

**UNIVERSITY OF DEBRECEN**  
**Faculty of Engineering**  
**Department of Mechanical Engineering**



**PROCEEDINGS OF THE**  
**5<sup>th</sup> INTERNATIONAL SCIENTIFIC CONFERENCE ON**  
**ADVANCES IN MECHANICAL ENGINEERING**  
**(ISCAME 2017)**

**12-13 October, 2017**

**Debrecen, Hungary**

organized by

**Department of Mechanical Engineering**  
**Faculty of Engineering, University of Debrecen**

and

**Working Commission in Mechanical Engineering**  
**Specialized Committee in Engineering**  
**Regional Committee in Debrecen, Hungarian Academy of Sciences**



**PROCEEDINGS OF THE  
5<sup>th</sup> INTERNATIONAL SCIENTIFIC CONFERENCE ON  
ADVANCES IN MECHANICAL ENGINEERING**

---



**Edited by**                    **Sándor BODZÁS PhD**  
                                      **Tamás MANKOVITS PhD**

**Technical editors**       **Levente CZÉGÉ PhD**  
                                      **Sándor HAJDU PhD**  
                                      **Sándor PÁLINKÁS PhD**  
                                      **Péter BALSÁ**  
                                      **Zsolt BÉKÉSI**  
                                      **Krisztián DEÁK**  
                                      **Dávid HURI**  
                                      **József MENYHÁRT**  
                                      **Tamás Antal VARGA**

**Publisher:**                **Department of Mechanical Engineering**  
                                      **Faculty of Engineering**  
                                      **University of Debrecen**  
                                      **2-4 Ótemető str. Debrecen, Hungary**  
                                      **Phone: +36 52 415 155**  
                                      **Web page: [old.eng.unideb.hu/gepesz](http://old.eng.unideb.hu/gepesz)**

**ISBN 978-963-473-304-1**



**PROCEEDINGS OF THE  
5<sup>th</sup> INTERNATIONAL SCIENTIFIC CONFERENCE ON  
ADVANCES IN MECHANICAL ENGINEERING**

---



**PROCEEDINGS**

**5<sup>th</sup> INTERNATIONAL SCIENTIFIC  
CONFERENCE ON ADVANCES IN  
MECHANICAL ENGINEERING  
(ISCAME 2017)**

**12-13 October, 2017  
Debrecen, Hungary**



**PROCEEDINGS OF THE  
5<sup>th</sup> INTERNATIONAL SCIENTIFIC CONFERENCE ON  
ADVANCES IN MECHANICAL ENGINEERING**



Chair of ISCAME 2017

**Tamás MANKOVITS, University of Debrecen, Hungary**

Scientific Program Committee of ISCAME 2017

**Ágnes BATTÁNÉ GINDERT-KELE, University of Debrecen, Hungary**

**Sándor BODZÁS, University of Debrecen, Hungary**

**Gábor BOHÁCS, Budapest University of Technology and Economics, Hungary**

**István BUDAI, University of Debrecen, Hungary**

**Levente CZÉGÉ, University of Debrecen, Hungary**

**Igor DRSTVENSEK, University of Maribor, Slovenia**

**János Péter ERDÉLYI, University of Miskolc, Hungary**

**Lajos FAZEKAS, University of Debrecen, Hungary**

**Csaba GYENGE, Technical University of Cluj-Napoca, Romania**

**Sándor HAJDU, University of Debrecen, Hungary**

**György JUHÁSZ, University of Debrecen, Hungary**

**Gábor KALÁCSKA, Szent István University, Hungary**

**Ferenc KALMÁR, University of Debrecen, Hungary**

**Imre KOCSIS, University of Debrecen, Hungary**

**Ákos LAKATOS, University of Debrecen, Hungary**

**Stanislav LEGUTKO, Poznan University of Technology, Poland**

**Zoltán MAJOR, Johannes Kepler University Linz, Austria**

**Ljubica MILOVIC, University of Belgrade, Serbia**

**Imre Norbert ORBULOV, Budapest University of Technology and Economics, Hungary**

**Sándor PÁLINKÁS, University of Debrecen, Hungary**

**Tibor POÓS, Budapest University of Technology and Economics, Hungary**

**Milan RACKOV, University of Novi Sad, Serbia**

**Istvánné RÁTHY, Óbuda University, Hungary**

**Tamás SZABÓ, University of Miskolc, Hungary**

**Edit SZÚCS, University of Debrecen, Hungary**

**György THALMAIER, Technical University of Cluj-Napoca, Romania**

**Zsolt TIBA, University of Debrecen, Hungary**

**László TÓTH, University of Debrecen, Hungary**

**Matej VESENJAK, University of Maribor, Slovenia**

**László ZSIDAI, Szent István University, Hungary**

Technical Assistance

**Beáta KÖVÉR, University of Debrecen, Hungary**

**Tamás Antal VARGA, University of Debrecen, Hungary**



## CONTENTS

<b>AL-MALIKI Hayder, KÁROLY Zoltán, KLÉBERT Szilvia, KALÁCSKA Gábor, SUKUMARAN Jacob, KALÁCSKA Ádám</b> <i>Surface characterization of polytetrafluoroethylene treated by atmospheric plasma</i>	1 – 8
<b>ANTAL Tamás, KERÉKES Benedek</b> <i>Novel drying techniques for the preservation of by-products of food industry</i>	9 – 16
<b>AZANE Thomas, BARKÓCZY Péter</b> <i>Comparison of the production and properties of ACCC conductors to other HTLS conductors</i>	17 - 21
<b>BADITA Liliana-Laura, ZAPCIU Aurel, GORNOAVA Valentin, VOCUREK Marian, MUNTEANU Iulian-Sorin</b> <i>Nanostructured thin films used to improve the tribological properties in mechatronic actuating systems</i>	22 – 28
<b>DE BATTISTA Péter Italo, SZABÓ József Zoltán, BAKUCZ Péter</b> <i>Detecting knocking combustion of large gas engine by deep recurrent neural network</i>	29 – 35
<b>BALOGH Gábor</b> <i>Recycling possibilities of end period nuclear fuel cells</i>	36 – 40
<b>BANJANIN Bojan, VLADIĆ Gojko, DELIĆ Gordana, ADAMOVIĆ Savka, KAŠIKOVIĆ Nemanja</b> <i>Influence of post-treatment methods on mechanical properties of PLA parts fabricated by fused deposition modeling</i>	41 – 47
<b>BELÉNYI Alpár, ACHIMAŞ Gheorghe</b> <i>Vibration measurement on reconditioned semi-hermetic compressor</i>	48 - 53
<b>BENCHABANE Ahmed Elmehdi, BARKÓCZY Péter</b> <i>Effects of surface treatment to the properties of railway contact wires</i>	54 – 58
<b>BODZÁS Sándor</b> <i>Comparative tooth contact analysis of X-zero gear drives in the function of the module changing</i>	59 – 67
<b>BOLDIZSÁR Csongor</b> <i>Optimization of wood biomass gasification process</i>	68 – 72
<b>BÖRÖCZ Péter</b> <i>Averaged vibration levels of vans in package delivery</i>	73 – 78



PROCEEDINGS OF THE  
5<sup>th</sup> INTERNATIONAL SCIENTIFIC CONFERENCE ON  
ADVANCES IN MECHANICAL ENGINEERING



<b>BUBONYI Tamás, LÉRÁNTH Gábor, BARKÓCZY Péter</b> <i>Automated image analysis of the inhomogenities in the microstructure of aluminum castings</i>	79 – 83
<b>BUSZNYÁK Tibor, LAKATOS István</b> <i>Automotive engineering possibilities in combining global positioning and vehicle diagnostic</i>	84 – 89
<b>CHMIELARZ Krzysztof, MARCINIAK Szymon</b> <i>Changes of microstructure and mechanical properties of nano crystalline steel X37CrMoV5-1 subjected to heat treatment as is used during nitriding</i>	90 – 95
<b>CSAVAJDA Péter</b> <i>Shock testing in the evaluation of packaging performance</i>	96 – 101
<b>DEÁK Krisztián, KOCSIS Imre</b> <i>Condition monitoring by applying advanced diagnostic method</i>	102 – 108
<b>DÓCS Roland, JOBBIK Anita</b> <i>Porous system modeling using multi-capillary method</i>	109 – 114
<b>DOVRAMADJIEV Tihomir</b> <i>3D computer processing and improvement of the geometry of received photogrammetric models through photo shooting with one camera</i>	115 – 122
<b>DUDÁS László, KAPITÁNY Pálma</b> <i>Combustion chamber and fuel mixture motion analysis of a new rotary engine</i>	123 – 128
<b>DUDÁS László</b> <i>The effect of profile variation on contact properties in case of quasi globoid worm gearing</i>	129 – 134
<b>ÉCSI Ladislav, ÉLESZTÖS Pavel, JANČO Roland</b> <i>An alternative to hyperelastic-based multiplicative plasticity models</i>	135 – 141
<b>ERDÉLYI Viktor, JÁNOSI László</b> <i>Digital twin and shadow in smart pork fatteners</i>	142 – 146
<b>FINŽGAR Miha, PODRŽAJ Primož</b> <i>Feasibility of remote photoplethysmography for implementation in mobile robots</i>	147 – 152
<b>FODOR Antal</b> <i>3D printed polymer specimens of fatigue test examination based on DMA tests</i>	153 – 157
<b>GEAMBAZU Elena Laura, MANEA Ciprian Alexandru, CSAKI Ioana, KARLSDÓTTIR Sigrún Nanna</b> <i>High entropy alloys in geothermal environment</i>	158 – 162



PROCEEDINGS OF THE  
5<sup>th</sup> INTERNATIONAL SCIENTIFIC CONFERENCE ON  
ADVANCES IN MECHANICAL ENGINEERING



<b>GORDIĆ Dušan, VUKAŠINOVIĆ Vladimir, ALEKSIĆ Aleksandar, NEŠOVIĆ Aleksandar</b> <i>Introduction of water management in food production plant: a case study margarine production facility</i>	163 – 171
<b>GRUJIĆ Ivan, STOJANOVIĆ Nadica, GLIŠOVIĆ Jasna, DAVINIĆ Aleksandar, MILOJEVIĆ Saša</b> <i>Modeling and aerodynamic simulation of the passenger vehicle</i>	172 – 177
<b>GULAN Ladislav, SCHMIDTOVÁ Carmen, IZRAEL Gregor</b> <i>Effective designing of modular structures variants of mobile working machines</i>	178 – 183
<b>HAGYMÁSSY Zoltán, PÁLINKÁS Sándor, BATTÁNÉ GINDERT-KELE Ágnes</b> <i>Examination the physical characterising of fertilizers</i>	184 – 187
<b>HAJDU Flóra, HORVÁTH Péter</b> <i>Comparison of bathlift constructions</i>	188 – 191
<b>HÉGELY László, SLEISZ Kristóf</b> <i>Optimization of batch extractive distillation with different methods</i>	192 – 197
<b>HNILICOVÁ Michaela, MATEJ Jaroslav, DADO Miroslav, HNILICA Richard</b> <i>Design of the supporting frame for the fire-fighting adapter using the shape generator</i>	198 – 202
<b>IHEMAGUBA Chukwuemeka, MAROSSY Kálmán</b> <i>Application of thermally stimulated discharge current method for investigation of fine structure of polymeric materials</i>	203 – 209
<b>JANČO Roland, ÉCSI Ladislav, ÉLESZTŐS Pavel</b> <i>Numerical solution of friction stir welding compared by experimental measurement</i>	210 – 215
<b>JOLDEȘ Nicolae Traian, GYENGE Csaba, ACHIMAȘ Gheorghe, POP-SZOVÁTI Anton-Gheorghe</b> <i>The waste and the environment</i>	216 – 221
<b>JÓNÁS Szabolcs, TISZA Miklós</b> <i>Clinching of DP600 steel sheets</i>	222 – 227
<b>JUHÁSZ János, BÁNYAI Tamás</b> <i>Logistic aspects of real time decisions in intelligent transportation systems</i>	228 – 234
<b>KÁDÁR Fanni, ERDŐDI István, HŐS Csaba</b> <i>Phase space analysis of a pressure relief valve</i>	235 – 240
<b>KALMÁR Csanád, HEGEDŰS Ferenc, FELHŐS Dávid</b> <i>Transient simulations of gas dynamics with different numerical schemes</i>	241 – 247



PROCEEDINGS OF THE  
5<sup>th</sup> INTERNATIONAL SCIENTIFIC CONFERENCE ON  
ADVANCES IN MECHANICAL ENGINEERING



<b>KAŠČÁK Ľuboš, SPIŠÁK Emil</b> <i>Mechanical joining methods of hot-dip galvanized steel sheets</i>	248 – 253
<b>KINCSES Dávid, MEZEI Lajos, HAJDU Sándor</b> <i>Review of wheel dynamic models at vehicle development</i>	254 – 260
<b>KLAPCSIK Kálmán, HEGEDŰS Ferenc</b> <i>Modelling of non-spherical bubble shape oscillations in viscous liquid</i>	261 – 267
<b>KOLOZSVÁRY Zoltán</b> <i>A few considerations on the state of the art and development trends in heat treatment and surface engineering</i>	268 – 273
<b>KOVÁCS Róbertné, KESZTHELYI-SZABÓ Gábor, SZENDRŐ Péter</b> <i>Optimization of operational parameters for microwave pre-treating system</i>	274 – 279
<b>LAKATOS István, NAGY Andor</b> <i>The development of the punctuality of railroad event recording in accident investigation</i>	280 – 288
<b>LÁNG Péter, ÖRSI Márton, HÉGELY László</b> <i>Comparison of batch and semi-continuous distillation</i>	289 – 295
<b>LATEȘ Daniel, CĂȘVEAN Marius, CIOLOCA Flaviu</b> <i>Application of the functions of a chatbot in the manufacturing process of a gear in IRUM company</i>	296 – 299
<b>LOVREC Darko</b> <i>Ionic liquid as a novel, high performance hydraulic fluid - selection process</i>	300 – 305
<b>LOVREC Darko</b> <i>Corrosion protection properties of ionic liquids</i>	306 – 311
<b>MAJDIČ Franc</b> <i>Research of carbon fibre hydraulic cylinder</i>	312 – 318
<b>MAJDIČ Franc</b> <i>Duration test of carbon fibre hydraulic cylinder: Water&amp;oil</i>	319 – 322
<b>MARCINIAK Szymon, SKOLEK Emilia, GOŁASZEWSKI Adam, ŚWIĄTNICKI Wiesław</b> <i>Thermal stability of carbide-free bainite in two nanocrystalline steels</i>	323 – 328
<b>MARKOVA Kremena</b> <i>How the user became authority</i>	329 – 333
<b>MENYHÁRT József, SZABOLCSI Róbert</b> <i>Batteries operation parameter analysis with fuzzy logic</i>	334 – 338



PROCEEDINGS OF THE  
5<sup>th</sup> INTERNATIONAL SCIENTIFIC CONFERENCE ON  
ADVANCES IN MECHANICAL ENGINEERING



<b>MODLA Gábor, LÁNG Péter</b> <i>Decrease of the energy demand of distillation with vapour recompression</i>	339 – 344
<b>MOHAMAD Barhm, SZEPESI Gábor, BOLLÓ Betti</b> <i>Review article: modelling and analysis of a gasoline engine exhaust gas systems</i>	345 – 357
<b>MOLNÁR András, BUZA Gábor, FAZEKAS Lajos, PÁLINKÁS Sándor, BATTÁNE GINDERT-KELE Ágnes</b> <i>Thermal sprayed and laser remelted wear resistant NiCrBSi coatings</i>	358 – 365
<b>MOLNÁR Bence</b> <i>Simulation framework for packaging dynamics of stacked units</i>	366 – 371
<b>MUHANDES Hasan, SALLOUM Weal</b> <i>Simulating the bruising damage of olive fruit during drop</i>	372 – 379
<b>NAGY Péter Tamás, PAÁL György</b> <i>Plane jets excited by vortices</i>	380 – 385
<b>NAGY Péter Tamás, PAÁL György</b> <i>The effect of spanwise flexible coating on the boundary layer transition</i>	386 – 390
<b>NEMES Csaba, BODZÁS Sándor</b> <i>Designing, modelling and analysis of straight turning tool geometry</i>	391 – 396
<b>PÁLINKÁS Sándor, FAZEKAS Lajos, BATTÁNE GINDERT-KELE Ágnes, MOLNÁR András, HAGYMÁSSY Zoltán</b> <i>Investigation of hot metal powder spray fusing of cultivator tines after tith</i>	397 – 405
<b>PETHŐ Dániel, BENKE Márton, MERTINGER Valéria, BARKÓCZY Péter</b> <i>The effect of thickness reduction on the recrystallization processes of cold rolled 3104 deep draw Al sheets</i>	406 – 417
<b>POÓS Tibor, SZABÓ Viktor, VARJU Evelin, HORVÁTH Dániel</b> <i>Introduction of freeze granulation technology</i>	418 – 421
<b>POÓS Tibor, HORVÁTH Dániel, TAMÁS Kornél</b> <i>Modeling the movement of the granular material in a static equipment with discrete element method</i>	422 – 427
<b>POÓS Tibor, VARJU Evelin, SZABÓ Viktor</b> <i>Determination of medicinal plants' porosity</i>	428 – 432
<b>POP-SZOVÁTI Anton - Gheorghe, BORZAN Marian, GYENGE Csaba, JOLDEȘ Nicolae</b> <i>Systems for counterbalancing the ram of the mechanical presses</i>	433 – 438



PROCEEDINGS OF THE  
5<sup>th</sup> INTERNATIONAL SCIENTIFIC CONFERENCE ON  
ADVANCES IN MECHANICAL ENGINEERING



<b>RACKOV Milan, KUZMANOVIĆ Siniša, PENČIĆ Marko, ČAVIĆ Maja, KNEŽEVIĆ Ivan</b> <i>Analysis of different concept ways of two-stage gear reducers design</i>	439 – 444
<b>RAZA Md Tanweer, SZEKERES András</b> <i>Thermo-hygro- mechanics in indian science philosophy</i>	445 – 454
<b>ROMÁN Krisztina, ZSOLDOS Gabriella</b> <i>Examinations of mechanical properties of different PVC/CPE blends</i>	455 – 459
<b>RÓNAI László, FÜVESI Viktor, VÖRÖS Csaba</b> <i>Designing of a water sampling unit</i>	460 – 465
<b>SEPSI Máté, ANGEL Dávid, CSEH Dávid, BENKE Márton, MERTINGER Valéria</b> <i>Residual stress monitoring for machine industry</i>	466 – 471
<b>SIDDIQUI Shiraz Ahmed, MAROS B. Mária, SZILAGYINÉ BÍRÓ Andrea</b> <i>Investigation of the tribological performance of wear resistant surface layers produced on automotive tool steel by duplex heat treatments</i>	472 – 478
<b>SKORIC Branko, MILETIC Aleksandar, TEREK Pal, KOVACEVIC Lazar, KUKURUZOVIC Dragan</b> <i>Influence of ion implantation on duplex hard coatings</i>	479 – 484
<b>SKRIBANEK Ádám, BODNÁR István, ISKI Patrik</b> <i>Optimizing an uninterruptible solar power system for inductive natured loads</i>	485 – 490
<b>STOJANOVIĆ Nadica, GRUJIĆ Ivan, GLIŠOVIĆ Jasna, MILOJEVIĆ Saša, DAVINIĆ Aleksandar</b> <i>Vanes shape optimization of ventilated disc brakes for heavy duty vehicles</i>	491 – 496
<b>STOJIC Boris, POZNANOVIĆ Nenad</b> <i>Experimental research of tractor tyre response to quasistatic passage over the singular road obstacle</i>	497 – 502
<b>STRAKA Luboslav, DITTRICH Gabriel</b> <i>Dielectric fluids applied during electrical discharge machining</i>	503 – 507
<b>STRAKA Luboslav, DITTRICH Gabriel</b> <i>Improving reliability indicators of technical systems</i>	508 – 512
<b>SZABÓ Sándor, FORGÁCS Attila, NAGY Gábor, SZIKRA Dezső</b> <i>Research, development and optimization of nuclear tomography</i>	513 – 518
<b>SZAKÁL Zoltán, PATAKI Tamás, KÁRI-HORVÁTH Attila</b> <i>Strength examination of adhesive bonded joints of steel against DBD treated PTFE and PA66 surfaces</i>	519 – 527



**SZALAI Judit**

*The development of evaluation system qualifying the iter diagnostic cable conduit the and satisfying the system requirements*

528 – 532

**SZENTESI Miklós Gergely, LAKATOS István**

*Road traffic accidents caused by mechanical failures in Hungary between 2012 and 2017*

533 – 539

**SZIKI Gusztáv Áron, SARVAJ CZ Kornél, SZÁNTÓ Attila**

*Dynamic simulation of a series wound DC motor applying the control design and simulation module of LABVIEW*

540 - 543

**SZÜLE Veronika, PERE Balázs**

*Solution of thermomechanical coupled problem using fem*

544 – 547

**TANASKOVIĆ Drakče, ĐORĐEVIĆ Branislav, SEDMAK Simon, VUČETIĆ Filip, GAJIN Marko**

*Repair welding of lower rails of a 30CrMoV9 steel transport beam and the conditions under which the welding procedure must be carried out*

548 – 555

**THALMAIER György, SECHEL Niculina, VIDA–SIMITI Ioan**

*Water leaching behaviour of carbamide space holder particles in TiAl foams*

556 – 559

**TIBA Zsolt, FEKETE-SZŰCS Dániel, MENYHÁRT József**

*Eliminating the positioning error of gamma knife; recommendations for the mechanical overhaul*

560 – 568

**TISZA Miklós**

*Lightweight manufacturing of automotive parts*

569 – 574

**TOMOR András, ANTAL-JAKAB Erik, KRISTÓF Gergely**

*Experimental investigation of a finite length lateral system in a dividing-flow manifold*

575 – 580

**TOMOR András, MERVAY Bence, KRISTÓF Gergely**

*Continuous parametrization of hydraulic losses caused by diameter transition in cylindrical pipes*

581 – 587

**TÓTH Kinga, VENCZEL Gábor, SZAMOSI Zoltán**

*Examination of biomethane production*

588 – 594

**UNGÁR Péter, SZABÓ Tamás**

*Designing a balancing machine for a plastic rotor*

595 – 600

**VÖRÖSKŐI Kata**

*Selection of packaging systems in automotive engine supply: The case of overseas transport*

601 – 606



**PROCEEDINGS OF THE  
5<sup>th</sup> INTERNATIONAL SCIENTIFIC CONFERENCE ON  
ADVANCES IN MECHANICAL ENGINEERING**



<b>ZÁKOPČAN Ján, JAVOREK Lubomír, BACHRATÝ Michal</b> <i>The influence of tool diameter and feed speed on feed force and torque moment during steel S233J0 drilling</i>	607 – 611
<b>ZÁKOPČAN Ján, JAVOREK Lubomír, BACHRATÝ Michal</b> <i>Dependence of the thrust force from the clearance angle and feed speed during drilling</i>	612 – 616
<b>SUPPORTING COMPANIES OF THE ISCAME 2017</b> <i>Introduction of the companies</i>	617 – 634
<b>THE DEPARTMENT OF MECHANICAL ENGINEERING</b> <i>Department staff and the mechanical engineering trainings</i>	635 - 639



## SURFACE CHARACTERIZATION OF POLYTETRAFLUOROETHYLENE TREATED BY ATMOSPHERIC PLASMA

<sup>1</sup>AL-MALIKI Hayder, <sup>2</sup>KÁROLY Zoltán PhD, <sup>2</sup>KLÉBERT Szilvia PhD, <sup>1</sup>KALÁCSKA Gábor DSc, <sup>3</sup>SUKUMARAN Jacob PhD, <sup>3</sup>KALÁCSKA Ádám

<sup>1</sup> Institute for Mechanical Engineering Technology, Szent István University

E-mail: [haidrlatif@gmail.com](mailto:haidrlatif@gmail.com)

<sup>2</sup>AKI, Research Centre for Natural Sciences

<sup>3</sup>Department of Electrical Energy, Metals, Mechanical Constructions and Systems, Ghent University

### Abstract

*Polytetrafluoroethylene surface was treated by atmospheric DBD plasma for 1 min in ambient conditions. The effect of DBD plasma introduces significantly increasing of the surface energy (wettability) within 24 hours after treatment. However, the surface starts recovering to the original state with aging. The surface elemental composition shows enhancing in oxygen-containing which suggests presenting the polar functional groups. The surface roughness exhibits a mild reduction within 24 hours after treatment. Whereas, the roughness values start to increase with the function of time.*

**Keywords:** PTFE, Surface Characterization, Atmospheric Plasma Treatment

### 1. INTRODUCTION

The effect of different plasmas on polymer surface characterization has been widely reviewed in literature especially during the last three decades. Earlier, achieved that exposure of PTFE to oxygen and argon plasma for a short time enhances the surface wettability while no morphological alter could be noted. However, longer time of oxygen plasma treatment is deeply etched PTFE surface [1]. In a related context, XPS results show that mild argon plasma treatment of PTFE surface is sufficient to cause substantial surface defluorination and oxidation [2]. The treatment of PTFE by low-power plasma utilizing a variety of feed gases (O<sub>2</sub>, Ar, N<sub>2</sub>, and NH<sub>3</sub>) resulting in light etching into the surface. However, the nature and extent of chemical modification varied considerably where Ar plasma was the most efficient and O<sub>2</sub> plasma the least [3]. Vacuum DBD plasma significantly improves the PTFE surface energy which owing to the changes in surface chemistry and microstructure [4]. Furthermore, Ar remote and direct plasma treatment of PTFE surface can modify the surface in morphology and composition, and form some polar functional groups which owing to the surface oxidation of PTFE films; thereby improvement in polymer wettability [5]. The influence of nitrogen plasma-based ion implantation (N PIII) introduces a sharply decreasing in the F/C atomic ratio, whereas topography measurements show an increase in the mean surface roughness [6]. In this paper, the PTFE surface characterization will be investigating in term of atmospheric DBD plasma treatment.



## 2. METHODS AND MATERIALS

### 2.1. Material and preparation

Polytetrafluoroethylene commercial type (distributed by Quattroplast Ltd., Hungary and produced by Ensinger GmbH, Germany), were utilized in bulk conditions: Polytetrafluoroethylene or virgin PTFE grad Docafion-PTFE-N. The mechanical properties of the used material are as follows: (tensile strength  $\sigma = 22$  MPa, glass transition temperature  $T_g = -20$  °C, shore D hardness = 55). Polymer samples were configured into pins with a diameter of 10 mm and thickness of 4 mm with an extruded surface for all tests except the topographical investigation where the surface was subsequently polished with wet SiC paper (grid numbers P1200 and P2000) and felt sheet towards required surface roughness. For more precision, the samples were cleaned in an ultrasonic bath with distilled water and 96% ethanol (Reanal, Hungary) before testing.

### 2.2. Plasma Treatment

The plasma was generated in the air and ambient atmospheric pressure by DCSBD plasma source at AKI, Research Centre for Natural Sciences. Plasma works depending on a coplanar DBD. The electrodes have comb-shape within a dielectric. The diffuse plasma is generated in thin 0.4 mm thick flat layer on alumina ceramic; the DCSBD was designated to be utilized primarily for flat surfaces treatment (Roplass s.r.o., Brno, Czech Republic), the apparatus is shown in Figure 1. The DCSBD electrode system was powered by AC High-Voltage source with frequency approx. (10-20) kHz and voltage approx. 20 kV peak-to-peak while the total discharge power in plasma during the experiments is 320 W. The total area of generated plasma is 170 cm<sup>2</sup>. The system is supported with oil recycling (cooling) system to maintain the system at the proper temperature range which keeps the gas temperature around 370 K. The DCSBD plasma is described in detail [7]. The plasma treatment was performed in dynamic treatment mode, and the distance between the treated polymer surface and DBD plate was 0.5 mm. The treatment has been done under air atmosphere conditions ( $T = 23$  °C,  $H = 50\%$ ). The treatment time for each specimen was 1 min determined by preliminary experiments and all the recent experiments were done within 24 hours from the treatment.

Surface treatment by atmospheric cold plasma:  
dielectric barrier discharge (DBD)

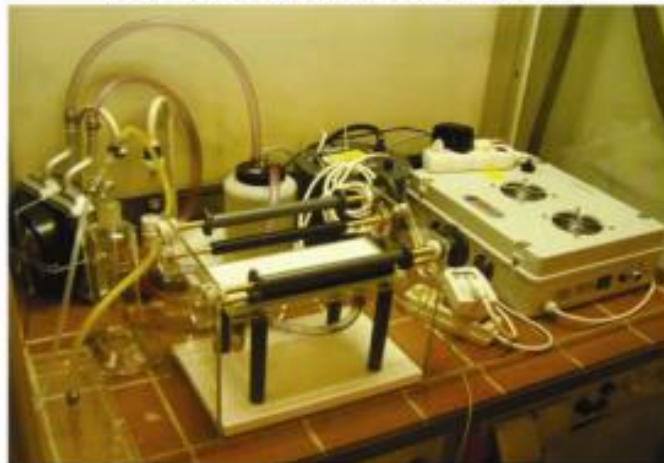


Figure 1 DBD laboratory test equipment used for polymer surfaces



### 2.3. Wettability

The wettability was evaluated according to contact angle measurements by using the static sessile drop method at 23 °C, with double distilled water and diiodomethane or CH<sub>2</sub>I<sub>2</sub> (Sigma–Aldrich, Reagent Plus 99% grade), applying the SEE System apparatus (Advex Instruments, Czech Republic) as shown in Figure 2. A Hamilton syringe was used to inject two µl droplets. The results of the contact angle are an average of 5 measurements, always performed on previously non-wetted parts of the samples. The surface energy component calculations based on Owens-Wendt method [8].



Figure 2 SEE System apparatus which used to evaluate the contact angle of polymer

### 2.4. Chemical composition

The X-ray photoelectron spectroscopy (XPS) was carried out on a XSAM 800 spectrometer (Kratos, Manchester, UK), as shown in Figure 3, equipped with a non-monochromatic Mg K $\alpha_{1,2}$  radiation source (1253.6 eV) operating under a fixed analyzer transmission mode (chamber pressure < 10<sup>-7</sup> Pa). The pass energy was set at 80 eV for survey spectra (wide scan) and 40 eV for high resolution (detailed) spectra. The wide scan spectra were recorded at 0.5 eV steps in the 50 to 1300 eV energy range while the detailed spectra were recorded at 0.1 eV steps for the respective main elements. As a reference, the C1s line for the hydrocarbon C-Hx component was set to a binding energy of 285.0 eV. The accuracy of binding energy determination was  $\pm 0.2$  eV. The data acquisition and processing were performed with the Kratos Vision 2 software, applying a Shirley type background subtraction and decomposition of the peaks by using a mixed Gaussian-Lorentzian shape (70/30 ratio) of equal full-width-at-half-maximum (FWHM). The quantitative analysis of the surface composition was based on integrated peak areas calculated by the XPS MultiQuent program [9] and is expressed in at.-%. The photo-ionization cross-section data of Evans et al. [10] and asymmetry parameters of Reilman et al. [11]. were experimentally utilized. The conventional model of the infinitely thick layer was used to estimate the surface chemical compositions.



Figure 3 X-ray photoelectron spectroscopy (XPS)

## 2.5. Surface topography

The surface roughness was evaluated from non-contact profilometry, using a 3D optical profilometer Coherence Correlation Interferometry (CCI) HD type (Taylor Hobson, Leicester, England), as shown in Figure 4, with an ultra-high precision closed loop piezoless z-scanner having a resolution in z-direction of  $0.1 \text{ \AA}$ . Fiber Lite DC-950 source was used to generate a white light illumination and measurements were done at 50 % light intensity. The elaborated surface area is  $330 \times 330 \text{ \mu m}^2$  for each sample, and vertical scanning interferometry imaged it, has an objective lens with magnification 50 x and numerical aperture (NA) = 0.55. The scanning arrays contained  $2048 \times 2048$  pixels with a field-of-view (FOV) =  $330 \text{ \mu m}$ , corresponding to a pixel size of  $0.165 \text{ \mu m}$ . The images were further processed by Talymap software (Digiserve) to calculate the 3D surface roughness parameters according to ISO 25178, including  $S_a$  (average roughness),  $S_z$  (maximum height),  $S_{ku}$  (kurtosis) and  $S_{sk}$  (skewness). The roughness values were determined as average from three measurements at independent surface locations, with repeatability  $S_a < 0.2 \text{ \AA}$ , more details about Coherence Scanning Interferometry in [12].



Figure 4 3D optical profilometer Coherence Correlation Interferometry (CCI) HD type



### 3. RESULTS

#### 3.1. Surface energy

The contact angle (water and CH<sub>2</sub>I<sub>2</sub>) values and surface energies are illustrated in Table 1. Whereas Figure 5 shows the surface energies change for pristine and a DBD plasma treated surface (after 24 hours and 80 days' shift time). From that, it can be noted the substantial change in the wettability, where the contact angles significantly decrease, thereby the surface energies were enhanced due to DBD plasma treatment based on Owens-wendt calculation. In parameters range, both the polar ( $\gamma_{pol}$ ) and dispersive ( $\gamma_{disp}$ ) components increased, in particular, the polar component was increased 3650% more than the reference state. After 80 days aging, the hydrophobic recovery takes place and resulting in decreasing the polar and dispersive component values. Thus, the polarity declined 72% than the initial state after treatment.

Table 1 Contact angle and surface energy values for pristine and treated surfaces

Sample	Q <sub>w</sub> (deg)	Q <sub>CH<sub>2</sub>I<sub>2</sub></sub> (deg)	$\gamma_{pol}$ (mJ/m <sup>2</sup> )	$\gamma_{disp}$ (mJ/m <sup>2</sup> )	$\gamma_{tot}$ (mJ/m <sup>2</sup> )
PTFE untreated	108 ±1.5	73±3.2	0.2	21.2	21.5
PTFE treated, 24h	75 ±1	56±1	7.5	30.9	38.4
PTFE treated, 80 days	98 ±16	75±7.1	2.1	20.2	22.3

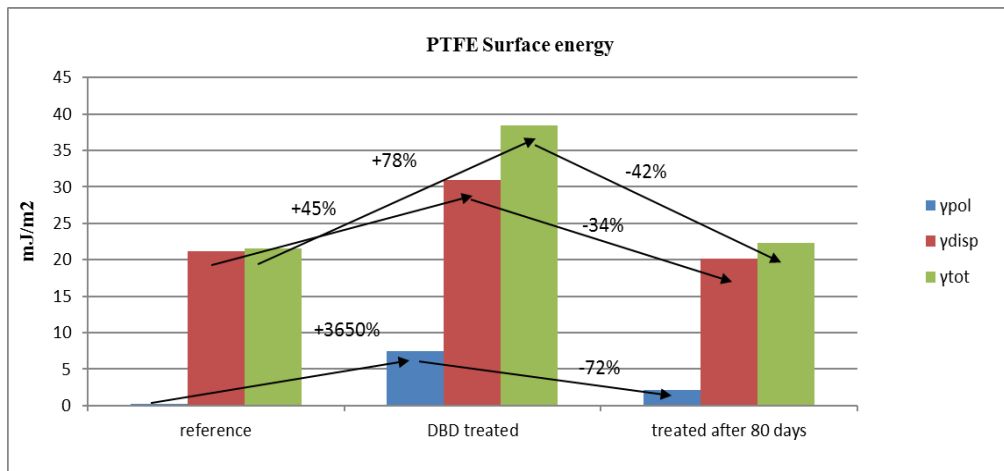


Figure 5 Surface energy parameters and tendency for pristine surface and after DBD plasma treatment (after 24 hours and 80 days)

#### 3.2. Chemical composition

XPS analyzed the surface chemical composition change. The elemental composition (at.-%) of PTFE is listed in Figure 6 for theoretical, pristine and treated surface respectively which calculated from the wide-scan XPS spectra. The effect of DBD plasma on the surface chemical composition has presented an improvement in the oxygen content and reduction in the fluorine and carbon content indicated by the increase of O/C atomic ratio and decrease F/C atomic ratio. The increased O content introduces the establishment of polar functional groups (oxygen-containing functional groups) onto the PTFE surface which in turn leads to improvement in wettability.

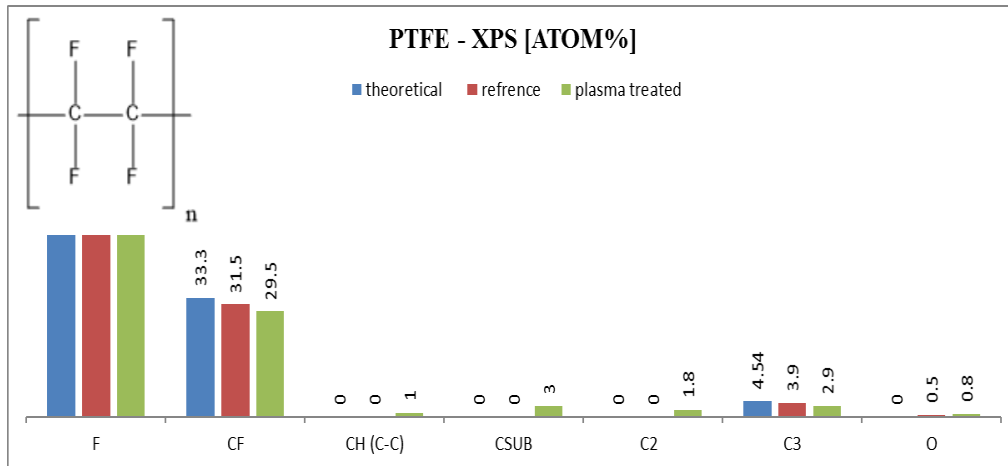


Figure 6 Analysis of chemical composition from high-resolution XPS spectra

### 3.3. Surface topography

Surface topography of pristine and plasma treated samples were monitored by non-contact profilometry, illustrated by 3D surface scan giving in Figure 7. The 3D surface roughness parameters change due to plasma treatment are shown in Figure 8. In general, the surface roughness was slightly decreased after DBD plasma. In parameters range, the average roughness  $S_a$  decreased 10%, the maximum height ( $S_z$ ) decreased 20%,  $S_{ku}$  (kurtosis) was destined closer to 3 value whereas  $S_{sk}$  (skewness) exposed reduction in the negativity value after plasma treatment. The values introduce mild flattened surface probably owing to the removal of the top layer and melting of the surface asperities, while the original polishing grooves remain visible. The aging effect was taken into consideration therefore the tests were repeated after 800 hours. PTFE exhibits increase in the surface roughness with the function of time which attributed to the surface recovery. The surface smoothening is characteristic for the used plasma processing conditions and measurements at microlevel scale.

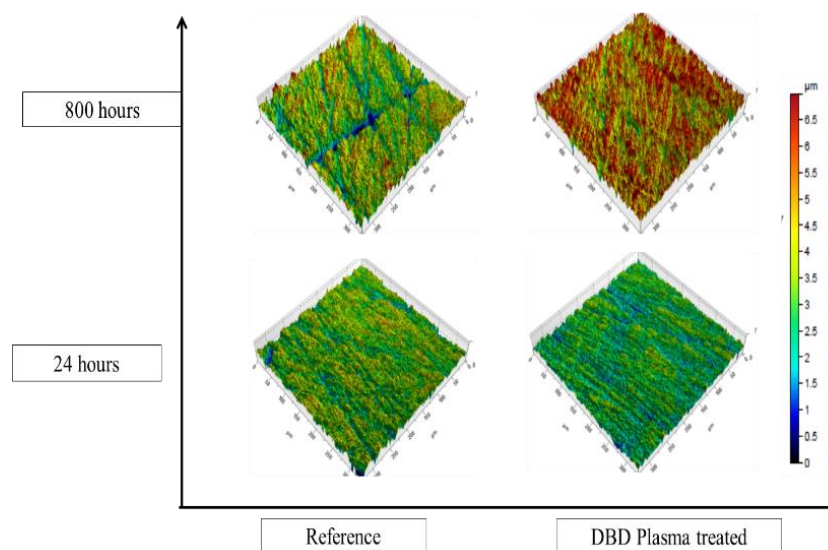


Figure 7 Non-contact Profilometry of pristine and treated samples of (330 x 330  $\mu\text{m}^2$  surface area)

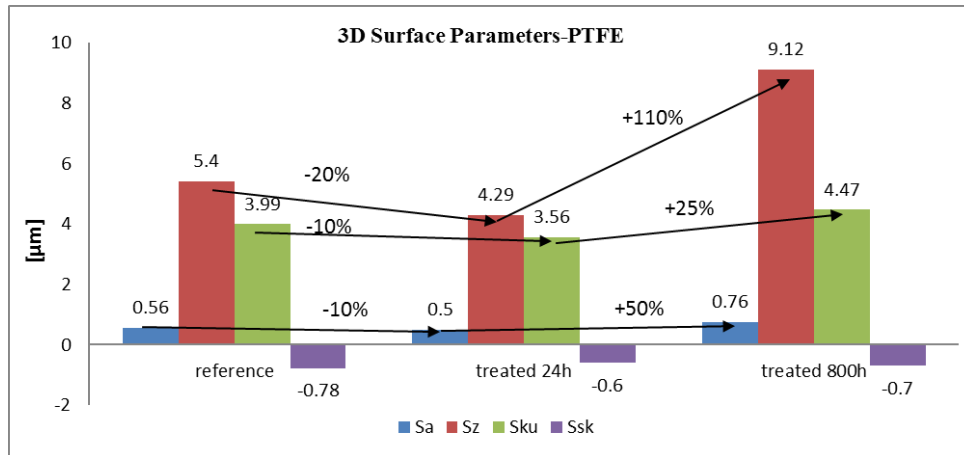


Figure 8 surface roughness parameters of pristine compared to plasma treated samples (after 24 hours and 800 hours)

## CONCLUSIONS

In conclusion, the surface characterization of polytetrafluoroethylene was investigated for pristine, and atmospheric DBD plasma treated surface within 24 hours and time shift. The SEE System apparatus evaluated the contact angle, and the surface energy was carried out based on Owens-Wendt method. The surface chemical composition was analyzed by XPS. The surface 3D topography was scanned by non-contact profilometry (CCI) HD type. Due to the atmospheric DBD plasma treatment, the surface energy components improve where the polar component increased 3650% than the virgin state. Surface chemical composition exposes increasing the oxygen content which leads to the establishment of polar functional groups. The 3D topographical scan shows a mild decrease in the surface roughness after plasma treatment where the average roughness was decreased 10%.

## ACKNOWLEDGEMENT

The research is supported by OTKA K 113039 and 3D topographical investigation was carried out in co-operation with Laboratory Soete, Gent University, Belgium.

## REFERENCES

- [1] Mona, M., Occhiello, E., Garbassi, F.: *Surface Characterization of Plasma-treated PTFE*. Surface and Interface Analysis, 16, 412-417., 1990.
- [2] Tan, K. L., Woon, L. L., Wong, H. K., Kang, E. T., Neoh, K. G.: *Surface modification of plasma-pretreated poly(tetrafluoroethylene) films by graft copolymerization*. Macromolecules, 26, 2832-2836., 1993.
- [3] Wilson, D. J., Williams, R. L. and Pond, R. C.: *Plasma modification of PTFE surfaces. Part I: Surfaces immediately following plasma treatment*. Surface and Interface Analysis, 31, 385-396., 2001
- [4] Liu, C. Z., Wu, J. Q., Ren, L. Q., Tong, J., Li, J. Q., Cui, N., Brown, N. M. D., Meenan, B. J.: *Comparative study on the effect of RF and DBD plasma treatment on PTFE surface modification*. Materials Chemistry and Physics, 85, 340-346., 2004.
- [5] Chena, W., Jie-ronga, C., Ru, L.: *Studies on surface modification of poly(tetrafluoroethylene)*



# INTERNATIONAL SCIENTIFIC CONFERENCE ON ADVANCES IN MECHANICAL ENGINEERING

12-14 October 2017, Debrecen, Hungary



- film by remote and direct Ar plasma*. Applied Surface Science, 254, 2882–2888., 2008.
- [6] Kereszturi, K., Tóth, A., Mohai, M., Bertóti, I., Szépvölgyi, J.: *Nitrogen plasma-based ion implantation of poly(tetrafluoroethylene)*. Applied Surface Science, 256, 6385–6389., 2010.
- [7] Černák, M., Černáková, L., Hudec, I., Kováčik, D., Zahoranová, A.: *Diffuse Coplanar Surface Barrier Discharge and its applications for in-line processing of low-added-value materials*. European Physical Journal, Applied Physics, 47, 22806., 2009.
- [8] Kostov, K.G., Hamia, Y.A.A., Mota, R.P., dos Santos, A.I.R., Nascente, P.A.P.: *Treatment of polycarbonate by dielectric barrier discharge (DBD) at atmospheric pressure*. Journal of Physics: Conference Series, 511, 12075., 2014.
- [9] Mohai, M.: *XPS MultiQuant: Multimodel XPS Quantification Software*. Surface and Interface Analysis. 36, 828–832., 2004.
- [10] Evans, S., Pritchard, R. G., Thomas, J. M.: *Relative Differential Subshell Photoionization Cross-sections (Mg K $\alpha$ ) from Lithium to Uranium*. Journal of Electron Spectroscopy and Related Phenomena, 14, 341–358., 1978.
- [11] Reilman, R. F., Msezane, A., Manson, S. T.: *Relative Intensities in Photoelectron Spectroscopy of Atoms and Molecules*. Journal of Electron Spectroscopy and Related Phenomena, 8, 389–394., 1976.
- [12] De Groot, P.: *Coherence Scanning Interferometry, In Optical Measurement of Surface Topography*. 187–208. Berlin: Springer. 2011.



## NOVEL DRYING TECHNIQUES FOR THE PRESERVATION OF BY-PRODUCTS OF FOOD INDUSTRY

*ANTAL Tamás PhD, KERÉKES Benedek PhD*

*Institute of Engineering and Agricultural Sciences, University of Nyíregyháza, Nyíregyháza, HU*  
*E-mail: [antal.tamas@nye.hu](mailto:antal.tamas@nye.hu), [kerekes.benedek@nye.hu](mailto:kerekes.benedek@nye.hu)*

### Abstract

*The by-products of food industry are produced in great amounts in Hungary. Elderberry- and sour cherry pomace was subjected to freeze- (FD), hot-air- (HA), vacuum- (VD), and hybrid drying (HA-FD and VD-FD) for preservation. They were dried to less than 3% (w.b.) moisture content using freeze-, hot-air-, vacuum-, and hybrid drying methods. The results show that hot-air and vacuum pre-drying play a substantial role in operational time of FD. The hybrid-drying had the higher drying rate, which reduced the drying time by 23.8–28.6% compared with FD method. There was no significant difference ( $P>0.05$ ) in the operational time between the HA and VD; HA-FD and VD-FD drying methods at dehydration of elderberry pomace. The HA, FD, VD and hybrid drying processes could give steady water activity values for long term storage of dried samples.*

**Keywords:** *by-product, single-stage drying, hybrid drying, drying characteristics, water activity*

### 1. INTRODUCTION

Many by-products have a substantial potential value as human and animal foodstuffs. The by-product food result from the processing of commercial crop in the food industry. By-product foodstuffs, which contain little economical value as edible foods for human consumption have become major sources of dietary nutrients (Fruit pomace rich is phenolic and anthocyanin contents). These materials are important in the food and fibre system, yet little research has characterized individual by-products [1].

The elderberry (*Sambucus nigra* L.) and sour cherry (*Prunus cerasus* L.) pomace are a by-product of food industry which is produced in great amounts in Hungary.

Drying is used as preservation method for prepare shelf-stable foods and as pretreatment for further processes, for example milling to make powdered products [2].

Hot-air drying (HA) is a one of the most frequently used, relative simple and economic dehydration process, having some disadvantages, including product darkening, hard texture, shrinkage, loss of chemical components and decrease in rehydration capacity [3].

Vacuum-drying (VD) is alternative method for drying of foods. If vacuum pressure decreasing can reduce the drying temperature and therefore improve the qualitative attributes of food products [4]. Because of the VD reduce the boiling point of water. The VD is applied successfully for many foods dehydrating, which are heat-sensitive [5]. Several studies reported that the quality of vacuum-dried products was superior to that of hot-air dried materials [6].

Freeze-drying (FD) or lyophilization is considered as the best dehydration method for the quality of final products, which has spongy structure, high rehydration rate, soft texture and prominent appearance. Nutrition and volatile aroma retention is high in the FD [7]. But at the same time, the FD is the more expensive process due to the cost of equipments and long operational time. The FD is usually applied in combination with convective pre- and post-drying [8]. Combined hot-air-freeze



drying (HA-FD) and vacuum drying-freeze drying (VD-FD) is a relatively new technique for the conservation of foods.

The objective of this work was to study the effect of different drying methods, i.e. hot-air-, vacuum-, freeze- and hybrid drying on the drying characteristics, drying time and water activity of elderberry- and sour cherry pomace samples.

## 2. METHODS

### 2.1. Moisture content (MC)

The oven method was used to determine the initial moisture content. A samples of about 10 g of elderberry- and sour cherry pomace were taken and dehydrated in an experimental dryer (model LP306, LaborMIM, Budapest, Hungary) at 105°C for 10 h. The initial moisture content of the elderberry- and sour cherry pomace samples were 40.41, 63.99% and 0.678, 1.777 kg water/kg dry matter expressed in wet- (w.b.) and dry basis (d.b.). The specimens were stored at 5°C in a refrigerator until used.

### 2.2. Drying experiments

Seed and stem were removed from peel by hand and sour cherry pomace was dried in dryers. The samples were spread on drying trays in a single layer and dried in hot-air-, vacuum- and freeze dryers. In each experiment, an amount of elderberry- (peels, pulp residues and seeds) and sour cherry pomace (peels and pulp residues) corresponding to 100 and 100 g were placed on a drying trays. The drying process would not stop until the equilibrium moisture content ( $M_e$ ) was achieved. All the drying experiments were replicated three times and the average values reported. The dehydrated samples were packed immediately into nylon bags after drying.

The following four different drying programs were applied in this research:

1. HA – pure hot-air drying under the total process with drying temperature (dt) of 60 and 80°C.
2. VD – pure vacuum drying under the total process with drying temperature (dt) of 60 and 80°C.
3. FD – pure freeze drying under the total process.
4. Hybrid drying (HA-FD/VD-FD) – intermittent hot-air- or vacuum pre- (dt=60 and 80°C) and freeze finish-drying.

#### 2.2.1. Hot-air drying (HA)

Hot-air drying was carried out in a hot-air tray dryer (model LP306, LaborMIM, Budapest, Hungary) at 60 and 80°C for 7 and 5h. The air velocity over the tray in the drying chamber was 1 m/s. Air humidity was regulated at  $\approx$ 20-25%. After 1h, the trays were taken out of the equipment, weighed, and then put back in the dryer. During the drying process, the weight of the samples was recorded to determine the moisture content. The final moisture content of elderberry- and sour cherry pomace was found to be 0.021 and 0.024 kg water/kg dry matter.

The temperature (material and air), air velocity, air humidity was measured using a Testo 4510 type meter (Testo GmbH, Lenzkirch, Germany). The mass was measured on an analytical balance (model JKH-500, Jadever Co., New Taipei, Taiwan) with a precision of  $\pm$ 0.1 g.

#### 2.2.2. Vacuum drying (VD)

The elderberry- and sour cherry pomace were dried in a vacuum oven (model Kambic VS-50C, Kambic Lab. Eq., Semic, Slovenia), consisting of a vacuum gauge, a temperature control unit, a



heating chamber and a vacuum pump (model V-710, Büchi Labortechnik AG, Flawil, Swiss). Vacuum drying was performed at 60 and 80°C, at 4-4.5×10<sup>3</sup> Pa for 7 and 5h. The specimens were placed in two stainless steel trays and the trays were withdrawn from the dryer and weighed every 1h using a digital balance (model JKH-500, Jadever Co., New Taipei, Taiwan) with 0.1 g precision. The final moisture content of the dried elderberry- and sour cherry pomace (0.025 and 0.026 kg water/kg dry matter) was assumed to be equilibrium moisture content.

### 2.2.3. Freeze drying (FD)

For vacuum-freeze drying, a laboratory-scale freeze dryer (model Armfield FT33, Armfield LTD, Ringwood, England) was used. The drying was carried out by maintaining the chamber pressure at 85-100 Pa, chamber temperature at 20°C and condenser temperature at -47°C. At an interval of 1h, the mass of samples was recorded to determine the moisture removal from material. The temperature of material was determined by a four thermocouple. The weight loss of the samples was followed by a data logger (model ES-138, Emalog, Budapest, Hungary) and a RS-232 attached to a PC computer, acquired the data readings from platform cell (model PAB-01, Emalog, Budapest, Hungary), which is placed within the sample chamber.

The final moisture content of elderberry- and sour cherry pomace was found to be 0.007 and 0.021 kg water/kg dry matter.

### 2.2.4. Hybrid dehydration (HA-FD and VD-FD)

A hybrid drying process consisting of a hot-air drying (60 and 80°C) or vacuum-drying (60 and 80°C) followed by freeze-drying was carried out. The drying parameters are in agreement with above-mentioned ones. The elderberry- and sour cherry pomace were dried in two stages: (1) Dried by a hot-air dryer (HA) where the samples (elderberry and sour cherry) were dehydrated for 2h and the moisture content of materials were 0.288 and 0.906 kg water/kg dry matter, respectively; (2) then, it was dried in a freeze dryer (FD) until the products reached the equilibrium moisture content (0.0078 and 0.016 in d.b.).

(1) Dried by a vacuum dryer (VD) where the samples (elderberry and sour cherry) were dehydrated for 2h and the moisture content of materials were 0.315 and 0.782 kg water/kg dry matter, respectively; (2) then, it was dried in a freeze dryer (FD) until the products reached the equilibrium moisture content (0.0078 and 0.0123 in d.b.).

The hybrid dried products (elderberry- and sour cherry pomace) obtained were labeled as HA2h-FD80°C<sub>elderberry</sub>, HA2h-FD60°C<sub>sour cherry</sub> and VD2h-FD80°C<sub>elderberry</sub>, VD2h-FD60°C<sub>sour cherry</sub>, respectively.

### 2.2.5. Drying curves

The drying curves were prepared by plotting the moisture ratio  $MR$  (dimensionless) vs. drying time  $t$  (h).

The moisture ratio ( $MR$ ) of the elderberry- and sour cherry pomace samples during drying was calculated using the following equation (1):

$$MR = \frac{M - M_e}{M_0 - M_e} \quad (1)$$



where  $MR$  is the moisture ratio,  $M$  is the moisture content (kg water/kg dry matter),  $M_e$  is the equilibrium moisture content (kg water/kg dry matter) and  $M_0$  is the initial moisture content (kg water/kg dry matter).

The sample moisture content –  $M$  – was calculated on a dry basis (d.b.) according to Eq. (2):

$$M = \frac{W_t - W_k}{W_k} \quad (2)$$

where  $W_t$  is the sample weight at a specific time (g) and  $W_k$  is the sample dry weight (g).

### 2.3. Water activity ( $a_w$ )

The water activity could be much more important to the quality and stability of food. Approximately 3 g of chopped dried pomace samples were placed in the sample holder of a Novasina Labmaster  $a_w$ -meter (model CH-8853, Novasina AG, Lachen, Switzerland). The temperature and duration for testing were at 25°C and 30 min. The tests were replicated three times.

### 2.4. Data analysis

The significance of differences between treatments was determined by ANOVA using the Duncan's test ( $p < 0.05$ ). The calculations were performed using PASW Statistics 18 (IBM Corp., Armonk, USA) software.

## 3. RESULTS

### 3.1. Drying time of elderberry- and sour cherry pomace

The time required for drying the pomace samples under different dehydration modes is presented in *Table 1*. Drying characteristics were slightly different among the two cultivars. It is observed that the total drying time required for HA and VD of the elderberry pomace is the shortest (5h). The reason of this, that the drying temperature higher (because the sour cherry is heat sensitive) and the initial moisture content of the elderberry pomace lower, than for the sour cherry pomace. The drying time required for an evaporated elderberry pomace sample was significantly ( $P < 0.05$ ) reduced from 19h at FD to 14h at HA-FD and VD-FD. The hot air pre- and vacuum pre- and freeze finish drying reduced ( $P < 0.05$ ) the traditional freeze drying time of elderberry pomace by about 26.31%.

Similar results were obtained by [9]. There was no significant difference ( $P > 0.05$ ) in operational time of elderberry pomace between the hybrid drying methods.

For example, the drying times for reaching about 0.012-0.026 kg water/kg dry matter moisture content of sour cherry pomace samples were about 7, 7, 15, 16 and 21 hours, respectively at HA, VD, VD-FD, HA-FD and FD. The statistically significant difference ( $P < 0.05$ ) in drying time was found between hybrid- and freeze drying. *Table 1* demonstrated that drying was completed after 15 and 16 hours for VD-FD and HA-FD, and this represents a 28.57 and 23.81% reduction ( $P < 0.05$ ) of drying time in comparison with FD.



Table 1 Effect of different drying methods on drying time and saving in duration of freeze drying

Drying method (Symbol)	Hot-air pre-drying period [h]	Vacuum pre-drying period [h]	Freeze finish-drying period [h]	Total drying time [h]	Reduction in FD drying time [%]
FD <sub>elderberry</sub>	-	-	19	19 <sup>b</sup>	-
FD <sub>sour cherry</sub>	-	-	21	21 <sup>c</sup>	-
HA80°C <sub>elderberry</sub>	5	-	-	-	-
HA60°C <sub>sour cherry</sub>	7	-	-	-	-
VD80°C <sub>elderberry</sub>	-	5	-	-	-
VD60°C <sub>sour cherry</sub>	-	7	-	-	-
HA2h-FD80°C <sub>elderberry</sub>	2	-	12	14 <sup>a</sup>	26.31 <sup>a</sup>
HA2h-FD60°C <sub>s.cherry</sub>	2	-	14	16 <sup>b</sup>	23.81 <sup>b</sup>
VD2h-FD80°C <sub>elderberry</sub>	-	2	12	14 <sup>a</sup>	26.31 <sup>a</sup>
VD2h-FD60°C <sub>s.cherry</sub>	-	2	13	15 <sup>a</sup>	28.57 <sup>a</sup>

abcMeans with different letters in the same column were significantly different at the level ( $P < 0.05$ )

FD, freeze-drying; HA, hot-air drying; VD, vacuum drying; HA-FD, hot-air drying-assisted freeze-drying; VD-FD, vacuum drying-assisted freeze-drying.

### 3.2. Drying curve of elderberry- and sour cherry pomace

Drying curve shows the profile change in dimensionless moisture ratio (MR) versus drying time (t). The effect of HA, VD, FD, HA-FD and VD-FD on drying characteristics curves of the elderberry- and sour cherry pomace during drying are shown in Figures 1-2. It was observed that moisture content decreases continuously with elapsed time in both materials. As expected, the HA and VD methods were carried out more rapidly than the FD method. The higher drying temperature – from 60°C to 80°C – produced a shorter drying time in case of elderberry- and sour cherry pomace. These results are in agreement with the observations of earlier researchers [10]. There was no significant difference ( $P > 0.05$ ) between the HA and VD processes, this trend similar at running of drying curve of elderberry- and sour cherry pomace.

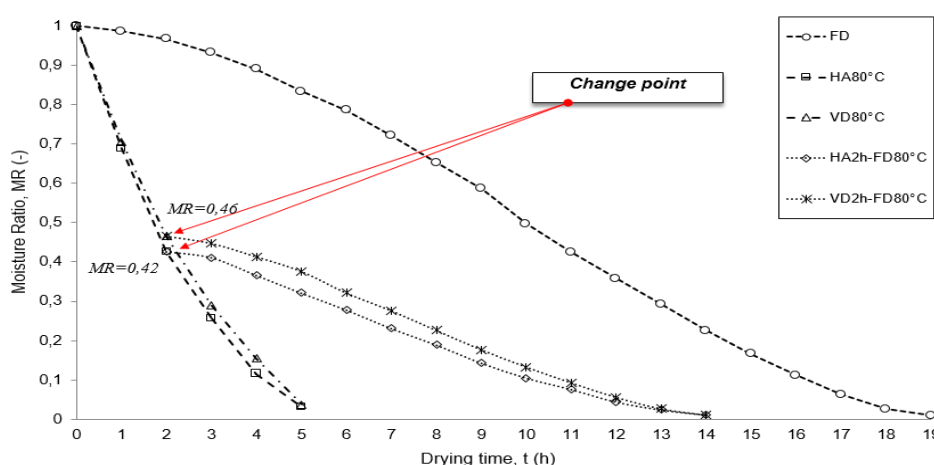


Figure 1 Drying curve of elderberry pomace

The drying curves at HA and VD indicated exponential decay, for elderberry pomace dehydration. The HA and VD processes needs only 5h. The moisture content of elderberry pomace rapidly decreases during first 2 hours of the dewatering process at HA and VD, and then decreases slower until the end of drying. This is so called equilibrium moisture content ( $M_e$ ) which is corresponding



to the equilibrium between the final product and the surrounding drying conditions. At this point water content of elderberry pomace decreased from 40.41% to 2.44-0.78% (w.b.) at all drying methods. On the other hand, the slope of the drying curve of elderberry pomace dried by HA and VD are steeper than the sour cherry pomace treated by HA and VD.

In addition, the *Figure 1* showed that the FD method needs the longest operational time (19h). This is because lyophilization, under vacuum conditions, supplies the sublimation heat by radiation. According to *Figure 1*, the drying curves of single-stage of FD and FD finish-drying have long-drawn “S” shape.

The dimensionless moisture ratios (MR) of elderberry pomace of HA- and VD-FD were reduced to 0.42 and 0.46 when were reached the change points (This point shows where joined the various drying methods in succession.), respectively.

Drying curve of sour cherry pomace undergoing HA, VD, FD and hybrid drying are shown in *Figure 2*. The plots in this figure is relative similar to typical dehydration trend, where the water content of sour cherry pomace decreases exponentially with drying time. A similar result was reported in an earlier study [11]. According to *Figure 2*, the drying curves of single-stage of FD and FD finish-drying have long-drawn “S” shape.

The initial moisture content of the sour cherry pomace of 63.99% and was reduced to the final moisture content ranged from 2.55 to 1.22% (w.b.). It is evident from examination of this curve that the drying of sour cherry pomace by HA and VD is much faster than drying by FD or HA- and VD-FD combination. The moisture content of sour cherry pomace rapidly decreases during first 3 hours of the dewatering process at HA and VD, and then decreases slower until the end of drying. The drying process was stopped after no further change in weights was observed ( $M_e$ ).

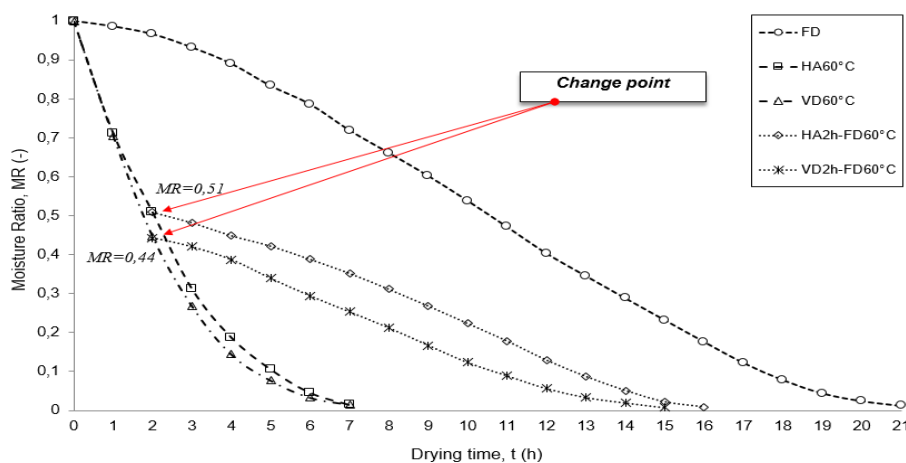


Figure 2 Drying curve of sour cherry pomace

The dimensionless moisture ratios (MR) of sour cherry pomace of VD- and HA-FD were reduced to 0.44 and 0.51 when were reached the change points (This point shows where joined the various drying methods in succession.), respectively.

### 3.3. Effect of different drying methods on $a_w$ and MC of samples

The *Table 2* indicate that the different drying methods were significantly affected the moisture content (w.b.) and water activity of by-products.



Table 2 Moisture content (MC) and water activity ( $a_w$ ) of elderberry- and sour cherry pomace

Symbol	Elderberry Pomace [%]*		Sour cherry Pomace [%]*	
	MC	$a_w$	MC	$a_w$
Fresh	40.41	0.958 <sup>d</sup>	63.99	0.951 <sup>f</sup>
FD	0.82	0.113 <sup>b</sup>	2.04	0.101 <sup>a</sup>
HA	2.12	0.345 <sup>c</sup>	2.4	0.273 <sup>d</sup>
VD	2.44	0.343 <sup>c</sup>	2.55	0.316 <sup>c</sup>
HA-FD	0.78	0.098 <sup>a</sup>	1.56	0.211 <sup>c</sup>
VD-FD	0.78	0.103 <sup>a</sup>	1.22	0.187 <sup>b</sup>

\*Moisture content (MC) in wet basis.

<sup>abc</sup>Means with different letters in the same column were significantly different at the level ( $P < 0.05$ )

FD, freeze-drying; HA, hot-air drying; VD, vacuum drying; HA-FD, hot-air drying-assisted freeze-drying; VD-FD, vacuum drying-assisted freeze-drying.

Elderberry pomace with initial moisture content of 40.41% (w.b.) were dried following four different drying methods, i. e. freeze-drying (FD), hot-air drying (HA), vacuum drying (VD) and hybrid drying (HA-FD and VD-FD) to a final moisture content of 0.78–2.44 % (w.b.).

Sour cherry pomace with initial moisture content of 63.99% (w.b.) were dried following four different drying methods, i. e. freeze-drying (FD), hot-air drying (HA), vacuum drying (VD) and hybrid drying (HA-FD and VD-FD) to a final moisture content of 1.22–2.55 % (w.b.). In the case of both samples, we achieved the lowest moisture content with the combined drying method.

Drying is one of the oldest methods of food preservation, where water activity is reduced by separating out water [12]. The water activity ( $a_w$ ) of dried apple cubes in all cases is below 0.6, hence the samples can be deemed to be safe from common microbial damage. The dried samples in the  $a_w$  range of 0.345 and 0.098 showed the microbiological stability. The  $a_w$  has a direct conjunction with the equilibrium moisture content. In this respect, the lowest and highest  $a_w$  values were found for hybrid- and vacuum dried elderberry pomace samples which had the lowest and highest final moisture content. Similar trend can be observed the other pomace samples (sour cherry).

The results of  $a_w$  at HA, VD; HA-FD and VD-FD elderberry pomace products showed no significant ( $P > 0.05$ ) differences in water activity between drying methods. Nevertheless, water activity of the FD dried sour cherry pomace was significantly lower ( $P < 0.05$ ) than the HA, VD, HA-FD and VD-FD dried ones. Summarize the results of  $a_w$ , the freeze and hybrid drying has the most favourable effect on the water activity of the pomace product.

## CONCLUSIONS

These results demonstrated elderberry pomace samples have shorter drying times than sour cherry pomace. There was no significant difference ( $P > 0.05$ ) in the operational time between the HA and VD; HA-FD and VD-FD drying methods at elderberry pomace, respectively. Similarly, there was no significant difference ( $P > 0.05$ ) in the operational time between the HA and VD drying methods at sour cherry pomace.

The total drying time of elderberry pomace required for HA-FD and VD-FD methods was 14h, reduced by 26.3% compared to pure FD. The total drying time of sour cherry pomace required for HA-FD and VD-FD methods was 16 and 15h, reduced by 23.8-28.6% compared to pure FD.

It can be observed that the drying curves of VD and HA following an exponential decay. Moreover the drying curves of FD have long-drawn “S” shape.



The water activity ( $a_w$ ) values of the dehydrated pomace products were in the range of 0.345-0.098. Besides, our results show that no microbial proliferation was occurred in the dried samples.

## REFERENCES

- [1] Mirzaei-Aghsaghali, A., Maheri-Sis, N.: *Nutritive value of some agro-industrial by-products for ruminants - A review*. World Journal of Zoology, 3(2), 40-46., 2008.
- [2] Lee, J.H., Rhim, J.W.: *Rehydration kinetics of vacuum-dried Salicornia herbacea*. Food Science and Biotechnology, 19(4), 1083-1087., 2010.
- [3] Lee, J.H., Li, Z.: *Mathematical modelling on vacuum drying of Zizyphus jujuba Miller slices*. Journal of Food Science and Technology, 50(1), 115-121., 2013.
- [4] Jaya, S., Das, H.: *A vacuum drying model for mango pulp*. Drying Technology, 21(7), 1215-1234., 2003.
- [5] Jaya, S., Das, H.: *Accelerated storage, shelf life and color of mango powder*. Journal of Food Processing and Preservation, 29(1), 45-62., 2005.
- [6] Orikasa, T., Koide, S., Okamoto, S., Imaizumi, T., Muramatsu, Y., Takeda, J., Shiina, T., Tagawa, A.: *Impacts of hot air and vacuum drying on the quality attributes of kiwifruit slices*. Journal of Food Engineering, 125, 51-58., 2014.
- [7] Jaya, S., Durance, T.D.: *Compressive characteristics of cellular solids produced using vacuum-microwave, freeze, vacuum and hot air dehydration*. Journal of Porous Materials, 16(1), 47-58., 2009.
- [8] Xu, Y.Y., Zhang, M., Tu, D.Y., Sun, J.C., Zhou, L.Q., Mujumdar, A.S.: *A two-stage convective air and vacuum freeze-drying technique for bamboo shoots*. International Journal of Food Science and Technology, 40(6), 589-595., 2005.
- [9] Pei, F., Yang, W., Shi, Y., Sun, Y., Mariga, A.M., Zhao, L., Fang, Y., Ma, N., An, X., Hu, Q.: *Comparison of freeze-drying with three different combinations of drying methods and their influence on color, texture, microstructure and nutrient retention of button mushroom (Agaricus bisporus) slices*. Food and Bioprocess Technology, 7(3), 702-710., 2014.
- [10] Ertekin, C., Yaldiz, O.: *Drying of eggplant and selection of a suitable thin layer drying model*. Journal of Food Engineering, 63, 349-359., 2004.
- [11] Prachayawarakorn, S., Soponronnarit, S., Wetchacama, S., Jaisut, D.: *Desorption isotherms and drying characteristics of shrimp in superheated steam and hot air*. Drying Technology, 20(3), 669-684., 2002.
- [12] Rahman, M.S.: *Food Preservation: Overview*. In: Handbook of Food Preservation. CRC Press Taylor & Francis Group, 11., 2007.



## COMPARISON OF THE PRODUCTION AND PROPERTIES OF ACCC CONDUCTORS TO OTHER HTLS CONDUCTORS

<sup>1,2</sup>AZANE Thomas, <sup>1,2</sup>BARKÓCZY Péter PhD

<sup>1</sup>Faculty of Materials Engineering, University of Miskolc

E-mail: [thomasazane@yahoo.com](mailto:thomasazane@yahoo.com)

<sup>2</sup>FUX Co., Miskolc

E-mail: [peter.barkoczy@fux.hu](mailto:peter.barkoczy@fux.hu)

### Abstract

*If the electric energy demand suddenly increases the reconductoring is the only one possibility to supply the necessary electric energy. In this case the application of the HTLS conductors gives the best result. The article compares the materials of the different HTLS conductors, and shows the specialty of the stranding of fully annealed trapezoidal shaped wires.*

**Keywords:** *conductors, sag, aluminium, heat resistant, composite.*

### 1. INTRODUCTION

Nowadays the utilities frequently meet an extra electric power demand in developing industrial areas or residential areas. When this demand is larger than the capacity of the electrical line, the operating temperature of the conductors increases more than the standardized limit. The high voltage and middle voltage overhead lines mostly built by ACSR conductor. ACSR conductors contains stranded steel core and stranded cold drawn aluminium wires. In this construction the strength of the aluminium wires plays a significant role in the strength and mechanical behaviour of the whole conductor. Long term operation over the maximal operating temperature means an annealing on the aluminium wires. During the annealing the aluminium wires continuously lose their strength, and there is a risk of the breakage, additionally due to the high temperature the sag of the conductors increasing extremely which causes operational problems (phase faults, short circuits, accidents) (1). In that case the utilities can replace the line or can build another. Both of them are long and expensive process. The lines have to be planed, the utility have to buy the field under the new towers, the legislation process too long. This process cannot solve the mentioned problem in short term. The HTLS (high temperature low sag) conductors were developed to solve this problem. If it's possible a simple reconductoring without the strengthening of the towers is enough. This means the replacement of the conductor which faster process than a new line building or a total reconstruction. The common feature of this conductors, that the maximal operating temperature is higher than an ACSR conductor, the sag value remains low at higher temperatures and contains special materials [1].

Recently more and more line reconductoring used ACCC conductor which is a protected conductor of CTC Global company (2). The ACCC conductor contains a carbon fibre reinforced composite core, and annealed trapezoidal shaped aluminium wires are stranded on it (3)s. Due to the increasing demand CTC Global search for cable manufacturers who can produce this type of conductor in high quality. FUX company. is the contractual producer partner of CTC Global in Eastern-Europe. But FUX Company regularly produce other HTLS conductors as ACSS and TACIR. It is important to compare this types of HTLS conductors according to the properties and production to present clearly the advantages of the conductors from the producer point of view. In this article we introduce the materials used in the conductors, and compare the properties of the conductor based on the materials.



Additionally, this article introduces the specialities of the production originated to the special properties of the materials. This article deals with these topics only. The electrical properties under high voltage, the stringing and installation and the operation of the lines discussed in the literature in several articles by utilities and development groups [3].

## 2. METHODS

HTLS conductors produced by FUX Zrt. The conductors tested in the Laboratory of Wire and Conductor Diagnostics. The Laboratory supervised by jointly FUX and University of Miskolc and situated at the plant of FUX. The mechanical properties of the conductor and the wires tested according to the standardized descriptions. The sag value measured on 30mm sample and calculated to longer span if it was necessary. The conductor heated up by current with a high current tester. The sag value is measured by optical sensors.

## 3. RESULTS

In HTLS conductors the conductive material is EC aluminium or aluminium alloy. In normal ACSR conductor hard drawn wires are used. If heat resistant alloys are used the state of the wires also hard drawn. The elevated temperature means an annealing to the hard drawn EC aluminum. If EC aluminium wires used in HTLS manufacturing the hard drawn aluminium wires are fully annealed before stranding. Table 1 shows a summary of the possible solutions. Several data can be found on the articles due to the different standards or measured data, but the ranges in all database are close together.

Table 1 Aluminium conducting materials and properties [2].

Aluminum Conducting Materials					
description	name	(% IACS)	Rm, MPa	Thermal limits, °C	
				Cont.	<10 hrs
Hard drawn	AL1	61	162-172	90	120
MS alloy	AL7	57,5	255-275	90	120
HS alloy	AL3	53	300-330	90	12
Fully annealed	-	63	55-96	250	250
Thermal resistant	AT1-TAL	60	165-186	150	180
High strength thermal resistant	AT2-KTAL	55	225-248	150	180
Ultra thermal resistant	AT3-ZTAL	60	160-180	200	240
Extra thermal resistant	AT3-XTAL	58	160-170	230	310

Table 1 clearly shows that from electrical and operational point of view the fully annealed aluminium is the best choice. The conductivity and the maximal operating temperature are the highest. But the strength of this alloy is the lowest. The annealed aluminium wires do not play a significant role in the strength of the conductor. It is handled during the calculations as an excess weight. Additionally, there is an extra technological step, the heat treatment, in the manufacturing technology. The heat treatment of the wires is expensive in contrast to the wire drawing alone. Additionally, due to the low strength the stranding also not easy as in the case of the hard drawn wires. It is necessary to handle by care the annealed wires. This can cause problems during the installation of the conductor. The strength of the thermal resistant aluminium wires comparable to the hard drawn wires. It can handle normal way. This used in cold drawn state, and the stranding and the installation do not require special attention. But the conductivity lower than the hard drawn wires, and the maximal operating



temperature is not as high as fully annealed wires. Additionally, the main alloying element is the zirconium which make extremely expensive the alloys.

Table 2 Core materials and properties [2].

Core materials			
description	E, GPa	Rm, MPa	specific weight, kg/dm <sup>3</sup>
HS Steel	200	1380-1450	7,8
EHS Steel	200	1516	7,8
EXHS Steel, Galfan coated	200	1965	7,8
Aluminum clad (20,3% IACS)	165	1100-1345	6,6
Galvanized invar alloy	162	1035-1068	7,8
Aluminum-oxide composite	215	1310	3,3
Carbon fibre composite	124	4295	1,9

Table 2 shows the properties of the core material. The steel wires stranded, and this strand is the core. The steel wires can be galvanized or aluminium clad due to the corrosion resistance. Extra high strength can be produced by Galfan coating, where few percentage aluminum is added to the zinc bath. The Galfan coating proves the same or better corrosion resistance but. FUX use EXHS steel in ACSS conductors. ACSS conductors consists of EXHS steel strand and fully annealed aluminium wires. The thermal resistance of the aluminium clad wires higher than the galvanized wires but the strength is lower. An advantage of the aluminium clad wires is that the aluminium coating has a good conducting properties so the resistivity of this type of conductors are lower. Invar wires has an extremely low thermal expansion. Therefore, the sag of this conductors are lower. FUX produce TACIR and ZTACIR conductors which consist of invar strands and thermal resistant aluminium alloys. The price of the invar wires are extremely high compare to the EXHS wires.

Table 2 show that one of the best core material is the carbon fibre reinforced composite material. The problem of this core is that the conductors with its patented by CTC Global. FUX start the production of the ACCC conductors in East-Europe with the permission of CTC Global. ACCC conductor consists of the mentioned carbon fibre reinforced composite core and fully annealed aluminium wires. Table 1 and Table 2 show that this combination has the best properties. The strength of the composite core is large enough to hold the extra weight of the aluminium. The resistivity of the conductor is low due to the low resistivity of the annealed wires. Additionally, the magnetic loss is missing, so the impedance of the line which is built-up with ACCC conductors is lower than a normal ACSR line. Figure 1 compares the sag of the ACCC conductor to an ACSR.

The price of the ACCC conductor is higher than the ACSR conductors due to the price of the composite material and the heat treatment. But the ACCC conductor contains trapezoidal shaped wires instead of rounded wires. Double power can be transmitted with the same diameter of ACCC conductor because the conductive cross section is larger due to the trapezoidal wires. This fact shows that in a reconductoring project the price of the ACCC conductor have to be compared to the ACSR with equivalent current carrying capacity.

The annealed trapezoidal wire production and stranding initiate a lot of technological problem. First of all, the geometry of the wires can be determined based on the conductor geometry. A geometrical modelling is used to calculate the dimensions of the trapezoidal wires. Figure 2 shows a geometrical model. The next step is the planning of drawing dies. During the cold drawing a round wire have to be deformed to trapezoidal one. More shaped die is necessary to distribute the material in the final die properly. Additionally, it has to take into consideration the properties of the rod breakdown machine.

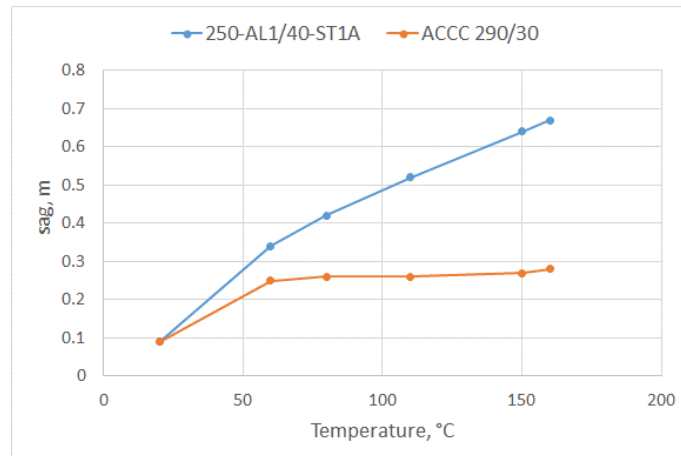


Figure 1 Comparison of the sag value of an ACCC and ACSR conductor

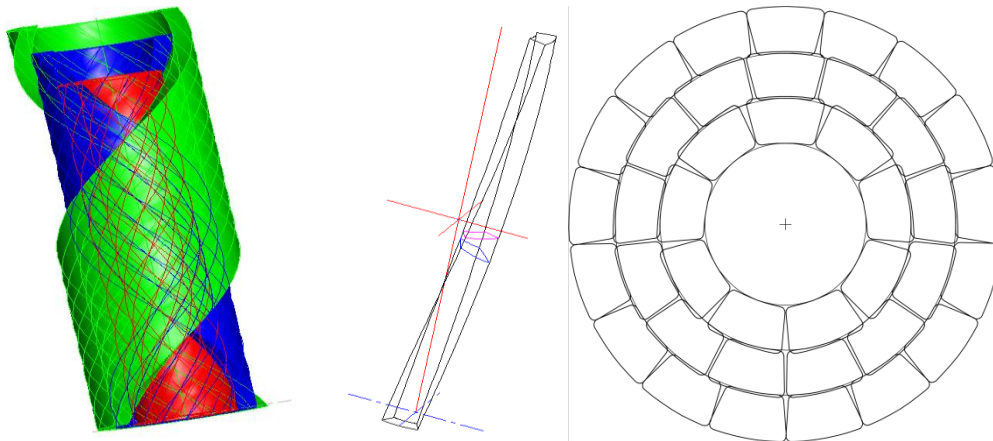


Figure 2 Sketch of the geometrical planning of the trapezoidal shaped wires.

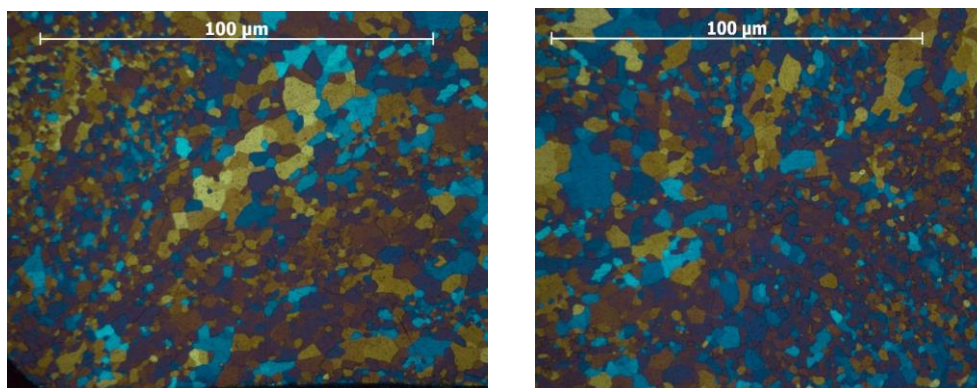


Figure 3 The microstructure of the annealed wires.

The difference of the shape between the round and trapezoidal wires means an inhomogeneous deformation distribution in the cross section of the wire. Volumes with higher extent of deformation recrystallize faster and has a finer annealed grain structure. Therefore, inhomogeneity is found in the microstructure of the annealed wire. Figure 3 shows the small and large grains in the microstructure. The left picture is taken from the edge of the cross section; the right is taken from the centre of the cross section. But this difference in the grain size does not cause problem during the stranding process. With the developed technology FUX produce the ACCC conductors.



## **CONCLUSIONS**

When the electric energy demand suddenly increases one possibility to replace the conductors is by the use of HTLS conductors. The maximal operating temperature of the HTLS conductors is higher, therefore the current carrying capacity of the line also bigger. The price of the HTLS conductors are higher than the ACSR conductors, but the reconductoring is cheaper than a total modernization or new line building. The article overviewed the materials of the HTLS conductors, and showed the ACCC as the best choice. But ACCC conductors consist of fully annealed trapezoidal shaped wires besides the carbon fibre reinforced composite core. This gives difficulties to the production technology. This difficulty can be solved by a design methodology and testing.

## **REFERENCES**

- [1] Filipovic V., Morgan, V.T., Findlay, R.D.: *A unified Model for Predicting the Electrical, Mechanical and Thermal Characteristics of Stranded Overhead Line Conductors*. Electrical and Computer Engineering, 1, 182-185., 1994.
- [2] Southwire.: *Southwire Overhead Conductor Manual*.
- [3] Alawar, A., Bosze, E.J., Nutt, S.R.: *A composite Core Conductor for Low sag at High Temperatures*. IEEE Transactions on Power Delivery, 20, 2193-2199., 2005.



## NANOSTRUCTURED THIN FILMS USED TO IMPROVE THE TRIBOLOGICAL PROPERTIES IN MECHATRONIC ACTUATING SYSTEMS

**BADITA Liliana-Laura PhD, ZAPCIU Aurel PhD, GORNOAVA Valentin, VOCUREK Marian, MUNTEANU Iulian-Sorin PhD**

*National Institute of Research and Development for Mechatronics and Measurement Technique, Bucharest, Romania*

*E-mail: [badita\\_l@yahoo.com](mailto:badita_l@yahoo.com)*

### **Abstract**

*This article briefly describes a part of the results obtained in a project with important applications in the field of mechatronics. The main objective of this project was to improve the tribological properties and, at the same time, to extend the lifetime of the moving components of the mechatronic systems. This was realized by depositing thin metallic films on the surfaces of friction couples components of mechatronic systems for ultra-precision measuring, positioning and adjustment. Thin nanostructured layers of Ti, Cr, Al and Ti+Al multilayer were deposited by the electron beam evaporation method on steel substrates of different types (OLC45, Rul1, C120, OSC8). Following the physico-mechanical and topographic analyses, it was observed that Cr is the deposited metallic layer exhibiting the highest hardness on all types of substrate. Ti has the best adhesion to all four substrates, but the other thin metallic layers have not been destroyed by scratching tests. In view of these results demonstrating the improvement of the tribological characteristics of the steel substrates used in mechatronics, these materials will be integrated into real mechatronic systems.*

**Keywords:** *thin films, mechatronic components, tribology, wear, roughness.*

### **1. INTRODUCTION**

In highly developed industries, the mechatronic components are found in a multitude of applications, such as modern cars, industrial robots, microrobots used in the military industry, nanorobots used in medical investigations, medical investigation equipment, prosthetic systems and artificial organs, audio, video recording systems, etc. [1].

Currently, micro and nanostructured thin films represent a solution to improve the constructive features and to increase the operational lifetime of mechatronic systems and components because they have tensile strength 20-50 times greater than the stainless steel and Young's modulus 5 times higher than the stainless steel. [2] These can help to reduce the wear and release of particles in different couplings. Increasing the system components durability, a different surface chemistry to reduce adhesive friction, coated parts that remain undisturbed could also help to this reduction.

Wear consists in the progressive loss of material that results from the interaction of the surfaces of the friction couples. [3] Between the wear and friction process there is interdependence in the sense that wear is a consequence of friction, and the condition of wear surfaces influences friction. In order to obtain materials with improved properties, different methods have been tried, but the most important, so far, is the method of depositing thin films on different substrates, having as main purpose the increase of the lifetime as well as the improvement of the physico-mechanical properties.



## 2. METHODS

### 2.1. Materials

In order to achieve the objectives proposed in this project, thin metallic layers were deposited on different steel substrates used in the mechatronic field. Taking into account the mechatronic components envisaged for the future applicative tests, nanostructured Al, Cr, Ti layers and Ti+Al multilayer were deposited on steel substrates. OLC45, Ru11, C120 and OSC8 steel substrates were used, because the first two types are employed for the production of gauges, bushings, actuators, measuring dowels, positioning supports, gauge body, and the last two are employed for the production of threaded gauges, probe heads, benchmarks, punches. The main physico-mechanical characteristics and chemical composition of these types of steel are shown in *Table 1*.

*Table 1* Chemical composition and physico-mechanical characteristics of the steels used in the present project

Substrate	Composition (%)						Physico-mechanical properties
	C	Si	Mn	P	S	Cr	Hardness HB
<b>OLC45</b>	0,42-0,50	0,15-0,40	0,60-0,80	0,030	0,030	-	207
<b>Ru11</b>	0,55-0,65	0,15-0,35	0,25-0,45	-	-	1,35-1,65	223
<b>C120</b>	1,90-2,20	0,10-0,60	0,20-0,60	-	-	11,0-13,0	248
<b>OSC8</b>	0,75-0,85	0,10-0,30	0,10-0,40	-	-	-	192

### 2.2. Deposition of thin layers and determination of their thickness

In these experiments the depositions of Ti, Cr, Al layers and Ti+Al multilayer on the four types of substrates were made by the electron beam evaporation method. This technique performs deposition of thin metallic layers to translate the geometries from the mask into the substrate followed by the lift-off. The deposition process was performed using a Temescal FC-2000 system, a fast cycle system, the thickness of the layers obtained being determined using the quartz crystal microbalance (QCM) method. [4]

### 2.3. Characterization of deposited thin layers

Thin films deposited for improving the resistance of mechatronic components in this project were physico-mechanically, structurally and topographically characterized. Following these characterizations, information about the degree of influence of the material used were obtained, for a future enhancement of substrates resistance.

To determine the hardness of the deposited thin layers, the HMV-2 system was used. The automatic reading system for Vickers hardness tests automatically measures the distance between the opposite corners of the fingerprint to find the Vickers hardness, based on the image of the fingerprint taken on the test surface and captured by the CCD camera. Measurements were made with this system under the following conditions  $T = 24^{\circ}\text{C}$ ;  $H = 50\%$ ,  $F = 98.07 \text{ mN}$ ,  $\text{HV}0.01$ , 10 sec. [4]

A CETR-UMT 2 system (*Figure 3a*) was used to determine the adhesion of thin layers. The device allows two sliding contact modes: reciprocating or unidirectional sliding contact. It allows the control of ambient temperature and humidity and provides protection against vibration. The tests



involved the execution of a measuring cycle in three steps, with a normal force of 5 N, a length of 5 mm, speed of 0.2 mm/s, having duration of 25 s.

The structural and topographic characterization of the deposited thin layers and subjected to scratch tests was realized using mainly atomic force microscopy (AFM) [5]. AFM measurements were performed with an NTEGRA Probe NanoLaboratory NT-MDT Microscope - *Figure 1b* [6]. Surfaces of 50/50  $\mu\text{m}$  situated in different locations of samples were scanned and topographic parameters (roughness, surface skewness, coefficient of kurtosis) were determined using NOVA SPM Software. The KLA TENCOR MICRO XAM 100 laser system for measurement of microgeometry surfaces has also been used for topographic characterization, to quantify the roughness and surface topography without contact, with high precision and speed [7].

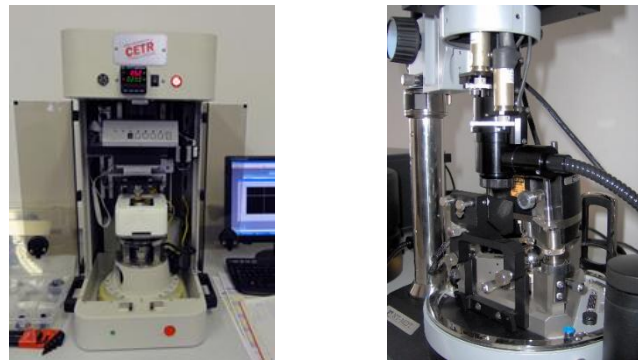


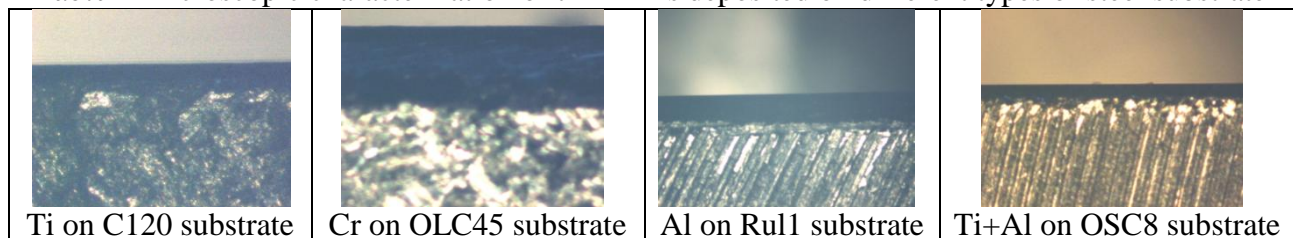
*Figure 1* Systems for the characterization of deposited thin layers. (a) CETR-UMT 2 system; (b) AFM microscope, NTEGRA Probe NanoLaboratory NT-MDT

### 3. RESULTS

#### 3.1. Structural characterization of deposited thin layers

Thin layers with different thickness Ti (100 nm), Cr (50 nm), Al (50 nm) and Ti+Al multilayer (thickness of 50 nm each layer, total thickness of the multilayer being 100 nm) were obtained on steel substrates (OLC45, Ru11, C120 and OSC8) after electron beam evaporation. From the characterization at the microscopic scale the complete joining between the layer and the substrate was observed (*Table 2*).

*Table 2* Microscopic characterization of thin films deposited on different types of steel substrate



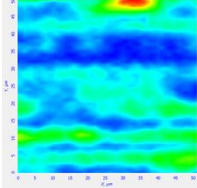
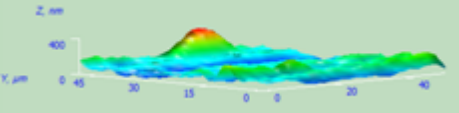
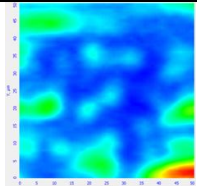
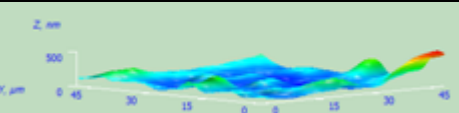
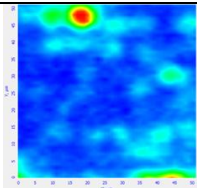
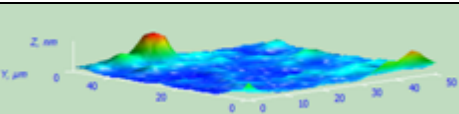
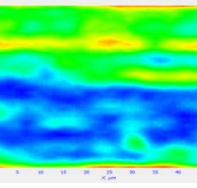
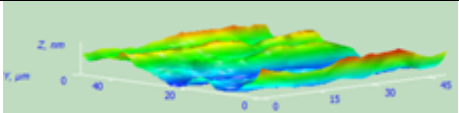
Following the nanometric characterization using AFM, the roughness  $R_a$  was used as an indicator of the deposited layer deterioration to obtain information on its uniformity. The surface skewness  $R_{sk}$  measures the asymmetry degree of a distribution and, together with the coefficient of kurtosis  $R_{ka}$ , characterizes the shape of the distribution. In *Table 3* are presented some of the results obtained by AFM characterization of the thin layers deposited and the calculation of the topographic parameters. After analyzing the average values of the roughness of the deposited layers, it was observed that the layers deposited on the OSC8 steel substrate have the most uniform surface. Ti is the layer with the



lowest value of roughness on all types of steel substrates, followed by Al and Cr. The Ti+Al multilayer has a more uniform distribution on the C120 steel substrate.

After analyzing the average values of the roughness of the deposited layers, it was observed that the layers deposited on the OSC8 steel substrate have the most uniform surface. Ti is the layer with the lowest value of roughness on all types of steel substrates, followed by Al and Cr. The Ti+Al multilayer has a more uniform distribution on the C120 steel substrate.

Table 3 AFM characterization of thin layers surfaces deposited on steel substrates

	 <p style="text-align: center;">Al<sub>50</sub> nm on OSC8 substrate</p>	<pre> Amount of sampling 2652 Max 400.656 nm Min 0 nm Peak-to-peak, Sz 400.656 nm Ten point height, Sz 137.679 nm Average 96.2767 nm Average Roughness, Sa 40.2764 nm Second moment 112.4816 Root Mean Square, Sq 95.3973 nm Surface skewness, Ssk 1.42007 Coefficient of kurtosis, Skk 4.32273 Entropy 5.88718 Redundance -11.111           </pre>
	 <p style="text-align: center;">Cr<sub>50</sub> nm on OLC45 substrate</p>	<pre> Amount of sampling 2601 Max 519.203 nm Min 0 nm Peak-to-peak, Sz 519.203 nm Ten point height, Sz 256.683 nm Average 90.8404 nm Average Roughness, Sa 43.1666 nm Second moment 122.142 Root Mean Square, Sq 71.7576 nm Surface skewness, Ssk 2.41547 Coefficient of kurtosis, Skk 8.47522 Entropy 5.90104 Redundance -8.91496           </pre>
	 <p style="text-align: center;">Ti<sub>100</sub> nm on C120 substrate</p>	<pre> Amount of sampling 2704 Max 526.375 nm Min 0 nm Peak-to-peak, Sz 526.375 nm Ten point height, Sz 261.094 nm Average 74.6464 nm Average Roughness, Sa 40.8964 nm Second moment 99.0815 Root Mean Square, Sq 65.1542 nm Surface skewness, Ssk 3.29409 Coefficient of kurtosis, Skk 15.1772 Entropy 5.76163 Redundance -8.44369           </pre>
	 <p style="text-align: center;">Ti+Al<sub>50+50</sub> nm on Ru11 substrate</p>	<pre> Amount of sampling 2601 Max 233.921 nm Min 0 nm Peak-to-peak, Sz 233.921 nm Ten point height, Sz 113.953 nm Average 81.4618 nm Average Roughness, Sa 45.8398 nm Second moment 97.1698 Root Mean Square, Sq 52.9694 nm Surface skewness, Ssk 0.433722 Coefficient of kurtosis, Skk -0.839309 Entropy 5.77284 Redundance -18.0366           </pre>

### 3.2. Physico-mechanical characterization of deposited thin layers

The main physico-mechanical properties determined were the hardness and adhesion of the thin films deposited.

As a result of hardness measurements, the variation in hardness of each type of metal depending on the substrate used was analyzed. The variation graph of these values is shown in *Figure 2a*. From the realized graph it can be seen that, among all the deposited metals, Cr is the hardest deposited metallic layer, followed by Ti and Al. The hardness of the Ti+Al multilayer has a value between the hardness of Ti and Al. On the surface of the OSC8 substrate the highest average value of hardness for all four types of nanoscale layers was obtained.

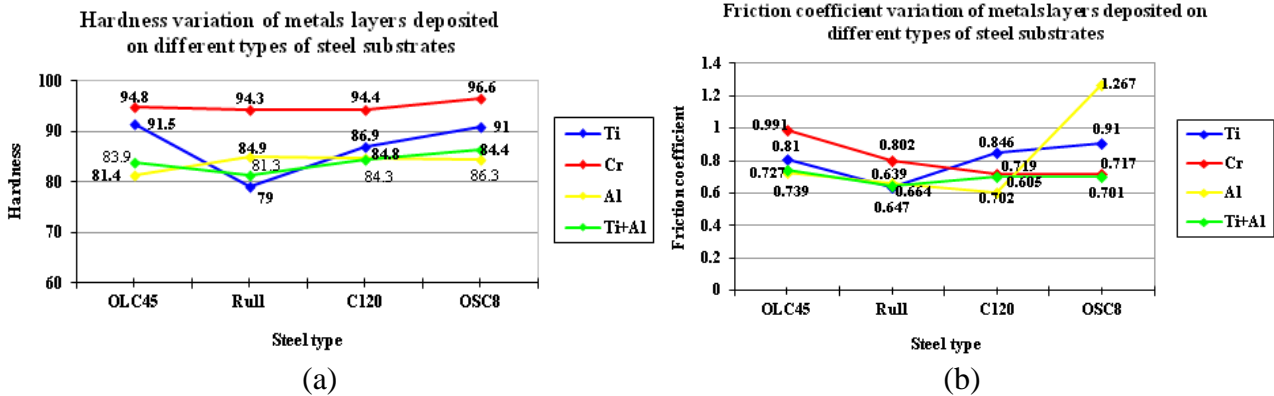


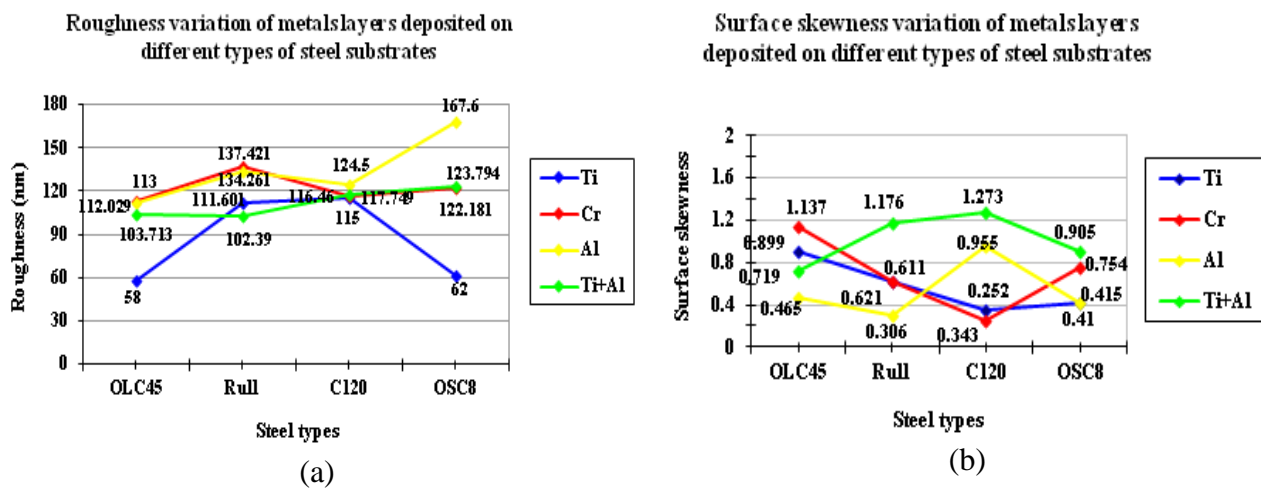
Figure 2 (a) Hardness variation of the Ti, Cr, Al layers and Ti+Al multilayer deposited on OLC45, Rull, C120 and OSC8 steel substrates; (b) Friction coefficient variation of the Ti, Cr, Al layers and Ti+Al multilayer deposited on OLC45, Rull, C120 and OSC8 steel substrates

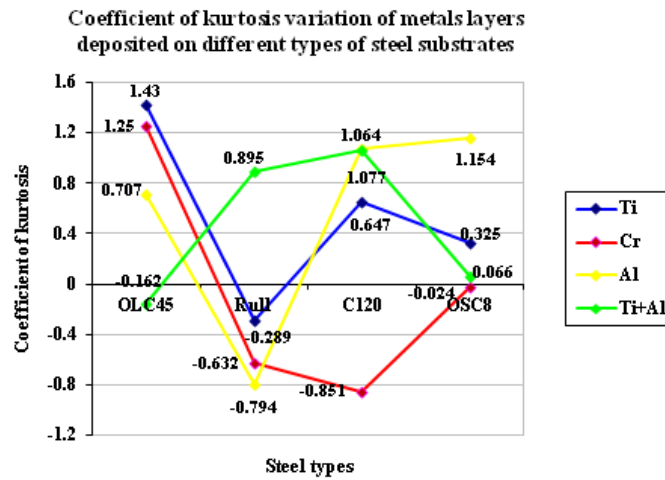
The adhesion of the deposited metallic layers was determined by scratch tests, mainly obtaining information on the friction coefficient (COF). The variation graph of the average COF values obtained from these tests is shown in Figure 2b. The average COF values are generated by the adherent structure of the deposited material and of the peeling resistance of the hardened superficial layer. Cr has the highest COF value when deposited on OLC45 and Rull1 steel substrates, Ti on C120 and Al on OSC8. Al thin layer has the lowest COF when it is deposited on OLC45 and C120 substrates. Ti has the lowest COF when it is deposited on Rull1, but the value of this coefficient increases when it is covered with Al and is deposited as multilayer on OSC8.

### 3.3. Topographic characterization of thin layers surfaces subjected to scratch tests

Several types of damages on the thin layers resulted from critical loads after the scratch tests. The main signs observed were: deformations and detachments of deposited layers, semicircular cracks of the coating, raising of the material on the edges, cutting of the base material and oxidation, but there are also areas with uniform surfaces, almost without defects.

The average values of the tribological parameters obtained from the topographic analysis of the thin layers surfaces subjected to the scratch tests were compared (Figure 3a, Figure 3b, Figure 3c).





(c)

Figure 3 Variation of roughness (a), surface skewness (b), coefficient of kurtosis (c) of the Ti, Cr, Al layers and Ti+Al multilayer deposited on OLC45, Ru11, C120 and OSC8 steel substrates and subjected to scratch tests

From the comparative graph of the roughness (*Figure 3a*) it can be seen that the Ti layer deposited on the OLC45, C120, OSC8 steel substrates and subjected to the scratch tests is the least damaged layer deposited on these substrates, thus proving the increased resistance of this metallic layer. Cr appears to be more damaged on OLC45 and Ru11 substrates, and Al on C120 and OSC8 substrates. The surface skewness was also graphically compared (*Figure 3b*) for all four types of substrates. The values of the surface skewness, in all cases, indicated a distribution of asymmetric layers to the right, so not a completely symmetrical distribution of these deposited materials. Coefficient of kurtosis (*Figure 3c*) indicates the shape of distribution obtained from the deposition of the material and subjected to the scratch test. The comparative graphical analysis revealed the lack of a value of this parameter indicating a normal distribution of deposited metallic layers.

## CONCLUSIONS

As a result of this study realized in the thin films field, the superior properties of nanostructured materials have been highlighted. Thin layers of Al and Cr with 50 nm thickness, Ti layer with 100 nm thickness and Ti+Al multilayer with the thickness of 100 nm on OLC45, Ru11, C120, OSC8 type substrates were obtained. On all four types of substrates, Cr is the thin film that has the highest hardness. The metallic layers with the most uniform surface are deposited on the OSC8 steel substrate. After studying the adhesion of the deposited layers, it was concluded that Al detaches itself the fastest from the C120 substrate type, Cr from the Ru11, Ti from the OSC8 substrate, and the Ti+Al multilayer detaches the fastest from the C120 substrate type. The values of the surface skewness showed that the Cr, Ti and Al layers have a symmetrical distribution on the OLC45, Ru11 and OSC8 steel substrates. Al and Cr layers have a symmetrical distribution following deposition on the C120 steel substrate. The other metallic layers have asymmetrical distribution on the other substrates. Taking into account the roughness values obtained after the scratch tests, it was observed that there was not a very large destruction of the layers. The fact that the scratch tests did not destroy very hard the surface of some layers was interpreted as a good adhesion of these layers on those types of substrates.



# INTERNATIONAL SCIENTIFIC CONFERENCE ON ADVANCES IN MECHANICAL ENGINEERING

12-14 October 2017, Debrecen, Hungary



Given the behavior of these nanostructured thin films in scratch tests, it was concluded that their integration into real mechatronic systems is useful. This is currently being done on mechatronic components in positioning and control systems.

## REFERENCES

- [1] Bolton, W.: *Mechatronics – electronic control systems in mechanical and electrical engineering*. Harlow: Pearson Education Ltd., 2008.
- [2] Buschan, B.: *Springer Handbook of Nanotechnology*. New York: Springer, 2007.
- [3] Gheorghe, Gh.I., Badita, L.L.: *Advanced micro and nanotechnologies in mechatronics*. Bucharest: CEFIN Publishing House, 2009
- [4] Gornoava, V., Gheorghe, Gh.I., Badita, L.L.: *Tribological characterization of the nanostructured thin films deposited by intelligent methods, for mechatronic and biomedical applications*. The Scientific Bulletin of Valahia University – Materials and Mechanics, 14(11): 69-74., 2016.
- [5] Binnig, G., Quate, C.F., Gerber, Ch.: *Atomic Force Microscope*. Physical Review Letters 56(9), 930-933., 1986.
- [6] <http://www.ntmdt-si.com/modular-afm/prima>
- [7] Badita, L.L., Gheorghe Gh., Bratu, V., Gornoava, V., Vocurek, M., Zapciu, A., Munteanu, I.S.: *Mechanical Characterization of Nanostructured Thin Films Used to Improve Mechatronic Components*. The Scientific Bulletin of Valahia University – Materials and Mechanics, 15 (12), 48-54., 2017.



## DETECTING KNOCKING COMBUSTION OF LARGE GAS ENGINE BY DEEP RECURRENT NEURAL NETWORK

*DE BATTISTA Péter Italo, SZABÓ József Zoltán PhD, BAKUCZ Péter CSc*

*Mechatronics Institute, Donát Bánki Faculty of Mechanical and Safety Engineering, Óbuda University*

*E-mail: [szabo.jozsef@bgk.uni-obuda.hu](mailto:szabo.jozsef@bgk.uni-obuda.hu), [bakucz.peter@bgk.uni-obuda.hu](mailto:bakucz.peter@bgk.uni-obuda.hu)*

### **Abstract**

*Knocking combustion analysis of a Deutz MWM 8 cylinder large gas engine based on recurrent neural networks will be presented. The knocking combustion is identified by deep learning technique. A framework for determining the knocking combustion of the sound vibration signals is discussed using a recurrent neural networks of the knocking probability sequences. Our proposed deep neural network consists of five layers, where the middle layer is a recurrent one. This build-up was trained to distinguish weak knocking combustion from strong ones and reached 98.79% accuracy on the test set.*

*Keywords: knocking phenomena, structure borne sound recurrent neural network, deep learning, gas engine*

### **1. INTRODUCTION**

Today, designing large gas engine control systems it is necessary to minimize exhaust emissions while maximizing power and fuel economy. The capability to maximize power and fuel budget by optimizing spark timing for a specified air/gas ratio is restricted by engine knock.

Knocking phenomena in combustion processes were observed from the very beginning of the large gas engine research [1]. Engine knock occurs when the temperature or pressure in the unburned gas-air system exceeds a threshold, causing chaotic ignition of the mixture. This harvests a shock wave that creates a hasty escalation in cylinder pressure. There are many factors that affect the manifestation of knocking, including mechanical, electrical, environmental and misuse [2].

A complicated issue of knocking combustion is the unpredictable, chaotically nature of their occurrence. Thoughtful of their heritages have been one of the major question in large gas engine technology in the last century [3].

The knocking system is taken as quasiperiodic and chaotic, meanwhile the time-frequency representation is tightfitting, because it illustrates when and how knocking motion between adjacent signals can be trapped in some resonance zones associated with quasi periodicity.

For identifying the knocking phenomena it is obvious to use neural networks. In the literature could be found different varieties of self-organizational imaginary neurocomputers, such as a synergetic computer by Haken [7], resonance neurocomputers by Grossberg [6], the chaotic memory by Nicolis [8], chaotic information processing and chaotic neural networks by Tsuda [8],

In the mechanical engineering literature widely used approach to analyze the knock signal in large gas engines is based on the signal to noise ratio (SNR). This procedure contains analyzing the structural vibration of the engine by using the time-frequency domain. The time-frequency depiction of the signal is then used to define numerous schemes characterized by a greater SNR than recent procedures.



Contemporary publications concentrated on the development and utilize of *spectral models* of the knocking procedure. Among the different articles, [4] analyzed the nonlinear facet of knocking and studied the system of vibration fluctuations in a gas engine.

The industrial articles focused on four main methods in knock detection analysis:

1. Band-pass filtering based methods.
2. Detection based on the Wigner-Ville Distribution (WVD).
3. Detection using the cross WVD.
4. Detection schemes based on the Choi-Williams distribution [4].

In this paper the vibration signal analysis of a Deutz MWM gas engine is based on the cognitive science; the deep learning techniques [5].

We want to customize deep learning to determine the knocking for each working cycle.

In order to work on the deep learning system properly, it is important defining the nonlinearity parameter that can be applied under any conditions. This parameter is derived by deep neural networks in possession of the distribution of the intensity of gas engine knocking.

Deep learning has been used to analyze the knocking system in [6] and in [7] where the main frequency was extracted by computing the frequency curve where the energy of the deep learning rate is maximum [8].

Sec. II describes the deep learning techniques generally and our proposed deep recurrent neural network build-up. In Sec. III, the chaos is identified in vibration knocking and the sound vibration data-preparation is described. Sec. IV presents the results of a multilayer perceptron and the proposed recurrent neural network. The paper is closed with a summary and conclusion section.

## 2. RECURRENT NEURAL NETWORK AND DEEP LEARNING

Deep learning is the term for high-level abstraction in artificial neural networks. In the practice, the high-level abstraction is feasible by using multiple level feature representation. This is advantageous compared to shallow architectures because deeper structures require less computational elements and can learn highly-varying functions [9]. Therefore, deep neural networks are the state-of-the-art methods in several machine learning related fields, like computer vision [10], speech recognition [11] and natural language processing [12].

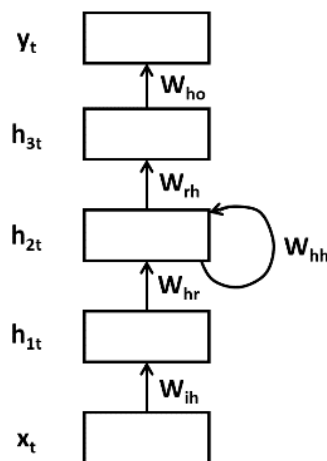


Figure 1 The deep transition-deep output recurrent neural network.



Deep learning based methods are also applicable for machine condition monitoring. They reached comparable or even better results compared to another machine learning methods [13].

One class of the neural networks is recurrent neural networks, which contain internal state feedback. This paper proposes a five layer deep transition-deep output recurrent neural network [14], where the internal state is feed-backed in the third layer. Figure 1 shows the architecture of this deep recurrent neural network.

The rectangles present the layers and the arrows show the weights between the layers. In vector form, the output evaluation is

$$\mathbf{h}_{1t} = \sigma(\mathbf{x}_t^T \mathbf{W}_{ih} + \mathbf{b}_{ih}), \quad (1)$$

$$\mathbf{h}_{2t} = \sigma(\mathbf{h}_{1t} \mathbf{W}_{hr} + \mathbf{h}_{2t-1} \mathbf{W}_{hh} + \mathbf{b}_{hr}), \quad (2)$$

$$\mathbf{h}_{3t} = \sigma(\mathbf{h}_{2t} \mathbf{W}_{rh} + \mathbf{b}_{rh}), \quad (3)$$

$$\mathbf{y}_t = \sigma(\mathbf{h}_{3t} \mathbf{W}_{ho} + \mathbf{b}_{ho}), \quad (4)$$

where  $\mathbf{h}_{1t}$ ,  $\mathbf{h}_{2t}$  and  $\mathbf{h}_{3t}$  are the hidden layers activations,  $\mathbf{h}_{2t-1}$  is the previous  $\mathbf{h}_2$  hidden layer activation,  $\mathbf{y}_t$  is the output vector,  $\mathbf{x}_t$  is the input vector and  $\sigma$  is the sigmoid activation function. The biases and the weights are denoted to the layers respectively, where  $\mathbf{b}$  is the bias vector and  $\mathbf{W}$  is the weight matrix. The layer notation ih the input-hidden, hr hidden-recurrent, hh hidden-hidden, rh recurrent-hidden and ho hidden-output is respectively.

The knocking combustion class is given at the output of last recurrence state. This structure is called many-to-one and shown in figure 2.

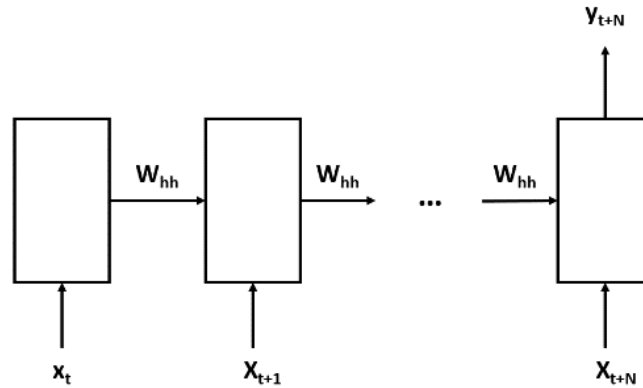


Figure 2 The many-to-one recurrent neural network structure.

Therefore, the classification error is measured on the output vector of the last sequence. Because, the desired machine learning task is a binary-classification, thus the used error function is cross-entropy [15].

$$J_{CE}(y, \hat{y}) = - \sum_{i=1}^N [y_i \ln(\hat{y}_i) + (1 - y_i) \ln(1 - \hat{y}_i)] \quad (5)$$

Where  $\hat{y}$  is the output of neural network and  $y$  is the desired output.



The predicted class is defined as:

$$Class = \begin{cases} 0, & \text{if } y \leq 0.5 \\ 1, & \text{if } y > 0.5. \end{cases} \quad (6)$$

## 2. KNOCKING COMBUSTION AND DATA-PREPARATION

### 2.1. Knocking combustion level identification

Our knocking combustion level definition is based on the signal-to-noise ratio measurement of pressure data. By using Savitzky-Golay filter [16] with polynomial order one and frame length 15, the data is filtered. Afterward, the filtered signal is subtracted from the original signal to get the noise. The absolute value of noise is integrated correspondingly the work cycle and the knocking combustion level is normalized.

### 2.2. Data-preparation

Every sound vibration signal based work cycle was normalized. Randomly, 35505 work cycles were chosen with their knocking combustion level. Afterward, the dataset was divided into a train, validation and test set by dividing into 60-20-20% respectively. For the binary classification, the weak knocking combustion class is labeled by zero, where the knocking combustion level is less or equal with 0.5. Figure 3 shows an example from weak knocking combustion class.

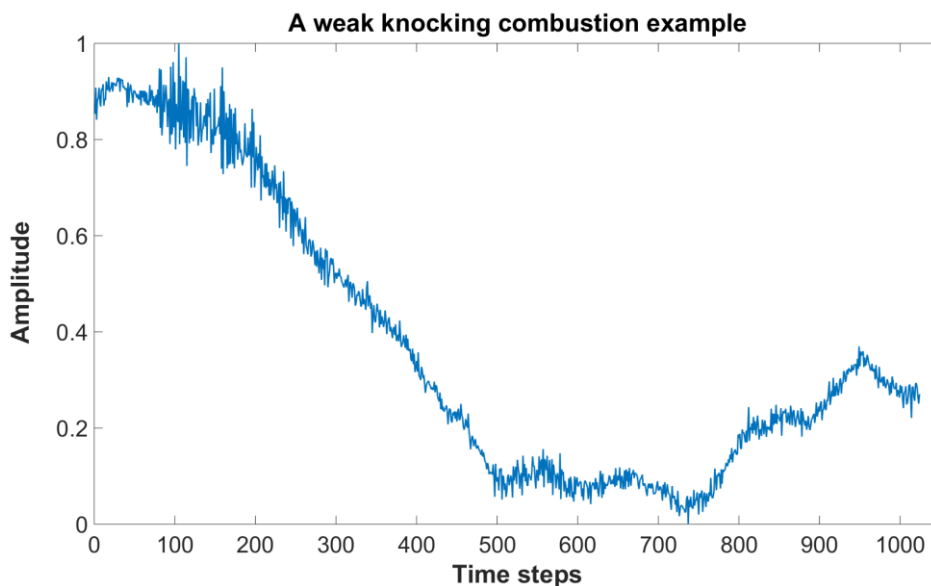
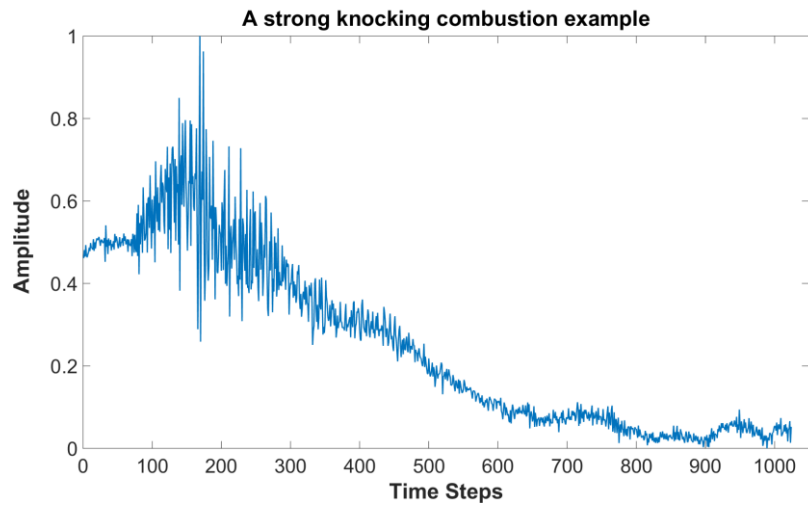


Figure 3 A weak knocking combustion example.

The strong knocking combustion class is defined oppositely and labeled by one. Fig. 3.2 shows an example from strong knocking combustion class.



*Figure 4 A strong knocking combustion example.*

### 3. RESULTS

#### 3.1. Measurement set-up

Our test engine is a Deutz MWM G234V8 large gas engine.



*Figure 5 Test engine Deutz MWM G234 V8.*

Figure 5. shows the basics of test gas engine and generator used for the knocking analysis. The working principle of the gas engine is the following: the gas is burnt in the cylinders of the engine, the energy shifts a crankshaft within the engine. The crankshaft shifts a generator which results in the alternation of electricity. Heat from the combustion process is discharged from the cylinders, which must be either reclaimed and used in a combined heat and power structure or dissipated via heaters placed near the to the engine.



### 3.2. Multilayer perceptron result

First, the general knocking combustion classification capability of neural networks was tested on a multilayer perceptron [17], which contains 1024 inputs, 100 hidden units and 1 output. The used training method is cross-validation [18], which chooses the best model, where the validation error is the least. The instances are in mini-batches with size 32. By applying ADAM adaptive gradient descent based optimizer with global learning rate  $5 \cdot 10^{-5}$  and the recommended hyper-parameters [19], the best model results are: training error 2.59%, validation error 2.41% and test error 2.75%.

### 3.3. Deep recurrent neural network result

To reduce the model size of neural network, the number of inputs is chosen to be 32. Because of a sound vibration work cycle consists of 1024 points, thus the deep recurrent neural network goes through 32 sequences. At the last sequence, the neural network gives the classification result as figure 6. shows that.

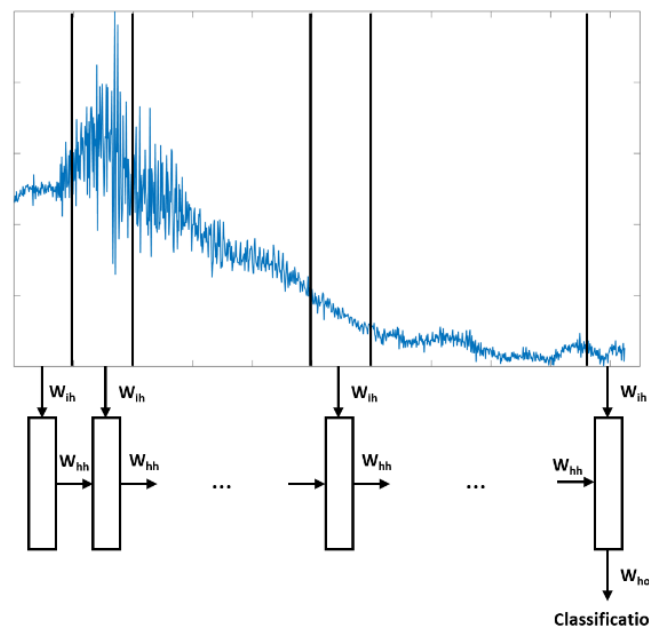


Figure 6 The evaluation principle of one work cycle.

Furthermore, the deep recurrent neural network contains a hidden layer with 30 units, a recurrent hidden layer with 25 units and a hidden layer with 5 units before the output layer and 1 output. This build-up is trained with the same hyper-parameters as the multilayer perceptron, except the global learning rate, which is initialized to  $10^{-3}$ . The results are the followings: training error 1.00%, validation error 1.25% and the test error 1.21%.

## SUMMARY AND CONCLUSION

Large gas engines can operate at maximum power and budget fuel when the spark timing is optimized for a specified air/gas ratio, which is restricted by the engine knock. Therefore, the combustion knocking level identification of gas engines is necessary. One possible solution is to use artificial neural networks as this paper has proposed. A multilayer perceptron reached 97.25% accuracy to distinguish strong from weak combustion knocking on the sound vibration based test



data set of a Deutz MWM G234 V8 gas engine. Although, the model is relatively big because it contains 102,601 parameters. By using single precision floating-point variables, this requires 400.78 kB memory. Therefore, a deep recurrent neural network has been proposed with 5 layers, where the middle layer is a recurrent one. This build-up contains together 2526 parameters, calculating also single precision floating-point variables, it requires 9.87 kB memory, which is more than 40 times smaller as the multilayer perceptron model and reached better accuracy on the same test data set, namely 98.79%.

## REFERENCES

- [1] J. Heywood, *Internal combustion engine fundamentals*, Springer Verlag, 1988.
- [2] F. Millo and C. Ferraro, "Knock in S.I. Engines: A Comparison between Different Techniques for Detection and Control," SAE Technical Paper 982477, 1998.
- [3] L. Duval and et al., "Noise robust spark ignition engine knock detection with re-dundant wavelet transform," in International Conference on Noise and Vibration, 2002.
- [4] Y. Bengio, A. Courville and P. Vicent, "Representation learning: A review and new perspectives," IEEE transactions on pattern analysis and machine intelligence, pp. 1798-1828, 2013.
- [5] L. Kovacs and J. Ratsaby, "Analysis of Linear Interpolation of Fuzzy Sets with Entropy-based Distances," Acta Polytechnica Hungarica, vol. 10, no. 3, pp. 51-54, 2013.
- [6] S. Grossberg, *The adaptive brain I: Cognition, learning, reinforcement, and rhythm*, Elsevier, 1987.
- [7] H. Haken, "Learning in Synergetic Systems for Pattern Recognition and Associative Action," Phys. B-Condensed Matter, pp. 521-526, 1988.
- [8] Hirsch and Morris, "Convergent activation dynamics in continuous time networks," Neural networks 2.5, pp. 331-349, 1989.
- [9] Y. Bengio, "Learning deep architectures for AI," Foundations and trends® in Machine Learning 2.1, pp. 1-127, 2009.
- [10] Janai, Joel and et al., "Computer Vision for Autonomous Vehicles: Problems, Datasets and State-of-the-Art," arXiv preprint, 2017.
- [11] Chan, William and et al., "Listen, attend and spell: A neural network for large vocabulary conversational speech recognition," in Acoustics, Speech and Signal Processing (ICASSP), 2016 IEEE International Conference on. IEEE, 2016.
- [12] Conneau, Alexis and et al., "Very deep convolutional networks for natural language processing," in arXiv preprint, 2016.
- [13] Zhao, Rui and et al., "Deep Learning and Its Applications to Machine Health Monitoring: A Survey," in arXiv preprint, 2016.
- [14] Pascanu, Razvan and et al., "How to construct deep recurrent neural networks," in arXiv preprint, 2013.
- [15] Nasr and et al., "Cross Entropy Error Function in Neural Networks: Forecasting Gasoline Demand," in FLAIRS Conference, 2002.
- [16] Savitzky and Golay, "Smoothing and Differentiation of Data by Simplified Least Squares Procedures," Analytical Chemistry, p. 1627-1639, 1964.
- [17] Pal, Sankar and Mitra, "Multilayer perceptron, fuzzy sets, and classification," IEEE Transactions on neural networks, pp. 683-697, 1992.
- [18] M. Browne, "Cross-validation methods," Journal of mathematical psychology, pp. 108-132, 2000.
- [19] Kingma, Diederik and Ba, "Adam: A method for stochastic optimization," arXiv preprint, 2014.



## RECYCLING POSSIBILITIES OF END PERIOD NUCLEAR FUEL CELLS

**BALOGH Gábor**

*Department of Mechanical Engineering, Faculty of Engineering, University of Debrecen*  
E-mail: [balogh.gabor@eng.unideb.hu](mailto:balogh.gabor@eng.unideb.hu)

### **Abstract**

*In the energy-dependent world of today, the energy is an important issue. At present, the production of energy does not cause a technological problem for us. We have many well-defined and effective technologies. The biggest problem is the storage of the generated energy. For this reason, alternative solutions are used, for example, in the automotive industry, when a diesel generator generates the energy required to drive electric motors and simultaneously charges the battery in the circuit. The limitation of the electric cars are the not enough effective accumulators. Beside that there are an existing technology to generate enough energy to long-term operation of a space shuttle, satellites, submarines, boats etc. This is the nuclear energy. For these application we already use small nuclear reactors, to generate energy. That's the technology which is efficient enough to create really small reactors – we can call the nano reactor or extra small smart nuclear reactor – in the safest possible design and start to use them for civil application, like cargo, trains, planes etc. Especially if we are able to recycle the end period fuel cells, which are able to give enough fuel for smaller application. The application of these technologies can reduce the pollution with the recycle use of the old cell for other decades. There are parallel advantages and they are more than disadvantages.*

**Keywords:** *nuclear power, recycling, renewable energy, re-used nuclear fuel cells*

### **1. INTRODUCTION**

In the energy-dependent world of today, the energy is an important issue. At present, the production of energy does not cause a technological problem for us. We have many well-defined and effective technologies. The biggest problem is the storage of the generated energy. For this reason, alternative solutions are used, for example, in the automotive industry, when a diesel generator generates the energy required to drive electric motors and simultaneously charges the battery in the circuit. The limitation of the electric cars are the not enough effective accumulators. Beside that there are an existing technology to generate enough energy to long-term operation of a space shuttle, satellites, submarines, boats etc. This is the nuclear energy. For these application we already use small nuclear reactors, to generate energy. That's the technology which is efficient enough to create really small reactors – we can call the nano reactor or extra small smart nuclear reactor – in the safest possible design and start to use them for civil application, like cargo, trains, planes etc. Especially if we are able to recycle the end period fuel cells, which are able to give enough fuel for smaller application. The application of these technologies can reduce the pollution with the recycle use of the old cell for other decades. There are parallel advantages and they are more than disadvantages. That could be a sign that we have to wake up and use the tools what we already have.



## 2. AVAIAABLE LITERATURES OF THE TOPIC

I have made a literature search for the related topics by review the last five years. I also try to find Hungarian language articles to see the rate of the published articles in this topic.

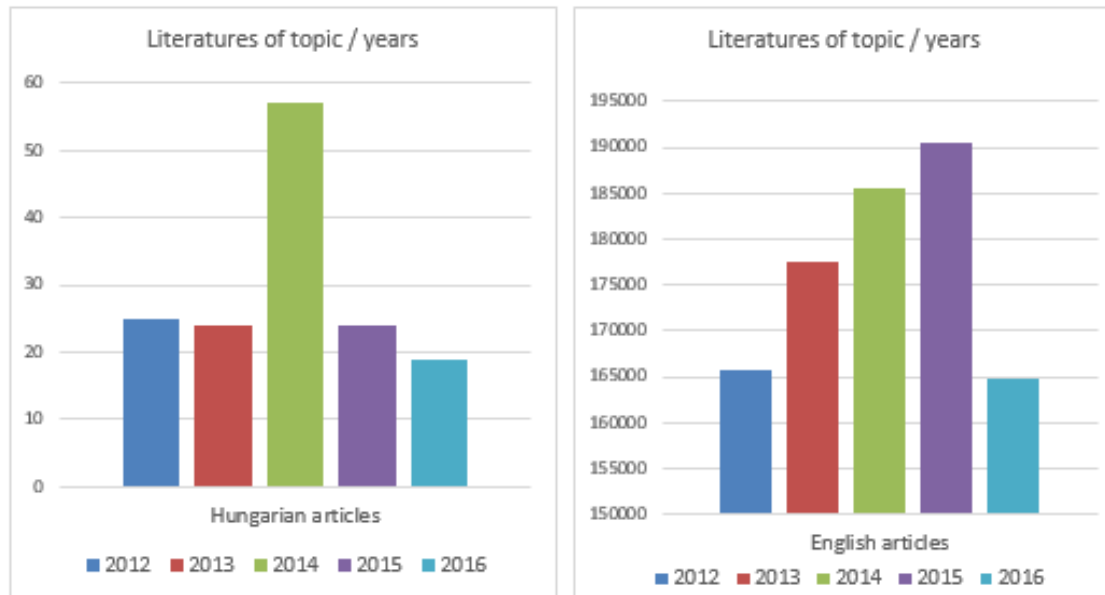


Figure 1 Available articles of the topic

As it can see on the figures the number of the published articles in this topic was rising until 2015. Nowadays the number of the published articles went down to 165000 beside that it's still a big number of publications. It could mean that the scientist finds this topic interesting and the recycling processes of the end period nuclear cells could be a possible solution for the treatment and recycling of nuclear waste beside that by technical approach we could generate a renewed energy source.

## 3. OVERVIEW OF DIFFERENT POSSIBILITIES

From the high number of published articles it comes there are a lot of theoretical solution for renew and recycle the end period nuclear fuel cells beside that we can found existing technologies, or possible technologies which were not tried out at the moment. So generally we can say that we have the solution but we need some experimental tests before we can start to use the recycling technology. I have read several articles and in this article I'd like to present two different solution for the problem. The first figure will present the process which named as [1]AIROX process. The figure represents the basic steps of the process both for recycling and renewing the fuel cells. In the original article the figure number was Figure 2-1. I keep this number, to make it easier to find it in the literature. For the conceptual flowsheet[2] I also keep the original figure number for the same reason.

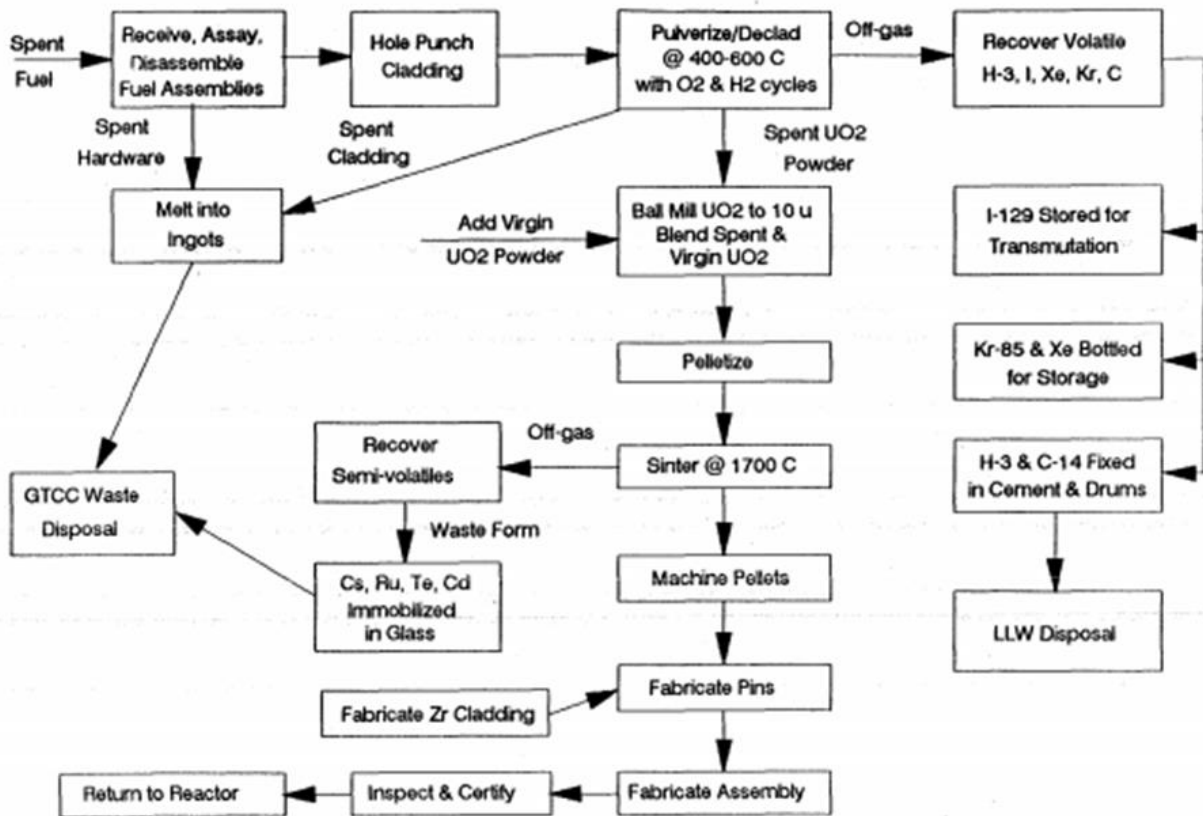


Figure 2 AIROX process [1]

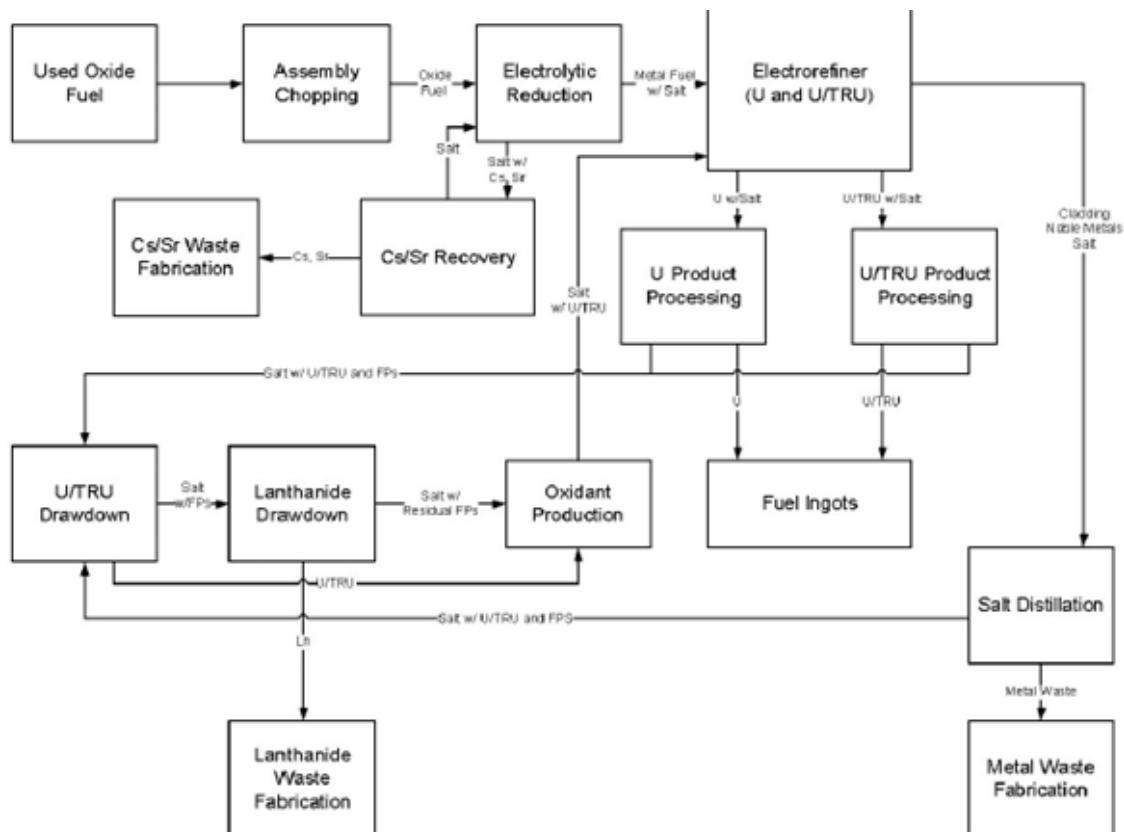


Figure 3 Conceptual Flowsheet for the Treatment of used LWR fuel [2]



This figure is represent a conceptual flowsheet for the treatment of used LWR fuel cell. If we have the solution for recycling we have to find the way to try it out practically and use them in everyday life.

#### 4. ADVANTAGES OF RECYCLING TECHNOLOGIES

Nowadays the nuclear power is applied in different transportation and exploration vehicles. The small nuclear reactors are a smart solution for produce enough energy for these applications for several years.

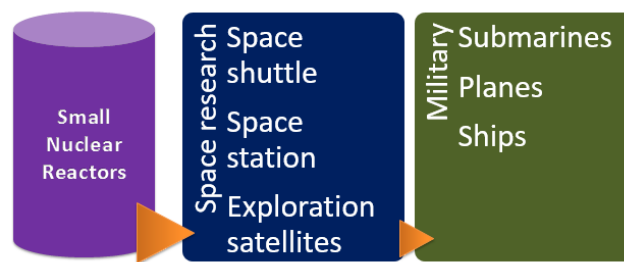


Figure 4 Application fields of small nuclear reactors

The possible solution can be born in the next few years to create an enough small and stable nuclear reactor (which could be based on applied nanotechnology) to generate power for high range of applications. At first we can solve the power supply of electrical mass transportation like buses, metro, trains, airplanes, then we can use this smart reactor to power cargo applications like trucks, trains, planes, boats. At least but not last several years later when it will became an everyday technology we can solve the electrical individual transportation power supply.

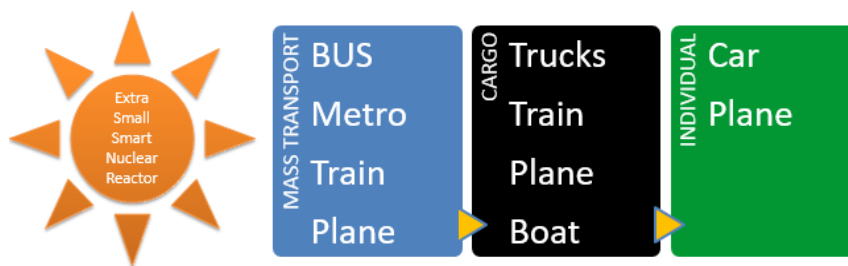


Figure 5 Further possible application fields of smart nuclear reactors

#### 5. POSSIBLE PROBLEMS WITH THE TECHNOLOGY

As a researcher we have to talk about disadvantages of this technology parallel with the advantages. There are a lot of factors that can cause serious problems. After we were able to crate the smart nuclear reactor, we have to issue of protection of the smart reactor must be addressed immediately. Some disadvantage factors are present at the figure below.



Figure 6 Possible Failures

## CONCLUSIONS

In the near future I think that the scientists and researcher will be able to build a small and smart nuclear reactor which will fulfil all the requirement both engineering and environmental approach. Beside that we can recycle the end period nuclear cells and use those fuel cells to power our smaller reactors. This could be a bright future of the nuclear technology.

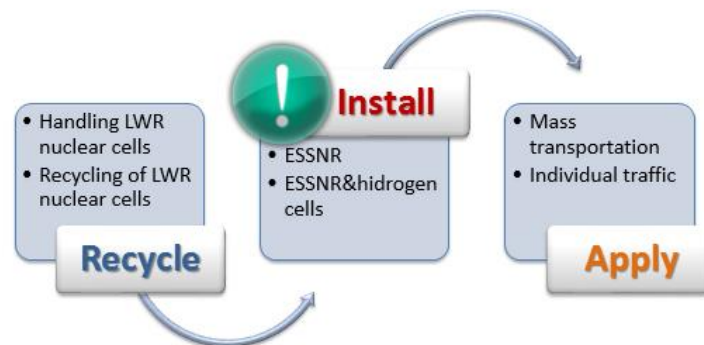


Figure 7 Schematic diagram of possible application technology

## ACKNOWLEDGEMENT

The publication is supported by the EFOP-[3.6.1-16-2016-00022](#) project. The project is co-financed by the European Union and the European Social Fund.

## REFERENCES

- [1] Majumdar, D. et al. Recycling of Nuclear Spent Fuel with AIROX Processing. United States: N. p., 1992. Web. doi:10.2172/10146308.
- [2] Williamson, M.A.; Willit, J.L.; Pyroprocessing flowsheets for recycling used nuclear fuel, Nuclear Engineering and technology, Volume 43, Issue 4, 2011, pp329-334. doi: 10.5516/NET.2011.43.4.329
- [3] Dresselhaus, M. S., & Thomas, I. L. (2001). Alternative energy technologies. Nature, 414(6861), 332-7. doi:http://dx.doi.org/10.1038/35104599



## INFLUENCE OF POST-TREATMENT METHODS ON MECHANICAL PROPERTIES OF PLA PARTS FABRICATED BY FUSED DEPOSITION MODELING

**BANJANIN Bojan, VLADIĆ Gojko PhD, DELIĆ Gordana, ADAMOVIĆ Savka PhD, KAŠIKOVIĆ Nemanja PhD**

*Department of Graphic Engineering and Design, Faculty of Technical Sciences, University of Novi Sad*

*E-mail: [bojanb@uns.ac.rs](mailto:bojanb@uns.ac.rs), [vladicg@uns.ac.rs](mailto:vladicg@uns.ac.rs), [gordana.delic@uns.ac.rs](mailto:gordana.delic@uns.ac.rs), [adamovicsavka@uns.ac.rs](mailto:adamovicsavka@uns.ac.rs), [knemanja@uns.ac.rs](mailto:knemanja@uns.ac.rs)*

### **Abstract**

*Fused Deposition Modelling (FDM) is one of the most commercialised 3D printing processes. In FDM process thermoplastic filament is used as a printing material. There are a lot of factors influencing the appearance of surface finish and mechanical properties of FDM printed parts. A fine surface finish can be obtained by optimisation of process parameters or by utilising one of the post-treatment methods. The aim of this research is to investigate the influence of two post-treatment methods on surface finish, dimensional accuracy and tensile strength of PLA parts printed by FDM technology. Results showed that both mechanical and chemical finishing method could improve surface finish but with the changes in dimensional accuracy. Samples treated with acetone solvent had reduced tensile strength but improved elongation at break showing greater ductility compared to untreated and sanded samples.*

**Keywords:** *3D printing, post-treatment, sanding, acetone bath*

### **1. INTRODUCTION**

Additive manufacturing, commonly referred to as 3D printing, has been around for more than thirty years, but recently it emerged in public and scientific circles as very promising and prolific technology. In additive manufacturing process material is added in the form of successive layers to produce the final product. Fused Deposition Modelling (FDM) is one of the most commercialised 3D printing processes. In FDM process thermoplastic filament is used as a printing material. The filament is drawn into the print head, melted and extruded through the nozzle onto printing surface in the form of semi-melted plastic threads. Cooling, threads solidify to form a layer of material. Additional layers are deposited on top of each other to form a 3D object. The FDM printer deposits material in a directional way thus producing parts with anisotropic behaviour [1]. 3D objects created by FDM are used not only as prototypes but also as functional parts. However, products manufactured with this technology has rough surfaces which often need to go through one of the post-processing methods. These rough surfaces are a consequence of extruded filaments (roads) in  $x$  and  $y$ -direction and deposited layers in  $z$ -direction of building plate.

#### ***1.1 Influence of process parameters on surface finish and mechanical properties***

Mechanical properties of FDM printed parts depend on various process-related parameters. Many authors investigated the influence of: extruder temperature [2], layer thickness [3], bead (road) width (width of the deposited filament) [4] orientation of model on printing plate [1,4], raster angle



[1,4,5], air gap [4], temperature of printing bed (envelope) and extruder [6], nozzle diameter, printing speed [7], part fill style (infill) [8] and number of shells (contour width) [9] on mechanical properties of FDM parts. Influence of different process parameters on surface finish was also investigated. Correlation between part deposition orientation and surface finish is investigated in the works of [10,11]. In the work of [12], efforts were made to establish the influence of layer thickness on the surface finish. Bakar and his co-workers [13] investigated how layer thickness, contour width and internal raster affect bonding quality between deposited filaments and its influence on surface finish. These researchers confirm that with appropriate setting of process parameters, better quality of surfaces on FDM printed parts can be obtained.

### ***1.2 Influence of post-treatment on surface finish and mechanical properties***

Post-treatment of FDM printed parts can be done by mechanical or by chemical treatment. Pandey et al. [14] investigated the use of hot cutter machining to improve the surface finish of printed parts. In the work of [15], FDM printed ABS parts were immersed in a dimethyl ketone and water solution for 180 to 420 seconds to obtain a better surface finish. Results showed that this chemical treatment could drastically improve the surface finish of ABS prototypes, improve flexural strength and reduce its dependency on the raster angle. However, the tensile strength of the specimens was decreased. Peroco et al. [16] also investigated the effect in dimethyl ketone and water solution for 300 seconds and found that reduction of surface roughness of ABS parts was up to 90% with improved mechanical properties in some cases. Post-treatment of polylactic acid (PLA) with dichloromethane was investigated in work of Jin et al. [17]. They used cold vapour method after which they concluded that this approach not only decreases the roughness of parts manufactured in FDM significantly, but also improves the toughness of PLA parts. There is also known that vapours of tetrahydrofuran can polish the surface of PLA parts, but its influence on mechanical properties of treated parts is not known. Also, the influence of acetone vapours or baths is not investigated on PLA samples. According to [18], acetone as a polar aprotic solvent ( $HSP_{\text{acetone}} = 20,1 \text{ MPa}^{1/2}$ ) are suitable solvent for PLA film ( $HSP_{\text{PLA}} = 21,2 \text{ MPa}^{1/2}$ ). If the HSP values of the organic solvent and the given polymer are near, the solvent is considered compatible with the polymer material. The aim of this paper is to investigate the influence of mechanical treatment and chemical treatment on surface roughness, dimensional accuracy and mechanical properties of PLA samples.

## **2. METHODS**

To investigate the influence of two different post-treatment methods on surface roughness, dimensional accuracy and mechanical properties of samples printed with PLA, tensile and visual assessment test were conducted.

### ***2.1 Specimens***

There are no defined standards related to testing mechanical properties of parts printed by FDM printing technology and the common choice for covering this issue is ASTM D638-14 standard [19] or its ISO 527-1 technical equivalent for the tensile test. Dimensions of printed samples are taken from this standard for Type I specimen.

### ***2.2 Procedure***

CAD model was created after choosing appropriate specimen geometry, using Autodesk Inventor Professional 2016. CAD model was then converted to STL (Stereolithography) file format required



by pre-processing software Makerbot Desktop, which prepares a model for the 3D printing process. PLA samples were printed using Makerbot Replicator 5th generation. Printing parameters were set to infill density 100%; layer thickness of 0,15 mm with three shells. Raster orientation was 0°/90° crisscross infill. Samples were printed with a head speed of 90 mm/s using rafts. Extruder temperature for PLA samples was set to 225 °C. Layers were printed perpendicular to each other. First layer at raster angle of 0° along the specimen length and next layer at raster angle of 90° (crisscross), and so on, up to the final 22nd layer. Finished specimens were separated from the raft and cleaned. Nine samples were printed in total. After printing, six of those nine samples undergo post-treatment (three for sanding and three for chemical treatment). Three samples were untreated and served as a control group. Dimensions of all samples before post-treatment and after the procedure were recorded using a digital calliper. Mechanical treatment of samples was done with fine grade sandpaper (100 grit and 320 grit) using continuous circular strokes under flow of cold water. Samples were sanded on each side for 3 minutes and 30 seconds with rougher (100 grit) and then for another 1 minute and 30 seconds with finer sandpaper (320 grit). Water was used in order to avoid heating of PLA material during the sanding process. Chemical treatment of PLA samples was done using acetone bath (p.a.  $\geq 99\%$ ). Optimum immersion time for sample testing gathered in pre-tests was found to be 40 seconds. After post-treatment, the tensile test was performed using Shimadzu Compact Tabletop Testing Machine EZ-LX equipped with a 2.5 kN load cell. Samples were loaded and tested at 5 mm/min loading rate. All tests are carried out at the temperature  $23 \pm 2^\circ\text{C}$  and relative humidity  $50 \pm 5\%$  as per ISO R291:2008 [20]. Data for tensile stress and strain were collected using Trapezium X software, and maximum tensile stress, strain and elastic modulus were automatically calculated. Finally, digital USB microscope Vitiny VT300 with the magnification of 10x was used to acquire images of the cross section in fracture zones of the samples and surfaces of the samples.

### 3. RESULTS AND DISCUSSION

Dimensions of printed samples before and after post-treatment are presented in Table 1. Mechanically treated samples had reduced dimensions due to the removing of the material during the sanding process. Chemically treated samples had increased dimensions compared to untreated ones but only to a small degree. This was probably due to a reaction where the extruded filament of PLA swelled after exposure to acetone.

Table 1 Dimensions of the PLA samples before and after post-treatment

	Sample number	Untreated		Mechanically treated		Chemically treated	
		Height (mm)	Width (mm)	Height (mm)	Width (mm)	Height (mm)	Width (mm)
Before post-treatment							
	Avg.	3,27	13,14	3,23	13,13	3,20	13,14
	StDev	0,02	0,0451	0,036	0,031	0,005	0,046
After post-treatment							
	Avg.	3,27	13,14	2,96	12,98	3,27	13,15
	StDev	0,02	0,0451	0,031	0,061	0,012	0,075

The appearance of the surface of untreated, mechanically and chemically treated samples are presented in Figure 1. Figures 1a, 1b and 1c represent the appearance of top layer surfaces and Figure 1d, 1e, 1f represent side surfaces of the specimens. It can be seen that the top surface of the untreated samples had visible filaments which are due to characteristics of FDM technology.



Staircase effect can be seen on the side surface of untreated samples which is a consequence of deposition of filaments in layers along  $z$ -axis. Mechanically treated samples produced a high polished top surface with barely visible filaments. This is the case in the areas where there are no gaps between filaments or other inconsistencies. Side surface was also polished with partially visible layers. To produce flat polished surface without visible layers or filaments (roads), chemical treatment is often used. In our case, acetone bath leads to surprisingly good result regardless of the fact that acetone is used commonly to dissolve ABS material. Chemical treatment produced top surfaces with uniform structure without visible filaments, but only at areas which did not have large gaps in the top layer. Staircase effect from side surfaces was eliminated.

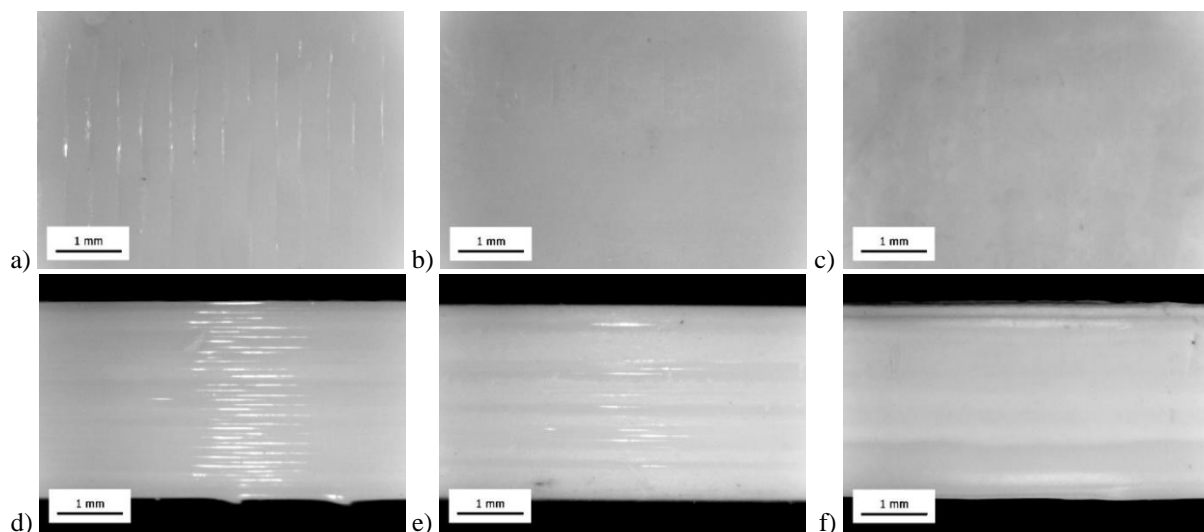


Figure 1 Appearance of top (a,b,c) and side surfaces (d,e,f) of differently treated PLA samples

Break stress values for untreated, mechanically treated and chemically treated samples were 37,58 MPa (StDev. = 2,67 Mpa), 33,72 MPa (StDev. = 1,37 MPa) and 21,37 MPa (StDev. = 0,41 MPa), break strain values were 2,32 % (StDev. = 0,071 %), 2,28 % (StDev. = 0,051 %) and 2,79 % (StDev. = 0,25 %) respectively. Elastic modulus values were 2057,11 MPa (StDev. = 50,4 MPa) for untreated, 2061,47 MPa (23,61 MPa) for mechanically treated and 1388,41 MPa (StDev. = 32,99 MPa) for chemically treated samples. Results showed that samples treated with either method caused degradation in tensile strength. There was a slight decrease in tensile strength of mechanically treated specimens and similar elongation at break values. Chemically treated samples were more ductile and had greater elongation at break values. These findings are in accordance with findings of [28]. Plastic nature of chemically treated samples can also be seen from stress-strain curves in Figure 2.

Figure 3 illustrates a close-up view of the fracture zones of untreated, mechanically and chemically treated samples of PLA respectively. Cross section in fracture zones shows that in the case of untreated and mechanically treated samples inter-layer bonds remained unchanged. Larger air gaps in mechanically treated sample (Figure 3b) are probably produced during printing and not during the sanding process. On the other side, there is a visible alteration of inside layers of the chemically treated samples (Figure 3c). It can be seen that acetone penetrated the porous inner structure of PLA samples which affects inter-layer bonds in the several top and bottom layers.

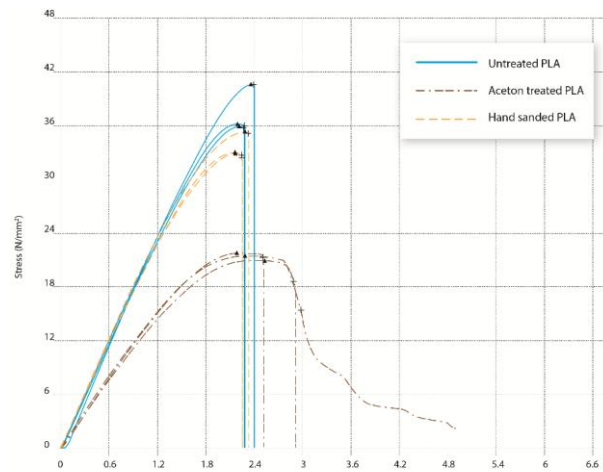


Figure 2 Stress-strain curve of differently treated PLA samples

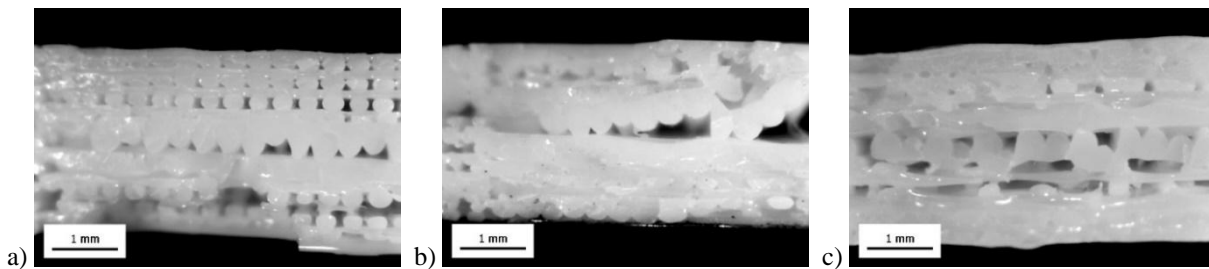


Figure 3 Cross section view of the fracture zones after tensile tests on a) untreated, b) mechanically treated and c) chemically treated samples

## CONCLUSIONS

The influence of mechanical and chemical post-treatment methods on dimensional accuracy, surface finish and tensile strength of PLA samples fabricated by FDM technology was investigated. It was found that both methods can improve the appearance of the PLA surface. Mechanically treated samples undergo reduction of sample dimensions compared to samples treated with acetone solution which in contrary had increased width and height values.

The appearance of top and side surfaces after post-treatment was improved compared to surfaces of untreated samples. The finished surfaces of mechanically treated specimens had the finest surface of all tested samples but with greater reduction in dimensions. Chemical treatment provided fine surface finish but with visible filaments on areas where they were not bond well due to the printing process. The tensile strength of untreated specimens was greater compared to specimens treated with both methods. Mechanically tested samples had similar tensile strength as untreated samples due to the unchanged inner structure of the part and inter-layer bonds. However, after chemical treatment, samples suffered changes in the structure of the polymer and inter-layer bonds not only on the surface but also in inner layers of the specimens. This method removed staircase effect on the side surface and also toughness of the samples due to improved elongation at break. Untreated and mechanically treated samples showed brittle behaviour compared to increased ductile nature of chemically treated samples. It can be concluded that acetone solution alters the PLA structure in such a way that finer appearance of the surface can be obtained but at the expense of mechanical properties. Finer control over the chemical treatment could probably provide better results in terms of dimensional stability. Further, a combination of mechanical and chemical finishing could lead to better surface finish. Testing PLA samples printed by FDM with different solvents, different



concentrations and exposure times could also provide better insights into post-processing parameters needed for the superior surface finish.

## ACKNOWLEDGMENTS

The research is supported by the Ministry of Education, Science and Technology Development of the Republic of Serbia, project number: 35027 “Development of software model for scientific and production improvement in graphic industry”

## REFERENCES

- [1] Ahn, S.H., Montero, M., Odell, D., Roundy, S., Wright, P.K.: *Anisotropic material properties of fused deposition modeling ABS*. Rapid prototyping journal, 8 (4), 248-257, 2002.
- [2] Drummer, D., Cifuentes-Cuéllar, S. and Rietzel, D.: *Suitability of PLA/TCP for fused deposition modeling*. Rapid Prototyping Journal, 18(6), 500-507., 2012.
- [3] Letcher, T., Rankouhi, B., Javadpour, S.: *Experimental study of mechanical properties of additively manufactured ABS plastic as a function of layer parameters*, In: ASME 2015 International Mechanical Engineering Congress and Exposition, American Society of Mechanical Engineers, V02AT02A018-V02AT02A018, 2015.
- [4] Bellini, A., Güçeri, S.: *Mechanical characterization of parts fabricated using fused deposition modelling*. Rapid Prototyping Journal, 9 (4), 252-264, 2003.
- [5] Tymrak, B.M., Kreiger, M. Pearce, J.M.: *Mechanical properties of components fabricated with open-source 3-D printers under realistic environmental conditions*. Materials & Design, 58, 242-246, 2014.
- [6] Sun, Q., Rizvi, G.M., Bellehumeur, C.T. and Gu, P.: *Effect of processing conditions on the bonding quality of FDM polymer filaments*. Rapid Prototyping Journal, 14(2), 72-80, 2008.
- [7] Žarko, J., Vladić, G., Pál, M., Dedijer, S.: *Influence of printing speed on production of embossing tools using FDM 3D printing technology*. Journal of graphic engineering and design, 8(1), 19-27, 2017.
- [8] Hwang, S., Reyes, E.I., Moon, K.S., Rumpf, R.C. and Kim, N.S.: *Thermo-mechanical characterization of metal/polymer composite filaments and printing parameter study for fused deposition modeling in the 3D printing process*. Journal of Electronic Materials, 44(3), 771, 2015.
- [9] Lanzotti, A., Grasso, M., Staiano, G., Martorelli, M.: *The impact of process parameters on mechanical properties of parts fabricated in PLA with an open-source 3-D printer*. Rapid Prototyping Journal, 21(5), 604-617, 2015.
- [10] Thrimurthulu, K., Pandey, P.M., Reddy, N.V.: *Optimum part deposition orientation in fused deposition modeling*. Int. J. Mach. Tools Manuf., 44, 585–594, 2004.
- [11] Garg, A., Bhattacharya, A., Batish, A.: *On surface finish and dimensional accuracy of FDM parts after cold vapor treatment*. Mater. Manuf. Process. 31, 522–529, 2016.
- [12] Anitha, R., Arunachalam, S., Radhakrishnan P.: *Critical parameters influencing the quality of prototypes in fused deposition modeling*, Journal of Materials Processing Technology, 118, (1–3), 385–388, 2001.
- [13] Bakar, N.S.A., Alkahari, M.R., Boejang, H.: *Analysis on fused deposition modelling performance*, Journal of Zhejiang University-SCIENCE A (Applied Physics & Engineering), 11/12, pp. 972-977, 2010.
- [14] Pandey, P.M., Reddy, N.V. and Dhande, S.G.: *Improvement of surface finish by staircase machining in fused deposition modelling*. Journal of Materials Processing Technology, 132,



# INTERNATIONAL SCIENTIFIC CONFERENCE ON ADVANCES IN MECHANICAL ENGINEERING

12-14 October 2017, Debrecen, Hungary



323-331, 2003.

- [15] Galantucci, L.M., Lavecchia, F. and Percoco, G.: *Quantitative analysis of a chemical treatment to reduce roughness of parts fabricated using fused deposition modeling*. CIRP Annals-manufacturing technology, 59(1), 247-250, 2010.
- [16] Percoco, G., Lavecchia, F. and Galantucci, L.M.: *Compressive properties of FDM rapid prototypes treated with a low cost chemical finishing*, Research Journal of Applied Sciences, Engineering and Technology, 19(4), 3838-3842, 2012.
- [17] Jin, Y., Wan, Y., Zhang, B. and Liu, Z.: *Modeling of the chemical finishing process for polylactic acid parts in fused deposition modeling and investigation of its tensile properties*. Journal of Materials Processing Technology, 240, 233-239, 2017.
- [18] Sato, S., Gondo, D., Wada, T., Kanehashi, S. and Nagai, K.: *Effects of various liquid organic solvents on solvent-induced crystallization of amorphous poly (lactic acid) film*. Journal of Applied Polymer Science, 129(3), 1607-1617, 2013.
- [19] ASTM International: *ASTM D638-14, Test Method for Tensile Properties of Plastics*. Pennsylvania, United States, 2014.
- [20] ISO 291:2008: *Plastics – Standard Atmospheres for Conditioning and Testing*, 2008.



## VIBRATION MEASUREMENT ON RECONDITIONED SEMI-HERMETIC COMPRESSOR

*BELÉNYI Alpár, ACHIMAȘ Gheorghe DSc*

*Department of Manufacturing Engineering, Technical University of Cluj-Napoca*

*E-mail: [alpar\\_belenyi@yahoo.com](mailto:alpar_belenyi@yahoo.com), [gheorghe.achimas@tcm.utcluj.ro](mailto:gheorghe.achimas@tcm.utcluj.ro)*

### **Abstract**

*The dilution of oil by the freezing agent is a problem met in the cooling industry. The semi-hermetic compressor suffered such a failure, where some pieces failed because of the unequal greasing. We have used different methods of reconditioning, where these pieces were reconditioned. After assembly, check and a free testing, comes the testing under work. There will be measured: the vibrations, the work pressures, the working temperatures and in the end a thermographic measurement. These measurements will be compared to the measurements made before reconditioning at failure compressor. After comparison, we will deduce the conclusion that the reconditioned compressor is functioning in the optimal parameters in work or not.*

**Keywords:** *recondition, vibration, semi-hermetic compressor, measurement, failure.*

### **1. INTRODUCTION**

Semi-hermetic compressor, type: DLEE-201, suffered a failure because of the dilution of oil caused by the freezing agent[1][2]. This failure is characterized, the oil presenting a huge affinity with the freezing oil being mixable with it. In the case of an elongated stop, it's possible to become diluted enough with the agent, to lose its lubing properties, like in our case. The damaged pieces in our compressor, because of the unequal lubing were: the eccentric shaft and the winch. After the effectuated researches, It was chose the following types, of reconditioning on the pieces[3]:

- eccentric shaft: the method of reconditioning through metalizing
- winch: the reconditioning through fabrication of two new winches

After the remedy of failures with the help of reconditioning, the compressor was assembled, the oil being changed with new oil, new stuffing etc.[1] After this, the compressor will be equipped back in the aggregate, while the aggregate will be vacuumed, after this it will be filled with clean freezing agent(R404A) and the compressor will be tested at work. Further the compressor will be placed under measurers, verifying functioning parameters (vibrations, temperatures, pressure, etc), which way we will prove the compressor is working under optimal parameters even after reconditioning, repairs.

In this article we will present vibration measurers of the reconditioned semi-hermetic compressor. The damaged compressor underwent vibration measurements before the damaged parts being repaired. These measures will be compared with the measures after reparations and reconditioning of the compressor. It was chose measuring with the following device: vibration measuring device (ME42).

### **2. DESCRIPTION OF MEASURING GAUGES**

ME 42 is a vibration measurer-analyzer machinery, failure detector ("machinery expert") hand device.[4]The ME42 measures machinery and bearings vibrations, RPMs, and optionally



temperature as well. But more importantly: the ME42 is a machinery expert! It's not just capable of measuring wideband vibrations, spectrum analysis, demodulation, acceleration measuring based and L type bearings analysis according to ISO 10816 standards but it also does a machinery failure diagnosis. The machinery failure detection capabilities of the ME42 are competing with many expert systems running on computers. Its biggest advantage is that the information concerning the possible failure is available – near the diagnosed machinery – right during the measuring. There's nothing better like getting information right near the machinery, which can help in deciding fast and effective about further analysis or immediate intervention.



*Figure 1* Vibration measuring device ME42

According to ISO 10816 this device is capable of the following functions:

- wideband measuring functions of vibrations;
- spectral analysis;
- temperature measurement;
- acceleration measurement;
- analysis of bearings;
- it's making failure detections of the equipment more efficient.

This device can be used by maintenance personnel, without them knowing the equipment at which it intervenes.

### **3. ANALYSIS OF COMPRESSOR VIBRATIONS**

It's one of the most used methods of detecting and diagnosing failures in electrical machine systems. Through this method are measured the system's vibrations, usually with a vibration measuring device, after which the spectrum of generated frequency is examined, for the identification of significant frequencies, from point of view of the machinery's condition. Some frequencies are part of the system's normal functioning. The modifications of some specific harmonic's amplitudes, could suggest the presence of a failure. The data can be collected periodic, utilizing a portable or fixed system like the ME42 device. Through vibrations we can detect failures such as: unbalance, problems in the chambers, structural resonance, rotation failures at electric machines, eccentricities, etc. The measurers are fast and they don't influence the system's functioning. For each electromagnetic system we define an own level of vibrations, any derivations from this indicating a problem, so that we can intervene before the system could deteriorate. Some standards also exist which set a specific level of vibrations and operating speeds for groups of equipments. These can be used as comparison references for setting a vibration level for specific equipments.[5]

At freezing compressors (in our case semi-hermetic compressor) all vibrations have specific properties, which are determined by the process the vibrations are generated.[6][7] Each compressor has different vibration imprint. When measuring the vibrations of a compressor, the vibrations'



speed is measured, the acceleration of vibrations in gravity and high frequency vibrations. These measurers are showcased on the graphic and are compared. These analysis of the vibrations will predict if we have any failure of the component piece. In our case of measuring the vibrations we focused on mechanism: eccentric shaft and winch because these pieces were damaged and they were reconditioned. An analysis of mechanic vibrations for a compressor requires a maximum of 30 different readings, at different points of the compressor, so we can get true analyses.

## 4. MEASUREMENTS AND RESULTS

### 4.1. Measuring of vibrations

We did 30 different readings on our compressor, on different points of the compressor (horizontal,vertical,axial) for vibration analysis. On the ME42 device we used the: *ISO-BRG functions*, where we considered the sums got in ISO. This graphical reading shows the vibration levels according to the ISO 10816-1. The optimal level of vibration is under 3 mm/s. We also used the function: *FFT/DEMODO* – this function is used for measuring manual vibrations. During the FFT from the time function of the signal becomes a frequency-amplitude function. In this function are represented the measured vibration's components of different frequency and magnitude. These 30 readings will be summarized and will be shown in an evaluation at final in a program.

#### a) Vibration measuring on the reconditioned compressor

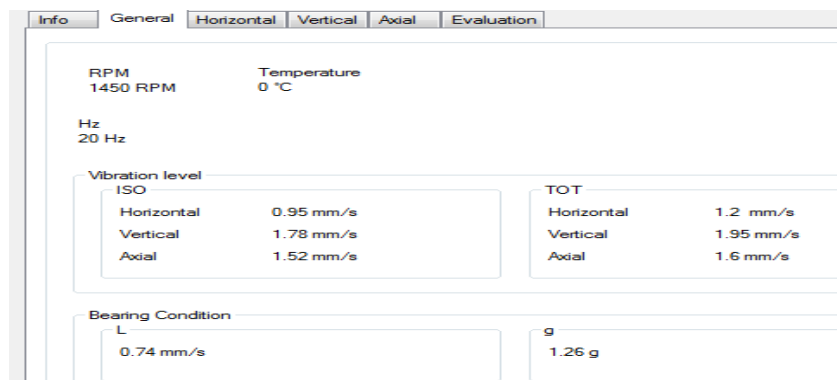


Figure 2 General measurements

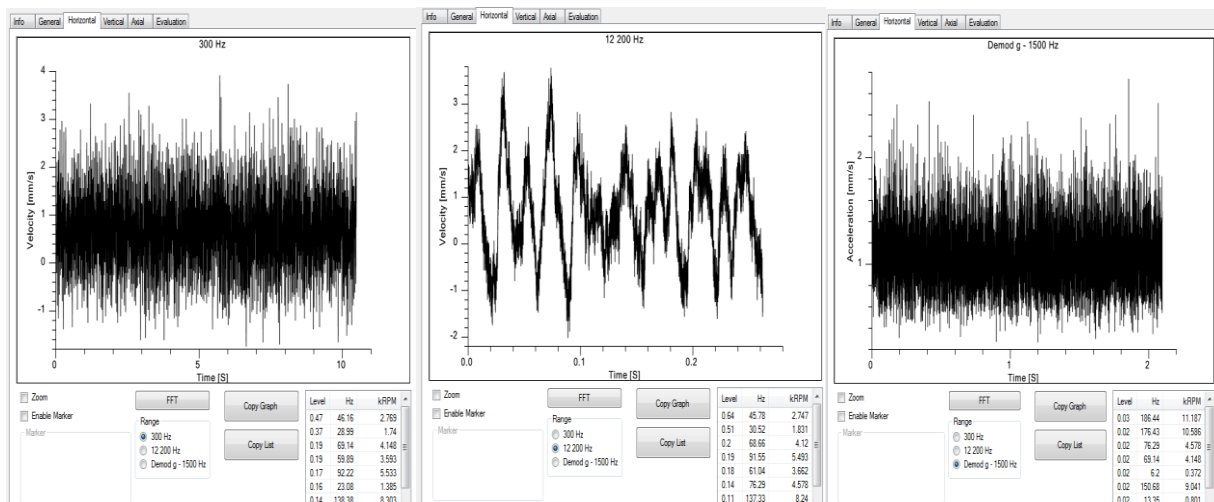


Figure 3 Horizontal vibration frequencies



# INTERNATIONAL SCIENTIFIC CONFERENCE ON ADVANCES IN MECHANICAL ENGINEERING

12-14 October 2017, Debrecen, Hungary

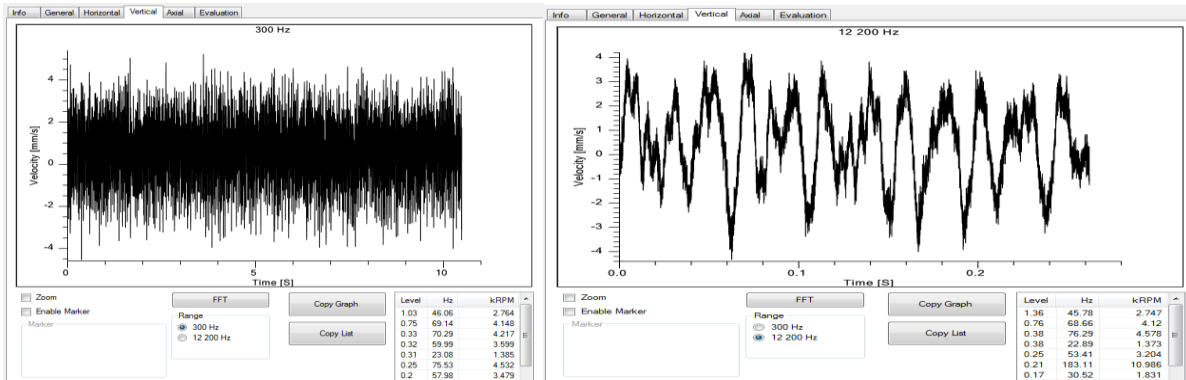


Figure 4 Vertical vibration frequencies

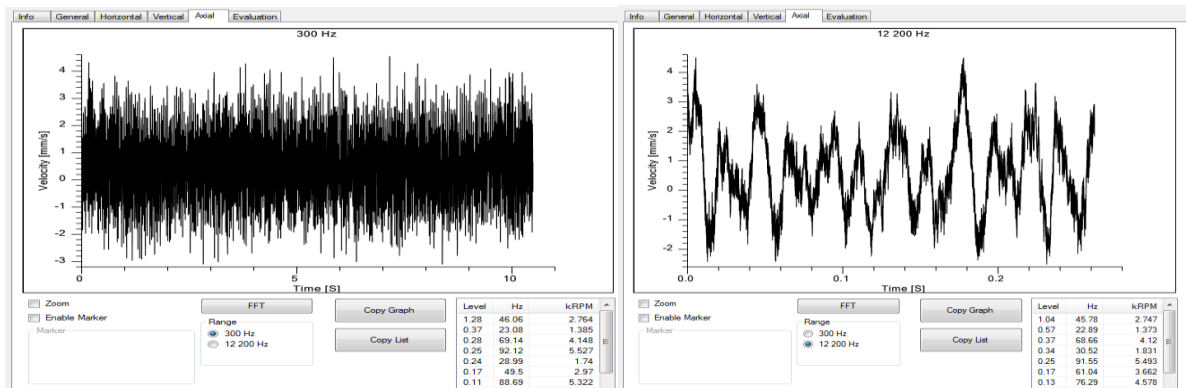


Figure 5 Axial vibration frequencies

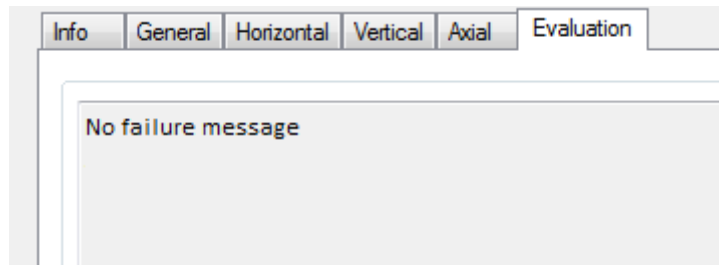


Figure 6 Evaluation of vibration measurements

## b) Vibration measuring on the failing compressor

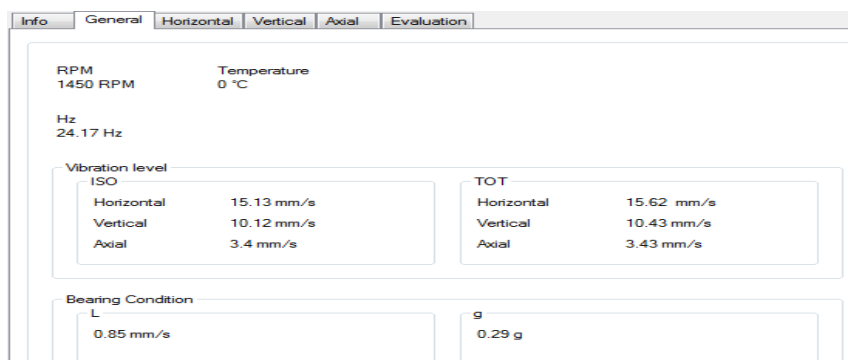


Figure 7 General measurements



# INTERNATIONAL SCIENTIFIC CONFERENCE ON ADVANCES IN MECHANICAL ENGINEERING

12-14 October 2017, Debrecen, Hungary

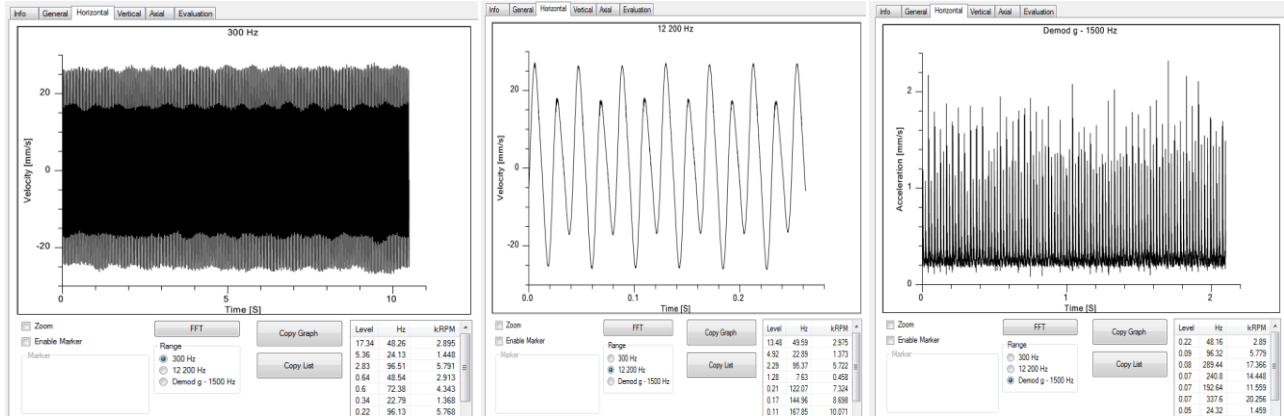


Figure 8 Horizontal vibration frequencies

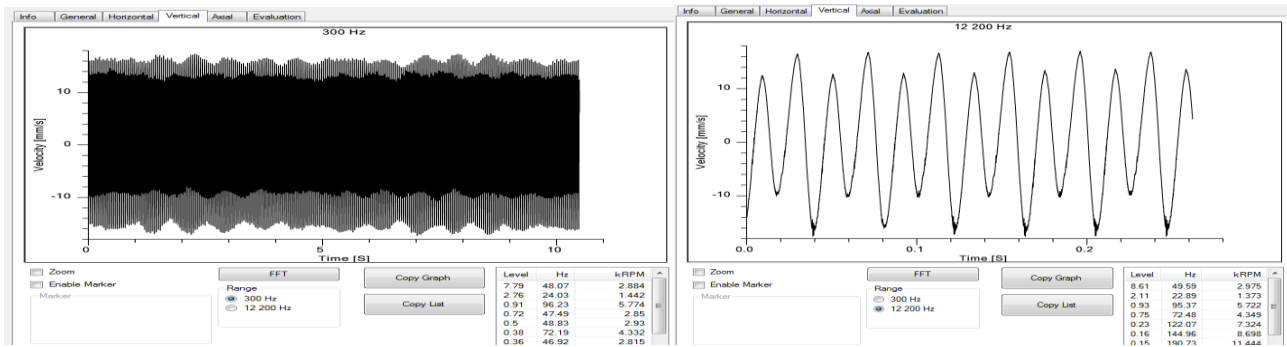


Figure 9 Vertical vibration frequencies

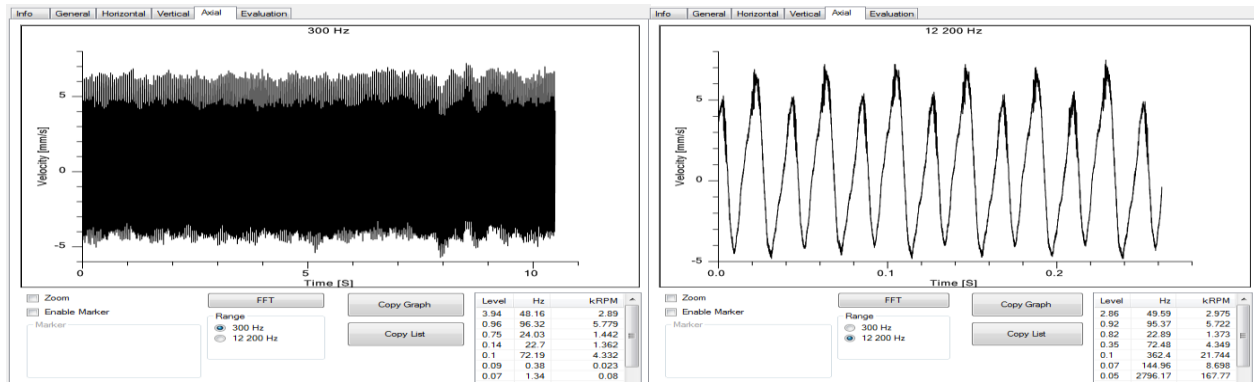


Figure 10 Axial vibration frequencies

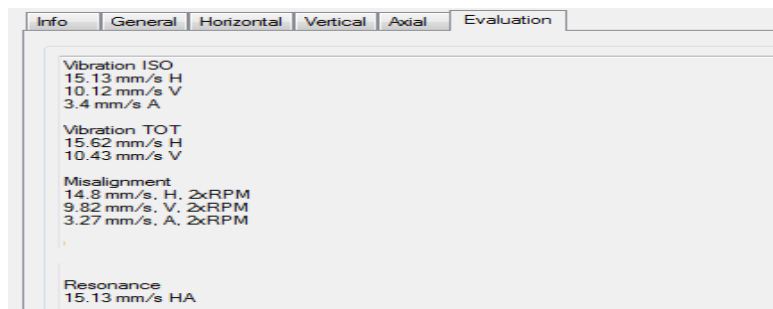


Figure 11 Evaluation of vibration measurements



#### 4.2. Results of measurements

In subchapter 4.1 was presented the measurements on the semi-hermetic compressor.

At reconditioned compressor, can see that we got good values. Vibration levels at general was: horizontal 0,95mm/s; vertical ;1,78mm/s; axial 1,52 mm/s and bearing level is 0.43mm/s. These values are very good, they do not exceed the limit of 3 mm/s, which would mean that we have something nerogorous. .Bearing level is under0,75mm/s( $0.43\text{mm/s} < 0.75\text{mm/s}$ ) what it means, the bearing after replacement works well.

At failing compressor we can see that the received values exceed the limit of 3mm/s. Vibration levels at general was: horizontal 15,13mm/s, vertical 10,12mm/s and axial 3,4mm/s and bearing wear is 0.84mm/s. Vibration evaluation was: total vibration 15,62mm/s at horizontal; 10,43mm/s at vertical. It was received value of misalignment: 14,8mm/s(2xRPM) at horizontal; 9,82mm/s(2xRPM) at vertical; 3,27(2xRPM) at axial and resonance 15.13mm/s horizontal and axial. These vibration values is meaning: parallel fault, both angle and paralel fault, diffuser and piston type problem. These vibration data predicts that in which and shaft area, we have wear or faulty. Bearing level is bad while it is bigger(0.84mm/s) than the normal value level (0.75mm/s).

If we compare the values received at both compressors, we can define that the reconditioned compressor has received good values, thi s works at the optimal parameters. At the failing compressor vibration values define that we have problems on the parts, which means that the we must intervene as soon as possible, to repair it.

#### CONCLUSIONS

With the help of vibration measurers which we effectuated we proved that the compressor is working with optimal parameters, after reconditioning the deteriorated pieces. The reconditioned compressor emits only acceptable operating vibrations, compared to the broken one which's vibrations go over the limit values. To measure other vibration frequencies as well on the reconditioned compressor, we will use other types of oil and freezing agent on the aggregate to see if the vibrations are the same when under work or if they are different.

In the future we will also utilize other methods of measuring on the reconditioned compressor and these are:

- analysis of functioning temperature and operating pressure;
- thermographic images and level of noises emitted by the compressor; etc.

These measurements are made with modern devices, which will be useful in the future as well from maintenance point of view, because if we check with these devices in specific intervals, with the utilized equipment we can prolong its life, discovering its failures. The goal of measurers is also introducing new elements in preventive maintenance by using them.

#### REFERENCES

- [1] I.Culescu, *Manualul mecanicului frigotehnist*, Editura de stat didactică, București 1962.
- [2] \*\*\*[www.termo.utcluj.ro/ufa/ufapdf/ufa14.pdf](http://www.termo.utcluj.ro/ufa/ufapdf/ufa14.pdf)
- [3] C.Mitroi, *Tehnologia recondiționării pieselor uzate*, Editura Tehnică, București 1968
- [4] \*\*\*[www.pim-kft.hu/termékkinálat](http://www.pim-kft.hu/termékkinálat)
- [5] Gh.Buzdugan, *Vibrații mecanice*, Editura didactică, București 1979
- [6] Shapiro U., *The role of estimating the stiffness of rolling element bearings in the analysis of semi-hermetic, twin, screw compressors*, International Compressor Engineering Conferenc 1992
- [7] Singh R. And Sodel W., *Journal of Sound and Vibration*(56,57,63), 1978



## EFFECTS OF SURFACE TREATMENT TO THE PROPERTIES OF RAILWAY CONTACT WIRES

<sup>1</sup>BENCHABANE Ahmed Elmehdi, <sup>2</sup>BARKÓCZY Péter PhD

<sup>1</sup>Faculty of Materials Engineering, University of Miskolc

E-mail: [benchabane.am@outlook.fr](mailto:benchabane.am@outlook.fr)

<sup>2</sup>FUX Co.

E-mail: [peter.barkoczy@fux.hu](mailto:peter.barkoczy@fux.hu)

### Abstract

*A surface treatment of bare overhead conductors is a well-known technology. It is examined and states that the same treatment can be applied on railway contact wires. In the case of railway catenaries, we use the additional advantages as shown in the case of overhead conductors. The article analyses the effect of the emissivity of the conductor to the operation of the catenary line.*

**Keywords:** *surface treatment, emissivity, wire, copper.*

### 1. INTRODUCTION

Cable producers regularly manufacture surface treated bare conductors. In case of high voltage bare overhead conductors, this is a usual product. Generally there are two main reasons for the heat treatment. First is to reduce the audible noise by coronary radiation. Second, is to terminate the gleaming of the conductor. Both treatments have an importance next to the residential areas where the two effects disturb people.

In the first case we change the nature of the surface. The as-manufactured conductors have a hydrophobic surface. The water does not wet the surface but forms big drops on the surface in rainy, moist or foggy weather. The large electric field can deform the drops, and initiate the coronary effect. The corona radiation produces an audible noise, which can reach a high level in larger moisture content of the air [3]. Besides the audible noise, the corona radiation means an additional loss in the transmission system, which means a comparable amount with the Ohmic loss in rainy periods. If a surface treatment can reduce the level of the audible noise, it will also reduce the corona loss. Therefore, several solutions can be found for this in the literature. FUX develops a technology which is based on a mechanical treatment without foreign material addition. With this treatment, the surface of the conductor becomes hydrophilic so when the water nearly perfectly wets the surface, it won't form drops on the conductor. So, the audible noise level becomes lower where it doesn't disturb people.

In the second case, the aim of the treatment is to avoid the gleaming of the conductor in crossings. The surface of the as-manufactured bare overhead conductor is shiny and smooth. To obtain the desired effect, FUX uses a chemical treatment to change the colour of the conductor's surface to dark grey (RAL 9700).

It is well known that the same effect occurs due to pollution and corrosion after 15-20 years. The surface of the conductor becomes grey (not as dark as RAL 9700) and the audible noise also decreases, but within the mentioned period we have to prove the same properties of the bare overhead conductors in the mentioned applications.

Both surface treatments change the emissivity of the conductors besides the primary effect. In both cases the emissivity of the surface increases. The larger emissivity proves larger cooling of the



conductor, therefore, due to enhanced cooling, the same load means a lower operating temperature. The resistivity of the conductor is smaller at lower operating temperatures, which means smaller Ohmic loss while taking into consideration the maximal operating temperature because a larger emissivity means larger current carrying capacity. This value can reach an 11% increment in high voltage bare overhead ACSR conductors.

Additionally, the changes in emissivity cause changes in icing of the conductor. Several articles deal with this phenomena where the basics of icing are extensively studied [1,2], but only few articles have mentioned the effect of the changes in emissivity. In bare overhead conductors, the icing is an important matter, because in emergency cases it can cause a catastrophe in the case of the conductor breakage. But it is important to know the relation between the weather conditions and the icing in particular areas.

The surface treatment of the conductors in railway catenaries is not a usual technique. The main reason is that there should be a robust electrical connection between the contact wire and the pantograph. Several researchers have examined this contact where the treatment has been performed without foreign material addition, and it can be applied in railway conductors, because this does not have an effect on the electrical connection to the pantograph.

This article shows the results of this treatment. Also, the effects on the overhead conductors and railway catenaries. The literature shows some models of icing and the effect of emissivity to the icing. The effect of the emissivity changes on the railway conductors is also analysed.

## 2. METHODS

The tested conductors and wires in the Laboratory of Wire and Conductor Diagnostics. The Laboratory supervised by jointly FUX and University of Miskolc and situated at the plant of FUX. The conductors were heated up with a high current tester and the temperature of the conductors was measured by thermocouples and using the thermo-vision. The resistivity, strength and elongation of the wires were measured according to the standard descriptions. The results were evaluated and analysed in the following section.

## 3. RESULTS

The effect of the surface treatment was tested by water spraying. After a certain time with a continuous spraying, the drops were visually analysed. After that, the main question was the size and the number of drops.

If the drops are not visible, this means the desired result was obtained. *Figure (1)* shows the water spraying test of the overhead conductors with and without the surface treatment.



*Figure 1* Results of the water spraying test of on as-manufactured ACSR conductor (left) and on a surface treated conductor (right)



As it can be seen on *Figure (1)*, large drops form on the surface of the as-manufactured conductor. Contrary to the first case, water drops were not formed on the surface treated conductor. Therefore we conclude that the applied surface treatment prevents the occurrence of corona radiations on the surface of the conductor as *Figure (2)* shows.



*Figure 2* Observation of corona radiation at VEIKI-VNL. Conductor on the left side is the surface treated.

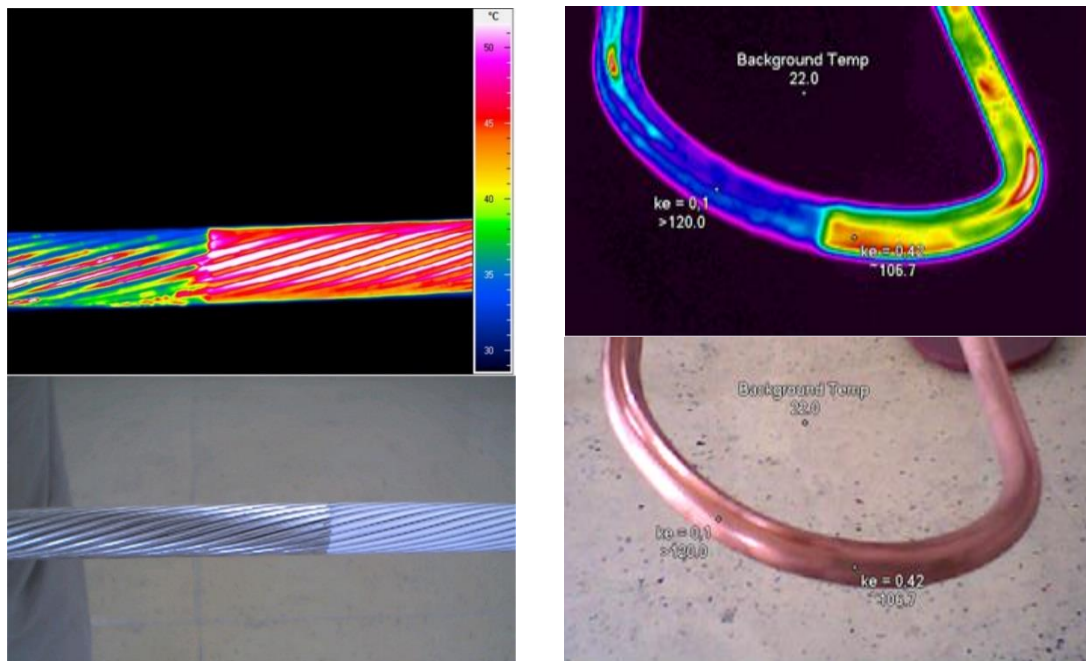


*Figure 3* Measurement of the emissivity of the surface treated conductors. Thermo-vision was used to determine the emissivity value. Both cases (overhead conductor and catenary contact wire) the emissivity 4x bigger in the surface treated area.

The emissivity of the conductors was measured by thermos-vision where the surface treatment was interrupted after a certain length. The same surface treatment was applied on an AC-100 contact wire as in the case of ACSR conductor. The conductors were heated up by current. *Figure (3)* shows the results of the observation, it can be seen that the treated surface gives more emissivity. The measured results show that the emissivity of the treated surface in both cases is nearly four



times bigger than the as-manufactured surface. The ampacity calculations shows that it means 11% increment in the current carrying capacity.

Elsewhere, it is proved by mechanical and electrical tests that the properties of the as-manufactured and the heat treated contact wires are nearly the same. *Figure (4)* shows the tensile strength of the wires, and the recrystallization behaviour. The strength and the starting temperature of the softening is the same in both cases. More cross sections and CU-ETP materials were tested [4].

The recrystallization starting temperature was determined based on 1h isothermal heat treatments.

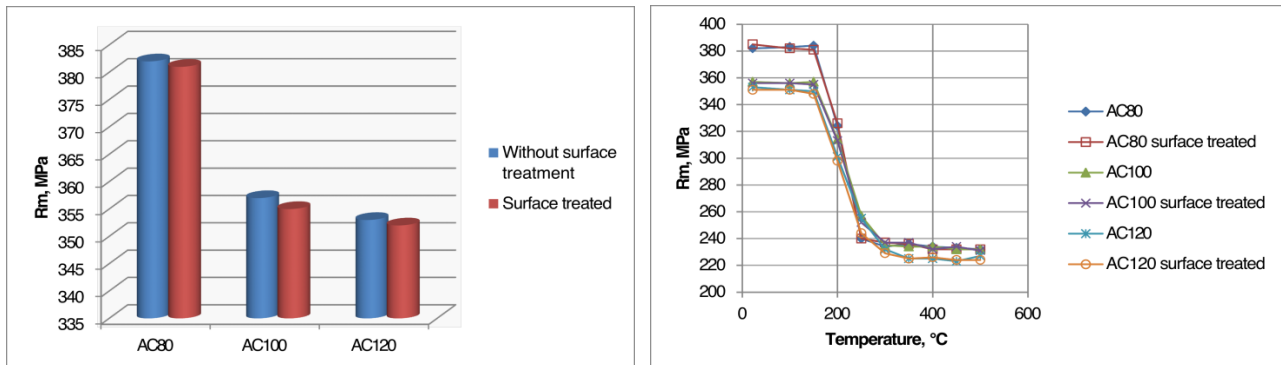


*Figure 4* Comparison of the tensile strength and the recrystallization start temperature (1h isothermal heat treatments). There is no difference between the surface treated and as-manufactured conductors.

The icing is an important matter in the railway catenary conductors because they are not under a continuous electrical load. Therefore, the risk of icing is larger and it is no possibility of heating the conductors with electrical load without train approaching. Articles show the effect of the surface treated bare overhead conductors against icing, but all study analyse the glaze ice accretion. This is the most dangerous case, because the glaze ice is an insulator layer on the conductor, and in a case of catenary conductors, the pantograph cannot touch the contact wire.

According to the models from the literature, the glaze ice forms when a water film exists between the conductor and the ice layer. This happens when the undercooling of the air at the conductor is not high, the conductor does not consume large heat from the air nor from ice. If the emissivity of the conductor becomes high, it can consume more heat from the environment. The undercooling becomes larger, and it could be possible that the liquid film disappears from the surface, then rime forms on the surface instead of the glaze ice. The analysis of the mentioned models are currently in progress to calculate the extent of this effect, but the surface treatment can produce a safer catenary system against icing. Because the pantograph can remove the rime from the conductor, but the glaze ice can destroy the structure of the pantograph.

## CONCLUSIONS

The surface treatment changes the emissivity of the surface of the conductors. This has a great effect to the current carrying capacity, and this also has some effect to the ice accretion. The article briefly introduces the basics of this effect and the operation consequences. FUX applies the same surface treatment on contact wires as applied in the case of bare overhead conductors. As the results and the properties of the new type of conductor were introduced previously, the new conductor's mechanical and electrical properties are the same as the as-manufactured one. Due to the emissivity increment, the current carrying capacity is greater in the surface treated conductor. In addition, the emissivity increment has a good effect to the icing, because the probability of the rime formation is larger than the as-manufactured conductors. The extent of this effect is now studied.



# INTERNATIONAL SCIENTIFIC CONFERENCE ON ADVANCES IN MECHANICAL ENGINEERING

12-14 October 2017, Debrecen, Hungary



## REFERENCES

- [1] Fochi Wang, Yuzhen Lv, Qing Zhang, Zhou You, Chengrong Li: *Ice Accretion on Different Aluminum Cable Steel Reinforced*. Annual Report Conference on Electrical Insulation and Dielectric Phenomena, p. 2, 2010.
- [2] Zsolt Péter, Masoud Farzaneh, László I. Kiss: *Assessment of the current Intensity for Preventing Ice Accretion on Overhead Conductors*. IEEE Transactions on Power Delivery, vol. 22, p. 567, Jan. 2007.
- [3] U.Straumann, H.J.Weber: *Potential Reduction of Audible Noise From New and Aged Overhead Transmission Line Conductors by Increasing Their Hydrophilicity*, ETH Zurich, Switzerland, 2010.
- [4] Barkoczy P: *Contact wires – conductivity is of prime importance*, Railway Pro, vol. IX, No 1-2., 2014



## COMPARATIVE TOOTH CONTACT ANALYSIS OF X-ZERO GEAR DRIVES IN THE FUNCTION OF THE MODULE CHANGING

**BODZÁS Sándor PhD**

*Department of Mechanical Engineering, University of Debrecen*

*E-mail: [bodzassandor@eng.unideb.hu](mailto:bodzassandor@eng.unideb.hu)*

### Abstract

*In this publication the connection of four gear drives will be analysed beside constant number of teeth in the function of the modul changing. Computer program will be developed for designing of x-zero gear drives. Using this program the x-zero gear drives could be generated with arbitrary numbers and parameters. Based on the connection statements the conclusions will be worked out.*

**Keywords:** modul, toothed gear, finite element, stress

### 1. INTRODUCTION

The objective of connection analysis and computer modelling is the analysis of the teeth of the gear drive in aspect of stress, strain and total deformation. Before the concrete production and commissioning the dimensions of the connection results for the effect of given loading is defined on the connection tooth surfaces. Based on the received simulation results the tooth geometry could be modifiable because of the better connection properties. After the connection results have been given good results the concrete production of the gear drives could be designed.

In case of toothed gear production the pitch circle diameter is rolled down without slip on the tool reference line. The tool reference line could be different from the tool center line. This effect is called tool stoppage gearing. The produced gear teeth is called a gear having addendum modification (Figure 1) [2, 4, 5, 6].

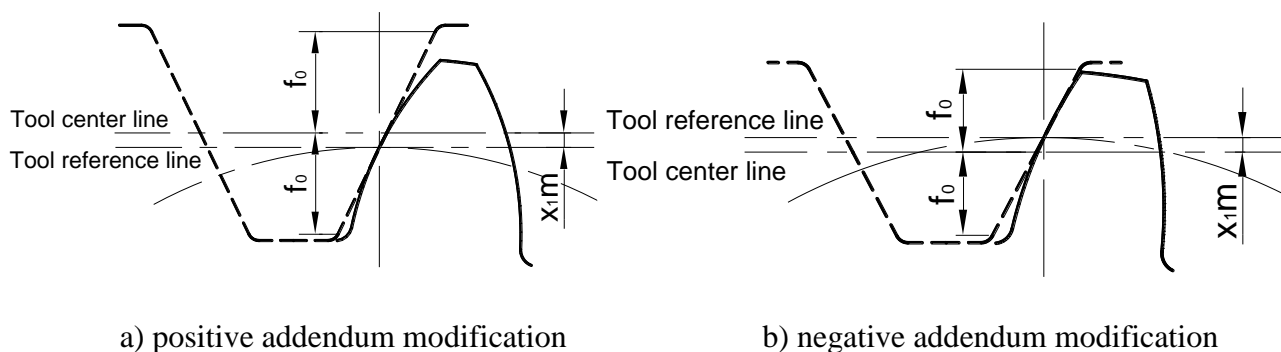


*Figure 1* Tool connection with gear tooth

The x-zero gear drive is an extreme case of the x-gear when addendum modification is not used ( $x_1=0$ ). The tool reference line is the tool center line [2, 4, 5, 6].



## 2. COMPUTER AIDED MODELLING

A computer program has been worked out for the modelling of x-zero gear drives. The modul and the number of teeth of the gears are asked from the user by the program. Knowing of these three parameters the other parameters of the gear drive are calculated by the program. After the calculations the gears are drawn by the software (Figure 2).

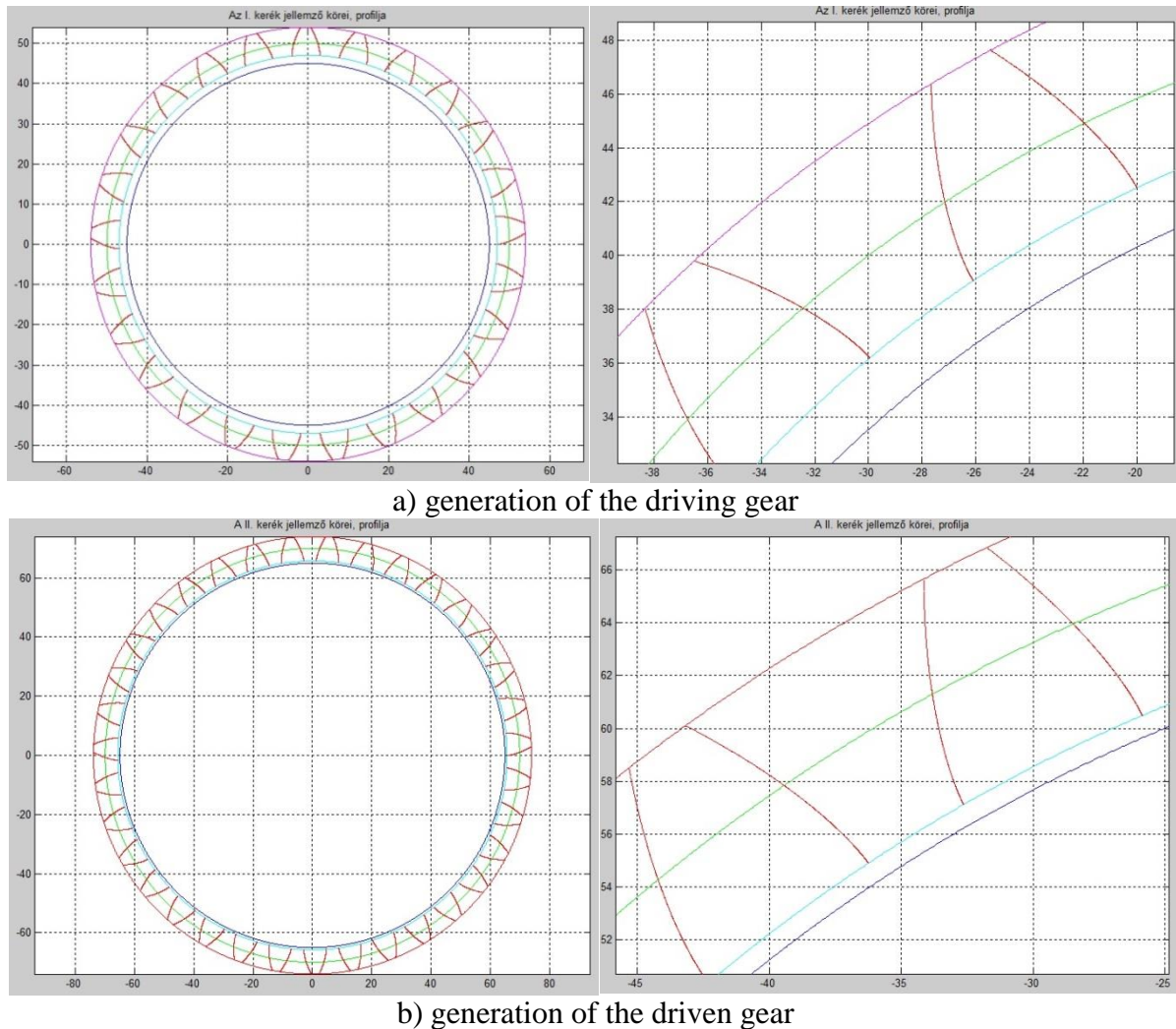


Figure 2 Generation of a concrete geometric X – zero gear drive

The received involute tooth profile points are saved in txt file. The parametric equation of the involute curve is [1, 6]:

$$\begin{aligned}x_{1F} &= \frac{d_{b1}}{2} \cdot (\cos \beta + \beta \cdot \sin \beta) \\y_{1F} &= \frac{d_{b1}}{2} \cdot (\sin \beta - \beta \cdot \cos \beta)\end{aligned}\tag{1}$$

Using of the received points the computer models of the gear drives could be designed to the finite element analysis with SolidWorks computer aided designing software.

Four gear drives have been designed [4, 6] and modelled [1] for the finite element analysis. The



number of teeth of the gear drives ( $z_1$ ,  $z_2$ ) are the same. Based on the modul standard the modules of the gear drives are changed with 0,5 mm scale [6]. During the analysis the driving gear having lower number of teeth that is why transmission ratio is slower. The calculated parameters of the gear drives could be seen on Table 1.

Table 1 The parameters of the designed gear drives

Parameters	Gear drive I.	Gear drive II.	Gear drive III.	Gear drive IV.
Axial modul (m)	4 mm	4,5 mm	5 mm	5,5 mm
Driving gear number of teeth ( $z_1$ )	25	25	25	25
Driven gear number of teeth ( $z_2$ )	35	35	35	35
Centre distance (a)	120 mm	135 mm	150 mm	165 mm
Addendum ( $h_a$ )	4 mm	4,5 mm	5 mm	5,5 mm
Clearance (c)	1 mm	1,125 mm	1,25 mm	1,375 mm
Dedendum ( $h_f$ )	5 mm	5,625 mm	6,25 mm	6,875 mm
Circular pitch (p)	12,566 mm	14,137 mm	15,708 mm	17,278 mm
Backlash ( $j_s$ )	0,628 mm	0,706 mm	0,785 mm	0,863 mm
Whole depth (h)	9 mm	10,125 mm	11,25 mm	12,375 mm
Working depth ( $h_w$ )	8 mm	9 mm	10 mm	11 mm
Tooth thickness ( $S_{ax}$ )	5,969 mm	6,715 mm	7,461 mm	8,207 mm
Pitch circle diameter of the driving gear ( $d_1$ )	100 mm	112,5 mm	125 mm	137,5 mm
Tip circle diameter of the driving gear ( $d_{a1}$ )	108 mm	121,5 mm	135 mm	148,5 mm
Root circle diameter of the driving gear ( $d_{f1}$ )	90 mm	101,25 mm	112,5 mm	123,75 mm
Basic circle diameter of the driving gear ( $d_{ak1}$ )	93,969 mm	105,715 mm	117,461 mm	129,207 mm
Pitch circle diameter of the driven gear ( $d_2$ )	140 mm	157,5 mm	175 mm	192,5 mm
Tip circle diameter of the driven gear ( $d_{a2}$ )	148 mm	166,5 mm	185 mm	203,5 mm
Root circle diameter of the driven gear ( $d_{f2}$ )	130 mm	146,25 mm	162,5 mm	178,75 mm
Basic circle diameter of the driven gear ( $d_{ak2}$ )	131,557 mm	148 mm	164,446 mm	180,89 mm
Transmission ratio (i)	1,4	1,4	1,4	1,4



### 3. TOOTH CONNECTION ANALYSIS

#### 3.1. Adoption of the finite element mesh

Coefficient of friction having 0,15 value has been set on the connection teeth zone. During the calculations tetrahedron mesh was used. Density of the meshing was automatic in outside of the connection teeth zone [5, 9]. Meshing having 0,6 mm dense has been set on the connection zone (Figure 3).

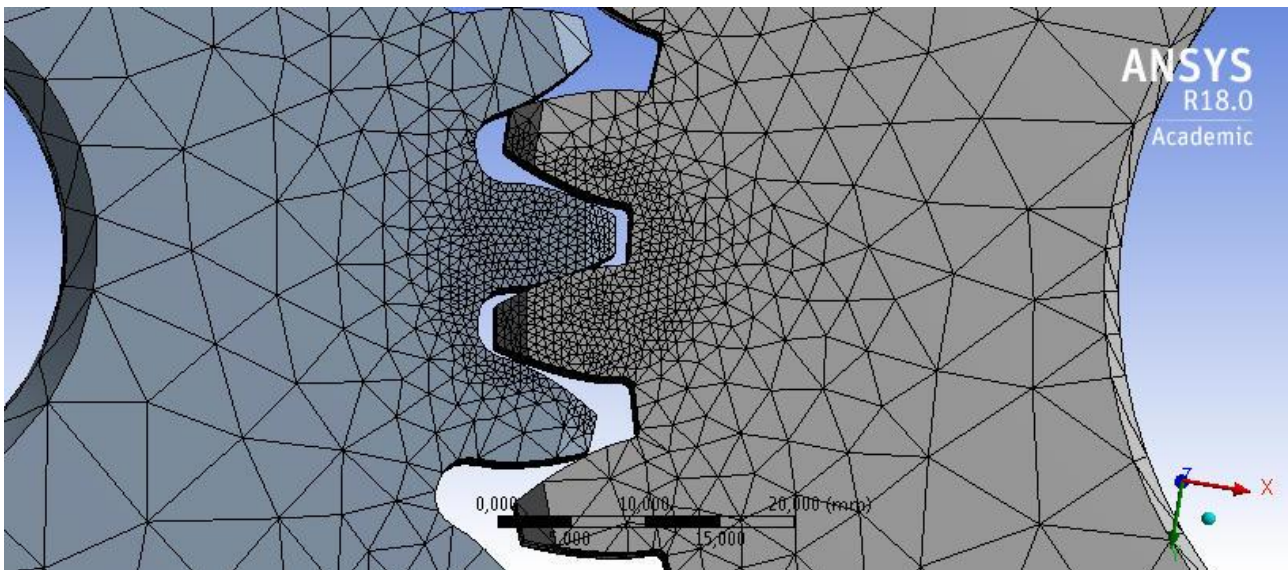


Figure 3 Adoption of finite element mesh

#### 3.2. Setting of loading and boundary conditions

During the analysis the gear drive material is structural steel (Figure 2). The driving gear is loaded with 20 Nm rotation moment (Figure 4).

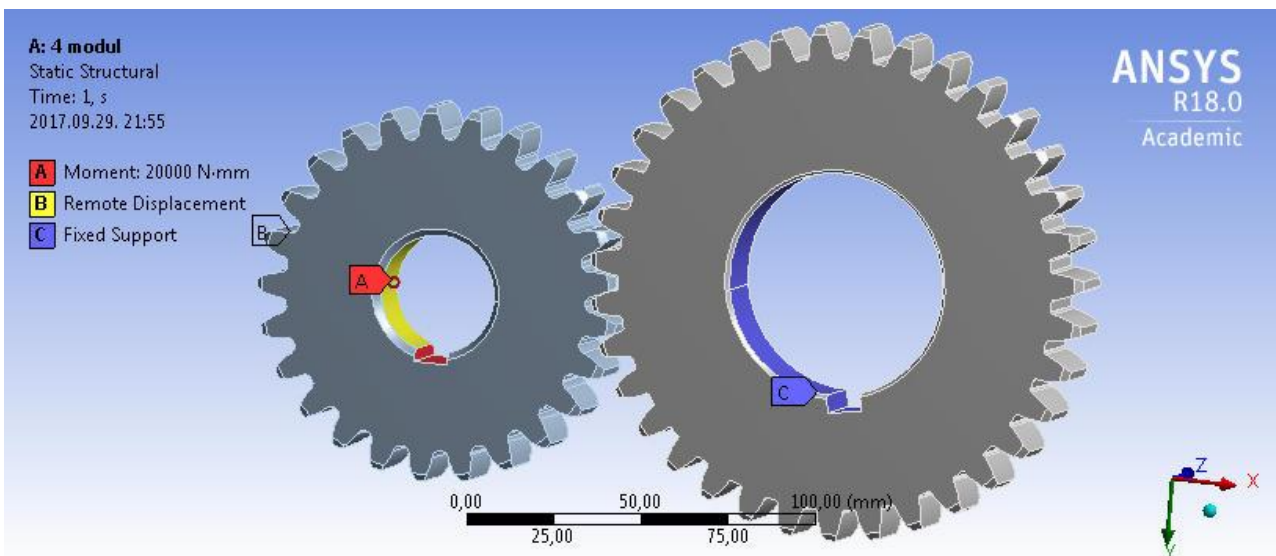


Figure 4 Setting of loading and boundary conditions



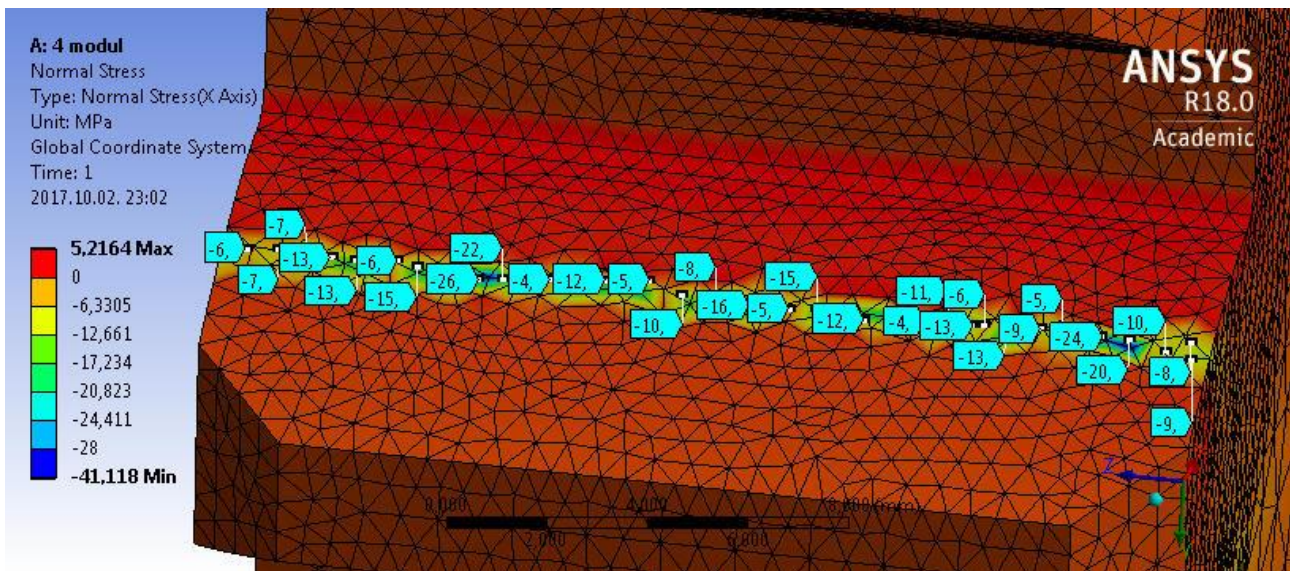
Table 2 Material parameters

Density	7850 kg/m <sup>3</sup>
Yield limit	250 MPa
Ultimate strength	460 MPa

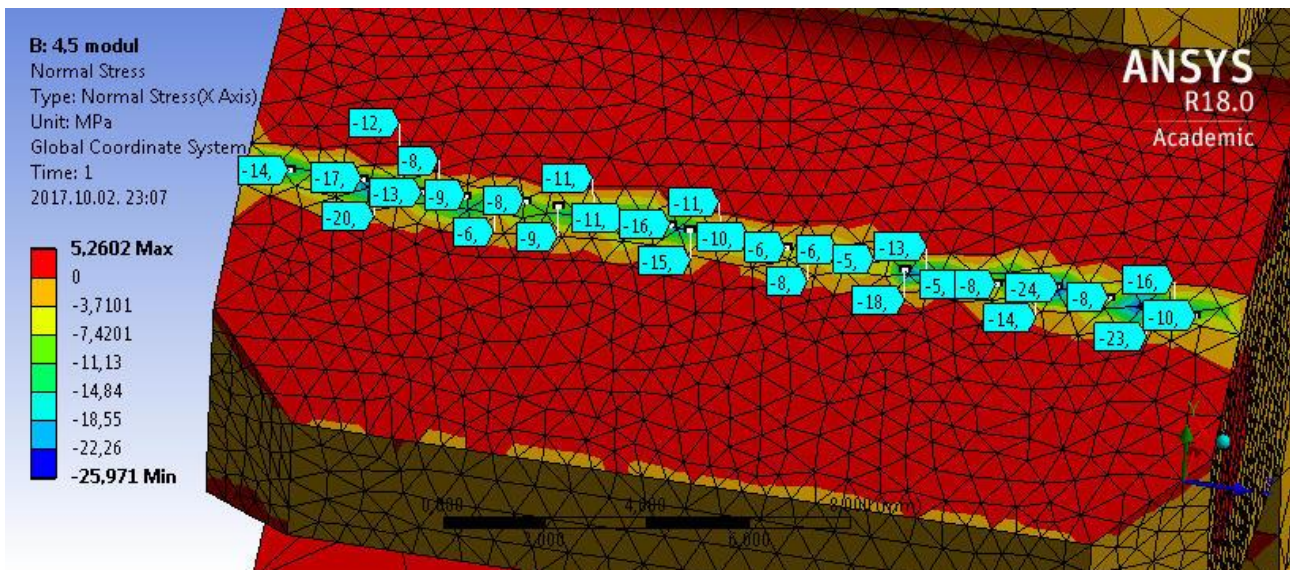
Five freedom degrees of the driving gear have been fixed. Only rotation around the axis of rotation has been permitted. Fix holding has been used for the driven gear (Figure 4).

### 3.3. Analysis of normal stress distribution

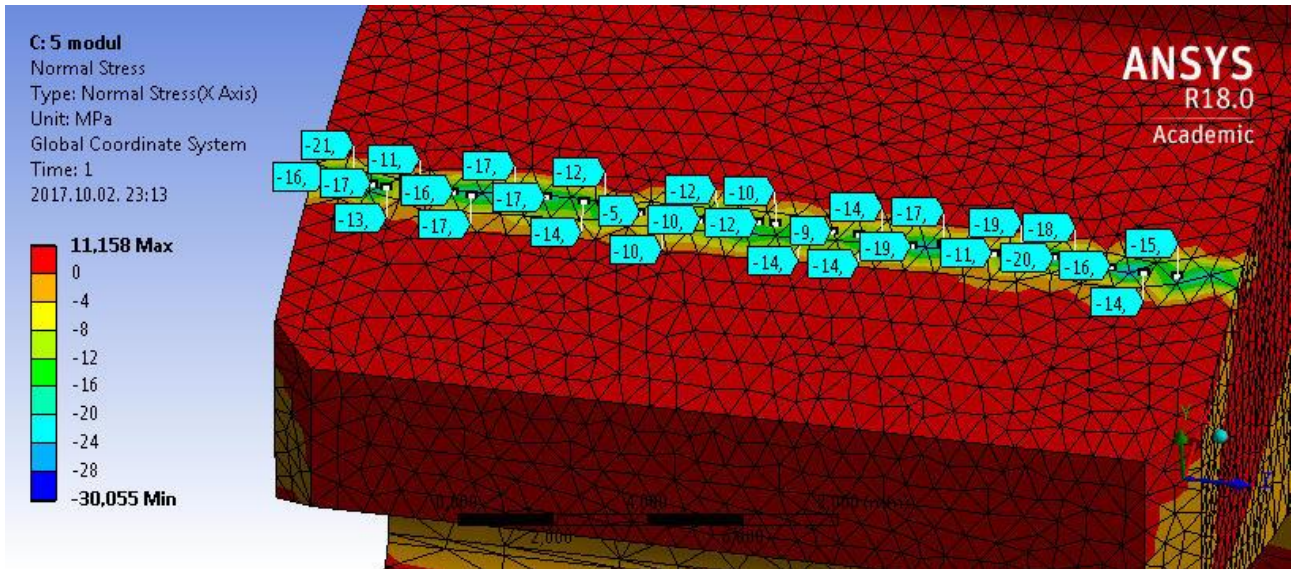
On Figure 5 the normal stress distribution could be seen by the effect of loading moment on the connection tooth surface of the driven gear.



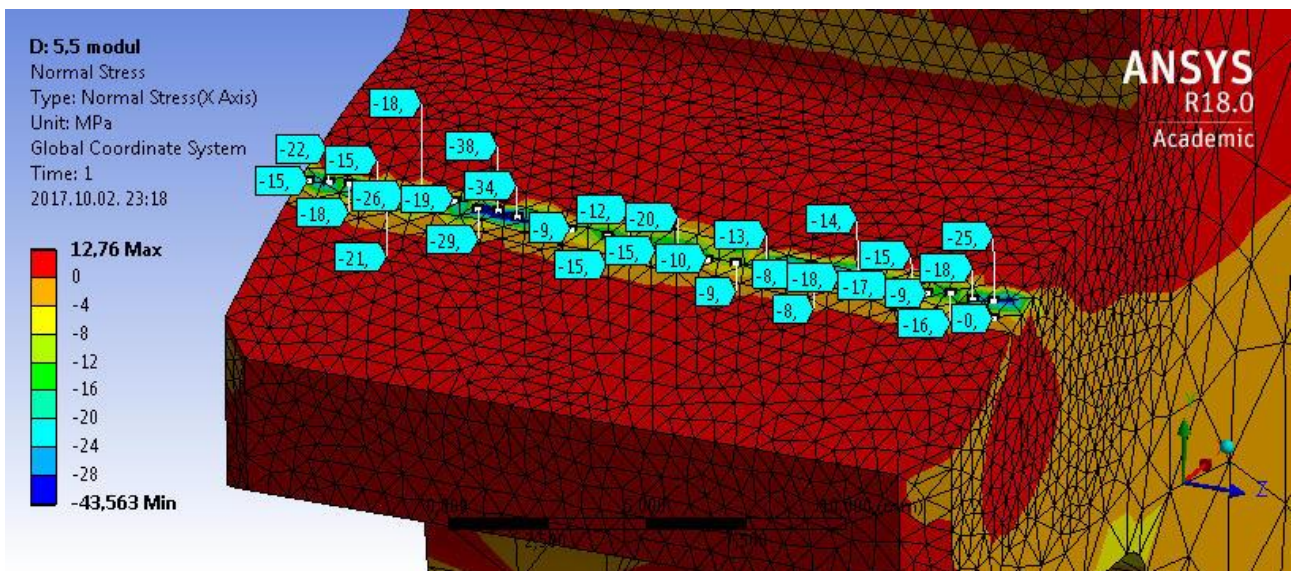
a) in case of 4 mm modul (the average normal stress on the tooth surface: -11,333 MPa)



b) in case of 4,5 mm modul (the average normal stress on the tooth surface: -11,466 MPa)



c) in case of 5 mm modul (the average normal stress on the tooth surface: -14,133 MPa)



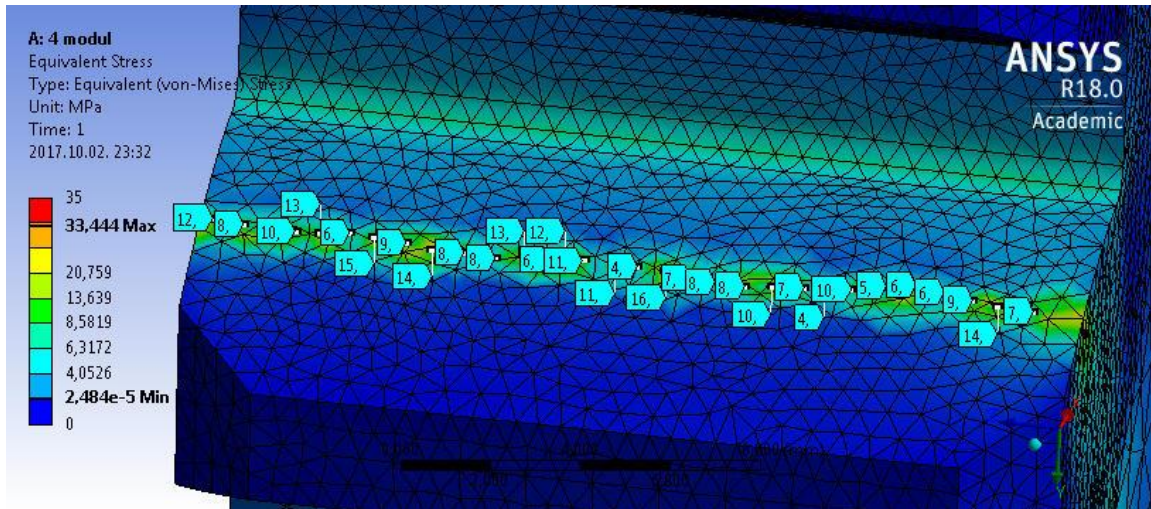
d) in case of 5,5 mm modul (the average normal stress on the tooth surface: -17,366 MPa)

Figure 5 Normal stress distribution on the tooth surface of the driven gear

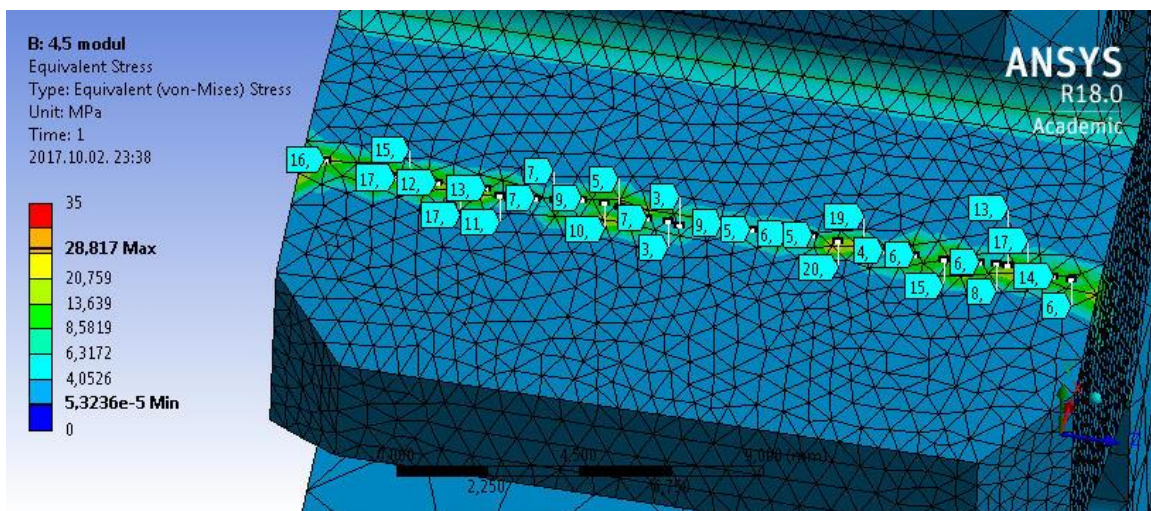
On Figure 3 the normal stress distributions in the function of the modul increase are reduced on the tooth surface of the driven gear on the connection zone. The root has bending and turning stresses.

### 3.4. Analysis of equivalent stress

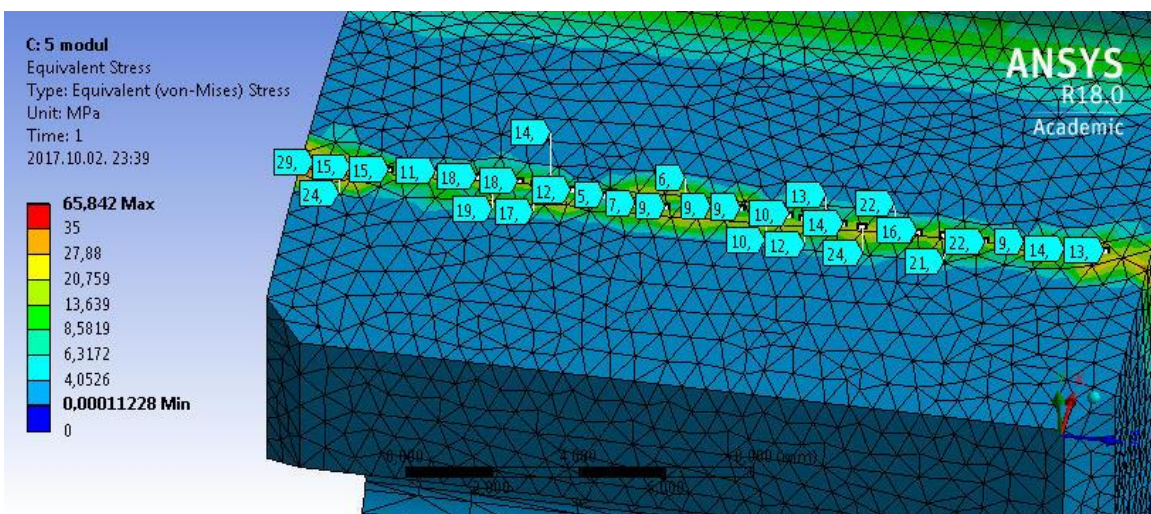
On Figure 6 the equivalent stress distribution could be seen by the effect of loading moment on the connection tooth surface of the driven gear.



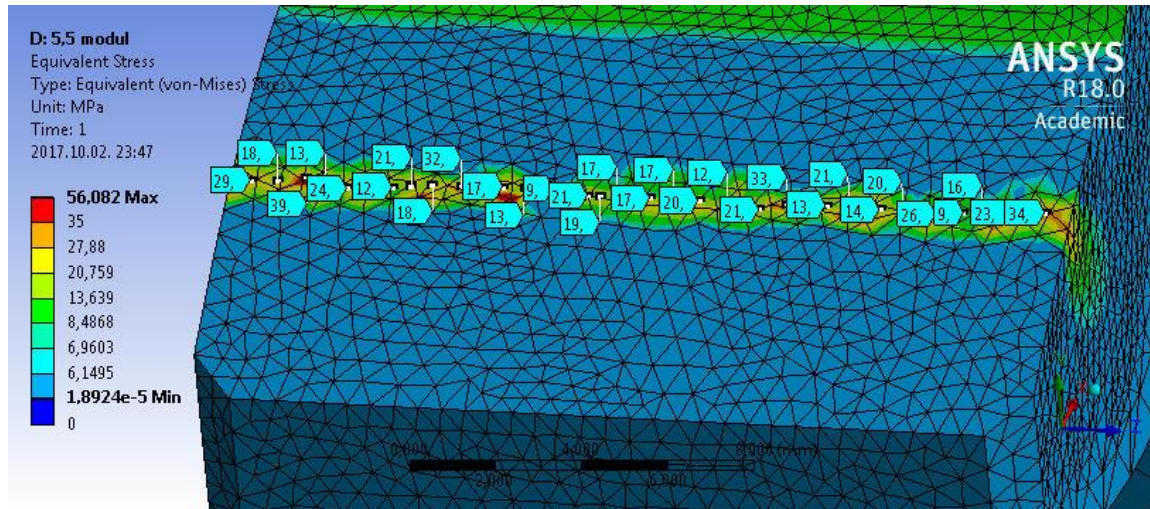
a) in case of 4 mm modul (the average equivalent stress on the tooth surface: 9,833 MPa)



b) in case of 4,5 mm modul (the average equivalent stress on the tooth surface: 10,033 MPa)



c) in case of 5 mm modul (the average equivalent stress on the tooth surface 13,33 MPa)



d) in case of 5,5 mm modul (the average equivalent stress on the tooth surface 22,22 MPa)

Figure 6 Equivalent stress distribution on the tooth surface of the driven gear

On Figure 6 the equivalent stress distributions in the function of the modul increase is increased on the tooth surface of the driven gear on the connection zone. The root has bending and turning stresses.

## CONCLUSION

In this publication the x-zero gear drives are designed beside the number of teeth constancy. Based on the standard the modules of the toothed gears have been changed with 0,5 mm step value. Computer software has been worked out for the easement of the designing process. Based on the teeth geometric parameters the CAD models of the gear drives have been worked out by SolidWorks designer software.

Beside similar loading and boundary conditions the evolved normal and equivalent stress dispositions have been analysed [7, 8, 10, 11] on the tooth surfaces of the driven gear by Ansys finite element software. As a result the effect of the modul increasing the normal stress values are decreased and the equivalent stress values are increased on the tooth surface of the driven gear on the connection zone.

## ACKNOWLEDGEMENT

This research was supported by the **János Bolyai Research Scholarship of the Hungarian Academy of Sciences**.

The work is partially supported by the **EFOP-3.6.1-16-2016-00022 project**. The project is co-financed by the European Union and the European Social Fund.

## REFERENCES

- [1] Bodzás, S.: *Computer aided designing and modelling of x-zero gear drive*, International Review of Applied Sciences and Engineering, volume 8, number 1, 2017, pp. 93-97, ISSN 2062-0810
- [2] Dudás, I.: *Gépgyártástechnológia III., A. Megmunkáló eljárások és szerszámaik, B. Fogazott alkatrészek gyártása és szerszámaik*, Műszaki Kiadó, Budapest, 2011.



# INTERNATIONAL SCIENTIFIC CONFERENCE ON ADVANCES IN MECHANICAL ENGINEERING

12-14 October 2017, Debrecen, Hungary



- [3] Dudás, L.: *Kapcsolódó felületepárok gyártásgeometriai feladatainak megoldása az elérés modell alapján*, Candidate thesis, Budapest, TMB, 1991., p.144., 2005. 06. 29.
- [4] Erney Gy.: *Fogaskerekek*, Műszaki Könyvkiadó, Budapest, 1983., p. 460.
- [5] Litvin, F. L., Fuentes, A.: *Gear Geometry and Applied Theory*, Cambridge University Press, 2004., ISBN 978 0 521 81517 8
- [6] Terplán Z.: *Gépelemek IV.*, Kézirat, Tankönyvkiadó, Budapest, 1975., p. 220.
- [7] Páczelt, I., Szabó, T., Baksa, A.: *A végeelem módszer alapjai*, Értékünk az ember, Humánerőforrás fejlesztési Operatív Program, Miskolci Egyetemi Elektronikus jegyzet
- [8] Szabó, F., Bihari, Z., Sarka, F.: *Termékek, szerkezetek, gépelemek végeelemes modellezés és optimalása*, Szakmérnöki jegyzet, Miskolc, 2006.
- [9] Litvin, F.L., Fuentes, A., Fan, Q., Handschuh R. H.: *Computerized design, simulation of meshing, and contact and stress analysis of face-milled formate generated spiral bevel gears*, Mechanism and Machine Theory, 2002, pp. 441-459, Elsevier
- [10] Mankovits, T.: *Numerical Analysis of Engineering Structures: Linear Elasticity and the Finite Element Method*, Debrecen: University of Debrecen, 2014. 181., ISBN:978-963-473-797-1
- [11] Mankovits, T., Szabó, T., Kocsis, I., Páczelt, I.: *Optimization of the Shape of Axi-Symmetric Rubber Bumpers*, Strojnicki Vestnik-Journal Of Mechanical Engineering 60:(1) pp. 61-71., 2014



## OPTIMIZATION OF WOOD BIOMASS GASIFICATION PROCESS

**BOLDIZSÁR Csongor**

*Department of Fluid and Heat Engineering, Faculty of Mechanical Engineering and Informatics,  
University of Miskolc*

*E-mail: [boldizsar.csongor.balint@gmail.com](mailto:boldizsar.csongor.balint@gmail.com)*

### Abstract

*Nowadays, bioenergy and biofuel via gasification from biomass has become of great interest, but there are still many unexploited possibilities for the utilization of biomass for energy purposes. For example, the utilization of agricultural and forest industry by-products and gases produced in the landfills can be mentioned. The synthesis gas generated by biomass gasification is suitable for utilize in heat and power generation in a combined-cycle power plant. The economy of energy production depends on the efficiency of the power plant, which can be optimized by selecting the composition of the biomass or the gasifying conditions properly. I have used thermokinetic modeling to determinate the compositions and the heating value of the synthesis gas. I have executed analysis for different compositions and moisture content of biomass. Based on the model, the operating condition of the gasifier can be optimized and the composition of the syngas can also be determined.*

**Keywords:** *biomass, gasification process, simulation*

### 1. INTRODUCTION

Hungary is commonly known as an agricultural country, and this is also unquestionable for the use of renewable energy sources, the domestic biomass potential is 328 PJ, of which 49.2 PJ is now utilized [1]. Due to its capacity, biomass can play a prominent role in regional and urban development as well as in the job creation of countryside. Biomass-based developments also realize the de-centralized energy generation by the creation of additional power plants, which may also provide income for the settlements.

In Hungary, there are several medium-sized biomass power plants, the largest of them the Mátra Power Plant (103 MW), the Pannongreen Group (85 MW), the AES Borsodi Power Plant (80 MW), Oroszlány Power Plant (49 MW), Ajka Power Plant (33 MW) and Bakony Bioenergia Group's power plant (30 MW). Most of the medium-sized power plants apply forestry or industrial wood waste, but for example in the biomass power plant at Szabadegyháza, which will be completed by the end of 2018, straw and sunflower pellets will be burned [2].

The biomass is considered as renewable energy source, however, only a finite amount of energy is applicable therefore the biomass for energy produce can only be realized in a limited way. The renewable cycling time of the energy source should be shorter than the rate it is used avoiding the excessive exploitation [2].

Gasification is one of the oldest methods of converting solid state fossil and renewable energy sources into combustible synthesis gas and liquid fuel. Gasification is a process with partial oxidation based on rapid heat dissipation of materials, which has a lower oxygen demand than the theoretical oxygen required for perfect combustion – ideal excess air ratio: 0.5 and ideal temperature: 800 °C). During the partial oxidation of the organic compounds found in the base

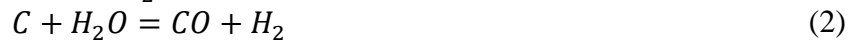


material synthesis gas is released, which can be used as a raw material, at chemical synthesis or as a fuel. The purified synthesis gas is usually utilized in a gas-engine or in a combined-cycle power plant, producing electrical and thermal energy, but it is significant in chemical synthesis, especially in methanol production as well [2].

## 2. METHODS

The main objective of the study was the simulation of the biomass gasification and the theoretical analysis of synthesis gas using the GASEQ program, depending on the composition of the input materials and the change of the technological parameters. Another objective was to calculate the energy efficiency measurements; the most important measurements are the chemical and energy conversion efficiency, as well as the heat and electricity energy efficiency that is influenced by the composition, moisture content and ash content of biomass, and the amount and type of auxiliary gas used [3].

The equilibrium model assumes that all the reactions are in thermodynamic equilibrium. It is excepted that the pyrolysis product burns and achieves equilibrium in the reduction zone before leaving the gasifier, hence an equilibrium model can be used in the downdraft gasifier. The reactions are the follows [3]:



As a starting point for modelling, the ingredient-forming molecule for the composition should be provided, followed by the list of constituents of the product as well as the working pressure and the temperature. In the ideal case, the input molecule would be the cellulose, but this compound was not included in the program, so phenol ( $C_6H_5OH$ ) was chosen for this purpose, which is an aromatic crystalline solid. In view of the fact the phenol molecule does not contain enough oxygen and hydrogen, it is necessary to apply a correction to make the chemical composition appropriate, before the simulation these corrections have been executed [4].

The reaction efficiency shows how much the energy content of the solid fuel appears in the produced gas product:

$$\eta_r = \frac{\dot{m}_g \cdot F_g}{\dot{m}_b \cdot F_b} \quad (5)$$

where  $\eta_r$  is the reaction efficiency,  $\dot{m}_g$  [kg/s] is the mass flow of the synthesis gas,  $F_g$  [MJ/kg] is the heating value of the synthesis gas,  $\dot{m}_b$  [kg/s] is the mass flow of the biomass and  $F_b$  [MJ/kg] is the heating value of the biomass [4].

The relative energy density increment shows the goodness of the biomass gasification technology compared to conventional combustion:

$$\Delta e_{rk} = \frac{e_{gasification}}{e_{combustion}} \quad (6)$$

where  $\Delta e_{rk}$  is the relative energy density increment,  $e_{gasification}$  [MJ/kg] is the gasification specific capacity and  $e_{combustion}$  [MJ/kg] is the conventional combustion specific capacity. At biomass



gasification Diesel-cycle efficiency (36%), and in the case of conventional combustion the efficiency of the Rankine-Clausius cycle (27%) have been used [4].

### 3. RESULTS

Two different wood types of biomass have been analysed during this study: pine (*Pinus*) and beech (*Fagus*), at constant pressure (1 atm) and constant temperature (800 °C), but with different moisture content and excess air ratio.

Table 1 Various biomass materials chosen (dry basis, weight percentage)

Material	C	H	O	N	Ash	HHV [MJ/kg]
Pine	52	6,07	41,55	0,28	0,1	14,1758
Beech	51,6	6,3	41,5	0	0,6	14,1523

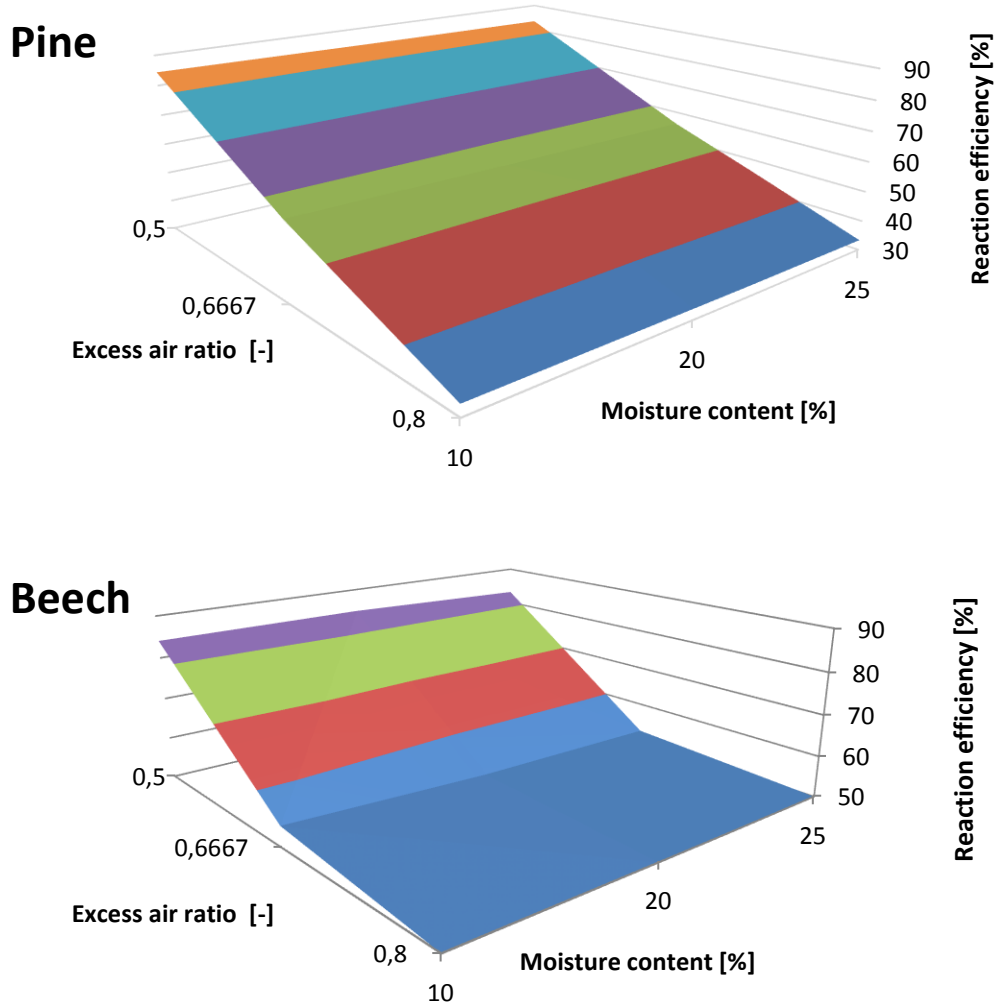


Figure 1 Effect of the excess air ratio and the moisture content in the beech and in the pine on reaction efficiency



Figure 1 shows the effect of the excess air ratio and the moisture content in the beech and in the pine on reaction efficiency when the bed is working at 800 °C. It can be observed from the figure that the reaction efficiency is almost constant with the moisture content, but highly decreasing with the excess air ratio. It is interesting to note that the reaction efficiency of the pine decreases steadily from 90% to 30%, but in case of beech gasification the efficiency steadily decreases from 90% to 50% when the excess air ratio increases from 0.5 to 0.6667. Despite further ascending of the excess air ratio the reaction efficiency is almost considered to be constant.

Figure 2 shows the effect of the excess air ratio and the moisture content in the beech and in the pine on energy density increment when the bed is working at 800 °C. It can be detected from the figure that the relative energy density increment is almost constant with the moisture content, but highly decreasing with the excess air ratio. The figure shows that the energy density increment is only positive when the value of excess air ratio is around 0.5 in case of pine and beech gasification, as well.

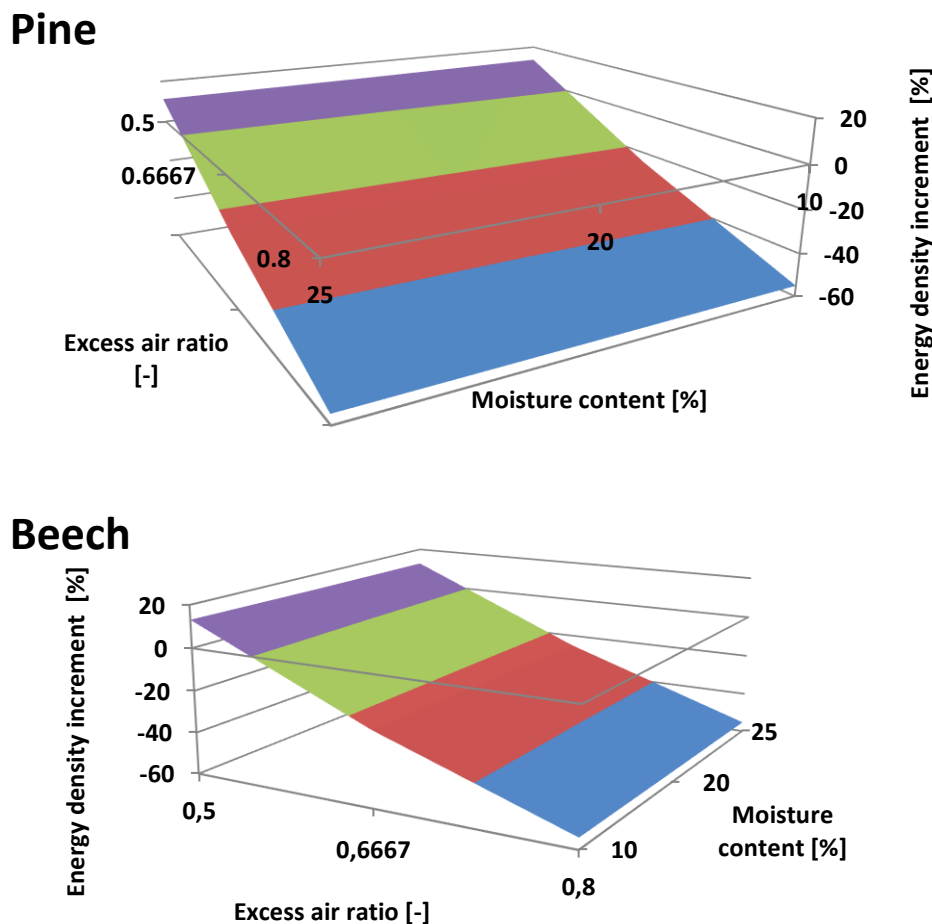


Figure 2 Effect of the excess air ratio and the moisture content in the beech and in the pine on energy density increment



Using the GASEQ program, the heat value of the synthesis gas produced by the gasification of biomass have been determined, depending on the moisture content. Figure 3 shows hardly noticeable difference between the heating value of pine and beech gasification, but it is seen that the calorific values decrease linearly with increase in moisture content.

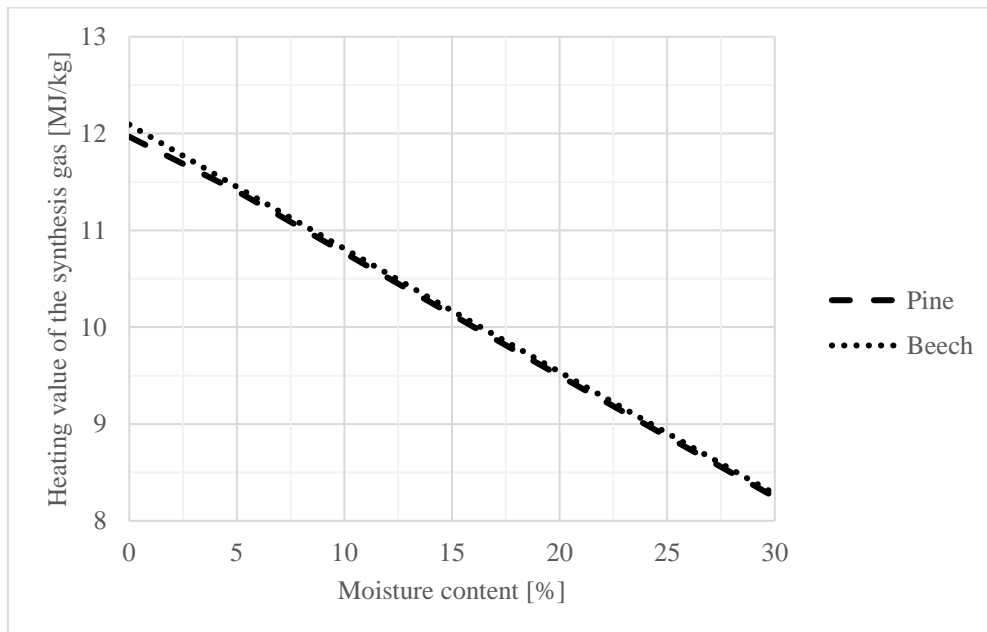


Figure 3 Effect of the moisture content on heating value of synthesis gas

## CONCLUSIONS

The modelling of the gasification process is performed using an equilibrium model. The calculations of the reaction efficiency and the relative energy density increment are illustrated. From the analysis the following conclusions are made:

1. The reaction efficiency is almost constant with the moisture content.
2. The reaction efficiency is highly decreasing with the excess air ratio.
3. The relative energy density increment is almost constant with the moisture content.
4. The relative energy density increment decreases linearly with the excess air ratio.
5. The calorific values of the synthesis gas decreases with the increase in moisture content for all the raw materials studied.

## REFERENCES

- [1] Gyulai, I.: *A biomassza dilemma*. Negyedik átdolgozott kiadás, Magyar Természetvédők Szövetsége, Föld Barátai Magyarország, 2010.
- [2] Dr. Bodnár, I.: *Fás szárú biomasszák és települési szilárd hulladékok termikus hasznosítása*. Miskolci Egyetem, 2017. p. 164. ISBN 978-963-12-7604-6.
- [3] Bodnár, I.: *Efficiency of co-Generated Power Production Based on Woody Biomass*. Journal of Computer Science and Control Systems. Vol. 10. Nr. 1., May 2017, pp. 5-10.
- [4] Bodnár, I.: *Fás szárú biomasszák pirolitikus hasznosításának termokinetikai modellezése*. GÉP magazin. A Gépipari Tudományos Egyesület Műszaki Folyóirata. LXVII. évfolyam 3. sz. 2016, pp. 5-12.



## AVERAGED VIBRATION LEVELS OF VANS IN PACKAGE DELIVERY

**BÖRÖCZ Péter PhD**

Széchenyi István University

E-mail: [boroczp@sze.hu](mailto:boroczp@sze.hu)

### Abstract

*This study measured the transportation vertical vibration levels that parcel pickup and delivery vans experience when carrying packages across the various road networks that were measured in Hungary. Nowadays, there continues to be an increase in courier parcel delivery services due to the growing of worldwide online economy and express parcel shipments. It is therefore important to measure and quantify the levels of vibration that occur inside the vehicle during transport, as it can be one of the primary sources of damages. The recorded acceleration data were analysed in terms of power spectral densities (PSD) and presented in the frequency bandwidths of 1 – 200 Hz. The results of the separated and averaged vertical vibration levels provide physical circumstances for testing conditions.*

**Keywords:** Van, PSD, vibration, package testing

### 1. INTRODUCTION

Small truck transport is one of the most widely form of parcel transportation used for the shipment of goods in Hungary. The parcel courier and express delivery services industry continues to experience growth as the global economy improves and online stores develop. The carriers generally provide services between metropolitan areas or urban centres and form a huge network that includes local pickup and delivery. The parcel delivery companies use many modes of transport and vehicles (Figure 1), but the packages can spend a significant portion of the entire transportation time on a van depending on inter alia the length of daily delivery route, the number of stopovers, the distant of centre hub from the destination, or the exact time of picking or delivering moment in a given daily route.

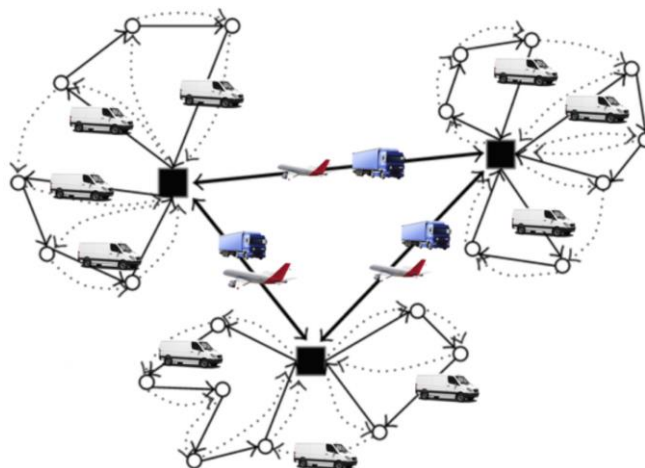


Figure 1 Parcel delivery structure with vans as the last or first leg



Previous studies have also measured and analysed the vibration levels and developed power spectral density (PSD) mainly for heavy trucks in various continents and regions such as North America [1], Brazil [2], India [3], Thailand [4], and recently in China [5]. In 2008, a study measured vibration levels in Spain. Results showed lower intensity for trucks with leaf spring and air-ride [7] as compared to other regions. There are also two papers for van vehicle measurement, but those do not focus on averaged vibration levels instead of analyse the effect of suspension system and payload conditions to the vibration levels [8], or analyse the statistical parameters of vibration intensity of van vehicle during traveling [9].

This research attempts to measure and analyse the vibration levels and intensity on van shipments on the major distribution roads in West-Hungary using acceleration data recorder to measure and record vibration events and present them in the form of PSD. The data from this study can be compared to vibration test profiles recommended in popular, widely used vibration test standards such as ASTM and ISTA. The data and results from this study can be used to compare packaging vibration test methods used by packaging engineers to develop optimized packaging for shipment in Hungary.

## 2. METHODS

### *Vehicle and route details*

In order to analyse the averaged vibration levels a FIAT Ducato (Figure 2a) van was used by carrier TNT. Table 1 contains the specifications of van used in this study. The van was monitored for approximately 8 hours of a total workday trip. The real duration the trucks were in motion was between 5.5–6.5 hours. The measurements were conducted with various payloads and speeds in range of 0-1140 kg and 1-130 km/h. The payload condition during shipping varies on a function of packages being delivered and picked up. The suspension system of observed van was a parabolic leaf spring at the rear axle (Figure 2b).



a)



b)

Figure 2 FIAT Ducato van used for the measurement and its suspension system b)

The van was a van with weight of 1975 kg and maximum possible payload of 1 525 kg, and 8.0m<sup>3</sup> container size. To determine the averaged effect of transportation circumstance such as road condition during shipping the small trucks travelled on various roads such as motorway, primary road, secondary road, tertiary road and city road, respectively. The total journey that travelled was 267 km.



### Instrumentation and setup

The vibration events during courier parcel delivery routes were measured by Lansmont (SAVER)<sup>TM</sup> 3X90 (Shock and Vibration Environment Recorder, Lansmont Corp., CA, USA). Then SaverXware<sup>TM</sup> software and MathLab R2014a software were also used for analysing the data. Table 1 contains the setting parameter for the survey, and Figure 3a and 3b shows the SAVER itself, and the location of the instrument in van. The recorder was mounted directly to the floor and located at the right rear of the vehicle cargo area.

Table 1. SAVER setup parameter

Timer trigger	30s
Recording time	2.048 s
Signal Trigger	2.5 G
Sample/sec	500 Hz
Sample size	1024
Resolution for PSD	0.48 Hz



a)



b)

Figure 3 SAVER a) and its location b) in van for this study

### Data analysis

In the case of vibration analysis power density (PD) levels were determined as function of frequency, based on the recorded random vibration acceleration levels. The average power density within a narrow band of frequencies (BW) of a given spectrum can be determined by  $G_{\text{rms}}$  values based on the number of samples for a given bandwidth. In this way  $G_{\text{rms}}$  is determined as the root mean square value of the acceleration in G's in the given bandwidth of frequency, based on a number of (n) samples.

$$PD = \frac{1}{BW} \sum_{i=1}^n (RMSG_i^2) / n \quad (1)$$

In this study, the data are presented and analysed from 1 to 200 Hz due to the fact that during transportation this is the typical frequency range within the vibration occurs damages. First, the recorded vibration data were filtered to remove all undesirable events such as any noise or non-vibration featured movements from the analysis, i.e. stopovers during daily transportations. This way data below 0.03  $G_{\text{rms}}$  were filtered out. This method was already used former by the Author [10].



The vibration environment then was represented by power density spectrum (PSD) showing a plot of the power density levels versus frequency. The energy within a specific frequency range can be obtained by integrating PSD within that frequency range and is usually represented in  $G_{rms}$  for the entire or portion of the spectrum. Computation of PSD is done directly by the method called Fourier transformation or computing autocorrelation function and then transforming it. Figure 4 shows an example of a PSD lot for normal truck vibration during transportation with lead spring suspension.

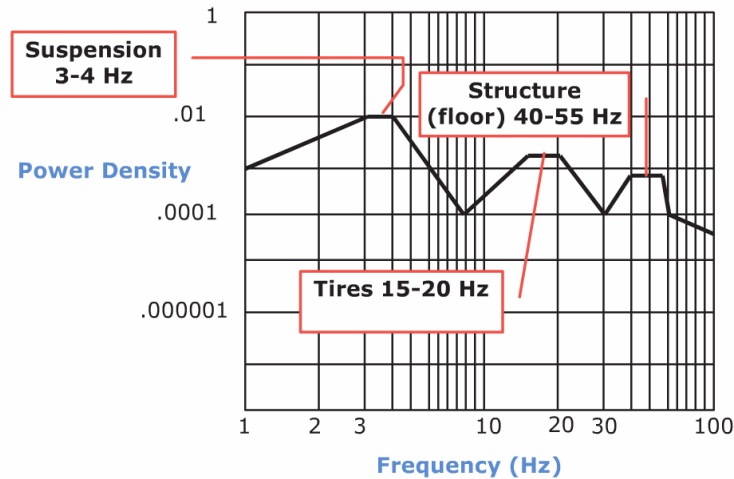


Figure 3

Figure 4 A typical PSD plot for heavy truck vibration

### 3. RESULTS

Figure 4 shows an acceleration signal measured in van with a time history of 220 seconds. For the analysis 849 samples were used, this was the total number of events recorded over 0.03  $G_{rms}$ . Figure 5 shows the vertical PSD spectrum for van vibration. As shown on the PSD spectrums, the measured vibration intensity in the low-frequency range (1–5 Hz and 13 – 18 Hz) was relatively high. After 100 Hz the PD levels decrease rapidly. The intensity (overall  $G_{rms}$ ) of vibration level on field measurement was 0.311 in 1 to 200Hz.

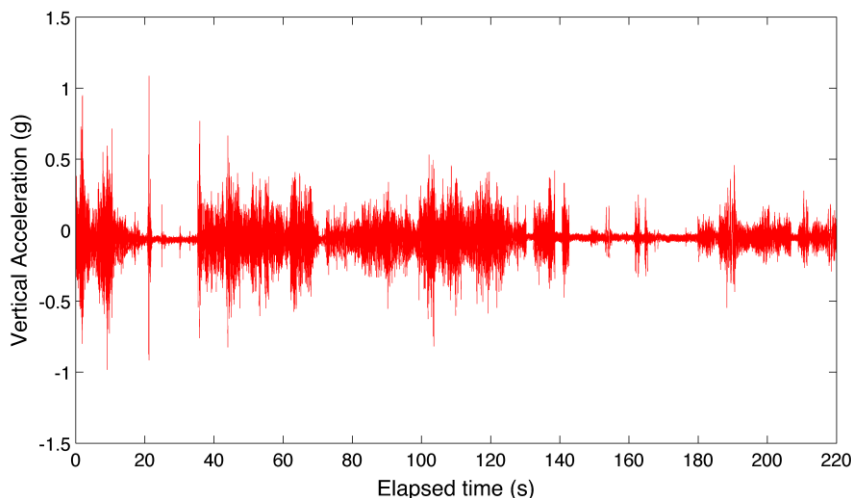


Figure 4 Sample of vertical vibration signal recorded

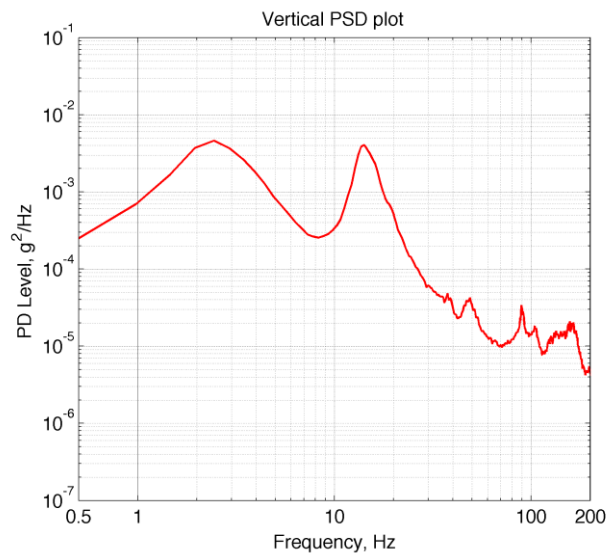


Figure 5 Sample of vertical vibration signal recorded

Table 2 Recommended test spectrum for van in package delivery

Frequency (Hz)	PD level (g <sup>2</sup> /Hz)
1	0,001
2	0,008
3	0,008
7	0,0005
10	0,0005
13	0,01
16	0,01
35	0,00006
55	0,00006
70	0,0003
100	0,0003
200	0,00005

## CONCLUSIONS

The PD levels of vertical vibration in frequency range of 1 – 200Hz was the highest between 2.5 Hz, and then 13 – 18 Hz. Over 60Hz the PD levels decreased rapidly. The recommended PD spectrum based on the measured data from this study can be used as test circumstances for vibration simulation condition of van.

## Acknowledgement

This work was supported by the project EFOP-3.6.1-16-2016-00017 of Széchenyi István University.

## References

- [1] Singh, J., Singh, S. P. and Joneson, E. Measurement and analysis of US truck vibration for leaf spring and air ride suspensions, and development of tests to simulate these conditions.



# INTERNATIONAL SCIENTIFIC CONFERENCE ON ADVANCES IN MECHANICAL ENGINEERING

12-14 October 2017, Debrecen, Hungary



- Packaging Technology and Science 2006; 19: 309–323. DOI: 10.1002/pts.732
- [2] Rissi GO, Singh SP, Burgess G, Singh J. Measurement and analysis of truck transport environment in Brazil. Packaging Technology and Science 2008; 21: 231– 246. DOI:10.1002/pts.797.
- [3] Singh SP, Sandhu APS, Singh J, Joneson E. Measurement and analysis of truck and rail shipping environment in India. Packaging Technology and Science 2007; 20: 381–392. DOI:10.1002/pts.764.
- [4] Chonhenchob V, Singh SP, Singh J, Sittipod S, Swasdee D, Pratheepthinthong S. Measurement and analysis of truck and rail vibration level in Thailand. Packaging Technology and Science 2010; 23: 91–100. DOI:10.1002/pts.881.
- [5] Zhou, R., Yan, L., Li, B., & Xie, J. Measurement of Truck Transport Vibration Levels in China as a Function of Road Conditions, Truck Speed and Load Level. Packaging Technology and Science 2015; 28: 949-957, DOI:10.1002/pts.2176
- [6] Singh SP, Marcondes J. Vibration levels in commercial truck shipments as a function of suspension and payload. Journal of Testing and Evaluation 1992; 20(6): 466–469.
- [7] Garcia-Romeu-Martinez MA, Singh SP, Cloquell-Ballester VA. Measurement and analysis of vibration levels for truck transport in Spain as a function of payload, suspension and speed. Packaging Technology and Science 2008; 21: 439–451. DOI:10.1002/pts.798.
- [8] Böröcz P and Singh SP. Measurement and analysis of delivery van vibration levels to simulate package testing for parcel delivery in Hungary, Packaging Technology and Science, Early View, (2017), doi: 10.1002/pts.2327
- [9] Böröcz P. Vibration Levels in Vans as a Function of Payload and Leaf Spring Sheet Number, Journal of Testing and Evaluation, Early View (2017)
- [10] Böröcz, P., and Singh, SP. Measurement and Analysis of Vibration Levels in Rail Transport in Central Europe. Packaging Technology and Science 2017, 30: 361–371. doi: 10.1002/pts.2225



## AUTOMATED IMAGE ANALYSIS OF THE INHOMOGENITIES IN THE MICROSTRUCTURE OF ALUMINUM CASINGS

<sup>1</sup>BUBONYI Tamás, <sup>1</sup>LÉRÁNTH Gábor, <sup>1,2</sup>BARKÓCZY Péter PhD

<sup>1</sup>Faculty of Materials Science, University of Miskolc

E-mail: [bubonyitamas@gmail.com](mailto:bubonyitamas@gmail.com)

<sup>2</sup>FUX Zrt., Miskolc

E-mail: [peter.barkoczy@fux.hu](mailto:peter.barkoczy@fux.hu)

### Abstract

*The fast cooling of the die casted aluminum products can cause an inhomogeneity in the microstructure. An automated image analysis method is developed and introduced to evaluate this inhomogeneity. This is based on the analysis of a tile image taken from the whole cross section of the castings. This article describes the method of analysis.*

**Keywords:** die casting, aluminum, microstructure, image analysis, hypo-eutectic

### 1. INTRODUCTION

The mechanical properties of the metals and alloys are strongly related to its microstructure. Some cases are easier to examine, evaluate and qualify the microstructure instead of performing mechanical tests. The testing of thin walled castings is a typical example. The most productive technology of this type of products is the die casting. During die casting, the cooling of the melt can be fast. The cooling rate has a great effect to the microstructure. The cooling rate the largest at the surface of the melt, next to the tool, the crystallization starts in the surface region, and fine microstructure develops. In the bulk the cooling rate is smaller due to the finite heat conduction of the solid and melt aluminium. In the bulk coarser structure can be found. The extent of this effect extremely depends on the thickness of the wall. So, in the case of thin walled castings the evaluation of the microstructure is not enough. Evaluation of the mentioned inhomogeneity is also necessary [1]. This means the analysis and evaluation of a large number of images. Image analysis is only one tool which can help in the evaluation of this number of images [2].

Image analysis is extensively developed in the last decade. Several fast algorithm and mathematical method were created to solve simple and complex problems. In materials science, the metallographic examinations use extensively image analysis mainly in the mentioned evaluation and qualification tasks [3]. As it was mentioned above in the case of castings, the comprehensive mechanical testing could be an extremely hard work or impossible. For this reason, there are image analysis systems nearly the all quality control lab of foundries [1].

Mainly hypo-eutectic aluminium-silicon alloys are used in die casting. The microstructure of this alloys contain primary aluminium dendrites and eutectic colonies. The eutectic colonies are built-up by silicon plates in an aluminium matrix. The aluminium and the aluminium matrix are ductile. For this it is necessary to measure the size of the aluminium dendrites and the eutectic colonies too. The dislocation free path is the important parameter which has a strong relation to the strength and the elongation of the material. There are more measures which can describe the size of the dendrites and eutectic colonies [4]. It is necessary to find that geometrical parameter which proportional to the dislocation free path.

Samples were examined which were produced according to [1]. Thin walled samples produced by



die casting with several thicknesses. This article shows the metallographic techniques, the algorithm of image analysis and the evaluation method.

## 2. METHODS

Samples were cut from the casted parts. The samples were mounted in resin. The cross sections of the samples were examined. The examined surface of the samples was grinded and polished. The polishing was made by 3 $\mu$ m diamond paste. The surface of the samples was etched by hydrofluoric acid. The whole cross section of the samples was necessary for the examination therefore tile images were taken by Zeiss AxioImager M1m microscope and Zeiss AxioVision software. The images were analysed.

The tile images were too large for the analysis, therefore 1024x512 pixel sized images were cut out from the tile images. The single images were analysed separately. The images were cut out as a moving window along the thickness of the sample. The longer measurements of the cut images were parallel of the surface of the casting. The windows moved through the thickness with  $\frac{1}{4}$  overlap. This proved a stability of the measured results. This analysis was performed in three independent positions. Figure 1 shows an illustrated sample of a 2mm wide sample.

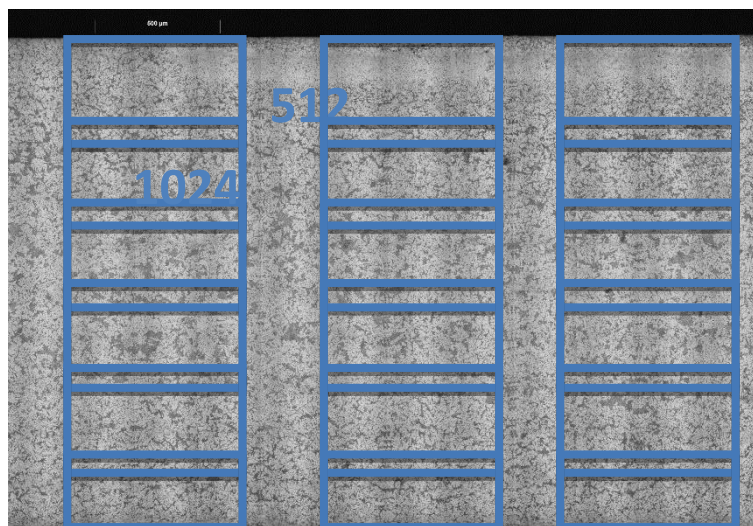


*Figure 1* The tile image with the analysed image. Images cut out from the tile image for analysis

The images are prepared for the segmentation. An automatic contrast method was applied. Automatic segmentation technique (moment) was used for distinguishing the eutectic area and the primary dendrites. Binary transformation also used to remove digital noise from the images. This digital noise means small white dots in the eutectic area. Binary open was applied to remove these dots. Figure 2 shows a grayscale image and a binary image.

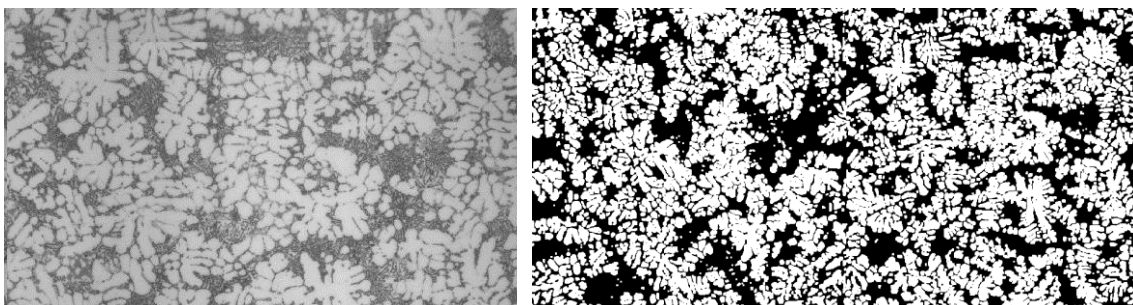




Figure 2 One grayscale image cut out from tile image and a binary image before measurement. The white areas are the primary dendrites, the black areas are the eutectic colonies. Both have complex shape. Simple parameters are necessary to measure which characterize the microstructures. The trivial choice is the specific surface of the dendrites, but this value has not a direct relation to the dislocation free path. The area fraction of the dendrites and the eutectics can be easily measured. The horizontal and vertical projected diameters also can be measured easily. A parameter was constructed based on these values according to (1).

$$WAPD = X_{dendrite} \overline{Proj}_{dendrite} + X_{eutectic} \overline{Proj}_{eutectic} \quad (1)$$

In the equation WAPD is the mentioned parameter.  $X_{dendrite}$  is the area fraction of the primary dendrites,  $X_{eutectic}$  is the area fraction of eutectic colonies.  $Proj_{dendrite}$  and  $Proj_{eutectic}$  are the average of the horizontal and vertical projected diameters. This parameter has a direct correlation of dislocation free path because of both volumes, the eutectic and primary dendritic, can be deformed in some extent. These parameters were measured on the images. All image means a position so it is possible to plot the results according to the wall thickness.

### 3. RESULTS

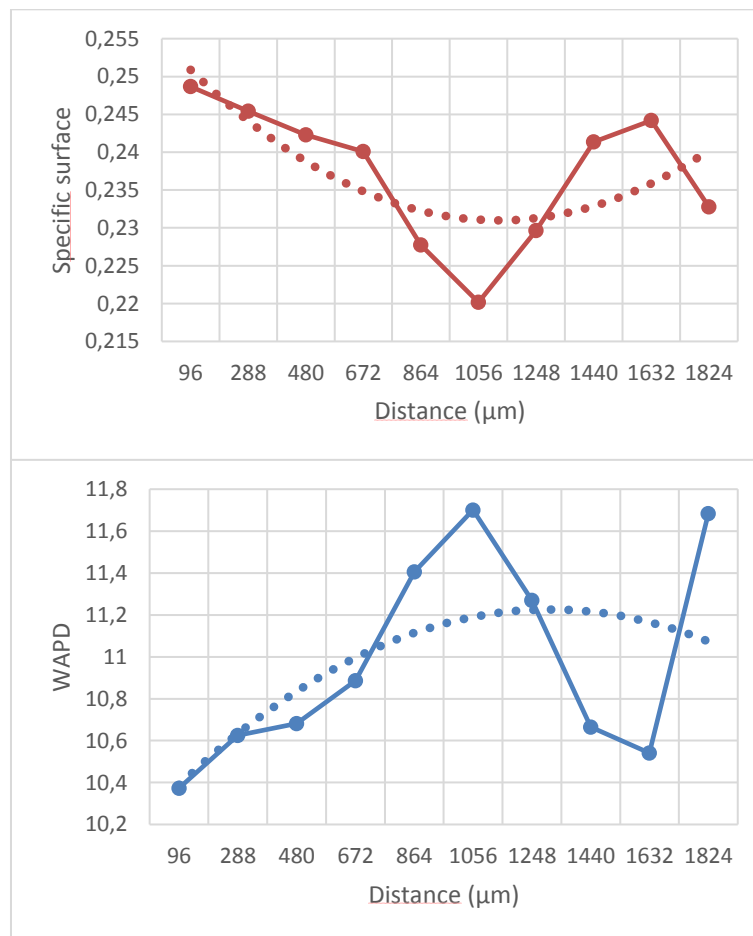


Figure 3 The results of the analysis of Figure 1. The upper graph shows the changes of the specific volume, the lower graph shows the changes of WAPD parameter along the thickness of the sample



Figure 3 shows the measured results of the 2mm wide sample. It can be seen on the graphs that the structure of the dendritic area and the eutectic colonies are finer in the surface of the sample than the middle. The fits with the prior observation. The graphs show a difference between the two sides of the sample. Probably this originated to the supply of the tool. In the warm side the microstructure is coarser.

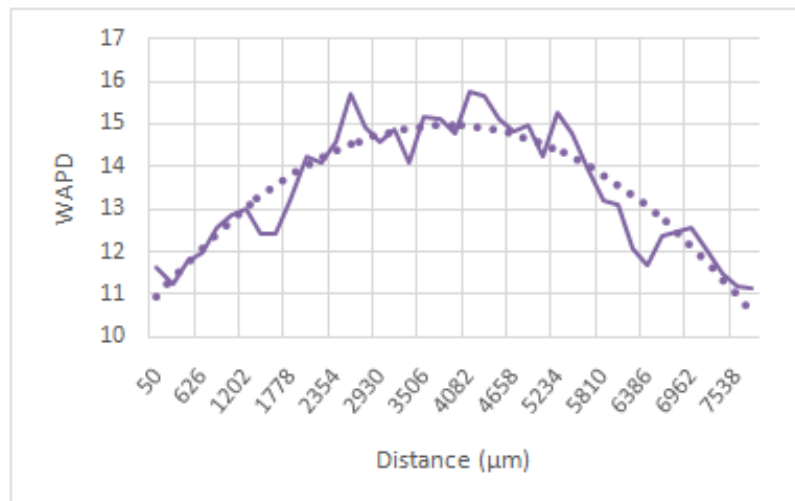
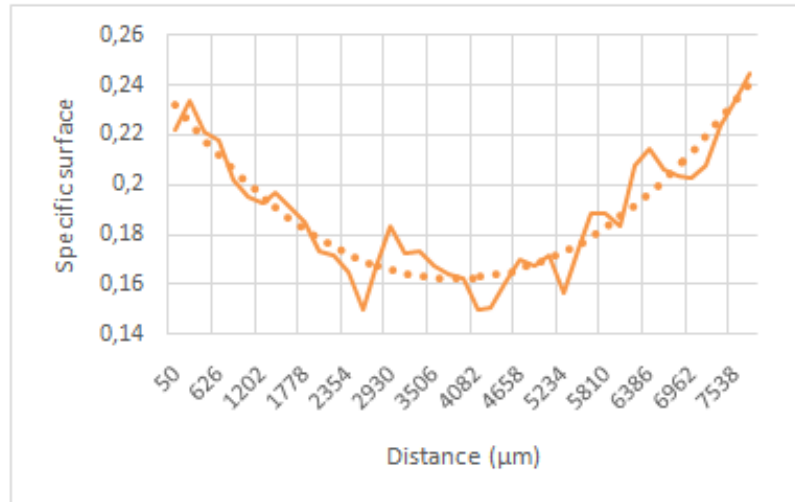


Figure 4 The results of the analysis of the 8mm wide sample. The upper graph shows the changes of the specific volume, the lower graph shows the changes of WAPD parameter along the thickness of the sample. The micrograph shows the tile image.

Figure 4 shows the results of the measurement of 8mm wide sample. It can be seen that much more images build up the tile image. It means a really large amount image to analyse. This only can perform by the introduced automated method. The results show the same. The structure finer next to the wall, and coarser in the middle. The comparison of the two samples shows that the difference between the surface and the bulk is larger in this case. The thickness of the sample is larger so the difference in the cooling rate is also larger. The larger difference in cooling rate causes larger inhomogeneity in the microstructure. Both examples show that the developed method is suitable for characterizing the inhomogeneity of the microstructure in hypo-eutectic castings. It can be seen in the graphs that the specific surface and WAPD parameter show the same and comparable. The specific surface can be measured easier and shorter computation time than WAPD parameter.



## **CONCLUSIONS**

Plates were casted from aluminum alloy in different thickness in a previous research. The microstructure, mainly the inhomogeneity in the microstructure was measured by image analysis method. A tile image was taken from the cross section of the image. Image sequence was cut out from the tile image along the wall thickness. Specific surface of the dendritic area, and a complex parameter (WAPD) were used to describe the whole image. All images indicate a position along the thickness of the wall. The mentioned measurements were plotted as a function of thickness. Both parameters clearly describe the inhomogeneity in the microstructure. But the measurement of the specific surface a fast method, and smoothly shows the differences. Based on the results the introduced method and the specific surface are suggested to characterise the inhomogeneity in thin walled castings.

## **References**

- [1] Léránth G., Barkóczy P.: Nyomásos öntvények vizsgálata, Miskolci Egyetem Közleményei: Anyagmérnöki Tudományok, Vol 37., pp 277-284, 2012
- [2] Leszek Wojnar: Image Analysis applications in materials engineering, CRC Press, 1999.
- [3] Qiang Wu, Fatima Merchant, Kenneth R. Castleman: Microscope Image Processing, Elsevier, 2008.
- [4] Gácsi Z., Barkóczy P.: Számítógépi képelemzés, [www.tankonyvtar.hu](http://www.tankonyvtar.hu)



## AUTOMOTIVE ENGINEERING POSSIBILITIES IN COMBINING GLOBAL POSITIONING AND VEHICLE DIAGNOSTIC

**BUSZNYÁK Tibor, LAKATOS István PhD**

Széchenyi István University

E-mail: [tibroclassix@gmail.com](mailto:tibroclassix@gmail.com) , [drlakatosi@gmail.com](mailto:drlakatosi@gmail.com)

### Abstract

*Our research examines an alternative way when global positioning (GPS) and on-board diagnostics are used to measure a vehicle's drive and performance characteristics, as well as to examine the accuracy of certain systems.*

*Relationship between speed, consumption and elevation is looked for in this paper, with the help of same-time on-board diagnostics and GPS terrain measurement at different speeds. Related literature both from Hungary and abroad in the topic has been studied for this reason, devices for the measurements have been set up, measurements have been planned and carried out. The conditions of the measurements as well as the digital data processing devices and methods are introduced.*

*As a first step, we prove that it is possible to deduce certain parameters of a combustion engine based on elevation data at standard speeds, and to create an elevation model based on the data of a combustion engine. Examining this relationship at a further level, consumption data and their changes are analysed at different speeds. In the first case, measurement was carried out under nearly standard terrain conditions on flat surface, whereas in the second one, which is the basis to the present essay, under changing elevation conditions. Data from several sources- a modelled consumption based on GPS data and calculated from on-board diagnostics data- are compared.*

**Keywords:** OBD, RTK GPS, elevation, consumption, vehicle

## 1. INTRODUCTION

A highly important demand on the customer's and thus the producer's side concerning modern vehicles is consumption. Its predictability is one of the most relevant issues for the everyday person and for the fleet owner as well, both for financial and environmental reasons. We wish to introduce an alternative way to measure the consumption characteristics of a vehicle with the help of global positioning and on-board diagnostics. High precision geodesic and vehicle diagnostic measurements were carried out both at standard and changing speeds. We examined whether it is possible to create a topographic elevation model with the help of the diagnostic data of a vehicle. In case it is, consumption can be predicted based on certain route and vehicle attributes.

## 2. METHODS

### Global Positioning Device System

Our method is the RTK (Real Time Kinematic) GPS (Global Positioning System). Mounting the device on the vehicle, the vehicle's spatial position can be identified with geodesic accuracy ( $\Delta h \sim 5-6$  cm,  $\Delta s \sim 3-4$  cm) at a given moment. A designed route can be driven along, the real elevation features of which can thus be modelled. The survey was carried out using GPS Trimble 5,800 device, capable of phase survey. The data were processed with the help of Trimble Survey Controller 12.22 control unit and ArcGIS 10.1 software [1].



### Onboard Diagnostic Device System

The second basis of the concept is OBD (On Board Diagnosis). OBD is an on-board diagnostic system. With the help of OBD, a vehicle's data generated throughout a given journey (speed, consumption and lambda sensor voltage) can be obtained. The device used for the survey was a Car Chip Pro Data Logger [2].

### Attaching the Devices to the Vehicle, Boundary Conditions

The surveys were carried out using a modern Ford B-Max car with an unladen weight of 1279 kg. The engine is a 3-cylinder, 100 HP, 74 KW new design 1 litre (999 ccm) EcoBoost engine with turbocharge, which can achieve 170 Nm torque. An OBD and a GPS device were attached to the car at the same time in order to make route modelling possible using two independent methods. Comparing the two sets of data, we can see whether there is a connection between them.

Before surveying, both GPS and OSB has to be attached to the vehicle. OBD can be mounted by simply plugging it into the vehicle's adequate socket. When mounting GPS, all the receiver's degree of freedom have to be fixed in a perpendicular position to the wheels' plane ensured with the use of bubble vial. Throughout the survey, every rapid change like using the brakes, a rapid turn or stop is to be avoided, that is the reason why a route with less traffic is to be chosen. To ensure the adequate work of the combustion engine, it is also worth carrying out measurement with as standard outward temperature as possible. Moreover, strong winds can also influence the data, so weather conditions have to be taken into consideration.

The control unit of GPS works with a T-Mobile SIM card, thus a priority condition is a minimum of GPRS connection. The receiver unit has to have a connection to at least 5 satellites at the same time, which means the designed route can not be lined by bigger objects that could influence the view or give shadow (mountains, trees, electrical wires) [3].

### Pre-processing Data

Correlation is sought for between elevation and consumption. To achieve this, the data of the two different devices have to be synchronised, without which data procession is impossible. As the Data Logger measures only air intake, it was corrected by lambda value, using the following formula:

$$\lambda = \frac{10(1 + U)}{14.64} \quad (1)$$

where:

- U: voltage of the lambda sensor,
- 14,64: air volume belonging to theoretical mixture rate (lambda=1)

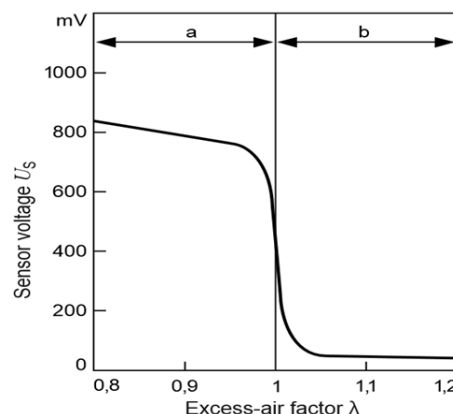


Figure 1 Characteristic of the lambda sensor [4]



### 3. RESULTS

#### Statistical Analysis, Single-variable Analysis

The analysis consists of two main phases. First, data gained at a standard 30 km/h speed ensured by tempomat were analysed. In this case, GPS elevation coordinates were used to generate direction tangent, which were generated from horizontal and vertical projections. Thus, an elevation angle was calculated for each point, the trend of whose can be compared to consumption.

$$r^2 = \frac{\sum_{i=1}^n (\hat{y}_i - \bar{y})^2}{\sum_{i=1}^n (\hat{y}_i - \bar{y})^2} = \frac{[\sum_{i=1}^n (x_i - \bar{x})(y_i - \bar{y})]^2}{\sum_{i=1}^n (x_i - \bar{x})^2 \sum_{i=1}^n (y_i - \bar{y})^2} \quad (2)$$

In other words, how consumption changes can be explained by elevation changes. Coefficient of determination gives information on this.

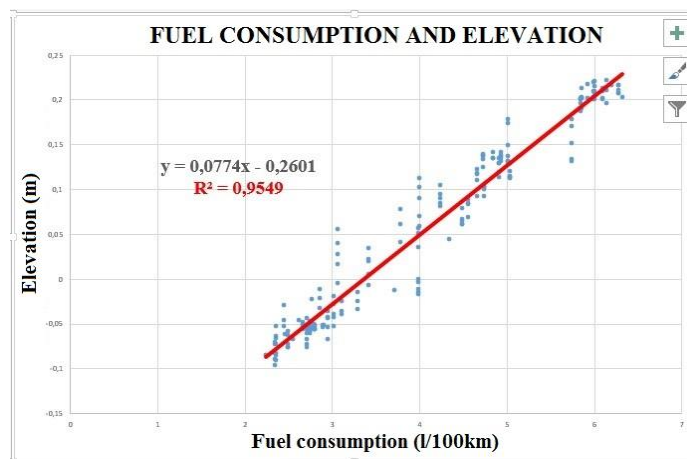


Figure 3 The function and correlation

The basic theory of the measurement that it is possible to predict consumption from elevation conditions at standard speed has been proven to be true at least at 95%. Next, with the help of the correlation function, real elevation conditions and those calculated from consumption are fitted and shown on diagrams.

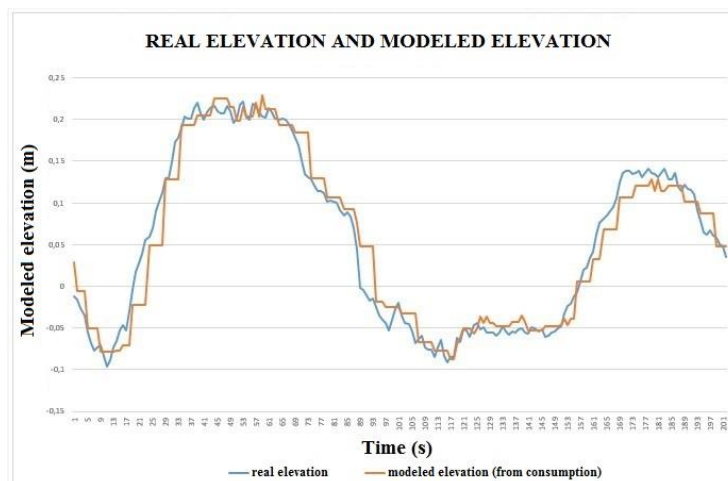


Figure 4 Trends at standard speed and changing elevation



As at the speed of 30 km/h, the two datasets correspond excellently, the analysis was carried out with data gained at speeds 40 and 50 km/h as well. The results are informative, at the speed of 40 km/h, coefficient of determination is 91.6%, at speed 50 km/h it is 83.7%. Noticably, the correlation gets slightly lower, which means that at higher speeds, other explanatory variables are to be introduced.

### Statistical Analysis, Multi-variable analysis

The parameter system was widened after the single-variable analysis. Changes of the correlation were examined when surveying at continuously changing speeds. This is in fact a real life situation modelled, with designed speeding and slowing. Consumption was to be predicted at changing speeds and changing elevation.

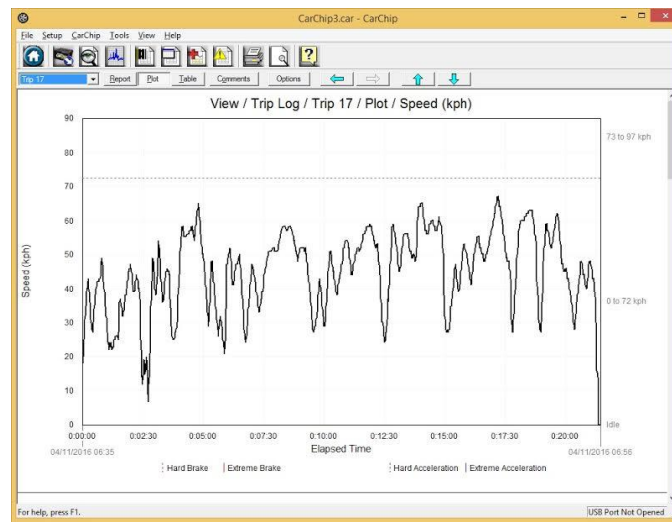


Figure 5 Log diary of changing speed section

Consumption is to be predicted at higher elevation and changing speed, so owing to the new parameters, a new mathematical tool has to be used. This mathematical tool is linear regression, where the needed variable can be predicted at a 95% significance level, with several explanatory variables.

$$SSE = \sum_{i=1}^N [y_i - f(x_i)]^2 = \sum_{i=1}^N [y_i - \omega_1 x - \omega_0]^2 \quad (3)$$

When selecting new variables, the energy need of the vehicle should be examined. Driveloading equation:

$$F = (\mu \times m \times g) + (m \times g \times \sin(\alpha)) + \left(\frac{1}{2} \times A \times \rho \times g \times v^2\right) + (m \times a) \quad (4)$$

The formula on the right shows that beside elevation changes, speed and its change are relevant, thus we have got the new parameter(s) to be introduced:

- acceleration work~ $\Delta(v^2)$ ,
- elevation difference (from potential energy)~ $\Delta h$ ,
- air resistance~ $v$ ,
- losses~ $U$  (constant).



Based on these, regression analysis can be done.

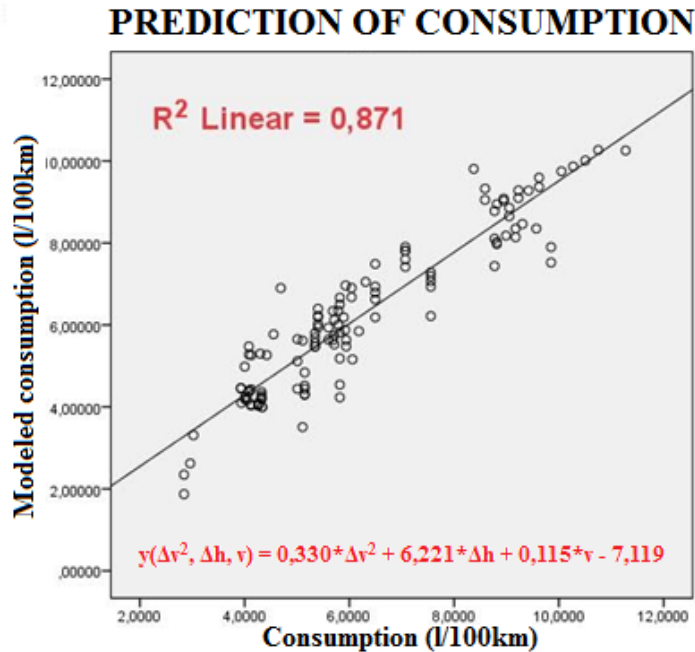


Figure 7 Prediction of consumption

The diagram of the real consumption is fitted to that of modelled consumption [5]. It can clearly be seen that change trends are similar, even through several variable analysis.

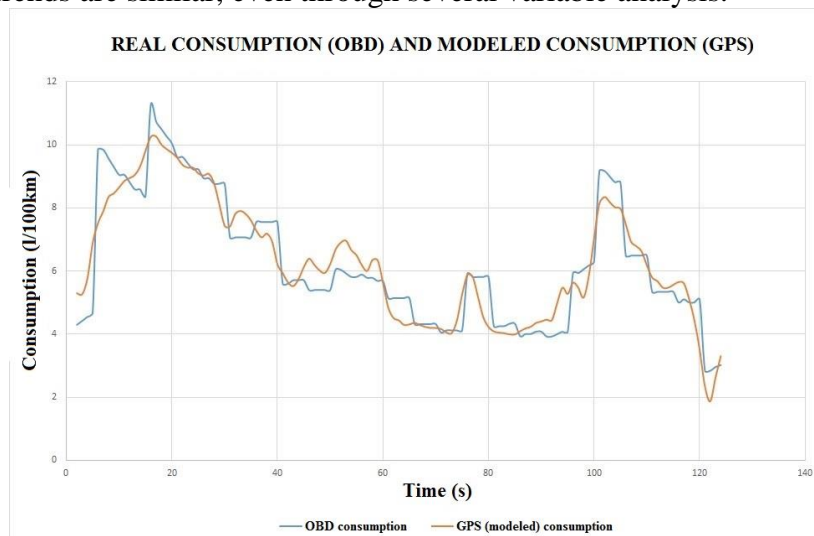


Figure 8 Trends at changing speed, changing elevation

## CONCLUSIONS

With diagnostic and positioning surveys, a database suitable for statistical analysis could be created. The theoretical issues set in advance were proven. The survey and data procession methods used in the research are highly usable with parameter systems adequate to certain circumstances.



# INTERNATIONAL SCIENTIFIC CONFERENCE ON ADVANCES IN MECHANICAL ENGINEERING

12-14 October 2017, Debrecen, Hungary



## ACKNOWLEDGEMENT

The research has been realised by the project: "Internationalisation, initiatives to establish a new source of researchers and graduates, and development of knowledge and technological transfer as instruments of intelligent specialisations at Széchenyi István University"

## REFERENCES

- [1] ESRI Arc GIS Editing Tutorial  
<http://help.arcgis.com/en/arcgisdesktop/10.0/pdf/editing-tutorial.pdf>
- [2] CarChip Software Version 2.3 Online Help Printable Version (6/11/2007)  
[http://www.carchip.com/Product\\_Docs/8226-46-21-45\\_CarChip\\_OnlineHelp.pdf](http://www.carchip.com/Product_Docs/8226-46-21-45_CarChip_OnlineHelp.pdf)
- [3] Trimble Survey Controller Help Revision A October 2008  
<http://www.geotrade.hu/index.php?page=letoltes&spage=fajl&id=220>
- [4] Characteristic of Lambda sensor  
[http://www.bosch-lambdasonde.de/en/lambdasonde\\_funktion.htm](http://www.bosch-lambdasonde.de/en/lambdasonde_funktion.htm)
- [5] Min Goo Lee, Young Kuk Park, Kyung Kwon Jung, Jun Jae Yoo: *Estimation of Fuel Consumption using In-Vehicle Parameters*. International Journal of u- and e- Service, Science and Technology Vol. 4, No. 4, December, 2011.



## CHANGES OF MICROSTRUCTURE AND MECHANICAL PROPERTIES OF NANO CRYSTALLINE STEEL X37CrMoV5-1 SUBJECTED TO HEAT TREATMENT AS IS USED DURING NITRIDING

*CHMIELARZ Krzysztof, MARCINIAK Szymon*

*Institute of Surface Engineering, Faculty of Material Science, Warsaw University of Technology  
E-mail: [krzysztof.chmielarz@nanostal.eu](mailto:krzysztof.chmielarz@nanostal.eu) , [szymon.marciniak@nanostal.eu](mailto:szymon.marciniak@nanostal.eu)*

### **Abstract**

*The aim of this study was to investigate changes that occur in nanobainitic microstructure of X37CrMoV5-1 hot work tool steel during annealing in a temperature range at which nitriding process is performed. Moreover the effect of these changes on mechanical properties of the hot work tool nanostructured steel was investigated. The purpose of these studies was to check if nitriding process could be successfully applied to the hot work tool nanobainitic steel. The possible phase transformations that could occur during various annealings were widely checked via dilatometric and microscopic survey. According to the research, annealing of X37CrMoV5-1 steel at temperature in the range between 500-600 Celsius leads to carbides precipitation and grain growth. After complete heat treatment steel presented a submicron bainitic microstructure with mechanical properties different than in the initial nanostructured state.*

**Keywords:** *Nanobainit, nanosteel, bainit nitriding, X37CrMoV5-1 nitriding, nanobainit temperature stability.*

### **1. INTRODUCTION**

One of the latest method of improving the mechanical properties of steel is nanostructuring through austempering in range of bainitic transformation temperatures (the so called nanobainitization) [1]. This process that indicates rapid cooling of steel slightly above Ms temperature and then annealing for several dozens of hours. Thanks to large overcooling of material a large density of bainitic ferrite nuclei appear, leading to a nano-sized plates of bainite separated by thin layers of retained austenite. The nanobainitic steels should contain an increased content (of about 1,5 wt.%) of silicon and/or aluminium which prevent carbide precipitations [1]. As a result a carbide free microstructure is formed. Especially important are carbon with concentration 0,6÷1,1 wt.% and manganese, which are responsible for tempering and for austenite stability, Nanobainitic steels are characterized by high mechanical properties – their hardness can get up to 700HV, with considerable elongation and high tensile strength and fracture toughness [2][3]. It is assumed that the nanobainitic steels could replace maraging steels which consistently have very good properties but are extremely expensive due to the large amount of alloying elements and complicated heat treatment [4]

The properties of nanobainitic steels may be insufficient for many applications, especially in heavy industry, i.e. mining. For example steels for gears or high-load components need to have higher hardness and fatigue resistance. In order to obtain such properties, steels are often subjected to nitriding processes. Usually, nitriding is carried out at temperatures between 500 – 600 °C. Unfortunately, at this temperatures nanobainitic microstructure is falling apart [5].

The question arises whether it is possible to combine both types of treatments: nanobainitizing and nitriding, while preserving properties of nanobainite in the core of the element and to get higher hardness on the surface. To answer this question the investigations of changes that occur in



nanobainitic microstructure of X37CrMoV5-1 hot work tool steel during annealing in a temperature range of nitriding process were carried out. Moreover the effect of these changes on mechanical properties of the steel was analysed.

## 2. METHODS

X37CrMoV5-1 steel is a tool steel for hot work. It is not typical kind of steel used to nitriding, but it can be nitrided with a satisfactory result. It is also possible to obtain nanobainitic structure [6], therefore it would be perfect material to nitride steel with nanocrystalline structure.

*Table 1* Chemical composition of tested X37CrMoV5-1 steel

	C [%]	Si [%]	Mn [%]	Cr [%]	Mo [%]	V [%]	Ni [%]	P [%]	S [%]
<b>X37CrMoV5-1</b>	0,37	1,01	0,38	4,91	1,2	0,34	0,19	0,02	0,004

The main device used for research was a differential inductive dilatometer Bähr DIL 805L that allows the measurement in a temperature range from -150 to 1500 °C with the accuracy of changes in length 0,05µm and 0,05 °C temperature changes. Charpy's impact strength was tested on Zwick/Roell RKP 450 hammer with energy 300J, tensile strength on INSTRON 1115 with extensometer at a tensile speed of 0.032mm/s and a pre-force of 20N. Microstructure was investigated by use of Nikon Eclipse MA200 light microscope and transmission electron microscope TEM JEOL 1200 operating at 120 kV.

## 3. RESULTS

In the first part of the work, heat treatment processes were carried out in a dilatometer, recording changes in elongation of the steel sample to reveal the phase changes that occur during the process. The nanostructurization process was performed on X37CrMoV5-1 steel atin 300 °C for 19 h to get stable nanobainitic microstructure. Then, in order to simulate nitriding process, the steel samples were annealed at 480 °C for 12 h. Those values could be considered as nitriding time and temperature respectively. During final cooling after annealing simulating the nitriding process martensitic transformation occurred in the specimen. This confirmed, that just according to our predictions, the austenite got unstable and underwent a martensitic transformation. It have established that it is impossible to carry out a conventional gas-nitriding process which permit preserve a nanobainitic microstructure. Therefore, a modification of the thermal processing was applied. The modification consisted of a periodic increase of the process temperature to a nitriding temperatures zone followed by a decrease in temperature to a nanobainitizing temperature (300°C) as shown on fig 1. It was expected that such a process would prevent the martensitic transformation during final cooling and would maintain good properties of the core. It was decided to increase the temperature after 2h 30min of austempering at 300 °C which correspond to the time when around 90% of bainitic ferrite is formed.

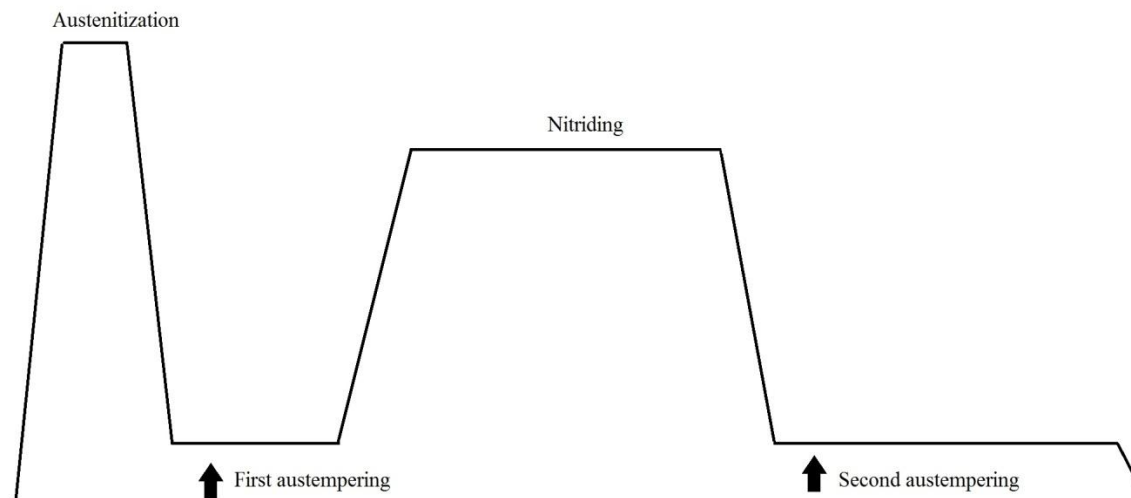


Figure 1 Schematics of proposed nitriding process

The thermal processing at nitriding temperatures simulated two steps nitriding – first at 490 °C for 1 h and second step at 550 °C for 24 h. Those parameters gave the best nitrated layers on X37CrMoV5-1 as it was shown in [7]. The second austempering at 300°C lasted 5 h which should be sufficient to stabilize retained austenite present in the microstructure. Unfortunately, at the end of the process martensitic transformation was observed. This phenomena could arise from the carbides precipitation process which occurred during prolonged annealing at 550°C. Dilatometric curve indicated that a rapid increase in carbide precipitation occurred after 15h of annealing at 550°C.

In order to decrease amount of carbide precipitation and to stabilize austenite it was decided to remove first step of nitriding and to shorten time of nitriding to 15 h. Thus, the second performed process consisted of: austenitization at 1030 °C, austempering at 300 °C for 2.5 hours, heating at 500 °C for 15 hours simulating nitriding followed by the second annealing at 300 °C for 5 hours. Again, during the final cooling martensitic transformation occurred. Therefore, in the third process time of second austempering was extended, in order to increase the amount of bainitic ferrite and to avoid the martensitic transformation. Four variants of the modified second austempering were performed, with the following parameters: 300°C – 10 h, 300 °C – 15 h , 300 °C – 35 h and two-step annealing 300 °C – 5 h and then 260 °C – 10 h (Table 2).

Despite increased length of the second austempering and increased amount of bainitic ferrite, at the end of each process the martensitic transformation occurred in all tested variants, although the longer was the time of austempering, the lower was the Ms temperature during final cooling and the smaller was amount of martensite. Unfortunately, this changes were disproportionately small to the extent of annealing time.

Since changing the second austempering time didn't give the expected results, it was decided to change the temperature of nitriding simulation. Except aforementioned 550 °C we also conducted simulations at different  $T_N$  temperatures: 500 °C, 530 °C, and 580 °C (table 2). The best result was obtained for initial nitriding simulation temperature – 550 °C. To our surprise decreasing temperature of nitriding simulations lead to increasing Ms temperature during final cooling of samples. A strong effect reflecting the carbides precipitation was observed on dilatometric curve during annealing at 580 °C. This process was confirmed during TEM observations. The TEM micrographs presented huge density of carbides inside grains and on grain boundaries. The TEM micrographs indicate also that the microstructure obtained after nitriding simulation has mainly submicron, not nano – sized grains.



Table 2 Parameters of described processes

Austenitisation	First austempering	Parameters of nitriding simulation: $T_N - t_N$	Second austempering
1030 °C – 15 min	300 °C – 2h 30 min	490 °C – 1h+550 °C – 24 h 550 °C – 15h 500 °C – 15h 530 °C – 15h 580 °C – 15h	300 °C – 5h 300 °C – 15h 300 °C – 35h 300 °C – 5h+260 °C 10h

The aim of the second part of the work was to compare mechanical properties of steel samples after nanobainitization performed at 300°C-19h and after the nitriding simulation process. Samples for nitriding simulation were prepared with the following parameters of heat treatment: austenitization at 1030 °C, austempering at 300 °C for 2.5 hours, heating at 550 °C for 15 hours, then second austempering at 300 °C for 5 hours. These parameters were chosen since they might have had promising microstructure and were economically justified.

Table 3. Comparison of properties of structures after nanobainitization and after simulation of nitriding.

Table 3

Austempering parameters	$R_{0,2}$ [MPa]	$R_m$ [MPa]	A [%]	Charpy Impact toughness [J/cm <sup>2</sup> ]	Hardness [HRC]
300 °C-19h	822	1709	12,9	19	52,9
300 °C-2,5h+550 °C-15h + 300 °C-5h	1604	1918	6,9	6,1	52,9

Both types of specimens differed significantly in mechanical properties. The samples after heat treatment simulating nitriding exhibited lower ductility and impact toughness, higher yield strength and similar hardness as compared to samples after nanobainitizing at 300°C-19h.. The low ductility and impact strength of samples after nitriding simulation could be explained by presence in the microstructure of martensite and carbides which precipitated on grain boundaries.. The higher yield strength and tensile strength that have samples after nitriding simulation could result from high density of carbides present in the microstructure (Photo 2).

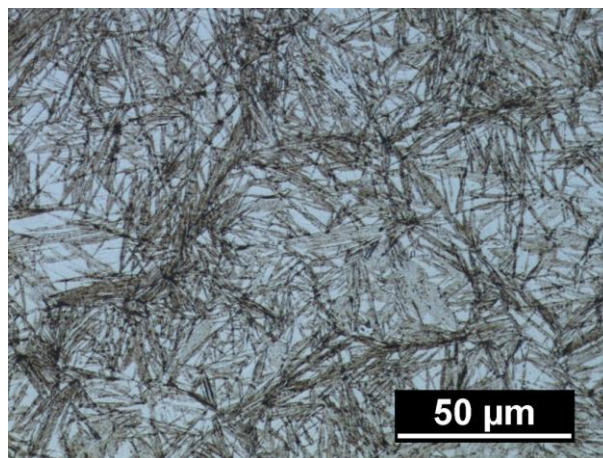


Photo 1 Structure of X37CrMoV5-1 steel after final nitriding simulation process. Bainite and retained austenite are visible.



Photo 2 Microstructure of X37CrMoV5-1 steel after final nitriding simulation process

The microstructure consists of bainitic ferrite plates and martensite laths with a huge density of strongly dispersed carbides.

## CONCLUSIONS

The annealing simulating nitriding at temperatures between 490 and 580°C of nanobainitic X37CrMoV5-1 steel led to strong changes in the nanocrystalline microstructure.

The changes consisted of formation of martensite, precipitation of carbides inside bainite and martensite grains and coarsening of a microstructure to the submicron size.

The observed changes led to reduction of ductility and impact toughness, to increase of yield and tensile strength.

Any of heat treatment variants did not permit to avoid changes in obtained microstructure and properties of the core during nitriding simulation. Described processes cannot be used to nitride nanobainitic steel, and further research on this field are required.

## REFERENCES

- [1] H. K. Dharamshi, H. K. D. H. Bhadeshia, C. Garcia-Mateo, P Brown "Bainite steel and method of manufacture thereof." Patent application publication No US 2011/0126946 A1 June 2011
- [2] F.G. Caballero, M.K. Miller and C. Garcia-Mateo „Design of Novel Bainitic Steels: Moving from UltraFine to Nanoscale Structures” JOM, volume 66, issue 5, 2014
- [3] H. K. D. H. Bhadeshia "Nanostructured bainite" Proceedings of the Royal Society A: mathematical physical and engineering sciences, volume 466, issue 2113, January 2010
- [4] K. Wasiluk, E. Skołek, W. Świątnicki "Microstructure and properties of surface layer of carburizer 38CrAlMo6-10 steel subjected to nanostrukturization by a heat treatment process" Archives of Metallurgy and Materials, volume 59, issue 4, 2014
- [5] E. Skołek, S. Marciniak, W. Świątnicki "Thermal stability of nanocrystalline structure in X37CrMoV5-1 steel" Archives of Metallurgy and Materials, volume 60, issue 1, 2015
- [6] S. Marciniak, E. Skołek, W. Świątnicki "The effect of stepped austempering of phase composition and mechanical properties of nanostructured X37CrMoV5-1 steel" " Archives of Metallurgy and Materials, volume 60, issue 1, 2015
- [7] B. Pachutko, L. Małdziński "Ocena grubości warstw azotowanych na stalach 38HMJ i WCL za pomocą przyrządów Wirotest", Obróbka Plastyczna Metali, tom 21, nr 1, 2010



## SHOCK TESTING IN THE EVALUATION OF PACKAGING PERFORMANCE

**CSAVAJDA Péter**

*Széchenyi István University*

E-mail: [csavajda.peter@sze.hu](mailto:csavajda.peter@sze.hu)

### **Abstract**

*Markets and consumers are located widely separated areas from manufacturers. That is why products became subject to transportation, handling and warehousing during the physical distribution. Each element includes hazard to the products such as vibration, shock or static and dynamic load. Packaging helps products arrive in good condition to the consumers. Use of packaging pre-shipment testing is performed to check and control the ability of packaging exposed to real physical stresses in the distribution environment. Manual and mechanical handling operations always generate risk of packages being dropped, thrown and bounce. These different dynamic effects are characterized by amplitude, duration and velocity change and can be reproduced by a free-fall drop tester or a shock machine. Furthermore, the standard procedures (distinguish?) make difference in not only between individual packaging and unit load, but also in the impact surfaces. This paper summarizes the key principles of shock testing in the evaluation of packaging performance.*

**Keywords:** *shock, free-fall drop, packaging, testing*

### **1. INTRODUCTION**

Physical distribution contains three logistic activities. Transportation moves products from point to point using different modes and equipment. Warehousing helps ensure availability to satisfy demand. Handling connects the parts of the logistics system, which include the following elements: manufacture to warehouse, warehouse to shipping equipment, and shipping equipment to retailer. Each activity includes hazards to the products and packages. Vibration, static and dynamic loads are also able to damage the goods, but numerous studies have shown that shock is the main reason for product damage during transportation [1-2]. Selection of the optimal packaging (cushioning) is a significant step in the defence against shock [3].

Thus, this study focuses on the theoretical factors and the laboratory simulation methods of shock. In general, shock means a rapid change in something over a very short period of time. Rapid changes in temperatures are also a type of shock, but this is not part of this paper. This study focus only on the mechanical shocks related to physical distribution of packages. In the logistics processes, it could be occurred during mechanical movement of the transportation (sudden stops and starts, turning, speed-up). The most common shock suffered by packages in the handling activities, result from handling drops. It also may result from being hit when another package dropped onto it. Automated material handling system, such as diverters on a conveyor belt, is also able to cause shock events on the packages.

The duration of the impact is the main factor of the shock event. It is depending on the quality and amount of the cushioning used to protect the product and on the rigidity of the impacted surface.

Beside primary packages, unit loads are also experience shocks relate to mechanized material handling systems, e. g. pallet truck, forklift, but they are suffered the most dangerous shocks result from horizontal static and dynamic effects, e. g. vehicle acceleration, vehicle turning.



## 2. FUNDAMENTALS OF SHOCK

Shock pulses are produced when a falling object strikes the ground. Impact velocity of the falling object is related to package damage:

$$V_I = \sqrt{2gh} \quad (1)$$

where

$V_I$  = impact velocity (m/sec)

$g$  = gravitational acceleration (m/sec<sup>2</sup>)

$h$  = drop height (m)

As *Figure 1* shows, they are characterized by measurement of amplitude (acceleration level), duration (length of time) and velocity change (sum of the absolute impact and rebound velocities).

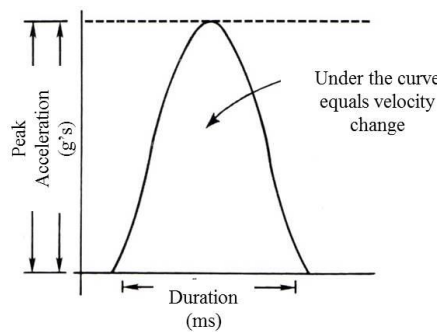


*Figure 1* Shock pulse

The relationship between impact velocity  $V_I$ , and rebound velocity,  $V_R$  is shown in *Figure 2*.

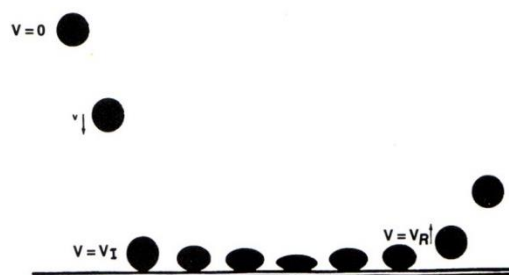


*Figure 2* The relationship between impact velocity and rebound velocity

The elasticity of impact is not perfect, so the result will not be  $V_I = V_R$ . The degree of elasticity can be defined by the coefficient of restitution,  $e$ .

$$e = \frac{v_R}{v_I} \quad (2)$$

where

$e$  = coefficient of restitution

$V_R$  = rebound velocity (m/sec)

$V_I$  = impact velocity (m/sec)



The value of “e” is usually between 0,3 and 0,5, but will have values between zero and one.

The total velocity change ( $\Delta v$ ) can be defined as  $\Delta v = |v_I| + |v_R|$ . Knowing that  $v_I = \sqrt{2gh}$  and  $v_R = ev_I$ , Equation 3 can be derived.

$$\Delta v = (1 + e)v_I = (1 + e)\sqrt{2gh} \quad (3)$$

where

$\Delta v$ =velocity change (m/sec)

e = coefficient of restitution

g = gravitational acceleration (m/sec<sup>2</sup>)

h = drop height (m)

Based on the possible values of the coefficient of restitution, velocity change falls between

$$\sqrt{2gh} \leq \Delta v \leq 2\sqrt{2gh} \quad (4)$$

### 3. PARAMETERS OF SHOCK EVENTS DURING DISTRIBUTION

Various previous studies have been done to quantify the impact and drop levels that packages experience during the distribution. These papers can be divided into 2 main categories based on the type of the shipment: palletized or non-palletized freight.

Singh et al. measured the environment within FedEx Second-day Air Delivery System for small and light-weight package. The authors concluded that neither the package size/weight nor the labels had any significant effect on the handling of packages. During 4 routes of 5 shipments, the maximum drop height was 1,851 m, but the drop height at 90% occurrence of the different types was only between 0,406 and 0,609. [4]

A study by Martinez et al. investigated the air parcel shipping environment for DHL and FedEx between Europe and United States. They did not find significant difference between the use or absence of warning labels. They conducted that a package suffered an average of 27 drops drop height at 95% occurrence was below 0,57 m. [5]

The paper of Singh et al. concluded that the handling environments within FedEx and UPS are not significantly different between ground shipping, second-day and next-day, regardless of package size and weight of packages. The 95% level drop heights are all within the range 0.46–0.86m. [6]

The paper of Singh et al. measured the environment of for small packages in next-day air shipments. The maximum drop heights are for 6 different packaging within the range 0.965–1.22m.

Singh et al. measured the environment for air package shipment. 99% of the drops occurred at or below 127 cm and 155 cm (61 in.) for domestic and international air package shipments, respectively. [7]

Zhong et al. investigated the small packages in the express shipping environment of China. They find negligible, slight and significant effects of the pictorial marking, package shape and handle holes. They conducted that 99% of the drops in the shipments of light and middle small packages occur below 40 cm; and those of heavy small packages occur below 30 cm. Although drops from heights greater than 0.5m seldom occur. [8]

Böröcz et al. measured the distribution environment a palletized LTL shipment between Central Europe and South Africa. They have found that the shock levels were generally very low when the



package system was being transported by ship and the most shock physical events happened when the unit was handled at the ports or during transfer between storage and loading on trucks. [9] The paper of Böröcz and Singh concluded that the recorded vibration signals also contains shock events, but these are not usable during the packaging testing, because the commonly used equipment does not suitable for this.

#### 4. SHOCK TESTS IN PACKAGING TESTING STANDARDS

Organizations, for example the International Organization for Standardization and American Section of the International Association for Testing Materials (ASTM) offers standards for different types of shock testing. *Table 1* summarizes the current standards.

*Table 1* Summary of the current testing protocols for shock

Standard	Type of Shock Test	Type of Equipment	Packaging form
ASTM D 5276, ISO 2248	Free-Fall Drop Tests	Free-fall drop tester	Non-palletized
ASTM D 6179, ISO 2876	Tip/Tip over Tests, Rotational Flat Drop Tests, Rotational Edge and Corner Drop Tests	-	Non-palletized
ASTM D 880, ASTM D 4003, ASTM 5277, ISO 2244	Inclined or Horizontal, Impact Tests	Inclined or Horizontal Impact tester	Palletized
ASTM D 5265	Bridge Impact Tests	Free-fall drop tester with edge hazard box	Non-palletized
ISTA 3E	Rotational Edge Drop	Lifting equipment	Palletized
ASTM D 5487	Vertical Shock Test	Shock test machine	Non-palletized

Based on these general standards, the International Safe Transit Association (ISTA) developed test protocols for different packaging form and different distribution channel. Among others, they offer protocols for Parcel Delivery System Shipments, Less-Than-Truckload (LTL) Shipment and Unitized Loads for Truckload Shipment. *Figure 3-6* show the method of different shock tests, rotational edge drop, free-fall drop, vertical shock test and horizontal impact test, respectively.



Figure 3-6 Test method of rotational edge drop, free-fall drop, vertical shock and horizontal impact test

Shock tests are also suitable to determine the acceleration of impact (g's) of the product with a triaxial accelerometer. An observed graph of an impact can be seen on Figure 7.

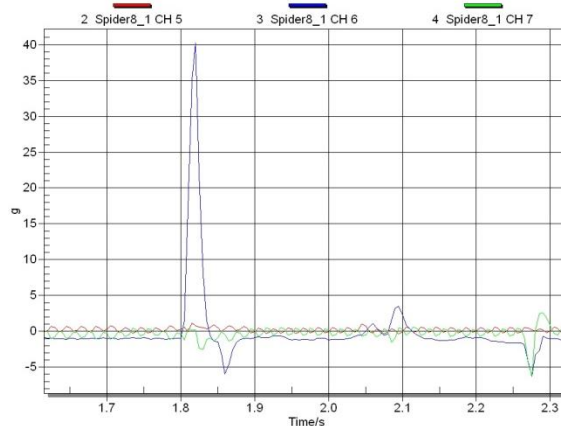


Figure 7 Input shock graph of a free-fall drop test

## CONCLUSIONS

Products have to be moved during the logistics processes. Many of the handling events performed by human and manual handling may create opportunities to drop packages. Packaging engineers have to be developing packaging systems, which decrease the effect of this hazard. Therefore, define the parameters and effects of shock are necessary. Based on these, suitable test programs can



# INTERNATIONAL SCIENTIFIC CONFERENCE ON ADVANCES IN MECHANICAL ENGINEERING

12-14 October 2017, Debrecen, Hungary



be developed and the evaluation of packaging system can be performed. Organizations, such as ISTA, ASTM, ISO issue standards with test programs, but the right choice of three elements, drop height, drop number and drop orientation is very important.

## ACKNOWLEDGEMENTS

The author acknowledges the financial support of this research by the Project EFOP-3.6.1-16-2016-00017. Internationalisation, initiatives to establish a new source of researchers and graduates, and development of knowledge and technological transfer as instruments of intelligent specialisations at Széchenyi István University.

## REFERENCES

- [1] Yam, KL.: *Encyclopedia of Packaging Technology*. John Wiley & Sons, Hoboken, New Jersey, USA, 2009.
- [2] Goodwin, D., Young, D.: *Protective Packaging for Distribution*. DEStech Publications, Lancaster, Pennsylvania, USA, 2011
- [3] Mojzes, Á., Böröcz, P.: *Decision Support Model to Select Cushioning Material for Dynamics Hazards During Transportation*. ACTA TECHNICA JAURINENSIS 8(2) 188-200, 2015
- [4] Singh, S. P., Burgess, G., Singh, J.: *Measurement and analysis of the second-day air small and light-weight package shipping environment within FedEx*. Packaging Technology and Science, 17(3), 119-127, 2006.
- [5] Garcia-Romeu-Martinez, M-A., Singh, S. P., Cloquel-Ballester, V-A., Saha, K.: *Measurement and analysis of international air parcel shipping environment for DHL and FedEx between Europe and United States*. Packaging Technology and Science, 20(6), 421-429, 2007.
- [6] Singh, S. P., Singh, J., Chiang, K. C., Saha, K.: *Measurement and Analysis of 'Small' Packages in Next-day Air Shipments*. Packaging Technology and Science, 23(1), 1-9, 2010.
- [7] Singh, S. P., Singh, J., Saha, K.: *Measurement and Analysis of Physical and Climatic Distribution Environment for Air Package Shipment*. Packaging Technology and Science, 28(8), 719-731, 2015.
- [8] Zhong, C., Li, J., Kawaguchi, K., Saito, K., and An, H.: *Measurement and Analysis of Shocks on Small Packages in the Express Shipping Environment of China*. Packaging Technology and Science, 29(8-9), 437-449, 2016.
- [9] Böröcz, P., Singh, S. P., Singh, J.: *Evaluation of Distribution Environment in LTL Shipment between Central Europe and South Africa*. Journal of Applied Packaging Research, 7(2):45-60, 2015.
- [10] Böröcz, P., Singh, S. P.: *Measurement and analysis of delivery van vibration levels to simulate package testing for parcel delivery in Hungary*. Packaging Technology and Science, Wiley online Library - Early View, 1-11, 2017.



## CONDITION MONITORING BY APPLYING ADVANCED DIAGNOSTIC METHOD

**DEÁK Krisztián, KOCSIS Imre PhD**

Faculty of Engineering, University of Debrecen

E-mail: [deak.krisztian@eng.unideb.hu](mailto:deak.krisztian@eng.unideb.hu), [kocsisi@eng.unideb.hu](mailto:kocsisi@eng.unideb.hu)

### Abstract

*Bearings have vital role in rotary machines. This article focuses on the detection of grinding defects. Vibration measurement in both time and frequency domains along with signal processing techniques such as the high-frequency resonance technique have been covered. For diagnosis of bearings wavelet transform gained remarkable roles in the previous years. Wavelet transform is an efficient tool for analyzing the vibration signal of the bearings because it can detect the sudden changes and transient impulses in the signal caused by faults on the bearing elements. In this article manufacturing faults on the outer ring of tapered roller bearings due to the grinding process in manufacturing are investigated. Five different wavelets, Haar, Gaussian, Coiflet, Mexican hat, Meyer are compared according to the Energy to Shannon Entropy ratio criteria and it is determined which is efficient for detecting the manufacturing faults*

**Keywords:** bearing, diagnosis, wavelet, entropy, grinding problem

### 1. INTRODUCTION

Patel et al. used envelope methods to reveal local faults on the races of deep groove ball bearings [1]. Kalman and H filter were applied by Khanam et al. to measure bearing faults especially in noisy condition with low signal-to-noise ratio when it was difficult to identify the useful components of the vibration signal [2]. Some studies used acoustic signal instead of vibration to identify bearing faults [3,4]. Acoustic emission measurement is a powerful method to detect cracks inside the bearing material which are the initial reasons of fatigue spallings Al-Ghamd and Mba applied this method combined with the traditional vibration analysis to determine the bearing outer race defect width directly from the raw signal [3]. Sawalhi and Randall made their researches to determine the fault size of the bearings from the vibration signal by analyzing the entry and exit impulses [5].

Because of its flexibility and computational efficiency several studies applied the wavelet analysis in bearing fault diagnosis [7-12]. Wavelets are perfect tools for fault feature extraction, singularity detection for signals, denoising and extraction of the weak signals from the vibration signals. These applications were presented by Peng and Chu [6]. Combination of envelope spectrum and wavelet transform for extraction of defect problems in bearings were used by Shi et al. [8]. Discrete wavelet transform with Daubechies-4 (db04) mother wavelets to analyze the combination of different faults on the races of ball bearings were used by Prabhakar et al. [7].

Wavelet filter based denoising is suitable method for detection of weak signatures in bearing fault diagnosis. This experiment was presented by Qiu et al. [10]. Symlet wavelets were used efficiently in the study of Kumar et al. [12]. In their study tapered roller bearings were analyzed to determine the fault size on the outer ring.

Symlet wavelets were used in several papers [7-11] to determine the problems of bearings and machines since its shape is adequate to solve the problem. Symlet-5 wavelet represents the entry



and impact events as the roller hits the defects during operation of the bearing. A detailed study was presented about the decomposition of the vibration signals using discrete wavelet transform with Symlet-5 by Kumar et al. [14]. Moreover, Symlet wavelet is a good tool for noise reduction in ECG signals because it could filter out the useful components of the complex signal from the noisy background [13].

Analytical Wavelet Transform (AWT) based acoustic emission technique for identifying inner race of radial ball bearing were applied by Kumar et al. [15].

Machine learning methods for optimization of parameters such as support vector machines were used by Mankovits et al. [16].

Approaches based on simulation using applied methods are analyzed by Szántó et al. [23-24.] where Matlab software are emphasized to find solutions for real applications.

## 2. ADVANCED INTEGRAL TRANSFORM FOR DIAGNOSIS

Wavelet transform is continuous or discrete and it is calculated by the convolution of the signal and a wavelet function. A wavelet function is a small oscillatory wave, which contains both the analysis and the window function. Continuous wavelet transform (CWT) generates the two dimensional maps of coefficients that is called scalogram.

$$CWT_f(a,b) = \frac{1}{\sqrt{a}} \int_{-\infty}^{\infty} f(t) \cdot \psi^* \left( \frac{t-b}{a} \right) dt \quad (1)$$

where  $a$  is the scale parameter,  $b$  is the translation parameter,  $f(t)$  is the signal in time domain,  $\psi$  is the 'mother' wavelet and  $\psi^*$  is the complex conjugate of  $\psi$  [19].

Discrete wavelet transform (DWT) applies filter banks for the analysis and synthesis of a signal. Filter banks contain wavelet filters and extract the frequency content of the signal in the pre-determined subbands. The discrete wavelet transform is derived from the discretization of continuous wavelet transform by adopting the dyadic scale and translation to reduce the computational time and can be expressed by the following equation [20]:

$$DWT_s(j,k) = \frac{1}{\sqrt{2^j}} \int_{-\infty}^{\infty} s(t) \cdot \psi^* \left( \frac{t-2^j k}{2^j} \right) dt \quad (2)$$

where  $j$  and  $k$  are integers,  $2^j$  and  $2^j k$  represent the scale and translation parameter respectively. The original signal  $s(t)$  passes through a set of low pass and high pass filters emerging as low frequency (approximations,  $a_i$ ) and high frequency (details,  $d_i$ ) signals at each decomposition level  $n$ . They are usually finite impulse response filters whose impulse response (or response to any finite length input) is of finite duration, because it settles to zero in finite time. Therefore, the original signal  $s(t)$  can be written as [4]:

$$s(t) = a_n + \sum_{i=1}^n d_i \quad (3)$$



### 3. SHANNON ENTROPY PRINCIPLE

Fault detection procedures based on time-frequency methods usually rely on visual observation of contour plots. It is also known that if the wavelet matches well with the shape of the signal at a specific scale and location a large transform value is obtained. However, a low transform value is obtained if the signal and wavelet do not correlate well. To avoid defects of visual observation a more precise way of determining the best suited wavelet is presented here.

The combination of the energy and Shannon entropy content of the wavelet coefficients of the signal, denoted by Energy to Shannon Entropy ratio is an appropriate indicator to choose the best wavelet for diagnosis and it can be calculated in the following form [21, 22]:

$$\xi(n) = E(n) / S_{entropy}(n) \quad (4)$$

The energy content of signal wavelet coefficients is given by:

$$E(n) = \sum_{i=1}^m |C_{n,i}|^2, \quad (5)$$

where  $m$  is the number of wavelet coefficients,  $C_{n,i}$  is the  $i$ th wavelet coefficient of  $n$ th scale.

The entropy of signal wavelet coefficients is given by:

$$S(n) = - \sum_{i=1}^m p_i \log_2 p_i \quad (6)$$

where  $(p_1, \dots, p_n)$  is the energy probability distribution of the wavelet coefficients, defined as:

$$p_i = |C_{n,i}|^2 / E(n) \quad (7)$$

### 4. EXPERIMENT

In this study an experimental test rig (Fig. 1.) has been constructed to measure properly vibration signatures of the tapered roller bearings.

The shaft in the test rig is supported by two tapered roller bearings. The one under investigation is No. 30205 tapered roller bearing. Four tapered roller bearings with different manufacturing defect width on the outer race (OR1-4) were investigated in our experiments (Table 1.). Defect on the outer race is a line (rectangular) shape grinding defect (Fig. 1.) The shaft is driven by an alternating current motor of 0.75 kW (made by Cemer), frequency of 50 Hz, and nominal speed of 2770 rpm which is reduced to 1800 rpm with variable speed drive device. Rubber V-belt between the electric engine and the shaft provides smooth running and low vibration which help accurate and precise measurements. Rubber bumpers are installed to reduce vibration of the electric motor to the bearing housing in order to minimize harmful vibrations. The arrangement provides option of different speeds controlled by Schneider ATV32HU22M2 variable speed drive device. In the experiment the speed of the shaft is measured using an optical tachometer with digital display to check the speed fluctuations. Additionally, the test rig can be used for acoustic measurements as well because an anechoic chamber is installed around the test bearing house with an appropriate features to suppress



outside noises and reduce echo time. Test bearing is spanned by screw mechanism to supply the sufficient axial force to the measurements. Constant spanning force during the measurements is measured by strain gauges in Wheatstone-bridge mode on the basis of difference in voltage measurement.

NI 9234 dynamic signal acquisition is used in the experiments with 4-channels to vibration measurements from integrated electronic piezoelectric (IEPE) and non-IEPE sensors. The NI 9234 delivers 102 dB of dynamic range. Input channels simultaneously digitize signals at rates up to 51.2 kHz per channel with built-in anti-aliasing filters [17]. PCB IMI 603C01 vibration transducer is used which is an industrial type platinum stock piezoelectric sensor with low noise level, sensitivity of 100 mV/g and frequency range of 0.27 to 10 kHz with top exit 2-pin connector [18]. The accelerometer is placed right above the previously ground surface of the top of the bearing house with screw mechanism perpendicular to the axis of the rotation of the shaft. 32 bit AMD Athlon II X2 M300 2.0 GHz processor is used for data processing which is carried out in Matlab and Labview environment. For visual validation of the defect sizes on the bearing rings Garant MM1-200 video microscope is applied that is an incremental measuring system, built-in image processing with 1.3 megapixel colour camera. Furthermore, Mahr MMQ 200 with precision roundness measuring axis, motorized vertical and horizontal measuring axis is used for roundness deviation measurement to determine both width and depth of the grinding marks.

In the experiments the energy content of the transient impulse and the signal-to-noise ratio are sufficiently large but additional effects of the structural and environmental vibrations could emerge despite of the vibration isolation system of the test rig.



Figure 1 Test rig for tapered roller bearing measurement (left) and outer ring (OR4) (right) in the experiment

Table 1 Geometrical parameters of grinding defects of outer rings (OR)

Type	Width(mm)	Depth ( $\mu\text{m}$ )
OR1 defect	0.6311	6.5
OR2 defect	1.2492	33.6
OR3 defect	1.4751	42.3
OR4 defect	1.6236	51.4

## 5. RESULTS

Fig. 5. presents the spectra of outer race defect of 0.6311 mm. The highest periodic transient impulse related energy content of the burst occurs at 2.09 kHz that causes 5 ms rate of periodicity



which is equal to 206.18 Hz BPFO frequency (Fig. 2.). The spectrum was measured in all outer rings with different fault sizes and they showed similar manner around the peak of 2.09 kHz.

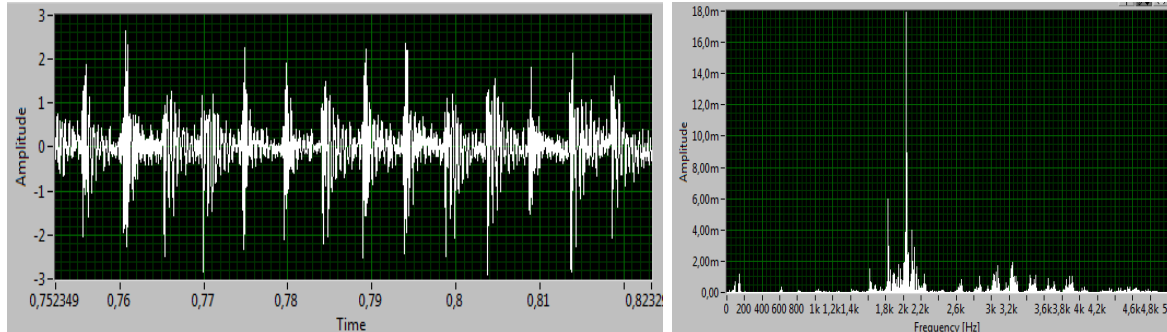


Figure 2 Typical raw time domain signal of bearing having 0.6311 mm of ground fault width on the outer race (left) and its spectra (right)

Total nine different wavelets are considered for the present study. An appropriate base wavelet should extract the maximum amount of energy, with minimizing the Shannon entropy of the corresponding wavelet coefficients. Calculated values of the Energy to Shannon Entropy ratios are in Table 2.

E/S values are calculated from the vibration signal at the wavelet center of 2.08 kHz. (Table 2.).

Table 2 Calculated values of Energy to Shannon Entropy ratios of wavelet functions,  $F_c=2.08$  kHz

	E/S	OR1	OR2	OR3	OR4	Mean
1.	Haar	44.63	71.68	91.17	103.56	77.76
2.	Gaussian	47.69	107.61	111.26	120.54	96.775
3.	Coiflet	51.23	62.12	84.78	91.58	72.4275
4.	Mexican hat	41.87	61.25	85.78	108.74	74.41
5.	Meyer	54.78	87.98	121.78	138.97	<b>100.87</b>

Values, after calculating the mean values of E/S ratio, are presented in Fig. 3. It is observed that Meyer wavelet gives the highest value that indicates to be the most efficient wavelet for both fault detection and possibly fault size estimation.

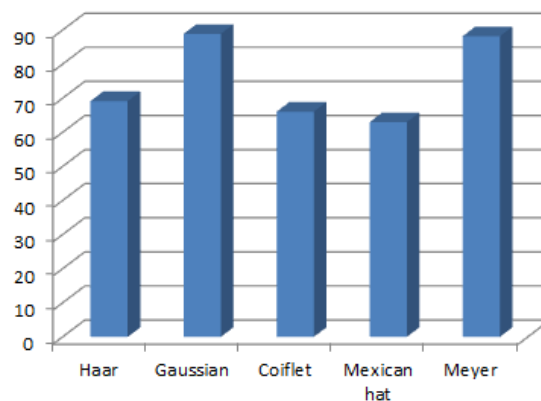


Figure 3 Energy to Shannon Entropy ratio values of wavelet functions,  $F_c=2.08$  kHz



## CONCLUSIONS

A technique based on wavelet transform using nine different real-valued wavelets has been proposed for measuring outer race manufacturing defect width of tapered roller bearings. Wavelet analysis is an efficient method to detect sharp edges in the vibration signal generated by tiny defects which emerge in the form of transient impulses.

Wavelet coefficients were determined at constant scale value of the scalograms of four outer rings with grinding manufacturing defects. Then, wavelet coefficients at the highest local maxima of the scalograms were calculated. Five wavelets were analyzed and it was determined that Meyer wavelet was the best for the manufacturing fault detection in all cases on the basis of the Shannon Entropy Criteria. Furthermore, the width measurement of the outer ring grinding fault was executed with all nine wavelets. The best wavelet previously chosen by Shannon Entropy Criteria creates the opportunity to determine the manufacturing defect width in the most accurate way because it presents the best correlation with the transients.

## ACKNOWLEDGEMENT

The publication is supported by the EFOP-3.6.1-16-2016-00022 project. The project is co-financed by the European Union and the European Social Fund.

## REFERENCES

- [1] Patel, V. N., Tandon, N., Pandey, R., K. (2012). Defect Detection in Deep Groove Ball Bearing in Presence of External Vibration Using Envelope Analysis and Duffing Oscillator. *Measurement*, vol. 45, p. 960.
- [2] Khanam, S., Tandon, N., Dutt, J. K. (2012). Fault Identification of Rolling Element Bearings from Vibration Signals: An Application of Kalman and H Filters. *LOWHUV 10th International Conference on Vibrations in Rotating Machinery (VIRM10)*, p. 703-713.
- [3] Al-Ghamd, A.M., Mba, D. (2006). A Comparative Experimental Study on the Use of Acoustic Emission and Vibration Analysis for Bearing Defect Identification and Estimation of Defect Size, *Mechanical Systems and Signal Processing*, vol. 20, p. 1537.
- [4] Elforjani, M., Mba, D. (2010). Accelerated Natural Fault Diagnosis in Slow Speed Bearings with Acoustic Emission. *Engineering Fracture Mechanics*, vol. 77, p. 112.
- [5] Sawalhi, N., Randall, R.B. (2011). Vibration Response of Spalled Rolling Element Bearings: Observations, Simulations and Signal Processing Techniques to Track the Spall Size. *Mechanical Systems and Signal Processing*, vol. 25, p. 846.
- [6] Peng, Z.K., Chu, F.L. (2004). Application of the Wavelet Transform in Machine Condition Monitoring and Fault Diagnostics. *Mechanical Systems and Signal Processing*, vol. 18, p. 199.
- [7] Prabhakar, S., Mohanty, A.R., Sekhar, A.S. (2002). Application of Discrete Wavelet Transform for Detection of Ball Bearing Race Faults. *Tribology International*, vol. 35, p.793.
- [8] Shi, D. F., Wang, W. J., and Qu, L. S. (2004). Defect detection for bearings using envelope spectra of wavelet transform. *ASME Journal of Vibration and Acoustics*, vol. 126, no. 4, p. 567.
- [9] Nikolaou, N. G., Antoniadis, I. A. (2002). Demodulation of Vibration Signals Generated by Defects in Rolling Element Bearings Using Complex Shifted Morlet Wavelets. *Mechanical Systems and Signal Processing*, vol. 16, no. 4, p. 677.
- [10] Qiu, H., Lee, J., Lin, J., Yu, G. (2006). Wavelet Filter-Based Weak Signature Detection Method and its Application on Rolling Element Bearing Prognostics. *Journal of Sound and Vibration*, vol. 289, p. 1066.



- [11] Junsheng, C., Dejie, Y., Yu, Y. (2007). Application of an Impulse Response Wavelet to Fault Diagnosis of Rolling Bearings. *Mechanical Systems and Signal Processing*, vol. 21, p. 920.
- [12] Kumar, R., Singh, M. (2013). Outer Race Defect Width Measurement in Tapered Roller Bearing using Discrete Wavelet Transform of Vibration Signal. *Measurement*, vol. 46, p. 537.
- [13] Awal, M. A., Mostafa, S. S., Ahmad, M. (2012). Quality Assessment of ECG Signal Using Symlet Wavelet Transform. *Proceedings of International Conference on Advances in Electrical Engineering*, p.129-134.
- [14] Chavan, M. S., Mastorakis, N., Chavan, M. N., Gaikwad, M. S. (2012). Implementation of SYMLET Wavelets to Removal of Gaussian Additive Noise from Speech Signal. *Recent Researches in Communications, Automation, Signal Processing, Nanotechnology, Astronomy and Nuclear Physics*, p. 37-41.
- [15] Kumar, R., Jena, D.P., Bains, M. (2010). Identification of inner race defect in radial ball bearing using acoustic emission and wavelet analysis. *Proceedings of ISMA 2010 including USD 2010 Leuven (Belgium)*, p. 2883–2891.
- [16] Mankovits, T., Szabó, T., Kocsis, I., Páczelt, I. (2014). Optimization of the Shape of Axisymmetric Rubber Bumpers. *Strojnicki vestnik-Journal of Mechanical Engineering*, vol. 60, no. 1, p. 61-71.
- [17] NI 9234 datasheet: <http://www.ni.com/datasheet/pdf/en/ds-316>, accessed on 2016-02-04.
- [18] PCB IMI 603C01 transducer, from [https://www.pcb.com/contentstore/docs/PCB\\_Corporate/IMI/Products/Manuals/603C01.pdf](https://www.pcb.com/contentstore/docs/PCB_Corporate/IMI/Products/Manuals/603C01.pdf), accessed on 2016-02-04.
- [19] Michel Misiti, Yves Misiti, Georges Oppenheim, Jean-Michel Poggi (2007). *Wavelets and their Applications*. ISTE Ltd.
- [20] Salguerio, J., Persin, G., Vizintin, J., Ivanovic, M., Dolenc, B. (2013). On-line Oil Monitoring and Diagnosis. *Strojnicki vestnik-Journal of Mechanical Engineering*, vol. 59, no. 10, p. 604-612.
- [21] Kankar, P.K., Sharma, S.C., Harsha, S.P. (2011). Fault diagnosis of ball bearings using continuous wavelet transform. *Applied Soft Computing*, vol. 11, p. 2300–2312.
- [22] Kankar, P.K., Sharma, S.C., Harsha, S.P. (2013). Fault diagnosis of rolling element bearing using cyclic autocorrelation and wavelet transform. *Neurocomputing*, vol. 110, p. 9-17.
- [23] Szántó, A., Szíki, G., Hajdu, S.: Elektromos hajtású tanszéki versenyautó járműdinamikai modellezése = Vehicle dynamics modelling of an electric driven race car. *IJEMS* 1 (2), 106-114., 2016.
- [24] Szántó, A., Szíki, G., Hajdu, S., Gábora, A.: Soros gerjesztésű egyenáramú motor szimulációja MATLAB környezetben = Simulation of a Series Wound DC Motor in MATLAB Environment. In: A XXII. Fiatal Műszakiak Tudományos Ülészak előadásai = Proceedings of the XXII-th International Scientific Conference of Young Engineers / szerk. Bitay Enikő, Erdélyi Múzeum Egyesület (EME), Kolozsvár, 367-370, 2017.



## POROUS SYSTEM MODELLING USING MULTY CAPILLARY METHOD

<sup>1</sup>DÓCS Roland, <sup>2</sup>JOBBIK Anita PhD

<sup>1</sup>Research Institute of Applied Earth Sciences, University of Miskolc

E-mail: [docs@afki.hu](mailto:docs@afki.hu)

<sup>2</sup>Research Institute of Applied Earth Sciences, MTA-ME Geoengineering Research Group  
University of Miskolc

E-mail: [jobbik@afki.hu](mailto:jobbik@afki.hu)

### Abstract

Covering Darcy's equation of single phase filtration in porous media, it can be clearly seen that a large amount of parameters are present. These petrophysical parameters were fused together into a single one, known as permeability, which describes the reciprocal value of resistance present at fluid flow in the porous material. As a result, making a truly difficult task of describing fluid flow into a rather simple one. But how efficient is this solution, covering such a complex system by a simple numerical value. In this paper, a model is covered, in which flow happens in a volume equal to the pore volume of the given sample, made of a number of steel capillaries equal in diameter. The number and diameter of the corresponding capillaries are found during an iteration process, in which the aim is to find the solution where the calculated pressure drop covering the steel capillaries, equals pressure drop measured between the two sides of the sample during permeability measurement.

**Keywords:** Darcy's equation, porosity, permeability, steel capillary, pressure drop.

### 1. INTRODUCTION

During fluid flow in porous media Darcy's equation of single phase filtration, is the one which describes forces acting in this particular case, with some simplifications. Regarding these simplifications, forces of compression, gravity and friction are the only ones taken into consideration, others like capillary- and forces of inertia are neglected. Also, in order to use the differential form of this equation, the following statements have to be met [1]:

- A certain volumetric element with known dimensions is considered in space with fix boundaries, in a way that random effects may be statically eliminated.
- Stream lines are building up the surface so that its base surfaces are perpendicular to it.
- Forces acting on the fluid volume inside the control volume are equal.
- Regarding to Newton's Law of motion, fluid body will accelerate until resultant acceleration is larger than zero, but will keep its velocity ( $u_i$ ).
- We seek a value for  $u_i$  such that the resultant acceleration equals the null vector.

In order of achieving simplicity without losing generality, a cylindrical element was taken as control volume shown in the following figure.

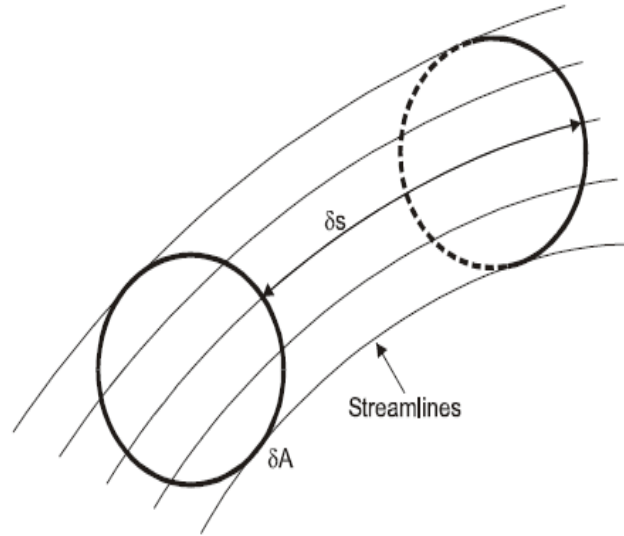


Figure 1 Control volume determined by Darcy [2]

Taking into consideration the above mentioned, the equation of single phase filtration in porous material covered by Darcy and Weisbach can be written up in the following form.

$$F_p + F_g + F_\mu = 0 \quad (1)$$

$$-\Phi \delta A \nabla p \delta s - \rho g \Phi \delta A i_3 \delta s - B \mu \delta A u \delta s = 0 \quad (2)$$

$$-\left( \nabla p + \mu \frac{B}{\Phi} u + i_3 \rho g \right) \Phi \delta A \delta s = 0 \quad (3)$$

Two parameters have to be introduced regarding porous media which are described in *Equation 3*. These are porosity ( $\Phi$ ) and the coefficient of the given system ( $B$ ). As a result,  $\Phi \delta A$  describes the cross sectional area in which fluid flow happens, and the ratio of  $B/\Phi$  can be written up as another key petrophysical parameter known as permeability ( $k$ ), which describes the resistance met by the fluid during flow (if saturated only with that given fluid) inside that given porous media. Both parameters can only be determined by data obtained in petrophysical measurements. In the knowledge of these parameters a simpler form of Darcy's Law can be used.

$$u = -\frac{k}{\mu} (\nabla p + i_3 \rho g) \quad (4)$$

It can be clearly seen that the task of modelling flow in these complex systems is a truly difficult one. Also it has to be taken into consideration that the above mentioned petrophysical parameters are the function of many individual properties starting from geology, sedimentation, compaction, fluid-rock behaviours (wettability and interfacial tension values). In order to be able to even start developing any sort of model that could imitate what happens in these systems data is required. The necessary data can be obtained from petrophysical measurements such as He porosimetry, permeability measurement (using gas and water), all of which can be performed in the Research Institute of Applied Earth Sciences-University of Miskolc.



## 2. FOUNDATION OF THE MODEL

Model by definition presents a part of a system in a simpler form, determined by a group of hypotheses described by the operator. Its duty is not to fully describe what happens in that particular system, but to get the same result by using the defined hypotheses [3]. If satisfactory result reached the model is capable of presenting the problem.

It could be clearly seen from the start that these systems from petrophysical point of view are such complex that even the task of defining these basic principles on which the model even works on is a rather difficult one. The problem mainly consists of parameters connection on one another. For example, permeability depends not on porosity, but rather on the pore size distribution, because between two systems of equal porosity, the one built up by bigger but less pores will have higher permeability than the one where smaller but more in number pores are present. As result making those principals inefficient where porosity would be only taken into consideration. Not to mention capillary forces which changes in function of wettability properties present between the rock and fluids at imbibition and drainage phases of displacement, in addition to pore size distribution as well.

In knowledge of the difficulties present the question was made that what other form of approach could be made in order to develop the model. A solution was to determine a flow volume equal in size as the pore volume and describe flow restrictions in this volume in a way so that the calculated pressure drop (at a given flowrate) between the two sides of the control volume would be equal to the one present during the measurement of absolute permeability determined by water. This effective flow volume of the system would be constructed of a number of capillary equal in diameter. Calculating pressure drops in smooth pipes is a rather simple procedure, where besides of the already known parameters (pipe geometry, fluid properties at given pressures and temperatures) only the velocity of flow and the frictional factor have to be determined.

$$\frac{dp}{dl} = \frac{g}{g_c} \rho \sin \alpha + \frac{\rho v dv}{g_c dl} + f \frac{\rho v^2}{2g_c d} \quad (5)$$

Assuming horizontal steady state flow, the effect of potential and kinetic energy changes can be neglected, resulting in pressure drops caused only by irreversible energy losses of friction.

## 3. DATA GATHERING

In order to describe the effective pore volume in which flow even happens, porosity ( $\Phi$ ), the ratio of pore volume ( $V_p$ ) to total bulk ( $V_b$ =samples measurable volume) volume has to be determined.

$$\Phi = \frac{V_p}{V_b} = \frac{V_b - V_s}{V_b} \quad (6)$$

One of the most commonly used method of pore volume determination is Helium pycnometry, which implements Boyle's law. Of all non-reactive gases, Helium has the finest particles which benefits solid volume ( $V_s$ ) determination of samples due to the fact that it can get into the smallest of pores. The apparatus consisting of two chambers (sample and reference) with known volumes, where pressures reached by existing Helium quantity are measured at isothermal conditions ( $T_a$ ).

If both chambers are empty, the previously adjusted pressure ( $p_1$ , reference pressure) at reference volume ( $V_R$ ) after expansion between both reference and sample chambers ( $V_R+V_C$ ) will drop to a



certain ( $p_2$ ) pressure.

$$V_s = V_c - V_R \left[ \left( \frac{p_1}{p_2} \right) - 1 \right] \quad (7)$$

The volume where gas expansion happens is decreased by the samples solid volume inside the sample chamber which will result a higher  $p_2$  pressure (for same  $p_1$ ) than it would in case of an empty chamber. In the process reference- and expansion pressures are recorded three times resulting in three calculated solid volumes for each sample. Finally, the standard deviation of the solid density (calculated from the dry weight and the determined volumes) is determined. If this value exceeds  $0,003 \text{ g/cm}^3$  the measurement has to be repeated until satisfactory condition reached. At lower standard deviation values, average of the calculated volumes determines the solid volume of the given sample with sufficient accuracy. In possession of both total and solid volumes of the given sample porosity can be determined easily using *Equation 6*.

In order to be able to determine flow restrictions of water inside the pore volume, a standard absolute permeability measurement is used. Where pressure difference between the two sides of the cylindrical sample with  $A$  cross sectional area and length of  $l$  in horizontal position is measured at a given flowrate of  $q$ . One thing has to be taken into consideration, both Darcy's law and the pressure calculation for smooth pipes requires laminar flow to be present. In order to achieve laminar flow, throughout permeability measurement of the given samples the lowest pressure differences were used where consistent flow was recorded.

By applying constant  $q$  flowrate and monitoring the pressure difference between inlet ( $p_1$ ) and outlet side ( $p_2$ =atmospheric pressure), time is measured which is required for a given volume of fluid to pass through the sample of known volume ( $A$ ,  $l$ ). Thus flowrate at the outflow and both permeability can be calculated. Because of constant pressure difference throughout the entire measurement, time periods for equal amount of fluid volume accumulation should be constant as well. As a result, permeability of the sample regarding that given fluid will be calculated as the average of each measured point.

$$k = \frac{q\mu\Delta l}{A\Delta p} \quad (8)$$

In the possession of the samples porosity and the value of the pressure difference recorded during steady state flow, all necessary data are at hand which are required for the model in order to calculate that number ( $c_i$ ) of capillaries with equal diameter ( $d_{ci}$ ) where pressure drops present will be equal of the one measured.

#### 4. CALCULATIONS IMPLEMENTED BY THE MODEL

Pressure drop calculations by Gábor T [4] were used as the foundation of the multy capillary model. After in knowledge of the input data required which are as mentioned porosity, and the average of pressure differences measured at steady state flow conditions. Assumption of the first value of capillary number is made which will be the starting value of the iteration process of finding the correct  $c$  and  $d_c$  values.



In the equation of flow velocity, parameter  $B_w$  is the so called Formation Volume Factor of water, which describes the ratio of water volume at standard and at given pressure and temperature conditions. In our case because of standard conditions  $B_w$  was equal 1.

$$v = 0.0119 \frac{q_w B_w}{c d_c^2} \quad (9)$$

In the process of finding these values another iteration term needs to be met, where the region of the flow according to the diagram described by Moody has to be at laminar profile ( $N_{Re} < 2300$ ). If the values of  $c$  and  $d_c$  calculated both met the criteria of laminar flow and pressure drop the cycle is finished.

$$N_{Re} = 124 \frac{\rho v d_c}{\mu} \quad (10)$$

Friction factor regarding laminar flow conditions can easily be calculated by *Equation 11*. After that pressure drop caused by friction was calculated by *Equation 12* in a single capillary, which because of equally distributed flow in all capillaries, multiplied by the number of the capillaries equals pressure drop throughout the entire system. The presented equations all use SI units.

$$f = \frac{64}{N_{Re}} \quad (11)$$

$$\Delta p_f = 1.294 \cdot 10^{-3} f \frac{l}{d_c} \rho v^2 \quad (12)$$

## 5. RESULTS

At start a total of three samples from different permeability regions were used in order to determine if the model can successfully met all requirements and reach satisfactory results. The parameters of these samples and the results of the capillary numbers and the corresponding capillary diameters are also listed in the following table.

*Table 1* Parameters and results regarding the observed samples

Sample ID	$\Phi_{He}$ , [%]	$k_w$ , [mD]	$q_{steady}$ , [cm <sup>3</sup> /h]	$(\Delta p_{steady})_{avg.}$ , [bar]	$\Delta p_{calculated}$ , [bar]	NRe	$c$ , [number]	$d_c$ , [cm]
S-1	17,62	22,87	97,00	0,6590900	0,6590690	25,29	7906,9407	0,01787
S-2	31,65	229,88	100,00	0,07190000	0,07189997	26,39	4324,1577	0,03230
S-3	27,72	830,34	99,56	0,019403333	0,01940330	39,97	2116,5146	0,04337

As it can be clearly seen in all cases, results achieved by the model reached satisfactory conditions both in case of laminar flow conditions and in calculated pressure drops at the given  $c$  and  $d_c$  values. The huge difference in permeabilities of chosen samples were in order to check if our model has any limits of its own due to the used simplifications.



# INTERNATIONAL SCIENTIFIC CONFERENCE ON ADVANCES IN MECHANICAL ENGINEERING

12-14 October 2017, Debrecen, Hungary



## CONCLUSIONS

In all three investigated cases, our multy capillary model made satisfactory results, taking into consideration the differences between calculated pressure differences and the ones measured during permeability measurement made by water. Samples were chosen in a way that their permeabilities would define a rather high spectrum, in order to define flaws if there any because of the used simplifications. The results show that the model is capable of presenting the effects of incompressible single phase fluid flow in a porous media of given porosity value, using the previously defined criteria. Achieving all necessarily elements of a working model and giving proper results.

## ACKNOWLEDGEMENT

The research was carried out in the framework of the GINOP-2.3.2-15-2016-00010 "Development of enhanced engineering methods with the aim at utilization of subterranean energy resources" project in the framework of the Széchenyi 2020 Plan, funded by the European Union, co-financed by the European Structural and Investment Funds.

## REFERENCES

- [1] Zoltán, E., Heinemann: *Fluid Flow In Porous Media*. Textbook Series Volume 1, Montanuniversitat Leoben Petroleum Engineering Department 2005. page 5-93.
- [2] Zoltán, E., Heinemann: *Fluid Flow In Porous Media*. Textbook Series Volume 1, Montanuniversitat Leoben Petroleum Engineering Department 2005. page 67.
- [3] Roland D., Anita J.: Additional problem overview of fluid flow in porous media, Debrecen ISCAME 2016 ISBN: 978-963-473-944-9.
- [4] Gábor, T.: *Production Engineering Fundamentals Vol. 1*. University of Miskolc Petroleum Engineering Department 2012. page 19-23.



## 3D COMPUTER PROCESSING AND IMPROVEMENT OF THE GEOMETRY OF RECEIVED PHOTOGRAMMETRIC MODELS THROUGH PHOTO SHOOTING WITH ONE CAMERA

*DOVRAMADJIEV Tihomir PhD*

*Technical University of Varna*

*E-mail: [dr.tihomir.dovramadjiev@gmail.com](mailto:dr.tihomir.dovramadjiev@gmail.com)*

### **Abstract**

*With the advancement of technology, the use of photogrammetric techniques is becoming more and more convenient as a mean for generating a computer-based 3D model of real-world imaging as a result of photo shooting. Depending on the assignment and the available equipment, photogrammetry is successfully applied in the field of shooting small and large-scale objects, architecture, geodesy, etc. This article discusses the possibilities of obtaining quality completed non-large models with the help of a photo camera and / or an analog photo camera from a smartphone. The obtained 3D models and masks are further processed with free access programs. Different successful practices for 3D finishing modeling have been demonstrated to obtain ultimate, successfully modeled samples.*

**Keywords:** *Photogrammetry, design, methodics, free software*

### **1. INTRODUCTION**

The realization of 3D computer models by using modern photogrammetry technology contains different specific stages that have their own individual features [1]. It is believed that for the production of quality finishing 3D models, a serious material base is necessary including expensive imaging equipment and high-cost exponential photogrammetric computer software systems. The present text examines the construction of the exemplary 3D computer model horseback bas-relief from the real existence of minimal material resources. In a sequence of steps, the important moments influencing the photogrammetry process are explained [2, 3].

Fig. 1 shows the process *photogrammetry metrology*. Photography in its broadest sense is a process that converts the real 3-dimensional world into flat 2-dimensional images. The camera is the device that makes this transformation or mapping from 3 dimensions to 2 dimensions [4, 5].

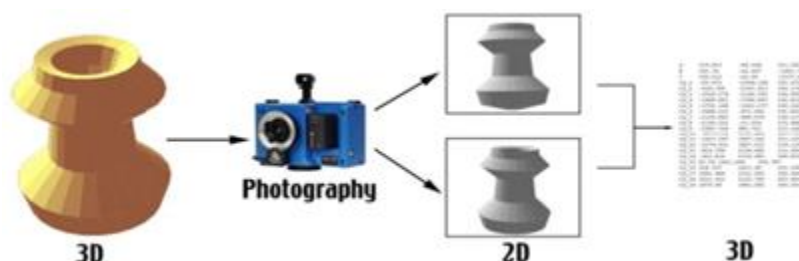


*Figure 1* Photogrammetry – Metrology process

Fig. 2 shows the process *photogrammetry triangulation*. Photogrammetry uses the basic principle of Triangulation, whereby intersecting lines in space are used to compute the location of a point in



all three dimensions. However, in order to triangulate a set of points one must also know the camera position and aiming angles (together called the orientation) for all the pictures in the set.

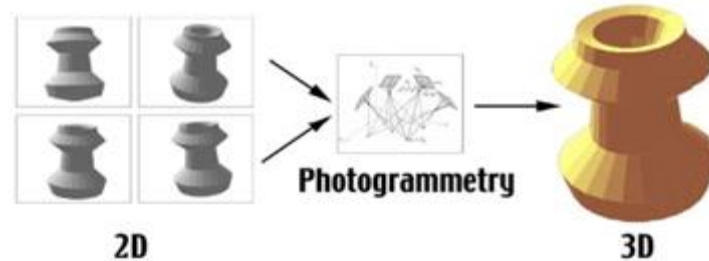


Figure 2 Photogrammetry – Triangulation process

Particularly important is the stage of calculating 3D geometry as a result of the taken photographs. Different software systems offer different options, with some dominating strengths or weaknesses in others, other strengths or weaknesses. The choice of free or paid software is crucial. Table 1 lists some of the best possible software products needed to fully implement quality 3D computer models [6 -19].

Table 1 Most useful free and paid software in photogrammetry & 3D reconstruction

FREE & OPEN SOURCE	PAID
Autodesk ReMake & VisualSFM	Autodesk ReCap, Agisoft PhotoScan & 3DF Zephyr and etc
Autodesk MeshMixer & MeshLab	ZBrush
Blender	Autodesk Maya, Autodesk 3DS Max, Cinema 4D, Rhinoceros, LightWave and etc

## 2. MATERIALS & METHODS

Given the available functionalities of free & open source software, the following programs were selected: **Autodesk ReMake**, **Autodesk MeshMixer** and **Blender** (fig. 3).



(a)



(b)



(c)

Figure 3 An useful and popular free & open source software – (a)Autodesk ReMake, (b) Autodesk MeshMixer, (c) Blender

Recently, AutoDesk ReMake [20] has become very popular due to its free license, including a wide range of functionalities and a convenient interface. Also, the ability to use cloud space and online data computation makes the program a preferred one.



Table 2 shows the capabilities of Autodesk ReMake's free and pro versions.

*Table 2* Functional capabilities of Autodesk ReMake – free and pro [21] (from September 2017 Autodesk ReMake move to ReCap)

Features	Autodesk ReMake	FREE	VS	PRO
<b>CREATE3D</b>	Photo to 3D (cloud computation) 125 photos max*	●		●
	Photo to 3D (cloud computation) 250 photos max			●
	Photo to 3D (local computation) 250 photos max			●
	1000+/50 gigapixel image input (BETA feature)**			●
<b>PREPARATION</b>	Huge mesh support (2+ billion polygons)	●		●
	Set units and scale*			●
	Scene clean up	●		●
	Mesh analytics	●		●
	Mesh fix, edit, re-topo and sculpt tools	●		●
	Set coordinate points/system			●
<b>EXPORT</b>	Quick3D mesh export (limited controls)	●		●
	Export with controls and texture baking			●
	Export high res. images with alpha channel	●		●
	Export videos (turntables and keyframe animation)	●		●
<b>3D PRINT</b>	3D print prep tools	●		●
	High res 3D print	●		●
	Various 3D printer support	●		●
<b>REPORT</b>	Measurements - distance	●		●
	Measurements - surface	●		●
	Measurements - volume	●		●
	Compare two models (diff. analysis)			●
<b>PUBLISH</b>	To online 3D viewer/explorer	●		●

\*This limitation will be eliminated in the promo period.  
\*\*Option available in pro version with additional fee.

After receiving the generated \* .obj file from Autodesk ReMake [22], it is desirable to process it further with Autodesk MeshMixer [23] specializing in 3D sculpting and 3D printing. Depending on the task, in Blender environment, the 3D model can be used for various purposes: creating realistic visuals, animations, games, etc. Table 3 lists the core capabilities of Autodesk MeshMixer and Blender.

*Table 3* Capabilities of Autodesk MeshMixer and Blender

Autodesk MeshMixer	Blender
Drag-and-Drop Mesh Mixing	Photorealistic Rendering The built-in Cycles rendering engine offers: GPU & CPU rendering, Realtime viewport preview, HDR lighting support, Permissive License for linking with external software.
Sculpting and Surface Stamping	Modeling Blender's modeling tools include: Keyboard shortcuts for a fast workflow, N-Gon support, Edge slide, collapse and dissolve, Grid and Bridge fill, Python. scripting for custom tools and add-ons
Robust Convert-to-Solid for 3D printing	Realistic Materials Key features are: Complete Node Support for full customization, Physically accurate shaders like glass, translucency and SSS, Open Shading Language (OSL) support for coding unique shaders.



# INTERNATIONAL SCIENTIFIC CONFERENCE ON ADVANCES IN MECHANICAL ENGINEERING

12-14 October 2017, Debrecen, Hungary



3D Patterns & Lattices	<b>Rigging</b> Blender offers an impressive set of rigging tools including: Envelope, skeleton and automatic skinning, Easy weight painting, Mirror functionality, Bone layers and colored groups for organization, B-spline interpolated bones.
Hollowing (with escape holes!)	<b>Animation toolset</b> Blender's animation feature set offers: Automated walk-cycles along paths, Character animation pose editor, Non Linear Animation (NLA) for independent movements, IK forward/inverse kinematics for fast poses, Sound synchronization.
Branching Support Structures for 3D printing	<b>Sculpting</b> Sculpting in Blender includes: 20 different brush types, Multi-res sculpting support, Dynamic Topology sculpting, Mirrored sculpting
Automatic Print Bed Orientation Optimization, Layout & Packing	<b>UV Unwrapping</b> Blender allows for: Fast Cube, Cylinder, Sphere and Camera projections, Conformal and Angle Based unwrapping (with edge seams and vertex pinning), Painting directly onto the mesh, Multiple UV layers, UV layout image exporting
Advanced selection tools including brushing, surface-lasso, and constraints	<b>Full Compositor</b> The compositor comes with: Impressive library of nodes for creating camera fx, color grading, vignettes and much more, Render-layer support, Full compositing with images and video files, Ability to render to multiLayer <u>OpenEXR</u> files, Multi-threaded
Remeshing and Mesh Simplification/Reducing	<b>Simulations</b> Blender's simulation tools include: Fluid – Realistic water and fluid simulations, Smoke – Billowing smoke with flames and scene interaction, Hair – Beautiful wafts of hair that blows in the wind and interacts with collisions, Cloth – Amazingly realistic cloth simulations for clothing and environments, Rigid Body Physics – Makes any object destructable and collidable, Particles – For creating things like rain, sparks and shrapnel.
Mesh Smoothing and Free-Form Deformations	<b>Game Creation</b> The game engine includes: Ability to port your models to any third-party game engine, Create or code your own game logic, Full <u>Bullet Physics</u> integration, Python scripting API for advanced control and AI, Support for all OpenGL dynamic lighting, toon shading, animated materials as well as Normal and Parallax Mapping, Playback of games inside Blender without compiling or preprocessing, 3D spatial audio using OpenAL.
Hole Filling, Bridging, Boundary Zipping, and Auto-Repair	<b>Camera and Object tracking</b> The Camera and Object Tracker includes: Auto and manual tracking, Powerful camera reconstruction, Real-time preview of your tracked footage and 3d scene, Support for Planar tracking and Tripod solvers.
Plane Cuts, Mirroring, and Booleans	<b>Library of Extensions</b> Some existing extensions include: Generators for trees, terrain, ivy and clouds, Fracture Objects, 3D Printing Toolbox, Rigify meta-rigging system, Import and Export format support for AfterEffects,



DirectX, Unreal Game Engine and more.	
Extrusions, Offset Surfaces, and Project-to-Target-Surface	Video Editing The Video Editor includes: Live preview, luma waveform, chroma vectorscope and histogram displays, Audio mixing, syncing, scrubbing and waveform visualization, Up to 32 slots for adding video, images, audio, scenes, masks and effects, Speed control, adjustment layers, transitions, keyframes, filters and more.
Interior Tubes & Channels	File Formats Including: <b>Image:</b> JPEG, JPEG2000, PNG, TARGA, OpenEXR, DPX, Cineon, Radiance HDR, SGI Iris, TIFF; <b>Video:</b> AVI, MPEG and Quicktime (on OSX); <b>3D</b> Alembic, 3D Studio (3DS), COLLADA (DAE), Filmbox (FBX), Autodesk (DXF), Wavefront (OBJ), DirectX (x), Lightwave (LWO), Motion Capture (BVH), SVG, Stanford PLY, STL, VRML, VRML97, X3D.
Precise 3D Positioning with Pivots	Flexible Interface Blender's interface also offers: Consistency across all platforms, No disruptive pop-up windows, Crisp text (support for retina on OSX).
Automatic Alignment of Surfaces	
3D Measurements	
Stability & Thickness Analysis	

Fig. 4 shows the Horse Bas-relief model (Figure 4a) and the capture apparatus, which is a simple smartphone with modest capabilities (fig. 4b). The actual Horse Bas-relief model is 5x5x5sm in size and is made of wood. The smartphone is a model Lenovo A2010 (launched in August 2015 year) [24]. The phone has a 4.50-inch touchscreen display with a resolution of 480 pixels by 854 pixels. The Lenovo A2010 is powered by 1GHz quad-core MediaTek MT6735 processor and 1GB of RAM. The phone packs 8GB of internal storage that can be expanded up to 32GB via a microSD card. As far as the cameras are concerned, the Lenovo A2010 packs a 5-megapixel primary camera on the rear and a 2-megapixel front shooter for selfies.



(a)



(b)

Figure 4 Object and apparatus (a) Horse bas-relief, (b) Lenovo A2010 – Camera 5-megapixel



### 3. RESULTS

Getting 3D geometry depends on the conditions in which the filming takes place. In the absence of sufficient daylight or professional photographic studio, a good option is to make a portable Chroma Key Studio. It is also important while photo shooting the required angles and positions of a single photo camera (smartphone in this case) to be respected. It should be kept in mind that free version of Autodesk ReMake has a limit of 50 photos that can be uploaded to the cloud space. Another option is the presence of a powerful personal hardware system. Given the limited conditions, the original three-dimensional geometry is created in two stages. Figure 5 shows part of the photos on the left (a) and right (b) sides of the Horse bas-relief.

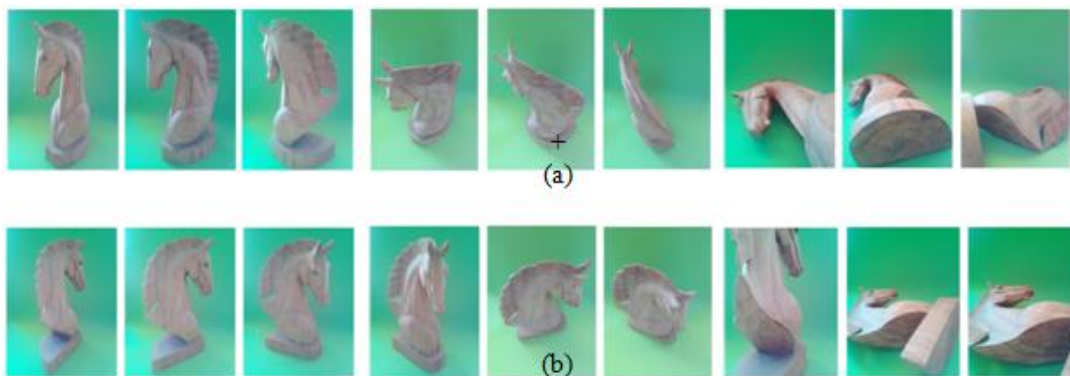


Figure 5 Part of the images of the actual Horse Bas-relief model (a) left side, (b) right side

After completion of the computing process in Autodesk ReMake environment, files are created in a format \*.mtl, \*.obj, \*.jpg (figure 6, (a) left side, (b) right side).



Figure 6 Resulting files from Autodesk ReMake (a) left side, (b) right side

The resulting files are imported into Autodesk MeshMixer for further processing (figure 7, (a) two parts in front view, (b) cut the useless elements (marked in red)).

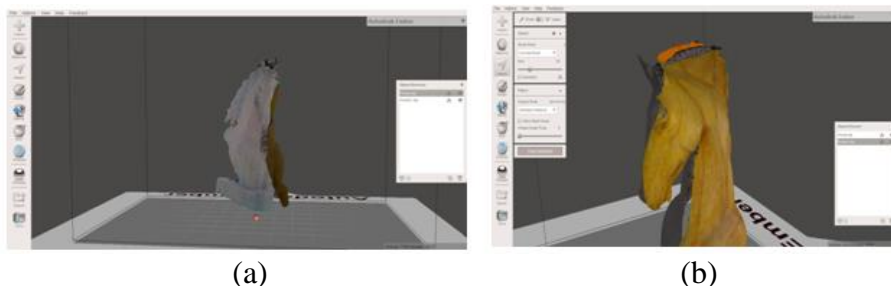


Figure 7 Additional processing in Autodesk MeshMixer (a) two parts in front view, (b) cut the useless elements (marked in red)



After cleaning, go to combine and make solid. Fig. 8 shows views of solid Horse bas-relief, (a) front view, (b) back view.

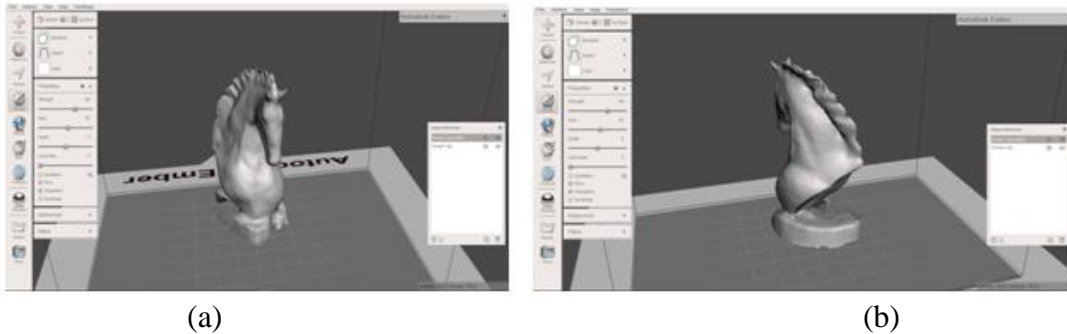


Figure 8 Solid Horse bas-relief (Autodesk MeshMixer interface), (a) front view, (b) back view

The model is now ready to finalize the design in Blender software. Initially, a completely new foundation is created and a final renderer with a selected texture is made. Figure 9 (a) shows the finished 3D model and (b) render with added texture - glass.

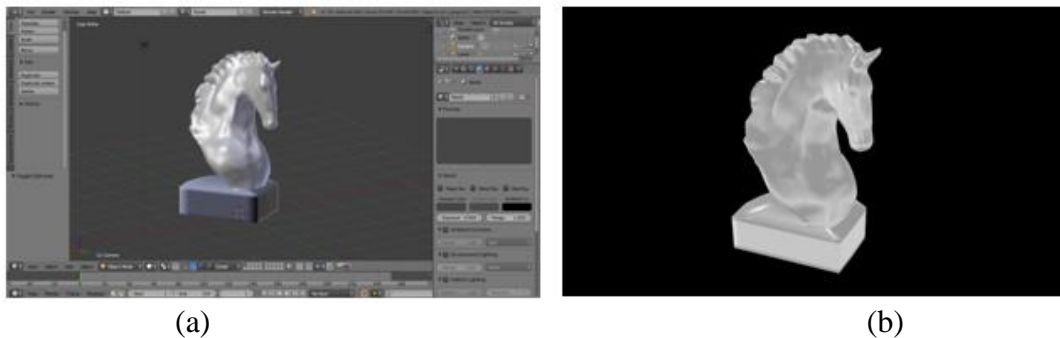


Figure 9 Horse bas-relief (Blender interface), (a) object mode, (b) rendered view + add glass texture

Figure 10 shows two additional final renderers in Blender where it is applied marble texture – (a) green marble, (b) white marble.



Figure 10 Horse bas-relief (Blender render views), (a) + green marble texture, (b) + white marble texture

## CONCLUSIONS

Photogrammetry is a complex process combining advanced technological tools and specific designer skills. It is considered that obtaining a precise 3D geometry is possible by using hi-tech



equipment, which requires good financial investment and appropriate computer modeling systems. Nevertheless if there is a lack of such equipment or it is not possible to use a professional one, the photo shooting of the object can be done with a simple smartphone. In this case the received photogrammetric data and the generated 3D object may need an additional manual modeling. The designer should be able to master programs such as Autodesk ReMake, MeshMixer and Blender programs, where sculpting tools are used. The article shows a fully completed and successful process of creating a virtual 3D model.

## REFERENCES

- [1] Paul Debevec, Christoph Bregler, Michael Cohen, Leonard McMillan, François Sillion, Richard Szeliski. SIGGRAPH 2000 Course 35 (Full Day). USA, 2000.
- [2] Tihomir Dovramadjiev. Improving 3D Geometry of the received photogrammetric models. ISEC & TUV. Coimbra, Portugal, Sept. 2017. <https://www.slideshare.net/TihomirDovramadjievP/improving-3d-geometry-of-the-received-photogrammetric-models-isec-coimbra-portugal-25-29-ix-2017-dr-eng-tihomir-dovramadjiev/1>
- [3] Pavel Ivanov. Three-dimensional Scanning of Objects Using a Mobile Phone. Photogrammetry Silhouette Technique. Helsinki Metropolia University of Applied Sciences. Finland, March 2017.
- [4] Geodetic Systems. <https://www.geodetic.com/v-stars/what-is-photogrammetry/>
- [5] [http://www.iqlaser.co.za/files/white\\_papers/Photogrammetry\\_basics.pdf](http://www.iqlaser.co.za/files/white_papers/Photogrammetry_basics.pdf)
- [6] Autodesk ReMake <https://remake.autodesk.com/about>
- [7] VisualSFM : A Visual Structure from Motion System <http://ccwu.me/vsfm/>
- [8] Autodesk ReCap <https://www.autodesk.com/products/recap/overview>
- [9] Agisoft PhotoScan <http://www.agisoft.com/>
- [10] 3DF ZEPHYR <https://www.3dflow.net/3df-zephyr-pro-3d-models-from-photos/>
- [11] Autodesk MeshMixer <http://www.mmmanual.com/>
- [12] MeshLab <http://www.meshlab.net/>
- [13] Blender <https://www.blender.org/>
- [14] ZBrush <http://pixologic.com/>
- [15] Autodesk Maya <https://www.autodesk.com/products/maya/overview>
- [16] Autodesk 3Ds Max <https://www.autodesk.com/products/3ds-max/overview>
- [17] Cinema 4D <https://www.maxon.net/en-us/>
- [18] Rhinoceros <https://www.rhino3d.com/>
- [19] LightWave <https://www.lightwave3d.com/>
- [20] Kyle Maxey. Autodesk Releases ReMake, a Photogrammetry Program for Everyone. June, 2016. <http://www.engineering.com/DesignSoftware/DesignSoftwareArticles/ArticleID/12318/Autodesk-Releases-ReMake-a-Photogrammetry-Program-for-Everyone.aspx>
- [21] Autodesk ReMake Free & Pro <http://www.cadtutor.net/forum/showthread.php?96975-Autodesk-Memento-Becomes-Autodesk-ReMake>
- [22] AUTODESK® REMAKE GETTING STARTED GUIDE. [https://remake.autodesk.com/assets/Autodesk\\_ReMake\\_Guide\\_01.pdf](https://remake.autodesk.com/assets/Autodesk_ReMake_Guide_01.pdf)
- [23] Trevor Williams. Basic Model Preparation with Meshmixer. Digital Media Tutorial . <http://digitalmedia.architecture.yale.edu/sites/default/files/files/Meshmixer.pdf>
- [24] Gadgest 360. <http://gadgets.ndtv.com/lenovo-a2010-2881>



## COMBUSTION CHAMBER AND FUEL MIXTURE MOTION ANALYSIS OF A NEW ROTARY ENGINE

*DUDÁS László PhD, KAPITÁNY Pálma*

*University of Miskolc, Hungary*

*E-mail: [itidl@uni-miskolc.hu](mailto:itidl@uni-miskolc.hu), [kapitanypalma@gmail.com](mailto:kapitanypalma@gmail.com)*

### **Abstract**

*The paper introduces a new patented internal combustion engine construction that has rotary working parts only. The internal combustion takes place in the cavities formed between the rotor and the rotary chamber. The rotation of these two parts of the engine are synchronised by the third rotary part of the engine, by the block gear. The accomplished work analyses the form of the combustion chamber along the working cycles of the motor and the motion path of the fuel mixture. It has been proved that in this type of rotary engine the motion path of the fuel mixture is unique among all the well known internal combustion engines having closed combustion chamber: it is linear.*

**Keywords:** *Rotary engine, internal combustion, rotor, rotary chamber, fuel mixture.*

### **1. INTRODUCTION**

There is no doubt that the internal combustion engines will exist in special areas along with the rapidly evolving electric engines and machines powered by them. So the improvement of possible new types of internal combustion engines is also important. The paper presents a new patented motor construction [1] that has rotary working parts only and characterised by closed internal combustion chambers. The construction, the advantages and disadvantages, the possibilities of manufacturing and assembling were analysed in previously published articles [2,3,4]. In the research work demonstrated in this paper the formation of the internal combustion cavities and the motion path of the fuel mixture along the working cycles will be analysed and demonstrated. First the geometry of the engine is discussed and the special distinctive characteristic signs will be reviewed. Then the explanation will deal with the dynamic formation and special features of the internal cavities where the working cycle sections – sucking, compression, ignition, combustion, expansion and exhaust happen. The third main part of the review will analyse the motion path formation of the fuel mixture and the gas in the working engine. In the end a summary will conclude the achieved results and new recognitions.

### **2. THE PATENTED ENGINE CONSTRUCTION**

The evolution history of screw compressor line and the progressive cavity pump line lead to the invention and patenting of the new rotary internal combustion engine that was published in [5] by one of the authors. The direct prequel of the invention was the FORCYL-type fluid pump [6]. Applying changing pitch along the rotor and the rotary chamber axes the modified helicoids produce increasing and decreasing volumes of the dynamically formed cavities between these two main parts of the motor. The patented engine construction (see Fig. 1) is similar to the original construction of Wankel rotary engine [7] with the fixed axes of the two main rotary parts, but the working cycles happens not in the plane of the rotation, but along the length of the axes of the



engine. Owing to this 3D feature the pitch modifications give maximal freedom for setting the compression and expansion cycle properties. In this construction the moving parts simple rotate, there is no alternating or planetary motion at all. As there is not direct contact between the rotor and rotary chamber surfaces, the rotation speed of the engine is limited by the rotation limits of the rolling bearings and the synchronising gears only. As a consequence, this engine can reach the extreme high 40 000 RPM, that is more than double of actual formula one car engines rev. The final realisation is planned using industrial ceramic materials for the parts of the motor.

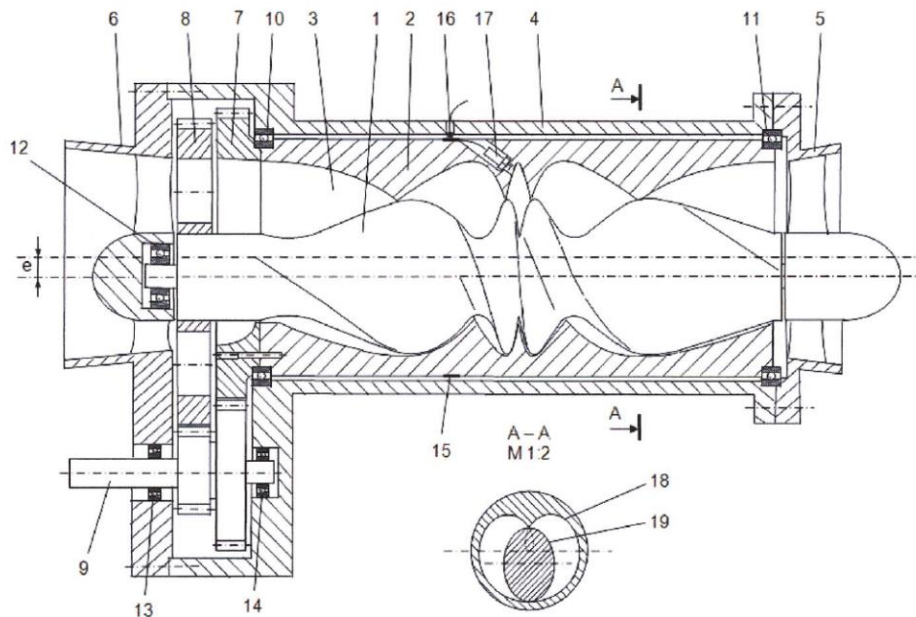


Figure 1 The patented rotary internal combustion engine

The next list summarizes the special distinctive characteristic signs of this motor:

- Prolonged or repeated sparking is also possible
- Two-stroke engine without any valves – no vibration and noise
- Compression and exhaust ratios can be controlled by any function
- There is no need for a tailpipe and muffler because the exhaust gas pressure may be as low as the environmental air pressure
- Mixture and exhaust gas are perfectly isolated
- There is no alternating motion – no vibration
- Very high rotational speed is possible: 40 000 RPM
- Very high temperature is applicable due to ceramic materials
- No need for water cooling
- Thermal fluctuation is minimal
- The friction between the rotor and the rotary house is drastically reduced because there is a very small gap.

Unfortunately there are some disadvantages also exist:

- Complex 3D surfaces, higher manufacturing cost
- Manufacturing and assembling precision is crucial
- Long internal cavities, more difficult combustion.



### 3. DYNAMIC FORMATION AND SPECIAL FEATURES OF THE CAVITIES

The cavities are formed dynamically between the rotary parts, namely between the rotor and the rotary chamber. These parts have own axes and there is a given eccentricity between them. The rotor and the chamber work as envelope surfaces in the relative motion. There is a very small gap between them and the dynamic effect happening on the fluid content of the fuel mixture and of the exploded gas act as sealing. In Fig. 2 the rotor is slightly enlarged to demonstrate the locations of the gaps on the rotary chamber surface in a given moment of rotation.

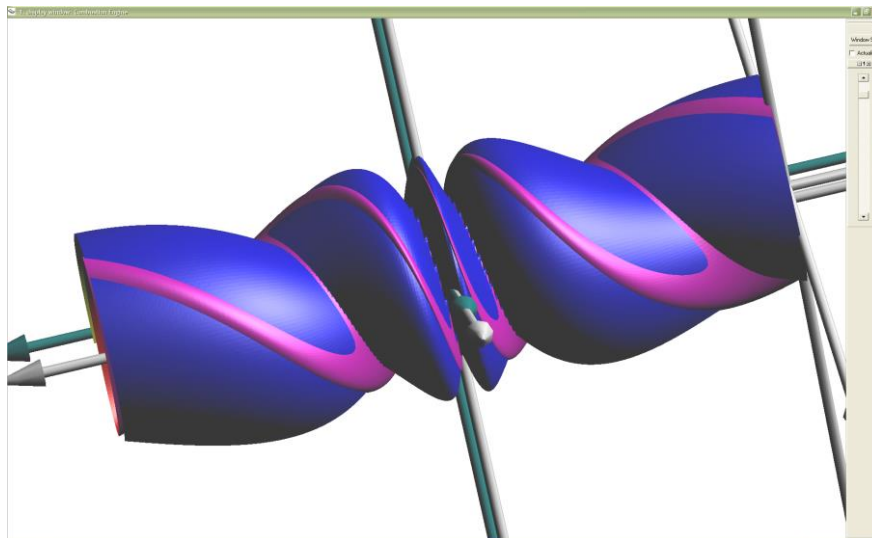


*Figure 2* The enlarged rotor surface intersects the chamber surface and indicates the gaps locations

In accordance with the orthogonal intersection subfigure shown in Fig. 1, the ellipse curve of the rotor and the quasi-cardioid curve of the chamber are touches each other in two or three points depending on the angle of rotation. The chamber rotates with doubled rotation velocity of the rotor. The surface parts of the rotor and the chamber surfaces that are closed around by the touching spatial curves form closed cavities. These similar shape cavities are longer or shorter depending on the local pitch values of the rotary parts. As these cavities shorten a compression effect happens, and on the other hand the cavities becoming longer make possible the dilatation of the expanding gas. Owing to the used Surface Constructor [8] kinematic surfaces designer and motion animator computer program – developed by one of the authors – it is easy to study the motion of the engine parts. Any part can be chosen as fixed reference object and the relative motion of the other can be analysed. Using this possibility the next features were detected:

- The chamber is a one start helicoids, the rotor is a two starts helicoids
- The pitch of the rotor is two times longer than the pitch of the chamber
- A cavity length is one and a half thread (540 grad) on the rotor and three full thread (1080 grad) on the chamber
- The next cavity opens at every 180 grad rotation of the two starts rotor (360 grad of the one start chamber)
- A three thread (1080 grad) length rotor is suitable for an engine, after a 540 grad sucking in period the closing cavity moves along the axis 270 grad while performs a compression. In the next 270 grad expands fully and at the end of this period the cavity starts to open



- At every 180 grad rotor turning (360 grad chamber turning) there is an ignition
- There are three closed moving fills at the same time in different cavities, plus one half opening and one half closing (not closed) cavities at the two ends, and while a full 1080 grad four stroke cycle (see Fig. 3) takes place six explosions happen.

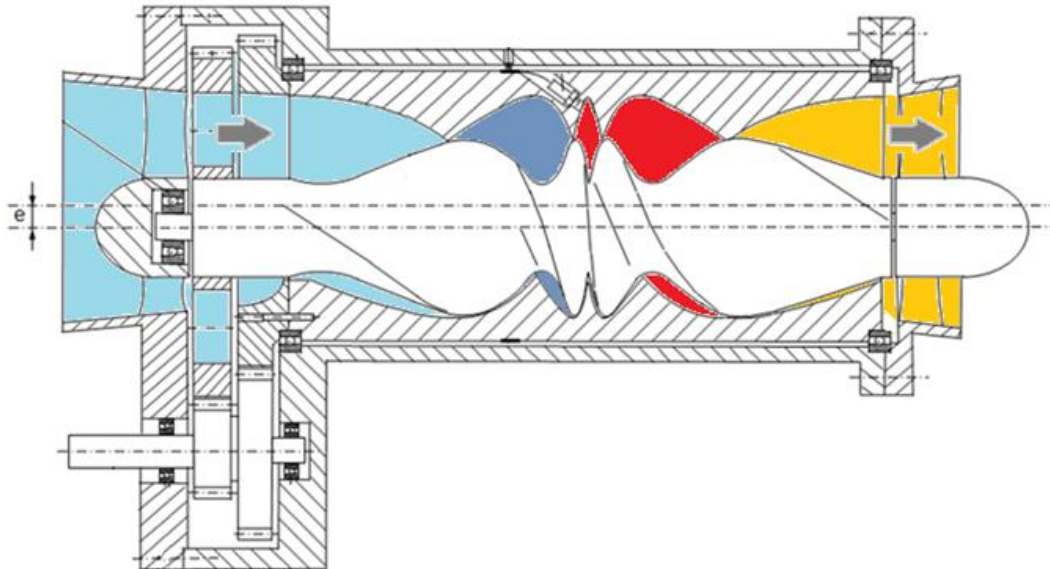


Figure 3 The four strokes of the engine are indicated by different colours

#### 4. MIXTURE MOTION PATH FORMATION OF THE WORKING ENGINE

The goal of this section is to prove the presumption that the motion path of the mixture is linear, parallel to the rotary axes of the rotor and the rotary chamber. This property of the investigated engine is unique among all the well known internal combustion engines having closed combustion chamber and is similar to turbines.

The linear motion of the mixture comes from that fact that the formed planar regions between the intersection curves of the rotor and the chamber are moves along the axes as the rotary parts rotate. One moment of the working is fixed and is shown in Fig. 4. The figure shows the orthogonal intersections in different locations of the engine and these intersections are assigned to the proper location of the rotor with numbers. The formation of one cavity has been emphasised with grey filling of its area. The formed cavities have a 'slug' form that is curved in a helical manner. The thickest intersection of this 3D formation is in the upper region of the chamber because the rotor axis is under the chamber axis with the  $e$  eccentricity as marked in Fig. 3. As this eccentricity is constant along the length of the engine, the thickest part of the cavity is always in the upper region of the chamber when moves along the engine. As a consequence, the shown intersections, one after another, go through the engine parallel to the axes direction. It can be interpreted another way also, considering the 'slug', it moves linearly along the axis direction and it changes its form only in axial direction, as a spring, because of the compression and expansion. This motion was checked by the SC computer program that could animate the motions.

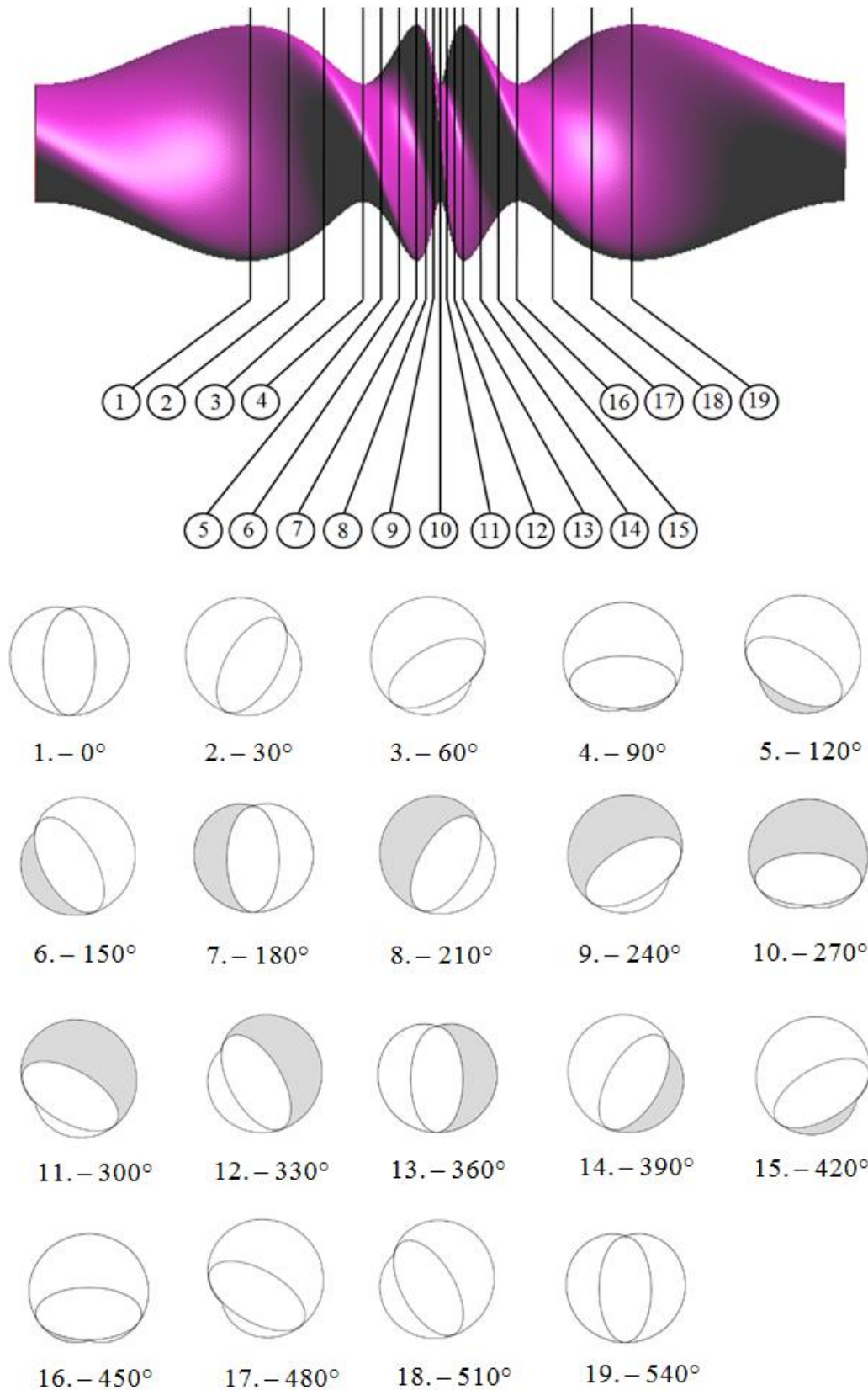


Figure 4 The orthogonal intersections of the rotor and the rotary chamber surface form closed regions



## SUMMARY

The paper introduced a new patented internal combustion engine construction that has rotary working parts only. First the construction was presented with its unique features, then the advantages of such a type engine were listed together with the disadvantageous properties. Then the dynamically formed closed cavities were analysed in conjunction with the rotational angle of the rotor and the strokes of the engine were demonstrated. The investigations are shown that an engine having three full threads of the double start rotor having elliptical orthogonal intersection curve is enough for a well-working engine, and in the case of such a construction six explosion will happen in every cycle. In the last part of the accomplished analysis it has been proved that in this type of rotary engine the motion path of the fuel mixture is linear along the axes of the rotary parts and this feature is unique among all the well known internal combustion engines having closed combustion chamber.

## ACKNOWLEDGMENTS

This research was partially carried out in the framework of the Center of Excellence of Mechatronics and Logistics at the University of Miskolc. The financial support is acknowledged. The authors also acknowledge the help of Máté Biró, who determined the intersection points used in Fig. 4.

## REFERENCES

- [1] Dudás, L.: *Rotary Piston Internal Combustion Engine*. Hungarian patent HU230082, 2015.
- [2] Dudás, L.: *Computer Aided Design of a New Combustion Engine Having Only Rotary Parts*, SAMI2015 IEEE 13th International Symposium on Applied Machine Intelligence and Informatics, PROCEEDINGS, January 22-24, 2015 Herl'any, Slovakia, pp.295-300. IEEE Xplore: DOI: 10.1109/SAMI.2015.7061892
- [3] Dudás, L. Biró, M., Novák, L. L.: *Construction Modeling and Manufacturing Analysis of a New Rotary Combustion Engine*, INES 2016 • 20th Jubilee IEEE International Conference on Intelligent Engineering Systems • June 30-July 2, 2016 • Budapest, Hungary pp.89-94. IEEE Xplore: DOI: 10.1109/INES.2016.7555099
- [4] Dudás, L.: *Developing a Rotary Internal Combustion Engine Characterised by High Speed Operation*. In: Jármái K., Bolló B. (eds) *Vehicle and Automotive Engineering. Lecture Notes in Mechanical Engineering*. Springer. 2017
- [5] Dudás, L.: *Térbeli forgódugattyús motorok evolúciója (Evolution of spatial rotary piston engines)* (In Hungarian), *Műszaki Füzetek 14.* (HU ISSN 2060-7954) Ed.: prof. dr. László Pokorádi, pp.284-292.
- [6] Micro Europe Kft.: *A Sokszögmegmunkálás Élvonulában (In the Frontline of Polygon Surface Machining)*, Available at: <http://www.microeurope.hu/indexsziv.html>, Accessed Febr. 19, 2012.
- [7] *NSU Wankel rotary engines and cars*, [http://cp\\_www.tripod.com/rotary/pg05.htm](http://cp_www.tripod.com/rotary/pg05.htm), Accessed: Oct. 2, 2017.
- [8] Dudás L.: *Modelling and Simulation of a New Worm Gear Drive having Point-like Contact*, *Engineering with Computers*, Volume 29, Issue 3, pp. 251-272. 2013.



## THE EFFECT OF PROFILE VARIATION ON CONTACT PROPERTIES IN CASE OF QUASI GLOBOID WORM GEARING

*DUDÁS László PhD*

University of Miskolc, Hungary

E-mail: [iitdl@uni-miskolc.hu](mailto:iitdl@uni-miskolc.hu)

### Abstract

The paper presents the effect of the profile variation on the contact properties of a new, hourglass-like quasi globoid worm gearing. This gearing type is a novel construction and needs deeper analysis. The generation of the worm is made moving the generating profile along a line that is not parallel to the axis of the worm. The head surface of this worm is a hyperbolic surface of revolution. The advantage of the generation and the machining that it doesn't need special teething machine, like the normal Cone-type worms, but a modified turning machine is adequate. The worm wheel is enveloped by the worm. As this worm gearing is new, the evaluation of the properties, advantages and disadvantages are missing. This paper would like to analyse three types of profile curves: linear, circular and elliptical and presents the form of the mating curves.

**Keywords:** Hourglass-like worm, worm generation, worm wheel tooth generation, mating properties.

### 1. INTRODUCTION

The hourglass-like worms and the gearings using such worms are known as very precise, loadable drives. The original Cone-type gearing is characterised by advantageous contact lines and an undercut region on the gear tooth surface. Because of the advantageous properties many research was accomplished to avoid drawbacks and improve the driving [1, 2, 3]. One of the disadvantages is the expensive cutting method of the worm and the required special teething machine. The circular generating motion characterises the cutting process, as can be followed in Fig. 1.

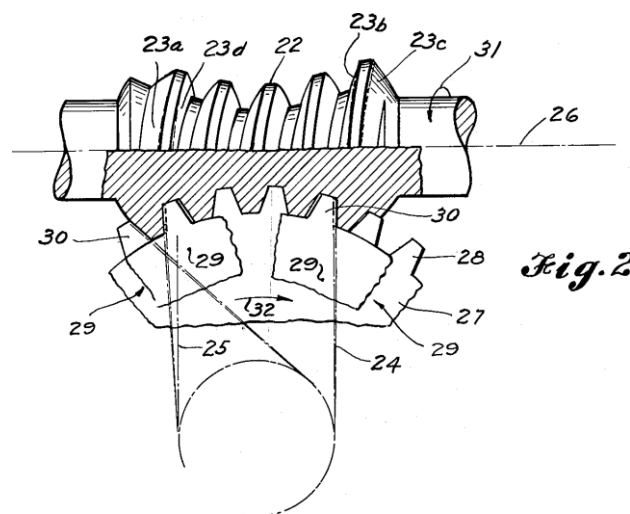


Figure 1 The circular motion of the generating edge in case of Cone-type globoid worm [1]



The innovations concerning the profile curve modification and using rotary tool for generating the worm resulted in better, more economical technologies [3, 4]. The author introduced in [5] a globoid-like novel gearing type that uses linear motion of the cutting tool, but this path is not parallel to the worm axis. To refresh the method Fig. 2 is borrowed from that paper.

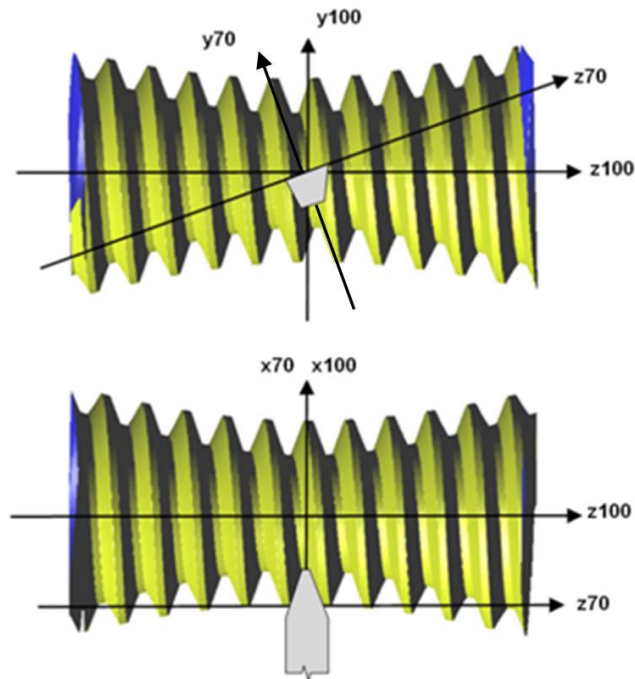


Figure 2 The generation of the tooth surface of the worm

Figure 2. shows the case when the edge of the tool is linear. This case was analysed in [5]. The enveloping of the worm wheel tooth surface and the generated segment of the worm wheel are shown in Fig. 3.

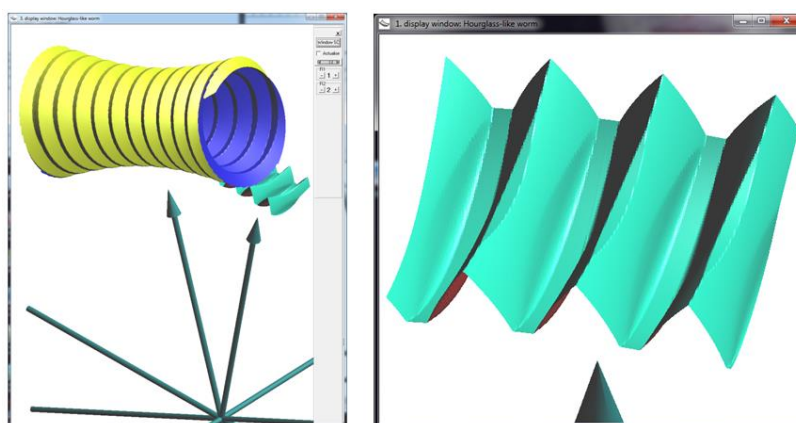


Figure 3 Generation of the worm wheel segment (left) and the segment having undercut region (right)

The results revealed that the worm wheel teeth may have large undercut region at the foot of the tooth.



Moreover the mating lines were also disadvantageous, almost parallel to the sliding velocity direction, as can be checked in Fig. 4.

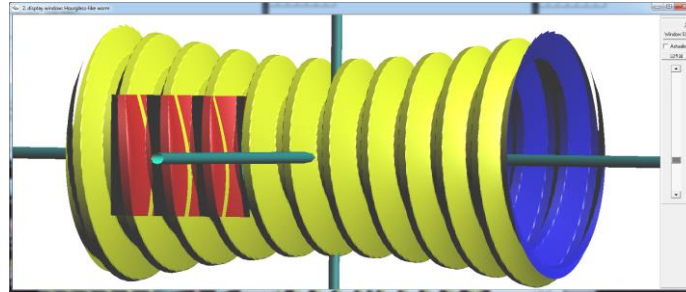


Figure 4 The characteristic curves on the inner side of the worm wheel segment

In the following two other profile curves, circle and ellipse will be used for sweeping the worm tooth surface and the mating worm wheel surface will be generated in the enveloping process. Then the form of the characteristic lines will be evaluated and compared. The modelling and the generation of surfaces were performed by the Surface Constructor (SC) 3D kinematic modeller computer program of the author.

## 2. CIRCLE GENERATOR PROFILE ON THE WORM

The theoretical cutting tool is positioned in the  $x70-z70$  coordinate plane, similarly to the case shown in Fig. 2 for the situation of linear edge. To improve the efficiency of the research the working tooth surfaces were modelled both for the worm and for the worm wheel only. A screenshot in Fig. 5 shows the model in SC with the axes of coordinate systems. Unfortunately the large undercut region could be detected in this case also, as shown in right side of Fig. 5. Applying larger distance of rotary axes this problem could be eliminated.

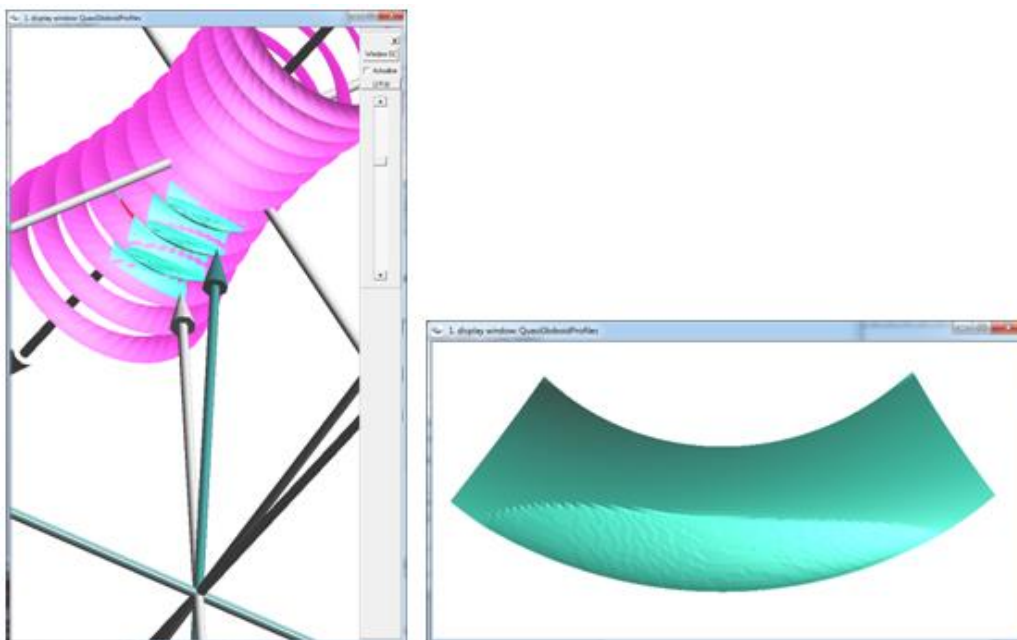


Figure 5 The model (left) and the undercut worm wheel tooth surface (right)

For the first it was surprising that the worm wheel tooth side is generated by the positive  $z100$  half of



the worm only. This happens because of the asymmetric location of the generating motion path to the centrally symmetric helicoids of the threads of the worm which originates from the ALPHA angle between  $z_{100}$  worm axis and  $z_{70}$  generating curve translation direction. The axial relocation of the generating profile doesn't modify this feature. In case of circle profile the enveloped worm wheel, the enveloping worm and the characteristic curve between them show similarity to the helical worm having linear profile form. Some moments of the relative motion of the worm and worm wheel are shown in Fig. 6. Only the effective positive half of the worm is used.

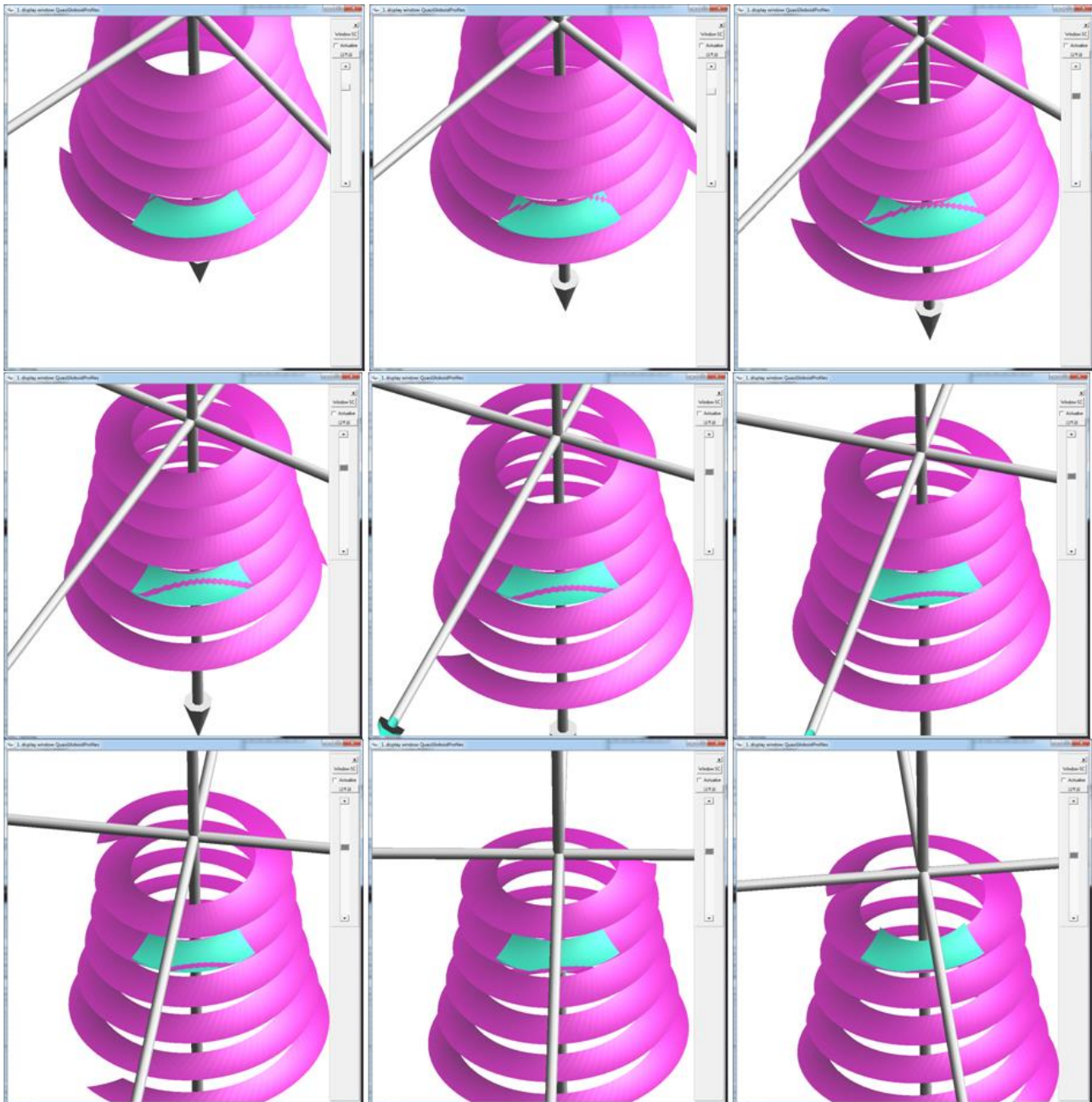


Figure 6 Characteristic curves of the mating worm and worm wheel tooth surfaces



## 2. ELLIPSE GENERATOR PROFILE ON THE WORM

The pictures of the mating surfaces of the gearing generated using ellipse profile curve are presented in Fig. 7. They are very similar to the curves of circular gearing.

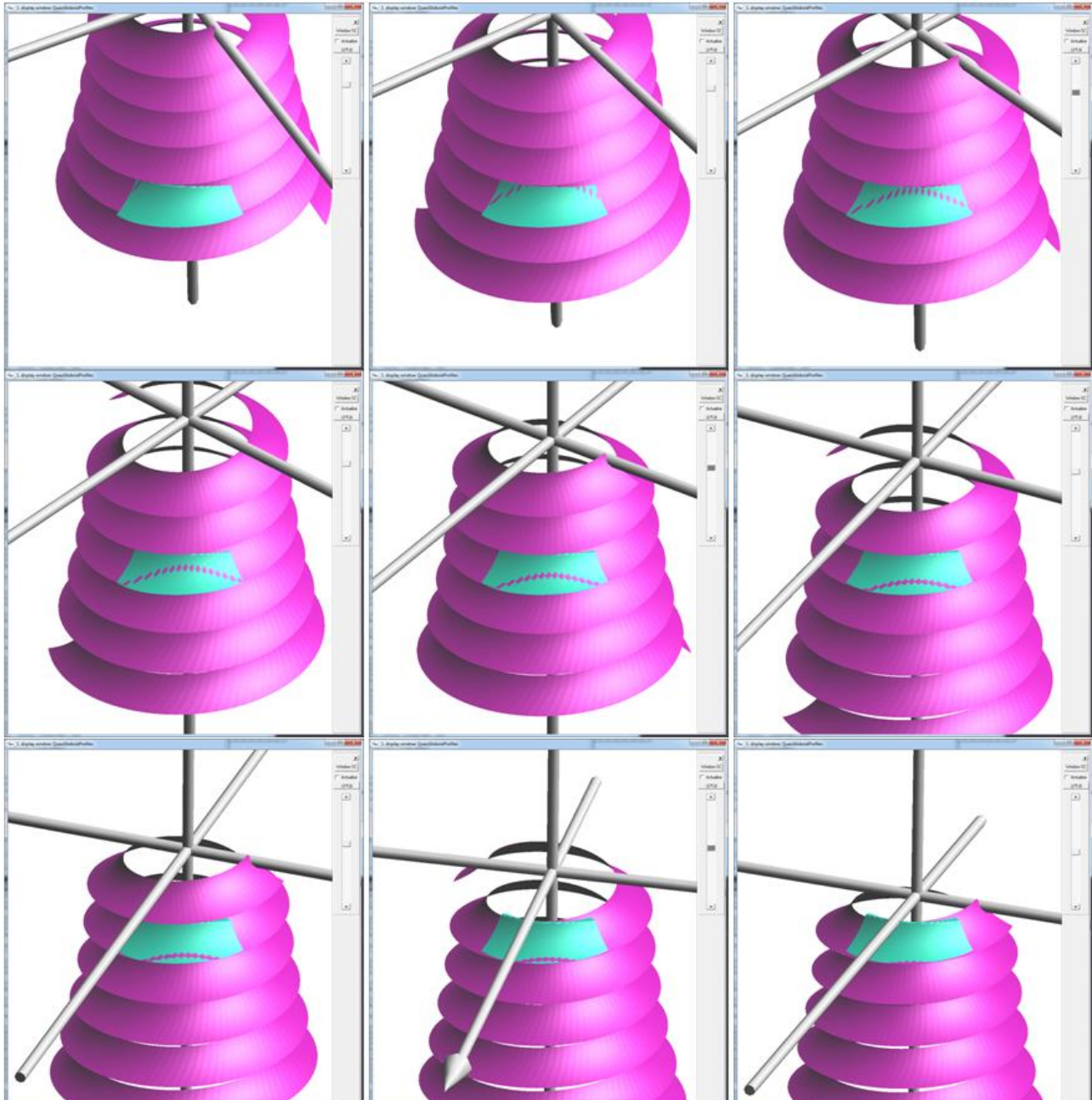


Figure 7 Characteristic curves of the mating worm and worm wheel tooth surfaces in case of elliptical generating curve

## 4. SUMMARY

The paper introduced a new worm gearing having hourglass-like worm. Despite of high similarity to globoid form, this type of worm can be generated without circular tool motion with a simple linear



feed and as a consequence it can be produced even on a normal lathe equipped with a tilted worm holder. The advantages and disadvantages are need additional investigations and modelling. Beside trivial advantages, like easy and cheap machining and the possibility of using the well-tried modification methods of cylindrical worm drives, the accomplished with SC (see Fig. 8) modelling revealed a special feature: the worm is not the usual, one half of the threads connect to the right hand side of the worm wheel teeth, and the threads of the other half connect to the left hand side of the worm wheel teeth. Foreseen analysis has to explore the balancing possibilities of the mating properties to improve the number of simultaneously connecting teeth.

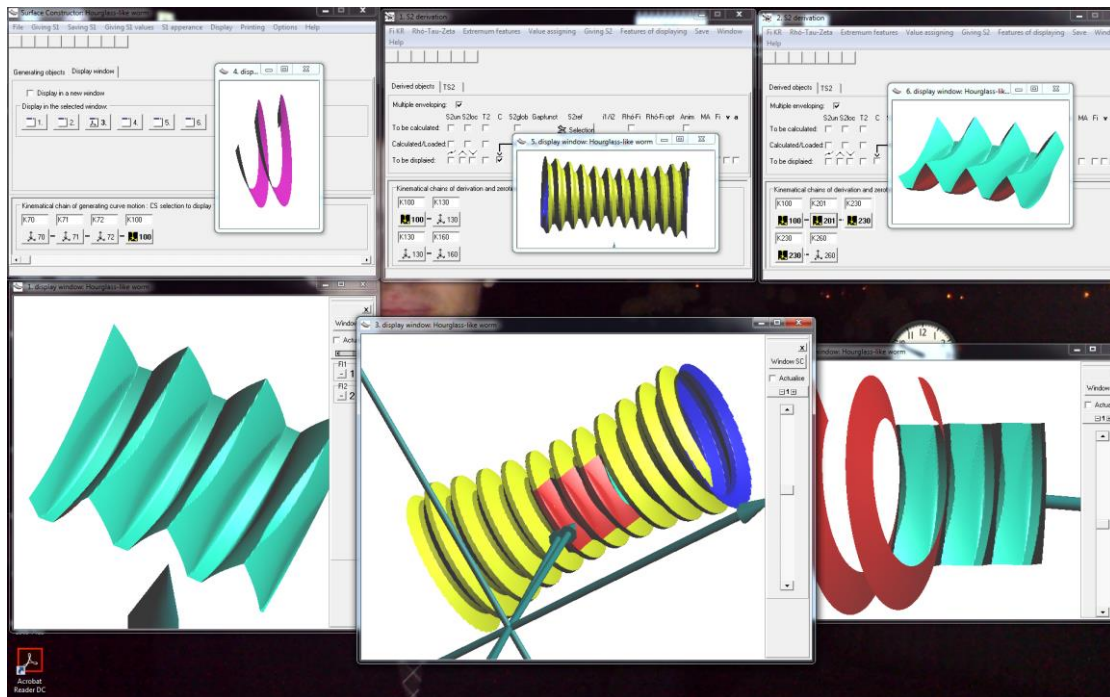


Figure 8 Snapshot of the computer screen in the midst of the analysis accomplished with Surface Constructor

## ACKNOWLEDGMENTS

This research was partially carried out in the framework of the Center of Excellence of Mechatronics and Logistics at the University of Miskolc. The financial support is acknowledged.

## REFERENCES

- [1] Skog, G.: *Gear worm thread generating machine*. US 2756641 A patent, 1956.
- [2] Wildhaber, E.: *Enveloping worm gearing*. US 2935886 A patent, 1960.
- [3] Kobayashi, T.: *Hourglass worm gear*. US 5325634 A patent, 1994.
- [4] Lunin, S. V.: *Globoid gear technology from ZAKGEAR* <http://www.zakgear.com/Wormoid.html>, Accessed: 10.10.2016.
- [5] Dudás, L.: *Generation and analysis of a new hourglass-like worm gearing*. PROCEEDINGS OF THE 4th INTERNATIONAL SCIENTIFIC CONFERENCE ON ADVANCES IN MECHANICAL ENGINEERING (ISCAME 2016) 13-15 October, 2016 Debrecen, Hungary, Eds. S. Bodzás, T. Mankovits



## AN ALTERNATIVE TO HYPERELASTIC-BASED MULTIPLICATIVE PLASTICITY MODELS

*ÉCSI Ladislav PhD, ÉLESZTÖS Pavel CSc, JANČO Roland PhD*

*Institute of Applied Mechanics and Mechatronics, Faculty of Mechanical Engineering, Slovak University of Technology in Bratislava*

*E-mail: [ladisav.ecsi@stuba.sk](mailto:ladisav.ecsi@stuba.sk), [pavel.elesztos@stuba.sk](mailto:pavel.elesztos@stuba.sk), [roland.janco@stuba.sk](mailto:roland.janco@stuba.sk)*

### Abstract

*Hyperelastic-based multiplicative plasticity models are commonly used for modelling of material deterioration of hyperelastic materials within the framework of finite-strain plasticity. The multiplicative split of the deformation gradient in the models, however, is rather incomplete and not quite consistent with the theory of nonlinear continuum mechanics as it neglects the displacement fields in the definitions of the deformation gradient and its parts. Besides, the models fix the order of elastic and plastic deformations, which may also question the correctness of the models from the physical point of view. In this paper an alternative to hyperelastic-based multiplicative plasticity models is presented. The related material models are based on a modified non-linear continuum theory for finite deformations of elasto-plastic media, which uses an additive split of the displacement field into an elastic and a plastic part, and which describes the plastic flow in terms of various instances of the yield surface and stress measures in the initial and current configurations of the modelled body. In this paper an alternative framework for modelling of the plastic flow in hyperelastic material is presented using the Ogden material and  $J_2$  plasticity, which have widespread use in numerical simulations of rubber-like solids, various polymers and biomaterials.*

**Keywords:** *finite-strain formulation, Lagrangian description,  $J_2$  plasticity, hyperelastic-based plasticity model, Ogden material.*

### 1. INTRODUCTION

Hyperelastic material models are commonly used for modelling material behaviour of rubber-like solids, various polymers, foams and biomaterials under elastic loading [1]. Without a need for completeness let us just mention a few concrete examples of hyperelastic material, such as the Ogden material [2, 3], the Hencky material [4], the Mooney–Rivlin material, the neo-Hookean material or their regularised (or compressible) alternatives, to model rubber-like solids and polymers [5]. The range of these materials have later on been extended by the Yeoh material [6], the Gent material [7], the Dill material [8] and the Bower material [9]. The Holzapfel material [10] was proposed to model carbon-black-filled rubber vulcanizates, while the Blatz-Ko material [11] or the Arruda-Boyce material [12] to model foamed, or compressible elastomers. From among the biomaterials the Ogden material or its regularised alternatives ought to be mentioned with widespread use in modelling soft tissues [1, 13].

When in addition the aforementioned materials undergo material deterioration, hyperelastic-based multiplicative plasticity models are used to model their behaviour within the framework of finite strain plasticity [13-15]. The related flow plasticity theories are based on a multiplicative split of the deformation gradient into an elastic part and a plastic part, while use hyperelastic constitutive equations, such as the ones mentioned above, to describe the stress-strain relationship in the material. In spite of the fact that they are generally accepted, the multiplicative split based flow plasticity theories are rather incomplete and not quite consistent with the theory of nonlinear



continuum mechanics as they employ a multiplicative split of the deformation gradient into an elastic part and a plastic part, in the definitions of which the displacement fields are neglected. The theories moreover fix the order of elastic and plastic deformations at each material point of the body, which may also question the correctness of the theories and the related material models from the physical point of view.

In this paper a modified framework for modelling of the plastic flow in hyperelastic material is presented, which allows for the development alternative material models which no longer exhibit the disadvantages of the hyperelastic-based multiplicative plasticity models. As a result, an alternative hyperelastic-based plasticity model using the Ogden material with  $J_2$  plasticity has been proposed. The material model is based on the first non-linear continuum theory of finite deformations of elastoplastic media, which uses an additive split of the displacement field into an elastic and a plastic part and which describes the plastic flow in terms of various instances of the yield surface and stress measures in the initial and current configurations of the body. Furthermore, the material model is objective and thermodynamically consistent every respect.

## 2. METHODS

The Lagrangian description within the frameworks of the modified non-linear continuum theory of finite deformations of elastoplastic media is used to describe the kinematics of deformation of the body. Though the non-linear continuum theory will not be detailed herein, it play a key role in the development of the presented framework for modelling material deterioration of hyperelastic material.

### 2.1 A short overview of the non-linear continuum mechanical theory of finite deformations of elastoplastic media

In order to develop a thermodynamically consistent material model within the framework of finite-strain plasticity, we assume that the plastic flow has alternative forms, defined in terms of various instances of the yield surface and stress measures in the body initial and current configurations. Starting with a multiplicative split of the deformation gradient, the proper form of the decomposition, consistent with the theory of nonlinear continuum mechanics, which includes displacement fields in the definitions of the deformation gradient and its parts, can be expressed as (Figure 1)

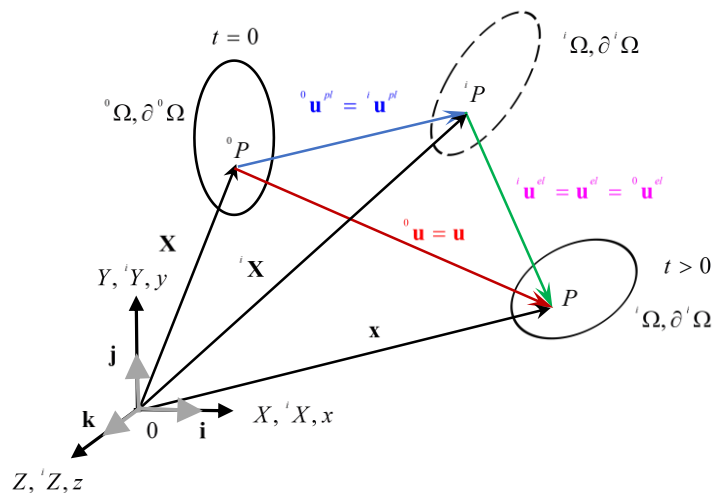


Figure 1 Multiplicative decomposition of the deformation gradient into an elastic part and a plastic part



$$\mathbf{F} = \frac{\partial \mathbf{x}}{\partial \mathbf{X}} = \frac{\partial \mathbf{x}}{\partial \mathbf{X}} \cdot \frac{\partial \mathbf{X}}{\partial \mathbf{X}} = \left( \mathbf{I} + \frac{\partial \mathbf{u}^{el}}{\partial \mathbf{X}} \right) \cdot \left( \mathbf{I} + \frac{\partial \mathbf{u}^{pl}}{\partial \mathbf{X}} \right) = \mathbf{F}^{el}(\mathbf{X}, t) \cdot \mathbf{F}^{pl}(\mathbf{X}, t). \quad (1)$$

In this form, however, the deformation gradient has neither a Lagrangian form nor an Eulerian form, because the plastic displacement field  ${}^0\mathbf{u}^{pl} = {}^0\mathbf{u}^{pl}(\mathbf{X}, t)$ , defined over the initial volume of the body, is in Lagrangian form, but the elastic displacement field  ${}^i\mathbf{u}^{el} = {}^i\mathbf{u}^{el}(\mathbf{X}, t)$ , defined over the intermediate volume of the body, is in Eulerian form. In order that the multiplicative split be in Lagrangian form, the elastic displacement field must have a Lagrangian counterpart,  ${}^i\mathbf{u}^{el} = {}^0\mathbf{u}^{el} = {}^0\mathbf{u}^{el}(\mathbf{X}, t)$ , defined over the initial volume of the body, so that the proper Lagrangian form of the multiplicative split of the deformation gradient is actually based on the additive decomposition of the Lagrangian displacement field into an elastic part and a plastic part  ${}^0\mathbf{u} = {}^0\mathbf{u}^{el} + {}^0\mathbf{u}^{pl}$ . Then the Lagrangian form of Eqn. (1) then takes its final form

$$\mathbf{F}(\mathbf{X}, t) = \mathbf{F}^{el}(\mathbf{X}, t) \cdot \mathbf{F}^{pl}(\mathbf{X}, t) = \left[ \mathbf{I} + \frac{\partial {}^0\mathbf{u}^{el}(\mathbf{X}, t)}{\partial \mathbf{X}} \cdot (\mathbf{F}^{pl})^{-1} \right] \cdot \mathbf{F}^{pl} = \mathbf{I} + \frac{\partial {}^0\mathbf{u}^{pl}}{\partial \mathbf{X}} + \frac{\partial {}^0\mathbf{u}^{el}}{\partial \mathbf{X}}. \quad (2)$$

In this case, however, neither the Green strain tensor  $\mathbf{E} = 1/2 \cdot (\mathbf{F}^T \cdot \mathbf{F} - \mathbf{I})$ , nor the Almansi strain tensor  $\mathbf{e} = 1/2 \cdot (\mathbf{I} - \mathbf{F}^{-T} \cdot \mathbf{F}^{-1})$  has decomposition into an elastic part and a plastic part, but additive decomposition exists when one evaluates the objective rates of the strain tensors. Then the material  $\dot{\mathbf{E}}$  and the spatial  $\mathbf{d} = \mathcal{L}_e(\mathbf{e})$  strain rate tensors can be expressed in the following forms

$$\dot{\mathbf{E}} = \frac{1}{2} \cdot (\dot{\mathbf{F}}^T \cdot \mathbf{F} + \mathbf{F}^T \cdot \dot{\mathbf{F}}) = \dot{\mathbf{E}}^{el} + \dot{\mathbf{E}}^{pl}, \quad \Rightarrow \quad \mathbf{d} = \mathbf{d}^{el} + \mathbf{d}^{pl}, \quad (3)$$

where

$$\mathbf{d} = \mathbf{F}^{-T} \cdot \dot{\mathbf{E}} \cdot \mathbf{F}^{-1}, \quad \mathbf{d}^{el} = \mathbf{F}^{-T} \cdot \dot{\mathbf{E}}^{el} \cdot \mathbf{F}^{-1}, \quad \mathbf{d}^{pl} = \mathbf{F}^{-T} \cdot \dot{\mathbf{E}}^{pl} \cdot \mathbf{F}^{-1}, \quad (4)$$

$$\dot{\mathbf{E}}^{el} = \frac{1}{2} \cdot \left[ \left( \frac{\partial {}^0\dot{\mathbf{u}}^{el}}{\partial \mathbf{X}} \right)^T \cdot \mathbf{F} + \mathbf{F}^T \cdot \frac{\partial {}^0\dot{\mathbf{u}}^{el}}{\partial \mathbf{X}} \right], \quad \dot{\mathbf{E}}^{pl} = \frac{\dot{\lambda}}{2} \cdot \left[ \left( \frac{\partial {}^p\Psi}{\partial \mathbf{P}} \right)^T \cdot \mathbf{F} + \mathbf{F}^T \cdot \frac{\partial {}^p\Psi}{\partial \mathbf{P}} \right], \quad (5)$$

$$\frac{\partial {}^0\dot{\mathbf{u}}^{pl}}{\partial \mathbf{X}} = \dot{\lambda} \cdot \frac{\partial {}^p\Psi}{\partial \mathbf{P}}, \quad \text{and} \quad \frac{\partial {}^p\Psi}{\partial \mathbf{P}} \neq \left( \frac{\partial {}^p\Psi}{\partial \mathbf{P}} \right)^T. \quad (6)$$

Here  $\mathbf{X}$  denotes the position vector of a material point and  $\mathbf{x} = \mathbf{X} + {}^0\mathbf{u}$  is the position vector of the corresponding spatial point after deformation. The deformation gradient  $\mathbf{F} = \mathbf{I} + \partial {}^0\mathbf{u} / \partial \mathbf{X} = \mathbf{I} + \partial {}^0\mathbf{u}^{el} / \partial \mathbf{X} + \partial {}^0\mathbf{u}^{pl} / \partial \mathbf{X}$  in this case can either be expressed as a function of the material displacement field  ${}^0\mathbf{u}$  alone, or as a function of its elastic  ${}^0\mathbf{u}^{el}$  and plastic  ${}^0\mathbf{u}^{pl}$  parts. The symbols in the above  $\dot{\mathbf{E}}^{el}, \dot{\mathbf{E}}^{pl} / \mathbf{d}^{el}, \mathbf{d}^{pl}$  denote the elastic and the plastic material/spatial strain rate tensors, where in the latter the plastic flow is defined by Eqn. (6)<sub>1</sub> as a product of a plastic multiplier  $\dot{\lambda}$  and an appropriate yield surface normal,  $\partial {}^p\Psi / \partial \mathbf{P}$ , defined in terms of the 1<sup>st</sup> Piola-Kirchhoff stress tensor  $\mathbf{P}$ . Here the symbol  $\mathcal{L}_e(\mathbf{e}) = \mathbf{F}^{-T} \cdot [\partial(\mathbf{F}^T \cdot (\mathbf{e}) \cdot \mathbf{F}) / \partial t] \cdot \mathbf{F}^{-1}$  denotes the Lie derivative of the Almansi strain tensor  $\mathbf{e}$ . It should be noted that both the elastic and the plastic strain-rate tensors have forms similar to the strain-rate tensor itself. Besides, it can be shown that the plastic flow defined by Eqn.



(6)<sub>1</sub> is not constrained, resulting in Eqns. (5)<sub>2</sub> and (4)<sub>3</sub> respectively, being the only non-degenerated forms of the material and spatial plastic strain rate tensors.

Let the instances of the yield surface be defined as  ${}^s\Psi = {}^s\Psi[{}^s\sigma_{eq}(\mathbf{S}), \mathbf{q}]$ ,  ${}^p\Psi = {}^p\Psi[{}^p\sigma_{eq}(\mathbf{P}), \mathbf{q}]$ ,  ${}^r\Psi = {}^r\Psi[{}^r\sigma_{eq}(\boldsymbol{\tau}), \mathbf{q}]$ ,  ${}^\sigma\Psi = {}^\sigma\Psi[{}^\sigma\sigma_{eq}(\boldsymbol{\sigma}), \mathbf{q}]$  in terms of the 2<sup>nd</sup> Piola-Kirchhoff stress tensor  $\mathbf{S}$ , the 1<sup>st</sup> Piola-Kirchhoff stress tensor  $\mathbf{P}$ , the Kirchhoff stress tensor  $\boldsymbol{\tau}$ , the Cauchy stress tensor  $\boldsymbol{\sigma}$  and a vector of internal variables  $\mathbf{q}$ . After changing the physical interpretation of the plastic flow and applying push-forward and pull-back operations to the material gradient of the plastic velocity field (Eqn. (6)<sub>1</sub>) as follows

$$\frac{\partial \dot{\mathbf{u}}^{pl}}{\partial \mathbf{x}} = \frac{\partial {}^0\dot{\mathbf{u}}^{pl}}{\partial \mathbf{X}} \cdot \mathbf{F}^{-1} = \dot{\lambda} \cdot \frac{\partial {}^\sigma\Psi}{\partial \boldsymbol{\sigma}}, \quad \frac{\partial \dot{\mathbf{u}}^{pl}}{\partial \mathbf{x}} = \frac{\partial {}^0\dot{\mathbf{u}}^{pl}}{\partial \mathbf{X}} \cdot \mathbf{F}^{-1} = \dot{\lambda} \cdot \frac{\partial {}^r\Psi}{\partial \boldsymbol{\tau}}, \quad \mathbf{F}^T \cdot \frac{\partial {}^0\dot{\mathbf{u}}^{pl}}{\partial \mathbf{X}} = \dot{\lambda} \cdot \frac{\partial {}^s\Psi}{\partial \mathbf{S}}, \quad (7)$$

it can be found that the yield surfaces are related by the following formulas

$$\frac{\partial {}^p\Psi}{\partial \mathbf{P}} \cdot \mathbf{F}^{-1} = \frac{\partial {}^\sigma\Psi}{\partial \boldsymbol{\sigma}}, \quad \frac{\partial {}^p\Psi}{\partial \mathbf{P}} \cdot \mathbf{F}^{-1} = \frac{\partial {}^r\Psi}{\partial \boldsymbol{\tau}}, \quad \mathbf{F}^T \cdot \frac{\partial {}^p\Psi}{\partial \mathbf{P}} = \frac{\partial {}^s\Psi}{\partial \mathbf{S}}. \quad (8)$$

It can also be verified, that the yield surfaces and the equivalent stresses  ${}^p\sigma_{eq}$ ,  ${}^s\sigma_{eq}$ ,  ${}^r\sigma_{eq}$ ,  ${}^\sigma\sigma_{eq}$  contained in them which meet the transformations defined by Eqn. (8) too, have the following properties:

$${}^p\sigma_{eq} = {}^s\sigma_{eq} = {}^r\sigma_{eq} = J \cdot {}^\sigma\sigma_{eq}, \quad (9)$$

$$\frac{\partial {}^s\Psi}{\partial \mathbf{S}} : \mathbf{S} = \frac{\partial {}^p\Psi}{\partial \mathbf{P}} : \mathbf{P} = \frac{\partial {}^r\Psi}{\partial \boldsymbol{\tau}} : \boldsymbol{\tau} = J \cdot \frac{\partial {}^\sigma\Psi}{\partial \boldsymbol{\sigma}} : \boldsymbol{\sigma}, \quad (10)$$

where Eqn. (10) is equivalent with the following equation

$$\dot{\mathbf{E}}^{pl} : \mathbf{S} \cdot dV_0 = \frac{\partial {}^0\dot{\mathbf{u}}^{pl}}{\partial \mathbf{X}} : \mathbf{P} \cdot dV_0 = \mathbf{d}^{pl} : \boldsymbol{\tau} \cdot dV_0 = \mathbf{d}^{pl} : \boldsymbol{\sigma} \cdot dv. \quad (11)$$

Here  $J = \det(\mathbf{F})$  is the Jacobian of deformation,  $dV_0$  is the volume of an infinitesimal volume element in the initial configuration of the body and  $dv = J \cdot dV_0$  is its spatial counterpart. Moreover, since they define the same admissible stress space and the same plastic flow respectively, one of the yield surfaces  ${}^s\Psi$ ,  ${}^p\Psi$ ,  ${}^r\Psi$ ,  ${}^\sigma\Psi$  has to be chosen as a reference yield surface to define the material model. Furthermore, when  ${}^\sigma\Psi$  or  ${}^r\Psi$  is chosen as a reference yield surface in the current configuration of the body, the contemporary flow plasticity theories will be recovered. It also ought to be noted that Eqns. (8)<sub>1</sub> and (8)<sub>2</sub> are constraint equations, making the contemporary strain rate additive decomposition based theories appear as if they had mixed finite-strain-small-strain formulations.



### 3. RESULTS

Eqns. (2)-(4) show that the deformation gradient multiplicative split based flow plasticity theories and the strain rate tensor additive decomposition based flow plasticity theories are variants of the presented nonlinear continuum mechanical theory based flow plasticity theories. Moreover, the two types of flow plasticity theories ought to be equivalent if they were properly formulated. In order to use the theory for modelling of deterioration of hyperelastic material, one needs to realise, that the proper deformation gradient, consistent with the theory of nonlinear continuum mechanics (Eqn. (2)), is independent of the order of elastic and plastic deformations. Then Eqns. (1) and (2) imply for the elastic part of the deformation gradient

$$\mathbf{F}^{el} = \mathbf{F}^{el}(\mathbf{X}, t) = \mathbf{I} + \frac{\partial^0 \mathbf{u}^{el}}{\partial \mathbf{X}} = \mathbf{F}(\mathbf{X}, t) - \frac{\partial^0 \mathbf{u}^{pl}}{\partial \mathbf{X}} = \mathbf{F} - \frac{\partial^0 \mathbf{u}^{pl}}{\partial \mathbf{X}}. \quad (12)$$

Furthermore, from Eqns. (6)<sub>1</sub> and (8) we have the following formula for the material gradient of the plastic displacement field

$$\frac{\partial^0 \mathbf{u}^{pl}}{\partial \mathbf{X}} = \int_0^t \frac{\partial^0 \dot{\mathbf{u}}^{pl}}{\partial \mathbf{X}} \cdot dt = \int_0^t \dot{\lambda} \cdot \frac{\partial^p \Psi}{\partial \mathbf{P}} \cdot dt = \int_0^t \dot{\lambda} \cdot \frac{\partial^r \Psi}{\partial \boldsymbol{\tau}} \cdot \mathbf{F} \cdot dt = \int_0^t \dot{\lambda} \cdot \frac{\partial^s \Psi}{\partial \boldsymbol{\sigma}} \cdot \mathbf{F} \cdot dt. \quad (13)$$

The constitutive equation of hyperelastic material is usually defined in terms of a strain energy function [1]. In our study there was used the Ogden material, the strain energy function of which can be expressed in any of the following forms [13]

$$\rho_0 \cdot {}_v \bar{\Psi}({}_v \lambda_1, {}_v \lambda_2, {}_v \lambda_3) = \sum_{p=1}^N \frac{\mu_p}{\alpha_p} \cdot ({}_v \lambda_1^{\alpha_p} + {}_v \lambda_2^{\alpha_p} + {}_v \lambda_3^{\alpha_p} - 3), \quad (14)$$

$$\rho_0 \cdot {}_B \bar{\Psi}({}_B \lambda_1, {}_B \lambda_2, {}_B \lambda_3) = \sum_{p=1}^N \frac{\mu_p}{\alpha_p} \cdot \left( {}_B \lambda_1^{\frac{\alpha_p}{2}} + {}_B \lambda_2^{\frac{\alpha_p}{2}} + {}_B \lambda_3^{\frac{\alpha_p}{2}} - 3 \right). \quad (15)$$

In Eqns. (14) and (15)  $\mu_p, \alpha_p$  for  $p=1, \dots, N$  are material properties and  ${}_v \lambda_i$  for  $i=1, 2, 3$  are the principal stretches or eigenvalues of the elastic left stretch tensor  $\mathbf{V}^e$ , while  ${}_B \lambda_i$  for  $i=1, 2, 3$  denote the eigenvalues of the elastic left Cauchy-Green tensor  $\mathbf{B}^e = \mathbf{F}^{el} \cdot (\mathbf{F}^{el})^T = (\mathbf{V}^e)^2$ . The two tensors can also be expressed in terms of their spectral decomposition

$$\mathbf{B}^e = \sum_{i=1}^3 {}_B \lambda_i \cdot \mathbf{n}_i \otimes \mathbf{n}_i = \mathbf{R} \text{diag} [{}_B \lambda_1 \quad {}_B \lambda_2 \quad {}_B \lambda_3] \mathbf{R}^T, \quad (16)$$

$$\mathbf{V}^e = \sum_{i=1}^3 {}_v \lambda_i \cdot \mathbf{n}_i \otimes \mathbf{n}_i = \mathbf{R} \text{diag} [{}_v \lambda_1 \quad {}_v \lambda_2 \quad {}_v \lambda_3] \mathbf{R}^T, \quad (17)$$

where  ${}_v \lambda_i = \sqrt{{}_B \lambda_i}$  and  $\mathbf{n}_i$  for  $i=1, 2, 3$  are the corresponding unit orthogonal eigenvectors. The rotation tensor then can be expressed in terms of the reference coordinate system triad  $\mathbf{i}, \mathbf{j}, \mathbf{k}$  as



$$\mathbf{R} = \begin{bmatrix} \mathbf{n}_1 \cdot \mathbf{i} & \mathbf{n}_2 \cdot \mathbf{i} & \mathbf{n}_3 \cdot \mathbf{i} \\ \mathbf{n}_1 \cdot \mathbf{j} & \mathbf{n}_2 \cdot \mathbf{j} & \mathbf{n}_3 \cdot \mathbf{j} \\ \mathbf{n}_1 \cdot \mathbf{k} & \mathbf{n}_2 \cdot \mathbf{k} & \mathbf{n}_3 \cdot \mathbf{k} \end{bmatrix} = \begin{bmatrix} n_{11} & n_{12} & n_{13} \\ n_{21} & n_{22} & n_{23} \\ n_{31} & n_{32} & n_{33} \end{bmatrix}, \quad \mathbf{R} \cdot \mathbf{R}^T = \mathbf{R}^T \cdot \mathbf{R} = \mathbf{I}. \quad (18)$$

The components of the principal Kirchhoff stress tensor  $\boldsymbol{\tau}_p = \text{diag}[\tau_1 \quad \tau_2 \quad \tau_3]$  then take the form [13]

$$\tau_i = 2 \cdot \rho_0 \cdot \frac{\partial_B \bar{\Psi}}{\partial_B \lambda_i} \cdot {}_B \lambda_i = \rho_0 \cdot \frac{\partial_V \bar{\Psi}}{\partial_V \lambda_i} \cdot {}_V \lambda_i \quad \text{for } i = 1, 2, 3, \quad (19)$$

while the Kirchhoff stress tensor itself can be calculated by back rotation of the principal stress tensor  $\boldsymbol{\tau}_p$  in the Kirchhoff stress space

$$\boldsymbol{\tau} = \sum_{i=1}^3 \tau_i \cdot \mathbf{n}_i \otimes \mathbf{n}_i = \mathbf{R} \boldsymbol{\tau}_p \mathbf{R}^T. \quad (20)$$

When plastic step takes place in the analysis, the procedure of the Kirchhoff stress tensor calculation presented above has to be extended by the plastic multiplier calculation. Moreover, since the trial stress calculation takes place in the principal Kirchhoff stress space in accordance with Eqn. (19), it is more advantageous to realize the plastic step in the principal stress space too. Then considering the Von-Mises material model with isotropic hardening, the yield surface  ${}^\sigma \Psi$  and the yield surface normal  $\partial^\sigma \Psi / \partial \boldsymbol{\sigma}$  too, will be functions of the principal Cauchy stress tensor expressed by the formulas

$${}^\sigma \Psi^1 = \sigma_{\text{eq}} - \sigma_y(\boldsymbol{\varepsilon}^{pl}) \leq 0, \quad \boldsymbol{\sigma} = \frac{\boldsymbol{\tau}_p}{J} = \frac{\text{diag}[\tau_1 \quad \tau_2 \quad \tau_3]}{J}, \quad J = \det(\mathbf{F}), \quad (21)$$

where

$$\sigma_{\text{eq}} = \sqrt{\frac{3}{2} \boldsymbol{\Sigma} : \boldsymbol{\Sigma}}, \quad \boldsymbol{\Sigma} = \boldsymbol{\sigma} - \frac{1}{3} \text{tr}(\boldsymbol{\sigma}) \cdot \mathbf{I}.$$

The corresponding spatial strain rate tensor  ${}^1 \mathbf{d}^{pl}$  and the accumulated plastic strain  $\boldsymbol{\varepsilon}^{pl}$  then take the forms

$${}^1 \mathbf{d}^{pl} = \dot{\lambda} \cdot \frac{\partial^\sigma \Psi^1}{\partial \boldsymbol{\sigma}} = \text{diag}[d_1^{dp} \quad d_2^{dp} \quad d_3^{dp}], \quad \boldsymbol{\varepsilon}^{pl} = \sqrt{\frac{2}{3} \cdot {}^1 \mathbf{d}^{pl} : {}^1 \mathbf{d}^{pl}} = \dot{\lambda}, \quad (22)$$

which with respect to Eqns. (13) and (20) imply the following final formulas for the spatial gradient  $\partial \dot{\mathbf{u}}^{pl} / \partial \mathbf{x}$  and the material gradient  $\partial \dot{\mathbf{u}}^{pl} / \partial \mathbf{X}$  of the plastic velocity fields

$$\frac{\partial \dot{\mathbf{u}}^{pl}}{\partial \mathbf{x}} = \mathbf{R} \cdot {}^1 \mathbf{d}^{pl} \cdot \mathbf{R}^T = \dot{\lambda} \cdot \mathbf{R} \cdot \frac{\partial^\sigma \Psi^1}{\partial \boldsymbol{\sigma}} \cdot \mathbf{R}^T = \mathbf{R} \cdot \text{diag}[d_1^{dp} \quad d_2^{dp} \quad d_3^{dp}] \cdot \mathbf{R}^T, \quad \frac{\partial \dot{\mathbf{u}}^{pl}}{\partial \mathbf{X}} = \frac{\partial \dot{\mathbf{u}}^{pl}}{\partial \mathbf{x}} \cdot \mathbf{F}. \quad (23)$$



## CONCLUSIONS

In this paper a modified framework for modelling of the plastic flow in hyperelastic material was presented using the first nonlinear continuum mechanical theory of finite deformations of elastoplastic media. An alternative hypoelastic-based plasticity model for the Ogden material with J2 plasticity was developed. Although, the material model is objective and thermodynamically consistent, it still needs to be implemented into a finite element code and verified its results. The resulting flow plasticity theory however does not exhibit any of the disadvantages of multiplicative split based flow plasticity theories, thus it presupposes a better solution to the problem.

## ACKNOWLEDGEMENT

This publication is the result of the project implementation: “Research of friction stir welding (FSW) application as an alternative to melting welding methods” no. 26240220031 supported by the Research & Development Operational Programme and funded by the ERDF. Funding from the VEGA grant 1/0740/16 resources is also greatly appreciated. The authors also would like to express their special thanks for the financial supports of the KEGA 060STU-4/2016 grant.

## REFERENCES

- [1] Hackett, R.M.: *Hyperelasticity Primer*, Springer, N.Y., 2016.
- [2] Ogden, R.W.: *Non-Linear Elastic Deformations*, Chichester, Ellis Horwood, 1984.
- [3] Ogden, R.W.: *Large Deformation Isotropic Elasticity – On the Correlation of Theory and Experiment for Incompressible Rubberlike Solids*, Proc. R. Soc. Lond. A, 326, 565-584, 1972.
- [4] Hencky, H.: *The Elastic Behavior of Vulcanized Rubber*, J. Appl. Mech., 1, 45-53, 1933.
- [5] Green, A.E., Zerna, W.: *Theoretical Elasticity*, Oxford University Press, 1954.
- [6] Yeoh, O.H.: *Characterization of Elastic Properties of Carbon-black-filled rubber vulcanizates*, Rubber Chem. Technol., 63, 792-85, 1990.
- [7] Gent, A.N.: *A New Constitutive Relation for Rubber*, Rubber Chem. Technol., 69, 59-61, 1996.
- [8] Dill, E.H.: *Continuum Mechanics: Elasticity, Plasticity, Viscoelasticity*, CRC, Boca Raton, 2007.
- [9] Bower, A.F.: *Applied Mechanics of Solids*, CRC, Boca Raton, 2010.
- [10] Holzapfel, G.A.: *Nonlinear Solid Mechanics: a Continuum Approach for Engineering*, Wiley, Chichester, 2000.
- [11] Blatz, P.J., Ko, W.L.: *Application of Finite Elasticity to the Deformation of Rubbery Materials*, Trans. Soc. Rheol., 6, 223–251, 1962.
- [12] Arruda, E.M., Boyce, M.C.: *A Three-dimensional Constitutive Model for the Large Stretch Behavior of Rubber Elastic Materials*, J. Mech. Phys. Solids, 41, 389-412, 1993.
- [13] De Souza Neto, E.A., Perić, D., Owen, D.R.J.: *Computational Methods for Plasticity, Theory and Applications*, Wiley, Singapore, 2008.
- [14] Simo, J.C., Hughes, T.J.R.: *Computational Inelasticity*. Springer, New York, 1998.
- [15] Nemat-Nasser, S.: *Plasticity, A Treatise on Finite Deformation of Heterogenous Inelastic Materials*, Cambridge University Press, Cambridge, 2004.



## DIGITAL TWIN AND SHADOW IN SMART PORK FETTENERS

*ERDÉLYI Viktor, JÁNOSI László CSc*

*Institute for Mechanical Engineering Technology, Szent István University*

*E-mail: [erdely.viktor@gmail.com](mailto:erdely.viktor@gmail.com), [janosi.laszlo@gek.szie.hu](mailto:janosi.laszlo@gek.szie.hu)*

### **Abstract**

*This paper introduces our ongoing research in the field of smart livestock farming. The base idea in this research is to take some industry based concepts, and adapt them into agriculture.*

*In Industry we live the fourth industrial revolution, which is not a technical, but an organization revolution. So in this concept there are two key ideas, which are digital twin, and digital shadow.*

*This article is about creating digital twin and digital shadow of a modern pig fattener. These models are based on the literature, and are identified on the data shared in these. However, these models can't be used on real systems before identifying them on the actual circumstances.*

*At this stage of research only digital twin of the product was created, and only some aspects of it. This however can simulate an average porkers feed consumption, weight growth and calculate the weight on certain stages of breeding. Further development is ongoing and our target is to make a fully functional model of a pig fattener.*

**Keywords:** *Industry 4.0, Agriculture, Smart livestock farming, Digital Twin, Digital Shadow*

### **1. INTRODUCTION**

Nowadays, the concept of Industry 4.0 is becoming more and more known. One of I4.0 core elements is modelling, known as *digital twin*, and *digital shadow*. These two are the digital equivalent of not only the production, but the product itself as well. The use of this concept in another production system, such as a pig fattener speaks for itself [2],[4].

This paper shows the so far achieved results of the ongoing research. In the smart livestock farming environment, the Digital Twin would be the digital model of the livestock with all the data from it, and the Digital Shadow is the computer counterpart of the production system itself. These, in the industry can be used to achieve predictive maintenance and predictive control which are advantageously affect the production parameters. So to examine its potential in the smart livestock farming, we have to make computer models both of the pigs, the pig fattening process and its assets.

### **2. METHODS**

As a first step in the research work, a general model of a pig farm will be designed. The model is based on the measured data found in the literature [3] The parameter identification is based on the same data, however to use the models as an aid to design a pig fattener farm, or use it to control an existing one, further identification is needed based on other farms using the same technologies. These models are intended as commonly usable wireframes. Figure 1 illustrates the structure of the currently used farms where typical time-based control is used. Figure 2, conversely, illustrates a solution where control is affected through continuous feedback. Figure 1 illustrates the structure of the currently used farms where typical time-based control is used.

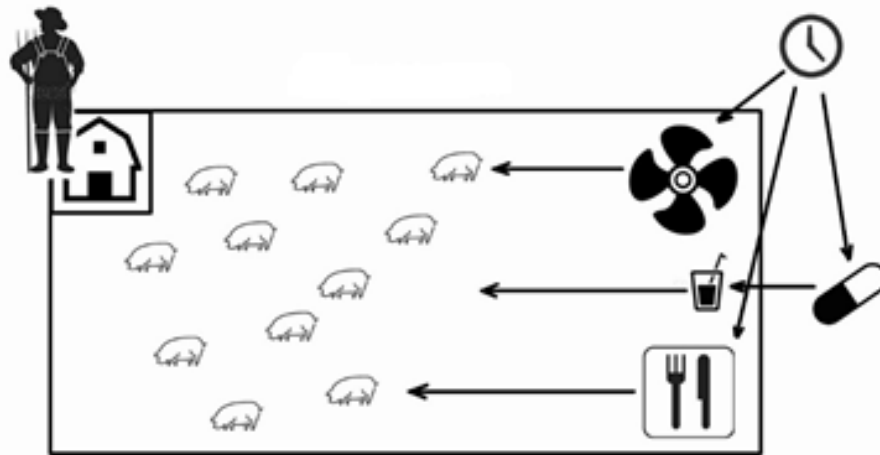


Figure 1 A graphical sketch of the current pig farm model

The model is based on a pig farm of this kind. In these feters, there are only few fully automated systems using closed control loop. The main feedback is the swineherd himself. Therefore, interestingly it is fairly complicated to model this current solution, it would be much easier, if there were no uncertain factors in control like humans. So in the first steps only the modeling of singular subsystems take place, then these will be interlocked with some uncertainty, based on measured data.

Of course, the best solution would be a feedback coupled system, like on Figure 2, where control is affected through continuous feedback. Fortunately, if the sub models are available, this model will be much easier to build.

The second-degree polynomial based on the weight gain data is the following equation:

$$\frac{dm}{dt} = a_m t^2 + b_m t + c_m. \quad (1)$$

The MATLAB *polyfit()* method results the following correlation coefficient:  $R^2=0,99698$ .

The effect of *feeding* is described in the following equation, in which I assumed the simplest case, that only  $c_m$  is concerned, and only linearly (intuition). The equation so prescribed

$$g(t, m) = a_g t^2 + b_g t + c_g m + d_g. \quad (2)$$

Parameter identification is done with the data found in literature.

$$\int_0^{t_{max}} (g_m - g(t, m))^2 dt \Rightarrow \min. \quad (3)$$

The *fminsearch()* method gave us the correlation coefficient of  $R^2=0,99677$ .

Formula (4) serves to determine parameter  $C_m$  in formula (1), which is assumed to be a linear relationship.

$$C_m(t) = a_c g(t, m) + b_c. \quad (4)$$

The relation (5) shows the substitution of equation (4) in formula (1).

$$\frac{dm}{dt} = a_m t^2 + b_m t + a_c g(t, m) + b_c \quad (5)$$



Equation (6) used to determine the coefficients of the so-modified (1) equation so it can be written that,

$$\int_0^{t_{\max}} (m_m - m_c(t))^2 dt \Rightarrow \min \quad (6)$$

The re-running of *fminsearch()* algorithm, shows us that the correlation is improved, numerically to  $R^2=0,99787$ .

*Italics font* expressions indicate the feedback points.

Figure 4. illustrates the solution of these models in Matlab Simulink environment.

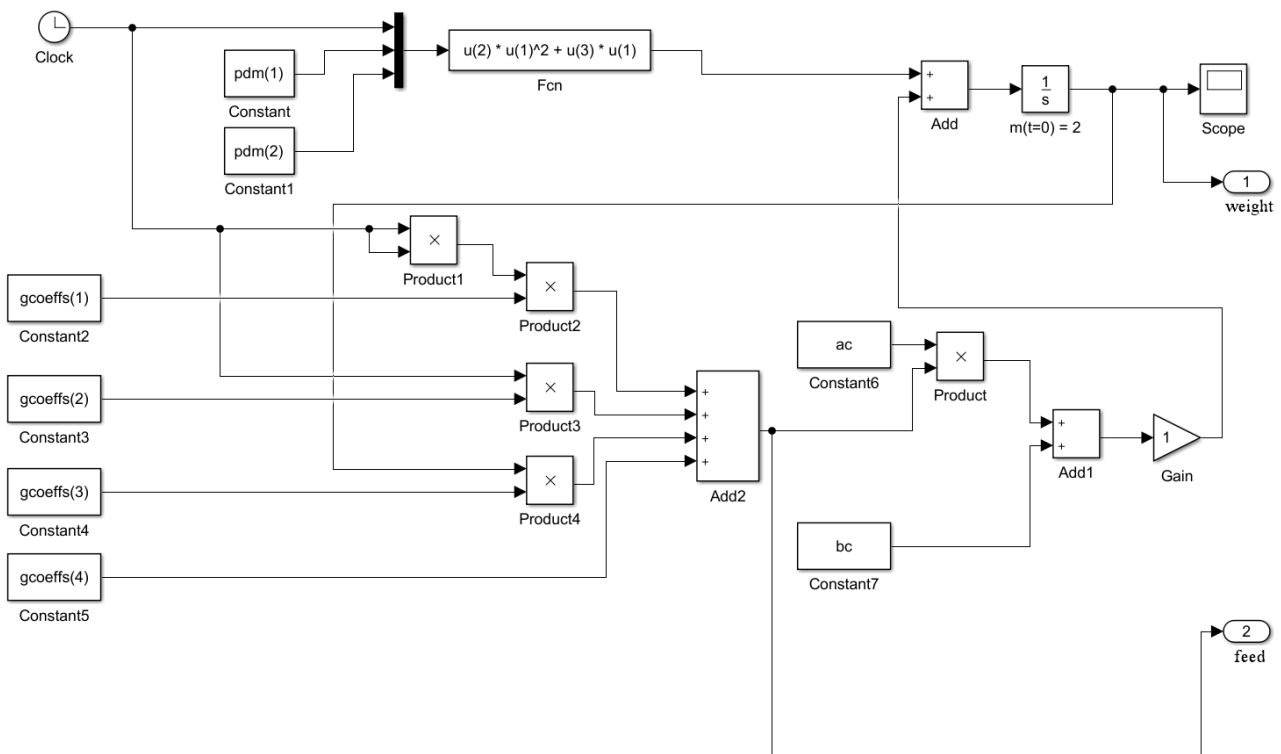


Figure 2 Solution of the porker model in Simulink environment

*Energy balance of pork*

$$c m \frac{dT}{dt} = \eta m_t H(m) - k A (T - T_k) \quad (7)$$

where:

- c - specific heat of pig, J/kg°C
- m - mass of pig, kg
- T - temperature of pig, °C
- t - time, s
- η - nutrient heat utilization efficiency, -
- mt - mass of feed, kg
- H - nutrient energy content, kJ/kg
- k - heat transfer factor, W/m<sup>2</sup>



- A - heat transfer surface of pork, m<sup>2</sup>  
Tk - ambient temperature, °C

According to the correlation (8), the energy content of the feed is dependent on the weight of the pig (ruling, 2003):

$$H(m) = \begin{cases} 14, & \text{if } m < 40 \\ 13.6, & \text{if } 40 \leq m < 70 \\ 13.4, & \text{else} \end{cases}, \frac{\text{MJ}}{\text{kg}} \quad (8)$$

Based on the known density and mass of the pig the volume on an equivalent mass and density sphere could be calculated:

$$V = \frac{m}{\rho} = \frac{4 \cdot r^3 \cdot \pi}{3}, \quad (9)$$

from which the sphere radius is expressed as follows:

$$r = \sqrt[3]{\frac{3m}{4\pi\rho}}, \quad (10)$$

where:

- V - volume of the sphere, m<sup>3</sup>  
r - radius of the sphere, m  
m - mass of the pig, kg  
ρ - density of the pig, kg/m<sup>3</sup>

Thus, the surface of the spherical swine model can be expressed as follows:

$$A = 4r^2\pi, \quad (11)$$

where:

- A - surface of the sphere, m<sup>2</sup>  
r - radius of the sphere, m

Parameters used at calculations:

- k = 4 W/m<sup>2</sup>  
η = 10<sup>-6</sup>  
c = 260 J/kg°C  
Tk = 30 °C  
T(t = 0) = 39.3 °C

### 3. RESULTS

The Digital Twin of the porker is under construction. The so far modelled aspect of it are giving the input parameters back if we run the simulation. On Figure 3 the measured values compared to simulated values to be seen. It is interesting, that the growth of the pig can't be described so accurately with an exponential equation, as with a simple second degree polynomic. One possible



explanation for this is that the pigs aren't held with ad libitum feeding. Further investigation is in progress.

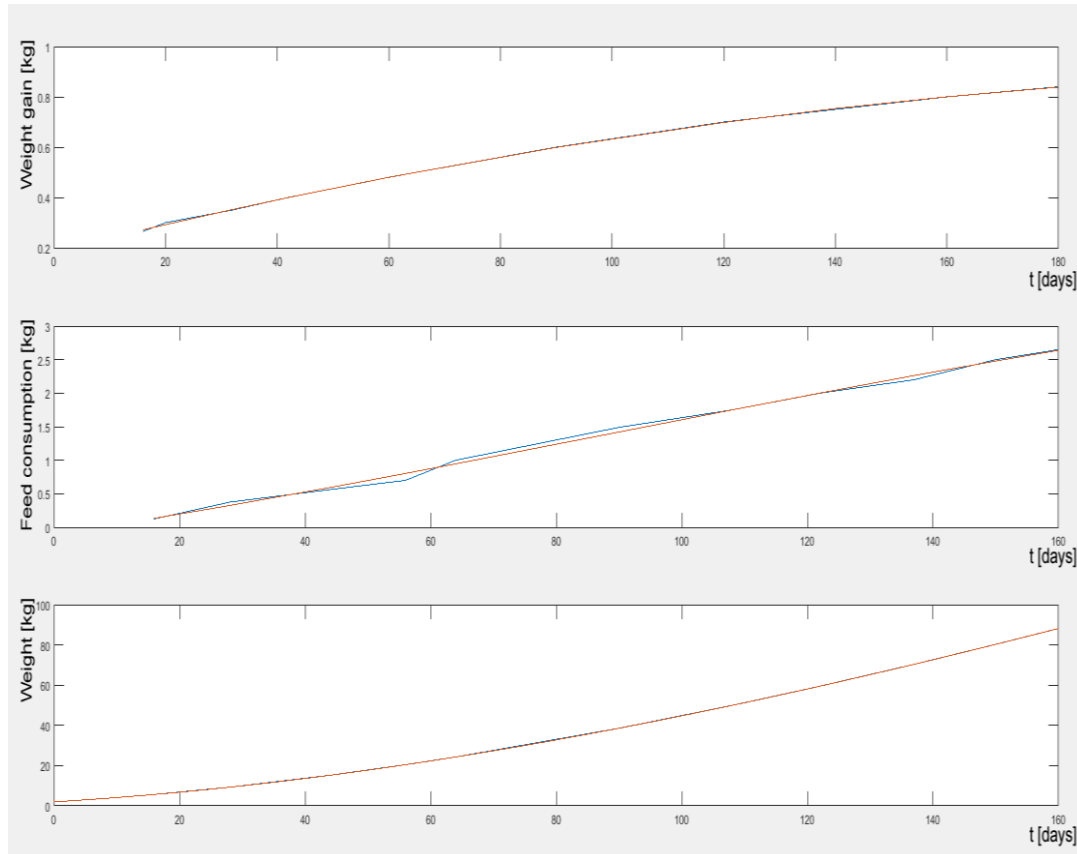


Figure 3 Results of the simulation of the porker model

## CONCLUSIONS

The build of an existing pig fattener farm – model is now ongoing. This model – after identification and validation- will be used to consider the possibilities of the use of an Industry 4.0 grade closed loop control system. Can it be used without a modification, and if the answer is no, then how should I modify the architecture to gain the output parameters.

In my further work, I will search such solutions, where the subsequent sub-processes of livestock farming are interconnected in a larger master system. That can be stated if the consecutive sub-systems are codified, and they can be connected to each other (compatible information contents), then the operation can be optimized in a larger system, and will work more efficiently.

## REFERENCES

- [1] Codex Pabularis Hungaricus (2004.)
- [2] Dieter, W. (2015.) Industrie 4.0 – die Zukunft der digitalen Fabrik, VVD-2015 Verarbeitungsmaschinen und Verpackungstechnik, Radebeul
- [3] Fenyvesi, L., Mátyás, L., Pazsiczki, I. (2004.) Technologies of pig husbandry, Hungarian Institute of Agricultural Engineering, pp. 10-11., Gödöllő, ISBN 963-611-426-9
- [4] Günter, S., Matthias, B., Jan, R., Martin, B. (2016.) Der Digitale Schatten in der Auftragsabwicklung, ZWF Zeitschrift für wirtschaftlichen Fabrikbetrieb: Vol. 111, No. 1-2, pp. 48-51.



## FEASIBILITY OF REMOTE PHOTOPLETHYSMOGRAPHY FOR IMPLEMENTATION IN MOBILE ROBOTS

*FINŽGAR Miha, PODRŽAJ Primož*

*Faculty of Mechanical Engineering, University of Ljubljana*

*E-mail: [miha.finzgar@fs.uni-lj.si](mailto:miha.finzgar@fs.uni-lj.si), [primoz.podrzaj@fs.uni-lj.si](mailto:primoz.podrzaj@fs.uni-lj.si)*

### **Abstract**

*Due to the increasing number of elderly people in their home environments monitoring of their health is of a big importance. The monitoring could be done by using the mobile robots, which can offer not only companionship and assistance, but can also perform various healthcare tasks. An exemplary aforementioned task is a heart rate measurement, which provides basic information about the health status of a human. One of the most promising measuring methods suitable for the implementation in the mobile robots is a contactless method called remote photoplethysmography. There are however numerous challenges that prevent an easy implementation of this method in mobile robots, such as limited computational capability and sensitivity of the remote photoplethysmography to motion artifacts. Therefore we reviewed studies dealing with the challenges and tested one of the state-of-the-art algorithms for rPPG signal extraction on lossy compressed data. Results of the review and our experiment show that feasibility of the remote photoplethysmography for implementation in mobile robots strongly depends on the used algorithm for rPPG signal extraction and degree of video compression.*

**Keywords:** *remote photoplethysmography, image processing, machine vision, mobile robotics*

### **1. INTRODUCTION**

The number of elderly people is increasing in Western societies. In order to ensure high quality of their lives, it is important to monitor their health and offer them early medical diagnosis and prevent complications. One of the basic physiological parameters that offers assessment of health status is heart rate. Golden standard for its measurement is electrocardiography (ECG) and an alternative approach are photoplethysmography-based (PPG-based) devices, such as a pulse oximeter. An important characteristic of the ECG and PPG methods is that a physical contact between skin and a measuring device is needed. Wearing intrusive devices usually causes discomfort, impairs mobility and can affect human's physiological state. Therefore a contactless measuring method would be highly beneficial. Furthermore, an intelligent system, which would first detect a human and then perform heart rate measurement would be even more favourable. A promising solution are mobile robots performing remote photoplethysmographic measurements, which offers extraction of heart rate. An example of such system is shown in *Figure 1*. In this paper feasibility of the implementation of the remote photoplethysmography in mobile robots is assessed.

#### **1.1 Remote photoplethysmography**

Remote photoplethysmography (hereinafter rPPG) is a non-invasive, contactless optical method which detects transmitted or reflected light from the skin. The skin surface-spectral reflectance comprises of two components: interface (specular) reflection and body (diffuse) reflection. Latter is due to scattering and absorption among the coloured scatterers (mainly melanin and haemoglobin)



in the layers below the surface, while former occurs at the interface of the air and skin surface [1]. Diffuse reflection contains a pulsatile component that is varied by the blood volume changes, which are synchronous with cardiac cycle [1]. See *Figure 2* for schematic representation of the interaction between light and skin. rPPG offers estimation of the heart rate [1-3], blood pressure [4], respiratory rate [5], blood oxygen saturation [6] etc. Basic rPPG system consists of a digital camera and dedicated light source. The main advantage of the method is the absence of the physical contact between a measuring device and the skin. This offers more reliable measurements as well as enables its usage in situations in which contact is highly undesirable (neonates, burn victims). The auspiciousness of the method has been increased after it has been shown that method can work without special dedicated lighting, but can use ambient lighting instead [2]. Method offers not only extraction of the physiological parameters, but also living skin detection [7], which is necessary in order to avoid detection of inanimate objects mimicking skin colour and/or appearance.

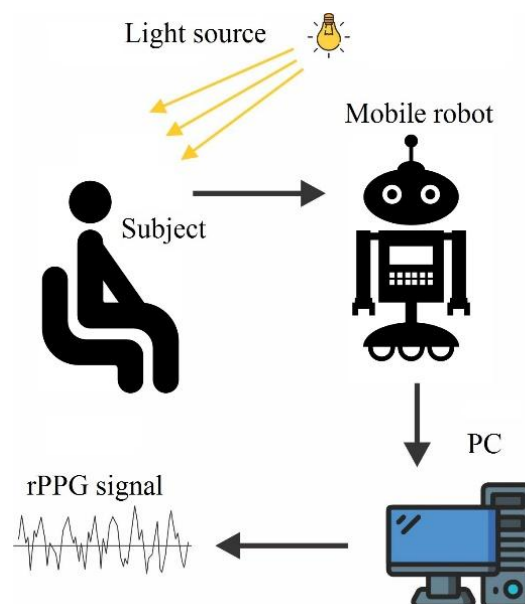


*Figure 1* Schematic representation of rPPG signal acquisition using mobile robot and offline PC

## 2. METHODS

### 2.1 Review of challenges regarding implementation of remote photoplethysmography on mobile robots

#### 2.1.1 Video data compression

Mobile robots have limited computational capability and storage capacity. Since raw, uncompressed RGB videos require a lot of storage it is necessary to introduce data compression or alternative data representation for rPPG signal extraction. Additionally, some software programs limit the maximum size of the input data that can be imported into them. One of the solutions is to store video data in an alternate colour space, e.g. YUV420p that emphasizes the luminance differences over chrominance differences [8]. Each pixel is given a luminance value, while chrominance values are subsampled. Problem of this approach is that chrominance data is the one carrying the pulsatile information [1]. Additionally, it is the spatial averaging of the pixels inside ROI that eliminates quantization noise and enables extraction of minute pulsatile variations [1]. The other solutions include intra-frame compression, which reduces spatial redundancy and inter-frame compression,



which reduces temporal redundancy [8]. An important limitation of dealing with compressed data is that state-of-the-art model-based algorithms may not be used due to the potential loss of pulsatile information and introduction of additional artifacts [9].

McDuff et al. tested the effect of video compression on the extraction of rPPG [8]. The authors studied the impact of video compression on pulse rate estimation from rPPG using blind source separation approach, i.e. independent component analysis (ICA). They reported significant signal-to-noise ratio (SNR) reduction when lossy compressed data was used instead of the raw data. There was a linear relation between increased constant rate factor and consequent bit rate and SNR drop. Bit rate of 10Mb/s offered reasonable SNR with acceptable pulse rate estimation error. Decrease of SNR was faster in videos with more motion artifacts. It was suggested that x265 compression codec is more appropriate than x264 when dealing with videos with a lot of motion artifacts.

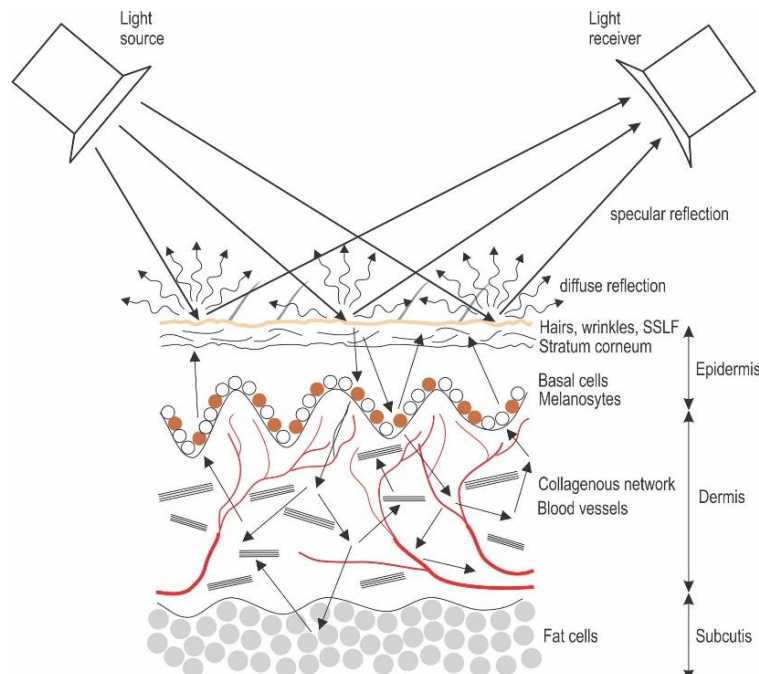


Figure 2 Schematic representation of skin interaction with light. Legend: SSLF – skin surface lipid film. Adopted from [1].

### 2.1.2 Motion artifacts

Robustness to motion artifacts in rPPG applications is a universal rPPG challenge, not specific to implementation of the method in mobile robots and will not be the focus of this paper. In general, the motion artifacts include any motion that influences the relative position between a camera, a subject and a light source. A special type of the motion artifacts are ballistocardiographic artifacts, which cannot be neglected in the non-fitness applications [10]. Motion artifacts that are due to the head movements were studied by Stricker et al., who recorded a benchmark database with different scenarios in 10 different participants [11]. Implementation of rPPG in mobile robots however introduces additional sources of motion artifacts, since digital camera is fixed on a moving object, i.e. mobile robot. It is obvious that video data acquisition should be performed when mobile robot is still, but even then there are some intrinsic sources of motion in terms of vibrations.



## ***2.2 Analysis of feasibility of Sub-band rPPG in combination with Plane-Orthogonal-to-Skin algorithms in rPPG extraction from lossy compressed video***

We believe that data compression is the most important issue, since it increases SNR, worsens performance of state-of-the-art rPPG algorithms for heart rate estimation and is more specific to our rPPG implementation proposal. In order to test this hypothesis we used videos from DEAP Dataset, a dataset for emotion analysis using EEG, physiological and video signals [12]. Dataset includes 60 s long frontal face videos in H.264 format (block-oriented and motion-compensated compression standard). We used 5 videos of 5 participants (2 males and 3 females) and calculated SNR for 3 different rPPG signals. First one was raw rPPG signal extracted from faces of the participants (spatial and temporally normalized signal), the second one was Butterworth filtered rPPG signal (4<sup>th</sup> order, lower cut-off frequency 40 min<sup>-1</sup>, upper cut-off frequency 220 min<sup>-1</sup>) and the third one was rPPG signal extracted with one of the state-of-the-art algorithms (Sub-band rPPG and Plane-Orthogonal-to-Skin [13]). We used modified SNR metric proposed by de Haan and Jeanne [1]. The metric was defined as the ratio of the energy within 5 bins around the fundamental frequency and the remaining energy within the spectrum defined by the expected frequency range of heart rate in humans (40-220 min<sup>-1</sup>). Fundamental frequency was defined based on the reference PPG measurements, which are also part of the dataset.

## **3. RESULTS**

*Figure 3* shows a video frame with displayed region of interest (ROI), which was manually selected. The position of ROI was kept throughout the entire video, since we assumed that there are no significant head motions. Results of the analysis are shown in *Table 1*. It is clear that there are inter-video SNR variations, which might be due to different distances between subjects and camera, camera focus settings and motion artifacts. Butterworth filtering improved SNR, whereas application of state-of-the-art algorithm on raw rPPG signals reduced the ratio, which means that used compression standard introduced artifacts, which prevent the extraction of the rPPG signal with improved SNR using the chosen algorithm.

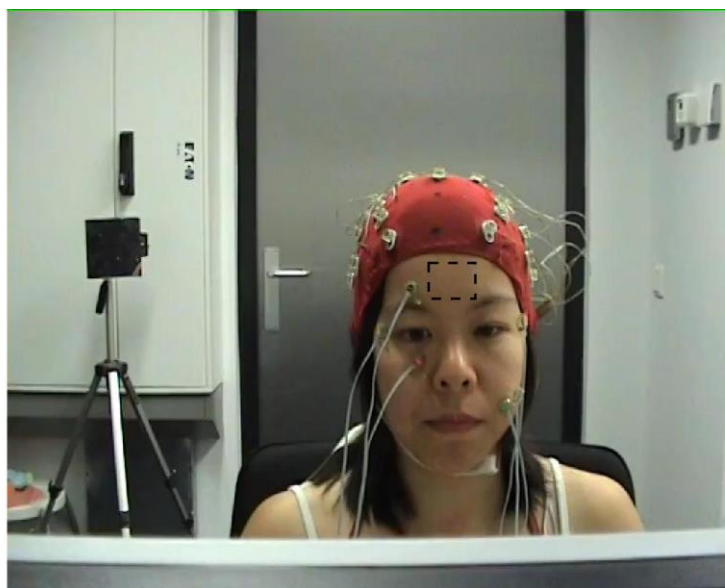


*Figure 3* An example of a video frame with the ROI marked with the dashed line



Table 1 SNR values comparison of different approaches of rPPG signal processing

Participant number/video number	SNR <sub>raw</sub> [dB]	SNR <sub>BF</sub> [dB]	SNR <sub>SB+POS</sub> [dB]
1/1	-4,41	-4,00	-5,71
2/1	-8,48	-8,02	-8,69
3/1	-3,81	-1,74	-5,70
4/1	-4,48	-3,82	-5,34
5/1	-12,65	-11,21	14,11

Legend: SNR<sub>raw</sub> – signal-to-noise-ratio of raw rPPG signal, SNR<sub>BF</sub> – signal-to-noise-ratio of Butterworth filtered rPPG signal, SNR<sub>SB+POS</sub> – signal-to-noise ratio of rPPG signal extracted using Sub-band rPPG (SB) and Plane-Orthogonal-to-Plane (POS) algorithms [13].

## CONCLUSIONS

Literature review and our short analysis show that there are two important issues regarding implementation of rPPG on mobile robots. First one is a universal rPPG challenge – reduction of sensitivity to motion artifacts, whereas the second is data compression issue. Latter suppresses pulsatile component and introduces additional noise, which makes it difficult for the state-of-the-art, model-based rPPG to extract the desired signal with high enough SNR. Our analysis show that the use of the one of the most promising rPPG algorithms does not work with the H.264 compression standard, since SNR of the raw rPPG signal was higher than that of the processed rPPG signal. The main challenge in the implementation of rPPG in mobile robots will be to find the trade-off between the data compression rate, rPPG algorithms' performance and used hardware in mobile robots.

## REFERENCES

- [1] de Haan, G., Jeanne, V.: *Robust pulse rate from chrominance-based rPPG*. IEEE Transactions on Biomedical Engineering, 60(10), 2878-2886. 2013.
- [2] Verkruysse, W., Svaasand, L.O., Nelson, J.S.: *Remote plethysmographic imaging using ambient light*. Optics Express, 16(26), 21434-21445. 2008.
- [3] Poh, M.Z., McDuff, D.J., Picard, R.W.: *Non-contact, automated cardiac pulse measurements using video imaging and blind source separation*. Optics Express, 18(10), 10762-10774. 2010.
- [4] Jeong, I.C., Finkelstein, J.: *Introducing Contactless Blood Pressure Assessment Using a High Speed Video Camera*. Journal of Medical Systems, 40(4), 77. 2016.
- [5] Nam, Y., Lee, J., Chon, K.H.: *Respiratory rate estimation from the built-in cameras of smartphones and tablets*. Annals of Biomedical Engineering, 42(4), 885-898. 2014.
- [6] Guazzi, A.R., Villarroel, M., Jorge, J., Daly, J., Frise, M.C., Robbins, P.A., Tarassenko, L.: *Non-contact measurement of oxygen saturation with an RGB camera*. Biomed Opt Express, 6(9), 3320-3338. 2015.
- [7] Wang, W., Stuijk, S., de Haan, G.: *Living-Skin Classification via Remote-PPG*. IEEE Transactions on Biomedical Engineering, 1-11. 2017.
- [8] McDuff, D.J., Blackford, E.B., Estep, J.R.: *The Impact of Video Compression on Remote Cardiac Pulse Measurement Using Imaging Photoplethysmography*. Automatic Face & Gesture Recognition (FG 2017), 2017 12th IEEE International Conference on, 63-70. 2017.
- [9] Wang, W., Brinker, A.d., Stuijk, S., Haan, G.d.: *Algorithmic Principles of Remote-PPG*. IEEE Transactions on Biomedical Engineering, 64(7), 1479-1491. 2016.



# INTERNATIONAL SCIENTIFIC CONFERENCE ON ADVANCES IN MECHANICAL ENGINEERING

12-14 October 2017, Debrecen, Hungary



- [10] Wang, W., Balmaekers, B., de Haan, G.: *Quality metric for camera-based pulse rate monitoring in fitness exercise*. Image Processing (ICIP), 2016 IEEE International Conference on, 2430-2434. 2016.
- [11] Stricker, R., Müller, S., Gross, H.-M.: *Non-contact video-based pulse rate measurement on a mobile service robot*. Robot and Human Interactive Communication, 2014 RO-MAN: The 23rd IEEE International Symposium on, 1056-1062. 2014.
- [12] Koelstra, S., Muhl, C., Soleymani, M., Lee, J.S., Yazdani, A., Ebrahimi, T., Pun, T., Nijholt, A., Patras, I.: *DEAP: A Database for Emotion Analysis Using Physiological Signals*. IEEE Transactions on Affective Computing, 3(1), 18-31. 2012.
- [13] Wang, W., den Brinker, A.C., Stuijk, S., de Haan, G.: *Robust heart rate from fitness videos*. Physiological Measurement, 38(6), 1023-1044. 2017.



## 3D PRINTED POLYMER SPECIMENS OF FATIGUE TEST EXAMINATION BASED ON DMA TESTS

**FODOR Antal**

*Vehicle Technology Department, Faculty of Engineering and Computer Science, John von Neumann University - GAMF*

*E-mail: [fodor.antal@gamf.kefo.hu](mailto:fodor.antal@gamf.kefo.hu)*

### **Abstract**

*Alongside the using of „technical materials”, the direct 3D printed different plastic also speeded up lately. Accordingly to this, it is often designed parts, which have to sustain extreme stress. The proper definition of material qualities is expensive; despite in every phase of designing, we need it to be done perfectly. In every industrial section, it is important to work with exact material characteristics, especially in fields where strict safety rules have to be kept (in connection with the lifespan) the design of fatigue tests of 3D printed polymer specimens. We planned the examinations on the way to avoid the critical temperature range shown by the DMA examinations' results in the bending point of the inner friction coming up in the local range. This information could be important for the Military to change the busted parts quickly and sound. That is the reason why we designed these examinations in this way, so, it could help for designers in the field of military, in development of security technology and improvement of recovery.*

**Keywords:** *Rapid Prototyping, Fatigue testing, 3D printing plastics, DMTA tests.*

### **1. INTRODUCTION**

Nowadays the break-through of plastic materials is significant, while we know less about its characteristics than we do about metals. Of course technical materials have strength indicators too, for example tensile strength, elongation or Young modulus, but we do not know their resistance against cyclic stresses in a wide range [1]. The fatigue qualities of plastic materials produced by rapid prototyping were not even defined yet or just in small numbers or in special occasions. We performed the planning of tests for injecting moulded, standard technical plastic samples. We will implement these experiences earned this way further on to design the tests for the same sized parts created by rapid prototyping, because of the financial reasons of producing methods to make these examinations. The previous investigation is completed with wide-ranged DMA examinations.

### **2. PLANNING OF THE FATIGUE INVESTIGATION PROCESS**

The essential of fatigue calibration is to invent the fatigue limit for each material. The standard prescribes a minimum of four samples, despite sometimes about 80 – 100 experiments are needed for a proper result. The literature often provides the ratio of measured strength values' (measured under fatigue limit and short-time stress). But an overall confirmed method of the failure of polymers is not worked out yet despite of the metal. The manufacturer companies give advices concerning to their own materials. Research on polymers has to be done with the use of modern, trustworthy and fast equipment's and technologies.

The behaviour of polymers under fatigue stress is greatly different from metals. Under the investigation, the flexibility modulus of steel is not changing, if it stays within the Hook flexibility



range. The damping of metals is smaller compared to polymers, and because of this, the heat of the specimen not increases significantly. In case of metals, the flexibility modulus and the amplitude of stress-changing do not or hardly change by the warming. Plastics have great inner attenuation, but have bad thermal conductivity, so specimens exposed to fatigue stress will increase their heat even under 10 Hz frequencies, and their flexibility modulus is decreasing as well [1]. DMA examinations give - in addition to many other - exact results on specimen's critical temperature which can serious impact on their results of fatigue stress tests (Figure 1).

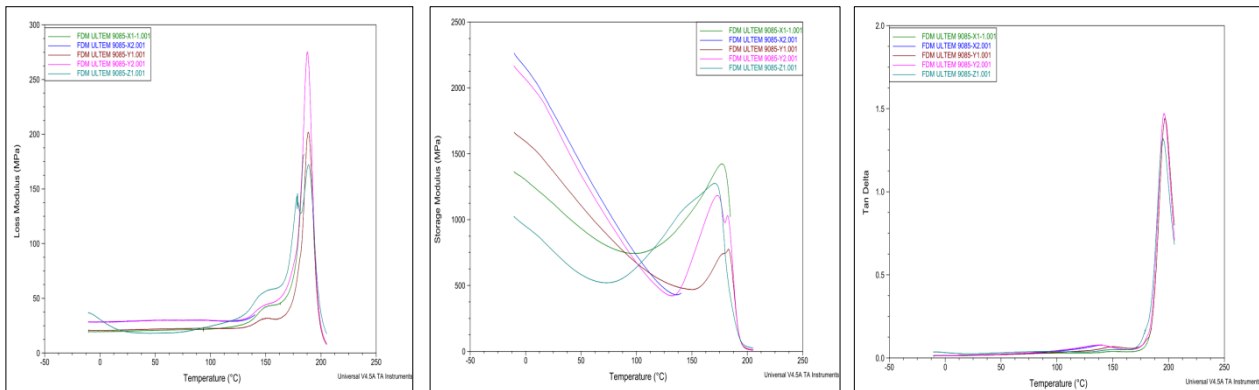


Figure 1 ULTEM 9085 DMA Loss-, Storage Tangens Delta modulus

The characteristics of technical plastics are defined in the specialized literature as a fully flexible and liquid mixture during the Dynamic Mechanical Thermal Analysis (DMTA) [2]. For the fatigue stress test it is very important to define the most essential part of it, the glass transition temperature. Usually the DMA test happens in the glassy status of the material, in which the temperature is increased acutely and progressive measures are taken until the material reaches its rubber condition. When the transition happens, the modulus of pressure and tension changes, which effects its fatigue properties in a measurably way [2, 3]. To define the fatigue limit, we have designed and produced a bender - fatigue equipment, which can examine 40 specimens at the same time. In this, the sample - in the axis, which is perpendicular to the longitudinal axis - is exposed to bending, so that the torque of the plane includes the longitudinal axis of the specimen.

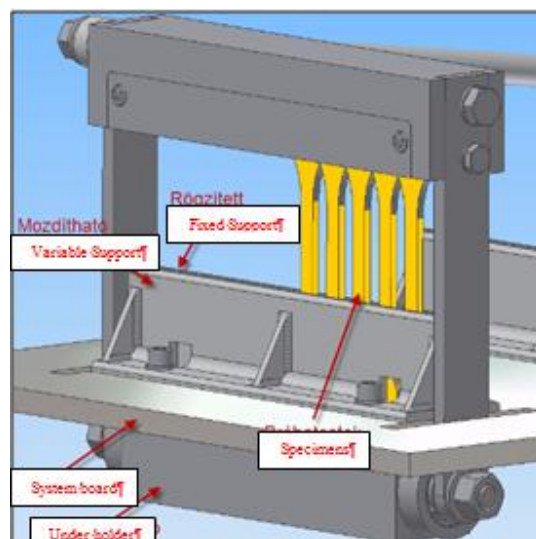


Figure 2 The shaping of holder



The torque loads the specimen in one or both end of it. The Figure 2 shows the shaping of the previously planned and produced forced-motion fatigue equipment, which is just for bending. [3][4] Approximately 55-60 specimens are needed for one of the research. In first step, we have to define the level of the stress. To do it, we stressed 5 - 10 specimens till they break - considered the length of each specimens - with our Instron 3366 tensile strength measuring equipment (Figure 3).

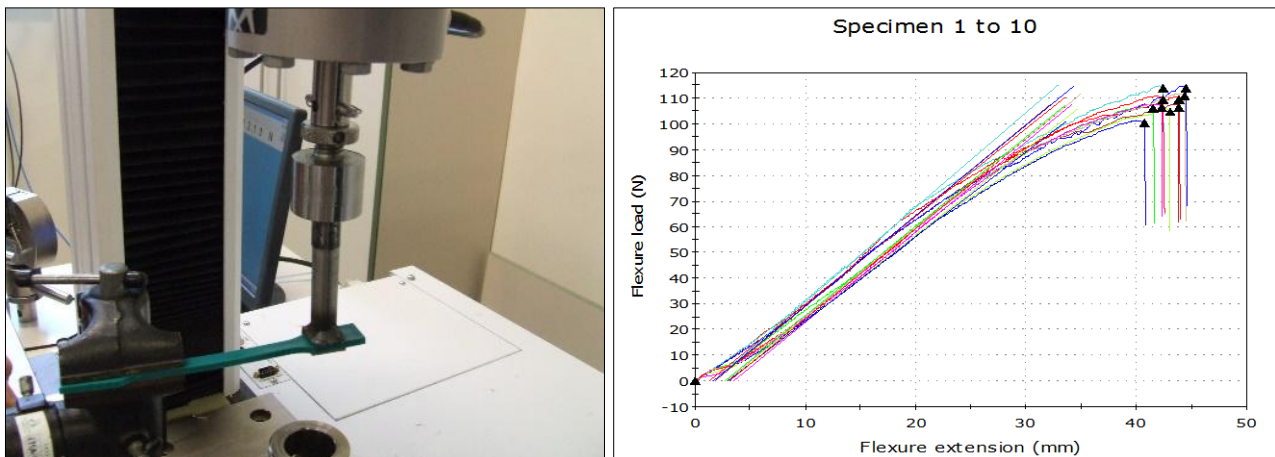


Figure 3 The results of bending experiment in case of PA3WG6 polymer

The 3th Figure shows that the samples broke at about 40 mm bending, approximately at 105 N stress level.

During the preparation of the pilot plan, in the first phase we monitored the warm-up of specimen coming from the inner cushioning and bad heat conduction with FLIR T360 infrared camera. We shot a record about the changing of the temperature. We can see the picture of the initial and the stabilized temperature on Figure 4.

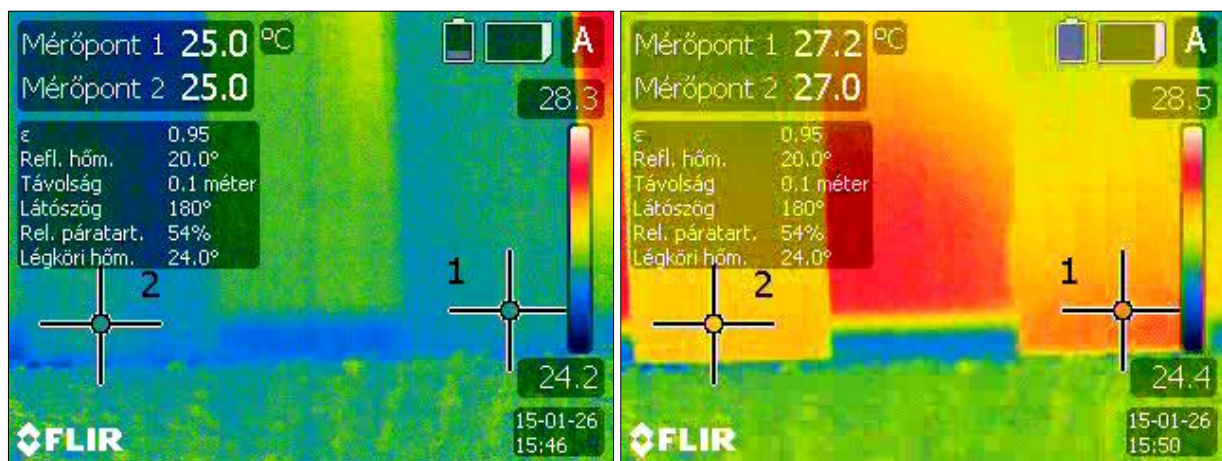


Figure 4 Temperature in the bending point

The heat has stabilized after about 4 minutes, approximately increasing 2°C (shown on Figure 4.) On the base of this has been defined the level of tension of fatigue test. According to our previous consultancies and researches in literature, we decided to choose the failure of 50%, which means the 20% of bending amplitude. This was set up in the eccentric discs put in the driven shaft (Figure 5) [3, 4].

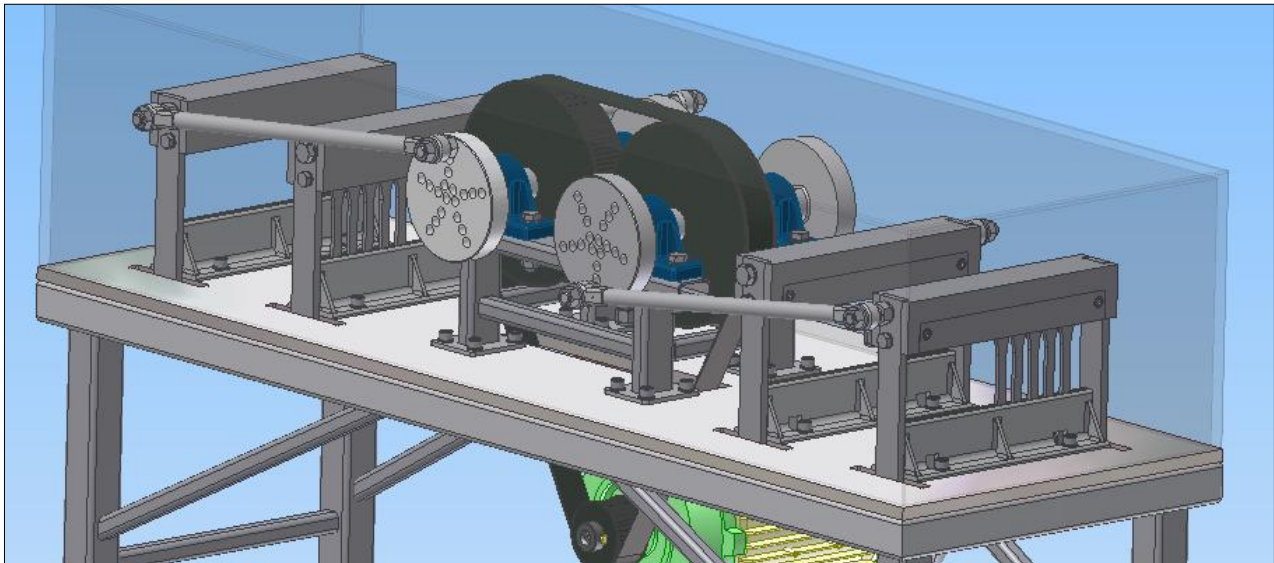


Figure 5 The buildup of bending equipment

We have set the experimental frequency to 2,5Hz. In the clamping head we placed 4x10 specimens. We performed the exhaustion, in four phases. We have stressed the samples with 1000 cycles in the first, 10.000 cycles in the second, 100.000 cycles in the third, and 1.000.000 cycles in the fourth phase.[3]

### 3. THE RESULTS

The whole experiment lasted for more than seven days. After each cycle, the equipment stopped based on the signal of its own counter. Once it stops, we could take out the stressed experimental samples.

The cycle number can be calculated in connection with the elapsed time, as we know the experimental frequency. According to this, after around 600 cycles the heat at the bending point will be stabilized.

Table 1: The results of the fatigue test

Number of load cycles	Tensile extension at Break (Standard) (mm)	Load at Break (Standard) (N)
0	5,3	3508,48
1.000	5,28	3377,83
10.000	4,66	3310,18
100.000	4,35	3289,88
1.000.000	2,67	2382,33

After performing the whole experimental series, according to the non-stressed, and the stress levels for each exhaustion cycles, we have axially tensioned them till they broke. In the first column of the 1st table above we show the exhaustion cycle number, in the second the tensile extension at break, and in the third the loads at break.



#### **4. SUMMARY**

For polymers, fatigue limit can't be defined as it can be for metals. Experiments are usually done till 10<sup>6</sup> cycle number. To do this or any other load cycle numbers, given experimental frequency, environmental temperature, moisture content and stress factor probability are given as an exhausting limit. Literatures often give the ratio of fatigue limit and the strength value measured during short tests. Despite of metals, in case of polymers, there isn't any method done on failure of them.[5][6] The manufacturer companies give advices to their own materials.

Because of the above mentioned facts, the available time and financial reasons we have performed the experiment with PA3WG6 technical plastic specimens. Defining the tendency of exhaustion limit, in a different way than usually, we did not perform the investigation in each stress level till break, but in the chosen stress level, after each cycle number we implemented tensile tests in the specimens.

With experiences earned within the experiments, we made the following conclusions.

The chosen stress level (amplitude) was proved to be too high. At the highest cycle number, 90% of the specimens broke, while the not-fully-destroyed pieces' stress levels did not decrease decently. The explanation of this phenomenon is that the existing PA3WG6 material specimen contains 30% glass fiber, so the fiber's destruction limit defined the maximal tensile force. The tensile elongation decreased significantly. The reason of this can be the exhaustion of the Polyamid matrix material. The tensile elongation decreased significantly. The reason of this can be the exhaustion of the Polyamid matrix material.

The material of chosen specimen is greatly different from the characteristics of materials produced by rapid prototyping. On the base of this, it can be declared, that this was not a lucky choice. In the second phase of the experiment, we will try the whole test series with lower stress level, and a material that does not have fiber reinforcements in it. Despite the results, it is proved that the process has been thought correctly, because the tendency of destruction limit has been reducing as we changed the stress levels.

#### **REFERENCES**

- [1] M.De Monte, E.Moosbrugger, K. Jaschek, M. Quaresimin: MultiaxialFatigue of a shortglassfibrereinforcedpolyamide 6.6 – Fatigue and fracturebehaviour, International Journal of Fatigue 32. 2010 pp.: 17-28.
- [2] Czvikovszky Tibor, Nagy Péter, Gaál János: A polimertechnika alapjai [www.tankonyvtar.hu/hu/tartalom/tkt/polimertechnika-alapjai/ch03s02.html](http://www.tankonyvtar.hu/hu/tartalom/tkt/polimertechnika-alapjai/ch03s02.html) 2017.08.22.
- [3] Antal Fodor, Dr. Pal Boza, Designing Fatigue Experiment for Investigating Polymer Specimens, De Gruyter Open MACRo 2015- 5th International Conference on Recent Achievements in Mechatronics, Automation, Computer Science and Robotics pp.: 269-274
- [4] Antal Fodor, Dr. Pal Boza, Development of endurance testing machine for the investigation of repeating use of polymer specimen, pp.: 243-249 AGTEDU 2010.
- [5] Antal Fodor, Dr. Pal Boza, Examination of snap joints using finite element method, AGTEDU 2009, pp.: 287-291,.
- [6] Antal Fodor, Dr. Pal Boza, The examination of non-linear behaviour of pieces used in extreme circumstances in condition of time using finite element method, OGÉT 2009 pp.:68-73.



## HIGH ENTROPY ALLOYS IN GEOTHERMAL ENVIRONMENT

<sup>1</sup>GEAMBAZU Elena Laura, <sup>1</sup>MANEA Ciprian Alexandru, <sup>1</sup>CSAKI Ioana PhD, <sup>2</sup>KARLSDÓTTIR Sigrún Nanna PhD

<sup>1</sup>University Politehnica of Bucharest

E-mail: [laura.geambazu@gmail.com](mailto:laura.geambazu@gmail.com)

<sup>2</sup>University of Iceland

E-mail: [snk@hi.is](mailto:snk@hi.is)

### Abstract

*This study aims to follow the geothermal environment corrosive effect influencing the high entropy alloys structure. A high entropy alloy with an improved hardness value and corrosive resistance suitable for the use in geothermal environment was developed. Geothermal steam, mainly composed of H<sub>2</sub>S and CO<sub>2</sub>, represents the main factor of the corrosion that occurs, other factors being erosion, abrasion and humidity. Our study revealed that high entropy alloy could be an option for improving the life of a component working in geothermal steam. The material was investigated visually and using an optical microscope to observe the deposited layer after exposure in geothermal steam. The main idea of this study is to describe the method used for producing the high entropy analysis and the corrosion results revealed a high corrosion rate for Al – high entropy alloy.*

**Keywords:** *high entropy alloys, geothermal, corrosive resistance*

### 1. INTRODUCTION

Corrosive resistant materials in the geothermal environment represent an important matter in the geothermal field. The purpose of the paper is to find the most suitable alloy that is intended to be used in geothermal environment, mainly to cover the surfaces of the geothermal installations components (turbine blades, rotors, etc.). For this matter, high entropy alloys had been taken into consideration, because of their tailored properties. High-entropy alloys (HEAs) are substances that are constructed with equivalent quantities of five or more metals. These alloys are currently the focus of significant attention in materials science and engineering because they have potentially desirable properties. [1]

The multi-principal element character of HEAs causes important properties and effects which are appropriate in the geothermal field use.

For this experiment, the samples were tested in Rreykjanesbær Power Plant, Reykjavik, Iceland, in the most active geothermal area and high temperatures from Iceland. [2] The current turbine blades are manufactured from stainless steel 630, but they are subjected to intense corrosion due to aggressive geothermal environment. [5-6]



Figure 1 Current working turbine



Figure 2 Corrosion affected blade



In order to have the required properties, the obtaining method represents an important factor that should be taken in consideration. According to literature, there are several methods tested, that have results when working with high entropy alloys. Vacuum Arc Remelting (VAR) represents the most viable solution in this case. [3, 4, 9]

For this experiment the high entropy alloys tested were CoCrFeNiMo and AlCrFeNiMn, alloys with an equiatomic composition.

## 2. METHODS

The samples were produced using the liquid-phase method – arc melting. We used disk shaped copper cast for our samples, with a melting electrical current of 600 Amps.

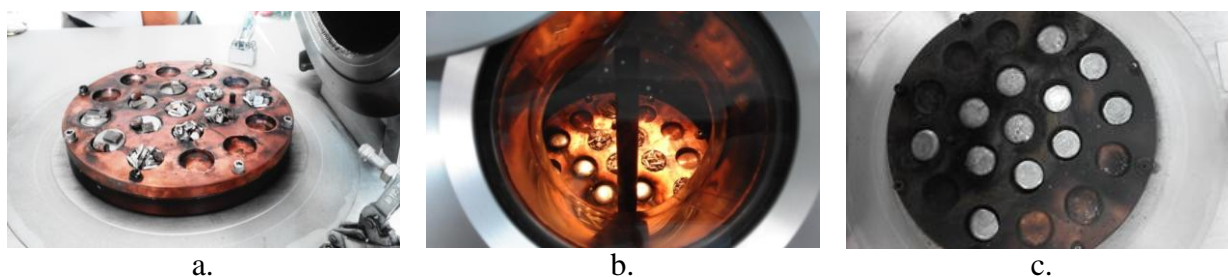


Figure 3 a. Before, b. during and c. after melting the materials in the furnace

On the surface can be seen inhomogeneity due to the obtaining method and after the electronic microscopy analyses the results shown a homogeneous structure.

The samples used for the geothermal corrosion test were prepared in accordance with ASTM\_G4\_Conduction corrosion tests in field applications at Innovation Center Iceland - Nýsköpunarmiðstöð Íslands, Reykjavik, Iceland.

The corrosion testing was done at Reykjanesbær Power Plant, a high temperature geothermal field in Iceland. A test chamber was prepared for the corrosion testing. The chamber pressure used was 1.65 MPa at a temperature of approx. 200°C. The chamber was connected to throttled steam, flowing in the exhaust pipe from the well.

The gas content of the steam from the inlet of turbine 2 (M20257) 2012-2014 is shown in table 1, also shown are the results for a sample from August 2008, in which all major gases were analyzed.

Table 1 Gas content of geothermal steam

Date	Sample No.	CO <sub>2</sub> (mg/kg)	H <sub>2</sub> S (mg/kg)	H <sub>2</sub> (mg/kg)	N <sub>2</sub> (mg/kg)	O <sub>2</sub> (mg/kg)	Ar (mg/kg)	CH <sub>4</sub> (mg/kg)	Total gas (mass-%)
17.10.2014*	20140362	6330	190	-	-	-	-	-	0.65
05.08.2008	20080323	5795	225	2.11	67.7	<0.01	1.71	0.45	0.61

\*the measurements are made every 6 years.[6-8]

The samples were kept in the testing chamber for a 30 days period, in order to obtain significant results for our study. At the end of the period, the samples exposed, were macro analyzed for the first results (figure 4, figure 5).



Figure 4. AlCrFeNiMn samples after exposure

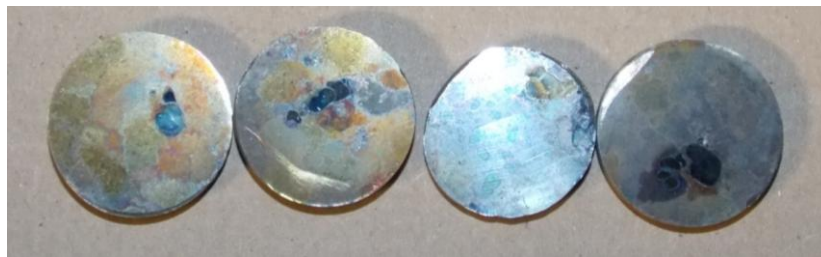


Figure 5 CoCrFeNiMo samples after exposure

The cleaning process was in accordance with ASTM\_G4\_Conduction corrosion tests.



Figure 6 a. AlCrFeNiMn before mechanical and chemical cleaning  
b. AlCrFeNiMn after mechanical and chemical cleaning

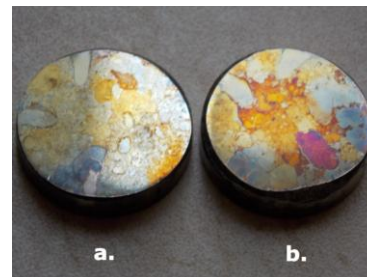
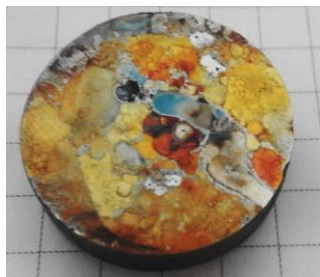


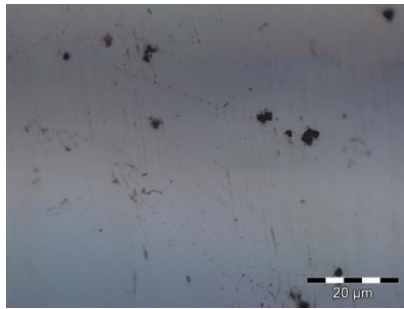
Figure 7 a. CoCrFeNiMo before mechanical and chemical cleaning; b. CoCrFeNiMo after mechanical and chemical cleaning

### 3. RESULTS

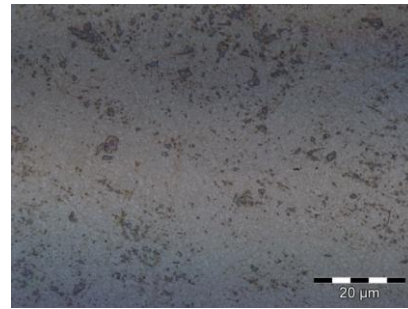
After the exposure in the geothermal steam, on the surface of both types of alloys, a deposited layer can be observed. For AlCrFeNiMn, a thick dark grey layer can be observed and after the mechanical and chemical cleaning, a mass loss of approximately 25%.

For CoCrFeNiMo alloy, on the surface can be observed a thin white deposited layer due to the geothermal steam but also an oxide layer. The structure was not affected by the corrosion and after the mechanical and chemical cleaning, a mass loss of approximately 0.00233%.

The obtained optical microscopy images are presented in figure 8.



a.



b.

Figure 8. Optical microstructure after exposure and cleaning of a. CoCrFeNiMo and b. AlCrFeNiMn

## CONCLUSIONS

After the corrosion process, macroscopic deposition layers could be seen on both types of high entropy alloys. CoCrFeNiMo samples had a low corrosion rate compared with AlCrFeNiMn samples. Taking in consideration the results, CoCrFeNiMo could represent a possible solution to be used in the geothermal environment.

Further research will be taken in consideration in order to improve the performance of CoCrFeNiMo high entropy alloy, but also obtaining this material through other more economical methods.

## ACKNOWLEDGMENTS

Research Grants 6 SEE/ 2016 EEA Grants Small Bilateral Projects;  
CNFIS-FDI-2017-0087

## REFERENCES

- [1] Tsai, Ming-Hung; Yeh, Jien-Wei, *High-Entropy Alloys: A Critical Review*, Materials Research Letters. 2 (3): 107–123. doi:10.1080/21663831.2014.912690, 2014
- [2] Kamal S., Jayaganthan R., Prakash S., *Evaluation of cyclic hot corrosion behaviour of detonation gun sprayed Cr<sub>3</sub>C<sub>2</sub>-25%NiCr coatings on nickel- and iron-based superalloys*, Surface and Coatings Technology, Volume 203, Issue 8, Pages 1004-1013, 15 January 2009
- [3] Sathiaraj G. Dan, Bhattacharjee P.P., *Analysis of microstructure and microtexture during grain growth in low stacking fault energy equiatomic CoCrFeMnNi high entropy and Ni-60 wt%. Co alloys*, Journal of Alloys and Compounds, Volume 637, Pages 267–276, July 2015,
- [4] Clay A., Tansley G.D., *Exploration of a simple, low cost, micro gas turbine recuperator solution for a domestic combined heat and power unit*, Applied Thermal Engineering, Volume 31, Issues 14–15, Pages 2676-2684, October 2011
- [5] Bolellia G., Bergerb L-M., Börnerab T., Koivuluotoc H., Lusvarghia L., Lyphoutd C., Markocsand N., Matikainenc V., Nylénd P., Sassatelli P., Trache R., Vuoristoc P., *Tribology of HVOF- and HVAF-sprayed WC-10Co4Cr hardmetal coatings: A comparative assessment*, Surface and Coatings Technology, Volume 265, Pages 125-144, 15 March 2015
- [6] Karlsdottir SN, Ragnarsdottir KR, Thorbjornsson IO, Einarsson A, *Corrosion testing in superheated geothermal steam in Iceland*, Geothermics, Vol.53, 281-290, 2015
- [7] Buzăianu A., Moțoiu P., Csaki I., Popescu G., Ragnarstottir K., Guðlaugsson S., Guðmundsson D., Arnbjornsson A., *Experiments on life cycle extensions of geothermal turbines by multi*



# INTERNATIONAL SCIENTIFIC CONFERENCE ON ADVANCES IN MECHANICAL ENGINEERING

12-14 October 2017, Debrecen, Hungary



*composite technology*, Geothermics, Volume 57, Pages 1-7, September 2015

- [8] Karlsdottir S.N., Ragnarsdottir K.R., Moller A., Thorbjornsson I.O., Einarsson A., *On-site erosion–corrosion testing in superheated geothermal steam*, Geothermics, Volume 51, Pages 170-181, July 2014
- [9] Pickering E.J., Muñoz-Moreno R., Stone H.J., Jones N.G. , *Precipitation in the equiatomic high-entropy alloy CrMnFeCoNi*, Scripta Materialia Volume 113, Pages 106–109, March 2016



## INTRODUCTION OF WATER MANAGEMENT IN FOOD PRODUCTION PLANT: A CASE STUDY MARGARINE PRODUCTION FACILITY

*GORDIĆ Dušan PhD, VUKAŠINOVIĆ Vladimir PhD, ALEKSIĆ Aleksandar, NEŠOVIĆ Aleksandar*

*Faculty of Engineering, University of Kragujevac*

*E-mail: [gordic@kg.ac.rs](mailto:gordic@kg.ac.rs), [vladimir.vukasinovic@kg.ac.rs](mailto:vladimir.vukasinovic@kg.ac.rs), [a.aleksic@hotmail.com](mailto:a.aleksic@hotmail.com),  
[aca.nesovic@gmail.com](mailto:aca.nesovic@gmail.com)*

### **Abstract**

*The food processing industry consumes relatively high volumes of water for different purposes (production, cleaning, heating and cooling). Beside, wastewater discharged from the production process has high organic load. The industry has huge potential for water conservation and reuse if audited properly.*

*This paper presents the results of water consumption auditing and identifying water consumption centres in a margarine production line in Serbia. Based on the results of the auditing and performed technological and economic feasibility studies, several measures related to reducing water consumption and increasing water reuse in production process were proposed, implemented and valuated. Implemented the measures the company significantly reduced specific water consumption (from 2.71 m<sup>3</sup>/t of produced margarine to 0.71 m<sup>3</sup>/t of produced margarine in two-year period). The study shows that water management activities (as a comprehensive and systematic approach for reducing water consumption, increasing water reuse and reducing wastewater creation) are environmentally and economically feasible in a margarine production company.*

**Keywords:** *margarine production, water consumption centres, specific water consumption, water conservation and reuse*

### **1. INTRODUCTION**

The perception of water being a never-ending and cheap resource with unlimited renewable capacity belongs to previous times and water conservation measures should be prioritized in all sectors (households, industry, agriculture, energy, public water supply). The world is facing the on-going risk of water shortages, particularly given the uncertain impacts of climate change.

Globally, industry uses approximately 20% of the freshwater extracted by humans, around twice as much as is used for household purposes [1]. Water is vital to many manufacturing processes, therefore its efficient use should be a priority in order to ensure that water shortage and increasing price of water have minimal effects on production. The economic reasons as well as environmental issues have led to reduction of water consumption during the past years.

Food processing systems consume extensive amounts of water since water has been traditionally a key processing medium throughout all steps in the food process as an ingredient and as a process aid (cleaning, heating and cooling). As a result of the need to use water in these processes, large volumes of wastewater are generated.

Cost of water used in food processing is the sum of costs of supply, disposal, loss of potential revenue from product discharged and the energy with the discharged effluent. Food processors may follow several strategies in order to reduce fresh water consumption and wastewater [6-10].



Margarine production basically involves the preparation of oil phase and water phase which are carefully mixed through proportionating systems (*Figure 1*). The resultant mixture is passed through a pasteurizer and then through chilling unit, where it is cooled to bring about emulsification and crystallization. Chilling unit is cooled by a separate ammonia cooling system.

In margarine production water is used as a raw material (part of the final product), but it is used for various processes and sub processes also: different heating and cooling processes, cleaning and cleaning-in-place (CIP) processes.

It should be also emphasized that wastewater discharged from the production process has high organic load. As a result, rivers with low water flows and ground-waters are dangerously polluted exceeding the values of parameters from water quality standards.

Beside, impact of warm waste water on the environment in terms of thermal pollution which is the degradation of water quality is also important. When water used as a coolant is returned to the natural environment at a higher temperature, the change in temperature decreases oxygen supply and affects ecosystem composition.

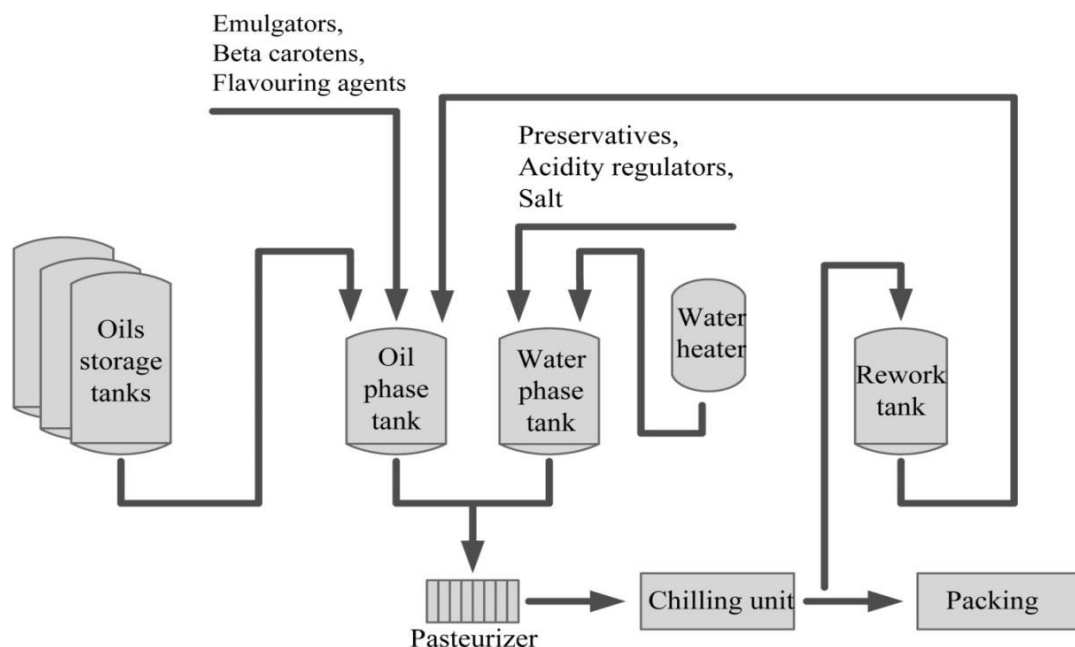


*Figure 1* Margarine production process

Analysed margarine production line facility in Serbia had a problem of increased water consumption that influenced increased production costs. Therefore, it was decided to initiate a project of introducing a water management practice in the factory in order to reduce total costs of margarine production. As a rule, making decisions about water management within companies is clearly dictated by costs associated to water supply and effluent discharge [14]. In order to be effective, water management must examine not only theoretical optimisation values, but also investigate practical, behavioural and communication issues [15]. Results of project development are presented in this paper.

## 2. METHODS

The first step in establishing the system of water management practice in a company is water consumption auditing. Water auditing is an analytical tool which quantifies water flows and quality within a predefined boundary [1]. The water consumption auditing starts with collecting and



analysis of information and data from processes. Data includes: lay-out of processes, water distribution system, sewage and drainage collecting system, equipment specifications, bills for water consumption and waste water disposal from previous period (at least one year), production volume from the period, readings of measuring equipment, etc. [11]

As a result of auditing, performance indicator of company's water consumption – specific water consumption (water consumption in  $\text{m}^3$  per ton of produced margarine) is determined. Whenever it is possible, determined specific water consumption should be compared with the specific water consumption of “similar” companies (same industry, similar production program, similar production volume).

The water management auditing also considers defining a water consumption centre (WCC). Each WCC represent different operating segment (plant, department, group of equipment or single equipment) in which important activities are performed with significant water consumption [7].

Based on readings of existing/portable measuring instruments and bills for water consumption water demand of each WCC is calculated. Consumption is to be prioritized by classification of consumed water quantities using the ABC curve concept where it is graphically possible to identify the highest water consumers. The ABC curve concept aims to sort items according to their relative importance [11]. Usually, this curve is split into three parts: “A”, “B” and “C”. “A” represents the most important items which require special attention, “B” is the intermediate group and “C” indicates the group with less importance.

Analysing collected data, the major locations and activities that correspond to the increased water consumption in the production process are identified. Depending on the results of monitoring adequate corrective and preventive actions are undertaken.

### 3. RESULTS

Analysing the data of water consumption for the base year (2014.), it was calculated that the water consumption in the company was  $14367 \text{ m}^3$ . Since annual margarine production was 5309 tonnes, specific water consumption was  $2.71 \text{ m}^3/\text{t}$  of produced margarine, which is significantly higher than the values from other branch companies in other European countries (*Table 1*).

*Table 1* Specific water consumption of some branch margarine producing companies

	<b>Spain</b>	<b>Belgium</b>	<b>Hungary</b>	<b>Romania</b>
Specific water consumption ( $\text{m}^3/\text{t}$ of produced margarine)	0.77÷0.82	0.84÷1.18	0.97÷1.05	0.87÷0.95

Ref: Data obtained from personal communication with plant managers of branch margarine producing companies

Therefore, the company management initiated an action to explore ways on how to reduce the water consumption to the level of other branch margarine producing companies. It was decided that for the activities only very limited budget was available i.e. the emphasis should be given on good housekeeping measures and improved maintenance of existing equipment.

Analysing available distribution network diagrams and measuring water consumption in the process, WCCs were mapped and marked. Different centres were designated based on type and temperature of water (*Figure 2*). Measured or calculated value of daily water demand of each WCC is presented in *Table 2*.



Table 2 Water demand of each WCC

WCC	WCC No	Water demand (m3/day)	Percentage
Cooling system	WCC2	21.75	46.93%
Pasteurization process	WCC1	9.63	20.78%
Cleaning	WCC4	5.21	11.24%
Raw water	WCC1	3.78	8.16%
Steam production	WCC5	3.75	8.09%
Hot water production	WCC3	2.23	4.81%

ABC curve (Figure 3) was created using the value of water consumption of each WCC. The major locations and activities that correspond to the highest water consumption in the process were identified. Three WCCs (cooling system, pasteurization process, cleaning) which consumption corresponded to almost 80% of total water consumption were in “A” range.

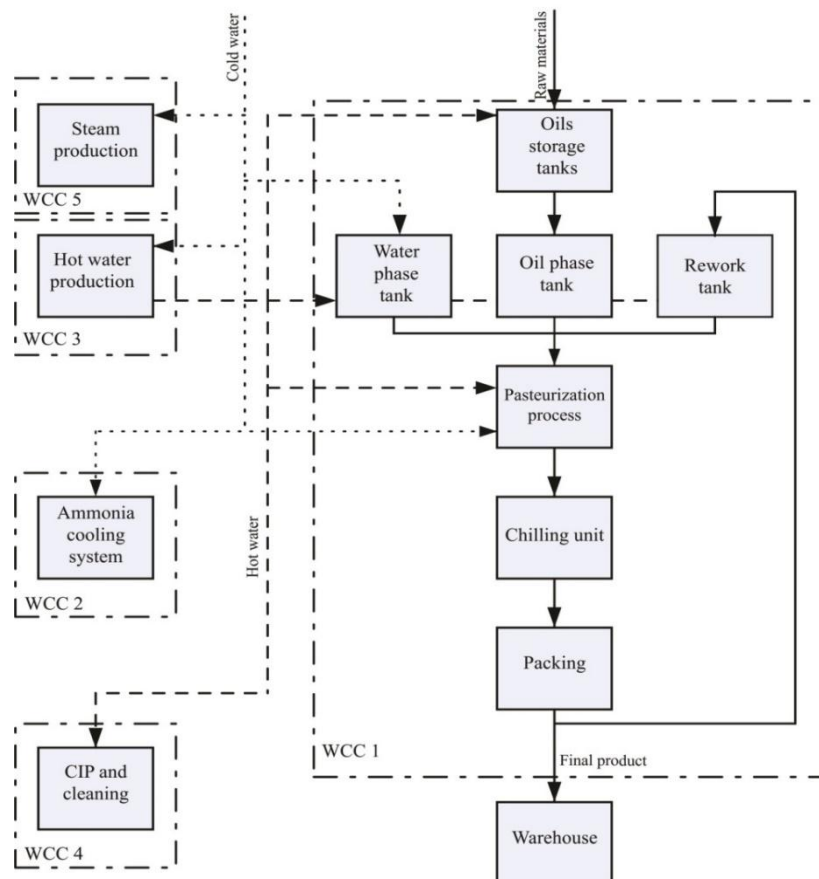


Figure 2 Water consumption centres (WCCs) in analysed margarine production

Since the biggest consumption was in cooling system, the first priority was given to cooling tower performance analysis. As a result of control and inspection of the cooling tower, it was established that it had been in a very poor condition as a result of poor maintenance. Therefore, the efficiency of the cooling tower was greatly reduced and the water consumption was significantly higher. The absence of any chemicals addition in make-up water led to the increase in precipitation and scale formation which also significantly undermined the efficiency of the system.

General overhauling of the cooling tower considered detailed cleaning and the installation of chemical dosing unit for the control of scale build-up and corrosion. The overhauled cooling tower



became operative at the beginning of 2015. Water consumption in the company was 9249 m<sup>3</sup> and margarine production was 4885 ton in 2015. It can be seen that while margarine production was decreased for 8%, water consumption decreased for 35.6% in 2015. In this way, specific water consumption was reduced from 2.71 m<sup>3</sup>/t to 1.89 m<sup>3</sup>/t of produced margarine which was remarkable result, but still above the targeted values presented in *Table 1*.

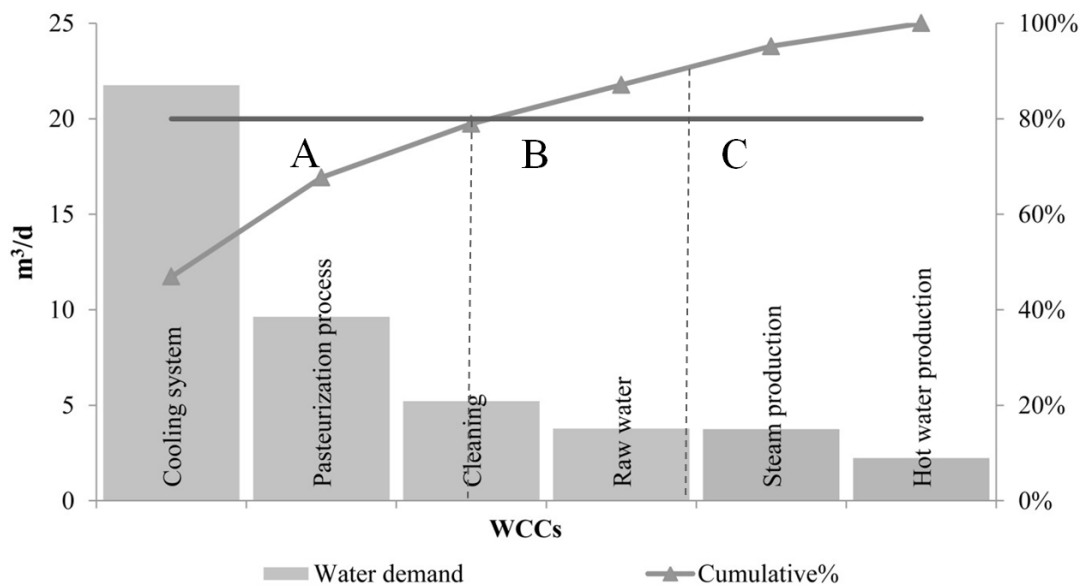


Figure 3 ABC curve - Water demand of WCCs

Since it was noticed that the water consumption for cooling processes is still significant, analysis was related to other possibilities of reducing water consumption in cooling processes. The main reason for such a high volume of water consumption is the fact that tap water used for ammonia compressor cooling was disposed after the cooling process to sewage as waste water. Therefore it was proposed to use conventional water cooling network with parallel configuration according to principles described in [13].

In the parallel configuration, make up cooling water is directly supplied to the pasteurizer and the compressor cooler as individual heat-exchangers. The hot cooling water from both heat exchangers is collected afterward in appropriate tank. Water is returned from the tank to the cooling tower (*Figure 4*).

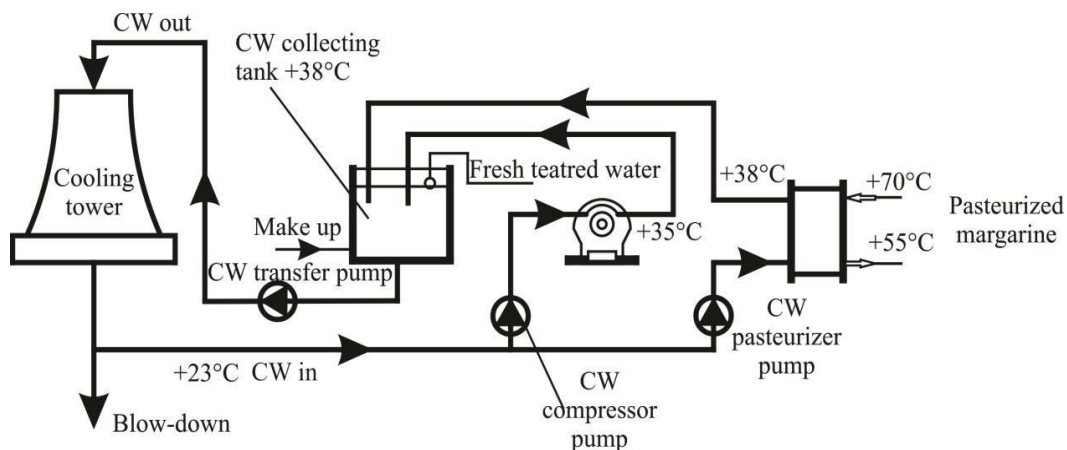


Figure 4 Implemented water reuse system



Additional benefit of modifying water reuse system was environmental protection since hot water (which temperature is 38 °C) is not discharged to sewer any more.

In order to create effective water management system, the other cost-effective measures to improve water consumption efficiency of the company were also evaluated. Measures related to the detection of physical losses, replacement of inadequate operations and operational improvements were considered in all WCCs. The proposed measures for reduction of the water consumption are shown in *Table 3*.

*Table 3* Measures for rational water use

WCC	Description of losses	Measures
WCC1, WCC3, WCC4	Water leaks identified at pumps, hose connectors and fittings	– Repairing identified leaks
WCC4	Cleaning floors and equipment	– Using detergents to dissolve fat, – Applying automated water gun for cleaning oily floor, – Promoting mop cleaning instead of wet cleaning always
WCC4	Unnecessary water wastage during vessels cleaning	– Replacing manual taps with push-button taps, – Proper awareness of rational water use
WCC4	CIP process	– Using ozonised CIP instead of conventional CIP, – Club flushing hot air along with ozonised water to achieve removal of loose fats, scaling and disinfection
WCC1, WCC2	Cooling tower water overflows	– Installing float valves, – Running tower on higher cycles using better cooling tower treatment chemicals.
WCC5	No purge control at the steam boiler (the concentration cycle was lower than ideal)	– Providing appropriate purge control

Some of the proposed measures are technical entirely, while some of them belong to the group of good housekeeping measures. Minimization of water usage is emphasized to management and employees.

All proposed measures and organizational activities were implemented in the process until 20<sup>th</sup> March 2016. Comparing the values of monthly specific water consumptions for two consecutive years (*Figure 5*), it can be concluded that specific water consumption was reduced by 59.23%, which presents a more than serious cut cost for a company. Beside, level of water consumption reached a level of 0.71 m<sup>3</sup>/t of produced margarine, which is even lower than values presented in *Table 1*.

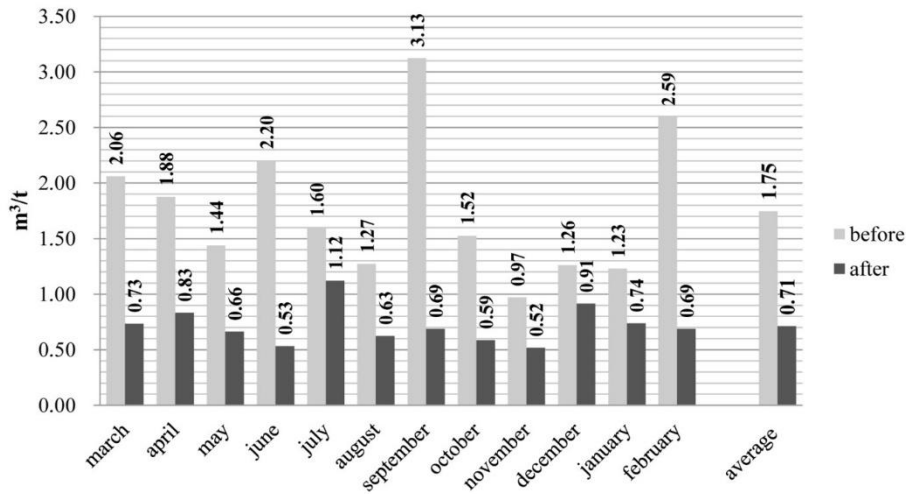


Figure 5 Specific water consumption [m<sup>3</sup>/t] for two-year period

Values of daily water demand measured at each WCC see in *Table 4*, had a different values then those presented in *Table 2*.

Table 4 Water demand of each WCC after implementing water management program

WCC	WCC No	Water demand (m <sup>3</sup> /day)	Percentage
Raw water	WCC1	3.48	29.72%
Steam production	WCC5	3.46	29.55%
Cleaning	WCC4	2.45	20.92%
Hot water production	WCC3	2.10	17.93%
Pasteurization process	WCC1	0.12	1.02%
Cooling system	WCC2	0.10	0.85%

Implementing water management practice completely modified the appearance of the ABC curve is showed in *Figure 6*. Now, two WCCs with highest water consumption (that are in “A” range) are raw water (water used in the process as a raw material) and steam production. In future development of the water management program should be more focused on those two WCCs. Pasteurization process and cooling system are in “C” range as lowest water consumption WCCs.

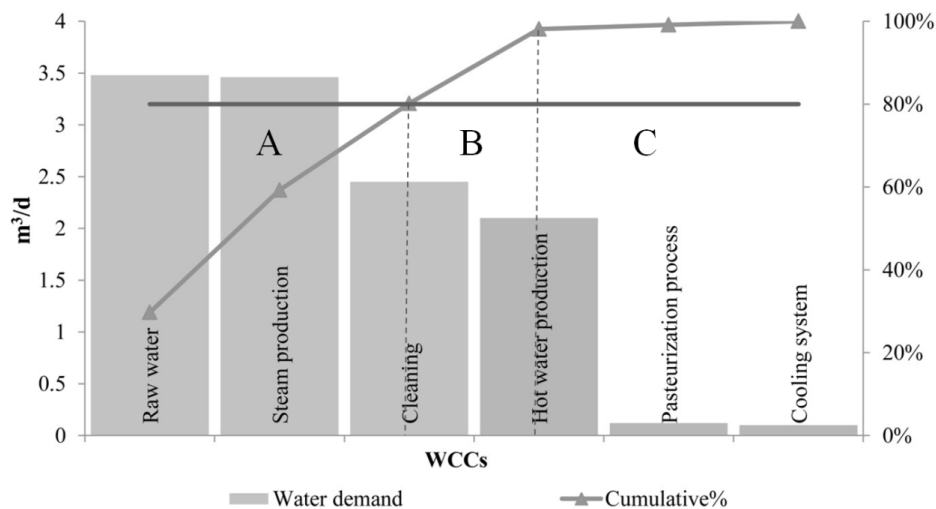


Figure 6 ABC curve - water demand of each WCC after implementing water management program



Considering that cost of non-treated industrial water for the company was 0.911 €/m<sup>3</sup>, for the production level of 4554.81 tonnes in 2016., annual savings was around 8600 €.

## CONCLUSIONS

This study shows that water management activities (as a comprehensive and systematic approach for reducing water consumption, increasing water reuse and reducing wastewater creation) are environmentally and economically feasible in a margarine production company. As a result of introduction of different water management activities, specific water consumption in the analysed company was decreased from 2.71 m<sup>3</sup>/t to 0.71 m<sup>3</sup>/t of produced margarine in two-year period. Taking into account total investment costs, annual operating costs and annual savings, payback period for implemented measures in analysed company is less than 1.5 year. Water consumption reduction in food processes can be a significant cut costs for a company.

Further developments of water management practice in the company should include continual monitoring of water consumption and analysing of additional technical opportunities for reducing water consumption with allocating more significant financial resources for implementation of the opportunities.

## REFERENCES

- [1] Barrington DJ., Prior A., Ho G.: *The role of water auditing in achieving water conservation in the process industry*, Journal of Cleaner Production, 52, 356-361., 2013.
- [2] Barrington DJ., Ho G.: *Towards zero liquid discharge: The use of water auditing to identify water conservation measures*, Journal of Cleaner Production, doi: 10.1016/j.jclepro.2013.11.065., 2013.
- [3] Briao VB., Tavares CRG.: *Effluent generation by the dairy industry: preventive attitudes and opportunities*, Brazilian Journal of Chemical Engineering, 24, 487-497., 2007.
- [4] Casani S., Knöchel S.: *Application of HACCP to water reuse in the food industry*, Food Control, 13, 315-327., 2002.
- [5] Casani S., Rouhany M., Knöchel S.: *A discussion paper on challenges and limitations to water reuse and hygiene in the food industry*, Water Research, 39, 1134-1146., 2005.
- [6] Ene SA., Teodosiu C., Robu B., Volf I.: *Water footprint assessment in the winemaking industry: a case study for a Romanian medium size production plant*, Journal of Cleaner Production, 43, 122-135., 2013.
- [7] Gordić D.: *Joint management of energy and environment in furniture industry (in Serbian)*, Kragujevac, Faculty of Engineering, 2011.
- [8] Jefferies D., Muñoz I., Hodges J., King VJ., Aldaya MM., Ercin AE., Milá Canals L., Hoekstra AY.: *Water Footprint and Life Cycle Assessment as approaches to assess potential impacts of products on water consumption: Key learning points from pilot studies on tea and margarine*, Journal of Cleaner Production, 33, 155-166., 2012.
- [9] Kist LT., Moutaqi SEL., Machado EL.: *Cleaner production in the management of water use at a poultry slaughterhouse of Vale do Taquari, Brazil: a case study*, Journal of Cleaner Production, 17, 1200-1205., 2009.
- [10] Lee WH., Okos MR.: *Sustainable food processing systems - Path to a zero discharge: reduction of water, waste and energy*, Procedia Food Science, 1, 1768-1777., 2011.
- [11] Matsumura EM., Mierzwa JC.: *Water conservation and reuse in poultry processing plant - A case study*, Resources, Conservation and Recycling, 52, 835-842., 2008.



# INTERNATIONAL SCIENTIFIC CONFERENCE ON ADVANCES IN MECHANICAL ENGINEERING

12-14 October 2017, Debrecen, Hungary



- [12] Milosavljevic N., Heikkila P. A.: *Comprehensive approach to cooling tower design*, Applied Thermal Engineering, 21(9), 899–915., 2001.
- [13] Panjeshahi MH., Ataei A., Gharaie M., Parand R.: *Optimum design of cooling water systems for energy and water conservation*, Chemical Engineering Research and Design, 87, 200–209., 2009.
- [14] Román Sánchez IM., Molina Ruiz JM., Casas López JL., Sánchez Pérez JA.: *Effect of environmental regulation on the profitability of sustainable water use in the agro-food industry*, Desalination, 279, 252–257., 2011.
- [15] Seneviratne MA.: *Practical Approach to Water Conservation for Commercial and Industrial Facilities*, Oxford England, Butterworth-Heinemann, 2007.
- [16] Barjoveanu G., Teodosiu C.: *Advanced treatment for pulp and paper wastewater recycling by membrane processes*, Environmental Engineering and Management Journal, 5, 145-167., 2006.



## MODELING AND AERODYNAMIC SIMULATION OF THE PASSENGER VEHICLE

**GRUJIĆ Ivan, STOJANOVIĆ Nadica, GLIŠOVIĆ Jasna PhD, DAVINIĆ Aleksandar PhD,  
MILOJEVIĆ Saša**

*Department for Motor Vehicles and Motors, Faculty of Engineering, University of Kragujevac*

*E-mail: [ivan.grujic@kg.ac.rs](mailto:ivan.grujic@kg.ac.rs), [nadica.stojanovic@kg.ac.rs](mailto:nadica.stojanovic@kg.ac.rs), [jaca@kg.ac.rs](mailto:jaca@kg.ac.rs), [davinic@kg.ac.rs](mailto:davinic@kg.ac.rs),  
[sasa.milojevic@kg.ac.rs](mailto:sasa.milojevic@kg.ac.rs)*

### Abstract

*Today, the vehicle aerodynamics has a significant place in the development of vehicle shape, as well as in increasing competitiveness in the automotive market. Aerodynamics has a big influence on improving the vehicle dynamics, reducing fuel consumption, increasing transverse vehicle stability, and increasing vehicle safety during the braking. The development of computer technology made it possible to detect the defects of a product in the early stages of development. This further aims at achieving a shorter time for creating a new one or modifying an already existing product. The simulation of the air flow effects is presented in the paper, using the ANSYS software package. Furthermore, an overview of the impact of the angle of the windscreen on the loads occurring on the vehicle itself is given, in order to improve the vehicle performance.*

**Keywords:** *shape development, vehicle dynamics, air flow, performance improving.*

### 1. INTRODUCTION

In a process of designing a more attractive vehicle, manufacturers must first know what customers want. Passenger vehicle is not just a means of transportation, also represents a person's personality. It can be said that design is the key for the success of a vehicle on the market. For this reason, marketing experts spend a lot of time exploring the desires and needs of the market, in terms of design, price, performance, comfort, and many other features. Of course, in addition to all other characteristics, the drag coefficient must not be omitted.

Aerodynamics is a science that deals with the movement of the air currents along the contour surfaces of the obstructed object [1]. The shape of the vehicle affects the dynamic behavior of the vehicle, fuel consumption, increases vehicle stability, increases vehicle safety during braking. How important is the vehicle's aerodynamics can be seen from the fact that it was noticed by the appearance of the first car body, and it became significant with the appearance of engines with larger power that enabled the development of high speeds.

During the vehicle movement, there is a friction of air with outer surface of the vehicle. There are two reasons why there is a friction between moving vehicles and air. The first is that it is almost impossible to make an ideal smooth surface, and the other is the viscosity of the fluid. By a vehicle moving, air is compressed in the front, while in the rear part of the vehicle, there is a dilution of particles [2]. The consequence of this is a frontal impact, where the air is opposing the vehicle's movement.

The evolution of car design through time is shown in *Figure 1*. The idea begins with an aerodynamic shape - a drop and a vehicle that has a similar look [3]. The vehicle's shape like the droplet was not suitable due to low quality roads and low engine power [4]. Then, in the next



## 2. 2D MODEL DEFINING OF BOUNDARY CONDITIONS

The main focus of paper is based on the aerodynamics of the vehicle. Before creating the final 3D model, it is necessary to determine how its shape influences on the resistance that occurs when vehicle moving. The analysis will be performed with the 2D model, *Figure 2*. The 2D model was created in the CATIA software package, while the analysis was performed in ANSYS, using the Fluid Flow (Fluent) module. A variable parameter whose influence will be tested during the analysis is the angle of inclination of the windshield,  $\alpha$ .

Three different values were selected for angle  $\alpha$ :  $30^\circ$ ,  $33^\circ$  and  $36^\circ$ .

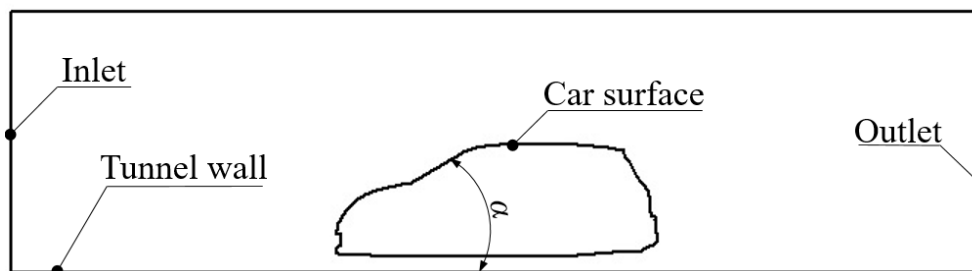


*Figure 2* 2D model

Regardless of whether it is a 2D or 3D model, it is necessary to define boundary conditions. The environmental condition under which the vehicle is being tested is defined with an air temperature of  $27^\circ\text{C}$ . The vehicle's speed is 100 km/h. Turbulent air flow occurs when a vehicle moving, so this is taken into account during the analysis. The air, in this case, is incompressible. The analysis uses the Navier-Stokes equations, and the SIMPLE algorithm is selected.

## 3. RESULTS

Numerical simulation of aerodynamics has a number of advantages. One of the most important is time saving, as well as the reduced cost of creating a new vehicle model.

The air pressure that occurs around the vehicle contour, when  $\alpha = 33^\circ$ , is shown in *Figure 3*. The maximum pressure values occur in the front of the vehicle. The reason for this lies in the fact that in this zone of the vehicle, there is compression of air due to the vehicle movement. There are slightly lower pressures in the rear of the vehicle, as the air is thinned. The vehicle with his movement compresses the air in the movement direction. The lowest pressure values are between the bottom of the vehicle and the ground.

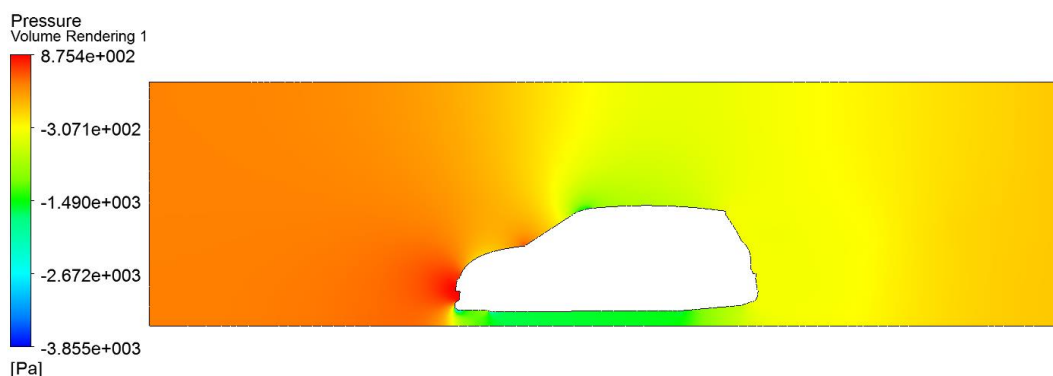


*Figure 3* Pressure contour



Changing the angle  $\alpha$ , more precisely with its increase, values of maximum pressure that occurs during the vehicle moving under the same boundary conditions of the analysis are reduced.

The display shows the effect of the pressure on the vehicle contour and is given in *Figure 4*, where it can be noticed that the maximum pressure values occur in the bumper area. It is understandable that there are higher air pressures in this zone, because in this way the vehicle has good cooling of the engine. Also, at the transition between the hood and the windshield, there are slightly higher pressures. The reason for this is the very shape of these surfaces, due to which such high pressure values are present.

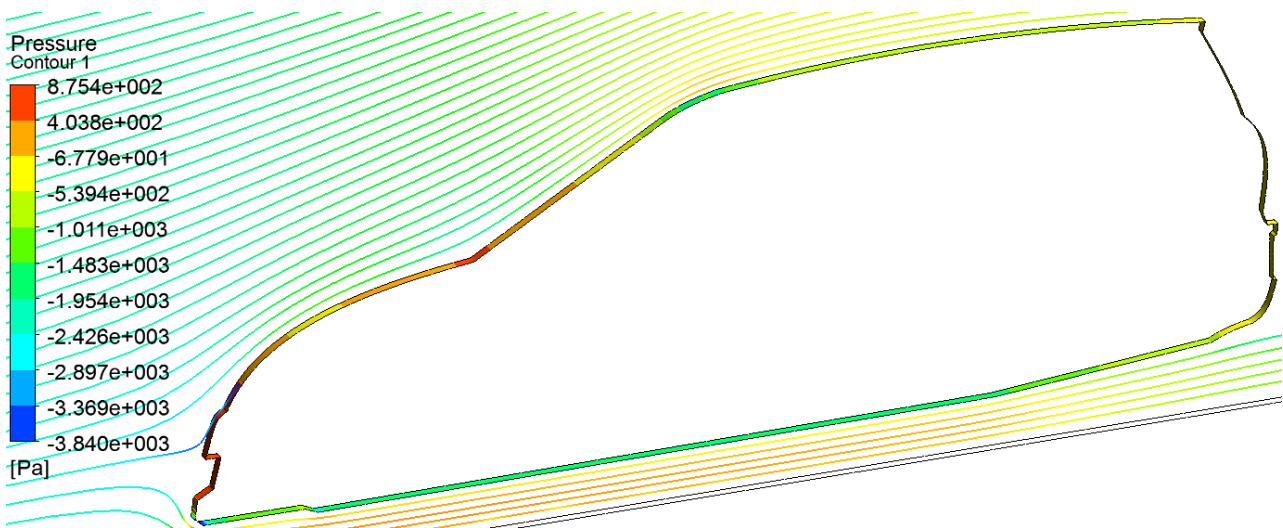


Figure 4 Pressure distribution on the contour of the vehicle and the air flow

Turbulence kinetic energy represents a measure of turbulent flow in the immediate proximity of the vehicle. In this case, turbulence kinetic energy is the result of the air flow and the movement of the vehicle. The values of the turbulent kinetic energy, when  $\alpha = 33^\circ$ , are shown in *Figure 5*. For the angle  $\alpha = 30^\circ$ , the kinetic energy is 101.953 J/kg, and for  $\alpha = 36^\circ$ , it is 101.796 J/kg. Based on the obtained values of turbulence kinetic energy, it can be noticed that there is no clear connection between the change of angle and turbulent kinetic energy. From other authors' research, it was found that the reduction of turbulent kinetic energy is accomplished by implementation of the spoiler.

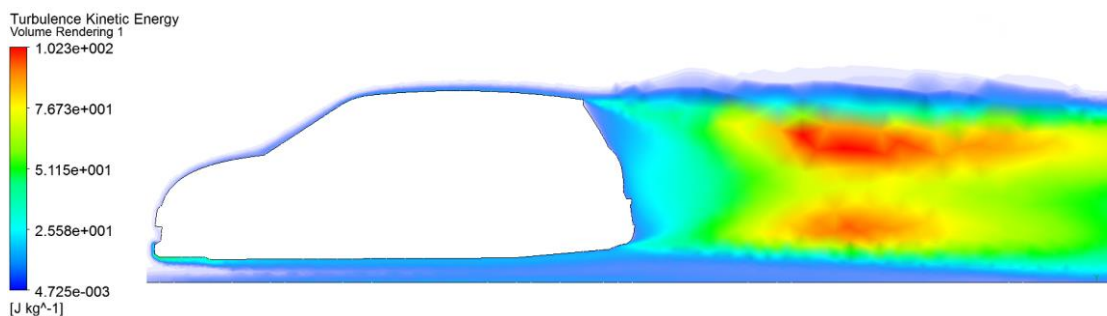


Figure 5 Turbulence kinetic energy

One of the most important indicators of the aerodynamics of the vehicle is the drag coefficient, and the values for the different angles of the windshield inclination are given in *Table 1*. As in the case



of turbulence kinetic energy, the same conclusions can be achieved for the drag coefficient. Taking into account that the aerodynamics of the vehicle is a very important parameter, which affects not only the aesthetic form of the car, but also the dynamics of the vehicle. Based on these values, it is necessary to find the optimum value of the incline angle of the windshield and thereby influences the reduction of resistance that occurs during the vehicle movement - air resistance.

Table 1 Drag coefficient in function of angle  $\alpha$

Angle, [°]	Drag coefficient, [-]
30	0.31438086
33	0.31487155
36	0.31443887

## CONCLUSIONS

In this study, the influence of the inclination angle of the windshield on the pressure, turbulence kinetic energy and drag coefficient is shown. With the rise of the inclination angle of the windshield, the pressure is reduced. The minimum values of the turbulence kinetic energy is obtained at an angle of 36°, which corresponds to the maximum angle in this analysis. While the smallest value of the drag coefficient occurs at angle of 30° - the minimum angle in this analysis. Using CFD numerical analysis provides an efficient and fast way to check the aerodynamics of the vehicle.

Future research should be based on a further reduction of a drag coefficient. Further study would be based on varying other vehicle parameters that also affect the drag coefficient. Furthermore, in addition to the parameters of the vehicle geometry, it is necessary to show the influence of the spoiler mounting. In addition to all this, the analysis should be done on a 3D model.

## ACKNOWLEDGEMENT

This paper was realized within the researching project “The research of vehicle safety as part of a cybernetic system: Driver-Vehicle-Environment” ref. no. 35041, funded by Ministry of Education, Science and Technological Development of the Republic of Serbia.

## REFERENCES

- [1] Janković, A.: *Vehicle Dynamics*. Kragujevac, 2008.
- [2] Simić, D.: *Motor vehicles*. Beograd, 1988.
- [3] Schütz, T.: *Hucho - Aerodynamik des Automobils Strömungsmechanik, Wärmetechnik, Fahrdynamik, Komfort*. Springer, 2013.
- [4] Hucho W.H.: *Aerodynamics of road vehicles: from fluid mechanics to vehicle engineering*. Butterworths, 1987.
- [5] Barreau, M., Boutin, L.: *Réflexions sur l'énergétique des véhicules routiers*. InterAction. Cachan cedex: Institut Universitaire de Technologie, 2008.
- [6] Parab, A., Sakarwala, A., Paste, B., Patil, V.: *Aerodynamic Analysis of a Car Model using Fluent- Ansys 14.5*. International Journal on Recent Technologies in Mechanical and Electrical Engineering (IJRMEE), 1(4), 7-13., 2014.
- [7] Zhang, Y., Zhang, Z., Luo, S., Tian, J.: *Aerodynamic Numerical Simulation in the Process of Car Styling*. *Applied Mechanics and Materials*. 16-19, 862-865., 2009.
- [8] Ali, M.Z., Khan, S., Mohan, N., Mandape, P.: *Aerodynamics*. IOSR Journal of Mechanical and



# INTERNATIONAL SCIENTIFIC CONFERENCE ON ADVANCES IN MECHANICAL ENGINEERING

12-14 October 2017, Debrecen, Hungary



Civil Engineering, 64-67., 2014.

- [9] Sharath Kumar, S.N., Umesh, C.K.: *Analysis of External Aerodynamics of Sedan and Hatch Back Car Models Having Same Frontal Area by Computational Method*. International Journal of Research in Mechanical Engineering & Technology, 6(1), 55-61., 2016.
- [10] Hu, X., Wong, E.T.T.: *A Numerical Study On Rear-spoiler Of Passenger Vehicle*. International Journal of Mechanical, Aerospace, Industrial, Mechatronic and Manufacturing Engineering, 5(9), 1800-1805., 2011.
- [11] Daryakenari, B., Abdullah, S., Zulkifli, R., Sundararajan, E., Mohd Sood, A. B.: *Numerical study of flow over ahmed body and a road vehicle and the change in aerodynamic characteristics caused by rear spoiler*. International Journal of Fluid Mechanics Research, 40(4), 354-372., 2013.



## EFFECTIVE DESIGNING OF MODULAR STRUCTURES VARIANTS OF MOBILE WORKING MACHINES

*GULAN Ladislav PhD, SCHMIDTOVÁ Carmen, IZRAEL Gregor PhD*

*Faculty of Mechanical Engineering, Slovak University of Technology in Bratislava*

*E-mail: [ladislav.gulan@stuba.sk](mailto:ladislav.gulan@stuba.sk), [carmen.schmidtova@stuba.sk](mailto:carmen.schmidtova@stuba.sk), [gregor.izrael@stuba.sk](mailto:gregor.izrael@stuba.sk)*

### **Abstract**

*The information about the degree of use of particular building modules is very important for a company producing mobile working machine, but also the information about the realization between costs invested on design activities and revaluating of these costs into produced machines. This information is important not only for already existing program, but also for decisions, which products, eventually modifications of already existing products include into production program in the future. For the purpose of such decisions, it is suitable to use evaluation of structures modularity via the so called coefficient of financial efficiency, which can help in decisions about creation, eventually change of production program.*

**Keywords:** *mobile working machine, flexible modular structure, coefficient of modular structure, modularity ratio, coefficient of financial effectivity*

### **1. MODULAR CONSTRUCTIONS OF MOBILE WORKING MACHINES**

The market of mobile working machines is filled in with a broad offer of various types and size classes of machines. Every producer must hence constantly follow and evaluate requirements of users, so as to be able objectively to determine production program for the future. On the basis of knowledge of contemporary situation are then designers able to create suitable structure of basic building modules, from which will then be possible to assemble required structural variants of mobile machines determined for realization of particular working technologies. Effectivity of in this way created structures can be assessed via modularity ratio. Modularity ratio expresses degree of use of building modules and regards various facts and relations among assembled machines, their structures, number of disponsible variants of particular modules as well as problems of creation of a mutual platform [1], [2].

Costs for development of a new mobile working machine usually exceeds the limit 0,5 million €, a new product must then inevitably be economically successful. Problems of creation of a suitable products structure on a mutual platform is solved in the stages of the project APVV „Research of a Modular Platform for an Oriented Segment of Mobile Working Machines“. This project created the basis for the development and design of new mobile working machines with type marking HON 200. In case of basic machines with type marking HON 200Z and HON 200T (Figure 1) the pre-production phase was finished including production and testing of prototype, process of approval of a new product and piece production was launched. Presented methodology of structures assessment should contribute to design process of a pilot production program, eventually to its subsequent expansion with further loadability classes.

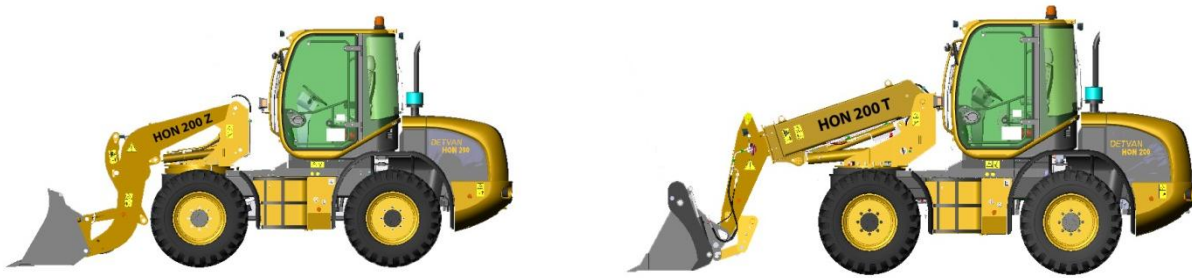


Figure 1 Loader HON 200Z and HON 200T

## 2. ASSESSMENT OF FINANCIAL EFFECTIVITY OF PROPOSED PRODUCTION PROGRAM

Prerequisite of a successful acting of a company producing mobile working machines on market, and its competitiveness, is also an offer of a sufficient assortment of machines enabling realization of more than one working technologies. This offer is usually objectified by requirements of users. These requirements have to be in the initial phase of design evaluated and required assortment has to be reduced by restriction of number of universal working machines, for which flexible modular structures on a mutual platform have to be created and their modularity ratio as the criterion for design of definitive variants of working machines will be assessed (Figure 2), [1], [2]. After considering contemporary requirements of users, the set of basic machines of a building sequence was widened with further variants and virtually a modular structure of a carrier HON 200 from existing building modules was created.

Created was then a machine group, which aside basic types HON 200Z and HON 200T is composed of articulated loader with Z-kinematics HON200 KZ, articulated loader with a telescopic

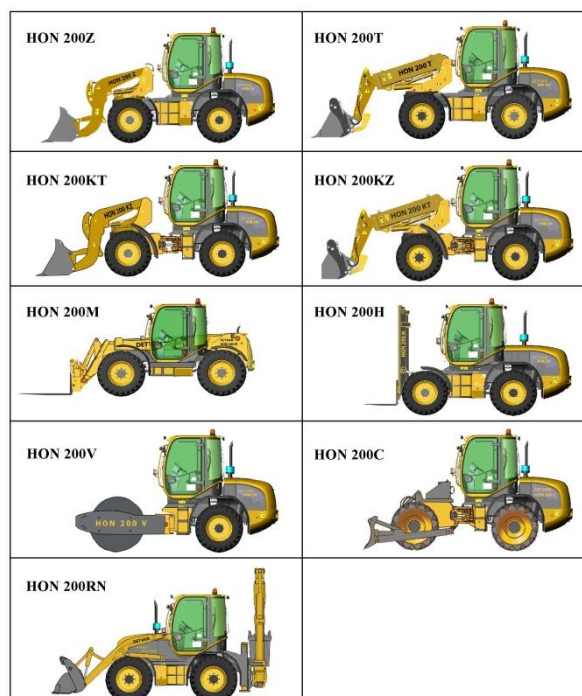


Figure 2 Modular structure of a carrier HON 200



equipment HON 200KT, manipulator HON 200M, high lift manipulator HON 200H, articulated dump cylinder HON 200V, articulated compactor HON 200C and backhoe loader HON 200RN (Figure 2).

For a production company is very important not only the information about degree of use of particular building modules, but also about relation between costs, which have to be spent on design activities and revaluating of these costs into products produced in frame of a particular production program[4], [5]. Such information is important not only for an already existing production program, but also for decisions, which further products, eventually modifications of already existing should be included into a production program.

For this purpose we define the so called coefficient of financial effectivity –  $k_{FE}$ , which can provide relevant support in decisions about creation, eventually widening of production program. Proposed methodology of evaluation can be realized with the use of chart. 1. In this table we consider a production program of  $\lambda$  machines  $S_1$  to  $S_\lambda$ . Particular machines are assembled from modules  $M_1$  to  $M_\rho$ .

Every module, which participates in creation of these machines can occur in one or several variants.

In this chart the following symbols are used:

$\rho$  – is the number of modules in consideration

$r = 1, \dots, \rho$  – is the sum index with respect to all modules for the computation of values  $S_V$  a  $S_{ZM}$

$S_V$  – is the sum of financial costs for procuration of all needed variants of all modules

$S_{ZM}$  – is the sum of evaluation of all variants of modules into all machine assemblies.

$F_{Mr} \cdot V_o$  - are financial costs needed for procuration of o-th variant of r-th module

$\omega_r$  - is number of variants of r-th module

$o = 1, \dots, \omega_r$  is the sum index for summing of financial costs needed for procuration of all variants of r-th module

$\sum_{o=1}^{\omega_r} F_{Mr} \cdot V_o$  - are financial costs needed for procuration of all variants of r-th module.

$S_V = \sum_{r=1}^{\rho} \sum_{o=1}^{\omega_r} F_{Mr} V_o$  are financial costs needed for

procuration of all variants of all modules

$\lambda$  – is the number of machines of a production program

$L = 1, \dots, \lambda$  – is the sum index regarding all the machines for computation of values  $S_V$  and  $S_{ZM}$

$F_{Mr} V_{SL}$  is financial value of the r-th module in that particular variant, which is used for the creation of the L-th machine, for  $r = 1, \dots, \rho$ ,  $L = 1, \dots, \lambda$

$\sum_{r=1}^{\rho} F_{Mr} V_{SL}$  - is the financial evaluation of all used modules

for the L-th machine, while mentioned evaluation is implied by creation of particular machine

$S_{ZM} = \sum_{L=1}^{\lambda} \sum_{r=1}^{\rho} F_{Mr} V_{SL}$  - is the evaluation of all used variants of all modules implied by creation of all

machines of particular production program.

Note: In computation of the

$S_{ZM} = \sum_{L=1}^{\lambda} \sum_{r=1}^{\rho} F_{Mr} V_{SL}$  - are the values of particular variants

in the sum applied in every machine while in computation of





decisions will be influenced by many factors, from which the most important are the needs of real market and affinity of working technologies, which will be performed by considered machines. On the basis of these criteria, the extent of modular solutions can be specified. For a factual case after a detailed research of market requirements and considering concrete possibilities and requirements of producer it would be purposeful to select for the pilot program the group of variant structures depicted in the (Figure 3).

For this group of machines, assurance of one working technology is characteristic - manipulation with material – using two types of working tools, loading shovel and manipulation forks. Just working technologies realized by these tools belong to the most widespread and users require very often their mutual exchangeability. But specific are carriers with their building modules, enabling various ways of machine control, their maneuverability and manipulation suitable for various areas of their use in praxis.

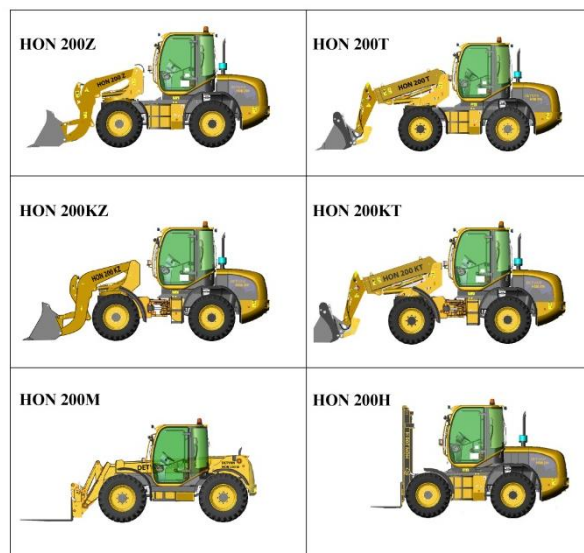


Figure 3 Pilot production program

## CONCLUSIONS

In the conclusion, it can be stated, that just modular structures enable flexible to create relevant production program of a company [2], [3]. These positive properties can briefly be summarized into the following points:

- flexibility for change of working technology
- flexibility for respecting of requirements of users
- positive influencing of logistic production chain
- shortening of design and technological production preparation
- shortening of innovation process and time needed for launching a product onto market
- decreasing of production costs
- simplification of production process
- diversity of products
- high number of variants.

Responsible producers of mobile working machines have to apply scientifically based methods of production program creation support, which is also proved by experience. Presented methodology of assessment of modular structures is the contribution to creation of economically successful and sophisticated technological solutions of products. It is gratifying, that scientific cooperation in



# INTERNATIONAL SCIENTIFIC CONFERENCE ON ADVANCES IN MECHANICAL ENGINEERING

12-14 October 2017, Debrecen, Hungary



development of these progressive methods is supported by agencies in the form of mutual scientific-research projects with production companies.

This contribution was supported by the Slovak Research and Development Agency under the contract No. APVV-15-0524 and the Scientific and Educational Grant Agency through financial support VEGA 1/0445/15.

## REFERENCES

- [1] Gulán, L.: *Modular Design of Mobile Working Machines*. Book, STU in Bratislava, 2000, ISBN 80-227-1397-X.
- [2] Gulán, L., Bukoveczky, J., Zajacová, E.: *Verification of modularity ratio on the set of mobile working machines*. In: Proceedings of the XV European conference of material handling teaching professors. 22. - 26. 9. 2004, Novi Sad, p. 18 – 23, 2004.
- [3] Gulán, L., Bukoveczky, J., Zajacová, E.: *The platform of machine assemblies of mobile working machines: Monograph on the occasion of 47th anniversary of the Faculty of Technical Sciences*, p. 185 – 186, UNS FTS Novi Sad 2007, ISBN 978-86-7892-038-7.
- [4] Gulán, L., Bukoveczky, J.: *Platform creation of modular working machines*. In: *Gép*, 4/2006. Published by the Scientific Society of Mechanical Engineering, p. 27 – 29, Hungary, 2006, ISSN 0016-8572.
- [5] Gulán L., Zajacová E.: *Architectonic structure of flexible constructions of mobile working machines: Monograph on the occasion of 48th anniversary of the Faculty of Technical Sciences*, (105 - 108 p), UNS FTS Novi Sad 2008, ISBN 978-86-7892-105-6.



## EXAMINATION THE PHYSICAL CHARACTERISING OF FERTILIZERS

<sup>1</sup>HAGYMÁSSY Zoltán PhD, <sup>2</sup>PÁLINKÁS Sándor PhD, <sup>2</sup>BATTÁNE GINDERT-KELE Ágnes PhD

<sup>1</sup>Department of Agrotechnology, Institute for Land Utilization, Technology and Regional Development, Faculty of Agricultural and Food Sciences and Environmental Management, University of Debrecen

E-mail: [hagymassy@agr.unideb.hu](mailto:hagymassy@agr.unideb.hu)

<sup>2</sup>Department of Mechanical Engineering, Faculty Engineering, University of Debrecen

E-mail: [palinkassandor@eng.unideb.hu](mailto:palinkassandor@eng.unideb.hu), [battane@eng.unideb.hu](mailto:battane@eng.unideb.hu)

### Abstract

In University of Debrecen, Department of Agrotechnology different type's fertilizer distributor was examined by authors within the framework of precision farming. Nowadays the cultivation technology requires distributing different types of fertilisers more accurately and evenly. Evenly distributed fertilisation is an important demand in agricultural technology. Because of this, it is necessary to develop fertiliser spreader machines continuously. In developing this machinery, it is essential to know the physical properties of fertilisers. We can determine the following characteristics: particle size and particle size distribution, bulk density, moisture content, and the angle of repose. This study deals with the main factors influencing fertilisation, including surface characteristic, particle (granule) shape, particle hardness, particle size range, specific particle weight..

**Keywords:** Precision application of fertilizer, Fertilizer characteristics

## 1. INTRODUCTION

The physical characteristics of the used fertilisers greatly differ from each other as they significantly affect the physical distribution of fertilisers applied on the soil. This research, we examined the physical characteristics of six different fertilisers widely used in nutrient replenishment. Fertilisers are indispensable in nutrient replenishment, which is an essential part of crop production. This environmental friendly and cost-effective method is the location-specific "precision" nutrient replenishment, which makes it possible to perform nutrient application adapted to the local endowments and needs of the given plot. The precision application of fertilisers is necessary in order to perform modern nutrient management, as it guarantees the stable yield and quality of culture crops without harming the environment. [3]

## 2. METHODS

In University of Debrecen the measurements were made in the material analysis laboratory of the Institute of Land Utilisation, Regional Development and Technology of the Faculty of Agricultural and Food Sciences and Environmental Management at 20°C and a relative humidity of 30-40 %. 50 kg airtight fertiliser bags were available for each type.



For the analyses, the following fertilisers were used:

1.  $\text{NH}_4\text{NO}_3$
2. YARA Mila 13:13:21
3. Genezis NS 21:24
4. Potassium chloride (60% Potash)
5. Genezis CAN 27%N
6. MAP NP 12:52

Moisture content was calculated from weight measured before and after transport. A 25g sample was heated for 72 hours to  $103 \pm 1^\circ\text{C}$  temperature in a drying oven. (*Figure. 1*) This examination had three replications. Samples were placed on aluminium trays. The heating samples were weighed using an analytical scale with 0.01g accuracy. The sensory evaluation of the particles, it can be concluded that their consistency is representative of each type. No agglutination and friability were observed with the samples.

Measurement of moisture content is an important, because it is greatly affected by the trajectory of fertilisers; therefore, this examination should be performed before the measurements to be carried out.



*Figure 1* The sieve, and the drying oven

Using a mechanical shaker, 100g samples of each fertiliser type were shaken for three minutes with three replications. A sieve analysis (*Figure. 1*) was performed to determine the characteristics of particle size distribution. The following sieve sizes were used: 1 mm; 1.25 mm; 2 mm; 2.5 mm; 4 mm. The sample and the leftover after sieving were weighed using an analytical scale with 0.01g accuracy. [1] [2]



*Figure 2* The digital calliper and the analytical scale



The ratio of the geometric effective diameter and the largest diameter,  $g_a = (d_1 d_2 d_3)^{1/3} / d_1$ , where  $d_1$  is the largest size and  $d_2$  and  $d_3$  are the two sizes perpendicular to  $d_1$ . In the case of a regular globe, this value is one unit. The bulk density measured by a 1000 cm<sup>3</sup> measurement pot of 100 mm diameter and 127.4 mm height was used to determine bulk density. Fertilisers were slowly poured into the measurement pot from a height of 150 mm without compaction and with three replications. After the top was skimmed off, the weight was measured using an analytical scale of 0.01g accuracy. (Figure. 2) [2]

### 3. RESULTS

Sample 2 contained the highest amount of moisture and the lowest amount of pulverised fraction (<1) as a result of the sieved fractioned measurement, which equals to 0.0g related to the examined sample; therefore, it does not cause any significant problem during the application of the fertiliser. Table 1 shows the moisture content and particle composition of the examined fertilisers. Sample 4 (potassium chloride) contained the lowest amount of moisture. This fertiliser type is mostly coarse and irregular shaped and it has the hardest particle. Accordingly, this fertiliser is the least hygroscopic and, as a result, it is the least sensitive of all examined fertilisers to the humidity of the storage environment. [3]

Table 1 Results of the measurement

Sample	storage (g)	total mass storage weight (g)	wet fertilizer (g)	total dry mass storage (g)	dry fertilizer (g)	water content (g)	moisture content %
1	10,63	35,76	25,13	34,71	24,08	1,05	4,18
2	10,73	35,80	25,07	34,54	23,81	1,26	5,03
3	10,64	35,71	25,07	35,37	24,73	0,34	1,36
4	10,64	35,48	24,84	35,37	24,73	0,11	0,44
5	10,69	35,89	25,2	35,15	24,46	0,74	2,94
6	10,71	35,73	25,02	34,62	23,91	1,11	4,44

The determination of particle fractions leads us to conclude to the evenness of dispersion. The amount of pulverised fraction is in a sample, the more hygroscopic and uneven the dispersion is. Table 2 show the measurement of the examined samples by fraction. [3]

Genezis NS 21:24 contained the highest amount of pulverised (<1) fraction and the highest amount of particles above 4mm, which is considered to be a relatively significant value. Because of this, this fertiliser type is rather variable in terms of its water binding capacity and dispersion. [3]

An unusually high value was there in the 2-2.5 mm range, which was provided by the NH<sub>4</sub>NO<sub>3</sub> sample. Therefore, 70.27% of the examined sample belongs into this range, which significantly exceeds the respective values of the other samples. Consequently, it can be concluded that there is a favourable impact on working width in the case of NH<sub>4</sub>NO<sub>3</sub>. The bulk density of fertilisers is in connection with the capacity demand which arises during transport. It can be observed that Genezis CAN 27%N has the highest bulk density which is related to its imperfect globularity (0.871). The results obtained during the measurement of globularity. Genezis NS 21:24 has the lowest bulk density; therefore, this fertiliser type calls for the highest capacity during storage and transport. [3]



# INTERNATIONAL SCIENTIFIC CONFERENCE ON ADVANCES IN MECHANICAL ENGINEERING

12-14 October 2017, Debrecen, Hungary



Table 2 Results of the particle size measurement

	1		2		3	
<b>Moisture</b>	0,44		2,94		4,44	
<b>Particle size</b>	g	%	g	%	g	%
<b>&lt; 1</b>	0,05	0,05	0,04	0,04	0,15	0,15
<b>1 - 1,25</b>	0,07	0,07	0,01	0,01	0,09	0,09
<b>1,25 - 2</b>	3,66	3,66	4,5	4,5	1,7	1,7
<b>2 - 2,5</b>	16,82	16,82	7,76	7,76	5,64	5,64
<b>2,5 - 4</b>	76,28	76,28	77,2	77,2	82,73	82,73
<b>&gt; 4</b>	3,28	3,28	10,1	10,1	9,68	9,68
<b>Total</b>	100,16	100	99,61	100	99,99	100

## CONCLUSIONS

The result may also provide a background for the production characteristics of the examined fertilisers, thereby reducing the pulverisation of fertilisers. The measured moisture content, space filling and fraction characteristics affect storage and transport properties. In addition, the change of working width and dispersion plays a very important role in the case of each fertiliser type. The obtained results show these characteristics of the examined fertilisers in a quantified way which leads us to conclude to the existence of even dispersion and even working width as these are indispensable factors in precision technology. Different fertiliser types were examined for their most significant physical characteristics from the aspect of the dispersion of fertiliser particles. [3]

## ACKNOWLEDGEMENT

This publication was supported by the project “Establishing a scale-independent complex precision consultancy system (GINOP-2.2.1-15-2016-00001)”.

## REFERENCES

- [1] Battáné Gindert-Kele, Á., Csizmazia, Z., Ancza, E.: Hagymássy, Z. (2002): *Műtrágyaszemcsék néhány fizikai jellemzője*. Kutatási és Fejlesztési Tanácskozás : Nr. 26. Gödöllő. 15-16. 2. kötet. 165-169. 2002
- [2] Gindert-Kele, Á. (2005): *Műtrágyaszemcsék fizikai jellemzői és mozgásuk elemzése*. Doktori (Ph.D) értekezés tézisei. Debrecen, 26. p. 2005
- [3] Balla Z., Tamás A., Vántus A., Hagymássy Z.: *Determining the main physical characteristics of fertilisers*. 6-th. Alps Adria Scientific Workshop, Columella. 305-308. 2017



## COMPARISON OF BATHLIFT CONSTRUCTIONS

*HAJDU Flóra, HORVÁTH Péter PhD*

*Department of Mechatronics and Machine Design, Faculty of Mechanical Engineering,  
Informatics and Electrical Engineering, Széchenyi István University  
E-mail: [hajdfl@sze.hu](mailto:hajdfl@sze.hu)*

### **Abstract**

*Having bath is difficult for old and disabled people. Fortunately there are several bathlift constructions ranging from simple motorized retractable chair placed in the bathtub to more difficult wall mounted bath hoists. An applicable bathlift must meet several requirements, which are safety, comfort, easy manufacturability and mount, low space occupation and low price. Each of the mentioned constructions have some advantageous features but none of them meet all the requirements. The main purpose of this paper is to find a bathlift construction combining the advantageous functions of bathlifts available. For this reason several bathlift constructions are analysed and compared in order to find their advantageous features. The paper concludes with a possible solution, which is the combination of known constructions supplemented by new functions.*

**Keywords:** *construction, bathlift,*

### **1. INTRODUCTION**

The age structure of the population in the EU is becoming older [1] and is expected to continue in the coming decades [2]. For old and disabled people getting in and out of bath can be difficult and also dangerous. To solve the problem there are several solutions from simple retractable chairs to more difficult wall mounted constructions. A good solution must meet several requirements, which are safety, comfort, easy manufacturability and mount, low space occupation and low price. In this paper different bathlift constructions are compared according to these requirements to find the best solution available.

### **2. METHODS: ANALYSIS OF AVAILABLE BATHLIFT CONSTRUCTIONS**

One of the most common solution is the motorized retractable chair placed in the bathtub (Figure 1.1). Its advantage is the simple construction, but it doesn't solve getting in and out of the bathtub, which can be dangerous because of slipping. For disabled people stepping over the edge of the bathtub is nearly impossible.

A similar construction is the Splash bathlift (Figure 1.2) [3]. It is one of the cheapest bathlift available on the market and it has low weight and occupies little space. It's great advantage, that the seat goes all the way down to the lowest point within the bathtub resulting in greater water immersion providing improved personal hygiene. This construction also does not solve getting in and out of the bathroom and the fixed backrest can be uncomfortable.

Similar simple constructions such as water pressure inflatable balloons (Figure 1.3) and band bathlifts (Figure 1.4) also do not provide solution for getting in and out of the bathtub (Figure 1).



Figure 1 Simple bathlift constructions[3]-[5] (1.retractable chair, 2. Splash bathlift, 3. water pressure inflatable balloon, 4. band bathlift)

Fixed constructions may transfer the person in and out of the tub, but their installation is difficult, sometimes needs great masonry work. The floor or wall mounted constructions (Figure 2.1 and 2.2). are complicated and occupy a lot of space from the bathroom. As they are loaded with high bending moment, thus they are robust. The advantage of ceiling mounted constructions (Figure 2.3) is that they occupy no space from the floor nor the bathtub. They are expensive, so only rich people and premium hospitals can afford them.



Figure 1 Fixed bathlift constructions [6] and mobile patient lift [8](right) (1. floor mounted, 2. wall mounted, 3. ceiling mounted, 4. mobile patient lift)

Mobile patient lifts (Figure 2. 4), which are even capable of moving the person from the bed into the bathtub are also known. They are often used in hospitals and retirement homes, where there is enough room for maneuver.

### 3. RESULTS: COMBINING THE ADVANTAGES

To develop a new construction we worked out a bathlift, which could lift the person into the bathtub using a circular trajectory. (Figure 3) [9]. Its greatest advantage is the simple construction (only one drive system is required), but it is heavy and needs additional installation work. Analysing the known solutions, it is clear that each one has some advantages features, but there is no perfect solution so far. In the Table 1 we evaluated the functions of the certain constructions. All properties get a score from 1 to 5, the more favourable the property the higher the score is. [10]. The ability of lifting legs over the tub side and applicability for lot of bathrooms are taken into account under Functionality. As for Complexity it is evaluated how difficult to assemble and disassemble the bathlift and how much changes required in the bathroom (e.g. drilling of walls).



Figure 2 The first bathlift construction [9]

Table 1 Comparison of bathlift constructions

Concept	Cost	Complexity	Functionality	Safety	Space	Comfort	Sum
Column chair (Splash)	5	5	2	2	4	2	20
Retractable chair	4	5	3	2	3	3	20
Floor mounted	2	3	4	3	1	3	16
Wall mounted	2	3	4	3	2	3	17
Celling mounted	1	1	5	3	4	3	17
Band	3	4	1	1	3	4	16
Inflatable balloons	4	4	1	1	4	4	18
Mobile patient lift	2	4	3	4	2	3	18
Circular trajectory (our construction)	3	3	4	3	3	3	19
New combined construction (Figure 4)	4	4	5	4	4	4	21

In Table 1 it can be seen that all constructions have advantages and disadvantages, but there is no perfect solution. It would be good to combine the advantages of different constructions to create a new construction (Figure 4.). The safe floor mounted bathlift can be combined with the easy construction of Splash bathlift using simple elements (lifting column) available on the market. The lifting column lifts higher, which solves the problem of lifting the leg above the bathtub. The seat has a turntable, which makes it easier to get in and out of the bathtub. Turning the seat can be easily executed with manual power, so it also combines the simple drive system of our self-developed construction too. The folding arm-rest makes the use of bathlift more comfortable and secure. If there is no need to use the bathlift, the seat can be easily removed. This construction has a simple supporting structure, which occupies only little space and requires no changes in the bathroom.

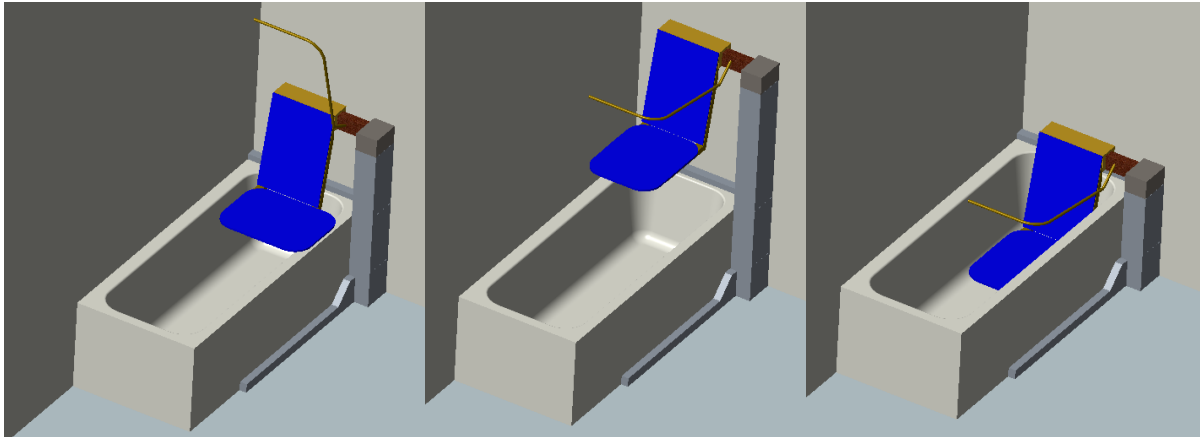


Figure 3 Combined bathlift construction. Left: boarding. Middle: lifting and turning. Right: bathing position

As it can be seen in Table 1. this construction can meet all the requirements appointed before.

## CONCLUSIONS

In this paper several bathlift constructions were compared. All constructions have advantages, but there is no perfect solution so far. Combining them a safe, simple and cheap construction could be created.

## ACKNOWLEDGMENTS

This study has been supported by EFOP-3.6.1-16-2016-00017 project.

## REFERENCES

- [1] European Commission: *EU employment and social situation*, Quarterly review, March 2013
- [2] Giannakouris K.: *Ageing characterises the demographic perspectives of the European societies*, Eurostat, 72/2008
- [3] <https://www.careco.co.uk/item-s-ba01001/splash-bath-lift/#tabsection>
- [4] <http://www.livingmadeeasy.org.uk/bath+lifts/>
- [5] <https://www.nrshealthcare.co.uk/bathroom-aids/bath-lifts/orca-bath-lift>
- [6] <http://www.abledata.com/indexing-terms/bath-lifts>
- [7] [https://www.pattersonmedical.co.uk/Supplies/ProductFamilyDetails/PIF\\_AA1305A](https://www.pattersonmedical.co.uk/Supplies/ProductFamilyDetails/PIF_AA1305A)
- [8] <https://hu.pinterest.com/dolphinlifts/hoists-and-lifting-disabled-patients/>
- [9] Hajdu F., Horváth P.: *Design of a new bathlift construction*, Naucni Izvestija: Scientific Proceedings of the Scientific-Technical Union of Mechanical Engineering 15/201: pp. 7-11. (2016), II International Scientific Congress. Varna, Bulgaria: 2016.06.20 -2016.06.23.
- [10] Pahl G., Beitz W.: *Konstruktionslehre: Methoden und Anwendung*, Springer, 1997



## OPTIMIZATION OF BATCH EXTRACTIVE DISTILLATION WITH DIFFERENT METHODS

**HÉGELY László PhD, SLEISZ Kristóf**

*Department of Building Services and Process Engineering, Faculty of Mechanical Engineering,  
Budapest University of Technology and Economics*

*E-mail: [hegely@mail.bme.hu](mailto:hegely@mail.bme.hu), [ksleisz@gmail.com](mailto:ksleisz@gmail.com)*

### **Abstract**

*Batch distillation is a frequently used method to separate liquid mixtures with variable amount and composition, for example in the pharmaceutical industry. Batch extractive distillation is applied for the separation of azeotropic mixtures. The optimization of these processes can greatly increase their efficiency and profitability. Stochastic optimization methods, such as genetic algorithms, are often used as they perform global optimization. However, genetic algorithms require a large number of objective function evaluations that makes them computationally intensive, especially for the optimization of dynamic processes, such as batch distillation. The downhill simplex algorithm is a promising faster, although local alternative. We perform the optimization of a batch and a batch extractive distillation waste solvent regeneration process by the simplex algorithm of Spendley and compare the results to those previously obtained using a genetic algorithm. The objective function (profit) is evaluated by dynamic simulation in a flow-sheet simulator. By starting the simplex from the optimum found by the genetic algorithm, it was verified that only very small improvements can be reached. The stand-alone applicability of the simplex algorithm is also studied by starting the optimization from a point further away from the optimum.*

**Keywords:** *optimization, batch distillation, extractive distillation, genetic algorithm, simplex.*

### **1. INTRODUCTION**

*Distillation is the most frequently used method to separate liquid mixtures, based on the differences in the volatility of the components. It is often performed in batch mode in the fine chemical, spirit and pharmaceutical industry, as well as in solvent recovery, as *batch distillation* (BD) can be used to separate mixtures of varying quantity and composition (flexibility of operation).*

*The main components to be recovered are produced in the *main cuts* (products). The polluting components and azeotropes are removed in off-cuts (fore-, intermediate and/or after-cut). The *off-cuts* may contain the main components in considerable quantity. The off-cuts can either be disposed of by incineration or can be recycled to the next batch in order to reduce the loss of the main components.*

*For the separation of *azeotropic mixtures* a special distillation method must be applied. In *batch extractive distillation* (BED, Yatim et al. [1]), an entrainer (En) is fed continuously into the column. The entrainer, which is not necessarily a new component, changes the relative volatilities favourably [2]. BED is usually applied to extract pollutants of moderate concentration from the main component to be recovered. However, if En reduces the volatility of the main component, it can be then extracted from beside the pollutants of low concentration forming minimum azeotropes with it. These pollutants can be removed in fore-cuts, which, however, cause a loss of the main component, since they contain it in considerable amount. On the basis of industrial experiences Lang et al. [3] suggested a new operational policy, with entrainer feeding already during the*



heating-up of the column.

Batch distillation can be made more efficient by optimizing the operational parameters of the process, such as the reflux ratios and termination criteria of the different steps. In the case of BED, the parameters of the  $E_n$  feeding should also be optimized. Feeding more  $E_n$  helps the separation of the azeotrope-forming components, but it also makes the recovery of the main component more difficult due to its dilution by  $E_n$ . This is especially a concern when the main component is extracted as the necessary  $E_n$  quantity is higher. Since batch distillation is a time-dependent process, dynamic optimization must be applied. Instead of finding the time-optimal profiles of the optimization parameters, an infinite-dimension problem, discretisation is applied. In the simplest case, the parameters can be constant, or they might be a stepwise constant, with different values at different steps of the process. Based on the objective function, Mujtaba [4] distinguished the following problem formulations for the optimization of batch distillation: minimum time, maximum distillate and maximum profit (productivity) problems.

The solution method of the problem is influenced by the modelling approach applied. If an equation-based modelling environment (e.g. MATLAB, GAMS) is used, the model equations are explicitly known and derivatives can be calculated. The problem, which is usually a MINLP one, is then solved by an appropriate algorithm (solver). Using a professional flow-sheet simulator is more convenient for modelling, but optimization can only be performed in this case by derivative-free optimization methods that treat the dynamic model of the process as a black box. Stochastic methods, such as genetic algorithms (GA), are popular, as they can find the global optimum. An example is the work of Hegely and Lang [5] who performed the optimization a BD and a BED multi-batch waste solvent regeneration process with off-cut recycle. The GA was coupled to CHEMCAD, which performed the dynamic simulation. The main drawback of the stochastic methods is their computational intensity. The number of objective function evaluations is high, and since every evaluation is a dynamic simulation, the optimization takes a significant amount of time (in the magnitude of days). Moreover, we do not have information about the distance of the real and the calculated optimum due to the stochastic nature of the method.

The computational intensity could be reduced by using deterministic methods, although at the cost that finding the global optimum is not ensured. A potential method is the downhill simplex method. The original version was proposed by Spendley et al. [6] and was later improved by Nelder and Mead [7], among others. The objective function is evaluated in every (i.e.  $n+1$ ) vertex of a simplex in the  $n$ -dimensional space of the optimization variables. In the method of Spendley et al. [7], the vertex with the worst value of the objective function is reflected through the centroid of the remaining vertices. Through repeated reflections, the simplex roughly follows the gradient of the objective function. If the simplex is reflected onto itself in two steps, then its size is reduced. This procedure is continued until the size of the simplex becomes smaller than a given value.

In the BD and BED processes optimized by Hegely and Lang [5], methanol was recovered from a mixture of acetone(A)-methanol(B)-tetrahydrofuran(C)-water(D)-toluene(E). Both processes consisted of six consecutive batches with off-cut recycle. The optimization was performed consecutively, as well, by maximizing the profit of the individual batches. The aim of this work is to perform the optimization of a single batch of both processes by using the simplex method of Spendley et al. [7] in order to test whether it could be applied as a faster but equally well performing alternative to GA.

## 2. THE SEPARATION PROCESS

The mixture contains 0.07 mass% A, 37.14 % B, 4.89 % C, 56.34 % D and 1.56 % E. The recovery of B is disturbed by the azeotropes B–C (30 % B, 59.5 °C) and B–E (71.5 % B, 63.6 °C). The boiling points of the components and all the azeotropes, with azeotropic compositions were given



by Hegely and Lang [5].

The BD separation consists of the following steps [5]:

0. Heating-up of the column under total reflux.
1. 1<sup>st</sup> fore-cut: removal of C and E (incinerated).
2. 2<sup>nd</sup> fore-cut: removal of C and E (recycled).
3. Main-cut: product B in high purity.
4. After-cut: removal B from the residue (recycled) so that it could be sent to biological purification.

For BED, heating-up (Step 0) can be divided into two parts: a. No water feeding until the vapour reaches the top. b. Water is fed continuously to the column causing an increase in  $x_{D,C}$ .  $x_{D,E}$  decreases, but to a lesser extent than by BD. Water feeding can be stopped at the end of Step 0b or it can be still continued during Steps 1 and 2. In the latter case, the loss of B can be further reduced, but this dilutes the mixture from which B is to be recovered and can also increase the amount of fore-cuts increasing the cost of incineration and energy.

The column has 26 theoretical plates (including the reboiler); further details can be found in Hegely and Lang [5]. The volume of the charge was 25 m<sup>3</sup> (20 °C). The prescribed purity of B was 99.5 mass%. The duration of Step 0 (for BD) was 360 min. For BED Step 0a was 160 min long, after which water feeding (of 15 °C) was started. Step 0b was 200 min long. The termination criteria for the different steps: 1.  $x_{D,C} < Cr_1$  (mass fraction of C in the distillate), 2.  $x_{D,C} < Cr_2$ , 3.  $x_{M,C,B} < 99.52$  mass%, 4.  $x_{SR,B} < 0.25$  % (in the still residue).  $Cr_1$  and  $Cr_2$  were optimization variables.

### 3. OPTIMIZATION METHODS

The objective function (OF) maximized is the profit of the production:

$$OF = p_B m_{mc} + c_{inc} m_{FC1} - c_{st} \frac{Q_{st}}{r_{st}} t - c_{cw} \frac{Q_{cond}}{c_{p,cw} \Delta T_{cw}} - c_{bio} m_{sr} - c_{sw} F_D t_F \quad (1)$$

where  $m_{MC}$  is the mass of the main-cut,  $m_{FC1}$  is that of the 1<sup>st</sup> fore-cut.  $p_B$  is the price of methanol (0.46 \$/kg),  $c_{inc}$  is the cost of incineration (0.21 \$/kg),  $c_{st}$  is cost of heating steam of 3 bar (57.6 \$/t),  $r_{st}$  is its heat of condensation (2,263.5 MJ/t),  $\dot{Q}_{st}$  is the heat duty (1,800 MJ/h) and  $t$  is the duration of the whole process.  $Q_{cond}$  is total heat withdrawn by the cooling water,  $c_{p,cw}$  is the specific heat of the cooling water and  $\Delta T_{cw}$  is the increase in its temperature.  $F_D$  is the flow rate,  $t_F$  is the duration of water feeding. The cost of cooling water ( $c_{cw}$ ), the cost of water fed as entrainer ( $c_{sw}$ ), and the cost of biological purification ( $c_{bio}$ ) are neglected (not debited to the solvent recovery plant).

The optimization is subject to the following inequality constraints: the main-cut must satisfy the purity specification, the C/B and E/B ratios in the second fore-cut cannot exceed those of the traditional BD process applied in the plant (0.1068 and 0.1203, respectively). The latter constraints ensure the recyclability of the second fore-cut.

The optimization variables were the reflux ratios of the steps:  $R_1$  (1<sup>st</sup> fore-cut),  $R_2$  (2<sup>nd</sup> fore-cut),  $R_3$  (main-cut),  $R_4$  (after-cut), the termination criteria of Steps 1 and 2 ( $Cr_1$  and  $Cr_2$ ), and for BED,  $F_D$  and  $t_F$  (even integer). The bounds for reflux ratios were 0.6 and 15. The lower bound of termination criteria was 0.05 mass%, the upper bounds were 40 % (Step 1) and 10 % (Step 2), respectively. The value of  $Cr_1$  was also an upper bound for  $Cr_2$ . The ranges of water feeding variables were:  $0 \leq F_D \leq 3,000$  kg/h;  $0 \leq t_F \leq 1,000$  min. By BED, the location of water feeding was fixed at the top plate of the column based on former experiences.

The optimization method used by Hegely and Lang [5] was a real-coded elitist GA written in VBA under Excel. The parameters of the GA: mutation probability: 5 %, population size: 30, crossover



probability: 70 %, number of generations: 100.

The simplex algorithm was also written in VBA. In this version of the algorithm, the length of the sides ( $a$ ) of the simplex are identical. However, the optimization variables can vary in intervals of different magnitudes, as determined by their bounds, meaning that OF is more sensitive to some variables. To avoid numerical problems, the values of the variables were transformed to percentages of their possible variation: the lower bound corresponds to 0%, the upper one to 100%.

Two versions of the algorithm was tested. In the first one (runs BD 1-4, BED 1-4, *Table 1*), the size of the simplex is constant: the initial side length equals to the final one ( $a=a_s=a_f$ ). Calculations were performed with different  $a$  values to study its effect. The initial simplices were generated from  $X_{GA}$ , the optimal point determined by GA. The length of sides ( $a$ ) was a parameter whose effect on the results was investigated. The optimization was stopped when the simplex became stuck, that is, the last iteration reflects the simplex back to its penultimate position.

In the second version of the algorithm, the simplex changed its size. When the simplex became stuck, a new simplex was generated from its best point, but with half of the previous side length. The optimization stopped with the run with the given final side length ( $a_f$ ). Apart from starting from  $X_{GA}$ , optimization was also performed for BED with the initial simplex generated from a point of experimental conditions ( $X_{exp}$ , [8]):  $R_1=R_2=5.25$ ,  $R_3=R_4=2$ ,  $Cr_1=20\%$ ,  $Cr_2=1\%$ ,  $t_F=400$  min,  $F_D=1100$  kg/h.

OF is evaluated by dynamic simulation using the flow-sheet simulator ChemCAD. The violation of constraints is penalized by changing OF to -10,000 \$ by GA or the income to 0 \$ by the simplex algorithm. The phase equilibria are described with the UNIQUAC model.

### 3. RESULTS

The optimal values of the variables and the profit and its elements obtain by GA are given in *Tables 1 and 2*, respectively [5]. OF was evaluated 3,000 times in each case. BED clearly outperforms BD, mostly due to the increase of the amount of the product, although the decrease in the incineration cost is also notable.

*Table 1* Optimal values of the optimization variables obtained by GA. [5]

	$R_1$	$R_2$	$R_3$	$R_4$	$Cr_1$ , [mass%]	$Cr_2$ , [%]	$t_F$ , [min]	$F_D$ , [kg/h]
BD	6.22	3.07	3.05	5.41	17.5	2.62	-	-
BED	7.74	3.41	3.48	4.72	18.7	3.83	574	283

*Table 2* Elements of the profit (GA, [5]).

	Income, [\$]	Incineration cost, [\$]	Steam cost, [\$]	Profit, [\$]
BD	2597	492	1638	467
BED	3003	390	1820	793

The details of the optimization runs (ID of the run, starting point,  $a_s$  and  $a_f$ , the number of iterations) with simplex are shown in *Table 3*, which includes the profit and its elements, as well. The optimal values of optimization variables are given in *Table 4*.

The results with constant size simplices (BD 1-4, BED 1-4) are either identical to those obtained by GA, or improve the profit only slightly. All the runs stop in a dozen or less iterations (reflections). The effect of  $a$  is not clear: for BD, higher, for BED lower values led to the increase of the profit. By BD, multiple points of the initial simplex violate constraints. By BD 1-3, this is also true for the final simplices indicating that the local gradient points toward the constraint, stopping the



optimisation on the constraint. By BD 4, the simplex is able to leave the constraint, and stops near the original optimum. This could be explained either by the existence of a local optimum (as point with higher profit were found later), or, more likely by the possibility that the simplex is so small that the numerical errors of the simulation significantly influences the run.

With varying size simplices, the simplex algorithm performs much better. The number of iterations is higher and the profit is increased to a greater extent. Moreover, there is a considerable change in the values of the parameters, meaning that the algorithm is able to leave the immediate vicinity of  $X_{GA}$ .

By BD (BD 5), the most important changes are the decrease of  $R_1$  and the increase of  $Cr_1$  and  $Cr_2$ . The result is a decrease of the quantity and duration of the first fore-cut. The decreased steam (1.4%) and incineration costs (2.4%) compensate the slight decrease of the income (0.5%). The profit increases by 4.7%.

Table 3 Details of the optimization runs with the simplex algorithm and their elements of profit.

	ID	Starting point	$a_s$ , [%]	$a_f$ , [%]	$N_{it}$	Income, [\$]	Incineration cost, [\$]	Steam cost, [\$]	Profit, [\$]
BD	1	$X_{GA}$	1		4	As obtained by GA			
	2		0.5		6	2609	492	1640	477
	3		0.05		5	2609	492	1640	477
	4		0.005		9	2609	492	1640	477
	5	5	0.625	67	2585	480	1615	489	
BED	1	$X_{GA}$	1		10	2999	389	1818	793
	2		0.5		9	3005	388	1822	794
	3		0.05		5	As obtained by GA			
	4		0.005		1	As obtained by GA			
	5		5	0.625	39	3017	386	1837	795
	6	$X_{exp}$	16	0.5	43	2873	376	1878	619

Table 4 Optimal values of the optimization variables obtained by the simplex algorithm.

	ID	$R_1$	$R_2$	$R_3$	$R_4$	$Cr_1$ , [mass%]	$Cr_2$ , [%]	$t_F$ , [min]	$F_D$ , [kg/h]
BD	1	As obtained by GA						-	-
	2	6.18	3.10	3.08	5.44	17.6	2.64		
	3	6.23	3.07	3.06	5.41	17.5	2.62		
	4	6.22	3.07	3.05	5.41	17.5	2.62		
	5	5.55	3.02	3.15	5.50	19.2	2.94		
BED	1	7.71	3.49	3.45	4.67	18.7	3.80	577	287
	2	7.78	3.39	3.48	4.73	18.7	3.82	577	277
	3	As obtained by GA							
	4	As obtained by GA							
	5	7.94	3.55	3.55	4.85	19.0	3.69	573	273
	6	5.74	5.59	4.08	2.46	21.2	2.39	434	1192

By BED, when starting from  $X_{GA}$  (BED 5), all the reflux ratios and  $Cr_1$  increases, while  $Cr_2$ ,  $t_F$  and  $F_D$  decrease. The quantity of the first fore-cut is slightly decreased. Although increasing the reflux ratios increases the duration of the process, the amount of the product is also higher. As a result, the profit is almost identical to that found by GA, even though the profit elements have different values. Optimization of BED was also started from  $X_{exp}$  (BED 6) to test whether the simplex algorithm can



approach the optimum starting from a point further away. At  $X_{exp}$ , the income was 2107 \$, the incineration cost 346 \$, the steam cost 1828 \$, and the profit -67 \$. The simplex algorithm was able to quickly find (in 43 iterations) a much higher value of OF than the starting value, but the results are still far from that of  $X_{GA}$ . Compared to the point found in BED 5 or to the results of GA,  $R_1$ ,  $R_4$  and  $Cr_2$  are lower,  $R_2$ ,  $R_3$  and  $Cr_1$  are higher.  $t_F$  is lower and  $F_D$  is significantly higher. The greatest changes are observed in  $R_4$  and  $F_D$ , but we must note that OF is not very sensitive to these variables, especially not to  $R_4$ . The value of  $F_D$  is close to that in  $X_{exp}$ . The profit is considerably lower (by 22%) due to lower income (by 4.8%) and higher steam cost (by 2.2%).

## CONCLUSIONS

The applicability of downhill simplex algorithm proposed by Spendley et al. [6] for the optimization of a batch distillation (BD) and a batch extractive distillation (BED) process was studied. The objective function to be maximized was the profit, which was evaluated by performing dynamic simulation with the flow-sheet simulator CHEMCAD. The optimization variables were the reflux ratios of the steps, the termination criteria of the fore-cuts and for BED, the parameters of the entrainer feeding (flow rate, duration). First, optimization was performed using constant size simplices, starting from the optimum determined earlier by a genetic algorithm [5]. The optimization stopped after less than a dozen iterations with slight or no increase in the profit, depending on the size of the simplex. Then, the optimization was repeated with variable size simplex. By BD, the profit increased by 5%, while by BED, the improvement was negligible. These results proved that the results of genetic algorithm had already been close to the global optimum, and no significant further improvement can be expected. By BED, an optimization run was also started from a point further away from the optimum. The simplex algorithm was unable to find the optimum, but it improved the profit greatly in only a small number of iterations.

## ACKNOWLEDGEMENT

This work was supported by NKFI-OTKA (Hungarian Scientific Research Fund, Project No.: K-120083).

## REFERENCES

- [1] Yatim, H., Moszkowicz, P., Otterbein, M., Lang, P.: *Dynamic simulation of a batch extractive distillation process*. Comput. Chem. Eng. 17, S57-62., 1993.
- [2] Luyben, W.L., Chien, I.L.: *Design and Control of Distillation Systems for Separating Azeotropes*. John Wiley & Sons, Inc., Hoboken, New Jersey, 421-422., 2010.
- [3] Lang, P., Kovacs, G., Kotai, B., Gaal-Szilagyi, J., Modla, G.: *Industrial application of a new batch extractive distillation operational policy*. IChemE Symp. Ser., 152. 830-839., 2006.
- [4] Mujtaba, I.M.: *Batch Distillation: Design and Operation*. Imperial College Press, London, 2004.
- [5] Hegely L., Lang P.: *Optimization of a batch extractive distillation process with recycling off-cuts*. Journal of Cleaner Production, 136, 99-110., (2016)
- [6] Spendley, W., Hext, G. R., Himesworth, F. R.: *Sequential Application of Simplex Designs in Optimisation and Evolutionary Operations*. Technometrics, 4(3), 441-461., 1962.
- [7] Nelder, J. A., Mead, R.: *A simplex method for function minimization*. Computer Journal, 7, 308-313., 1965.
- [8] Hegely, L., Lang, P., Kovacs, G.: *A new batch extractive distillation operational policy for methanol recovery*. Chem. Eng. Trans. 35, 949-954., 2013.



## DESIGN OF THE SUPPORTING FRAME FOR THE FIRE-FIGHTING ADAPTER USING THE SHAPE GENERATOR

<sup>1</sup>*HNILICOVÁ Michaela PhD, <sup>2</sup>MATEJ Jaroslav PhD, <sup>3</sup>DADO Miroslav PhD, <sup>3</sup>HNILICA Richard PhD*

<sup>1</sup>*Department of Forest Harvesting, Logistics and Ameliorations, Faculty of Forestry, Technical University in Zvolen, T. G. Masaryka 24, 960 53 Zvolen, Slovak Republic*

<sup>2</sup>*Department of Mechanics, Mechanical Engineering and Design, Faculty of Environmental and Manufacturing Technology, Technical University in Zvolen, Študentská 26, 960 53 Zvolen, Slovak Republic*

<sup>3</sup>*Department of Manufacturing Technology and Quality Management, Faculty of Environmental and Manufacturing Technology, Technical University in Zvolen, Študentská 26, 960 53 Zvolen, Slovak Republic*

### Abstract

*This post describes a use of the new Autodesk Inventor model package, namely the shape generator. It evolves and imitates the evolutionary approach of nature in the form of generative design. The use of the shape generator package is showed on a design of the carry frame of a fire fighting adapter placed on a forest wheeled skidder.*

**Keywords:** *supporting frame, shape generator, design, software, construction.*

### 1. INTRODUCTION

The Shape Generator, introduced in Autodesk Inventor R2 2016, is technology in some features similar to topological optimization. It uses the principles of generative design, in which it is necessary to define a set of parameters, respectively rules, while the internal Shape Generator algorithm in the cycle generates the component design itself unless an optimal solution is found. Topology optimization is a tool based on the finite element method and defined criteria to optimize the initial solution in order to achieve the goal. However, the result may be expensive or unmanageable by common production techniques, although with the continued development of technology, the manufacturing criteria can also be applied. At present, the solution is an additive manufacturing technology, 3D printing. [3]

Generative design simulates the natural evolutionary approach. Designers or engineers inserted aims to software for generative design, along with parameters such as materials, production methods and cost requirements. Then, using cloud computing, the software examines all possible permutations of the solution and generates design alternatives. It tests and learns from every iteration what works and what does not. Using a generic design does not result in one solution but a potentially large number. [1]

Generic design covers these optimization methods [1]:

- Form synthesis - With this approach, designers or engineers input their goals and constraints, and the software runs artificial intelligence-based algorithms to produce a wide range of design alternatives.
- Lattice and surface optimization - This method applies internal lattices and optimized surface structures to an existing component to make it lighter and stronger.



- Topology optimization - This approach reduces the weight of an existing component by running analysis to remove unnecessary material, while meeting or exceeding performance criteria.
- Trabecular structures - This method precisely scales and distributes tiny pores through solid materials, and creates surface roughness to mimic bone in medical implants to help patients heal.

For more information on this topic can be found in the project Dreamcatcher [2]. We decided to use this relatively new tool and present, in short, the results and experiences we achieved.

## 2. METHODS

By solving the submitted paper, we mainly tried to present a new approach to the design of lightweight, structurally efficient parts. The Shape Generator provides an intelligent strategy to maximize the stiffness of the parts based on the specified limitations.

Work methodology consisted of the following activities:

- defining the model envelope (volume),
- carry out a geometry is optimized based on user input, such as loading condition, anticipated pressure, and targeted weight reduction threshold,
- detailed construction design of supporting frame for the fire-fighting adapter,
- FEA analysis of the model and its modifications if needed.

## 3. RESULTS

Scheme frame holder tanks were processed in Autodesk Inventor using the Shape Generator. This tool works quite differently from conventional optimization tools, so in short lists and its use. A common optimization task optimizes the parameters of the finished model. It can be of dimensions such as length, cross-section, type cross-section, material, etc. However, the basic structure of the model must already be known and the optimization only improves it. The result is good but only if the quality and original design. Shape Generator uses a different approach based on locally adding material only where it is needed. It requires the definition of boundary conditions, ergo places where the model will be mounted where they work force and their size. Next, it is necessary to define the maximum possible envelope of the model, i.e. volume model that can take in all directions. As a result, we have obtained an amorphous volume, in the form of a finite element network, which we have used as a guide for the frame holder construction of a standard material (Fig. 1 to Fig. 4).

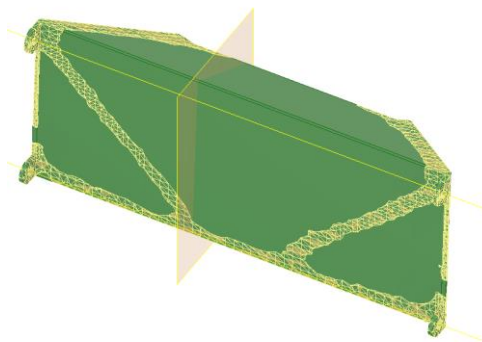


*Figure1* The front view of the defined envelope of the model and the resulting network created by the Shape Generator

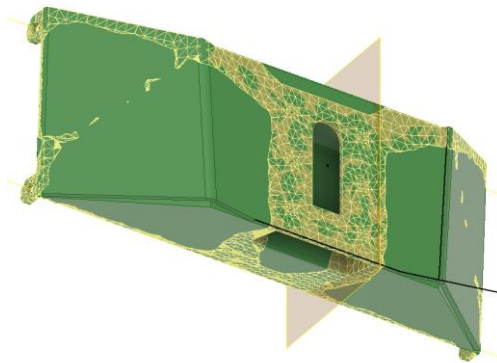


*Figure 2* Rear view of the defined envelope of the model and the resulting network created by Shape Generator

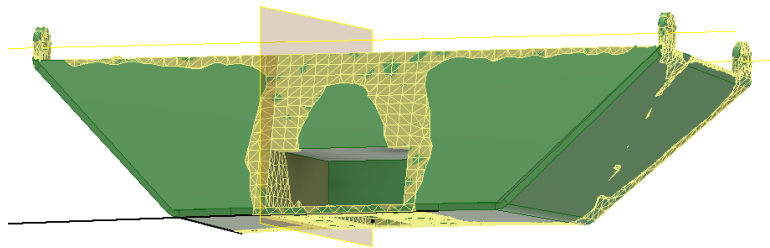


*Figure 3* The bottom view of the defined envelope of the model and the resulting network created by the Shape Generator

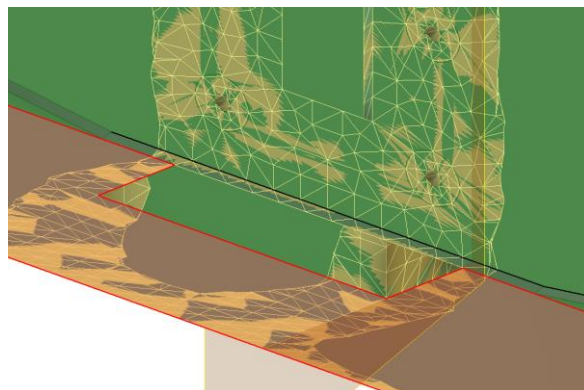


*Figure 4* A detailed view of the defined envelope of the model and the resulting network created by the Shape Generator

On the basis of the resulting amorphous model as a finite element mesh, we started the draft supporting frame of the fire-fighting adapter. The supporting frame will carry a fire-fighting adapter consisting of the composite tank, the protective frame, the pump and the fire-fighting equipment. The resultant shape of the carrier frame is shown in Fig. 5.



Figure 5 Design of the supporting frame for the fire-fighting adapter

Based on FEA analysis (Fig. 6), we made minor changes to increase the strength of the frame. These adjustments are illustrated by the red dots in Fig. 7. The results after the reload are reduced to an acceptable level (Fig. 8).

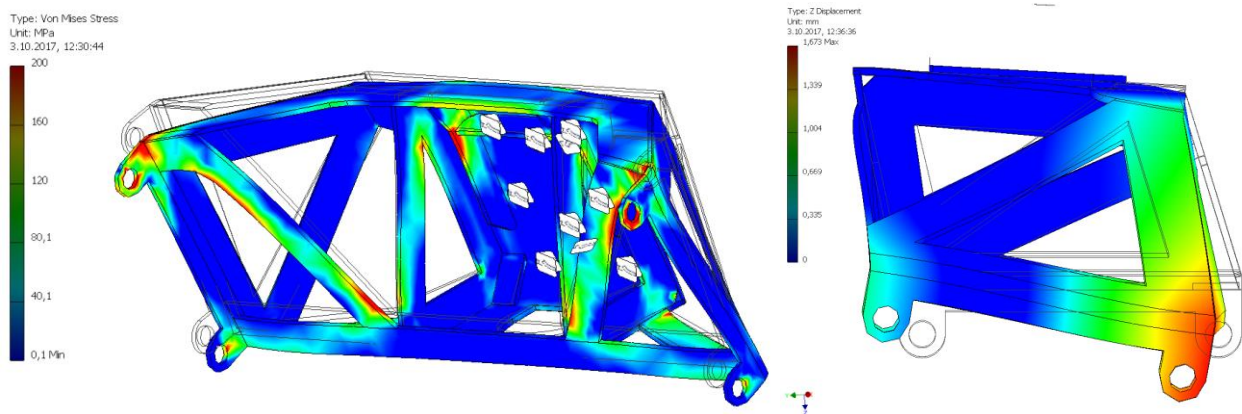


Figure 6 FEA analysis – max Von Mess Stress 461 MPa, max z displacement 1,67 mm

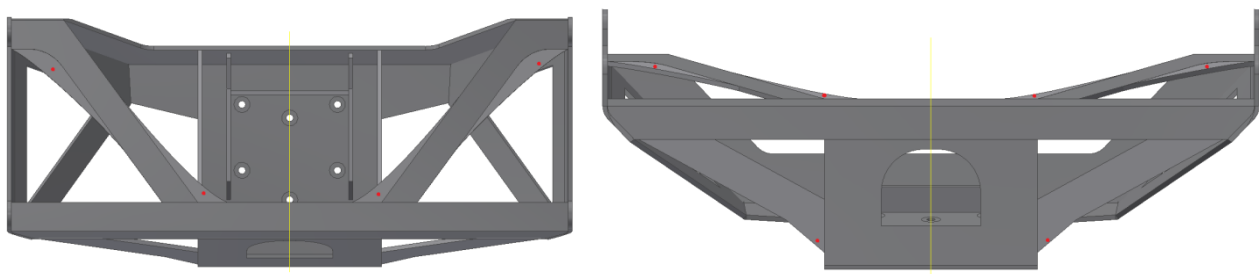


Figure 7 Modifying the supporting frame

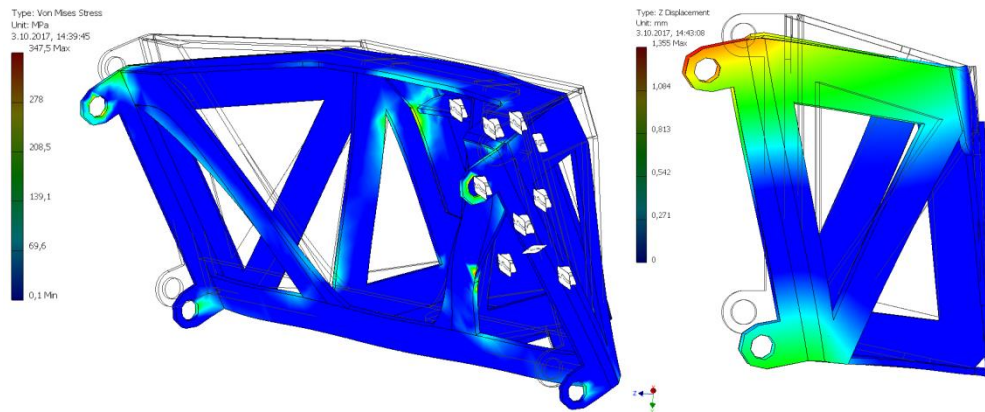


Figure 8 FEA analysis – max Von Mess Stress 347 MPa, max z displacement 1,355 mm

It means that the Shape Generator does not prescribe a detailed construction solution. The tool provides a help only, and the final design is influenced at least by a manufacturing method. However, in a case of an additive manufacturing method, the product can be manufactured, e.g. printed, directly, using the tool's output. From point of view of the overall design, the frame created with the tool's support achieved lower weight in comparison with designs based on one's individual experiences. Conclusions resulting from the present design of a design element will be tested under realistic conditions when the tank is waterlogged and functionally and operationally tested.

## CONCLUSIONS

Based on the procedures and results presented in this post, we can conclude that the presented software package is an excellent tool for designing and creating structural parts of different constructions. The basics of designing now consist in creating the structure of the model and its subsequent optimization. By using the shape generator, it is enough to define its maximum volume bounded by boundary conditions. Output is then an indication of the structure of the model that can be take form in all directions. We have verified this fact on the part proposed by us, and we will address this solution also in the future. After determining the boundary conditions Shape Generator own algorithms determine where you need to add mass and where it is unnecessary.

## ACKNOWLEDGMENT

This work was supported by the Slovak Research and Development Agency under the contract No. APVV-14-0468 „Development of an auxiliary device and its technological employment to increase the efficiency of extinguishing forest fires“.

## REFERENCES

- [1] Autodesk: Generatívny dizajn / Generative design. [cit. 13.9.2017] online: <https://www.autodesk.com/solutions/generative-design>
- [2] Autodesk Research: Project Dreamcatcher. [cit. 14.9.2017] online: <https://autodeskresearch.com/projects/dreamcatcher>
- [3] Michael Thomas: The More Things Change - Generative Design. [cit. 13.9.2017] online: <https://designandmotion.net/autodesk/the-more-things-change-generative-design/>
- [4] Shigley, J. E., Mischke, Ch. R., Budynas, R. G. 2010. Konstruování strojních součástí / Mechanical Engineering Design. VITIUM (2010), ISBN 9788021426290, 1159 p.



## APPLICATION OF THERMALLY STIMULATED DISCHARGE CURRENT METHOD FOR INVESTIGATION OF FINE STRUCTURE OF POLYMERIC MATERIALS

*IHEMAGUBA Chukwuemeka, KÁLMÁN Marossy PhD*

*Department of Polymer Engineering, Faculty of Materials Science and Engineering, University of Miskolc*

*E-mail: [chukwuemeluck@yahoo.com](mailto:chukwuemeluck@yahoo.com), [polkal01@uni-miskolc.hu](mailto:polkal01@uni-miskolc.hu)*

### **Abstract**

*Thermally stimulated discharge current method have been used for the investigation of fine structure of polymeric materials. In the research, both solids and liquid materials were investigated. The study was performed on some disk-shaped, gold plated solid film samples prepared from polymeric materials such as polybutadien, CPVC, plum gum, polyamide, PUR, etc. These materials were synthesized using either compression molding, reaction casting, solution casting or by mixing and roll milling processing techniques at BorsodChem Vinyl Technology's Laboratory. Gold plated solid samples were used thereby avoiding air gaps. Liquid samples such as polyol, Biocizer, DOP, DUP, DINCH, etc, were also investigated using TSD. DSC technique was used in addition for the liquid samples for comparison purposes. For DSC on liquid samples no sample preparation was required, while for TSD 8mm disk shaped borosilicate glass paper was used as carrier due to its high tolerance to heat and extreme resistance to severe temperature changes and low polarizability.*

*From the TSD result of the liquid samples a major transition peak was observed at temperatures well below their melting point. This was observed for all liquid samples tested, which may be as a result of the molecular movement and segmental motion of their side chains, although this phenomena have not been recorded in literature before. It was also observed that the shift of the low temperature peak depends on the length of the alkyl group on the molecule. In the solid polymers, over the glass transition several other transitions were observed. In case of polymer alloys, the individual glass transitions appeared in the measured depolarization curve.*

*Thus the results obtained shows that TSD does not just study the structure of polymeric materials, but it is an excellent tool for fine structure investigation of both solid polymers and liquid additives.*

**Keywords:** *Polymers, thermally Stimulated discharge (TSD), relaxation, glass transition, differential scanning calorimetry (DSC)*

### **1. INTRODUCTION**

Scientists, engineers and researchers have constantly and effectively carry out researches and experiments, in other to study, determine and characterize different materials. Experiments and tests such as mechanical, corrosion, electrical, dielectric tests, etc., has been used to unravel the properties and to determine the best area of application of engineering materials [1-3].

However, these tests are not enough to fully characterize polymeric, dielectrics and some other crystalline and non crystalline materials.

In view of this, tests and equipments such as differential scanning calorimetry (DSC), dynamic mechanical analysis (DMA), dielectric analysis (DEA), thermally stimulated discharge (TSD), and so many others were introduced and developed.



DSC measures the enthalpy changes that occur as a result of change in physical and chemical properties of the material as a function of either temperature or time [4-5]. DEA is used for the determination of cure state and material activation energy [6-9]. DMA is most important for the study of visco-elastic behavior of polymers or to study the mechanical performance or behavior of materials as the temperature is altered [9]. While on the other hand, TSD/TSDC studies the structural property changes in materials as they undergo changes in temperature, in the presence (polarization) and absence (depolarization) of electric field.

Although this (TSD) method does not or cannot be used to measure any engineering data, such as hardness tensile strength, etc, it has been described as a powerful tool or method for the study and characterization of dielectrics, polymers, co-polymers, di-polymers, some crystalline and non-crystalline materials [19-20]. The technique is basically for the detection of transitions which depends on the changes in mobility of molecular scale dipolar structural units [18]. The technique helps one to understand and evaluate relaxation processes, molecular parameters (such as relaxation frequencies, distribution functions, activation energy) in these materials [7, 9-12]. It possesses a high resolution power as compared to DSC, DMA, and other thermal analyses techniques. [18]. One of its major industrial applications is in the manufacturing of capacitors.

TSD method can be traced back to 1936 to Frei and Droetzinger from Germany, with the title 'Liberation of electrical energy during the fusion of electrets' [9], while according to G.M. Sessler, it was first applied systematically by Fiecchi and his group, noting that, although a similar work was done in early 1936 [13-16].

## 2. METHODS

The method employed for this research is that of thermally stimulated discharge. It is basically the study of polymeric materials by simple mechanism which involves heating up the sample to a temperature well above its melting point, applying electric field at this temperature, leaving it at this temperature for some time to make room for uniformity, then cooling it at a specific rate to low temperatures below the freezing point, after which the polarization field is short circuited. It is then left at this temperature for some time and the heating up of the sample takes place again at constant rate to the initial higher temperature. The essence is to study the characteristics of materials as they undergo changes in temperatures in the presence (polarization) and absence (depolarization) of applied field.

The relaxation time  $\tau$  which is temperature dependent characterizes the relaxation processes in materials and controls both the polarization and depolarization. It is given by the Arrhenius law represented by equation 1 below [18].

$$\tau_{(T)} = \tau_0 e^{\left(\frac{A}{RT}\right)} \quad (1)$$

Where  $\tau_0$  is a constant (pre-exponential factor), A is the activation energy and R is the universal gas constant.

And the polarization as a function of time at temperature T is given by the following equation [18]

$$P_{(t)} = P_0 \left(1 - e^{-\frac{t}{\tau}}\right) \quad (2)$$

Where  $P_0$  is the equilibrium polarization at a given temperature T, and applied field E.

The figure 1 below shows the schematic diagram of the TSDC experimental setup, while figure 2 shows the process which takes place during TSD test.

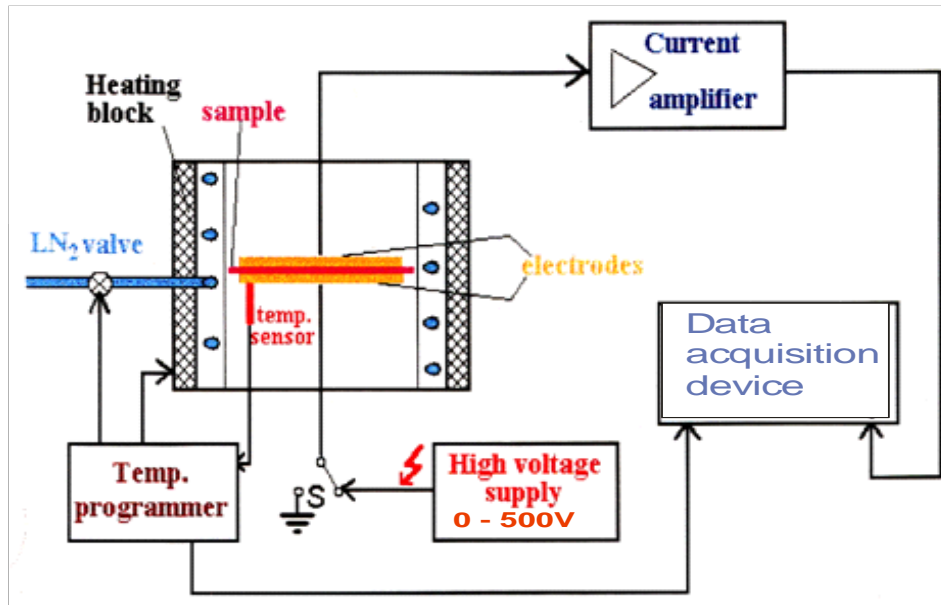


Figure 1 schematic diagram of the TSDC experimental setup [18]

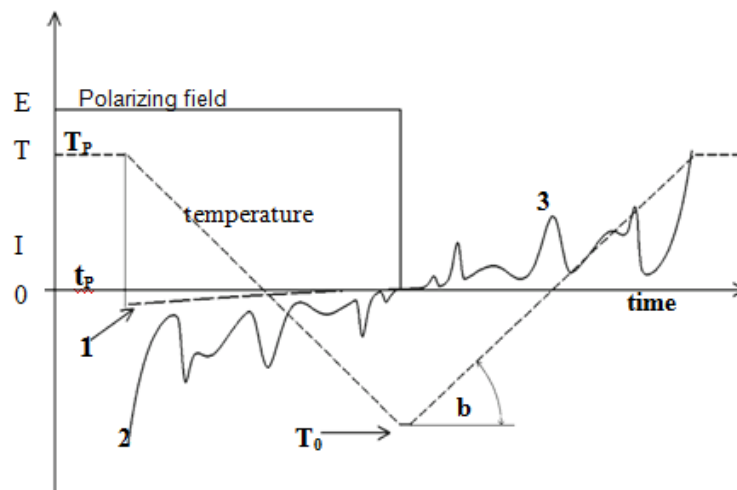


Figure 2 Schematic diagram of the TSDC experimental setup [18]

The electric field  $E$  polarizes the sample at polarizing temperature  $T_p$  for a certain time  $t_p$  and then cooling down takes place.

$I$  is the conductive,  $2$  is the polarization current. Getting to the initial temperature  $T_0$  the electric field is turned off (sample short circuited) and heated by a heating rate  $b$ , to obtain the depolarization current  $3$

The principle is based on the knowledge that when a polymeric material (or any insulator) is kept in an electric field, its particles become oriented in the direction of the applied field; the higher the field the more oriented the particles become. The disorientation of particles takes place when the field is removed thereby current is generated by the charges. However, this disorientation can be hindered by cooling the sample in the presence of the field thereby forming a permanently polarized material (electret) [17]. The differential scanning calorimetry method was used as well for investigating further the liquid materials for the sake of comparison, since the TSD test gave an



unexpected result. The table below shows the experimental condition of the investigated materials as well as their processing techniques.

*Table 1* Specification and Experimental Condition of Sample

Solid samples	preparation method	Liquid samples		
			preparation method DSC	TSD
Gelatene	Solution casting	Diocetyl phthalate (DOP)	<b>No sample preparation required for TSD</b>	<b>8mm diameter Borosilicate glass paper was used as fluid carrier</b>
Plum gum	Solution casting	vestaline		
Poly amide	compression molding	Di Iso Decyl Phthalate (DIDP)		
Polybutadien base copolymer	Compression molding	Di Undecyl Phthalate (DUP)		
Polyurethane	reactive casting	Diisotridecyl Phthalate (DTDP)		

### 3. RESULTS

TSD results obtained after resolution of peaks are shown below for the tested materials

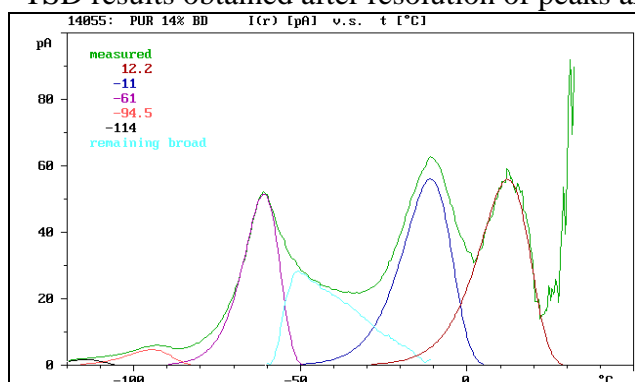


*Figure 3* TSD result and resolved peaks for PUR

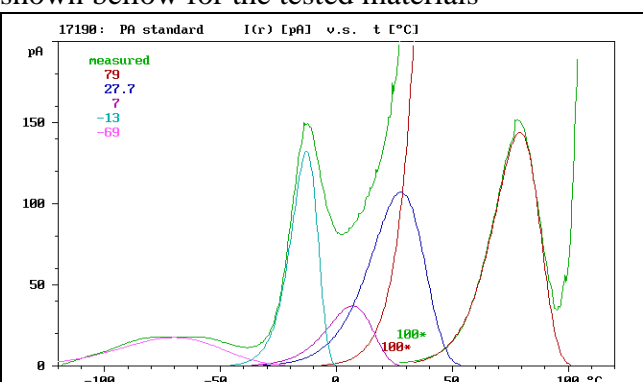


*Figure 4* TSD result and resolved peaks for PA

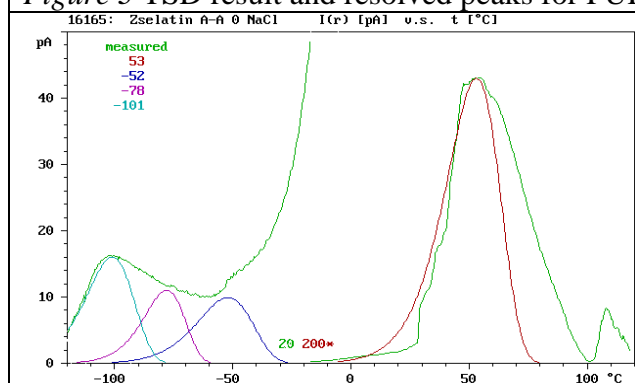


*Figure 5* TSD result and resolved peaks for Gelatene

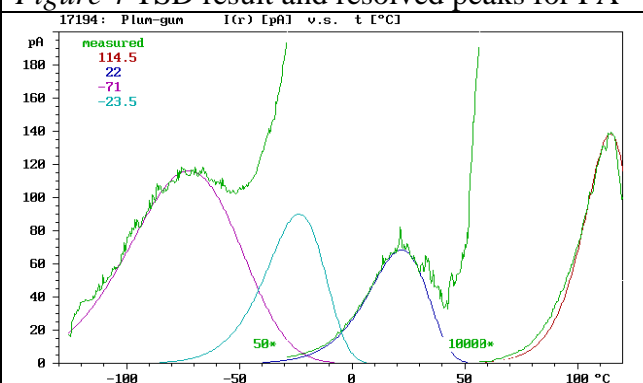


*Figure 6* TSD result and resolved peaks for Plum-gun



As seen in the above results, the noisy transition peaks was resolved and multiple transitions were obtained, revealing some initially hidden transitions in the polymer chains both below and above their glass transition temperatures

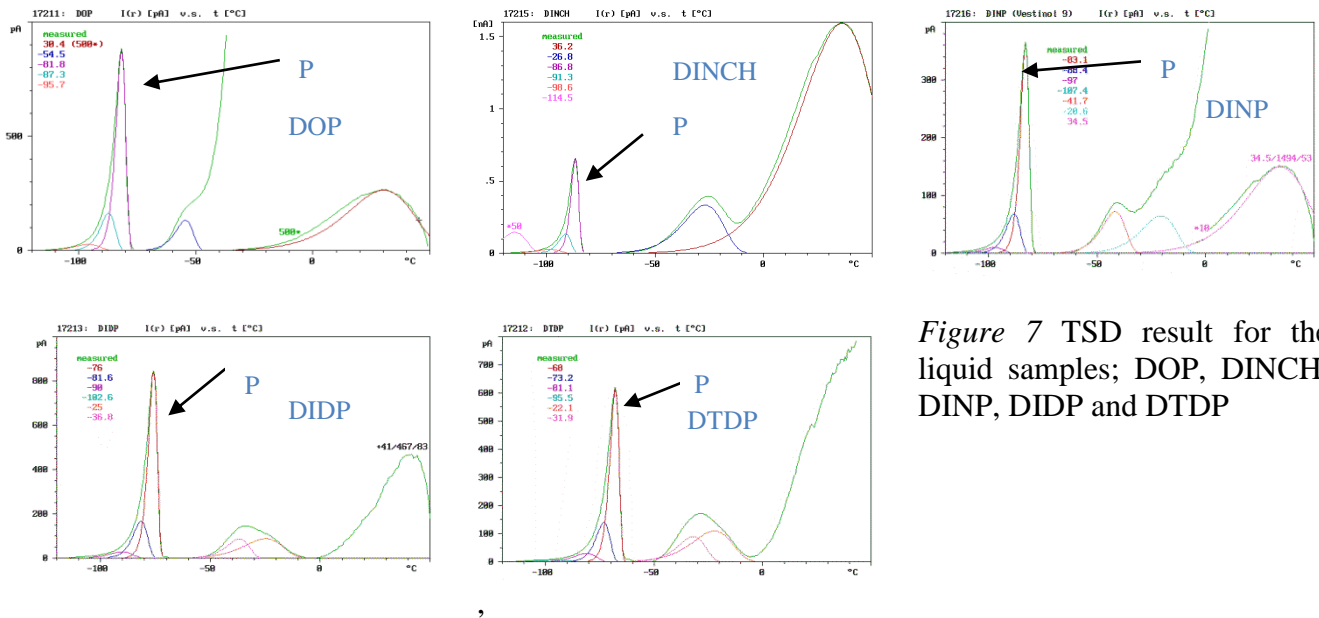


Figure 7 TSD result for the liquid samples; DOP, DINCH, DNP, DIDP and DTDP

The result shows that there are pronounced transition peak (p) well below the melting points of these materials, which may be as a result of the molecular movement and segmental motion of their side chains, even at this low temperature.

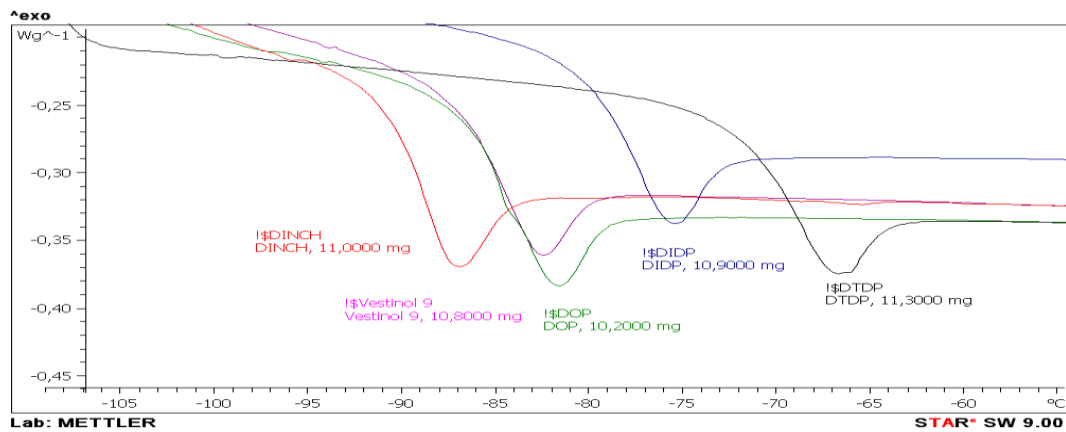


Figure 8 combined DSC result for DOP, DINCH, Vestinol 9, DIDP, DTDP and DNP for comparison

From the DSC result above, it is evident that the lower transition peaks for all the tested materials are similar. It is seen that the shift of the low temperature peak depends on the length of the alkyl group on the molecule; that is as the number of carbon chain in the compound increase; from DOP (8 carbon); Vestinol 9 (9); DIDP (10); DNP (11 carbon); DTDP (13 carbon), the lower the transition temperature.



## CONCLUSIONS

Solid Polymeric materials and liquid additives have been characterised using TSD and DSC was used in addition for the liquid materials for comparison purposes, due to a shocking result obtained from their TSD test. Results show that even frozen liquids show transition well below their melting point. And the analysis of these transitions could explain the low temperature behaviour of plasticised polymers

## ACKNOWLEDGEMENT

I wish to acknowledge the support of the Stipendium Hungaricum Scholarship, tempus Public foundation, and the Nigeria Federal Scholarship Board, for their efforts in making this research possible.

## REFERENCES

- [1] Kantesh, B.: *Physical and Mechanical Properties of Polymers Biosurfaces: A Materials Science and Engineering Perspective*. 329–44. 2015.
- [2] Kantesh, B.: *Physical and Mechanical Properties of Polymers Biosurfaces: A Materials Science and Engineering Perspective*. 329–44. 2015.
- [3] Api, P., Olorunniwo O. E., Ige, O.O.: *Corrosion Resistance Through the Application of Anti-Corrosion Coatings*. *Developments in Corrosion Protection*. 241–70., 2014.
- [4] Alegria, A., Goitiandia, L., Colmenero, J.: *On the Interpretation of the TSDC Results in the Study of the  $\alpha$ -Relaxation of Amorphous Polymers*. *Polymer Journal*, 2915–23., 1996.
- [5] Turnhout, J. V.: *Thermally Stimulated Discharge of Polymer Electrets*. *Polymer Journal*, 2, 173–191., 1971.
- [6] Havriliak, S., Negami, S.: *A Complex Plane Representation of Dielectric and Mechanical Relaxation Processes in Some Polymers*. *Polymer*, 8, 161–210., 1967.
- [7] Neagu, E., Pissis, P., Apekis, L., Gomez Ribelles, L. G.: *Dielectric Relaxation Spectroscopy of Polyethylene Terephthalate (Pet) Films*. *Journal of Physics D: Applied Physics*, Volume 30
- [8] Huan L. L., *The Handbook of Dielectric Analysis and Cure Monitoring*, Lambert Technologies, 2014.
- [9] J van Turnhout, 'Thermally Stimulated Discharge of Polymer Electrets', *Polym J*, 2.2 , 173–91., 1971.
- [10] Kleemann, T. A.: *An Investigation into Solid Dielectrics*. 231, 2012.
- [11] Shunli Z., *Thermally Stimulated Depolarization Current*. Shunli Zhao, 74., 2014.
- [12] Rosu, D., Varganici C. D., Visakh, P. M., et-al.: *Thermal Degradation of Polymer Blends, Composites and Nanocomposites*. 17–50., 2015. (txt bk)
- [13] Kryszevski, M., Zielinski, M., Sapiuha, S.: *Analysis of Relaxation Processes in Methacrylate Polymers by Thermally Stimulated Discharge*. *Polymer*, 17.3, 212–16., (1976).
- [14] Wikipedia, [https://en.wikipedia.org/wiki/Thermally\\_stimulated\\_current\\_spectroscopy](https://en.wikipedia.org/wiki/Thermally_stimulated_current_spectroscopy), 7/08/2017
- [15] Sessler, G. M.: *Topics in applied Physics*, volume 33, Springer Science & Business media
- [16] Mulayam, S., Gaur, B., Singh, R.: *Thermally Stimulated Current and Differential Scanning Calorimetry Spectroscopy for the Study of Polymer Nanocomposites*. 315–21., 2010
- [17] Wenxiang, X., Qinglin, D., Huaifa M., et-al.: *Interfacial Effect on Physical Properties of Composite Media: Interfacial Volume Fraction with Non-Spherical Hard-Core-Soft-Shell-Structured Particles*. *Scientific Reports*, 5.November, 16003., 2015.



# INTERNATIONAL SCIENTIFIC CONFERENCE ON ADVANCES IN MECHANICAL ENGINEERING

12-14 October 2017, Debrecen, Hungary



- 
- [18] Marossy, K.: *Practical Approach to Thermally Stimulated Discharge (TSD) Method on Polymers*. Journal of Thermal Analysis and Calorimetry. 129.1, 161–70., 2017.
- [19] Shalloway, M.: *An Investigation of Electrets*, Msc Thesis, Georgia Institute of Technology. 1951.
- [20] Somdee, P.: *Heat conductive Polyurethanes*, PhD Student, University of Miskolc, Hungary



## NUMERICAL SOLUTION OF FRICTION STIR WELDING COMPARED BY EXPERIMENTAL MEASUREMENT

*JANČO Roland PhD, ÉCSI Ladislav PhD, ÉLESZTŐS Pavel CSc*

*Institute of Applied Mechanics and Mechatronics, Faculty of Mechanical Engineering, Slovak University of Technology in Bratislava*

*E-mail: [roland.janco@stuba.sk](mailto:roland.janco@stuba.sk), [ladislav.ecsi@stuba.sk](mailto:ladislav.ecsi@stuba.sk), [pavel.elesztos@stuba.sk](mailto:pavel.elesztos@stuba.sk)*

### **Abstract**

*Friction Stir Welding (FSW) is one of the most effective solid state joining processes. It enables to weld materials which cannot be welded by conventional methods. As a result, it has many applications in various industries. Numerical simulation of the process moreover can provide valuable information about the evolution of the physical quantities accompanying the FSW, such as temperature distribution, local metallurgical phase proportions, stress and strain distributions, which can directly or indirectly be determined during the welding process. Proper numerical simulations furthermore require modelling the interactions between thermal, metallurgical and mechanical phenomena in the material. The aim of this paper is to describe a thermal-fluid-flow-structural simulation of FSW using the finite element method and the way of controlling the temperature values at selected points. The numerical results are compared with experimental results.*

**Keywords:** *Friction Stir Welding (FSW), aluminium alloy, Finite element method, Thermal-fluid-flow-structural analysis, Experimental measurement.*

### **1. INTRODUCTION**

Friction stir welding (FSW) is a relatively new joining technology. It was developed and patented by The Welding Institute (TWI), United Kingdom in 1991 [1]. The FSW is a solid state welding process and is particularly suitable for the creation of good quality butt and lap joints. It has also been proved to be ideal for welding materials which cannot be welded by conventional fusion welding. Figure 1 depicts the scheme of the friction stir welding process.

Since the welding zone is isolated from the atmosphere during FSW there is low probability of creation of voids in the welding zone as well as the defects commonly associated with fusion welding. Moreover, the residual deformations associated with the welding technology are smaller too, due to the fact that the material is not melted during the welding process. FSW has many applications in aerospace, automobile and shipbuilding industries [4, 5, 6].

FSW is particularly suitable for welding aluminium alloys, because no additional material is required for the welding process. The major disadvantage of the process however is that it is difficult to control the microstructure of the material, the residual stresses and the deformations associated with the welding process, which directly affect the mechanical properties of the material, as well as the quality of the welded joint, or the geometry of the construction. In fact, high residual stresses can lead to an unexpected geometry, or [4] result in a great deterioration of the fatigue life of the material.

From the physical point of view, the FSW simulation is a multi-physical finite element simulation, which takes into account the strong coupling between the thermal, metallurgical and mechanical



phenomena, various internal processes and the dependence of the material properties of the welded material on temperature, accumulated plastic strain or metallurgical structure [2, 3]. Since the finite element analysis is sensitive to the imposed boundary conditions, careful considerations are needed when modelling the contact between the welded sheets and the rotating tool during the numerical simulation of the FSW.

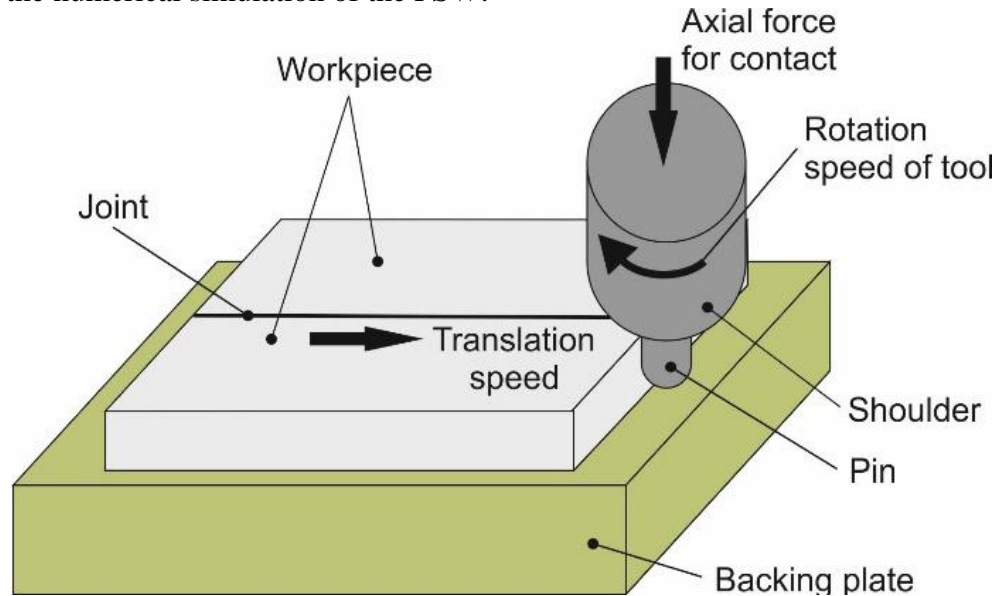


Figure 1 The scheme of the FSW process

## 2. THERMAL-FLUID-FLOW NUMERICAL ANALYSIS USING THE SYSWELD FINITE ELEMENT CODE

The aim of this section is to describe the first stage of the FSW numerical simulation of an aluminium alloy AlMg4.5Mn0.7 sheet without phase changes using the FSW module of the SYSWELD commercial finite element code [7, 8]. The actual numerical analysis consists of two stages, namely the thermal-fluid-flow analysis stage in order to determine the temperature field and the velocity field in the welded material and a following structural analysis stage in order to determine the stress field and the associated displacement and strain fields in the welded material. Here the first stage of the analysis is presented.

In the thermal-fluid-flow analysis the welded sheets are considered to be as a viscous fluid which flows around a rotating tool with its axis of rotation fixed at the location of the pin of the FSW device. The thermal properties for the sheet and backing plate are listed in Tab. 1. In the numerical analysis there was considered a friction coefficient of 0.238, a linear welding velocity of 1.67 mm/s and 41.89 rad.s<sup>-1</sup> rotation velocity of the tool. The room temperature was 15 °C and the heat transfer coefficient 19 W/(m<sup>2</sup>.K). The geometry of the pin was defined by the following data. The lower diameter of the pin was 4.64 mm, the upper diameter 12 mm and its length was 4.5 mm. The tool was made from a ceramic material [7].

Figure 2 depicts the finite element model of the sheet, the backing plate and the tool used in the analysis. The numerical analysis was carried out using the SYSWELD® commercial package. Fig. 3 shows a few selected results coming from the finite element analysis.

## 3. MEASUREMENT OF TEMPERATURE DURING FSW

To verifying the results of the numerical analysis, there was carried out an experimental measurement of the temperature field of the welded sheet. The measurement took place in the



Welding Research Institute - Industrial Institute of SR in cooperation with the staff of the Institute of Automation, Measurement and Applied Informatics, Faculty of Mechanical Engineering, Slovak University of Technology in Bratislava. Figure 4 depicts the FLIR® SC660 camera used in thermography to determine the temperature distribution on the surface of the sheet and Fig. 5 the actual temperature distribution at a particular time instant during the experiment.

Table 1 Material properties of the sheet and backing plate

T [°C]	Sheet (Aluminium alloy)			Backing Plate (Steel)		
	$k \left[ \frac{W}{mm \cdot ^\circ C} \right]$	$\rho \cdot 10^{-6} \left[ \frac{kg}{mm^3} \right]$	$c \left[ \frac{J}{kg \cdot ^\circ C} \right]$	$k \left[ \frac{W}{mm \cdot ^\circ C} \right]$	$\rho \cdot 10^{-6} \left[ \frac{kg}{mm^3} \right]$	$c \left[ \frac{J}{kg \cdot ^\circ C} \right]$
20	0.130	2.750	898.0	0.068	7820	430
120		2.730	951.0			500
220		2.710	1003.0	0.059	7800	550
320		2.690	1055.0			580
420		2.660	1108.0	0.047	7730	610
500						650
587	0.170	2.630	1195.0			
600				0.036	7653	710
644		2.450	1200.0			
700					7613	790
800				0.029		865
900				0.027		565
1450				0.033		
1600					7190	630
2447		2.230	1300.0			707

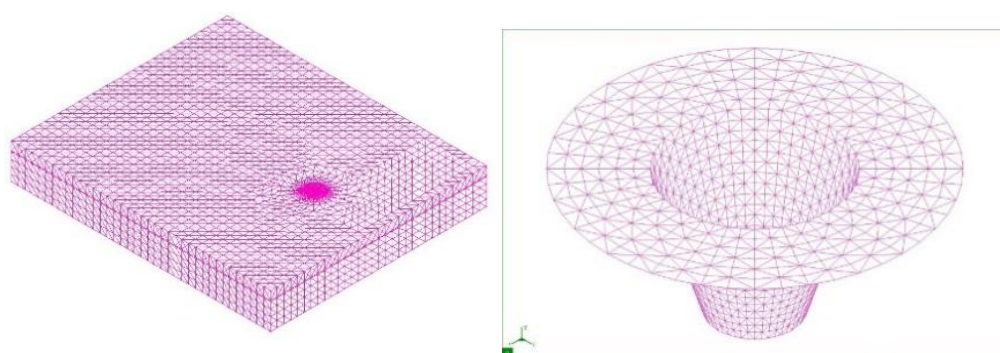


Figure 2 FEM model of the sheet and backing plate and the FEM model of the tool

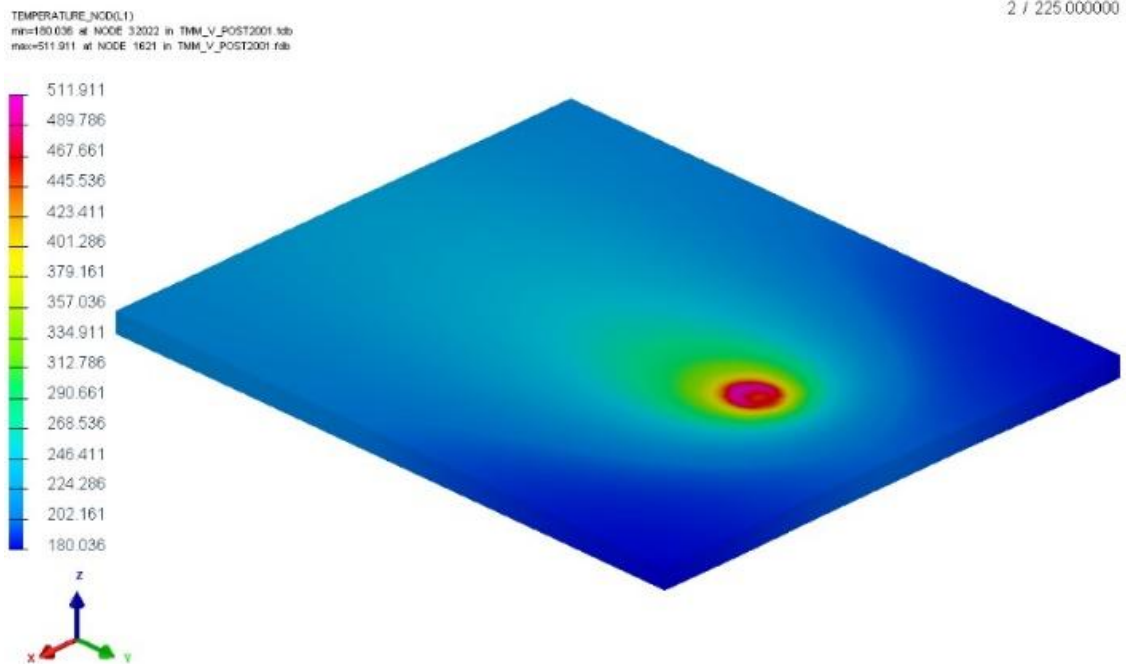


Figure 3 Temperature field (°C) at time 225 s

### 3. RESULTS

The temperature time history coming from the analysis and the experiment at a selected location is shown in the Figure 6. As it can be seen in the figure, the calculated and the measured temperature time histories are quite similar with almost identical maximum values which justify the chosen modelling methodology.



Figure 4 Experimental measurement taken with camera FLIR® SC660

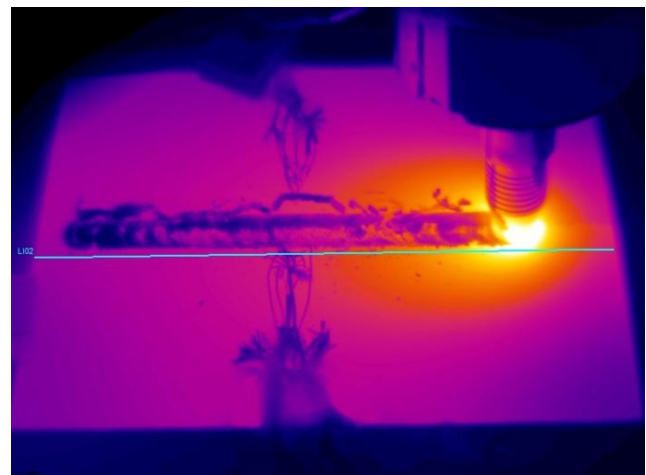


Figure 5. Thermal field measured by a thermal camera

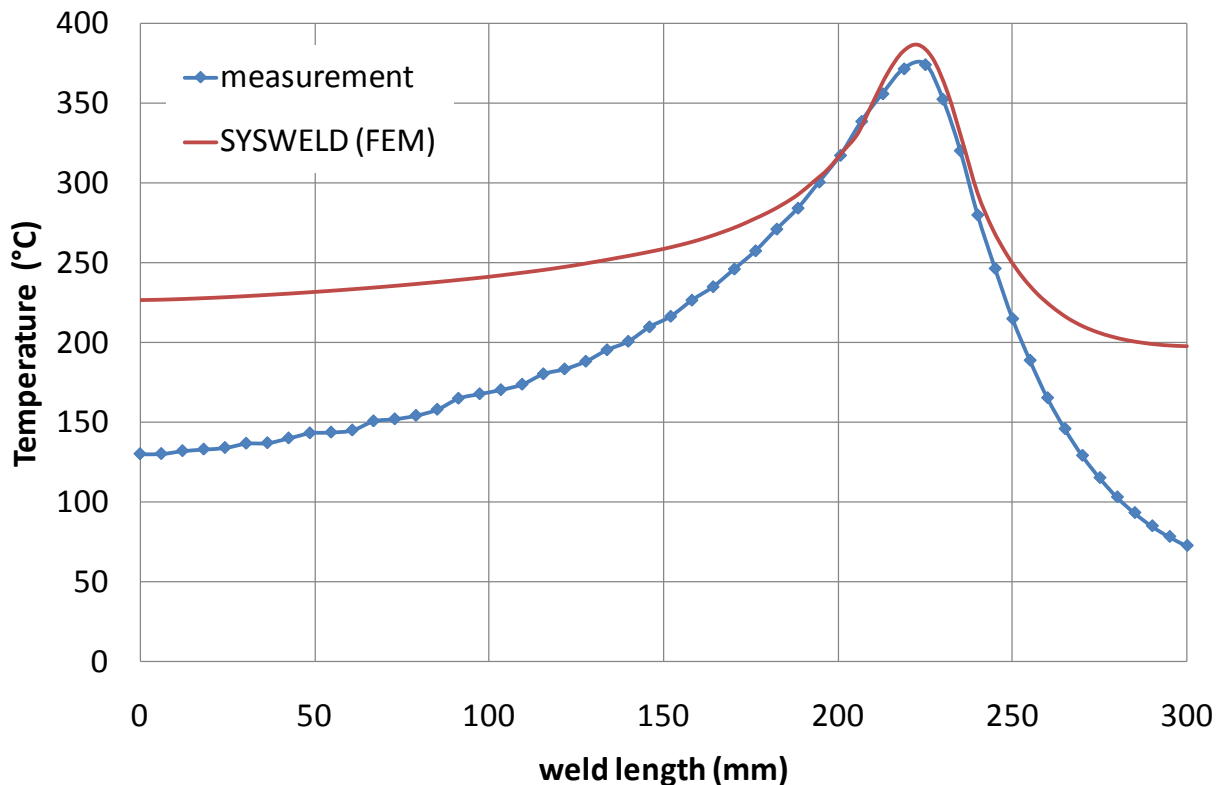


Figure 6 Comparison of temperature time histories coming from the analysis and experiment

## CONCLUSIONS

In this paper a thermal-fluid-flow analysis welded sheets using the Sysweld commercial finite element code and the experimental verification of the welding process was carried out using friction-stir welding. The analysis results are in the range of an acceptable tolerance with the experimental results. As a result, the simplified modelling methodology of the welded material as a fluid flow appear to be a suitable tool for temperature field assessment during friction-stir welding.

## ACKNOWLEDGEMENT

This publication is the result of the project implementation: Research of friction stir welding (FSW) application as an alternative to melting welding methods no. 26240220031 supported by the Research & Development Operational Programme funded by the ERDF. The research was also supported by the grant from Grant Agency of VEGA no. 1/0740/16 titled "Mathematical model proposal for numerical simulation of creep behaviour of TiAl intermetallic alloys".

## REFERENCES

- [1] Chen, C.M., Kovacevic, R.: *Finite element modeling of friction stir welding - thermal and thermomechanical analysis*, International Journal of Machine Tools & Manufacture, 43, 1319-1326, 2003
- [2] Frigaard, Ø., Grong, Ø., Midling, O.T.: *A Process Model for Friction Stir Welding of Age Hardening Aluminium Alloys*, Metallurgical and Materials Transactions A, 32A: 1189-1200, 2001



# INTERNATIONAL SCIENTIFIC CONFERENCE ON ADVANCES IN MECHANICAL ENGINEERING

12-14 October 2017, Debrecen, Hungary



- [3] Feulvarch, E., Robin, V., Boitout, F., Bergheau, J.M.: *3D Modelling of Thermofluid Flow in Friction Stir Welding*, Including Metallurgical and Mechanical Consequences. *Mathematical modelling of weld phenomena* 8, 1-24, 2007
- [4] Trebuña, P., Pástor, M., Trebuña, F., Šimčák, F.: *The analysis of failure causes of the rotor shaft of steam turbines*. *Metalurgija* 56 (1-2): 233-236, 2017
- [5] Halama, R., Fajkos, R., Matusek, P., Babkova, P., Fojtik, F., Vaclavek, L. (2011) *Contact defects initiation in railroad wheels - Experience, experiments and modelling*. *WEAR* 271 (1-2): 174-185
- [6] Frydryšek, K., Michenková, Š., Nikodým, M. (2014) *Straight beams rested on nonlinear elastic foundations – Part 1 (Theory, experiments, numerical approach)*. *Applied Mechanics and Materials* 684: 11-20
- [7] Jančo, R., Écsi, L., Élesztos, P. (2016) *FSW Numerical Simulation of Aluminium Plate by Sysweld – Part I*. *Journal of Mechanical Engineering – Strojnícky časopis* 66 (1): 47-52. doi: 10.1515/scjme-2016-0010
- [8] Jančo, R., Écsi, L., Élesztos, P. (2016) *FSW Numerical Simulation of Aluminium Plate by Sysweld – Part II*. *Journal of Mechanical Engineering – Strojnícky časopis* 66 (2): 29-36. doi: 10.1515/scjme-2016-0016



## THE WASTE AND THE ENVIRONMENT

*JOLDEȘ Nicolae Traian, GYENGE Csaba PhD, ACHIMAȘ Gheorghe PhD, POP-SZOVÁTI Anton-Gheorghe*

*Department of Industrial Engineering, Technical University of Cluj-Napoca, Romania*

*E-mail: [joldeș\\_nicolae@yahoo.com](mailto:joldeș_nicolae@yahoo.com), [Csaba.Gyenge@tcm.utcluj.ro](mailto:Csaba.Gyenge@tcm.utcluj.ro),*

*[Gheorghe.Achimaș@tcm.utcluj.ro](mailto:Gheorghe.Achimaș@tcm.utcluj.ro), [anton\\_pops@yahoo.com](mailto:anton_pops@yahoo.com)*

### Abstract

*One of the methods of reducing the quantity of solid waste, which are evacuated is limiting the consumption of raw materials used in the manufacturing processes. Under the pressure of ecology many countries have begun to give special attention to the protection of natural resources and to environment. In this sense, the recycling of waste can and must save resources of raw materials and energy, while reducing environmental pollution. The goals and targets of waste management for Romania are set by the Treaty of Accession of Romania to the European Union. The Accession Treaty provides the basis for developing relevant legislation on waste management and strategic documents. All national, regional and local waste management targets are covered by the obligations that have been undertaken in the country under the Accession Treaty.*

**Keywords:** *waste, environment, waste management, waste recovery, recycling technologies.*

### 1. INTRODUCTION

Pollution and environmental protection are currently considered as very important issues humanity is facing in general. Transformations that take place globally in terms of the environment call for solutions that are theoretically and conceptually grounded to maintain the planet's ecological balance.

It can be stated with certainty that the irrational development, the excessive urbanization, the demographic explosion, the massive destruction of the forests, are permanently a potential pressure with negative effects on the environment.

Under these circumstances, where the World Commission on Environment and Development, as well as a number of non-governmental organizations, put pressure on governments that do not sufficiently address environmental issues, a new concept emerged, namely the concept of "Sustainable Development". It is necessary to understand that sustainable development must be involved in finding optimum solutions regarding the economic sizing in all the fields, for discovery and application of nonpolluting technologies, for developing an ecological agriculture, for environment protection.

An important role in the realization of this concept lies with the economic agents who have to reorient their technologies towards less polluting technologies, which generate fewer waste, which have low material and energy consumptions, with as little environmental impact as possible and which present reduced environmental risks.



## **2. ENVIRONMENT PROTECTION IN THE CURRENT ECONOMY**

Increasing pollution can be stopped by a policy in line with the concept of sustainable development. In this sense, the future technologies must pursue reduction of raw materials and energy consumptions, to avoid technology losses, to save energy and mineral resources, to reduce to maximum the polluting emissions and the waste, to eliminate any irrational use of all resources.

Clean technologies that are less polluting for the environment and which in the future have to be extended in all countries are relatively expensive and not at hand for poor countries. Economic enterprises need to be stimulated to change their technologies, reduce their waste volume, and process their own waste, install air filtration systems and waste water treatment plants to minimize the negative effect of the economic activity on the environment.

We can assert with certainty that the main causes of environmental degradation are due to economic activities, whether industrial, or agricultural, construction or transport activities. We will have to find technical and technological solutions to reduce the negative effect of these activities on the environment and at the same time must make efforts to bring back all areas affected by pollution.

## **3. REDUCING WASTE GENERATION**

A new discipline "Solid Waste Management" has appeared for waste management, with the following activities:

- waste generation research;
- tracking how waste is stored;
- waste collection control;
- waste transportation control;
- control of waste primary processing;
- tracking waste recovery;
- waste storage supervision.

The purpose of this new discipline is to ensure the ecological management of all material resources including wastes in order to protect the environment in accordance with market economy principles, conservation of natural resources and generally in accordance with the new concept of "Sustainable Development".

The National Waste Recycling Strategy focuses mainly on the following:

- preventing generation of waste through promoting clean technologies and of eco-production;
- waste recovery by optimization of the collecting and selecting systems of waste;
- elimination of waste that can no more be recovered in ecological pit.

To achieve these objectives, it is necessary:

- creating a specific legislative framework;
- encouraging waste recovery and reuse activities;
- promoting clean technologies;
- stimulation of raw materials and energy consumption reduction;
- promoting scientific research into the use of waste;
- achieving educational programs.

Based on some technical and economic nature criteria, the following concepts regarding the reduction and recovery of waste can be formulated:

- the use of basic technological processes that no longer produce waste;
- waste recovery within the area of the units;



- waste recovery also outside the area of the units;
- the use of clean technologies.

In case of application of these procedures, even if there appear less waste, important economic results are guaranteed from diminishing the raw material consumption.

#### 4. RECYCLING THROUGH MODERN TECHNOLOGIES

The study will be developed in a county located in the North-West region of Romania, and its horizon is 30 years.

Analysis of the actual situation (Fig. 1) related to the relationship with the waste management and generation provided the following results:

- the amount of municipal waste generated is about 60 tons / year, of which:
  - 62% comes from urban areas;
  - 38% from rural areas.

The total amount of solid waste from the municipal town is presented in Table 1.

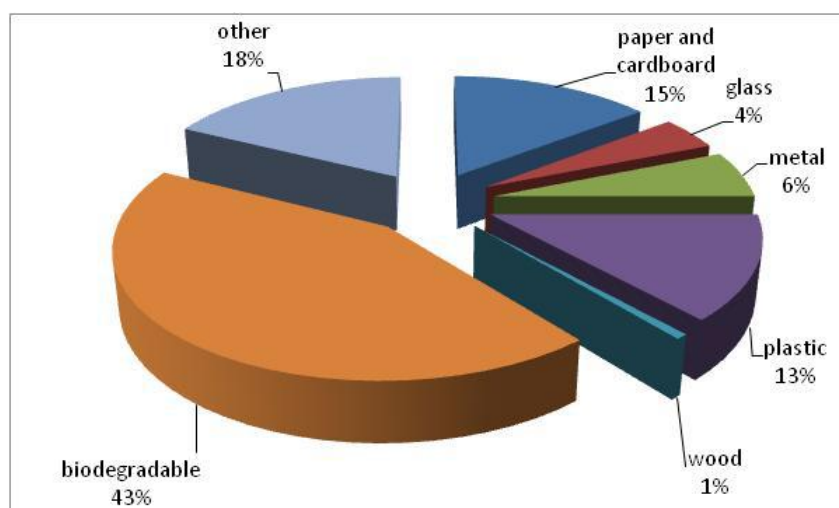


Figure 1 Waste composition at the county level.

Table 1. The average composition of the collected waste (2007).

Waste type	Urban area	Rural area	County average	County average
-	%	%	%	t/year
Paper and cardboard waste	16	12	14,6	8,615
Glass waste	4		4,4	2,610
Metal waste	5	8	6,1	3,663
Plastic waste	14	12	13,3	7,881
Wood waste	1	0	0,6	367
Biodegradable waste	42	46	43,4	25,925
Other waste sand, maturing	18	17	17,6	10,491
Total	100	100	100	59,552



This analysis is important because it offers a base for the future design of the waste management system.

The actual waste management (2017) is unsuitable as it can be seen below:

Waste collection:

- collection is organized by unauthorized operators;
- selective collection is implemented only in few areas (15%);
- the existing equipment is old and not sufficient.

Biological treatment of the waste:

- untreated biodegradable waste (the impossibility to achieve the targets imposed by the legislation);
- the lack of waste treatment facilities.

Waste recycling:

- selective collection is implemented only in areas where there are PHARE Projects;
- manual sorting of the waste.

Waste disposal:

- inadequate disposal (4 non-conform storage yards);
- mixed waste disposal with not treated waste;
- the absence of a conform waste storage yard.

In Figure 2 is presented the generation of package waste, for the period of time from 2005 – 2007.

Per capita, the generation of biodegradable waste is 142 kg / year. Approximately 62% (21,450 t / year) of biodegradable waste is generated in urban areas, corresponding to 215 kg / capita / year, while in rural areas the figure is 92 kg / capita / year.

The package waste quantity was estimated in the county under analysis to ca. 18.000 tons.

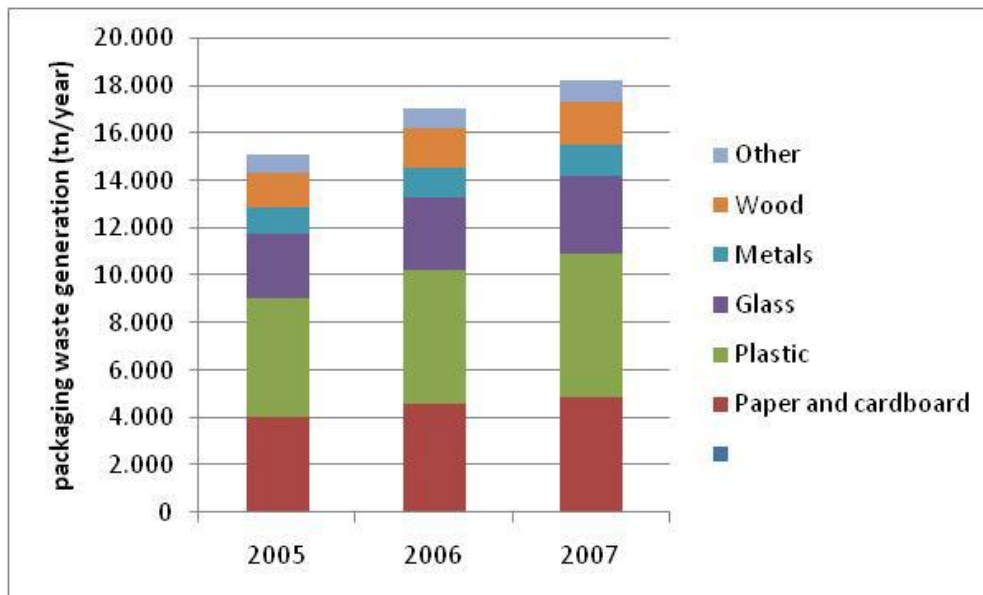


Figure 2 Package waste generation in the analyzed county (t/year)

#### 5. 4 R – RECYCLING, RECOVERY, REPAIR, REUSE

Reducing the consumption of material needed to produce a piece of equipment, as any other product, is beneficial both in terms of manufacturing costs, especially under the ecological cost.

Under the ecological aspect the material consumption used for the manufacture of an equipment, can be estimated by:



# INTERNATIONAL SCIENTIFIC CONFERENCE ON ADVANCES IN MECHANICAL ENGINEERING

12-14 October 2017, Debrecen, Hungary



- the evident costs;
- costs not included;
- costs of persistence and storage of materials.

The consequences of fabrication of the quantities of materials included in the structure of the equipment contribute to:

- thermal pollution;
- chemical pollution;
- contribution to the destruction of the ozone layer ;
- the displacement of large masses of ore.

Dematerialization of the design activity is considered as a priority direction of reducing the effects of the impact on the natural environment.

From the programs of the manufacturers of technical equipment and research institutes with this profile, the following trends are outlined:

- design of technical equipment with increased life-cycle;
- rebuilding and recycling of equipment;
- equipment modernization.

The life-cycle of the equipment can be extended through rebuilding, repair, recycling and reuse of their components, actions known under the name of the “4R”. At the moment, rebuilding have exceeded 20% from the world production of equipment and generates less waste.

Sustainable development is that development which satisfies the needs of the present without compromising the possibility of future generations to satisfy their own needs.

Sustainable development tries to respond to five great imperatives that is:

- integration of the nature conservation and of development;
- basic human needs satisfaction;
- equity and social justice;
- opportunity for social self-determination and cultural diversity;
- maintaining the ecologic integrity.

The three “E” of the sustainable development, economy, ecology (environment) and equity (social), represent a set of relative condensed values, which have to guide the process of change.

## CONCLUSIONS

Based on technical and economic criteria, conclusions can be drawn regarding the reduction and recovery of waste, namely:

- the use of basic technological processes that no longer produce waste;
- recovery of waste within the units;
- recovery of waste outside the units;
- the use of clean technologies.

The strategy at national level regarding the recovery of waste lines out mainly the following:

- preventing generation of waste through promoting clean technologies and of eco-production;
- waste recovery by optimization of the collecting and selecting systems of waste;
- elimination of waste that can no more be recovered in ecological pit.

The risks of pollution which appear, impose establishing of protection measures which have to be



# INTERNATIONAL SCIENTIFIC CONFERENCE ON ADVANCES IN MECHANICAL ENGINEERING

12-14 October 2017, Debrecen, Hungary



taken into consideration at the use of waste.

## REFERENCES

- [1] Bengtsson, L., Seman, P.O., *Waste management and recovery Landfilling*. First edition, Editor William Hogland, LTH, Lund, 1996.
- [2] Drost, U., ş.a., *Report on the operating trial with auto motive shredder residue*. International Automotive Recycling Congress, Geneva, 2004.
- [3] Duca, Gh., Scurlatov, Y., *Ecological Chemistry*, Chişinău, 2002.
- [4] Mattisson, C., *Waste management and producer responsibility in Sweden*. Chalmers University of Technology, Goteborg, Sweden, 2003.
- [5] McDougal, F., White, P., Franke, M., Hindle, P., *Integrated solid waste management – a life cycle inventory*. Blackwell Publishing, 2001.
- [6] Tornebz, L., and others, *Waste management and recovery, Exercises in waste management and recovery*. Lund, 1997.



## CLINCHING OF DP600 STEEL SHEETS

<sup>1</sup>JÓNÁS Szabolcs, <sup>2</sup>TISZA Miklós DSc

<sup>1</sup>Knorr-Bremse Vasúti Jármű Rendszerek Hungária Kft.

E-mail: [szabolcs.jonas@knorr-bremse.com](mailto:szabolcs.jonas@knorr-bremse.com)

<sup>2</sup>University of Miskolc

E-mail: [miklos.tisza@uni-miskolc.hu](mailto:miklos.tisza@uni-miskolc.hu)

### Abstract

*This study deals with the clinch joints especially the clinching of high strength steels. DP600 type of steel sheets was tested. The thickness of the sheets was 1 mm. The joining procedure was made by a round TOX tool. The DP600 steels are dual phase (ferritic-martensitic) types (AHSS – advanced high strength steels). Non standardized impact tests were performed and the results were analysed to determine which the best joint is. For deeper understanding of the joints non-linear finite element simulations were performed in the ANSYS system. In this paper the results of the comparison of the tested clinched joint and the FEA simulations was presented. After the model validation further FEA simulations were carried out the behaviour of the sheets with different frictional conditions between the “upper” sheet and the punching tool. The comparison based on the size of the undercut. The results show the dependency of the effect of the frictional coefficient.*

**Keywords:** DP600, clinch joint, impact test, FEA

## 1. INTRODUCTION

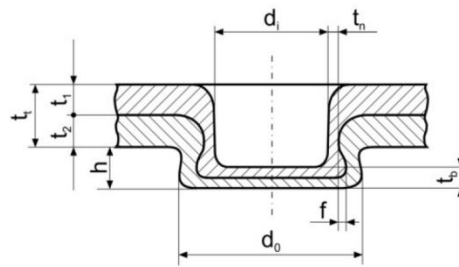
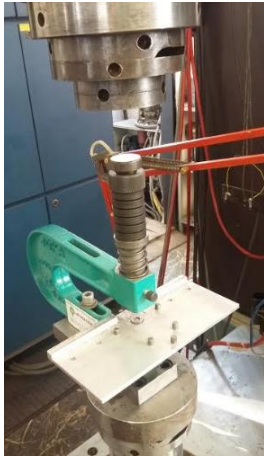
These joints are used mostly in automotive, computer and aircraft industries, but for instance according to the standards not allowed to use in food industry. This article is the first results of this research programme. The goal of the research is to determine the optimal parameters of clinched joints of high strength steels and aluminium. Furthermore to find a solution for fatigue evaluation and to replace some welded joints to clinched joints because of the cost of clinched joints are lower. The most difficult goal is to use the lowest number of tests and use the articles and other available material and test data to determine the relevant parameters. The clinch joints are quite new types of joints, the first patent was accepted in 1989. This joint can be done between 2-3 thin sheet plates. The material of the plates can be ferrous or non-ferrous, so this joint can realize dissimilar joints without any added material (weld material or glue). The joint made by metal plastic forming by a special tool. After the patent the increasing industrial needs of this type of joints led the researchers to analyse the joint much more deeply. Several studies carried out the geometry optimization of the clinching tool to get better joints by different optimization methods. Other studies were carried out on the so-called hybrid joints. These joints have an adhesive layer between the sheets. These joints have higher strength but these joints need much more time because the adhesive layer's drying is a time-consuming process [1], [2].

## 2. METHODS

In this study DP600 type of advanced high strength steel was tested. Each type of steel is used in automotive industry. The clinching tool was set up in an MTS servo-hydraulic testing machine. The maximum load which the tool can survive is 50kN. The set up can be seen in Figure 1. The



specimens were pre-drilled for this application. Two holes were drilled which centralized the specimens on the one hand and prevented them moving on the other hand.



$d_o$  - outer diameter  
 $d_i$  - inner diameter  
 $f$  - interlock  
 $h$  - forming height of the joint  
 $t_b$  - thickness of the bottom  
 $t_n$  - thickness of the neck (is zero with both side cut elements)  
 $t$  - total sheet thickness  
 $t_1$  - single sheet thickness, punch side  
 $t_2$  - single sheet thickness, die side

Figure 1 Clinching tool (TOX) and the relevant geometrical parameters of the joint [8]

The first few clinch processes were made to determine the loads required to restrain the sample in order to reach the 50kN maximum tool load. For each joint the bottom thickness was measured by a micrometer.

To reduce time to find the best joint with a given tool, measured impact test was performed. The basic idea to use impact test was that the joint with the highest value of impact energy should be the best joint. Based on previous studies the best choice of thickness of the bottom layer was already quite well known, so only 3 thicknesses were tested [4],[5] and [6]. From these impact energy values the highest was analysed for the further testing. For the tests a standard Charpy impact tester was used which was instrumented. The clamping device was developed for these types of tests. The Figure 2 shows the testing machine and the device with a specimen after clinching.



Figure 2 Impact testing machine (300 J) – Machine and clamping device of the specimens

It can be seen that the relationship between the maximal clinching force and the bottom thickness is linear (Figure 3) and at the same time the impact energy and bottom thickness diagram (Figure 4) also shows a slightly linear relationship between the two values. The thickest specimen has the highest impact energy and the lowest maximal clinching force. It means the better joint has a lower joining energy need compare to the worst case.

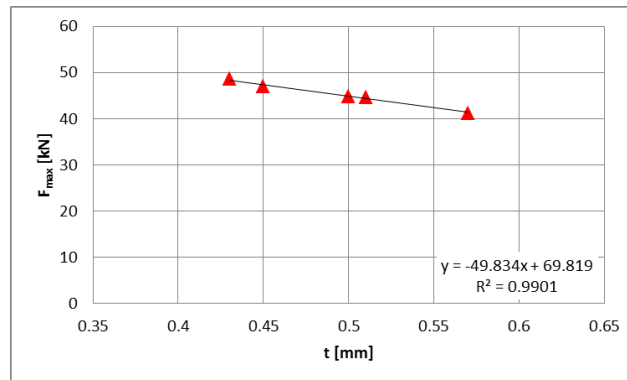


Figure 3 Maximum clinch force – bottom thickness relationship

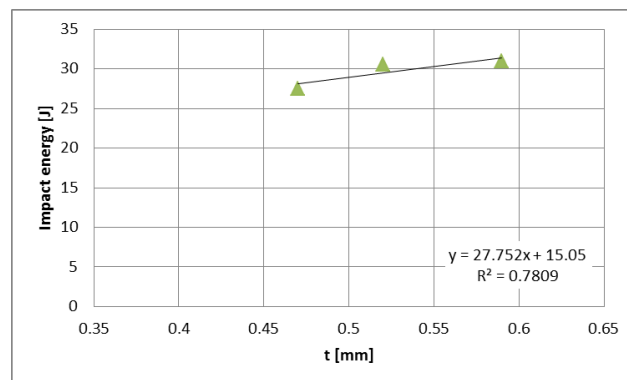


Figure 4 Impact energy – bottom thickness relationship

After the measurement a microscopic investigation has been done. The grinded section can be seen in Figure 5. The extended grains can be observed due to the forming procedure. The undercut can be also seen on the section. This curve between the formed sheets will be used to compare different simulated cases.

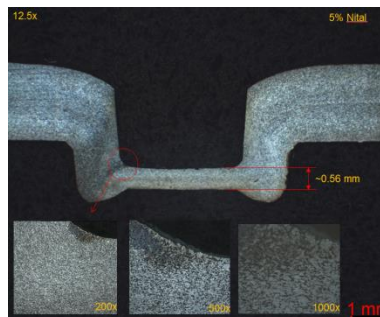


Figure 5 Microscopic investigation - cross section of the specimen after clinching

The FE simulation model was built in ANSYS WB 17.2 [3]. A 2D axisymmetric model was presented below (Figure 7.). The sheets can handle as circular sheets. The tools were taking account as linear elastic materials. The sheets have multilinear isotropic hardening material model. The material model can be seen in Figure 6. The material law is fitted to the measured flow curve. The contact zones and the sheets also have a high mesh density. The boundary conditions applied to the model can be seen in Figure 7. The tools prescribed in all degrees of freedom on their sides and the punching tool is displacement controlled. It has got a -2.8mm displacement in the vertical direction till the end of the simulation. Between the parts Augmented Lagrange contact behaviour was applied. The frictional coefficient between the sheets is 0.2, other contact 0.01.

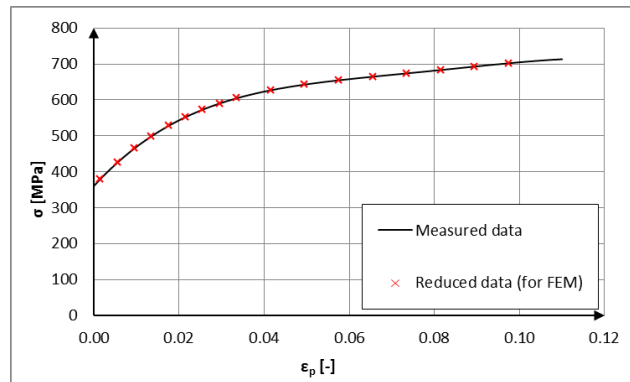


Figure 6 DP600 true stress-true plastic strain curve

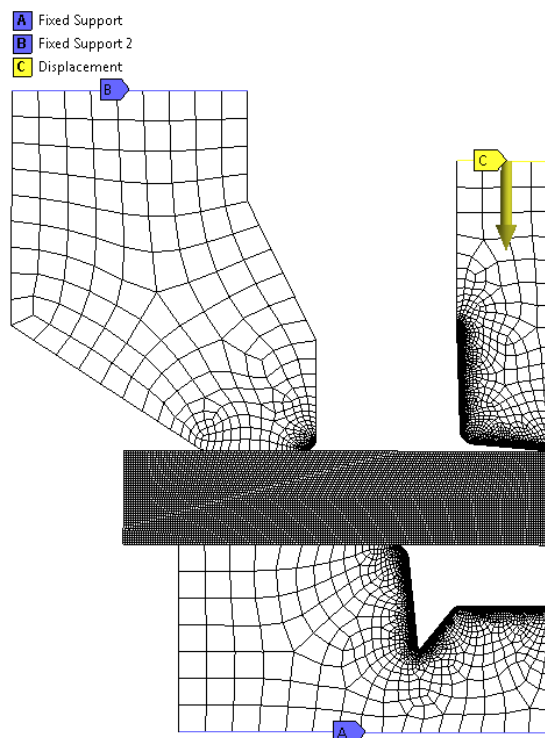


Figure 7 Boundary conditions of the model

### 3. RESULTS

The results of the simulation can be seen in Figure 8. The figure shows the equivalent plastic strain distribution of the sheets. The most affected zones are the neck region of the upper sheet where the punching tool is contacted with it and between the two sheets.

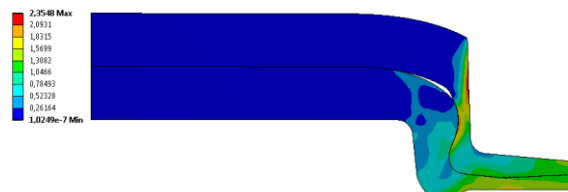


Figure 8 Equivalent plastic strain distribution of the sheets



The Figure 9 shows the measured and simulated sections of the sheets. The results show good agreement with each other; we can say that the FE model is valid. With this model further simulations can be made to analyse the behaviour of the sheets with different frictional conditions.

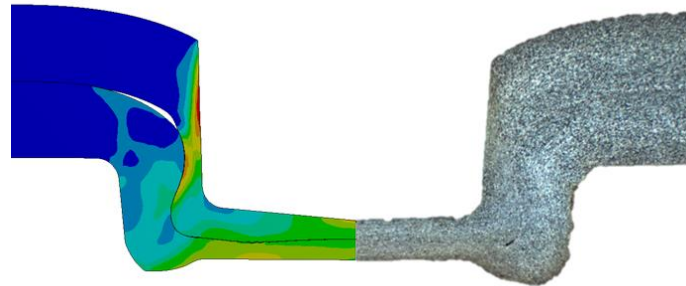


Figure 9 Comparison of the measured and simulated joints

The frictional behaviour between the punching tool and the upper sheet were changed from 0.001 to 0.2. The curve of the undercut was compared to each other. The results show that the frictional behaviour is highly affected on the size of the undercut [8].

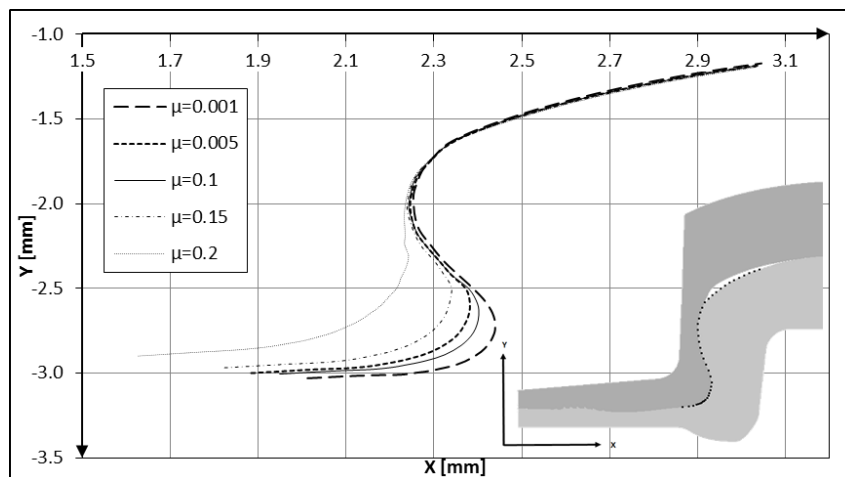


Figure 10 Comparison of the undercuts with different frictional coefficient

## CONCLUSION

The impact tests show a slightly linear relationship between the bottom thickness of the joined sheets and impact energy values for DP600 type of sheets. A valid FE model has been built up and sensitivity analysis was done. The frictional coefficients highly effect on the curve of the undercut. This effect shows that the punching tool should dry enough to make a good clinched joint. Further analysis and tests need to prove this phenomenon for other types of materials also.

## REFERENCES

- [1] T. Sadowski, T. Balawender, P. Golewski: *Technological aspects of manufacturing and numerical modelling of clinch-adhesive joints*, Springer (2015)
- [2] L. Kascák E. Spisák: *Clinching as a non-standard method for joining materials of dissimilar properties*, Zeszyty naukowe politechniki rzeszowskiej Nr. 284. Mechanika z. 84 2012



# INTERNATIONAL SCIENTIFIC CONFERENCE ON ADVANCES IN MECHANICAL ENGINEERING

12-14 October 2017, Debrecen, Hungary



- [3] ANSYS WB 17.2 User's guide
- [4] P. Z. Kovács, M. Tisza: *Investigation and Finite element modelling of technological parameters of clinched joints*, Miskolci Egyetemi Közlemények, Miskolc, X. kötet, (2015) pp.
- [5] M. Tisza, G. Gál, A. Kiss, Z. Z. P. Kovács, Zs. Lukács: *Alakítható nagyszilárdságú anyagok klincs kötése*, Multidiszciplináris tudományok, 4. kötet (2014) 1. sz. pp. 49-58.
- [6] P. Z. Kovács, M. Tisza: *Klincs kötés technológiai paramétereinek vizsgálata, végelelemes modellezése*, Anyagmérnöki Tudományok, 39/1 (2016) pp. 7-18
- [7] Chan-Joo Lee, Jae\_Young Kim, Sang-Kon Lee, Dae-Cheol Ko, Byung-Min Kim: *Parametric study on mechanical clinching process for joining aluminum alloy and high-strength steel sheets*, Journal of Mechanical Science and Technology 24 (2010) pp. 123-126
- [8] W-G. Drossel, M. Israel, T. Falk: *Robustness evaluation and tool optimization on forming applications*, 9th Weimar Optimization and Stochastic Days, 2012



## LOGISTIC ASPECTS OF REAL TIME DECISIONS IN INTELLIGENT TRANSPORTATION SYSTEMS

*JUHÁSZ János, BÁNYAI Tamás PhD*

*Institute of Logistics, Faculty of Mechanical Engineering and Informatics, University of Miskolc*  
*E-mail: [juhaszj@uni-miskolc.hu](mailto:juhaszj@uni-miskolc.hu), [alttamas@uni-miskolc.hu](mailto:alttamas@uni-miskolc.hu)*

### **Abstract**

*The current way that supply chain operations are realized to handle physical objects is unsustainable. Intelligent transportation systems (ITS) based on geographic information systems (GIS) improves the efficiency, mobility and safety of supply chain operations through application of wireless communication based technologies. This paper deals with a methodological approach for real time planning of transportation operations. It first looks into hyperconnected supply chain processes and identifies key advantages of ITS solutions. The main contribution of the paper is the conceptualization of the real time, dynamic planning of transportation tasks to minimize the operation costs and ecological footprint. The complexity of the optimization problems led to the development of a metaheuristics algorithm based on harmony search. This contribution shows by means of a scenario that real time planning supports cost efficient, economical hyperconnectivity.*

**Keywords:** *hyperconnected supply chain, logistics, optimization, heuristics*

### **1. INTRODUCTION**

To achieve economic and environmental sustainability, utilization of technological and logistic resources has become a key challenge for the logistics sector, especially in the field of transportation. Hyperconnected supply chain solutions are based on the cooperation of networking partners. This cooperation aims to enable highly efficient and sustainable supply chain solutions based on intelligent transportation systems and geographical information systems using up-to-date technologies.

Due to the large amount of researches on the field of intelligent transportation systems the most relevant scientific results have to be summarized before to elaborate the model, algorithm and solution. However the main research field of ITS is focused on application in road transportation, but a wide range of literatures are discussing ITS solutions in the field of rail [1], maritime [2] and air [3].

In the current globalized economic environment, planning and controlling of an efficient distribution and transportation network is considered as a competitive advantage for every company, which has to answer at minimum costs at the customers' demands, while ecological aspects [4] and safety [5] are also taken into consideration.

The complexity of transportation systems related to hyperconnected global supply requires up to date methods to find near-optimal parameters for the operation of the processes. The optimization methods of large scale, multi-objective design problems [6] are mostly heuristic methods. Much literature has been published in the field of ITS-design heuristic or metaheuristic based algorithms, like particle swarm optimization (PSO) methods or ant colony optimization (ACO). ACO applications are aiming to distribution and collection processes of supply chain, like pickup and delivery problems [7]. The main focus of PSO is the vehicle routing problems [8].



The optimization of large scale ITS problems can be based on simulation techniques, like multi-agent based simulation which makes it possible to support real time decisions in systems with uncertainties, in a stochastic environment [9]. Traditionally, the investment costs of the latest ITS solutions and techniques are increasing depending on the complexity of the system, therefore low cost companies are looking for low cost solutions, like smart phone based freight logistics transport information management optimisation and asset tracking solution [10].

One of the main streams of literature in the field of ITS addresses the development of city logistics solutions, focusing on the use of real time traffic information in urban freight distribution [11], design of truck ban scheme [12] or minimization of operational costs of city transportation systems. The design of intelligent transportation systems covers a wide range of tasks, but most of the researchers are focusing on routing problems, like fleet use optimization with time window constraints [13] or flow scheduling optimization in capacitated vehicle routing problem (CVRP) with unsplit demands [14].

The aim of this paper is to investigate an integrated model of real time assignment of available, running transportation tasks to additional demands, which takes into consideration the transportation related costs. This paper is organized as follows. Section 1 presented a literature review, which summarizes the research results related to intelligent transportation systems in supply chain operation. Section 2 describes an integrated model, which focuses on operation cost. Section 3 demonstrates the numerical analysis of the model. Conclusions and future research directions are discussed in Section 4.

## 2. MODELING OF A REAL TIME ITS BASED DECISION MAKING PROBLEM

Within the frame of this chapter two different models of assignment of transportation resources (trucks) and transportation demands are described. The first model represents the supply chain process, where ITS is not applied, therefore no information is available for real time scheduling and assignment of trucks and additional transportation demands, see in *Figure 1*. This model represents a traditional supply chain, which is not suitable for hyperconnected global logistics services.

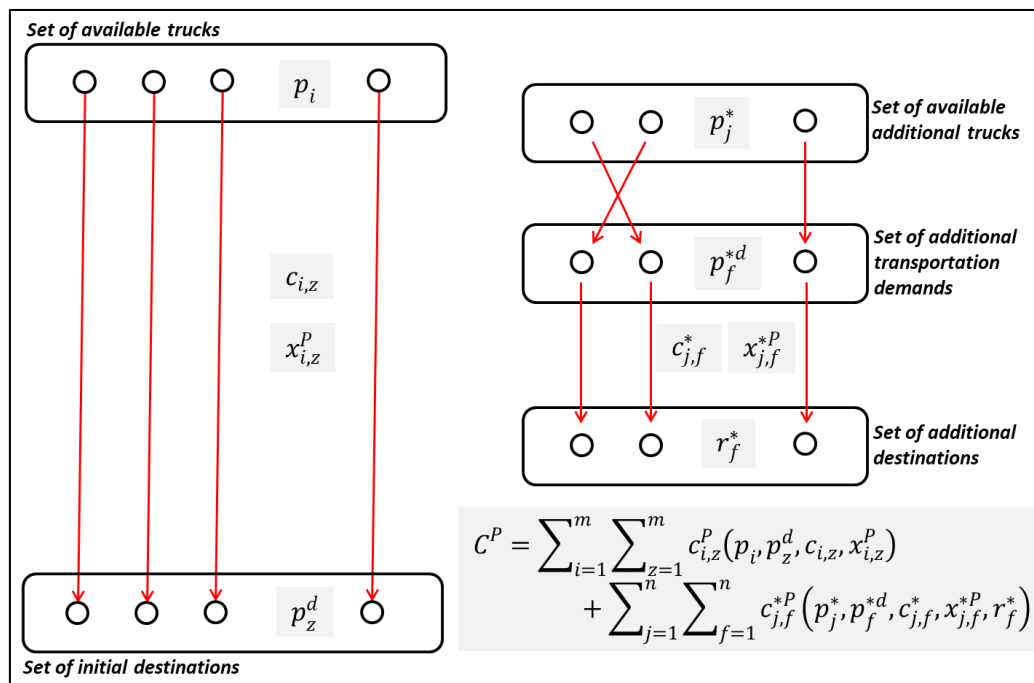


Figure 1 Flow scheduling without real time decision possibilities



The objective function of the optimization is the maximization of the cost difference between the operation cost of flow scheduling without real time scheduling and the operation cost of flow scheduling with real time scheduling of available trucks:

$$C = C^P - (C^{RT1} + C^{RT2} + C^{RT3}) \Rightarrow \max., \quad (1)$$

where  $C^P$  is the operation cost of the traditional flow scheduling without the possibility of ITS based real time scheduling,

$C^{RT1}$  is the operation cost of flow scheduling of available trucks to initial destinations with real time scheduling,

$C^{RT2}$  is the operation cost of flow scheduling of available additional trucks with real time scheduling,

$C^{RT3}$  is the operation cost of assignment of available trucks and additional destinations with real time scheduling.

The operation cost of the traditional flow scheduling can be calculated as follows:

$$C^P = \sum_{i=1}^m \sum_{z=1}^m c_{i,z}^P(p_i, p_z^d, c_{i,z}, x_{i,z}^P) + \sum_{j=1}^n \sum_{f=1}^n c_{j,f}^{*P}(p_j^*, p_f^{*d}, c_{j,f}^*, x_{j,f}^{*P}, r_f^*) \quad (2)$$

where  $c_{i,z}^P$  is the operation cost of the route, where the  $i^{th}$  truck is assigned to the  $z^{th}$  initial destination,

$p_i$  is the position of the  $i^{th}$  available truck,

$p_z^d$  is the position of the  $z^{th}$  initial destination,

$c_{i,z}$  is the specific transportation cost of the  $i$ - $z$  relation, where the  $i^{th}$  truck is assigned to the  $z^{th}$  initial destination,

$x_{i,z}^P$  is the element of the assignment matrix,

$c_{j,f}^{*P}$  is the operation cost of the route, where the  $j^{th}$  available additional truck is assigned to the  $f^{th}$  additional transportation demand and destination,

$p_j^*$  is the position of the  $j^{th}$  available additional truck,

$p_f^{*d}$  is the position of the  $z^{th}$  additional transportation demand,

$c_{j,f}^*$  is the specific transportation cost of the  $j$ - $f$  relation, where the  $j^{th}$  available additional truck is assigned to the  $f^{th}$  additional transportation cost,

$x_{j,f}^{*P}$  is the element of the assignment matrix.

$r_f^*$  is the length of the transportation route of the  $f^{th}$  available transportation demand – additional destination assignment.

The second model represents the supply chain process, where geographical and other information is available through ITS, therefore the additional transportation tasks of the system can be assigned to available transportation resources, see in *Figure 2*. This model represents the supply chain kmodel of hyperconnected global logistics services.

We write for the operation cost of flow scheduling of available trucks to initial destinations with real time scheduling:

$$C^{RT1} = \sum_{i,z \in \Theta} c_{i,z}^{RT}(p_i, p_z^d, c_{i,z}, x_{i,z}^{RT}) \quad (3)$$

where  $\Theta$  is the set of assigned available trucks and initial destinations,

$x_{i,z}^{RT}$  is the element of the assignment matrix in the case of real time decision possibilities.

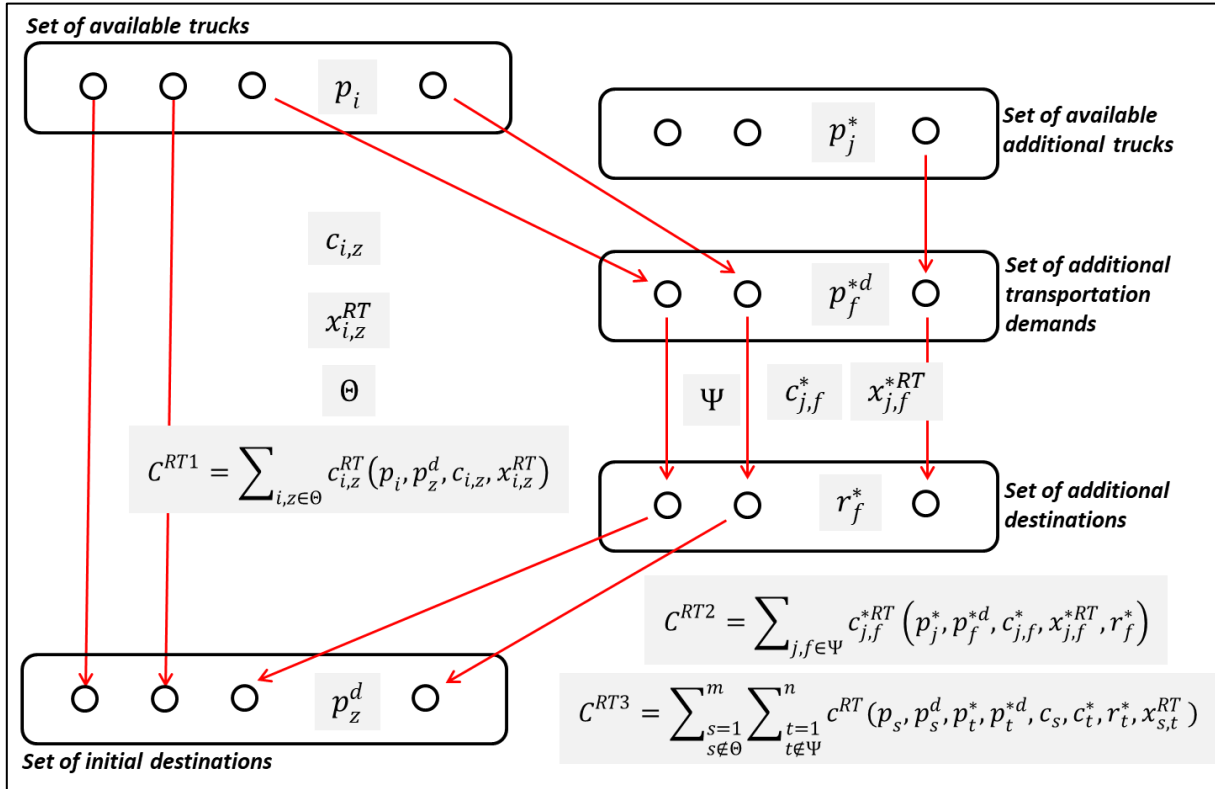


Figure 2 Flow scheduling with real time decision possibilities

We write for the operation cost of flow scheduling of additional available trucks to additional transportation demands with real time scheduling:

$$C^{RT2} = \sum_{j,f \in \Psi} c_{j,f}^{*RT}(p_j^*, p_f^{*d}, c_{j,f}^*, x_{j,f}^{*RT}, r_f^*) \quad (4)$$

where  $\Psi$  is the set of assigned additional available trucks and additional transportation demands,  $x_{j,f}^{*RT}$  is the element of the assignment matrix of additional available trucks and additional transportation demands in the case of real time decision possibilities.

The operational cost of routes assigned by available trucks to additional transportation demands can be calculated as follows:

$$C^{RT3} = \sum_{\substack{s=1 \\ s \notin \Theta}}^m \sum_{\substack{t=1 \\ t \notin \Psi}}^n c^{RT}(p_s, p_s^d, p_t^*, p_t^{*d}, c_s, c_t^*, r_t^*, x_{s,t}^{RT}) \quad (5)$$

where  $s$  is the index number of available truck, which is assigned to additional transportation demands,

$t$  is the index number of additional transportation demands and destinations, which are assigned to an available truck,

$x_{s,t}^{*RT}$  is the element of the assignment matrix;  $x_{s,t}^{*RT} = 1$ , if the  $s^{th}$  available truck is assigned to the  $t^{th}$  additional transportation demand and destination, otherwise 0.

The above described mathematical model represents an NP-hard optimization problem. For the solution of this problem we have used a genetic algorithm based heuristic, where the possible solutions (assignment of available trucks and additional transportation demands) are described with entities of a population.



### 3. CASE STUDY

Within the frame of this chapter two scenarios will be presented to demonstrate the efficiency of the real time decisions in hyperconnected supply chain solutions. The above described model makes it possible to define the optimal assignments of available trucks to additional transportation demands and destinations. Scenario 1 describes a traditional supply chain, where no real time assignment is possible. The parameters of the available routes are described in *Table 1*.

*Table 1* Available routes in Scenario 1

From	GPS lat.	GPS long.	To	GPS lat.	GPS long.	Route [km]	Cost [\$]
Polgár	47.8476 34	21.07582 8	Hajdúböszörmény	47.6563 42	21.517236	72.0	226.80
Gödöllő	47.5984 75	19.32026 7	Érd	47.4131 11	18.11415.	69.2	217.98
Bőny*	47.6522 29	17.87339 1	Vát	47.2635 84	16.739490	107.0	337.05
Szeged*	46.2949 58	20.08727 5	Szigetszentmiklós	47.3794 12	19.030156	168.0	529.20
Pécs	46.0144 96	18.24394 7	Nagyrecse	46.4780 53	17.071908	152.0	478.80
Békéscsaba	46.6771 83	21.02384 1	Furta	47.1565 16	21.498999	74.8	235.62
Siófok	46.9008 00	18.07087 7	Szolnok	47.1290 02	20.137859	208.0	655.20

If the location of additional trucks is in Veszprém (47.115871; 17.903504), then the transportation costs of additional transportation demands is shown in *Table 2*. As *Table 1* and *Table 2* shows, the total cost of this solution is 5332.95 \$.

*Table 2* Additional routes in Scenario 1 without real time assignment

From	GPS lat.	GPS long.	To	GPS lat.	GPS long.	Route [km]	Cost [\$]
Kiskunhalas	46.4644 55	19.46321 4	Fülöpháza	46.8722 50	19.455489	423	1332.45
Csopak	46.9723 14	17.91586 8	Sümege	46.9601 65	17.298232	147	463.05
Abda	47.6998 57	17.53864 4	Simaság	47.4340 51	16.836823	272	856.80

In the case of Scenario 2 two additional routes are assigned to available trucks (routes signed with \* in *Table 1*) and the cost is 1814.4 \$. The cost of additional transportation demands including the deleted routes from *Table 1* is 1641.15 \$, so the total cost of supply chain solution is 3455.55 \$, which represents a saving of about 35 % of the solution without real time decisions.



# INTERNATIONAL SCIENTIFIC CONFERENCE ON ADVANCES IN MECHANICAL ENGINEERING

12-14 October 2017, Debrecen, Hungary



Table 3 Additional routes in Scenario 2 with real time assignment

From	Route [km]	Cost [\$]
Szeged – Kiskunhalas – Fülöpháza - Szigetszentmiklós	242	762.30
Veszprém – Csopak – Sümeg – Veszprém	145	456.75
Bőny – Abda – Simaság - Vát	134	422.10

## CONCLUSIONS

The solutions of intelligent transportation systems make it possible to make real time decisions in supply chain networks aiming economic and environmental sustainability and utilization of capacities. The described mathematical model makes it possible to optimize the assignment of available transportation resources (trucks) and additional transportation demands instead of using new resources. The described NP-hard problem is solved with genetic algorithm based heuristic. As the analysed scenarios showed, significant financial savings are available using the mentioned method. However, there are also directions for further research. Although the transportation routes as distances among the locations are considered in this paper, the capacities of vehicles are not taken into consideration. In further studies, the model can be extended to a more complex model including additional constraints related to time window.

## ACKNOWLEDGEMENT

The described research was carried out as part of the EFOP-3.6.1-16-00011 “Younger and Renewing University – Innovative Knowledge City – institutional development of the University of Miskolc aiming at intelligent specialization” project implemented in the framework of the Szechenyi 2020 program. The realization of this project is supported by the European Union, co-financed by the European Social Fund.

## REFERENCES

- [1] Becker, F., Zell, M.: *The state of the art in positively guided rail transport systems for underground mining*. Mining Report, 150(1-2), 34-47., 2014.
- [2] Chen, L., Zhang, D., Ma, X., Wang, L., Li, S., Wu, Z., Pan, G.: *Container Port Performance Measurement and Comparison Leveraging Ship GPS Traces and Maritime Open Data*. IEEE Transactions on Intelligent Transportation Systems. 17(5), 1227-1242., 2016.
- [3] Zhang, H.-H., Yang, X.-L., Fan, W., Wang, Z.-Y., Liao, Z.-H.: *Guidance control strategy for air traffic flow in terminal areas*. Advances in Mechanical Engineering, 8(10), 1-12., 2016.
- [4] Dongmin, X., Dingyi, Youfang, H., Bin, Y.: *A study of cost and emissions considering speed optimization in trans eurasia transportation based on intelligent transportation*. International Journal on Smart Sensing and Intelligent Systems, 9(1), 191-214., 2016.
- [5] Khaliq, K.A., Qayyum, A., Pannek, J.: *Novel routing framework for VANET considering challenges for safety application in city logistics*. Advances in Intelligent Systems and Computing, 548, 53-67., 2017.
- [6] Deqqaq, H., Abouabdellah, A.: *A bi-objective optimization for a green distribution network with transportation modes selection*. Proceedings of the 11th International Conference on Intelligent Systems: Theories and Applications. Article number 7772295. 2016.
- [7] Seng, D., Wang, Q., Fang, X., Zhang, X.: *Application and analysis of logistics distribution routing based on ant colony algorithm*. Revista de la Facultad de Ingenieria, 32(3), 423-431.,



2017.

- [8] Jianjun, W., Yubo, T.: A particle swarm optimization algorithm for grain logistics vehicle routing problem. Proceedings of the Second ISECS International Colloquium on Computing, Communication, Control, and Management, 364-367., 2009
- [9] Wojtusiak, J., Warden, T., Herzog, O.: *Machine learning in agent-based stochastic simulation: Inferential theory and evaluation in transportation logistics*. Computers and Mathematics with Applications, 64(12), 3658-3665., 2012
- [10] Muna, J.T., Prescott, K.: *Affordable freight logistics transport information management optimisation and asset tracking solution using smartphone GPS capabilities*. Proceedings of the 18th World Congress on Intelligent Transport Systems and ITS America Annual Meeting. 1254-1262., 2011.
- [11] Flamini, M., Nigro, M., Pacciarelli, D.: *The value of real-time traffic information in urban freight distribution*. Journal of Intelligent Transportation Systems: Technology, Planning, and Operations, 1-14., 2017.
- [12] Qureshi, A.G., Taniguchi, E., Thompson, R.G., Teo, J.S.E.: *Application of exact route optimization for the evaluation of a city logistics truck ban scheme*. International Journal of Urban Sciences, 18(2), 117-132., 2014.
- [13] Zhang, Q., Zhen, T., Zhu, Y., Zhang, W., Ma, Z.: *A hybrid intelligent algorithm for the vehicle routing with time windows*. Lecture Notes in Computer Science, 5226, 47-54., 2008.
- [14] Liu, M., Zhu, C., Wu, C.: *Lower bound analysis of the capacitated vehicle routing problem with unsplit demands*. Chinese Journal of Electronics, 15(1), 85-90., 2006.



## PHASE SPACE ANALYSIS OF A PRESSURE RELIEF VALVE

*KÁDÁR Fanni, ERDŐDI István, HŐS Csaba PhD*

*Department of Hydrodynamic Systems, Budapest University of Technology and Economics*  
*E-mail: [kadarfannigml@gmail.com](mailto:kadarfannigml@gmail.com), [ierdodi@hds.bme.hu](mailto:ierdodi@hds.bme.hu), [cshos@hds.bme.hu](mailto:cshos@hds.bme.hu)*

### Abstract

*The system under investigation consists of a direct spring operated pressure relief valve mounted on a vessel. A reduced order model was assembled based on [1], with which the valve response was analysed as a function of the system flow rate. It was found that at low flow rates impacting oscillations occur, which after a short period-two section turn into chaotic solutions, and finally at larger flow rates the system is stabilised. Coexisting, exponentially stable solutions also appeared in the oscillating range, which coupled with the fact that the amplitude of the oscillation was monotonously increasing with the flow rate hinted that there should also be a repelling limit cycle between the basins of attraction of the stable node and the attracting limit cycle. In the article this was confirmed by the shown phase planes.*

**Keywords:** *pressure relief valve, instability, coexisting solutions, phase space, numerical model*

### 1. INTRODUCTION

Pressure relief valves are generally used as the last line of defence against overpressure in both hydraulic and pneumatic systems. In this paper the direct spring operated configuration is investigated, in which the valve disc is pressed against the seat by a pre-compressed spring. Its main advantage is reliability due to the simplicity of the construction and the low number of moving parts. However, this construction is prone to harmful oscillations [2], which increase both the mechanical wear and the pressure losses, thus greatly reducing the discharge flow rate and endangering the protected system. In this paper our goal is to show the behaviour of a given hydraulic relief valve at various driving flow rates.

### 2. MATHEMATICAL MODEL

Our model is based on the one presented in [1], and consists of a vessel with direct spring operated pressure relief valve installed directly on it without any connecting pipes (*Figure 1*). The equation of motion for the valve is

$$m\ddot{x} + k\dot{x} + s(x + x_0) = Ap, \quad (1)$$

where  $m$  is the reduced mass of the moving parts,  $x$  is the valve lift,  $k$  is the damping coefficient,  $s$  is the spring stiffness,  $x_0$  is the pre-compression of the spring,  $A$  is the cross-sectional area of the seat and  $p$  is the overpressure in the vessel. Note that while more precise approximations exist [4, 5, 3] for the total fluid force on the right-hand side, this simple approximation is sufficient for our qualitative analysis. For the vessel we have the equation of mass conservation, which is

$$\frac{d(\rho V)}{dt} = \rho(Q_{in} - Q_{out}), \quad (2)$$



where  $\rho$  is the density of the fluid (with barotropic assumption),  $V$  is the volume of the vessel,  $Q_{in}$  is the driving flow rate, and  $Q_{out}$  is the discharge flow rate. The latter can be calculated from

$$Q_{out} = A_{ref}(x)C_D \sqrt{\frac{2}{\rho}p}, \quad (3)$$

where  $A_{ref}$  is the reference area, and  $C_D$  is the discharge coefficient. In the case of disc-shaped valves, the former is the cylindrical surface between the valve and the seat [3], and as such can be calculated by

$$A_{ref} = D\pi x, \quad (4)$$

where  $D$  is the seat diameter.

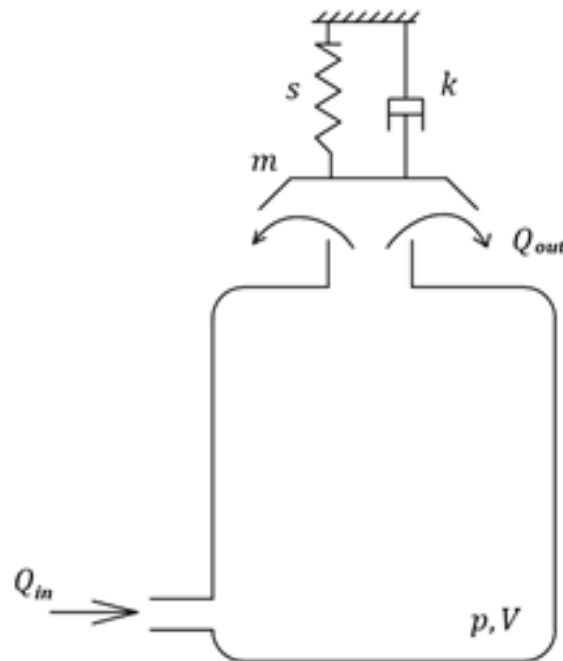


Figure 1 The modelled system

Following the method presented in [1] we get from Equations (1)-(4) that

$$y_1' = y_2, \quad (5)$$

$$y_2' = -\kappa y_2 - (y_1 + \delta) + y_3, \quad (6)$$

$$y_3' = \beta(q - \sqrt{y_3}y_1), \quad (7)$$

where  $y_1$ ,  $y_2$ ,  $y_3$  are the dimensionless valve lift, valve velocity and vessel overpressures,  $\kappa$  corresponds to the damping coefficient,  $\delta$  is the dimensionless pre-compression,  $\beta$  is the stiffness parameter of the system, and  $q$  is the non-dimensional driving flow rate.



Furthermore, the interaction between the valve and the seat is taken into account by a mapping. If at the moment of the collision the valve velocity is sufficiently low and the net force acting on it points towards the seat, then the valve remains closed, otherwise it bounces back according to

$$y_2^+ = ry_2^-, \quad (8)$$

where the  $-$  and  $+$  signs refer to the states before and after the collision, and  $r$  is the coefficient of restitution.

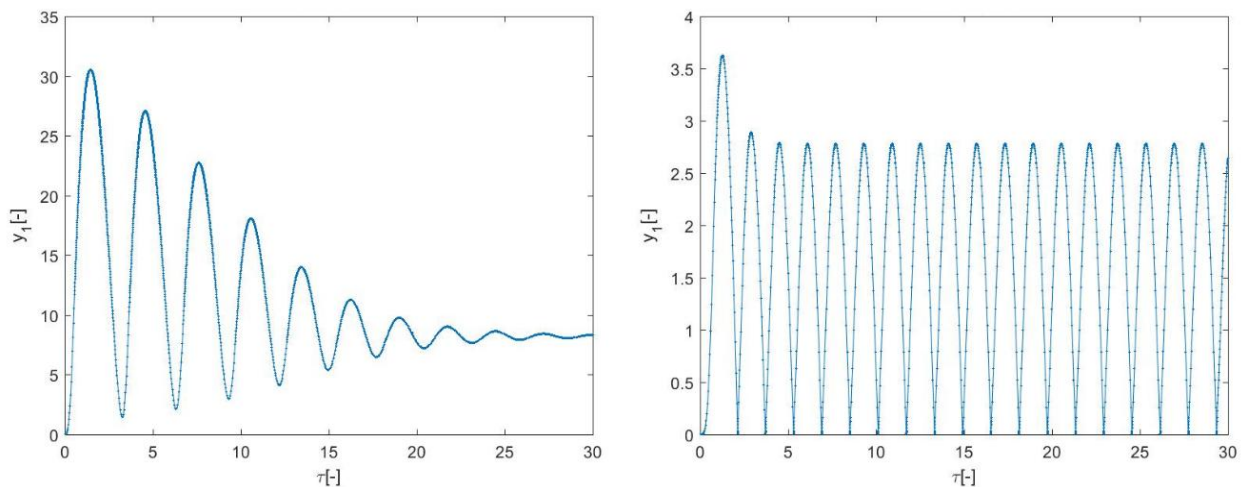


Figure 2 Valve lift versus time during an exponentially stable ( $q = 35$ , left) and a periodic ( $q = 3$ , right) solution

### 3. RESULTS

The same dimensionless quantities were chosen as in [1], i.e.  $\beta = 20$ ,  $\delta = 10$ ,  $\kappa = 0.7$ , and  $q$  was the varied parameter. An exponentially stable and a periodic solution are illustrated by Figure 2. A series of simulations were conducted starting from  $q = 0$  and up to  $q = 40$ , then back to  $q = 0$  again. All calculations were initialized from the last time step of the previous one. From this sweep, the local minimum and maximum values of the lift versus the driving flow rate can be seen in Figure 3. At low flow rates only periodic solutions exist, which first turn into period-two solutions at around  $q = 17$ , then into chaotic oscillations from around  $q = 21$ . The system stabilises at  $q = 29$ . Furthermore, in the  $13 < q < 29$  zone we have coexisting exponentially stable solutions as well. The dashed line illustrates the unstable equilibrium solution, and was analytically calculated from  $y_1' \equiv y_2' \equiv y_3' \equiv 0$ .

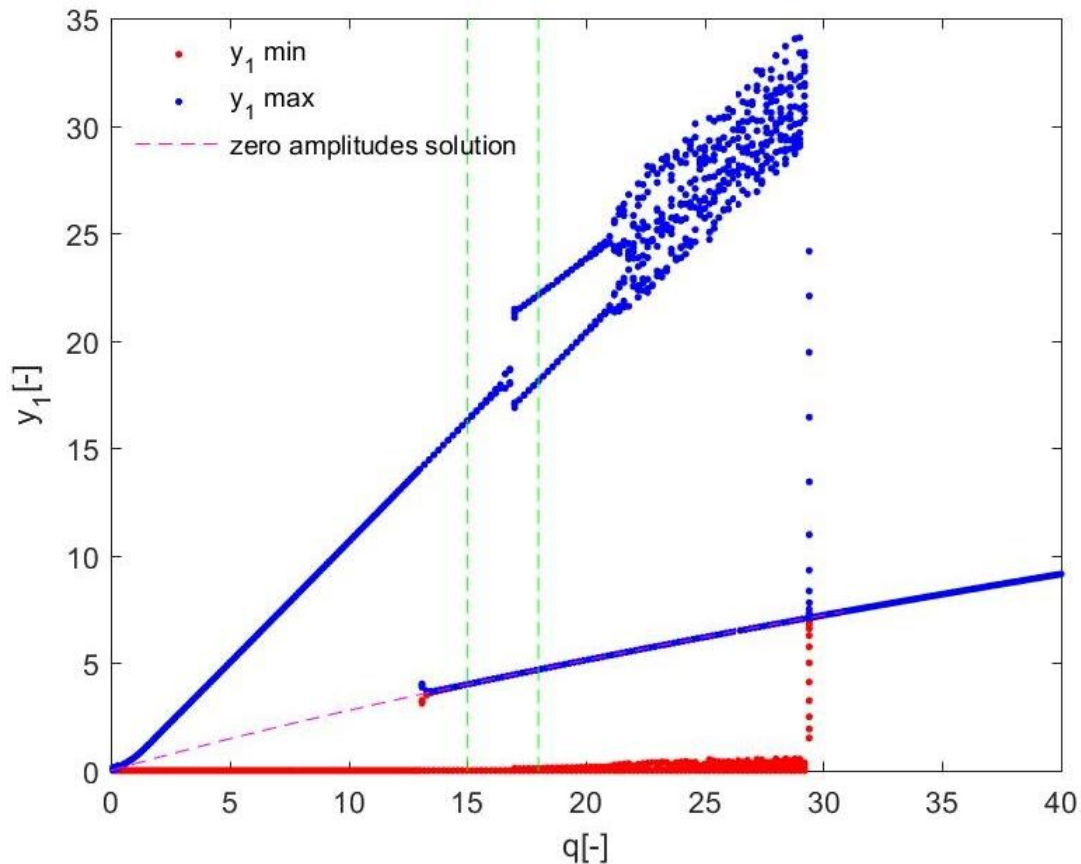


Figure 3 The local minimum and maximum values of the lift versus the driving flow rate

The figure also suggests that in the coexisting region there is a repelling limit cycle somewhere between the exponentially stable and the periodic (or chaotic) solutions. This is confirmed by the projection of the phase portrait (Figure 4): the light blue and the light orange colours illustrate the basins of attraction of the exponentially stable and the periodic solutions, respectively. From the figure it is evident that there exists a repelling limit cycle between the two. Note that the system is autonomous, therefore the trajectories do not cross each other – it only seems so because of the projection. The fully three-dimensional phase space for the  $q = 18$  case can be seen in Figure 5 with the exponentially decaying and the period-two solutions. Here it is clearly visible that the trajectories indeed do not cross each other.

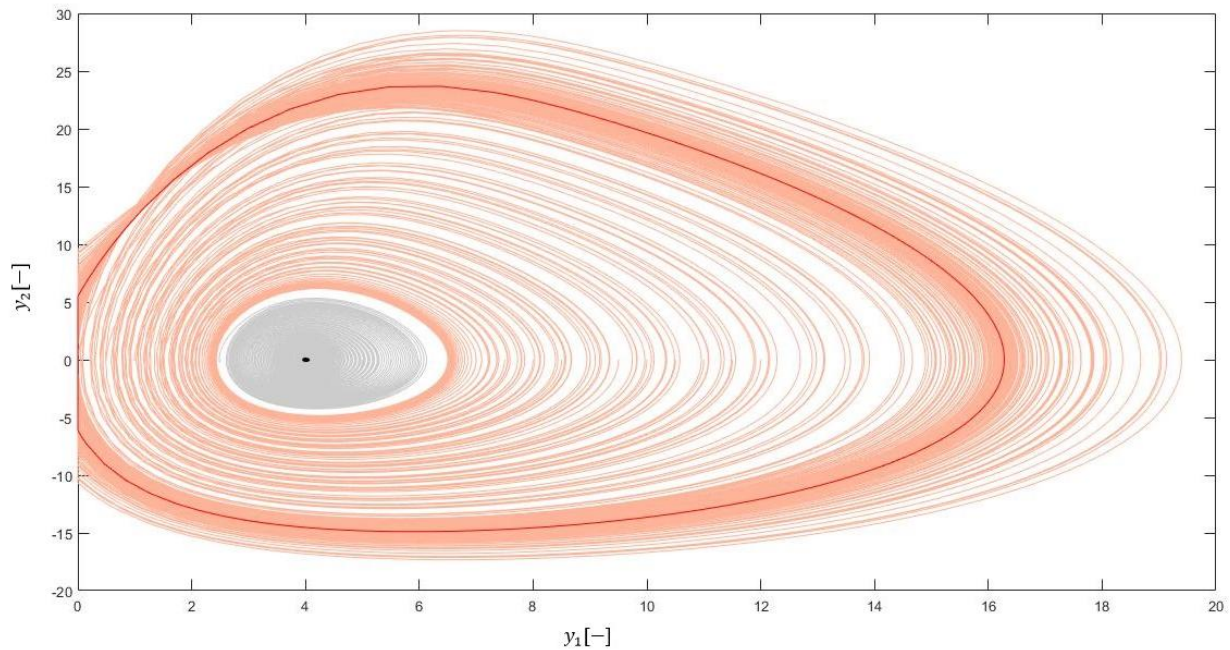


Figure 4 Projection of the phase portrait to the  $y_1$ - $y_2$  plane and the basins of attraction at  $q = 15$

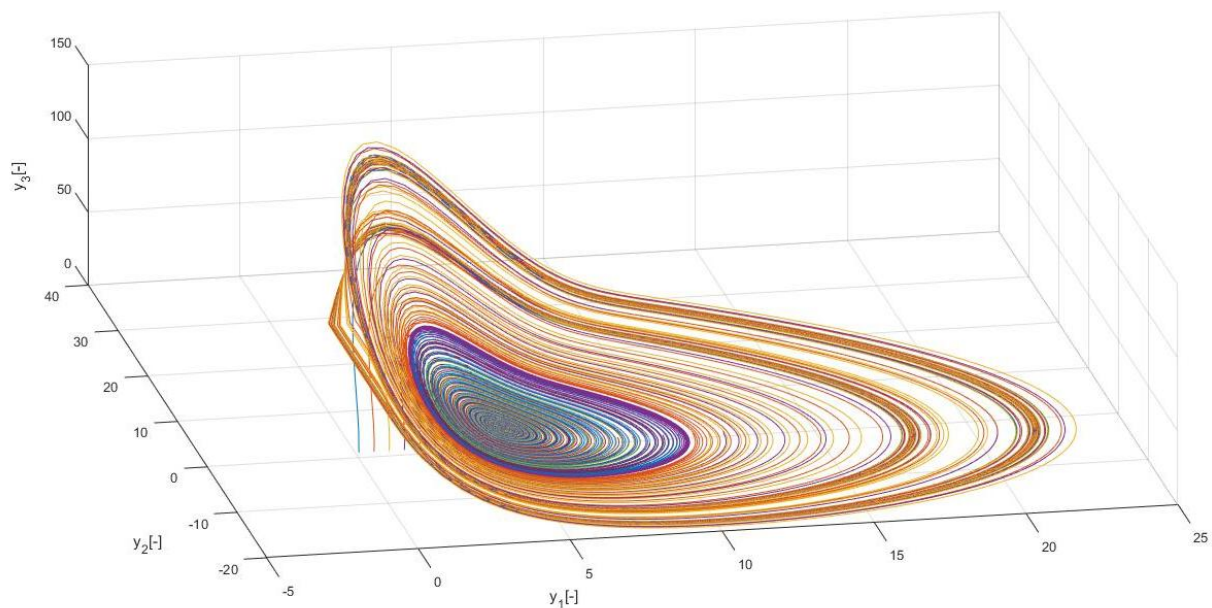


Figure 5 Phase space and the basins of attraction at  $q = 18$

## CONCLUSIONS

A mathematical model was adapted with which numerical simulations were made possible on a simple hydraulic vessel-valve system. It was shown that for given system parameters, depending on the flow rate it one can reach exponentially stable, periodic, period-two, and even chaotic solutions. Phase space analysis also confirmed that in the flow rate range of coexisting solutions, there exists a repelling limit cycle between the attracting node and the attracting limit cycle.



# INTERNATIONAL SCIENTIFIC CONFERENCE ON ADVANCES IN MECHANICAL ENGINEERING

12-14 October 2017, Debrecen, Hungary



## ACKNOWLEDGEMENTS

This project was supported by the OTKA Grant K116549 of Csaba Hős.

## REFERENCES

- [1] Licskó, L., Champneys, A., Hős, Cs.: *Nonlinear Analysis of a Single Stage Pressure Relief Valve*. International Journal of Applied Mathematics, 39, 4-12., 2009.
- [2] Darby, R.: *The dynamic response of pressure relief valves in vapor or gas service, part I: Mathematical model* . Journal of Loss Prevention in the Process Industries, 26, 1262-1268., 2013
- [3] Hős, Cs., Champneys, A., Paul, K., McNeely, M.: *Dynamic behaviour of direct spring loaded pressure relief valves in gas service: Model development, measurements and instability mechanisms*. Journal of Loss Prevention in the Process Industries, 31, 70-81., 2014
- [4] Moussou, P., Gibert, R.J., Brasseur, G., Teygeman, Ch., Ferrari, J., Rit, J.F.: *Instability of pressure relief valves in water pipes*. Journal of Pressure Vessel Technology, 132, 2010
- [5] Viel, A.: *Strong Coupling of Modelica system-level models with detailed CFD models for transient simulation of hydraulic components in their surrounding environment.*, Proceedings of the 8th Modelica Conference, Dresden, 2011



## TRANSIENT SIMULATIONS OF GAS DYNAMICS WITH DIFFERENT NUMERICAL SCHEMES

<sup>1</sup>KALMÁR Csanád, <sup>2</sup>HEGEDŰS Ferenc PhD, <sup>3</sup>FELHŐS Dávid PhD

<sup>1,2</sup>Department of Hydrodynamic Systems, Faculty of Mechanical Engineering, Budapest University of Technology and Economics

E-mail: [cskalmar@hds.bme.hu](mailto:cskalmar@hds.bme.hu), [fhegedus@hds.bme.hu](mailto:fhegedus@hds.bme.hu)

<sup>3</sup>Knorr-Bremse Railway Systems Hungary Ltd.

E-mail: [david.felhos@knorr-bremse.com](mailto:david.felhos@knorr-bremse.com)

### Abstract

The effect of different numerical schemes was investigated in the case of transient gas dynamics. The partial differential equation system of continuity, momentum and energy was solved for a one dimensional pipe flow. A couple of members of the so-called Lax-Wendroff family of schemes were used. The models were compared with analytical solutions and with measurement results as well. We observed that some methods are comfortable to use, but some of them cannot resolve some specific cases such as shock waves, etc. The numerical results agree well both with the solutions of some analytical cases and with measurements as well.

**Keywords:** Gas dynamics, numerical schemes, Lax-Wendroff, shock waves

### 1. INTRODUCTION

Developing numerical methods in order to solve difficult ordinary or partial differential equations have always been in the centre of attention amongst researchers. Several explicit, semi-explicit and implicit schemes with different order and accuracy have been introduced since the last century [1]. Each of them has multiple advantages and disadvantages depending on what kind of applications they are being used on.

In order to apply a suitable numerical method, it is necessary to define the following three requirements: *consistency*, *stability*, and *convergence* [2]. These three conditions cover different aspects of the relations between the discretized equations, the numerical solution and the exact, analytical solution of the differential equation. Consistency expresses that the discretized equations should tend to the differential equations to which they are related to when  $\Delta t$  and  $\Delta x$  tend to zero. Stability means that the difference scheme should not allow errors to grow indefinitely; that is, to be amplified without bound, as we progress from one time step to another. More precise definitions of stability can be found in [3]. Finally, convergence means that the numerical solution should approach the exact solution of the differential equation at any point  $x_i = i\Delta x$  and time  $t_n = n\Delta t$ . As it can be seen, the conditions of consistency, stability and convergence are related to each other, and the precise relation is contained in the fundamental *Equivalence Theorem of Lax*, a proof of which can be found in [1].

The complex behaviour of several numerical schemes are investigated in this study. The applied system of equations is the one-dimensional, non-linear equations of gas flow in conservative form (also called inviscid Euler-equations) [2]. These equations have the opportunity to show the advantages and disadvantages of some certain numerical schemes.



## 2. GOVERNING EQUATIONS

The governing equations of a one-dimensional, transient flow in a tube with variable cross-section are the equations of continuity, momentum and energy, respectively. These three equations can be written in a compact vectorial form:

$$\frac{\partial \vec{U}}{\partial t} + \frac{\partial \vec{f}}{\partial x} = \vec{Q}, \quad (1)$$

where  $t$  and  $x$  are the time and spatial coordinates, respectively;  $\vec{U}$  is called the conservative variables,  $\vec{f}$  is the fluxes of the conservative variables, and  $\vec{Q}$  is any kind of source terms. More explicitly, these can be written as follows:

$$\vec{U} = \begin{pmatrix} \rho A \\ \rho v A \\ \rho e A \end{pmatrix}, \quad \vec{f} = \begin{pmatrix} \rho v A \\ (\rho v^2 + p) A \\ (\rho v e + p v) A \end{pmatrix}, \quad \vec{Q} = \begin{pmatrix} 0 \\ F_p + F_f \\ 0 \end{pmatrix}, \quad (2)$$

where  $\rho$  is the density,  $A = A(x)$  is the cross-section,  $v$  is the velocity,  $p$  is the pressure,  $F_p$  and  $F_f$  are the forces due to the variable cross-section and friction, respectively. The total energy  $e$  is written as

$$e = c_v T + v^2, \quad (3)$$

where  $c_v$  is the isochoric specific heat, and  $T$  is the temperature. The relation between  $T$ ,  $\rho$ , and  $p$  is expressed by the ideal gas law:

$$\frac{p}{\rho} = RT, \quad (4)$$

with  $R$  being the specific gas constant. The force acting on the gas by the wall due to variable cross-section can be computed as

$$F_p = p \frac{dA}{dx}. \quad (5)$$

Wall friction is modelled by a friction term  $F_f$ , which can be calculated with the well-known Blasius-formula:

$$F_f = A \frac{\lambda \rho}{D} \frac{v |v|}{2}, \quad (6)$$

where  $\lambda$  is the friction coefficient. It can be seen, on the other hand, that heat diffusion and the viscous effects are totally neglected in the equations.

Our task is to discretize these equations in a way that satisfies the three conditions mentioned above. The problem is that many of the well-known discretizing schemes (upwinding, central space-centred, etc.) become unstable on velocities approaching sound speed, which is a fairly common phenomenon in gas dynamics. Therefore, it is necessary to introduce more complex schemes in order to solve the equations in these types of conditions.



### 3. APPLIED METHODS

The first method we use maybe the most fundamental scheme introduced by Richtmyer and Morton [1]. This scheme, known as the *Richtmyer* scheme, is at the basis of many modern two-step predictor-corrector methods which are able to handle non-linearities in a straightforward way. An intermediate state is introduced which can be considered as the solution at a time  $t = (n + 1/2)\Delta t$ . The scheme is defined as

$$U_{i+\frac{1}{2}}^{n+\frac{1}{2}} = \frac{1}{2}(U_i^n + U_{i+1}^n) - \frac{\tau}{2}(f_{i+1}^n - f_i^n), \quad (7a)$$

where  $\tau = \Delta t/\Delta x$ . The subscript  $i$  and  $n$  are related to spatial and time discretization, respectively. This first step is identical to the first-order Lax-Friedrichs scheme [4]. The second step is a so-called *leapfrog* step applied at  $(n + 1/2)$ :

$$U_i^{n+1} = U_i^n - \tau \left( f_{i+\frac{1}{2}}^{n+\frac{1}{2}} - f_{i-\frac{1}{2}}^{n+\frac{1}{2}} \right), \quad (7b)$$

where the flux terms are evaluated at the half time step. It can be proven that this scheme is second order in both space and time. A more general version of this scheme is developed by Lerat and Peyret [5][6].

Another Lax-Wendroff discretization is the two-step predictor-corrector scheme of *MacCormack* [7]. This scheme is probably the most widely applied version of the Lax-Wendroff schemes. Predictor values are defined at  $(n + 1)$  and at point  $i$ , followed by a corrector step, where  $\bar{f}_i = f(\bar{U}_i)$ :

$$\bar{U}_i = U_i^n - \tau(f_{i+1}^n - f_i^n) \quad (8a)$$

$$U_i^{n+1} = \frac{1}{2}(\bar{U}_i + U_i^n) - \frac{\tau}{2}(\bar{f}_i - \bar{f}_{i-1}). \quad (8b)$$

The first step is a first-order forward discretization in space, which is actually unstable for supersonic velocities. The second, corrector step is a backward first-order scheme, is unstable for subsonic flows. However, it can be proven that the combined scheme is stable and of second order in both time and space. It is important to mention that an alternative of MacCormack's scheme is to reverse the order of the predictor and corrector steps.

The third scheme is being examined here is developed by *Casier et al.* [8], and it can be considered as a generalization of MacCormack's scheme. The scheme can be written as follows:

$$\left(\xi + \frac{1}{2}\right)\overline{\Delta U}_i = -\tau(f_{i+1}^n - f_i^n) + \left(\xi - \frac{1}{2}\right)\overline{\Delta U}_{i-1} \quad (9a)$$

$$\left(\xi + \frac{1}{2}\right)\overline{\overline{\Delta U}}_i = -\tau(f_i^n - f_{i-1}^n) + \left(\xi - \frac{1}{2}\right)\overline{\overline{\Delta U}}_{i+1} \quad (9b)$$

$$\Delta U_i^n = \frac{1}{2}(\overline{\Delta U}_i + \overline{\overline{\Delta U}}_i), \quad (9c)$$



where  $\Delta U_i^n = U_i^{n+1} - U_i^n$ . Here, the parameter  $\xi$  is an arbitrary choice, and it can be clearly seen that the scheme reduces to (8) with  $\xi = \frac{1}{2}$ . This scheme is a semi-explicit scheme, and can be solved by a single sweep through the mesh.

All of these numerical schemes are conditionally stable, therefore, it is necessary to consider the time step selection in each one of them. Both (7) and (8) has the stability condition of  $|\sigma| \leq 1$ , where  $\sigma = a\tau$  with  $a$  being the propagation speed. The scheme (9) is stable if the condition  $|\sigma| \leq 2\xi$ , which gives the opportunity to increase time step as  $\xi$  increases.

As it can be observed, all three methods need special consideration on the boundary points. Probably the most widely applied tool for boundary treatment is the method of characteristics. We present only a brief summary of this method here, a detailed review can be found in [2]. The main concept of this technique is that three characteristic quantities are conserved along their respective characteristic lines. By solving these three equations the three primitive variables (pressure, density and velocity) can be determined, temperature and total energy can be calculated by using (3) and (4).

#### 4. NUMERICAL RESULTS

To compare the different numerical schemes, we solve the equations for four different test cases, three of them are simple problems with known analytical solutions, and the fourth is a measurement case of filling a reservoir.

The first example is the so-called Fanno-flow, in which the gas flows through a straight tube. The pressure difference on the ends of the tube equals to the pressure drop due to friction. The velocity is growing in the flow direction, but if the outflow velocity reaches Mach number 1, the mass flow rate through the pipe cannot be increased by increasing the pressure difference. Figure 1 shows a state with subsonic and supersonic outflow on the left and right hand side, respectively. It can be observed that if the outflow is subsonic, the pressure on the end of the pipe equals to the ambient pressure. However, when the outflow velocity reaches Mach number 1 (graphs on the right hand side), the pressure on the outlet separates from the ambient pressure, because no information can propagate into the pipe in this case.

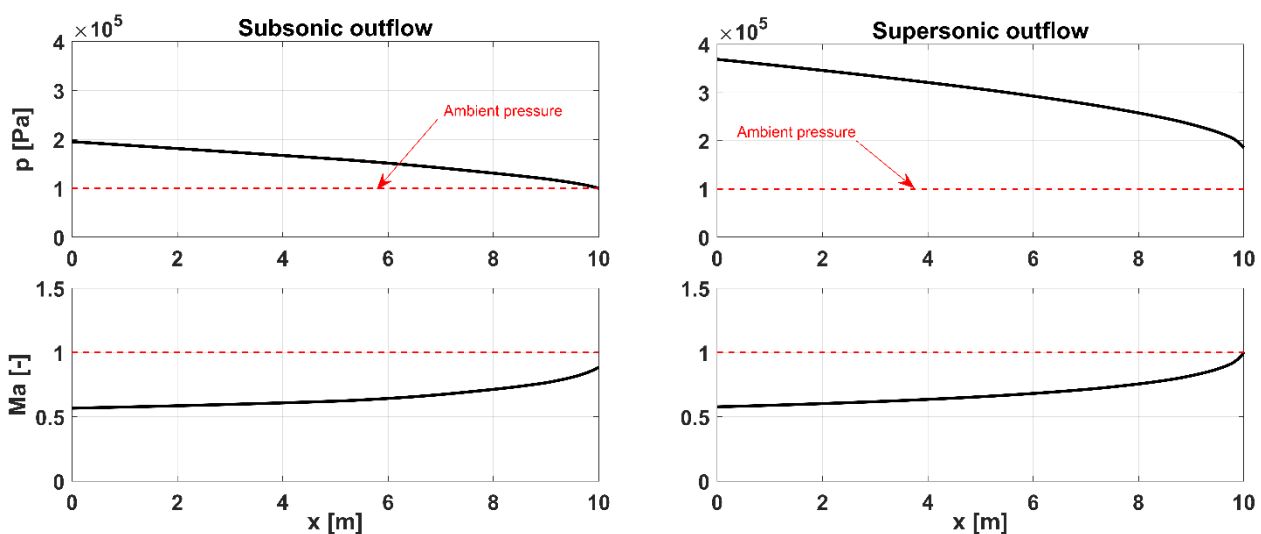


Figure 1 Pressure and Mach number distributions of a Fanno-flow. The two graphs to the left hand side are in subsonic; the two to the right side are in supersonic outflow case.

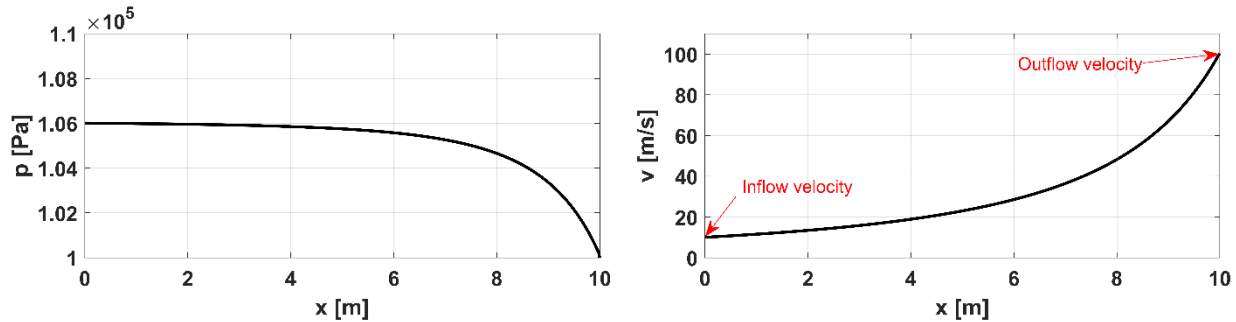


Figure 2 Pressure and velocity distributions in a frictionless converging nozzle.

The second example is a frictionless flow in a converging nozzle. In this case, for given inflow parameters, the outflow conditions can be determined analytically by solving the energy equation. Figure 2 shows the pressure and velocity distributions in this example with a specific geometry. As computed in [9], for this current geometry, for inflow velocity of 10 m/s the outflow velocity should be 100 m/s; the correspondence is clearly seen in the velocity distribution diagram.

It has to be mentioned that the results completely agreed with all the three examined numerical schemes in the first two examples. However, in the case of the third example, the well-known Laval-nozzle, the schemes behaved quite differently. In a converging-diverging nozzle, over a given pressure difference between the two boundaries, a steep shock wave evolves somewhere in the diverging zone. Neither of the schemes of Richtmyer nor MacCormack were able to resolve this shock wave precisely. The Casier scheme, however, produced really good resolution around the shock wave. The pressure distributions in a Laval-nozzle can be seen on Figure 3 with Richtmyer's scheme on the left, and Casier's scheme on the right hand side.

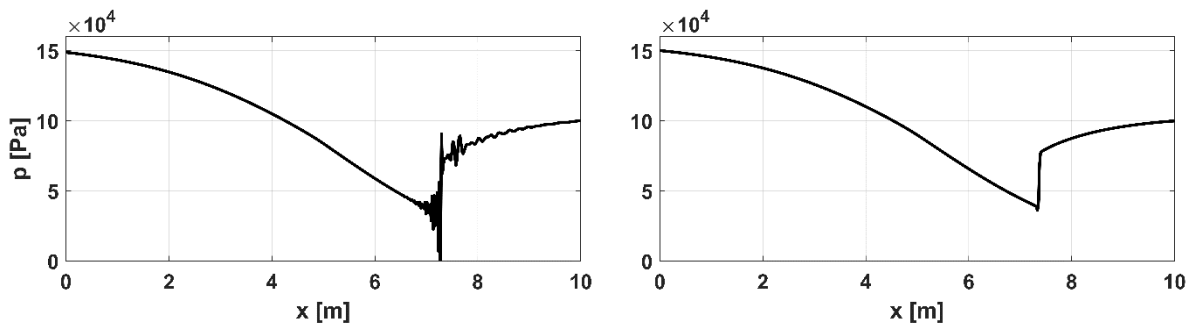


Figure 3 Pressure distributions in a Laval-nozzle with Richtmyer's scheme on the left and Casier's on the right hand side.

The last example is a real measurement case, in which a reservoir of 50 L volume is being filled to 9.8 bar from a pressure supply through a pipeline with given geometry. The length of the tube was 4.5 m, the diameter was 20 mm. The simulation was computed by Casier's scheme taking advantage of the opportunity to increase the time steps. The results of the measurement and simulation can be seen on Figure 4. The blue line denotes the supply side pressure versus time. The red and green lines are the simulated and the measured reservoir pressures versus time, respectively. The result from the measurement and simulation are fitting fairly well. It can be seen that the



reservoir pressure follows the supply pressure by a little delay due to the complex geometry of the pipeline.

## CONCLUSIONS

The behaviour of three different numerical schemes were investigated in order to solve the non-linear system of equations of gas dynamics. According to the result of the examples, it can be stated that the Richtmyer's and MacCormack's scheme can be used in the absence of shock waves. On the other hand, Casier's method can handle steep shock waves properly, thus it can be used in almost any problems of gas dynamics. However, the selection of the parameter  $\xi$  is not evident and needs further investigations. Comparisons with more measurement cases will be done in the near future as well.

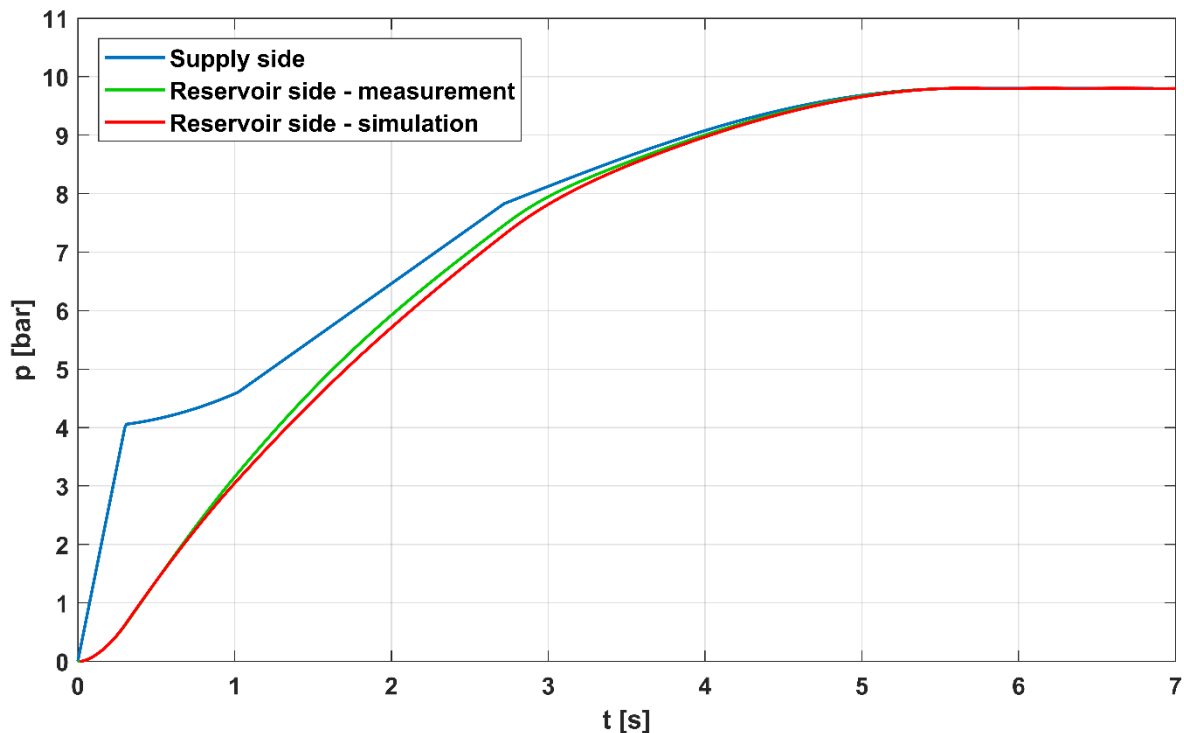


Figure 4 Supply side (blue line) and reservoir side (red line – simulation, green line – measurement) pressures versus time in the measurement test case.

## ACKNOWLEDGEMENT.

The recent study and publication was realized within the *Knorr-Bremse Scholarship Program* supported by the Knorr-Bremse Railway Systems Budapest.

## REFERENCES

- [1] Richtmyer, R. D., and Morton, K. W.: *Difference Methods for Initial Value Problems*. Comm. Pure and Applied Mathematics, 17, 267-93. 1967.
- [2] Hirsch, C.: *Numerical computations of internal and external flows*. ISBN 0 471 91762 1. John Wiley and Sons, 1983.
- [3] O'Brien, G. G., Hyman, M. A., and Kaplan, S.: *A study of the numerical solution of partial*



# INTERNATIONAL SCIENTIFIC CONFERENCE ON ADVANCES IN MECHANICAL ENGINEERING

12-14 October 2017, Debrecen, Hungary



- differential equations*. Journal Mathematics and Physics, 29, 223-51. 1950.
- [4] Lax, P. D.: *Weak solutions of non-linear hyperbolic equations and their numerical computation*. Comm. Pure and Applied Mathematics, 7, 159-93. 1954.
- [5] Lerat, A., Peyret, R.: *Non centered schemes and propagation problems*. Computers and Fluids, 2, 53-52. 1974.
- [6] Lerat, A., Peyret, R.: *The problem of spurious oscillations in the numerical solution of the equations of gas dynamics*. Lecture Notes in Physics, Vol 35, pp. 251-256, New York: Springer Verlag. 1975.
- [7] MacCormack, R. W.: *The effect of viscosity in hypervelocity impact cratering*. AIAA Paper 69-354. 1969.
- [8] Casier, F., Deconinck, H., and Hirsch C.: *A class of bidiagonal schemes with implicit boundary conditions for the solution of Euler's equations*. AIAA Paper 83-0126, AIAA 21<sup>st</sup> Aerospace Sciences Meeting. 1983.
- [9] Környei, T.: *Termodinamika*. Műszaki Kiadó, 45076. 2005.



## MECHANICAL JOINING METHODS OF HOT-DIP GALVANIZED STEEL SHEETS

**KAŠČÁK Ľuboš PhD, SPIŠÁK Emil PhD**

*Institute of Technological and Material Engineering, Technical University of Košice*  
E-mail: [lubos.kascak@tuke.sk](mailto:lubos.kascak@tuke.sk), [emil.spisak@tuke.sk](mailto:emil.spisak@tuke.sk)

### Abstract

*The optimization of a car body in terms of cost can be achieved by using different materials in various positions of the car in order to utilize specific properties of each different material. It is not always possible or effective to use conventional joining methods such as resistance spot welding, therefore clinching and clinchriveting seem to be possible alternatives. The paper evaluates the properties of joints made by clinching and clinchriveting techniques. Hot-dip galvanized steel sheets such as microalloyed steel H220PD, extra deep-drawing grade steel DC06 and drawing grade steel DX51D+Z were used for the experiments. In order to evaluate the properties of the clinched joints, the following tests were performed: tensile test – to determine the load-bearing capacity and the force-elongation diagrams and a metallographical observations for evaluation of the joints' structures. Clinching and clinchriveting proved to be suitable methods for joining the tested car body steel sheets.*

**Keywords:** *clinching, clinchriveting, tensile test, metallography*

### 1. INTRODUCTION

Hot-dip galvanized steel sheets have been widely used in car body production to improve the corrosion resistance and service life of vehicles. Resistance spot welding is a common joining method for car body parts. Welding of galvanized steel sheets requires to use higher values of welding parameters such as welding current, electrode pressure and welding time due to the shunting effect of zinc coating; electrodes need to withstand more pressure and higher temperature in the process of welding, resulting in a sharp decline of electrode service life [1,2]. The electrode tip is alloyed with the zinc coating on its working face, which defiling the electrode. Zinc coating could increase the resistance and enlarge the welding spot, bringing follow-up treatment difficulties. The following difficulties may also turn up for resistance spot welding of galvanized steel sheets: it is prone to have cracks, pores and soft tissues in the internal areas of the welding spot [3,4]. Resistance spot welding is not suitable for joining different materials because of oxide layer on the sheet, different thermal conductivity, and fusion point. Therefore the mechanical joining methods have been proved effective for joining lightweight materials. Mechanical fastening encompasses a broad range of methods, from threaded fasteners to different forms of rivets and mechanical interlocking methods [5,6]. Among these mechanical fastening technologies, the mechanical clinching and the clinchriveting technology have been developed rapidly.

Hot-dip galvanized steels sheets or non-weldable sheets can be joined by clinching or clinchriveting without damaging the surface. Dissimilar material sheets with different melting point and mechanical properties can be joined effectively by these clinching methods as well. Plastic deformation of the sheets forms the joint in the mechanical clinching processes, so the chemical properties have negligible effect on the joining of different material [6,7].

The paper focuses on the evaluation of the joints made by clinching and clinchriveting methods which are utilized in car body production.



## 2. METHODS

The clinching process is a combination of drawing and forming that locks together sheets. Sheet metal parts are deformed locally without the use of any additional elements – *Figure 1*. A mechanical interlock is produced between the metal sheets by the material flow in the mechanical clinching [5]. The sheets can be hooked together by the mechanical interlock which has a high strength. The strength of the mechanical clinched joint mainly depends on the geometrical parameters of the joint profile which is mainly influenced by process parameters and clinching dies [8].

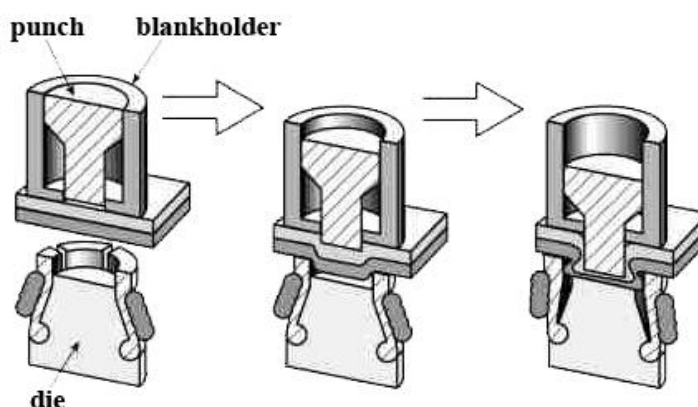


*Figure 1* Principle of clinching

The ClinchRivet is a cold process for joining two or more sheets by directly piercing the sheets with a special rivet (*Figure 2*). Since the ClinchRivet process does not require a pre-drilled hole unlike the conventional riveting, the joining speed is the same level with that of the spot resistance welding, and the equipment is similar [8].

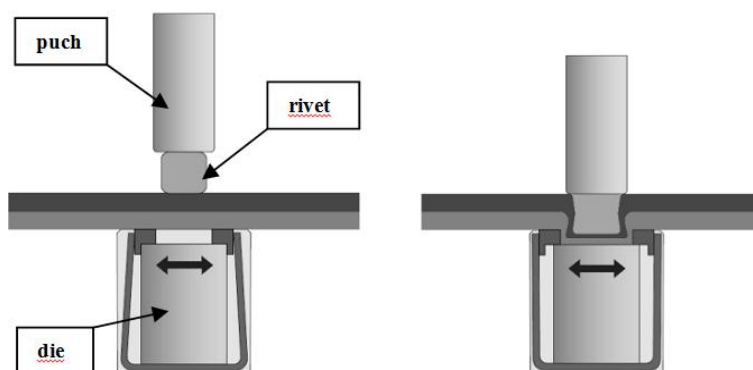


*Figure 2* Principle of clinchriveting

The joint is formed by a rivet – *Figure 3*. The punch, under the pressure conveyed by a hydraulic power device, pushes the rivet to penetrate into the top plate, and the die shape causes the rivet to flare within the lower sheet in order to form a mechanical interlock. This process therefore requires access to both sides of the joint [9,10].



Figure 3 Rivets for clinchriveting process

The following materials were used for joining by both methods: microalloyed steel HSLA H220PD with the thickness of 0.8 mm, extra deep-drawing grade steel DC06 with the thickness of 0.7 mm and DX51D+Z with the thickness of 0.9 mm. The chemical composition and the basic mechanical properties of the joined steel sheets are shown in *Table 1* and *Table 2*.

Table 1 Chemical composition (in [%] of wt) of materials

Material	C	Mn	Si	P	S	Al	Cu	Ni
H220PD	0.012	0.435	0.119	0.057	0.002	0.041	0.040	0.013
DC06	0.020	0.071	0.010	0.017	0.002	0.055	0.038	0.011
DX51D	0.064	0.178	0.007	0.016	0.002	0.120	0.041	0.002
Material	Cr	Ti	V	Nb	Mo	Co		
H220PD	0.046	0.033	0.012	0.052	0.009	0.047		
DC06	0.022	0.062	0.008	0.023	0.009	0.035		
DX51D	0.023	0.002	0.005	0.015	0.004	0.019		

Table 2 Basic mechanical properties of joined steel sheets

Material	R <sub>p0.2</sub> [MPa]	R <sub>m</sub> [MPa]	A <sub>80</sub> [%]
H220PD	238	382	36
DC06	170	270-330	41
DX51D+Z	≥ 140	270-500	23

The same material combinations for the joining were used:

- *Samples A*: H220PD ( $a_0 = 0.8$  mm)
- *Samples B*: DC06 ( $a_0 = 0.7$  mm)
- *Samples C*: DX51D ( $a_0 = 0.9$  mm)

The tensile test was performed for evaluation of the load-bearing capacity of the joints. The samples with dimensions of 40 x 90 mm and 30 mm lapping according to STN 05 1122 standard were prepared for the experiments (*Figure 4*). Ten samples were created for every combination of sheets. It was not necessary to clean the surfaces of samples before clinching and clinchriveting. The clinchriveting method was realized with the steel rivets of  $\varnothing 5$  mm diameter. The metallographical observations for evaluation of the joints' structures was utilized as well.

The carrying capacities of the SPR joints were evaluated according to the above-mentioned standard. This test was used for measuring the maximum load-bearing capacity  $F_{max}$  of the joints. The test was carried out on the metal strength testing machine TIRAtest 2300 produced by VEB TIW Rauenstein with the loading speed of 8 mm/min.

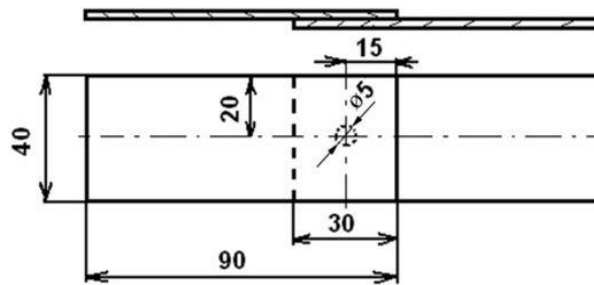


Figure 4 Sample for tensile test

### 3. RESULTS

Tensile tests were executed under displacement control conditions on the specimen configurations in order to characterise the static behaviour of the joints. The maximum shearing load was the most significant value obtained from the load-displacement curves. The form of the curves indicates the behaviour of the joints under loading.

The average maximum load-bearing capacity of clinchriveted joints (CR) were about 4800 N for sample A, about 3800 N for sample B and about 4800 N for sample C. During the riveting process the rivet and the riveted sheets undergo massive deformation to form the mechanical interlock. This energy is stored within the interlock leading to higher energy absorption. Load-displacement curves of CR joints were compared with curves of clinched joints (CL), as is shown in Figure 5.

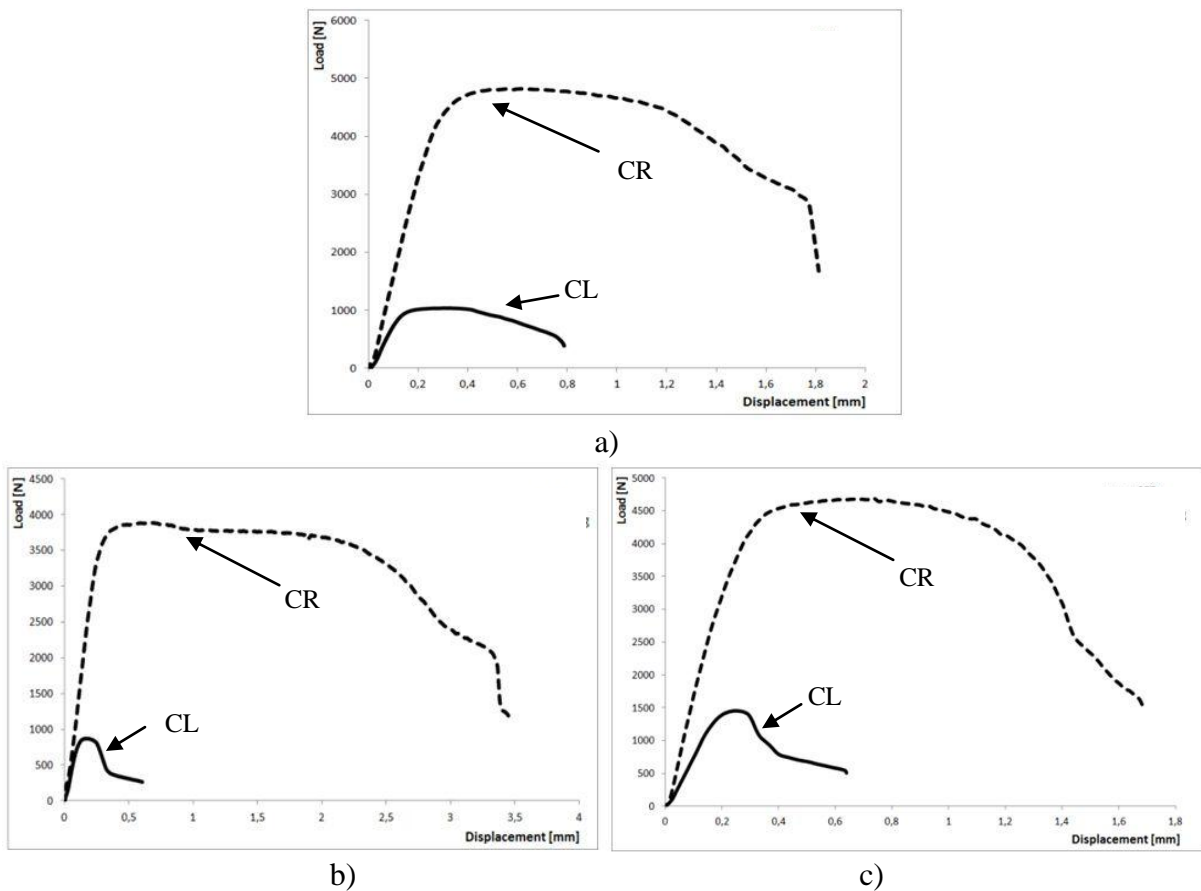
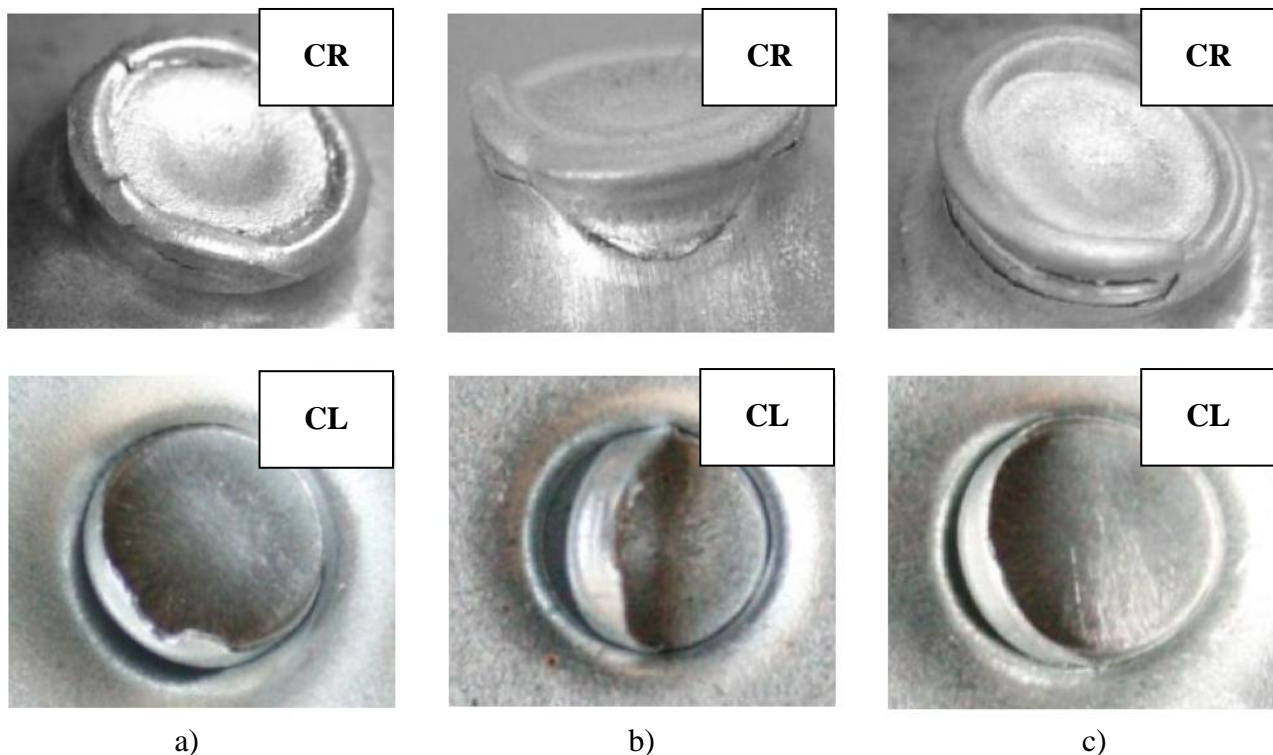


Figure 5 Load-displacement curves of clinched joints (CL) and clinchriveted joints (CR):  
a) H220PD, b) DC06, c) DX51D



The shearing loads are significantly higher for clinchriveted joints than clinched joints. On average, the CL joints reached 21% (for samples A), 22% (for samples B) and 30% (for samples C) of carrying capacities of CR joints. The capacity for deformation in the case of CL joint is considerably smaller than the CR joint.

CR joints failed in the manner of a press-stud in combination with the mode of one edge of the joint fails. CL joints failed at the neck of the joint – *Figure 6*. Both modes result in loosening of the joint after quite small displacements. In the press-stud mode, insufficient deformation produces minor interlocking of the sheets and will lead to failure. In the second mode, there is insufficient material in the neck of the joint and loading will result in failure in the neck; excessive elongation in the region of the joint neck, causing crack formation.



*Figure 6* Failures of clinchriveted joints (CR) and clinched joints (CL): a) H220PD, b) DC06 and c) DX51D

## CONCLUSIONS

The high-speed mechanical fastening technique clinching and clinchriveting are young joining methods, but become more and more popular during the last decades. The main advantage of mechanical joining technology is low running costs due to the fact that the processed components are not heated. Only die, punch and rivets in clinchriveting method are used to form the sheet components to finish the whole joining process. The incomparable advantages of clinching and clinchriveting are as follows: no joining hot-stress has been produced, no poisonous gas has been given off, the energy consumption is low, and this process leads to no damage to surface coating and does not require any premanufacturing of holes to the joined materials.

The methods of clinching and clinchriveting are suitable for joining the tested hot-dip galvanized steels sheets. All tested samples of clinchriveted joints reached higher values of load-bearing capacity in comparison with clinched joints. The maximum load values of clinched joints and



# INTERNATIONAL SCIENTIFIC CONFERENCE ON ADVANCES IN MECHANICAL ENGINEERING

12-14 October 2017, Debrecen, Hungary



clinchriveted joints were 1020 N and 4790 N for the samples of H220PD materials, 853 N and 3857 N for the samples of DC06 materials, and 1467 N and 4798 N for the samples of DX51D materials. The load-bearing capacity of these samples were sufficient and the metallographical observation confirmed no occurrence of cracks or failures in the area of joints during both joining processes. Using the rivets in clinchriveting method led to significant increasing of load-bearing capacity in comparison to the clinching method.

## ACKNOWLEDGEMENT

The described work was carried out as part of a project VEGA 1/0441/17.

## REFERENCES

- [1] Mei, L., Yi, J., Yan, D., Liu, J., Chen, G.: *Comparative study on CO<sub>2</sub> laser overlap welding and resistance spot welding for galvanized steel*. Materials and Design, 40, 433-442., 2012.
- [2] Kaščák, L., Mucha, J., Slotá, J., Spišák, E.: *Application of modern joining methods in car production Processes Examples Strength*. Rzeszów: Oficyna Wydawnicza Politechniki Rzeszowskiej, 2013.
- [3] Aslanlar, S.: *The effect of nucleus size on mechanical properties in electrical resistance spot welding of sheets used in automotive industry*. Materials and Design, 27, 125-131., 2006.
- [4] Hwang, I.S., Kang, M.J., Kim, D.C.: *Expulsion reduction in resistance spot welding by controlling of welding current waveform*. Procedia Engineering, 10, 2775-2781., 2011.
- [5] Chen, C., Zhao, S., Cui, M., Han, X., Zhao, X., Ishida, T.: *Effects of geometrical parameters on the strength and energy absorption of the height-reduced joint*. The International Journal of Advanced Manufacturing Technology, 90, 3533-3541., 2017.
- [6] Mucha, J., Witkowski, W.: *The experimental analysis of the double joint type change effect on the joint destruction process in uniaxial shearing test*. Thin-Walled Structures, 66, 39-49., 2013.
- [7] Mucha, J., Kaščák, L., Spišák, E.: *The experimental analysis of forming and strength of clinch riveting sheet metal joint made of different materials*. Advances in Mechanical Engineering, 2013, 1-11., 2013.
- [8] Johnson, P. et al.: *Online visual measurement of self-pierce riveting systems to help determine the quality of the mechanical interlock*. Measurement, 42, 661-667., 2009.
- [9] Abe, Y. et al. *Self-piercing riveting of high tensile strength steel and aluminium alloy sheets using conventional rivet and die*. Journal of Materials Processing Technology, 209, 3914-3922., 2009.
- [10] Sun, X., Khaleel, M.A.: *Performance Optimization of Self-Piercing Rivets through Analytical Rivet Strength Estimation*. Journal of Manufacturing Processes, 7, 83-93, 2005.



## REVIEW OF WHEEL DYNAMIC MODELS AT VEHICLE DEVELOPMENT

KINCSES Dávid, MEZEI Lajos, HAJDU Sándor PhD

Department of Mechanical Engineering, Faculty of Engineering, University of Debrecen

E-mail: [davidkincses@gmail.com](mailto:davidkincses@gmail.com), [mezei.lajos14@gmail.com](mailto:mezei.lajos14@gmail.com), [hajdusandor@eng.unideb.hu](mailto:hajdusandor@eng.unideb.hu)

### Abstract

In this paper the possibilities of wheel dynamic modeling are shown. The type of wheel dynamic models what can be used for modeling are presented. Our aim is to investigate a simpler, less parametric function (as the Pacejka Magic formula), that provide correct accuracy. Non-linear curve fitting is used between the data of the Magic formula and the examined functions. The fitted curves and the Magic formula are compared on different slip ranges. The most suitable curves for each range are selected.

**Keywords:** wheel modeling, slip, curve fitting

### 1. THEOREYTICAL BACKGROUND OF WHEEL DYNAMIC MODELING

The wheels are mainly supposed to transfer forces between the road and the vehicle, so the vehicle can be controlled by the driver. The wheel is functioning also as a low-pass filter in the suspension. The high frequency vibrations, (that caused by the small scragginess of the road) are reduced by this filter. The forces taking effect on a wheel, which rolls on horizontal road, can be active or passive forces. As the first example for the active forces is the vertical load. This is passed across through the centerline of the wheel. That, from the total mass of the wheel and the part of the vehicle's mass on the wheel is summed up. The second example is the horizontal tractive force, with the vehicle's shaft pushes or pulls the wheel (actually at the contact point between the wheel and the road is woken). The wheel is rotated around its center by the rotating/braking torque.

Passive forces are only working on a wheel if, that rolls on horizontal road and any of the active forces is taking effect. For example, the reaction force, which is waking on the surface between the wheel and the road. Since the wheel does not contact with the ground in a point, but on a surface, so the reaction force takes effect like distributed load, what is substituted as a concentrated force in calculations. The point of application of reaction force is vertical correlate to the axis of symmetry. In the direction of driving this force is shifting, that causes the rolling resistance/drag.

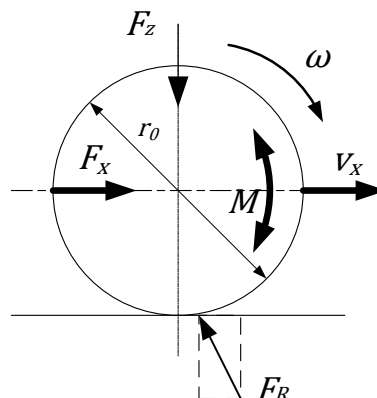


Figure 1 Forces and torques on wheel



The slip is actually the effect of the speed difference between the wheel and the vehicle. The slip of the wheel extends always. 0 [%] slip value does not occur in reality. Driving and braking slip is distinguished. In driving case the wheel's peripheral speed is larger than the vehicle's, and in the braking case, the vehicle's is larger.

Slip calculations:

$$s_{driving} = \frac{r_0\omega - v_x}{r_0\omega} \quad (1)$$

$$s_{braking} = \frac{v_x - r_0\omega}{v_x} \quad (2)$$

### 1.1 Theory of modeling

For simulations, different complexity of models of wheels can be used. There are complex wheel models, that rely on low number of measured data. These models work theoretically, with high calculation needs, but do not need many measurements for their parametrization. The other option is the experimental modeling, with huge amount of measurement data. The realistic value of these procedures is much better, but a lot of measurements have to be made to parametrize them properly. Of course, none of these proceedings can only be theoretical or just experimental, both of them requires the other process's "help".

Huge amount of wheel model born over the years. One of the most accurate and most commonly used model is the Pacejka's Magic Formula. This is the model, that describes the reality as accurately as possible.

## 2. INTRODUCTION OF INQUIRY

Several of scientists tried to create a similar but simpler model than Pacejka's Magic Formula. The aim of our study is to select from among these available models one, that functions with fewer parameters. An important aspect for selecting the model is that, it should be simple but properly accurate. Since there are many models available, so without being exhaustive, we examine the models, based on our previous literature research.

### 2.1 Presentation of examined functions

In our studies, three functions are compared with Pacejka's magic formula. These are the Burckhardt; the Kiencke and Daiss; and finally the DeWit functions.

Pacejka's Magic formula:

$$f_x(s) = c_1 * \sin (c_2 \arctan(c_3 s - c_4(c_3 s - \arctan(c_3 s))))), \quad (3)$$

Burckhardt:

$$f(s) = c_1(1 - e^{c_2 s}) - c_3 s, \quad (4)$$

Kiencke and Daiss:

$$f(s) = k_s \frac{s}{c_1 s^2 + c_2 s + 1}, \quad (5)$$



Dewit:

$$f(s) = c_1\sqrt{s} - c_2s. \quad (6)$$

In the above functions, the  $c_1$ ,  $c_2$ ,  $c_3$  and  $c_4$  tags are the input parameters, and  $s$  is the variable of the functions, which is actually the value of the wheel's slip. It is noticeable, that the Pacejka's Magic formula has four input parameters. An empirical model is described by this function, that approximates the reality supremely. At the same time, many input parameters are required, so a large number of measurements is needed. The other models in the comparison (Burckhardt, Kiencke and Daiss, DeWit), work with fewer input parameters. These will be compared to Pacejka's Magic formula later on.

## 2.2 The theory of curve fitting

Empirical wheel models are matched to measured data, see In that case, the Magic formula is given. The models that work with fewer parameters are needed to fit on the data generated by Pacejka's Magic formula. The model suits the most, which approximates the data provided by Pacejka's Magic formula. In our enquiry it has given "n" pieces of value-pairs.

$$(F_i, s_i) \quad (i = 1, 2, \dots, n) \quad (7)$$

Usually, we assume, that between the point there is a function connection, based on theoretical considerations.

$$F = f(s; c_1, c_2, \dots, c_m) \quad (8)$$

In that case, this can be the function shown in correlation (4)-(6) Generally, during measurement, the measured points are modified by random errors. Now, the values obtained by the function  $F_i$  and 7 correlations are different from each other:

$$F_i - f(s; c_1, c_2, \dots, c_m) = \varepsilon_i \quad (9)$$

This difference need to be reduced by using the least squares method so, the total of:

$$S(c_1, c_2, \dots, c_m) = \sum_{i=1}^n \varepsilon_i^2 \quad (10)$$

has to minimized. We are looking for the

$$S(c_1, c_2, \dots, c_m) = \sum_{i=1}^n [F_i - f(s; c_1, c_2, \dots, c_m)] \quad (11)$$

function's minimum in the function of  $c_i$  values. If the function  $f$  can be differentiated according to the parameters  $c_i$ , then the minimum's necessary but not sufficient condition is:

$$\frac{\partial S}{\partial c_1} = 0; \quad \frac{\partial S}{\partial c_2} = 0; \quad \dots; \quad \frac{\partial S}{\partial c_m} = 0 \quad (12)$$

There are many methods to solve the multivariate extreme value problem.



### 3. RESULTS OF THE TESTS

The previously mentioned curve fitting was performed using a mathematical program for all three functions. Initially, the tests were performed in 0-100 [%] slip range with curve fitting. Then, based on the experience gained here, it was concluded, that is subservient to perform the study on reduced slip ranges.

#### 3.1 Curve fitting on the entire slip range

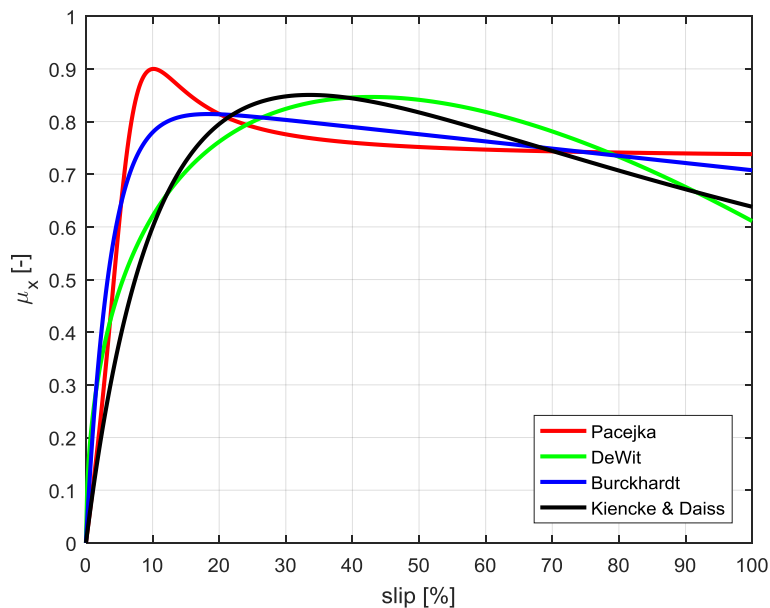


Figure 2 Curve fitting on the 100 [%] slip range

In this case, the curve fitting was performed on the full 0-100 [%] slip range. It is noticeable, that the examined functions do not approximate the locations neither the values obtained with the Magic formula. Moreover, even the shape of the curves is significantly different.

#### 3.2 Curve fitting on partial slip range

Since in reality very high slip values do not often occur, the curve fitting on lower ranges is started and examined there. If a certain range from the point of fitting is distinguished, than in this range the curves will resemble the desired shape logically. However, the rest of the curves will substantially differ, because the curve fitting did not take on that part of the function.

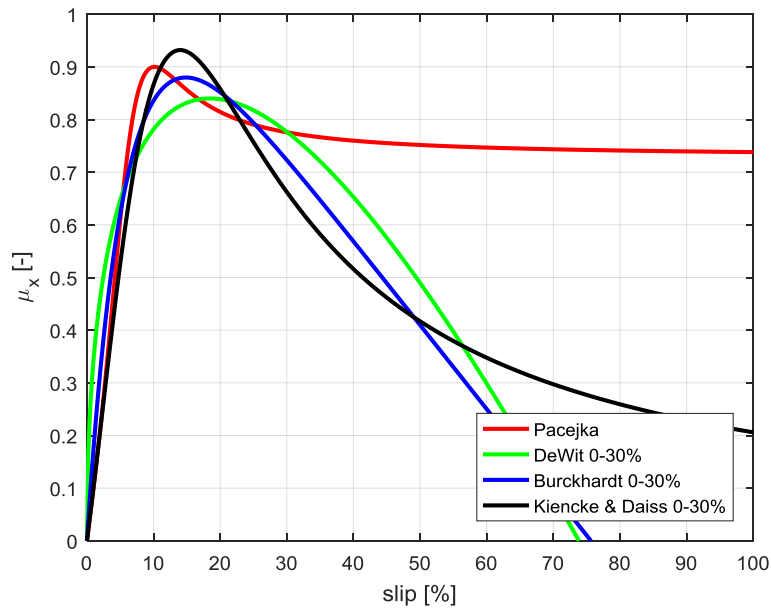


Figure 3 Curve fitting on the 0-30 [%] slip range

First, the curve fitting was performed in the 0-30 [%] range. It is noticeable, the shape, the peak value, and the peak position are much closer to the desired one.

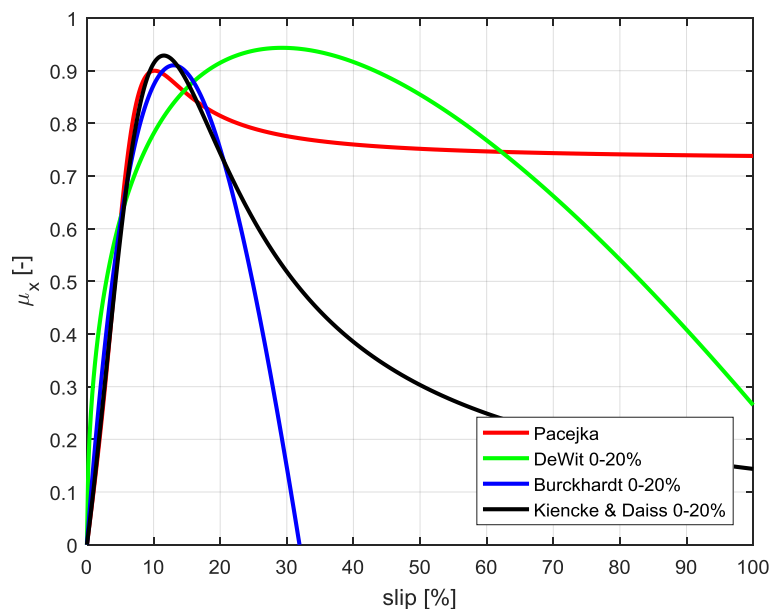


Figure 3 Curve fitting on the 0-20 [%] slip range

Then the 0-20 [%] slip range was studied. It is noticeable, that the DeWit function differs widely from the data. The other two functions behave more favourably and approximate more to the desired shape in the examined range.

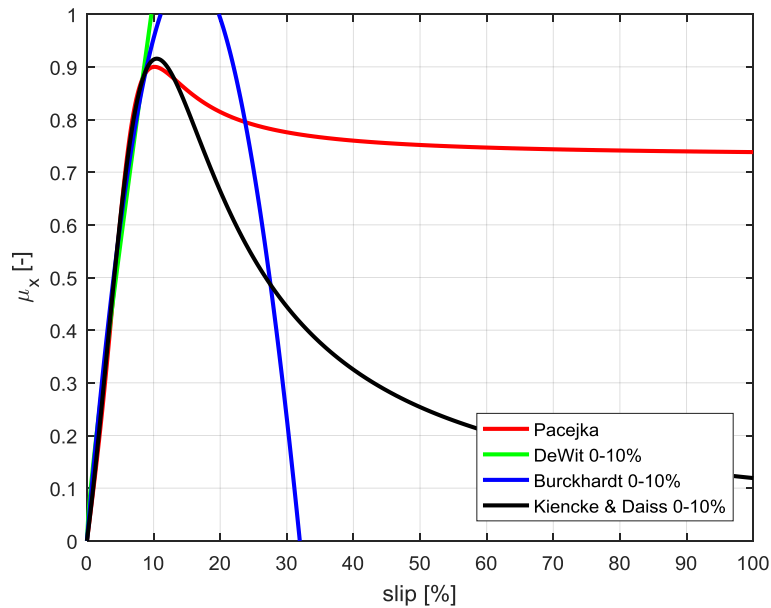


Figure 3 Curve fitting on the 0-10 [%] slip range

Finally, a curve fitting is occurred in the 0-10 [%] range. In this section, both the DeWit and the Burckhardt function, which have not been corresponsive before, are very close to the Magic formula. The Kiencke and Daiss function is the one, that is very close to the shape of Pacejka Magic formula.

### 3. RESULTS

We can say that the curve fitting method worked well in the case we are looking at. By decreasing the ranges, a significant improvement in the curves in the relevant ranges is achieved. It should be noted, however, that if you want to make dynamic simulations in the 0-100 [%] slip range, the Pacejka Magic formula is the only available model, because this is the most appropriate for this purpose because of its accuracy. For the most commonly occurring slip ranges are the 0-10 [%] and 0-20 [%], the Kiencke and Daiss function is the best possibility. This is the function that can provide accurate precision in the vehicle dynamics models.

### ACKNOWLEDGEMENT

The publication is supported by the EFOP-3.6.1-16-2016-00022 project. The project is co-financed by the European Union and the European Social Fund.

### REFERENCES

- [1] Carlos Canudas-de- Wit, Panagiotis Tsiotras, Efstathios Velenis, Michael Basset and Gerard Gissinger: *Dynamic Friction Models for Road/Tire Longitudinal*. 2002.10.14..
- [2] Gáspár Péter, Szabó Zoltán, Bokor József: *Járműdinamika és Irányítás*. 2015.
- [3] Mezei Lajos, Kincses Dávid, Dr. Hajdu Sándor: *Gépjármű keréken ébredő erők mérése, Tudományos Diákköri Konferenciára készített dolgozat*, 2016.12.05
- [4] Havancsák Károly: *Mérési Adatok Kezelése és Értékelése*. International 2012
- [5] Hans B. Pacejka: *Tire and Vehicle Dynamics*. 2005



# INTERNATIONAL SCIENTIFIC CONFERENCE ON ADVANCES IN MECHANICAL ENGINEERING

12-14 October 2017, Debrecen, Hungary



- [6] Szíki, G: *Computer program for the calculation of the performance parameters of electromobiles..* Int. Rev. Appl. Sci. Eng 2 1-6., 2011
- [7] Szíki, G., Juhász, G., Nagyné Kondor, R., Juhász, B.: *Determination and Solution of the Motion of Equation of a Pneumatic Drive Vehicle.* In: Proceedings of the 1st Agria Conference on Innovative Pneumatic Vehicles - ACIPV 2017 / ed. László Pokorádi, Óbuda University, Institute of Mechatronics and Vehicle Engineering, Budapest, 55-58, 2017.
- [8] Szántó, A., Szíki, G., Hajdu, S.: *Soros gerjesztésű egyenáramú motorral hajtott versenyautó dinamikai modellezése.* In: Műszaki tudomány az Észak-Kelet Magyarországi régióban 2016 / szerk. Bodzás Sándor, Debreceni Akadémiai Bizottság Műszaki Szakbizottsága, Debrecen, 587-591, 2016.



## MODELLING OF NON-SPHERICAL BUBBLE SHAPE OSCILLATIONS IN VISCOUS LIQUID

*KLAPCSIK Kálmán, HEGEDŰS Ferenc PhD*

*Department of Hydrodynamic Systems, Faculty of Mechanical Engineering, Budapest University of Technology and Economics*

*E-mail: [klapcsik@hds.bme.hu](mailto:klapcsik@hds.bme.hu), [fhegedus@hds.bme.hu](mailto:fhegedus@hds.bme.hu)*

### **Abstract**

*The surface mode oscillation of a harmonically excited bubble has been investigated numerically in highly viscous glycerine. The radial bubble motion was modelled by the Keller-Miksis equation while the surface modes were modelled by an integro-differential equation, and a simplified model using boundary layer approximation. The comparison of the two models shows remarkable agreement under different scenarios, which implies that the simpler model may be suitable to explore stability limits on parameter spaces. We also observed that the high viscosity can stabilize the surface oscillations.*

**Keywords:** *Shape-stability, non-spherical bubble oscillation, Keller-Miksis equation, high viscosity, boundary layer approximation*

### **1. INTRODUCTION**

When a liquid is irradiated with ultrasound, the usually micron-sized bubbles presented in the liquid form clusters and start to oscillate around their equilibrium size. This phenomenon is called acoustic cavitation. If a bubble collapse during its oscillation, the collapse may induce extreme conditions, such as high pressure, and temperature, or shock waves [1]. These extreme conditions can be exploited in various fields of industry; for example, ultrasonic pasteurization, sonochemistry, polymer research, or cancer therapy. The efficiency of these applications highly depends on the dynamics of the bubbles, which has been studied intensely in the last decades.

The harmonically driven bubbles show a feature rich dynamics on the parameter space of the excitation. One can find periodic collapse-like oscillations, damped oscillations, or chaotic motions depending on the parameter values. An interesting question is that what kind of motion can survive the continuous acoustic irradiation. A natural limitation is, when the bubble loses its spherical symmetry and during the oscillations the surface waves overwhelm the bubble.

We investigate the bubble-dynamics in glycerine, which has approximately three orders of magnitude higher viscosity than water's on room-temperature. The high viscosity leads to a huge damping effect on the radial motion of bubble [2]. The main is to find out how viscosity can stabilize the surface oscillations and delay the disintegration of bubbles, hence the bubble may survive even higher-amplitude oscillations and stronger collapses than in pure water, which is necessary for efficient applications.

The radial oscillation was modelled by the well-known Keller-Miksis [3] equation, which is a second order ordinary nonlinear differential equation that takes into account the liquid compressibility, and viscous damping. The dynamics of non-spherical modes were described by the model of Prosperetti [4], and by using the boundary layer type approximation [5]. It should be pointed out that these models neglect the nonlinear effects and the coupling between different modes [6]. Nevertheless, the good agreement between the experiments and numerical solutions



[7,8] demonstrated that the linear theory is sufficient to qualitatively explore the domain of shape-stable bubbles.

## 2. RADIAL BUBBLE OSCILLATION

The radial oscillation of the bubble was modelled with the well-known Keller-Miksis equation [3]

$$\left(1 - \frac{\dot{R}}{c_L}\right) R \ddot{R} + \left(1 - \frac{\dot{R}}{3c_L}\right) \frac{3}{2} \dot{R}^2 = \left(1 + \frac{\dot{R}}{c_L} \frac{d}{dt}\right) \frac{(p_L - p_\infty(t))}{\rho_L} \quad (1)$$

which takes into account the liquid compressibility, where  $R(t)$  is the time dependent bubble radius, and the dots stand for the derivatives with respect to time. In the above equation  $c_L$  is the speed of sound in the liquid,  $\rho_L$  is the density of the liquid,  $p_\infty(t)$  is the time dependent pressure far away from the bubble and  $p_L$  is the pressure at the bubble wall on the liquid side. The bubble content composed by non-condensable gas and vapour, thus the pressure inside is the sum of partial pressures of both components. The mechanical balance of normal stresses across the bubble wall is

$$p_G + p_V = p_L + \frac{2\sigma}{R} + 4\mu_L \frac{\dot{R}}{R}, \quad (2)$$

in which  $p_G$ ,  $p_V$ ,  $\sigma$ , and  $\mu_L$  are the gas pressure, vapour pressure, surface tension, and liquid dynamic viscosity, respectively. In this study, we investigate harmonically excited bubbles

$$p_\infty(t) = P_\infty + p_A \cdot \sin(\omega t), \quad (3)$$

where  $p_A$  and  $\omega/2\pi$  are the pressure amplitude and frequency of sound waves, while  $P_\infty = 1\text{bar}$  is the ambient pressure which was constant. Assuming adiabatic gas behaviour with  $\gamma = 1.4$  polytropic exponent the gas content obeys a simple polytropic state of change

$$p_G = p_{G0} \left(\frac{R_0}{R}\right)^{3\gamma}. \quad (4)$$

A common way to prescribe the size of the bubble is to set the reference radius equal to the size of bubble at rest  $R_0 = R_E = 0.1\text{mm}$  (unexcited system with  $p_A = 0$ ). Now, the reference gas pressure is expressed as

$$p_{G0} = \frac{2\sigma}{R_E} - (p_V - P_\infty). \quad (5)$$

In present case, to investigate the effect of high viscosity the chosen liquid was glycerine, which has three orders magnitude higher viscosity than of water. All the material properties of glycerine depend only on the ambient temperature [9], while the pressure dependence can be negligible.

## 3. SURFACE WAVES

When bubbles oscillate with fairly large amplitude, the spherical shape is not valid anymore, and then the bubbles start to oscillate non-spherically in the sound field. To calculate the non-spherical modes on the bubble's surface, a small initial perturbation is prescribed [4]



$$r(\theta, \vartheta, t) = R(t) + a_n(t)Y_n^m(\theta, \vartheta) \quad (6)$$

where  $R(t)$  is the instantaneous bubble radius, which comes from the radial oscillation model (Keller-Miksis (1)),  $Y_n^m(\theta, \vartheta)$  is the surface harmonics of degree  $n$  and order  $m$ , and  $a_n$  is the distortion amplitude. In linear theory, the dynamics of a perturbation is independent from the order  $m$  of the spherical harmonics, and independent ordinary differential equations can be derived for the distortion amplitudes  $a_n$ . The derivation of Prosperetti [4] leads to an integro-differential equation

$$\begin{aligned} \ddot{a}_n + \left[ 3 \frac{\dot{R}}{R} + 2(n+2)(2n+1) \frac{\mu_L}{\rho_L R^2} \right] \dot{a}_n \\ + (n-1) \left[ -\frac{\ddot{R}}{R} + (n+1)(n+2) \frac{\sigma}{\rho_L R^3} + 2(n+2) \frac{\mu_L \dot{R}}{\rho_L R^3} \right] a_n \\ + n(n+1) \frac{\dot{R}}{R^2} \int_{R(t)}^{\infty} \left( \frac{R^3}{r^3} - 1 \right) \frac{R^n}{r^n} U(r, t) dr \\ - 2n(n+1)(n+2) \frac{\mu_L}{\rho_L R^3} \int_{R(t)}^{\infty} \frac{R^n}{r^n} U(r, t) dr = 0. \end{aligned} \quad (7)$$

Here,  $U(r, t)$  is the toroidal component of liquid vorticity, whose evolution in time is described with the following partial differential equation

$$\frac{\partial U}{\partial t} + \frac{\partial}{\partial r} \left( \frac{R^2}{r^2} \dot{R} U \right) = \frac{\mu_L}{\rho_L} \frac{\partial^2 U}{\partial r^2} - n(n+1) \frac{\mu_L}{\rho_L r^2} U, \quad (8)$$

with boundary conditions at infinity  $U(\infty, t) = 0$  and at  $r = R(t)$

$$U(R(t), t) + 2R^{n-1} \int_{R(t)}^{\infty} r^{-n} U(r, t) dr = \frac{2}{n+1} \left[ (n+2) \dot{a}_n - (n-1) \frac{\dot{R}}{R} a_n \right]. \quad (9)$$

At  $t = 0$  the liquid is assumed to be at rest, so that the vorticity is  $U(r, 0) = 0$ . The bubble collapse transports vorticity into the liquid, see Eq. (8) which acts back to (Eq. (7)) the dynamics of  $a_n$ . The exact stability analysis requires to solve the Keller-Miksis equation (1) coupled with Eqs. (7)-(9). However, since vorticity is considerable only within a small boundary layer  $\delta$  around the bubble, the integrals in Eq. (7) and (9) can be approximated by the (integrand at  $R(t)$ )  $\times \delta$  thus we obtain a boundary layer type approximation (BLA) [9] of Eq. (7)

$$\begin{aligned} \ddot{a}_n + \left[ 3 \frac{\dot{R}}{R} - 2(n-1)(n+1)(n+2) \frac{\mu_L}{\rho_L R^2} + 2 \frac{n(n+2)^2}{1+2\delta/R} \frac{\mu_L}{\rho_L R^2} \right] \dot{a}_n \\ + (n-1) \left[ -\frac{\ddot{R}}{R} + (n+1)(n+2) \frac{\sigma}{\rho_L R^3} \right. \\ \left. + 2 \frac{\mu_L \dot{R}}{\rho_L R^3} \left( (n+1)(n+2) - \frac{n(n+2)}{1+2\delta/R} \right) \right] a_n = 0. \end{aligned} \quad (10)$$



Hilgenfeldt et al. [9] suggested to define the boundary layer thickness  $\delta$  for large bubbles  $R \gg \delta$  by the diffusive length scale  $\sqrt{\nu_L/\omega}$ , and for small bubbles  $R \ll \delta$  do not let the boundary layer to be larger than the bubble itself, thus a cutoff needs to be defined as  $R/2n$ . We may choose the minimum from above approximations

$$\delta = \min \left( \sqrt{\frac{\mu_L}{\rho_L \omega}}, \frac{R}{2n} \right). \quad (11)$$

For numerical solution, we rewrote the above equation system into as a first order dimensionless differential equation system, by introducing dimensionless variables, namely, the dimensionless bubble radius  $x_1 = R/R_E$ ; the dimensionless distortion amplitude  $\alpha_{1,n} = a_n/R_E$ ; and their derivatives with respect the dimensionless time  $\tau = t/(2\pi/\omega)$ ; the dimensionless bubble wall velocity  $x'_1 = x_2$  and dimensionless distortion amplitude velocity  $\alpha'_{1,n} = \alpha_{2,n}$ . During the work, we define the relative frequency  $\omega_R = \omega/\omega_E$ , where  $\omega_E$  is the undamped linear eigen-frequency of radial bubble oscillation [1].

Additionally, we map the vorticity from the semi-infinite  $[R(t), \infty[$  interval onto a fixed  $[1, 0[$  domain by introducing the new spatial coordinate  $z = R(t)/r$ . The governing equation of the vorticity (8) is transformed into a set of ordinary differential equation by Chebyshev spectral collocation method exploiting parity properties [10] of the Chebyshev polynomial. The integrals over variable  $z(r)$  was evaluated by Gaussian quadrature [11]. The computations were carried out by an initial value problem solver, the numerical method was a 4th order Runge-Kutta scheme with 5th order error estimation.

### 3. NUMERICAL RESULTS

To compare the different models, first we solved the Keller-Miksis equation from randomly prescribed initial conditions and integrate it forward in time until the solution converged to a periodic or chaotic orbit. Then, we couple one of the surface models to the Keller-Miksis equation, with an initial perturbation that was prescribed as 10% of bubble radii  $R$ , and continue the integration. In Fig. 1., we demonstrate the results of such computations at  $T_\infty = 30^\circ\text{C}$  and  $70^\circ\text{C}$  temperature and at pressure amplitude  $p_A = 0.1 \text{ bar}$ ,  $0.75 \text{ bar}$  and  $1.1 \text{ bar}$  for the 2<sup>nd</sup> surface mode, where the dimensionless surface distortion amplitude is plotted with respect dimensionless time. The blue solid and red dashed lines denote the results of BLA approximation (10) and solutions of the complete integro-differential equation (7)-(9), respectively.

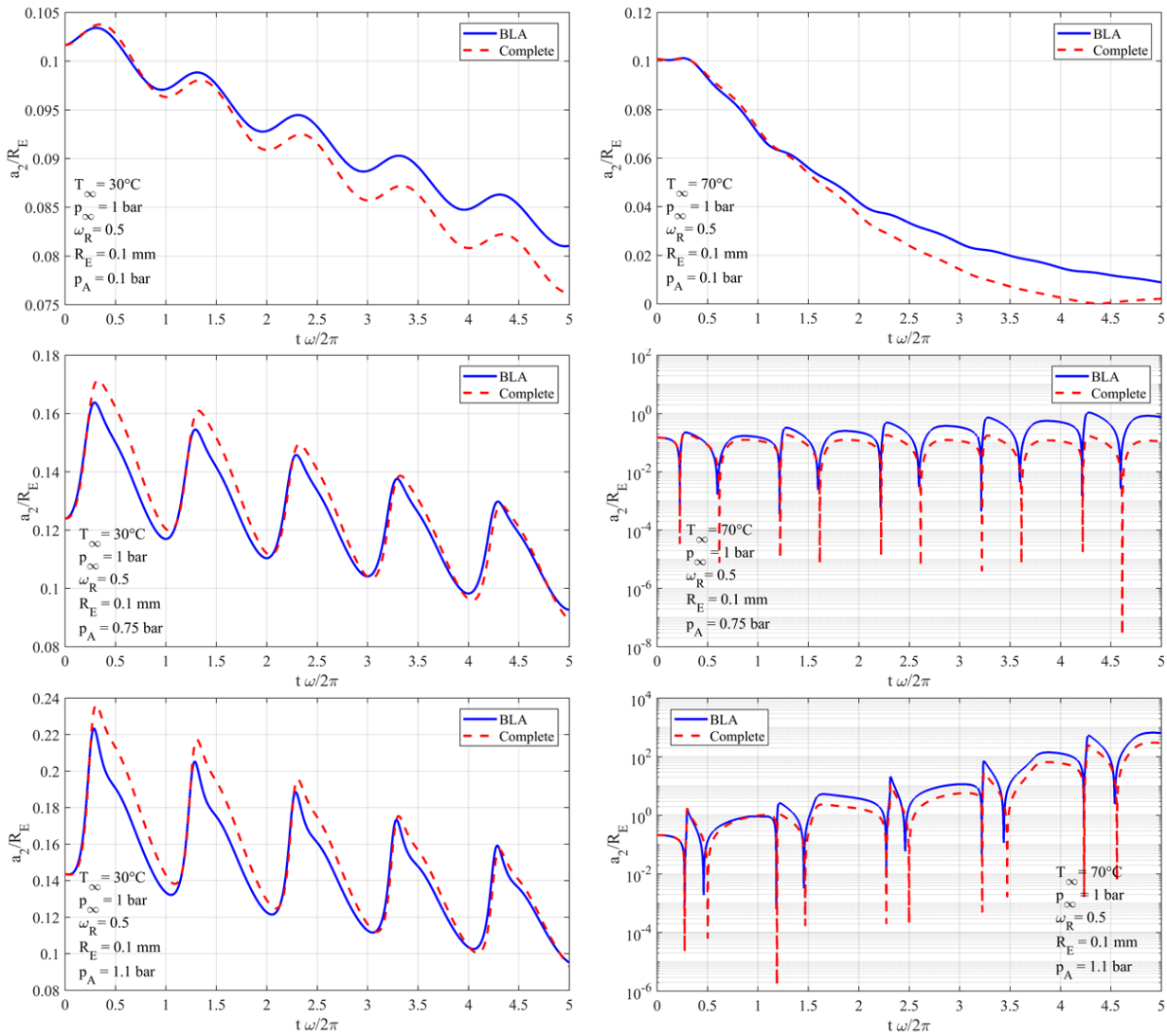


Figure 1 Comparison of dimensionless non-spherical distortion amplitudes for the 2<sup>nd</sup> mode obtained by BLA (blue) and the complete model (red).

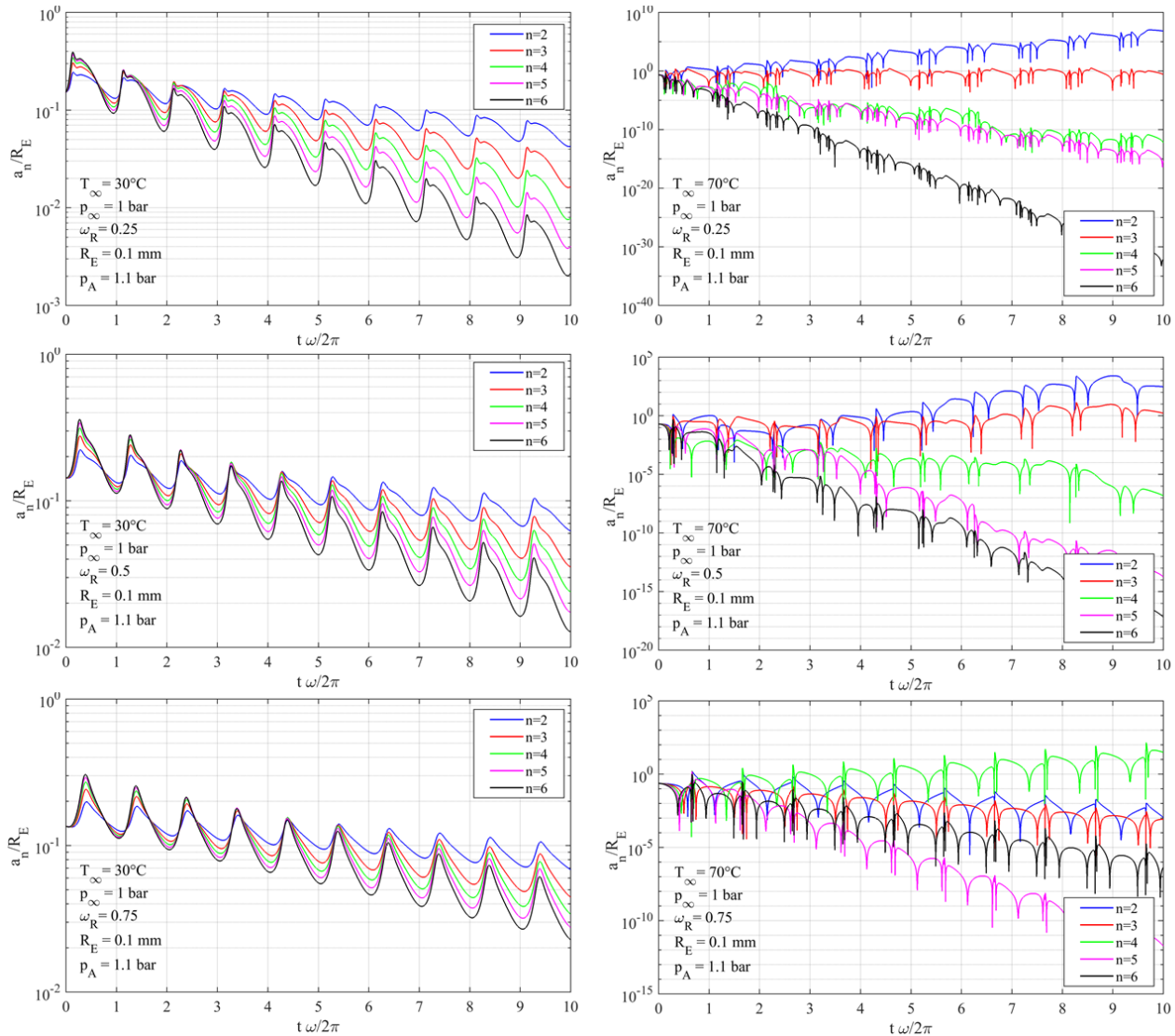


Figure 2 The dimensionless bubble distortion amplitude for excited bubble for mode numbers from 2 to 6 obtained by BLA approximation.

The figures show remarkable agreement between the models. However, the BLA model slightly underestimates the damping rate of the viscosity; since the complete model usually decays faster for stable bubbles, or grows slower for unstable bubbles. From the graphs, one can conclude that even at the high pressure amplitude ( $p_A = 1.1 \text{ bar}$ ), the 2<sup>nd</sup> surface mode is stable at  $T_\infty = 30^\circ\text{C}$ . At  $T_\infty = 70^\circ\text{C}$  however, the mode becomes unstable and growth rapidly. To better visualize this rapid growth, the last two graphs in the right hand side are plotted in logarithmic scale.

To investigate the behaviour of higher modes, we perform the above computations for mode numbers 2 to 6 using the BLA approximation. Figure 2 shows the results of such computations at ambient temperature  $30^\circ\text{C}$  and  $70^\circ\text{C}$ . The simulations were performed at constants pressure amplitude  $p_A = 1.1 \text{ bar}$  with the frequency values  $\omega_R = 0.25, 0.5,$  and  $0.75$ . The graphs shows that at high temperature at  $\omega_R = 0.25$  and  $0.5$  the unstable modes are the 2<sup>nd</sup> and 3<sup>rd</sup> modes, while at  $\omega_R = 0.75$  only the 4<sup>th</sup> mode is excited. It is known that the most unstable mode arises for  $\omega = 2\omega_n$  where  $\omega_n = \sqrt{(n-1)(n+1)(n+2)\sigma/(\rho_L R_E^3)}$  is the natural frequency of surface mode oscillations [7,8]. Since surface tension  $\sigma$  and liquid density  $\rho_L$  are almost constant between  $30^\circ\text{C}$  and  $70^\circ\text{C}$  the natural frequencies are approximately  $\omega_n/\omega_E \cong 0.13, 0.24,$  and  $0.36$  for mode



# INTERNATIONAL SCIENTIFIC CONFERENCE ON ADVANCES IN MECHANICAL ENGINEERING

12-14 October 2017, Debrecen, Hungary



numbers 2, 3 and 4, respectively. This explains, why the 2<sup>nd</sup> 3<sup>rd</sup> and 4<sup>th</sup> modes are the excited ones in the graphs. However, Lowering the temperature, however, even these the unstable modes become stable, see graphs at the left hand side.

## CONCLUSIONS

The spherical stability of a harmonically excited bubble in the highly viscous glycerine has been investigated numerically. The radial motion of the bubble was modelled by the Keller-Miksis equation, while the surface waves were modelled by the integro-differential equation derived by Prosperetti, and a the model using boundary layer type approximation. The comparison of models for the 2<sup>nd</sup> mode showed a remarkable agreement, which implies that the simpler model may be sufficient in the exploration of the shape-stable oscillations. It was also observed that the unstable modes become stable with lowering the temperature (increasing the viscous damping). Although the viscosity can stabilize the surface waves, viscous damping also softens the collapse strength. In application point of view, the main aim is to find a compromise between shape-stable oscillation and the collapse strength. However, this requires to scan the given parameter spaces, which will be done in the future.

## ACKNOWLEDGEMENT.

This research was supported by the ÚNKP-17-3-I. New National Excellence Program of the Ministry of Human Capacities; and by the János Bolyai Research Scholarship of Hungarian Academy Sciences.

## REFERENCES

- [1] Brennen, C.E.: *Cavitation and bubble dynamics*. Oxford University Press, New York, 1995.
- [2] Fujiwara, T., Shima, A.: *Nonlinear oscillations of bubbles in compressible hydraulic oils*. J. Acoust. Soc. Am. 68(5), 1502-1508., 1988.
- [3] Keller, J.B., Miksis, M.: *Bubble oscillations of large amplitude*. J. Acoust. Soc. Am., 68 (2), 628-633., 1980.
- [4] Prosperetti, A.: *Viscous effects on perturbed spherical flows*. Q. Appl. Math. 34, 339-352., 1977.
- [5] Hilgenfeldt, S., Lohse, D., Brenner, M. P.: *Phase diagrams for sonoluminescing bubbles*, Phys. Fluids 8(11), 2808-2826., 1996.
- [6] Shaw, S.J.: *Translation and oscillation of a bubble under axisymmetric deformation*, Phys. Fluids 18, 072104. 2006.
- [7] Versluis, M., Goertz, D.E., Palanchon, P., Heitman, I.L., van der Meer, S.M., Dollet, B., de Jong., N., Lohse, D.: *Microbubble shape oscillations excited through ultrasonic parametric driving*. Phys. Rev. E 82, 026321. 2010.
- [8] Xi, X., Cegla, F., Mettin, R., Holsteins, F., Lippert, A.: *Study of non-spherical bubble oscillations near a surface in a weak acoustic standing wave field*. J. Acoust. Soc. Am. 135(4), 1731-1741., 2014.
- [9] Haynes, W.M.: *CRC handbook of chemistry and physics*. 95<sup>th</sup> edn. (CRC press, Internet Version, 2015)
- [10] Boyd, J.P.: *Chebyshev and Fourier spectral methods*. 2<sup>nd</sup> edn New York, Mineola, Dover Publications, 2001.
- [11] Hao, Y., Prosperetti, A.: *The effect of viscosity on the spherical stability of oscillating gas bubbles*. Phys. Fluids 11(6), 1309-1317., 1999.



## A FEW CONSIDERATIONS ON THE STATE OF THE ART AND DEVELOPMENT TRENDS IN HEAT TREATMENT AND SURFACE ENGINEERING

**KOLOZSVÁRY Zoltán PhD**

SC.PLASMATERM SA, Romania

E-mail: [zoltan.kolozsvary@plasmaterm.ro](mailto:zoltan.kolozsvary@plasmaterm.ro)

### Abstract

*The rapid development of science and technology at the beginning of the 21<sup>st</sup> century has its effects on materials science and the related fields as well. New materials and new areas of the materials science, the increasing role of the materials triangle: nano-bio- info is radically influencing our concept on materials science in every aspect.*

*Heat treatment and surface engineering are important part of materials science and are important in offering a possibility to increase the application area of both the classical and emerging materials with a strong effect on sustainable development as well. In a rough approach heat treatment is modifying the properties of the bulk material, whereas the surface engineering is offering the required properties to the material surface without a significant modification of the structure and properties of the substrate.*

*The paper is intending to present a short overview on the state of the art and present trends in heat treatment and surface engineering with an emphasis on those for conventional materials. However, a few aspects of emerging materials are also considered.*

*Technological processes and advanced equipment are briefly outlined and evaluated. A few aspects of research and development in the specific area are also shown.*

**Keywords:** *heat treatment, trends, surface engineering*

### 1. INTRODUCTION- GENERAL REMARKS

It seems very risky trying to make a projection on the future development in any branches of technology and this is even more true if materials and materials science are concerned. Beyond any doubt, energy efficiency and environment are the main drivers to orientate research and development in any industrial field, even if the trends are frequently -at least- controversial. Life cycle assessment and the circular economy are more and more in focus of attention for sustainable development.

In the history of mankind the strong interdependence between the science and technology and the society was extremely strong, even if that was not always evident. This interdependence is even stronger at the beginning of the 21<sup>st</sup> century. The problem of our age seems to be in the increasing time-gap between the progress of science and technology on one side and society on the other. The increasing volume of information and the speed of data processing and transmission didn't find a balance with human perception of real values and their use for the society. The gap between the different segments of the society is increasing alarmingly. The astonishing achievements of science and technology are poorly reflected in the general level of the human society. It is a commonplace, after a period of accumulation at the beginning of the 21<sup>st</sup> century this spiral was significantly speeding up. The time-gap between the development of science and technology on one side and the human society on the other is mainly depending on the speed and possibilities of communication but apparently the overwhelming speed and amount of information may not be efficiently handled. The



# INTERNATIONAL SCIENTIFIC CONFERENCE ON ADVANCES IN MECHANICAL ENGINEERING

12-14 October 2017, Debrecen, Hungary



industrial development is more and more depending on the possibilities of data processing and automation. This has the effect of losing an important part of skilled workforce for traditional operations and the professional knowledge is restricted to a very narrow field. This trend is generally reflected in the industry even if apparently the progress is astonishing.

Trying to make any projection for the future may also consider the scenario presented in a recent interview by the CEO of Daimler Benz (Mercedes Benz)...who said "...their competitors are no longer other car companies but Tesla (obvious), Google, Apple, Amazon ..... Software will disrupt most traditional industries in the next 5-10 years. ...Most car companies will probably become bankrupt. Traditional car companies try the evolutionary approach and just build a better car, while tech companies (Tesla, Apple, Google) will do the revolutionary approach and build a computer on wheel ..... Electric cars will become mainstream about 2020. Cities will be less noisy because all new cars will run on electricity. Electricity will become incredibly cheap and clean: Solar production has been on an exponential curve for 30 years, but you can now see the burgeoning impact..." / 1 /.

(Reading these predictions is unavoidable to think of the famous science-fiction of Aldous Huxley: " Brave new world" written almost a century ago. ....)

This vision is also connected to the achievements of materials science, in the group of emerging materials, respectively the info materials. However even with these science -fiction visions classical materials have to give support to our machines, buildings, trains and airplanes...at least for the 21<sup>st</sup> Century

...should it be the near future... or a vision which may be or may not be reality or at least not in the timeframe outlined?... There are many controversial predictions of the general development and even more in the automotive industry but for the next two- three decades we may probably accept a more conventional development

Materials and -certainly- materials science is of fundamental importance for any industrial development. Dealing with materials it is important to consider two -rather distinct- areas: the "conventional" and the "emerging" materials /2. Global 21China.../ This is especially important when heat treatment and surface engineering are in focus. In the period of 2005 and 2015 on the initiative of the International Federation for Heat Treatment and Surface Engineering (IFHTSE) run a program under the name of GLOBAL 21 (Heat Treatment and Surface Engineering at the beginning of the 21<sup>st</sup> Century ) As the author of the present paper was the coordinator of the program there was a possibility to scan the documentary material sent by a number of highly recognized authors (G.Krauss, T.Bell, K.Funatani, H.W.Zoch, G.Totten and many others) Projections, ideas and solutions presented in these papers fundamented the core of this presentation. The paper doesn't intend to give details of development trends in heat treatment and surface engineering but to outline the main stream of this development and to show the most important factors of influence.

When heat treatment is considered first of all iron and steel are the main areas of interest. Heat treatment of other industrial alloys is of a much smaller importance, even if aluminum and other metals and alloys are also treated and strongly developing. The explanation may be connected to the overwhelming share of steels in the world economy and the spectacular development of both the steel industry and the innovation in the related field. Just to point out a few interesting data:

- "In the 1980s it took 10.1 hours of human labor to produce a ton of steel. Today, it takes 1.9 hours..." /3 Steel Times International May/June 2016 pg.9/
- Energy efficiency and environment are of primary importance. This aspect is slowing down the use of aluminium in the automotive industry, even if both the technological development and the specific weight act in its favour. "Producing primary aluminium ingot in North America currently generates at least four times the emissions of producing steel...! 9-ton CO<sub>2</sub>e/ton for steel



# INTERNATIONAL SCIENTIFIC CONFERENCE ON ADVANCES IN MECHANICAL ENGINEERING

12-14 October 2017, Debrecen, Hungary



vs 8.9-ton CO<sub>2</sub>e/ton for aluminium.....” and the problem of close cycled economy also act in this direction. Steel is recycled five times more than the sum of all other metals combined....

The automotive industry is one of the most important drivers in technological development for the materials science. Examples may be quoted: AHSS are high strength (generally greater than 500MPa) and applied in body structures.... dual phase steels (DP) 500-1200 MPa with martensite in the ferrite microstructure combines excellent formability and high strength /4. Steel’s top dog in automotive, D.W. Anderson, Steel Times International May/June 2016 pg.29/. For this combination of high strength and ductility Molybdenum as alloying element in steels may have a spectacular growth in the near future. /5. Molybdenum-reducing car weight. Tim Outteridge; Steel Times International May/June 2015 p.51/

Evaluating trends in heat treatment and surface engineering, the survey on development has to consider trends in:

- technological processes
- equipment and instrumentation
- “philosophy” in process control
- Xxxxxxxx

The technological development of heat treatment (and -certainly- that of surface engineering) will have to consider:

- New materials with specific heat treatment needs
- The reduction of specific energy needs of technological processes
- Decreasing or -if possible- elimination of environmental damage
- Reducing the production costs
- Increasing the service life of products and enhancing recycling

The category of new materials is very large but their influence on heat treatment and surface engineering is more limited. Certainly, the innovation in the steel industry is the main factor and even if just a few trends are exemplified their importance may not be neglected. New structural steels are and will be developed. Just a few examples:

- low carbon structural steels with reduced sensibility to grain coarsening thus allowing higher carburizing temperatures, above 1010 C
- new steels for very high-speed induction hardening
- new nitriding steels for improved case-substrate properties.

An important expectation is a reliable databook on interdependence of machinability, deformability etc. and the steel structure resulted from specific heat treatment.

The emerging materials may significantly influence the surface engineering. In this respect nanomaterials are in frontline, making a “bridge” between conventional and emerging materials as nano- coatings seem to gain ground rather fast. Biomaterials and materials for bio-mechanical and bio-medical applications also are of increasing importance. “Copying the nature” is an important preoccupation in the whole scientific world. Special coatings or deposits will bring unexpected improvement of specific service properties in many areas. Protective and repellent coatings, easy-clean, anti-fouling, self-cleaning, dirt-resistant, self-healing, conductive and scratch-proof coatings find application in most diverse fields. In fact, the surface engineering has to cover the most versatile functions as thermal barrier; conductivity; thermal insulation; easy clean; scratch resistance, anti-corrosion; stain repellent. ( Photo catalysis is also a particular case with outstanding interest for new energy sources / 6. Cordt Zollfrank; Bioinspired material surfaces – Science or Engineering? 2013, ScienceDirect, [www.sciencedirect.com/](http://www.sciencedirect.com/)

There is a specific new field where heat treatment will also have to gain ground, even if today this is not yet in focus. This is the additive manufacturing with a fantastic increase in its applications and perspectives. If originally only was used for prototypes and specific applications like orthopedic prostheses, in future (and even today) almost there are no limits. However it is rationally expected



# INTERNATIONAL SCIENTIFIC CONFERENCE ON ADVANCES IN MECHANICAL ENGINEERING

12-14 October 2017, Debrecen, Hungary



to develop new heat treating and surface engineering procedures in order to cover the expected service properties. It may be expected to develop low temperature processes (as nitriding, nitrocarburizing) in order to minimize the distortion. However this doesn't seem to be a simple process.

The computer modelling and simulation in materials science enhances the development of tailor-made materials, alloys. The simulation is a relatively simple tool for predicting the material properties function of composition and structure. A specific area of modelling and simulation covers also a series of heat treatment operations, including quenching, carburizing, a.s.o. For the time being simulation and computer modelling for nitriding is less feasible as this is a non-equilibrium process and evaluating all the factors of influence faces difficulties and uncertainties.

Generally speaking the technological development of heat treatment (and -certainly- that of surface engineering) will have to consider:

- The reduction of specific energy needs of technological processes
- Decreasing or -if possible- elimination of environmental damage
- Reducing the production costs
- Increasing the service life of products and enhancing recycling

A few years ago (in 1998) ASM launched the study for the future of heat treating "Vision 2020" /...7./ targeting:

- Reduce *energy consumption* by 80%
- *Zero emissions*
- Reduce process time by 50%
- Reduce production costs by 75%
- Reduce investment cost by 50%
- Increase the furnace service life 10-fold
- Zero distortion

Unfortunately, very few of these targets seem to be achieved in these almost 20 years, but the trend will have to continue.

Considering basic technology in heat treatment of steels no spectacular changes may be expected as the structural constituents responsible of specific properties are those well known today, innovation mainly concerns the methods and equipment for the structural modifications. (Most of these changes have their origin in increasing restrictions by environmental considerations and increasing cost of energy.)

A brief overview suggests, the vacuum technology and low temperature processes will increase their share. The largest utilization of vacuum technology is in aviation, but automotive, medical equipment and tool production also have an important share. (Data collected from the world sales of equipment give a clear indication of the changes) /8. Ten new trends in heat treatment. Global prospective. Janus Kowalewski Proceedings of the 28<sup>th</sup> ASM Heat Treating Society Conference, October 20-22 2015, Detroit, USA/

No matter from which side we approach the problem of future development an important aspect is the trend of digitalization. This is concerning not only the furnace control systems aiming increased reliability and efficiency but also an instantaneous communication with the company production software. The real-time process sensors will evaluate the process and provide immediate solutions in case of process deviation. This way a total process control of the manufacturing may be achieved, with a special importance for serial production (automotive but not only).

Many of the earlier predicted changes did not materialize. These are mainly connected to the combination energy-environment like the switch from electric heat-treating furnaces to gas-fired units. This is bringing us back to the question of energy and environment. The biggest polluter our days is the electrical energy generation. Even if electric current generation using renewable



# INTERNATIONAL SCIENTIFIC CONFERENCE ON ADVANCES IN MECHANICAL ENGINEERING

12-14 October 2017, Debrecen, Hungary



resources- first of all solar power- may offer solutions, the poor performance of transport and especially of storing electrical energy remains one of the biggest problems of our age.

The annual global heat treatment market volume is estimated to 75-85 billion USD, whereas the estimated annual equipment sale is between 4.4 to 5.5 billion USD. (Roughly some 300 companies in 34 countries are manufacturing heat treating furnaces /9. Kowalewski Industrial Heating 2/2012 CH /Global HT/

It is not the subject of the present paper to list all those innovations the furnace builder companies introduced and continuously develop for better performance. Better isolating materials, use of the heat emanating from the workpieces during cooling, changes in furnace configuration, control of NO<sub>x</sub> emissions etc. are all of interest.

Instrumentation and specific software are in focus of attention. The results of heat treatment depend first of all on the treating parameters: treating temperature, heating rate, cycle-time, parameters of the furnace atmosphere, cooling conditions. The most significant progress at the beginning of the 21<sup>st</sup> century is in the field of process control. "In the future the furnace control system will include real-time process sensors that will evaluate the process and provide immediate solutions or electronic notification of the furnace operators in the case of process deviation"/Kowalewski/

Carbon potential control in carburizing or in any furnace atmosphere using oxygen probe was an important step in the second half of the last century. Controlling the nitriding atmosphere using H-probe is./10 Spies a.o. /.....and solide electrolyte oxygen probe with the necessary specific software improve significantly the reliability of the procedure. The reliable process control in gaseous nitrocarburizing is even more important as the structure and properties of the compound layer heavy depend on nitrogen and carbon potential and the influence of oxygen in the process. / 11./ A simultaneous control of nitrogen and carbon potential in different gaseous mixtures in furnace atmosphere may guarantee a predictable structure of surface layer even in ferritic nitrocarburizing and postoxidation / 12. New Measurement and Control Techniques for Predictable Results in Ferritic Nitrocarburizing ;Jens Baumann 24th National Conference on Heat Treatment with International Participation 2012, Jihlava, Czech Republic /

A controlled porosity compound layer may improve also the possibilities of boundary lubrication in critical applications especially for tools and dies for plastic deformation. In framework of an EU financed joint project /.../ investigations are in progress for using nano graphite in nitrocarburized compound layer with controlled porosity.

The simple and reliable control techniques for ferritic nitrocarburizing is a rather acute problem. Different solutions are applied for controlling the nitrogen and carbon potential but further development of sensors and data processing is expected. /12/

## SUMMARY

Heat treatment and surface engineering is more and more in focus of attention in industrial development. Basically the factors of influence are first of all the general concern for energy and environment but the development of new materials is also a decisive factor. The spectacular achievements of sensor techniques and data processing is in many respect remodelling the technologies even if no significant modifications are on horizon for the basic knowledge in steel metallurgy. Emerging materials in nano-bio- info categories are expected to modify especially the surface engineering possibilities and technologies.

No matter how we approach the global economical development, one key factor is the ever increasing thirst for energy

A more efficient, less polluting energy generation is in focus of attention but we have to be aware, a real "green energy" will not be able to replace the fossil energy sources in the next 20-30 years. It has to be accepted, the key problems of the future is the transport and storage of the energy



# INTERNATIONAL SCIENTIFIC CONFERENCE ON ADVANCES IN MECHANICAL ENGINEERING

12-14 October 2017, Debrecen, Hungary



The role of politicians may not be overvalued, but unfortunately very few encouraging signs are visible. The decisions are mostly focused on national and narrow sighted interests even in the European Union and the overwhelming volume of “shop window” birocratic regulations only increase the cost of production without giving a real answer to global environment problems.

In this context the heat treatment is energy consumer but in the same time much more energy saver through the increased service life and efficiency of the products.

A significant example is the group of nitriding, nitrocarburizing treatments as it forms a bridge between the “traditional” thermochemical treatments (salt bath, gaseous nitriding, nitrocarburizing) and the more efficient, new generation plasma, active screen a.o. technologies. It represents a way to create energy efficient, environment friendly technologies based on traditional ones.

## REFERENCES

- [1] Mercedes CEO Describes Inventions of the Future ,July 28, 2017 By Steve Beckow [goldenageofgaia.com/2017/07/28/288896https://theplebiscitenaija.wordpress.com/.../the-future-from-a-recent-interview-the-md...](https://goldenageofgaia.com/2017/07/28/288896https://theplebiscitenaija.wordpress.com/.../the-future-from-a-recent-interview-the-md...)
- [2] Surface engineering: a bridge between ‘avant-garde’ and conventional materials and technologies 20.Congress of IFHTSE, Beijing 2012 KZ RW
- [3] Steel Times International May/June 2016 pg.9
- [4] Steel’s top dog in automotive, D.W. Anderson, Steel Times International May/June 2016 pg.29
- [5] Molybdenum-reducing car weight. Tim Outteridge; Steel Times International May/June 2015 p.51
- [6] Cordt Zollfrank; Bioinspired material surfaces – Science or Engineering? 2013, ScienceDirect, [www.sciencedirect.com/](http://www.sciencedirect.com/)
- [7] "Heat Treating Vision 2020." (ASM Vision 2020). Heat Treating 1998: Proceedings of the 18th Conference USA
- [8] Ten new trends in heat treatment. Global prospective. Janus Kowalewski Proceedings of the 28<sup>th</sup> ASM Heat Treating Society Conference, October 20-22 2015, Detroit, USA/
- [9] Kowalewski Industrial Heating 2/2012 CH /Global HT/
- [10] Spies Sensor controlled gas nitriding and nitrocarburizing of ferrous materials– possibilities and limits H.-J. Spies
- [11] Z. Kolozsváry: Beitrag zur Untersuchung der Reaktionskinetik in Carbonitrireatmosphären und Möglichkeiten Ihrer Regelung und Überwachung, HTM 1973, Nr.1, p 112-115
- [12] New Measurement and Control Techniques for Predictable Results in Ferritic Nitrocarburizing ;Jens Baumann 24th National Conference on Heat Treatment with International Participation 2012, Jihlava, Czech Republic /
- [13] IFTHSE Global 21 heat treatment and surface engineering in twenty –first century Activ screen plasma nitriding and nitrocarburizing of steels- an overview. H.-J. Spies. I. Burlacov, K. Börner, H. Biermann Institute for Materials Engineering, TU Bergakademie Freiberg
- [14] An industrial system enabling the use of a patented, lab-proven materials processing technology for Low Cost forming of Lightweight structures for transportation industries. Grant agreement no.: 604240 Grant.No. FP7-NMP-2013-SME-604240 LoCoLite



## OPTIMIZATION OF OPERATIONAL PARAMETERS FOR MICROWAVE PRE-TREATING SYSTEM

<sup>1</sup>KOVÁCS Róbertné, <sup>2</sup>KESZTHELYI-SZABÓ Gábor DSc, <sup>3</sup>SZENDRŐ Péter DSc

<sup>1</sup>Technical Department, Faculty of Engineering, University of Szeged

E-mail: [veszelov@mk.u-szeged.hu](mailto:veszelov@mk.u-szeged.hu)

<sup>2</sup>Department of Process Engineering, Faculty of Engineering, University of Szeged

<sup>3</sup>Institute of Mechanics and Machinery, Faculty of Mechanical Engineering, Szent István University

### Abstract

In this study the influence of magnetron power (PM), flow rate (FR) and number of treating (NT) on biogas production was investigated using  $2^3$  factorial design. Pre-treating of wastewater was carried out in a continuous flow microwave treating system. Minimum and maximum values for PM (300-700W), FR ( $6-25\text{Lh}^{-1}$ ) and NT (1-5) were adopted as the base of the operation of the magnetron and the irradiation power consumption for wastewater treatment ( $1.5\text{ Wg}^{-1}$  and  $2.5\text{ Wg}^{-1}$ ) [2]. NT was observed to have the largest effect on specific energy demand (SED)

**Keywords:** pre-treatment, biogas, microwave, anaerobic digestion.

### 1. INTRODUCTION

Growing pressure due to growing population and increasing in general demand for water means that more wastewater treatment plants are to be expected and the ones that already exist should be increased in wastewater volume to be treated. Waste water dispensed directly into the environment without proper treatment is an impact on community well-being and the livelihood of the population. Accordingly wastewater treatment is an imperative in human ecosystems that intend to maintain a satisfactory balance between resource consumption and resource renewal. Instead of disposing and discharging waste water to the environment, it is useful to return it to the economic cycle after proper treatment. We can not only decrease water consumption, but also get other useful energy sources, in form of biogas. Anaerobic digestion is a technology can be used to treat wastewater as it reduces the pathogen content, stabilizes it requiring no oxygen or other chemicals. In addition methane is generated by the degradation of organic matter, such that in certain cases an energy surplus can be obtained.

Anaerobic degradation seems to be an obvious solution as the wastewater generated by food industry contains very high levels of organic matter. But most of the organic matter is located within the semi-rigid structured microbial cell membrane contains glycan fibres cross linked with peptide chains. It is capable to protect the cell from osmotic lyses but because of this reason cell wall is resistant to biodegradation. The increase in biodegradability is very important improvement in waste water treatment, because it results in more methane produced per mass.

Several pre-treatment techniques have been studied to improve the biodegradability, mainly by disintegrating or solubilising cell walls prior to digestion, such as mechanical disintegration by various means (ball milling, special thickening, high pressure homogenizer), thermal disintegration (heating or freezing and thawing of biomass) or chemical disintegration (acids, bases, oxidants) [1]. In some cases, a combination of more than one of the techniques was used. These studies revealed that the breakup of cell walls increases the biodegradability of the substrate and causes an increase in the rate of biodegradation.



The application of microwaves (MW) is one of the pre-treatment techniques. Additionally, it was reported that biogas production increased with the application of microwaves and that it was higher than the gas production obtained in tests subjected to the same temperature but with conventional heating, suggesting that other effects besides the thermal effect would occur when using this technique. This effect is usually called the athermal effect; however, it is not clear if this effect really exists. [4]

### Materials and Methods

Meat industrial wastewater was collected in a Hungarian medium-sized meat processing company; the sampling point was after the grease tap. Sewage originates from meat processing technology, mainly from the flushing and rinsing process of equipment (slicing and packaging machines, smoking chambers). To remove grit, particles and other large-sized solids a cloth filter was used.

Table 1 Characteristics of wastewater

Parameter	Value
Total solid (TS) (mgL <sup>-1</sup> )	3210±296
Total organic carbon (TOC) (mgL <sup>-1</sup> )	834,1±35,3
Lipid(mgL <sup>-1</sup> )	115,1±21,7
Protein (mgL <sup>-1</sup> )	379,4±21,2

### Microwave pre-treating system

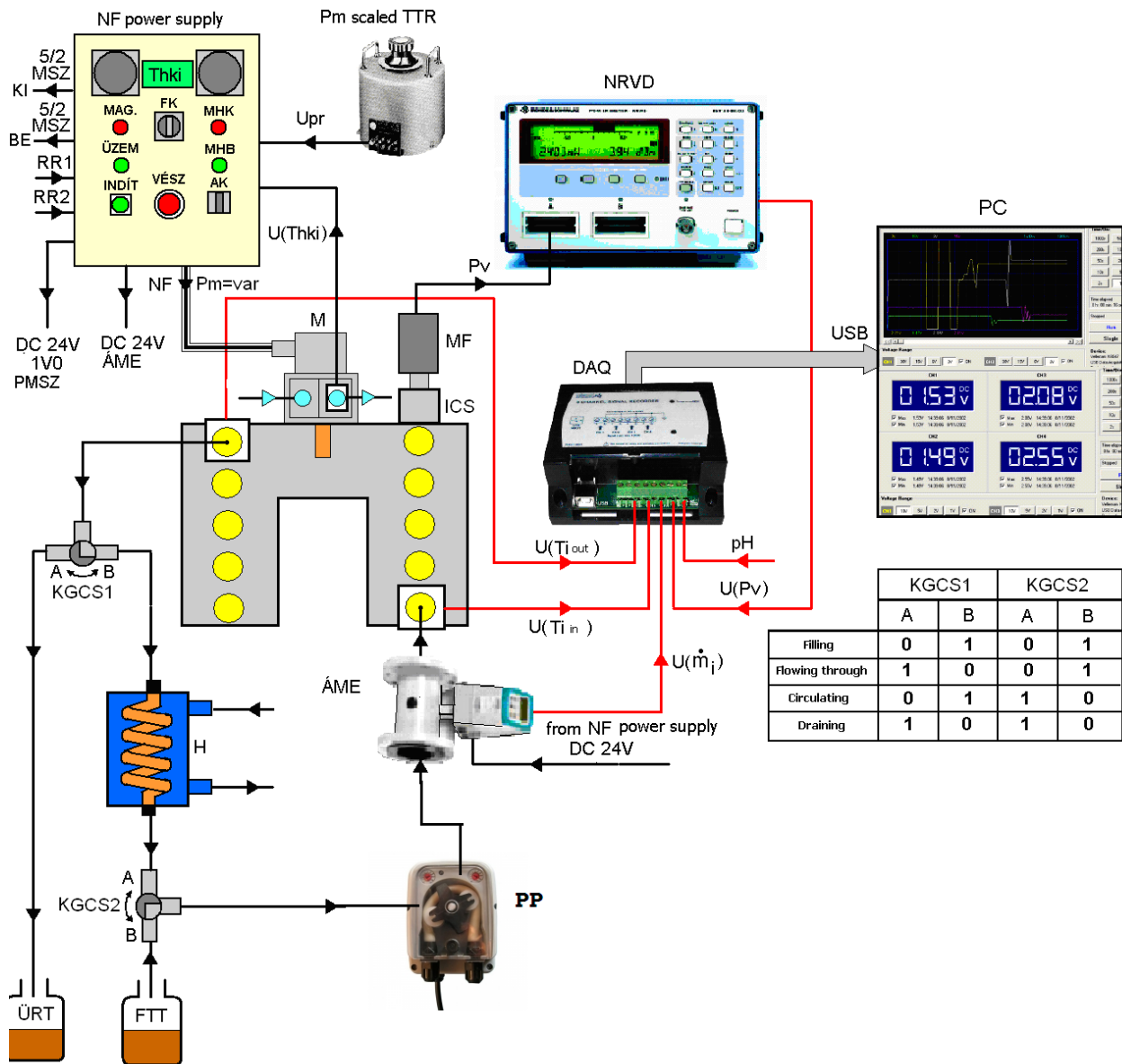
Microwave pre-treating system (Fig. 1) contains a water-cooled, variable-power magnetron (M) operating at 2450 MHz. High-voltage power supply (NF power supply) feeding the magnetron consists of two transformers, one of them produces cathode heating voltage and heating current, the other produces the anode voltage which can be controlled by the primary circuit of an external auto-transformer. With this device (PM scaled TTR) the power of the magnetron can be set as well. Electromagnetic energy of the magnetron spread over a resonant slot. Getting through this slot the energy gets in the toroidal resonator. [5]. During the operation of toroid resonator energy is given to the treated material. As a result of energy transmission the temperature of the material rises and the dielectric properties change continuously. The effect of the microwave energy intake, variable power, impedance and dielectric relationships are formed in the microwave resonator. Some of these can be measured (eg. power dissipation, reflected power), some of them can only be determined by calculation, knowledge of the other parameters [6]. Material is transferred in the continues-flow microwave treating system by a peristaltic pump (PP) with variable flow.

### Fermentation process, biogas measurement

Anaerobic digestion (AD) tests were carried out under controlled mesophilic temperature range (35±0,2 °C). in 12 mini continuously stirred laboratory scale reactors with 250 mL total volume, equipped with Oxitop C.

### Experimental

The influence of PM, FR and NT on biogas production was investigated at maximum and minimum level, yielding a 2<sup>3</sup> factorial design as shown in Table 2. Minimum and maximum values for PM (300-700W), FR (6-25Lh<sup>-1</sup>) and NT (1-5) were adopted as the base of the operation of the magnetron and the irradiation power consumption for wastewater treatment (1.5 Wg<sup>-1</sup> and 2.5 Wg<sup>-1</sup>) [2].



	KGCS1		KGCS2	
	A	B	A	B
Filling	0	1	0	1
Flowing through	1	0	0	1
Circulating	0	1	1	0
Draining	1	0	1	0

*Table 2* Assignment of operational parameters in the 2<sup>3</sup> factorial design

Run	Power of the magnetron [W]	Flow rate [Lh <sup>-1</sup> ]	Number of treatings [db]
1	+	+	+
2	+	+	-
3	+	-	-
4	-	+	+
5	-	-	+
6	-	+	-
7	+	-	+
8	-	-	-



### 3. RESULTS AND DISCUSSION

#### Specific energy demand

Pre-treatment conditions and accordingly energy demand were very different, therefore specific energy demand was determined. Due to the nature of the parameter, the lowest value is the best in terms of energetic.

$$SED = \frac{E}{BP} \quad (1)$$

where BP is biogas production, E is the energy demand of pre-treatments was calculated from the power of the magnetron ( $P_M$ ) and the time of irradiation (t).

$$E = P_M \cdot t \quad (2)$$

In Table 3, *SED*-values for each run within the experimental design are given. Runs 5 and 6 exhibit highest and lowest *SED*. To define precisely the relative effect of each operating parameter, the main effects as well as the two and three factor interactions were calculated [3].

Table 2 PM, FR, NT used in the composite design and response associated

No.	PM [W]	FR [Lh <sup>-1</sup> ]	NT [-]	t [s]	E [J]	SED [ $\frac{J}{ml}$ ]
1	700	25	5	360	252000	845
2	700	25	1	72	50400	183
3	700	6	1	300	210000	646
4	300	25	5	360	108000	420
5	300	6	5	1500	450000	1510
6	300	25	1	72	21600	87
7	700	6	5	1500	1050000	3125
8	300	6	1	300	90000	310

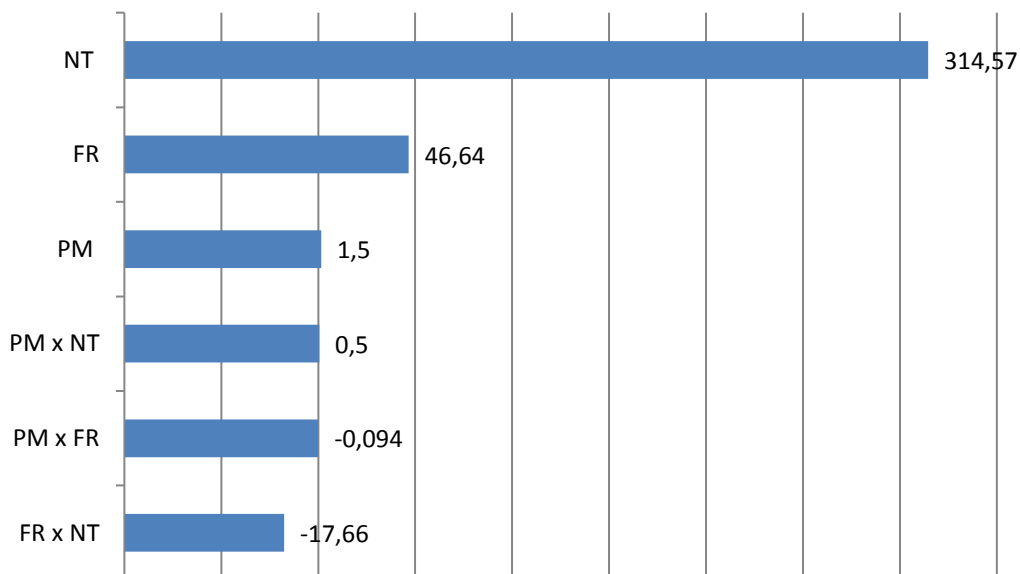


Figure 2 Main effects of the operational parameters on SED and interactions



As shown in Fig. 2, NT was observed to have the largest effect on SED.

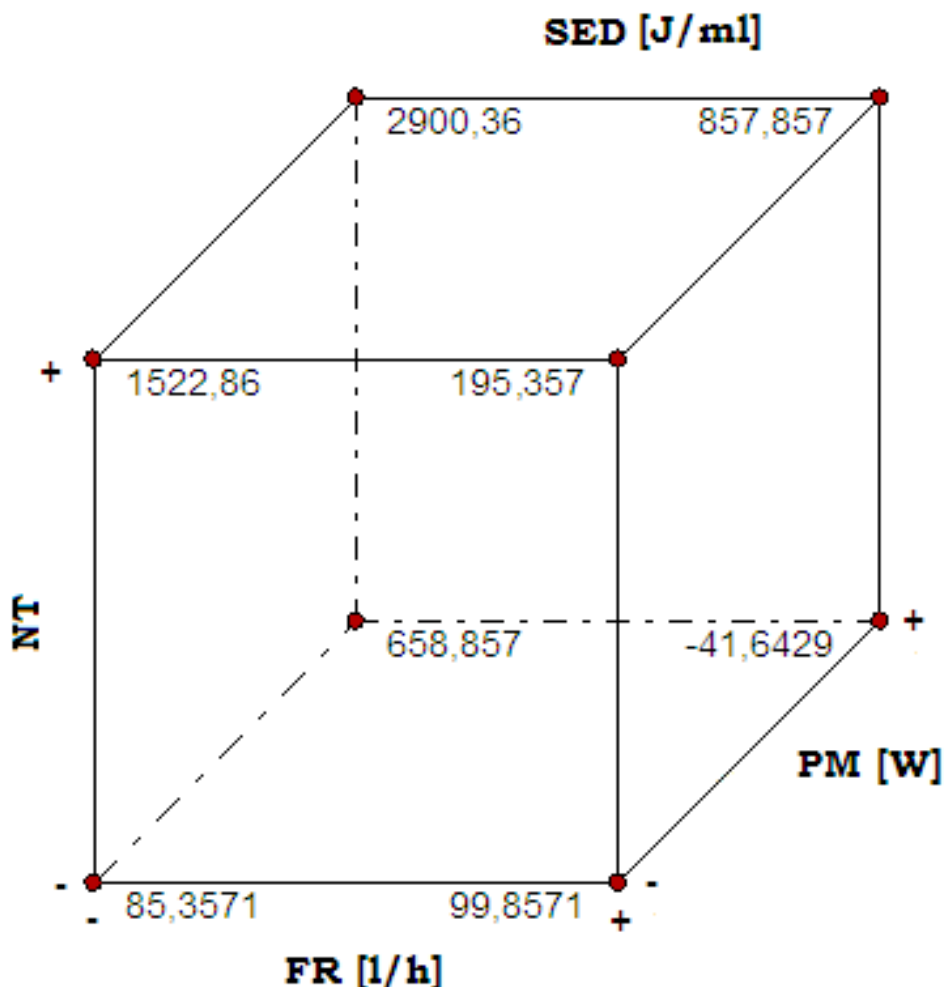


Figure 3 Main effects of the operational parameters on SED and interactions

As shown in Fig. 3, FR/PM by NT interactions evidently arise from a difference in sensitivity to NT for both operational parameters. With NT at (-), a change in FR and PM affected SED increase by 573,5 and 14,5, respectively. At high NT (+), an increase of FR or PM affected fouling decidedly stronger as a decrease in SED of 1377,5 and 700,5, respectively has been observed.

## REFERENCES

- [1] Andreottola, Gianni, and Paola Foladori. (2006). A review and assessment of emerging technologies for the minimization of excess sludge production in wastewater treatment plants. *Journal of Environmental Science and Health. Part A, Toxic/hazardous substances & environmental engineering* 41 (9), 1853-72.
- [2] S Beszédes, Z László, ZH Horváth, G Szabó, C Hodúr (2011) Comparison of the effects of microwave irradiation with different intensities on the biodegradability of sludge from the dairy- and meat-industry *Bioresource technology* 102 (2), 814-821
- [3] G.E.P. Box, W.G. Hunter, J.S. Hunter (Eds.), *Statistics For Experimenters*, Wiley, New York, 1978.



# INTERNATIONAL SCIENTIFIC CONFERENCE ON ADVANCES IN MECHANICAL ENGINEERING

12-14 October 2017, Debrecen, Hungary



- [4] Hong, Seung M, Park, J. K., & Lee, Y. O. (2004). Mechanisms of microwave irradiation involved in the destruction of fecal coliforms from biosolids. *Water Research*, 38, 1615-1625.
- [5] Kovács P V R, Beszédes S, Ludányi L, Hodúr C, Szabó G (2012), Development of a continuous flow microwave toroidal cavity resonator 11th INTERNATIONAL SCIENTIFIC CONFERENCE MMA 2012: ADVANCED PRODUCTION TECHNOLOGIES, Novi Sad: University of Novi Sad, 2012. pp. 357-360.
- [6] J. Zhu, A.V. Kuznetsov, K.P. Sandeep (2007) „Mathematical modeling of continuous flow microwave heating of liquids”, *International Journal of Thermal Sciences*, Vol. 46, 328–341.



## THE DEVELOPMENT OF THE PUNCTUALITY OF RAILROAD EVENT RECORDING IN ACCIDENT INVESTIGATION

LAKATOS István PhD, NAGY Andor

Department of Road and Rail Vehicles, Faculty of Mechanical Engineering, Informatics and Electrical Engineering, Széchenyi István University  
E-mail: [lakatos@sze.hu](mailto:lakatos@sze.hu)

### Abstract

The railroad accidents are the same age as the railroad itself. The paper is to present the development of data recording on the scene of an occurred railroad accident, from the manual procedures, to the modern event recorders.

**Keywords:** Railroad, accident, investigation, event recorder

### 1. INTRODUCTION

The railroad accidents are present since the railroad itself. These events are carrying numerous disadvantages, coming from the serious or fatal injuries, and/or a serious damage of property. The railroad companies are eagerly seeking for the roots of these causes, and from the very beginning, procedures were laid down in order to carry out data recording. The railroad needed proof for the mistrustful population, that the steam-powered “iron horses” those went on their way with relatively big speed compared to the horse carriages – can be trusted, and they are not dangerous.<sup>1</sup> To blow away these bad feelings, railroad companies published their investigations. For every investigation, we need stone hard evidences. These evidences are the product of the accident investigation. The more punctual the data is, the more accurate is the outcome. This basic principle has not changed at all during all the years until nowadays. Just we started to implement more and more accurate data recording methods, as the time went on. We do not separate the nature of the data itself, only examining the methods, that where, and how the data is recorded, and how is this affected by the technical development of the equipment available.

### 2. DATA COLLECTION METHODS

Upon examining the continuity of an accident, a clear assignment has to be carried out, between the data signals, and the timestamp, when the data has been recorded. We need to monitor the data, that helps us track down the movement of a railroad vehicle, with all the environmental variables available. These variables can be seen in *Table 1*.

*Table 1* Variables that are affecting railroad operation, in terms of data (evidence) collection

Data type to be collected	Realization
Communication	Telegraph tape, ear witness, tape recorder, DSR
Vehicle movement (from-to)	Significant points (track, signal, switch, gate)
Vehicle speed	[m/sec] measured or calculated, on paper or digital record

<sup>1</sup> Parliament of the United Kingdom: The Locomotive Act 1865, Highways and Locomotives Amendment 1878



# INTERNATIONAL SCIENTIFIC CONFERENCE ON ADVANCES IN MECHANICAL ENGINEERING

12-14 October 2017, Debrecen, Hungary



Event logging	Actions done or omitted, manual or digital logging with timestamp (permissions, reporting etc.)
Environment variables	Meteorological conditions that are affecting visibility or friction
Actions of staff	Operations carried out by operating staff (braking, accelerating, switch handling, signal box operations) with timestamp

At first sight, these variables in *Table 1*. seem to be simple. The fact is, that these are the most important, and most complex data what we are using in reconstructing scenes, and events. Without recording the data with the chronological point, sometimes not even the occurrence can be proven. There is a saying: “The most simple method is the most efficient.” this is not exactly true here. Let’s see the variables listed in *Table 1*.

## Communication

In the beginning, where there were no telecommunication methods at all, railroad used messengers to exchange messages. These were in written form, it has to be delivered from one traffic controller to the neighbouring station’s controller, who had to sign it, and keep a copy, then the messenger had to deliver back the signed message to the origin station. This is far not the most effective method, but everything was written. Except the time. The time could not be assigned to the action itself. As the technical improvements were realized, semaphore, and telegraph poles were installed to make the communication faster. Telegraph operators had to keep a record about what they have transmitted or received, and when. In this case the timestamp has been added to the message, but its punctuality highly depended on the operator. The telegraph poles accelerated the communication, the clockwork-like tape writers recorded the message itself, but the time of the transmission was also depending on the operator. When the telegraph has been upgraded to local battery telephone, the possibility of quality voice recording was not yet available, just as some stations still lacked electricity, so controllers used ear witnesses to avoid misunderstanding of traffic related information. The messages were written into the stations telecom logbook, and the timestamp punctuality also depended on the people. This was the used method, until the tape recorder became available. Due to its installation price, in Hungary, it was only installed on main lines, and cargo terminals. The biggest problem was still the adding of a timestamp. This has only been solved with the DSR (Digital Sound Recorder).

### a) Vehicle movement

The movement of the vehicles were only registered manually in the stations logbook. Arrival, departure (or transit), shunting, and their secondary control were also logged by the station controller. As all of these procedures require numerous staff, these orders, checks, were given in written form, and also transmitted verbally. Only after the receiver has repeated the message verbally, could they undersign the notification of the order. (This procedure still lives!)<sup>2</sup>. When the wireless radio equipment became available, the radio communication was also recorded like the telephone, and nowadays we can download the recordings from the telephone to the handheld radio communication, just as we would download an mp3 file from the internet, with timestamp accurate to decimal seconds.

Vehicle movement is also influenced by the implementation of signalling systems, where transport critical actions were also logged. In the beginning with plumbing the necessary lever, where it can be seen that it has been removed, then, electric counters. They were also lacking timestamp, but the

<sup>2</sup> Hungarian State Railways (MÁV) F.2 Traffic Regulations: 15.8.4.



signalling system used nowadays, has the possibility, to record every logical event (signalling contacts, relays, etc.). These are the ancestors of the event recorders in the scope of infrastructure.

b) Vehicle speed

In the beginning, the speed was directly measured, but despite that the dimensions were various, they calculated the speed out of the time, and the distance components. Practically all the instruments are doing the same nowadays, using the accurate wheel diameter driving it through numerous mechanical, optical or electrical systems. The principle is to generate the signal somewhere, and transmit it to the driver, without altering it. If we can visualize it to the driver, the next step is to add a pen, and a clock, and it starts to record the speed. This is how the first speed recorders have worked. Now we have changed the cogwheels to optical equipment, and substituted the pen with electronic memory and digital display. The speed will always be an analogue data that we need to record, together with the distance. Everything else can be logged as a logical value nowadays.

c) Event logging

As we can see, almost all the data were recorded with a pen and a logbook before. As the time goes on, and more and more complex systems are to be implemented by the railroad, their event recorders, DSR's, DVR's are substituting the human, making the logging more and more accurate, nowadays with 3 decimals punctuality. Previously we could not say if the signalman has set the signal back to "Stop!" or not, today this event is recorded with at least 3 variables with timestamps.

d) Environment variables

These are the temperature, rail temperature, humidity, visibility, rain volume, wind direction and speed, sunlight direction and its disturbance in visibility. These were recorded by the station staff before, and they had to carry out numerous measurements during the day, and log them. Nowadays, it is done by automatic stations, and DVR's. If there is an accident for example, where it must be determined if the sunlight angle was enough to disturb the visibility of a signal, it is enough to check any of the digital video recorders, that has timestamp also, to see how it went.

Every railway staff knows that the rain is not dangerous when it is raining a while ago. Track conditions are not significantly differ from the dry stage. But when it begins to rain, it becomes slippery as an ice skate ring.

e) Actions of staff

These are the data, those can save lives, help saying out a releasing verdict, and help improving rail safety. Some other ones from points a)-e) can be calculated, assumptions can be made that can be confirmed by other sources, witnesses, but if we need to monitor the behaviour of our staff without the possibility to alter the information, we definitely do need the event recorder. (Our rail-ancestors would give significant amount of gold for this possibility.) We can monitor the opening of a door, pressure existence in a brake cylinder, fire or smoke detection, we can answer every question that can be answered by "yes" or "no" with this equipment. Let us go back in time a bit: 70 years ago, if there was an accident – a train hit a carriage on the tracks – where there is a possibility, that it could have been avoided, if the staff would have been using the emergency brake. If we don't know the speed, and numerous data what the event recorder can present nowadays, it is impossible to judge. Today, we can calculate what was the distance between the train and the carriage, when did the driver apply emergency brake, etc. Everything is clear.

### **3. DATA SAFETY AND EVENT RECORDING**

We have come to the point, where we do record all the data that is necessary, but this recorded data needs to be converted to evidence, and must be protected. Obviously, there is no such thing as total safety. Papers can be wet, burn, the ink can lose its colour. Sound recordings on tape can be damaged by magnetic fields, files can be deleted, the entire computer can be physically damaged.



First, we need to protect the data, in the event recorder, against loss, and alteration. Against loss, all the actions carried out on the event recorder (from now on EVR) must be logged, even the opening its hatch door. We need to log the connecting attempts, to the recorder. This is to prevent unauthorized access to the data. We need to protect the data from the recorder itself, so we use short term memory, and long term too, with temporary memories, in which the data is stored, and periodically written to the short term memory (STM) then in longer periods to the long term memory (LTM). Upon authorized access, the EVR disconnects all memories from the continuous incoming signals, usually disabling the usage of the equipment, in order to prevent data loss. The EVR needs to produce such file type, that has an unique identifier, and only that software is able to handle it, that is bundled to it. If the checksum is altered, the data will not be readable. In most cases, the EVR is locked into a special compartment, that can only be opened with special keys, only held by authorized personnel. The EVR has also a special casing, protected from heat, humidity, electric overload, and physical effects.

We need to collect data, to record them. For to have data, we need signal. For signals, we need sensors. There are digital, and analogue type of signals to be distinguished. We need to store them different ways. Digital signals can be stored easily: we record the timestamp and the signal at the moment when it has been changed, and consider it unchanged, until another signal comes in, that it has been changed, then we register it with a timestamp. So, for example if we need to register that if the parking brake was applied or not, there will be signals that it was “ON” in this time, and “OFF” at that time. The interval between the two signals are to be considered to have the same signal that it had at the previous time of change, until the next. We do not add a line to a data record that it has been “remaining” the same. IT is different by the measurement of analogue signals. Speed can be registered in every milliseconds, or bigger intervals, but to achieve the aim – punctuality – we need to store as much as possible. Here, the hysteresis must be determined, what is the requirement for STM, and LTM. The bigger the hysteresis is, the more interpolation will be applied. (From the point of “evidence” view, the interpolation is an “assuming” method, despite its wide usage). This method helps to save a lots of valuable storage space.

How does a modern EVR work? Let’s think it over from the point of view of the investigator. We illustrate its features with the Hassler Teloc 1500-type EVR. This is widely used in Hungary.

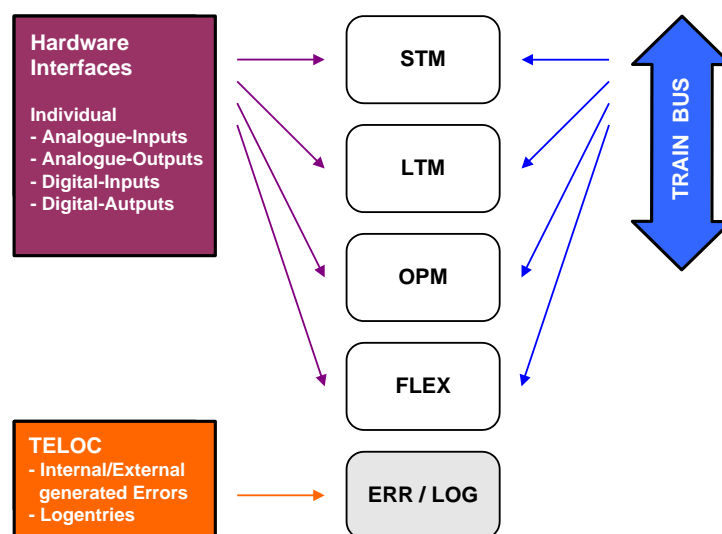


Figure 1 Memory distribution of the Teloc 1500 (Source: Hassler)

The Teloc is a modular system. For to be able to retrieve vital data from the EVR, it must be carefully planned, what we are about to monitor, because usually the more signals we monitor, the



less time will we be able to record. It is useless to duplicate every signal meaning (i.e. “The door is closed” and “The door is not open”) when there is no significant probability exists to affect traffic safety. This EVR plays a significant role in the vehicle’s operation in many cases, but from our point of view, we only need the data out of it, that has been recorded. The memory distribution can be seen on *Figure 1*.

The STM memory (short term) contains data from a short time interval. The signals are recorded with a high resolution, since the extract and detailed recording of speed as well as digital and analogue signals of the last covered distance are used for accident data analysis. Also known as residual distance memory.

The LTM (long term) contains less data, and analogue signals are often interpolated, but the registration period can be up to 8-10 months. The OPM contains the operational data such as train identifier, software versions, and we do not use it by investigation. The FLEX memory is a variable purpose memory, this can be extended, and its use depends on programming. The ERR/LOG memory contains data about the equipment itself (external link usage, restart, etc.). There is always a software necessary to read out, and visualize the data recorded.

The sampling frequency rate is 50Hz (20 milliseconds), from every digital inputs, but for the EVR to record it as a true or false signal, it must be at least 100ms long. It may happen, that a signal occurs for 15ms, but that will not be recorded.<sup>3</sup> (*See Figure 2*).

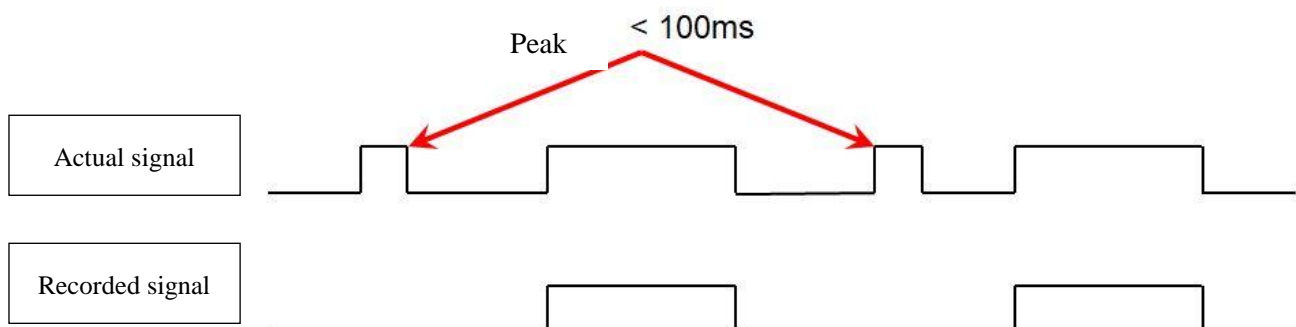


Figure 2 EVR signal selection (Source: Hassler)

For analogue inputs, the method can be seen in *Figure 3* below:

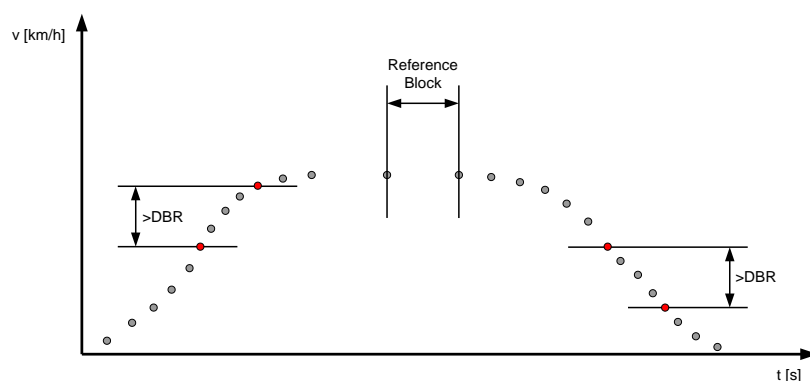
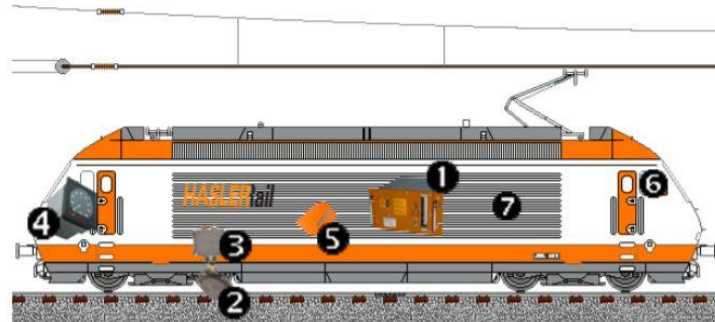


Figure 3 The principle of analog data recording (Source: Hassler)  
DBR means “Deviations Before Writing”

<sup>3</sup> Hassler Rail AG: Teloc 1500 Data acquisition and monitoring system manual EN.0300.085, 2.2.2.



The EVR is not similar on all of the trainsets. The basic layout is, not to mention the monitored signals can be seen on *Figure 4*.



*Figure 4* Typical layout of an EVR system. 1 – EVR, 2- impulse generator, 3 – terminal, 4 – speedometer, 5- external shock resistant memory, 6 – driver display unit, 7 – carbody shell (Source: Hassler)

The typically used analogue (A) and digital (D) signals upon accident investigation (at last, but not least) are the following:

- a) Axle speed (A)
- b) Wheel diameter (A)
- c) Train load (A)
- d) Train serial number (A)
- e) Driver ID (A)
- f) Traction effort demand (A)
- g) Brake effort demand (A)
- h) Reference speed (A)
- i) Train total mileage (A)
- j) Traction power present (D)
- k) All brakes applied (D)
- l) Fire and smoke detected (D)
- m) Doors are closed (D)
- n) Train stopped ( $v=0$  m/s – D)
- o) Safety systems bypasses (D – I eg. TCMS, SIFA etc.)
- p) Traction authorisation (D)
- q) All brakes released (D)
- r) AUX converter operates (D)
- s) Minimum air reservoir pressure present (D)
- t) Emergency brake applied (D) and its sub-lines (because of passenger activation, overspeed etc.)
- u) Horn, or other signals applied (D)

The EVR has presented us all the data necessary. The last step is the investigator, to come to the final conclusion. This process cannot be automatized. There is a sample of a record, on *Figure 5*.



# INTERNATIONAL SCIENTIFIC CONFERENCE ON ADVANCES IN MECHANICAL ENGINEERING

12-14 October 2017, Debrecen, Hungary

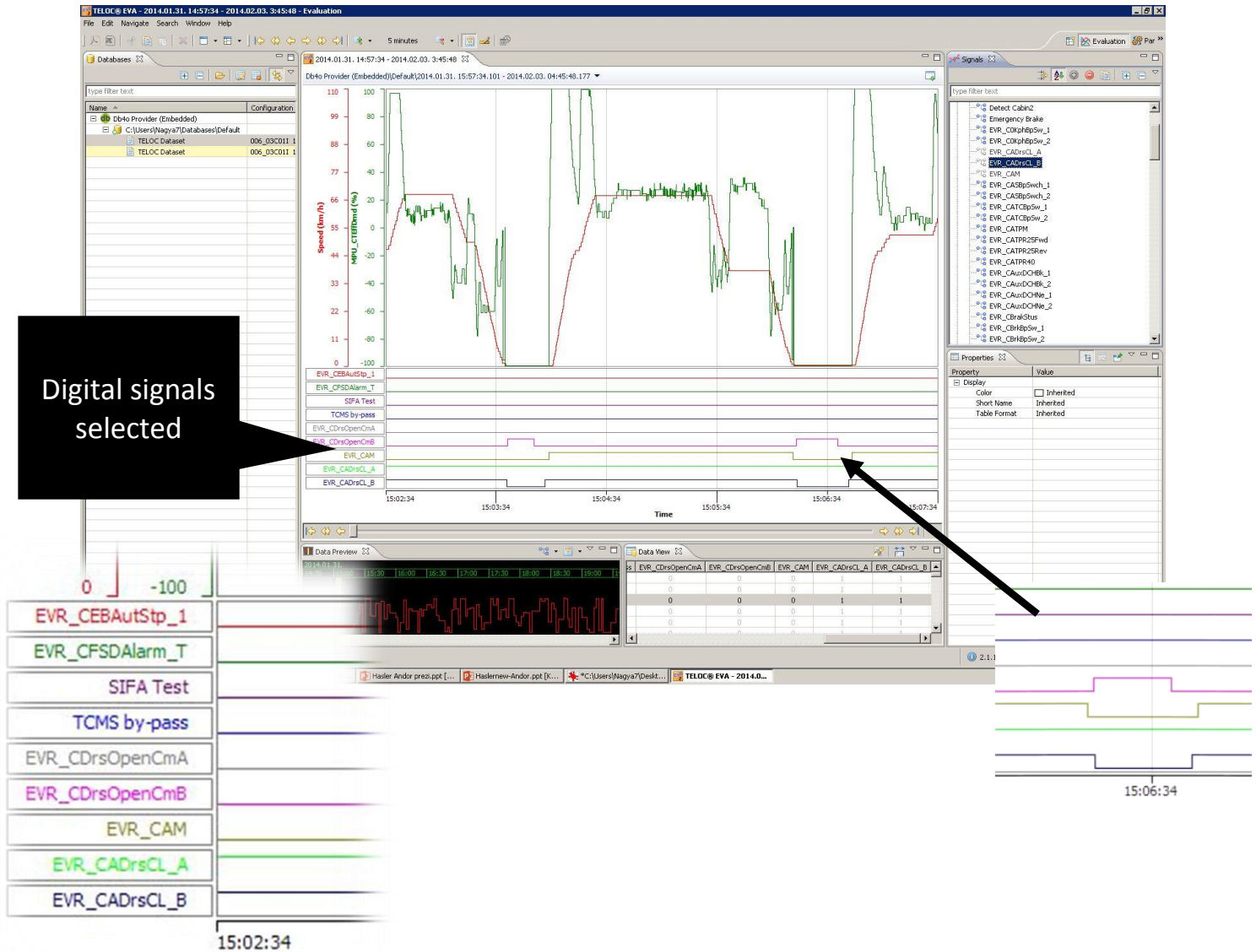


Figure 5 Typical EVR event list (Source: A.Nagy)

On the left bottom side, we can see the variables selected for showing. The aim of this investigation was to determine whether the doors were closed on the train, or not before the emergency brake applied upon a false side door opening. Just for showing, we have selected some more variables, like fire and smoke detection (EVR\_CFSDAlarm\_T), automatic emergency brake trigger device status (EVR\_CEBAutStp\_1). Down below, on Figure 6. there is the old version of event recorder. The paper was very sensitive, but very basic data, like speed, and emergency brake usage was written on it. There were no technical possibilities to read out these variables like the Teloc 1500.



*Figure 6* Clockwork based tape recorder, a pin scratches the signs into a waxed paper tape (Source: Hassler)

#### 4. CASE STUDY

We will present an accident case, step by step, and meanwhile compare the possibilities of collecting evidence from the old, and the new data recording systems.

The case: collision between a standing car, and a locomotive arriving the station, to an occupied track. The locomotive cannot stop within the brake distance, because of wheel slide. The case seems to be obviously locomotive driver issue.

<b>Event:</b>	<b>Old methods, without digital recorders</b>	<b>New method, with event recorders.</b>
The loco is heading towards the station, when it starts raining.	Departure from previous station has been logged, its “paper-pen” like register is writing the speed-distance graph. Permanent speed cannot be proven, as the register’s sample interval is too big. Brake application cannot be proven. The beginning time of the rain cannot be proven. The loco driver is notified about the entry for occupied track, and according to him, he held the brake test on the way. Cannot be proven.	The EVR continuously records the movement of the loco. It clearly says, when did it rain, as the rain sensor on the loco switched on the windshield wipers. There were no braking attempts from the loco driver side. Continuous traction effort is requested, there were no braking.
The loco is passing the entry signal, and goes right on the first switch, where it supposed to hold 30 km/h speed limit.	Entering the station (timestamp) cannot be proven, the first attempt can be seen for braking, but the register’s paper shows 0km/h, as the loco slides on the track, with 60km/h. Cannot be proven. According to him, he applied the brake. This is true, because in other case, the loco would not slide.	The EVR registers when it did pass the entry signal, and registers the speed for 60km/h, without braking signals, the horizontal accelerometers indicate moderate vibration. The signalling event recorder shows, that the isolated rails behind the entry signal were occupied for such a time, that is indicating 60km/h The driver then tries braking, but the whole loco slides with all



# INTERNATIONAL SCIENTIFIC CONFERENCE ON ADVANCES IN MECHANICAL ENGINEERING

12-14 October 2017, Debrecen, Hungary



		the wheels, as it can be seen that the wheel slide protection is working. Brake applied signal on.
The loco slides into the freight car.	Loco driver applied emergency brake. Wheel slide protection (WSP) is not present. All the wheels are stopped. No speed indication. Synchronous slide. The rest is just seen on pictures.	Wheel slide protection is not working, all wheels are stopped. The train follows all the happenings. The applied emergency brake just makes the situation worse, all the wheels are stopping.

The study shows, that numerous data disappeared in that era, where the event recorders were not available. Obviously, the comparison is not perfect, as most probably, the older vehicle would not even be able to be attached to an EVR. The technical level of the vehicles developed much faster than the infrastructure, and as the necessity of event recording appeared in other fields, their development has become faster, meanwhile the development of the railroad-only specialised equipment remained in the same pace.

## ACKNOWLEDGEMENT

The research has been realised by the project, "Internationalisation, initiatives to establish a new source of researchers and graduates, and development of knowledge and technological transfer as instruments of intelligent specialisations at Széchenyi István University"

## REFERENCES

- [1] Parliament of the United Kingdom: The Locomotive Act 1865, Highways and Locomotives Amendment 1878. Vic.28-29, The Houses of Parliament, London, 1865
- [2] Hungarian State Railways (MÁV): F.2. Traffic Regulations (Forgalmi Utasítás), Budapest, 2007
- [3] Hassler Rail AG: Manual for Teloc 1500 Data acquisition and monitoring system Hassler Bern, 2009



## COMPARISON OF BATCH AND SEMI-CONTINUOUS DISTILLATION

LÁNG Péter DSc, ÖRSI Márton, HÉGELY László PhD

Department of Building Service and Process Engineering, Faculty of Mechanical Engineering,  
Budapest University of Technology and Economics

E-mail: [lang@mail.bme.hu](mailto:lang@mail.bme.hu)

### Abstract

Batch distillation is frequently applied for the separation of liquid mixtures with variable amount and composition. Semi-continuous distillation differs from the batch distillation in that one part of the feed is continuously fed during the distillation. The heating surface of the reboiler must be always covered by liquid. This determines a minimum volume of residue at the end of the batch. In the case studied, the less volatile component (B) must be produced from a dilute aqueous solution in high purity which cannot be reached in one batch because of the above constraint. Different batch and semi-continuous operational policies are studied by dynamic simulation with a professional flow-sheet simulator, and compared on the basis of the specific energy demand of B production.

**Keywords:** batch distillation, semi-continuous distillation, dynamic simulation, operational policies

### 1. INTRODUCTION

By *distillation* the components of a liquid mixture are separated on the basis of the difference of volatility. In a binary mixture the more volatile component is A whilst the less volatile is B. This energy demanding separation method is the most widespread one in the chemical industry. The main parts of a distillation equipment: column (with plates or packing), condenser and reboiler. By *continuous distillation* (CD) there is continuous feeding (usually liquid at its boiling point), continuous distillate and bottoms withdrawal and the column operates at steady state. The feed plate divides the column into rectifying and stripping sections. If the location of feed plate is optimal the concentration of liquid on this plate is near to that of the feed.

If the amount of mixture to be separated (feed) is smaller and varying and the feed composition also varies *batch distillation* (BD) is applied. The whole amount of feed is filled into the reboiler, the distillate is continuously withdrawn, whilst the bottoms product (residue) remains in the reboiler. There is no steady state except for the end of heating up under infinite reflux ratio ( $R=\infty$ ). The advantages of BD are the flexibility and that multicomponent mixtures can be separated with a single column.

*Semi-continuous distillation* differs from the BD in that one part of the feed is continuously fed (usually) into the reboiler during the distillation.

By BD the feed is processed in several batches. The whole amount of liquid to be processed (charge) is filled into the reboiler. The volume of the liquid in the reboiler (residue) is continuously decreasing. The residue becomes more and more dilute for A, therefore if the reflux ratio (R) is kept constant, the mass fraction of component A in the distillate ( $x_D$ ) decreases, too. The reboiler can be heated with a heating jacket (providing a relatively low, eventually decreasing active heating surface area), and/or a tube bundle or heating spiral in the reboiler. The heating surface of the reboiler must be always covered by liquid. This determines a minimum volume of residue at the end of processing of each batch. The product is more frequently A (obtained as distillate), but in some



cases B (obtained as residue). In certain cases, B must be produced from a dilute solution in high purity which cannot be reached in one batch because of the above constraint.

There are the following possibilities (operational policies) to produce B in the purity prescribed:

1. To leave the residue in the reboiler and to fill the next amount of fresh feed onto it until the purity prescribed of B is reached (BD1 policy).
2. If an additional tank is available, at the end of the batches the reboiler is drained, the residues are collected in the tank. After processing several batches when the necessary amount of residue (containing enough B) has been collected, the residues collected are redistilled (BD2 policy).
3. Semi-continuous operation of the BD column (SCD policy) when one part of the feed is introduced continuously into the reboiler.

The aim of the paper is

- to study different BD and SCD operational policies by dynamic simulation,
- to compare the energy demand of these operational policies.

The simulation calculations are performed with the ChemCad professional flow-sheet simulator ('CCBATCH'). In the case studied an organic component (B) must be produced in high purity from its dilute aqueous solution (water is component A) in an existing BD column.

## 2. VAPOUR-LIQUID EQUILIBRIUM CONDITIONS

The most important data of the components are shown in *Table 1*.

*Table 1.* Data of the components

Component	MW g/mol	$T_{bp}$ °C	$\rho_L^{20}$ kg/m <sup>3</sup>	$C_{P,L}$ J/gK	Latent heat J/g	Antoine-constants		
						A	B	C
Water (A)	18.02	100	998	4.19	2257	7.52940	1435.264	208.302
Organic (B)	87.12	128.3	999	2.00	456.7	7.16030	1447.70	210.000

For the equilibrium and enthalpy calculations Margules (constants:  $a_{12}=0.4816$ ,  $a_{21}=0.0085$ ) and Latent Heat models are applied. The y-x measured and calculated data are shown in *Figure 1*.

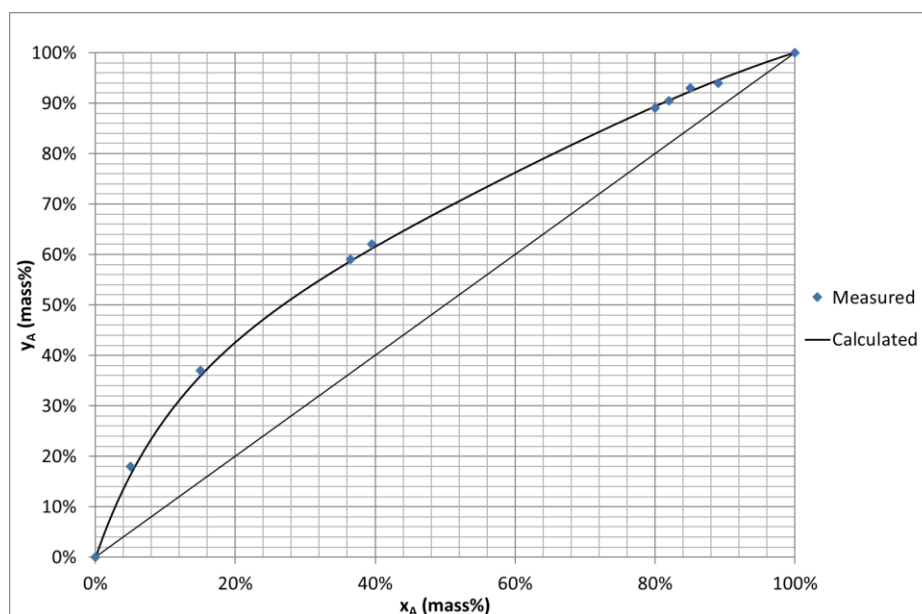


*Figure 1* Measured and calculated y-x equilibrium curves (P=1.013 bar)



### 3. RESULTS

The feed contains 90 mass% water ( $x_F=0.9$ ). The prescribed product compositions:  $x_{D,av}=0.99$  and  $x_W=0.005$ . The data of the column (operating at atmospheric pressure) are as follows. The volume of the reboiler:  $10\text{ m}^3$ , the maximum and minimum liquid volume in it  $8$  and  $2\text{ m}^3$ , respectively. Number of theoretical plates (in the CC model):  $N=32$  (including the total condenser and reboiler). The hold-ups: condenser:  $0.08\text{ m}^3$ , column:  $0.08\text{ m}^3$ . The flow rate of distillate:  $1\text{ t/h}$ . The reflux ratio ( $R$ ) is so determined that at the end of each step the average composition of the distillate ( $x_{D,av}$ ) collected in this step equals to  $0.99$ . The hold-up remaining in the condenser and column are separately collected. The feed is always liquid at its boiling point. The different operational policies are compared on the basis of the specific energy demand of the production of  $B$ .

#### 3.1 Continuous distillation

Before the different BD and SCD policies the CD was simulated. From material balances the ratio of the distillate and bottoms flow rates:  $D/W=9.94\text{ kg/kg}$  ( $D/F=0.90863\text{ kg/kg}$ ). For the given  $N$  the optimal location of the feed plate ( $f=19$ ) is where the lowest reflux ratio ( $R=0.683$ ) is needed hence the energy demand of the separation prescribed is minimal. The specific energy demand is  $37.83\text{ MJ/kg B}$ .

#### 3.2 Batch distillation policies

The BD policies differ from each other in what happens with the off-spec residues whose  $B$  content is still too low, that is their  $A$  content ( $x_W$ ) is still higher than  $0.005$ .

##### a. BD1 policy

In all steps the reboiler is filled up onto  $8\text{ m}^3$ . At the end of heating up of the column the hold-up in the reboiler ( $U_N$ ) is  $7.84\text{ m}^3$ . The distillation is finished when  $U_N$  reaches the minimum ( $2\text{ m}^3$ ) or  $x_W$  decreases to  $0.005$  (in the last, 4-th batch). The *off-spec residues remain in the reboiler* and the next amount ( $6\text{ m}^3$ ) of fresh feed is filled onto it. Figure 2 shows the evolution of the  $x$ -profile during Batch 1 (together with the optimal CD profile).

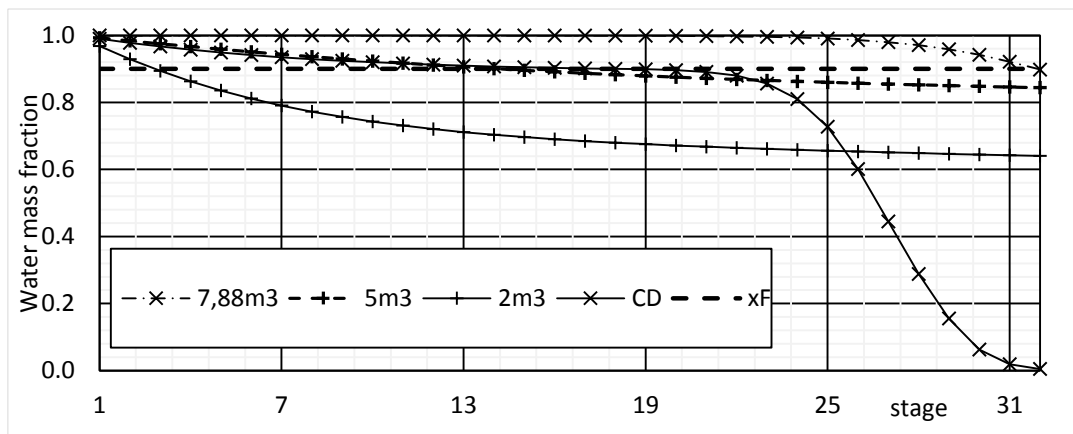


Figure 2  $x$ -profiles for different reboiler hold-ups (Batch 1 of BD1, CD)

It can be noticed that the location of the plate where  $x$  equals to  $x_F$  is getting higher with time.



The results for the end of the steps are shown in *Table 2*.

*Table 2. Results of BD1 policy*

Step	charge		R	$\Delta t$	SQ	distillate		residue	
	kg A	kg B		h		MJ	kg A	kg B	kg A
1	7200	800	0.78	5.85	23408	5795	56	1280	720
2	6680	1320	0.84	5.85	25515	5796	55	780	1220
3	6180	1820	1.18	5.85	28677	5798	53	304	1696
4	5704	2296	2.2	5.70	40068	5654	47	13	2139

The overall energy demand of one production cycle is 118668MJ, hence the specific energy demand is  $118668/2139=55.5$  MJ/kg B.

### *b. BD2 policies*

In all steps the reboiler is filled up onto  $8 \text{ m}^3$ . The distillation is finished when the minimum volume ( $2 \text{ m}^3$ ) is reached. The reboiler is then drained and *the residues are collected in a tank* and when the amount of residue (containing enough B) collected is enough, it is redistilled. By this policy the first 4 (or 3) steps are identical to Step 1 of BD1 policy. The necessary amount of B can be already collected in 3 steps (with  $6 \text{ m}^3$  residue), but we can still collect  $2 \text{ m}^3$  residue in a 4-th step in order to fill up the reboiler onto its maximum volume for the redistillation.

The results are shown in *Table 3* (for the first 4 steps the total amounts are given).

*Table 3. Results of BD2a policy (4 residues collected)*

Step	charge		R	$\Delta t$	SQ	distillate		residue	
	kg A	kg B		h		MJ	kg A	kg B	kg A
1-4	28800	3200	0.78	23.4	93633	23180	224	5120	2880
5	5120	2880	2.25	5.12	37454	5074	47	14	2718

The specific energy demand:  $131087/2718=48.2$  MJ/kg B.

If the residues of only 3 steps are collected and redistilled in the 4-th step the following results are obtained (*Table 4*):

*Table 4 Results of BD2b policy (3 residues collected)*

Step	charge		R	$\Delta t$	SQ	distillate		residue	
	kg A	kg B		h		MJ	kg A	kg B	kg A
1-3	21600	2400	0.78	17.55	70224	17385	168	3840	2160
4	3840	2160	2.03	3.82	26065	3970	31	12	2020

The specific energy demand:  $96289/2020=47.7$  MJ/kg B. *Figure 3* illustrates evolution of the charge composition ( $x_{CH}$ ) from batch to batch for the different BD policies.

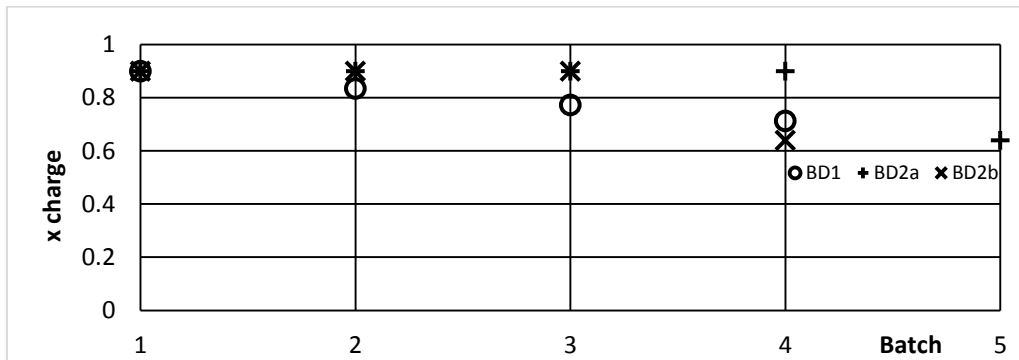


Figure 3 The variation of charge composition for the different BD policies

### 3.2 Semi-continuous policy (partial continuous feeding)

By this policy the reboiler is filled up until its maximal volume, the column is heated up, then after reaching the steady state one part of the feed is continuously introduced into the reboiler. The goal is to produce both the distillate and residue products of prescribed purity at the same time (at the end of the last step). The reboiler hold-up ( $U_N$ ) is kept constant (which can be made at different levels between the maximum and minimum volumes) so the flow rate of the continuous feeding equals to that of the distillate ( $1 \text{ m}^3/\text{h}$ ). There is a minimum amount of feed (cca.  $14\,500 \text{ kg}$ ), which must be continuously introduced in order to have at least the minimum amount of B in the system (more than  $2000 \text{ kg}$ ). Hence the minimal duration of continuous feeding is cca.  $14.5 \text{ h}$ .

First (by SDCa policy)  $U_N$  is kept all the time near to its maximal value ( $7.84 \text{ m}^3$ ). Even if a very high reflux ratio ( $R=4$ ) is applied  $x_W$  cannot be reduced in this step to  $0.005$  even if the distillate is too pure. The evolution of  $x_{D,av}$  and  $x_W$  in Step 1 are shown for different reflux ratios in Figure 4.

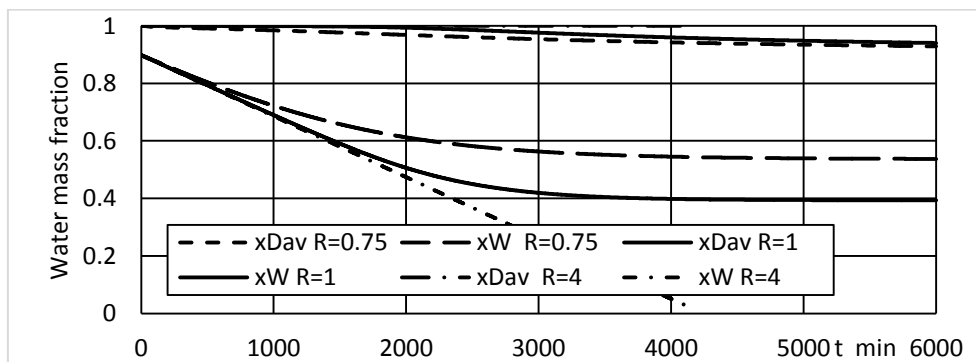


Figure 4 Evolution of  $x_{D,av}$  and  $x_W$  in Step 1 of SDCa policy (maximal  $U_N$ ;  $R=0.75, 1, 4$ )

$x_W$  decreases with time nearly linearly for a longer time, then slower and slower and finally it reaches a minimum, which is above  $0.005$ . Therefore an additional BD step without continuous feeding (Step 2) is needed with a higher  $R$ , at the end of which both purity requirements are satisfied. Both steps are finished when  $x_{D,av}$  falls onto  $0.99$ .

Step 1 was studied for different reflux ratios ( $R_1$ ) gradually decreased from  $4.0$  to  $0.75$ . At  $R_1=0.75$   $x_{D,av}$  fell onto  $0.99$  too early (at  $t=9.2 \text{ h}$ ). The (minimal) reflux ratio for Step 2 ( $R_2$ ) was determined for two different appropriate  $R_1$  values. The results are shown in Tables 5 and 6.



*Table 5 Results of SCDa policy (maximal  $U_N$ ;  $R_1=1.0$ )*

Step	R	$\Delta t$	SQ	distillate		residue	
		h	MJ	kg A	kg B	kg A	kg B
1	1.0	37.16	167043	36797	371	3742	4111
2	2.8	3.84	32889	3803	38	20	3998

The specific energy demand for  $R_1=1.0$  is  $199932/3998=50.0$  MJ/kg B

*Table 6 Results of SCDa policy (maximal  $U_N$ ;  $R_1=0.9$ )*

Step	R	$\Delta t$	SQ	distillate		residue	
		h	MJ	kg A	kg B	kg A	kg B
1	0.9	26.74	114187	26478	267	4671	3182
2	2.4	4.80	36717	4752	49	15	3043

The specific energy demand for  $R_1=0.9$  is 49.6 MJ/kg B, which is only slightly lower than for  $R_1=1.0$  in spite of the fact that both  $R_1$  and  $R_2$  are lower.

The evolution of  $x_{D,av}$  and  $x_W$  in the two steps is shown in *Figure 5* (the distillates of the two steps are collected separately).

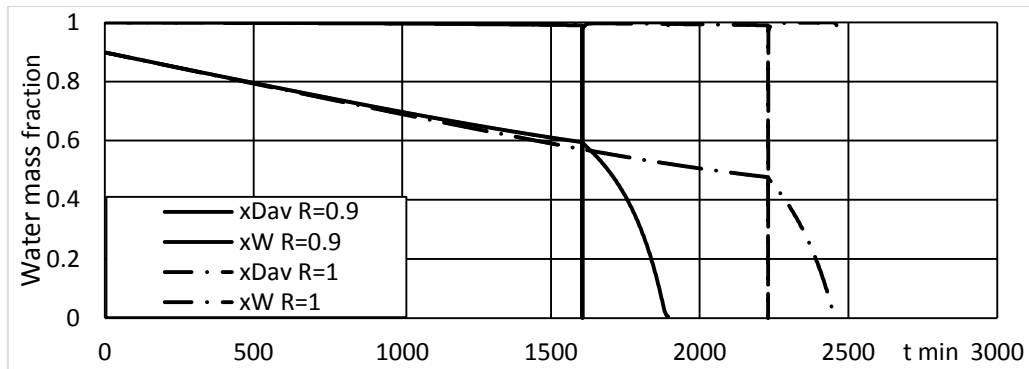


*Figure 5 Evolution of  $x_{D,av}$  and  $x_W$  by SCDa policy ( $R_1=0.9, 1.0$ )*

The SCD policy was also studied for the case where the reboiler hold-up is kept at a reduced value ( $5 \text{ m}^3$ ). In this case before the two steps of SCDa there is a BD step when the reboiler hold-up is decreased to  $5 \text{ m}^3$  under the lowest  $R_1$  (at the end of which  $x_{D,av}$  equals to 0.99). In Step 2  $R_2=0.9$  gave still too short duration (13.26 h). The results are shown in *Table 7*.

*Table 7 Results of SCDb policy (reduced  $U_N$ ;  $R_2=1.0$ )*

Step	R	$\Delta t$	SQ	distillate		residue	
		h	MJ	kg A	kg B	kg A	kg B
1	0.67	2.86	10773	2832	28.3	4230	762
2	1.0	20.46	91978	20260	204	2412	2581
3	2.4	2.5	19142	2475	25	12	2485

The specific energy demand is 49.1 MJ/kg B, which is only slightly lower than that of SCDa (for the same R of the step with continuous feeding). However this policy is more complicated and it is not sure that the whole surface area of the heating mantle is covered by liquid.



# INTERNATIONAL SCIENTIFIC CONFERENCE ON ADVANCES IN MECHANICAL ENGINEERING

12-14 October 2017, Debrecen, Hungary



We can state that SCD policies gave better results than BD1 policy. However their energy demands were near to those of BD2 policies. Their main advantage that  $U_N$  can be kept at the maximum and the interruption of the production (filling up, heating up and draining of the reboiler) is much more seldom (much less dead time).

## CONCLUSIONS

Different batch (BD) and semi-continuous distillation (SCD) operational policies were studied by dynamic simulation with the ChemCad professional flow-sheet simulator and compared on the basis of the specific energy demand. In the case studied, the less volatile component (B) must be produced from a dilute aqueous solution in high purity, which cannot be reached in one batch, because of the minimum volume of the residue at the end of the batch necessary for wetting the whole heating surface. We concluded for the BD policies that it is better to empty the reboiler at the end of the batches, and redistill the residues collected (BD2) than filling the next amount of fresh feed on the residue of the previous batch (BD1). The energy demand of SCD policy where continuous feeding is applied into the reboiler was near to that of BD2 under lower dead times.

## ACKNOWLEDGEMENT

This work was supported by the NKFI-OTKA (project No. 120083).



## APPLICATION OF THE FUNCTIONS OF A CHATBOT IN THE MANUFACTURING PROCESS OF A GEAR IN IRUM COMPANY

<sup>1,3</sup>LATEȘ Daniel PhD, <sup>2</sup>CĂȘVEAN Marius, <sup>2,3</sup>CIOLOCA Flaviu

<sup>1</sup>“Petru Maior” University of Târgu Mureș

E-mail: [ddan005@gmail.com](mailto:ddan005@gmail.com)

<sup>2</sup>Technical University of Cluj Napoca

E-mail: [marius.casvean@yahoo.com](mailto:marius.casvean@yahoo.com)

<sup>3</sup>IRUM, Târgu Mureș

E-mail: [cioloca.flaviu@irum.ro](mailto:cioloca.flaviu@irum.ro)

### Abstract

*In this paper we will use the concept of chatbot in the production process of the gear wheels from a company. The paper highlights the important aspects of using this concept by exemplifying existing applications on the market today. In this paper, a demonstration program will be carried out in which the operation processes of the gears realization will be integrated. At the end of the paper we will conclude by showing the functional aspects of the application. This was made in relation to the added benefit of the implementation of the chatbot on the technology of toothed wheel manufacture.*

**Keywords:** chatbot, manufacturing process, gear

### 1. CHATBOT CONCEPT DEFINITION AND APPLICATIONS

Brennan defined a chatbot as an artificial construction designed to converse with it. Chatbots, in specialized literature are defined as automated or semi-automated software designed in particular to interact with users. They are meant to respond quickly to user's questions and extract relevant information from a huge amount of data. In general, bots run simple and repetitive tasks at a rate much faster than a human being could do. Built on the principle of neural networks, chatbots are endowed with a certain degree of artificial intelligence and become more and more effective in giving answers. Based on these answers, the robot guides you through a series of site designs that you can further customize to fit your needs.

Among the obstacles of computers, understanding of words or sentences cannot be count, but understanding the meaning of those words. Moreover, the difficulties of computerized systems are not only to understand the meaning of those words but rather to understand the limitless flexibility of expression and the way in which those words are used together for the purpose of communicating an expression. Another important advantage of the chatbot is represented by the fact that it can work non-stop and the transfer of information from a human person to such a device can be done without too much difficulty or effort. This communication takes place through digital technology, which can also be matched by the positive aspects of chatboots. In the field of mechanical engineering, for example, the rapid development of chatbot systems has opened a new niche for communication between a human and a chatbot, the latter providing support in coordinating technological processes, their status, or inventory of raw materials. Among the various situations that can be automated, organizational processes seem more common, so using a chatbot system reduces operational costs, especially in terms of maintaining a particular service. In the medical field, using chatbot systems as a communication device for translational medicine will reduce costs and time for routine operations.



Among the negative aspects of chatbots would be the fact that sometimes they have too many functions and slow down the interpretation and processing of information. Another one is that the delivery of a response is delayed, or sometimes they have an interface which is too complex.

Applications for communication between a human person and a conversational entity are found in many areas, from complex aircraft or vehicle systems, smart phone applications to their integration into the medical field, or various commodity catalogs. In some contexts, the computer-mediated communication name is assigned. Within a company, these systems can be used for more sophisticated purposes, such as supporting a hiring interview for a potential future employee, communicating organizational issues, thus replacing a person from human resources.

The first attempt to build a chatbot was ELIZA, which was created in the 1960s by Joseph Weizenbaum, to emulate a psychotherapist in clinical treatment. Another specific example of such an application is the ALICE Chatbot System (Artificial Linguistic Internet Computer Entity).

It was developed and implemented by Wallace in 1995 to allow people to introduce knowledge about the chatbot dialogue model based on the ALICE open source software. In another example, Webber developed a similar ALICE chatbot, called Virtual Patient Bot (VPbot), which simulates a patient that some students will be interviewing. The entrance is introduced as text by the student, and the patient's response is presented as a textual and spoken word. The chatbot can also assist a human being in shopping, business or companies. At one point, a chatbot may even remind the interlocutor of the need to practice and try new words and expressions.

## 2. REALIZING A CHATBOT IN THE GEAR WHEELS MANUFACTURING PROCESS

Gears are used to transmit translation or rotation movements at varying powers. This makes the gears one of the most used machine parts. Thus, a series of processes have been developed to achieve the shape of the flank and the shape of the teeth of the gear wheels. From the point of view of the tooth profile, there are several widely used profiles (especially in industry): the evolving profile, the cycloidal profile and the profile composed of circular arcs.

The phases of toothed wheel manufacture are defined as the workplace processing operation. The technological operations for gears are:

1. Cutting - full semi-finished
2. Forging
3. Turning - grinding, finishing
4. Grooving(through broaching / mortising) - channels up
5. Tothing
6. Thermal treatment
7. Correction: interior, exterior.

A chatbot is thought to check the tracking card, based on multiple choices. Depending on the complexity of the program, the chatbot structure develops in pyramidal form. In this paper a demo application has been made. The first step to build the program is to integrate all of the manufacturing processes mentioned above into a pyramid structure. This pyramidal shape can be seen in Figure 1, in a simplified version on a certain technological stage, namely for making the outer teeth of the toothed wheel. In the pyramid structure we can see simplified names: MTE, MTI, MTM which means the machines that make the respective operation and codes: code 25, code 42, code 50, code 64 etc, which means the technological operation of the toothed wheel. By acting, we can have access to the information, or we can go back to the previous stage.

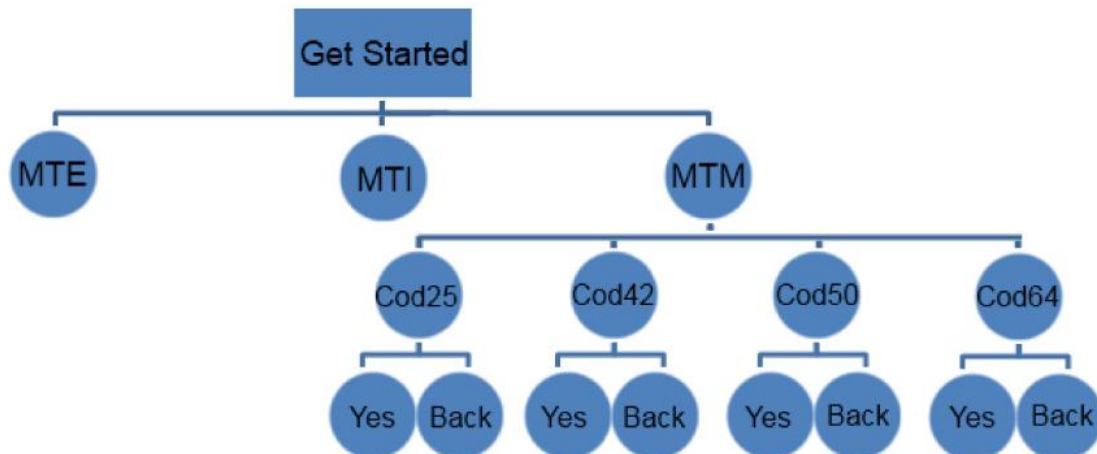


Figure 1 The structural pyramid of the chatbot

Figure 2 illustrates on an online application a part of the chatbot program that is related to the toothed wheel manufacturing process. With the help of this application, the operator can access the documentation bases that help him achieve the teething process in this case. This program can give you information about the piece's execution drawing, the semi-finished piece on stock, information about the batch of parts, the location of the parts at the time, the time to complete the parts, the reject of the parts, etc.

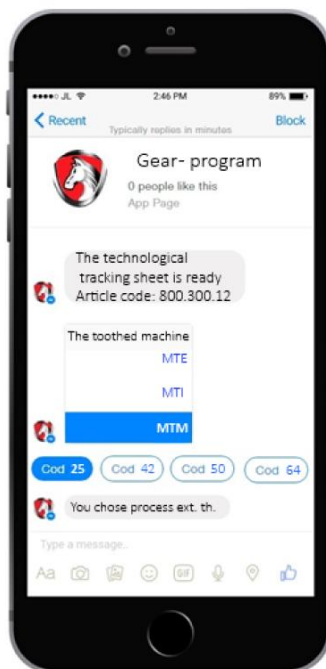


Figure 2 The chatbot application

## CONCLUSIONS AND RESEARCH DIRECTIONS

Most chat robots nowadays still have problems when it comes to becoming effective in interacting with a web service and often lead to frustrating experiences because of their rather restrictive nature. All of these applications are constantly being developed, included in the current research fields, where simulation of a natural language is explored. Integrating automated conversation systems, supplemented by spoken natural language, along with other devices, is a good solution for



a variety of tasks. Any task that needs analysis and reasoning, with enough information, can be interfaced by a chatbot with a human person. Systems of this type are of future in the sense that many routine and time-consuming operations will be taken over by them, giving employees around the world time to handle creative and innovative tasks. The biggest challenge of a chatbot is to receive the information and understand correctly what it wants to communicate, so that it can also provide coherent information.

By using the chatbot in the paper it was noticeable that the information can be structured much easier, can be checked, can be analyzed. With the realized chatbot you can interact with multiple choices or voice recognition, which offers ease of use. It has been noticed that using this program brings benefits such as: collects and evaluates data, simplifies complex program control, lower error margin, makes the use of human capital more efficient, reduces administrative effort. We wish to continue the studies to implement this chatbot in the making process of gears with the tracking of lots of pieces to follow this program realized in the paper.

## ACKNOWLEDGEMENTS

We would like to express our gratitude to SC IRUM SA for the moral and financial support for the realization of this article. We also want to thank the organizers of the event for organizing such a scientific conference that helps us publish articles on engineering.

## REFERENCES

- [1] Abashev, A., Grigoryev, R., Grigorian, K., Boyko, V.: *Programming Tools for Messenger-Based Chatbot System Organization: Implication for Outpatient and Translational Medicines*. BioNanoScience, vol. 7, pg. 403-407, 2017.
- [2] Fryer, L., K., Ainley, M., Thompson, A., Gibson, A., Sherlock, Z.: *Simulating and sustaining interest in a language course: An experimental comparison of Chatbot and Human task partners*. Computers in Human Behavior, vol. 75, pg. 461-468, 2017.
- [3] Hill, J., Ford, R., W., Ferraras, I., G.: *Real conversations with artificial intelligence: A comparison between human-human online conversations and human-chatbot conversations*. Computers in Human Behavior, vol. 49, pg. 245-250, 2015.
- [4] Jia, J., CSIEC: *A computer assisted English learning chatbot based on textual knowledge and reasoning*. Knowledge-Based Systems, vol. 22, pg. 249-255, 2009.
- [5] Jiyoun Jia: *The Study of the Application of a Web-Based Chatbot System on the Teaching of Foreign Languages*. Institute for Interdisciplinary Informatics, University of Augsburg, Germany, 2004.
- [6] Kowalski S., Pavlovska, K., Goldstein, M.: *Two Case Studies in Using Chatbots for Security Training*. Information Assurance and Security Education and Training pp 265-272, WISE 2009.
- [7] Lates, D., Mihnea, D., B., Cioloca, D., F.: *Utilizarea chatbot-ului în tehnologia de fabricație a mașinilor*. Conferința națională multidisciplinară, ISBN 978-973-126-528-5, Cugir, 2017.
- [8] Mihnea, D., B., Lates, D.: *Implementarea Chatbot-ului pe Tehnologia Vehiculelor Articulate*. Sesiunii de comunicări științifice a cercurilor științifice studențești, Universitatea Petru Maior, 2017.
- [9] Nikolaos Polatidis: *Chatbot for admissions*. Computers and Society, 28 Aug 2014.
- [10] Shawar, B., A., Atwell, E.: *Chatbots: are they really useful?*. LDV Forum, pg. 29-49, 2007.
- [11] Zah, M., Csibi, V., Lates, D.: *Reprezentarea grafică și analitică a curbelor cicloidale prin Matlab*. Conferința națională multidisciplinară, ISBN 978-973-126-528-5, Cugir, 2013.
- [12] <http://www.experionglobal.com/blog-post/chatbots-the-new-face-of-employee-service/>



## IONIC LIQUID AS A NOVEL, HIGH PERFORMANCE HYDRAULIC FLUID - SELECTION PROCESS

LOVREC Darko PhD

University of Maribor, Slovenia

E-mail: [darko.lovrec@um.si](mailto:darko.lovrec@um.si)

### Abstract

Ionic liquids (ILs), a combination of cations and anions, are molten organic salts with very low melting point, below 100 °C or lower. They have been recognized as very promising high-performance lubricants and have attracted considerable attention within the field of tribology. Due to its remarkable lubrication and anti-wear capabilities, as compared with lubrication oils in general use, they represent very promising candidate for the use as a hydraulic fluid. But, despite the excellent individual properties, it is very difficult to find an ionic liquid that would combine the majority of good physical-chemical properties, characteristic for the modern hydraulic fluids, e.g. high performance mineral based hydraulic oils. For a very well-known and widely used hydraulic oils, a numerous testing procedures have been used for practically all properties. In case of ionic liquids, the situation is completely different - one possibility represents the use the same methods as in case of conventional hydraulic fluids.

**Keywords:** ionic liquids, hydraulic fluid, properties, selection process, test procedures.

### 1. INTRODUCTION

Due to numerous good features, the ionic liquids should be an ideal candidate for a new lubricant, suitable for use under harsh conditions, where conventional oils and greases or solid lubricants fail [1] **Hiba! A hivatkozási forrás nem található.** A large number of studies have already been carried out in this area so far, but only few with ionic liquids suitable for use within hydraulic systems. The choice of cation and anion in an ionic liquid (IL) as well as the design of ion side chains determine the fundamental properties of ILs, which permits the creating of tailor-made lubricants and lubricant additives [2].

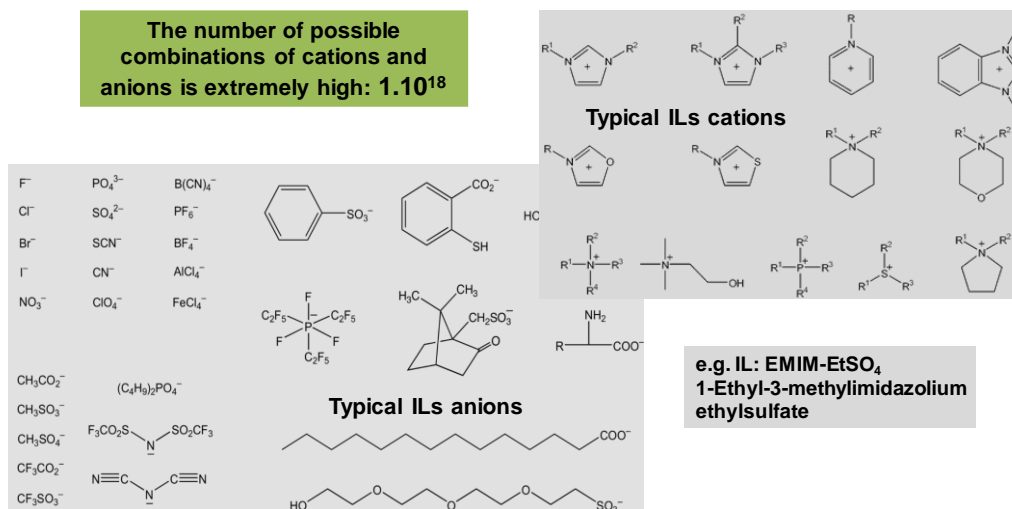


Figure 1 Enormous combination of anions and cations



When combined specified cation with the anions, you will obtain another salt – which if it does not work by trial and error but intentionally, can be synthesised into a completely new material with entirely new properties. In our case, we are looking for liquid salts, which would have the characteristics of a perfect hydraulic fluid. The number of possible combinations is extremely high, that is why the best ionic liquid is supposed to be adapted for different usage:  $1.10^{18}$  – see *Figure 1*.

The many benefits of using IL lubricants include:

- reduced parasitic energy loss by reducing friction,
- extended device life and maintenance cycles because of wear reduction,
- expanded high temperature lubricant usage because of high thermal stability,
- safer transportation and storage because of non-flammability.

In addition, ILs don't evaporate like most other liquids, one of the reasons they hold so much promise as lubricants.

## 2. METHODS

Even after selecting the “more suitable candidates” for use as hydraulic liquids, the work with ionic liquids is not as uniformly definite as with other lubricants. It is because of their unique properties that ionic liquids frequently impose the use of special laboratory equipment.

The majority of laboratory measurements were carried out by a wide assortment of “classical” analytical methods, out of which many were also applicable for ionic liquids, for example measurements of viscosity, density, corrosion, Karl Fischer titration, UV/VIS spectroscopy, FTIR spectroscopy, thermo-gravimetric analysis, measurements of lubricating and foaming properties. These tests can be carried out in conventional lubricant labs using the conventional measuring devices and standards:

- flash and fire points by Cleveland Open Cup tester; ASTM D 92,
- flash-point by Pensky-Martens Closed Cup Tester; ASTM D 93,
- determination of density by a densimeter; ISO 12185,
- kinematic viscosity at 40 °C and 100 °C; ASTM D 445,
- determination of viscosity index; ASTM D 2270,
- determination of corrosion within a humid chamber; DIN EN ISO 6270-2,
- determination of corrosiveness to copper; ASTM D130,
- determination of demulsifying properties; ASTM D 1401,
- determination of foaming in lubricating oils; ASTM D 892,
- determination of welding point and wear diameter; IP 239-85,
- determination of pour-point; ASTM D 97.

Summarised descriptions of executing the individual measurements, sample amounts and the equipment used mainly relate to the usual lubricants in accordance with the relevant standard. In addition, tests of ionic liquids (as lubricants) based on processes intended particularly for the testing of mineral based oils (liquid lubricants) and as such served as a starting-point. One of the duties within the framework of the research was the assessment of adequacy when using the existing standardised processes for testing ionic liquids as lubricants.

In addition to the mentioned and used standard tests, special purposeful measurements of physical-chemical properties were also used for testing the ionic liquids as well as comparing liquids. Some of these tests, e.g. measurement of breakdown voltage, filtration capacity, Stribeck's curve, contact



angle, or e.g. to check a compatibility with other materials used within hydraulic system: compatibility with reservoir paint coats, compatibility with different sealing material, measurement of compressibility and sound propagation... These tests need to be carried out with special measurement equipment, in specialised laboratories and/or under specific conditions, requirements or procedures. Some of these methods are adapted for testing the ionic liquids and are not standardized. [3]

Also in presented paper, some measurements were performed in conformity with the standard, but less of the usual test methods and some in conformity with adapted methods. The principal target of those measurements was to determine suitability of use within a real hydraulic system. The measurement results allowed the definition of directions for selecting of the hydraulic system and its component parts.

Those special, purposive tests were performed in order to become more familiar with the important properties of ionic liquids and to compare them with usual lubricants. On the basis of such measurement results, a lot of useful information and directions will be acquired for constructing components suitable for use with ionic liquid and/or systems incorporating these liquids.

### 3. RESULTS

Generally, the analyses were conducted by standard testing methods that are normally used for laboratory analysis of conventional hydraulic fluids. In some cases, we are forced to use, otherwise standard testing methods, which are not typical for hydraulic fluids. These methods allow to obtain additional information. Analyses were carried out in comparison with classical mineral based hydraulic oil (Hydrolubric VG 46). In the following, the laboratory measurements results only of two important properties will be pointed out: lubricating properties measurement, and compatibility testing with paint coat.

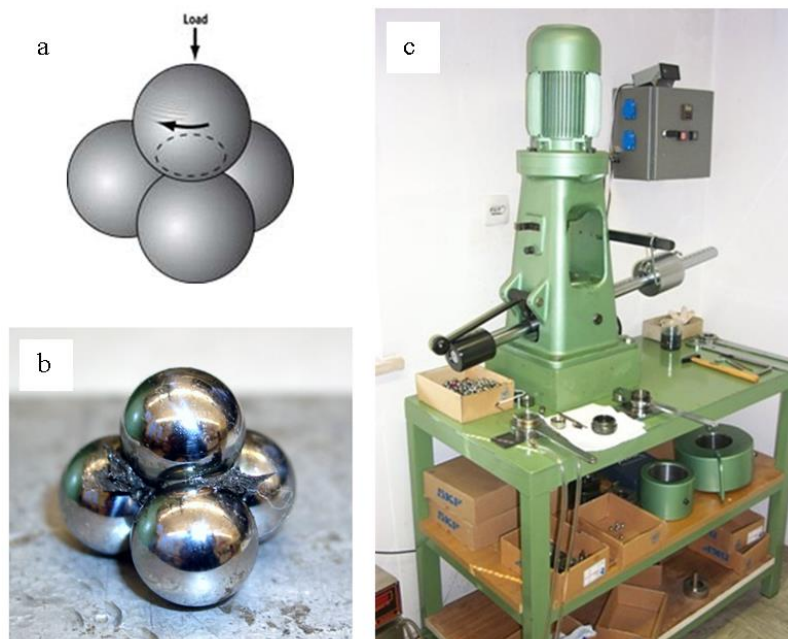


Figure 2 Principle of welding-point measurement a), b), Four-Ball device Hansa Press c)

Hydraulic liquid lubricating properties, a basic important property for hydraulic fluids, can be determined and verified in different ways. One of these are the measurements of the welding-point and wear test according to standardised procedure (e.g. IP 239-85), with the use of four-ball



apparatus Hansa Press, as shown in *Figure 2c*. This method based on load application to four standardised steel balls of 12.7 mm diameter. The top rotating ball slips onto the lower three fixed balls at constant loading and at constant rotating velocity of  $1440 \text{ min}^{-1}$  (*Figure 2a* and *2b*). The welding-point measurement and the wear test of lubricating oils, emulsions and greases can be performed on the same apparatus.

The welding-point is measured at specific loading and/or to ball pressure for 10 seconds. The top ball rotates and presses with the test loading against the lower three immovable balls dipped into the tested liquid. The measurement result is given in kg and comprises two numbers (e.g. 140/160). The first number indicates the maximum loading at which ball welding did not occur during the test (10 s). The second number indicates the minimum loading at which complete steel ball welding and/or automatic deactivation of the device occurred during the test.

The wear test lasts much longer, namely for  $60 \text{ min} \pm 1 \text{ min}$  at constant temperature and loading, depending on the tested hydraulic liquid. The ball wear depends on the loading, velocity, duration of the test and the properties of the lubricant tested. As all parameters, except the lubricating properties are constant, the result and/or the ball wear depends only on the lubricating properties of the liquid tested. After completion of the test, the wear test result is obtained by measuring the wear of the lower three steel balls under a microscope, where the diameters of the wear cavities are measured on the three immovable balls. The wear extent is defined as the average diameter of ball wear under known conditions. [4]

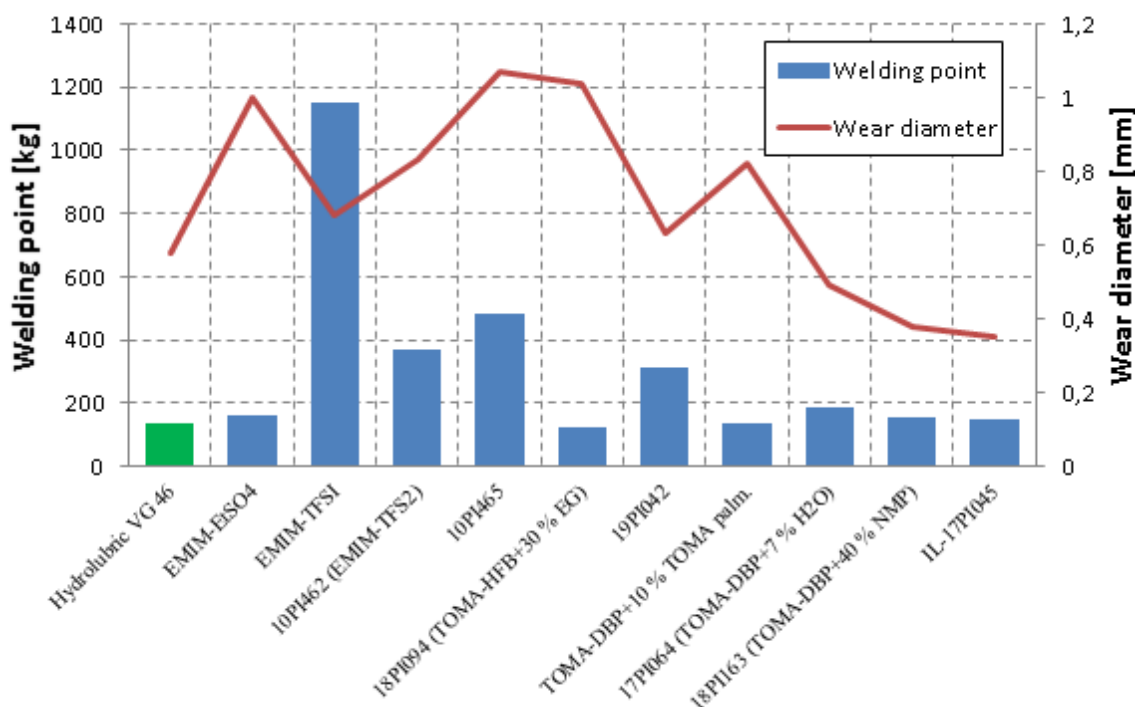


Figure 3 Lubricating properties in comparison with mineral hydraulic oil

Figure 3 shows the comparison between the welding points and wear diameters for different samples of ionic liquids compared with mineral hydraulic oil ISO VG46. The lubricating properties of some ionic liquid samples are considerably better than those of the mineral oil. Some samples have an exceptionally high welding point, for example EMIM-TFSI had as much as 1150 kg, which pointed out exceptional properties at extreme pressures but, interestingly, the wear diameter was even greater than that of the mineral oil, implying that the anti-wear properties were worse. As in the case of hydraulic oils the anti-wear properties are more important that liquid would be



potentially more suitable for use in gearings, maybe even as metalworking fluid during metal machining. In regard to other liquids with high welding points the limitation was, in particular, bad corrosive protection in the presence of moisture or in proper viscosity for the use in hydraulic systems.

Apart from the standard tests used for conventional hydraulic fluids, it is necessary to carry out some additional, unconventional tests for the practical use of new ionic liquids within hydraulic system. One such test is certainly testing the compatibility of ionic liquid with e.g. a reservoir colour coating.

Most hydraulic systems' tanks are painted inside and outside. Therefore, it is very important that the used hydraulic liquid should be compatible with the used paint coatings. We performed a comparison test between the compatibilities of two ionic liquids IL-EMIM-EtSO<sub>4</sub> and IL-17PI045 with two fire resistant hydraulic liquids Hidrol HFC 46 (HFC type) and Quintolubric 888-68 (HFD-U type). For the test we used the samples of metal plates as used by the tank manufacture. The metal plate samples were painted with two paints used for the tanks' interiors and exteriors. The interior is painted with epoxy priming coat, whilst the exterior is additionally coated with epoxy thick-layer finishing coat. Some metal plate samples were painted only with the interior paint and some were still additionally coated with the paint for the tank exterior.

The test was performed so that about 40 ml of each liquid were poured into glass cups; then single metal plate samples coated with the paint coat for the tank interior and a metal plate sample coated with the paint coating for the tank exterior were introduced into them. At the beginning of testing the entire metal plates were wetted with the test liquid; during testing the bottom part of the metal plate was permanently dipped into the liquid, whilst the top part was above the surface level, as shown in *Figure 4*.

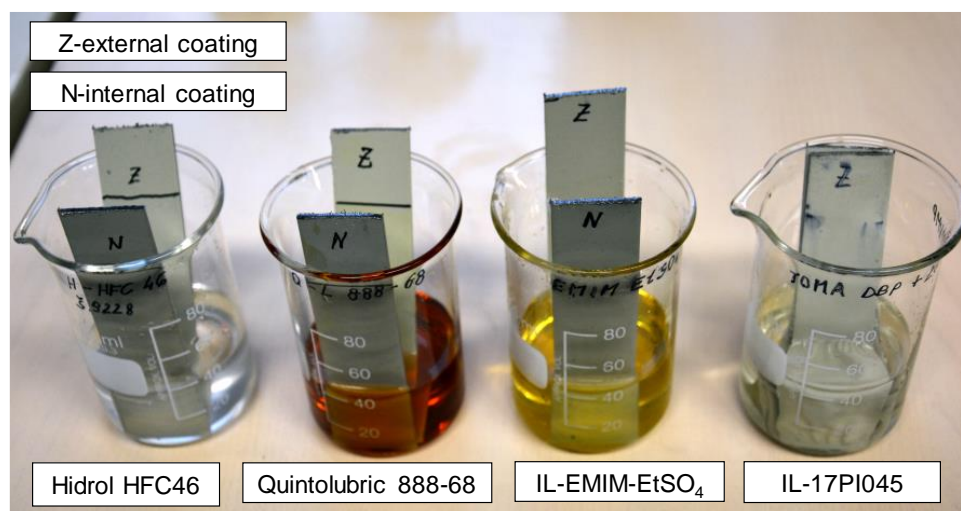


*Figure 4* Test of compatibility with protection paint

Already after a few days of testing, it was proved that the ionic liquid IL-17PI045 was incompatible either with the paint coat for the tank's interior or with the coat for the tank's exterior. The paint coat wrinkled and peeled off on the part of the metal plate permanently dipped in the test liquid.

On the other three tested liquids, after more than 7 months of testing, no changes in the condition of the painted metal plate occurred either on the permanently dipped part of the metal plate or on the wetted part above the surface level. The ionic liquid IL-EMIM-EtSO<sub>4</sub> and the two fire resistant hydraulic liquids Hidrol HFC 46 and Quintolubric 888-68 are, consequently, compatible with the usual paint coats of the tank's metal plates.



## CONCLUSIONS

Despite the excellent individual properties, it is very difficult to find an ionic liquid that would combine the majority of good characteristics, required for use within a modern hydraulic system. In the presented paper the research results were focused only on two properties – lubricating properties tested using a standard testing method, and testing the compatibility of ionic liquid with paint coat, using a non-conventional, practically testing method.

So, some ionic liquids proved to have excellent lubricating properties at high pressures but their properties at lower loadings were worse. By measuring the welding point and the wear diameter on a four-ball apparatus, it was discovered that e.g. the liquids IL-17PI045 and EMIM-EtSO<sub>4</sub> had better lubricating properties than the mineral hydraulic oil. For the use within hydraulic system other, additional test regarding friction further research and test need to be carried out (e.g. determination of the friction coefficient - Stribeck's curve) to have complete information regarding the lubricating properties. On the other side, the non-standardized, practically tests are necessary, to get the answer regarding the compatibility with different material used within hydraulic system.

Before using a new type of hydraulic fluid, we need to obtain all the necessary information on important fluid properties. To this end, we have to carry out a very extensive and relatively expensive selection process.

## REFERENCES

- [1] Kalb, R.: *Ionic liquids – A new generation of high-tech engineering liquids*. Proceedings of international conference Fluid Power 2015, 17.-18. September 2015, Maribor, Slovenia: 49-77., 2015.
- [2] Feng, Z., Yongmin, L., Weimin, L.: *Ionic liquid lubricants: designed chemistry for engineering applications*, Chemical Society Reviews (2009), vol. 9, no. 38, 2590-2599., 2009.
- [3] Kambic, M., Kalb, R., Tasner, T., Lovrec, D.: *High bulk modulus of ionic liquid and effects on performance of hydraulic system*, The Scientific World Journal, 1-10, doi: 10.1155/2014/504762., 2014.
- [4] Kambic, M., Kalb, R., Lovrec, D.: *Lubrication properties of ionic liquids suitable for use within hydraulic systems*. Proceedings of International Conference Fluid Power 2015, 79-93, 2015.
- [5] Kambic, M., Lovrec, D.: *Problems of testing new hydraulic fluids*. Fluid Power 2017, Conference proceedings, <https://dk.um.si/IzpisGradiva.php?id=68230>, University of Maribor Press. Maribor, 281-293., 2017.
- [6] Lovrec, D., Tic, V.: *Energy saving novel lubricants*. 10<sup>th</sup> international conference on sustainable and environmental protection: materials, conference proceedings, University of Maribor Press. 2017, 119-129, doi: <https://doi.org/10.18690/978-961-286-056-1>, 2017.



## CORROSION PROTECTION PROPERTIES OF IONIC LIQUIDS

*LOVREC Darko PhD*

*University of Maribor, Slovenia*

*E-mail: [darko.lovrec@um.si](mailto:darko.lovrec@um.si)*

### **Abstract**

*As ionic liquids are salts, it would be expected that the corrosion protection capacity would be one of the parameters, the most difficult to approach regarding the properties of the conventional hydraulic liquids, particularly the mineral-based oils. That was confirmed in by the laboratory test, particularly during the corrosion test in the humid chamber, where most tested ionic liquids proved to be considerably worse than the mineral hydraulic oil. This test is more rarely used for the testing of hydraulic liquid but is very useful for quick estimates, as because of tightened-up conditions the time until occurrence of corrosion is distinctively shortened. Besides, the corrosion protection capacity was determined by the standard method of determining corrosiveness to copper and the internal method of determining corrosion in the open air.*

**Keywords:** *ionic liquids, hydraulic fluid, corrosion protection, test procedures, humid chamber.*

### **1. INTRODUCTION**

The corrosion resistances of unprotected metals or those protected by metallic or non-metallic coatings is very important property of any hydraulic fluid. The corrosion test in a humid chamber, according to standard DIN EN ISO 6270-2 is a very rigorous test. This test is more rarely used for the testing of hydraulic fluid but is very useful for quick estimates, as because of tightened-up conditions the time until occurrence of corrosion is distinctively shortened. The tests in corrosion chambers are very suitable for comparing materials with known corrosion resistance and those in the course of testing. The measurements were performed at constant atmosphere up to the appearances of the first signs of corrosion and sometimes after that in order to gain additional information. It can be seen that some of ILs are real stimulator of rust.

Besides, the corrosion protection ability was determined by the standard method of determining corrosiveness to copper and the internal method of determining corrosion in the open air.

### **2. METHODS**

The aim of the test in the humid chamber is to inspect the corrosion resistances of unprotected metals or those protected by metallic or non-metallic coatings within the atmosphere of wet water vapour. The humid chamber is a closed container the bottom of which is covered with heated distilled water. In that way, the relative humidity in the chamber is always 100 %. The tests are often performed with interruptions. *Table 1* shows the individual testing circumstances as defined by that standard.

For the tests in the humid chamber the following apparatus and accessories are used:

- humid chamber HK 400,
- sheet metal plate – plate material: ST 1405 (according to DIN 1623, part 1), with thickness 0.7 to 0.8 mm, Ra = 0.6 to 1.9  $\mu\text{m}$ , and size 150 mm x 210 mm,
- emery paper, grain size 120,



- distilled water,
- acetone,
- ethanol.

Table 1 Atmospheric types in corrosion tests in a humid chamber

Test atmosphere	Code	Cycle duration (h)	Test period(s)	Air temperature (°C)	Relative humidity (%)
Constant	K	-	-	40 ±3	100
Alternating condensation atmosphere	A1	24	8 h (including warm-up)	40 ±3	100
			16 h (including cooling down, chamber open)	18 to 28	<100
	A2	24	8 h (including warm-up)	40 ±3	100
			16 h (including cooling down, chamber closed)	18 to 28	100

The humid chamber must be placed in a space without aggressive atmosphere, with room temperature and relative air humidity of not more than 75 %. It must be so positioned that it is protected against air draught and direct sun rays. The humid chamber bottom has to be filled with distilled water up to 10 mm to 12 mm level. The water level must be checked each time prior to heating. The test plates have to be placed within the test space at the same level. If the samples are to be placed one above another, they must be so arranged that the condensed water from the upper samples and horizontal supports does not fall onto the lower ones. The samples (sheet metal plates) must be so placed in the test space that:

- the sample distance from the device wall is at least 100 mm,
- the distance between the sample bottom edge and the water level is 400 mm to 450 mm,
- spacing between samples is at least 20 mm.

Simultaneously, only those samples not affecting each other in any way may be tested. Before application of the protective agent to sheet metal plate the latter should be cleaned to metallic lustre by emery paper and degreased first by acetone and then still with ethanol. The polished, degreased and dry sheet metal plate should be thinly coated, using a clean soft paint brush, with protective agent having to completely cover the cleaned surface, and then introduced into the humid chamber. When the samples have been introduced into the testing space and the humid chamber door closed, heating has to be activated. The required temperature of 40 °C ±3 °C must be reached within 90 minutes, condensed water having to form on the samples.

During the test in constant atmosphere (K), the constant temperature (40 °C ±3 °C) must be maintained throughout the testing. Testing has to be effected in so many cycles that the first visible signs of corrosion – brown stains (1 cycle=24 h) appear. When testing in an alternating condensation atmosphere (A1), heating must be interrupted after 8 hours, reckoning from the heating activation, the humid chamber door opened and left open for 16 hours. In this way, the first cycle is at an end. Then, the distilled water level has to be checked, water added if necessary, and the device closed. The new cycle starts by the activation of heating. Testing should continue over so many cycles that the first signs of corrosion (1 cycle=24 h) appear. When testing in an alternating



condensation atmosphere (A2), heating must be interrupted after 8 hours, reckoning from the heating activation, while the testing device should remain closed for 16 h. In that way, condensed water remains on the samples throughout testing. In that way, the first cycle is finished. The distilled water level in the chamber has to be checked, water added if necessary, and heating activated. A new cycle then begins. Testing continues over as many cycles until the first visible signs of corrosion appear (1 cycle=24 h). In all three cases, the changes in the sheet metal surface should be observed.

The report on the test results should contain descriptions of the test samples and possible previous treatments, testing circumstances (atmosphere K, A1 or A2), and a number of cycles or testing duration.

Determination of corrosiveness to copper (Cu) is performed according the standard ASTM D130. The polished copper plate has to be dipped into the sample at a prescribed temperature and time. Corrosiveness is expressed by values 1 to 4 obtained by comparing corroded copper plate with freshly polished standard plate by assessing the appearance of the test plate as shown in *Figure 2* (ASTM Copper Strip Corrosion Standards).

The copper plate has to be polished first with coarse and then with fine emery paper. The polished plate has to be cleaned with absorbent cotton. The sample has to be poured into the test tube and the freshly polished and cleaned copper plate dipped into it. The test tube has to be placed into the bath at the specified temperature 50 °C or 100 °C and specified time of heating (usually for 3h). After three hours, heating must be stopped, the plate taken out of the test tube and corrosiveness assessed with the standard copper plates (etalons), as shown in *Figure 2*.

The results are given as the corrosiveness to Cu with the designation of the corrosion degree determined from the table or by comparison with the etalon, by stating the temperature and duration of the test. For example: If the sample was tested at 100 °C, heated for 3 hours, and the corrosion determined is 4c, the result can be written as follows: Corrosiveness to copper (3h / 100 °C): 4c.

Corrosion in the open air was tested using a non-standardised, practical test. Identical steel plates and material were used, as for the determination of corrosion in the humid chamber. The plate preparation was also the same. Then, the plate was coated with the ionic liquid sample and in the continuation of the test possible changes of the surface appearance were observed at room conditions.

### 3. RESULTS

The corrosion protection capacity in a humid chamber was determined by the method described in chapter 2. The measurements were performed at constant atmosphere up to the appearances of the first signs of corrosion and sometimes also after that in order to gain additional information.

More than 25 different samples of ionic liquids were tested. *Table* shows only a part of comparisons between times up to the occurrences of corrosion of only some of them, comparably with mineral hydraulic oil Hydrolubric VG 46 and fire-resistant hydraulic liquid Quintolubric 888-68 (HF DU type). Good properties of the tested samples are marked in green and the bad ones in red. It can be seen that corrosion protection in most cases did not amount to even 1 cycle (24 hours). In that case, the times in minutes or hours up to the occurrences of the first signs of corrosion are stated in parentheses. In most cases, the corrosion protection in comparison with the mineral hydraulic oil was worse, particularly in comparison with the fire-resistant liquid, where the corrosion protection capacity was exceptional and amounted to 7 cycles, which was already comparable with the purpose agents for corrosion protection. In rare cases, the corrosion protection capacity was comparable or even superior to that of the mineral hydraulic oil, as can be seen for the last three samples in the table. According to the viscosity suitable for use in most hydraulic systems, the last



two samples in particular are interesting. *Figure 1* shows the sample comparably with the sample of the mineral hydraulic oil Hydrolubric VG46 after 24 hours (1 cycle) since the beginning of the test.

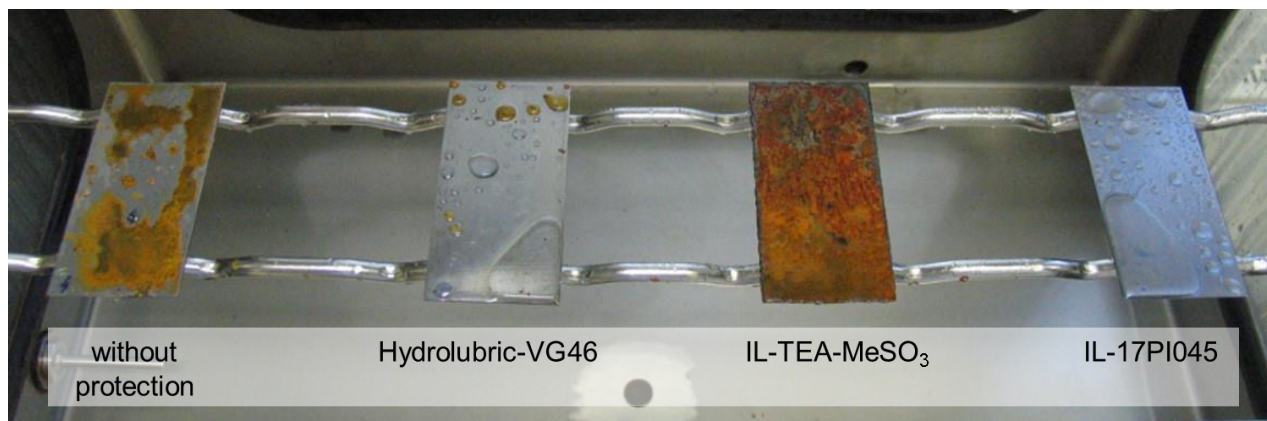


*Figure 1* Test in humid chamber after 24 h

*Table 2* Corrosion protection capacity of different IL

Sample	cyclus=24 h
Hydrolubric VG46	0 (3h)
Quintolubric 888-68	7 h
IL-EMIM-EtSO <sub>4</sub>	0 (15 min)
IL-EMIM-TFSI	0 (1.5 h)
IL-10PI 453-1	0 (5 h)
IL-10PI 453-2	0 (1 h)
IL-10PI 453-4	0 (30 min)
IL-10PI 453-5	0 (45 min)
IL-16PI062-2	0 (4 h)
IL-16PI062-1	0 (5 min)
IL-17PI064	1
IL-18PI163	0 (3.5 h)
IL-17PI045	0-1 (>7.5 h)

The data in *Table table2* shows that the corrosion protection capacity with sample IL-17PI045 did not deteriorate. That is also confirmed by *Figure 1*, showing the condition of that sample in comparison with some other samples, amongst them also with mineral hydraulic oil after 24 h since the test start. At that time, the first signs of corrosion were already also present on the metal plate protected by sample IL-17PI045. In the next days of testing in the humid chamber, the condition of the ionic liquid IL-17PI045 sample also did not importantly deteriorate and that this time the ionic liquid sample also proved to be better than the mineral oil.

The test of corrosiveness to copper was also carried out because of the presence of non-ferrous metals based on copper in the hydraulic components. The test was carried out according to standard ASTM D 130 in accordance with the procedure described in point 0, where the two ionic liquid samples IL-17PI045 and EMIM-EtSO<sub>4</sub> were heated for 3 hours at 100 °C. The procedure and the results are shown in *Figure 2*.



Figure 2 Performing the corrosiveness test to copper (left) and determination of corrosiveness to copper for IL-17PI045 (right)

After completion of heating the appearance of the copper strip was compared with the etalon as shown in *Figure 2 (right)*. There were no visible changes, meaning that the result of that test is 1a. Consequently, both ionic liquids are compatible with materials containing copper.

Results regarding the corrosion test in open air under normal humidity conditions show, that in case of mineral hydraulic oil the corrosion did not appear even after a long time period (>60 days), whilst in the cases of some ionic liquids it had already appeared after 20 to 30 minutes. In the case of ionic liquid EMIM-EtSO<sub>4</sub> the corrosion already occurred also after 3 days – *Figure 3*.



Figure 3 Test of corrosion in the open air for EMIM-EtSO<sub>4</sub> after 4 days

Corrosion in the open air:

- mineral hydraulic oil: >60 days,
- some IL: 20 to 30 min,
- IL-EMIM-EtSO<sub>4</sub>: 2 to 3 days,
- IL-17PI045; > 4 months

In the case when the metal plate, after coating with ionic liquid IL-17PI045, was left in the open air at room temperature, corrosion did not appear even after 3 months. Therefore, testing that liquid in the open air was interrupted after 4 months.



## CONCLUSIONS

Within the framework of this research, most of work was devoted to finding such an ionic liquid that would offer sufficient corrosion protection in hydraulic systems even in the presence of moisture and would comply with all other properties that hydraulic liquids must satisfy. Corrosion protection was extensively tested in a humid chamber; in addition, the tests of corrosiveness to copper and corrosion in the open air were performed. It has been found that most ionic liquids do not ensure proper protection against corrosion, particularly in the presence of moisture/water.

The humid chamber corrosion test is a very rigorous test. In practice, the hydraulic components parts were after machining protected by a purpose anticorrosion agent. Therefore, directly impact of ionic liquid on metal surface is not featured in the same extend as in case of humid chamber test and unprotected metal surface. According to the results of the compatibility test, corrosion problems should not to be expected in the practical use of ionic liquids in the hydraulic system, unless water is present in the system.

## REFERENCES

- [1] Freemantle, M.: *An introduction to ionic liquids*. Cambridge: The Royal Society of Chemistry, Thomas Graham House, Science Park, Milton Road, 2010.
- [2] Predel, T., Schlücker, E., Wasserscheid, P., Gerhard, D., Arlt, W.: *Ionic liquids as operating fluids in high pressure applications*. Chem. Eng. Technol., vol 30, no. 11, 1475-1480, 2007.
- [3] Uerdingen M., Treber, C., Balsler, M., Schmitt, G., Werner, Ch.: *Corrosion behaviour of ionic liquids*. Green Chemistry, vol. 5, no. 7, 321-325, 2005.
- [4] Yu, Bo, Bansal, D. B., Qu Jun: *Oil miscible and non-corrosive phosphonium-based ionic liquids as candidate lubricant additives*. Wear, vol. 289, 58-64, 2012.
- [5] Li, D., Cai, M., Feng, D., Zhou, F., Liu, W.: *Excellent lubrication performance and superior corrosion resistance of vinyl functionalized ionic liquid lubricants at elevated temperature*. Tribology International, vol. 44, no. 10, 1111-1117, 2011.
- [6] Kambic, M., Kalb, R., Lovrec, D.: *Lubrication properties of ionic liquids suitable for use within hydraulic systems*. Proceedings of International Conference Fluid Power 2015, Congress centre Habakuk, Maribor, Slovenia. Maribor: Faculty of Mechanical Engineering, 79-93, 2015.
- [7] Kambic, M., Kalb, R.: *Corrosion and lubrication properties of some ionic liquids*. Ventil : revija za fluidno tehniko in avtomatizacijo, ISSN 1318-7279, Oct. 2013, vol. 19, no. 5, 364-368, 2013.
- [8] Lovrec, D.: *Possible use of ionic liquids as a technical fluid*. V *IN-TECH 2011: proceedings*, International Conference on Innovative Technologies, Bratislava, Slovakia, 100-103, 2011.
- [9] Kambic, M., Kalb, R.: *Comparison of ionic liquids with conventional mineral oils*. Proceedings of International Conference Fluid Power 2013, 19th-20th September 2013, Congress centre Habakuk, Maribor, Slovenia. Maribor: Fakulteta za strojništvo, 61-70, 2013.



## RESEARCH OF CARBON FIBRE HYDRAULIC CYLINDER

*MAJDIČ Franc PhD*

*Faculty of Mechanical Engineering, University of Ljubljana*  
*E-mail: [franc.majdic@fs.uni-lj.si](mailto:franc.majdic@fs.uni-lj.si)*

### **Abstract**

*Paper presents the information about possibility of using tap water without any additives as a hydraulic liquid instead of the nowadays widely used mineral hydraulic oil. Hereinafter we present the most important basic properties of tap water, its impact on the environment, the current use of water hydraulics and state of the art. After that follows a presentation and a description of the carbon fibre water hydraulic cylinder, test rigs, procedures of the tests, main parameters of the tests and results of hydraulic and tribological investigations. The carbon fibre tube was able to withstand a burst test up to a pressure of 62 MPa. Composite hydraulic cylinder was after 100 km of total stroke of rod under load in oil without damage. In water only 42 km of total rod stroke was done, because a major damage of the sliding surface and consequently a damage of piston seal occurred. Results of basic tribological tests with five different seals type and three different sliding surface is presented on the end. The lowest coefficient of friction (0,12) was observed with Polytetrafluoroethylene with bronze in contact with clear epoxy gel without nanoparticles.*

**Keywords:** *hydraulic, water, hydraulic cylinder, carbon fibre, tests*

### **1. INTRODUCTION**

Despite being environmentally friendly, water hydraulic systems are not involved in many applications. When we talk about water hydraulics, we are referring to the use of tap water without any additives for the hydraulic fluid instead of conventional hydraulic fluids that can harm the environment.

Interestingly, it was water that was the first fluid used in industrial power-control hydraulics, more than two hundred years ago [1]. However, in the early years of water hydraulics there were many problems associated with both durability and functionality.

During the 19th Century, after the oil industry began to develop [2, 3], there was no further use of water hydraulics. Oil-based hydraulic machines worked better and for longer time than the equivalent water hydraulic machines. The reasons for the replacement of water hydraulics were linked to the low volumetric and mechanical hydraulic efficiencies, corrosion and high wear for the materials known at that time.

However, mineral hydraulic oil is not the best solution. The main problem is related to polluting the natural environment and in particular to the spoiling of drinking water. One so-called "soft" solution is to use a bio-degradable hydraulic oil [4, 5], but the problem is with the additives, which tend not to be totally degradable. For this reason, in the early 1990s, many countries [2, 6 and 8] began with research into the possibilities of using tap water as a hydraulic fluid.

On this place it is convenient also to mention the use of pneumatics instead of mineral oil hydraulics when we need only lower working forces [7]. For such cases it is especially environmentally suitable when we use bio-oil as lubricant or particularly when we use unlubricated compressed air, for which the components are already some decades available on the market for the field of industrial pneumatics.



The current situation on the market is that the available water hydraulic components are not persuading customers that they can replace oil-based systems and so lead to a significant increase in use [6].

Using water instead of mineral oil as the pressure medium entails significant changes in the physical parameters [9]. Compared to mineral oil water differs, in the following physical parameters which are important for PCH: about 30- times lower viscosity (at 20°C) and thus poorer lubrication, a more than 12 million-times higher vapour pressure (at 50°C), and 33 to 60 % higher bulk modulus (at 20°C). Water also provokes corrosion of parts that are not corrosion resistant.

In the paper, prototype of the hydraulic cylinder with carbon fibre tube is presented. Pressure burst test of carbon fibre cylinder tube have been done. Two lifetime test of composite cylinder, the first in mineral hydraulic oil and the second in water have been done. Due to the premature failure of the composite cylinder tube in the water, numerous tribological tests of tubes with different coatings and different seal materials were carried out.

## 2. METHODS

Lightweight carbon fibre tube of hydraulic cylinder (Figure 1, pos. 4) in contact with the piston rod seal and guiding rings (Fig. 1, pos. 5) are the main parts of the observed specimen.

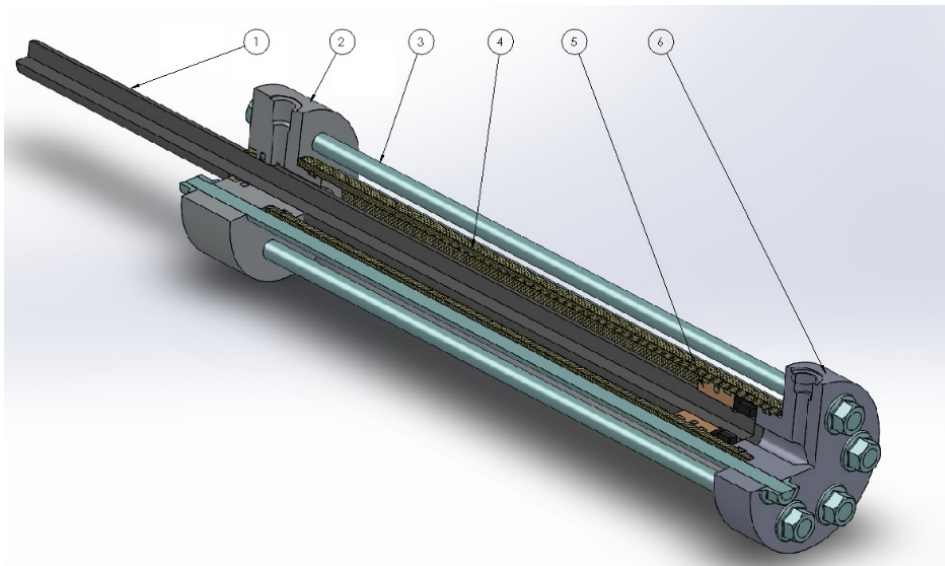


*Figure 1* Tested carbon fibre water hydraulic cylinder ( $\text{\O}40$  mm /22 mm x 305 mm); 1 – the piston rod, 2-the cylinder head, 3-the holding screw, 4-the carbon fibre cylinder tube, 5-the cylinder piston, 6-the bottom of the cylinder.

A lot of hydraulic tests with carbon fibre cylinder have been done. First we made high pressure burst test (Fig. 2) of carbon fibre tube with mineral hydraulic tube. Then we made lifetime test of composite cylinder with mineral hydraulic oil and with tap water [10]. Since we have got short lifetime of carbon fibre and piston seal contact surface in water compared to mineral hydraulic oil, we made tribological investigation on different composite surface layout (resin). Tribological investigation have been done on standardised test rig, Cameron plint TE77 (Fig. 3). Coefficient of friction on five different materials of piston seals (NA300, NI150, PTFE B, PTFE C and PTFE G) in contact with three different composite tube sliding surfaces (clear gelcoat, gelcoat with  $\text{Al}_2\text{O}_3$  and gelcoat with  $\text{SiO}_2$ ) at two normal forces (20 N and 50 N) at the constant sliding velocity of 0,4 m/s have been investigated.



*Figure 2* High pressure burst test of hydraulic cylinder carbon fibre tube with mineral oil in safety chamber.

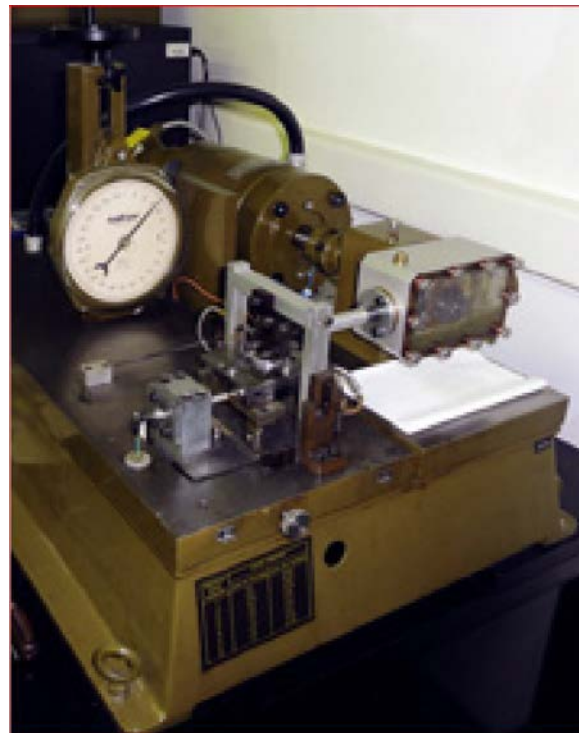


*Figure 3* Test rig Cameron plint TE77 for tribological investigations of different tube resin surfaces and different seal materials in water.

### 3. RESULTS

High pressure burst test with mineral hydraulic oil have been done with 10 MPa stepping increase of pressure. Carbon fibre tube of hydraulic cylinder have bursted at pressure of 63 MPa (Fig. 4). Due to the very high wear on the piston rod seals the measurements could not be performed. It turns out that the wear of the seal on the piston of a specimen moving in a carbon fibre tube [10] is reaching permissible and expected limits, while the wear of the seal on the piston rod is very high and does not satisfy the minimum needs, and exceeded all the expected boundaries.

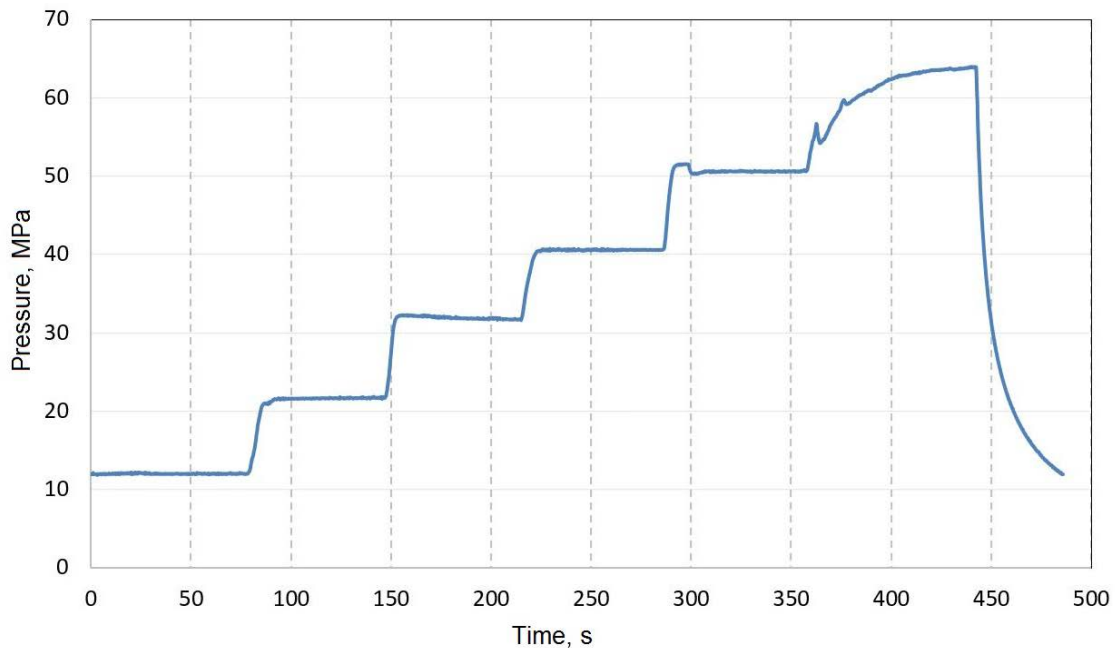


Figure 4 Increasing the oil pressure in the burst test of carbon fibre tube.

Figure 5 shows external leakage (oil drop) of carbon fibre cylinder tube during the successfully completed oil hydraulic duration test due to porous composite structure.

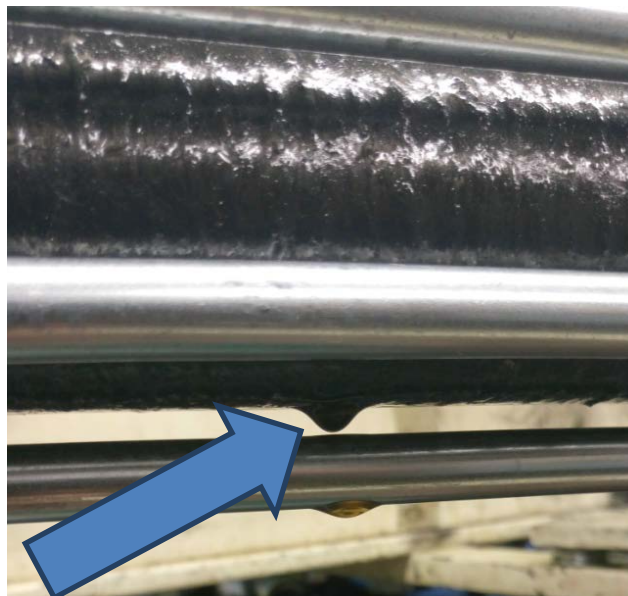


Figure 5 External leakage of carbon fibre tube during lifetime oil hydraulic test.

Figure 6 shows results of measurement of coefficient of friction for five different sealing material on the inner composite tube surface coated with epoxy gel including  $\text{Al}_2\text{O}_3$  nanoparticles at 20 N of normal load. The worst material pair was NA300 (Polyurethane) with maximum friction coefficient 0,85 at start and time stable coefficient 0,37. The lowest constant coefficient of friction, 0,2 was observed with material PTFE G.

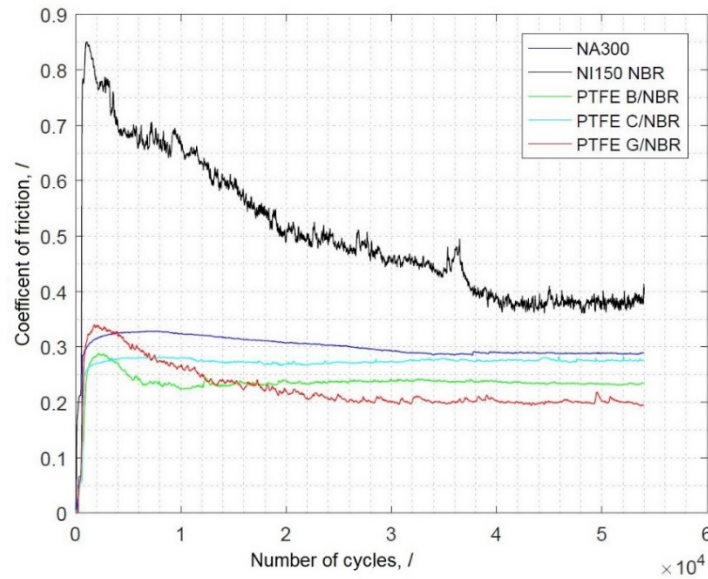


Figure 6 Measured coefficient of friction between five different sealing materials on composite surface coated with gel included  $\text{Al}_2\text{O}_3$  nanoparticles at 20 N of normal load and velocity 0,4 m/s.

Figure 7 shows results of measured coefficient of friction for five different sealing materials on three different sliding surfaces of composite tube. The highest coefficient (0,51) was observed at NI150 seal (nitrile rubber) in combination with gelcoat without additional nanoparticles. The lowest coefficient of friction (0,12) was observed also at gelcoat surface without nanoparticles in combination with PTFE B seal (Polytetrafluoroethylene with bronze).

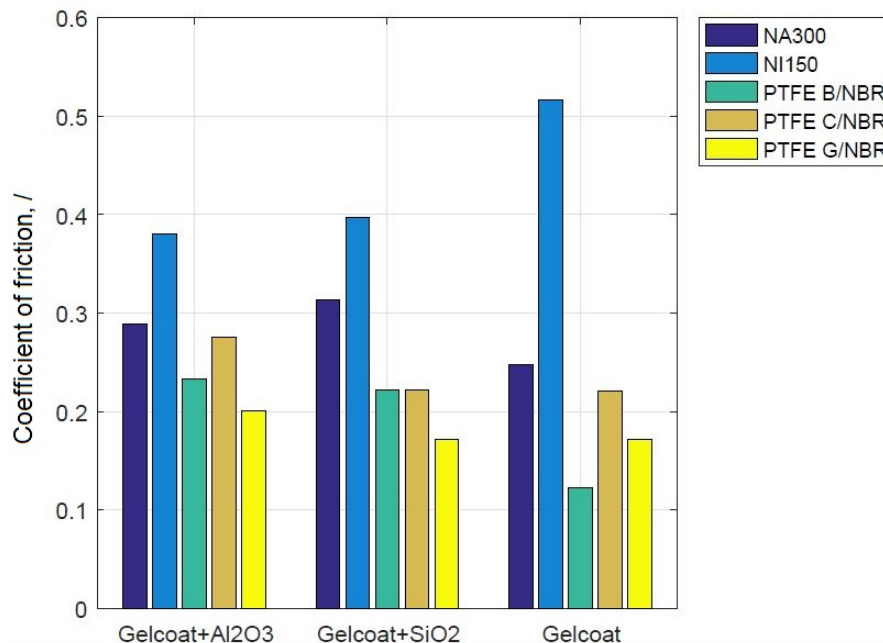


Figure 7 Measured coefficient of friction between five different sealing materials on three different composite surfaces at 20 N of normal load and velocity 0,4 m/s.

Figure 8 shows transpose film formed on the worst (with seal NI150 - left) and the best (with seal PTFE B - right) material pair. In both cases were epoxy gelcoat without additional nanoparticles. Seal NI150 is very soft, so it left some material on the surface of tube gelcoat. Mentioned deposition of soft seal material (nitrile rubber) cause accelerated wear.

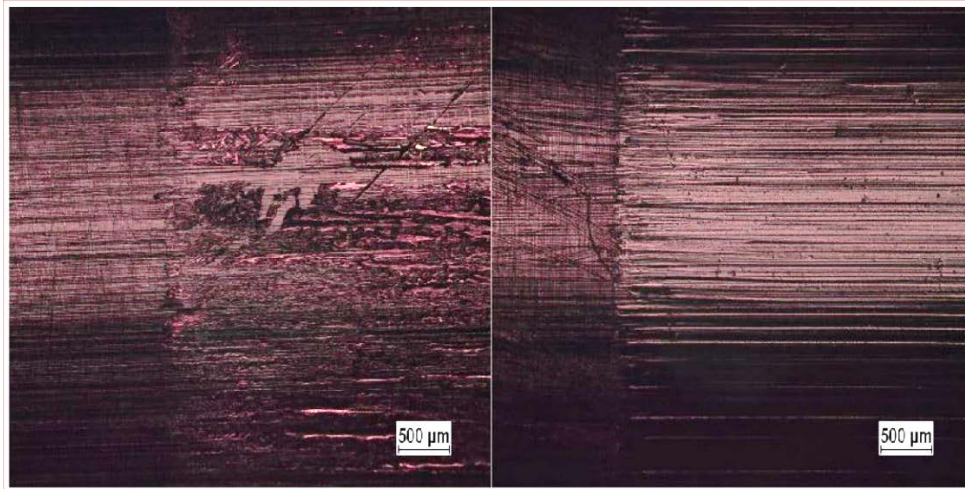


Figure 8 Transpose film formed on the epoxy gelcoat of the tube in contact with seal NI150 (left) and with seal PTFE B (right) at normal force of 20 N

## CONCLUSIONS

High pressure burst test of carbon fibre tube have been done in oil hydraulics. Burst pressure was 62 MPa. Two long term tests of carbon fibre cylinder have been done in oil and in water. After 100 km of total cylinder rod stroke in oil there was no significant change of internal leakage. Composite cylinder in water lasted only 42 km of total stroke due to increased damage to the sliding surface inside of tube and consequent damage to the piston seal. Tribological investigations of three different surfaces in pair with five different piston rod seals have been done due too short lifetime of the composite tube in water. The most promised piston seal materials are PTFE B, PTFEG and also PTFE C. About better sliding surface inside of composite tube is just in the way of coefficient of friction hard to decide. Long term wear basic tribological test of mentioned material pair are needed. Next step will be to prepare new prototype of composite hydraulic cylinder with correct sliding surface material and correct sealing material.

## REFERENCES

- [1] Bramah, J.: *The Hydraulic Press*. U K Patent No. 2045, 1795.
- [2] Trostmann, E.: *Water Hydraulics Control Technology*. Lyngby, , Technical University of Denmark, 1996.
- [3] Murrenhoff, H.: *Grundlagen der Fluidtechnik Teil 1, Hydraulik*. 5th ed., IFAS, Aachen, 2007.
- [4] Kalin, M., Majdič, F., Vižintin, J., Pezdinik, J., Velkavrh, I.: *Analyses of the Long-Term Performance And Tribological Behaviour of an Axial Piston Pump Using Dimond-like-Carbon-Coated piston Shoes and Biodegradable Oil*. Journal of Tribology, vol. 130, 2008.
- [5] Kalin, M., Majdič, F., Vižintin, J., Pezdinik, J.: *Performance of axial piston pump using DLC-coated piston shoes and biodegradable oil*. The 12th Nordic Symposium on Tribology, Helsingor, Denmark, 2006.
- [6] Koskinen, K., Leino, T., Riipinen, H.: *Sustainable development with water hydraulics – possibilities and challenges*. Proceedings of the 7th JFPS Interantional Symposium in Fluid Power, Toyama, Japan, Vol. 1, pp. 11 – 18, 2008.
- [7] Šitum, Ž.: *Applying Different Controller Structures for Position Control of Pneumatic Servo System*. Strojarstvo 48, 5–6, 261–271, 2006.



# INTERNATIONAL SCIENTIFIC CONFERENCE ON ADVANCES IN MECHANICAL ENGINEERING

12-14 October 2017, Debrecen, Hungary



- 
- [8] Kitagawa, A.: *Co-operation between Universityes and Water Hydraulic Companies in Japan*. The Sixth Scandinavian International Conference on Fluid Power, Tampere, Finland, 1999.
- [9] Trostmann, E., Frolund, B., Elesen, B. H., Hilbrecht, B.: *Tap Water As A Hydraulic Pressure Medium*. Marcel Dekker, New York, 2001.
- [10] Majdič, F.: *Duration test of carbon fibre hydraulic cylinder: water&oil*. International scientific conference on advances in mechanical engineering, Debrecen, Hungary, 2017.



## DURATION TEST OF CARBON FIBRE HYDRAULIC CYLINDER: WATER&OIL

*MAJDIČ Franc PhD*

*Faculty of Mechanical Engineering, University of Ljubljana*

*E-mail: [franc.majdic@fs.uni-lj.si](mailto:franc.majdic@fs.uni-lj.si)*

### **Abstract**

*Power control hydraulics is very common in industry and other fields. Lower weight of hydraulics, especially for mobile systems, and protection of the natural environment are two trends that are becoming more and more popular. Presented work shows results of investigation on lightweight carbon fibre tube of hydraulic cylinder. Two long term tests were done, first with mineral hydraulic oil and second with tap water. Hydraulic cylinder and circuit for long term tests rig are presented. Results of long term oil hydraulic test show that there are no visible increase of internal leakage after 100 km of total stroke of cylinder rod under load. Rod of carbon fibre cylinder stop to move after 42 km in water hydraulic test. It is obvious, that tribological circumstances in contact of piston seals and carbon fibre tube, lubricated with water are not suitable for long term use.*

**Keywords:** *Hydraulic, water, oil, carbon fibre, cylinder*

### **1. INTRODUCTION**

Power control hydraulics is an important way of science that is present in many branches of industry, such as in the automotive, aerospace, construction, forestry, food processing, agriculture, etc [1]. Hydraulic cylinders are the most used actuators. The lower weight of the hydraulic components is becoming increasingly important, especially in mobile hydraulic machines. New, lightweight materials such as composites can replace traditionally used steel. Lower weight of mobile hydraulic machines means less fuel consumption and consequently less CO<sub>2</sub>. This was the reason for researches on composite hydraulic cylinders. Environmental trends also warn us about the danger of polluting nature with harmful hydraulic liquids [2-4]. Water hydraulics is one of the alternative for such pollution [5]. Presented results of investigation of composite carbon fibre hydraulic cylinder tube was compared in water and oil.

### **2. METHODS**

The goal of the presented work was to investigate duration time of carbon fibre tube of hydraulic cylinder (Figure 2) in mineral hydraulic oil and in water. Figure 1 shows hydraulic circuit of test rig for duration test of water hydraulic cylinder. Hydraulic test rig in Laboratory for fluid power and controls is shown in Figure 3. Investigated composite hydraulic cylinder  $\Phi 40/22 \times 305$  (pos. 8) is in both cases (oil and water hydraulic duration test) loaded with standard oil hydraulic cylinder  $\Phi 50/25 \times 400$  through two pressure relief valves (pos. 27 and 29) and two check valves (pos. 28 and 30). Tested cylinder is driven by, in the first case by oil and in the second case by water hydraulic pump (pos. 2). Oil and water hydraulic test rig for driving the tested cylinder are very similar, each is made by standard – on market accessible hydraulic components.





Figure 3 Hydraulic test rig with observed carbon cylinder in the front.

### 3. RESULTS

Two long term test of carbon fibre cylinder was done, first with oil and second with tap water. Figure 4 shows results of measured internal leakage during test. Maximum oil leakage 2,3 ml/min was observed at cylinder rod outside of tube at 100 km of total stroke. Leakage increasing of oil hydraulic composite cylinder was after 100 km of total stroke very low, there was no obvious sliding surface damage on piston seal or inside tube sliding surface observed.

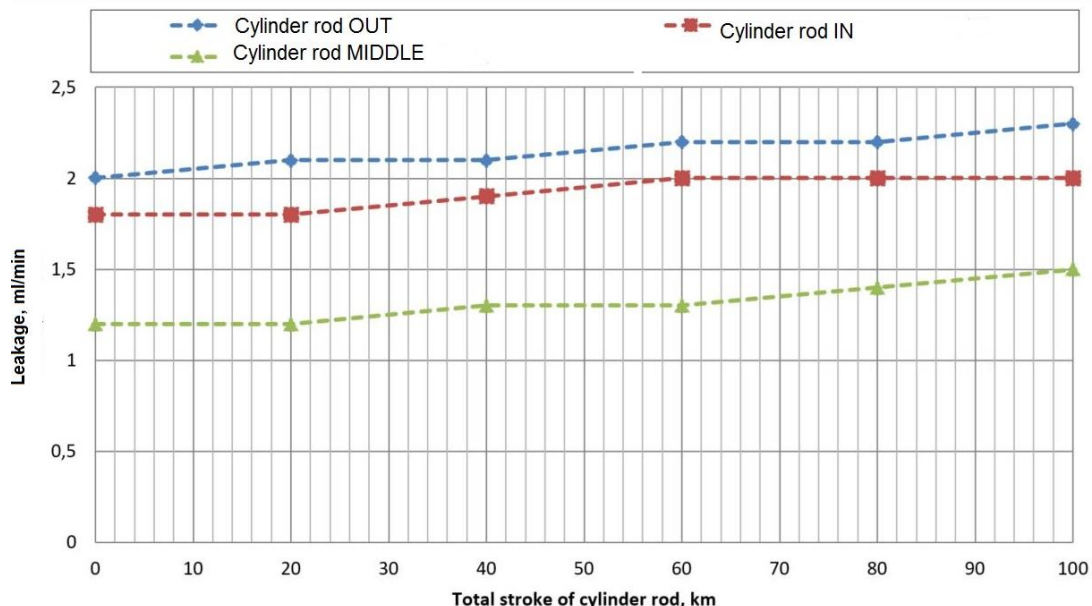


Figure 4 Results of duration test of carbon fibre cylinder in oil hydraulics.

Duration test of carbon fibre cylinder in water was prematurely stopped at 42 km due to the significant worn sliding surface of carbon fibre tube and piston seals (Fig. 5, 6 and 7). It is obvious that water as a hydraulic pressure medium requires different material pairs and better quality of contact surfaces as requires mineral hydraulic oil.

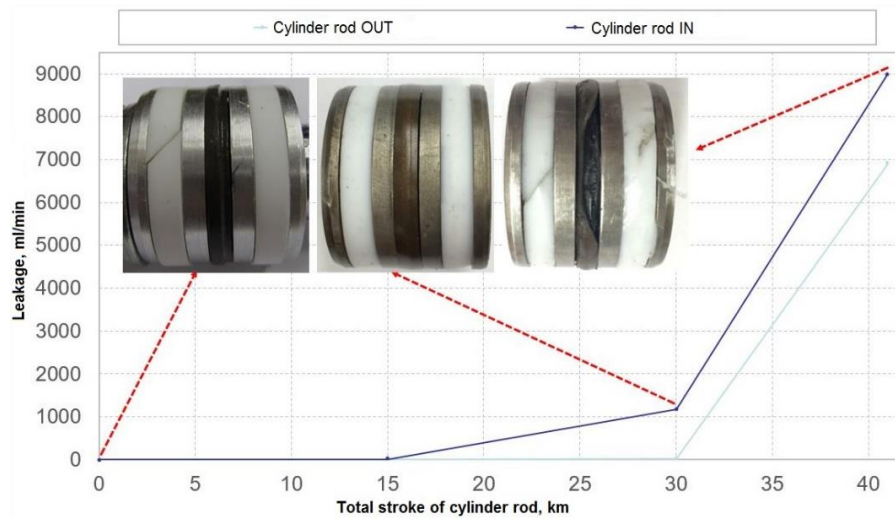


Figure 5 Results of duration test of carbon fibre cylinder in water hydraulics.



Figure 6 Worn carbon fibre inside tube ( $\Phi 40$  mm) sliding surface (left), worn tube particles (right) after duration test in water.

## CONCLUSIONS

A huge difference between water and oil lifetime was observed. Carbon fibre cylinder with oil was after 100 km of total stroke still useful, however water hydraulics cylinder stopped at 42 km due to destroyed tube sliding surface and piston seals.

Carbon fibre cylinder tube has to be improved in terms of construction and tribological sliding surface sustainability. One of our further plan will be tribological researches of different sliding surface contacts of carbon resin and different seals geometry and materials to get better and longer to-use contact of lightweight hydraulic cylinder in water.

## REFERENCES

- [1] Pezdirnik, J., Pikon, J.: *Oil hydraulics in industry*. Ironwork educational centre, Jesenice, 1980.
- [2] Trostmann, T.: *Water Hydraulic Control Technology*. Lyngby, Technical University of Denmark, 1996.
- [3] Majdič, F.: *Water as a hydraulic pressure fluid, doctoral thesis*, Ljubljana, 2010.
- [4] Majdič, F, Pezdirnik, J., Kalin, M.: *Water as a hydraulic pressure fluid in power-control hydraulics – 2. part*. Ventil, 4, 242–249, 2006.
- [5] Trostmann, E.B., Frolund, B., Elesen, B. H., Hilbrecht, B.: *Tap Water As A Hydraulic Pressure Medium*. Marcel Dekker, New York, 2001.



## THERMAL STABILITY OF CARBIDE-FREE BAINITE IN TWO NANOCRYSTALLINE STEELS

MARCINIAK Szymon, SKOLEK Emilia PhD, GOŁASZEWSKI Adam, ŚWIĄTNICKI Wiesław DSc

Faculty of Materials Science and Engineering Warsaw University of Technology

E-mail: [szymon.marciniak@nanostal.eu](mailto:szymon.marciniak@nanostal.eu) , [emilia.skolek@wimpw.edu.pl](mailto:emilia.skolek@wimpw.edu.pl) ,  
[adam.golaszewski@nanostal.eu](mailto:adam.golaszewski@nanostal.eu) , [wieslaw.swiatnicki@wimpw.edu.pl](mailto:wieslaw.swiatnicki@wimpw.edu.pl)

### Abstract

*The aim of the study was to compare the thermal stability of nanocrystalline carbide-free bainite in hot-work X37CrMoV5-1 steel and in 35CrSiMn5-5-4 structural steel in the range of nitriding temperatures. In both steels, the nanocrystalline structure was obtained during isothermal quenching at a temperature lying in bainitic transformation zone. The thermal stability of the studied microstructures was assessed by the use of dilatometric tests and electron microscopy (TEM) observations. The dilatational changes were recorded during continuous heating of the studied steel samples and its isothermal annealing at a temperature that was higher than the temperature of the isothermal quenching.*

*TEM observations were carried out before and after the isothermal annealing for both steels. The dilatometric and TEM investigations accordingly confirmed the higher thermal stability of the nanocrystalline structure in X37CrMoV5-1 steel. Eight-hour annealing of that sample at 400°C caused minimal changes in its microstructure, while in 35CrSiMn5-5-4 steel the content of residual austenite decreased significantly and precipitation of carbides occurred. The investigations allowed to identify the changes occurring in carbide-free bainite with residual austenite when subjected to increased temperature. It was shown, that the thermal stability of nanobainitic microstructure of steel depends on its chemical composition.*

**Keywords:** Heat treatment; Carbide-free bainite; Nanocrystalline structure; Thermal stability

### 1. INTRODUCTION

Carbide-free bainite in which the grain size is less than 100 nm in at least one direction is called nanobainite [1]. The nanobainite is composed of plates of bainitic ferrite separated by thin layers of stable residual austenite. Its distinctive feature is the lack of carbide precipitates. During the bainitic transformation the austenite gets carbon-enriched, which improves the thermal stability of austenite during cooling to room temperature. Bhadeshia and Caballero have shown [2,3], how nanostructured bainite can be formed, during quenching with isothermal annealing at the lower range of temperature of bainitic transformation. A nanobainitic structure can be created in steels of a suitable chemical composition. The crucial factor is sufficient content of carbon (0.6-1.1%) and silicon (1,5-2%), which hinders the cementite precipitation [4,5]. However, obtaining a nanobainitic structure is also possible in steels containing less carbon and silicon [6,7]. Steels with nanobainitic microstructure exhibit a very good balance between ductility and strength, which is better than balance exhibited by steels with conventional bainite or tempered martensite obtained by use of conventional heat treatments. In addition, isothermal quenching provides an increase of fracture toughness, greater resistance to friction wear and a decrease in distortion during quenching. Such features are desirable for production of tools, gears and many other machine parts. However, hardness of nanobainitic steels can be too low for many applications. Nitriding processes, among others, are often used to improve the hardness of steel. In addition, the effective nitriding process



requires a temperature higher than temperature of isothermal quenching at which nanobainite is formed. The question arises, if the nanobainitic microstructure has sufficient thermal stability to perform the nitriding process at elevated temperature. In order to verify such a possibility an investigation of microstructural changes occurring at temperatures of nitriding process were performed. The subject of this paper was to investigate the thermal stability of the nanobainitic microstructure in two steel grades: X37CrMoV5-1 hot-work tool steel and 35CrSiMn5-5-4 structural steel. The influence of chemical composition of steel on thermal stability of nanobainitic microstructure was discussed. The mechanical properties of steels after thermal stability tests were analysed.

## 2. METHODS

The study was performed on the X37CrMoV5-1 and 35CrSiMn5-5-4 steels. Chemical compositions of these steels are given in *Table 1*.

*Table 1* Chemical composition of tested steel

Steel	C	Si	Mn	Cr	Mo	V	Ni
X37CrMoV5-1	0,37	1,01	0,38	4,91	1,2	0,34	0,19
35CrSiMn5-5-4	0,35	1,3	,095	1,31	0,02	0,006	0,14

Samples of X37CrMoV5-1 steel were subjected to a thermal treatment consisting of austenitization at 1030°C followed by quenching down to 300 °C and isothermal annealing at this temperature for 19 hours. Samples of 35CrSiMn5-5-4 steel were subjected to a thermal treatment consisting on austenitization at 900 °C followed by quenching down to 350 °C and isothermal annealing at this temperature for 1,5 hours. All dilatometric studies were conducted with a Bahr DIL805L quenching dilatometer. The steel samples were shaped as 10 mm long rods of 3 mm diameter. Temperature stability tests were conducted during continuous heating at 0.3 °C/min up to 600 °C as well as during isothermal annealing that lasted 8 hours. The heating rate during the isothermal tests was 200 °C/s.

The analysis of a microstructure of the heat treated samples was carried out with the use of a TEM JEOL 1200 EX transmission electron microscope. In order to characterise the properties of steels, static tensile tests were performed with the initial strain rate of 0,001 s<sup>-1</sup> on samples with the diameter of 6 mm on the Zwick/Roell Z250 testing machine with the use of an extensometer.

## 3. RESULTS

At the first step, the dilatometric measurements were performed during continuous heating up to 600°C of both steels with the nanocrystalline structure (*Figure 1*). The grey line obtained for the tool steel is obviously straight, which attests the lack of significant phase transformations. The black line represents the result obtained for the structural steel. In this case a divergence from the straight line begins at above 400°C and ends at 485°C. This indicates a much lower thermal stability of the nanostructure in the structural steel than in the hot work tool steel. The observed transformation is probably due to the carbide precipitation process.

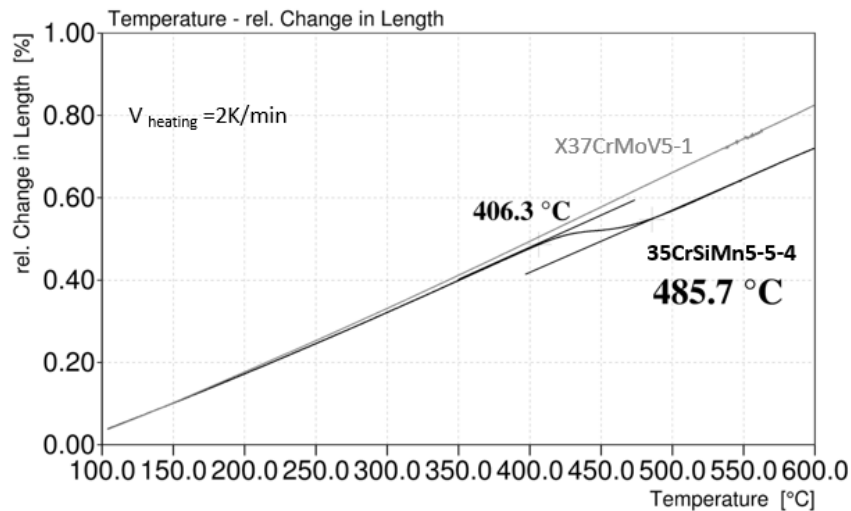


Figure 1 Dilatometric plot presenting transformations that occur during continuous heating

The second dilatometric test consisted of isothermal annealing of the nanostructure at 400 °C, which was a higher temperature than the temperature of the isothermal quenching during the heat treatment, but a lower temperature than the temperature of the transformations that occurred during the continuous heating. A change in length of hot work tool steel specimen represented by the grey line was much smaller than a change in length of the structural steel sample. In that case there was a significant decrease in length of the sample (the black line on Figure 2). That process began almost with the start of the isothermal annealing and lasted for eight hours (which was the duration of the isothermal annealing). However, the rate of that process diminished with the time. It can be concluded that the thermal stability of the nanobainitic microstructure of structural steel is lower than that of the tool steel.

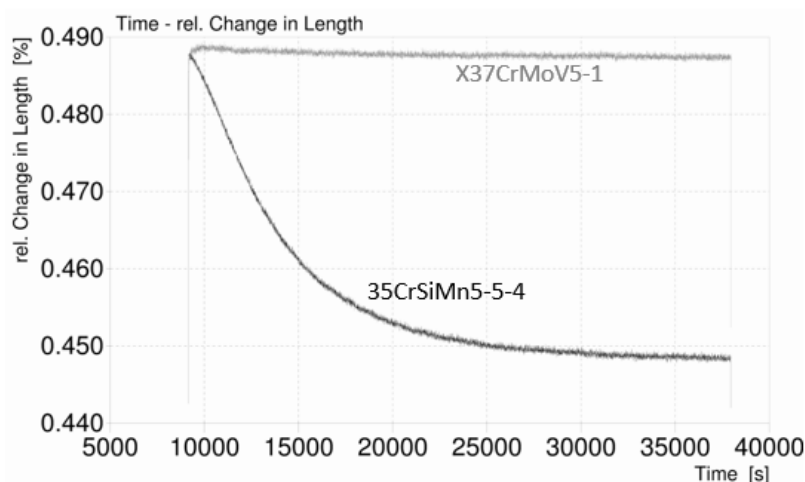
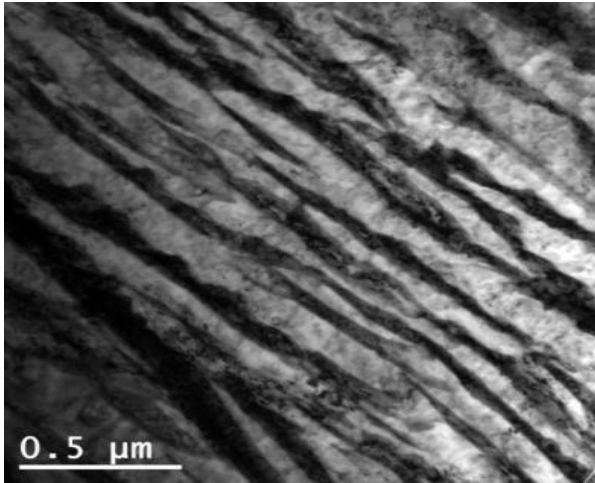


Figure 2 Dilatometric plot presenting a comparison of sample length changes during 8-hour isothermal annealing at 400 °C

In order to explain the results of dilatometric tests a TEM observations were performed on samples subjected to thermal stability tests. The microstructure of the tool steel after dilatometric annealing was similar to the initial nanobainitic microstructure (Figure 3), which continued to exhibit characteristic alternating layers of austenite and ferrite plates. No presence of carbides was noticed.



That confirmed that the nanobainitic microstructure of the hot work tool steel did not undergo any substantial changes during isothermal annealing.



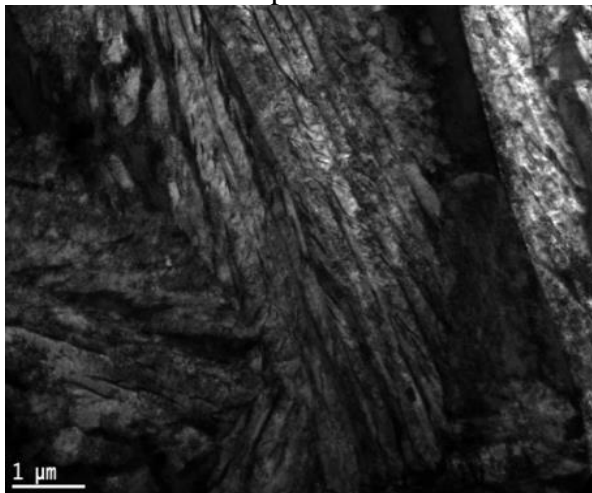
Before annealing



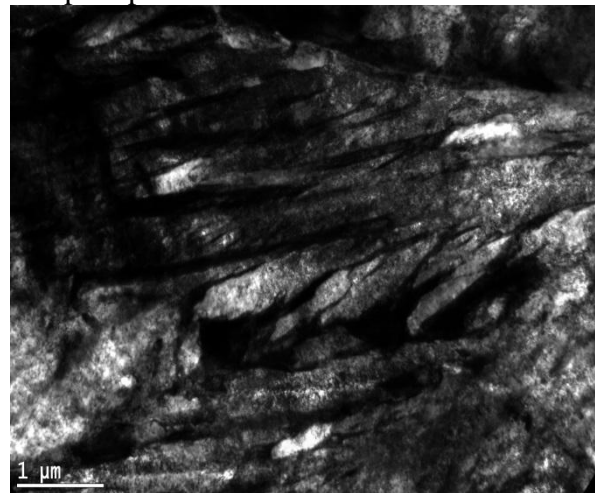
After annealing

Figure 3 Microstructure of X37CrMoV5-1 nanobainitic steel before and after annealing with 400°C-8h

On the contrary a strong microstructural changes were observed in the structural steel (Figure 4). The austenite content was smaller than at the initial state and the analysis of diffraction images disclosed diffraction spots that arose from the cementite precipitates.



Before annealing



After annealing

Figure 4 Microstructure of 35CrSiMn5-5-4 nanobainitic steel before and after annealing with 400°C-8h

The mechanical tests also revealed that the isothermal annealing of the structural steel decreased its strength and plasticity (Figure 5). The decrease of strength can be explained by cementite precipitation that led to the decrease of carbon content in ferrite and hence to reduction of carbon strengthening effect. Moreover the decrease of carbon content led to destabilisation of retained austenite which then transformed to ferrite during isothermal annealing. The resulting decrease in the content of austenite brought to the reduction of ductility.,

The changes of mechanical properties of the tool steel were different to those displayed by the structural steel. The annealing improved both, the strength and the ductility of the tool steel (Figure 6). The increase of plasticity can be explained the fact that the carbon content in the austenite was



equalised at high temperature and hence the stability of the austenite was improved. The high content of austenite with homogeneous carbon concentration can make the Transformation Induced Plasticity (TRIP) phenomena more effective during the deformation of steel which in turn can increase the total elongation. Steel can achieve higher stress level during tensile test when elongation increases, what explains the increase of steel's strength.

The obtained results show, that the temperature stability of the 35CrSiMn5-5-4 nanobainitic steel is too low to allow for an efficient nitriding process. However it can be supposed, that the nanostructured X37CrMoV5-1 steel can be subjected to low-temperature nitriding processes at about 400°C without the risk of decrease of the mechanical properties of the steel core.

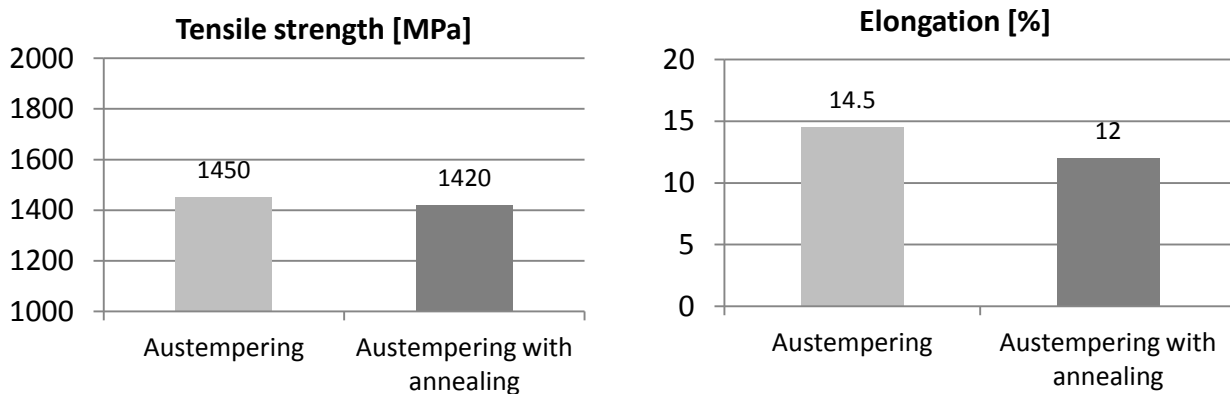


Figure 5 Mechanical properties before and after annealing of 35CrSiMn5-5-4 nanobainitic steel

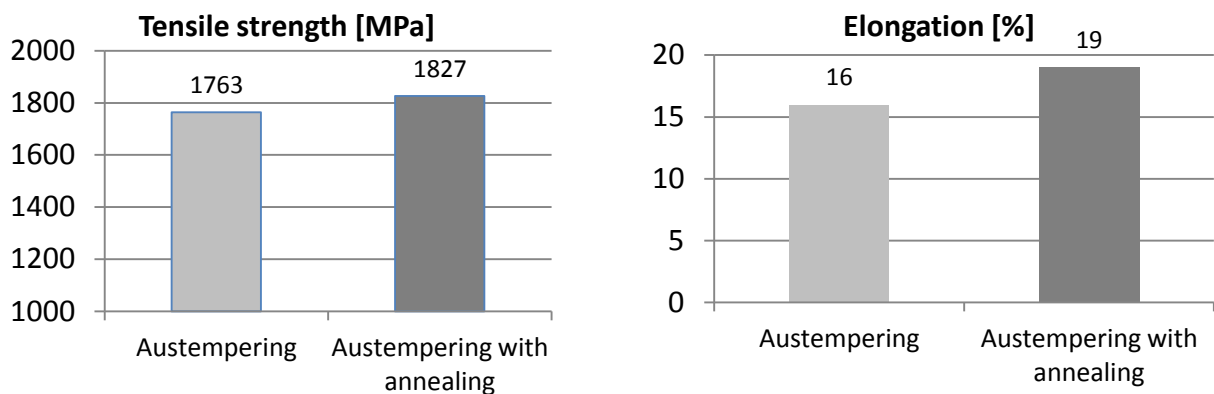


Figure 6 Mechanical properties before and after annealing X37CrMoV5-1 nanobainitic steel

## CONCLUSIONS

Nanostructured X37CrMoV5-1 steel is stable up to 400°C. During 8 hour annealing no carbides precipitation occurs and the mechanical properties get improved.

The temperature stability of 35CrSiMn5-5-4 nanobainitic steel is worse than in the case of the tool steel. 8 hour annealing causes carbides precipitation and deterioration of mechanical properties.

Thermal stability of nanobainitic steels depends on their chemical composition.

## ACKNOWLEDGEMENT

The results presented in this paper have been obtained within the project "Production of nanocrystalline steels using phase transformations" – NANOSTAL (contract no. POIG 01.01.02-



# INTERNATIONAL SCIENTIFIC CONFERENCE ON ADVANCES IN MECHANICAL ENGINEERING

12-14 October 2017, Debrecen, Hungary



14-100/09 with the Polish Ministry of Science and Higher Education). The project is co-financed by the European Union from the European Regional Development Fund within Operational Programme Innovative Economy 2007-2013 and by the Warsaw University of Technology

## REFERENCES

- [1] Beladi H., Adachi Y., Timokhina I., Hodgson P.D., *Crystallographic analysis of nanobainitic steels* Scripta Materialia 60 (2009) 455–458
- [2] Bhadeshia, H. K. D.H.: *Nanostructured Bainite*, Proceedings of the Royal Society A, 466, 2010
- [3] Caballero F.F.G., Bhadeshia H.K.D.H.: *Very strong bainite* Current Opinion in Solid State and Materials Science 8 (2004) 251–257
- [4] Bhadeshia, H. K. D.H., Garcia-Mateo C., Brown P.: *Bainite steel and methods of manufacture thereof*, United States Application US20110126946 (2011)
- [5] Burian W., Marcisz J., Garbarz B., Starczewski L.: *Nanostructured Bainite-Austenite Steel for Armour Construction*, Archives of Metallurgy and Materials. 59, 1211 (2014).
- [6] Skołek E., Marciniak S., Świątnicki W.: *Determination of phase composition in commercial Cr-Si-Mn steel after austempering treatment*, Inżynieria Materiałowa 2014/2, 199-202
- [7] Świątnicki W. A., Pobiedzińska K., Skołek E., Gołaszewski A., Marciniak S., Nadolny Ł., Szawłowski J.: *Nanocrystalline structure formation in steels using bainitic transformation*, Inżynieria Materiałowa, XXXIII, nr 6, 524-529 (2012)



## HOW THE USER BECAME AUTHORITY

**MARKOVA Kremena PhD**

Technical University of Varna

E-mail: [kremenacankova@abv.bg](mailto:kremenacankova@abv.bg)

### Abstract

*The user's mistrust in the expert authority forces him to take the position of self-built "authority". This new position can be skillfully conducted, managed, directed in a particular direction. Reason was given to the user to "live through" product design as if he was an author or at least a co-author. These levels of co-authorship can be cooperative design, demystifying the authority of the specialist, creating a gaming situation - design as entertainment and more. As a result, the current foundations of the designer profession are changing as well as the meaning of the term "expert".*

**Keywords:** *authority, expert, product, design*

### 1. INTRODUCTION

In the beginning, it is important to specify the notion of "authority" and the meaning given to it by the author, namely: a person to whom the power to rule on a matter has been delegated, who has the right to control; an acknowledged source of information. In other words - expert authority, based on knowledge, learning, experience, skills. Today, a number of rights are undoubtedly delegated to the average consumer and the opportunity to take its own decisions, but one is what he has won by himself - to be authority ; to be convinced, that for many questions he is erudite more than the specialists and to show this fact.

What are the reasons: global mistrust in the political system, in the law system, in the educational system; rewriting of historical facts, seen up until now as bases, the mass circulation of conspiracy theories, facilitated by technologies etc.

Due: for the user has no information which is secure, there is no foundation - philosophical, social, based on unwavering expert authority, which can not be broken down, refuted. And since he can not believe in anyone /anything, the user only believes in his own judgment, in his own self-built "authority". And that applies to all areas of human intervention, including design.

### 2. METHODS

The meaning of design is to serve people, that is its essence. The founders of the design profession and those who affirm it build their authority on the basis that they are the creators, they set the rules. No other experts. And even when ideas evolve or confront themselves based on a selected aesthetics, disputes are still held at expert level. Whether the design is a model of culture – a means of educating society by managing its needs and tastes; whether the design is the process of operating the product, the product itself is only auxiliary element; advocates the thesis, that design is making of illusions - to make visually appealing products - the right of conclusion is given only to the specialist.

Mistrust of expert authority today, this trend, nevertheless it is possible to be cleverly managed, cleverly guided in the desired direction by those same expert authorities. If the goal is to tolerate the user's "expert" opinion, to caress his ego - so be it! Managing the principle "Give them what they want!". But this is not about collecting information in consumer centers. It's not a question of fads



or vogues - such as concrete bed side table (Thomas Bina) or iron that looks like a locomotive (Henry Dreyfuss). The chosen method is: guiding user behavior when contacting the product, by deliberately giving him an illusory power to manifest himself as "authority". In other words - the consumer's suspicion in expert authority is tolerated by the expert, who gives the consumer reason to "live through" product design as if he was an author or at least a co-author.

The research methods in the papers are based on the selection and analysis of publicly available information concerning design of lighting fixtures.

### 3. RESULTS

What are the levels of co-authorship /authorship when the user can express his authority:

#### Co-design, cooperative design

In this case, the type and the final number of the elements of the article are fixed, as well as the parameters of its functioning. There are 1, 2 or 3 elements to be ordered, arranged by the user, usually at places indicated by the designer, but giving the user a sense of complicity, for his own importance.

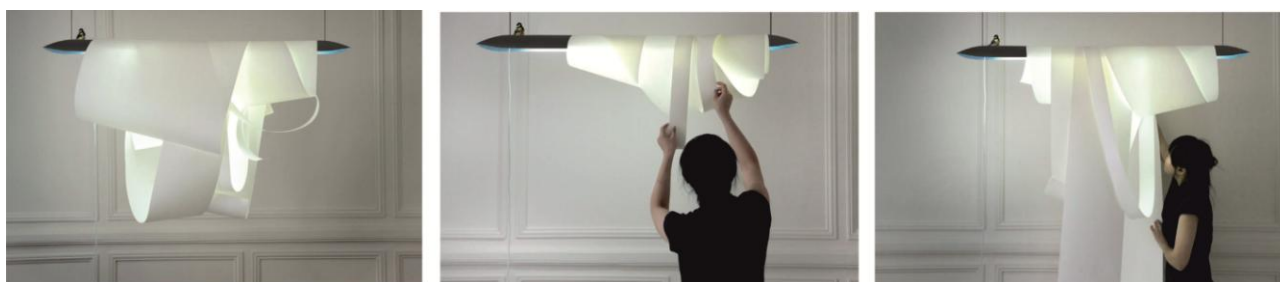


*Figure 1* **Angelin** lamp by **Constance Guisset** - Metal structure and neon, surrounded by three rolls of paper. The intensity of the light varies depending on the configuration and density of the paper strips. An active approach to co-authorship with the user.



*Figure 2* **Fresh** desk lamp by **Victor Vetterlein** - The five elements are fixed at the base, but the user is "free" to determine their positions in its own configurations, he is given the freedom to "customize" the lamp.

Another possibility of co-authorship arrives when the user is allowed not only to assemble ("create") the product himself but also to add some small personal element.

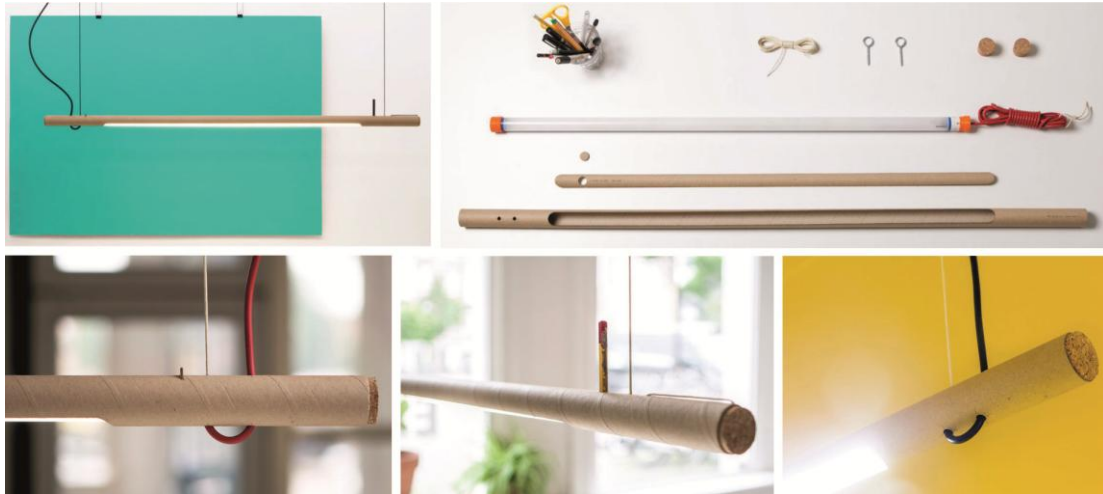


*Figure 3 R16 by **Waarmakers** - An active approach to co-authorship - the user assembles the product himself in order for the product to fulfill its purpose; customization is limited to selecting the color of the cable and embedding its own element in the system - the pencil that will become the switch.*

### **Demystifying the authority of the specialist**

The approach in this case convincingly opposes the tradition of the designer profession - to create models to be categorical, a specific example of the technologies and cultural processes of an era. This approach provides for the use of certain elements in a system, but does not specify their number, configuration relative to one another and to the occupied space; allows for a factual, physical change in the structure of the product, as well as the addition of elements, that were not originally foreseen in the set of elements of the purchased product; or the replacement of original items with others, at the discretion of the user.



*Figure 4 Tetra light by **Peter Liversidge and Asif Khan** - Components can be joined and re-arranged using connecting tubes of various lengths.*



*Figure 5 Zettel by **Ingo Maurer** - The luminaire gives the user enough "space" for his own creativity and may be formed with a loose or dense structure. The provided Japanese paper can be replaced by the user with any other format or non-format paper, with any texts or images.*



### Game

It gives the opportunity for self-expression to the user, as he is involved in a game situation. Typically, possible configurations for changing the vision /structure of the article are final, not a large number. However, the user actively experiences his "authorship", personalizing the editorial product through satisfaction from the created gaming situation.



Figure 6 **Frank Table Lamp** by **Pana Objects** - an article created with the idea for its main function and being an inanimate pet.



Figure 7 **Bite Me** edible desk lamp by **Victor Vetterlein** - made of biodegradable plastic derived from vegetable glycerin, agar and gelatin made from sea algae. When the lamp is no longer useful or desired, the lighting strip is removed and the lamp may be eaten or thrown into the garden as compost.

### Create with their own hands

This level of "co-authorship" in fact does not give the user a great scope for self-expression. In particular, this involves following an instruction, a sequence of steps to achieving the desired specific, defined form of the product. There is no choice or substitution of elements - the user does not transform anything, does not impose anything of personal significance - he repeats the steps mentioned, but does so with his own hands. This fact gives him the reason to be personify as the "author" of the editorial product.

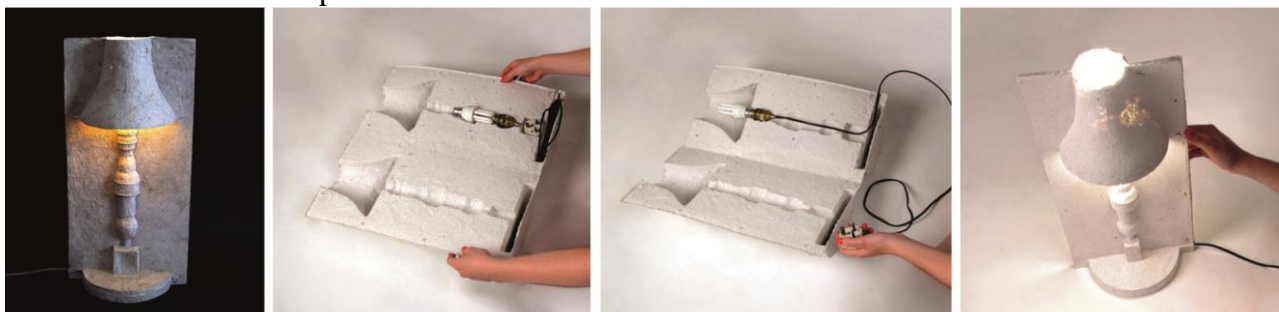


Figure 8 **Packaging Lamp** by **David Gardener** - the user's intervention is embedded in the ability of the product to perform its main function.

### CONCLUSIONS

Driven or not, the change of public opinion on the nature of the design profession is already under way. In this process, the change in attitude towards culture as a place of entertainment is also very



# INTERNATIONAL SCIENTIFIC CONFERENCE ON ADVANCES IN MECHANICAL ENGINEERING

12-14 October 2017, Debrecen, Hungary



important. The mistrust of the ordinary consumer in the authority of the experts is transformed into an increase in the role of his ego and self-captured "expert" position, including design issues. At the same time, the user is given the opportunity to participate in the processes of "creating" the elements of his own environment. This gives him the reason - figuratively or not - to acquire the status of author, of authority.

## REFERENCES

- [1] Markova, K.: *The consumer as author*. International Scientific Congress "Machines. Technologies. Materials 13-16.09.2017, Varna, Bulgaria, Year I, Issue 5, Volume V "Machines", "Ergonomics & design", 392-394., ISSN 2535-003X (ONLINE).
- [2] Constanceguisset.com  
<<http://www.constanceguisset.com/en/creations/Design/Prototypes/angelin>>(30.07.2017).
- [3] Dezeen.com<<https://www.dezeen.com/2008/08/14/packaging-lamp-by-david-gardener/>>(10.10.2017).
- [4] Dezeen.com<<https://www.dezeen.com/2012/11/21/bite-me-edible-desk-lamp-victor-vetterlein/>>(10.10.2017).
- [5] Dezeen.com<<https://www.dezeen.com/2008/10/13/tetra-light-by-peter-liversidge-and-asif-khan/>>(10.10.2017).
- [6] Dezeen.com<<https://www.dezeen.com/2016/06/26/video-r16-lamp-led-waarmakers-lighting-cardboard-packaging-design-diy-movie/>>(10.10.2017).
- [7] Dezeen.com<<https://www.dezeen.com/2012/01/03/fresh-by-victor-vetterlein/>>(10.10.2017).
- [8] Ingo-maurer.com<<https://www.ingo-maurer.com/en/products>> (30.07.2017).
- [9] Pana-objects.com <<http://www.pana-objects.com/index.php/product/frank/>>(30.07.2017).



## BATTERIES OPERATION PARAMETER ANALYSIS WITH FUZZY LOGIC

<sup>1</sup>MENYHÁRT József, <sup>2</sup>SZABOLCSI Róbert PhD

<sup>1</sup>Department of Mechanical Engineering, Faculty of Engineering, University of Debrecen,  
E-mail: [jozsef.menyhart@eng.unideb.hu](mailto:jozsef.menyhart@eng.unideb.hu)

Institute of Mechatronics and Vehicle Engineering, Donát Bánki Faculty of Mechanical and Safety  
Engineering, Óbuda University

E-mail: [szabolcsi.robort@bgk.uni-obuda.hu](mailto:szabolcsi.robort@bgk.uni-obuda.hu)

### Abstract

*This research and industrial project related to the monitoring of the State of Charge (SoC) of the batteries supplemented with consumption problems at high safety level. The article presents the authors' research and main results on State of Charge estimation and the measuring accuracy of SoC. The main findings of the research and development tasks show amount of accuracy problems in the daily usage. The authors describe the definition of parameter deviation and State of Charge and describe the Fuzzy logic analysis with sigmoid function to define parameter deviations in State of Charge.*

**Keywords:** *state of charge, parameter deviation, Fuzzy logic, sigmoid function*

### 1. INTRODUCTION

The Battery State of Charge (SoC) estimation and accuracy are key elements of the battery management system. The accurate of SoC estimation can make better performance of the batteries on short and long term, too. These properties of the SoC accuracy can ensure higher security level of the electric vehicles battery system. The main purpose of this article is to describe the main properties of State of Charge, parameter deviation, fuzzy logic and sigmoid functions. The fuzzy logic can help to prepare a better SoC strategy. The article will focus on investigation of the brand-new way to analyse the measurement errors and their effects on the battery systems' quality and functionality.

### 2. PARAMETER DEVIATION – INACCURACY

Accuracy is a very important definition in engineering life. It is a description of random errors in the technical systems, and, it is to describe and to measure of statistical variability. We can find two definitions of accuracy in different literatures. The accuracy is an important definition to describe the systematic errors in a technical system. The accuracy is a measure of statistical bias. These important properties make the difference between a result and the "true value". The ISO standard call this fact to trueness. The ISO defines to types of errors: these are the random and the systematic. A high accuracy requires high precision and high trueness. A given set of data from a series of measurements, the numbers can be said to be right if the given values are (very) close to the average value of the quantity being measures. The measured results can be accurate if the values are close to the true values of the quantity being measured. The two definitions are independent of each other. It means that the data can be accurate, either accurate, precise, both or neither too. [1] [2] [3] [4]

The closeness of a measured value to a standard or known value is the accuracy. The precision



shows the closeness of two or more measurements to each other. Important to know: the precision is independent from accuracy. So, you can be precise but inaccurate in the same time or you can be accurate but imprecise. It is always depends on a lot of external factor which have an effect on your work or your processes and devices. [1] [2] [3] [4]

### 3. STATE OF CHARGE

The State of Charge (SoC) is an equivalent definition of a fuel gauge for a battery system in a full electric driven vehicle, hybrid vehicle or plug-in hybrid vehicle. In the practice the units of SoC are in percentage results. 0% means the battery is fully discharged, the 100% means that the battery is fully charged. Important to know: the SoC has an alternate form, what we call Depth of Discharge (DoD). It is an inverse method of SoC so: 100% means that the battery is fully discharged, the 0% means that the battery is fully charged. The SoC is a good performance indicator when the operators or engineers would like to discuss the current state of battery in use. DoD is important when the researchers would like to investigate or check the lifetime of the battery. [5] [6]

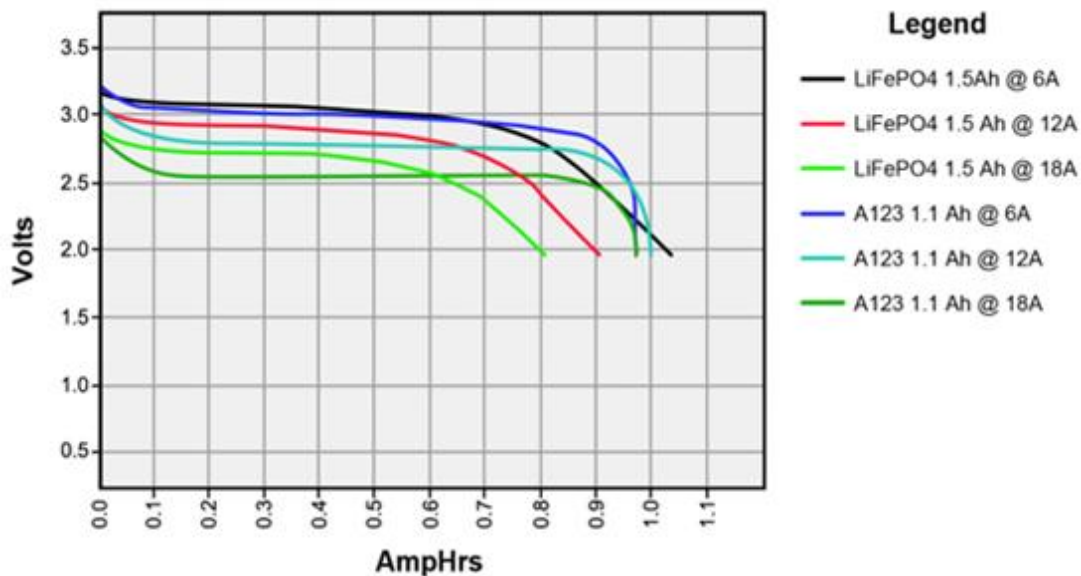


Figure 1 State of Charge example [5]

The SoC can't be measured directly, but we can find a lot of methods, which help us to estimate the SoC result. We know two types: offline and online methods. In offline techniques the batteries desire to be charged and discharged in constant. This method can give a very good result about the State of Charge of the battery. Important to know the offline methods have a high cost and they can interrupt the performance of the batteries. Nowadays the researchers try to investigate more and more online techniques to SoC investigation. We know 5 important techniques in practice, which are [5] [6]:

- chemical
- voltage
- current integration
- Kalman filtering
- pressure



#### 4. MEASURING ACCURACY OF BATTERY STATE OF CHARGE

In the practice we know lots of types of State of Charge measuring methods. Honestly, these methods are not really accurate. The easiest measurement method is that by voltage (see previous chapter). This method is very simple, but it is not correct because of the battery cell materials and the different temperatures are affecting the results of the voltage measurement. These effects can disturb the charge and overcharge process of the batteries, i.e. it is a very critical regime from the point of view of safety use of the batteries. This method can give a wrong SoC reference. [5] [6] [7] The voltage based SoC system is impractical. The engineers know many reasons. For precise result the batteries must rest in the open circuit. This process needs 4 hours. Important to know a lead acid battery need more time, they recommended 24 hours. These properties show the problems of the voltage system, it is not proper for a battery in active duty. The voltage system cannot use at nickel and lithium batteries. The lead acid has some important features like plate compositions which have to be check during the SOC estimation by voltage. The calcium is a very good example, it can raise the voltage by 5-8% with heat, but the cold reduces it. [5] [6] [7]

The surface charge can indicate other problems, too. It can make a high voltage instantly after the charge, it can make a false result. The user can avoid this failure with a short discharge before the measurement. The battery voltage must float without any load applied during the measurement of State of Charge. Most of the SoC measurements based on the voltage system thanks to the simplicity of this method. [5] [6] [7]

#### 5. FUZZY LOGIC

The founder of Fuzzy logic was Lofti Zadeh, who made his first publications about fuzzy in the middle of the 60's. He analysed the examined different types of truth provinces and their boundaries which are often blurred. Amount of literatures give a view about fuzzy logic [8][9][10][11][12]. In [8] are case studies about parameter deviation and fuzzy logic.

*“The following study: [8] describes the main steps of Fuzzyfication and introduces the generally applied functions.” [11]*

The sigmoid function is an important mathematical function, i.e. we often find it as logistic function. This function has a special shape curve, i.e. it looks like "S". The function has a lot of special properties, these are the following [11]:

- it has a positive derivate everywhere
- it is bounden differentiable real function

The sigmoid function often uses in logical systems, a lot of study write about the usage like a logical criteria. The function can take values on the range from 0 to 1 or in some case -1 to 1. The sigmoid function often uses in the field of artificial intelligence or is can use like an activation function. The fuzzy logic often uses sigmoid function. [11]

*“The fuzzy membership functions make an imaging in the analysed set and describe it in the 0 – 1 interval. The  $\mu$  membership function describes the result of the analysis on a 0 – 1 interval. The  $\mu$  values can take any result between 0 and 1.” [11]*

The general formula able to determine the Fuzzy membership function of parameter tolerances is given in the following form [11] [12]:

$$\mu = \frac{1}{1 + e^{a_i(b_i-x)}} \quad (1)$$



In Equation 1  $x$  stands for the input parameter, the  $a_i$  and  $b_i$  are scalar coefficients, which can change the shape of the membership function. The  $a_i$  coefficient affects the slope of the function, i.e. the  $b_i$  coefficients can determine the midpoint of the membership function. [11] [12]

The previous formula can give a 2D representation about the function. The following formula can show a 3D view [11] [12]:

$$\mu(x, y) = \left( \frac{1}{1 + e^{a_i(b_i - x)}}; \frac{1}{1 + e^{a_j(b_j - x)}} \right) \quad (2)$$

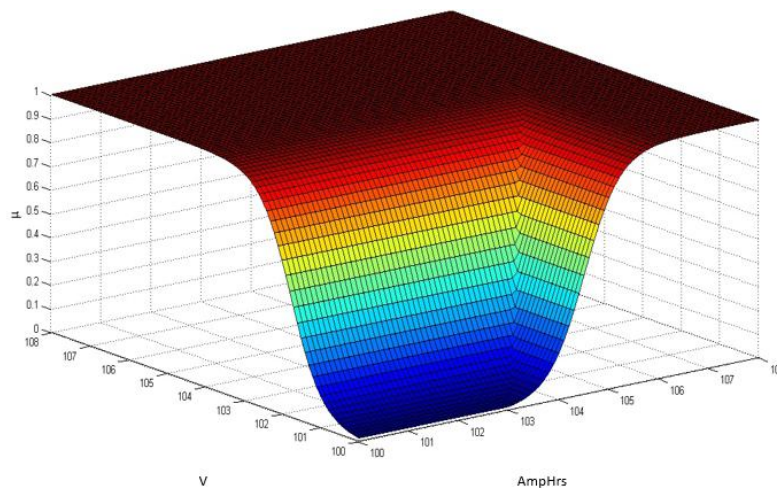


Figure 2 3D surface of a fictional SoC

The Fig. 2 illustrates a possible point of view of a fictional SoC. The figure contains the main parameters of SoC and the result of  $\mu$ . The  $\mu$  result between 0,7 and 0,8 can give a result to a parameter deviation during State of Charge measurement.

## CONCLUSIONS

The State of Charge is presented. The main properties and characteristics of the State of Charge were determined in the article. Sigmoid function implemented in the article is effectively used by many soft computing methods. The combining of sigmoid function and State of Charge inaccuracy the engineers and researchers can get a better SoC parameters in a real life and the batteries can work with a higher efficiency and with a higher safety. In the future works the authors will make investigation on lithium polymer batteries in a real electric vehicle. The measurement data will be analysed with MATLAB software.

## ACKNOWLEDGEMENT

The work/publication is supported by the EFOP-3.6.1-16-2016-00022 project. The project is co-financed by the European Union and the European Social Fund.

## REFERENCES

- [1] Bureau International de Poids et Mesures: Guides in Metrology, url: <https://www.bipm.org/en/publications/guides/>, Download: 2017.10.28.
- [2] Controlled Environments, Econtamination Control for Life Sciences and Microelectronics:



Beyond NIST – Traceability: What really creates Accuracy? Magazine, Vol. 13. No 9., 1-3., September, 2010

- [3] Significant Digits, url: <http://digipac.ca/chemical/sigfigs/contents.htm>, Download: 2017.10.28.
- [4] labwrite.ncsu.edu: *Accuracy an Precision*, url: <https://labwrite.ncsu.edu/Experimental%20Design/accuracyprecision.htm>, Download: 2017.10.28.
- [5] Battery University: BU.903 How to Measure State – of – Charge, url: [http://batteryuniversity.com/learn/article/how\\_to\\_measure\\_state\\_of\\_charge](http://batteryuniversity.com/learn/article/how_to_measure_state_of_charge) Download: 2017.10.28.
- [6] Electropedia, Battery and Energy Technologies: *State of Charge (SoC) Determination*, url: <http://www.mpoweruk.com/soc.htm>, Download: 2017.10.28.
- [7] Tawaki: *How accurate is the measuring of a battery state of charge?* url: <http://www.tawaki-battery.com/accurate-measuring-battery-state-charge/>, Download: 2017.10.28.
- [8] L. Pokorádi: *Rendszerek és folyamatok modellezése*, Capmus Kiadó, Debrecen 2008.
- [9] Z.C. Johanyák: *Fuzzy Modeling Of Thermoplastic Composites' Melt Volume Rate*, Computing and Informatics, Vol. 32, 2013, No 4, ISSN 1335-9150, pp. 845-857.
- [10] Z.C. Johanyák and J. Kovács: *Fuzzy Model based Prediction of Ground-Level Ozone Concentration*, Acta Technica Jaurinensis, Series Intelligentia Computatorica, ISSN 1789-6932, Vol. 4. No. 1. 2011, pp. 113-126.
- [11] R. Szabolcsi, J. Menyhárt: *Battery Voltage Limit Analysis with Support Vector Machine and Fuzzy logic*, Advances in Military Technology, Vol.12. No.1., 21-32. 2017.
- [12] L. Pokorádi, J. Menyhárt: *Electric Vehicles' Battery Parameter Tolerances Analysis by Fuzzy, Logic Proceedings of the 11th IEEE International Symposium on Applied Computational Intelligence and Informatics SACI 2016*. 412 p.  
Konferencia helye, ideje: Timisoara, Románia, 2016.05.12-2016.05.14. Budapest: IEEE, 361-364., 2016.



## DECREASE OF THE ENERGY DEMAND OF DISTILLATION WITH VAPOUR RECOMPRESSION

*MODLA Gábor DSc, LÁNG Péter DSc*

*Department of Building Services and Process Engineering, Faculty of Mechanical Engineering,  
Budapest University of Technology and Economics*

*E-mail: [mgabor-bp@freemail.hu](mailto:mgabor-bp@freemail.hu) , [lang@mail.bme.hu](mailto:lang@mail.bme.hu)*

### **Abstract**

*Distillation is one of the most widely used separation methods in the chemical industry in spite of its very high energy demand. A great number of attempts have been made to reduce the energy demand of distillation processes. One of them is the application of a mechanical heat pump technology (like vapour compression or vapour recompression) for distillation columns.*

*In this study two process flow-sheets for vapour recompression (VRC) system are investigated and compared for the separation i-butane/n-butane by rigorous simulation. In the first system only the top vapour leaving the column is compressed (VRC-1) and used for heating the reboiler, whilst in the second system the amount of working fluid (WF) compressed is increased by recycling (VRC-2). The influence of the relevant operational parameters (optimization variables) for the two VRC processes is studied by rigorous simulation with a professional flow-sheet simulator (ChemCad) in order to minimise the compressor power. The results show that the VRC-2 system is more efficient, it has lower investment cost and shorter pay-back time than the well-known VRC-1 system.*

**Keywords:** *heat pump in distillation, vapour recompression, separation i-butane/n-butane, simulation*

### **1. INTRODUCTION**

Distillation is one of the most widely used separation methods in the chemical industry in spite of the fact that its energy requirement is extremely high. A great number of attempts have been made to reduce the energy requirement of distillation processes one of them is the application of a heat pump for distillation column. Mechanical heat pump technologies like vapour compression and vapour recompression are useful ways to improve the energy quality and to reduce the greenhouse emissions. Their disadvantages include high investment cost and process complexity [1].

A comprehensive review of different heat pump (HP) systems for continuous distillation was given by Bruinsma and Spoelstra [2]. They gave a detailed, clear description about the theory of vapour recompression (VRC) as well. They also considered novel heat pumps for distillation (thermoacoustic, compression resorption, adsorption heat pumps, heat integrated distillation columns). Kiss et al. [3] summarized all HP technologies (including the thermal VRC, cyclic distillation, Kaibel and dividing wall columns). They proposed a practical selection scheme of energy efficient distillation technologies. In study of Diez et al. [4] the separation i-butane/n-butane was selected to analyse several distillation assisted heat pump processes when compared to conventional distillation. This conventional process, along with top vapour recompression, bottom flashing and absorption heat pumps, were simulated by using the HYSYS software platform, in order to determine the best alternative economically. They stated that distillation with both top vapour recompression and bottom flashing heat pumps allows a reduction of operation (energy) costs by 33% and 32%, respectively. Fonyo and Benko [5] analysed various heat pump assisted



process configurations for i-butane/n-butane separation using a design strategy based on preliminary screening, rigorous steady state simulation and economic evaluation. The influence of heat pump type, heat load, column temperature difference, utility cost, exchanger minimum approach temperature on the energetic aspects and economic range of application was studied.

In this study two VRC processes (one is well-known in the literature [4,5], the other one is less-known) are investigated and compared for the well-known industrial separation problem, the separation of i-butane/n-butane mixture (C4 split) by rigorous simulation. The effects of the main operational parameters of the heat pump system is studied.

The goals of this paper are:

- to present and investigate two process flow-sheets for vapour recompression system (VRC),
- to study the separation of i-butane/n-butane mixture by simulation with a professional flow-sheet simulator,
- to study the influence of the relevant operational parameters (optimization variables) for the two VRC processes,
- to minimise the compressor power and pay-back period.

The rigorous simulation calculations are performed with the ChemCad professional flow-sheet simulator. For the vapour-liquid equilibrium and enthalpy calculations the Soave-Redlich-Kwong equation of state is applied.

## 2. FUNDEMANALS

### 2.1 Conventional distillation column

Figure 1 gives the flow-sheet for the separation of i-butane/n-butane. Based on the work of Diez et al. [4] the column operates at 7.0 bar and the column pressure drop is 0.2 bar. The column has 32 theoretical stages ( $N=32$ ) without the total condenser and partial reboiler. The flow rate of the equimolar feed ( $F$ ) is 100 kmol/h and it is supplied as saturated liquid ( $q=1.0$ ) at a pressure of 7.1 bar. The mole fraction of i-butane in the top product ( $D$ ) is specified as 0.9, and that of n-butane in bottom product ( $W$ ) is specified as 0.9; hence the temperature of the distillate (and condenser) is 51.37 °C and the temperature of the bottom product (and the reboiler) is 63.05 °C. The top temperature is 51.68 °C. The condenser cooling requirement is  $Q_c=6915$  MJ/h and the reboiler heating requirement is  $Q_r=6919$  MJ/h. Feed stage is the 16-th.

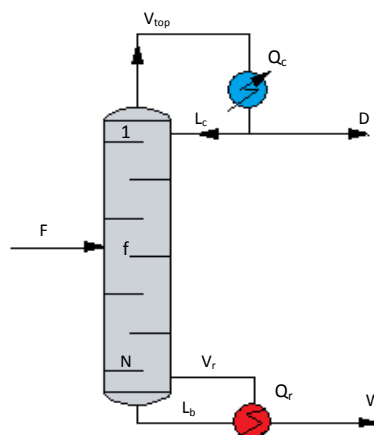
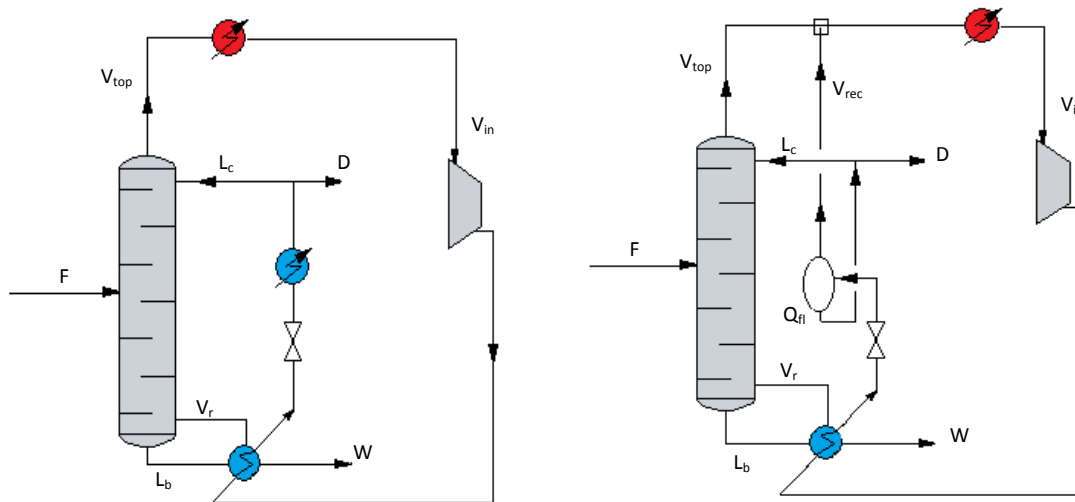


Figure 1 Conventional distillation column with total condenser and partial reboiler

## 2.2 Vapour recompression system

In vapour recompression systems the working fluid (WF) is the top vapour ( $V_{top}$ ). The working fluid is led to a compressor after its eventual superheating (in order to prevent the partial condensation in the compressor, that is, to protect it from the liquid break). Then it leaves the compressor and enters the reboiler, where (after losing the small heat of superheating) it is condensed and eventually it cools down further (the heat is transferred to the liquid in the reboiler). After that its pressure is reduced by a throttle valve (expander) where one of the WF is vaporised. From this point there are two possibilities. In the first case (Figure 2a, VRC-1), which is well-known in the literature, the vapour part of the working fluid stream is condensed totally in the after-cooler; one part of the liquid is the reflux ( $L_c$ ) and the other part is the distillate ( $D$ ). In the second case (Figure 2b, VRC-2) the vapour part of the working fluid stream leaving the throttle valve is only partially condensed then it is separated to liquid ( $L_c+D$ ) and vapour ( $V_{rec}$ ). The vapour is recycled (mixed with the top vapour) increasing the quantity of the WF compressed. (The liquid part is partially refluxed to the top of the column similarly to the former case.)



a) VRC without flashing (VRC-1)  
(traditional, well-known)

b) VRC with flashing (VRC-2)  
(proposed)

Figure 2 Vapour recompression systems (VRC)

### Compressor power

The compressor power can be calculated from the following equation:

$$MP = z \cdot \frac{\mu}{\mu-1} V^{vol.in} P^{in} \left[ \left( \frac{P^{out}}{P^{in}} \right)^{\frac{\mu-1}{\mu}} - 1 \right] \quad (1)$$

where

$$\frac{\mu-1}{\mu} = \frac{(k-1)}{\eta_{eff}} \quad (2)$$

$z$  is the compressibility factor,  $V^{vol.in}$  is the volumetric flow rate of vapour at the inlet of compressor, and  $k$  is the ratio of heat capacities ( $c_p/c_v$ ).

At the calculations the operation of compressor is polytropic and its efficiency is 70%.



### 2.3 Pay-back calculation

The payback period of investment (PBP) is determined by combining investment costs (IC), depreciation cost (DC) and the yearly savings (YS). The investment cost is estimated by the formulas of Douglas [6].

Investment cost of the compressor:

$$IC = \left( \frac{M \& S}{280} \right) \cdot 517.5 \cdot (1.34 \cdot MP)^{0.82} \cdot (2.11 + F_d) \quad (3)$$

where M&S is the Marshall-Swift index (1483 for the year 2012),

MP is the compressor motor power [kW],

$F_d=1$ .

Depreciation cost:

The estimated useful life of the compressor is 10 years, hence the depreciation cost is:

$$DC = \left( \frac{IC}{10} \right) \quad (4)$$

Yearly saving:

We suppose that the yearly working hour is 6000.

$$YS = 6000 \cdot [QR \cdot UP_{steam} - MP \cdot UP_{el}] - DC \quad (5)$$

where QR is the heat duty of the reboiler [GJ/h],

MP is the compressor motor power [GJ/h]

$UP_{el}$  is the unit price of electricity (30 \$/GJ\*),

$UP_{steam}$  is the unit price of heating (steam, 14 \$/GJ\*).

\*Unit prices are based on information obtained from a Hungarian industrial company.

Payback period:

$$PBP = \frac{IC}{YS} \quad (6)$$

## 3. PARAMETRIC STUDY AND OPTIMISATION

For both configurations the minimal compressor power, where the minimal temperature difference in the reboiler ( $\Delta T_r=10$  °C) is ensured and there is no liquid in the compressor (liquid break is avoided), is determined.

First the influence of the relevant parameters (optimisation variables) is studied. For the simpler configuration (VRC-1), where the ratio of WF compressed to that of leaving the column ( $\beta$ ) is fixed there is only one variable, which is the pressure at the outlet of the compressor. For the more flexible configuration (VRC-2), where  $\beta$  is also variable, after studying the influence of the individual parameters optimisation of two variables is performed.

First the outlet pressure of the compressor ( $P^{out}$ ) is estimated. By supposing that the WF of 73.05 °C leaving the reboiler (having the composition of top vapour) is saturated liquid  $P^{out}=11.44$  bar.

### 3.1 VRC-1 ( $\beta=1$ )

At  $P^{out}=11.44$  bar the temperature of the WF is 61.90 °C which is too low, therefore  $P^{out}$  must be increased (Table 1, where  $q_r$  is the heat condition of the WF leaving the reboiler).

On the increase of  $P^{out}$  MP strongly increases. The temperature of the WF leaving the reboiler increases (and at 18.41 bar it reaches 73.05 °C), but it becomes more and more sub-cooled ( $q_r$  increases). In the after-cooler more and more heat (Q) must be withdrawn.



Table 1 The influence of  $P_{out}$  (VRC-1)

Compressor				Reboiler			After-cooler
$P_{out}$ [bar]	MP [kW]	$T_{out}$ [°C]	$T_{out\_dp}$ [°C]	$T_{r\_out}$ [°C]	$T_{r\_out\_bp}$ [°C]	$q_r$ -	Q [MJ/h]
11.44	185.0	73.98	73.04	61.95	72.78	1.117	-661.6
16.00	323.4	91.35	89.32	69.68	89.10	1.257	-1159.7
18.00	374.4	98.06	95.41	72.51	95.20	1.325	-1343.3
18.40	384.1	99.35	96.57	73.04	96.37	1.340	-1378.1
18.41	384.6	99.38	96.59	73.05	96.39	1.340	-1379.0
19.00	388.3	101.26	98.27	73.82	98.07	1.363	-1429.3

### 3.2 VRC-2 ( $\beta > 1$ , variable)

First the influence of  $\beta$  is studied at  $P_{out}=11.44$  bar (Table 2), then that of  $P_{out}$  (Table 3).

Table 2 The influence of  $\beta$  (VRC-2,  $P_{out}=11.44$  bar)

$\beta$ -	Compressor			Reboiler			Flash
	MP [kW]	$T_{out}$ [°C]	$T_{out\_dp}$ [°C]	$T_{r\_out}$ [°C]	$T_{r\_out\_bp}$ [°C]	$q_r$ -	Q [MJ/h]
1.05	194.3	73.9	73.04	61.95	72.78	1.117	-661.0
1.10	203.5	73.9	73.04	71.41	72.78	1.015	-728.2
1.15	212.7	73.8	73.01	72.75	72.75	0.993	-744.8
1.20	222.0	73.8	73.04	72.75	72.75	0.930	-794.7
1.30	240.4	73.9	73.04	72.75	72.75	0.859	-857.8

On the increase of  $\beta$  MP proportionally increases. The temperature of the WF leaving the reboiler increases; it gets closer and closer to its boiling point and after reaching it on the further increase of  $\beta$  its vapour content increases. In the WF passing through the reboiler the mole fraction of the i-butane ( $x_{WF}$ ) slightly increases since the vapour recycled from the flash is in equilibrium with the liquid distillate ( $y_{rec}=0.9215$ ). At the given  $P_{out}$  the temperature of the WF leaving the reboiler remained slightly below 73.05 °C.

The influence of  $P_{out}$  is studied at  $\beta = 1.1$  (Table 3).

Table 3 The influence of  $P_{out}$  (VRC-2,  $\beta=1.1$ )

$P_{out}$ [bar]	Compressor			Reboiler			Flash
	MP [kW]	$T_{out}$ [°C]	$T_{out\_dp}$ [°C]	$T_{r\_out}$ [°C]	$T_{r\_out\_dp}$ [°C]	$q_r$ -	Q [MJ/h]
11.00	186.4	71.95	71.21	70.53	70.95	1.0046	-666.7
11.50	205.8	74.11	73.26	71.48	73.00	1.0170	-736.4
12.00	224.5	76.21	75.24	72.40	74.99	1.0295	-803.8
12.36	237.6	77.69	76.14	73.05	76.34	1.0387	-851.0
12.50	242.6	78.26	77.17	73.29	76.92	1.0423	-869.0

The influence of  $P_{out}$  similar as it was in the case of VRC-1, but due to the increased amount of WF compressed the temperature of the WF leaving the reboiler already reaches 73.05 °C (at  $P_{out}=12.36$  bar). However the WF cools below its boiling point.



MP can be still decreased by optimisation, where the optimisation variables are:  $\beta$  and  $P^{\text{out}}$ . The optimisation can be performed with sensitivity analysis with two variables or with a single variable by applying a controller maintaining  $T_r^{\text{out}}=73.05$  °C by manipulating  $P^{\text{out}}$  or  $\beta$ . The results are shown in Table 4.

Table 4 Optimal results for VRC-2

$\beta$	Compressor				Reboiler			Flash
	$P^{\text{out}}$ [bar]	MP [kW]	$T^{\text{out}}$ [°C]	$T^{\text{out}}_{\text{dp}}$ [°C]	$T_r^{\text{out}}$ [°C]	$T_r^{\text{out}}_{\text{bp}}$ [°C]	$q_r$ -	Q [MJ/h]
1.125	11.515	210.1	74.17	73.31	73.06	73.06	0.99454	-755.7

In the optimum the WF leaving the reboiler is saturated liquid ( $q_r$  is very close to 1.0). The pay-back for the VRC-1 (the motor power is 385 kW) is 6.5 year, while it is only 2.3 year for VRC-2 (MP is 210 kW).

## CONCLUSIONS

In this study two vapour recompression processes, a well-known in the literature (VRC without flashing) and a less-known (VRC with flashing) were investigated and compared for the separation of the mixture i-butane/n-butane by rigorous simulation with the flow-sheet simulator ChemCad. The influence of the relevant operational parameters (optimization variables) for the two VRC processes was studied in order to minimise the compressor power.

The result showed that the VRC with flashing is more flexible, more energy-saving and it has less investment cost and better pay-back (2.3 versus 6.5 year) than the VRC without flashing.

## REFERENCES

- [1] You X., Rodriguez-Donis I., Gerbaud V.: *Reducing process cost and CO2 emissions for extractive distillation by double-effect heat integration and mechanical heat pump*, Applied Energy, 166, 128–140., 2016.
- [2] Bruinsma, D.; Spoelstra, S.: *Heat pumps in distillation*. In: Proc. Distillation and Absorption 2010, 21–28, Eindhoven (NL), 2010.
- [3] Kiss A. A., Landaeta S. J. F., Ferreira C. A. I.: *Mastering Heat Pumps Selection for Energy Efficient Distillation*, Chem. Eng. Trans., 29, 397-402, 2012.
- [4] Diez E, Langston P, Ovejero G, Romero M. D.: *Economic feasibility of heat pumps in distillation to reduce energy use*, Appl. Therm. Eng, 29, 5, 1216–1223, 2009.
- [5] Fonyo Z., Benko N.: *Comparison of various heat pump assisted distillation configurations*, Trans. IChemE, 76, A, 348-360, 1998.
- [6] Douglas, J. M.: *Conceptual Design of Chemical Processes*; McGraw-Hill: New York. 1989.



## REVIEW ARTICLE: MODELLING AND ANALYSIS OF A GASOLINE ENGINE EXHAUST GAS SYSTEMS

*MOHAMAD Barhm, SZEPESI Gábor PhD, BOLLÓ Betti PhD*

*Faculty of Mechanical Engineering and Informatics, University of Miskolc*

*E-mail: [pywand@gmail.com](mailto:pywand@gmail.com), [szepesi@uni-miskolc.hu](mailto:szepesi@uni-miskolc.hu), [aramzb@uni-miskolc.hu](mailto:aramzb@uni-miskolc.hu)*

### **Abstract**

*The engine exhaust gas behaviour is strongly influencing the engine performance. This paper presents the modelling and analysis of four stroke - gasoline engine exhaust gas systems. An automotive example is considered whereby the pulsating exhausts gas flow through an exhaust pipe and silencer are considered over a wide range of speeds. Analytical procedures are outlined enabling the general analysis and modelling of vehicle engine exhaust gas systems also in this paper presents the numerical simulation of modern structure of exhaust pipe. Investigation in CFD was performed on four parameters comprises manifold temperature, manifold pressure, exhaust piping system and exhaust gas velocity. Results of CFD simulation was showed in the form of pressure, velocity contours and streamline.*

*The objective of this paper to provide latest technique through literature review to investigate the effects of gas flow inside the exhaust system and around the system on gasoline engine.*

**Keywords:** *exhaust gas, modelling, CFD, exhaust manifold, SI engine.*

## **1. INTRODUCTION**

### **1.1 Simulation of an exhaust system**

An exhaust system piping used to guide reaction exhaust gases away from a controlled combustion inside a gasoline engine. The entire system conveys burnt gases from the engine and includes one or more exhaust pipes. An exhaust pipe must be carefully designed to carry toxic and noxious gases away from the users of the machine. Indoor generators and furnaces can quickly fill an enclosed space with poisonous exhaust gases such as hydrocarbons, carbon monoxide and nitrogen oxides if they are not properly vented to the outdoors.

Also, the gases from most types of machine are very hot; the pipe must be heat-resistant, and it must not pass through or near anything that can burn or can be damaged by heat.

Motorcycle exhausts come in many varieties depending on the type of engine and its intended use. A twin cylinder may flow its exhaust into separate exhaust sections, such as seen in the Kawasaki EX250, or they may flow into a single exhaust section known as a two-into-one 2-1.

Larger engines that come with 4 cylinders, such as Japanese super sport or passenger cars (such that Honda's and Toyota,) often come with a twin exhaust system. A "full system" may be bought as an aftermarket accessory, also called a 4-2-1 or 4-1, depending on its layout. In the past, these cars would come standard with a single exhaust. EU noise and pollution regulations have generally stopped this practice, forcing companies to use other methods to increase performance of the vehicles. The heat transfer in exhaust system directly affects the performance and the emission characteristics of the internal combustion engine. For improvement in the performance of an engine, it is necessary to control the temperature in automotive exhaust system.



## **2. INTERNAL GAS FLOW CHARACTERISTICS ANALYSIS**

The automotive exhaust system is exposed to high temperature as the hot gases from combustion chamber passes through it. The uniform distribution of heat is needed to enhance life of exhaust system components. Heat transfer studies in the exhaust system is necessary to understand the physical phenomena takes place in it which is required to design purpose of exhaust system. Higher performance of engine can be achieved by normal operating condition which can be limited by controlling exhaust system temperature. Internal combustion engine is an important prime mover used in the various field like automotive, power generation and industry application. Exhaust manifolds are affected by thermal stresses and deformations due the temperature distribution, heat accumulation or dissipation and other related thermal characteristics. Heat transfer affects the performance, emission and durability of the engine as well as the design, material choice and fatigue life of vehicle components. Engine heat transfer and cooling is necessary for improvement of engine performance. Measuring the exhaust gas temperature from automotive exhaust system is useful to understand the engine processes. The exhaust gases coming out from engine are at very high speed and at high temperature. Exhaust system of an automobile from which exhaust gases coming out from combustion chamber have silencer which is integral part of exhaust system. High temperature in exhaust system leads to thermal, vibration and fatigue failures causing the cracks in silencer. So, it is necessary to study the heat transfer analysis for hot section of exhaust system for better performance of automobile.

Thermal mass and external insulation to exhaust system is main factor which affects the inlet gas temperature of catalytic converters. Under normal operating conditions, catalytic converters are most effective to reduce air pollution from internal combustion engines. The exhaust gases flowing through the exhaust system need to be cooled before reaching the catalytic converter to increase performance of catalytic converter. The heat transfer analysis in automotive exhaust system is necessary because their importance in the design and optimization phases of exhaust after-treatment system. Heat loss between the engine out and before the catalyst converter will determine the energy gain of the catalyst thus affect the temperature rise of the catalyst which affect catalyst life time. A significant number of researches have been done for exhaust manifold, exhaust piping and catalytic converter packaging design for automotive exhaust system to improve performance based on heat transfer analysis of exhaust system. The resulting heat transfer expression based on experiments and mathematical modelling used in computational models for the design of exhaust system parts and optimization phases to facilitate the selection of suitable material and designed system for better performance.

Plotnikov et al. [1] analyse the influence of cross-profiling of inlet and exhaust pipes on the gas exchange processes in four strokes - internal combustion engine the study carried out mainly by means of experimental investigations of gas-dynamics for different rotation crankshaft frequencies (from 600 to 3000 rpm) at different excess pressures in the exhaust process (from 0.05 to 0.2 MPa) as show in figure 1. The speed of the air flow ( $w$ ) and local heat transfer coefficient ( $\alpha_x$ ) was also determined.

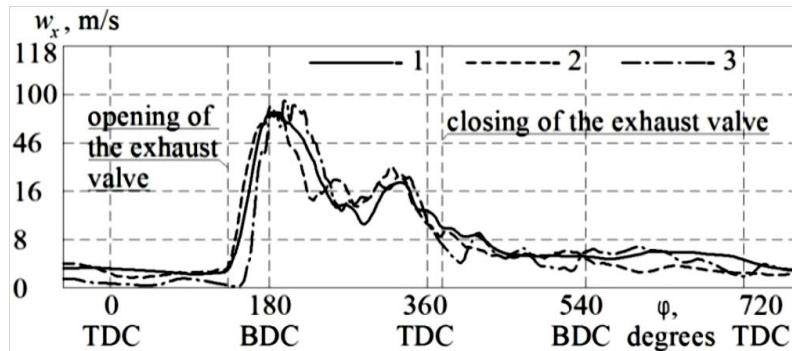


Figure 1 The dependences of the local ( $l_x = 140$  mm,  $d = 30$  mm) velocity of the gas flow  $w_x$  in the exhaust pipes of different cross-section from the crankshaft rotation angle  $\varphi$  at an initial excess pressure  $p_b = 0,2$  MPa and for the rotational speed  $n = 1500$  rpm. Cross section shape: 1 – circle; 2 – square; 3 – triangle [1]

Dependences of the local volumetric flow  $V_x$  through the exhaust pipe of different geometric shapes from the engine speed ( $n$ ) were obtained by processing the graphs of the gas flow rate for a particular engine cycle. The experimental points depending  $V_x = f(n)$  for different constant excess pressure before the valve are shown in Figure 2 (dependencies are approximated by linear functions).

Three typical phase diagrams can be provided for the exhaust pipe with a circular cross-section: I – section of the gas flow rate increase (from 600 to 1500 rpm); II – section of the constant gas flow rate (from 1500 to 2600 rpm); III – section of the recession (from 2600 rpm). Reduction of exhaust gas flow at high frequency rotations of the crankshaft is associated with the formation of these modes of stagnant areas in the outlet conduit and the reduction of gas-dynamic flow section.

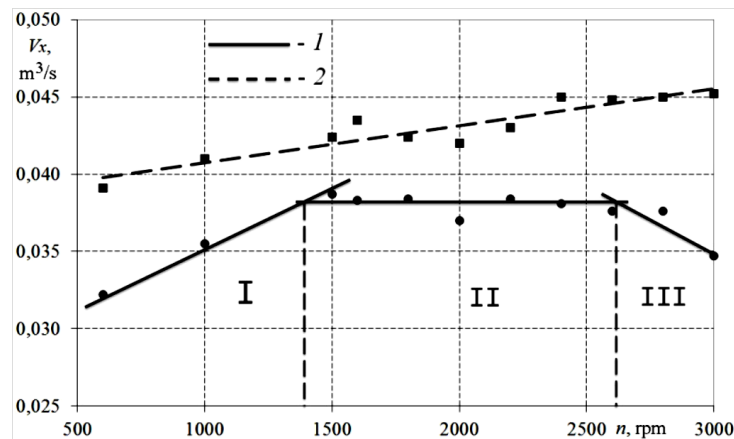


Figure 2 The dependences of the local volumetric flow of gases  $V_x$  through the exhaust pipes with different cross-sections from the rotational speed of the crankshaft  $n$  at an initial excess pressure  $p_b = 0,1$  Mpa. Cross section shape: 1 – circle; 2 – square [1]

The gas flow rate through the exhaust piping monotonically increases with the rotational speed. This continuous growth is due to the increase in the real engine cyclic pressure in the exhaust process, which leads to a decrease in engine specific work, also due to the stabilizing effect of the turbulent vortex structures formed in the corners of the square channel so the volumetric flow rate of air through the "square" exhaust pipe is greater on average by 25 % compared with a cylindrical



pipe. It should be noted that when determining the optimal geometric characteristics of exhaust systems of the engines (including the length and location of the profiled sections) should take into account the specifics of turbulent structures.

Marupilla Akhil Teja et al. [2] studied gasoline engine exhaust manifold using computational fluid dynamics, the partial differential equations (Euler equations, Navier-Stokes) been solved for the entire region, it has been presented that the research methodology depending on three-dimensional model of airflow in the outlet systems with the application of standard numeric methods.

The model may be the basis for performing changes in geometry of outlet system concerning minimizing the flow losses and shaping the dominant resistance has been affirmed in the space of direction change where the highest-pressure differences appear. This has been affirmed patchy distribution of pressure and velocity of fumes in the cross-section area of outlet ducting, which indicates the deficiencies in development of manifold. The result shows that maximum and minimum wall shear along the walls of exhaust manifold obtained are  $2 \times 10^7$  Pa and 3.77 Pa respectively. The increase of flow velocity appears in the field of manifold, which is the result of decreasing the field of section space. The conducted considerations suggest the necessity of changes in geometry of manifold. The Figure 3 shows that the static pressure of exhaust gases coming from the cylinder is varies with engine speed. The Figure 4 shows that velocity of the exhaust emission gases increases with the increase of engine speeds. The inhomogeneous flow at the end of exhaust manifold can produce the phenomenon of vortex flow and air separation, which cause the temperature distribution no uniform, also cause the carrier component damage, and then affect the engine's work.

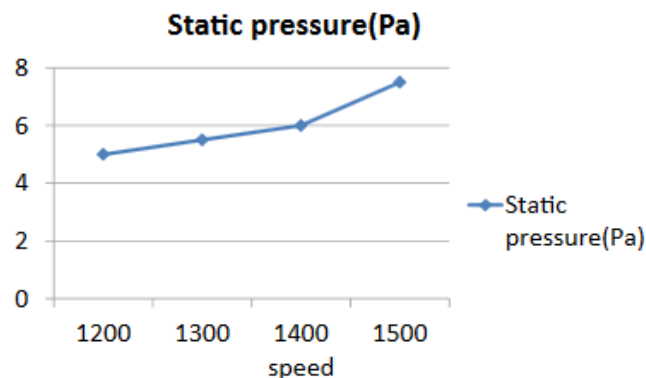


Figure 3 Static pressure versus speed [2]

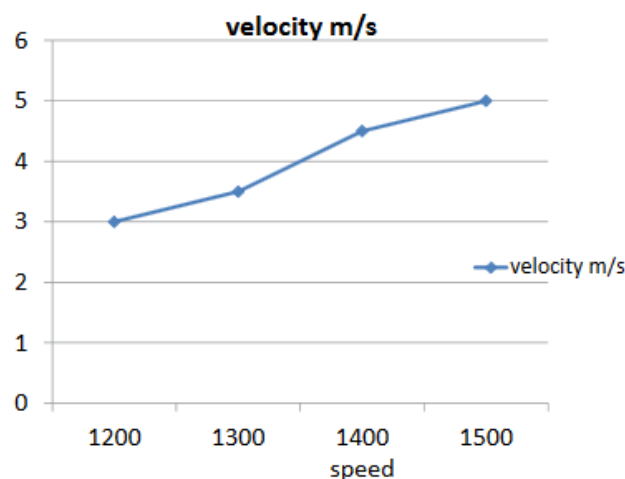


Figure 4 Velocity of gas versus engine speed [2]



This paper presents the modelling and analysis of four stroke - gasoline engine exhaust gas systems. An automotive example is considered whereby the pulsating exhausts gas flow through an exhaust pipe and silencer are considered over a wide range of speeds. Table 1 shows that the static pressure and the flow rate of exhaust gases coming from the cylinder is varies with engine speed.

Table 1 Wall shear [2]

Speed (rpm)	Flow rate (m <sup>3</sup> /s)	Static Pressure (Pa)×10 <sup>8</sup>	Turbulent Kinetic Energy (m <sup>2</sup> /s <sup>2</sup> )×10 <sup>7</sup>	Velocity (m/s)×10 <sup>4</sup>	Wall shear (Pa)×10 <sup>8</sup>
1200	3.143	5	3.6	3	20.8
1300	4.516	5.5	5.5	3.54	6.72
1400	4.981	6	3.5	4	18.5
1500	5.627	7.5	4	5	4.3

Investigation in CFD was performed on four parameters comprises manifold temperature, manifold pressure, exhaust piping system and exhaust gas velocity. Results of CFD simulation was showed in the form of pressure and velocity contours and streamline.

The engine causes the airflow in the exhaust manifold to oscillate with a frequency that is a multiple of the engine speed, as a result of the oscillating airflow, the pressure in the exhaust manifold will also oscillate. The exhaust manifold pressure is a crucial variable for an internal combustion engine, affecting the torque production and the emissions through variations in the mass flow and in the residual mass fraction in the cylinder. The gas flow velocity is the main basis for evaluating the gas wave propagation inside exhaust manifold. Kanupriya et al. [3] studied and identify the back pressure of an SI engine using alternative fuels. Traditional manifold optimization has been based on tests on the exhaust manifold. The research based on CFD analysis to determine flow and thermal characteristics. Figure 5 shows the pressure graph for three types of fuels (gasoline, alcohol and LPG), also velocity profiles and the temperature graph, of the exhaust manifold, it can be observed that the pressure and

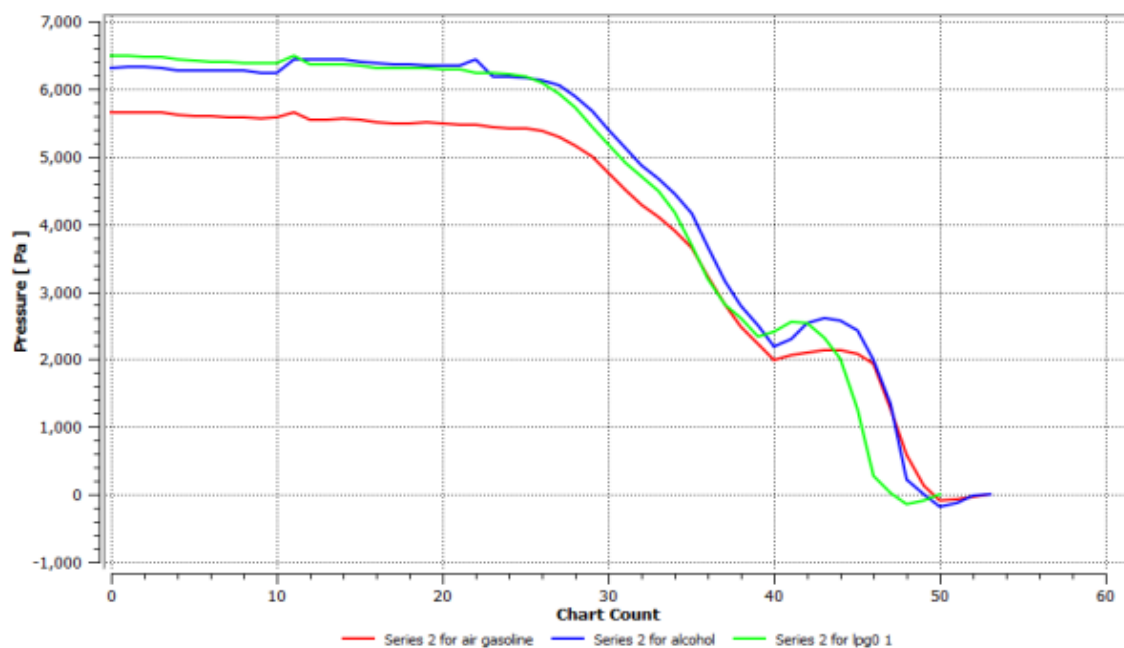


Figure 5 Pressure graph for gasoline, alcohol and LPG [3]



the temperature of flue gases in all the cases decrease as the gases proceed towards the outlet of the exhaust manifold. In some cases, the temperature rises due to collision and rubbing among the gas molecules as show in figure 6.

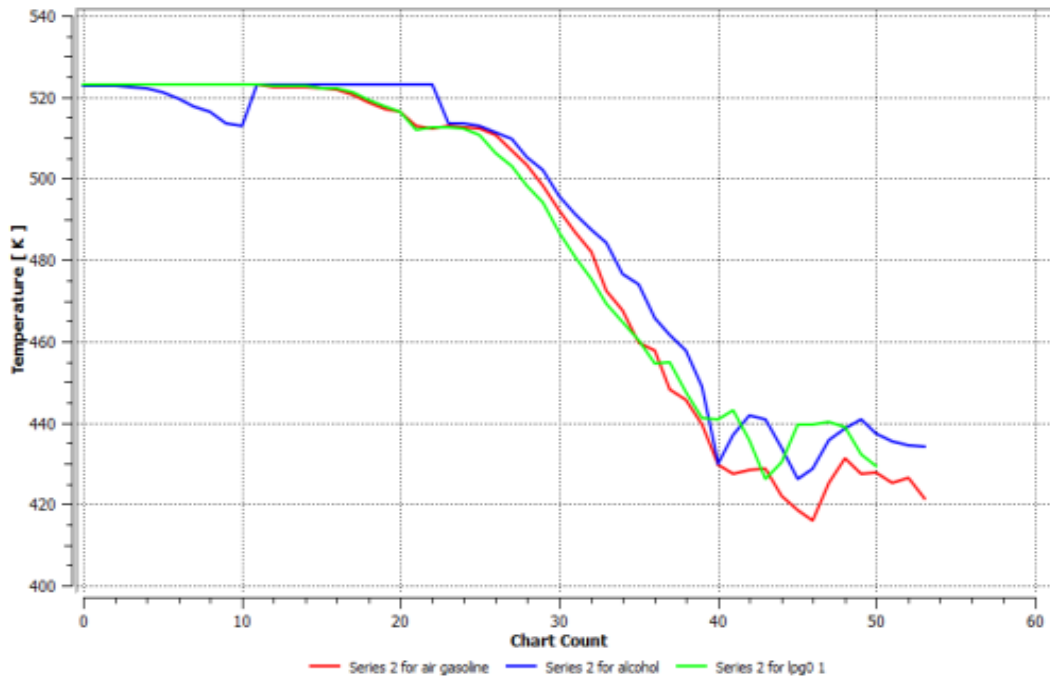


Figure 6 Temperature graph for gasoline, alcohol and LPG [3]

The velocities of the flue gases from all the three fuels remain almost identical at their respective positions in the duct as shows in figure 7. There is also some observable turbulence at the intersections of main duct and individual ducts from cylinders also near the end of the manifold due to mixing of gases and high velocity.

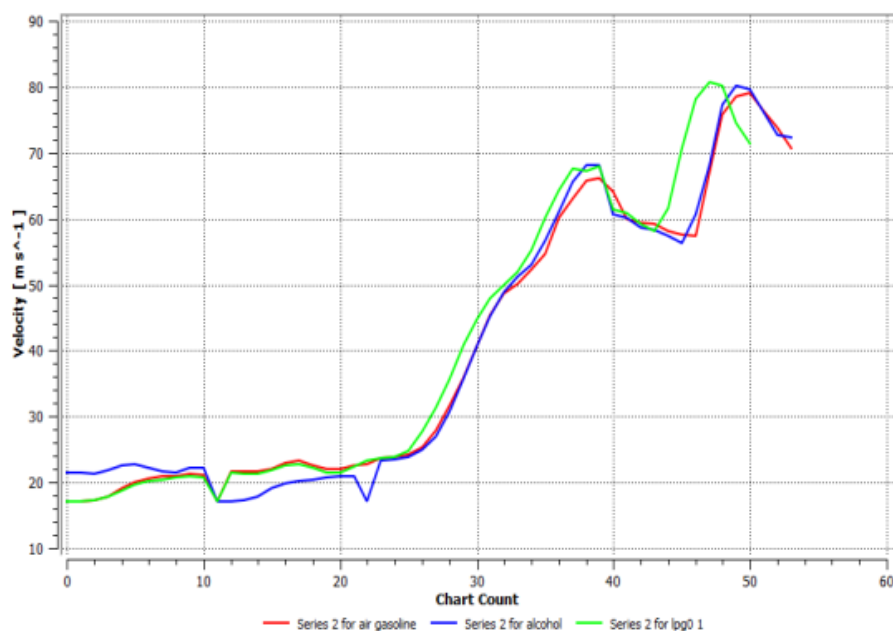


Figure 7 Velocity graph for gasoline, alcohol and LPG [3]



Durat et al. [4] carried out CFD and experimental analysis on thermal performance of exhaust system of a spark ignition engine. An experimental study was carried out to compare the CFD and heat transfer analysis of gas flow in the exhaust pipe. In the experiments, the temperatures at inlet and outlet of the exhaust pipe were measured and the study 3-D transient CFD analysis has been performed for the whole exhaust pipe. In this paper, SolidWorks flow Simulation is used to simulate the structure of a certain type of engine. It is convenient and intuitive to analyse the three-dimensional model of the exhaust pipe, the analysis process is visual, and easy to adjust the parameters, the analysis results were intuitive, determine whether the structure meets the design requirements quickly. Also, Shear Stress Transport (SST) turbulence model was used in this work. Turbulence models based on the RANS equations are known as Statistical Turbulence Models due to the statistical averaging procedure employed to obtain the equations, it accounts for the transport of the turbulent shear stress and gives highly accurate predictions of the onset and the amount of flow separation.

The Reynolds Averaged Navier-Stokes (RANS) transport equation is [4]:

$$\frac{\partial P}{\partial t} + \frac{\partial}{\partial x_j}(\rho U_j) = 0 \quad (1)$$

$$\frac{\partial \rho U_j}{\partial t} + \frac{\partial}{\partial x_j}(\rho U_i U_j) = -\frac{\partial \rho}{\partial x_i} + \frac{\partial \rho}{\partial x_i} + \frac{\partial}{\partial x_j}(\tau_{ij} - \rho u_i u_j) + S_m \quad (2)$$

Where:

$u$ : Fluctuating velocity component,  $m\ s^{-1}$

$\tau$ : Molecular stress tensor,  $kg\ m^{-1}s^{-2}$

$S_m$ : Momentum source,  $kg\ m^{-2}s^{-2}$

$\rho$ : Density,  $kg\ m^{-3}$

$P$ : Pressure, Pa

$t$ : time, s

$U$ : Averaged velocity component,  $m\ s^{-1}$

The continuity equation has not been altered but the momentum and scalar transport equations contain turbulent flux terms additional to the molecular diffusive fluxes. These are the Reynolds stresses,  $\rho u_i u_j$  [4]

$$-\rho u_i u_j = \mu_t \left( \frac{\partial u_i}{\partial x_j} + \frac{\partial u_j}{\partial x_i} \right) - \frac{2}{3} S_{ij} (\rho k + \mu_t \frac{\partial U_k}{\partial x_k}) \quad (3)$$

Where:

$\mu_t$ : The eddy viscosity or turbulent viscosity,  $kg\ m^{-1}\ s^{-1}$ , which must be modeled. RANS energy equation is:

$$\begin{aligned} & \frac{\partial \rho h_{tot}}{\partial t} - \frac{\partial P}{\partial t} + \frac{\partial}{\partial t} + \frac{\partial}{\partial t}(\rho U_j h_{tot}) \\ & = \frac{\partial}{\partial x_j} \left( \lambda \frac{\partial t}{\partial x_j} - \rho u_j h \right) + \frac{\partial}{\partial x_j} [U_i (\tau_{ij} - \rho u_i u_j)] + S_E \end{aligned} \quad (4)$$

Where:

$h_{tot}$ : is total enthalpy,  $m^2\ s^{-2}$

$\lambda$ : Thermal conductivity,  $kg\ m\ s^{-3}K^{-1}$

$S_E$ : Energy source,  $kg\ m^{-1}s^{-3}$

$$h_{tot} = h + \frac{1}{2} U_i^2 + k \quad (5)$$

where:

$k$ : is turbulent kinetic Energy,  $m^2\ s^{-2}$



$$k = \frac{1}{2} u_i^2 \quad (6)$$

Hussain et al. [5] also studied experimentally and numerically, the flow characteristic in inlet and exhaust manifolds of single cylinder spark ignition engine by using FLUENT software package to accomplish this research work, the main parameter that affects the flow in pipes and inside the cylinder. Pressure, temperature and flow pattern are the outputs of the programs. The pressure, temperature and velocity variations in the cylinder with respect to crank angle during gas exchange in the inlet manifold are shown in figure 8a-c, and during gas discharge in the exhaust manifold for an engine speed (2500 rpm) are shown in Figure 9a-c. It is observed that most graphs exhibit almost similar characteristics between numerical and experimental magnitudes at engine speed (2500 rpm).

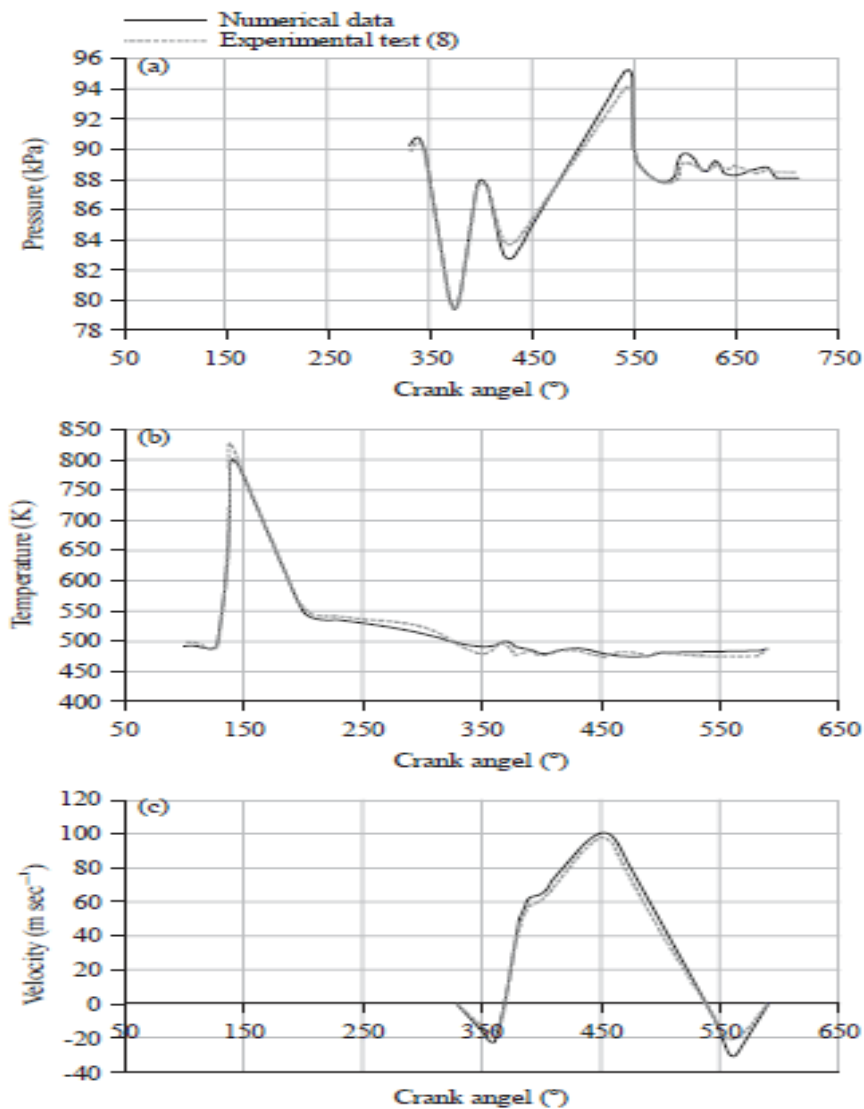


Fig. 8(a-c): (a) Pressure, (b) Temperature and (c) Velocity distribution in the cylinder with respect to crank angle during gas discharge in the exhaust manifold [5]

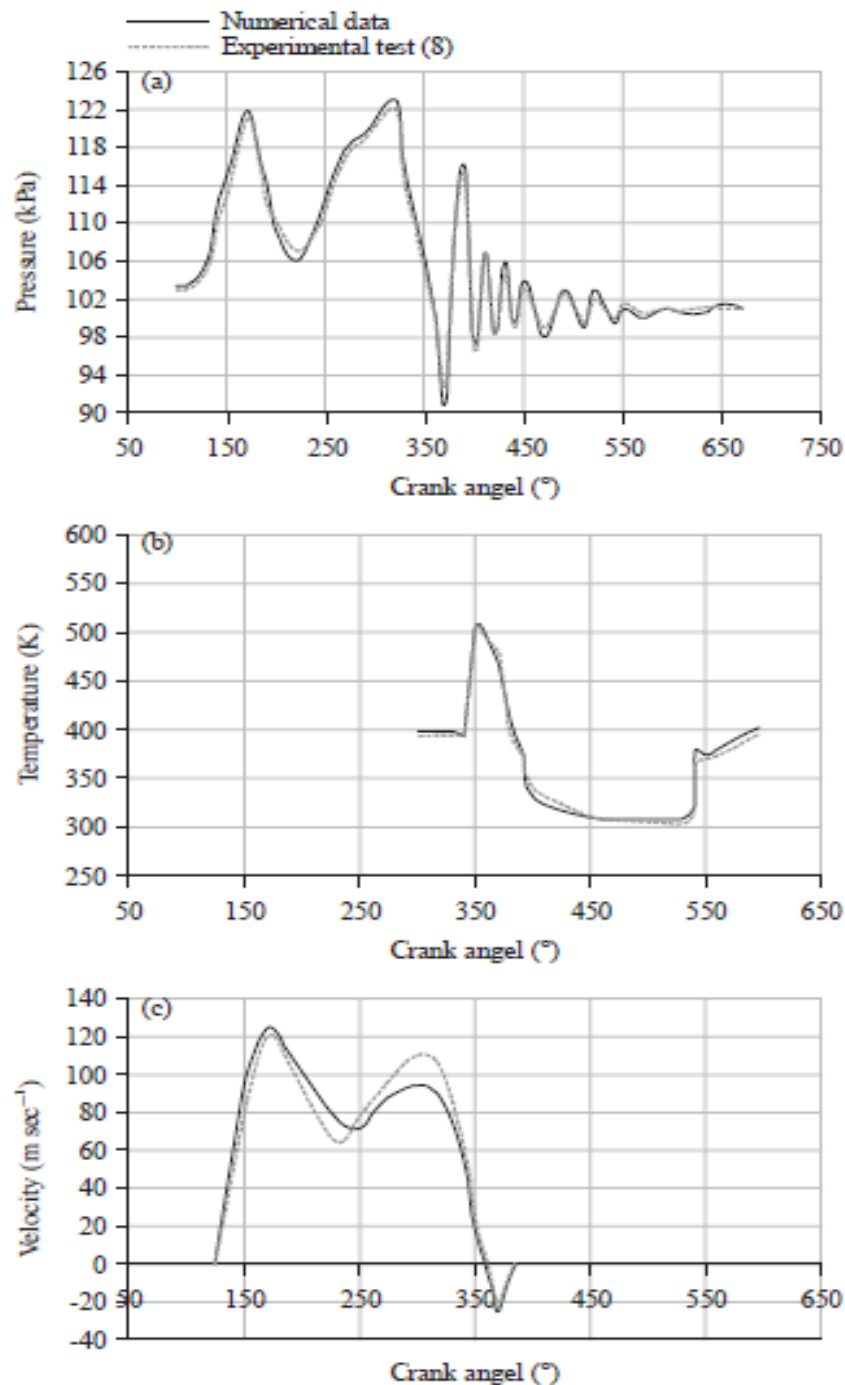


Figure 9 (a-c): (a) Pressure, (b) Temperature and (c) Velocity distribution in the cylinder with respect to crank angle during gas discharge in the exhaust manifold [5]

Liu et al. [6] studied the compatibility of automotive exhaust thermoelectric generation system, catalytic converter and muffler. The research work tried to vary the installation position of thermoelectric generator and proposed three different locations. They identified the three positions for installation of thermoelectric generator as location at the end of exhaust system, location between catalytic converter and muffler and location at upstream of catalytic converter and muffler. Simulation and experiment were developed to compare thermal uniformity and pressure drop characteristics over the three operating cases. From the simulation and experiment, heat exchanger in case location between catalytic converter and muffler obtained more uniform flow distribution,



higher surface temperature and lower back pressure than in other cases. At the same time, the catalytic converter and muffler could keep normal working in case location between catalytic converter and muffler, providing a theoretical and experimental basis for the exhaust gas waste heat recovery system.

Dattatray et al. [7] studied the thermal analysis for motor bike exhaust silencer for ensuring reduction in hot spot through design improvement. They design the silencer made with hot spot reduction and made improvement in the life of the components of exhaust system. They used high temperature heat resistance powder coating for mufflers of automobile application with enhanced aqueous corrosion, high temperature corrosion which started from the generation of the hot spot at front end of muffler. They analysed the modified design of silencer for heat transfer and proposed best suitable solution for reduction in hot spots in the exhaust sub-system.

Saider et al. [8] studied the various technologies to recover exhaust heat from internal combustion engine. The focus of the study is to review the latest developments and technologies on waste heat recovery of exhaust gas from internal combustion engine. This research includes thermo - electric generators, organic Rankine cycle, six stroke cycle internal combustion engine and new development in turbocharger technology.

Petkovic et al. [9] carried out experimental verification of developed mathematical model of the heat transfer in exhaust system. They developed 1-D mathematical model of unsteady heating up of the exhaust system parts. Experimental investigations carried out to measure temperature at various locations on the exhaust pipe for different gas flow rates. The gas was air supplied by a compressor. The calculation was carried out in gas dynamics software package Solid works and Flow works, which uses a finite volume method, the movement of the fluid is modelled by the Navier-Stokes equations.

Martins et al. [10] studied the internal combustion engine cooling at different operating condition by means of heat pipes for recovery of thermoelectric exhaust energy. They used thermoelectric generator for exhaust system at the hot source that is exhaust pipe for electric generation in automotive application. Sorin et al. [11] presented a study estimating the instantaneous character of heat transfer coefficient in exhaust pipes for the continuous and intermittent flows. The experimental results show that for the same mean mass flow, the heat transfers in the case of an intermittent flow are 20 to 40 percent higher than those which prevail in the continuous flow case. Estimation of instantaneous heat transfer coefficient in the entrance region of cylindrical channel seat of an intermittent gas flow. The authors concluded that, transient solution of the heat transfer equations was necessary to find out the instantaneous character of heat transfer coefficient.

Kar et al. [12] studied the method of measuring the instantaneous exhaust gas temperature by thermocouples. Thermocouples do not measure the instantaneous exhaust gas temperature because of their limited dynamic response. A thermocouple compensation technique has been developed to estimate the time constant in situ. This method has been commissioned in a simulation study and a controlled experiment with a reference temperature. The studies have shown that the signal bandwidth must be restricted, since noise will be amplified in the temperature reconstruction. The technique has been successfully applied to some engine exhaust measurements.

Kilicarslan et al. [13] experimentally performed in terms of engine speed at laboratory conditions by using of an exhaust gas analyzer and the special software called (NetDyn) and (WinDyn). The exhaust gas temperature and excess air coefficient are also measured as a function of the engine speed during the experiments. The variation of exhaust gas temperature with engine speed is depicted in Figure 10.

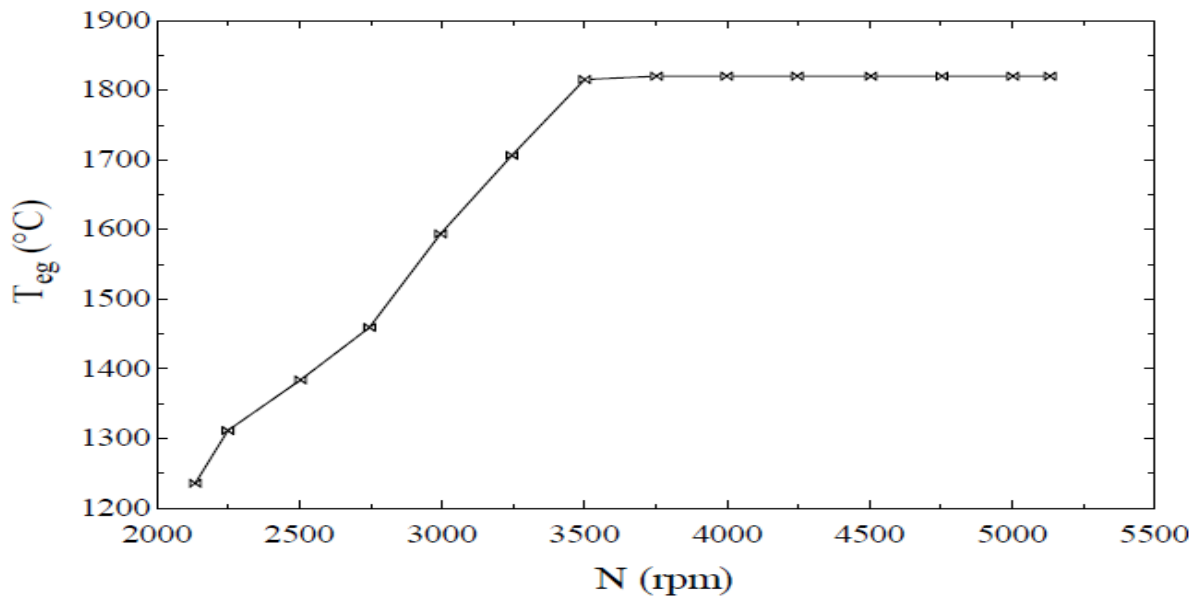


Figure 10 Exhaust gas temperature with engine speed [13]

The exhaust gas temperature raises with engine speed, reaches to the highest value of 1820°C at an engine speed of 3751 rpm and it remains constant beyond this speed. Zidat et al. [14] studied a basic heat transfer analysis to assess and rank the relative impact of thermal mass, external heat insulation and internal gas flow on the exhaust manifold outlet temperature. Using a simple heat balance in the exhaust manifold, the importance of exhaust gas flow is highlighted. They reported that an increase in wall thickness will increase the mass and the external heat transfer (through the increase of the external diameter) but will not change the internal heat transfer. According to the model, an increase in the internal diameter will decrease the internal heat transfer and will also increase the mass and the external heat transfer. Finally, the air gap case will reduce the external heat transfer and will increase the overall mass of the exhaust manifold. The effect of changes in internal heat transfer is more than ten times the effect of mass or external insulation changes during the first 15 seconds of a cold start.

### 3. MATHEMATICAL MODEL

The equations governing the fluid flow and determining the velocity, temperature profiles, and other parameters when analyzed in the pipe, results in complex calculations and hard analytical solution. This problem can be mitigated with the adoption of numerical methods, such as finite difference method (FDM) and finite volume method (FVM). FDM is a numerical method generally used to study heat transfer and fluid flow dynamics. In the analysis of exhaust systems, the FDM has been employed to verify the energy availability of exhaust. The exhaust gas fluid flow and heat transfer was simulated via FDM to design optimization of the exhaust system. Jianmin et al. [15] used mathematical equations for describing the flow field of entire exhaust system were analysed. The study provides a theoretical basis for designing complex system.

#### 3.1 Governing Equations

Under the condition of multidimensional compressible steady flow, the mass and momentum conservation equation are as follows [15]:



$$\frac{\partial}{\partial x_j} (\rho u_j) = 0 \quad (7)$$

$$\frac{\partial}{\partial x_j} (\rho u_j u_i - \tau_{ij}) = -\frac{\partial p}{\partial x_i} + S_i \quad (8)$$

Where  $S_i$  is the source term, which represent the catalytic converter resistance.  $\tau_{ij}$  is the stress tensor, for Newtonian flow described as follows:

$$\tau_{ij} = 2\mu(S_{ij} - \frac{1}{3}\frac{\partial u_k}{\partial x_k}S_{ij}) - \rho\overline{u_i u_j} \quad (9)$$

Where  $\mu$  is the molecular dynamic viscosity coefficient;  $\delta_{ij}$  is Kroneker number;  $\rho\overline{u_i u_j}$  is Reynolds stress tensor. The fluid deformation rate tensor is given by the following formula:

$$S_{ij} = \frac{1}{2}\left(\frac{\partial u_i}{\partial x_j} + \frac{\partial u_j}{\partial x_i}\right) \quad (10)$$

### 3.2 Turbulence Model

Using a standard  $k - \varepsilon$  model to calculate the Reynolds stress to solve the flow control equations above [15]:

$$\rho\overline{u_i u_j} = -2\mu S_{ij} + \frac{2}{3}(\mu_i \frac{\partial u_k}{\partial x_k} \rho k) \delta_{ij} \quad (11)$$

where  $\mu_\tau$  is the turbulent viscosity, given by the following formula:

$$\mu_\tau = \frac{C_\mu \rho k^2}{\varepsilon} \quad (12)$$

$k - \varepsilon$  are turbulent kinetic energy and turbulent energy dissipation rate respectively. Their transport equations are:

$$\begin{aligned} \frac{\partial}{\partial x} \left( \rho \mu_j k - \frac{\mu_{eff}}{\sigma_k} \frac{\partial k}{\partial x_j} \right) &= \mu_\tau S_{ij} \frac{\partial u_i}{\partial x_j} - \rho \varepsilon - \frac{2}{3} \left( \mu_\tau \frac{\partial u_i}{\partial x_i} + \rho k \right) \frac{\partial u_i}{\partial x_j} \\ \frac{\partial}{\partial x_j} \left( \rho \mu_j \varepsilon - \frac{\mu_{eff}}{\sigma_\varepsilon} \frac{\partial \varepsilon}{\partial x_j} \right) &= C_{\varepsilon 1} \frac{\varepsilon}{k} \left\{ \mu_\tau S_{ij} \frac{\partial u_i}{\partial x_j} - \frac{2}{3} \left( \mu_\tau \frac{\partial u_i}{\partial x_i} + \rho k \right) \frac{\partial u_i}{\partial x_i} \right\} \\ &\quad - C_{\varepsilon 2} \rho \frac{\varepsilon^2}{k} + C_{\varepsilon 4} \rho \varepsilon \frac{\partial u_i}{\partial x_i} \end{aligned} \quad (13)$$

In the formula above  $\mu_{eff} = \mu + \mu_\tau$  ; The empirical coefficients  $C_\mu, \sigma_k, \sigma_\varepsilon, C_{\varepsilon 1}, C_{\varepsilon 2}, C_{\varepsilon 4}$  of determined according to Table 2.

Table 2 Coefficient of experience [15]

$C_\mu$	$\sigma_k$	$\sigma_\varepsilon$	$C_{\varepsilon 1}$	$C_{\varepsilon 2}$	$C_{\varepsilon 4}$
0.09	1.0	1.22	1.44	1.92	-0.33

## CONCLUSION

The following conclusions can be drawn:

The study of CFD analysis on the effects of exhaust gas behaviour generated in exhaust system of 4-stroke gasoline engine, provided a knowledge to the designer and researcher in the internal combustion field.

Maximum velocity of flue gases is achieved near the outlet of exhaust manifold as the pressure at that position is low so the gases rush out of the exit of the duct.



This study was confirming that the changes of overall length of exhaust piping, numbers of bend pipes/elbow is directly affecting the rise of backpressure and a tad drop in efficiency of power generation.

These investigations shown the effect of back pressure where it is an undesired effect because as the back pressure increases so does the amount of gas residuals in the cylinder head, therefore, impedes the efficiency of the induction process.

The literatures prove that the wave action decrease the gas temperature inside exhaust system.

## REFERENCES

- [1] L.V. Plotnikov, B.P. Zhilkin, Yu.M. Brodov.: *The Influence of Cross-profiling of Inlet and Exhaust Pipes on the Gas Exchange Processes in Piston Engines*. ICIE., 2016.
- [2] Teja MA, Ayyappa K, Katam S, Anusha P.: *Analysis of Exhaust Manifold using Computational Fluid Dynamics*. Fluid Mech Open Acc 3: 129., 2016.
- [3] Kanupriya Bajpai, A. Chandrakar, A. Agrawal, S. Shekhar.: *CFD Analysis of Exhaust Manifold of SI Engine and Comparison of Back Pressure using Alternative Fuels*. JMCE., 2017.
- [4] Durat, M., Parlak, Z., Kapsiz, M., Parlak, A.: *CFD and experimental analysis on thermal performance of exhaust system of a spark ignition engine*”, Journal of Thermal Science and Technology, Vol. 33(2), pp.89-99, 2013.
- [5] Hussain H. Al-Kayiem, Hasanain A. Abdul Wahhab and A. Rashid A. Aziz.: *Computational Analysis of Flow Characteristic in Inlet and Exhaust Manifolds of Single Cylinder Spark Ignition Engine*. Asian Journal of Applied Sciences, 10: 102-115., 2017.
- [6] Liu, X., Deng, Y. D., Chen, S., Wang, W. S., Xu, Y., Su, C. Q.: *A case study on compatibility of automotive exhaust thermoelectric generation system, catalytic converter and muffler*. Case Studies in Thermal Engineering, Vol. 2, pp.62–66, 2014.
- [7] Dattatray, D. G., Shinde, V. B., Kulkarni, S. S.: *Thermal analysis for motor bike exhaust silencer for ensuring reduction in hot spots through design enhancement*. International Journal of Advanced Engineering Research and Studies, Vol. II/ IV, pp.134-137., 2013.
- [8] Saidur, R., Rezaei, M., Muzammil, W. K., Hassan, M. H., Paria, S., Hasanuzzaman, M.: *Technologies to recover exhaust heat from internal combustion engines*. Renewable and Sustainable Energy Reviews, Vol. 16, pp.5649–5659., 2012.
- [9] Petkovic, S., Pesij, R., Lukic, J.: *Experimental verification of mathematical model of the heat transfer in exhaust system*. Thermal science, Vol. 15(4), 1035-1048., 2011.
- [10] Martins, J., Brito, F. P., Goncalves, L. M., Antunes, J.: *Thermoelectric energy recovery with temperature control through heat pipes*. SAE paper 01-0315., 2011.
- [11] Sorin Anthony, Bourouga, Brahim & Anthoine, Pierre.: *Experimental study of periodic heat transfer coefficient in the entrance zone of an exhaust pipe*. International Journal of Thermal Sciences, 47.1665–1675., 2008.
- [12] Kar, K., Roberts, S., Stone, R., Oldfield, M.: *Instantaneous Exhaust Temperature Measurements Using Thermocouple Compensation Techniques*. SAE paper 01-1418., 2004.
- [13] Ali Kilicarslan and Mohamad Qatu.: *Exhaust gas analysis of an eight-cylinder gasoline engine based on engine speed*. 14-16, ICEP., 2016.
- [14] Zidat, S., and Parmentier, M.: *Exhaust Manifold Design to Minimize Catalyst Light-off Time*. SAE paper, 01, 0940.,2003.
- [15] Jianmin Xu and Shuiting Zhou.: *The Analysis for Flow Field of Automotive Exhaust System Based on Computational Fluid Dynamic*. The Open Mechanical Engineering Journal, 20, 8, 587-593., 2014.



## THERMAL SPRAYED AND LASER REMELTED WEAR RESISTANT NICRBSI COATINGS

<sup>1</sup>MOLNÁR András, <sup>2</sup>BUZA Gábor PhD, <sup>3</sup>FAZEKAS Lajos PhD, <sup>3</sup>PÁLINKÁS Sándor PhD,  
<sup>3</sup>BATTÁNE GINDERT-KELE Ágnes PhD

<sup>1</sup>University of Miskolc

E-mail: [a.molnar2007@gmail.com](mailto:a.molnar2007@gmail.com)

<sup>2</sup>BAYATI Budapest

E-mail: [buzabzaka.hu](mailto:buzabzaka.hu)

<sup>3</sup>Department of Mechanical Engineering, Faculty of Engineering, University of Debrecen

E-mail: [fazekas@eng.unideb.hu](mailto:fazekas@eng.unideb.hu), [palinkassandor@eng.unideb.hu](mailto:palinkassandor@eng.unideb.hu), [battane@eng.unideb.hu](mailto:battane@eng.unideb.hu)

### Abstract

The paper describes the some differences of laser coating (laser cladding or laser spraying) process in comparison to thermal spraying. Laser coating is a novel coating process, which produces coatings with high density, metallurgical bonding and low heat input to the substrate. Laser coating types and coating properties are reviewed and compared with thermally sprayed coatings. Typical application areas of laser coatings are presented.

**Key Words:** laser coating, HPDDL surface treatments

### 1. INTRODUCTION

Laser coating, also referred as “laser cladding” or “laser spraying” (note: in this paper the process is called laser coating), is an advanced coating technology for improving surface properties of various components and equipment

Table 1 Comparison of Thermal Spraying and Laser Coating

Process	Thermal Spraying	Laser Coating
Heat Source	Combustion Flame, Electric or Plasma Arc	High Density Laser Radiation
Bond Strength	Low to Moderate*	High Metallurgical bonding
Coating Structure	Lamellar; from porous to nearly Dense*	Dense; Crack and pore free layers
Heat Load to Workpiece	Wery low to moderate*	Low to moderate
Dilution	Nil	Low
Coating thickness	0.05 – some mm' s	Typically 0.5 – 3 mm
Coating Materials	Wide Range of metals, alloys, Hardmetal, Ceramics, Polimers	Metal And Alloys; with hard particles; hardmetals; Ceramics
Productivity	Low to High*	Low to Moderate/(high)*
Cost	Low to High	Moderte to High

\*Depends on type of Process.

These coatings have extremely dense, crack-free and non-porous microstructures (Table 1.). Laser coatings show also excellent metallurgical bonding to the base material, have uniform composition and coating thickness. Laser coating produces also very low dilution and low heat input to the



component [1-3]. Table 1 compares the characteristics of laser coating with thermal spraying. It is apparent that such characteristics as:

- high intensity, focusable and controlled heat source
- excellent coating properties obtained
- low dilution (min. 1-5 %)
- minimum changes in base material due to low heat load
- controlled coating thickness
- reasonable productivity and cost make laser coating attractive for industrial coating of new components and in repair.

Laser coating of new components gives them surfaces with high resistance against wear, corrosion and high temperatures.

Besides new manufacturing, the process has shown its importance also in maintenance and repair of worn components, often resulting in component performances superior to those of uncoated ones. Research and development of laser coating processes, properties of coated structures, and industrial applications has been very active during the last years f.ex. in Finland, primarily due to the rapid development of high power laser technology and recent launching of industrial laser coating activity. Industrial use of laser coatings is expected to increase markedly during the following next years.

## 2. LASER COATING AS A COATING PROCESS

### High power lasers for surface treatments

Several basic properties of lasers make them very useful for a number of industrial applications including laser materials processing. These properties include directionality, monochromaticity, coherence, and high brightness of the laser light. Laser equipment operating with high power levels, i.e. the “high power lasers”, can produce highly energetic and well focusable laser beams that are usable in marking, drilling, cutting, welding, hardening and laser coating.

Table 2 presents the characteristics of different type of high power lasers available for materials processing. Carbon dioxide (CO<sub>2</sub>) lasers are the most traditional high power lasers and are available in power levels up to several tens of kilowatts. CO<sub>2</sub> lasers have characteristics of very high power and power density, moderate efficiency, reliable operation and excellent beam quality (low “beam-parameter-product” number).

*Table 2 High power lasers for laser materials processing*

Property	CO <sub>2</sub>	Nd:YAG Lp	Nd:YAG Dp	HPDL
Wavelength [μm]	10.6	1.06	1.06	0.8 – 0.94
Efficiency [%]	5 - 10	1 - 3	10 - 12	30 - 50
Power max. [kW]	40	4	4	8,5
Average power density [W/cm <sup>2</sup> ]	10 <sup>6-8</sup>	10 <sup>5-7</sup>	10 <sup>8-9</sup>	10 <sup>3-5</sup>
Service period [h]	2000	200	10000	10000 - 20000
Fiber coupling	No	Yes	Yes	Yes
Beam parameter product [mm x mrad]	12	25 - 45	12	100 - 1000

Lp lamp pumped, Dp Diode pumped



The high wavelength of 10.6 mm results in a relative low absorption of the laser beam by metals, e.g. steels. It is common that an absorption enhancing pretreatment, such as graphitizing of the metal surface, is frequently needed in laser transformation hardening of steel surfaces by a CO<sub>2</sub> laser.

### 3. DIODE LASER CLADDING ADVANTAGES

High-power diode laser systems offer unique advantages for cladding compared to other currently available technology.

When compared to arc welding methods, diode laser systems offer lower heat distortion, reduced dilution (typically < 4%), lower porosity (< 1%) and better surface uniformity. Together, these properties largely eliminate the need for post-processing and its associated time and monetary expense. The high quench rate of the diode laser produces a finer grain structure in the clad leading to better corrosion resistance. Furthermore, these benefits generally apply at any power level and hence, deposition rate; unlike most arc welding processes, in which clad quality suffers with increasing power and deposition rate.

Finally, the line beam shape of the free-space laser can process large areas rapidly with a high degree of control over clad width and thickness. Both the diode laser and thermal spraying techniques avoid significant heat input into the part and minimize dilution (Table 3.).

Table 3 High-power diode laser systems offer unique advantages for cladding compared to other currently available technology

Cladding process	Power [kW]	Deposition Rate [lb/hr]	Efficiency [lb/kW x h]	Heat input Distortion	Notes
<b>Submerged Arc Welding (SAW)</b>	32	50	1.6	20	1000 A x 32 V 7/32" Wire
<b>Gas Metal Arc Welding (GMAW)</b>	17	15	0.9	10	500 A x 30 V 3/32" Wire
<b>Gas Tungsten Arc Welding (GTAW)</b>	10	15	1.5	8	500 A x 15 V + „Hot Wire” Power
<b>Plasma Arc Welding (PAW)</b>	10	15	1.5	3	500 A x 15 V + „Hot Wire” Power
<b>High Power Diode Laser (HPDL)</b>	8,5	8	2	1	Powder cladding Rate, Expect Greater Efficiency and Higher Deposition with „Hot Wire” Power and „Hot Wire” Power 2

However, unlike thermal spraying, diode laser cladding forms a true metallurgical bond with the base material. The result is better adhesion and wear resistance. Furthermore, metallurgically



bonded clads produced with the diode laser limit the cracking and de-lamination most often associated with mechanical coatings.

When compared to other lasers, diode laser (Figure 1) systems offer superior output characteristics and also a number of practical advantages. One reason for this is that the shorter wavelength output of the diode laser is better absorbed by cladding materials than the light of the Nd:YAG and especially the mid-infrared CO<sub>2</sub> laser. This means that a diode laser can melt a given clad material using substantially less output power than a CO<sub>2</sub> laser.

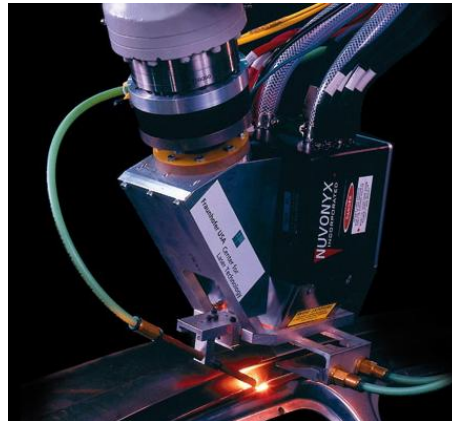


*Figure 1* High power diode laser in operating

In addition, diode lasers offer a substantial cost advantage over other laser types. One reason for this is that their electrical efficiency (conversion of input electrical energy to useful light output) is four times higher than for CO<sub>2</sub> lasers, about three times higher than diode-pumped Nd:YAG lasers and nearly twice that of currently available fiber lasers. When combined with the higher absorption rate this translates into lower operating costs, a smaller carbon footprint and increased deposition efficiency.



*Figure 2* Complete modern HPDDL system (Coherent Highlight 8000)

Power costs are further reduced because the diode laser has instant “on” capability, meaning there is no standby power consumption (Figure 2.). Even larger savings results from reduced maintenance costs which are orders of magnitude less for the diode as compared to other lasers.

Maintenance downtime is also minimized because the physically compact diode laser can be more rapidly replaced than bulkier laser type, and replacements can even be shipped via expedited courier services.



#### 4. MICROSTRUCTURE OF COATING

Scanning electron microscope techniques with energy dispersive spectroscopy ZEISS EVO MA 10 instrument (SEM–EDS) were used to metallographic investigation and analyse the coatings microstructures (*Figure 3 – 4*). Specimens for micro-structural analysis were firstly ground and polished to a mirror finish and then etched with solution of 1HCl:10HNO<sub>3</sub>:10H<sub>2</sub>O. Figure 3 and 4 shows the structure obtained spraying and after laser remelting. It can be clearly seen that the matrix phase is a solid solution of Ni with some Cr and Fe providing a dendrite structure; there is an interdendrite lamellar eutectic phase made up mainly of Ni and small amounts of Si.

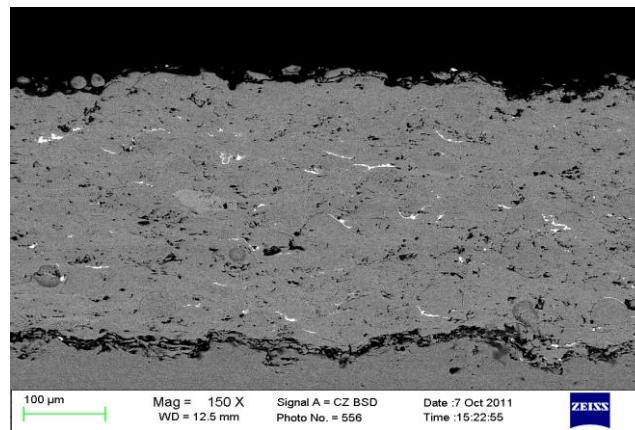


*Figure 3* HVOF thermal sprayed coating (M = 150x)

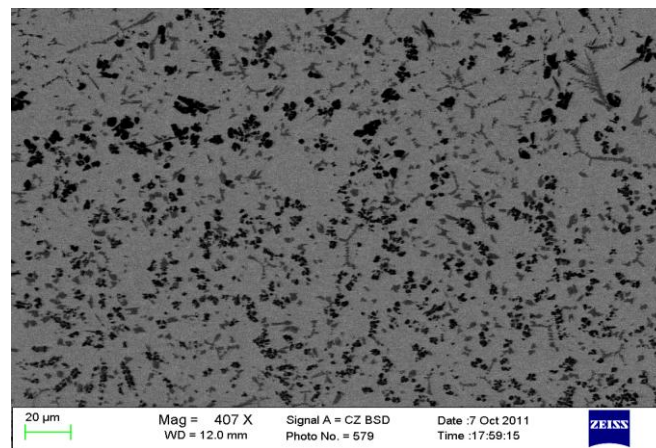


*Figure 4* Typical Results Laser remelted NiCrBSi coating (M = 407x)

#### SEM - EDXMA analysis

The UB5 - 2760 branded NiCrBSi dust-strewn and tested a laser beam remelted samples EDXMA SEM electron microscope method. The analysis EDXMA FS-sprayed and remelted samples with similar chemical composition. Figures 6 and shown in full section of the layer with a laser beam remelted layers chemical composition evolution. The contents of the analysis EDXMA conspicuous layers of high-Cr, which refers to the presence of hard phases.

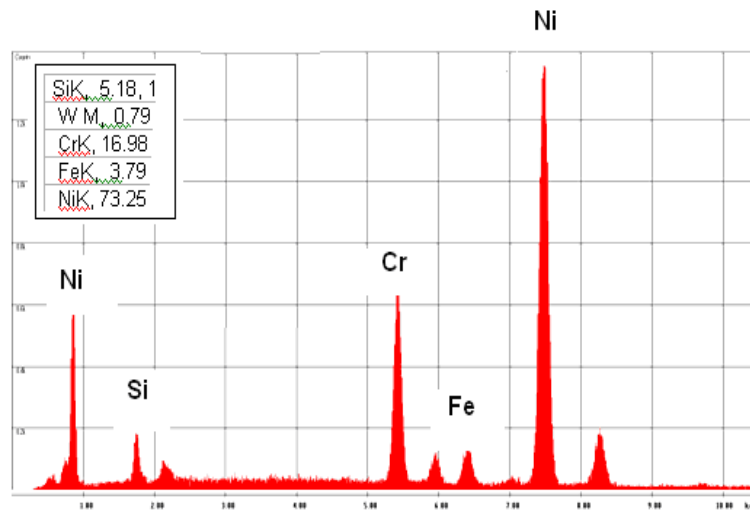


Figure 5 The USB-2760 laser beam remelted coating EDXMA Analysis

## 5. WEAR TESTS

Tests were carried out in a wear testing machine with a pin on disc configuration under dry sliding conditions without eliminating the debris formed (Figure 6.). Specimen and counter body were cleaned using methanol to avoid the presence of humidity and other non-desirable films such as grease. Most requirements of the ASTM standard G99-95 were followed (ASTM G99-95, 1995).

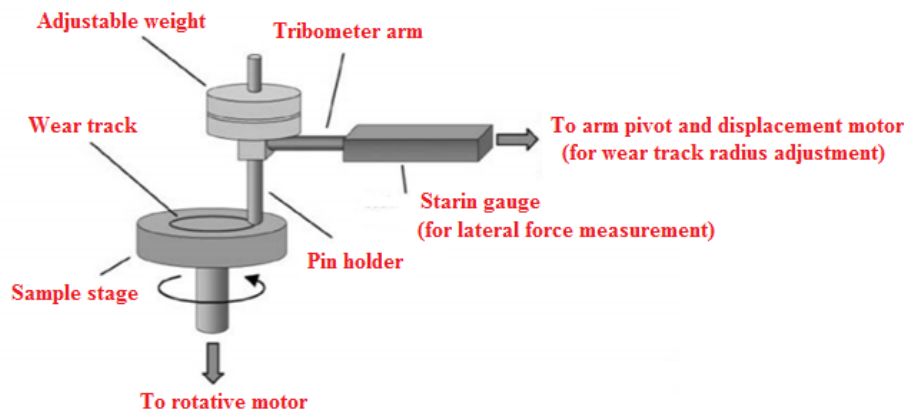


Figure 6 Wear test princip by ASTM G99-95, 1955

Cylindrical pins made of alumina (aluminium oxid) with diameter 3 mm. The cylinders were positioned in such a way that the nominal contact area was maintained constant during the tests in spite of the wear process. The disc, made of the coating under study, rotates horizontally at sliding speed of 1m/s. A dead weight loading system was used to perform the tests at nominal normal pressures of 16 MPa. The coefficient of friction was obtained by means of a torque transducer. The total sliding distance was 20.000 m. After the wear tests, the worn volume were calculated measuring the transversal area of the wear groove (A), by using SEM. The worn volume is calculated using the following equation:

$$V = 2\pi RA$$

where  $R$  is the distance between the centers of the disc and the pin. According to Archard law (Archard, 1953), the worn volume,  $V$ , is proportional to the sliding distance,  $L$  and the applied normal load,  $F$ :

$$V = kFL$$



where the proportionality constant  $k$ , is called specific wear rate and it is usually quoted in units of  $\text{mm}^3/\text{Nm}$  (Table 4.). It represents the volume of material removed by wear (in  $\text{mm}^3$ ) per unit of sliding distance (in m) and per unit of normal load (N). The measure of  $k$  is helpful for comparing wear rates of the coating (Figure 7.).

Table 4 Test results ( $k$ ) for different technologies

Technology	$k$ [ $\times 10^{-5}$ [ $\text{mm}^3/\text{Nm}$ ]]
HVOF FS	3.4
HVOF FS + laser remelting	4.4
Laser cladding	1.6

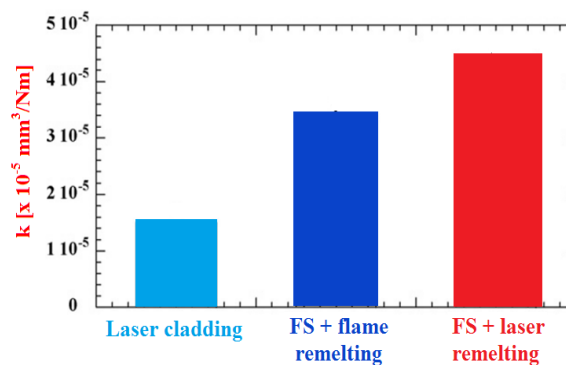


Figure 7 Wear coefficients  $k$  for the different coating technology

Table 5 Typical technological parameters at Coherent Highlight 4000L

Substrate material	Mild Carbon Steel
Cladding material	Hoganas C22 Hastelloy
Laser type	Coherent Highlight 4000L
Laser power	4 kW
Spot size	1 x 12 mm
Travel Speed	0.6 m/min
Powder Feed Rate	25 g/min
Step Size	8 mm
Clad Thickness	0.5 mm
Process notes	Helium cover gas

The following Figure 8. presents some typical cladding results obtained with Coherent HighLight diode lasers and should indicate the quality, capabilities and flexibility that can be readily obtained with this process technology.



Figure 8 Print Roller Shaft



# INTERNATIONAL SCIENTIFIC CONFERENCE ON ADVANCES IN MECHANICAL ENGINEERING

12-14 October 2017, Debrecen, Hungary



## CONCLUSIONS

All coatings show a similar microstructure composed mainly of a Ni solid solution matrix with dendrites structure and common phases precipitated on it with different distribution and size. Laser remelted coatings show a uniform distribution of small and rounded precipitates, which results in a harder material,

Results show that in situ laser remelting induces the growth of a dendrite microstructure that strongly decreases the HVOF FS-sprayed coating porosity,

*Wear behaviour* Laser Cladding coatings show higher wear resistance than HVOF FS and, especially HVOF FS + laser,

In particular, diode lasers produce a high quality clad with excellent physical characteristics and a true metallurgical bond, yet without the heat input into the part associated with non-laser remelting.

In addition, they are more economical to operate than other cladding laser sources and their small physical size and optional fiber delivery simplify their integration and use.

## ACKNOWLEDGEMENT

The publication is supported by the EFOP-3.6.1-16-2016-00022 project. The project is co-financed by the European Union and the European Social Fund.

## REFERENCES

- [1] P. Vuoristo<sup>1</sup>, J. Tuominen, J. Nurminen, Tampere University of Technology, Institute of Materials Science, Tampere Laser coating and thermal spraying - process basics and coating properties
- [2] Keith Parker Cladding with High Power Diode Lasers Sr. Business Development Direct Diode & Fiber Laser Systems
- [3] Coherent Adds High-Power From Saint Louis Coherent's latest acquisition strengthens the company's presence in the materials processing market.
- [4] E. Toyserkani, A. Khajepour, S. Corbin, Laser Cladding, CRC Press, 2005, 260 p.
- [5] J.F. Ready (ed.), LIA Handbook of Laser Materials Processing, Chapter 8: Surface Treatment: Glazing, Remelting, alloying, cladding, and cleaning, Laser Institute of America, 2001, p. 263-297.
- [6] S. Nowotny, S. Scharek, R. Zieris, T. Naumann, E. Beyer, Innovations in laser cladding, ICALEO 2000: Laser Materials Processing Conference; Dearborn, MI; USA; 2-5 Oct. 2000. pp. A11-A15.
- [7] J. Tuominen, P. Vuoristo, T. Mäntylä, S. Ahmaniemi, J. Vihinen, P. Andersson, Corrosion behavior of HVOF-sprayed and Nd-YAG laserremelted high-chromium, nickel-chromium coatings M, Journal of Thermal Spray Technology. Vol. 11, no. 2, pp. 233-243. June 2002
- [8] J. Tuominen, J. Laurila, J. Vihinen, P. Vuoristo, T. Mäntylä, L. Olausson, T. Peltola, Comparison of CO<sub>2</sub> and High Power Diode Laser (HPDL) Cladding, 21st International Congress on Applications of Lasers & Electro-Optics ICALEO 2002, October 14-17, 2002, Arizona USA, CDROM



## SIMULATION FRAMEWORK FOR PACKAGING DYNAMICS OF STACKED UNITS

*MOLNÁR Bence*

*Department of Logistics and Forwarding, Széchenyi István University, Győr*

*E-mail: [molnar.bence@sze.hu](mailto:molnar.bence@sze.hu)*

### **Abstract**

*The main goal of the packaging is to protect the products during the distribution from damage or destruction. The damages may occur many and varies hazards from the distribution environment. From these hazards, this study focus to the mechanical shock and vibration motion and these hazards simulation in the laboratory. The standards of the packaging testing are ignoring the simulation of the motion stacked packages upper layer. This paper main goal to draw attention to different motion between the upper and lower layer of stacked units and the stacked unit simulation is not properly solved.*

**Keywords:** *Packaging, Testing, Vibration, Stacked packaging*

### **1. INTRODUCTION**

The main goal of the packaging is to protect the products during the distribution from damage or destruction. The damages may occur many and varies hazards from the distribution environment, and in the packaging–product system occur significant financial disadvantages. But, on the other hand the over-packing solution can be a surplus and extra cost of the protection of product. [1] That is the reason of mapping the physical conditions during transportation by researchers, and new testing perspectives are carried out. The environmental hazard during the distribution may be climatic or mechanical hazards and their combination. The climatic hazard may be the combination of too high or low temperature and relative humidity. The most significant mechanical hazards the shocks and vibrations in addition the static load. This paper focuses on shock and vibration effect and their simulation in the laboratory.

The hazards of the distribution exactly predict is usually difficult or impossible. Many of previous study focus on the measurement of the vibration and shock properties of different distribution system. They measured the accelerations with a data logger on the load surface of the different transport vehicle on various shipping roots. From this data, the vibration power level depends on the type of the transport vehicle [2] and its suspension [3], speed and the payload, and not least the quality of the shipping route. [4] Important fact in these study that the measure point is located near the load surface of the transport vehicle therefore they focus only the vibration of the platform (*Figure 1*). As the *Figure 1* shows the motion in the upper layer of the packaging is not recorded in the most of researcher's papers.

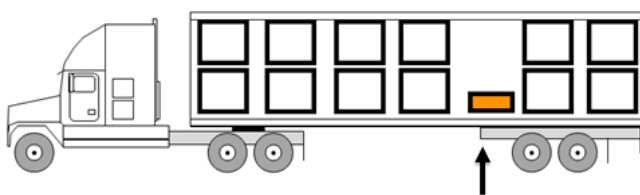


*Figure 1* Location of data logger for measurements as usual

In order to understand the motion of the stacked unit, field measurements are needed from the all of



layer during the distribution.

## 2. FUNDAMENTALS OF PACKAGING TESTING

As mentioned in the previous chapters the environmental hazards during the distribution can cause damages in the product-packaging system. Now this paper focus on the vibration and shock hazard simulation. These hazards can be simulated in the laboratory. Shocks and vibration base is the accelerations from the platform, what we can characterized by  $g$  value and the duration of the acceleration The mechanical shocks are the large acceleration changes during the short period of the time. These impacts occur when the packages dropped or the packaging impact each other during the transportation. The ISTA and ASTM standards provide simulation process of mechanical shock, such as the drop test and incline impact test. (Figure 2)



Figure 2 Rotational edge drop test to cause shock impulse in Lab

Vibration motion can be characterized by frequency and amplitude. In the reality a vibrational forces experienced by products and packages in distribution are not the result of single frequency, sinusoidal vibration. The vibration of truck bed, for example, is random in nature as shown in the graph of (Figure 3).

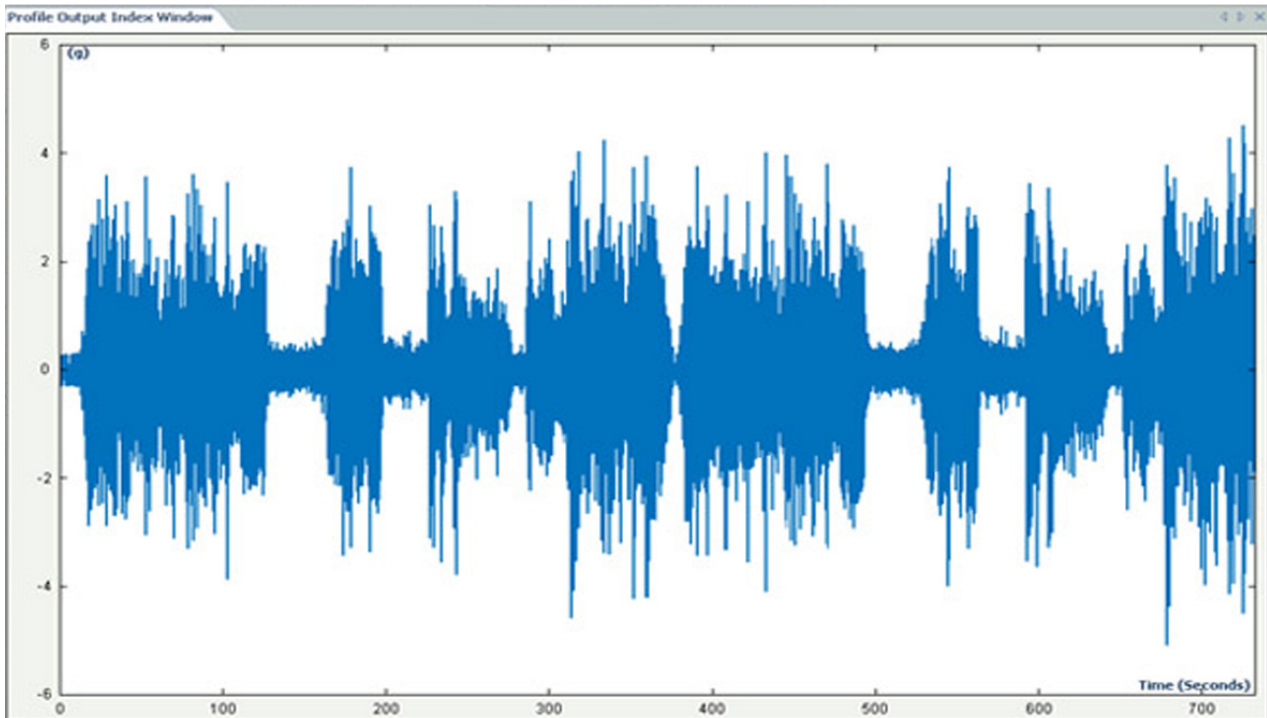


Figure 3 Acceleration signal in time history

To be able to use the real time vibration data for the laboratory simulation, first of all the acceleration-time function must be converted to acceleration-frequency function by Fourier analyses. After that conversion we get a Power Spectral Density (PSD) function. (Figure 4). For the vibration testing in the laboratory we use the PSD plot. The vibration intensity is characterized by overall  $G_{rms}$  value, which is calculated from the curve area. This function is the base of the vibration test standards and the control software of the vibration tables can use also.

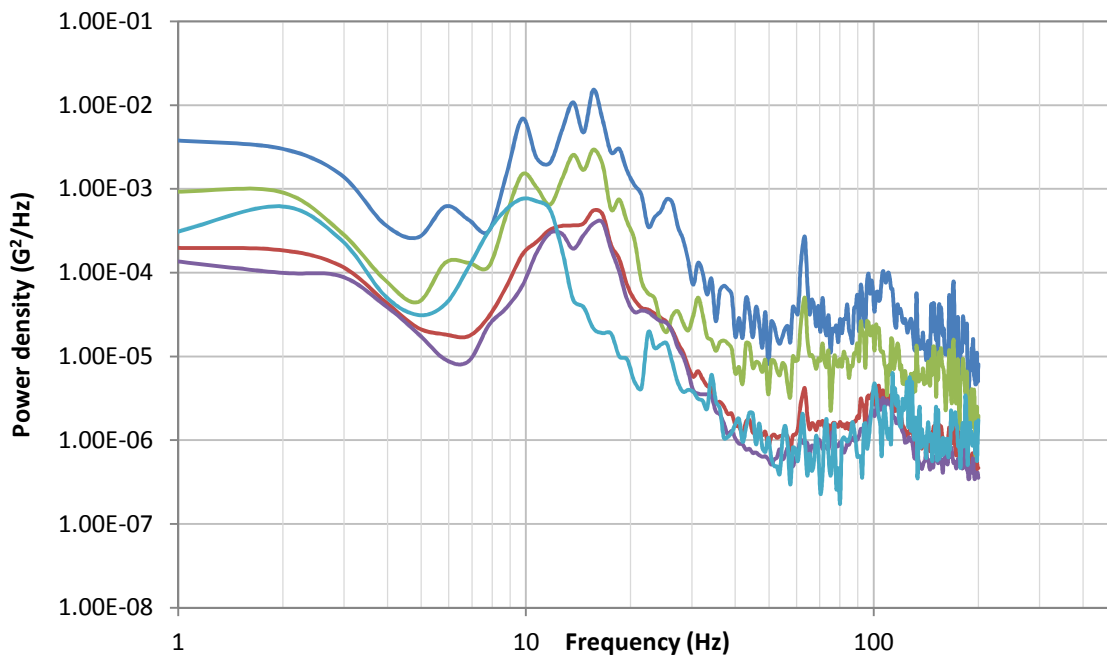


Figure 4 PSD plots of field measurements of truck trailer transport



Most of packaging testing standard, such as ISTA series, ASTM D4169, ISO 13355, require the vibration test and give a PSD profile for the test. These standards PSD are various, because its intensity depends on the simulating vehicle properties. They give PSD specification for truck, rail or air transport simulation. Important thing, these standards specify the vibration table motion and it is simulating the vibrations of the truck surface. Shown in the picture below (*Figure 5*) a vibration test system with single-unit packaging.



*Figure 5.* Servo hydraulic vibration system in Lab

### 3. STACKED UNITS TESTING

The vibrational motion of single-unit packaging has been thoroughly studied, against stacked packaging units. The stacked packaging unit behavior is not fully understood, because dynamic contact force appears between the packaged products during the transportation. A study by Wang et al. investigated the contact force between the three layers of packages on vibration table. The results of this study were the determination of contact force between the vibration table and the bottom layer of stack is larger than between the middle and top layer. [5] The contact forces and PSD levels of various layer depends on many properties of the packaging system, such as the weight, contact surface, center of gravity or the cargo securing. Fang et al. studied the statistical characteristics of maxima of contact force in stacked packaging units under random vibration. From this paper it can be realized that the vibration and contact force between the stacked units show the non-Gaussian distribution. [6] It can be seen from previous two papers that the stacked unit vibration testing is not solved. The vibration controller use Gaussian distribution function for the random acceleration signal. Thus, the stacked packaging testing is not solvable with a single-unit packaging. Currently, if we want to test the suitability of packaging in stack, we must test all of layer of stacked units (*Figure 6*).



Figure 6. Random vibration testing of stacked unit

The stack packages vibration simulation has a few infrastructural limits, such as the pay of the vibration tables and the inner height of the laboratories. Therefore, the maximum layer during the test depends on the packages geometrical size and their weight. Usually, the testable maximum layer on vibration tables is 2 packages.

## CONCLUSIONS

The stacked unit dynamic simulation in the laboratory is not a solved problem yet. The response motion of the upper layers in stacked packages can be very various. The packaging testing standards provide PSD spectrum only simulate the vibrations of the platform. Thus, the whole stack of units must be testing to confirm the suitability of packaging, which transported in stacked. This procedure usually not achievable, therefore it is necessary new vibration profiles where the PSD is similar to motion in real distribution.

## REFERENCES

- [1] Böröcz P.: *Analysing the functions and expenses of logistics packaging systems* ,In: Kóczy Á. László (szerk.Proceedings of FIKUSZ 2009: Symposium for young researchers, Budapest, Hungary, 2009.11.13 Budapest, Budapest Tech, 2009. pp. 29-39.
- [2] Böröcz, P., and Singh, SP.: *Measurement and Analysis of Vibration Levels in Rail Transport in Central Europe*. Packaging Technology and Science 2017, 30: 361–371. doi: 10.1002/pts.2225
- [3] Böröcz P.: *Vibration Levels in Vans as a Function of Payload and Leaf Spring*, Sheet Number, Journal of Testing and Evaluation, Early View (2017)



# INTERNATIONAL SCIENTIFIC CONFERENCE ON ADVANCES IN MECHANICAL ENGINEERING

12-14 October 2017, Debrecen, Hungary



- 
- [4] Singh SP, Saha K, Singh J, Sandhu APS.: *Measurement and analysis of vibration and temperature levels in global intermodal container shipments on truck, rail and ship*, Packaging Technology and Science 2012; 25(3): 149–160. DOI:10.1002/pts.968.
- [5] Wang, Z. -W., and Fang, K.: *Dynamic Performance of Stacked Packaging Units*. Packag. Technol. Sci., 2016, 29: 491–511. doi: 10.1002/pts.2232
- [6] Fang, K., and Wang, Z.-W.: *The Statistical Characteristics of Maxima of Contact Force in Stacked Packaging Units under Random Vibration*. Packag. Technol. Sci., 2017, doi: 10.1002/pts.2313



## SIMULATING THE BRUISING DAMAGE OF OLIVE FRUIT DURING DROP

<sup>1</sup>MUHANDES Hasan, <sup>2</sup>SALLOUM Weal

<sup>1</sup> Faculty of Mechanical Engineering, Szent István University

E-mail: [hasanmuhandes@gmail.com](mailto:hasanmuhandes@gmail.com)

<sup>2</sup>Dept. of Agricultural Machinery Engineering, Faculty of Mechanical Engineering, University of Aleppo

E-mail: [w\\_salloum@yahoo.com](mailto:w_salloum@yahoo.com)

### Abstract

*During of olive fruits harvesting, they subjected to bruising cause from its drop on earth or shock by tree branches or harvesting machine elements, which cause some bruising that has negative effect on table or oil olive specification. The research was conducted to knowledge the engineering and mechanical properties of olive fruits and determine the proper kind of receivers and its angles. By studying a model of olive fruit on receivers by finite element method for several types of receivers and variable angles, to reduce the force and stress of the impact as much as possible. The mechanical properties of olive fruits were calculated as (Poisson factor, density, spring stiffness). It found that the stress of bruising was  $4.7 \text{ N/cm}^2$  at the first velocity,  $5 \text{ N/cm}^2$  at the second velocity and  $5.4 \text{ N/cm}^2$  at the third velocity, for the same dropping high and same receiving angle. Also found that throwing fruit at  $0^\circ$  angle produces less stress.*

**Keywords:** Mechanical Properties of olive, Stress in fruit, olive fruit.

### 1. INTRODUCTION

It is necessary to study the physical and mechanical properties of agricultural materials to knowing the behavior of these material under the mechanization of agricultural process [4] [6] [7]. [9] stated that the detachment is caused by cumulative damage due to stress cycles and occurs after a number of bending cycles. The total number of cycle decreases with increasing applied stress. The finite element method simulation were utilized to found the effect of the factors cause the fruit damage [2]. Also these problems can be solved by advanced methods using programming [8]. The simulation of apple fruit damage during its drop on several surfaces at deferent drop high were occur using Ansys program [5]. Physical properties are variety significantly for length, diameter, sphericity and hardness of strawberry fruit [1]. The Young modulus and Poisson ratio of apple fruit were calculated by applying compression load [5].

### 2. OBJECTIVES

Conservatism good harvested fruits properties by:

- The study of geometry and mass of the fruits.
- The study of the forces resulting from the impact of falling to ground or receiver.
- Choice several types of receiver and choose different angles to put the receiver, so as to mitigate the force of the impact as much as possible or reduce the surface or the depth of the bruise occurring as result of impact.

### 3. MATERIALS AND METHODS

a- Geometric dimensions of the fruit of the olive:



the definition of geometrical dimensions of the fruit by measuring the length of the fruit, diameter and weight. By using the following equation to calculate the theoretical size of the fruit [5]:

$$V = \left(\frac{\pi}{6}\right) \times L \times D^2 \quad (1)$$

L: length of the fruit [mm], D: diameter of the fruit [mm]

The choice of three types of receptors are (fabric, nylon, ground "soil"), and then a choice of three different angles of the receptor (fabric - nylon) which is: (0-15-30) degree.

1- Young modulus:

Several of olive fruits have been subjected to pressure in order to draw a stress-strain diagram.

From this diagram shown in *Figure 2* Young's modulus was:  $E = 27586.2 \text{ N/m}^2$



*Figure 1* Olive fruits exposed to the process pressure

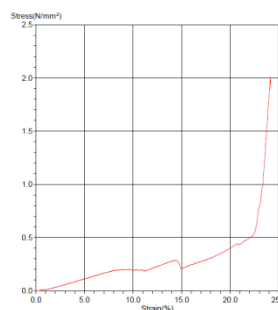


*Figure 2* Stress-strain diagram for olive fruit

2- Poisson's ratio:

A longitudinal strain to accidental strain rate.

Where a olive fruit was exposing to certain pressure force and compressed for a certain distance 1[mm] (accidental strain) is emotion output account (longitudinal strain) reaching 0.12 mm

$$\mu = \frac{0.12}{1} = 0.12 \quad (2)$$

3- determination of the density of adenoids structure:

The weight of 10 fruits (adenoids structure + nut), which amounted to 41.3 g, ten fruits were placed in the water so she slide water weight was 42.7 g.

Then it was removed adenoids structure and retain the nuts, where its weight is 6.4 g, and the nuts placed in the water, where the water slide the weight of 4.4 g.

adenoids structure weight of then fruits:  $41.3 - 6.4 = 34.9 \text{ g}$

adenoids structure of then fruits slide water weight:  $42.7 - 4.4 = 38.3 \text{ g water}$

And the volume of the water resulting from the displacement is:

$$V = \frac{W}{\rho} = \frac{38.3 \times 10^{-3}}{10^3} = 38.3 \times 10^{-6} \text{ m}^3 \quad (3)$$

And therefore the specific weight of the adenoids structure is:

$$\rho = \frac{W}{V} = \frac{34.9 \times 10^{-3}}{38.3 \times 10^{-6}} = 911.27 \frac{\text{kg}}{\text{m}^3} \quad (4)$$



b- nut specifications:

to determine the kind of nut material and its specifications 10 nuts were weighted and dried for 24 hours at 105 °C to evaluate the moisture content. The results indicate that the moisture content of studied olive fruit nut were 20%. This result was compared with several kind of wood, it is close to palsa.

2- receptors specifications:

a- determination of spring stiffness:

two types of receptors were studied (fabric and plastic), For each one the Sample width was 50 mm and the length was 200 mm and subjected to tension force, the force-elongation diagram was drawn.



Figure 3 Fabric sample during tensile process

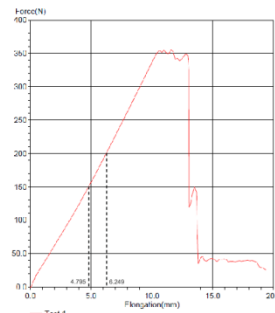


Figure 4 A force-elongation diagram to fabric sample

Two point was taken from the diagram and calculate static stiffness:

- for the fabric sample:

$$K = \frac{F}{U} = \frac{200 - 150}{6.249 - 4.795} = \frac{50}{1.45} = 34.387 \frac{N}{mm} = 34387 \frac{N}{m} \quad (5)$$

[



Figure 5 Plastic sample during tensile process

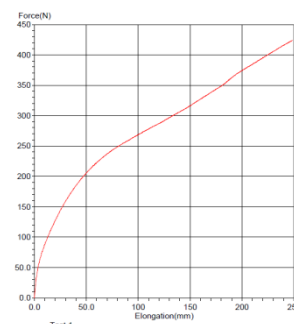


Figure 6 A force-elongation diagram to nylon sample

- for the plastic sample:

$$K = \frac{F}{U} = \frac{30 - 10}{1.54 - 0.37} = \frac{20}{1.17} = 17.094 \frac{N}{mm} = 17094.017 \frac{N}{m} \quad (6)$$

b- determination of thickness and the specific weight of the receptors:

For fabric thickness been identified and it was 0.78 mm, and then took the square of 10×10 cm<sup>2</sup> and weighted 2.905 g was calculated specific weight:

$$\rho = \frac{W}{V} = \frac{2.905 \times 10^{-3}}{0.1 \times 0.10 \times 0.78 \times 10^{-3}} = 372.4359 \frac{kg}{m^3} \quad (7)$$



For plastic thickness been identified and it was 0.47 mm, and then took the square of  $10 \times 10 \text{ cm}^2$  and weighted 5.182 g was calculated specific weight:

$$\rho = \frac{W}{V} = \frac{5.182 \times 10^{-3}}{0.1 \times 0.1 \times 0.47 \times 10^{-3}} = 1102.553 \frac{\text{kg}}{\text{m}^3} \quad (8)$$

#### 4. MODELING PROCESS

For starting the modeling of fruit drop some considerations were taken as:

The nut is homogeneous and has an ellipse shape with 15.78 mm and 6.63 mm dimensions, as shown in *Figure 7*. Also we consider that the adenoids of olive fruit has ellipse shape with 20.32 and 12.44 mm dimensions, as shown in *Figure 8*.

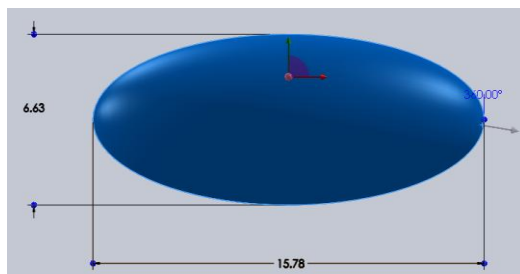


*Figure 7* Nut of the olive fruit.

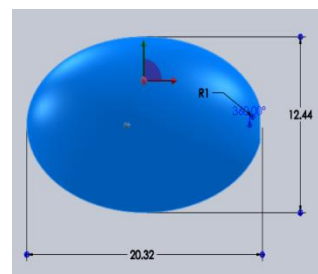


*Figure 8* Adenoids structure of the olive fruit

The nut and the adenoids of olive fruit were assembled.

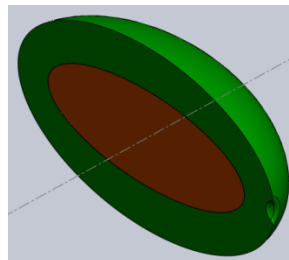


*Figure 9* A section in olive fruit after assembly

Before beginning of modeling we consider the following conditions:

- Material properties: ISOTROPIC material properties in all directions and Homogeneous.
- We consider that the free fall of the fruit of placing vertical.
- A deferent high of dropping to receptors.
- In this research we use a digital program called COSMOS to calculate the stresses and transitions.
- In this research we use tetrahedral element.

Free fall of the fruit:

the kind of falling is free and the falls high were (1-1.5-2-2.5 m) were selected from the list of the modeling and the gravity plane was determined.

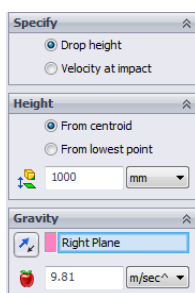


Figure 10 the introduction of high falls

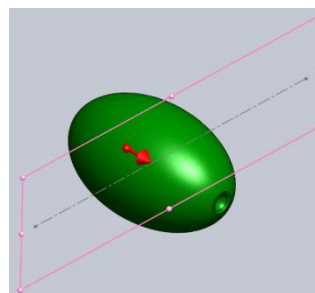


Figure 11 determine gravity plane

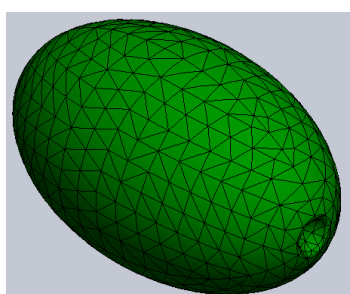


Figure 12 Division process (mesh) for fruit

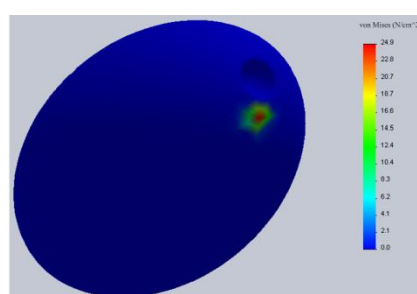


Figure 13 Stress values after the modeling process

The analysis of stress resulting in fruit values gave in Figure 13

## 5. RESULTS AND DISCUSSIONS

1- Impact of receptors and its angle on stress resulting in fruit:

a- Fabric receptors:

b-

Table 1 Effect of fabric receptors and its angle on fruit stress

falling high [m]	stress at 0° [N/cm <sup>2</sup> ]	stress at 15° [N/cm <sup>2</sup> ]	stress at 30° [N/cm <sup>2</sup> ]
1	6.4	3.83	1.13
1.5	8.2	4.8	1.466
2	9.76	5.6	1.733
2.5	11.1	6.33	1.9667

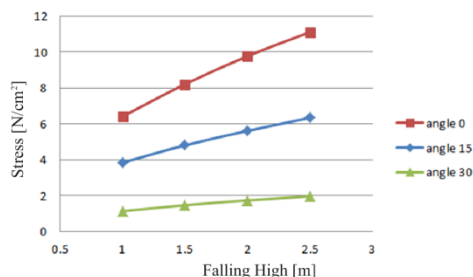


Figure 14 The relationship between stress and falling high at different angles for the fabric receptors

Figure 14 illustrated the relationship between stress and high falls at different angles for fabric receptors. It is noted that the increase in height of the fall of the fruit increases stress, and that the inclination angle of the receptor have an impact on stress as it is a decrease of this angle increases



stress. Due to the decrease vertical force on the fabric receptor.

b- Plastic receptors:

Table 2 Effect of plastic receptors and its angle on fruit stress

falling high [m]	stress at 0° [N/cm <sup>2</sup> ]	stress at 15° [N/cm <sup>2</sup> ]	stress at 30° [N/cm <sup>2</sup> ]
1	1	33	24.06
1.5	1.5	41.4	30
2	2	47.66	34.9
2.5	2.5	52.86	39.13

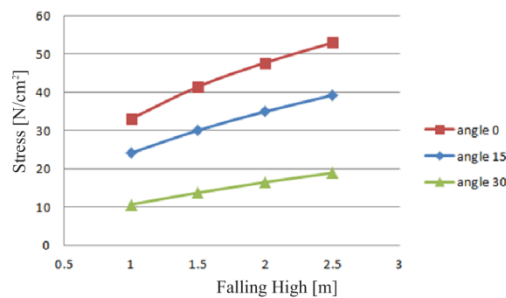


Figure 15 The relationship between stress and falling high at different angles for the plastic receptors

It is noted that the increase in height of the fall of the fruit increases stress, and that the inclination angle of the receptor have an impact on stress as it is a decrease of this angle increases stress.

c- Ground "Soil" receptors:

The soil is defined as a rigid receptors

Table 3 Effect of Soil receptors and its angle on fruit stress

falling high [m]	stress at 0° [N/cm <sup>2</sup> ]
1	9892.13
1.5	11431.63
2	12986.33
2.5	15192.66

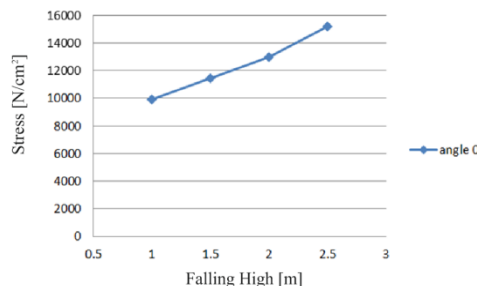


Figure 16 The relationship between stress and falling high for the soil receptors

It is noted that the increase in height of the fall of the fruit increases stress.

Throw fruits with primary velocity:

Was conducted experiment with primary velocity and relying on the strength of return spring, where it



was a choice of three Quicken extrusion due to three forces returned, velocities were identified following values: (1.15 - 2.31 - 3.47) m/s. It is selected from the list of the modeling process as a kind of falling is free fall and the high of falls (1-1.5-2-2.5 m) and is determined gravity plane.



*Figure 17* Throw fruits with primary velocity

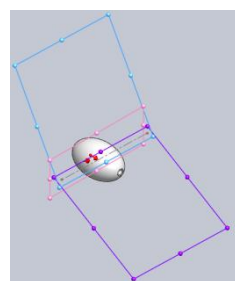


*Figure 18* Gravity plane, velocity plane and receptor plane

The impact of extrusion speed on the resulting stress in the bruise and throw it at fixed angle: It has been compared to stresses resulting in fruits at a fixed angle (15) and found the following:

*Table 4* The relationship between the high falls, extrusion speed and stress resulting in fruit

falling high [m] velocity [m/sec]	1 m	1.5 m	2 m	2.5 m
1.15	3	3.9	4.7	5.4
2.31	3.4	4.2	5	5.6
3.47	4	4.8	5.4	6.1

From *Figure 19* we note that the increase on speed throwing fruit rowing stress resulting in fruit, and that an increase rise of falling increases stress.

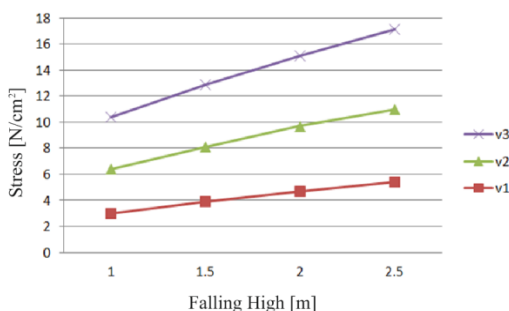


*Figure 19* The relationship between the high falls, extrusion speed and stress resulting in fruit

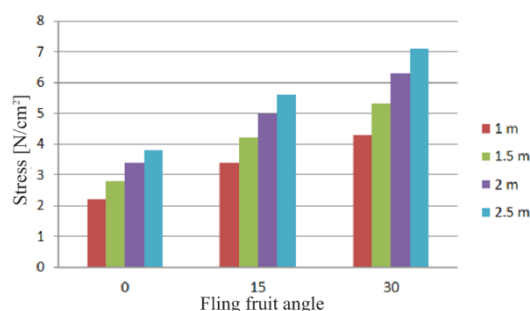


*Figure 20* The influence of extrusion angle and high falls on the resulting stress

The impact of extrusion angle on the resulting stress in the bruise and throw it at fixed extrusion speed: Been compared to stresses resulting in fruits at a fixed speed extrusion, the second speed (2.31 m/s) and found the following:



Table 5 The influence of extrusion angle and high falls on the resulting stress

falling high [m]	stress at 0° [N/cm <sup>2</sup> ]	stress at 15° [N/cm <sup>2</sup> ]	stress at 30° [N/cm <sup>2</sup> ]
1	2.2	3.4	4.3
1.5	2.8	4.2	5.3
2	3.4	5	6.3
2.5	3.8	5.6	7.1

From Figure 20 also note that the increase in fruit fling angle increases stress.

## CONCLUSION

- Increase in height of the fall of the fruit increases stress, and that the inclination angle of the receptor have an impact on stress as it is a decrease of this angle increases stress. Due to the decrease vertical force on the fabric receptor.
- For a fixed falling high, fabric receptor had less impact on stress for all studied angles.
- Increase on speed throwing fruit increases stress in fruit, and that an increase rise of falling increases stress.
- Increase in fruit throwing angle increases stress.

## REFERENCES

- [1] Aliasgarian, S., Ghassemzadeh, H.R., Moghaddam, M., Ghaffari., H.: *Mechanical Damage of Strawberry During Harvest and Postharvest Operations*. World Applied Sciences Journal 22 (7): 969-974, 2013.
- [2] Celik, K.H, Rennie, A.E.W., Akinci, I.: *Deformation behaviour simulation of an apple under drop case by finite element method*. Journal of Food Engineering 104, 293–298, 2011.
- [3] Mohsenin N.: *Physical Properties of Plant and Animal Materials: Structure, Physical Characteristics, and Mechanical Properties*. New York: Gordon and Breach Science, 1986.
- [4] Chen, H., De Baerdemaeker, J.: Modal analysis of the dynamic behaviour of pineapples and its relation to fruit firmness. Trans. ASAE 36, 1439–1444, 1993.
- [5] Salloum W.,Sefrani, Y., Sido, A. H.: *Physical and Mechanical Factors Affecting The Fruit During Transport and Handling*. Engineering Scientific Series, Aleppo University Research Journal, v. 85, 2010.
- [6] Shertz, C.E., and Brown, G.K.: *Basic considerations in mechanization citrus harvest*, Trans. ASAE, 3: 343-346, 1968.
- [7] Salloum, W.: *A study on design factors of a tree shaker for fruit harvesting*. Unpublished master of science, University of Ain Shams, 1996.
- [8] Topakci, M., Celik, H.K., Canakci, M., Rennie, A.E.W., Akinci, I., Karayel, D.: *Deep tillage tool optimization by means of finite element method: case study for a subsoiler tine*. J. Food Agric. Environ. 8 (2), 531–536, 2010.
- [9] Wang, J., and Shellenberger, F.A.: *Effects of cumulative damage to stress cycles on selective harvesting of coffee*, Trans. ASAE, 10 (2): 252-255, 1967.



## PLANE JETS EXCITED BY VORTICES

*NAGY Péter Tamás, PAÁL György PhD*

*Department of Hydrodynamic Systems, Faculty of Mechanical Engineering, Budapest University of Technology and Economics*

*E-mail: [pnagy@hds.bme.hu](mailto:pnagy@hds.bme.hu), [paal@hds.bme.hu](mailto:paal@hds.bme.hu)*

### Abstract

*The description of feedback mechanism is one of the crucial points in the understanding of the edge tone phenomenon. A method was developed by which any incompressible flow can be excited with a known vortex field. An analytical approximation of the vortex field is suggested. A plane jet at Reynolds number 100 is excited to investigate the effect of the fluctuating vortex field. The excitation procedure is implemented in a commercial computational fluid dynamics (CFD) simulation software ANSYS CFX 16.2. According to the results the jet is more sensitive to the excitation near the orifice than further downstream.*

**Keywords:** *vortex excitation, potential vortex, plane jet, edge tone model*

### 1. INTRODUCTION

The edge tone is one of the basic aeroacoustic flow configurations. In the simplest case, the fluid exits from a narrow rectangular nozzle into the free space. Along the jet, a disturbance wave develops that propagates downstream. At a certain distance, a wedge element (the edge) is placed in front of the nozzle. When the disturbance wave hits this edge it acts back to the jet origin and somehow initiates a new disturbance wave. The feedback mechanism is not clear whether it is caused by an acoustic wave or the formed vortices at the edge, via the Biot-Savart mechanism.

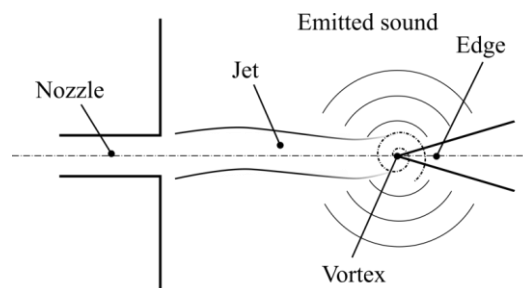


*Figure 1 Sketch of the edge tone flow configuration*

Fabre and Hirschberg [1] summarized many lumped models of flue instruments and the edge tone. They draw the conclusion that although these models explain some global observations, they do not fully reveal the physical mechanism. Our aim is to understand the afore-mentioned feedback mechanism and to create a simple, mathematical model. In this paper, the interaction of a known vortex field and an incompressible flow field is modelled. The authors hope that with the further extension of this model the feedback mechanism will be revealed. In Section 2., the governing equations of the interaction will be derived and presented. In Section 3., an approximation is derived for the vortex field. The excitation method is implemented in a commercial CFD code. The interaction of the vortex field and the plane jet is investigated. Its settings and results are presented in Section 4. Finally, concluding remarks are made.



## 2. MATHEMATICAL MODEL

Let us split the velocity field and the pressure field into two parts: into the jet flow and the excitation (the vortex) field. The former one is denoted with  $j$  in subscript while the latter one with  $e$ . The total velocity field has to fulfil the governing equations. The incompressible continuity equation is:

$$\frac{\partial(u_j + u_e)}{\partial x} + \frac{\partial(v_j + v_e)}{\partial y} + \frac{\partial(w_j + w_e)}{\partial z} = 0 \quad (1)$$

where  $u, v, w$  are the velocity components. The momentum equations read as:

$$\begin{aligned} \frac{\partial(u_j + u_e)}{\partial t} + (u_j + u_e) \frac{\partial(u_j + u_e)}{\partial x} + (v_j + v_e) \frac{\partial(u_j + u_e)}{\partial y} + (w_j + w_e) \frac{\partial(u_j + u_e)}{\partial z} = \\ = -\frac{1}{\rho_0} \frac{\partial(p_j + p_e)}{\partial x} + \nu \Delta(u_j + u_e) \end{aligned} \quad (2)$$

$$\begin{aligned} \frac{\partial(v_j + v_e)}{\partial t} + (u_j + u_e) \frac{\partial(v_j + v_e)}{\partial x} + (v_j + v_e) \frac{\partial(v_j + v_e)}{\partial y} + (w_j + w_e) \frac{\partial(v_j + v_e)}{\partial z} = \\ = -\frac{1}{\rho_0} \frac{\partial(p_j + p_e)}{\partial y} + \nu \Delta(v_j + v_e), \end{aligned} \quad (3)$$

$$\begin{aligned} \frac{\partial(w_j + w_e)}{\partial t} + (u_j + u_e) \frac{\partial(w_j + w_e)}{\partial x} + (v_j + v_e) \frac{\partial(w_j + w_e)}{\partial y} + (w_j + w_e) \frac{\partial(w_j + w_e)}{\partial z} \\ = -\frac{1}{\rho_0} \frac{\partial(p_j + p_e)}{\partial z} + \nu \Delta(w_j + w_e), \end{aligned} \quad (4)$$

where  $\rho_0$  is the density,  $\nu$  is the kinematic viscosity of the fluid,  $p$  is the pressure and  $\Delta$  is the Laplace operator. The excitation field fulfils the governing equations and some of the terms can be eliminated. Let us rearrange the equations; express the governing equations for the unexcited jet flow and collect the extra/excitation terms in  $S_m$ . The origin of these terms lies in the non-linear convective terms.

$$\frac{\partial u_j}{\partial t} + u_j \frac{\partial u_j}{\partial x} + v_j \frac{\partial u_j}{\partial y} + w_j \frac{\partial u_j}{\partial z} = -\frac{1}{\rho_0} \frac{\partial p_j}{\partial x} + \nu \Delta u_j + S_{m,x}, \quad (5)$$

$$\frac{\partial v_j}{\partial t} + u_j \frac{\partial v_j}{\partial x} + v_j \frac{\partial v_j}{\partial y} + w_j \frac{\partial v_j}{\partial z} = -\frac{1}{\rho_0} \frac{\partial p_j}{\partial y} + \nu \Delta v_j + S_{m,y}, \quad (6)$$

$$\frac{\partial w_j}{\partial t} + u_j \frac{\partial w_j}{\partial x} + v_j \frac{\partial w_j}{\partial y} + w_j \frac{\partial w_j}{\partial z} = -\frac{1}{\rho_0} \frac{\partial p_j}{\partial z} + \nu \Delta w_j + S_{m,y}, \quad (7)$$

where the extra terms are

$$S_{m,x} = -\left( u_j \frac{\partial u_e}{\partial x} + u_e \frac{\partial u_j}{\partial x} + v_j \frac{\partial u_e}{\partial y} + v_e \frac{\partial u_j}{\partial y} + w_j \frac{\partial u_e}{\partial z} + w_e \frac{\partial u_j}{\partial z} \right), \quad (8)$$

$$S_{m,y} = -\left( u_j \frac{\partial v_e}{\partial x} + u_e \frac{\partial v_j}{\partial x} + v_j \frac{\partial v_e}{\partial y} + v_e \frac{\partial v_j}{\partial y} + w_j \frac{\partial v_e}{\partial z} + w_e \frac{\partial v_j}{\partial z} \right), \quad (9)$$



$$S_{m,z} = - \left( u_j \frac{\partial v_e}{\partial x} + u_e \frac{\partial v_j}{\partial x} + v_j \frac{\partial v_e}{\partial y} + v_e \frac{\partial v_j}{\partial y} + w_j \frac{\partial v_e}{\partial z} + w_e \frac{\partial v_j}{\partial z} \right) \quad (10)$$

from Eqs. (2)-(4). It has to be mentioned these terms are not source terms in the strict sense of the word since they are not independent of the solution. Furthermore, this way of modelling of the interaction has the benefit that the vortex velocity will not directly appear in the simulated velocity field of the jet. Only the effect of the vortex field is taken into account.

### 3. THE VORTEX FIELD

A proper formula of the vortex must be defined which not only fulfil the governing equations but that describes well a real vortex field and that can be handled numerically. The simplest model is the potential vortex. It describes well the vortex field far from its centre. At the same time, the potential vortex is singular at the centre and its velocity field is also unrealistic near to centre. An improvement is made to handle this issue. An extra term was added to the velocity formulae which read as

$$u(x, y, z, t) = - \frac{\Gamma(y - y_0)}{2\pi((x - x_0)^2 + (y - y_0)^2 + r_0^2)}, \quad (11)$$

$$v(x, y, z, t) = \frac{\Gamma(x - x_0)}{2\pi((x - x_0)^2 + (y - y_0)^2 + r_0^2)}, \quad (12)$$

where centre is at  $x_0, y_0$  coordinates,  $\Gamma$  is the circulation and  $r_0$  is the extra term in the denominator. If  $r_0$  is zero this description will be identical to that of the original potential vortex. The extra term is related to the size of vortex, it prevents the velocity field to become singular. Furthermore, these expressions are differentiable everywhere. This property is important since the derivatives of the velocity field have to be calculated during the interaction, too. The formulae will approximate well the velocity fields of a rigid body rotation if  $|x - x_0| < r_0/2$  and a potential vortex if  $|x - x_0| > 3r_0$ , as shown in Fig. 2.

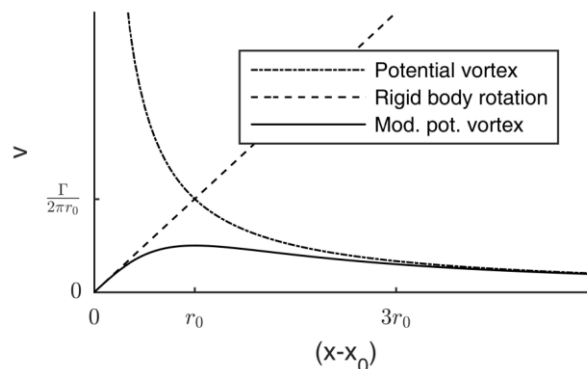


Figure 2 The velocity field of three various vortex description models

In the edge tone the generated circulation is not constant at the tip. As the jet moves up-and down periodically, the circulation of generated vortex field changes periodically and this is approximated by a harmonic variation here:

$$\Gamma(t) = \Gamma_0 \sin(\omega t), \quad (13)$$

where  $\omega$  is the angular frequency.

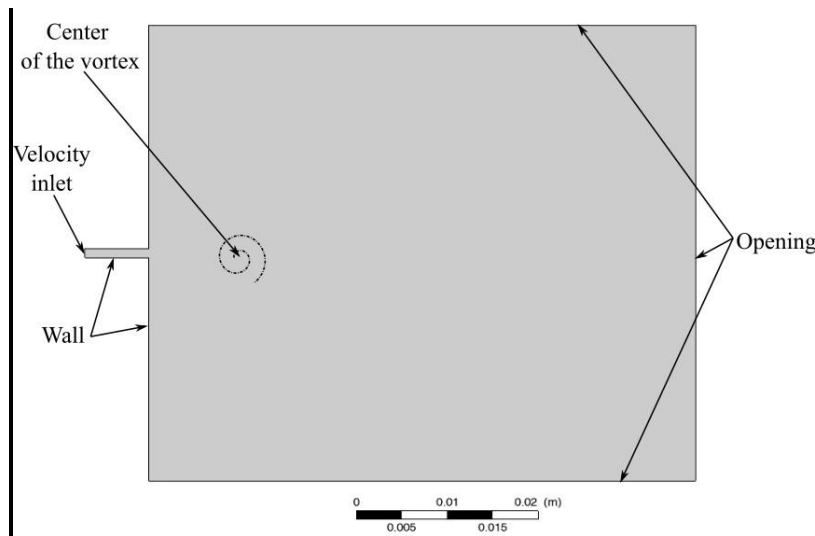


Figure 3 The CFD configuration and boundary conditions of the excited plane jet

#### 4. CFD SIMULATION

The interaction of the vortex and the plane jet is investigated with a commercial CFD code, ANSYS CFX. The 2D setup can be seen in Fig. 3. At the end of the nozzle, parabolic inlet velocity profile is prescribed. At both sides of the orifice, rigid wall and at the far field, opening boundary conditions are defined. The width of the orifice is  $h=1$  mm. The definition of the Reynolds-number is

$$\text{Re} = \frac{hU_{\text{Mean}}}{\nu}, \quad (13)$$

this flow configuration. It is set to 100, the kinematic viscosity is  $\nu = 1.545 \cdot 10^{-5} \text{m}^2/\text{s}$ , and the average velocity of the inlet velocity profile is  $U_{\text{Mean}} = 1.545 \text{ m/s}$ . The time step is  $5 \cdot 10^{-5} \text{ s}$  and the total simulation time was 2 s. The vortex centre is defined at  $x_0 = 10 \text{ mm}$ ,  $y_0 = 0 \text{ mm}$ . The amplitude of its circulation is  $\Gamma_0 = 10^{-5} \text{ m}^2/\text{s}$ , the angular frequency is  $\omega = 772.5 \text{ rad/s}$ , meaning the Strouhal-number of excitation  $\text{St} = \omega h / U_{\text{Mean}} = 0.5$ . The size of the vortex is  $r_0 = 0.1 \text{ mm}$ . The maximum velocity of this excitation field is around 8 mm/s and the velocity amplitude of the vortex is around 0.16 mm/s at nozzle.

The result of the simulation can be seen in Figure 4. There a typical velocity field is plotted at  $t = 0.57 \text{ s}$ . The displacement of the jet is visible only far from the orifice, at the end of the domain since the excitation is not so strong. The velocity components are monitored at 150 locations placed at the centreline of the jet. The transversal velocity signals are Fast Fourier Transformed using Matlab 2017a. In each spectrum, a strong peak is obtained at the excitation frequency, as expected. This means that our model is able to excite the flow and the jet responds with the same frequency as the excitation frequency. The amplitude of the transversal velocity at the excitation frequency ( $v_{j,a}$ ) is plotted as the function distance from the orifice in Fig. 5. (a). The amplitude of the perturbation velocity grows almost exponentially in the investigated domain. The growth rate of this disturbance is determined as [2]

$$\mu = \frac{1}{v(x)} \frac{dv(x)}{dx}. \quad (14)$$



If the amplitude grows exponentially, this value will be constant. However, this value continuously decreases from the orifice that can be seen in Fig. 5 (b). Two other curves are added to this figure based on our previous research. One curve is calculated from a simulation, where the flow is excited by an acoustic wave with the same frequency as here (not published yet). The acoustic wave propagates in the transversal direction. The last one (dashed line) is obtained from linear stability analysis [3] with the so-called Orr-Sommerfeld equation [2]. If the flow is not excited externally, this latter one will describe well the growth rate of disturbances if  $x/h > 2$  [3]. The differences of the other curves compared to this curve sign the locations where the external field (acoustic or vortex) excites the flow. We can see that in both cases, the differences are the largest close to the orifice and the differences become small after  $x/h > 4$ . There is only one exception, around the location,  $x/h = 10$ , where the vortex centre is placed. However, this difference is still not significant. These observations confirm the fact: the flow is more sensitive to external excitation at the orifice.

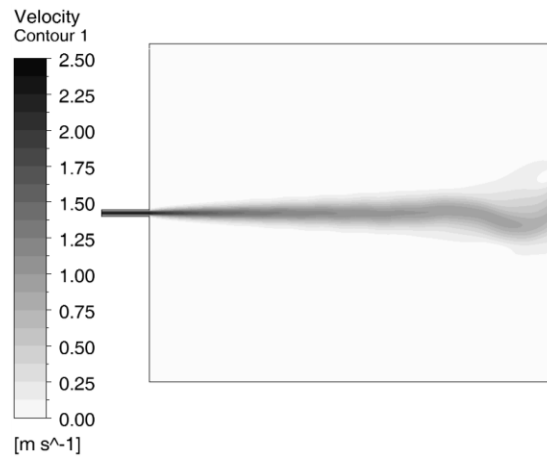


Figure 4 The velocity field of the simulation at  $t = 0.57$  s

In the next step, the vortex and acoustic excitation procedures are compared to each other, with respect to their effectiveness. Let us define the average kinetic energy of the excitation as

$$\bar{E}_e = \frac{1}{2} \rho \frac{\int_0^T \int_0^{x_1} \int_{y_1}^{y_2} (u^2 + v^2) dx dy dt}{T x_0 (y_2 - y_1)} \quad (15)$$

where  $T$  is the period of excitation. This corresponds to the amount of energy invested to the generation of the excitation field. This value is evaluated on the initial part of the domain, where the excitation process occurs:  $x_1 = 4h, y_1 = -2h, y_2 = 2h$ . The outcome of the excitation is the periodic motion of the jet, whose energy is measured by the previously calculated amplitudes of the fluctuating transversal velocity. Let us define the average kinetic energy of the perturbation wave at the cross section  $x_2$  as:

$$\bar{E}_j(x_2) = \frac{1}{4} \rho v_{j,a}^2(x_2) \quad (16)$$

The ratio of these two values determines, how receptive the jet to the respective perturbation is. This value is evaluated at  $x_2 = 5h$ , since according to the previous observation, the excitation has no effect downstream of  $x = 4h$ . The ratio is 330 in the case of acoustic excitation and 1921 in the case of vortex excitation. This means that the vortex field is more effective in exciting the jet. At the same time, the average kinetic energy does not depend on the definition of the integration domain in



the case of the acoustic field of a plane wave, while it does in the case of vortex field. If the vortex centre is also included in this finite domain, the previous ratio will be radically reduced.

## CONCLUSIONS

A procedure has been developed by which any incompressible flow can be excited with a known vortex field. The vortex field is described by an analytical formula. It handles the rigid body rotation at the near field and the hyperbolic decay in the far field. A plane jet is excited at a Reynolds number of 100 to investigate the effect of the fluctuating vortex field. The implementation is done in a commercial CFD code. The amplitude and the growth rate of the generated disturbance field are calculated. The growth rate is much larger close to the orifice. The results are compared to our previous research where the excitation effect is excluded. According to the comparison, the plane jet is more sensitive to the excitation near the orifice than further downstream.

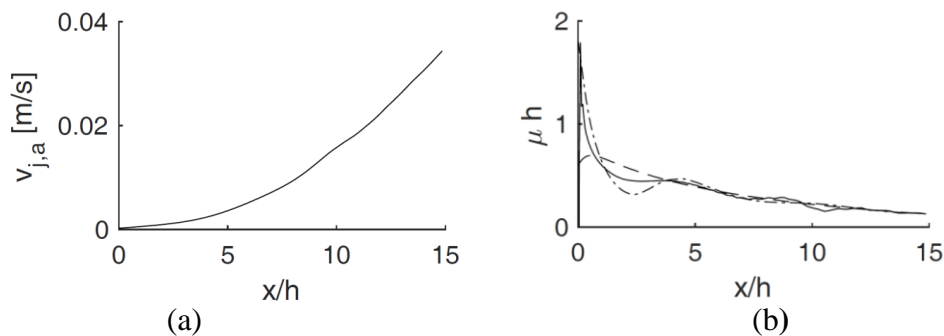


Figure 5 (a) The amplitude of the transversal velocity component at excitation frequency ( $v_{j,a}$ ) as a function of the distance from the orifice. (b) The growth rate of the disturbances wave (generated by excitation) as a function of the distance from the orifice: in the case of vortex excitation (continuous line), acoustic wave equation (dash-dot line, based on previous research) and linear stability analysis (dashed line, based on previous research)

## ACKNOWLEDGEMENT

Authors are indebted to Dr. László Kullmann of the Budapest University of Technology and Economics for the idea and fruitful discussions concerning the excitation procedure and the description of the vortex field. The work has been performed within the framework of the NKFI project K124939.

## REFERENCES

- [1] Fabre, B. and Hirschberg, A.: *Physical Modeling of Flue Instruments: A Review of Lumped models*, Acta Acust. united with Acust., 486:12, 2000.
- [2] Schmid, P. J., Henningson D. S.: *Stability and Transition in Shear Flows*, Applied Mathematical Sciences, Vol 142., 2001.
- [3] Nagy, P. T., Paál, G.: *On the sensitivity of planar jet*, International Journal of Heat and Fluid Flow 62 114-123. 2016.



## THE EFFECT OF SPANWISE FLEXIBLE COATING ON THE BOUNDARY LAYER TRANSITION

*NAGY Péter Tamás, PAÁL György PhD*

*Department of Hydrodynamic Systems, Faculty of Mechanical Engineering, Budapest University of Technology and Economics*

*E-mail: [pnagy@hds.bme.hu](mailto:pnagy@hds.bme.hu), [paal@hds.bme.hu](mailto:paal@hds.bme.hu)*

### **Abstract**

*The laminar-turbulent transition is investigated in a boundary layer flow over a coated wall. The coating consists of small elements which can move in streamwise and in some cases additionally in spanwise directions. The growth rate of disturbances is determined for a spanwise rigid and flexible wall with a linear approximation. The results show that the compliance of the coating in spanwise direction does not influence streamwise propagating waves and does not change the critical Reynolds number, where the transition begins. However, the spanwise flexibility of the coating may delay the transition in the non-linear regime, which cannot be further investigated with the presented techniques.*

**Keywords:** *boundary layer coating, delaying laminar-turbulent transition,*

### **1. INTRODUCTION**

One of the most crucial problems facing mankind, is the overusage of energy. Furthermore, the problem is not only that the most of the energy resources are finite; the excessive CO<sub>2</sub> emission is probably associated with climate change, too. According to estimations, water transport accounts for about 3% percent of the total CO<sub>2</sub> emission. A container ship consumes 300-400 tones of fuel per day and the amount of fuel of one ship costs around 10 million pounds per year.

The aim of our research is the development of a special coating on ships, which can reduce the friction drag. There are several ways to do that [1]. We focus only on the initial region of the watercraft, where the laminar-turbulent transition occurs. Our aim is to delay this transition and reduce the drag. The coating consists of miniature mass-spring-damping systems that have two degrees of freedom. They can move in streamwise and spanwise directions. In this paper, the spanwise flexibility of the coating on the transition will be investigated. A spanwise flexible and a rigid coating will be compared to each other.

The description of the coating and its mathematical model will be presented in next section. In Section 3, the results obtained with the model are shown. Finally, concluding remarks are made.

### **2. MATHEMATICAL MODELL**

The laminar-turbulent transition can be predicted by linear stability analysis. Above a so-called critical Reynolds-number, the boundary layer loses its stability, and any perturbation grows exponentially and after a certain distance turbulent boundary layer develops. The critical Reynolds-number and the growth rate of the disturbances can be predicted by linear stability analysis: an infinitesimally small perturbation is added to the basic flow. The basic flow is assumed to be time-independent and parallel meaning that the streamwise velocity component is much larger than the transversal one and the base velocity field does not change in streamwise direction. These approximations are fully valid for in a case of channel flow but self-similar flows, like the boundary



layer, can also be modelled properly this way. The flow is investigated at various cross sections (at various streamwise locations) which can be imagined as the boundary layer is split into a series of infinitesimal short “channels”. The basic flow is assumed to be the Blasius self-similar solution and the perturbation fields should be calculated. The disturbance field is assumed in a wave form

$$\hat{q}(x, y, z, t) = q(y) e^{i(\alpha x + \beta z - \omega t)}. \quad (1)$$

which propagates in the  $x, z$  plane.  $\hat{q}$  is any perturbation field (the pressure or the velocities),  $q$  is the eigenfunction,  $\alpha, \beta$  are the wave numbers in streamwise and spanwise directions respectively,  $\omega$  is the angular frequency. The disturbance has to fulfil the governing equations that are presented for the case of Blasius flow, where the transversal ( $V$ ) velocity is small, assumed to be 0 and the spanwise ( $W$ ) velocity is 0. The continuity equation for the perturbation is:

$$i(\alpha u + \beta w) + v' = 0. \quad (2)$$

where  $u(y), v(y), w(y)$  are the eigenfunctions of the velocity components of the perturbation field, and ' means the derivative of a function with respect to  $y$ .

The momentum equations read in non-dimensional form for an incompressible Newtonian fluid

$$i(-\omega + \alpha U)u + \frac{\partial U}{\partial y}v = -\frac{i\alpha}{\rho_0}p + \frac{1}{Re}(u'' - (\alpha^2 + \beta^2)u). \quad (3)$$

$$i(-\omega + \alpha U)v = -\frac{1}{\rho_0}p' + \frac{1}{Re}(v'' - (\alpha^2 + \beta^2)v). \quad (4)$$

$$i(-\omega + \alpha U)w = -\frac{i\beta}{\rho_0}p + \frac{1}{Re}(w'' - (\alpha^2 + \beta^2)w). \quad (5)$$

where  $p$  is the pressure and  $Re$  is the Reynolds-number. The velocity scale is the far-stream velocity ( $U_\infty$ ) and the length scale is the displacement thickness  $\delta^*$  for the non-dimensionalization procedure. This means the Reynolds-number is defined as:

$$Re = \frac{U_\infty \delta^*}{\nu}. \quad (6)$$

where  $\nu$  is the kinematic viscosity of the fluid.

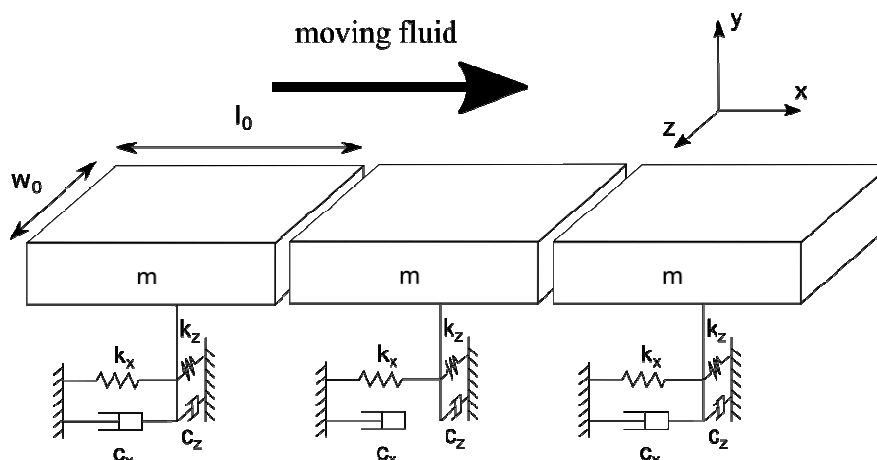


Figure 1. Sketch of the investigated coating

The problem is to find such kind of  $u(y), v(y), w(y), p(y)$  eigenfunctions and  $\alpha, \beta, \omega$  values which



fulfil Eqs. (2)-(5) and the proper boundary conditions. The boundary conditions in the far field are trivial, the perturbations have to vanish,  $\lim_{y \rightarrow \infty} \{u, v, w, p\} = \{0, 0, 0, 0\}$ . The far-field location was  $y = 20$  in the numerical procedure.

Describing the flexible wall with proper boundary conditions is a more complicated task. The wall consists of small elements with the mass ( $m$ ) which are shown in *Figure 1*. They are fixed via two springs ( $k_x, k_z$ ) and dampers ( $c_x, c_z$ ) in  $x$  and  $z$  directions. The wall cannot move in the transversal direction, meaning  $v(0) = 0$ . In streamwise ( $x$ ) and spanwise ( $z$ ) directions, the shear stress moves the miniature element of the coating. After writing the second law of Newton to an element with the external force caused by the shear stress and applying Fourier transformation, the following expressions can be derived:

$$u(0) = \frac{1}{-\tilde{m}i\omega + \tilde{c}_x + \tilde{k}_x i/\omega} u'(0), \quad (7)$$

$$w(0) = \frac{1}{-\tilde{m}i\omega + \tilde{c}_z + \tilde{k}_z i/\omega} w'(0). \quad (8)$$

where  $\tilde{m}, \tilde{c}, \tilde{k}$  are the non-dimensional mass, damping and stiffness parameters. They can be calculated as:

$$\tilde{m} = \frac{m U_\infty}{w_0 l_0 \mu}, \quad \tilde{c} = \frac{c \delta^*}{w_0 l_0 \mu}, \quad \tilde{k} = \frac{m \delta^{*2}}{U_\infty w_0 l_0 \mu} \quad (9)$$

where  $w_0, l_0$  the width and the length of the element. If the coating is rigid in spanwise direction, the boundary condition was  $w(0) = 0$ . The fourth boundary condition for the pressure can be arbitrary since we are looking for the eigenfunctions of the problem,  $p(0) = 1$  was prescribed to avoid the trivial solution.

The problem was discretized on a non-equidistant grid on  $y \in [0, 20]$  domain by a second order central difference scheme which leads to a linear equation system in the form,

$$\mathbf{A} \mathbf{q} = \mathbf{b}, \quad (10)$$

where  $\mathbf{q} = [\mathbf{u}, \mathbf{v}, \mathbf{w}, \mathbf{p}]^T$  is the solution vector. We assumed a spatial stability problem meaning that during the solution  $\beta, \omega$  were free parameters and our task is to determine the eigenvalue,  $\alpha$ . Eq. (12) was solved without prescribing one of the boundary conditions,  $v(0)=0$ , and  $\alpha$  is changed by Newton-Raphson method, until this missing BC is fulfilled. The wave number,  $\alpha$  is a complex number. Its real and imaginary parts determine the phase speed and the growth rate of the disturbance wave, respectively. If the imaginary part is negative, the growth rate is positive and the disturbance wave will grow exponentially in space. The lowest Reynolds-number, where any disturbance wave with positive growth rate exists, is called the critical Reynolds-number. Above this value some disturbances will grow exponentially (see Eq. (1)) and after a certain distance, the flow becomes turbulent.

### 3. RESULTS

The critical Reynolds number is around 520, for a rigid wall with the parallel flow assumption. In our previous work (not published yet) we found such kind of  $\tilde{m}, \tilde{c}_x, \tilde{k}_x$  parameters for which the critical Reynolds-number was increased to 1200 with the coating but it was flexible only in streamwise direction. These parameters are  $\tilde{m} = 0.2, \tilde{c}_x = 0.05, \tilde{k}_x = 0.001$ . Here, the effect of flexibility in spanwise direction is investigated.

It is well known according to the Squire theorem [2] that disturbances have the largest growth rate



in a two dimensional case when the wave propagates in the streamwise direction ( $\beta = 0$ ). First, this kind of disturbance was investigated. If  $\beta$  is set to 0, the spanwise flexibility has not effect on the results compared to the streamwise flexible wall. This can be seen in Figure 1. (a), where the dashed line (streamwise flexible) and dashed dot line (spanwise flexible) cover each other. It can be concluded that the spanwise flexibility has no effect on the largest growth rate. Furthermore, it has no effect on the critical Reynolds-number.

In the same figure, we can see also the stabilization effect of the coating. The continuous line shows the growth rate of the disturbance wave in the case of absolutely rigid wall which was positive for the angular frequencies between 0.04 and 0.12. At the same time, the coated wall remained stable for all frequencies since the growth rate was negative everywhere.

In the next step we investigated  $\beta = 0.1$  cases. Here, the spanwise flexibility has effect on the results. For certain parameters higher for others lower growth rates were obtained. After tuning the parameters, we found such parameters where the spanwise flexibility reduced the amplification of the disturbances wave almost for all frequencies. The results are shown in Figure 2. (b) for  $\tilde{c}_z = 3, \tilde{k}_z = 0.001$  parameters. Here, we can see that the growth rates are almost everywhere lower than those in the case of spanwise rigid coating. Further certain conclusions cannot be obtained since linear stability investigation methods are able to predict only the critical Reynolds-number. At the same time, it is well-known that the development of turbulent flow is a three dimensional phenomenon where disturbances propagate both in streamwise and slightly in spanwisely directions. This means that the spanwise flexible coating may help further delay the transition. Unfortunately, the presented model is inadequate to investigate this statement in its full depth.

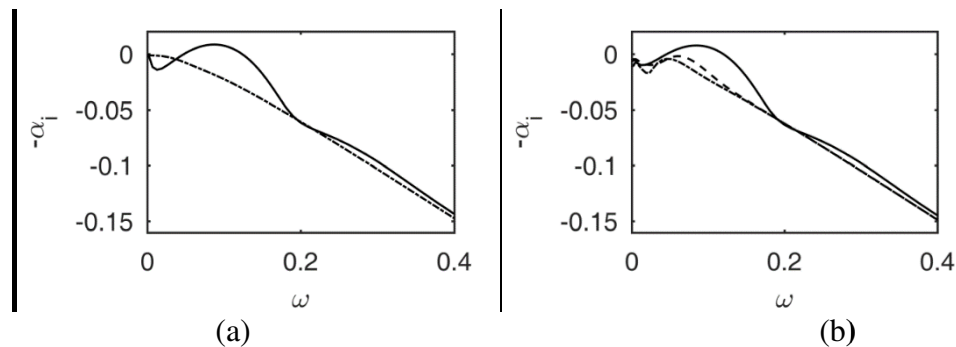


Figure 2 The growth rates ( $-\alpha_i$ ) of the disturbance waves as functions of the angular frequency at  $Re=1200$  in the case three different wall configuration: rigid wall (continuous line), streamwise flexible wall (dashed line), streamwise and spanwise flexible wall (dash-dot line). The parameters of flexible wall were:  $\tilde{m} = 0.2, \tilde{c}_x = 0.05, \tilde{k}_x = 0.001, \tilde{c}_z = 3, \tilde{k}_z = 0.001$ . (a)  $\beta = 0$ , (b)  $\beta = 0.1$ .

## CONCLUSIONS

The growth rate was calculated for a spanwise rigid and flexible wall in a linear approach. The result of the investigation was that the compliance of the coating in spanwise direction does not influence the critical Reynolds number. Spanwise flexibility of the coating has no effect on the growth rate of streamwise propagating disturbances. However, it may delay the transition in the non-linear domain but this cannot be fully investigated with the presented techniques.

## ACKNOWLEDGEMENT



# INTERNATIONAL SCIENTIFIC CONFERENCE ON ADVANCES IN MECHANICAL ENGINEERING

12-14 October 2017, Debrecen, Hungary



P.T. Nagy was supported by the ÚNKP-17-3 New National Excellence Program of the Ministry of Human Capacities.

## REFERENCES

- [1] Gad-el Hak, M.: *Flow control: passive, active, and reactive flow management*. Cambridge University Press, ISBN-13 978-0-521-77006-4, 2000.
- [2] Schmid, P. J., Henningson D. S.: *Stability and Transition in Shear Flows*. Applied Mathematical Sciences, Vol 142., 2001.



## DESIGNING, MODELLING AND ANALYSIS OF STRAIGHT TURNING TOOL GEOMETRY

*NEMES Csaba, BODZÁS Sándor PhD*

*Department of Mechanical Engineering, University of Debrecen*  
*E-mail: [csabanemes94@gmail.com](mailto:csabanemes94@gmail.com), [bodzassandor@eng.unideb.hu](mailto:bodzassandor@eng.unideb.hu)*

### **Abstract**

*We execute the planning, modelling and examination of straight turning tool geometry with the help of a software in the modelling space. Our aim is to create a programme that – given some lengths and angles – calculates the corresponding geometry. It establishes that as a wireframe model in a file format that is easily transmittable to the CAD softwares of today, so any additional changes can be done there. An optimal geometry can be defined for the best possible chipping conditions using finite element simulation and with given technological parameters and material quality standard.*

**Keywords:** *computer program, finite element method, turning, modelling, simulation*

### **1. INTRODUCTION**

The edge geometry of the turning tools have a significant impact on the turning process [2, 5, 9] because utilizing the optimal edge geometry results in favorable turning circumstances, which is an important economic aspect.

The ideal process is created by considering certain parameters. For example, one can strive for extending tool life; increasing specific removal of material; removing material in the most beneficial splinter shape (fragmented, elementary, continuous chip, etc.) or improving the quality of the machined surface. It is possible to work on more than one of these features simultaneously but of course that requires certain compromises [1, 4, 6].

The modelling software has been developed for the fast and easy creation of turning tools with different edge geometry parameters. Modelling such tools is difficult and time consuming and also it is easy to make mistakes due to the activity's complexity. Our program defines the model mathematically, which means the model will always be exact. We will elaborate later on how the software functions and how it is supposed to be used. The software's function description and the user's guide is provided later in this document.

It is important to know that the program complies with not only the professional expectations but many further requirements too – these are the criteria of a modern software. It must have a graphic interface instead of the outdated keyboard control. It must run fast and must not overload the computer. It must have functions that facilitate the operation, etc.

### **2. THE MODEL CREATOR SOFTWARE**

The geometry of the traditional lathe tool is described by spatial lines, which means that for defining the tool, we need to do certain simplifications. We ignore the pellet fixing and the curved surfaces, meaning that we also ignore the tool point's filleting and the groove-type chip breaker. The mountable hard metal pellet of the tool is not portrayed either. All these can be easily corrected with the help of the CAD program.



We illustrate the Cartesian right angled (right handed) coordinate system in a way that the tool's contact surface is on the X-Y dimension and the Z-axis crosses the tool's point. The simplification and the illustration of the coordinate system results in the following model, defined by spatial lines. The wireframe model is made of 26 spatial lines (Figure 1).

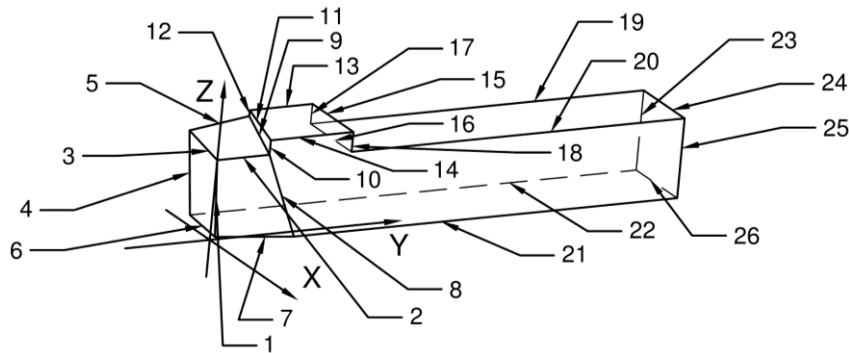


Figure 1 Wireframe model with extensional lines

All spatial lines cross each other, creating so-called pivots. One has to name all these pivots, we named them after the alphabet's letters (Figure 2).

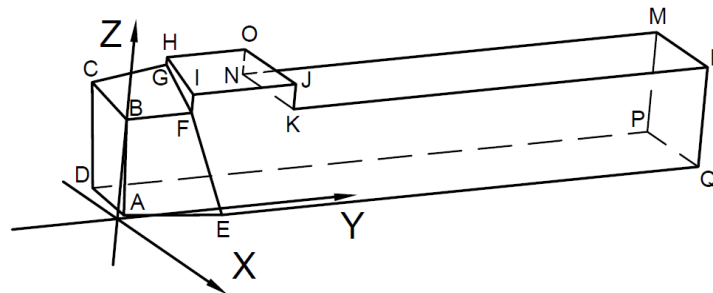


Figure 2 Wireframe model with pivots

Since the pivots are also situated in the space, they are identified through X-Y-Z coordinates. The geometry of the turning tools are characterized by angles and lengths; the equations of the spatial lines must be organized so that after entering these angles and lengths, the program is able to compute the location of the pivots within the modelling space. We develop the wireframe model by connecting the right pivots with lines.

The figures below illustrate the adequate lengths (Figure 3) and angles (Figure 4) we need to enter to define the wireframe model.

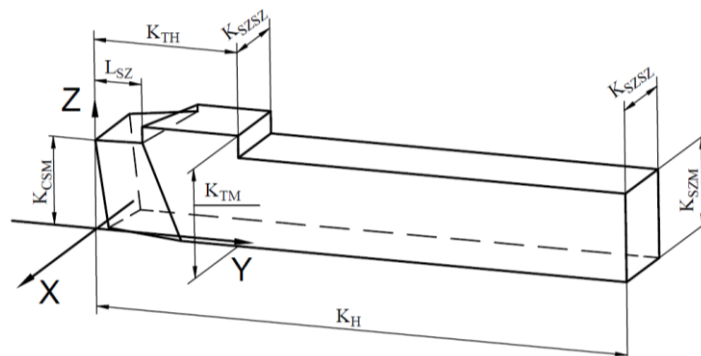


Figure 3 Linear dimensions for the determination of the wireframe model

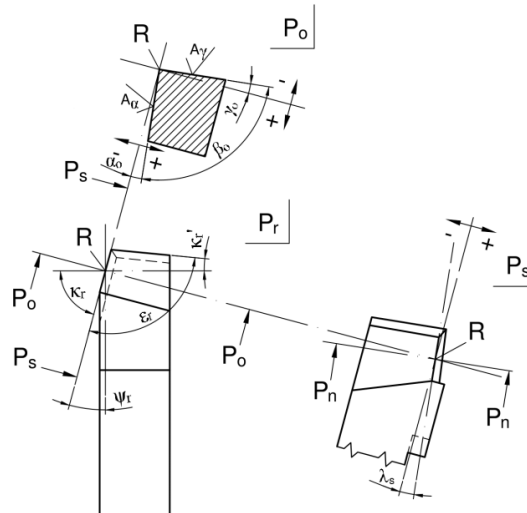


Figure 4 Angle scales for the determination of the wireframe model

The orthogonal tool angle system has been chosen to describe the size of the angles to maintain simplicity [5]. We attempted to describe a turning tool with the least possible number of parameters, then we programmed the equations and developed the modelling program. The program is able to operate without a development environment. The graphic interface is available after opening the program (Figure 5).

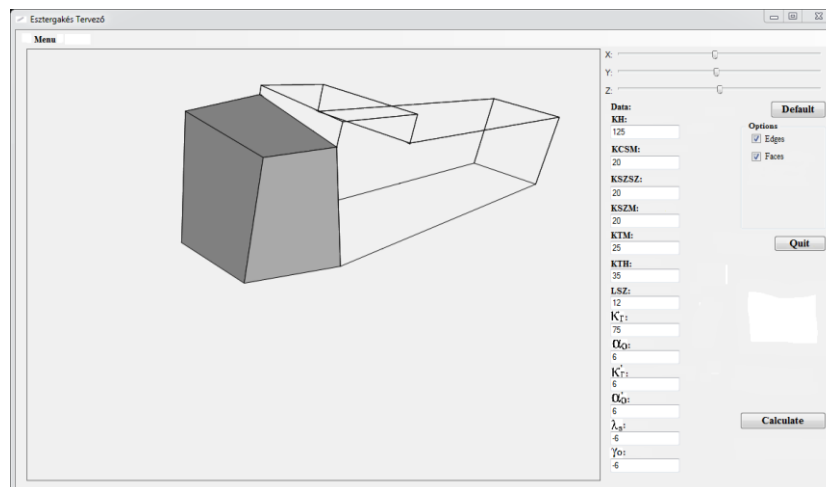


Figure 5 The appearance of the model creator software after running it

The program has two subparts. The interface is on the right side, this is where data entries are made and this is where the icons for saving the model and closing the program are situated. The display is on the left side, this is where the wireframe model based on the given measurements is projected. The model can be rotated by using the X-Y-Z slides. The edges and surfaces can be enabled under the “Options” button, resulting in a model covered by surfaces. The original conditions can be restored by clicking on “Default”, while “Calculate” summons the usual pop-up window that allows us to save the values under a preferred name to the preferred location in the preferred file format. The wireframe model generated by the modelling software is compatible with CAD programs in which further modifications can be made.

After importing the model, it needs to be covered with planes and surfaces. This activity creates a delimited waterproof space – the inner space of the tool. The coating is done by the CAD software



automatically upon opening the file in order to accelerate the process of modelling. The converting command – varying from program to program – transforms the model into a solid body. The most important difference between a model covered by surfaces and a solid body that the latter is considered a “solid material” by the program. This is why the conversion is needed and this is how modifications can be actualized. Sections can be made and parts can be added or removed. The net lines can be deleted by the blending command, so that the model – after applying the groove-type chip breaker and the nose radius filleting – looks like the following (Figure 6).

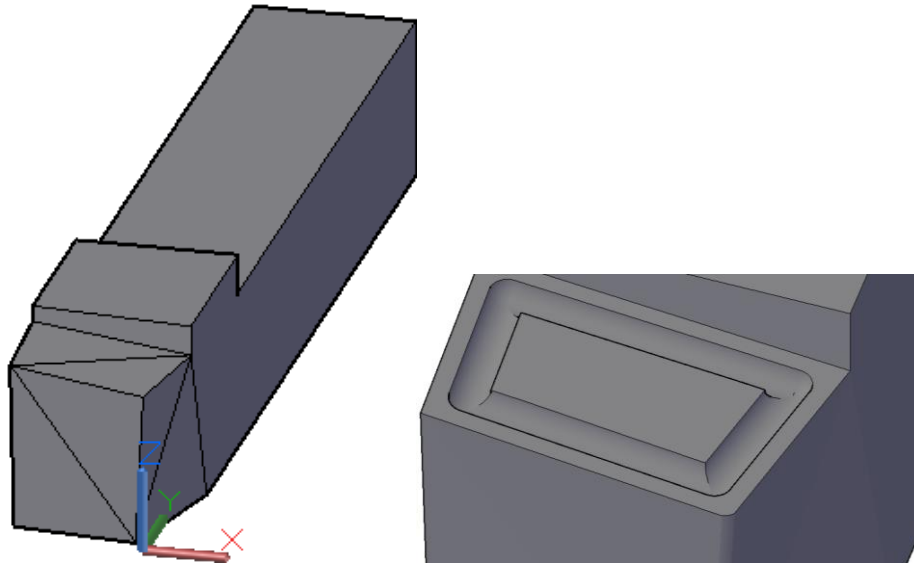


Figure 6 Solid-state model in the CAD software

#### 4. SIMULATION

During the simulations we used one work piece quality and one tool material quality, but the simulations have been run with two different edge geometries.

The tool body as a whole is not important to us while running simulations, so we focused on only a part of the edge geometry (the working part) and ignored the rest. The working part is somewhat similar to the mountable hard metal pellet that is used in practice. Nose radius filleting was used in one of the simulations and dropped in the other.

The **Johnson-Cook** model of material [8] has been utilized in the finite element simulations.

The yield point in the model is dependent on the plastic deformation, the speed of deformation and the temperature. The following formula describes the relationship between the pieces.

$$\sigma = (A + B \cdot \varepsilon_p^n) \left[ 1 + C \cdot \ln \left( \frac{\dot{\varepsilon}}{\dot{\varepsilon}_0} \right) \right] \left[ 1 - \left( \frac{T - T_r}{T_m - T_r} \right)^m \right] \quad (1)$$

This equation, also published by **Johnson-Cook** [8], describes the material wearing:

$$\varepsilon^f = \underbrace{[D_1 + D_2 e^{D_3 \sigma^*}]}_{\text{pressure dependence}} \underbrace{\left[ 1 + D_4 \ln \left( \frac{\dot{\varepsilon}}{\dot{\varepsilon}_0} \right) \right]}_{\text{strain rate dependence}} \underbrace{\left[ 1 + D_5 \left( \frac{T - T_r}{T_m - T_r} \right) \right]}_{\text{temperature dependence}} \quad (2)$$

where:

A	[MPa]	initial yield stress
B	[MPa]	hardening constant
C	[–]	strain rate constant



$\varepsilon_p$	[-]	effective plastic strain
$\dot{\varepsilon}$	$\left[\frac{1}{s}\right]$	rate of the von Mises plastic equivalent strain
$\dot{\varepsilon}_0$	$\left[\frac{1}{s}\right]$	reference strain rate
$\sigma$	[MPa]	von Mises tensile flow stress
$\varepsilon^f$	[-]	strain to fracture
$D_1, D_2, D_3, D_4, D_5$	[-]	material constants

## 5. RESULTS

The results are all within the maximum error of 10%. The figure below illustrates the heat generation during lathe work (Figure 7).

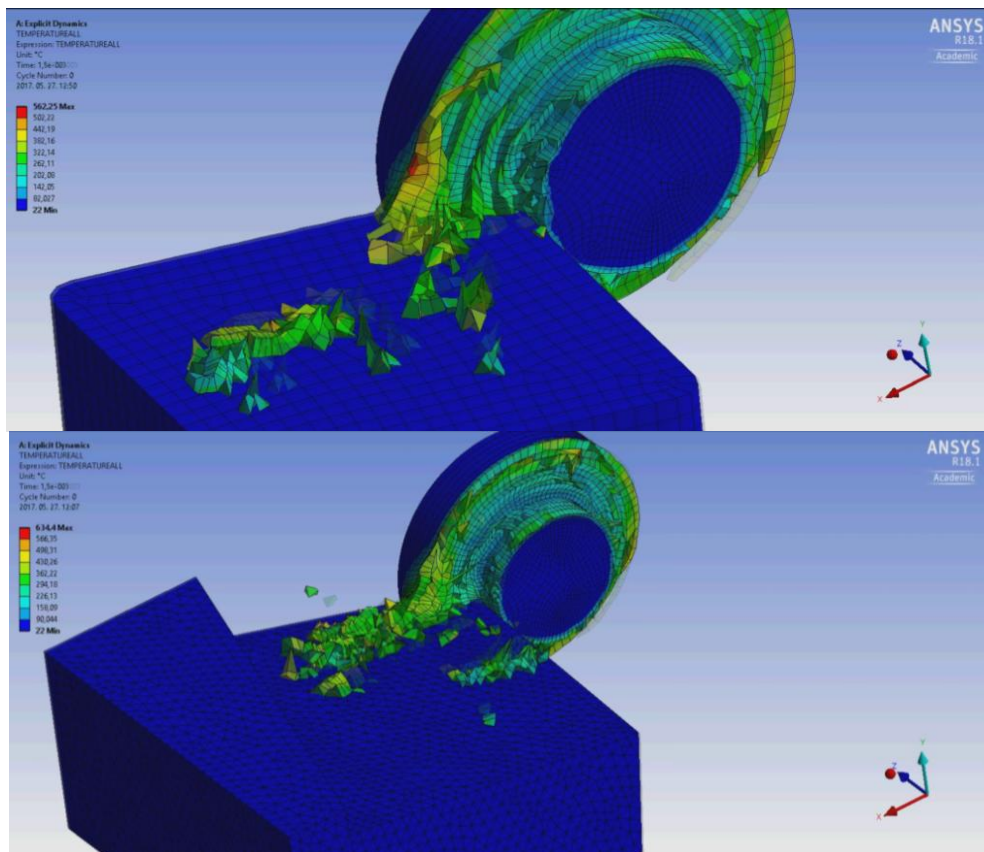


Figure 7 Results

We decided not to include the technical parameters that resulted in these outcomes because those parameters may or may not be true. This, however, does not prevent us from realizing the effect of the nose radius filleting, as by using it almost 100 °C less heat is generated than when there is no filleting. Hereby we would like to express our gratitude towards the Department of Mechanical Engineering of the University of Debrecen for their support and for providing us with opportunities to run the simulations and use the CAD softwares.



## CONCLUSIONS

We have performed the analysis of the lathe tool, we have determined the formulas of the spatial lines, and then finally we placed them in the proper formation.

Our software was developed via programming and has been tested for malfunctioning in several ways. The program, which has a graphic interface, operates without a development environment.

The computer program helps us to create lathe tool type of models in the modelling space quickly and easily.

The produced models are compatible with CAD softwares, meaning that the geometry can be edited freely. The models – after being converted into solid bodies – can be opened with finite element softwares for further analysis on hoe edge geometry influences the chipping.

Several finite element simulations has been done and the result has been assessed.

## REFERENCES

- [1] Bakondi K., Kardos Á.: A gépgyártás technológiája, I. Forgácsolás, *Második kiadás, Tankönyvkiadó, Budapest, 1966., p. 382.*
- [2] Bálint L.: A forgácsoló megmunkálás tervezése, *Műszaki Kiadó, Budapest, 1958.*
- [3] Ducsay J.: Forgácsolási eljárások, *Tankönyvmester Kiadó, Budapest, 2013., ISBN 978-963-275-082-8*
- [4] Dudás I.: Gépgyártás-technológia I., A gépgyártás-technológia alapjai, *Műszaki Kiadó, Budapest, 2011., ISBN 978-963-16-4030-4*
- [5] Dudás I.: Gépgyártás-technológia II., Forgácsoláselmélet, a technológiai tervezés alapjai, *Műszaki Kiadó, Budapest, 2007., ISBN 978-963-16-6003-6*
- [6] Fridrik L.: Forgácsolás I., (Forgácsoláselmélet), *Miskolci Egyetemi Kiadó, 2011, p. 206.*
- [7] Gyáni K.: Gépgyártástechnológia alapjai I., *Tankönyvkiadó, Budapest, 1979, p. 131.*
- [8] Johnson G. R., Cook W. H.: A constitutive model and data for metals subjected to large strains, high strain rates and high temperatures, *Proceedings 7th International Symposium on Ballistics, The Hague, 19-21 April 1983, p. 541-547.*
- [9] Kozma F.: Forgácsoláselmélet, *Kossuth Lajos Tudományegyetem, Műszaki Főiskolai Kara, Debrecen, 1995.*
- [10] Kozma F.: Forgácsolás technológiája I. (Esztergálás, Gyalulás, Vésés és Üregelés), *Kossuth Lajos Tudományegyetem, Műszaki Főiskolai Kara, Debrecen, 1996.*
- [11] Mankovits T., Huri D.: Modellezés és szimuláció (A lineáris rugalmasságtan és a végelem-módszer), *Debreceni Egyetem, 2015.*
- [12] Nemes Cs., Bodzás S.: Egyenes esztergakés tervezése, modellezése és vizsgálata, *Műszaki Tudomány az Észak – Kelet Magyarországi Régióban 2017, Konferencia Előadásai, Nyiregyháza, 2017.06.01., p. 333-339, ISBN 978-963-7064-35-7*
- [13] Páczelt I., Szabó T., Baksa A.: A végelem-módszer alapjai, *készült a HEFOP 3.3.1-P.-2004-09-0102/1.0 pályázat támogatásával, 2007.*
- [14] Y. Zhang, J.C. Outeiro, T. Mabrouki: On the Selection of Johnson-Cook Constitutive Model Parameters for Ti-6Al-4 V Using Three Types of Numerical Models of Orthogonal Cutting, *15th, CIRP Conference on Modelling of Machining Operations, Procedia CIRP, Volume 31, 2015, p. 112-117. Downloaded: 2017.08.10., <http://www.sciencedirect.com/science/article/pii/S2212827115002504>*



## INVESTIGATION OF HOT METAL POWDER SPRAY FUSING OF CULTIVATOR TINES AFTER TILTH

<sup>1</sup>PÁLINKÁS Sándor PhD, <sup>1</sup>FAZEKAS Lajos PhD, <sup>1</sup>BATTÁNE GINDERT-KELE Ágnes PhD,  
<sup>2</sup>MOLNÁR András, <sup>3</sup>HAGYMÁSSY Zoltán PhD

<sup>1</sup>Department of Mechanical Engineering Faculty Engineering, University of Debrecen  
E-mail: [palinkassandor@eng.unideb.hu](mailto:palinkassandor@eng.unideb.hu), [fazekas@eng.unideb.hu](mailto:fazekas@eng.unideb.hu), [battane@eng.unideb.hu](mailto:battane@eng.unideb.hu)

<sup>2</sup>Department of Mechanical Technology, Faculty of Mechanical Engineering and Informatics,  
University of Miskolc

E-mail: [a.molnar2007@gmail.com](mailto:a.molnar2007@gmail.com)

<sup>3</sup>Institute of Land Use, Technology and Regional Development, Faculty of the Agricultural and  
Food Sciences and Environmental Management, University of Debrecen

E-mail: [hagymassy@agr.unideb.hu](mailto:hagymassy@agr.unideb.hu)

### Abstract

*Wear is known to be as the degradation of material under plethora of service conditions and is considered as one of the major issue of the material used in engineering. Many types of wear have been recognized such as abrasive, erosive, corrosion, oxidation etc. Abrasive wear is probably the most significant cause of mechanical damage of equipment components coming in contact with abrasive bodies. For combating with wear problem various methods have also been developed such as hard facing, cryogenic treatment, coating and heat treatment of components which are chosen on the basis of various conditions under which the component has to perform the desired work. The wear of the component depends on its surface characteristics like roughness, microstructure and hardness. The abrasive wear in agriculture equipments is the most common problem. The high wear rate of ground engaging tools led to huge loss of material, recurring labor, downtime and replacement costs of worn out parts. Hardfacing is commonly employed method to improve surface properties of tillage tools.*

**Keywords:** wear, abrasive wear, agricultural equipments, ground engaging tools

### 1. INTRODUCTION

Surface engineering is one of the most relevant current fields of research. The events that occur on the surface, such as wear, corrosion or stress concentration create regions prone to crack nucleation, which under static or dynamic loading will eventually lead to most components and structures failures [1]. Wear is the degradation of metal surface, showing a continuous loss of material, due to relative motion between that main metal surface and another materials or substances whichever come in the contact with the original one. Wear is a major problem in industry and its direct cost is estimated to vary between 1 to 4% of gross national product [2].

Wear is a major problem in the excavation, earth moving, mining, automobiles, machines and mineral processing industries and occurs in a wide variety of items, such as bulldozers blades, excavator teeth, drill bits, crushers, slusher, ball and roll mills, chutes, slurry pumps and cyclones [3]. The wear behaviour of material is related to parameters such as shape, size of component, composition and distribution of micro constituents in addition to the service conditions such as load, sliding speed, environment and temperature [4]. The complex nature of wear has delayed its investigations and results in isolated studies towards specific wear mechanisms. The wear of the



component depends on its surface characteristics like roughness, microstructure and hardness. Friction and wear of materials are generally considered important properties in engineering practice [5]. Many types of wear have been recognized such as abrasive, erosive, adhesive, corrosion, oxidation and surface fatigue wear etc. Wear of solids is treated as the mechanical process. However, other chemical processes, oxidation and corrosion are exceptions of this rule. The abrasive wear and the contact fatigue are the most important from technological point of view. It was estimated that the total wear of component can be identified 80-90% as abrasion and 8% as fatigue wear. Contribution of other types of wear is small [6]. So, abrasive wear is probably the most significant cause of mechanical damage of equipment components coming in contact with abrasive/erosive bodies. The abrasive wear is caused by sharp particles sliding or flowing across a metal surface at varying speeds and pressure, thereby grinding away material like small cutting tools.

It has been estimated that 50% of all wear problems in industry are due to abrasion, and as such, much laboratory work has examined and sought to rationalise the abrasive wear behaviour of a wide range of material [8]. However two body abrasive wear generally arise when particles are in sliding movement, between hard and rough surface, and are able to move freely. Machinery that is operating in sandy environment is vulnerable to sand particles entering and becoming entrapped between components, causing abrasive wear [9]. In a study Hokkirigawa et al (1978) observed three abrasive wear mechanisms using scanning electron microscopy (SEM): microcutting, microploughing and wedge formation. Figure 1 (a) shows the microcutting mechanism, whereas Fig.1 (b) shows the microcutting with less deep grooves. Fig.1(c) shows the micro-ploughing mechanism and Fig.1 (d) shows the wedge formation.

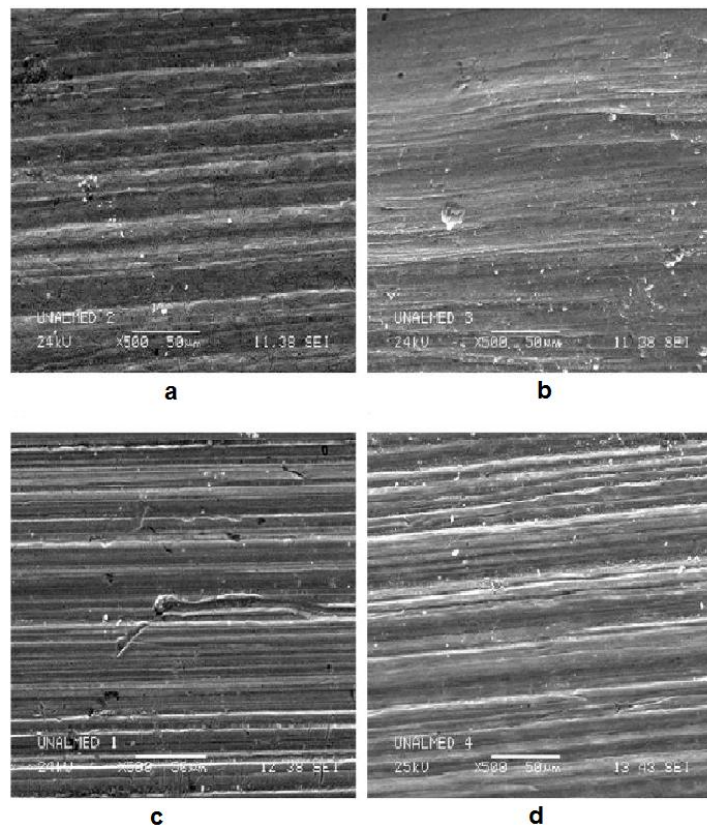


Figure 1 Abrasive wear mechanisms; (a) and (b) microcutting, (c) microploughing, (d) wedge formation.



## **2. ABRASIVE WEAR IN AGRICULTURAL EQUIPMENTS**

The problem of wear has mainly been concentrated on industrial related to large industries, but the interaction between agricultural tillage equipment and soil constitutes a complicated tribological problem [10]. In addition the optimizing tillage is one of the major objectives in mechanized farming to achieve economically viable crop production system [11]. Farmers and equipment operators often complain about high wear rate of ground engaging tools in some dry land agricultural areas. The problems faced with recurring labour, downtime and replacement costs of exchanging the worn out ground engaging components like ploughshares [12]. Worn out tools results in poor tillage or seeding efficiency, poor weed control and higher fuel penalties. Carbon or low alloy steels are generally preferred to make tillage tool under low stress abrasive wear [13]. Tillage having composites with alumina ceramics and boron, medium and high carbon heat treated steels offers great potential the severity of abrasive wear in soil-engaging components [14]. Hardness of tillage tool, grain structure and its chemical composition are also the influential factors in determination of wear rate. Wear due to highly abrasive soils have surface damage characterized by scoring, cutting, deep grooving and gauging, and micro machining caused by soil constituents moving on a metal surface [15].

The wear of tillage implements in most soils is caused by the stones and gravel content. In addition wear on parts of a plough body, more systematically, depends on the wear resistance of the plough parts which in term is dependent on their thermal processing and shape, the tillage conditions, as plough area (or time), plough speed and tillage depth, the normal forces between the soil and the surfaces of the plough area, the proportion, hardness, sharpness and shape of soil particles, the moisture content of the soil, the density and mechanical properties of the soil (hardness, shear strength and brittleness) and environmental effects and weather changes [16]. Wear resistance of plough is mainly associated with their surface hardness and shape of ploughshare, which in turns related to the soil type and the cutting edge thickness. The wear and wear rate determination of tillage tool is necessary because it seriously affects production planning, tillage quality, repair cost of tillage component, energy consumption for tillage process each time performed and finally the production cost of agricultural product [17]. Several studies on the evaluation of abrasive wear resistance have found that using hard deposits in welding processes is a good alternative to recover parts under abrasive wear [18].

## **3. GROUND ENGAGING TOOLS**

The mouldboard „flat feet” hoes is the most widespread tillage tool in the world and the biggest consumer of energy in agriculture [19]. For the design of an energy efficient mouldboard „flat feet” hoes in different operating conditions, an understanding of the interactions of different „flat feet” hoes, soils and operational parameters is essential [20]. The „flat feet” hoes and the mouldboard are the main soil engaging parts of the mouldboard „flat feet” hoes here is the part with the highest wear rate [21]. The „flat feet” hoes wear not only effects its working life but directly changes its initial shape, which is one of the most important factors influencing ploughing quality. The comparison between a new and a worn out ploughshare with changes in initial shape is shown in Figure 2. The wear of the „flat feet” hoes also lead to frequent work stoppages for replacement, downtime and results in direct costs through the important effects of higher fuel consumption and lower rates of work [22].



#### 4. REMEDIAL MEASURES

Wear is considered a genuine problem with engineering material globally, for instance, it has been reported that there is total losses in agricultural sector due to wear is about \$940 million every year in Canada [23] the similar losses costing about \$4.4 million in Turkey every year [24]. Research is going on over the years to reduce the wear either in the form of using a new wear resistance material or by improving the wear resistance of the existing material by addition of any wear resistance alloying element etc.



*Figure 2* A worn and a new out „flat feet” hoes

In order to combat with problem of wear several attempts have been made, and surface treatment has been considered as the most appropriate method [25]. In this various surface modification processes has been found so far, such as carburizing, boriding, nitriding, cryogenic treatment, heat treatment processes, coating and hardfacing. Hardfacing and coating are generally preferred for abrasion wear as cryotreatment found its application in the high-cycle fatigue fields [26]. Hardfacing process is considered as the effective and economical method to reduce wear problem by increasing hardness of the component [27]. Hardfacing is commonly employed method for functionalizing surfaces subjected to severe wear, corrosion or oxidation, which has transformed itself into a field of broad application and development, both in manufacturing of new components and in the repair and extension of useful life across a vast range of industries [28]. The hardfacing not only has a high wear and impact resistance, anti-corrosive behavior of deposited metal, but also can restore the dimensions of worn out components. In addition, the hardfacing may produce a thick deposited layer with a high deposition rate and resulting hardened layer has a high bonding strength with the matrix [29].

The systematic study of various consumable and welding processes applied to hardfacing, is of great interest for the optimization of the design of the consumables and for the evaluation of fine tuning of the welding procedures. The working life of equipment or of a mechanical component exposed to mechanical wear on its surface has been prolonged through the use of wear resistance alloys. Greater benefits can be and of the deposition process. We tried to increase of „flat feet” hoes life time with spray fuse welding methods (Figure 3).

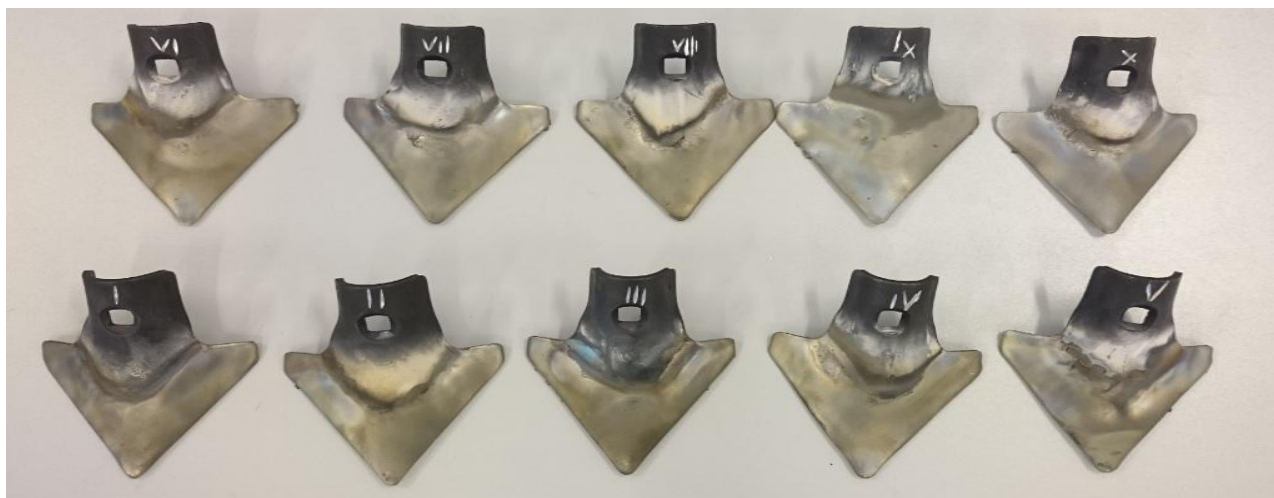


Figure 3 Spray fused „flat feet” hoes

The selection of deposition process is as important as the selection of the alloy to be deposited, i.e. it must be based on various factors such as the operating conditions, characteristics of the base material, the geometry and dimensions of the part, the cost/benefit ratio of the component to be coated and processing cost. The wear resistance of tillage tools depends mainly upon surface hardness. We are presenting our results in Table 1.

Table 1 Mass changing of spray fused hoes in g before- and after using

No of sample	Performed procedures: Spray welding by using	Mass of workpiece [g]		
		Before use	After use	Difference [g]
1.	10009 Borro Tec powder	246,89	199,1	46,98
2.	10009 Borro Tec powder	245,82	187,33	58,49
3.	10009 Borro Tec powder	251,57	198,41	53,16
4.	N 60 Mogul powder	248,54	197,34	51,2
<b>5.</b>	<b>N 60 Mogul powder</b>	<b>258,01</b>	<b>227,24</b>	<b>30,77</b>
6.	N 60 Mogul powder	248,66	193,21	55,45
<b>7.</b>	<b>Deloro 60 powder</b>	<b>253,49</b>	<b>220,09</b>	<b>33,4</b>
8.	Deloro 60 powder	249,83	191,27	58,56
9.	N 40 Mogul powder	265,92	159,05	106,87
10.	N 40 Mogul powder	256,94	184,68	72,26

## 5. THE USE OF COMPLETE WORKPIECES FOR SOIL PREPARATION

The experimental workpieces were given to János Illyés agricultural entrepreneur in Hajdúszovát who mounted them on the combinator seen in Figure 4 and performed the soil-preparation of a land of 200 hectare. The mass of tines was measured both before using them and after the soil-preparation of the land of 200 hectare. The obtained results are demonstrated in Table 1. The worn experimental workpieces are shown in Figure 5. It can be stated that Sample No. 5 (indicated by red



colour in the Table) and Sample No. 7 (indicated by blue colour in the Table) wore in the less extent of the samples treated by hot metal powder spraying. Such a result could be anticipated at these samples as this powder had got the highest hardness (60 HRC). In case of the samples No. 9 and 10, a powder-type with a hardness of 40 HRC was applied – a significant material loss was experienced at these samples – so we are not going to deal with this type of powder during our further experiments. A scattering can be observed as far as the material-loss of samples treated by the powders of identical types is concerned. It can be explained by the fact that the load of cultivator tines mounted on the agricultural machine was not equal; the tines overlap each other and the tines working in the tractor wheel track were exposed to a higher abrasive power owing to the compression of soil.



Figure 4 The combinator used for tillage



Figure 5 The experimental workpieces after use



The increase in material hardness results in decrease in wear rate. We showed the intermediate layer on Figure 6 – when we made a hard coating spray fused NiCrBSi coating on steel substrate. Certainly, there has to be a relationship between tool hardness and hardness of particles in order to keep effective wear resistance but also to be borne in mind is the fact that high hardness implies brittleness [30]. Studies on the wear resistance of the materials subjected to the impact of abrasive particles are usually carried out at many research centres. The research determined the wear resistance of material under laboratory conditions and includes selection of adequate grades of steel [31]. On the other hand, determination of effect different implement designs and different working conditions on the wear and its distribution on a given element requires field testing. This is due to the difficulties in laboratory simulation of changes in load, which occur during work in soil [32]. In laboratory conditions several methods are employed to determine the wear resistance of materials like dry sand rubber wheel test, pin on disc test etc. When comparison is made between the laboratory and in field experiments, it can be concluded that the actual field environment, in which the impacts or contacts to the tillage tool components occurs due to factors such as hard soil particles as the stones, gravels, rocks and roots during working in field could not be achieved satisfactorily in the laboratory merely through wear test machine [33-34].

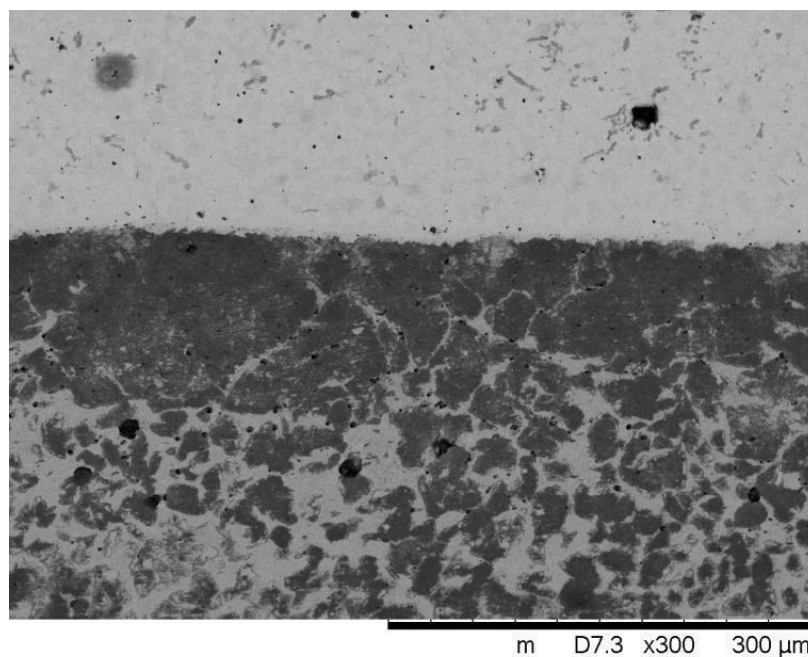


Figure 6 Intermediate layer at number of 8 probe piece (M=300X)

## CONCLUSIONS

Wear is considered as the major problem in engineering and agricultural components. To combat with wear problem, hardfacing is the most versatile process among many alternatives to improve the life of the worn out components and reducing the cost of replacement. Hardfacing reduces the downtime because parts last longer and fewer shutdowns are required to replace them. To determine wear in agricultural sector, in-field tests are necessary due to the difficulties in laboratory simulation of changes in load, which occur during work in soil. The performance of the components variations in conditions in actual environment could not be achieved through laboratory tests.



## ACKNOWLEDGEMENT

The publication is supported by the EFOP-3.6.1-16-2016-00022 project. The project is co-financed by the European Union and the European Social Fund.

## REFERENCES

- [1] J. Gandra, D. Pereira, R.M. Miranda, R.J.C. Silva and P. Vilaça, “*Deposition of AA6082-T6 over AA2024-T3 by friction surfacing - Mechanical and wear characterization*”, *Surface & Coatings Technology*, vol. 223, pp. 32–40, 2013.
- [2] Philip D Goode, *Nuclear Instruments and Methods in Physics Research Section B: Beam Interactions with Materials and Atoms*, Volume 39, Issues 1–4, Pages 521–530, 1989.
- [3] Sarkar AD, Clarke J , *Friction and wear of aluminium silicon alloys*, *Wear*, Volume 61, Issue 1, Pages 157–167, 1980.
- [4] Al-Mangour, B., R. Mongrain, E. Irissou, and S. Yue. 2013. *Improving the strength and corrosion resistance of 316L stainless steel for biomedical applications using cold spray*. *Surface & Coatings Technology* 216:297–307.
- [5] S. Ma, S. Zheng, D. Cao and H. Guo, “*Anti-wear and friction performance of ZrO<sub>2</sub> nanoparticles as lubricant additive*”, *Particuology*, vol. 8, pp. 468–472, 2010.
- [6] Alfred Zmitrowicz, “*Wear patterns and laws of wear*”, *A Review Journal of Theoretical and Applied Mechanics*, Warsaw, vol. 44, no. 2, pp. 219-253, 2006.
- [7] K. Hokkirigawa, K. Kato, “*An experimental and theoretical investigation of ploughing, cutting and wedge formation during abrasive wear*”, *Tribol international*, vol. 39, no. 6, pp. 570-574, 2006.
- [8] Eyre T S , *Wear characteristics of metals* ,*Tribol. Int.* 10 , 203-212,1976.
- [9] Woldman M, van der Heide E , Schipper D J , Tinga T, Masen M A, *Investigating the influence of sand particle properties on abrasive wear behaviour*, 294-295, Page 419-426, 2012.
- [10] Natsis A, Petropoulos G , Pandazaras C, *Influence of local soil conditions on mouldboard ploughshare abrasive wear*, *Tribology International*, 41, 151-157, 2008.
- [11] Jayasuriya H P W, Salokhe V M , *SW—Soil and Water: A Review of Soil–tine Models for a Range of Soil Conditions*, *Soil and Water*, doi:10.1006/jaer.2000.0692.
- [12] G.R. Quick, “*Tillage tool wear – some governing factors, measuring techniques and materials for wear resistance*”, *Agricultural Engineering Development International Rice Research Institute*. Phillipines, 1989.
- [13] H-J Yu , Bhole SD , *Development of a prototype abrasive wear tester for tillage tool materials*, *Tribol Int*, 23(5):309-16, 1990.
- [14] Foley AG , Lawton PJ , Mclees VA . *The use of alumina ceramic to reduce wear of soil-engaging components*. *J Agric Eng Res* , 30(1):37-46, 1984.
- [15] S.A. Ferguson, J.M. Fielke, T.W. Riley, “*Wear of cultivator shares in abressive south Australian soils*”, *J. Agric. Engg. Res.*, vol. 69, pp. 99-105, 1998.
- [16] Bayhan Y, *Reduction of wear via hardfacing of chisel ploughshare*, *Tribology International* 39 , 570-574, 2006.
- [17] A. Natsis, G. Papadakis, J. Pitsilis, “*The influence of soil type, soil water, and share sharpness of mouldboard plough on energy consumption, rate of work and tillage quality*”, *J Agric. Engg. Res.*, vol. 72, pp. 171-176, 1999.
- [18] I.M. Hutchings, *Tribology : “Friction and wear of engineering materials”*, Cambridge University Press ; 1992.



# INTERNATIONAL SCIENTIFIC CONFERENCE ON ADVANCES IN MECHANICAL ENGINEERING

12-14 October 2017, Debrecen, Hungary



- [19] V. Cracium, D. Leon, “*An analytical method for identifying and designing a mouldboard plough surface*”, Trans. ASAE, vol. 41, no. 6, pp. 1589-1599, 1998.
- [20] D.S. Shrestha, G. Singh, G. Gebresenbet, “*Optimizing design parameters of mouldboard plough*”, J Agric. Engg. Res., vol. 78, no. 4, pp. 337-389, 2001.
- [21] G. Wiese, E.H. Bourarach, “*Handbook of agricultural engineering*”, Plant Production Engineering, vol. 3, pp. 184-217, 1999.
- [22] E.Y.H Bobobee, K. Sraku-Lartey, S.C. Fialor, E.A. Canacoo, S.K. Agodzo, A. Yawson, “*Wear rate of animal drawn ploughshares in selected Ghanian soils*”, Soil Tillage Res., vol. 93, no. 2, pp. 299-308, 2007.
- [23] Ulusoy E. *A research on determination of wearing of some tillage tool shares*. Ege University. J AgricFac (390), 1981.
- [24] Gupta D, Sharma A K, *Investigation on sliding wear performance of WC10Co2Ni cladding developed through microwave irradiation*, wear, 271, 1642-1650, 2011.
- [25] Ivusic V, Jakovljevic M. *Protection of agricultural machinery from wear*. In: Proceedings of the international conference “Science and Practice of Agricultural Engineering,” Djakovo, Croatia, p. 275-83, 1992.
- [26] Bayhan Y, *Reduction of wear via hardfacing of chisel ploughshare*, Tribology International 39, 570-574, 2006.
- [27] Buchely M F, Gutierrez J C, Leon L M, Toro A, *The effect of microstructure on abrasive wear of hardfacing alloys*, Wear 259, 52-61, 2005.
- [28] Agustí'n Gualco, Herna'n G. Sroboda, Estela S. Surian and Luis A. deVedia, “*Effect of post weld heat treatment on the wear resistance of hardfacing martensitic steel deposits*”, Welding International, vol. 24, no. 4, pp. 258-265, 2010.
- [29] CHEN Bing-quan CHAI Cang-xiu PENG JUN-bo, “*A high Fe-Aluminium matrix welding filler metal for hardfacing aluminium-silicon alloy*”, Journal of Wuhan University of Technology – Mater. Sci. Ed., vol. 18, no. 1, pp. 25-28, 2003.
- [30] Y. Bayhan, “*Reduction of wear via hardfacing of chisel ploughshare*”, Tribol. Int., vol. 39, no. 6, pp. 570-574, 2006..
- [31] Zygmunt Owsiak, “*Wear of spring tine cultivator points in sandy loam and light clay soils in southern Poland*”, Soil and Tillage Research, vol.
- [32] A.G. Folay, P.J. Lawton, A.W. Barker, V.A. McLees, 1984. “*The use of alumina ceramic to reduce wear of soil engaging components*”, J Agric. Engg. Res., vol. 30, pp. 37-46, 1984.
- [33] B Par, U Er, “*Wear of ploughshare components in SAE 950 C steel surface hardened by powder boriding*”, Osmangazi University, Bati Meselik, 26480 – Eskishir, Turkey, Wear 261, pp. 251-255, 2005.
- [34] Parvinkal Singh Mann and Navjeet Kaur Brar: *Tribological aspects of agricultural equipments*, International Research Journal of Engineering and Technology (IRJET) Volume: 02 Issue: 03 | June-2015



## THE EFFECT OF THICKNESS REDUCTION ON THE RECRYSTALLIZATION PROCESSES OF COLD ROLLED 3104 DEEP DRAW AL SHEETS

*PETHŐ Dániel, BENKE Márton PhD, MERTINGER Valéria PhD, BARKÓCZY Péter PhD*

*Institute of Physical Metallurgy, Metalforming and Nanotechnology, University of Miskolc  
E-mail: [femdani@uni-miskolc.hu](mailto:femdani@uni-miskolc.hu), [embenke@uni-miskolc.hu](mailto:embenke@uni-miskolc.hu), [femvali@uni-miskolc.hu](mailto:femvali@uni-miskolc.hu),  
[fembarki@uni-miskolc.hu](mailto:fembarki@uni-miskolc.hu)*

### Abstract

*The present paper reports about the examination of the microstructure and texture variation during the annealing heat treatments of cold rolled 3104 type deep draw Al alloy sheets as a function of thickness reduction. The variation of the microstructure was examined by optical microscopy and Scanning Electron Microscopy and the variation of the texture was examined by means of X-ray diffraction. Detailed ODF analysis revealed that up to 90% thickness reduction, particle stimulated (PSN) recrystallization was the sole process during 1 hour of annealing at 673 K, resulting an isotropic structure. However, at 96% thickness reduction, extended recovery dominated over PSN, resulting in strong Cu texture component. Afterwards, PSN dominated over genuine discontinuous recrystallization during subsequent annealing resulting a close to random orientation with weak recrystallization components.*

**Keywords:** *aluminium, texture, recrystallization.*

### 1. INTRODUCTION

The 3104 type Al is a common material for deep drawing products. The proper thickness of the semi-product is achieved by hot and/or cold rolling steps. The main problem in the deep drawing process is that the texture developed during the rolling and/or the annealing heat treatments results an anisotropic formability. This anisotropy is often referred as “plastic anisotropy”. The stronger the texture is, the stronger plastic anisotropy results which may lead to earing [1-5].

Since annealing heat treatments are usually the last processes that affect the crystallographic texture before the deep drawing, the characterization of the recrystallization processes and the resulting textures are of great importance. It is known that besides genuine discontinuous recrystallization that results the classic recrystallization textures, the Cube and/or Goss, there are other types of recrystallization processes as well, which result in completely different textures. For instance, if particles with sizes  $\geq 1 \mu\text{m}$  are present, the particle stimulated nucleation (PSN) process is promoted in the vicinity of particles, the so-called deformation zones that form around the particles through the interaction between dislocations and the particles by introducing nucleation sites which results in a random grain structure [3]. If the genuine discontinuous recrystallization is suppressed through the prevention of all high angle grain boundary movements, extended recovery can be activated. High deformations also favour extended recovery. Since there is no high angle grain boundary movement, the deformation texture is preserved during extended recovery. Extended recovery can even sharpen the deformation texture by healing out of the dislocations within the formed subgrains thus decreasing the orientation scatter [6]. If these recrystallization processes occur simultaneously, the resulting texture will be their mixture. If one of the recrystallization processes is favoured, it will result in a dominating texture over the others. Finally, the recrystallization process in general can be quite complicated since it may cover many processes



being different from each other. The occurrence of these processes and the developed recrystallization texture strongly depend on many parameters, such as microstructure, deformation degree, rolling texture, etc.

The aim of the present paper is to characterize the rolling and recrystallization textures developed during the cold rolling steps and annealing heat treatments prior to the deep draw process of a 3104 type Al alloy as a function of thickness reduction. The types of the observed recrystallization processes are also discussed.

## 2. METHODS

The composition of the examined 3104 type Al is summarized in Table 1. After a preheating to 723 K, the 3104 Al sheets were rolled to the initial  $h_0=4.8$  mm thickness in the first rolling step. The hot-rolled sheets were subsequently annealed at 673 K for 1 hour. The annealed sheets were then cold-rolled at room temperature with different thickness reductions to  $h_1=1.5$  mm, 1 mm, 0.5 mm or 0.2 mm thicknesses, respectively. The thickness reductions were calculated as  $\varepsilon=(h_0-h_1)/h_0*100$ . Accordingly, the calculated degrees of thickness reductions were:  $\varepsilon=69\%$ ,  $79\%$ ,  $90\%$  and  $96\%$ . Sample pairs were cut from the sheets after the cold rolling. The first ones of the pairs were in cold-rolled state, getting the mark "R" (referring to the cold-rolled state of the sheets). These samples were labelled as  $\varepsilon/R$ . The second ones of the pairs were annealed after the cold rolling at 673 K for 1 hour. These samples were marked with "A" (referring to the annealed state). These samples were labelled as  $\varepsilon/A$ , respectively. Furthermore, annealed samples with thickness reduction of  $\varepsilon=96\%$  were additionally annealed at 653 K, 673 K and 693 K for 2 hours or for 4 hours. These were labelled for instance as 96A/653/2 or 96A/693/4, respectively. The samples were quenched in water after all of the annealing treatments.

Table 1 The composition of the examined alloy [m/m%]

Si	Fe	Cu	Mn	Mg	Cr	Zn	Ti
0.13	0.60	0.20	1.06	1.0	0.005	0.029	0.014

The samples were prepared by mechanical polishing and Barker etchant (Struers Electropol 5) for the grain structure examinations and 0.5% solution of HF etchant for the Scanning Electron Microscope (SEM) examinations. The preparation for texture measurements included mechanical polishing and etching in Al macro-etchant (2 ml  $\text{HNO}_3$ , 2 ml HCl, 1 ml HF). Structure examinations were carried out in the Complex Laboratory of Image- and Structure Analysis (LISA) of the Institute of Physical Metallurgy, Metalforming and Nanotechnology of the University of Miskolc (which attained the Strategic Research Infrastructure rating in the National Research Infrastructure Survey and Roadmap [7]). Optical microscope examinations were performed with a Zeiss Axiovert 40 type microscope using polarized light, SEM examinations were carried out using a Zeiss EVO MA10 SEM equipped with (EDS) and macrotexture measurements were performed with a Bruker D8 Advance diffractometer equipped with an Eulerian cradle ( $\text{CoK}\alpha$  tube). Incomplete pole figures were measured of the Al {111}, {200} and {220} plane series on the surface of the samples. The parameters of the measurements were: rotation angle,  $\varphi$ : 0-360°, measurement time,  $t_{\text{rotation}}=360\text{s}$ , tilt angle,  $\chi$ : 0-75°,  $\Delta\chi=5^\circ$ , background correction time:  $t=25$  s. The same pole figures of pure Al powder (min. 98% Al, 160  $\mu\text{m}$ ) were measured with the same parameters for the defocusing correction. The ghost-corrected pole figures and the texture index (T) were calculated using the harmonic method with Bruker's DiffracPlus Basic TexEval 2.5 software. The calculations were performed for cubic crystal symmetry and orthorhombic sample symmetry in accordance with the rolling operations (rolling direction: RD, transverse direction: TD and sheet normal direction: ND)



[8, 9]. No additional pole figures were calculated and no positivity refinement was used during the calculations [10]. The Orientation Distribution Functions (ODFs)  $f(g)$  were calculated from the data of the ghost-corrected pole figures. The orientations  $g$  are given by the Euler angles  $\varphi_1$ ,  $\Phi$ , and  $\varphi_2$ . The textures are represented with iso-intensity lines on the equidistant sections ( $\Delta\varphi_2=5^\circ$ ) through the reduced Euler angle space with  $0^\circ \leq \{\varphi_1, \Phi, \varphi_2\} \leq 90^\circ$ . Volume fractions with  $11^\circ$  radius were calculated for the most important orientations (texture components) of Al and Al alloys after rolling: Cu (C), S, Brass (B), and after recrystallization: Goss (G), Cube, a Goss component rotated  $19^\circ$  around ND (GossND), Cube component rotated  $20^\circ$  around ND (CubeND), R and P. The texture components with their designations, Miller indices  $\{hkl\}\langle uvw \rangle$  - where the first set of Miller indices refers to the sheet normal and the second to the rolling direction - and their approximated Euler angles are listed in Table 2.

Table 2 The designations, Miller indices, Euler angles of the most important texture components of Al and Al alloys after rolling and recrystallization (approximated)

Designation	Miller indices $\{hkl\}\langle uvw \rangle$	Euler angles			
		$\varphi_1$	$\Phi$	$\varphi_2$	
C	$\{112\}\langle 111 \rangle$	$90^\circ$	$30^\circ$	$45^\circ$	Rolling Texture Components
S	$\{123\}\langle 634 \rangle$	$59^\circ$	$34^\circ$	$65^\circ$	
B	$\{011\}\langle 211 \rangle$	$35^\circ$	$45^\circ$	$0^\circ/90^\circ$	
G	$\{011\}\langle 100 \rangle$	$0^\circ$	$45^\circ$	$0^\circ/90^\circ$	Recrystallization Texture Components
Cube	$\{001\}\langle 100 \rangle$	$0^\circ$	$0^\circ$	$0^\circ/90^\circ$	
GossND	-	$19^\circ$	$45^\circ$	$0^\circ/90^\circ$	
CubeND	$\{001\}\langle 310 \rangle$	$20^\circ$	$0^\circ$	$0^\circ/90^\circ$	
R	$\{124\}\langle 211 \rangle$	$53^\circ$	$36^\circ$	$60^\circ$	
P	$\{011\}\langle 122 \rangle$	$65^\circ$	$45^\circ$	$0^\circ/90^\circ$	

### 3. RESULTS

#### 3.1 Microstructure

The application of the Barker etchant gives a colour contrast between the grains with different crystallographic orientations under polarized light. This method was used to examine the microstructures of the rolled and annealed samples. The microstructure variation during the 673 K 1 hour annealing heat treatments are presented through the microstructures of the cold rolled and annealed samples exposed to the lowest ( $\epsilon=69\%$ ) and largest ( $\epsilon=96\%$ ) thickness reductions. Figure 1 (a) shows the microstructure of the 69/R sample and Figure 1 (b) shows the image of the 69/A sample.

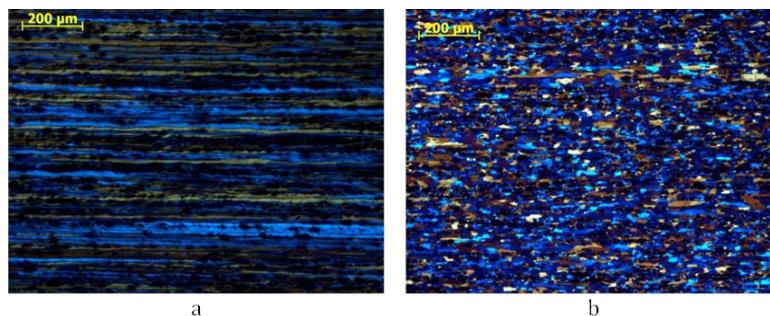
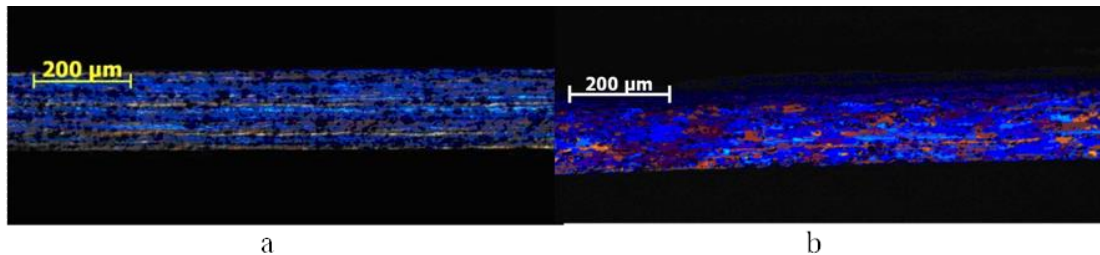


Figure 1 Microstructures of the sheets exposed to  $\epsilon=69\%$  thickness reduction (a) as-rolled state and (b) rolled and annealed at 673 K for 1 hour



In *Figure 1* (a) severely elongated grains and a texture due to the rolling deformation are clearly visible. In *Figure 1* (b) the rolled grain structure disappeared and a recrystallized structure with equiaxial grains can be seen. A random orientation dominates over a minor texture. *Figure 2* (a) shows the microstructure of the 96/R sample and *Figure 2* (b) shows the microstructure of the 96/A sample.



*Figure 2* Microstructures of the sheets exposed to  $\epsilon=96\%$  thickness reduction (a) as-rolled state and (b) rolled and annealed at 673 K for 1 hour

In *Figure 2* (a) the severely deformed grain structure and a strong texture can be seen. According to *Figure 2* (b), the annealed sample still possesses a minor elongated structure, but the recrystallized state obviously dominates. A strong texture also can be observed because of the weak colour contrast.

To follow the microstructure change during the additional annealing, the microstructures of the 96A/653/2 (*Figure 3* (a)) and 96A/693/4 (*Figure 3* (b)) samples are presented.

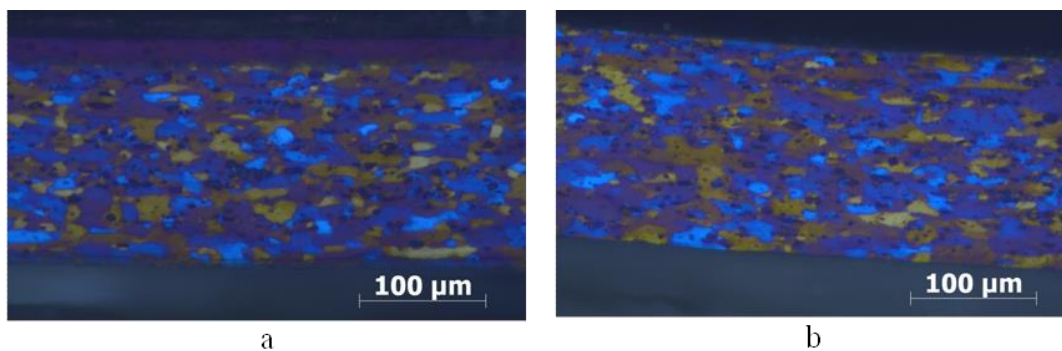


*Figure 3* Microstructures of the sheets exposed to  $\epsilon=96\%$  thickness reduction (a) additionally annealed at 653 K for 2 hours and (b) at 693 K for 4 hours

According to *Figure 3* (a) and (b) the rolled structures completely disappeared and the equiaxial grain structures dominate due to the additional heat treatments. A random orientation dominates over a weak texture in both samples. No significant difference can be observed between the microstructures of the two samples.

To reveal secondary phases, SEM and EDS examinations were performed on the rolled and annealed samples. The SEM image of the 69R sample is shown in *Figure 4*. The results of the EDS measurements at the points of *Figure 4* are summarized in *Table 3*. The EDS measurement at point 3 was an area scan, while at other points spot measurements were performed.

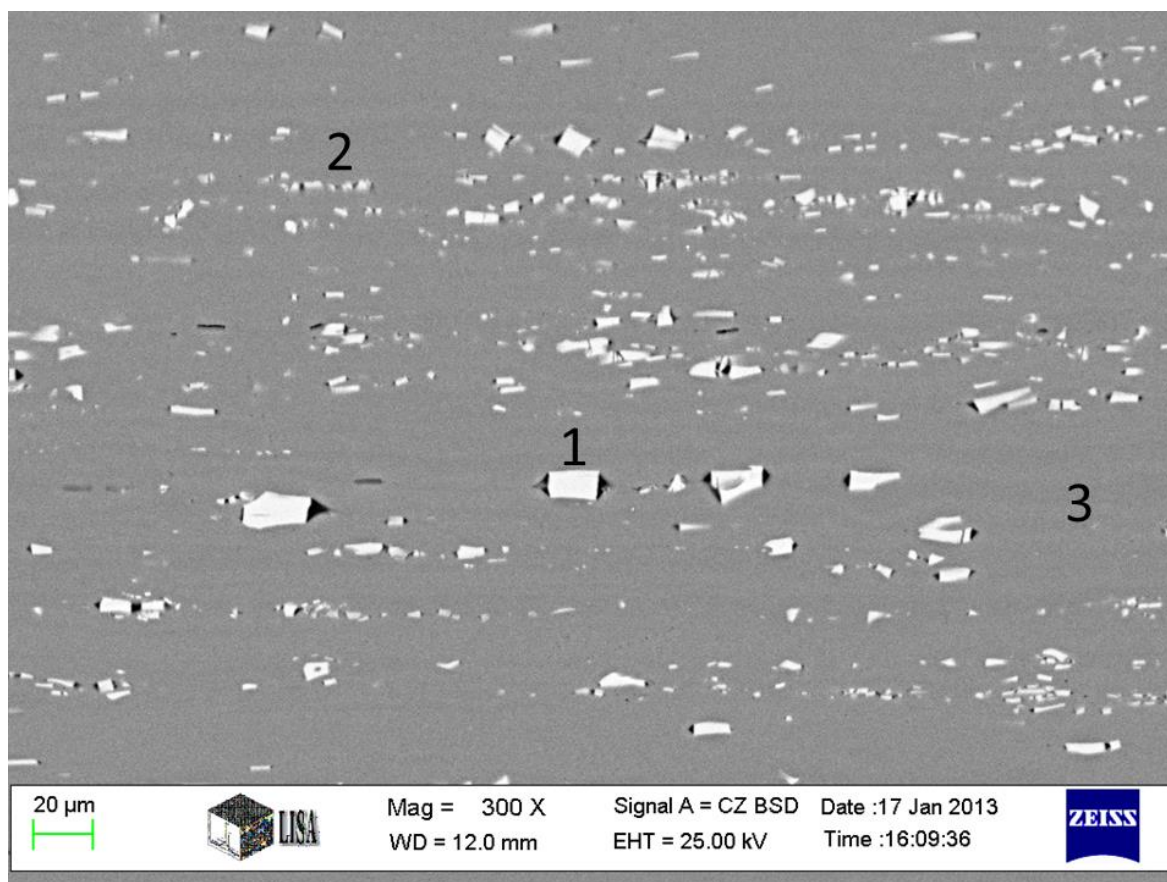


Figure 4 SEM image of the sample exposed to  $\epsilon=69\%$  thickness reduction

Table 3 The results of the EDS examinations of the points marked in Figure 4. [m/m%]

	1	2	3
Al	balance	balance	balance
Mn	10.62	6.64	0.68
Mg	-	0.99	1.72
Fe	13.16	12.22	0.19
Cu	0.99	0.79	0.32
Si	-	3.72	-

Particles of precipitations can be observed within the matrix in Figure 4. The larger particles with  $\sim 10 \mu\text{m}$  size consist of Fe, Mn and Cu, while the smaller ones with a few  $\mu\text{m}$  size contain all of the main alloying elements. Regarding the precipitations, there were no differences between the rolled and annealed samples or the samples exposed to different thickness reductions. Thus, the particles formed probably before the cold rolling of the sheets.

### 3.2 Texture

The variation of the texture due to the 673 K 1 hour annealing heat treatment is presented through ODF cuts of the samples exposed to the smallest (69%) and the largest (96%) thickness reductions.

In Figure 5 (a) the ODF cuts of the 69/R sample show the typical texture of rolled Al and Al alloys with the characteristic rolling texture components. [3, 6, 8, 11-13].

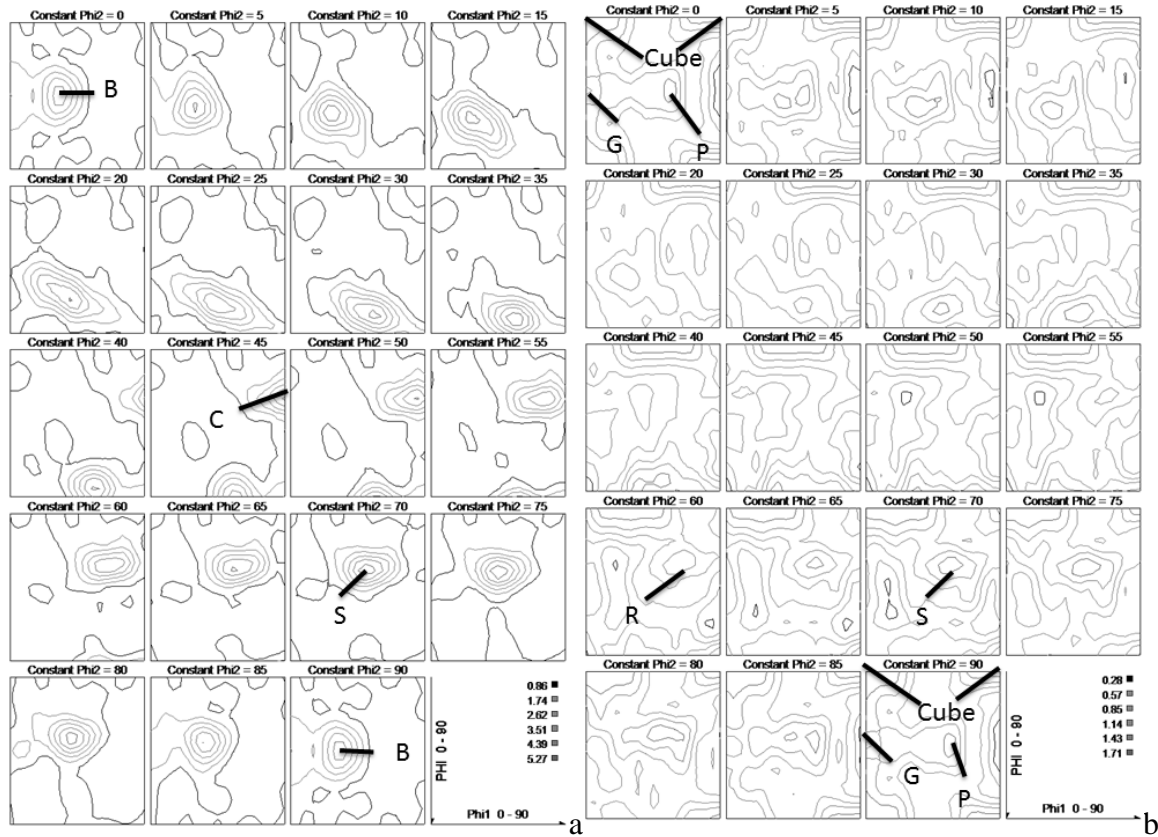


Figure 5 ODF cuts of the sheets exposed to  $\epsilon=69\%$  thickness reduction (a) as-rolled state and (b) annealed at 673 K for 1 hour with the typical texture components of Al and Al alloys (C: Copper, S, B: Brass, G: Goss, Cube, R, P)

According to the ODF cuts of the 69/A sample in Figure 5 (b) a nearly isotropic structure developed due to the annealing, where the rolled and recrystallized texture components can be recognized with very low intensities [3, 5, 6, 8, 11-13].

Figure 6 (a) show the ODF cuts of the 96/R sample with sharp rolling texture. The rolled texture components have higher intensities compared to the 69R sample (Figure 5 (a)) due to the larger thickness reduction. The ODF cuts of the annealed 96/A sample in Figure 6 (b) also show a sharp rolling texture with somewhat lower intensities compared to the as-rolled state. Only the P component appears weakly from the recrystallization components.

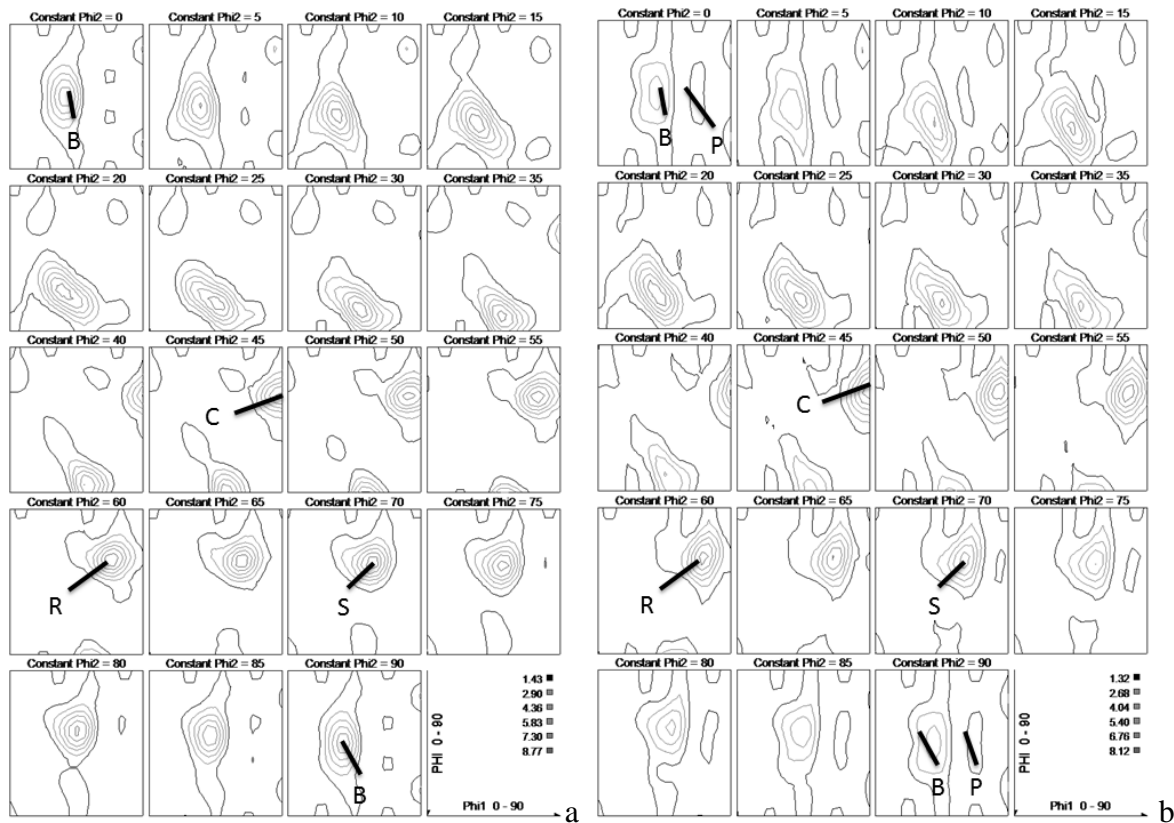


Figure 6 ODF cuts of the sheets exposed to  $\epsilon=96\%$  thickness reduction (a) as-rolled state and (b) annealed at 673 K for 1 hour with the typical texture components of Al and Al alloys (C: Copper, S, B: Brass, G: Goss, Cube, R, P)

The variation of the volume fractions of the main texture components and the texture index (T) of the rolled sheets as a function of thickness reduction are summarized in Figure 7 (a). The variation of the volume fractions of the texture components and the texture index (T) of the annealed sheets as a function of thickness reduction are summarized in Figure 7 (b).

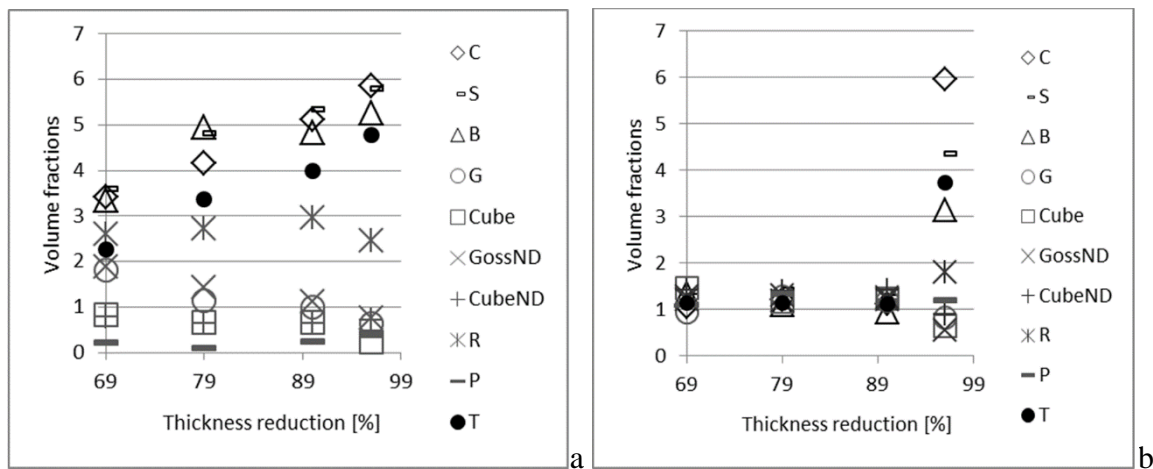
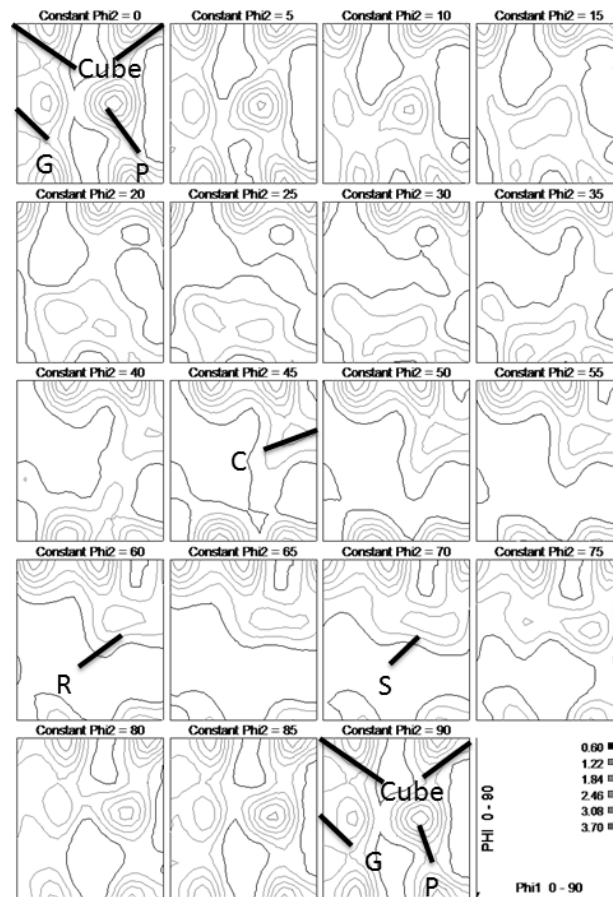


Figure 7 Variation of the texture components (C: Copper, S, B: Brass, G: Goss, Cube, GossND: Goss rotated around normal direction, CubeND: Cube rotated around normal direction, R, P) and texture index (T) versus thickness reduction of the (a) as-rolled sheets, (b) annealed sheets



In *Figure 7 (a)* it can be seen that as the thickness reduction increases, the volume fractions of the rolling texture components and the texture index increase while the volume fractions of the recrystallization texture components slightly decrease. (The R component from the recrystallization texture components seems to increase up to 90% thickness reduction together with the rolling texture components. This is due to the small angular difference between the R and S components.) According to *Figure 7 (b)* the volume fractions of the rolling texture components dropped, but the volume fractions of the recrystallization texture components did not increase notably. Thus, the resulting structures are isotropic. This trend stands only up to 90% thickness reduction. At 96% thickness reduction the volume fractions of the Brass (B) and S components decreased (but not dropped as did for smaller thickness reductions), but the volume fraction of the Cu (C) component increased. Thus, the Cu texture dominates in the annealed sample at 96% thickness reduction. The texture developed after the additional annealing heat treatments of the 96A sample is shown in *Figure 8*. through ODF cuts of the 96A/693/4 sample.



*Figure 8* ODF cuts of the additionally annealed sheets at 693 K for 4 hours with  $\epsilon=96\%$  thickness reduction with the typical texture components of Al and Al alloys (C: Copper, S, G: Goss, Cube, R, P)

In *Figure 8* the recrystallized texture components can be seen with low intensities. The mixture of the low intensity recrystallization texture components results in a structure which is close to isotropic. The highest intensities can be found close to the Cube orientation but rotated around  $\varphi_1$  (ND) with  $\sim 20^\circ$  giving the CubeND orientation, in the P orientation and close to the Goss orientation but rotated around  $\varphi_1$  (ND) with  $\sim 19^\circ$  giving the GossND orientation.



The variation of the volume fractions of the main texture components and the texture index as a function of the additional annealing temperature are shown in *Figure 9* (a) and (b). *Figure 9* (a) shows the results of the 96A samples after 2 hours of additional annealing treatments and *Figure 9* (b) shows the results of the 96A samples after 4 hours of additional annealing treatments.

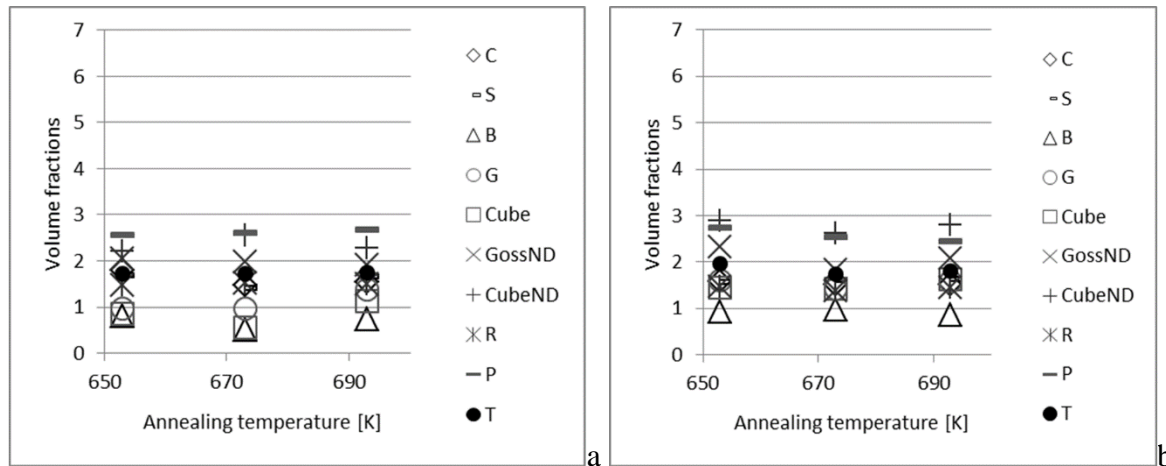


*Figure 9* Variation of the texture components (C: Copper, S, B: Brass, G: Goss, Cube, GossND: Goss rotated around normal direction, CubeND: Cube rotated around normal direction, R, P) and texture index (T) of the sheets exposed to  $\epsilon=96\%$  thickness reduction versus additional annealing temperature for (a) 2 hours annealing time, (b) 4 hours annealing time

In *Figure 9* (a) and (b) it can be seen that the volume fractions of the rolling texture components dropped due to the additional annealing heat treatments. The volume fractions of the P, the CubeND and the GossND components increased while the other recrystallization components did not. No notable changes can be seen in the textures as the temperature and/or time of the additional annealing changes.

## 4. DISCUSSION

### 4.1 Deformation

During the microstructure and texture examinations of the cold rolled 3104 Al samples it was observed that the grains within the sheets became elongated due to the rolling (*Figure 1* (a) and 2 (a)) and consequently the rolling texture developed with Cu, S, and Brass orientations typical of Al and Al alloys (*Figure 5* (a) and 6 (a)). The volume fraction values of the Cu, S, and Brass orientations were around the same, thus no rolling texture component dominated over the others. As the thickness reduction increased, the volume fractions of the rolling texture components increased (*Figure 7* (a)).

### 4.2 Recrystallization up to 90% thickness reduction

Up to 90% thickness reduction, the elongated grains disappeared and equiaxial grains formed during the subsequent annealing (*Figure 1* (b)). The rolling texture disappeared and a random structure developed with very weak recrystallization texture components (including the P orientation) during the 673 K 1 hour annealing heat treatment (*Figure 5* (b) and 7 (b)). The observed particles within the samples (*Figure 4*) and the random recrystallization texture suggest that particle stimulated nucleation (PSN) process occurred during the annealing. From the results it



can be concluded that up to 90% thickness reductions the stored energy introduced by the cold rolling initiated PSN recrystallization which was aided by the increased energy of the deformation zones of the resident particles.

#### **4.3 Recrystallization at 96% thickness reduction**

At 96% thickness reduction, new equiaxial grains visibly formed, but some of the elongated grains remained (*Figure 2 (b)*). The deformation texture remained (*Figure 6 (b)*), of which the S and Brass components weakened, but did not disappear, furthermore, the Cu component strengthened (*Figure 7 (b)*) due to the 673 K 1 hour annealing heat treatment. The different texture component change compared to the smaller thickness reductions proves that other recrystallization processes were also activated besides PSN. The increase in the volume fraction of the Cu component suggests that extended recovery dominated in grains with Cu component orientation. The extended recovery was confirmed by microstructure examinations where some elongated grains were still visible, being probably grains in the Cu component orientations (*Figure 2 (b)*).

As for the Brass and S components, the decrease of their volume fractions (but not drop to random volume fractions) suggests that PSN recrystallization and extended recovery competed in the grains of these orientations. PSN was activated due to the increased energy of the deformation zones, but extended recovery was also activated at the 96% thickness reduction. While PSN decreased the volume fractions of the Brass and S components, extended recovery preserved them.

For 96% thickness reduction it can be concluded that at this deformation degree extended recovery was also activated besides PSN. Extended recovery was the dominating process in the Cu orientation, whereas PSN overcame the extended recovery in the Brass and S orientations.

#### **4.4 Recrystallization at 96% thickness reduction during additional annealing**

During the additional annealing heat treatments of the samples exposed to 96% thickness reduction, equiaxial grains formed and the elongated grains completely disappeared (*Figure 3 (a) and (b)*). The rolling texture disappeared and a close to random texture developed where the Cube, a close to Cube orientation but rotated around  $\varphi_1$  (ND) with  $\sim 20^\circ$  giving the CubeND orientation, the Goss, a close to Goss but rotated around  $\varphi_1$  (ND) with  $\sim 19^\circ$  giving the GossND orientation and the P orientation developed with small volume fractions (*Figure 8. and 9. (a) and (b)*).

The appearance of the CubeND and the GossND, thus, the rotations of the cube and Goss components around ND and the appearance of the P component were caused by the resident particles [3]. The drop of the deformation texture components suggests that PSN was the main process during the additional annealing heat treatments. This means that the extended recovery during the former 673 K 1 hour annealing did not release all of the stored energy since PSN was still activated during the present additional annealing. The appearance of the weak recrystallization texture, the Cube, CubeND, Goss, GossND and P components is the evidence of that the genuine discontinuous recrystallization was not completely suppressed by the PSN.

It was shown that genuine discontinuous recrystallization was not activated during the 673 K 1 hour annealing in the sheets up to 90% thickness reduction. For those samples a random structure was formed by PSN. It is obvious that from this random structure the recrystallization texture with Cube and Goss (CubeND and GossND) orientations will never form, no matter how long annealing heat treatment might be subsequently applied. However, genuine recrystallization was activated during the additional annealing treatments of the sheets with 96% thickness reduction. There were two differences between the conditions of the samples that finally exhibited a pure random structure (formed by PSN) and the ones that finally exhibited a random structure with weak CubeND and GossND orientations (formed by genuine discontinuous recrystallization). The first difference was



the thickness reduction or, consequently, the magnitude of the stored energy. It seems that genuine discontinuous recrystallization occurred only if the stored energy resulting from the deformation was sufficiently high. However, this difference was not the direct cause of the activation of the genuine discontinuous recrystallization, since most of the stored energy was released by the extended recovery and PSN for the following genuine discontinuous recrystallization. Thus, the stored energy of the sheet after 96% thickness reduction and annealing was probably lower than that of the sheet after 90% thickness reduction [14, 15]. The second difference was that the initial structure before the genuine discontinuous recrystallization of the 96% thickness reduction sheet was a structure with a single dominating Cu orientation over the others, while the initial structures before the PSN of the sheets up to 90% thickness reduction were equivalent mixtures of the Cu, Brass and S components. The domination of the single Cu orientation over the others was proven to be a preferred structure to activate the genuine discontinuous recrystallization. This dominating Cu orientation was the direct cause of the appearance of the genuine discontinuous recrystallization. Of course, the structure with the dominating Cu orientation over the others (thus, the direct cause) originated from the different thickness reductions (the indirect cause).

## CONCLUSIONS

Microstructure and texture examinations were performed on cold rolled and annealed deep draw 3104 Al alloy sheets exposed to different thickness reductions ranging from 69% to 96%. The microstructure examinations and detailed ODF analysis revealed that the resident particles of precipitations and the degree of thickness reduction strongly influenced the type of the occurred recrystallization processes during the annealing heat treatments.

Up to 90% thickness reduction, only the particle stimulated nucleation (PSN) process occurred while at 96% thickness reduction extended recovery was the dominant process in the Cu oriented grains and PSN dominated over the extended recovery in the Brass and S oriented grains. PSN dominated over the genuine discontinuous recrystallization during the additional annealing heat treatments of the samples exposed to 96% thickness reduction.

## ACKNOWLEDGEMENT

The present research was supported by the TÁMOP-4.2.1.B-10/2/KONV-2010-0001 project in the framework of the New Hungarian Development Plant. The realization of this project is supported by the European Union, co-financed by the European Social Fund.

## REFERENCES

- [1] O. Engler, S. Kalz: Simulation of earing profiles from texture data by means of a visco-plastic self-consistent polycrystal plasticity approach, *Mat. Sci. Eng. A* 2004; 375: 350-362
- [2] O. Engler, L. Löchte, J. Hirsch: Through-process simulation of texture and properties during the thermomechanical processing of aluminium sheets, *Acta Mater.* 2007; 55: 5449-5463
- [3] O. Engler, J. Hirsch: Texture control by thermomechanical processing of AA6xxx Al-Mg-Si sheet alloys for automotive applications – a review, *Mat. Sci. Eng. A* 2002; 336: 249-262
- [4] O. Engler, J. Hirsch: Polycrystal-plasticity simulation of six and eight ears in deep-drawn aluminium cups, *Mat. Sci. Eng. A* 2007; 452-453: 640-651
- [5] K. Yoshida, T. Ishizaka, M. Kuroda, S. Ikawa: The effects of texture on formability of aluminium alloy sheets *Acta Mater.* 2007; 55: 4499-4506



# INTERNATIONAL SCIENTIFIC CONFERENCE ON ADVANCES IN MECHANICAL ENGINEERING

12-14 October 2017, Debrecen, Hungary



- [6] O. Engler, M.-Y. Huh: Evolution of the cube texture in high purity aluminum capacitor foils by continuous recrystallization and subsequent grain growth, *Mat. Sci. Eng. A* 1999; 271: 371-381
- [7] <https://regisztr.nekifut.hu/ki/434>
- [8] U. F. Kocks, C. N. Tomé, H.-R. Wenk: *Texture and Anisotropy Preferred Orientations in Polycrystals and their Effect on Materials Properties*, Cambridge University Press; 1998.
- [9] O. Engler, V. Randle: *Introduction to Texture Analysis Macrotexture, Microtexture and Orientation Mapping*, Second edition, CRC Press; 2010.
- [10] Bruker Advanced X-ray Solutions: *DiffractionPlus TEXEVAL Texture Evaluation Program Version 2.4 User's Manual*; 2002.
- [11] H.-C. Kim, C.-G. Kang, M.-Y. Huh, O. Engler: Effect of primary recrystallization texture on abnormal grain growth in an aluminum alloy, *Scripta Mater.* 2007; 57: 325-327
- [12] O. Engler: An EBSD local texture study on the nucleation of recrystallization at shear bands in the alloy Al-3%Mg, *Scripta Mater.* 2001; 229-236
- [13] O. Daaland, E. Nes: Origin of cube texture during hot rolling of commercial Al-Mn-Mg alloys, *Acta Mater.* 1996; 44: 1389-1411
- [14] S. Diligent, E. Gautier, X. Lemoine, M. Berveiller: Lattice orientation dependence of the stored energy during cold-rolling of polycrystalline steels, *Acta Mater.* 2001; 49: 4079-4088
- [15] G. Guiglionda, A. Borbely, J. H. Driver: Orientation-dependent stored energies in hot deformed Al-2.5%Mg and their influence on recrystallization, *Acta Mater.* 2004; 52: 3413-3423



## INTRODUCTION OF FREEZE GRANULATION TECHNOLOGY

*POÓS Tibor PhD, SZABÓ Viktor, VARJU Evelin, HORVÁTH Dániel*

*Department of Building Services and Process Engineering, Budapest University of Technology and Economics*

*E-mail: [poos@mail.bme.hu](mailto:poos@mail.bme.hu), [szabo.viktor@mail.bme.hu](mailto:szabo.viktor@mail.bme.hu), [varjuevelin@mail.bme.hu](mailto:varjuevelin@mail.bme.hu), [daniel.horvath.nk@gmail.com](mailto:daniel.horvath.nk@gmail.com)*

### **Abstract**

*Granulation is a widely used process in diverse sectors of the industry, one of them is freeze granulation. Besides pharmaceutical applications (eg. vitamins, vaccines, inhalers), this technology is often used in the chemical industry (eg. environmentally friendly batteries), the ceramic industry (powder sintering) and the food industry (eg. coffee powder). The aim of our work is gathering knowledge about the process and the equipment of freeze granulation and to compare it with other granulator processes on the basis of literature. Subsequently, we will propose a design of a freeze-granulator measuring station (main elements and instruments) at the Department of Building Services and Process Engineering of the Budapest University of Technology and Economics, which could be used for researches and student measurements. The spray-drying equipment in the departmental laboratory can be used later to compare its results to our measuring station's.*

**Keywords:** *freeze granulation, spray dryer, literature review, measurement*

### **1. INTRODUCTION**

Granulation may be defined as a size enlargement process which converts fine or coarse particles into physically stronger and larger agglomerates having good flow property, better compressibility of powders, improve content uniformity and eliminate excessive amounts of fine particles. Granulation is one of the most important unit operation in the production of pharmaceutical granules, ceramics, and foodstuffs. Particle size of the granules is mainly affected by the quantity and feeding rate of granulating liquid. Pharmaceutical granules typically have a size range between 0.2 and 4.0 mm, depending on their subsequent use [1].

Generally, there are three different method of granulation:

- Dry granulation.
- Direct compression.
- Wet granulation.

Wet granulation that utilize a liquid in the process and dry granulation that requires no liquid. The type of process selection requires thorough knowledge of physicochemical properties of the material, and required flow and release properties. Among currently available technologies, spray drying, freeze granulation, and fluid bed granulation are worth of note [2]. During spray drying, a powder suspension is sprayed into a hot air drying chamber. During drying, the droplets shrink to form powder granules. These granules may be more or less spherical and/or hollow depending on the slurry formulation (i.e. powder load and additives) and drying temperature [3]. Binder migration during the drying can additionally reduce the homogeneity and thereby quality of the granules, leading to inhomogeneities of the particles [4].

Freeze granulation is an alternative to spray drying, solving many of its limitations. During freeze granulation, droplets are rapidly frozen in liquid nitrogen before being recovered and subsequently



freeze-dried. Freezing being a fast process, diffusion dynamics are insufficient to induce any binder migration, thereby better preserving the granule homogeneity [5]. Additionally, the granules do not shrink during the whole process and therefore maintain their shape and powder density — consequently allowing higher granule deformability compared to spray drying.

Besides the high degree of granule homogeneity, freeze granulation technology offers several other advantages [6]:

- Control of granule density by the solids content of the suspension.
- Mild drying prevents serious oxidation of non-oxides and metals.
- No cavities in the granules.
- Low material waste, high yield.
- Small (50 – 100 ml suspension) as well as large granule quantities can be produced to equal quantity.
- Easy clean of the equipment (latex binder can be used).
- Possibility to recycle organic solvents.

## 2. FREEZE GRANULATION TECHNOLOGY

Freeze granulation technology is the combination of spray freezing and freeze drying. *Figure 1* shows an illustration of the process. Spray freezing is the first step in the freeze granulation process where a suspension is atomized, sprayed with a nozzle into a chamber with liquid nitrogen, with temperature around  $-196\text{ }^{\circ}\text{C}$ . The small droplets are then instantaneously frozen with a minimum of ice crystal growth. The frozen material (granules) are then transferred to a freeze dryer where the ice is removed by sublimation, i.e. never go through a liquid state that ensure homogeneity preservation without any segregation effects as in the case of conventional drying with air. The temperature in the freeze dryer is about  $-30\text{ }^{\circ}\text{C}$  [7].

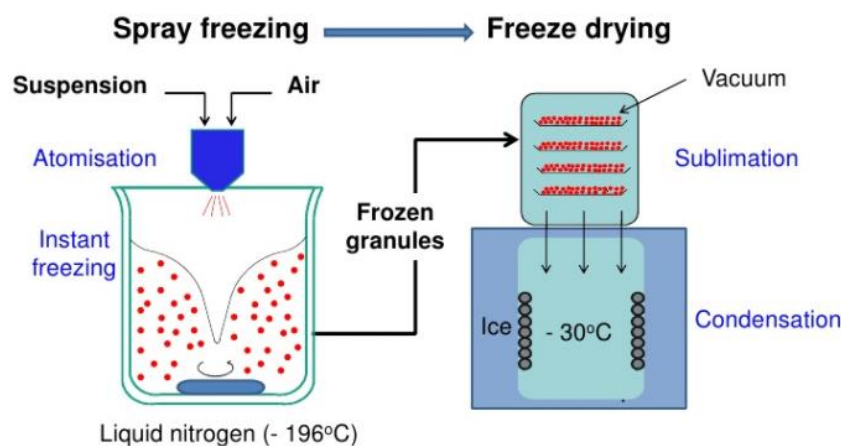


*Figure 1* Illustration of the freeze-granulation process [8]

The granule size distribution will be controlled by the suspension rheology (flow properties) and the process parameters (pump speed and air pressure). Normally, a certain size distribution-width is achieved with an average size, typically, around  $100\text{--}200\text{ }\mu\text{m}$ . In a comparison between the sintering performance of pressed specimens using granules obtained by freeze granulation or spray-drying the effect of homogeneity is clearly illustrated in *Figure 2*.

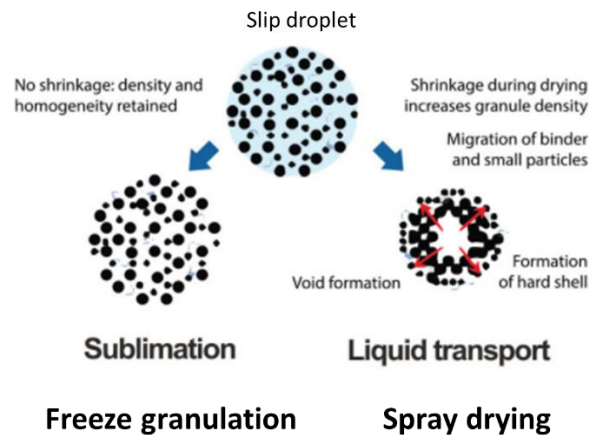


Figure 2 Comparison of freeze granulation and spray drying [8]

Several companies and research labs around the world have applied the freeze granulation process. Typical ceramic powders are oxides ( $\text{Al}_2\text{O}_3$ ,  $\text{ZrO}_2$ , and  $\text{SiO}_2$ ), nitrides ( $\text{Si}_3\text{N}_4$ ) and carbides ( $\text{SiC}$ ), but also nanopowders, diamonds and pharmaceuticals like proteins and enzymes [9].

### 3. METHODS

A full-scale plant spray dryer device is available in the laboratory of Department of Building Services and Process Engineering. Figure 3 shows a photo of the apparatus.



Figure 3 Spray dryer equipment

The spray dryer device is used for laboratory measurements. During the measurements, coffee suspension is atomized to drops, then dried in a drying chamber. The apparatus is equipped with instruments, e.g. thermometers, air humidity meters and pressure-difference meters. The atomizer rotates with 36000 1/min, the diameters of the coffee droplets are between 1 – 600  $\mu\text{m}$ . The quality of the drops made with the spray dryer and with the planned freeze granulator, and their operational parameters will be compared. Our work is still in the literature review state. Our work is still in the literature review state.



## CONCLUSIONS

Freeze granulation gives spherical, free-flowing granules. The good microstructure and homogeneous distribution of the granules enhance the sintering performance. The method should be well suited for composite systems, pharmaceutical use, or other fields of consumption where a uniform distribution and high quality of components required. The purpose of our work is to research the actual literature of this technology, than install a pilot-plant apparatus, which is suitable for pharmaceutical application. Our future plan is to compare the freeze granulation with the spray drying manufacturing the same type of material, which can be the basis of the scaling up this technology. The impact of operational parameters will be examined. Developing a mathematical model provides better economical operations and higher productivity. As an additional benefit, freeze granulation technology can be integrated to the education, which field is still less elaborated.

## ACKNOWLEDGEMENTS

This paper was supported by Gedeon Richter's Talentum Foundation (H-1103 Budapest, Gyömrői str. 19-21, Hungary), and by the Hungarian Scientific Research Fund (NKFIH/PD-116326).

## REFERENCES

- [1] Shinde, N., Aloorkar, N., Kulkarni, A., Bangar, B., Sulake, S., Kumbhar, P.: *Recent Advances in Granulation Techniques*. Asian Journal of Research in Pharmaceutical Science, 4 38–47., 2014.
- [2] Shanmugam, S.: *Granulation techniques and technologies: recent progresses*. BioImpacts : BI, 5 (1), 55–63., 2015.
- [3] Walker, W.J.J., Reed, J.S., Verma, S.K.: *Influence of Slurry Parameters on the Characteristics of Spray-Dried Granules*. Journal of the American Ceramic Society, 82 (7), 1711–1719., 1999.
- [4] Hidber, P., Graule, T.J., Gauckler, L.J.: *Competitive Adsorption of Citric Acid and Poly(vinyl alcohol) onto Alumina and Its Influence on the Binder Migration during Drying*. Journal of the American Ceramic Society, 78 (7), 1775–1780., 1995.
- [5] Lyckfeldt, O., Rundgren, K., Sjöstedt, M.: *Freeze Granulation for the Processing of Silicon Nitride Ceramics*. Key Engineering Materials - KEY ENG MAT, 264 281–284., 2004.
- [6] Solanki, H.K., Basuri, T., H.Thakkar, J., Patel, C.A.: *Recent Advances in Granulation Technology*. International Journal of Pharmaceutical Sciences Review and Research, 5 (3), 48–54., 2010.
- [7] Rundgren, K., Lyckfeldt, O.: *Development of Water Based Processing of Silicon Nitride Materials*. 26th Annual Conference on Composites, Advanced Ceramics, Materials, and Structures: A: Ceramic Engineering and Science Proceedings, 23 2–10., 2008.
- [8] *Test-granulation-arkiv, PowderPro*, <http://powderpro.se/category/test-granulation-en/>, 2017.
- [9] Rundgren, K., Lyckfeldt, O., Sjöstedt, M.: *Improving Powders with Freeze Granulation*. Ceramic Industry, 40–44., 2003.



## MODELING THE MOVEMENT OF THE GRANULAR MATERIAL IN A STATIC EQUIPMENT WITH DISCRETE ELEMENT METHOD

<sup>1</sup>POÓS Tibor PhD, <sup>1</sup>HORVÁTH Dániel, <sup>2</sup>TAMÁS Kornél PhD

<sup>1</sup>Department of Building Services and Process Engineering, Budapest University of Technology and Economics,

E-mail: [poos@mail.bme.hu](mailto:poos@mail.bme.hu), [daniel.horvath.nk@gmail.com](mailto:daniel.horvath.nk@gmail.com)

<sup>2</sup>Department of Machine- and Product Design, Budapest University of Technology and Economics,

E-mail: [tamas.kornel@gt3.bme.hu](mailto:tamas.kornel@gt3.bme.hu)

### Abstract

*In this study the measurements of direct shear box test were done on the assembly of hulled millet where different moisture contents were set. The moisture content dependent internal friction angle and cohesion of the aggregation were determined. With the use of a discrete element software the model of the direct shear box test was improved and simulations were done. The results of the simulation and measurement were compared. The aims of this study were to develop the DEM model of the laboratory direct shear box test and find appropriate parameter settings which will be used in further studies.*

**Keywords:** *direct shear box, internal friction angle, cohesion, discrete element method*

### 1. INTRODUCTION

There are several technologies in the food and pharmaceutical industry which include mixing, drying and the transportation of granular materials. For design and maintenance, it is necessary to know the physical and mechanical properties of the chosen material.

Due to the rapid technological advances of our day, simulation is the preferred method to provide fast, cost-efficient approximation of the kinetic and thermodynamic processes in granular materials with sufficient accuracy. The aim of this research is to modelling the internal friction angles and cohesions of granular materials with different moisture contents. We have created the model of the direct shear box in the applied Yade discrete element software (DEM) which is suitable for the calibration of the appropriate parameter set of the examined granular material [1].

There are numerous and different types of shear boxes [2, 3] for different sizes of granular materials to determine the internal friction angle and cohesion of the particle assembly. The laboratory direct shear box test presented in our research is suitable for geotechnics, polymer technology, chemical and food industries.

### 2. MATERIAL AND METHOD

The evaluation method of the selected shear box test is provided by MSZE CEN ISO / TS 17892-10 [4]. The design of the instrument, the evaluation of the measurement results and the presentation of the granular material used are described below.

#### 2.1. The examined material

During the research, the examined granular material was hulled millet which physical and mechanical properties were investigated with different moisture content. Spherical elements were



utilized in the DEM simulation, because this simple particle shape was so close to the geometry of the real hulled millet. The equivalent particle diameter of the aggregate was  $1.7 \pm 0.1$  mm. Before the measurements began, the aggregate was wind classified so as to remove the dust, other contaminants and ensure the nearly same size. Subsequently, water was added to the granular material and stirring occasionally for ten hours to allow the water to enter inside the material and not just into the surface capillaries. We have produced six different moisture contents (wet basis,  $x=11.2\%$ ,  $16.1\%$ ,  $18.7\%$ ,  $23.6\%$ ,  $24.1\%$ ,  $28.2\%$ ).

## 2.2. The laboratory measuring equipment

The actual design of the device is shown on the left side of *Figure 1*, while the schematic [4] is shown on the right side of *Figure 1*, where ‘1’ indicates the load plate, ‘2’ the porous plate, ‘3’ the examined sample, ‘4’ the load cell.

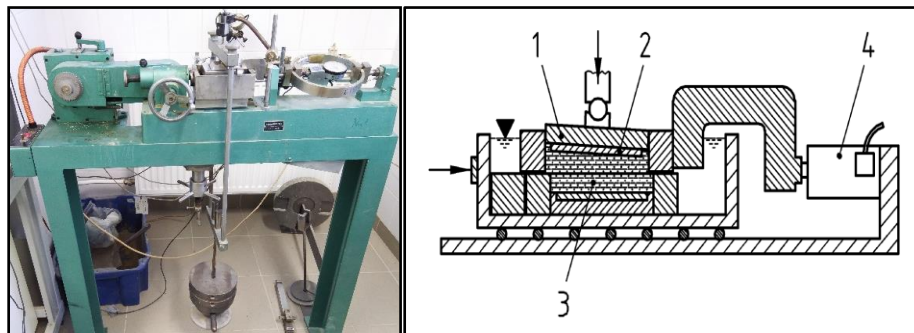


*Figure 1* Real (left) and schematic (right) illustration of the laboratory shear box device [4]

The selected standard laboratory direct shear box equipment had a granular material with an inner dimension of  $60 \times 60 \times 30$  mm, a shear speed of  $0.02$  mm/s and a shear length of  $7.5$  mm. The tests were performed using three different normal stress  $11.96$  kPa,  $19.61$  kPa and  $29.42$  kPa, respectively. While higher preloads were utilized the granules began to crumble, which was not able to increase the pre-load sufficiency.

## 2.3. Materials and methods

The evaluation was performed on the basis of MSZE CEN ISO / TS 17892-10 standard [4]. The shear force was measured during the shear test using different normal loads and moisture content.

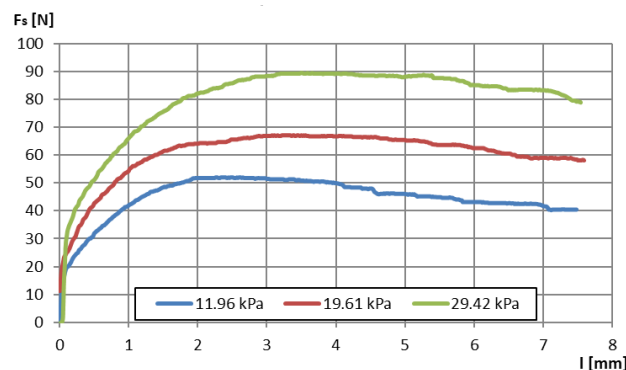


*Figure 2* The shear force measured by the laboratory direct shear box test with  $16.1\%$  moisture content and three pre-loads



The maximum shear stress can be calculated from the maximum shear force ( $F_{max}$ ) in *Figure 2* and the shear cross section ( $A$ ):

$$\tau_{max} = \frac{F_{max}}{A} \quad (1)$$

The maximal shear stress and the stress resulting from the normal load are represented by a pair of points, and then aligned with a linear trend line, the graph of *Figure 3* was obtained:

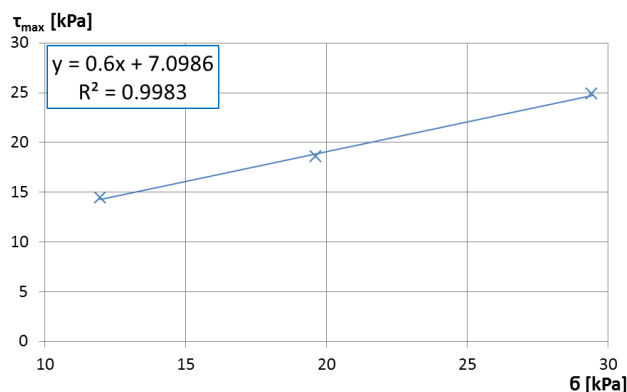


*Figure 3* Maximum shear stress as a function of normal stress

The steepness of the aligned trend line equals the internal friction angle of the aggregate. The straight line and the y-axis engagement give the cohesion of the aggregate [4].

### 3. THE DISCRETE ELEMENT MODEL

In this study, the Yade open source DEM software was used [5]. Several contact models are available to describe the rheological processes between granules in this DEM program (e.g. friction, cohesive, capillary). The frictional cohesive contact model (CohFrictMat) were utilized, because of the nature of the investigated granular material [8]. The Yade DEM software uses an explicit integral system with respect to time, which iterates between the movement and the force-displacement law [6]. The first step in explicit time integral is to set the value of forces to default, then refresh the bounds. Afterwards the collisions are detected. The software then calculates the forces from displacements based on the engine settings. From these forces the acceleration is calculated, the velocity is refreshed, then these data (forces, displacements) are recorded. Finally, the time step is increased by  $\Delta t_i$  and the bodies on the program display are refreshed, then the cycle starts again.

#### 3.1. The setup of the DEM simulation

In order to take into account the moisture content, the CohFrictMat contact model were utilized, which enable the simulation of adhesion [7, 8]. *Figure 4* shows the model of the direct shear box device under the simulation process which was improved in the Yade DEM software.

The model of the direct shear box was created from rigid wall elements called 'facetBoxes'. The bottom box (Number 2 in *Figure 4*) was opened on the upper side and upper box (Number 1 in *Figure 4*) was opened below and above. We created two more box sides to prevent the particles falling out during shearing.

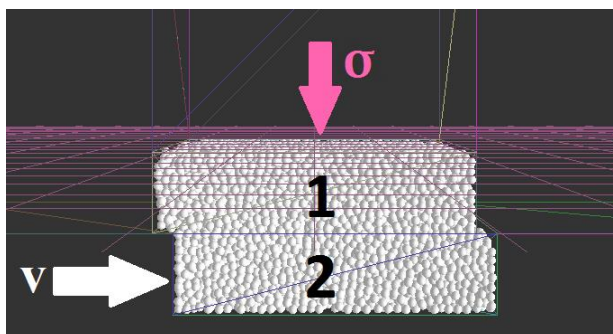


Figure 4 The simulation process of the direct shear box test in Yade DEM software (1: upper box, 2: lower box,  $\sigma$ : normal stress,  $v$ : shear direction)

The first stage of the simulation was the gravitational deposition, i.e. the filling of the shear box with particles, until the unbalanced force [6] decreased to less than 0.001. Then we turned on the cohesions between the particles with the ‘setCohesionOnNewContacts’ command and then using a wall element to provide the normal constant preload (marked with  $\sigma$  on Figure 4) on the assembly. As a result of the movement of the particles during shearing, the particle assembly modifies the displacement of the plate utilized for preloading even in the opposite direction. Therefore, this plate used for preload was controlled by the upward and downward movement as a function of the force exerted on it, so that the applied plate as wall element provided a constant pre-load with this servo mechanism. The shearing speed was set to 1 mm/s and the shear length was 8 mm. During the simulation, the shear force acting on the shear direction side of the upper box, the change of the unbalanced force, the position of the wall element providing the normal load and the force applied to it were recorded. Table 1 summarizes the material parameters of the direct shear box model.

Table 1 Material properties of the measuring equipment in the DEM software [9]

Measured particle density [kg/m <sup>3</sup> ]	Selected Young modulus [GPa]	Selected poisson ratio [1]	Measured friction angle [°]
7750	200	0.3	40.1

In the simulations, the global damping which create an opposite force against the accelerating particles was 0.5 and the time step was  $4.94 \cdot 10^{-6}$  s. The mechanical parameters of the modelled hulled millet are summarized in Table 2, which was taken from porosity measurement, the laboratory direct shear box test, and preliminary simulation experiments [9, 10].

Table 2 Material properties of the hulled millet in the DEM method

Moisture content [%]	Measured particle diameter [mm]	Measured particle density [kg/m <sup>3</sup> ]	Selected Young modulus [MPa]	Selected poisson ratio [1]	Measured friction angle [°]	Calibrated cohesion strengths [kPa]	Calibrated eta [1]
23.6	1.7±0.1	1402	20 [9]	0.2	40.1	60	0.05

The shape of the hulled millet grains was modelled by spherical particles. During the simulations 21,000 particles were used to fill the DEM model of the shear box. The shear and normal strengths ( $\tau$ ,  $\sigma$ ), which simulates the strength of the bonds between the particles (occurred by liquid bridges) were the same. Also the value of eta as the dimensional rolling and twisting strengths were the



same, which could be used for increasing the internal friction of the particle set with the interference of particles.

#### 4. RESULTS

The method of evaluation is described in *Section 2.3*. The obtained internal friction angles and cohesions from laboratory direct shear test are shown in *Figure 5*.

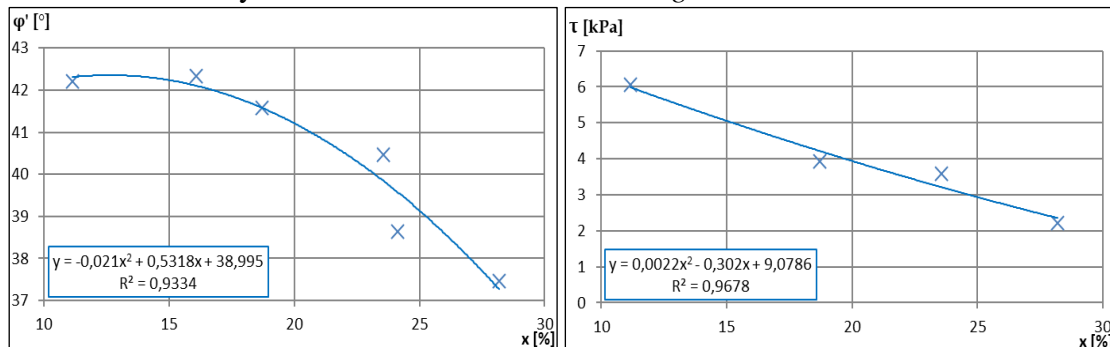


*Figure 5* The measurement results of the laboratory direct shear box test. On the left side, the internal friction angle, on the right side the cohesion dependence on the moisture content (wet basis) for hulled millet

Both the internal friction angle and the cohesion were polynomially decreased depending on the moisture content.

During the DEM modeling, the simulations were performed with the moisture content of 23.6%. We compared the simulated and the measured results in *Figure 6*, where the maximum shear stress was represented as a function of normal stress.

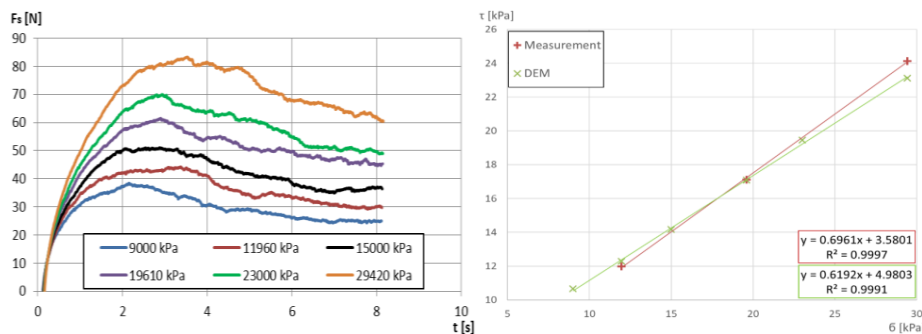


*Figure 6* On the left side, the simulated shear force for hulled millet of 23.6% moisture content by the time, and on the right side the maximum shear strength dependence on the normal stress by measurement and DEM simulation

During the DEM modeling, we performed simulations with six pre-loads in order to obtain more accurate results. It has been known that the model yielded the expected results with the parameter setting for a moisture content (*Table 2*), as the points were on a straight line (*Figure 6* on the right). The highest difference between the measured and the discrete elemental method was 4.1%. Based on the setting parameters (*Table 2*) and the results from the measurements (*Figure 6* on the left), it can be determined that the difference between the set (macromechanical) and the particles (micromechanical) cohesions are one order of magnitude higher. Furthermore, during the simulations, it was found that the steepness of the trend line increased by increasing the eta



parameter in the shear strength normal stress diagram (*Figure 6* right), while the axial section decreased considerably by decreasing the cohesions.

## CONCLUSIONS

The standard laboratory direct shear box tests with hulled millet was used with different moisture contents in this study. The effect the proportion of moisture content on cohesion and internal friction angle of the aggregate were investigated. We found that both parameters were polynomially decreased with the increase of the moisture content. Using DEM we created the model of the direct shear box and then simulated with a given moisture content. The geometry of the particles were approximated by sphere, and a cohesive contact model (CohFrictMat) was used to take into account the effect of moisture. The results of measurements and simulations were compared with a maximum deviation of 4.1%. Based on this experience, the steepness of the failure envelope (maximum shear strength - normal stress diagram) can be adjusted by increasing the eta parameter and the "shifting" by increasing the micro cohesion values ( $\sigma, \tau$ ). The results showed that the improved DEM model will be appropriate for further researches to determine additional moisture dependent micro-mechanical parameters.

## ACKNOWLEDGEMENTS

This paper was supported by Hungarian Scientific Research Fund (NKFIH/PD-116326).

## REFERENCES

- [1] Cundall, P.A., Strack, O.D.L.: *Discrete numerical model for granular assemblies*. Geotechnique, 29 (1), 47–65., 1979.
- [2] Suhr, B., Six, K.: *On the effect of stress dependent interparticle friction in direct shear tests*. Powder Technology, 294 (Supplement C), 211–220., 2016.
- [3] Yang, H., Xu, W.-J., Sun, Q.-C., Feng, Y.: *Study on the meso-structure development in direct shear tests of a granular material*. Powder Technology, 314 (Supplement C), 129–139., 2017.
- [4] *MSZE CEN ISO/TS 17892-10: Geotechnikai vizsgálatok. Talajok laboratóriumi vizsgálata. 10. rész: Közvetlen nyíróvizsgálat (ISO/TS 17892-10:2004)*, 2004.
- [5] Šmilauer, V., Catalano, E., Chareyre, B., Dorofeenko, S., Duriez, J., Gladky, A., Kozicki, J., Modenese, C., Scholtès, L., Sibille, L., Stránský, J., Thoeni, K.: *Dem formulation*. In *Yade Documentation 2nd ed.* The Yade Project, 37., 2015.
- [6] Šmilauer, V., Gladky, A., Kozicki, J., Modenese, C., Stránský, J.: *Using and programming*. In *Yade Documentation 2nd ed.* The Yade Project, 149., 2015.
- [7] He, Y., Peng, W., Tang, T., Yan, S., Zhao, Y.: *DEM numerical simulation of wet cohesive particles in a spout fluid bed*. Advanced Powder Technology, 27 (1), 93–104., 2016.
- [8] Bourrier, F., Kneib, F., Chareyre, B., Fourcaud, T.: *Discrete modeling of granular soils reinforcement by plant roots*. Ecological Engineering, 61 (Part C), 646–657., 2013.
- [9] Horabik, J., Molenda, M.: *Parameters and contact models for DEM simulations of agricultural granular materials: A review*. Biosystems Engineering, 147 (Supplement C), 206–225., 2016.
- [10] Poós, T., Horváth, D., Tamás, K.: *The compare of angles of repose with discrete element method and measurement*. 8th International Scientific Conference, 65–70., 2017.09.07-09.



## DETERMINATION OF MEDICINAL PLANTS' POROSITY

*POÓS Tibor PhD, VARJU Evelin, SZABÓ Viktor*

*Department of Building Services and Process Engineering, Faculty of Mechanical Engineering,  
Budapest University of Technology and Economics*

*E-mail: [poos@mail.bme.hu](mailto:poos@mail.bme.hu), [varjuevelin@mail.bme.hu](mailto:varjuevelin@mail.bme.hu), [szabo.viktor@mail.bme.hu](mailto:szabo.viktor@mail.bme.hu)*

### **Abstract**

*The role of medicinal plants in therapy is changed in different ages, closely linked to the state of the level of the therapy. Their special active agent content makes herbs suitable for healing and health preservation. The moisture content of harvested plants is generally very high, around 60-80%. If the moisture content is not significantly reduced, it enables maturation of harmful biological processes. Different characteristics of drying process are necessary to beware of to choose the appropriate drying method and apparatus. In this study the porosity of five different medicinal herbs are determined by an air pycnometer from these needed drying characteristics.*

**Keywords:** *medicinal plants, porosity, drying, air pycnometer.*

### **1. INTRODUCTION**

No doubt that synthetic drugs have played a vital role in the enhancement of human living standards during the past century; still, herbal medicine has regained its momentum again in recent years. Instead of focusing only on curing an illness, people pay more attention nowadays to improve the whole body's immune system so as to prevent the attack of diseases. Besides their traditional pharmaceutical usage, herbs have also become one of the important sources for drug discovery and production [1]. A significant number of medicinal plants are pharmaceutical raw materials, which can be extracted from the active agent by various procedures. These materials are marketed after determination of the exact active agent content, or are used as raw materials of drugs or combinations of drugs by further processing [2].

The aim of medicinal plants processing is turning herbs into some form of drugs, pure active agents or medicaments. Primary processing involves collecting or harvesting, cleaning, drying, qualification, etc. The moisture content of harvested plants is generally very high, around 60-80%. If the moisture content is not significantly reduced, it enables maturation of harmful biological processes. Because of this, valuable active agents of herbs can be destroyed and the external properties of drugs can become unfavourable. The fundamental requirement to prevent harmful processes is the reduction of moisture content as quickly as possible [2, 3].

During the drying process, the maximum bed height is also an important parameter to be determined because the thicker the bed, the more difficult it is to ensure a uniform quality at the end of the operation. In order to influence product quality, the goal is to familiarize with drying properties as precisely as possible, including bulk density and porosity, to be calculated from the former. Knowledge of porosity contributes to the determination of the flow resistance of the bulk of plants and of volume decrease during drying.

During our research work five herbs were investigated, as shown in *Figure 1*.



Figure 1 The studied medicinal plants (a – Common yarrow, b – Giant goldenrod, c - Wormwood, d – Walnut leaf, e –Wild carrot)

## 2. APPARATUS AND MEASURING METHOD

In order to measure herb porosity, an air pycnometer was available for us at the Department of Building Services and Process Engineering, the arrangement of which is shown by the drawing in Figure 2.

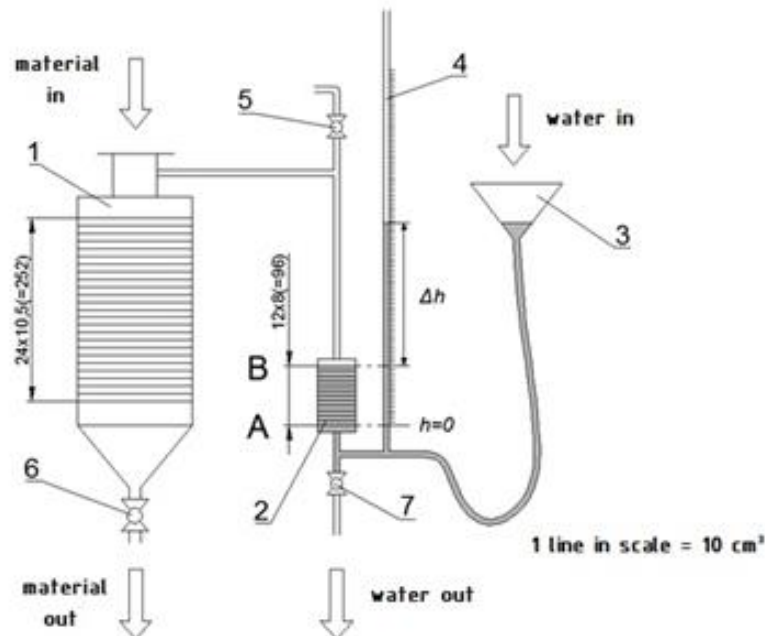


Figure 2 Schematic diagram of air pycnometer (1 – measuring vessel, 2 – compression tank, 3 – funnel, 4 – scaled measuring pipe, 5 – ball valve, 6 and 7 – ball valve)

Before the measurement, the moisture content was determined with reference to dry matter by using small samples for each herb. In the course of the measurement, the bulk density of the material concerned was to be measured first; afterwards the material density of the plant was specified by the air pycnometer.



As long as the density of a granular material is a constant value, its bulk density will vary between two limit values as a consequence of the arrangement of the bulk of material. In the course of the measurement, material of a given volume must be filled in the measuring vessel, to be followed by weight measurement.

The plant weight is known; its volume can be measured indirectly by determining the volume of air displaced by the herb. If the volume of air enclosed in the measuring instrument is measured without the material placed in, and then together with the material placed in, the difference of the two air volumes measured will yield the plant volume.

When measuring the volume of air enclosed in the measuring instrument, ball valve (6) and (7) were closed on the empty measuring instrument and ball valve (5) was left open. The sealing ring and the cap was placed on top (1) of the measuring vessel, fixed by a triclamp binder. Water was filled in the funnel (3) until the water level in the compression tank (2) reached mark 'A'. The funnel was first in the bottom position, where the water level was in line with mark 'A'. After precise level adjustment, ball valve (5) was closed, thereby the air was locked in the system. By lifting the funnel and constantly supplementing the water running out of the funnel, the water level in the compression tank was set to mark 'B'. The water level can be read from the scaled measuring pipe (4). The water can be drained from the system first by opening tap (7), then tap (5).

The course of measurement with the material placed in corresponds to the above, with the difference that the material of known mass is placed in the measuring vessel before fixing the cap.

### 3. EVALUATION METHOD

Upon closing tap (5) shown in *Figure 2* after finishing the measurement, the air enclosed in the system is at atmospheric pressure, that is,  $p_0$ , and its volume is  $V_0$ . After setting the fluid level in the compression tank to correspond to mark 'B', the air inside is compressed to a volume  $V_0 - V_{AB}$ , where  $V_{AB}$  is the volume between marks 'A' and 'B'. Deviation  $\Delta h_0$  on the scaled measuring pipe can be used for stating the pressure of the space inside after compression:

$$p = p_0 + \rho_v \cdot \Delta h_0 \cdot g \quad (1)$$

where  $\rho_v$  is the density of water [ $\text{kg/m}^3$ ],  $g$  is gravitational acceleration [ $9.81 \text{ m/s}^2$ ], and  $\Delta h_0$  is the displacement of water level in the measuring pipe in case of an empty measuring vessel [m]. The formula to be stated for isothermal change of state:

$$p_0 \cdot V_0 = (p_0 + \rho_v \cdot \Delta h_0 \cdot g) \cdot (V_0 - V_{AB}) \quad (2)$$

Therefore the volume of the air enclosed in the empty instrument will be:

$$V_0 = \frac{p_0 + \rho_v \cdot \Delta h_0 \cdot g}{\rho_v \cdot \Delta h_0 \cdot g} \cdot V_{AB} \quad (3)$$

This is followed by a measurement with herbs placed in the instrument. Then  $\Delta h_i$  can be calculated from the value read from the scaled measuring pipe. Volume of the air enclosed:

$$V_i = \frac{p_0 + \rho_v \cdot \Delta h_i \cdot g}{\rho_v \cdot \Delta h_i \cdot g} \cdot V_{AB} \quad (4)$$

where  $\Delta h_i$  is the displacement of water level in the measuring pipe after feeding in herbs with a



mass of  $m_i$  [m].

The difference between the two volume figures will yield the volume of the material examined. Therefore, the volume of a material of known mass  $m_i$  will be:

$$V_0 - V_i = \frac{p_0}{\rho_v \cdot \Delta h_0 \cdot g} \cdot \frac{\Delta h_i - \Delta h_0}{\Delta h_i} \cdot V_{AB} \quad (5)$$

From this, material density can be determined:

$$\rho = \frac{m_i}{V_0 - V_i} = \frac{m_i}{V_{AB}} \cdot \frac{\rho_v \cdot \Delta h_0 \cdot g}{p_0} \cdot \frac{\Delta h_i}{\Delta h_i - \Delta h_0} \quad (6)$$

In order to diminish measurement errors, measurements need to be conducted on several material samples of different weights and density must be approximated by linear regression. By rearranging equation (6), the invert of the deviation of the water level in the measuring pipe will be a linear function of the mass examined.

$$\frac{1}{\Delta h_i} = -\frac{\rho_v \cdot g}{\rho \cdot p_0} \cdot \frac{m_i}{V_{AB}} + \frac{1}{\Delta h_0} = a \cdot m_i + b \quad (7)$$

By plotting the measured points in a  $1/\Delta h_i - m_i$  diagram, steepness  $a$  of the first-degree trend line fitted to the points will be yielded. On the basis thereof, the average density value searched for will be:

$$\rho_{average} = -\frac{\rho_v \cdot g}{a \cdot p_0 \cdot V_{AB}} \quad (8)$$

The second part of evaluation involves the determination of porosity ( $\varepsilon$ ). By definition, porosity means the proportion of the volume of intergranular space to the total volume:

$$\varepsilon = \frac{V_h}{V + V_h} \quad (9)$$

This highly depends on the shape of granules: porosity may decrease if the set of granules consists of particles of different sizes and shapes arranged irregularly, whereas porosity may increase if the set consists of stringy or shell-shaped granules.

In order to determine porosity, either volumes or densities are required to be measured, since formula (9) can also be stated with densities:

$$\varepsilon = 1 - \frac{V}{V + V_H} = 1 - \frac{\frac{V}{m}}{\frac{V + V_H}{m}} = 1 - \frac{\frac{1}{\rho}}{\frac{1}{\rho_H}} = 1 - \frac{\rho_H}{\rho} \quad (10)$$

#### 4. RESULTS

Measurements were conducted and measurement results were evaluated according to the specifications described in Chapter 2 and 3. *Table 1* includes the values of bulk density, average



material density and average porosity, as calculated for the different herbs.

Table 1 Porosity measurement results for the different herbs

	X, [kg/kg]	$\rho_H$ , [kg/m <sup>3</sup> ]	$\rho_{\text{average}}$ , [kg/m <sup>3</sup> ]	$\epsilon$ , [-]
<b>Common yarrow</b>	5.094	101	1426	0.93
<b>Giant goldenrod</b>	1.462	117	1598	0.93
<b>Wormwood</b>	3.153	85	986	0.91
<b>Walnut leaf</b>	2.983	56	1973	0.97
<b>Wild carrot</b>	8.335	172	1068	0.84

The largest deviation from the values measured was presented by the large-surfaced walnut leaf, which considerably differs from granular substances in terms of structure. The measured bulk density values can be regarded as realistic; on the other hand, porosity figures show that the herbs fill the space available in an extremely loose arrangement, therefore they cause relatively low air resistance during drying.

## CONCLUSIONS

The aim of medicinal plants processing is turning herbs into some form of drugs, pure active agents or medicaments. The special active agent content makes suitable herbals for healing and health preservation. The key element in herbs and spices processing is drying. Different characteristics of drying process are necessary to beware of to choose the appropriate drying method and apparatus. In this study the porosity of five different medicinal herbs are determined by an air pycnometer from these needed drying characteristics. Knowledge of porosity contributes to the determination of the flow resistance of the bulk of plants and of volume decrease during drying.

## ACKNOWLEDGEMENTS

This paper was supported by Gedeon Richter's Talentum Foundation (H-1103 Budapest, Gyömrői str. 19-21, Hungary), and by the Hungarian Scientific Research Fund (NKFIH/PD-116326).

## REFERENCES

- [1] Dr. Szőke, É., Balázs, A., Kéry, Á., Then, M.: *Knowledge of Herbal and Drug Science Pharmacognosy - Phytochemistry, the use of Herbals*. Semmelweis Egyetem, 2012.
- [2] Borbélyné Dr. Hunyadi, É., Dr. Kutasy, E.: *Cultivation and processing of herbs*. Debreceni Egyetem, 2012.
- [3] Varró, A.B.: *The effect of medicinal herbs*. Kódexfestő Könyvkereskedés Kft., 2011.



## SYSTEMS FOR COUNTERBALANCING THE RAM OF THE MECHANICAL PRESSES

**POP-SZOVÁTI Anton - Gheorghe, BORZAN Marian PhD, GYENGE Csaba PhD, JOLDEȘ Nicolae**

Department Manufacturing Engineering, Technical University of Cluj-Napoca, Romania  
E-mail: [anton\\_pops@yahoo.com](mailto:anton_pops@yahoo.com), [Marian.Borzan@tcm.utcluj.ro](mailto:Marian.Borzan@tcm.utcluj.ro), [Csaba.Gyenge@tcm.utcluj.ro](mailto:Csaba.Gyenge@tcm.utcluj.ro),  
[joldes\\_nicolae@yahoo.com](mailto:joldes_nicolae@yahoo.com)

### Abstract

*Conventional mechanical eccentric or crank presses are used in most cold pressing operations but are most suitable for stamping operations. On the active surface of the executing body which is the ram, the upper parts of the punching or stamping tools are mounted. The dynamics of the alternative rectilinear movement of the ram are ensured by the main drive of the press generated by the kinetic energy of the fly-wheel, the transmission moments of the toothed wheels gears are all driven by the main electric motor.*

*Our research team has studied secondary actions that are complementary to the main actions but not without importance, because their role is materialized by: increasing the sustainability of the press, operating safely, obtaining quality pressed products and time saving. The objective of the study is the role the ram's pneumatic counterbalancing system in the operation of the mechanical presses and the development directions of the system.*

**Keywords:** *mechanical presses, ram (slide), pneumatic counterbalancing, cold pressing, computer-assisted.*

### 1. INTRODUCTION

The main role of the system is to counterbalance the weight of the ram, the weight of the upper part of the tool and to eliminate the wear-on to the connecting bolt between the ram and the connecting rod, to eliminate the movement between the crank and the sliding bearings of the mechanical presses with cranks, or to eliminate the movement between eccentric gear drive and sliding of the connecting rod at the eccentric mechanical press. In fact, the balancing system also positively influences other aspects in the quality of the pressing operation.

### 2. PNEUMATIC SYSTEMS FOR COUNTERBALANCING THE RAM

Assembly system for counterbalancing the ram of a press consists of one or more pneumatic linear motors (cylinder-piston assembly) which makes the link between the ram of the press and the frame. Typically, the cylinder is the stationary part fixed to the frames foot, and the piston is the active part which makes the connection with the ram.

In *Figure 1* it is shown the construction of a pneumatic linear motor that represents the assembly of the system for counterbalancing the ram.

The weight of the ram represents minimum pneumatic pressure in the cylinder for counterbalancing the ram, meaning that is the counterbalancing pressure of the ram without tools. At this value of pneumatic pressure in the system we add the value corresponding to the weight of the upper part of



the tools mounted on the active surface of the ram. The pneumatic controller is located in the general control panel with pneumatic regulators.

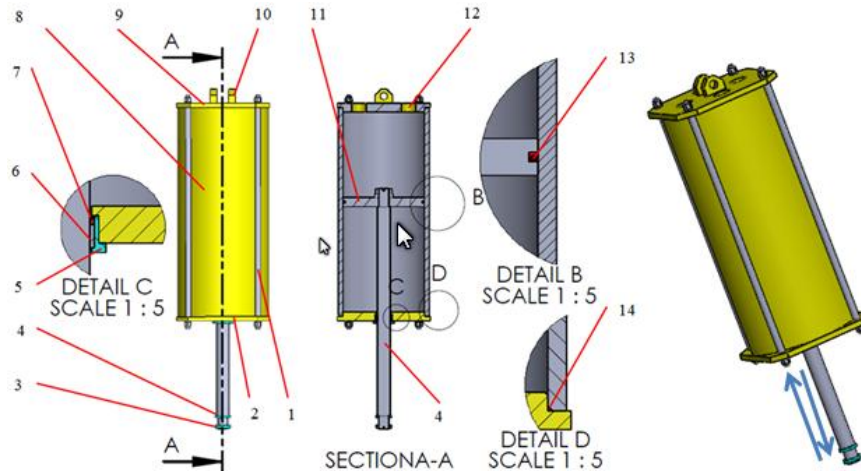


Figure 1 Counterbalancing cylinder of the ram with the components sections

1 - stud with nut for fixing the caps; 2 - lower lid; 3 - self-locking nut; 4 - washer; 5 - support; 6 - sliding bearing; 7 - sealing sleeve; 9 - top cap; 10 - bossage; 11 - piston; 8 - cylinder; 12 - reaming against vacuum formation; 13 - sealing sleeve; 14 - O ring seal.

Adjusting the ram counterbalancing force is a must in order to ensure efficient and safe press operation.

The pneumatic counterbalancing device of the ram should provide: ease of adjustment, the force required to counterbalance the ram, the compressed air pressure value in the system will vary by no more than 20% during a double ram race, protection for the main electric motor.

In Figure 2 a shows the pneumatic scheme of a mechanical press where the piston rod is under traction. Figure 2 b shows the pneumatic scheme of a mechanical press where the piston rod is subjected to compression.

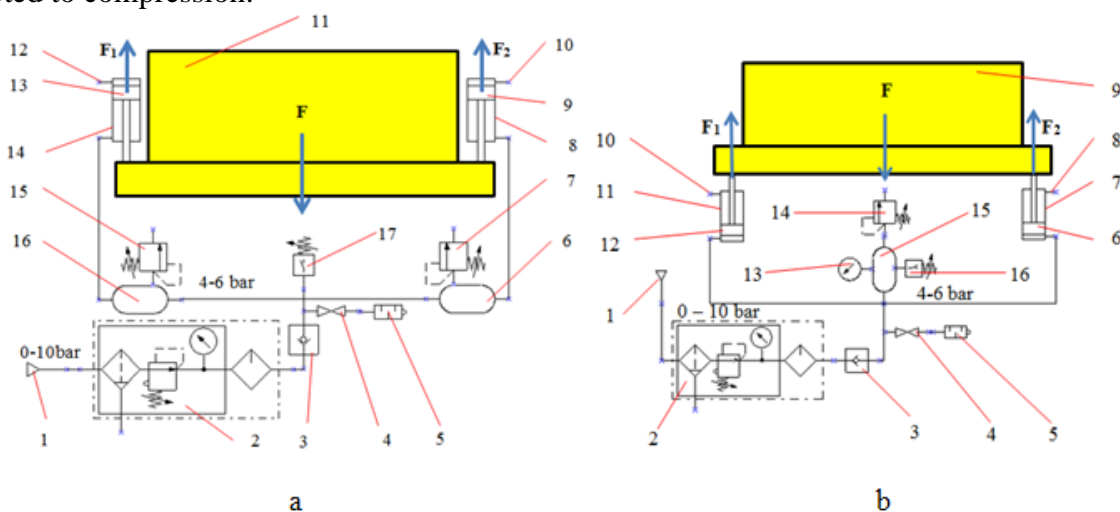


Figure 2 a - Pneumatic diagram of the counterbalancing system of the ram and of a mechanical press with the enclosed frame and pistons rod under tension;

Figure 2 b - The pneumatic scheme of the rams counterbalancing system and of a mechanical press with closed frame and with the piston rod subjected to compression



In the *Figure 2* were made notations:

F - the pressing force direction of the ram;  $F_1$  and  $F_2$  - the counterbalancing forces of the ram.

*Figure 2 a*: 1 - compressed air source; 2 - pneumatic group consisting of a drain filter, pressure regulator and lubricator; 3 - sense valve; 4 - rapid depressurization valve; 5 - noise damper; 6 and 16 - pneumatic accumulators; 7 and 15 - safety valve; 8 and 14 - stationary cylinder; 9 and 13 - piston; 10 and 12 - anti-vacuum reaming; 11 - the presses ram; 17 - pressure switch.

*Figure 2 b*: 1 - compressed air source; 2 - pneumatic group consisting of a drain filter, pressure regulator and lubricator; 3 - sense valve; 4 - rapid depressurization valve; 5 - noise damper; 6 and 12 - pistons; 7 and 11 - cylinders; 8 and 10 - anti-vacuum reaming; 9 - the presses ram; 13 - manometer; 14 - safety valve; 15 - pneumatic accumulator; 16 - pressure switch;

Press builders are giving increasingly more importance to the rams counterbalancing system of the mechanical presses with a closed frame with two connecting rods. The linear motor construction is similar in most cases, it only differs in where they are located, and their number (*Figure 3*).

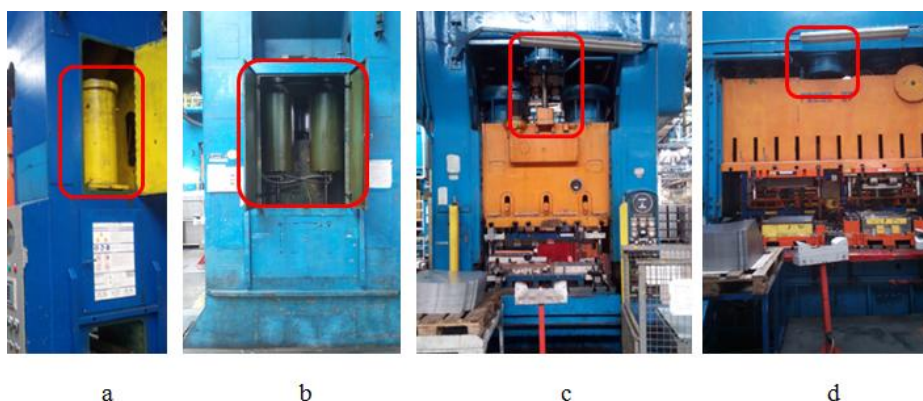


*Figure 3* Modes of positioning of the ram counterbalancing system with closed frame press (framed in red)

- a* - Closed frame press fitted with a counterbalancing system included laterally one on each side of the pillars;
- b* - Closed frame press fitted with a counterbalancing system included laterally with 2 on each side of the pillars;
- c* and *d* - Closed frame press fitted with a counterbalancing system included between the middle of the upper crossbar and the ram.

The cylinder is fastened to the presses frame and the piston end engages the ram where the alternate movement of descending and ascending causes the piston to move linearly in the cylinder. The minimum pneumatic pressure required in pneumatic counterbalancing cylinders to counterbalance the weight of the ram without tools being mounted on the press ram.

$$F = W_r + W_t, \quad [N] \quad (1)$$

Where: F - the ram counterbalancing force created by the pneumatic pressure in the piston-cylinder assembly;  $W_r$  - the weight of the ram;  $W_t$  - the weight of the upper part of the tools mounted on the press ram.

For a constant counterbalance, the pneumatic pressure value from the counterbalancing system should be slightly higher due to the pneumatic pressure fluctuation from the ram's alternate traction



motion and the kinetic energy variation of the flywheel. The variation of the pneumatic pressure in the counterbalancing system should not exceed 20%.

Then the expression of the force required to counterbalance the ram becomes:

$$F = W_r + W_t + f, \quad [\text{N}] \quad (2)$$

where:  $f$  - is additional force.

$$f = \frac{F \cdot 20}{100}, \quad [\text{N}] \quad (3)$$

### 2.1 Advantages of the ram counterbalancing system

The counterbalancing device of the ram disposes of such games arising from wear of the reaming from within connecting rod.

The direction of the force in the piston cylinder is opposite to the ram's descent direction and is the same as the direction of the ram's climb force.

Advantages of the Ram Counterbalancing System:

- eliminates the play caused by the wear of the reaming from within the connecting rod, of the crank sliding bearings, and the eccentric press axles;
- facilitates the precise stopping of the ram in TDC, which is especially necessary in the "single race" mode;
- the press brake in TDC is safer because the clutch brake is protected;
- by optimally adjusting the pneumatic pressure in the counterbalancing system the mechanism for adjusting the length of the blades during the adjustments is protected;
- elimination of games allows correct adjustment and measurement of the parallelism between the table and the active surface of the ram;
- compensates the kinetic energy consumed by the fly-wheel during technological operations;
- protects the main electric motor when climbing the ram by compensating the lost energy from the mechanical kinetic energy accumulator;
- Ensures constant gearshift of the transmission through constantly and even contact between the toothed wheels.

### 2.2 Adjusting the pneumatic pressure in the counterbalancing system

The compressed air in the accumulation and compensation vessel enters the linear motor and constantly operates the piston upward, thus cushioning the shocks resulting from the shearing of the blank to the stamping operations.

With a pressure regulator in the pneumatic panel with regulators, it is possible to adjust the pneumatic pressure in the rams counterbalancing system, according to the graph located on the press frame, indicating the force developed according to the pressure. The operator must know exactly the weight of the upper part of the tool for correct adjustment of compressed air pressure in the counterbalancing system. *Figure 4* is a graph of the counterbalancing force of a press whose ram has a weight of 100 kN. The ram's counterbalancing force is calculated as the sum of the forces resulting from the total number of counterbalancing cylinders existing in a press.

From the graph we see that the counterbalancing of the ram requires a pneumatic pressure of 4 bars. To this value add the pressure required to counterbalance the weight of the upper parts of the tools.

These results were calculated with the relationship:

$$F_{\text{ech.}} = P \cdot S_p, \quad [\text{N}] \quad (4)$$



where:  $F_{ech}$  = counterbalancing force, [N];  $S_p$  = piston surface, [m<sup>2</sup>].

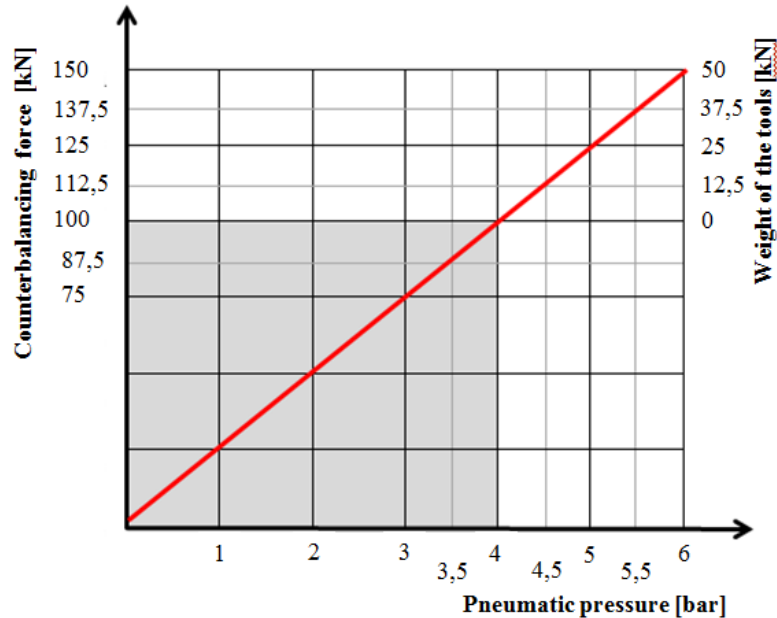


Figure 4 Graph showing the counterbalancing forces of the ram depending on the amount of air pressure supplied

### 2.3 Aspects related to the tribology of the counterbalancing system

Tribology includes aspects of the technical condition of the machinery, the technical criterion, functionality, technological and establishing economic condition and limits the processes for determining the physical wear and moral.

Components of the linear pneumatic engine for ram counterbalancing are constantly in direct and mobile contact by the alternative rectilinear movement of the ram.

The linear motor cylinder and piston are two elements that form friction coupler where direct contact is avoided by the oil layer provided by the press lubrication equipment. If the press lubrication system is not suited for the movement, the sliding creates friction between the cylinder and the piston, the resistance encountered by the pistons movement inside the cylinder increases.

The important role of the ram counterbalancing system requires strict adherence to preventive maintenance schedules. If sounds characteristic of dry friction are heard from the system, manual lubrication is applied through the reaming's to prevent vacuum formation.

It is important to lubricate the compressed air with which the system is fed by including it in the pneumatic circuit of the lubricants. The compressed air always lubricates the sealing sleeves in the counter balancers cylinder-piston assembly. The piston rod sliding bearing is lubricated by the central lubrication system of the press.

## 3. RESULTS

The modernization of existing presses in industrial companies for the cold pressing of sheet metal is an advantageous method for the implementation of advanced technologies. Our research team has explored the possibilities of achieving the performance of computer-assisted presses. The computer-assisted press control mode with the PLC program (programmable logic controller) is simple



because multiple PLC connections can be added to control and control the pneumatic and hydraulic systems.

The control of the ram counterbalancing system is performed through an interface with the operator on a touch panel inherent to the press control panel. The program stops the press operation if the pneumatic value of the counterbalancing system does not fall within the programmed range.

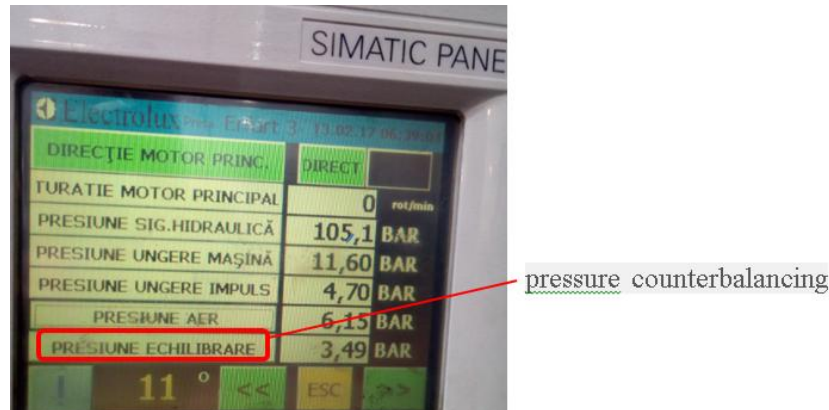


Figure 5 Touch panel with ram pressure counterbalancing monitoring

## CONCLUSIONS

The secondary action is complementary to the main drive, it is concretized by the additional actions required for the complex tools, or improves the precision and prevention of damage to the press mechanisms.

Worldwide press builders are increasingly using servomotors for the main drive of the ram. The use of electric servomotors for secondary presses is a challenge for our team. In the main operation with a press servomotor it is necessary also the secondary actuation of the counterbalancing with servomotor.

## REFERENCES

- [1] Pop – Szováti, A., Gyenge, Cs., Borzan, M.: *Dynamic analysis of vibration and noise metal forming presses*. Debreceni műszaki közlemények, 2014/2.
- [2] Pop - Szováti, A., Gyenge, Cs, Borzan, M.: *Specific achievements in the direction of the automated assembly through adhesion of household machines*. ANNALS of Engineering Faculty Hunedoara – International Journal of Engineering, Tome XIII [2015] – Fascicule 4 [November], ISSN:1584-2673.
- [3] Pop - Szováti, A., Gyenge, Cs, Borzan, M.: *The study of mechanical presses drives using cold plastic deformation*. Proceedings of the 3rd International Scientific Conference on Advances in Mechanical Engineering (ISCAME 2015) 19 November 2015, Debrecen, Hungary.
- [4] Pop - Szováti, A., Gyenge, Cs, Borzan, M.: *Optimization methods of the drives for mechanical presses*. Proceedings of the 4th International Scientific Conference on Advances in Mechanical Engineering (ISCAME 2016), 13 October 2016, Debrecen, Hungary.
- [5] Taylan Altan and A. Erman Tekkaya: *Sheet metal forming. Processes and Application*. ASM International, USA, ISBN-13: 978-1615038442, 2012.



## ANALYSIS OF DIFFERENT CONCEPT WAYS OF TWO-STAGE GEAR REDUCERS DESIGN

**RACKOV Milan PhD, KUZMANOVIĆ Siniša PhD, PENČIĆ Marko, ČAVIĆ Maja PhD, KNEŽEVIĆ Ivan**

*Faculty of Technical Sciences, University of Novi Sad*

*E-mail: [racmil@uns.ac.rs](mailto:racmil@uns.ac.rs), [kuzman@uns.ac.rs](mailto:kuzman@uns.ac.rs), [mpencic@uns.ac.rs](mailto:mpencic@uns.ac.rs), [scomaja@uns.ac.rs](mailto:scomaja@uns.ac.rs), [ivanknezevic@uns.ac.rs](mailto:ivanknezevic@uns.ac.rs)*

### **Abstract**

*There is no standard which defines particular shape and concept way of design of gear reducers. Therefore, manufacturers of gear reducers have open field for defining their own shape and design, or to copy the good concept design that already exist. Depending on the applied way of gear reducer design, technical characteristics of gear reducers can be different. Sometimes they achieve larger load capacity or higher gear ratio, but the best way is to improve both these characteristics. However, in order to achieve some advantage at the market, smaller manufacturers of gear reducers apply their own way of design. In this way they are able to provide different solution for better technical characteristics of gear reducer. This paper gives an overview of different concept ways of two-stage gear reducers design with different ways of assembling.*

**Keywords:** *two-stage gear reducer, different concept ways of design.*

### **1. INTRODUCTION**

Mechanical gear transmissions are mechanisms used to transfer mechanical energy from driving machine to operating machine where the number of revolution and operating torque are changed and sometimes direction of rotation, also. Mechanical gear drives can be divided in different ways, but depending on the direction of using, there are universal and special gear drives. Universal gear reducers are used for most of machines, but special are used for special case in certain machines and only for a particular purpose [1, 2].

Because of too complicated matter, this paper deals only with two-stage universal gear transmissions, but only with gear reducers ( $i > 1$ ), while gear multipliers ( $i < 1$ ) and simple gear units ( $i = 1$ ) will not be analysed here. Also, because of easier analysing, only universal gear reducers with spur and helical external gearing will be researched here, with normal backlash, i.e. industrial reducers. However, because of compact design, reducers with internal gearing (planetary gearboxes) are very used today no matter on their high price, but they will not be analysed here.

Universal gear drives are produced with axis heights according to the standard row R10. This height defines gear reducer size, so they are produced like a family of different sizes. But soon, gear ratio of gear reducer is increased, so the axis height is also increased, and now reducers are produced with axis height in a standard row R20/2. In the area of the most used gearbox sizes, some manufacturers produce so-called intermediate sizes with the axis heights in a row R20. [3]

### **2. PROBLEM DESCRIPTION**

In the area of universal gear reducers, there is no any technical standard which defines the relations between load capacity, gear ratios and axis heights. Therefore, larger load capacity of some gear reducers manufacturers has advantage for lower gear ratio and, vice versa, smaller load capacity of the



gearbox achieves higher values of gear ratio. However, there are some manufacturers who produce gear reducers with smaller or larger load capacity for higher or lower gear ratio, but solved with different gear reducer design.

Design of housing for two-stage gear reducer depends on what manufacturer wants to obtain: large load capacity or high gear ratio, or both of these. However, it also depends on the size of gear drive, on the way of elements mounting (bearings, gears, etc.) and on the way of covering the housing (from top side, from front side, or from top and front side) [2]. However, for all these different design solutions of housing, the most important is common axis height and the largest capacity and highest gear ratio. Therefore, there is a large competition between manufacturers to produce the gear drive with the better technical characteristics, but with smaller dimensions, weight and necessary oil quantity.

Two-stage gear units can be installed in separate housing for two-stage gear reducer (*Figure1-1*) [4], or in the universal housing for two- and three-stage gear reducers (*Figure1-2*) [5]. Of course, there are manufacturers which produce both type of housing, two-stage and three-stage gear reducer housing [6, 7, 8]. It is understandable that producing of two-stage gear reducers in special housing for only two-stage gear pairs has slightly lower production costs than using universal housing for two- and three-stages of gear pairs.

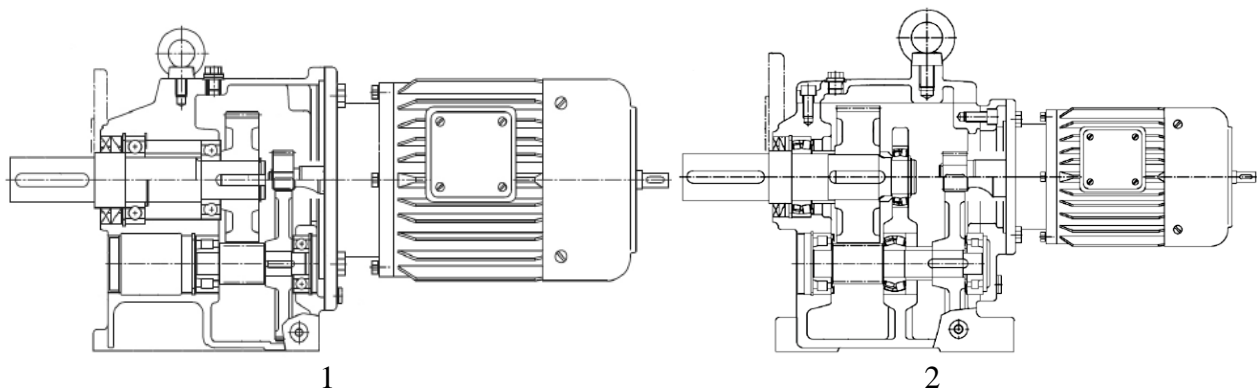


*Figure 1* Two-stage universal gear unit with special housing for two-stage gear reducer (1) and with universal housing for two- and three-stage gear reducers (2) [4, 5]

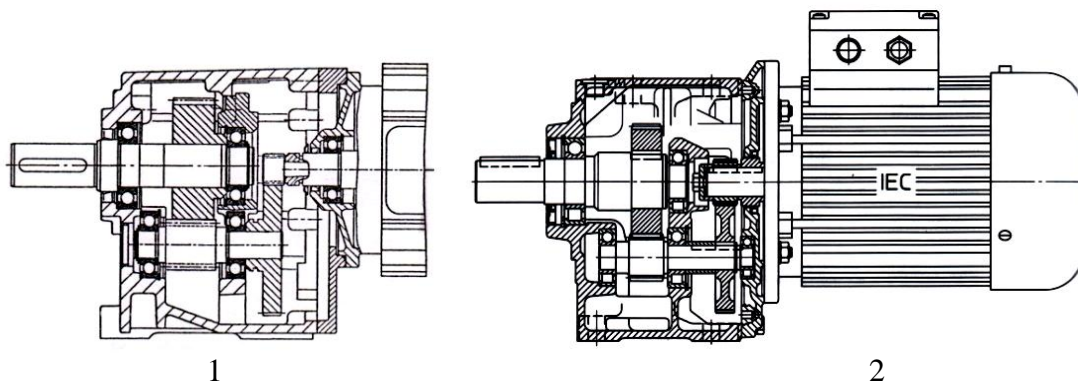


*Figure 2* Gearmotor with special reducer motor Lenze (1) and gearmotor with standard electric motor ROSSI(2)[7, 8, 9]

Most of gear reducers' manufacturers use special reducer motor which has shaft with smaller diameter than standard IEC electric motor. This allows the installation of smaller gears. Also, special reducer motor can have a hole in the free end of the shaft where small pinions are pressed, so gear ratio can have high values (*Figure 2-1*) [9]. Although, there are manufacturers which use



standard IEC electric motor, but also achieve relatively high gear ratio (*Figure 2-2*) [7, 8]. Since the gear drives are highly used mechanisms, there are a large number of manufacturers of different gear units. Certainly, there are different design solutions, but due to their long-term continuous improvement; they are brought to almost perfection. However, there is still continually improving at all stages of the production and exploitation of gear reducer. Strong competition has influenced the fast development of universal gear reducers, so now there are different concept solutions. Some concepts were created in order to increase the load capacity of the gear unit ( $T_N$ ), or to increase the gear ratio ( $i$ ), or to reduce the consumption of materials, the production costs (prices), the time of assembly, etc. These solutions are resulted from the tendency to be better than competition in some characteristic, and to achieve some advantage in some part of the market. Although many solutions were created from the tendency to make a different solution from the competition in order to avoid possible copyright disputes.

### 3. DIFFERENT CONCEPT WAYS OF TWO-STAGE GEAR REDUCERS DESIGN

It is evident that universal gear reducers are produced in several different variants. Market demands, the size of the series, and also the manufacturers' resources affect the most conception of the gear reducer. The gearbox concept defines the shape, disposition of the components and the way of assembly. However, the size of the series does not only depend on the number of reducers being produced, but also on the size (dimensions), and on their axial height.

During adopting the technical characteristics and the concept solution of universal gear drives, it is necessary to adopt the most advantageous on the basis of the different potential solutions. Based on the derived solutions of the universal gear reducers analyzed in this paper, it can be seen that almost every manufacturer of the gearbox has different technical characteristics and a different concept solution of the gearbox, so it is difficult to determine which solution is most favourable.

Axis heights of gear reducers are different and it is a problem, since the gears are mounted in the different way in the housing. There are also different approaches in defining the load capacity and gear ratio, and the applied materials can be different, especially for smaller axis heights. Manufacturers of gear reducers realize their own concept solution to make the gear drive different than the other solutions in order to achieve better characteristics or to avoid the possibility of being sued for copying somebody's other solution. Producers try to provide greater rigidity and the housing stability by appropriate shape and the mass distribution, and all that affects the technical characteristics.

The arrangement of gears is also important since it affects to loading of bearings, their size and possibility of installation and service. It is taken into consideration that only one bearing supports axial force at output shaft in order to reduce bearing costs and to obtain simple installation.

Rigidity of output shaft is provided by mounting the gears between the bearings. It also ensures application of shaft with smaller diameters. The gears should be positioned in the middle between bearings, so that the teeth mating should be as more correct as possible.

Gear drives with shafts distributed in the form of triangle are most commonly used because the drives compactness is the greatest in that case. So far, it has been common for gear drives to be manufactured with coaxial shafts, but in recent times it is more often used an inconsistent position of the input and output shaft in order to increase the gear ratio. On the basis of the analyzed characteristics of concept solutions of two-stage universal gear drives [5, 6, 7, 8, 9, 10, 11], four cases are evident (*Figure 3*). The solutions in *Figure 3-a*, *3-c* require the application of a housing with a single chamber, while the solutions in *Figure 3-b*, *3-d* require the application of the housing with two chambers.

If the reducer is only used as a two-stage, the cheapest and best solution is with the overhanged output gear and the second and third gears between the bearings (*Figure 3-a*). For transferring less torque, it is also good solution to have an output gear between the bearings and the second gear as



overhanged (*Figure 3-b*). While for transferring large torques the solution with the output gear between the bearings and the third gear shaft supported in three bearings is the best, but the most expensive solution (*Figure 3-c*). The fourth solution (*Figure 3-d*) with all the gears between the bearings corresponds most for two-stage gear drive, but only when all the gears are in one chamber.

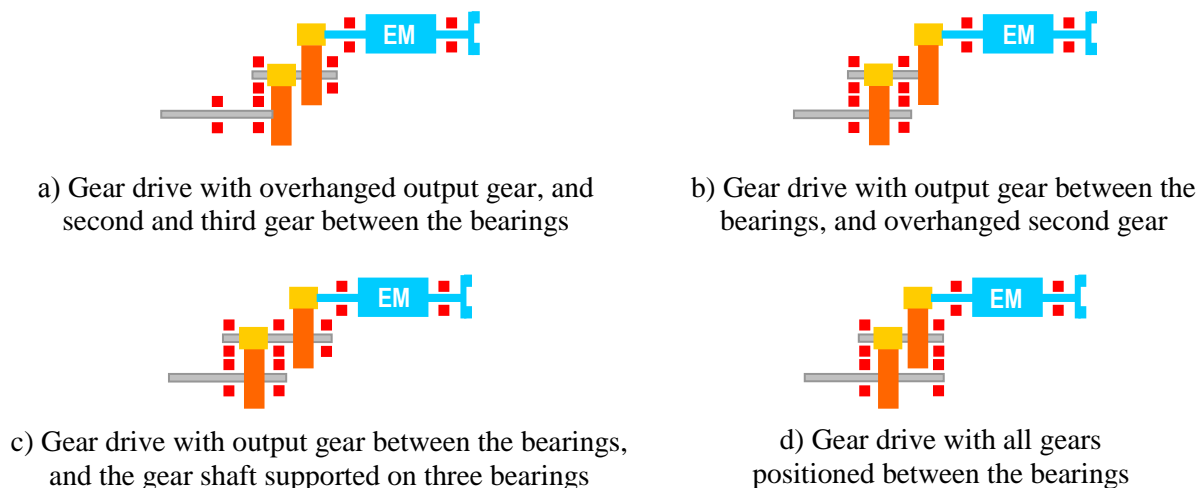


*Figure 3* Possible concept solution of universal two-stage gear drives with mounted special electric motor

World famous manufacturers of gearboxes use equally all concept solutions of two-stage gear units. The most expensive solution, with the third gear shaft supported on three bearings is used only by the largest gearbox manufacturers (SEW, Siemens-Flender, Nord and Rossi). Depending on the axis height, some manufacturers also offer two concepts of gearboxes, but always use the shaft mounted in three bearings for higher axis heights, or larger nominal torques. Manufacturers that produce two-stage reducers in separate housing use the first solution and manufacturers that use the same housing for two-stage and three-stage gear units typically use the other solution.

Based on the analyzed characteristic solutions of the housing of different gear units, the following division of the housing can be performed with respect to the openings on it: housing with an opening in slow-motion chamber, housing with an opening in both chambers, housing with a lower middle wall, housing with removable middle wall, housing with interflange and housing with a front cover.

The selection of the concept solution also depends on the desired stiffness of the housing and easy assembly. Based on the analyzed characteristic solutions of gear reducer housing, it can be concluded that the modern gear drives are produced in one-piece and two-piece variant. From the point of stiffness of the housing, one-piece housing is most suitable (*Figure 4*), but they do not provide high gear ratio. Two-piece housings are less rigid and especially if they have an opening for inserting large gears, when they have to be further strengthened [2].

Today there is a tendency to achieve high gear ratios, so the large driven gears are used. Therefore, there is a need to make the front opening of the housing. For high gear ratio, it is necessary to make top side opening on the gearbox housing, since opening at the front side is defined by the flange of the electric motor and it is too small. Housings with large front openings are not so strong, but the possibility of easy installation gives them a certain advantage.

There are several ways of mounting two-stage universal gear units, since there is large number of parts and different conceptual solutions. By analyzing the characteristic solutions of the two-stage gearboxes, a selection of the mounting method can be made depending on the gear unit manufacturer (*Figure 4*). Also, certain manufacturers, in order to get the best technical characteristics of their gear units, use different mounting modes depending on the axis height. On



the basis of the analyze, it is considered that two-stage gear units are manufactured in one-piece housing, while in the case of two- and three-stage gearboxes, two-part housings are also used [12]. Modern gear units are most often made in one-piece housing, since such construction has greater rigidity. The basic lack of one-piece housing is reduced gear ratio. Manufacturers try to solve this problem by applying an appropriate interflange or top side opening on the housing, so that the larger gears can be mounted into the housing.

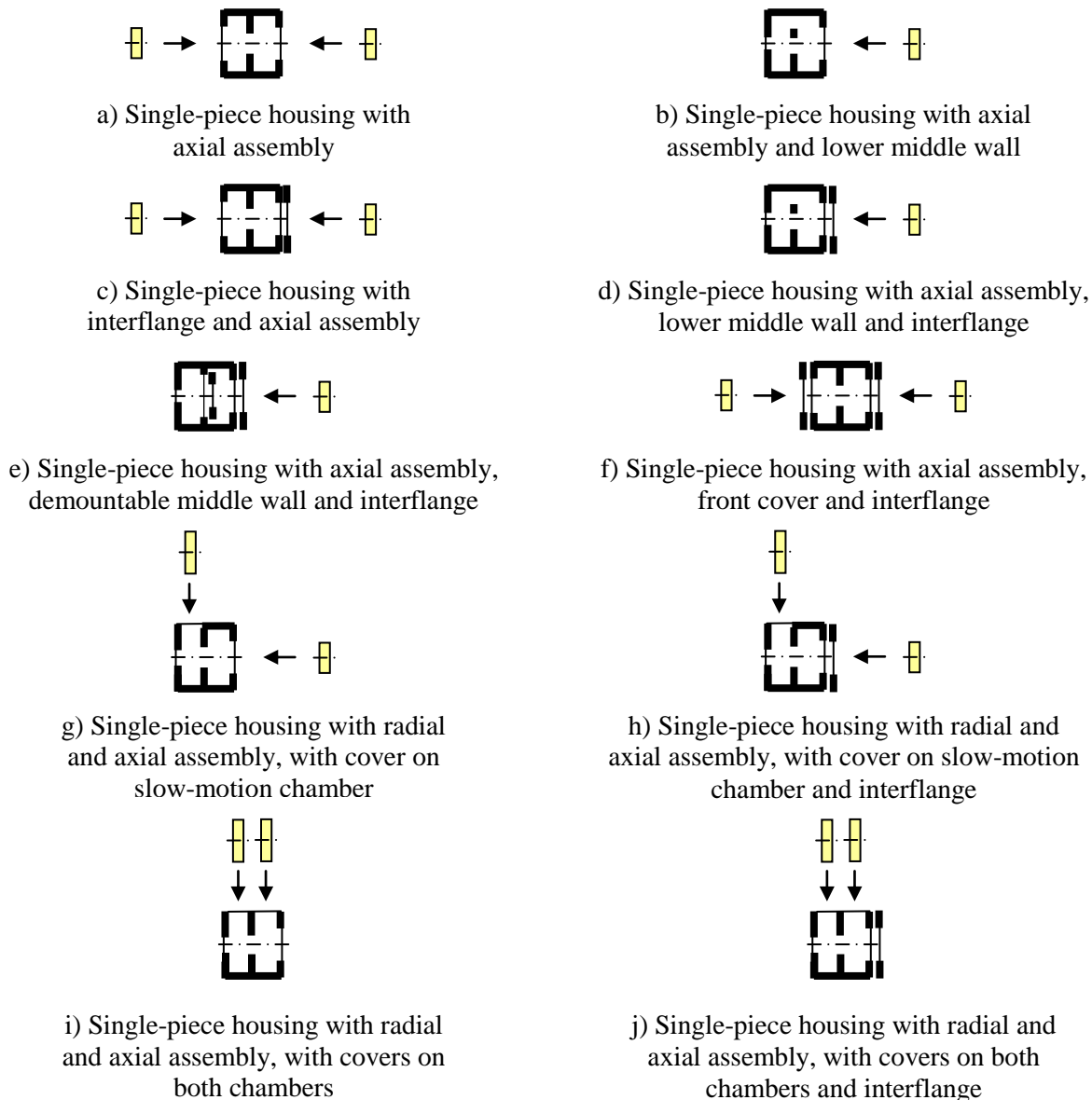
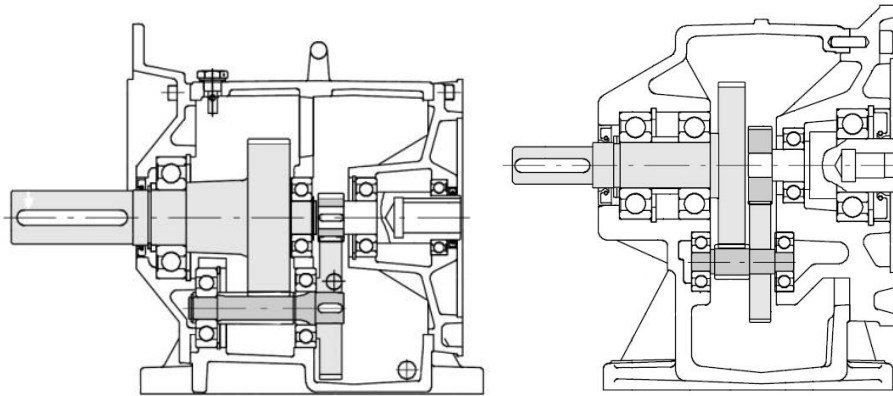


Figure 4 Characteristic concept ways of two-stage gear reducer assembly [12]

Axial mounting is most commonly used in smaller two-stage gearboxes, while radial mounting is used for gearboxes of larger axis heights, where it is necessary to install large gears as simple and easy as possible. The most commonly used mounting method for smaller sizes of two-stage gears is axial mounting in one-piece housing with interflange. In larger two-stage gear units, the most common way of assembly is radial mounting in single-piece housing with interflange. However, manufacturer Lenze GST constantly uses an axial mounting method using a demountable middle wall. Based on the analyzed characteristic solutions of the two-stage gearbox [2], it can be seen that the manufacturer SEW uses a housing without an interflange. Manufacturers Rossi ES07 and KEB are trying to copy



this SEW gearbox using a housing without an interflange, while other manufacturers use interflange. This resulted with lower values of gear ratio [2]. The characteristic solution is the gearbox produced by Pujol with an interflange which is in the same time also adapter for the installation of standard motors. Thanks to this, this gearbox provides great gear ratios due to small pinions (*Figure 5*).



*Figure 5* Cross section of universal two-stage gear reducer of the S series (1) and I series (2) (solution of the company Pujol) [13]

## CONCLUSIONS

The fact that there is a large number of universal gear drives manufacturers around the world tells about the importance of these products and the need for large-scale investments and efforts to create even more perfect gear units. Different concept designs, types and ways of installation are the result of different ways of improving the technical characteristics of universal two-stage gear units. This paper notes and describes different concepts of universal gear reducers, where the study of their parameters provides additional analysis of the quality of different concept solutions.

## REFERENCES

- [1] Kuzmanović, S., Rackov M.: *Development Tendencies of Universal Gear Reducers*. Proc. of the 3<sup>rd</sup> Inter Conf. on Power Transmissions (BAPT), Kallithea, Greece, 145–148., 2009.
- [2] Rackov M.: *Conceptions of Development of Universal Gear Reducers*. Ph.D. thesis (in Serbian), University of Novi Sad, Faculty of Technical Sciences, Novi Sad, Serbia, 2013.
- [3] Kuzmanović, S. *Universal Gear Reducers with Cylindrical Gears (in Serbian)*. University of Novi Sad, Faculty of Technical Sciences, Novi Sad, Serbia, 2009.
- [4] NORD Drivesystems, Constant Speeds, G 1000.
- [5] NORD Drivesystems, *Standard Helical Gearboxes*, G 2000.
- [6] NORD Drivesystems, *Standard Helical Gearboxes*, G 2016.
- [7] Rossi, *E04 Coaxial Gear Reducers and Gearmotors*, 2015.
- [8] Rossi, *STANDARDFIT Coaxial Gearmotors ES07*, 2015.
- [9] Lenze, *L-force, Getriebemotoren*, 2016.
- [10] SEW Eurodrive, *Catalog – Gear Units*, 06/2016.
- [11] Siemens, *MOTOX Geared Motors*, D 87.1, 2016.
- [12] Kuzmanović, S., Vereš, M., Rackov, M.: *Analysis of Characteristical Mounting Ways of Gear Wheels in Universal Gear Reducers*. Zeszyty Naukowe Politechniki Poznańskiej, Seria: Budowa Maszyn i Zarządzanie Produkcją, 11, 81–91., 2009.
- [13] Pujol Muntalà, *Geared Units*, Polígono Industrial La Serreta, 2015.



## THERMO-HYGRO- MECHANICS IN INDIAN SCIENCE PHILOSOPHY

**RAZA Md Tanweer, SZEKERES András CSc**

*Budapest University of Technology and Economics*

E-mail: [mdl1tan@gmail.com](mailto:mdl1tan@gmail.com), [szekeres@mm.bme.hu](mailto:szekeres@mm.bme.hu)

### Abstract

*The basic purpose of the paper is defined. First, to show the science philosophy (sphil) and math aspects of the science, mainly of the Thermo-hygro-mechanics (THM). Second, find Indian scientists from the last century and time older age who contributed to the science, usually to the THM. We reached also the side result, that the contribution of Indians on this field is comparable to the result of the Europeans. According to this goal, after the introduction the paper gives a brief summary on the THM based on our previous paper. Similarly, some examples on the sphil and math aspects of THM and finally this list of Indian scientists with their results.*

**Keywords:** thermo, hygro, mechanics, science philosophy and indian science

### 1. INTRODUCTION

The thermo-hygro-mechanics (from now on THM) is the general, interdisciplinary science philosophy as considered in the following in our paper. The steps of its evolution are the following: thermal stresses (TS), thermoelasticity (TE), generally thermomechanics (TM) and THM [1].

According to our opinion, basically the THM has quatro roots:

A very practical and the main one, ie. more and more materials of our life are thermoscopic and hygroscopic, supposing that all of them are more or less deformable, mentioning only two of them, ie. composites and biotissues.

Another root is a theoretical one, namely the coupled fields, or more generally the interdisciplinarity. The new materials and procedures require them and the new theories [2].

The third root is the possibility given by the new informatics and generally the techniques, let us call all of them together as "tools". Good example is the FEM, that became a replacement of the experiment, see eg. the photo-elasticity, or the electrical analogy based experiments replacing the physical experiments.

Finally, the interaction between the new theories induced tools and the new tools generated new theories give a special raise to the THM.

### 2. THERMO-HYGRO-MECHANICS (THM)

THM is based on the following well elaborate disciplines: thermodynamics(TD), hygro elasticity (HE), and elasticity(E). The basic laws are the following: Hooke's law, Duhamel Neumann Law(D-N), generalized Duhamel-Neumann law, Fourier and Fick laws, Soret and Dufour effects, and Gough-Joule effect. The mathematical tool is given generally by the continuum mechanics(CM) [1,2].

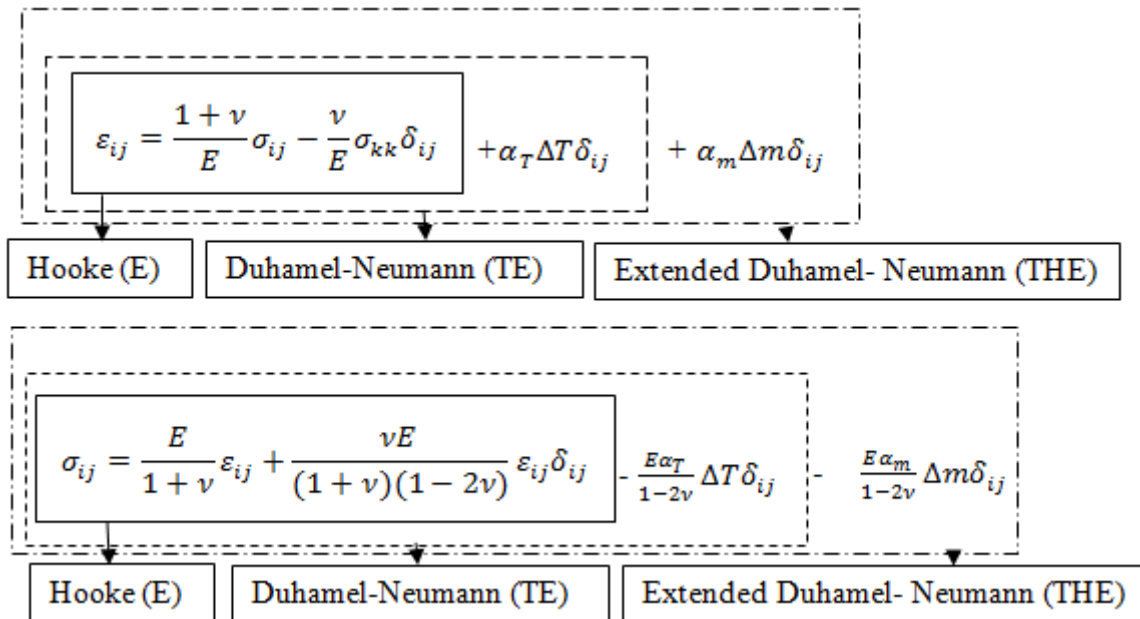


Figure 1 Constitutive Equation

### 3. THM AND SCIENCE PHILOSOPHY

In this part we are going to display a few problems of the aspects of math (mathematics/al) and phil (science philosophy/cal), especially, the math side of the phil and vice versa, the phil side of the math [3].

Let us start with the mentioning of a few basic parts of math that are organic parts also the THM. First of all, the PDES (partial differential equation), that are used, eg. to describe the problem, see eqs. or in the SSP (second sound phenomenon), see [4,5].

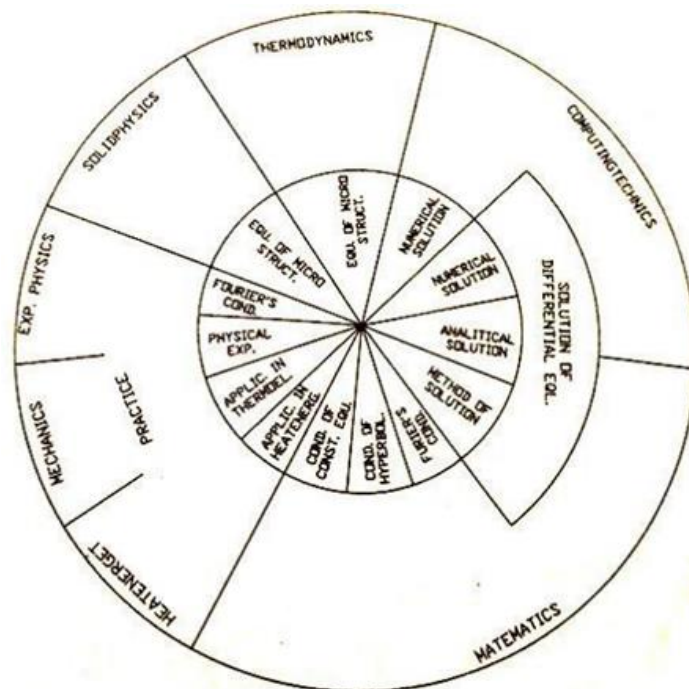
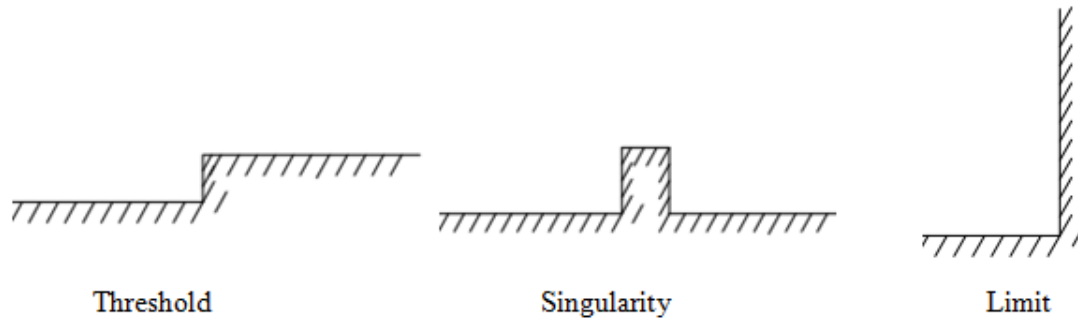


Figure 1\* Second Sound Phenomenon(SSP) Method



The *Figure 1\** shows a special table with also the math in it for the modification method in SSP. Example could be the Hooke's law and its advanced expressions, ie. Duhamel Neumann eqs. (See *Figure 1*, constitutive eqs.) Or, being at the Hooke's law, we may mention the spfil considerations on math (see [6]).



*Figure 2\** Threshold, Singularity, Limit

Approaching the spfil, several questions come up. Let us mention first the following notions: threshold, limit and singularity (see *Figure 2\**). The geometry an evidence, but how to express them by the means of math? Or, the scientific steps to the truth (see *Figure 3\**). The question is the role of the math in the different steps.

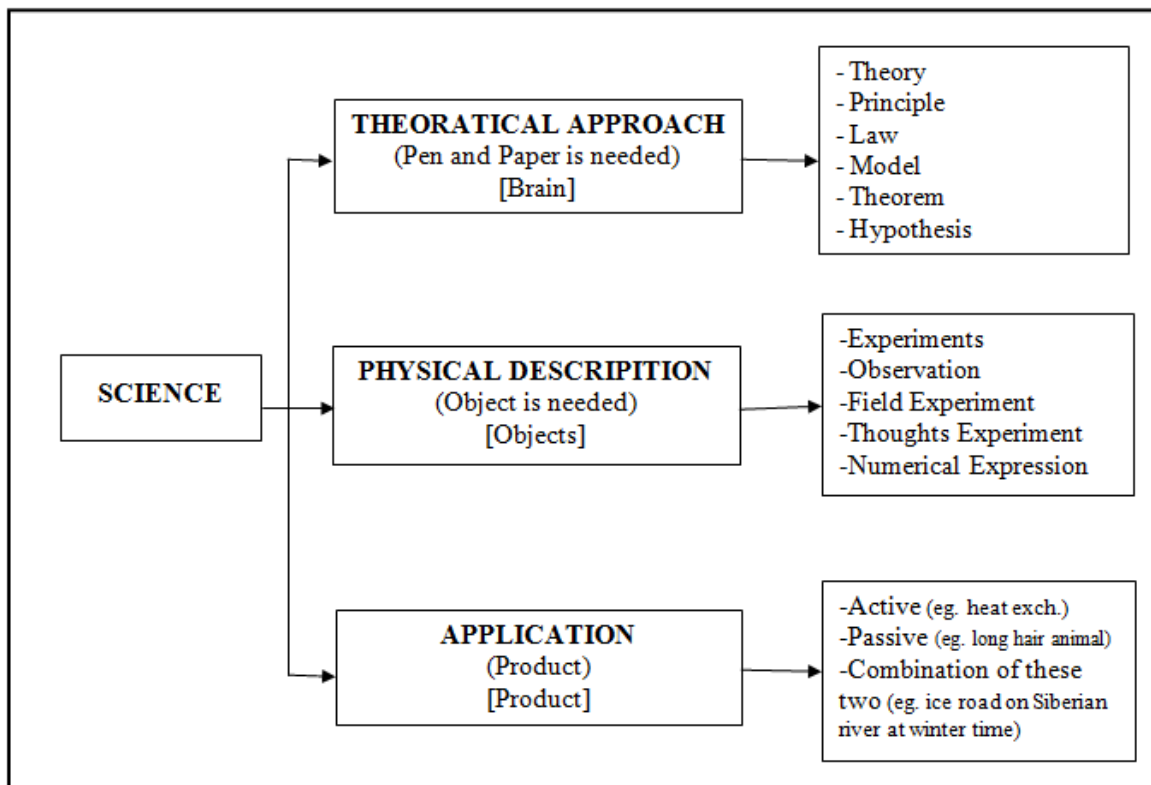


*Figure 3\** THM to use in Science History

Or, the most basic notions of the science, the time and the space. According to our opinion, they are so natural, that no need to define them. But there is the danger to neglect their role, of course, in some special cases.



#### 4. INDIAN SCIENTISTS TO SERVE IN THEIR WHOLE LIFE THIS FIELD OF SCIENCE

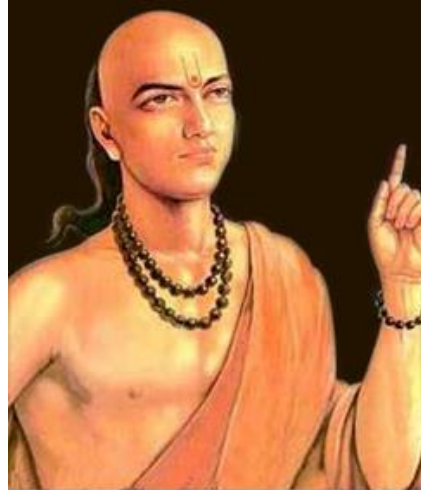


*Figure 4* Aryabhata

Born: 476AD. Died: 550AD. Aryabhata was the first of the major mathematician-astronomers from the classical age of Indian mathematics and Indian astronomy.[7] Father of Astronomy. Zero was invented by Aryabhata an Indian Mathematician in late 5th century. Aryabhata is also invented trigonometry function of Sin and Versine.

##### MORE HISTORY ABOUT ZERO:

It is also said that Aryabhata invented the number 0. Aryabhata was one of the world's greatest mathematician- astronomer. Aryabhata devised a number system, which had no Zero, as a positional system, but used to denote empty space. There is evidence that a dot had been used in earlier manuscripts to denote an empty space in positional notation. He gave the world the digit "0" (zero) for which he become immortal. He was the first mathematician to use the concept of zero. He used zero for the first time to define decimal system. It is said that he was aware of the concept and even used it is calculations. He certainty did not use the symbol, but French mathematician Georges Irfah argued that knowledge of zero was implicit Aryabhata's place value system as a place holder for the powers of the ten with null coefficient [8].



*Figure 5* Srinivasan Ramanujan



# INTERNATIONAL SCIENTIFIC CONFERENCE ON ADVANCES IN MECHANICAL ENGINEERING

12-14 October 2017, Debrecen, Hungary



**Born:** December 22, 1887, Erode, India. **Died:** April 26, 1920, Kumbakonam, India. Srinivasan Ramanujan was an Indian mathematician who lived during the British Rule in India. Though he had almost no formal training in pure mathematics, he made substantial contributions to mathematical analysis, number theory, infinite series, and continued fractions, including solutions to mathematical problems considered to be unsolvable. Ramanujan initially developed his own mathematical research in isolation; it was quickly recognized by Indian mathematicians [9]. In 1900, he worked on his own math summing geometric and arithmetic series. He solved cubic equation (1902),  $ax^3+bx^2+cx+d=0$

Reply to – The number 1729 is ‘dull’:

No, it is a very interesting number; it is the smallest number expressible as a sum of two cubes in two different ways, the two ways being [10]

$$1^3+12^3 \text{ and } 9^3+10^3=1729$$

First found by Ramanujan. It's my favourite formula for pi.

$$\frac{1}{\pi} = \frac{\sqrt{8}}{9801} \sum_{n=0}^{\infty} \frac{(4n)!}{(n!)^4} \times \frac{26390n + 1103}{396^{4n}}$$

Pi to Million (1,000,000) digits [11].

**pi** =3.1415926535 8979323846 2643383279 5028841971 6939937510  
 5820974944 5923078164 0628620899 8628034825 3421170679  
 8214808651 3282306647 0938446095 5058223172 5359408128  
 4811174502 8410270193 8521105559 6446229489 5493038196  
 4428810975 6659334461 2847564823 3786783165 2712019091  
 4564856692 3460348610 4543266482 1339360726 0249141273  
 7245870066 0631558817 4881520920 9628292540 9171536436  
 7892590360 0113305305 4882046652 1384146951 9415116094  
 3305727036 5759591953 0921861173 8193261179 3105118548  
 0744623799 6274956735 1885752724 8912279381 8301194912.



Figure 6 C.V. Raman

**Born:** November 7, 1888, India. **Died:** November 21, 1970, India. Sir Chandrasekhara Venkata Raman was an Indian physicist born in the former Madras Province in India presently called as Tamil Nadu, who carried out ground-breaking work in the field of light scattering, which earned him the 1930 Nobel Prize for Physics. He discovered that when light traverses a transparent material, some of the deflected light changes wavelength. This phenomenon, subsequently known



# INTERNATIONAL SCIENTIFIC CONFERENCE ON ADVANCES IN MECHANICAL ENGINEERING

12-14 October 2017, Debrecen, Hungary



as Raman scattering, results from the Raman effect. In 1954, India honoured him with its highest civilian award, the Bharat Ratna [12]. He was the first Asian and first non-white to receive any Nobel Prize in the sciences.

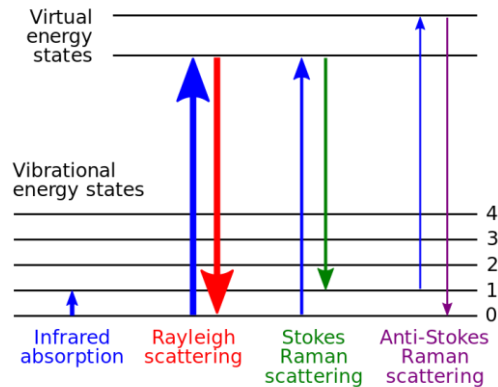


Figure 7 Energy level diagram showing the state involved in Raman Signal



Figure 8 Homi J. Bhabha

**Born:** October 30, 1909, India. **Died:** January 24, 1966, France, Homi Jehangir Bhabha was an Indian nuclear physicist, founding director, and professor of physics at the Tata Institute of Fundamental Research. Homi Jehangir Bhabha an Indian born scientist who played an important part in contribution to The Quantum Theory was born on October 30, 1909 in Bombay. He was the first one to become the Chairman of Atomic Energy Commission of India. Father of Indian Nuclear Program. Bhabha Presented, with Heitler, the Cascade Theory of Electron Showers, in 1937. Electron-positron scattering was later named “Bhabha Scattering” [13]. There are two leading-order Feynman diagrams contributing to this interaction: an annihilation process and a scattering process. The Bhabha scattering rate is used as a luminosity monitor in electron-positron colliders.

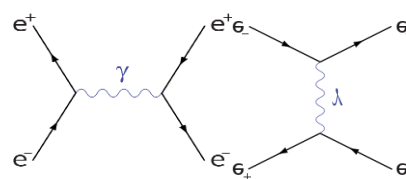


Figure 9



# INTERNATIONAL SCIENTIFIC CONFERENCE ON ADVANCES IN MECHANICAL ENGINEERING

12-14 October 2017, Debrecen, Hungary



Bhabha recognized heavy electron particle in cosmic rays and called them “MESON”. Mesons are unstable subatomic particles composed of one quark and one antiquark. They are part of the hadron particle family – particles made of quarks. The other members of the hadron family are the baryons – subatomic particles composed of three quarks. Three Atomic Reactors (‘Apsara’, ‘Cirus’ and ‘Zerlina’) are the result of his efforts.



Figure 10 Satyendra Nath Bose

Born: January 1, 1894, India. Died: February 4, 1974, India. Satyendra Nath Bose was an Indian physicist from Bengal specialising in theoretical physics. He is best known for his work on quantum mechanics in the early 1920s, providing the foundation for Bose–Einstein statistics and the theory of the Bose–Einstein condensate. The class of particles that obey Bose Einstein statistics, bosons, was named after Bose by Paul Dirac. A boson is a particle which has a whole number spin ('spin' is a quality assigned to subatomic particles). Bosons carry energy. A photon is an example of a boson as it has a spin of 1. Bosons are different from Fermions, which are particles that make up matter, because they obey Bose-Einstein statistics.

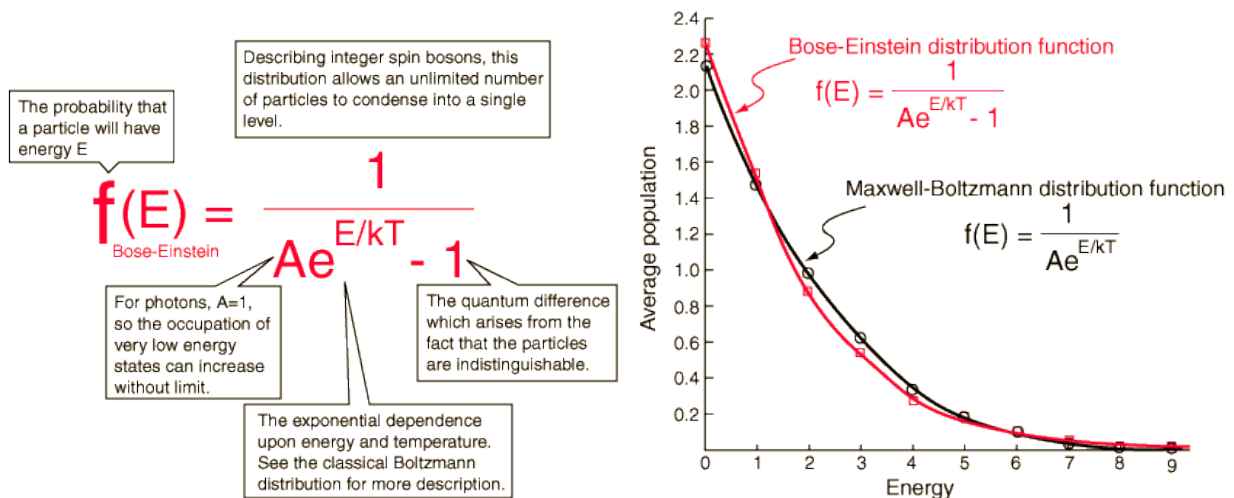


Figure 11 Bose-Einstein distribution equation [14]



# INTERNATIONAL SCIENTIFIC CONFERENCE ON ADVANCES IN MECHANICAL ENGINEERING

12-14 October 2017, Debrecen, Hungary



*Figure 12 S. Chandrasekhar*

Born: October 19, 1910, Pakistan. Died: August 21, 1995, United States. Subrahmanyan Chandrasekhar was an Indian American astrophysicist who was awarded the 1983 Nobel Prize for Physics with William A. Fowler "for his theoretical studies of the physical processes of importance to the structure and evolution of the stars". His mathematical treatment of stellar evolution yielded many of the best current theoretical models of the later evolutionary stages of massive stars and black holes. The Chandrasekhar limit is named after him. Chandrasekhar worked on a wide variety of physical problems in his lifetime, contributing to the contemporary understanding of stellar structure, white dwarves, stellar dynamics, stochastic process, radiative transfer, the quantum theory of the hydrogen anion, hydrodynamic and hydromagnetic stability, turbulence, equilibrium and the stability of ellipsoidal figures of equilibrium, general relativity, mathematical theory of black holes and theory of colliding gravitational waves.

## CHANDRASEKHAR LIMIT:

The Chandrasekhar limit is the maximum mass of a stable white dwarf star. This limit was initially ignored by the community of scientists because such a limit would logically require the existence of black holes, which were considered a scientific impossibility at the time. White dwarfs resist gravitational collapse primarily through electron degeneracy pressure. The Chandrasekhar limit is the mass above which electron degeneracy pressure in the star's core is insufficient to balance the star's own gravitational self-attraction. Consequently, white dwarfs with masses greater than the limit would be subject to further gravitational collapse, evolving into a different type of stellar remnant, such as a neutron star or black hole. The currently accepted value of this limit is about

$$1.4M_{\odot} (2.765 \times 10^{30}\text{kg})$$

where,  $M_{\odot}$  is Solar Mass.



*Figure 13 Meghnad Saha*



Born: October 6, 1893, Bangladesh. Died: February 16, 1956, India. Meghnad Saha was an Indian astrophysicist best known for his development of the Saha ionization equation, used to describe chemical and physical conditions in stars. Saha was the first scientist to relate a star's spectrum to its temperature, developing thermal ionization equations that have been foundational in the fields of astrophysics and astrochemistry.

$$\frac{N_{i+1}}{N_i} = \frac{2Z_{i+1}}{n_e Z_i} \left( \frac{2\pi m_e kT}{h^2} \right)^{3/2} e^{-\chi_i/kT}$$

The diagram illustrates the Saha ionization equation with color-coded labels for its components:

- RATIO OF POPULATIONS OF IONIZATION STATES  $i$  AND  $i+1$** :  $\frac{N_{i+1}}{N_i}$
- ELECTRON NUMBER DENSITY**:  $n_e$
- PARTITION FUNCTIONS FOR  $i$  AND  $i+1$** :  $Z_i$
- ELECTRON MASS**:  $m_e$
- BOLTZMANN CONSTANT**:  $k$
- PLANCK CONSTANT**:  $h$
- IONIZATION ENERGY**:  $\chi_i$

Figure 14 Saha ionization equation (Saha equation) [15]



Figure 15 A.P.J. Abdul Kalam

Born: October 15, 1931, Rameswaram, India. Died: July 27, 2015, Shillong, India. Avul Pakir Jainulabdeen Abdul Kalam, was an Indian scientist who worked as an Aerospace engineer with Defence Research and Development Organisation (DRDO) and Indian Space Research Organisation (ISRO) [16]. Missile Man of India. He was tested AGANI and PRITHVI missile. He was Scientist, Professor, Author, Engineer and President of India. Known for his crucial role in the development of India's missile and nuclear weapons programs. He thus came to be known as the *Missile Man of India* for his work on the development of ballistic missile and launch vehicle technology. He also played a pivotal organisational, technical, and political role in India's Pokhran-II nuclear tests in 1998, the first since the original nuclear test by India in 1974 [16]. He was the project director of India's first Satellite Launch Vehicle (SLV-III) which successfully deployed the *Rohini* satellite in near-earth orbit in July 1980; Kalam had first started work on an expandable rocket project independently at DRDO in 1965. Kalam made an effort to develop the Polar Satellite Launch Vehicle (PSLV) and SLV-III projects, both of which proved to be successful [16]. "If you want to SHINE like a sun, First BURN LIKE A SUN." A. P. J. Abdul Kalam.



# INTERNATIONAL SCIENTIFIC CONFERENCE ON ADVANCES IN MECHANICAL ENGINEERING

12-14 October 2017, Debrecen, Hungary



Speak 5 Lines to yourself every morning.....

1. I Am the Best
2. I Can Do It
3. God Is Always with Me.
4. I Am Winner
5. Today Is My Day

## REFERENCES

- [1] Szekeres, A.: *Thermo-Hygro-Elasticity (THE)*. Encyclopedia of Thermal Stresses, 5918-5924., 2013.
- [2] Szekeres, A.: Cross-Coupled Heat and Moisture Transport: Part 1 - Theory, Journal of Thermal Stresses, 35:248-268, 2012.
- [3] Szekeres, A., Divya, J., Kishan A., Md, Tanweer R., Danial, R., Sushil, K. T.: *Thermo-Hygro Mechanics from different aspects*. 14<sup>th</sup> Joint European Thermodynamics conference 2017, 21-25., 2017.
- [4] S. Feih, Z. Mathys, G. Mathys, A. Gibson, M. Robinson és A. Mouritz: *Influence of water content on failure of phenolic composites in fire*. Polymer Degradation and Stability, 1. kötet93., 376-382., 2008.
- [5] Szekeres, A.: *Equation Syatem of Thermoelasticity Using the Modified Law of Thermal Conductivity*. Periodica Polytechnica, Mech. Eng., vol. 24, no. 3, 253-261., 1980.
- [6] Farkas I., Szekeres A.: *Application of the Modified Law of heat Conduction and state Equation to Dynamical Problems of Thermoelsaticity*. Periodica Polytechnica, Mech. Eng., vol.28, nos. 2-3, 163-170., 1984.
- [7] <http://www.famous-mathematicians.com/aryabhata> (08/10/2017)
- [8] <https://www.slideshare.net/DivyaRajput6/history-of-zero-mathematics> (08/10/2017)
- [9] <http://www-groups.dcs.st-and.ac.uk/history/Biographies/Ramanujan.html> (04/10/2017).
- [10] Berndt, B. C., Chan, H. H. L., Zhang, Ch.: *Radicals and units in Ramanujan's work*. Acta Arith. 87, 145–158., 1998.
- [11] <https://crypto.stanford.edu/pbc/notes/pi/ramanujan.html> (15/09/2017).
- [12] <https://quantumredpill.wordpress.com/2013/03/09/spectral-lines> (08/10/2017).
- [13] [https://en.wikipedia.org/wiki/C.\\_V.\\_Raman](https://en.wikipedia.org/wiki/C._V._Raman) (08/10/2017).
- [14] [www.physi.uni-heidelberg.de/~menzemer/PP\\_SS2012/TestQED\\_10.pdf](http://www.physi.uni-heidelberg.de/~menzemer/PP_SS2012/TestQED_10.pdf) (31/09/2017)
- [15] <http://hyperphysics.phy-astr.gsu.edu/hbase/quantum/disbe.html> (08/10/2017)
- [16] Abdul Kalam, A. P. J.: *The wings of fire*. Auto-Biography Book, 1999.



## EXAMINATIONS OF MECHANICAL PROPERTIES OF DIFFERENT PVC/CPE BLENDS

**ROMÁN Krisztina, ZSOLDOS Gabriella PhD**

*Institute of Ceramics and Polymer Engineering, University of Miskolc*

*E-mail: [polkrisz@uni-miskolc.hu](mailto:polkrisz@uni-miskolc.hu), [femzsgab@uni-miskolc.hu](mailto:femzsgab@uni-miskolc.hu)*

### **Abstract**

*The objective of this work is to investigate the effect of using CPE polymer as additive on the mechanical properties of rigid PVC foams. The individual and combined effect of CPE concentration in the polymer on the mechanical properties of the rigid foam is reported. The good mechanical property of blending polymer with polymer provides more specific application opportunities in industrial areas. The CPE material can give higher stability. We produced samples of blends from PVC and CPE materials and neat PVC mixtures by extrusion. The properties of the two types of samples are obtained by mechanical tests: tensile-, flexure-, impact-, hardness tests and density measurements. Based on the results the differences can be determined in the material properties as function of distinct composition of the materials.*

**Keywords:** *PVC/CPE blend, foams, tensile and impact test, mechanical properties, hardness test, density measurements*

### **1. INTRODUCTION**

The PVC [poly(vinylchloride)] is often mixed with other polymers to improve properties of hardness and toughness. Chlorinated polyethylene (CPE) is commonly used to modify the structure of the PVC. Nowadays, the use of polymer blends and alloys has become increasingly important in the development of advanced engineering materials. Impact modification of PVC with CPE is an area of great interest to the polymer industry [1]. The PVC/CPE blend's structures are complex, because the morphology of the polymer blend changes with concentration and processing and it has a significant effect on the impact behaviour of the PVC. In this paper we compare the mechanical properties of a selected PVC/CPE blend with common PVC rigid foam. The rigid polymer foams are currently used as insulating material; the extrusion profiles used are as shades, pipes and for other industrial purposes [2].

### **2. MATERIALS**

CPE (chlorinated polyethylene) with a chlorine content of 32% and PVC with K values = 58 (suspension type) were used in blending. The PVC/CPE blend's density is 0,9261 g/cm<sup>3</sup>. Density of neat foam is 0,7027 g/cm<sup>3</sup>. The common foam contains the necessary production additives (processing aids, fillers and stabilizers, etc.) [3].

Sample preparation:

The polymer powders were mixed with stabilizers, additives and a foaming agent in a high-speed dry mixer to 110 °C. The PVC/CPE ratios are 100/20. Specimens were die-cut for all measurements from sheets obtained by extrusion at T= 180 °C [4].



### 3. METHODS

The temperature during measurement affects mechanical properties of PVC materials, such as tensile-, flexural-, strength or hardness. The properties of the foams also depend on cell morphology, such as cells size and shape, cell wall thickness and the density of the material [5].

Below are some examples of methods which can be used for testing [5]:

Foams: tension and compression test, impact strength, shear-strain behavior and torsion testing

The additives influence the tests also; they have an impact on the selection of the testing methods [6]:

impact modifiers: impact strength, toughness, plastic deformation, tensile stress and modulus, fillers: flexural modulus, thermal stabilizers: tensile test.

The investigations were carried out with INSTRON 5566 instrument for tensile and flexural tests. The INSTRON testing machine was used to determine tensile and flexure strength and specimens modulus values. The impact strength measurement was carried out in CEAST 6545 equipment and for the hardness tests Zwick/Roell Shore A equipment was used.

The standard test method for determining properties of plastics is ASTM D638-10. The standard test method for determination of flexural properties is: ISO 178:2010[7].

Most tests were carried out in both machine and cross directions on the samples. The two different directions are important to get an accurate picture of the strength and orientation of the test specimens.

Tensile test:

Figure 1 and 2 show the tensile test results. The FB means the Foam Blend, the FN is the Foam Neat. The M is the machine the C is the Cross direction of the specimen.

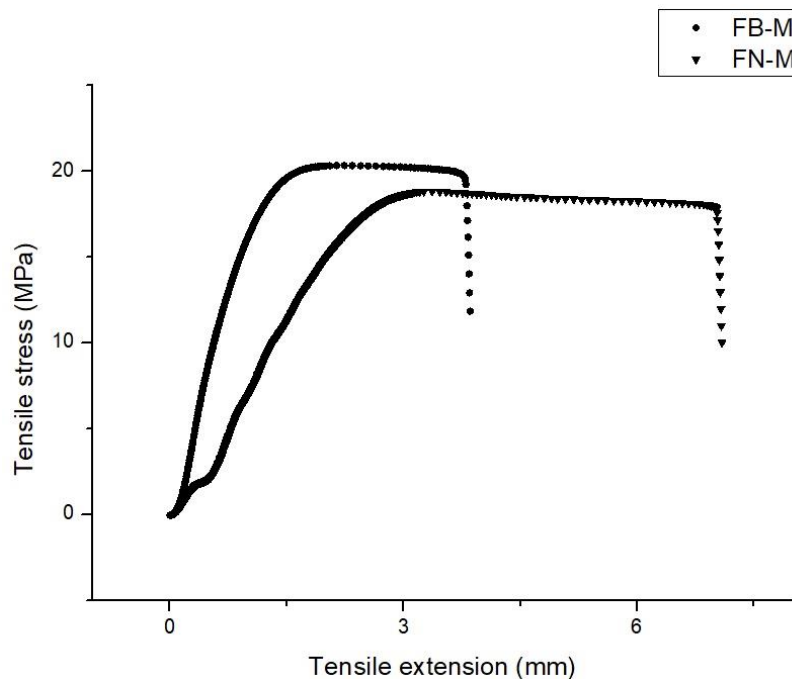


Figure 1 Tensile strength values in machine direction

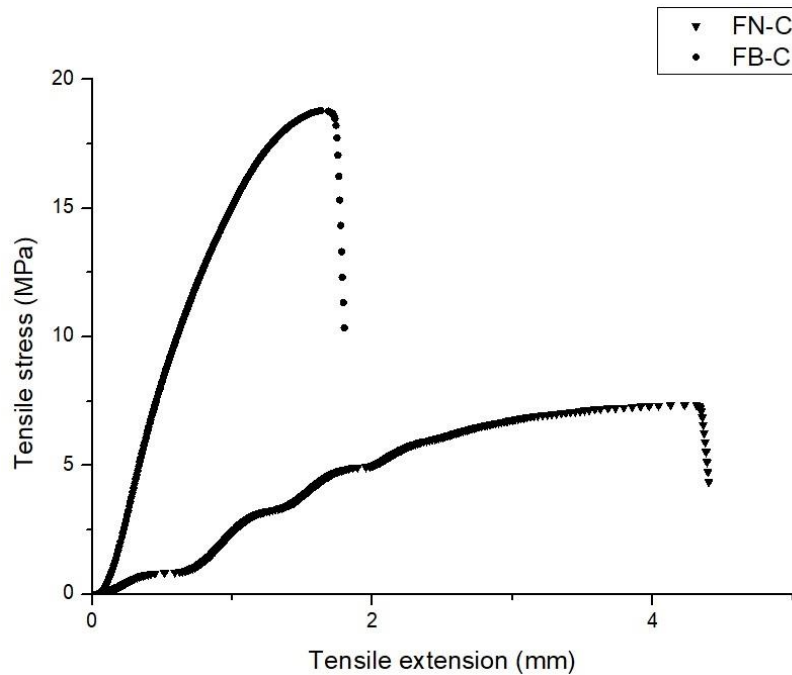


Figure 2 Tensile strength values in cross direction

Based on *Figure 2* the neat foam has much lower strength values, but ultimate yield of blend was much smaller.

Table 1 Results of tensile test

Specimen number	Max. Tensile stress [MPa]
FN-M	18.83
FN-C	7.35
FB-M	20.34
FB-C	18.79

The tensile test's results show an increase in the tensile strength of FB foam. It can be seen that the CPE increases the strength values, while the normal foam shows much less strength in both the cross and in the machine direction.

Impact test:

The tests were carried out using a 4J hammer. *Table 2* contains the average values of 7 samples for each measurement types (machine, cross direction).

Table 2 Result of impact test

Specimen number	Impact bending strength [kJ/m <sup>2</sup> ]
FN-M	2,19
FN-C	1.41
FB-M	2,61
FB-C	<b>3,47</b>

The results show the higher bending ductility of the blended foam in every direction.



#### Flexural test:

A minimum of ten samples were tested and an average value of flexural strength was determined. From *Table 3* and *4* it is visible that the results of the test are similar to the result to *Table 1*. In this case, the structure of the blend is more resistant of the force than the neat mixture. The blend has better strength for both cross- and machine directions than the average PVC foam.

*Table 3* Result of flexural strength

Specimen number	Flexure stress [MPa]
FN-M	25.19
FN-C	7.47
FB-M	33.25
FB-C	27.83

*Table 4* Results of flexural modulus

Specimen number	Modulus [MPa]
FN-M	762.00
FN-C	234.76
FB-M	1070.68
FB-C	949.65

#### Hardness test:

The hardness means the mechanical resistance of a material setting against the mechanical penetration of a harder specimen [8]. Many measurements are performed according to standards ISO 868 or ASTM D 2240 [9]. Usually Shore A is used for plasticized PVC and other flexible plastic. Shore hardness D is used for harder materials; rigid PVC or rigid PVC foams [10]. There are different Shore hardness scales for measuring the hardness a wide variety of materials. Usually the Shore A is used for measuring foam samples, but in this case because the blend had higher stability and strength values the Shore D method was used [9].

*Table 5* Results of hardness test

Specimen number	Mean
FN	39,76
FB	55.05

CPE had not only increased the density values but the hardness of the foam as well, which is shown in *Table 5*. To make the result comparable the hardness tests were performed using Shore D equipment for both samples.

## CONCLUSIONS

It is well known that the mechanical properties of polymer are closely related to their multiphase structure and morphology. Results indicate that the blend with CPE has better mechanical properties. According to the measurements, it can be concluded that the interface between PVC and CPE has a certain isotropic orientation. This behavior caused the foam blends higher cross directional toughness as it is shown at *Table 2*. It can be seen that with CPE, the tensile strength of the blend reached a maximum 18-20 MPa. In contrast the neat foam reached only about 7-18 MPa. Furthermore, the flexural test results show that the modulus and strength values in all cases were



# INTERNATIONAL SCIENTIFIC CONFERENCE ON ADVANCES IN MECHANICAL ENGINEERING

12-14 October 2017, Debrecen, Hungary



higher (machine and cross direction). Finally, CPE affected the strength values, also because it greatly modified the cellular structure of the foam generated from the blended polymer.

## REFERENCES

- [1] Maksimov, R. D., Ivanova, T., Zicans, J.: *Thermal and elastic properties of poly(vinyl chloride) (PVC)+ Chlorinated polyethylene (CPE) blends*. Springer-Verlag, 2003.
- [2] Jamel, M. M., Khoshnoud, P., Gunashekar, S., Abu- Zahra, N.: *Enhancement of Dimensional Stability of rigid foams using E-Glass Fibers*. Journal of Minerals and Materials Characterization and Engineering, Vol.3, 2015.
- [3] Titow, W. V.: *PVC Technology*. Fourth Edition, England, 86-103., 1984.
- [4] Gendron, R.: *Thermoplastic foam processing*. 76-79., 2005.
- [5] Wypych G.: *PVC Degradation & Stabilization*. 3rd Edition, Toronto, 186-198., 2015.
- [6] Reddy, C. V., Ramnarayanan, R., Babu, P. R.: *A study on effect of filler (SiO<sub>2</sub>) on mechanical properties of Glass/Epoxy (HT cure) composite*. International Journal of Research in Engineering and Technology
- [7] International Organization for Standardization: [www.iso.org/standard/45091.html](http://www.iso.org/standard/45091.html) (2017.10.08)
- [8] Dr. Tisza M.: *Anyagvizsgálat*. University of Miskolc, 81-105., 2010.
- [9] Miner Elastomer Products Corporation: <https://minerelastomer.com/technical-data/tecspak-features/shore-shore-d-comparison/>
- [10] Matweb: <http://www.matweb.com/reference/shore-hardness.aspx>



## DESIGNING OF A WATER SAMPLING UNIT

<sup>1</sup>RÓNAI László, <sup>2</sup>FÜVESI Viktor PhD, <sup>2</sup>VÖRÖS Csaba

<sup>1</sup>Robert Bosch Department of Mechatronics, University of Miskolc  
E-mail: [ronai.laszlo@uni-miskolc.hu](mailto:ronai.laszlo@uni-miskolc.hu)

<sup>2</sup>Research Institute of Applied Earth Sciences, University of Miskolc  
E-mail: [fuvesi@afki.hu](mailto:fuvesi@afki.hu), [voros@afki.hu](mailto:voros@afki.hu)

### Abstract

*This paper is dealt with the design of a water sampling unit, which will be used for the H2020 Unexmin project to explore abandoned and flooded mines in Europe. The three dimensional modeling of the sampler unit is investigated. Furthermore the assembling and controlling elements are described. Valco dead-end flowpath selector valve for high pressure is used to distribute the samples among the tanks. A Maxon drive system with controller was built in to drive the valve. Unique controller board is designed to handle the whole communication of the center system and control the unit.*

**Keywords:** water sampler, valve, BLDC motor, flooded mines

### 1. INTRODUCTION

A water sampling unit (WSU) is necessary to determine that the flooded mines are consist productive zones or not. The WSU is used for the project called Unexmin [1]. The sampler unit will be built in a spherical shaped autonomous robot, which called UX-1. The diameter of the hull is 600 mm. The robot can dive 500 m deep to map the mine and collect information about the valuable minerals. The UX-1 besides the sampler unit will contains sensors and actuators, e.g., pH sensor, thrusters, multispectral camera.

Several water sampling units have been designed since in the middle 1900s [2]-[6]. The main field for these units was the oceanography [2]-[4]. A 128 channel water sampling system was developed by Kei Okamura et al. to collect samples from hydrothermal areas [3]. Four piezoelectric pumps were used to store the incoming samples. The sampling units of the oceanography usually handle high pressures. The review process of some available papers are important to create an adequate sampling unit for purposes of mapping flooded mines.

The sampling unit can take 16 independent samples between 1-60 bar. A Valco [7] made special valve handles the distribution of the samples. The flowpath selector was designed to use it high pressures. The rated pressure of the valve is 345 bar at 75 °C. The body of the selector valve is made from Nitronic 60. The tank unit is made from polyoxymethylene to avoid dissolutions. Each tank can store up to 7 cm<sup>3</sup> mine water due to laboratory measurements. The air inlet option was created for the process of backward sampling to renew the samples. The pressurized air will push the adequate piston to flush the sampled water to laboratory analysis. The block scheme of the unit is shown in Figure 1.

A Maxon type BLDC motor [8] with an encoder and a ceramic version of planetary gearhead can produce more than 4 Nm torque, which is enough to rotate the rotor of the valve. EPOS4 position controller [8] is suitable for control the motor.

The larger particles from mine water could damage the valve and the seal systems. Therefore a 15 micron filter is used to prepare the incoming water.

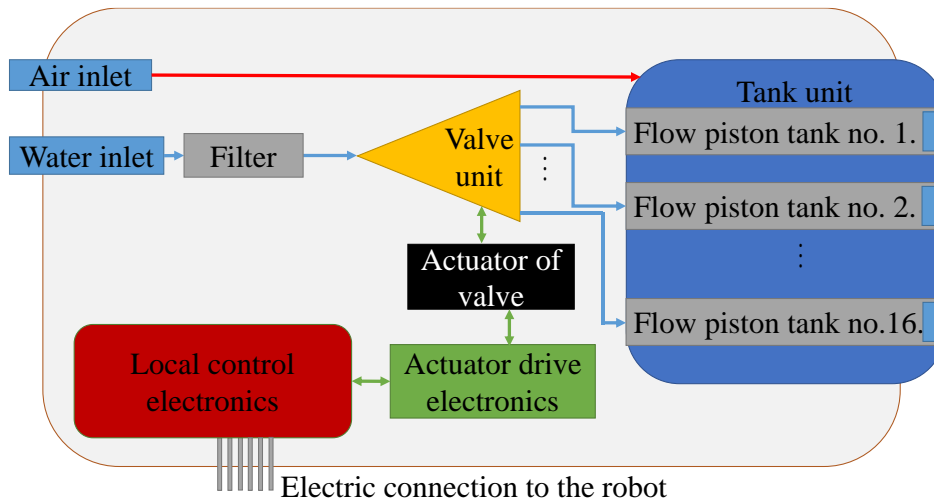


Figure 1 The block scheme of the water sampling unit

The supervision and control of the communication is achieved by a unique control board. The board contains a PIC microcontroller, which is able to communicate with the UX-1 via RS-485. The central unit of the UX-1 will send the instructions to the sampling unit. The required power of the unit is 12 V, which will be produced by the UX-1.

The modeling of the sampling unit is discussed in Section 2. The assembling and testing steps are given in Section 3.

## 2. MODELING OF THE WATER SAMPLER UNIT

The first step was to determine the required elements of the sampling unit, e.g., electronics, valve, storage, etc. The available space for the WSU in the UX-1 is very small. Thus the active sample collection method was cancelled, the more straightforward pressure difference method was applied. The readymade 3D model of the system is shown in Figure 2.

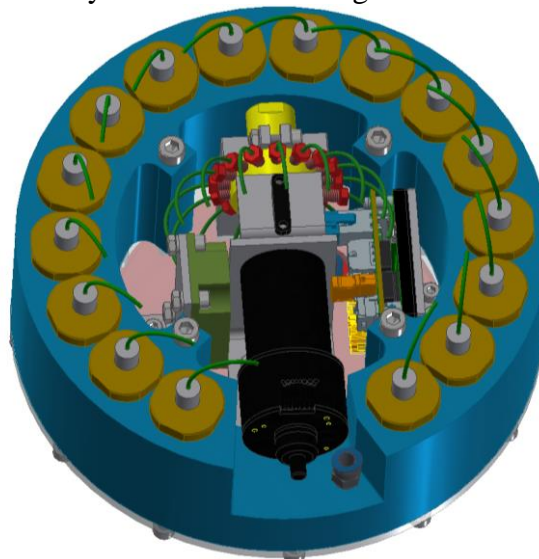


Figure 2 The 3D model of the WSU

The whole designing process was made in Inventor 2016 CAD system. Several unique elements



were designed. A mounting module was created on the UX-1 for installation of the WSU. The mounting unit will be welded into the outer spherical frame of the UX-1. PEEK tubes and connectors were chosen to connect the elements to each other. The half section of the unit is shown in Figure 3. The element consists connectors for the water and the air.

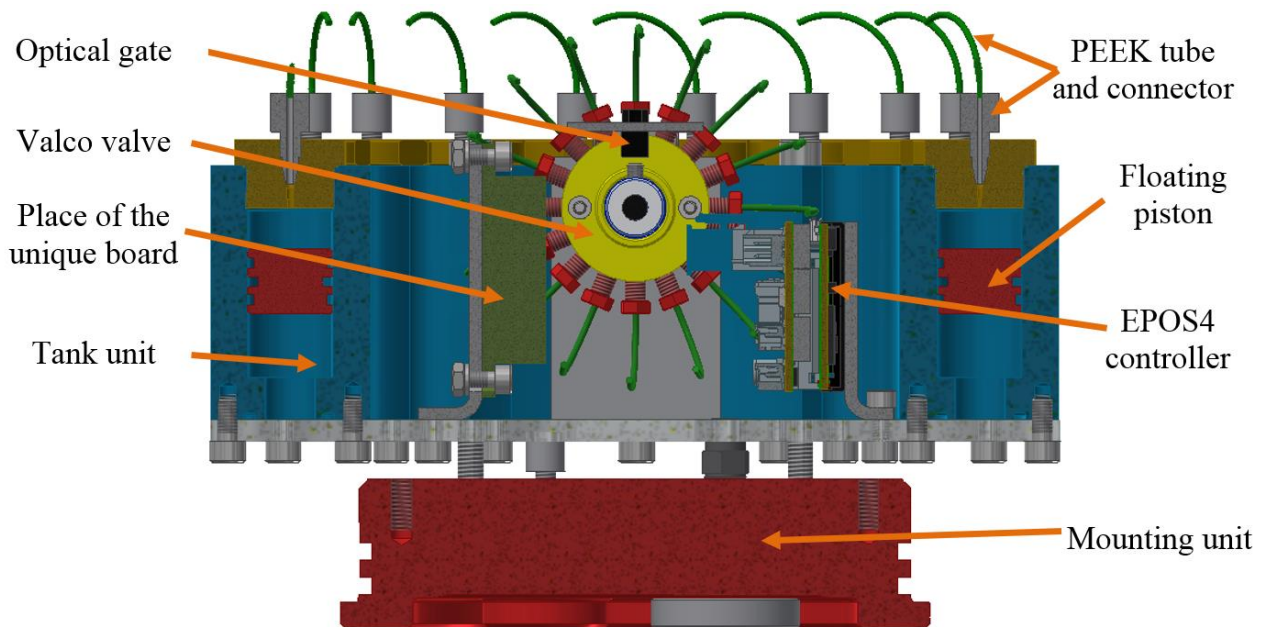


Figure 3 The half section of the sampler

The dimensions of the piston are shown in Figure 4. Professional sealing system was used to close the samples into the tank. The height of the WSU is 126 mm (with the mounting unit). The diameter is  $\varnothing 200$  mm.

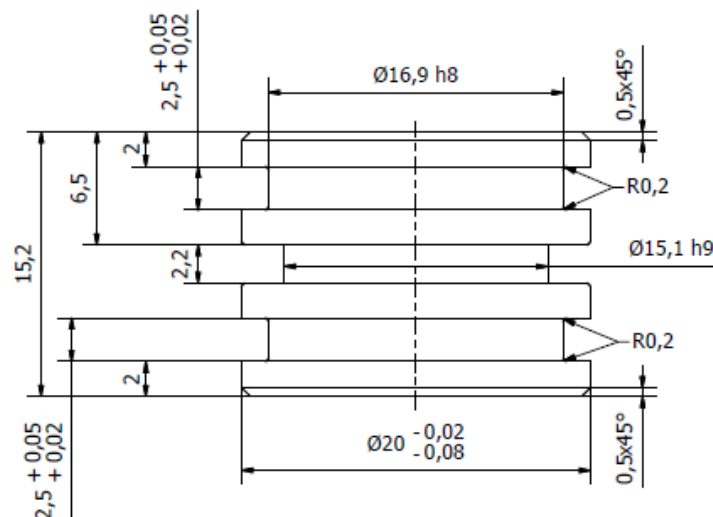


Figure 4 The dimensions of the flow piston

The sampling method contains four main steps. First of all the reference point of the motor is searched. An optical gate is used to sense the reference point. Thereafter the rotor of the valve is rotated to an intermediate position. The UX-1 is sending a sampling command, when a productive zone can be found. Therefore the rotor is rotated to the first sampling position. When the first tank is filled, the rotor of the valve is moved to an intermediate position. From this point the process is



repeated until free space is available. The sampling time was determined in different pressures during the testing method. The unique controller board control the sampling depending the actual pressure.

The model of the UX-1, with the WSU is shown in Figure 5. The hull of the unit is moved to the left to show the water sampler unit in a built in state.

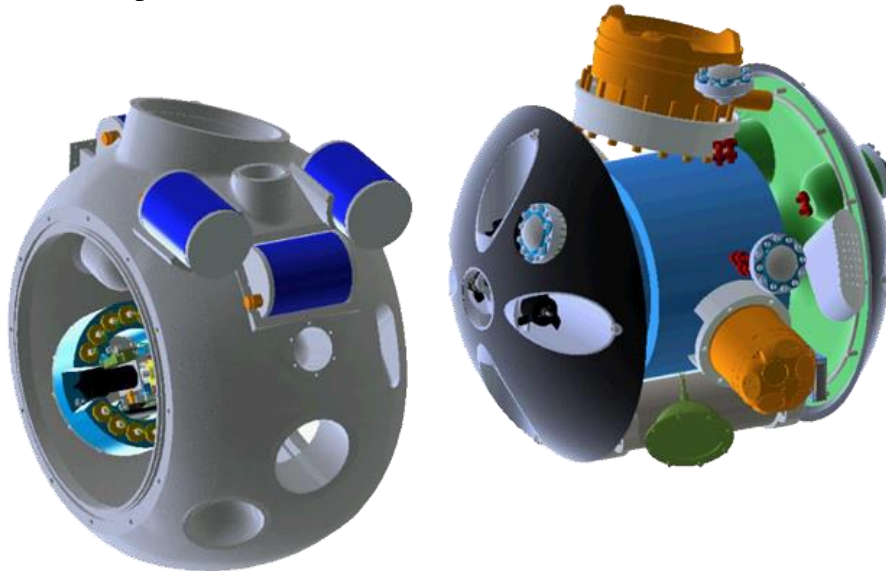


*Figure 5* The model of the UX-1 autonomous robot

### 3. ASSEMBLING AND TESTING

The assembled WSU is shown in Figure 6. The motor and the valve rotor is connected via a small coupling. The blue pipe is needed for the air flow to do the backward sampling.

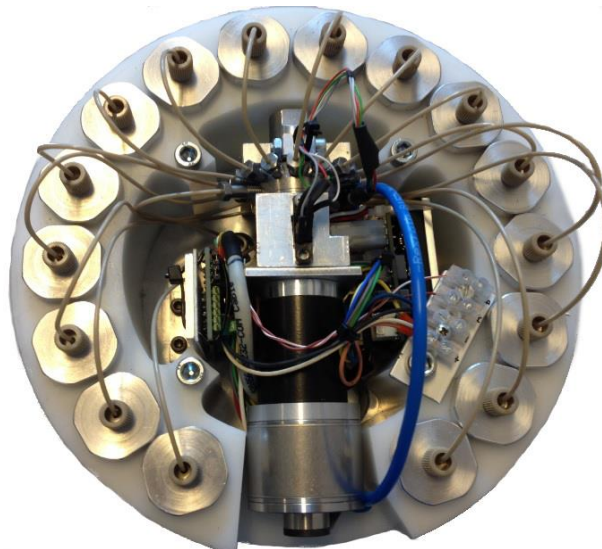


*Figure 6* The readymade WSU

Laboratory tests were performed to measure the sampling time at different pressure values. The block scheme of the measuring method is shown in Figure 7.

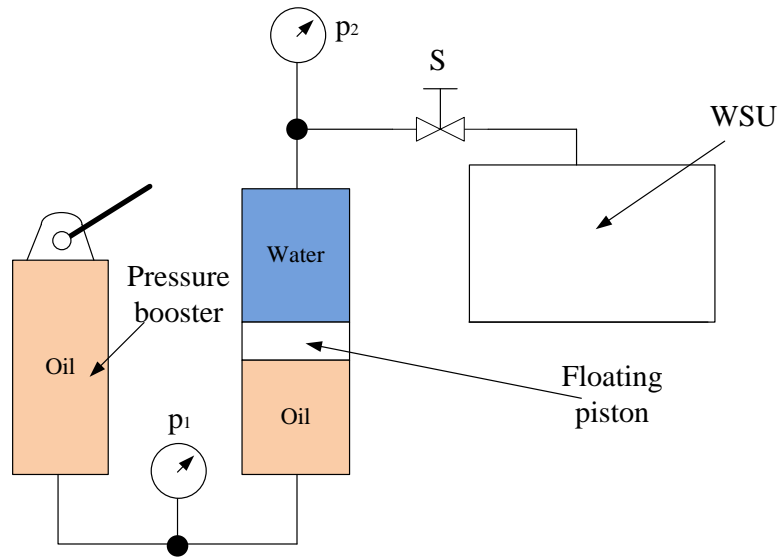


Figure 7 The block scheme of the test

The  $p_1$  and  $p_2$  manometers are indicating the current pressure level. The  $S$  is a ball valve. The pressure can be freely adjusted up to 60 bar. The required pressure range of the project is simulated. The seven main steps of the testing process are the following:

1. Set up the expected pressure via the pressure booster
2. Slowly open the ball valve
3. Using a timer to determine the filling time
4. Pumping the pressure booster to keep the pressure
5. When the filling process is completed, stop the timer
6. Closing the ball valve
7. Setting up the next pressure value

During the measurement at most  $7 \text{ cm}^3$  samples were taken. Every measurement was repeated to get more accurate time of the sampling process. The diagram of the measured sampling times is shown in Figure 8. A total of five measurements were performed.

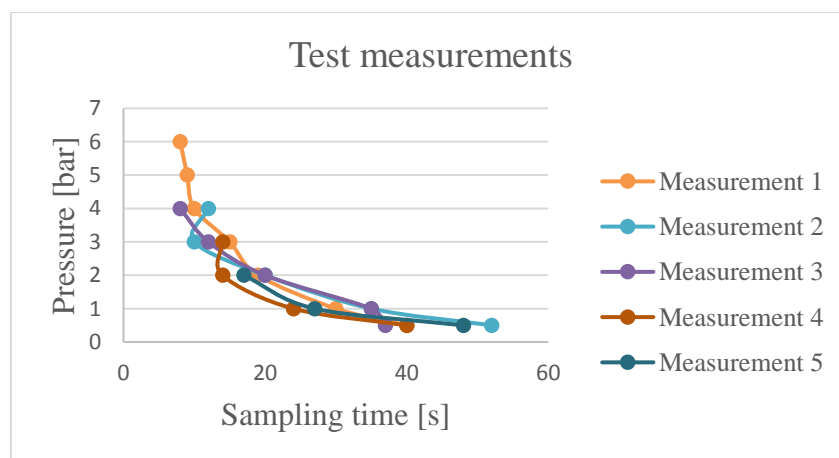


Figure 8 The measurement result in the function of the sampling time

After evaluating the results. The results are shown in Table 1.



Table 1 The results of the filling time test

Pressure [bar]	Average filling time [s]
0,5	43
1	30
2	18
3	13
4	10
5	9
6	8
Above 7	5

## CONCLUSIONS

A water sampling system has been designed and manufactured to take samples from abandoned flooded mines. Inventor software was used to create the model and the drawings of the unit. New elements have been made for the WSU. The whole system is very small, due to the available free space of the UX-1.

Some of the WSU elements were designed and manufactured individually, and some commercial parts were purchased and used, e.g., EPOS 4 position controller, valve unit and Maxon motor. After these processes the unit was assembled in laboratory conditions.

The laboratory and the field tests of the WSU were successfully completed. Therefore the applicability of the designed system is no doubt.

## ACKNOWLEDGEMENT

The UNEXMIN project has received funding from the European Union's Horizon 2020 Research and Innovation programme, under the Grant Agreement number 690008.

## REFERENCES

- [1] Unexmin project: <http://www.unexmin.eu/>
- [2] Breier, J.A., Gomez-Ibanez, D., Reddington, E., Huber, J.A., Emerson, D.: *A precision multi-sampler for deep-sea hydrothermal microbial mat studies*. Deep Sea Research. I, 83–90., 2012.
- [3] Okamura, K., Noguchi, T., Hatta, M., Sunamura, M., Suzue, T., Kimoto, H., Fukuba, T., Fujii, T.: *Development of a 128-channel multi-water-sampling system for underwater platforms and its application to chemical and biological monitoring*. Methods in Oceanography, 75-90., 2013.
- [4] Dodd, P. A., Price, M. R., Heywood, K. J., Pebody, M.: *Collection of Water Samples from an Autonomous Underwater Vehicle for Tracer Analysis*. Journal of Atmospheric and Oceanic Technology, Vol. 23, 1759-1767., 2006.
- [5] Ore, J.-P., Elbaum, S., Burgin, A., Zhao, B., Detweiler, C.: *Autonomous Aerial Water Sampling*.
- [6] Dhull, S., Canelon, D., Kottas, A., Dancs, J., Carlson, A., Papanikolopoulos, N.: *Aquapod: A Small Amphibious Robot with Sampling Capabilities*. Intelligent Robots and Systems (IROS), DOI: 10.1109/IROS.2012.6385733, 2012.
- [7] Valve, V.: *Valco Cheminert catalog*. 2005.
- [8] Maxon online catalog: <https://www.maxonmotor.com/maxon/view/catalog/>



## RESIDUAL STRESS MONITORING FOR MACHINE INDUSTRY

*SEPSI Máté, ANGEL Dávid, CSEH Dávid, BENKE Márton PhD, MERTINGER Valéria PhD*

*Institute of Physical Metallurgy, Metalforming and Nanotechnology, University of Miskolc  
E-mail: [femsepsi@uni-miskolc.hu](mailto:femsepsi@uni-miskolc.hu)*

### Abstract

*Determination of the residual stress state is highly important because it has a strong effect on the lifetime of the component and it can cause deformation or failure during the manufacturing. Nowadays, the residual stress characterization became an everyday requirement in the machine industry. Several methods exist for measuring the residual stress, with this paper our purpose is to introduce the non-destructive residual stress measuring by XRD, and show quantitative characterization and results from the machine industry. Two examples are presented about the stress monitoring during the manufacturing, while one is during fatigue test.*

**Keywords:** *Residual stress, Non-destructive measurement, XRD, Fatigue*

### 1. INTRODUCTION

Forasmuch as every producing process (casting, heat treating, different kinds of metal deformation processes and surface compressing methods, etc.) influences the residual stress state, therefore it can be very complex and various within the materials [1,2]. If we conscious in the effect of these processes it is possible to reach such a state in the material which can enhance its lifetime and quality, and with an optimized process, the costs could be reduced [3-5]. In this manuscript a series of residual stress measurements using X-ray diffraction were performed with different purposes. One example shows the importance of the residual stress evaluation during the whole process line the other example shows the evidence about the relationship between the stress state and the manufacturing scrap.

### 2. METHODS

Lattice spacing in crystalline materials can be determined by X-ray diffraction analysis. The fundamental equation of X-ray diffraction analysis is Bragg's law, which describes the interrelation between the interplanar distance  $d$ , the incident angle  $\theta$  (angle between the incident beam and the diffracting lattice plane), the wave length  $\lambda$  of the X-ray used and the order number  $n$  of the diffraction.

$$n \lambda = 2d \sin\theta \quad (1)$$

If stress is present, this interplanar distance becomes larger (tensile stress) or smaller (compressive stress). Assuming linear elastic distortions, the related normal stresses can be calculated:

$$\sigma = \frac{d_{\psi} - d_0}{d_0} \frac{E}{(1+\nu) \sin^2 \Psi} \quad (2)$$

where  $d_0$  and  $d_{\psi}$  are the interplanar distances of the strained material in the normal and in the tilted position defined by the angle  $\psi$  respectively.  $E$  (Young modulus) and  $\nu$  (Poisson number) are the elastic parameters of the material. The present manuscript gives an overview on the measurement possibilities by an innovative equipment of the Institute of Physical Metallurgy, Metalforming and



Nanotechnology at the University of Miskolc. The equipment is a Stresstech Xstress 3000 G3R type X-ray diffractometer developed especially for non-destructive residual stress measurements. The presented diffractometer has a remarkable innovation compared to the traditional ones. In the case of traditional diffractometers the sample is tilted by precision mechanics. The revolutionary construction of the G3R tilts the device instead of the specimen, which allows measurements without sample cutting, so the true stress state of the component is unaffected. Furthermore, there are no sample size and weight limits for the measurements [6]. This method provides residual stress values from 10  $\mu\text{m}$  depth of the surface layer (depending on material type, applied generator power, Bragg-angle). A Cr radiation was used to measure the {211} reflections of the samples. For stress calculations, the following material constants were used: Poisson's ratio  $\nu = 0.3$ , Young's modulus  $E = 211000 \text{ MPa}$ . The measured parameters (the investigated variables) such as maximum tilting angle, the number of tilting and spot size (the diameter of the beam on the examined surface) were changed during the test. The exposure time was chosen based on the requirement of proper signal/background ratio, so it was changing, and it is given at the presence of results chapter.

### 3. RESULTS AND CONCLUSIONS

The reproducibility of the XRD measurement is shown in Fig.1. The measurements were done 10 times on the shot peened surface of a steel component, without changing the parameters or the position of the sample. We can state that the value of standard deviation is excellent.

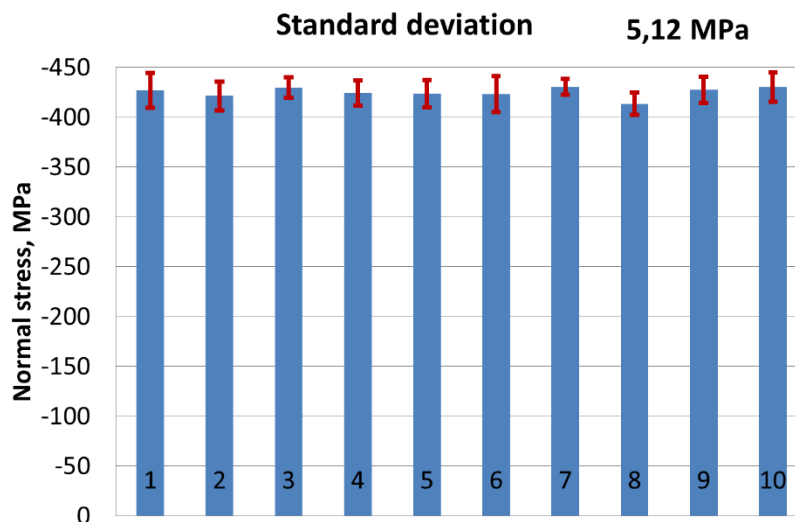


Figure 1 Reproducibility of the stress measurements on the shot peened steel surface

#### *Stress monitoring during the process*

The examined bearing rings were made of 100CrMn6 alloy according to the EN ISO 683-17 standard. The outer and the inner rings were evolved from a common semi-product. The first step of the process was hot forging at 1190°C. The next step was the turning. This was followed by the severing and the separation of the inner and outer rings. After severing, the rings were hardened at 835°C for 40 minutes then cooled in a 190 °C salt bath and a subsequent tempering at 200°C for 25 minutes was done. Finally, the hardened rings were finish-grinded. The stress states were measured after the hot forging (1. process), the turning of outer ring (2. process), severing (3. process) and heat treatment (4. process). The tangential residual stresses were measured at 12 positions (labelled from 0 to 11) on the middle perimeter of outer rings. The locations of the 12 measured positions were the same after each technological step. Data were recorded in 5 tilting positions in  $\Omega$  mode in



the  $-35^{\circ}$  to  $35^{\circ}$  interval with 10 sec exposure time and 1 mm spot size. The state of the rings after the different process steps, the measured position and the results are shown in Fig. 2. Scatter of the measurements never exceeded  $\pm 20$  MPa, therefore they are not marked. The measured residual stress values of the rings after the 1st processing step is compressive. Due to turning (2. process), the compressive stresses of the ring changed to intensive tensile stresses. The severing (3. process) did not make any detectable changes in the stress state, while the heat treatment (4. process) induced a near stress-free, relaxed condition. It is evident that the stress values of the rings vary between 600 and -200 MPa during the processing line. Even the final stress state is quite convenient if the distortion or microcrack have formed after turning due to the high tension stress those are unchanged and still exist after the heat treatment. So it is a typical example that the stress state control at the final state is not sufficient to detect the reason of failure of a component.



Figure 2 Stress distribution of the bearing rings after different process steps.

In case of other example residual stress measurements were carried out during the finishing manufacturing technology steps (hardening, grinding, shot peening) of spiral bevel gears to see through the evolution of the residual stress during the full manufacturing. The examined component is prone to fracture during straightening after the hardening heat treatment. The aim of the stress monitoring is to find out the role of residual stress in the component's failure. The measurements were performed using 3 tilting positions in both  $\pm$  directions. The measurements were carried out on two components, having the same history of production. One of the components had eccentricity values within the tolerances of the manufacturer (labelled as "good" component), while the other one had eccentricity outside the tolerances (labelled as "bad" component). The measurement locations were determined at two spots critical from the aspect of the component, on the six tooth tops and on the axle part, where occasional fracture typically occurred. The measurements were carried out in two different measurement directions (axial, tangential) in each point as shown in Fig. 3.



Based on the stress measurement results, there is no difference between the "good" and "bad" components tooth tops neither in axial nor in tangential directions. On both components, the stress distribution is uniform and the stress values are similar. In forged state, the measured stresses are compressive, which turned into tensile after machining. After hardening, the stress state changes in general. Grinding had no major effect on the tooth top and the shot peening step increased the already existing compressive stresses, as it was expected. The stress evolution during the full manufacturing changes between 600MPa and -500MPa as it is shown in Fig.3. The measured stresses on the axle indicate that there is a difference between the stress values of the "good" and "bad" components. The stress distribution is irregular in both components. The stresses are compressive in nature after the various technology steps. The values change between 0MPa and -700MPa. So the stress asymmetry was calculated. From the aspect of bending, the critical stress component is the axial stress of the axles. Thus, stress asymmetry was calculated only in the axial direction. The stress asymmetry results are shown in the Fig.4. Since stress state prior to hardening is relaxed at the austenization temperature, stress asymmetry was calculated only for technology steps after hardening. After hardening, the maximal value of stress asymmetry of the "bad" component is about 200 MPa, while that of the "good" component barely reaches 100 MPa. It is important to note that the maximal stress asymmetry occurs in the plane of measurement points 5 and 11. In grinded state, the plane of the maximal stress asymmetry is still the plane of the points of 5 and 11, The plane of the high stress asymmetry matches with the plane of measured highest eccentricity. Thus, stress asymmetry is proven to be suitable to characterise the component's bending stress.

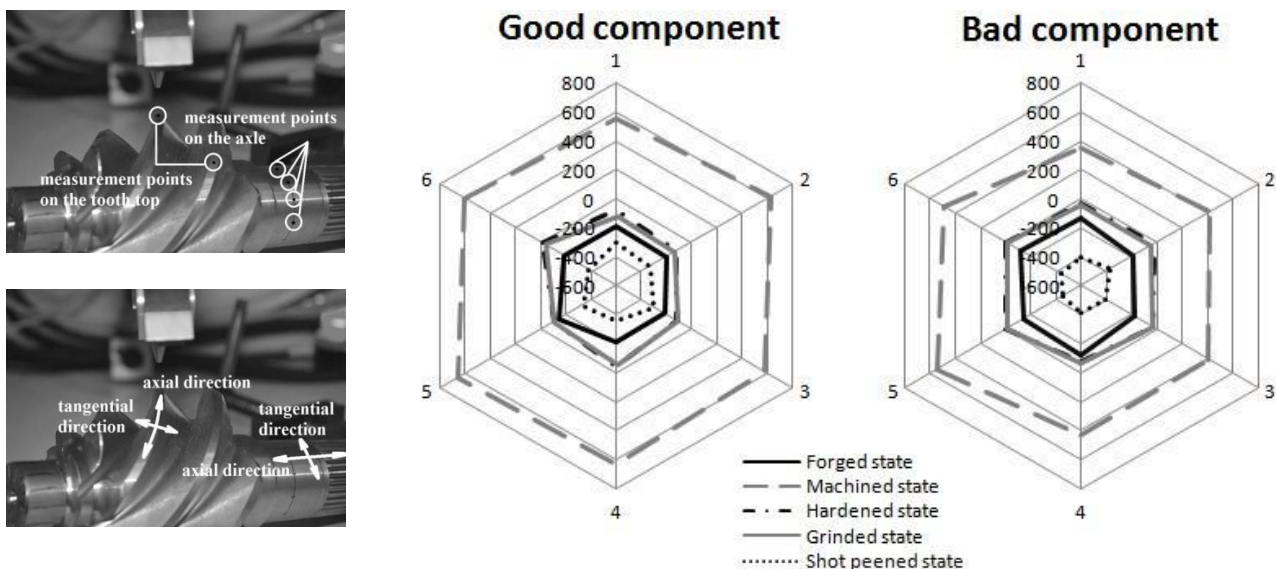


Figure 3 The measured points and directions and the variation of stress distribution on the tooth tops after the examined technology steps. Axial stress components

### Stress monitoring during fatigue

The stability of surface compressive residual stress on hardened, shot peened 42CrMo4 steel specimens during fatigue load was investigated. This is a widely used steel in the vehicle industry especially in the case of surface compressed machined elements. The residual stress state of machine elements can change during application, therefore it is necessary to describe how these changes are related to the operational parameters. The residual stress state was recorded in shot peened state and monitored during the fatigue tests. The fatigue test was stopped after certain cycles until the specimens fractured. The stress state was measured after each fatigue test stops and the



stress relaxation is given in the percentage of the initial stress state in function of cycle number. The specimens were induction hardened and oil quenched. To measure the temperature of the specimens and to control the inducer, Ni-NiCr thermocouple was soldered to the surface. First, the specimens were rapidly heated to 1000°C during a few seconds then the temperature was held for 2 seconds. When the sample reached 850°C, the thermocouple was cut from the specimens and the specimens were immersed in quenching oil media. During the immersion the longitudinal axis was perpendicular to the surface of the media. The tempering was carried out at 600°C in an inductive furnace for half an hour, and specimens were subsequently cooled in air. The shot peening was performed at the Rába Automotive Holding Plc. This means that the parameters of the applied peening method were industrial parameters. The peening time was 9 minutes. Two Almen C strips were fixed on the sample holders to control the peening. The values of the Almen C probes were 0.26 and 0.24. The used peening balls were made of 1.8 mm diameter steel wire (430 HV), cut in 1.8 mm length pieces and conditioned for 4 hours. The minimal peening coverage was 150%. The average speed of the balls, which left the peening wheels was 55 m/s. As an average 117 J/mm<sup>2</sup> energy was imparted with the surface.

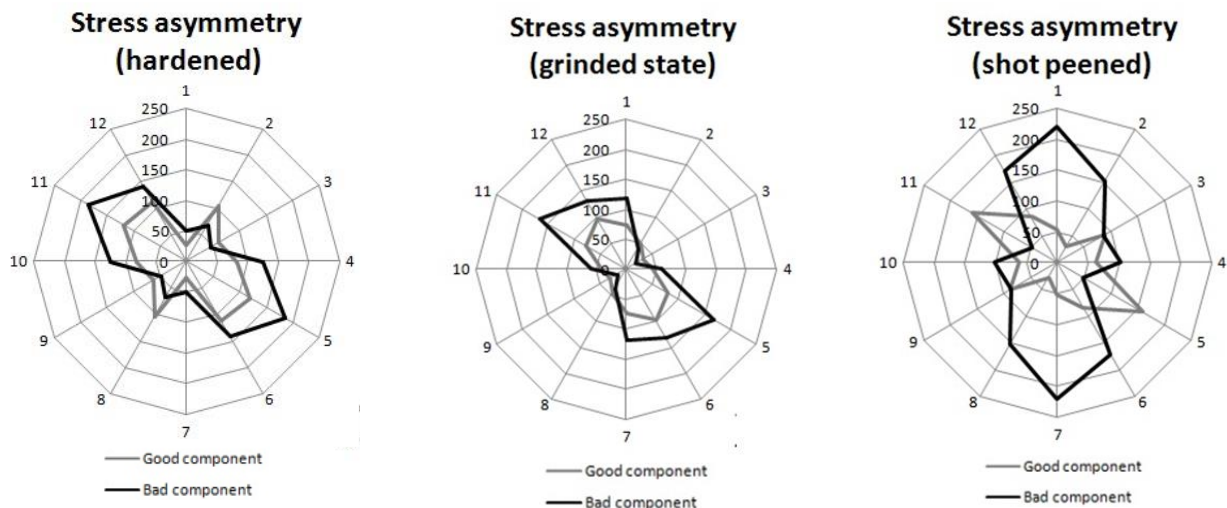


Figure 4 Stress asymmetry calculated after the different technological steps along the critical circumference of the axle. Axial stress component.

The residual stress was calculated according to the  $\sin 2\psi$  method. Reflections were obtained in  $\psi$  geometry from 3 tilting positions in the  $-45^\circ/+45^\circ$  range. The axial residual stress state was recorded at 3 spots with 3 mm spot size areas, on each side of each specimen in the initial shot peened state and during the fatigue loads. The same areas were investigated in each step of the monitoring. The sample geometry was quadratic (7x7 or 5x5). The stress was measured with less error (scatter) than  $\pm 10$  MPa in every point. The fatigue load was tensile-compressive, the stress ratio ( $R\sigma$ ) was -1 ( $R\sigma = \sigma_{\min}/\sigma_{\max}$ ;  $\sigma_{\max} = 350; 500$  MPa); so the absolute values of the tensile and compressive stresses were equal. The cyclic load was implemented by an MTS type universal electro-hydraulic testing machine of the Institute of Materials Science and Technology at the University of Miskolc. The Fig. 5 shows the results. The sample marked with H was only hardened, so the enhanced lifetime due to the shoot peening is evident. The significance of the fatigue stress amplitude is multiple: the higher stress level results shorter lifetime, and higher extent of residual stress relaxation. No systematic effect is connected to the sample size. The stress relaxation rate shows an increased level by increasing the fatigue stress amplitude. It is evident that the rate of the stress relaxation is very fast in the first thousand of the cycles.

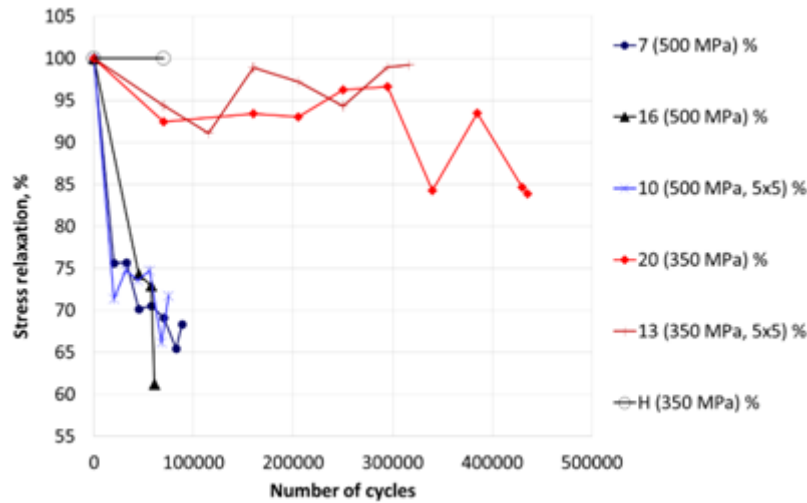


Figure 5 Compressive stress relaxation during fatigue at 500 and 350 MPa stress level.

## SUMMARY

Monitoring the residual stress evaluation of a spiral bevel gear and bearing rings during manufacturing were performed. The stress varied in a very wide range even from -100 MPa compression to the 600 MPa tension between the different manufacturing steps. It was experimentally shown that the high stress asymmetry matches with the plane of measured highest eccentricity. Thus, stress asymmetry is proven to be suitable to characterise the component's bending stress. Compressive stress relaxation after shot peening was also investigated during fatigue. It was stated that the higher fatigue stress amplitude indicates larger extent of residual stress relaxation. The absolute value of the initial residual stress state does not have systematic effect during the relaxation. The higher relaxation has no correlation with the value of the initial residual stress.

## ACKNOWLEDGEMENT

This research work was supported through the New National Excellence Program of the Ministry of Human Capacities.

## REFERENCES

- [1] García Navasa, V, Gonzaloa, O, Quintanaa, I, Pirling T: *Residual stresses and structural changes generated at different steps of the manufacturing of gears: Effect of banded structures*, Materials Science and Engineering, A 528, .5146-5157, 2011
- [2] Kim, J.C., Cheong, S.K, Nog, H.: *Residual stress relaxation and low- and high-cycle fatigue behavior of shot-peened medium-carbon steel*, International Journal of Fatigue, 114-122,2013.
- [3] Dalacia, K., Karlssona, B, Svenssona, L.E.:*Stability of shot peening induced residual stresses and their influence on fatigue lifetime*, Mat. Science and Engineering A, 1008-1015, 2010.
- [4] Cseh, D., Mertinger, V., Lukács, J.: *Residual Stress Evolution During Fatigue Test of a Shot Peened Steel Sample*. Materials Science Forum Vol. 752. 95-104., 2013
- [5] Angel, D., Benke, M., Cseh, Dávid., Mertinger, V.: *Residual stress evolution during the production of an automotive component*. MultiScience XXIX microCAD International Multidisciplinary Scientific Conference, proceedings, 2015
- [6] Sepsí; M, Cseh, D.,Filep,Á., Benke, M., Mertinger, V.: *Innovation Methods for Residual Stress Determination for the Automotive Industry*, Lecture notes in mech. eng.F12, 483-499., 2017



## INVESTIGATION OF THE TRIBOLOGICAL PERFORMANCE OF WEAR RESISTANT SURFACE LAYERS PRODUCED ON AUTOMOTIVE TOOL STEEL BY DUPLEX HEAT TREATMENTS

*SIDDIQUI Shiraz Ahmed, MAROS B. Mária PhD, SZILAGYINÉ BÍRÓ Andrea*

*Institute of Materials Science and Technology, University of Miskolc*

*E-mail: [ahmedshiraz432@gmail.com](mailto:ahmedshiraz432@gmail.com), [maria.maros@uni-miskolc.hu](mailto:maria.maros@uni-miskolc.hu), [biro.andrea@uni-miskolc.hu](mailto:biro.andrea@uni-miskolc.hu)*

### **Abstract**

*Advances in thin film deposition techniques during the 20th century have enabled a wide range of technological areas. The presented research work involves on one hand, characterization of a duplex treated, i.e. plasma nitrided and PVD coated X42Cr13 tool steel with special emphasis on the tribological performance. On the other hand, it deals with the complex tribological characterization of the produced surface layer. PVD processes have a wide range of industrial applications involving aerospace, automotive, surgical/medical components, moulds and dies, semiconductors and cutting tools. These processes can be employed to deposit virtually any metal, alloy, refractory or inter-metallic compound materials on low temperature substrates with excellent bonding strength and ability of controlling the microstructure.*

*Therefore, it is a well established hypothesis based on our research that surface engineering including surface treatments (plasma nitriding technology) and PVD coatings is one of the most effective and flexible solutions for tribological problems. Coatings change the performance of the tribological systems by inducing residual compressive stresses, decreasing the friction coefficient, increasing the surface hardness, significantly modifying the surface chemistry or changing the surface roughness. So, they improve the wear resistance of surfaces and extend the lifetime of complex, relevant components. The major conclusion drawn can be stated that Duplex layers have a better tribological properties comparing to the surfaces being just nitrided (uncoated)*

**Keywords:** *duplex heat treatment, plasma nitriding, PVD coating, wear, scratch*

### **1. INTRODUCTION**

In tribological applications, using PVD coatings is an effective and innovative technology to reduce friction and protect the substrate surface from wear and corrosion. The wear and friction of the mechanical components have a significant economic impact. Wear is a phenomenon that occurs in frictional loading conditions, causing material loss, surface degradation of materials, decreases the lifetime of machining tools, increases risk of failures etc. The most critical parts of machine elements are their surfaces, in point of view of characteristic stresses or environmental reactions. However, the tribological response of a PVD coating system depends on many factors (coating properties, counterpart, substrate, interface and operational conditions). There has been recent advancements and growth in this field, several coating methods and new deposition techniques are being continuously developed, for instance PVD, CVD and PAVD (plasma assisted vapour deposition).

Duplex treatment can be any heat treatment method combining two or more different surface technologies to build a two- or multi layer composite surface structure on an arbitrary substrate material with the purpose of improving the loadability and durability of the component surface not



achievable by neither individual processes alone . Duplex treatments mean combining two different surface technologies to produce more suitable layer: coatings are very hard, but the hardness difference can occur problems, such as galling and bad adhesion; hardness of layers produced by surface modification technologies lower than the coating and thus wear properties are moderated. A combination of thermal surface treatment processes (hardening, remelting, alloying, cladding) with a thermochemical treatment (carburizing, nitriding, nitrocarburising, boriding) and/or hard coating (PVD, CVD) brings into account highly technically advantageous effects in relation to the material's mechanical, chemical and physical performance of the surface layer. The combination of these technologies means eliminating of limitations of each of them, thus and enhanced surface properties as shown in *Figure 1*.

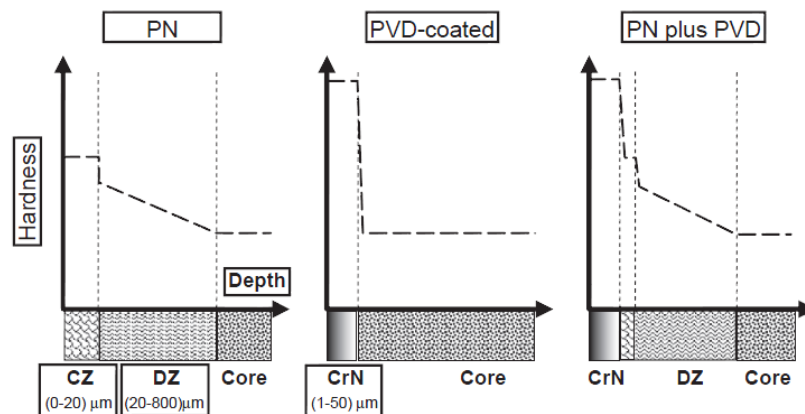


*Figure 1* Hardness versus distance from the surface for soft steels with a plasma nitriding treatment (PN), PVD coating, and combination nitriding plus PVD coating (CZ: compound zone, DZ: diffusion zone) *Hiba! A hivatkozási forrás nem található.*

The general objective of combined surface treatment technologies is to improve and modify the materials resistance to complex tribological loads, including,-

- Abrasive/adhesive wear in connection with high pressure intensity (typical for forming and cutting tools, as well as highly loaded automotive components)
- Adhesive/abrasive wear and contact fatigue (typical for automotive components, e.g., bearings, gear wheels, camshafts, crank shafts)
- Corrosion (components working in corrosive media, e.g., pumping elements).
- Increased hardness ,toughness, and fatigue strength

## 2. METHODS

Investigated Material:

The specimen is made of a high alloyed plastic mould tool steel DIN X42Cr13/W-Nr 1.2083. The tool steel grade 1.2083 has a high chromium content and is wear and corrosion resistant. The standard chemical composition is given in *Table 1*.

*Table 1* Standard chemical composition in weight%; EN ISO 4957:2001, DIN 17350 (1980)

C	Si	Mn	P	S	Cr
0.38-0.45	Max 1.0	Max 1.0	Max 0.030	Max 0.030	12-13.50

Step 1. Sample cutting from the steel rod- there is a big steel rod available from the manufacturer. This rod is bought and the sample of desired geometrical dimension is cut out from the entire rod.

Step 2. Bulk heat treatment of the base material



Precipitation hardening was applied on each sample. The characteristic time-temperature diagram of the treatment is shown in *Figure 2(a)*

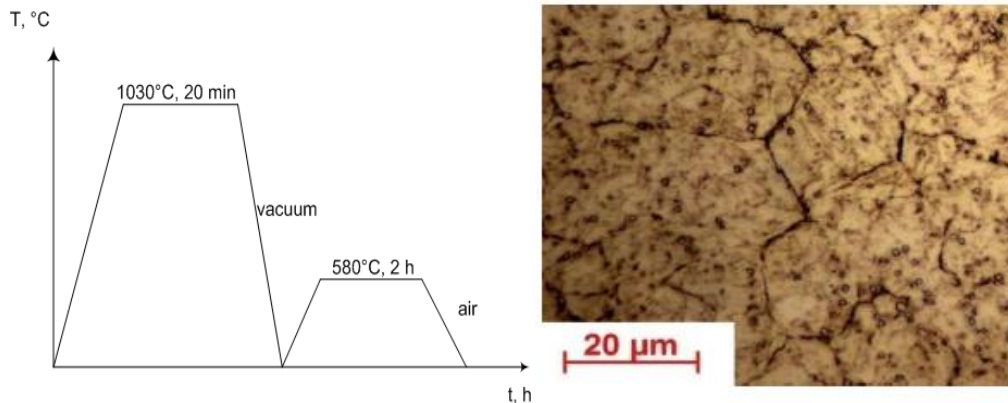


*Figure 2 (a)*\_Austenitization and Quenching + Precipitation Hardening and**(b)** Microstructure of base material (N=1000)

### Step 3. Grinding

Usual grinding operation was performed by the equipment of the Institute of Materials Science and Technology.

### Step 4. Nitriding

Nitriding procedure was done under the following conditions:

- Temperature of the process: 520°C
- Duration of the process: 8 hours;
- Pressure: 2 mbar = 200MPa;
- The Voltage: 600 V;
- Source of nitrogen: decomposed ammonia.

The applied thermochemical treatment resulted in a nitrided layer of the specimen. The obtained microstructure is illustrated by *Figure 3*

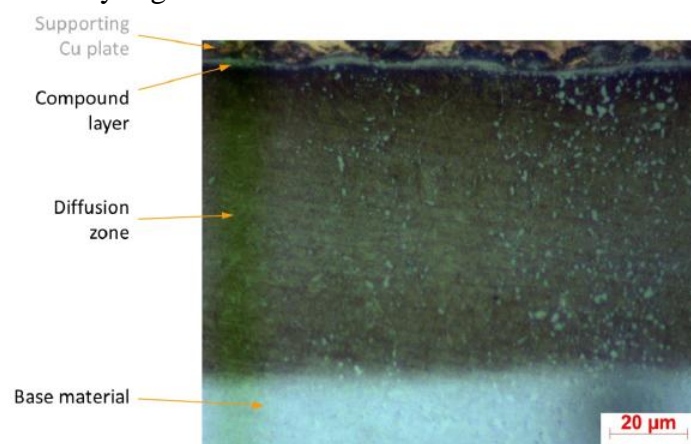


*Figure 3* Microstructure of the nitrided layer developed on the surface of the precipitation hardened tool steel

*Step 5.a): Surface preparation I.:* Grinding + Polishing (getting a polished surface of samples before PVD)

*Step 5.b): Surface preparation II.:* Grinding + Glass bead blasting (cleaning the surface before PVD)



### Step 6. PVD Coating

PVD coating were applied both on the differently nitrided and for comparison, on the non-nitrided samples. Coating material: Certess DDT (trade name), upper layer structure WC+a- C:HW+a-C:H; the coating thickness is about 3-4  $\mu\text{m}$ . This coating was prepared in Budapest by the manufacturing firm Techniques Surfaces, Hungary, i.e. TS Hungary (<http://www.tshungary.hu/>), subsidiary company of the HEF Group.

The following combination was prepared and in this work I shall demonstrate the most important hypothesis regarding effect of surface preparation prior to PVD.

Table 2 Experiment details

Probe number	Nitriding	Surface condition before PVD	PVD	Nomination	Color
P13	-	Polished	Yes	P+PVD	Magenta
P14	-	Glass Bead Blasted	Yes	GBB+PVD	Dark Green
P15	550°C, 8h	Polished	Yes	N(550°C)+P+PVD	Light Green
P16		Glass Bead Blasted	Yes	N(550°C)+GBB+PVD	Orange
P17		-	No	N(550°C)	Blue
P18	520°C, 8h	Glass Bead Blasted	Yes	N(520°C)+GBB+PVD	Cyan
P19		-	No	N(520°C)	Purple
P20		Polished	Yes	N(520°C)+P+PVD	Red

## 3. RESULTS

In order to characterize the adhesion between the PVD coating and the substrate (nitrided or un-nitrided) we used scratch testing method.

### Scratch Test ( Overall conclusion)

Comparison of the effect of surface preparation prior to PVD on the scratch behaviour of the samples nitrided at 520 °C.

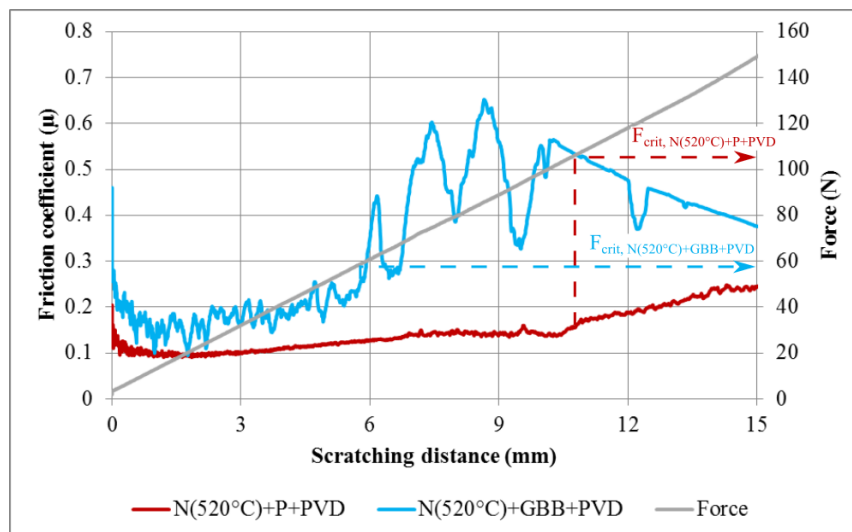


Figure 4 Comparison of friction coefficient curves obtained for nitrided(520 °C) samples having differently prepared surfaces below the PVD coating



The friction coefficient curve obtained for the P+PVD sample is much more uniform and smooth, than that of the GBB+PVD one. The value of the critical force in case of GBB+PVD specimen is lower compared to the P+PVD specimen. The sample which has a glass bead blasted surface prior to PVD coating shows higher friction coefficient values along the whole scratching distance and the curve contains several peaks referring to sharp surface irregularities

It can be stated based on the above results: polished specimen has a lower/better value of coefficient of friction and higher/better critical force than that of glass bead blasted specimen; hence polishing gives improved surface properties by giving smoothness to the surface.

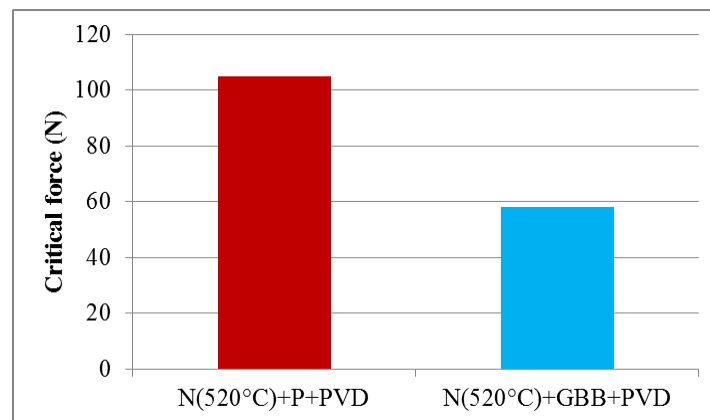


Figure 5 Comparison of critical forces obtained during scratching of nitrided (520 °C) samples having differently prepared surfaces below the PVD layer

#### Ball on disk Test

This test is performed to carry out wear testing of the specimen. The ball-on-disc tests were accomplished using the following test parameters

- ZrO<sub>2</sub> ball;
- F=60 N and 120 N;
- t=60 min;
- v=50 mm/s

During evaluating the friction behaviour of the tested samples –as it was the case during analysing the scratching behaviour – the friction coefficient curves will be presented and evaluated in a purposefully ordered way, i.e. the influence of the following factors on the wear behaviour in case of normal loads of F=60 and 120 N will be analysed:

Effect of different surface preparation prior to PVD on the wear behaviour of the coated samples having a substrate nitrided at 520 °C ( $F_N=60$  N)

Friction coefficient curve obtained for the glass bead blasted N(520 °C)+GBB+PVD sample has the most smooth and continuous curve with no significant variation in magnitude, representing the lowest friction coefficient values of  $\mu \sim 0.1$ . The reason behind is justified by the unique surface characteristics obtained after the process of glass bead blasting, which has been carried out on the specimen prior to applying the DLC layer by the PVD process.

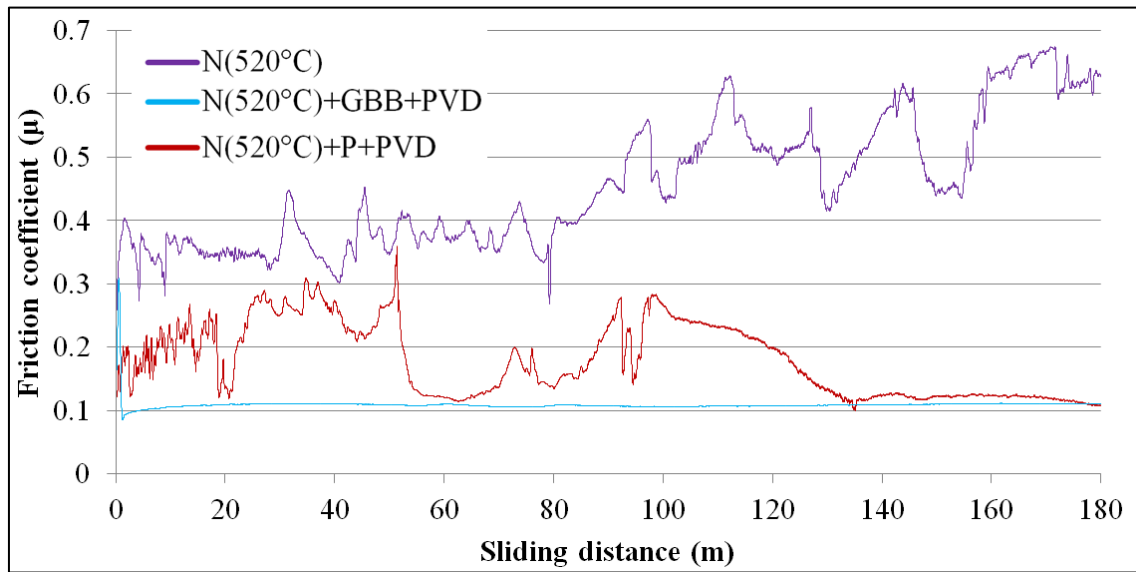


Figure 6 Comparison of friction coefficient curves obtained for samples having nitrided ( $T= 520$  °C) substrates and differently prepared surfaces below the PVD coating ( $F_N= 60$  N)

Effect of different surface preparation prior to PVD on the wear behaviour of the coated samples having a substrate nitrided at 520 °C ( $F_N=120$  N)

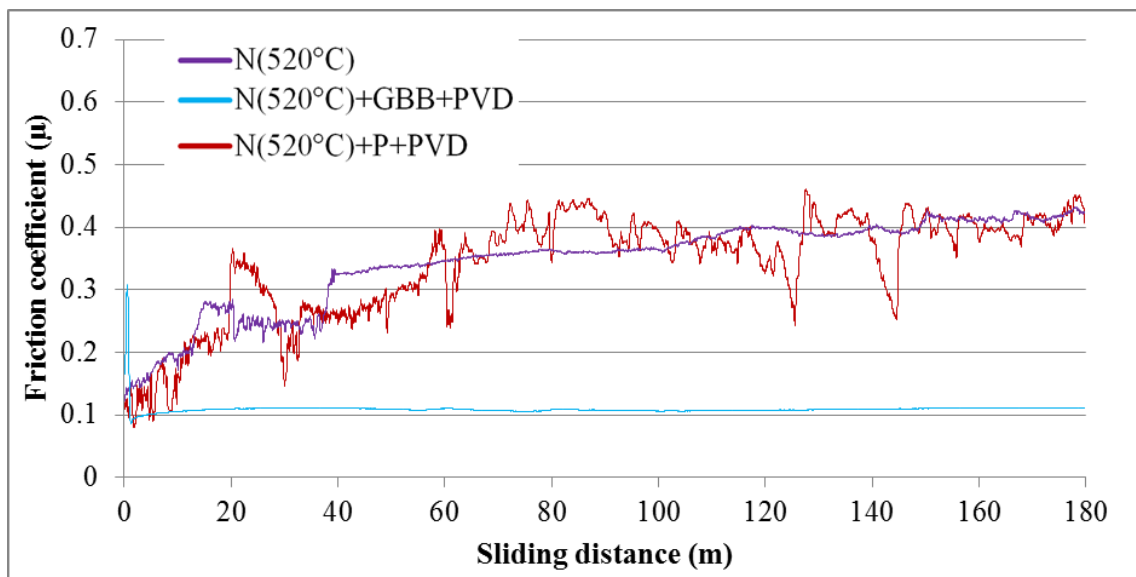


Figure 7 Comparison of friction coefficient curves obtained for samples having nitrided ( $T= 520$  °C) substrates and differently prepared surfaces below the PVD coating ( $F_N= 120$  N)

In both cases, i.e. for  $F=60$  N and 120 N we can establish that friction coefficient values are significantly higher for the  $N(520$  °C)+P+PVD and  $N(520$  °C) samples, than for the  $N(520$  °C)+GBB+PVD samples.

The possible reason could be that a GBB surface provides better conditions for the PVD coating to be intact with the substrate. As the coating was not removed from the surface it could remain coherent. The “better conditions” for PVD may involve, on the one hand compressive residual stresses in the outermost surface layer, due to the GBB process, on the other hand improved microgeometrical, mechanical and physico-chemical properties of the surface, like, lower average



# INTERNATIONAL SCIENTIFIC CONFERENCE ON ADVANCES IN MECHANICAL ENGINEERING

12-14 October 2017, Debrecen, Hungary



roughness, higher microhardness, less contamination, and higher chemical reactivity, providing better adhesion for the DLC layer to the substrate. In case of N(520 °C)+P+PVD the slope is kept on varying for this curve the reason for which is supposedly the presence of debris originated from both the sliding counterpart, i.e. ZrO<sub>2</sub> ball and the broken coating material.

## CONCLUSIONS

Scratch testing was done to characterize the adhesion of the coating and to evaluate the resistance of the surface to damage caused by a sharp indenter. The results were studied and the curves of the friction coefficient vs. scratching distance, as well as normal force vs. scratching distance were created. The results obtained showed that polishing of the surface prior to PVD coating leads to a better, smoother and more uniform friction coefficient curve during scratching, i.e. to lower value of friction coefficient as compared to that of the specimens which was glass bead blasted (cleaned). The critical force causing extreme damage or detachment of the coating, was also determined and it became a vital parameter in comparison of various surface preparations. Hence the overall hypothesis justified the priority of polishing the substrate surface prior to PVD coating to get the most desired scratching performance.

Ball on disc testing method was used to characterize the wear performance of the investigated materials. Based on these tests, the following conclusions have been derived: Duplex layers have better tribological properties comparing to the surfaces being just nitrided (uncoated).

GBB+PVD – i.e. glass bead blasted +PVD coated – surface layer has lower friction coefficient comparing to the P+PVD – polished and PVD coated –layer in case of the duplex treated samples.

## REFERENCES

- [1] Vetter J., et al.: *Surface treatment selections for automotive applications*. Surface & Coatings Technology 200, 1962 – 1968., 2005.
- [2] Holmberg, K., Matthews, A.: *Coatings Tribology- Properties, techniques and applications in surface engineering*. Elsevier Tribology Series 28, Elsevier Science, B V The Netherlands, 442., 1994.
- [3] Sergeson, R.: *Investigation in Nitriding, reprinted from American Society for Steel Treaters (ASST) Nitriding Symposium, 1929*. Source Book on Nitriding, P.M. Unterweiser and A.G. Gray, Ed., American Society for Metals, 26–55., 1977.
- [4] Holmberg, K., Ronkainen, H., Matthews, A.: *Tribology of thin coatings, b aVTT Manufacturing Technology*. PO Box 1704, FIN-02044 VTT, Finland bThe Research Centre in Surface Engineering, The University of Hull, 1999.



## INFLUENCE OF ION IMPLANTATION ON DUPLEX HARD COATINGS

*SKORIC Branko PhD, MILETIC Aleksandar PhD, TEREK Pal PhD, KOVACEVIC Lazar PhD, KUKURUZOVIC Dragan*

*Center for Surface Engineering and Nanotechnology, University of Novi Sad  
E-mail: [skoricb@uns.ac.rs](mailto:skoricb@uns.ac.rs)*

### Abstract

*The mechanical properties of new hard coatings based on a multilayer structure have been investigated at the nanometre scale. A multilayer structure consist of nitrated layer on steel substrate and hard coating deposited by Physical Vapor Deposition and Ion Beam Assisted Deposition. In the present investigation the subsequent ion implantation was provided with  $N^{2+}$  ions. This paper describes the use of the nanoindentation technique for determination of hardness and elastic modulus. The results are analyzed in terms of load-displacement curves, hardness, Young's modulus, unloading stiffness and elastic recovery. The analysis of the indents was performed by Atomic Force Microscope. Coating is often in tensile stress with greater microhardness. The stress determination follows the conventional  $\sin^2\Psi$  method, using a X-ray diffractometer*

**Keywords:** *coatings, ion implantation, microstructure, adhesion, nanohardness*

### 1. INTRODUCTION

Thin hard coatings deposited by physical vapour deposition (PVD), e.g. titanium nitride (TiN) are frequently used to improve tribological performance in many engineering applications [1]. In surgical stomatology insertion of bioinert TiN buffer layer at metallic substrate could be used [2]. Ion bombardment during vapour deposition of thin films, called ion beam assisted deposition (IBAD), exerts a number of effects such as densification, changes in grain size, crystallographic orientation, morphology and topography of the films [3]. In this paper, we present the results of a study of TiN films which are deposited by a Physical Vapor Deposition and Ion Beam Assisted Deposition. Subsequent ion implantation was provided with N ions. Ion implantation has the capabilities of producing new compositions and ructures unattainable by conventional means. Implantation may result in changes in the surface properties of a material, including hardness, wear, coefficient of friction and other properties.

### 2. METHODS

The substrate material used was high speed steel type M2. Prior to deposition the substrate was mechanically polished to a surface roughness of  $0.12\ \mu\text{m}$  (Ra). The specimens were first austenized, quenched and then tempered to the final hardness of 850 HV. In order to produce good adhesion of the coating, the substrates were plasma nitrated at low pressure ( $1 \times 10^{-3}$  Pa), prior to deposition of the coating. The PVD treatment was performed in a Balzers Sputron installation with rotating specimen. The deposition parameters were as follows: Base pressure in the chamber was  $1 \times 10^{-5}$  mbar. During etching, bias voltage was  $U_b=1$  kV, current  $I_d=50$  mA. During deposition substrate temperature was  $T_s=200$  °C, partial pressure of Ar was  $P_{Ar}=1 \times 10^{-3}$  mbar and partial pressure of  $N_2$  was  $P_{N_2}=3 \times 10^{-4}$  mbar. Prior to entering the deposition chamber the substrates were cleaned. The IBAD system consists of an e-beam evaporation source for evaporating Ti metal and 5-cm-



diameter Kaufman ion source for providing argon ion beam. Base pressure in the IBAD chamber was  $1 \times 10^{-6}$  mbar. The partial pressure of Ar during deposition was  $(3.1-6.6) \times 10^{-6}$  mbar and partial pressure of N<sub>2</sub> was  $6.0 \times 10^{-6}-1.1 \times 10^{-5}$  mbar. The ion energy ( $E_{Ar}=1.5-2$  keV), ion beam incident angle ( $15^\circ$ ), and substrate temperature  $T_s=200$  °C, were chosen as the processing variables. Deposition rate  $a_D=0.05-0.25$  nm/s. Quartz crystal monitor was used to gauge the approximate thickness of the film. After deposition, the samples were irradiated with 120 keV, N<sup>2+</sup> ions at room temperature (RT). The Ion Source is a multiply charged heavy ion injector, based on the electron cyclotron resonance effect (ECR), *Figure 1*. The implanted fluencies were in the range from  $0.6 \times 10^{17}$  to  $1 \times 10^{17}$  ions/cm<sup>2</sup>.

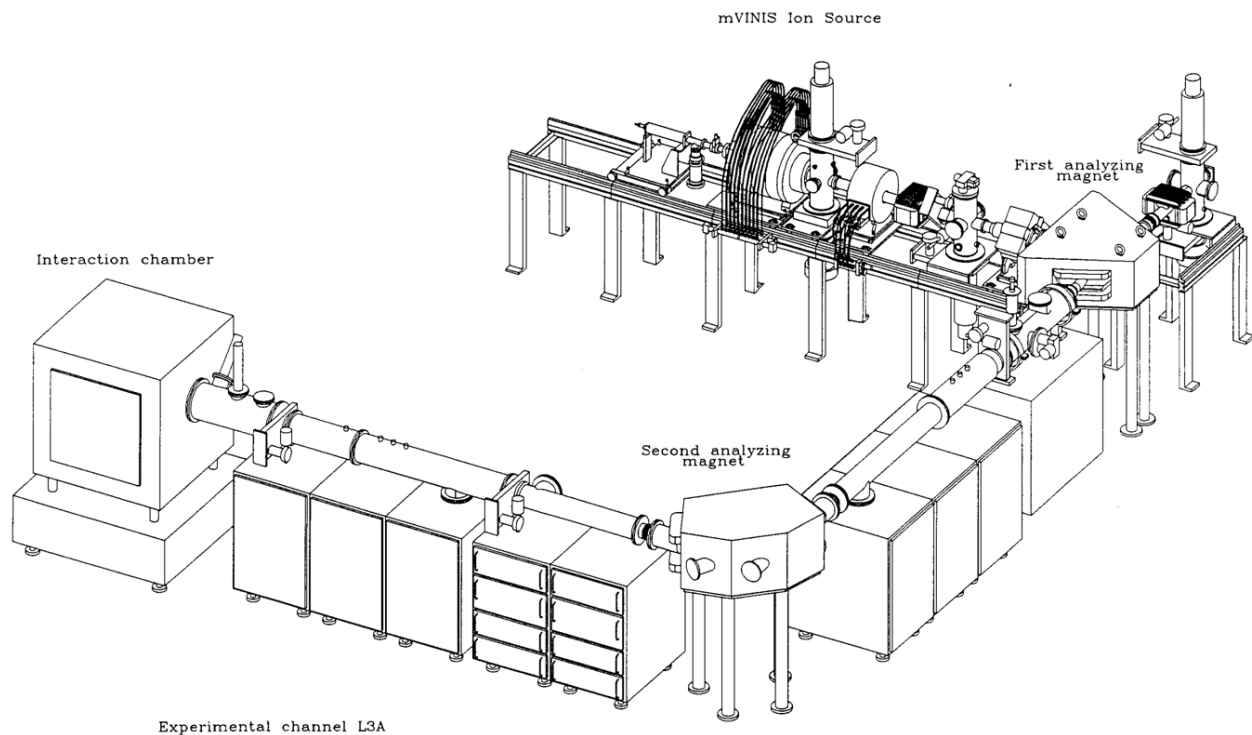


*Figure 1* Experimental channel L3A

A pure titanium intermediate layer with a thickness of about 50nm has been deposited first for all the coatings to enhance the interfacial adhesion to the substrates.

The mechanical properties on coated samples were characterized using a Nanohardness Tester (NHT) developed by CSM Instruments. Nanoindentation testing was carried out with applied loads in the range of 10 to 20 mN. A Berkovich diamond indenter was used for all the measurements. The data was processed using proprietary software to produce load–displacement curves and the mechanical properties were calculated using the Oliver and Pharr method.

Scratch adhesion testing was performed using commercially available equipment (REVETEST CSEM) fitted with a Rockwell C diamond stylus ( cone apex angle of  $120^\circ$ , tip radius 200  $\mu$ m). Acoustic Emission (AE) is an important tool for the detection and characterization of failures in the framework of non-destructive testing. The analyzed AE signal was obtained by a scratching test designed for adherence evaluation. Detection of elastic waves generated as a result of the formation and propagation of micro cracks.

X-ray diffraction studies were undertaken in an attempt to determine the phases present, and perhaps an estimate of grain size from line broadening. The determination of phases was realized by



X-ray diffraction using PHILIPS APD 1700 X-ray diffractometer. The X-ray sources were from CuK with wavelength of 15.443 nm (40 kV, 40 mA) at speed 0.9°/min. The surface roughness was measured using stylus type (Talysurf Taylor Hobson) instruments. The most popular experimental XRD approach to the evaluation of residual stresses in polycrystalline materials is the  $\sin^2\Psi$  method. The method requires a  $\Theta$ - $2\Theta$  scan for every  $\Psi$  angle around the selected diffraction peak and, in order to emphasize the peak shifts,

### 3. RESULTS

The nitrogen to metal ratio (EDX), is stoichiometries for IBAD technology and something smaller from PVD (0.98). For sample with additional ion implantation, value is significantly different, smaller (0.89). It is possibly diffused from the layer of TiN to the interface.

All the results of nanohardness are obtained with the Oliver & Pharr method and using a supposed sample Poisson's ratio of 0.3 for modulus calculation. The nanohardness values are shown in *Table 1*.

*Table 1* Surface nanohardness (load-10mN)

Unit	pn/IBAD	PVD	pn/PVD/II
GPa	21.6	32.6	42.6

The nanoindentation elastic modulus was calculated using the Oliver–Pharr data analysis procedure. The individual values of E are the different for all measurements, *Figure 2*.

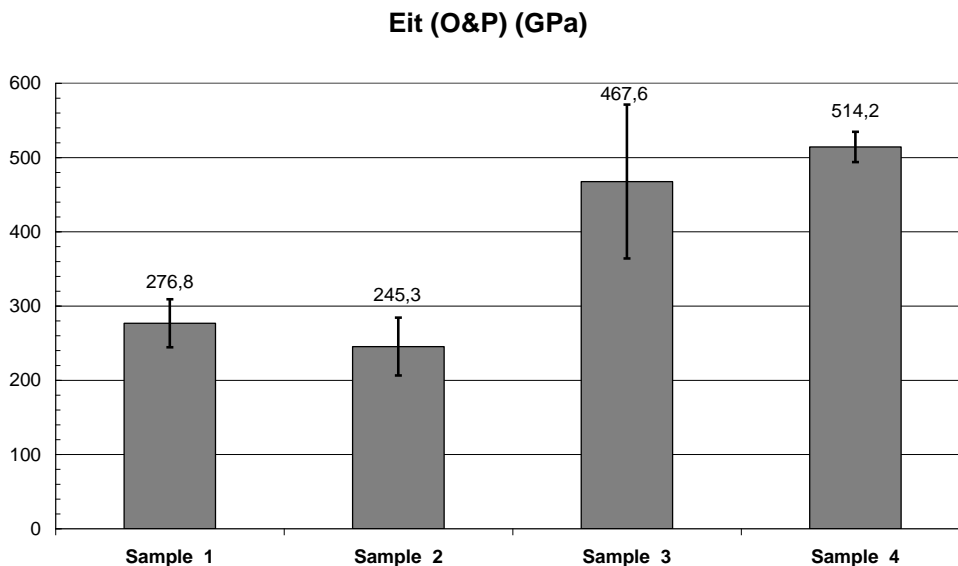


*Figure 2* Young's elastic module

The errors related to the measurements and estimations were different and for duplex coating with ion implantation is less than 4%. Good agreement could be achieved between the  $E_c$  values and nanohardness.

For each adhesion measurement, the penetration (Pd), the residual penetration (Rd), the acoustic emission (AE) and the frictional force are recorded versus the normal load. The breakdown of the coatings was determined both by AE signal analysis and scanning electron microscopy. AE permits an earlier detection, because the shear stress is a maximum at certain depth beneath the surface, where a subsurface crack starts



It was found that the plasma-nitriding process enhanced the coating to substrates adhesion. In some places of hard coatings cohesive failure of the coating and the delamination of the coating were observed, *Figure 3*.

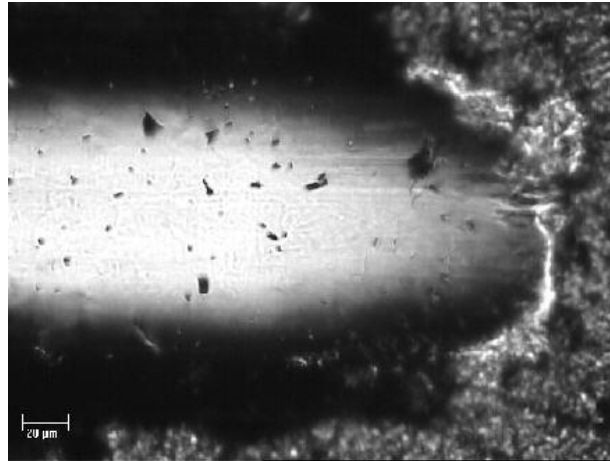


*Figure 3* SEM morphology of scratch test pn/TiN(PVD)

The simplest form of X-ray diffraction (XRD) characterization of thin film microstructure is Cohen-Wagner plot, *Figure 4*.

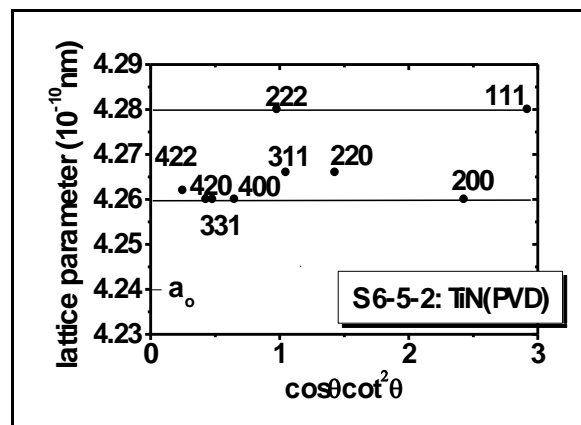


*Figure 4* The Cohen-Wagner plot, lattice parameters  $ahkl$  vs.  $\cos^2 \theta$

The anisotropy of lattice parameters,  $ah_{hh} \gg a_{hoo}$ , is characteristic for compact film. The coating morphology was evaluated using the well-known structure zone model of Thornton. All observed morphologies are believed to be from region of zone I (PVD) and from the border of region zone T (IBAD). It has been suggested [5], that the transition from open porous coatings with low microhardness and rough surface, often in tensile stress to dense coatings films with greater microhardness, smooth surface occurs at a well defined critical energy delivered to the growing film.

The microstructure of the TiN film, *Figure 5*, shows a columnar structure reaching from the substrate to the coating surface.

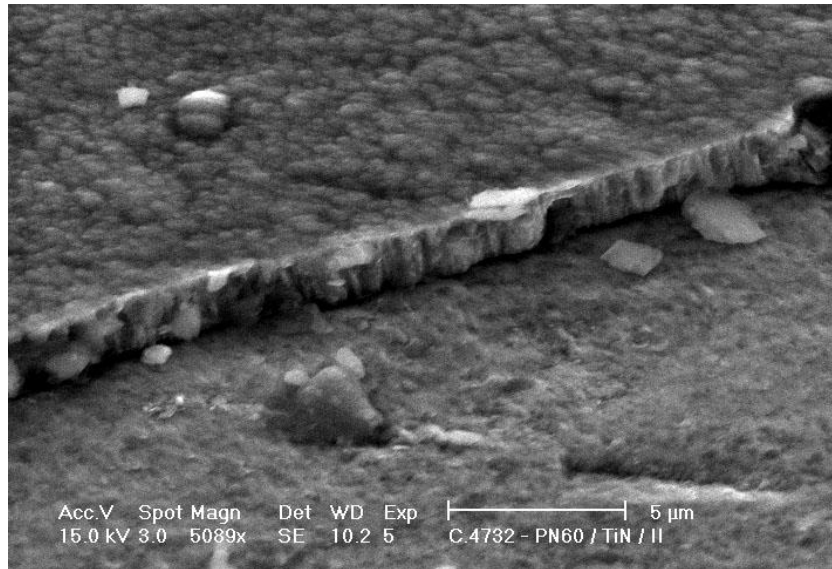


Figure 5. Surface morphologies of pn/TiN(PVD)/II

The specimen for these investigation was broken and the fracture surfaces were inspected. The width of column, for plane (422), is derived from the width of the diffraction peaks (Scherrer formula),  $t = \frac{0.9\lambda}{\beta \cos \frac{\theta}{\lambda} \cos \theta}$  of TiN ( $\lambda=0.154\text{nm}$ ,  $\Theta=62.5^\circ$  and  $\beta=0.056\text{rad}$ ), and it is 70 nm.

Because of low deposition temperature, it is possible that another planes also have small width of columns. The stress determination follows the conventional  $\sin 2\Psi$  method. Stress determination was performed using a PHILIPS XPert diffractometer. The (422) diffraction peak was recorded in a  $2\Theta$  interval between  $118^\circ$  and  $130^\circ$ , with tilting angle:  $\psi_0^1=0^\circ$ ,  $\psi_0^2=18.75^\circ$ ,  $\psi_0^3=27.03^\circ$ ,  $\psi_0^4=33.83^\circ$ ,  $\psi_0^5=40^\circ$ . A typical result for compact film, with residual stresses  $\sigma = -4.28\text{Gpa}$ , has TiN(PVD).

## CONCLUSIONS

The experimental results indicated that the mechanical hardness is elevated by penetration of nitrogen. Nitrogen ion implantation leads to the formation of a highly wear resistant and hard surface layer.

The deposition process and the resulting coating properties depend strongly on the additional ion bombardment.

Nitrogen implantation into hard TiN coatings increases the surface hardness and significantly reduces the tendency of the coatings to form microcracks when subjected to loads or stresses.

The present coating method can produce dense structures, high hardness and the high critical load values can be achieved. Tribological tests confirm that these composite coatings are wear resistant and provide very low friction coefficient

## ACKNOWLEDGEMENT

The authors would like to thank to The Provincial Secretariat for Higher Education and Scientific Research of Vojvodina, which supported this work by grant.



# INTERNATIONAL SCIENTIFIC CONFERENCE ON ADVANCES IN MECHANICAL ENGINEERING

12-14 October 2017, Debrecen, Hungary



## REFERENCES

- [1] Zheng, S., Sun, Y., Bell, T., Smith, J.M.: *Mechanical properties microprobing of TiN coatings deposited by different techniques*. The Fourth European Conference on Advanced Materials, 177-184., 1995.
- [2] Škorić, B., Schrittwieser, R., Cavaleiro, A.: *Nano metrology in biomedical engineering*. ETIKUM 2014 International scientific conference, 71-75., 2015.
- [3] Ensinger, W.: *Ion bombardment effects during deposition of nitride and metal films*. Surface and Coatings Technology, 99., 1-13., 1998.
- [4] Pharr, M., Harding, D.S., Oliver, W.C., in: Nastasi, M., et al.: *Mechanical Properties and Deformation Behavior of Materials Having Ultra-Fine Microstructures*. Kluwer, Dordrecht, 449., 1993.
- [5] Griepentrog, M., et al.: *Properties of TiN hard coatings prepared by unbalanced magnetron sputtering and cathodic arc deposition using a uni- and bipolar pulsed bias voltage*. Surface and Coatings Technology, 74-75., 326-332., 1995.



## OPTIMIZING AN UNINTERRUPTIBLE SOLAR POWER SYSTEM FOR INDUCTIVE NATURED LOADS

*SKRIBANEK Ádám, BODNÁR István PhD, ISKI Patrik*

*Institute of Electrical and Electronic Engineering, Faculty of Mechanical Engineering and Informatics, University of Miskolc*

*E-mail: [skribike@gmail.com](mailto:skribike@gmail.com), [vegybod@uni-miskolc.hu](mailto:vegybod@uni-miskolc.hu), [iskip95@gmail.com](mailto:iskip95@gmail.com)*

### **Abstract**

*This study deals with the optimization of an uninterruptible solar power system in case of different inductive natured loads, such as a drill or a boiler pump. After a short description of solar energy utilization, the examination of an off-grid solar system is presented. The experimental system is built up from two polycrystalline solar panels, an MPPT charge controller, a battery, an inverter and an automatic switching station. After describing the compiled system, the system efficiencies, maximum power, current and voltage waveforms together with other measurement results in case of different electrical loads are presented. The examination of the final systems operability and the switch-over are examined, then the expected and measured results are compared and explained.*

**Keywords:** *solar, off-grid, UPS, polycrystalline, MPPT*

### **1. INTRODUCTION**

Energy is one of the central elements of our world. Renewable energy sources, mainly the Sun increasingly come to the view nowadays, so the subject of examining solar power production is very actual. The Sun is not only the base of ground life, but the central planet of our Solar System too. Fusion processes are taking place inside of the Sun, where hydrogen atoms combine into helium atoms. The weight loss (4 million *ton/sec*), that comes into being during the reaction transforms into energy. About 180 million *kWh* energy is released during the formation of 1 *kg* helium. The energy of solar radiation is  $1.37 \text{ kW/m}^2$  at the border of our atmosphere, this is called *solar constant*. The energy of this solar radiation at the earth's surface is much lower, about  $1.000 \text{ W/m}^2$  can be measured at a sunny day. Third of this number is direct radiation and the rest is called scattered light [3].

If the energy that reaches the top of the atmosphere counts as 100%, then the direct radiation on the surface is 33% while the scattered is only 18% of that energy. The sum of these two numbers means the global radiation. 10% of the global radiation is reflected by the surface. The composition of the radiation defines its utilizability.

Two ways of solar energy utilization is distinguished. These are the so called passive and the active forms. The passive solar energy utilization means energetically more favorable orientation of buildings. The conscious building orientation is discernible since the ancient times, to take advantage of the solar radiation.

Active solar energy utilization happens with the help of solar panels. With the panels, it is possible to produce electricity or directly heat from solar radiation. Heat production means heating water for different reasons. Energy production nowadays can happen even at the roof of a family house in an environmental friendly way. It is important to mention, that the maximum electrical power can be produced only if the load resistance equals to the internal resistance of solar panels [1, 2].



## 2. VOLTAGE, CURRENT AND POWER OF SOLAR PANELS

$U_{oc}$  open circuit voltage and  $I_{sc}$  short circuit current can be measured on an unloaded solar panel. If any electrical load is connected to it, the  $I$  current and  $U$  voltage of the panel will always be lower than  $U_{oc}$  and  $I_{sc}$  values. The  $I$  current is the difference between the photo current ( $I_{photo}$ ) and the so called dark current ( $I_{dark}$ ). The dark current exponentially depends on the temperature and linearly depends on the  $I_s$  saturation current because of the semiconductor characteristic of solar panels. This is described by the following equation [1, 4, 5]:

$$I = I_{photo} - I_{dark} = I_{photo} - I_s \left[ \exp\left(\frac{eU}{kT}\right) - 1 \right] \quad (1)$$

The short circuit current (2) and the idle voltage (3) can be expressed by the substitution of  $U=0$  and  $I=0$ . The idle voltage logarithmically depends on the current values and linearly on the thermic voltage ( $U_T$ ). According to these [1]:

$$I_{sc} = I_{photo} , \quad (2)$$

$$U_{oc} = \frac{kT}{e} \ln\left(\frac{I_{photo}}{I_s} + 1\right) = U_T \ln\left(\frac{I_{photo}}{I_s} + 1\right) \quad (3)$$

The  $U$ - $I$  characteristics can be seen in *Figure 1*, in case of different intensities of illumination.

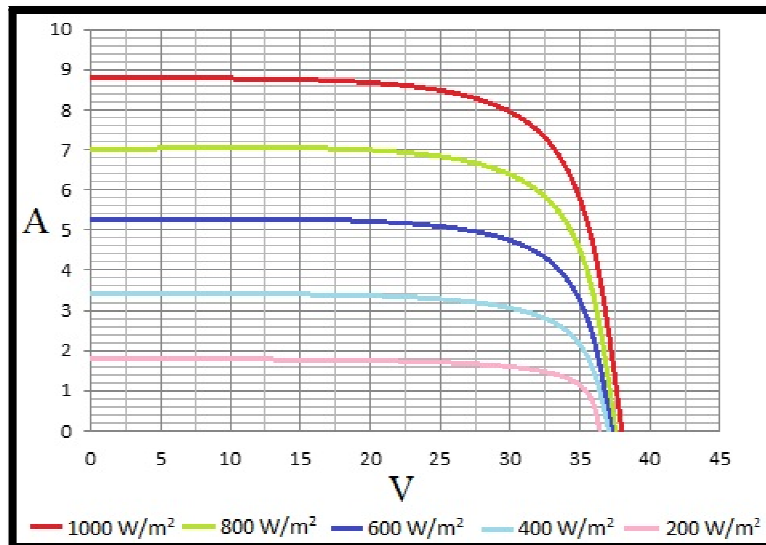


*Figure 1* Voltage-ampere characteristics of solar panels in case of different intensities

It can be seen, that the short circuit current is directly proportional to the intensity of illumination, as the value of the photo current increases together with the light intensity increase, and (2) says, that the photo current equals to the short circuit current. It can also be seen in (3), that the idle voltage logarithmically depends on the intensity of illumination on the earth's surface.

The effective electrical power ( $P$ ) of the solar panel can be determined by the multiplication of the  $I$  ampere and  $U$  voltage measured on the  $R$  resistance [1, 4, 5]:



$$P = IU = I_{sc}U - I_s U \exp\left(\frac{U}{U_T} - 1\right) \quad (4)$$

The value of the load resistance ideally equals to the internal resistance of the solar panel. The so called fill factor ( $\varphi$ ) shows how the multiplication of operating voltage and amperage relate to the multiplication of open circuit voltage and short circuit amperage [4, 5]:

$$\varphi = \frac{U_m I_m}{U_{oc} I_{sc}} \quad (5)$$

The value of the fill factor depends on the illumination and on the chosen operating point [4, 5]. The value of  $\varphi$ , in case of solar panels used in practice, moves between 0.75 and 0.85. It can be seen that the fill factor shows how the square of the maximum operating power (grey square) relates to the square of the multiplication of  $I_{sc}$  and  $U_{oc}$  in *Figure 2*.

The maximum efficiency of the solar panel ( $\eta_{max}$ ) can be counted by dividing the maximum operating power of the solar panel and the light power ( $P_{light}$ ) on the effective surface [4, 5]:

$$\eta_{max} = \frac{I_m U_m}{P_{light}} = \frac{\varphi I_{sc} U_{oc}}{P_{light}} \quad (6)$$

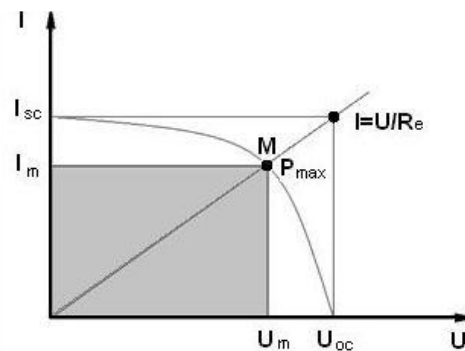


Figure 2 The operating point (OP) of maximum power

We examined a regular, nine years old monocrystalline solar panel in practice. The specifications of the solar panel, which are given by the manufacturer are the following:  $U_{oc}=21,6$  V;  $I_{sc}=4,8$  A. During our examination we created a Sun Simulator which illuminated the solar panel. We measured the open circuit voltage and short circuit current while using the simulator. The results were the followings:  $U_{ocm}=16,7$  V;  $I_{scm}=2,3$  A. The difference between the given and the measured values are mainly caused by the age of the solar panel together with the fact that we used a simulator at the laboratory instead of the natural sunlight. We measured the voltage and current in case of an ideally loaded solar panel. The results were the followings:  $U_m=14,3$  V;  $I_m=1,8$  A. From the measurement results, it is possible to count the fill factor:

$$\varphi = \frac{U_m I_m}{U_{ocm} I_{scm}} = \frac{14,3 \text{ V} \times 1,8 \text{ A}}{16,7 \text{ V} \times 2,3 \text{ A}} = \frac{25,74 \text{ W}}{38,41 \text{ W}} \approx 0,67 \quad (7)$$

There is only a little difference between the usual and the counted fill factor. The difference is also caused by the aging of the solar panel.



### 3. THE MEASURING SYSTEM

Measurements were made with two CFSR-SP250W polycrystalline solar panels operating in parallel. The maximum power of each solar panels is 250 W, but the value of the electrical power is affected by the temperature dependence of the PV, the intensity of illumination, the resistance of the electrical load, the age of the solar panel and the orientation. During the measurements, MPPT (Maximum Power Point Tracking) charge controller was applied, which follows and sets the right load resistance [6]. The two solar panels were placed on the roofing at the University of Miskolc.



Figure 3 Solar panels and the compiled system

The solar cables, the battery and the inverter are directly connected to the charge controller. The maximum current of the charge controller is 30 A and it was charging a 90 Ah, 12 V car battery with a maximum of 720 A starting current. DC was transformed to AC by a 12V/230V inverter. The switching between the two energy sources was provided by a US-12N automatic switching station. A boiler pump with 3 power levels and an electric drill was applied as electrical loads. With the help of the right instruments, it was possible to measure the voltages, currents and powers on both DC and AC sides.

The compiled system proved to be functional. The blackout was simulated by switching the household power off manually. As the effect of the simulated blackout, the switching station automatically switched-over to the alternative energy source, and the load was operating flawlessly. When the household power was switched back on, the switching station switched back to it in a short time.

### 4. RESULTS

During the efficiency measurement inductive natured loads were applied, such as a boiler pump and an electric drill. The battery was disconnected from the system while the boiler pump operated, but in case of the drill it was connected too, because of the high amperage while starting the operation. Solar panels were not able to provide enough energy for starting.

It means, that the battery is essential to apply, otherwise motoric appliances will not be able to operate by the help of the solar system. In case of connecting a higher electrical load to the system than the maximum power of solar panels, the extra energy is provided by the battery.

Figure 4 shows system efficiencies in case of different level loads. It is easy to see that higher electrical load means higher system efficiency. This is mainly caused by the inverter, which's maximum power is 1 kW. The closer load value to the 1 kW means the higher efficiency.



Table 1 Results of the measurement

	Boiler Pump			Drill
	I. level	II. level	III. level	
$P_{pv}$	-17.1 W	-34.4 W	-57.5 W	-235 W
$P_{battery}$	0 W	0 W	0 W	-135 W
$P_{load}$	8 W	23 W	44 W	308 W
Efficiency	46.78%	66.86%	76.50%	83.24%

The efficiency of the system almost equals to the efficiency of the inverter. This is mainly caused by its cooling system, which consumes relatively much energy, together with the energy loss of voltage transformation from DC to AC.

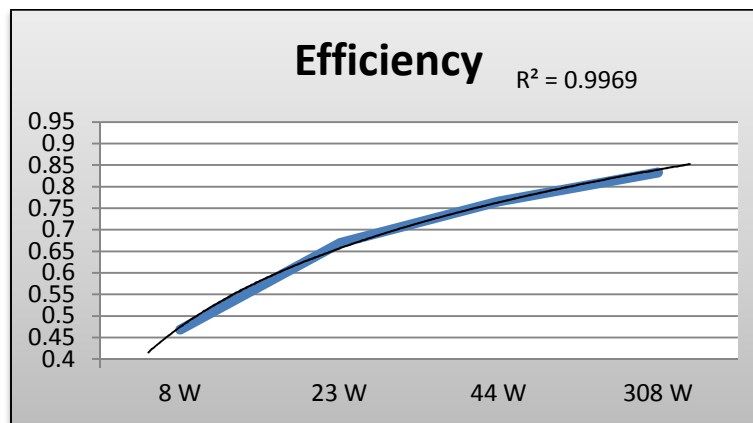


Figure 4 System efficiencies depending on the load

As the maximum power of the solar panel is limited at constant intensity, it is obvious, that if their voltage increases, their current will decrease and vice versa. This can be seen in Figure 5. On the left, we can see the voltage and the current of the solar panels, while the right picture shows their power.

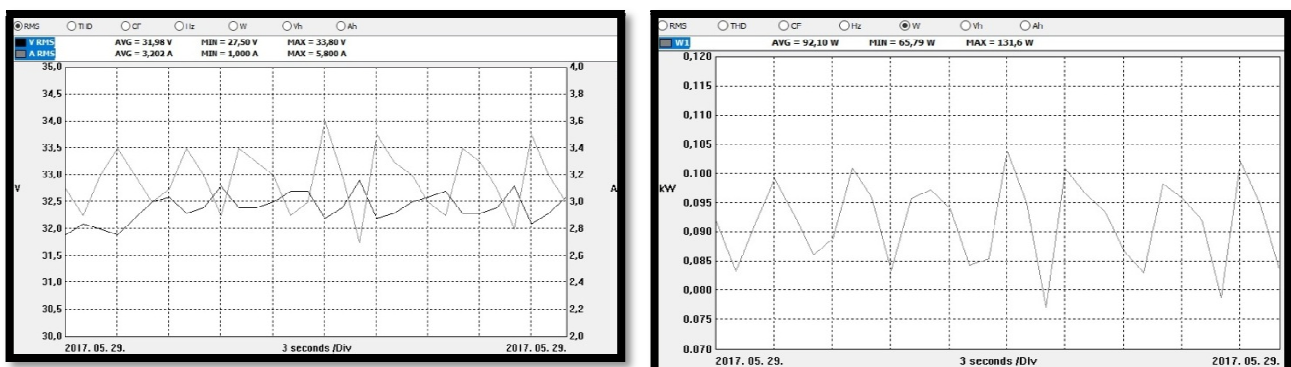


Figure 5 Voltage, current and power of solar panels

Consuming more energy than the maximum power of solar panels means, that all of the energy produced by solar panels are consumed. The waveforms of the solar panels are smoothed this time, as they provided their maximum power. This can be seen on Figure 6.

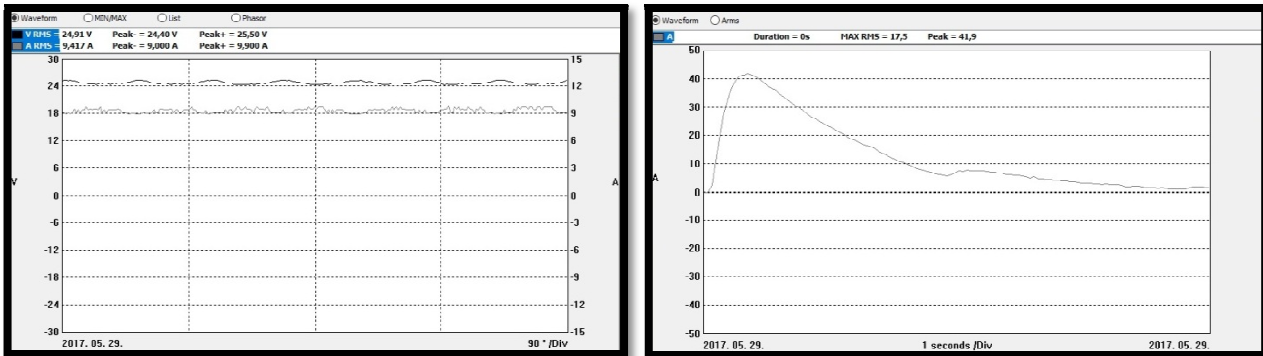


Figure 6 Voltage and current of solar panels (left); Starting current of battery (right)

The right side of *Figure 6* shows the starting current of the battery in can of starting the boiler pump. The maximum of this current is almost 42 A in this case. It is obvious, that the solar panels are not able to produce this high current at the operating voltage level, not even for a moment. Of course starting a higher electrical load, such as the applied electrical drill means even higher amperage, so it is proven, that there is a significant need for the battery not only for storing the energy, but for the starting transients too.

## CONCLUSION

The designed and compiled system proved to be functional. The MPPT mode is necessary for producing the maximum power because of the intensity and temperature dependence of solar panels, which can be counted by the mentioned equations. It is important to find and set the internal resistance of solar panels as load resistance.

The blackout of the household power was simulated by switching off the circuit breaker of household power manually. The switching station automatically recognized it and switched-over to the alternative energy source until the blackout was over. This proved that the compiled system works as a safe uninterruptable power supply system (UPS).

As it can be seen, that the battery is a very important part of the system, because in case of inductive natured loads, the starting current is provided by it. Also important to mention that the battery is the only part of the system that can store energy and provide it even at night, in case of a blackout. Solar energy together with other renewable energy utilization may be the solution of our energy problems, but it is still needed to develop the current technologies to reach higher efficiencies.

## REFERENCES

- [1] Szász, Cs.: *Optimal control of Photovoltaic Modules Energy Efficiency*. Journal of Computer Science and Control Systems, Vol. 10. Nr. 1., 29-34., 2017.
- [2] Hersch, P.: *Basic photovoltaic principles and methods*. United States Department for Energy, USA, 1982.
- [3] Dr. Mizsei, J.: *Napelemek laboratórium*. Segédlet. Budapest, 2003.
- [4] King, L.D., Kratochvil, A.J., Boyson, E.W.: *Temperature Coefficients for PV Modules and Arrays: Measurement Methods, Difficulties, and Results*. 26th IEEE Photovoltaic Specialists Conference, Anaheim, California, 1997.
- [5] Dubey, S., Sarvaiya, J.N., Seshadri, B.: *Temperature Dependent Photovoltaic (PV) Efficiency and Its Effect on PV Production in the World-A Review*. Energy Procedia 33., 311–321., 2013.
- [6] Malik, A.Q., Damit, S.J.B.H.: *Outdoor testing of single crystal silicon solar cells*. Renewable Energy 28., 1433–1445., 2003.



## VANES SHAPE OPTIMIZATION OF VENTILATED DISC BRAKES FOR HEAVY DUTY VEHICLES

*STOJANOVIĆ Nadica, GRUJIĆ Ivan, GLIŠOVIĆ Jasna PhD, MILOJEVIĆ Saša, DAVINIĆ Aleksandar PhD*

*Department for Motor Vehicles and Motors, Faculty of Engineering, University of Kragujevac*  
*E-mail: [nadica.stojanovic@kg.ac.rs](mailto:nadica.stojanovic@kg.ac.rs), [ivan.grujic@kg.ac.rs](mailto:ivan.grujic@kg.ac.rs), [jaca@kg.ac.rs](mailto:jaca@kg.ac.rs),  
[sasa.milojevic@kg.ac.rs](mailto:sasa.milojevic@kg.ac.rs), [davinic@kg.ac.rs](mailto:davinic@kg.ac.rs)*

### **Abstract**

*Braking system represents a very important system for all types of motor and trailer vehicles. The basic task of the braking system is reducing the vehicle speed until it stops or slows down to a lower speed. Furthermore, the braking system should also ensure that the vehicle is kept in a steady state. To achieve that the vehicle has a shorter braking distance, it is necessary to reduce the flywheel masses. The purpose of this paper is to reduce the weight of the venting disc, which is partly responsible for the value of braking distance achieved. Besides that, it must be ensured that deformations and stresses remain in the limits. Optimization is performed by ANSYS software package. The application of virtual experiments gives quick answers in developing a new or improving the already existing part. It also enables corrections of the product itself, as well as competitiveness on the market.*

**Keywords:** *braking system, flywheel masses, braking distance, competitiveness on the market*

### **1. INTRODUCTION**

Optimization is defined as the science for determining the "best possible" solution [1]. Having the best solution, or solution that is close to the best, leads to savings in material and energy (whose resources are limited) or achieving financial profit or achieving the highest reliability or safety in operation. Optimization aims to minimize negative effects (effort, costs, etc.) or to maximize positive effects (profit).

The optimization process for a particular system can be formally separated into two levels. The first level represents the need for a uniquely defined problem and the establishment of the exact relations of influence parameters and solutions in the conditions in which it should function. The second level is the choice of some of the known or the development of a new methodology for solving the problems.

The braking system is one of the most important parts of motor and trailer vehicles. As a motor vehicle cannot function without drive unit, it can also not be imagined without a braking system. In addition to stopping and slowing down the vehicle, the braking system also has other tasks, and above all, together with other systems, allows the control of the vehicle speed in accordance with traffic conditions, driver's wishes and other circumstances [2].

Disc brakes are a typical example of axial brakes, in which the pressure on the friction surface is realized in the direction of the axis of the rotational element. Due to the already emphasized importance of the brake system for vehicle safety, it is necessary that the vehicle users comply with the manufacturer's recommendations; otherwise different problems arise during the exploitation. Often in practice, the common requirement for selecting such parts is a lower price, which should not have a decisive role in selection. Friction pairs made of disc and brake pads should be selected



so that when activated, such a friction coefficient in the contact surface is achieved, which will ensure a fast and safe slowing or stopping [3].

Agnihorti and Chopra [4] were looking for the best materials and the best design in order to reduce heat loads. While Kajabe and Navthar [5] analyzed how changing the shape of the disc brake affects the braking, mass, manufacturing costs, stresses, and the heat dissipation into the environment. Amouzgar et al. [6] analyzed the disc brake for the heavy-duty vehicles. Their goal was to reduce the mass, as well as the maximum temperature that is a by-product of the braking. The variables that are analyzed are the braking load, the Young module and the thickness of the back plate. Furthermore, the shape of the rib affects the mass, as well as the accumulation of heat on the disc itself. One such study was carried out by Kumar et al. [7].

The aim of the research presented in this paper is to reduce the mass of the braking disc. The disc brakes together with the wheel, rotate and with their moment of inertia affect the braking distance. Of course, the influence of other rotary masses cannot be ignored. Thus, in braking, the inertial force of the brake disc together with the wheel, as well as other rotary masses, continues to tend to have the same angular velocity as before the activation of the braking system. In this paper, consideration is given to the reduction of the mass of the braking disc. As the disc mass is larger, the inertial force is larger too, so it is necessary to reduce it in any way. Some of the ways to achieve this goal are the use of aluminum for the construction of the lid, then the optimization of the construction itself, as well as the reduction of constructive parameters. By reducing the weight of the brake disc, the mass of one of the rotating bodies would be reduced, as would the braking distance. The optimization of the parameters of disc ribs—constructive parameters is performed in the paper.

## 2. 3D MODEL OF DISC BRAKE FOR HEAVY DUTY VEHICLES

Disc brake model is created in CATIA software package, shown on *Figure 1*. Assembly itself consists of a large number of parts, so it has a large mass. That's why it is very important to reduce the mass in any way. A part that is very interesting and for can be said to have the greatest influence on the braking distance, unlike the other parts, is a brake disc.

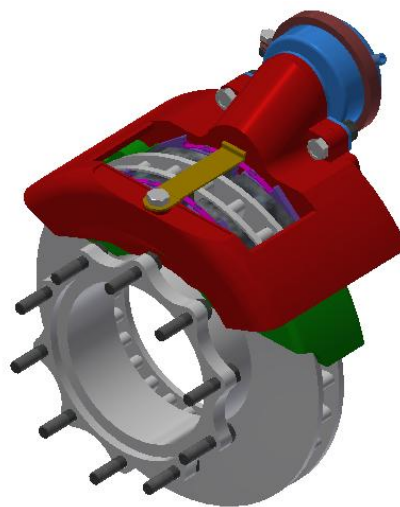


*Figure 1* Vented disc brake for heavy-duty vehicles

The maximum diameter of the brake disc for heavy-duty vehicles can be up to 430 mm. The diameter of the analyzed disc in this paper is 430 mm; the disc height is 130 mm, and the disc



thickness of the disc with ribs is 45 mm [8]. A disc with roll-shaped ribs is observed (*Figure 2*), while the diameters are marked with letters; the dimensions of the diameters are shown in *Table 1*. The disc is made of steel (*Table 2*). One such disc with the characteristics of the materials that are shown in *Table 2* has mass of the 23.523 kg.

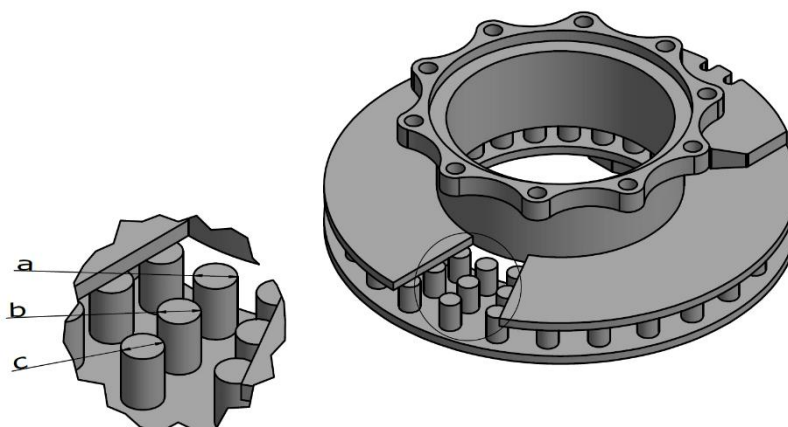


*Figure 2* Vented braking disc with detail

*Table 1* Ribs diameter of braking disc

Letters	Diameter, [mm]
<i>a</i>	15
<i>b</i>	20
<i>c</i>	25

*Table 2* Material characteristics of friction pair [9]

	Disc	Pad
Density, [kg/m <sup>3</sup> ]	7250	1400
Young's module, [GPa]	138	1
Poisson ratio, [-]	0.28	0.25

Before starting the analysis, it is first necessary to define boundary conditions. The conditions in which the analysis was carried out: an ambient temperature of 22°C, vehicle speed before braking is 80 km/h, which corresponds to an angular velocity of 41.89 rad/s, the coefficient of friction occurring in the friction pair is 0.336 [10].

The size of the final elements in part regions where the material is not taken away should not be so fine, compared with the parts where the material is taken away. In this case, the size of the final elements of the brake discs should be fine (fine discretization), so for this reason the number of nodes and elements is slightly higher. The mesh consists of 318654 nodes and 197662 elements.

When optimizing shapes, it is necessary to choose where materials can be taken away, and where it is not. In this case, the material may be taken away from the ribs, while it is not allowed from other regions.

### 3. RESULTS

The goal of optimization is to reduce mass of the brake disc, without compromising other characteristics of the part itself. Such a braking disc, obtained using the Shape Optimization Module



in ANSYS software package, should meet the same conditions that it had before the optimization itself.

As the diameters of the outer rolls are the largest, it can be noticed in *Figure 3 (a)* that most of the material is taken away from them. After the optimization, the rollers would have hollow cross-sections, with most of the material being taken off in roll-disc plate connection region, while in the middle, their cross-section will remain unchanged. *Figure 3 (b)* shows the disc after optimization, the removed material is displayed in red.

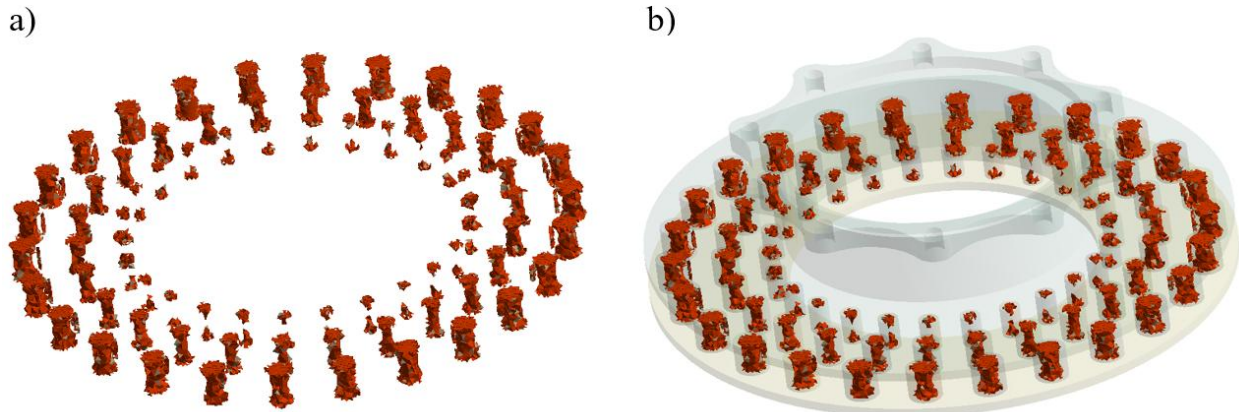


*Figure 3 (a)* Display of roller mass reduction by 20%, *(b)* A detailed view of the brake disc on which it takes off 20% of the material

For the application of Shape Optimization Module, it is necessary to define how many percentages it takes to reduce the mass, in this case the braking disc. *Table 3* shows how much the brake disc's mass decreases by 4%, 5% and 6%.

*Table 3* Braking disc's mass after optimization

	<b>Braking disc's mass after optimization, [kg]</b>
4%	22.6654
5%	22.3647
6%	22.0728

The display of the ribs of the brake disc with material that is taken away is given in *Figure 4 (a)* where 4% of the total weight of the brake disc is taken, while in *Figure 4 (b)* 6%.

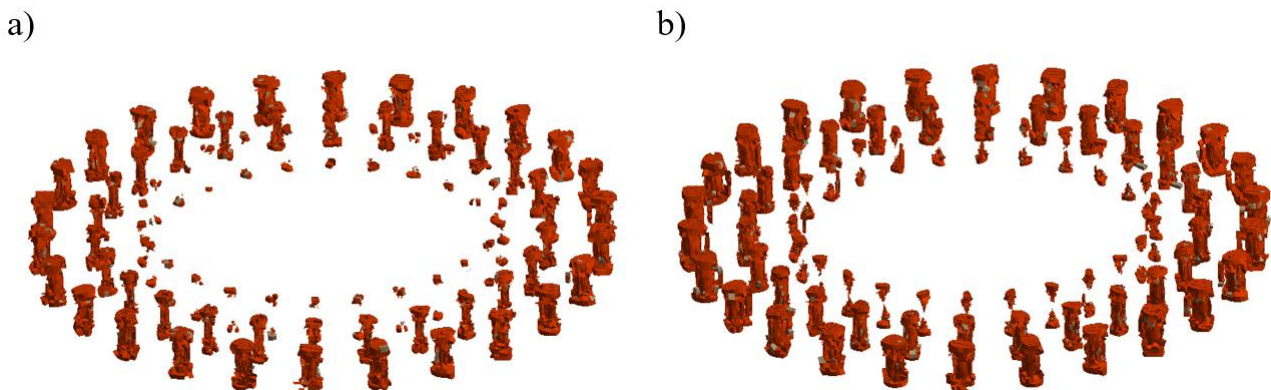


*Figure 4 (a)* Display of mass reduction of 15%, *(b)* display of mass reduction of 25%



It can be concluded that as the percentage of removal of material from the disc ribs is increased, material removed from the central and inner ribs increases, while it can be said that from the outer ribs that the material removed from the outer ribs is almost not changed with the increase in the percentage of the reduction in the mass of the brake disc.

The deformation and stress condition of the brake disc, in relation to the reduction of mass is shown in *Figure 5*. The initial value of the deformation and stress on the diagrams corresponds to the values recorded before the optimization of the brake disc.

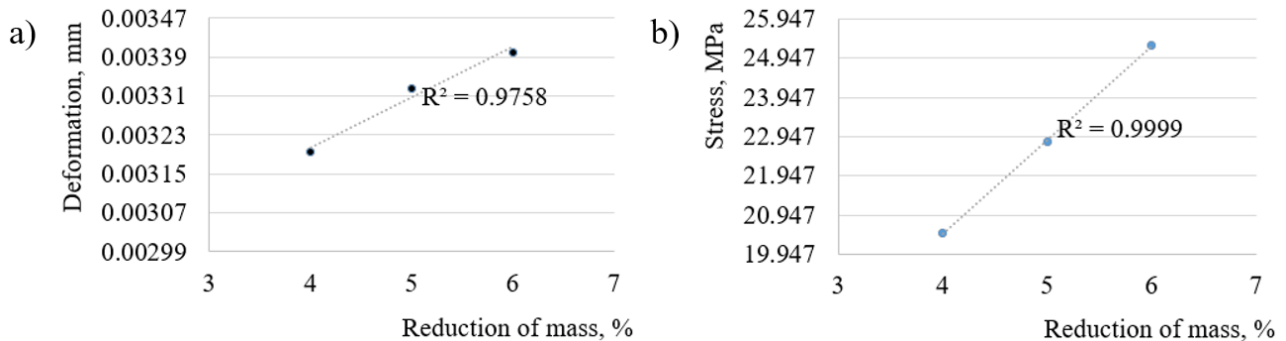


*Figure 5* (a) Deformations in function of mass reduction, (b) stresses in function of mass reduction

By analyzing *Figure 5 (a)* and *(b)*, it can be noticed that deformations and stresses increases linearly with decreasing of mass. The deformation values do not change to the extent that a brake disc can break. Furthermore, as can be seen from *Figure 5 (b)*, the stresses do not exceed the yield strength limit value, so there will not be plastic deformations of the brake disc. In case the stresses exceed the values of the yield strength, a distortion of the brake disc would occur, and when braking, the braking pads would not fit the entire surface of the disc. This would further negatively affect the braking distance as well as the stability in the braking process, and this would impair the safety of a driver as well as other traffic participants.

## CONCLUSIONS

The brake disc's mass obtained by the optimization process is still high; however, the weight is essentially reduced. Heavy duty vehicles can have 2, 3 or 4 axles (they can have more), so that on each axle we have two brake discs, the weight can be reduced up to 11 kg. Comparing the mass of a 10t-weighted vehicle with reduced mass achieved through the optimization process of the brake discs is insignificant. Regardless, reducing the weight of the brake discs has a major influence on the braking distance value.

Further research would be based on experimental research, where it is necessary to make such a disc that is obtained after optimization and examine how it behaves in different exploitation conditions.

## ACKNOWLEDGEMENT

This paper was realized within the researching project "The research of vehicle safety as part of a cybernetic system: Driver-Vehicle-Environment" ref. no. 35041, funded by Ministry of Education, Science and Technological Development of the Republic of Serbia.



## REFERENCES

- [1] Marjanović, N.: *Mathematical optimization of technical systems*. Faculty of Engineering University of Kragujevac, Kragujevac, 2014.
- [2] Todorović, J.: *Braking of Motor Vehicles: Theory, design, maintenance, testing*. Beograd, Institute for Textbooks and Teaching Resources, 1988.
- [3] Bendix Spicer Foundation Brake LLC: *The Compelling Case for Air Disc Brakes in Heavy Truck Braking: a White Paper*. Elyria, Ohio, 2011.
- [4] Agnihorti, V., Chopra M.K.: *Optimized Thermo –Structural Analysis of Solid and Vented Disc Brake Using Finite Element Method (A Case Study)*. IOSR Journal of Mechanical and Civil Engineering, 11(4), 40-49., 2014.
- [5] Kajabe, R.S., Navthar, R.R.: *Optimization of Disc Brake Rotor with Modified Shape*. International Journal of Research in Aeronautical and Mechanical Engineering, 3(3), 52-60., 2015.
- [6] Amouzgar, K., Rashid, A., Stromberg, N.: *Multi-Objective Optimization of a Disc Brake System by Using SPEA2 and RBFN*. ASME 2013 International Design Engineering Technical Conferences & Computers and Information in Engineering Conference, 2013.
- [7] Ranjith Kumar, G., Thriveni, S., Rajasekhar Reddy, M., Harinath Gowd, G.: *Design Analysis & Optimization of an Automotive Disc Brake*. International Journal of Advanced Engineering Research and Science (IJAERS), 1(3), 24-29., 2014.
- [8] UAB ECOBALTIC, [http://www.ecobaltic.lt/files/stabdziu\\_dalys/nca104720.pdf](http://www.ecobaltic.lt/files/stabdziu_dalys/nca104720.pdf)
- [9] Belhocine A.: *Numerical investigation of a three-dimensional disc-pad model with and without thermal effects*. Thermal science, 19(6), 2195-2204., 2012.
- [10] Glišović, J.: *Theoretical and experimental investigations of high-frequency noise of disc brakes*. PhD dissertation, Faculty of Engineering University of Kragujevac, Kragujevac, 2012.



## EXPERIMENTAL RESEARCH OF TRACTOR TYRE RESPONSE TO QUASISTATIC PASSAGE OVER THE SINGULAR ROAD OBSTACLE

*STOJIC Boris PhD, POZNANOVIĆ Nenad PhD*

*Department for Mechanization and Design Engineering, Faculty of Technical Sciences, University of Novi Sad*

*E-mail: [bstojic@uns.ac.rs](mailto:bstojic@uns.ac.rs), [npoz@uns.ac.rs](mailto:npoz@uns.ac.rs)*

### **Abstract**

*In this paper enveloping behaviour of tractor tyre was investigated for the case of quasistatic passage of the tyre over the singular road obstacle of rectangular shape. This relatively simple approach is intended to provide results for further theoretical study and development of appropriate modeling techniques dealing with tyre enveloping behaviour. Shapes of tyre response curves were determined for different obstacle dimensions and three levels of tyre ground contact length representing different tyre load conditions. whereby tyre load change was substituted by pressure variation. Impact of tyre load on the response form was clearly determined, and it was observed that tyre radial stiffness changes degressively with deflection. Results tended to exhibit significant fluctuations, probably originating from mechanical properties of the physical tyre structure.*

**Keywords:** *tractor, tyre, vibration, enveloping behaviour*

### **1. INTRODUCTION**

Despite high level of technological development of agricultural tractors nowadays, it is recognized that optimization of their vibration behaviour in view of human operator exposure to vibration still represents challenging engineering task [3]. Most significant vibration excitation comes from short-wavelength ground irregularities, typically encountered by agricultural tractors during field operations. Since wavelength of these irregularities is generally in the order of magnitude of tyre ground contact length, tyres deform locally due to their elasticity, thereby enveloping those irregularities. This way tyres transform real road geometry into effective vibration excitation. In order to study vehicle vibration, it is therefore necessary to address tyre enveloping behaviour in appropriate way. It is however not simple to study this mechanism using pure theoretical approach, since it is influenced by several complex phenomena such as large tyre deformations, geometric and material non-linearity, complex geometry, viscoelasticity and non-isotropic behaviour of composite material. It is therefore helpful to collect experimental data to support further theoretical investigations.

Goal of this paper is to introduce experimental setup, approach and basic results of investigations of the response of the tractor tyre that rolls quasistatically over the singular obstacle of rectangular shape. Results of investigations based on this simplified approach should subsequently serve as basis for further theoretical study and development of appropriate modeling techniques to deal with tractor tyre enveloping behaviour.

### **2. BASIC PROPERTIES OF TYRE ENVELOPING BEHAVIOUR**

If tyre rolls over uneven ground whose irregularities have wavelength of the order of magnitude



similar to tyre contact length, wheel centre will not follow exact ground geometry (as would be the case when using point-contact rigid follower instead of elastic tyre), but will travel along the path of different shape. If tyre motion happens in quasistatic manner, than tyre response (in view of the wheel centre trajectory shape) will have greater length and lower height compared to single road irregularity causing this response. This is the result of both tyre geometry and elasticity, and can be described as geometric low-pass filtering of the original road profile. Wheel centre trajectory is thereby considered effective road profile, since this motion represents real vehicle vibration excitation. This mechanism is depicted in *Figure 1*. Choosing quasistatic mode, it is possible to focus analysis purely on tyre enveloping behaviour, not taking into account tyre internal dynamics and vibration properties.

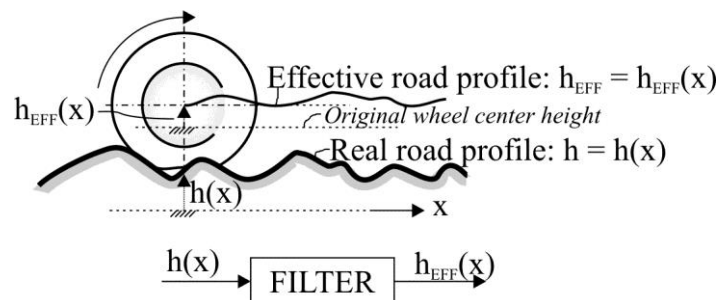


*Figure 1* Concept of effective road profile:  $h(x)$  - ground profile shape,  $h_{\text{EFF}}(x)$  - wheel centre trajectory based on  $h(x)$  and transformed by tyre filtering mechanism,  $x$  - direction of motion

In the paper [2], it was shown that quasistatic response of the tyre rolling over the singular obstacle can be approximated by superimposing two spatially shifted curves, so-called "basic functions". It was determined by experimental investigations that spatial shift between two curves grows with rising tyre load, while the shape of basic curves itself depends on the shape and size of the ground obstacle and has to be determined empirically for certain tyre and for every given obstacle. This concept is illustrated by the *Figure 2*.

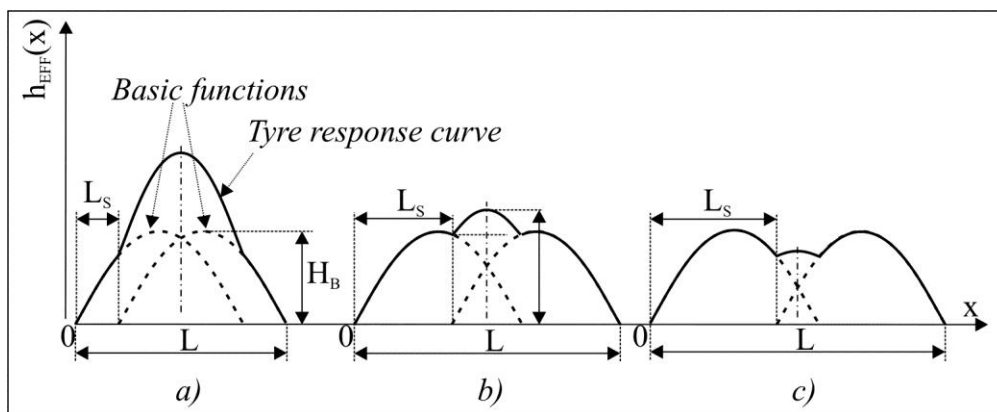


*Figure 2* Tyre response curve shape determined by two superimposed basic functions:  $x$  - wheel longitudinal motion,  $h_{\text{EFF}}(x)$  - vertical displacement of the wheel centre,  $L$  - total length of tyre response,  $L_s$  - spatial shift between basic curves,  $H_B$  - height of the single basic curve; a) light tyre load, b) moderate load, c) heavy load

### 3. EXPERIMENTAL SETUP AND METHOD

Tyre response curves were obtained by measuring horizontal and vertical displacement of the wheel rolling very slowly over the obstacle, trying to realize quasistatic conditions i.e. to avoid all kinds of



dynamic excitation of the tyre structure. Experimental facility used in these investigations is depicted in the *Figure 3*. It was described in more details in [6] and [7].

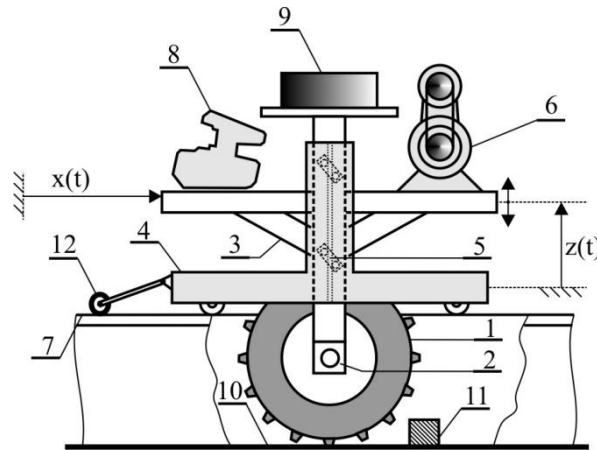


*Figure 3* Composition of the test facility: 1-tested wheel, 3-wheel mounting frame, 4-wheel guiding cart, 11-road irregularity

Experimental measurements were made with the tyre of the size 12.4R28. For ground excitation, single obstacle of rectangular shape has been selected, because results obtained this way are relatively simple for analysis, interpretation and comparison to each other. Besides, other authors have also used such approach in similar investigations, e.g. [1, 4, 5, 9]. Obstacles of following dimensions in terms of length  $\times$  height [mm] were used: 100 $\times$ 50, 200 $\times$ 50, 300 $\times$ 50, 100 $\times$ 100, 200 $\times$ 100, 300 $\times$ 100 and 200 $\times$ 150. Schematic view of the tyre rolling over obstacle is depicted in the *Figure 4*, with length and height of the obstacle denoted  $L_{\text{Obst}}$  and  $H_{\text{Obst}}$  respectively.

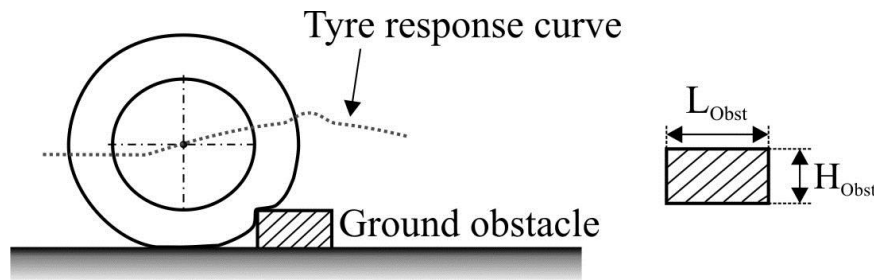


*Figure 4* Response of the tyre rolling over rectangular obstacle

Effect of varying tyre load was obtained by using different pressure values, because in [8] it was shown that tyre contact length can be used as singular parameter of enveloping behaviour, comprising effects of both load and pressure. Therefore tyre load was kept constant and three level of tyre pressure were used so as to obtain three levels of contact length [mm]: 280, 330 and 380. For every obstacle, measurements were carried out using all of these conditions. Significant level of result fluctuations was observed, so in order to compensate for this, every measurement was carried out 10 times.

#### 4. RESULTS AND DISCUSSION

Results of measurements are shown graphically in the *Table 1*. Since quasistatic response is not influenced by internal damping of tyre structure, response curve should be symmetrical assuming that radial tyre elasticity is distributed evenly, with vertical axis of symmetry passing through the



middle of the obstacle, i.e. also of the response curve itself. This property is depicted in the *Figure 5*. Taking this into account, it was deemed appropriate to represent results only through first halves of obtained curves shown in the *Table 1*.

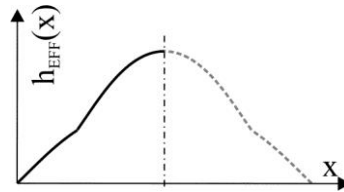


*Figure 5* Symmetry of the tyre response curve

*Table 1* Results of the measurements: dimensions of obstacles ( $L_{Obst} \times H_{Obst}$ ) denoted below graphs

Contact length: 280 mm	Contact length: 330 mm	Contact length: 380 mm

In order to quantify experimental results, main dimensions of curves shown in the *Table 1* are given in the *Table 2*.



Table 2 Main dimensions of obtained curves

	Tyre contact length: 280 mm			
Obstacle length × height [mm]	100×50	300×50	300×100	200×150
Half response length [mm]	350	450	520	530
Response height [mm]	32÷38	52	98	140
	Tyre contact length: 330 mm			
Obstacle length × height [mm]	100×50	300×50	200×100	300×100
Half response length [mm]	380	490	500	550
Response height [mm]	10÷26	50	90	95
	Tyre contact length: 380 mm			
Obstacle length × height [mm]	100×50	200×50	100×100	200×150
Half response length [mm]	380	450	560	580
Response height [mm]	12	18÷35	25÷35	100

Measurement results exhibited fluctuations, which though varied strongly between individual measurements. In some cases repeatability of obtained curves was high, while in other cases there was more fluctuations, and there were also some cases exhibiting bifurcation. To address the origin of these fluctuations, it should be started from the point that tyre load capacity is based on two main mechanisms: first, on mechanical properties of viscoelastic tyre structure (structural load capacity), and second, on pressurized air inside the tyre (pneumatic load capacity). One can expect that structural component is more prone to giving rise to fluctuations, due to effects such as e.g. non-homogenous distribution of tyre radial elasticity, or internal viscoelastic damping whose impact though could not be eliminated completely. Beside this, fluctuations can be also caused by other properties of tyre physical structure, such as e.g. deviations in tyre roundness, impact of lugs and their position with respect to the obstacle and so on. Such expectation is supported by the observation that fluctuations tended to be generally greater for larger contact length, corresponding to tyre pressure that can be considered low for given load, hence leading to greater contribution of structure load capacity to tyre response with regard to the share of pneumatic load capacity.

Further, measurement results for bigger ratio  $H_{\text{Obst}} / L_{\text{Obst}}$  were generally also characterized by more pronounced fluctuations. This condition means larger local deformations, which generally again stresses role of structure load share in overall tyre response. This further supports original assumption about impact of physical tyre structure of tyre on results fluctuations.

Another important observation that was made is that height in the middle of the response curve, obtained in case of contact length of 380mm, for obstacle 100×50mm, had negative value. This indicates degressive change of tyre radial elasticity vs. deflection.

## CONCLUSIONS

In this paper experimental setup and basic investigation results are shown for tyre enveloping behaviour. Investigations were carried out using single obstacle of rectangular shape as ground excitation profile. Results show typical forms of enveloping curves, which can be used to support further theoretical investigations of this phenomena or to develop appropriate physical or empirical models of tyre enveloping behaviour. Impact of tyre load on the response form was clearly determined, whereby load change was simulated by change of tyre pressure. It was observed that tyre radial stiffness changes degressively with deflection, diminishing after reaching certain



# INTERNATIONAL SCIENTIFIC CONFERENCE ON ADVANCES IN MECHANICAL ENGINEERING

12-14 October 2017, Debrecen, Hungary



maximum. In many cases results exhibited significant fluctuations, which can most probably be attributed to mechanical properties of the physical tyre structure. These fluctuations have in any case to be appropriately averaged if used for modelling or model parametrization.

## REFERENCES

- [1] Badalamenti, J. M., Doyle, G. R.: *Radial-Interradial Spring tyre Models*. Journal of Vibration, Acoustics, Stress and Reliability in Design, 110(1), 70-75., 1988.
- [2] Bandel, P., Monguzzi, C.: *Simulation model of the dynamic behavior of a tyre running over an obstacle*. tyre Science and Technology, 16(12), 62-77., 1988.
- [3] Scarlett, A.J. et al: *Whole-body vibration on agricultural vehicles*. Research report, Silsoe Research Institute and RMS Vibration Test Laboratory for the Health and Safety Executive, HSE Books, Silsoe, 2005.
- [4] Schlotter, V.: *Einfluss dynamischer Radlastschwankungen und Schräglaufwinkeländerungen auf die horizontale Kraftübertragung von Ackerschlepperreifen*. Dissertation, Universität Stuttgart, 2005.
- [5] Schmeitz, A. J. C.: *A Semi-Empirical Three-Dimensional Model of the Pneumatic Tyre Rolling over Arbitrarily Uneven Road Surfaces*. Doctoral thesis, Delft University of Technology, 2004.
- [6] Stojić, B., Poznanović, N., Poznić, A.: *Research and Modeling of the Tractor tyre Enveloping Behavior*. Journal of Vibration and Control, Volume: 23 issue: 2, page(s): 290-304., 2017.
- [7] Stojić, B., Poznić, A.: *Determination of Basic Mechanical Parameters of the Tractor Tyre by Using Universal Approach*. 9th International Symposium "Machine and Industrial Design in Mechanical Engineering", Balatonfüred, HU, FTN Novi Sad, 49-54., 2016.
- [8] Stojić, B.: *Istraživanje mogućnosti korišćenja kontaktne dužine traktorskog pneumatika kao jedinstvenog eksploatacionog parametra envelope kretanja*. Traktori i pogonske mašine 19(3), str. 23-28., 2014.
- [9] Zegelaar, P. W. A.: *The Dynamic Response of Tyres to Brake Torque Variations And Road Unevennesses*. Doctoral thesis, Delft University of Technology, 1998.



## DIELECTRIC FLUIDS APPLIED DURING ELECTRICAL DISCHARGE MACHINING

*STRAKA Luboslav PhD, DITTRICH Gabriel*

*Technical University of Kosice*

*E-mail: [luboslav.straka@tuke.sk](mailto:luboslav.straka@tuke.sk), [gabriel.dittrich@tuke.sk](mailto:gabriel.dittrich@tuke.sk)*

### **Abstract**

*Electrical discharge machined is currently one of the actively developing machining methods. In technical practice, it is often used for machining high strength, electrically conductive materials. By means of electroerosive machining, for example, complicated shapes of mold cavities for the casting of pressurized metals, molds for injection molding, cutting tools, and the like can be produced. The quality of the cut surface by electrical discharge machining is dependent on several factors. In addition to setting the main technological parameters (MTP) and process parameters (PP) it depends also on the properties of the dielectric fluid used. The paper deals with the influence of selected properties of the dielectric fluid quality machined surface by electrical discharge machining.*

**Keywords:** *electrical discharge machined (EDM), main technological parameter (MTP), process parameters (PP), dielectric fluid, quality of the machined surface*

### **1. INTRODUCTION**

EDM currently has an important position between progressive machining. Its long-lasting development has reached a level from which it can compete with the very precise technologies of machining metal materials. It is particularly distinguished by the high geometric precision of the machined surface [1] and by the high quality of the machined surface in terms of roughness parameters [2]. In practice, it is mainly used as the final machining technology [3], but also as the primary technology in tool making. The quality of the machined surface after EDM is influenced [4] by a number of factors. These include the main technological parameters (MTP) and process parameters (PP), but also the properties of the dielectric fluid.

### **2. BASIC CHARACTERISTICS OF DIELECTRIC FLUIDS USED IN EDM**

Dielectric fluid (or dielectric) refers to a fluid with high electrical resistance. It is a fluid that leads very little or no electrical current at all. The condition is that its electrical conductivity is less than  $150 \mu\text{S} \cdot \text{cm}^{-1}$ . Modern EDM equipment operate with a dielectric fluid whose electrical conductivity values range from 1 to  $10 \mu\text{S} \cdot \text{cm}^{-1}$ . Parameters of electrical conductivity of the dielectric fluid change during machining, therefore it is necessary to modify them. Editing is done using devices that are part of the EDM machine. Another important parameter of the dielectric fluid is its acidity. It is necessary that the pH be in the range of 7.5 to 8.5. At present, two types of dielectrics are the most commonly used. There are dielectrics based on deionized water and oil-based dielectrics. The use of a particular dielectric type depends on the machining method. In the case of undemanding EDM operations [5], it is preferable to use a dielectric on the basis of deionized water. This type of dielectric is entirely sufficient to isolate the electrical discharge between the tool and the workpiece, to ensure sufficient intensity of their cooling and leaching of electro-erosion products. Its advantage



is mainly ecologically clean operation, high chemical stability and a favourable price. Modern electrical discharge machines are equipped with a device for the treatment of deionized water. It is adjusted by means of filters filled deionization resin. This ensures the required properties and purity for electrical discharge machining. The disadvantage of deionized water is its corrosive aggression. This is particularly true for metal workpieces made of tool steels and high-speed steels during long machining times. For this reason, various anti-corrosion preparations are added to the dielectric fluid to prevent or at least reduce the impact of corrosion during machining. [6]

The second comparatively frequently used type of dielectric fluid is an oil-based dielectric [7]. This type of dielectric is mainly used in the production of parts where great emphasis is placed on the dimensional accuracy and the quality of the machined surface. The main advantage of using this type of dielectric is to prevent corrosion during and after EDM. This property is a major factor, especially in the case of long-term machining, which ranges in a matter of tens of hours. However, oil-based dielectrics also have a number of disadvantages. This is mainly about reduced productivity, worse rinsing properties and higher operating costs. The productivity of the machining process is reduced in comparison to the deionized water dielectric mainly due to the use of lower discharge electric currents. Reducing the discharge energy results in a reduction of the gap between the tool and the workpiece of the so-called gap, which is reflected by the reduction of the feed rate. However, in general, at the same rate of discharge energy, the quality of the eroded surface in terms of roughness parameters using an oil-based dielectric is better than the surface quality made using a dielectric on the basis of deionized water. [8] Another disadvantage of the use of dielectric fluids based on oil, the risk of ignition during machining. Therefore, when using this type of dielectric is necessary during electrical erosion observe a series of security measures.

### 3. REQUIREMENTS FOR PROPERTIES OF DIELECTRIC FLUIDS USED IN EDM

On the dielectric fluids used in EDM is asked a series of specific requirements. One of the basic requirements for the properties of dielectric liquids is their desired electrical resistance and pH. Only with respect to the limit values of these parameters can the dielectric provide the necessary deionization of the discharge channel between the tool electrode and the workpiece. The overview of the requests required on the features of the water-based dielectric fluid used in the EDM is shown in the *Table 1*.

*Table 1* Basic requirements for the water-based dielectric fluid properties

Required property	Parameter value
<i>Electrical conductivity</i>	⇒ $\leq 150 \mu\text{S} \cdot \text{cm}^{-1}$
<i>Neutrality</i>	⇒ value pH $7,5 \div 8,5$
<i>Purity</i>	⇒ the most suitable filtered water without particles of organic origin (deionized = demineralized water)
<i>Content of chemical elements</i>	⇒ chlorides $\text{Cl}^- < 20 \text{ mg} \cdot \text{l}^{-1}$ ⇒ sulphates $\text{SO}_4^{2-} < 20 \text{ mg} \cdot \text{l}^{-1}$ ⇒ hardness $\text{Ca}^{2+} < 120 \text{ mg} \cdot \text{l}^{-1}$ ⇒ inappropriate presence of NaCl, especially chlorine content

In addition to the deionization of the discharge channels, it is also the role of the dielectric fluid to remove the eroded material particles from the gap between the tool electrode and the workpiece. For this reason, its viscosity is also an important feature. It plays an important role especially in dielectric fluids based on oil. The following *Table 2* shows an overview of selected physical properties of an oil-based dielectric fluid used in EDM.



Table 2 Selected physical properties of an oil-based dielectric fluid

Property	Parameter value
Electrical conductivity	⇒ $\leq 1 \mu\text{S} \cdot \text{cm}^{-1}$
Density at 15 °C	⇒ 0,7 - 0,9 g.cm <sup>-3</sup>
Viscosity at 40 °C	⇒ 1,0 - 4,0 mm <sup>2</sup> .s <sup>-1</sup>
Flash point °C	⇒ 80 - 120 °C
Burning point °C	⇒ 120 - 150 °C
Content of aromatics	⇒ < 0,01%
Acid number (mgKOH/g)	⇒ Max 0.02

The required properties of the dielectric liquids both on the water and the oil basis used in the EDM can be summarized in the following points:

low electrical conductivity of the dielectric fluid that provides the required resistance between the tool and the workpiece so that the passage of the current between them results in a discharge; low viscosity and good wettability for rapid recovery of work gap insulation between tool and workpiece during individual discharge cycles; required pH value and high chemical neutrality to minimize corrosion of the workpiece; a sufficiently high flash point of the dielectric fluid to prevent its self-ignition; sufficient chemical stability of the dielectric fluid during electro-erosion with respect to poisonous gas release and unpleasant odor; the chemical elements contained in the dielectric fluid do not interfere with the integrity of the surface of the workpiece or tool electrode.

The use of a particular type of dielectric fluid for a particular EDM operation in addition to the properties mentioned above also determines its availability, production and operating costs.

#### 4. EFFECT OF DIELECTRIC FLUID ON THE SURFACE QUALITY AFTER EDM

The type as well as the quality of the dielectric fluid itself have a significant impact on the performance and the resulting quality of the machined surface in terms of roughness parameters  $R_a$  and  $R_z$ . Due to the electro-erosion process, the dielectric fluid is polluted by the electro-erosion products as well as the tool electrode as well as the workpiece. Therefore, in order to maintain the desired properties of the dielectric fluid during EDM, it is necessary to continuously modify it. As a result of contamination of the dielectric fluid may result in decreased performance electroerosion process by 50%. In rare cases, extensive contamination of the dielectric fluid can lead to an interruption of the electro-erosion process. This adverse effect is manifested mainly at the greater depths and complicated shapes of the tool electrode, where removal from the eroded metal particles is more difficult. This leads to a reduction in the MRR. In some cases, the electro-erosion process may be completely stopped due to pollution. In the following *Figure 1*, a change in the performance of the electroerosion process defined by the MRR parameter can be observed as well as the change in the quality of the machined surface in terms of the roughness parameter  $R_a$  using a water and oil based dielectric fluid.

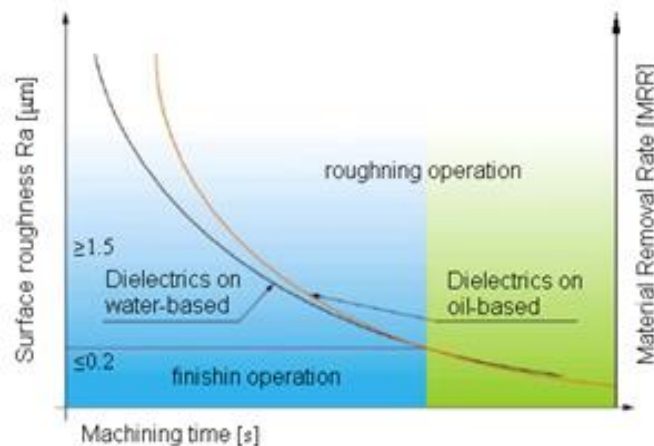


Figure 1 Influence of water and oil based dielectric fluid to change the quality of machined surface in terms of roughness parameter Ra and change of MRR power parameter

As mentioned above, the quality of the machined surface varies depending on the type of dielectric fluid used. From the graphical dependence on Figure 1, it can be observed that in fine finishing EDM operations ( $Ra \leq 0.2 \mu\text{m}$ ) the roughness parameter Ra of the machined surface is almost identical when using a dielectric fluid based on both water and oil. However, a substantial difference in final quality occurs at higher outputs, i.e. for roughing EDM operations ( $Ra \geq 1.5 \mu\text{m}$ ). It can be observed that at the same length of machining time, we will achieve higher MRR performance using an oil-based dielectric fluid compared to a water-based dielectric fluid. However, the higher performance achieved is at the cost of a higher roughness value of the machined surface Ra.

## CONCLUSIONS

The resulting quality level of machined surface after EDM is, in addition to the main technological parameters (MTP) and process parameters (PP), also dependent on the physical and chemical properties of the dielectric fluid used. Its inappropriate parameters have a significant negative impact on one of the most important qualitative indicators of the machined area, i.e., to the roughness parameter. In addition, the type and quality of the dielectric fluid has an impact on the roughness parameters also on the performance of the electro-erosion process itself. The aim of the paper was to point out the importance of a suitable choice of the type and parameters of dielectric fluid for individual EDM operations. It compares the influence of dielectric fluid based on water and oil on the roughness parameter of the machined surface Ra and the performance of the electroerosive process in EDM roughing and fine finishing.

## REFERENCES

- [1] Čada, R., Zlámalič, J.: *Materials comparison of cutting tools functional parts for cutting of electrical engineering sheets*. Transactions of the VŠB, Technical University of Ostrava, Mechanical Series, LVIII/1, 1892., 2012.
- [2] Kiyak, M., Cakir, O.: *Examination of machining parameters on surface roughness in EDM of tool steel*. Journal of Materials Processing Technology, 1-3, 141-144., 2007.
- [3] Saha, S.K., Chaudhary, S.K.: *Experimental investigation and empirical modeling of the dry electrical discharge machining process*. International Journal of machine tools and manufacturing, 49, 297-308., 2009.



# INTERNATIONAL SCIENTIFIC CONFERENCE ON ADVANCES IN MECHANICAL ENGINEERING

12-14 October 2017, Debrecen, Hungary



- [4] Sidhom, H. et al.: *Effect of electro discharge machining (EDM) on the AISI316L SS white layer microstructure and corrosion resistance*. The International Journal of Advanced Manufacturing Technology, 1-4,141-153., 2012.
- [5] Singh, S., Maheshwari, S., Pandey, P.C.: *Some investigations into the electric discharge machining of hardened tool steel using different electrode materials*. Journal of Materials Processing Technology, 149, 272–277., 2004.
- [6] Straka, L.: *Analysis of Wire-Cut Electrical Discharge Machined Surface, Study of Heat-Affected Zone Depth in Wire-Cut Electrical Discharge Machined (WEDM) Surface with Brass Electrode*. LAP LAMBERT Academic Publishing, Saarbrücken, 108., 2014.
- [7] Straka, L., Hašová, S.: *Prediction of the heat-affected zone of tool steel EN X37CrMoV5-1 after die-sinking electrical discharge machining*. Proceedings of the Institution of Mechanical Engineers, Part B: Journal of Engineering Manufacture, 1-23., 2016.
- [8] Straka, L., Čorný, I., Piteľ, J., Hašová, S.: *Statistical Approach to Optimize the Process Parameters of HAZ of Tool Steel EN X32CrMoV12-28 after Die-Sinking EDM with SF-Cu Electrode*. Metals, 7(2), 1-22., 2017.



## IMPROVING RELIABILITY INDICATORS OF TECHNICAL SYSTEMS

*STRAKA Luboslav PhD, DITTRICH Gabriel*

*Technical University of Kosice, Slovakia*

*E-mail: [luboslav.straka@tuke.sk](mailto:luboslav.straka@tuke.sk), [gabriel.dittrich@tuke.sk](mailto:gabriel.dittrich@tuke.sk)*

### **Abstract**

*The main priority of the designing technical systems is their high quality and reliability. These aspects ensure required safety and durability throughout running of the enterprise. Reliability of technical systems is 60% to 70% already predestined in the designed phase. During running of the technical system it is possible to influence its reliability only to the minimum extent of upgrade. However, all upgrades which were made during the use technical systems are much more costly than those which would have been done during its design or correction adjustments during their production. The article describes the individual possibilities of increasing selected indicators of reliability of technical systems both in the design stage and in the phase of their operation.*

**Keywords:** *reliability, safety, technical system (TS), operation.*

### **1. INTRODUCTION**

The overall reliability of the technical systems is already predestined in the designed phase. It can be partially corrected during construction in various constructions or more precisely system edits. All adjustments which were made to increase the reliability of the technical systems after the production phase (its physical realization) substantially increase the cost of securing the technical system. At the same time increasing the lack of the reliability of the technical system until its operational phase is in many cases very complicated and demanding and in some cases impossible.

### **2. IMPROVING THE RELIABILITY INDICATORS OF TECHNICAL SYSTEMS AT THE DESIGN STAGE**

In general, increasing the reliability of technical systems at design stage can be characterized as the combination of all activities aimed at achieving the required level of important reliability indicators. [1] It is usually an attempt to achieve as low a value as possible of the failure rate  $\lambda$ . This also improve the values of all important reliability indicators such as the probability of running of the enterprise  $R(t)$  without any breakdowns, the likelihood of failure  $Q(t)$ , the average time to failure or more precisely between disorders  $T_s$ , guaranteed operating time  $T_\alpha$  and others. To reduce the resulting value failure rate  $\lambda$  of technical system has a meaning only in some cases. At a certain stage of increasing the reliability of the technical system there is only a minimal decrease in the failure rate parameter  $\lambda$ , but its production costs are substantially increasing. [2] For this reason, it is necessary to increase the reliability of the technical systems at the design stage to optimize with regard to their economic efficiency of production.

One of the relatively effective ways to increase reliability of the technical systems at design stage is to design its structure from elements with favourable confidence indicators. [3] It is also necessary to choose the minimum necessary set of technical means that are necessary fulfil the required range and the quality of its functions. It is extremely undesirable to implement superfluous or even unnecessary elements into the system that would reduce the reliability of the system as a whole.



During the calculation of important indicators of reliability is largely considered, the series and parallel of reliability model or more precisely, with their combination. [4] Reliability of the serial system is generally dependent on the reliability of the weakest system locations, i.e. from those with the highest probability of failure  $Q(t)$ . [5] Therefore, if we want to improve the overall reliability of the technical system, the change must be necessarily performed with its weakest elements. This means that we replace the elements with high failure rate  $\lambda$  behind the elements with lower failure rate. Only after we can achieve an increasement in the reliability of the system as a whole without backup. To obtain components with low failure rate is possible with e.g. implementation more advanced technology production. [6] However, we can find here a number of limiting factors. These are mainly the mechanical, physical and chemical properties of the materials used as well as the limitations of the currently [7] available manufacturing technologies.

Improving the reliability of the technical system in the design phase without the usage of backup elements can be achieved:

a) by decreasing the value of the failure rate  $\lambda_i$  of the individual elements of the technical systems, i.e. using higher quality elements than standard (elements for which the reliability tests are performed or are screened by screening tests).

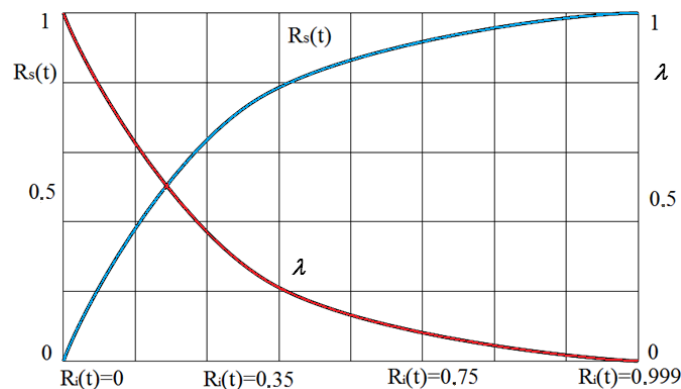


Figure 1 An example of a reduction the total failure rate  $\lambda$  of a technical system composed of  $n$  substantial elements by replacing them with elements with a higher probability of survival  $R(t)$

where:  $R_s(t)$  – is a probability of survival of the technical system,  $\lambda$  - total failure rate of the technical system,  $R_i(t)$  – the probability of survival of the  $i$ -th element of the technical system,  $n$  – number of elements of the technical system in serial involvement.

b) by minimizing the total number of  $n$  substantial elements of the technical system in serial connection,

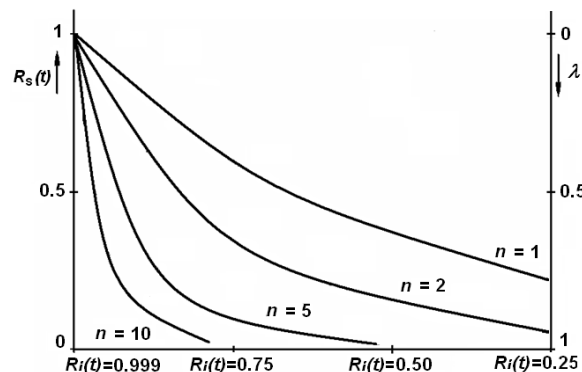


Figure 2 An example of reducing the total failure rate  $\lambda$  of the technical system by reducing the number  $n$  of the substantial serial links of elements and subsystems



where:  $R_s(t)$  is a probability of survival of the technical system,  $R_i(t)$  – the probability of survival of the  $i$ -th element of the technical system,  $n$  – number of elements in serial connection,  $\lambda$  – total failure rate of the technical system.

If all the available means and procedures have been utilized to minimize the partial failure rate of the individual elements of the technical system, but even if the required overall reliability of the technical system [8] in the design phase has not yet been achieved, the other option is to back up the selected elements. In essence, it is about the application of additional elements, or more precisely technical means whose main task is to substantially increase the reliability [9] of the technical system as a whole.

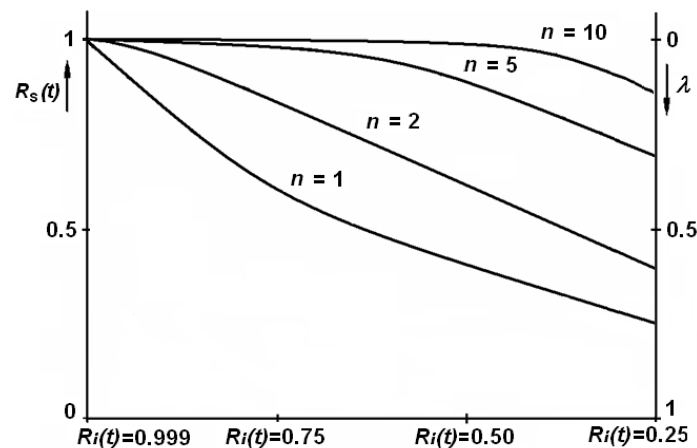


Figure 3 An example of reducing the total failure rate  $\lambda$  of the technical system through by backing up the weakest elements

where:  $R(t)$  – is a probability of survival of the technical system,  $R_i(t)$  – the probability of survival of the  $i$ -th element of the technical system,  $n$  – number of elements in serial connection,  $\lambda(t)$  – total failure rate of the technical system.

According to the mutual relationship of the basic and the backup element of the technical system we distinguish configurable and functional backups. During application configurable backup the reserved elements of the same type are backed up. The advantage of this type of backup is conceptual simplicity, which it predestines for more frequent usage. [10] The second relatively common type of backup is a functional backup, where a backup element of another type is added to the backed element. [11] The condition of the usability (functionality) of this type of backup is that all backup elements [12] must be able to perform the same or at least a similar function which is performed by the basic (main) element of the technical system.

When selecting a specific backup method and the type of the backup element, it is necessary to rely on the admissibility or more precisely inadmissibility of the short-term disruption of the serviceability of the technical system as a whole. If are asked increased requirements for trouble-free operation of the technical system, it is appropriate to use a configuration backup of elements or more precisely subsystems in combination with static backups. For example, in vital technical systems, will usually become used to it backups by the entire independent system, although much better results show backup of individual elements. If a short-term failure or more precisely short-term interruption of operation is allowed during the operation of the technical system, then it is preferable to use a functional backup of the elements or subsystems in combination with dynamic (substitution) backup method. In this case, it is best to exclude critical elements and back up only the weakest places in the system.



### 3. IMPROVEMENT OF RELIABILITY INDICATORS OF TECHNICAL SYSTEMS IN THE OPERATIONAL PHASE

As it was mentioned earlier, the additional increase the reliability of the technical systems putted into service is in practice many times technically and economically very difficult. Unfortunately, in some cases, even impossible. However, if it is necessary to increase the reliability of the technical system putted into service, we have to approach each of the technical systems individually. The simplest way is to replace the weakest elements of the technical system with elements which have lower failure rate  $\lambda$ . However, if it is not about the older technical system, but it is almost a new system where all available means have been used to ensure the highest possible reliability, this method is unlikely to be applied. [13] The second option, which is financially more expensive, is the additional application of backup elements. The main constraint is the spatial arrangement and the volume increase of the structure here. The third possibility of increasing the reliability of the technical system putted into service is a suitable modification of its operating mode and the appropriate choice of the system of planned preventive maintenance of its individual elements. [14] This is mainly about limiting the established operating modes e.g. by reducing the mechanical, electrical, thermal, chemical load of the technical system. These partly reduce the adverse impact of attrition and also partially eliminating the aging of its individual elements. In general, this method can be considered as ideal and at the same time financially not a very demanding way to maintain the technical system, preferably in the longest possible operating condition.

### CONCLUSIONS

The main aim of the article was to describe the various possibilities of improvement selected indicators of reliability of technical systems in the design phase, but also after their commissioning. As it was mentioned in the article, by improving selected indicators of reliability of the technical system it is important to decide whether it is beneficial to increase the system's passive reliability or to choose to back up essential elements of the technical system. The first way to increase the reliability of the technical system can be used in case that for various reasons, such as spatial, the number of system elements cannot be increased. At the same time, it is a more economical option. In the case of choice to increase the reliability of the technical system in the form of a deposit, i.e. by inclusion redundant elements or even entire subsystems, it is important to choose the backup type. It is also crucial whether increased requirements for faultless operation of the technical system are required or not. If the increased requirements for trouble-free operation of the technical system are required, it is recommended to use a configuration backup of elements or subsystems in combination with static backups. If the increased requirements for trouble-free operation of the technical system were not required, it is recommended to use a functional backup of elements or subsystems in combination with a dynamic (substitution) backup method.

### REFERENCES

- [1] Bigoš, P., Faltinová, E.: *Reliability of technical systems. Spoľahlivosť technických systémov (in Slovak)*. TU Košice, 171., 2011.
- [2] Birolini, A.: *Reliability Engineering: Theory and Practice*. Springer, 630., 2014.
- [3] Dhillon, B.S.: *Reliability, Quality, and Safety for Engineers*. CRC Press, 240., 2004.
- [4] Fabian, S., Straka, Ľ.: *Operation of production systems. Prevádzka výrobných systémov (in Slovak)*. FVT Prešove, 252., 2008.



# INTERNATIONAL SCIENTIFIC CONFERENCE ON ADVANCES IN MECHANICAL ENGINEERING

12-14 October 2017, Debrecen, Hungary



- [5] Fabian, S., Straka, Ľ.: *Theory of products reliability and systems in application examples. Teória spoľahlivosti výrobkov a systémov v aplikačných príkladoch (in Slovak)*. TU Košice FVT Prešov, 106., 2007.
- [6] Kahancová, E.: *Reliability and Diagnostics. Spoľahlivosť a diagnostika (in Slovak)*. ES VŠT Košice, 1989.
- [7] Kreidl, M., Šmíd, R.: *Technical diagnostics. Technická diagnostika (in Slovak)*. Praha, 2006.
- [8] Mykiška, A.: *Safety and reliability of technical systems. Bezpečnosť a spoľahlivosť technických systémů (in Czech)*. ČVUT Praha, 206., 2006.
- [9] Novák, M., Šebesta, V., Votruba, Z.: *Safety and reliability systems. Bezpečnosť a spoľahlivosť systémů (in Czech)*. ČVUT Praha, 195., 2003.
- [10] Straka, Ľ. Fabian, S.: *Modelling of selected reliability indicators of prototype PAM equipment. Applied Mechanics and Materials*, 460, 91-98., 2014.
- [11] Straka, Ľ., Gerková, J., Hašová, S.: *Proposal of preventive maintenance plan of experimental equipment. Key Engineering Materials*, 669, 523-531., 2016.
- [12] Straka, Ľ.: *Operational reliability of mechatronic equipment based on pneumatic artificial muscle. Applied Mechanics and Materials*, 460, 41-48., 2014.
- [13] Straka, Ľ., Fabian, S.: *Modelling of selected reliability indicators of prototype PAM equipment. Applied Mechanics and Materials*, 460, 91-98., 2014.
- [14] Stodola, J.: *Operation reliability and diagnostic. Provozní spoľahlivosť a diagnostika (in Czech)*. Brno, 320 p., 2002.



## RESEARCH, DEVELOPMENT AND OPTIMIZATION OF NUCLEAR TOMOGRAPHY

*SZABÓ Sándor PhD, FORGÁCS Attila, NAGY Gábor, SZIKRA Dezső PhD*

*ScanoMed Ltd. H - 4032 Debrecen Nagyerdei Körút 98*

*E-mail: [szabo.sandor@scanomed.hu](mailto:szabo.sandor@scanomed.hu)*

### **Abstract**

*We present some optimization possibilities in the field of nuclear tomography. Filtering and combination of different high voltages during X-ray screening, are presented. We show advantages of multimodal tomography, then some phantom measurements and steps for optimizing of multipinhole SPECT collection, are presented. We had prepared special phantom for optimization of tomographic imaging and with the help of the multidisc phantom we set the optimum length of palette movement during multi-pinhole SPECT collection.*

**Keywords:** *Tomography, X-ray, SPECT, PET, Optimization*

### **1. INTRODUCTION**

Nuclear tomography includes several diagnostic methods, single photon emission tomography (SPECT), positron emission tomography (PET), also combined hybrid modalities SPECT and/or PET with X-ray - computed tomography (CT) and/or nuclear magnetic resonance imaging (MRI). Nuclear tomography is an intensively developing area of medical diagnosis [1]. Wide range of diseases and organs can be detected and investigated via these techniques. Tumors, perfusion problems, heart, brain, bone diseases and all the tissue can be investigated [2]. There are several other possibilities of use nuclear methods [3]. Detection of cracks, control of impurities, check of appropriate mechanical connections and movements etc. can be performed in the different field of industry and mechanical engineering. The methods have been used in medical service for decades, but quality and features of tomography techniques, also other industrial applications of nuclear tomography are developing intensively nowadays. Research, development and optimization of methods progress in several areas, e.g.:

- Developing and optimization of detectors and detector structures.
- Developing and optimization of apertures and collimators.
- Developing and optimization of palettes, sample holders and mechanisms.
- Developing and optimization of nuclear sources, radiopharmaceuticals.
- Developing and optimization of reconstruction methods, evaluation of projections and images.
- Developing and optimization of software systems.

In this paper some innovative, new and promising results and methods will be presented. Optimization of projected images by filtering and combination of different high voltages during X-ray screening, features of hybrid, X-ray combined with SPECT & PET technology, also a possible way of optimization of modern SPECT aperture systems, will be presented.



## 2. METHODS

Nano Scan SPECT/CT and PET/MRI equipment manufactured by MEDISO Ltd. were used for preparing 2D X-ray projections and 3D X-ray (CT), SPECT and PET tomograms. In order, to investigate the role of filtering, removable 0.8mm thick (99.5%) Al sheet was used between the X-ray source and flat – detector panel. Surface of detector panel was protected with carbon fibre sheet. Special cone beam configuration was used for setting the appropriate zoom parameters. In order, to get the optimized picture, the appropriate filtered beam was prepared by 30 than 70 kV accelerating voltage. The prepared separated projection images were fusioned. Images were displayed with different color palettes, and the results were compared. MEDISO – Nucline evaluation software was used.

For presentation of advantages of the multimodal techniques, Sc-44 isotope was prepared with the elution of Ti-44/Sc-44 generator, providing activity typically in the range of 1-4 MBq [4, 5]. Morphology of Ti-44 was investigated by SPECT and dynamic process of elution of Sc-44 was tracking with PET. The holder tube of reaction, gaskets, nuts and threaded pipe ends were investigated with CT.

We used commercial, also unique phantoms for optimization of collection protocols of modern multi-pinhole SPECT aperture systems. Multi-disk phantom was created from 6 piece of Styrofoam disks (20mm thickness, 110mm diameter) placed 4mm distance next to each other. The whole setup was inserted into a hollow plastic cylinder tube. Phantom was filled with Tc-99m water solution, and imaging was performed with MEDISO triple head, multi-pinhole SPECT system. Scan parameters were 72 views, 128x128 image matrix, 0-8 cm axial bed motion. Total counts were ~100Mcts.

## 3. RESULTS

### Optimization of projected images by filtering and combination of different high voltages during X-ray screening

In most cases suggestion is to use Al filter during preparation of X-ray projections and tomograms. Filter can increase the signal to noise ratio, and can decrease the radioactive dose. With the help of filtering we can exclude the useless photons from the point of view of imaging. Filtering can increase the image quality. However, in some cases the contrast can be less appropriate, therefore we checked the role of filtering in the case of imaging of electronic, plastic, ceramic, also biological systems. In *Figure 1 A* and *B* we show projection image of an electronic microchip, performed with and without Al filter.

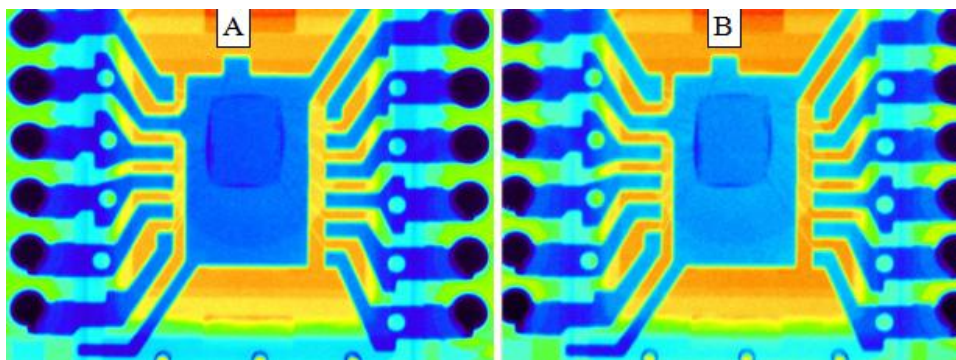


*Figure 1* Projection images about electronic microchip.  
A: prepared with Al filter. B: prepared without Al filter.



Measurements confirmed, that AI filtered images are more appropriate. Signal to noise ratio is better, and contrast is good enough to successfully separate the different characteristic areas. Since we confirmed the effectiveness of filtering, we continued the experiments with AI filtered X-ray beam, but various high voltages 30 and 70 kV were used to generate X-ray photons. After fusion of the images prepared with 30 and 70 kV, also via different color palettes, we could enhance appearance of various characteristic part of microchip. In *Figure 2 A* and *B* we present two representative results.

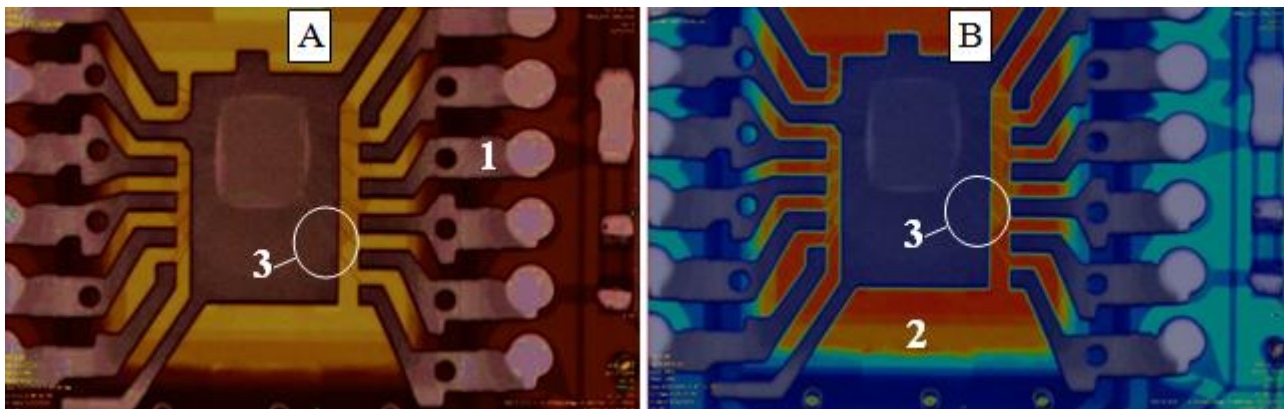


*Figure 2* Representative results after fusion of X-ray projections using 30 and 70 kV.

In *Figure 2A* the structure and defects of electronic wires, in *Figure 2B* the structure of semiconductor layers is highlighted better. Even the 0.01mm diameter details can be tested successfully. The areas marked with 1, 2 and 3 represent the above. (1 electronic wires, 2 semiconducting layers, 3 tiny connections)

#### **Advantages of multimodal, X-ray (CT) combined SPECT & PET technology:**

Extending 2D imaging, 3D images were prepared from a Ti-44, Sc-44 and plastic holder system. CT (X-ray tomography) is sensitive to the holder, and to filled granules, while with SPECT and PET technique distribution of Ti-44 and Sc-44 can be measured, respectively.

Sc-44 Removing from Titanium during elution.  
Direction of washer fluid is also signed.

Plastic holder of Ti → Sc generator.

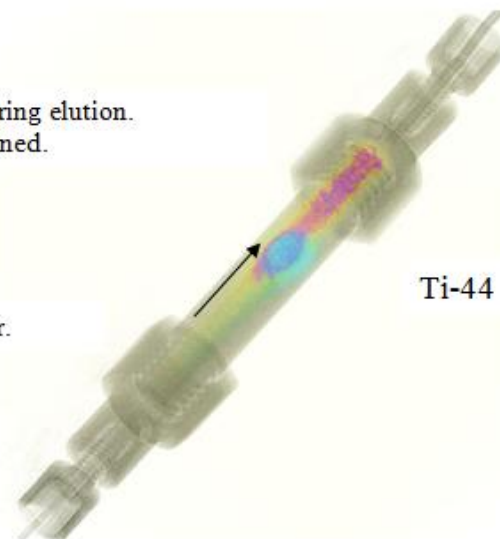


*Figure 3* Multimodal image from Ti-44, Sc-44, plastic holder system



Figure 3 represents that multimodal imaging technique can sum the features, and advantages of various modalities. In our case the CT is sensitive to the bulk high density materials, the SPECT can follow up the distribution, path and dynamics of gamma photon emitting tracers, while the PET show, dynamics and distribution of positron emitting tracers. In multimodal image, we can evaluate all the above. On the one hand, these techniques can be very useful for research and development of different industrial areas, on the other hand the development and optimization of multimodal technique, itself, is also important.

#### Possible way of optimization of modern SPECT aperture systems:

There are spectacular results within development of SPECT and multimodal SPECT technologies. Organ specific multipin-hole aperture was developed and optimized for brain investigation. In Figure 4, we present typical parameters that need to be optimized for collection.

##### Characteristic parameters to be optimised:

- Detector radius → Phantom measurement with homogeneous cylinder
- Start position → Phantom measurement with homogeneous cylinder
- Number of projections → Phantom measurement with radial „STAR phantom”
- Palette movement → Phantom measurement with multi-disc phantom

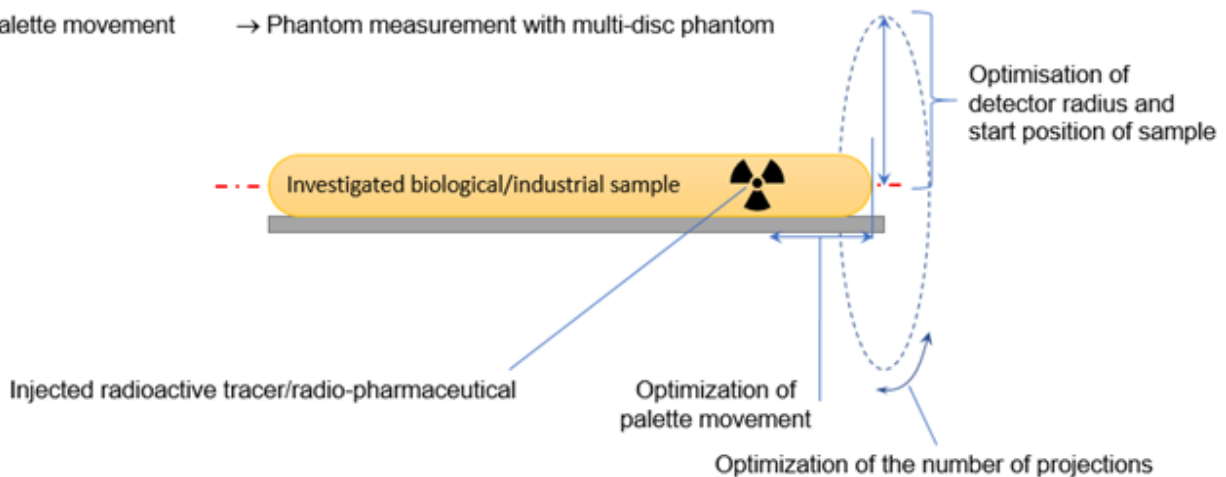


Figure 4 Characteristic parameters, need to be optimized for achieve the ideal gamma-photon collection protocol, during SPECT investigation. Phantom measurements, appropriate for optimization process are also presented.

We have prepared multidisc phantom for optimization of palette movement during tomographic imaging and measurement (Figure 5). During SPECT collection, various type sample holder/palette movement can be defined. The reconstructed SPECT image shows that display of multidisc structure is sensitive to the length of palette movement, and suitable for optimization of that. In case of not optimized length, blur and distortion artefacts appeared. If the palette moved through the optimal length, blurred and distorted areas have disappeared.

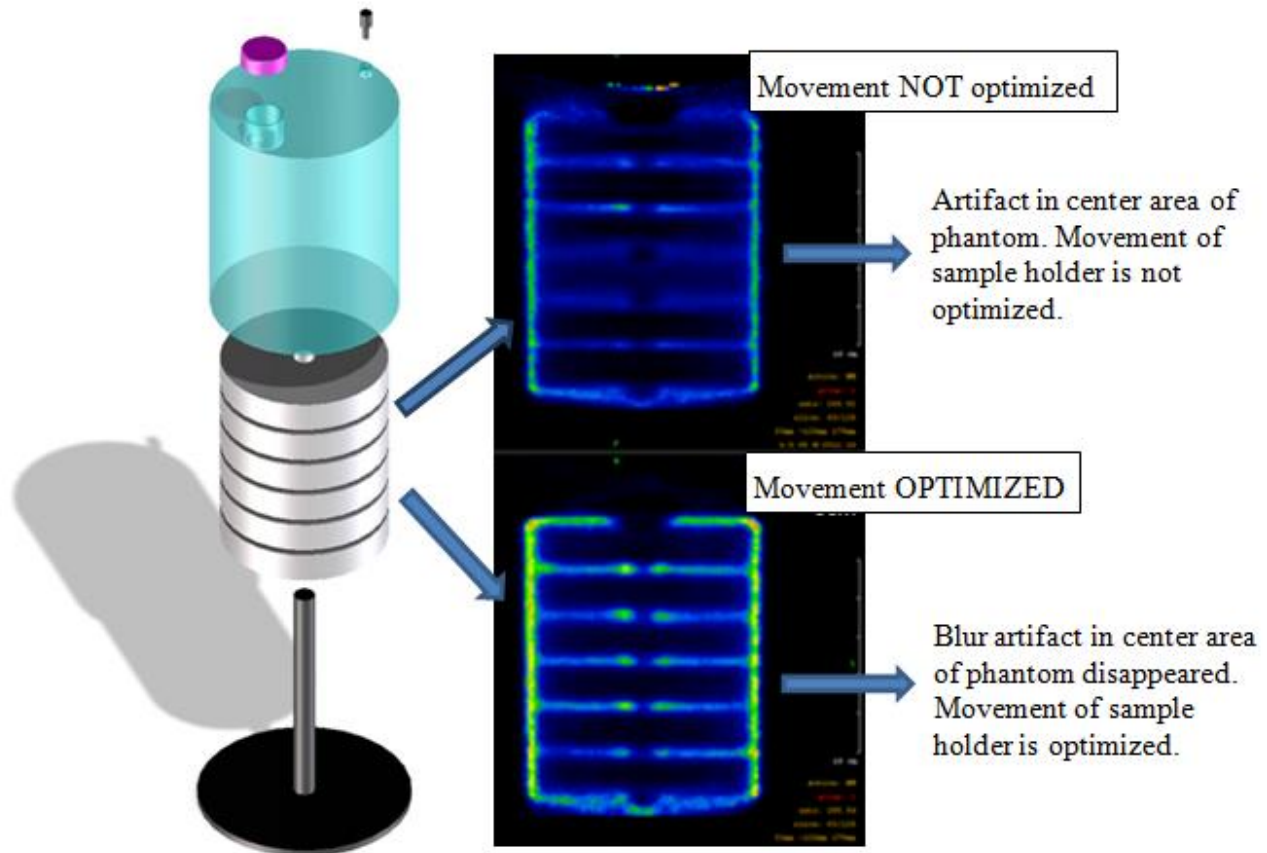


Figure 5 Multidisc phantom for optimization palette movement. The SPECT images show the blurred and distorted, also artifact free pictures from phantom, after unfit and optimized length.

## CONCLUSIONS

We presented some optimization possibilities in the field of nuclear tomography. Filtering and combination of different high voltages during X-ray screening, can optimize projections and computed tomograms. During multimodal tomography, the advantages of each method can be achieved. Phantom measurements can be appropriate for optimizing tomographic collections. Especially with the help the multidisc phantom we developed the optimum length of palette movement during multi-pinhole SPECT imaging.

## ACKNOWLEDGMENTS

Special thanks to MEDISO Ltd. for the opportunity of use nano-SPECT/CT, nano-PET/MRI and the latest Triple Head multi-pinhole SPECT equipment.

## REFERENCES

- [1] Paige, B., Umesh D. O., Andrew T. T., Akiva M.: *Diagnostic Imaging, Nuclear Medicine*. Elsevier, ISBN: 978-0-323-37753-9, 2016.
- [2] Kertész, I., Vida, A., Nagy, G., Emri, M., Farkas, A., Kis, A., Angyal, J., Dénes, N., Szabó, J. P., Kovács, T., Bai, P., Trencsényi, G.: *In Vivo Imaging of Experimental Melanoma Tumors using the Novel Radiotracer <sup>68</sup>Ga-NODAGA-Procaïnamide (PCA)*. J Cancer. 2017 Feb



# INTERNATIONAL SCIENTIFIC CONFERENCE ON ADVANCES IN MECHANICAL ENGINEERING

12-14 October 2017, Debrecen, Hungary



25;8(5):774-785. doi: 10.7150/jca.17550. e-Collection 2017

- [3] Yuri M. Tsipenyuk, David A. Bradley: *Nuclear methods in science and technology*. Fundamental and applied physics series, Institute of Physics Publishing, Bristol and Philadelphia IOP publishing Ltd. ISBN 0-7503-0422-7, 1997.
- [4] Roesch F.: *Scandium-44: Benefits of a Long-Lived PET Radionuclide Available from the 44Ti/44Sc Generator System*. Current Radiopharmaceuticals, 5, 187 – 201, Bentham Science Publishers 2012.
- [5] Nagy, G., Szikra, D., Trencsényi, G., Fekete, A., Garai, I., Giani, A., Negri, R., Masciocchi, N., Maiocchi, A., Uggeri, F., Tóth, I., Aime, S., Giovenzana, G., Baranyai, Z.: *AAZTA: An Ideal Chelating Agent for the Development of 44Sc PET Imaging Agents*. Angew. Chem.-Int. Edit 56 (8), 2118-2122., 2017.



## STRENGTH EXAMINATION OF ADHESIVE BONDED JOINTS OF STEEL AGAINST DBD TREATED PTFE AND PA66 SURFACES

*SZAKÁL Zoltán PhD, PATAKI Tamás PhD, KÁRI-HORVÁTH Attila PhD*

*Institute for Mechanical Engineering Technology, Szent István University*

*E-mail: [szakal.zoltan@gek.szie.hu](mailto:szakal.zoltan@gek.szie.hu), [tamas.pataki@gek.szie.hu](mailto:tamas.pataki@gek.szie.hu), [kari-horvath.attile@gek.szie.hu](mailto:kari-horvath.attile@gek.szie.hu)*

### Abstract

*During our work, we examined the features of the bonding of the polymers (PTFE, PA66), which are qualified as engineering material. In the course of the research we apply acrylic base and cyanoakrylate adhesives. In this work we used the DPD plasma treated of polymers of surface. The specimen of plasma treated increase the energy of surface. For qualifying the glued bonding we used specimens with lapped bonding made according to standard DIN EN 1465 and by breaking then we used tensile-test machine according to standard ISO 527-1. We make a proposal based on the results, onto the bandage forming coming close to the strength of the base material relating to the examined polymers.*

**Keywords:** *adhesion bonding, adhesive, gluing, polymer, DBD treated surface, PA66, PTFE*

### 1. INTRODUCTION

The development and adoption as well as testing of sticking technologies of machine parts made of engineering plastics [3,4,5,15,16,23] comes into the foreground rather continually. One of the main motivators of this is the industry, where the forming quick high-strength and elastic component contacts have got crucial importance. Here during production (sticking body and casing elements) and repairing (broken plastics, the bonding of windscreens) structural adhesives are used equally [2,6]. Due to this currently not only the development of polymer composites is going on, but the market of the bonding materials was transformed in the past 5-10 years totally. New and newer adhesives appear with additional surface treatment materials, which help the adhesion of cements and the increase of their strength.

The advantage of adhesion bonding:

- the constructional margin is growing,
- homogenous stress distribution,
- does not harm the structural materials,
- different structural materials can be bonded,
- may reduce the number of the machine elements,
- more aesthetic appearance.

We planned an overall experiment series, with the use of the most used engineering polymers and the new adhesion materials, with adhesives applied widespread in the industry in our present research. The adhesive substances are recommendation by Henkel Magyarország Ltd, we chose it from a product line of Loctite.

The choice of the superglue and commonly-used one expands on structural adhesives, these are acrylic bases, and in the case of the superglues cyanoacrylate types [11]. We had it in our sight at the examination of engineering polymers qualified previously not at all bonding or as bonding hardly like polyolefin [7,9], and the fluorine polymers [10,18,19,21]. With plain polymer on a surface without the special surface treatments. We carried out according to the ISO 527-1 standard



the shear test of lap joint made by the DIN EN 1465 standard with tensile-test machine. In the literature all the polyolefin [1,12,26], all the fluorine [4,19,20,23,24,25] polymer basis articles, which added a footing to our examinations, are attached to the adhesive and mechanics features of plastics [8,13,14,17].

We call those non-metallic substances an adhesive, that the firm surfaces with the surface adhesion (adhesion), and their own solidity join (cohesion). The sticking is an operation when a mediatory substance, the mucilage connects the surfaces of the solids with its help, and the peculiarities of the surfaces to be connected do not change.

The material to be bonded must fulfil two conditions:

- The mucilage has to moisten the polymer. The surface energy of plastic has to be higher or equal with the surface tension of the mucilage.
- The polymer surface must have adhesion friendly characteristics. This means that a chemical and physical interaction has to come into existence between the mucilage and the surface boundary layer.

In this case, the stock is unsuitable for gluing if these conditions do not come true, or the surfaces demand preparative treatment.

## 2. METHODS

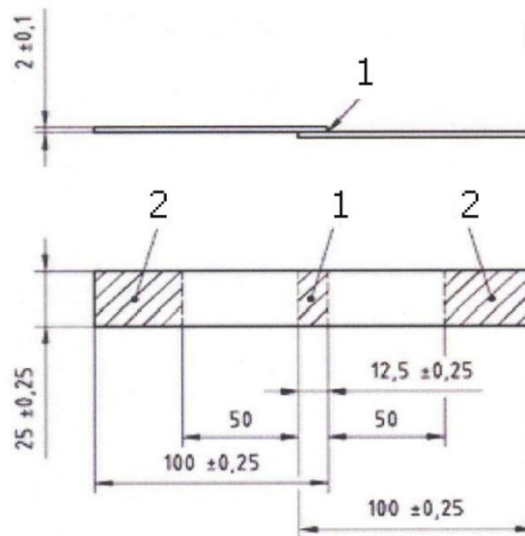
The Table 1 shows the tested materials and to them owing (the Loctite made a choice based on Technical Data Sheet (TDS) recommendation) adhesive systems. [11] We examined selected materials on the experiment series with themselves and sticking with a general construction steel. The test methods were performed on natural polymers, this was the basis of the test. The DBD plasma treatment was performed by modifying the surface energies of the polymers. On the treated specimens, the adhesive bonding shown in Table 1 was again performed.

Table 1 Gluing experiment plan

Material mates	Adhesive
PTFE - PTFE	Superglue: Loctite 406 (Cyanoacrylate)
	Structural adhesive: Loctite 3035 (acrylic)
PTFE – S235 steel	Superglue: Loctite 406 (Cyanoacrylate)
	Structural adhesive: Loctite 3035 (acrylic)
PA66 – PA66	Superglue: Loctite 406 (Cyanoacrylate)
	Structural adhesive: Loctite 9466 (epoxy)
	Structural adhesive: Multibond 330 (acrylic)
PA66 – S235 steel	Superglue: Loctite 406 (Cyanoacrylate)
	Structural adhesive: Loctite 9466 (epoxy)
	Structural adhesive: Multibond 330 (acrylic)

### 2.1. The strength tests of the bonded connections

We examine the specimens prepared for the experiment plan adequately on a tensile-test machine, according to DIN EN 1465 standard. Although the standard mentions more solutions onto the forming of the specimens, we elected the simple overlap joining. Its disadvantage, is tensile-tests that not clear shearing stress affects the gluing, identical forming is at disposal of all of the specimens at the same time. The knowledge of the absolute result is not necessary in the interest of the comparison because of this. We executed 5 repetitions in the course of our measurements.



*Figure 1* The adhesive bonding specimen and method  
1 , surface of adhesive gluing  
2, surface of clamping surface

The specimens used for the gluing were made by sawing from a 2mm thick plate in an identical size. The dimensions of the specimens are shown *Figure 1*. We fit the specimens with 12,7mm long overlap to each other, for the forming of the bandage. We chose the lap based on standard DIN EN 1465. The requirements made on the gluing of the specimens:

- simultaneously the gluing of 5 specimens,
- overlap size are  $12,5 +_{-0,1}$  mm,
- having identical compressive force,
- the specimens should not stick to the apparatus.

We bonded the specimens (what useful for tensile stress test) in the apparatus which can be seen on the *Figure 2*. We bonded two pieces of specimens can be seen on the Figure it together. We degreased the specimens with Loctite 7200 detergents before the bonding. We used Loctite 406 and Loctite 3035 adhesive gluing specimens.



*Figure. 2* The apparatus used for the gluing

The process of bonding technology:

- We cleaning the surface of specimen (Loctite 7061)
- We treated the plastic surfaces with the primer implement first.
- We the necessary adhesive placed on the specimens.
- Finish we laying on one another on the specimens.



We made the bonding according to Loctite Technical Data Sheet (TDS) regulations. The TDS grants the preparation method of gluing surface, the time of adhesive of application and his solidification time.

### 2.3 DBD plasma treats method

About DBD plasma treatment H. Al-Malaki -G. Kalacska wrote more. They investigated the relationship between surface treatment of polymers and surface energy [28].

The atmospheric pressure ambient air plasma was generated by DCSBD plasma source. The principle of DCSBD plasma is based on a coplanar DBD where comb shape electrodes are embedded in a dielectric. The diffuse plasma is generated in thin 0.3 mm thick flat layer on alumina ceramic which designates the DCSBD to be used especially for treatment of flat surfaces. The DCSBD electrode system was powered by AC HV source of frequency approx. 14 kHz and voltage approx. 20 kV peak-to-peak and the total power in plasma during the experiments was 400 W. The area of generated plasma of DCSBD is 170 cm<sup>2</sup>, thus the surface energy density and volume energy density at power of 400 W are approximately 2 W cm<sup>2</sup> and 80 W cm<sup>3</sup>, respectively. The DCSBD plasma is described in detail [27]. The plasma treatment was performed in dynamic treatment mode and the distance between the treated polymer surface and DCSBD ceramic was 0.3 mm. The treatment has been done under air atmosphere conditions (T= 23°C, H= 50%), the apparatus shown in *Figure 3*. The treatment time for each specimen was 1 min.

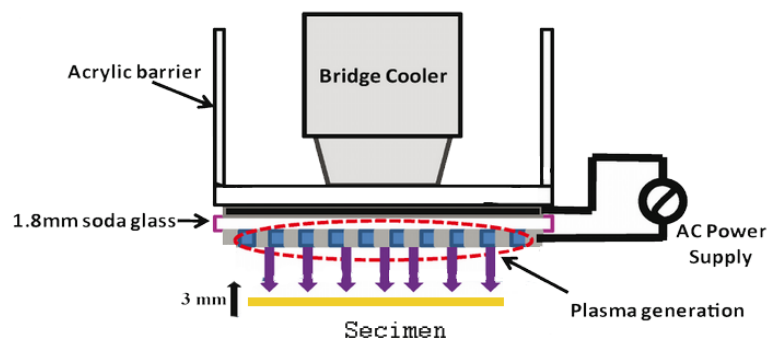


*Figure. 3* The plasma process

### 2.4 The tested materials

#### *Adhesives*

The Loctite adhesives what were used are reactionary adhesives. Their application happens in a fluent state, and they are consolidated by a reaction between the surfaces. Loctite gave the adhesives for our experiment series. Technical data of the selected adhesives Table 2. contains.

**Loctite 406:** This superglue is designed for bonding of plastics and elastomeric materials where very fast fixturing is required. His benefit, is that is resists up to 120<sup>0</sup> temperature and has got low viscosity The Loctite 770 polyolefin primer increases the gluing solidity in case of the polymers which can be sticked difficultly. His fixing time is 2-10mp. It is colourless, transparent material.

**Loctite 330:** General purpose acrylic based adhesive. Adhesive gluing for bonding plastic with good impact resistance. Two-component scrubber, a mixture of a gel-like base and a thin fluid activator. Curing time is 3 minutes. In principle, the shear strength of the bonded bond is 30 MPa.



**Loctite 9466:** Structured adhesive for increased bond strengths with increased toughness. Two-component epoxy adhesive, it is a product with 1:1 mixing ratio, that mixes during carrying up to the surface thanks its tabulated from. Suitable for bonding metals, ceramics and most plastics. The recording time is 180 minutes and pot life is 60 minutes. The maximum shear strength of the bonded bond is 32 MPa.

Table 2. Technical data of adhesives

	Loctite 406	Loctite 330	Loctite 9466
Technology	Cyanoacrylate	Acrylic	Epoxy
Chemical Type	Ethyl cyanoacrylate	Urethane methacrylate ester	Epoxy
Components	One part without mixing	One part – requires no mixing	Two component - requires mixing
Cure	Humidity	With activator	Room temperature cure after mixing
Working Time, 25 °C, (before assembly):	3min	3min	7 min
Fixture Time	5-10 sec	30 min	1 h
Full strength	24 h	6 h	24 h
Shear Strength	8-15 N/mm <sup>2</sup>	15-30 N/mm <sup>2</sup>	5-32 N/mm <sup>2</sup>

### ***The main materials***

We most important aim at the selected the materials was that witch materials is the most used in the industries. Of course the basic material was a simple structure steel. The two plastic what we toggled between the uncounted plastic what use the industry nowadays, the polytetrafluorethylene and the polyamide.

### ***Construction steel (S 235 JR N)***

The one with a general function, not alloyed one of the most widespread kinds of steels, with a low carbon content (0.17%) and tensile strength is at  $R_m = 400-500 \text{ N/mm}^2$  disposal generally. It is easily workable, because of this its use is wide-ranging. For sticking standpoint it can be put among the easily bonding materials, so for any steels in the commerce it can be used with prescribed adhesive.

### ***Polytetrafluorethylene (PTFE)***

Its construction is partly crystalline, thermoplastic substance partly. His tensile strength 16-25 MPa and the elongation 270-400 %. Because of the construction of the Teflon molecule it cannot be stucked, since the incomparably bigger one fluorine atoms surround totally the coal atoms, a cohesive contact cannot be created with adhesive substance. The chemical stability is good for the Teflon one, and sticking his anti-adhesion surface demands a special procedure.

### ***Polyamide (PA66)***

Polyamides are nitrogen-containing heteropolymeric polymers that contain -CO-NH bonds in the main chain. Polyamides are crystalline materials having a preferred mechanical property. Polyamides are capable of absorbing the water content of the air, thereby increasing their volume and reducing their strength. His material tensile strength 70-110 MPa.



### 3. RESULTS

We make known the test results carried out during research with different construction adhesive of those plastic which can be glued hardly and are widely used in practice. During our work we stucked PA66 and PTFE plastic with themselves and with construction S235 IR N steel. The tensile test diagram of the examined polymers is visible on the *Figure 4*. We summarized in the table 3. the typical polymer tensile load values.

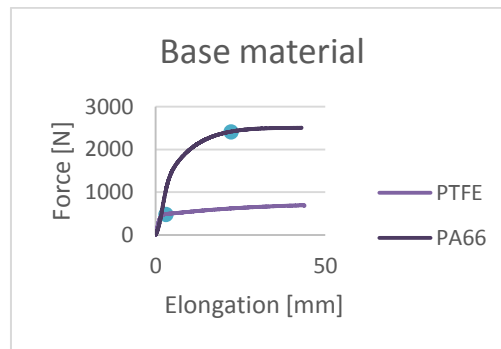


*Figure. 4* The tensile-test diagram of the base polymers

We made the tensile test according to a standard ISO 527-1. From the diagrams verifiable, that PA66 behaved rigidly in the first section, the rest of the plastic behaved toughly. The PTFE was softer, than the PA66 material, and in the second section was the plastically behaved too. The force marked (with a dot) value exceeded considerable stretching can be experienced on the tensile-test strength diagram. The specimens do not tear yet due to the metamorphosis, but their shape is lost already, this influences the solidity of the stucked bandages significantly.

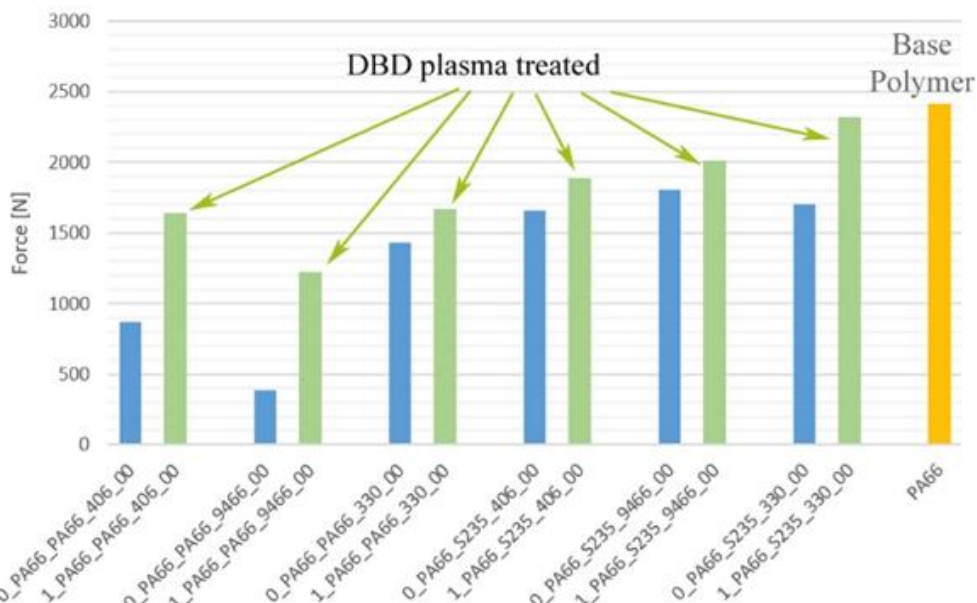


*Figure 5* The results of the PA66 and S235JRN mates with different adhesives

Adhesives 406 and 9466 are brittle, but PA66 is able to withstand a large deformation, so adhesives disengage from the plastic surface as a result of the load. The results of measurements on PA66 and PA66 are weak, as the specimens are deformed. The adhesive has been removed from the surface of



the specimens. The results of the PA66 and S234 JRN test results are good because the steel did not allow deformation. The surface of polymeric specimens was treated with DBD plasma, after which the measurement results were better. When bonding PA66 and steel specimens, the surface treatment did not provide much better breaking strength. With the increase in surface energy, the glue is more adherent to the surface of the specimen. In the polymer-polymer specimens connection, adhesives 406 and 9466 were performed very well. In practice, it is desirable to perform surface treatment on the surface of the polymers when the polymer is soft and the adhesive is brittle.

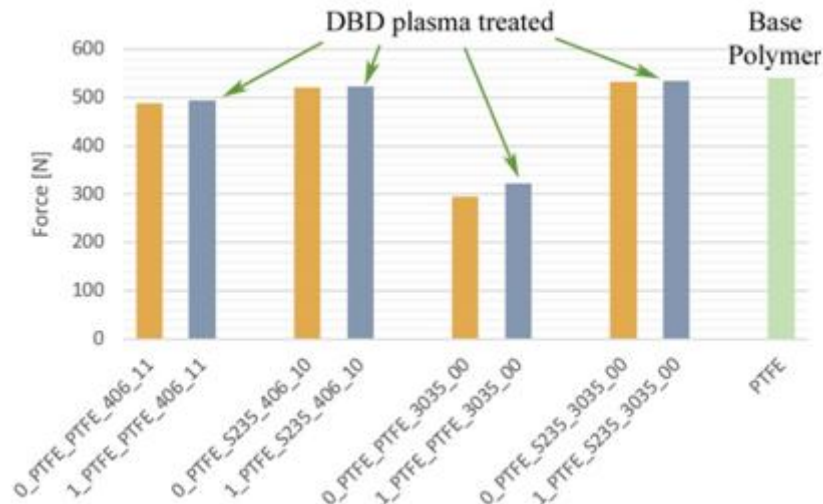


Figure 6 The results of the PTFE and S235JRN mates with different adhesives

The PTFE material has a lower strength than the PA66 polymer, it is softer. Figure 6 shows that there is no difference between the strength of the base and the treated surface test specimens. With the tested adhesives, the materials can be well glued. In the case of PTFE polymer, expensive plasma treatment is not required. This plastic is well adhesive with commercially available structural adhesives.

## CONCLUSIONS

During our present research work we made a series of experiment with the most used engineering polymers and the new adhesion adhesives applied widespread in the industry. The material choosing included to the superglues and to the structural glues used generally which house got acrylic base, epoxy basis and case of superglues they are cyanoacrylate types. We have carried out the experiments of those engineering plastics to be rated not or hardly glueable polymers (PP, UHMWPE HD1000, HD500, PTFE). Present article reports on the results of gluing experiments made on a surface, which were made without special surface treatments. In this paper we also reported on the effect of the DBD plasma surface treatment. Due to the treatment of the surface of the plastics, the bond strength increases in general.

In case of mating polymer and steel beyond choosing the adhesive, the glue must be able developing good adhesion connection with both surfaces, that adhesive should be preferred which is more optimal for the steel. Such case can take place, in the technical practice when it has to be produce glued bonding of polymer-polymer elements, beside the highest strength within reach of the given material. Then it should be consider that between the connection, made by lap it is expedient so put an intermediate rigid steel plate with this method the deformation ability of the bonding can be reduced. The smaller deformation results lower load on the glued bonding, the built in rigid part means a negligible effect so the whole structure.



For soft material, a soft glue should be used to create a strong bond. When applying soft and brittle material, use the surface treatment procedure and use a hard glue.

## ACKNOWLEDGEMENT



SUPPORTED BY THE ÚNKP-17-4 NEW NATIONAL EXCELLENCE PROGRAM OF THE MINISTRY OF HUMAN CAPACITIES”

## REFERENCES

- [1] A.M. Guedes Pinto, A.G. Magalhães, F. Gomes da Silva, A.P. Monteiro Baptista (2008) Shear strength of adhesively bonded polyolefins with minimal surface preparation International Journal of Adhesion and Adhesives, Volume 28, Issue 8, December 2008, Pages 452-456
- [2] Bernd R. Burchardt, Peter W. Merz (2006). Chapter 6 - Elastic Bonding and Sealing in Industry. Handbook of Adhesives and Sealants, Volume 2, 2006, Pages 355-480, xl-xlii
- [3] C. Ageorges Ing, MSc, PhD, L. Ye BSc, MSc, PhD (auth.)(2002).-Fusion Bonding of Polymer Composites-Springer-Verlag London (2002)
- [4] E. Stammen, K. Dilger 9 - Adhesive bonding of textiles: applications. Joining Textiles, 2013, Pages 275-308
- [5] Füzes L. (2013): Tapadási problémák műanyagok ragasztásakor, festésekor, Műanyagipari szemle 2013. 06 p.
- [6] J. Daniels (1984). Design implications of adhesive bonding in car body construction. International Journal of Adhesion and Adhesives, Volume 4, Issue 1, January 1984, Pages 5-8
- [7] Jiri George Drobny (2014). 7 - Polyolefin-Based Thermoplastic Elastomers. Handbook of Thermoplastic Elastomers (Second Edition), 2014, Pages 209-218
- [8] Ji-Zhao Liang, Qiang Du, Gary Chi-Pong Tsui, Chak-Yin Tang (2016) Tensile properties of graphene nano-platelets reinforced polypropylene composites. Composites Part B: Engineering, Volume 95, 15 June 2016, Pages 166-171
- [9] Laurence W. McKeen (2016) . 9 - Polyolefins and Acrylics. Fatigue and Tribological Properties of Plastics and Elastomers (Third Edition), 2016, Pages 261-277
- [10] Laurence W. McKeen (2016). 1 - Fluoropolymers. Fluorinated Coatings and Finishes Handbook (Second Edition), 2016, Pages 1-127
- [11] Loctite: <http://tds.loctite.com>
- [12] M. Kalnins, J. Ozolins (2002). Formation of a boundary layer of polyolefins adhesively bonded to steel. International Journal of Adhesion and Adhesives, Volume 22, Issue 3, 2002, Pages 179-185
- [13] M. Zrida, H. Laurent, V. Grolleau, G. Rio, M. Khelif, D. Guines, N. Masmoudi, C. Bradai (2010). High-speed tensile tests on a polypropylene material. Polymer Testing, Volume 29, Issue 6, September 2010, Pages 685-692
- [14] Mohammadreza Eftekhari, Ali Fatemi (2016). Tensile behavior of thermoplastic composites including temperature, moisture, and hygrothermal effects. Polymer Testing, Volume 51, May 2016, Pages 151-164
- [15] Obermayer S.(2013): Die Kunst starker Verbindungen Kunststoffe, 103. k. 6. sz. 2013. p. 78–80.
- [16] Sabreen S.R.(2011): Solving the problems of plastics adhesion. Plastics Engineering, 67. k. 4. sz. 2011. p. 6–8.



# INTERNATIONAL SCIENTIFIC CONFERENCE ON ADVANCES IN MECHANICAL ENGINEERING

12-14 October 2017, Debrecen, Hungary



- [17] P. Poelt, A. Zankel, M. Gahleitner, E. Ingolic, C. Grein (2010). Tensile tests in the environmental scanning electron microscope (ESEM) – Part I: Polypropylene homopolymers. *Polymer*, Volume 51, Issue 14, 24 June 2010, Pages 3203-3212
- [18] Sina Ebnesajjad (2015) 4 - Fluoropolymers: Properties and Structure. *Fluoroplastics (Second Edition)*, 2015, Pages 22-38
- [19] Sina Ebnesajjad (2015). 1 - Introduction to Fluoropolymers *Fluoroplastics (Second Edition)*, 2015, Pages 1-6
- [20] Sina Ebnesajjad (2015). 17 - Surface Treatment of Fluoropolymers for Adhesion. *Fluoroplastics (Second Edition)*, 2015, Pages 564-588
- [21] Sina Ebnesajjad (2015). 21 - Applications of Polytetrafluoroethylene and Fluoropolymers, *Fluoroplastics (Second Edition)*, 2015, Pages 461-478
- [22] Sina Ebnesajjad, Arthur H. Landrock (2015). Chapter 12 - Testing of Adhesive Bonds. *Adhesives Technology Handbook (Third Edition)*, 2015, Pages 339-352
- [23] Sina Ebnesajjad, Arthur H. Landrock (2015). Chapter 8 - Adhesive Applications and Bonding Processes. *Adhesives Technology Handbook (Third Edition)*, 2015, Pages 206-234
- [24] Vacuum (1980). Adhesive bonding of ion-beam-textured metals and fluoropolymers. *Vacuum*, Volume 30, Issues 8–9, 1980, Page 35
- [25] Yukihiro Kusano, Masato Yoshikawa, Itsuo Tanuma, Kazuo Naito, Masuhiro Kogoma, Satiko Okazaki (1994). Plasma surface treatment of fluoropolymers at atmospheric pressure. *Advanced Materials '93*, 1994, Pages 657-660
- [26] Zeena Cherian, Richard Lehman (2005). Effects of adhesive type and polystyrene concentration on the shear strength of bonded polystyrene/high-density polyethylene blends. *International Journal of Adhesion and Adhesives*, Volume 25, Issue 6, December 2005, Pages 502-506
- [27] Cernák M., Cernáková L., Hudec I., Kováčik D., Zahoranová A.: 2009. Diffuse Coplanar Surface Barrier Discharge and its applications for in-line processing of low-added-value materials, *European Physical Journal: Applied Physics*, Vol. 47, pp. 1-6. <http://dx.doi.org/10.1051/epjap/2009131>
- [28] H. Al-Maliki – G. Kalácska (2017); The Effect of Atmospheric DBD Plasma on Surface Energy and Shear Strength of Adhesively Bonded Polymer; *Hungarian Agricultural Engineering*, Volume 31, Pages 52-58, HU ISSN 0864-7410



## THE DEVELOPMENT OF EVALUATION SYSTEM QUALIFYING THE ITER DIAGNOSTIC CABLE CONDUIT THE AND SATISFYING THE SYSTEM REQUIREMENTS

*SZALAI Judit*

*Department of Machine and Product Design, Faculty of Mechanical Engineering, Budapest  
University of Technology and Economics*

*E-mail: [szalai.judit@gt3.bmehu](mailto:szalai.judit@gt3.bmehu)*

### **Abstract**

*In this paper we aim to reveal methods that can decrease the time spent on the mechanical elements development increasing the efficiency of the process. The challenge in this scheme is the optimization of a large number and variety of components in the ITER diagnostic system. During our work we compared the engineering requirements with the specific requirements of a fusion power plant. Our goal is to create a method that survey complex demands, accomplish evaluation and the final integration of the inspected mechanical design.*

**Keywords:** *design concept, ITER, product development, thermal-mechanical modelling*

### **1. INTRODUCTION**

The ITER's (International Thermonuclear Experimental Reactor) mission is to demonstrate the feasibility of fusion power and prove that the tokamak type of magnetic confinement device can work without negative impact. The final ITER design with the diagnostic cable ducts on the vacuum vessel wall shown in *Figure 1*.

Developing and understanding of effects in the presence of spatially varying nuclear and electromagnetic fields are also important to developing innovative design methods to control the resultant forces.

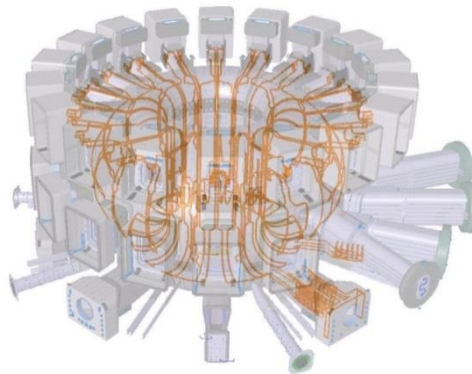


*Figure 1* The final ITER design with the diagnostic cable ducts on the vessel wall

Specifically, the project aims are to find the life-time of diagnostic cable ducts in the vessel's walls from the neutron bombardment and the heating and erosion by the high-temperature plasma. The final ITER design with the diagnostic cable ducts on the vacuum vessel wall shown in *Figure 1*. The summary of requirements on the diagnostic cable ducts are shown in *Figure 2*.



## Requirements on the diagnostic cable ducts

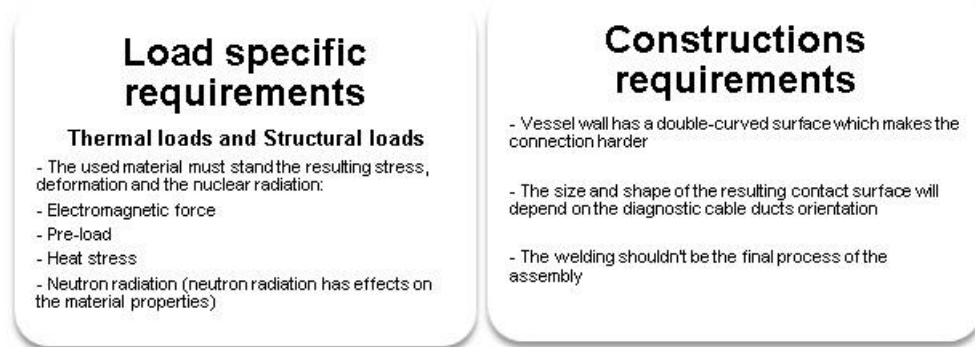


Figure 2 Summary of requirements on the diagnostic cable ducts

We must investigate the behaviour of structural materials affected by the plasma radiation, including strong band radiation (14 MeV electrons) and the strong cyclic thermal stress too. The high temperature and radiation results thermal aging embrittlement and radiation damage, which leads to reduction of material toughness. The reduced toughness leads to the spreading of existing unstable cracks which ultimately leads to failure. Due to the stress deformations and tensions are formed in the wall of the constructions, which under high temperature causes creeping in the material. [1]

## 2. METHODS

The procedure is based on the safety analysis and the strength model calculation. To control the barrier effects the survey of engineering and other special requirements is important. Firstly, the exclusive general engineering requirements: geometry (space requirements, compatibility, manufacturability, strength (static, dynamic). Secondly, the specific requirements in the fusion space: strong magnetic fields, internal heat generation, high thermal gradients, nuclear erosion. The goal of this comprehensive survey of requirements, evaluation and integration of mechanical design. The uncertainties need to be compensated during the design process with safety factors. This procedure ensures that the structure failure probability is properly is reduced to zero. The role of the calculations is to make the design to withstand the operational transients. The places of the diagnostic cable ducts at the vacuum vessel are shown *Figure 3*. The diagnostic cable ducts with the mineral insulated cables (MI cables) at the vacuum vessel shown in *Figure 2*. The MI cables will be used throughout the vacuum vessel environment to convey electrical signals to and from magnetic coils, bolometers, vacuum vessel instrumentations and thermocouples. These stainless steel sheathed cables vary in diameter from 1,5 mm to 4,8 mm. The diagnostic cable ducts which are located on the vessel wall where designed with pure extruded aluminium insert plates, lodged between each layer of cables, culminating with a sub-base plate, linking the diagnostic cable ducts to the vessel inner surface. The entire system can be treated with a distributed as a network, and we need such thermal model that describes the intended behaviours of the thermal components and is independent from circumstances, since the thermal simulation will answer questions on the thermal cooling design.

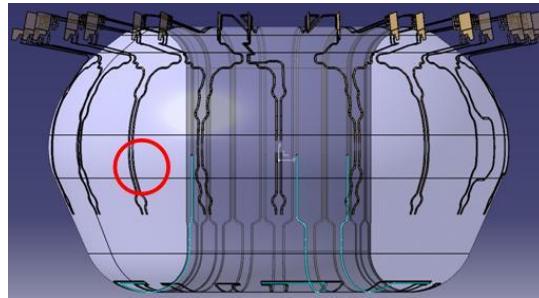


Figure 3 The final ITER design with the diagnostic cable ducts on the vacuum vessel wall

The highest heat charge to be taken into account when composing the structural design – affecting in the course of the fusion process the vacuum vessel and the shielding blocks – amounts to 360 °C in the case of the shielding blocks from the side of the plasma and to less than 150 °C in the case of the wall of the vacuum vessel.

In the cables and cable ducts of the diagnostic system the heat development in the internal volume stemming from neutron and gamma radiation will take up a value between 0,024-0,12 W/cm<sup>3</sup>.

The electromagnetic loads occurring during disruptions shall result in significant mechanical moments and forces on the diagnostic cable ducts and be joining constructions. The materials and design must ensure that the structure is able to withstand the loads on operating temperature.

Focused requirements of thermo-mechanical model: describe with reasonable accuracy regardless of boundary conditions, the integrated parts of a given change in temperature, time-varying excitation effect and the effect of heat dissipated by other components are able to take into account.

The main requirement that we focus on: the temperature variation ( $\Delta T$ ) along their length must not exceed 10 K, and since thermal conduction is the most effective method for heat transfer in ultra-high vacuum environment, it is therefore important to maintain close contact between the cables and the internal surface of the vessel over the diagnostic cable ducts length of travel. The force and torque components from acting on the diagnostic cable ducts are show in *Figure 4*.

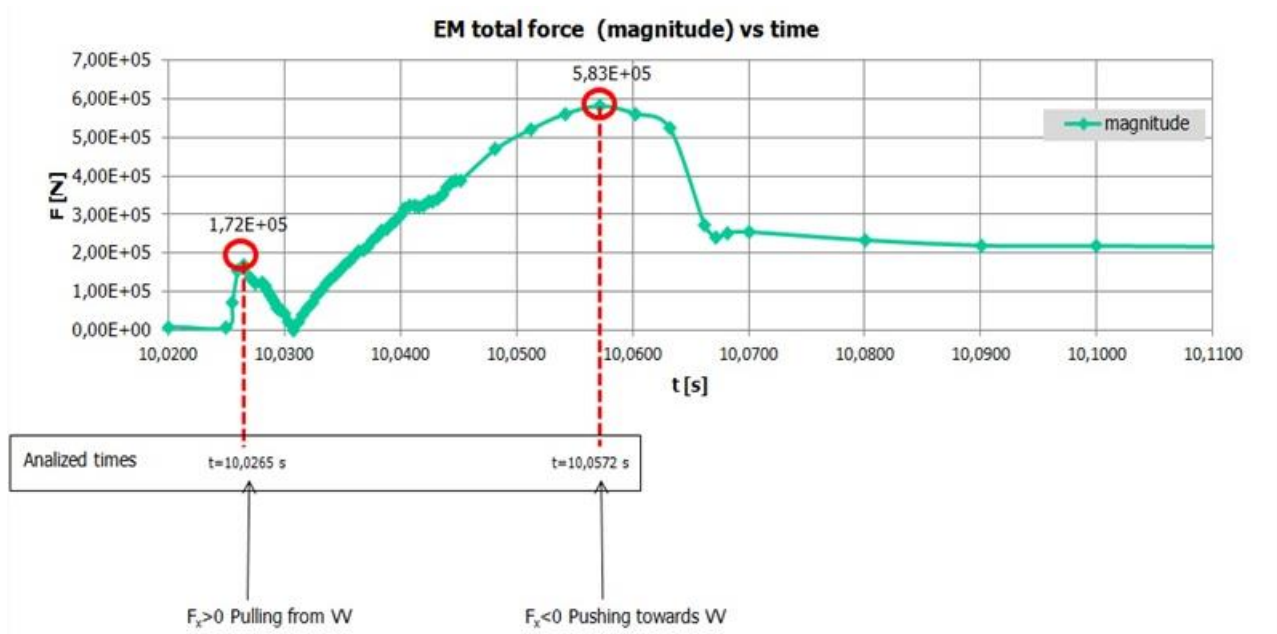


Figure 4 Force and torque components from acting on the diagnostic cable ducts



### 3. RESULTS

The structure is subjected to three types of thermal loads: plasma heat flux on the plasma facing surfaces, volumetric heat generation caused by neutron irradiation and the coolant temperature of the vacuum vessel front surface in contact with the back surface of the diagnostic cable ducts housing.

Table 1 Numerical material properties

Numerical material properties						
316I(N)-IG1 steel						
Temp. (C)	Coefficient of thermal expansion $10^{-6}(1\text{ }^{\circ}\text{C})$	Thermal conductivity (W/m $^{\circ}\text{C}$ )	Young's mod. (GPa)	Poisson's ratio	Density (kg/m $^3$ )	Yield point (MPa)
20	17	14	193	0,3	7966	271
100	17	15	186	0,3	7932	220
350	17	19	166	0,3	7824	155
NiCr19FeNb5Mo (Alloy 718)						
20	13	13	199	0,3	8200	343
100	13	13	195	0,3	8200	329
350	14	16,8	185	0,3	8200	293

Thermal boundary conditions are as follows: coolant temperature calculated as an average of inlet and outlet temperatures, heat transfer coefficient between coolant diagnostic cable ducts and vacuum vessel wall. The numerical materials properties are summarized in *Table 1* were chosen from ITER material properties handbook. [2]

Based on thermal-mechanical calculations, the numbers and locations of the anchor points of the diagnostic cable ducts can be optimized. The effect of heat loads was simulated with FEM. The 3D-models of of the diagnostic cable ducts in the FEM analysis are shown in *Figure 5*. For the simulations  $M_{\text{rad}}$ ,  $F_{\text{rad}}$  and  $M_{\text{ver}}$  values were used. Moments were represented by force couples. Assuming welded contact between the loom and the vacuum vessel was set to be fixed.

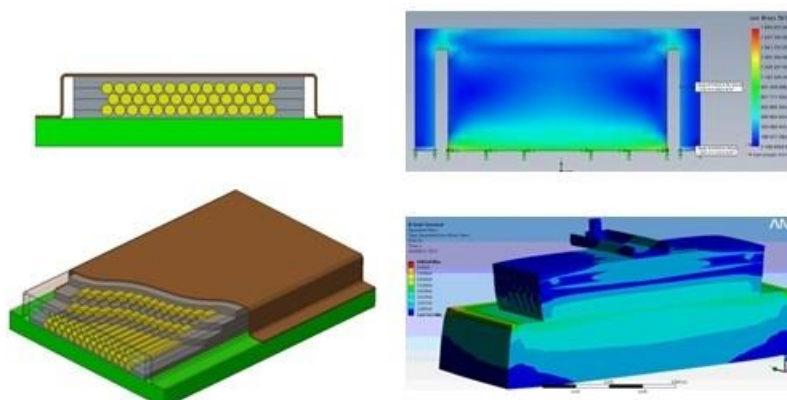
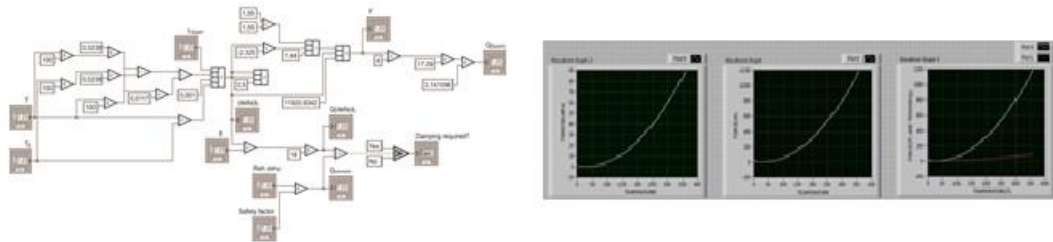


Figure 5 The models of FEM analysis and the results of thermo-mechanical simulations

As a result of the optimization of the bond, the stresses were lower with this solution of the structure of the diagnostic cable ducts. The block diagram of the optimization algorithm is shown



on *Figure 6*. The algorithm calculates and shows the numeric results for the exerted forces. The algorithm uses graphical interface for the calculation of exerted forces in the construction of the diagnostic cable ducts. The user interface contains input fields where each material, condition and geometry variable can be specified for the calculation's equations. With pressing the start button under the input fields the program calculates and shows the numeric results for the exerted forces with the defined parameters.



*Figure 6* The block diagram of optimization system and the numeric results for the exerted forces with the defined parameters

## CONCLUSIONS

Based on thermal-mechanical calculations, welding, in this case, were successfully replaceable with the anchor element, and the new concept allows deforming the structure of diagnostic cable ducts. As a result of the optimization of the diagnostic cable ducts, the stresses were lower with this solution. The thermal, static and fatigue analysis for the preliminary design of diagnostic loom are performed to obtain its temperature distribution and verify its structural integrity. The geometry of the diagnostic cable ducts constructions was determined by the positions on the vacuum vessel wall, and by observing the design requirements. The model then was examined with FEM analyses, the two main objectives of which was the determination of stress and temperature distributions. The effects of heat loads were simulated with FEM methods, and results of these simulations helped optimizing the geometry of the diagnostic cable ducts.

## REFERENCES

- [1] Friedberg, R.: *Plasma Physics and Fusion Energy*. Cambridge University Press, 2007.
- [2] EN 10302:2008, Summary of Material Data For Structural Analysis of the ITER Vacuum Vessel Supports3 VTZHT\_v1.0



# INTERNATIONAL SCIENTIFIC CONFERENCE ON ADVANCES IN MECHANICAL ENGINEERING

12-14 October 2017, Debrecen, Hungary



## ROAD TRAFFIC ACCIDENTS CAUSED BY MECHANICAL FAILURES IN HUNGARY BETWEEN 2012 AND 2017

*SZENTESI Miklós Gergely, LAKATOS István PhD*

*Department of Road and Rail Vehicles, Széchenyi István University,*

*E-mail: [szentesi.miklos.gergely@gmail.com](mailto:szentesi.miklos.gergely@gmail.com) , [lakatos@sze.hu](mailto:lakatos@sze.hu)*

### **Abstract**

*The purpose of this study is to provide a summary about the accidents which happened because of the vehicle's major technical failures in Hungary between 2012 and 2017, and to analyse what kind of major technical failures could have caused them to be light, serious or fatal. Based on the collected data, it can be said that two major technical problems have led to accidents: either a blow-out of the tyres or the failure of the braking system. These problems are usually the consequences of over-running, too old tyres, or overloaded tyres and the lack of maintenance period of the braking systems. The research also has a secondary purpose, and we would like to point out what future technical developments need to be made in order, to reduce the ever-increasing number of technical failure accidents.*

**Keywords:** *brake failure, tyre blow-out, road crash, Hungary*

### **1. INTRODUCTION**

According to the announcement of the Association of Hungarian Automobile Importers (MGE), it can be observed that the number of vehicles sold in Hungary in the last few years is constantly increasing compared to the bottom out in 2010. Due to the escalating number of registered vehicles, there is an upsurge in the number of automobiles per inhabitant. Unfortunately, this increasing value will bring the rise of the number of accidents. Analyzing the chart below, it is obvious that more accidents occur in the capital city and in its region, than in other counties. This, of course, due to the fact, that the number of vehicles in the highly urbanised areas is much higher. This thus attracts the fact that the number of mechanical malfunctioning accidents is higher.

Investigating more densely populated areas, more accidental data will we explore. This process can be divided into separate parts, one of which is considered the most important, the age of the vehicles. During our research, we did not only screen for location, time and failure type but also vehicle age. The result of the screening is that in the case of brake failure accidents, an older (at least 10 years old) vehicle is the victim of the accident. Naturally, the numbers are also influenced by the imported vehicles from abroad, because the imported used car market reaches its heyday. On these vehicles, the tyres are usually worn out, the brakes and the main components of the vehicle are no longer working properly (only in certain cases).

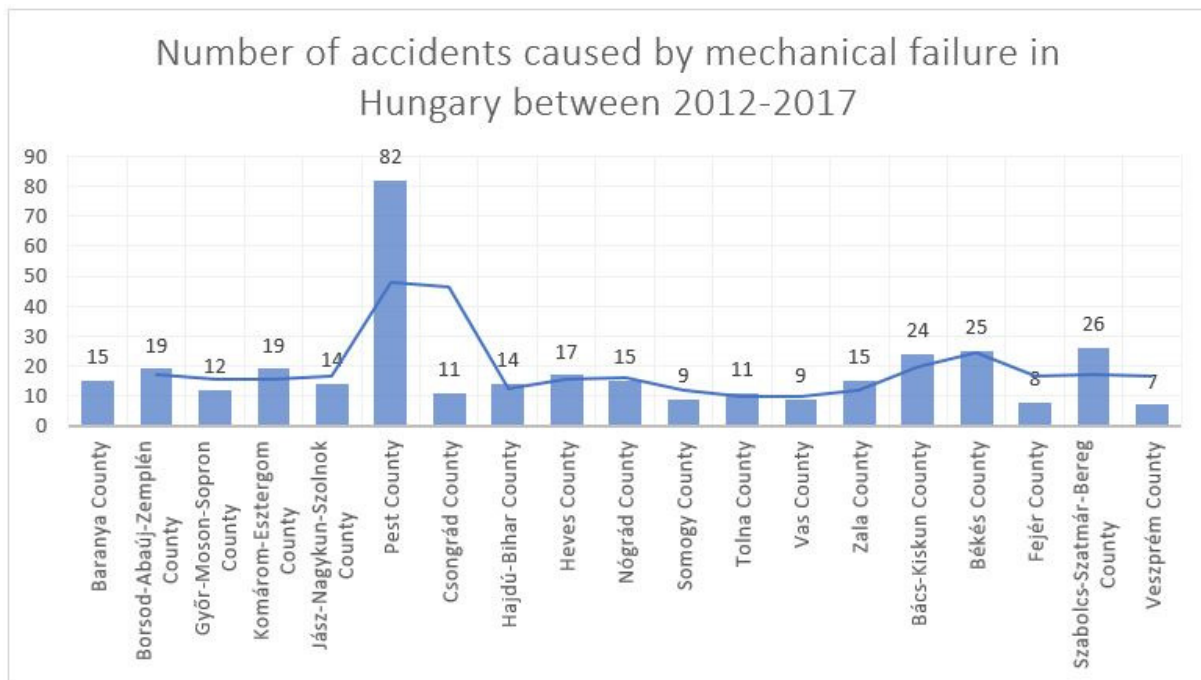


Figure 1 Number of accidents caused by mechanical failure in Hungary between 2012 and 2017, shown by countries

## 2. MEASUREMENTS AND EVALUATION

### 2.1 Road crashes caused by tyre blow-outs

In the analysis of accidents, two of the technical problems with a high prevalence is the wear and tear of tyres. This can be traced back to two main reasons: first, the technical conditions of imported cars and the second is the choice of an inadequate maintenance period. Vehicle owners, generally want to save money, and that's the main reason why they can make a big mistake by "winter tires as all seasons" attitude. When reading such crash reports, the vehicle was overloaded several times, the tyre was worn out, the traveling speed was high, the wheel was operated with too much pressure, and last but not least the car had old tyres.

In these cases there was a surprisingly high possibility of a traffic accident with a car. The most typical case for passenger cars is the over-wear and tear of older tyres (repeatedly inappropriate seasonal - winter or summer – tyre usage was the source of the problem). The number of tyre blow-out accidents analyzed by the chart shows, that it has a higher probability in the more densely populated areas. According to the Accident Report, it is generally a highway, single or dual carriageway in the case of tyre blow-out accidents.

After Passenger cars were directly truck related accidents. In the analysis of the accident reports of these vehicles, overloading them overwhelmingly could have caused the tyres' blow-out effects. Analyzing truck accident data, the severity of the incidents were mainly light and serious injuries, while the number of fatalities were less fortunate.

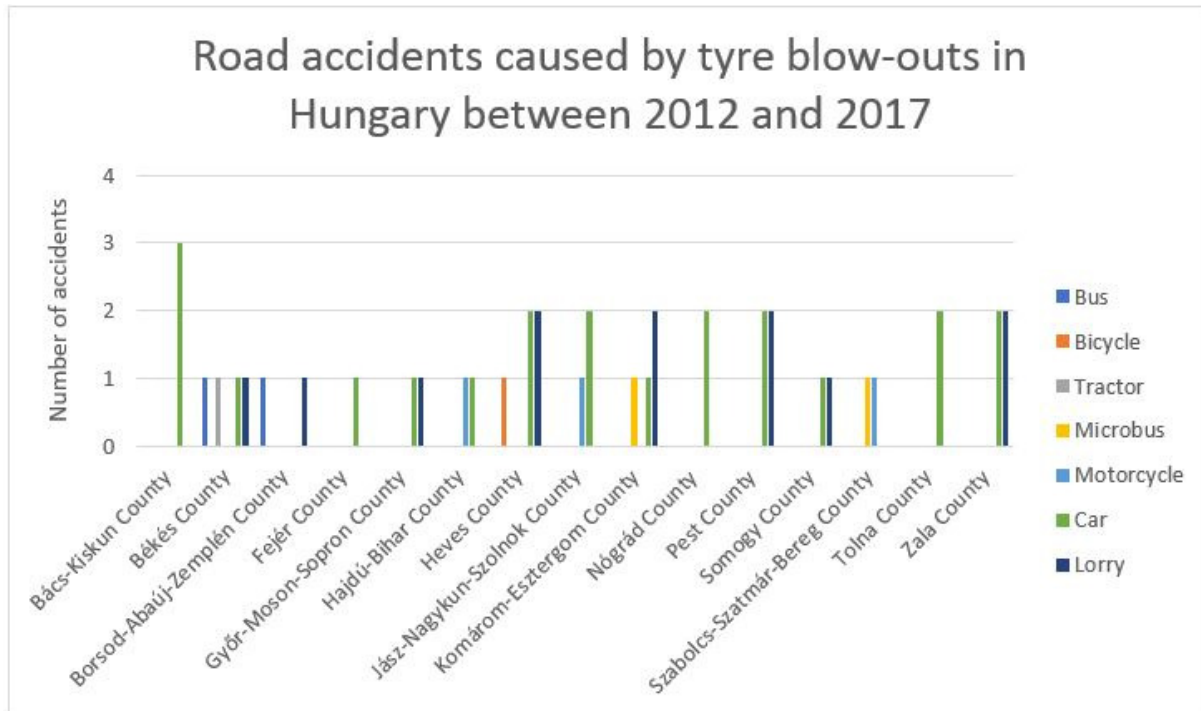


Figure 2 Road accidents caused by tyre blow-outs in Hungary between 2012 and 2017

## 2.2 Road crashes caused by brake failures

When analyzing brake failure crashes, it usually turns out that the owner tried to save money on the maintenance costs. Skipped the proper examination of the main components of safety and, if necessary, the replacement of the crucial parts. This can lead to severe or even lethal personal injury. The braking system must be maintained at all times, especially when traveling with the vehicle periodically. The braking equipment is the most critical device on the vehicles, so you always have to replace the parts with the right quality of replacement parts.

We have often found a description of excessive wear on the brake pads or brake discs during our accident investigation site readings. Excessively worn brake discs and brake pads will significantly increase the braking distance, therefore reducing braking performance, causing the overall efficiency of the service braking system to be nowhere near to its original condition.

A significant percentage of accidents occurred due to excessive wear and tear, but there were several other cases where the lack of brake fluid (brake system leakage) caused a road accident. It can also be said that the drivers did not have the right speed or that the vehicle was loaded more than its maximum permissible load.

The braking percentage for the whole vehicle can be calculated using the following formula:

$$lsz_e = \frac{\sum F}{m_{\ddot{o}} * g} * 100$$

Where:

- $\sum F$  is the required braking force, which is the sum of the braking force generated by the wheel structures



- $m_3$  the maximum permissible mass of the vehicle
- $g$  the difficulty acceleration

It is clear from the formula that if the vehicle is operated with the maximum permissible mass, the braking force exerted by us, is still sufficient to stop the vehicle safely. In the case where the maximum gross weight of the vehicle is exceeded, the percentage of braking effectiveness decreases, so naturally, the braking distance increases and it is harder to stop the vehicle with the same braking force.

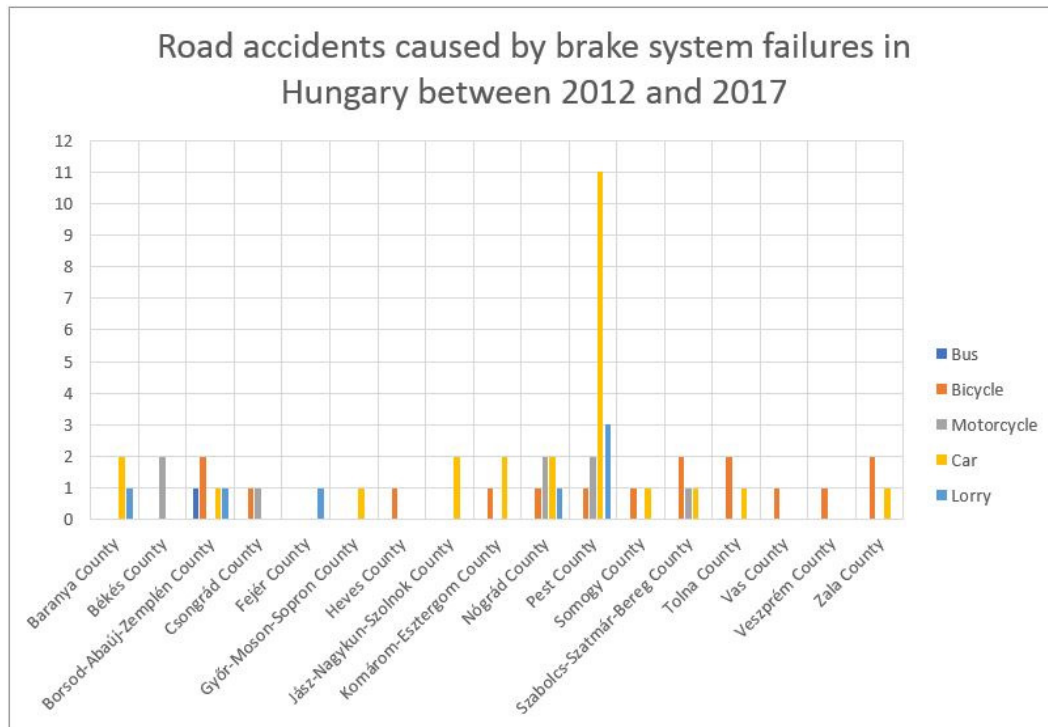


Figure 3 Road accidents caused by brake system failures in Hungary between 2012 and 2017

In the diagram of accident data, the brake failure of passenger cars is prominent. This usually means that there are many crash injuries, often within a populated area, and as is shown in the figure, such accidents occur more often in areas with higher population density. From analyzing the data, it can be observed that, for five years, only for Pest County approx. 49 cases were recorded, which also demonstrates a higher accident rate for more densely populated areas. Analyzing the accident data, it can be observed that light and serious injuries are suffered by the people involved in the accident. Fortunately, the number of fatalities is low but not negligible.

### 2.3 Comparison of passenger cars in EU

According to the Federal Office for Motor Vehicles' (Germany) data, only 38% of the vehicles are regularly serviced (based on tests in Germany), and 23% of those were considered as serious problems.

The main problems were involved with the lighting equipments (25%), braking system failures (almost 20%) and undercarriage, including wheels, tyres (14%). However, the number of defective vehicles has been decreasing gradually over the last couple of years. In 2000,



# INTERNATIONAL SCIENTIFIC CONFERENCE ON ADVANCES IN MECHANICAL ENGINEERING

12-14 October 2017, Debrecen, Hungary



almost half of the vehicles revealed technical mistakes. This was of course influenced by the age of the vehicle.

In 2012, 8.34 million cars fell into this category, by 2014 this number rose to 8.73 million, accounting for more than 44% of the checked vehicles. Compared to the ever-changing world trends, DEKRA carried out a survey of the widespread use of vehicles in Germany and found that the Germans kept their vehicles for an extended period of time. This is clearly indicated by the fact that compared with the western trend, where they are replaced after some vehicles, the average age of vehicles is lower, while in Germany the average age of vehicles is 9.2 years. According to data from European vehicle manufacturers, the average age of vehicles in the European Union in 2014 was almost 9.7 years, in 2006 it was only 8.4.

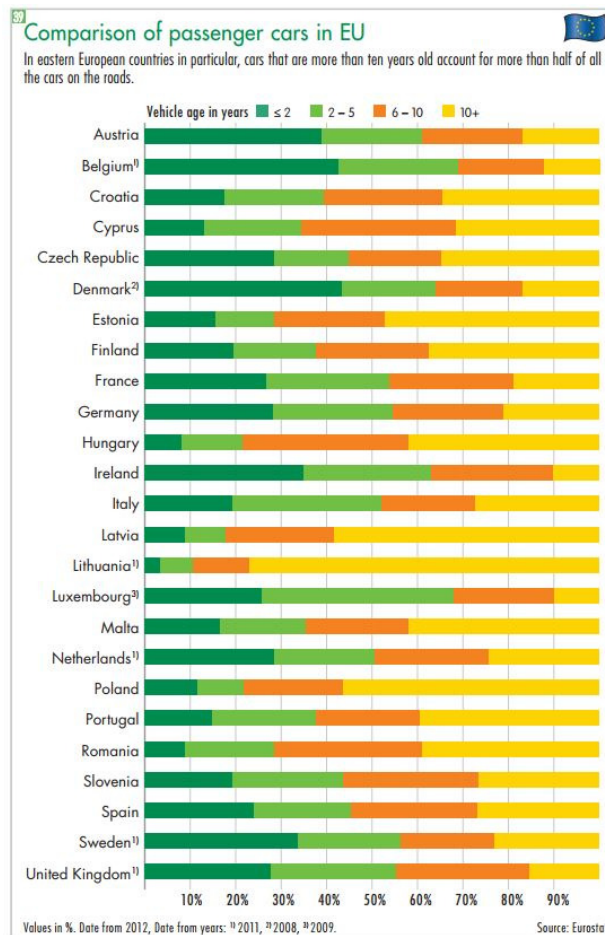


Figure 4 Comparison of passenger cars in EU

Thus it can be said, that society has become "greener", which means less waste for society. This brings the fact, that older vehicles need more attention to the good mechanical condition, a so-called preventive maintenance program (PM) has to be kept on a regular basis. The research of DEKRA supports the above, namely that the number of accidents from technical failure in Hungary is greatly influenced by the average age of 6-10 or even 10 years of our vehicles.

Analyzing the diagram, it can be seen, that in Hungary the overwhelming majority of older vehicles are available, with vehicles over 10 years old providing almost 42% of the total



# INTERNATIONAL SCIENTIFIC CONFERENCE ON ADVANCES IN MECHANICAL ENGINEERING

12-14 October 2017, Debrecen, Hungary



amount of vehicles, 40% of the vehicles are 6 to 10 years old, vehicles of 2-5 years old add another 10 % while vehicles under 2 years old give up to 8% of our total vehicle fleet.

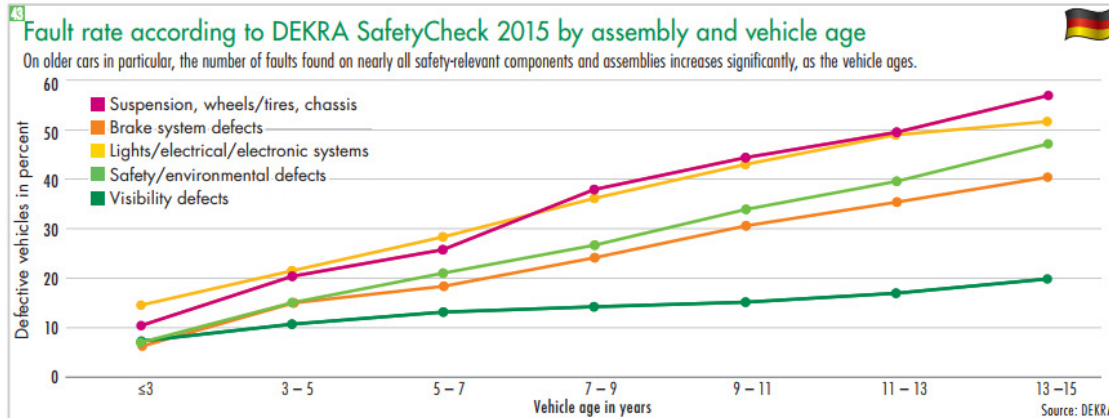


Figure 5 Fault rate according to DEKRA SafetyCheck 2015 by assembly and vehicle age

Continuing the thought, according to DEKRA's data, it can be stated that according to the tests conducted in 2015, the higher age of a vehicle, the higher possibility of failure. For example, the braking system was defective in more than 30% of the 73,000 vehicles surveyed by DEKRA in vehicles between 13 and 15 years old. For vehicles tested by DEKRA, not only the braking system, but also the components of the chassis, electronic systems and safety systems have been inspected. According to the study, when the vehicle grows older, the failure of the devices tested above exceeds the number of failures in modern state by more than 100% compared to ten years of aging.

### 3. RESULTS

Road accident due to a mechanical error has occurred in Hungary in a total of 340 cases in the last five years, of which a road accident due to tyre blow-out occurred in 42 cases (12.35%), passenger cars in 21 cases (50%), and lorries 12 times (28, 57%) are included in the statistical data. In the remaining 9 cases (21.42%) bus, bicycle, minibuses and tractors were involved in an accident.

As a result of the research, the accident due to the failure of the braking system was 57 cases (16.76%), of which 25 cases were caused by passenger cars and 7 were cases of lorry. Thus, a total of 43.86% of passenger cars and 12.28% of lorries from the accident caused by the failure of all braking systems are present in the total accident rate accidents. The remaining 25 cases (43.85%) are also made up of buses, bicycles, minibuses and tractors.

### CONCLUSION

Because in Hungary the average age of our vehicles is 6-10 years or over 10 years, therefore continuous maintenance / inspection is of paramount importance.

To avoid blow-out air loss on the tyre, a higher level of user attention is required. The number of such cases can be reduced by constantly checking our tyres, not just visually. When increasing the load on vehicles, should be taken into consideration not to overload the tyres and to operate them at the right pressure. In addition, special attention should be paid to check the size of the tread and to use suitable tyres for the season. This requires more stringent



# INTERNATIONAL SCIENTIFIC CONFERENCE ON ADVANCES IN MECHANICAL ENGINEERING

12-14 October 2017, Debrecen, Hungary



attention not only from the user side but also from the control side, which can be solved if the police also check the vehicles whether they have been fitted with safe and legal tyres or not.

Testing of the braking devices is also of paramount importance, from a user's point of view it is necessary to consider a different attitude, which should be the examination of the vehicles braking equipment for a given period of kilometers. This should not only cover certain parts, but a comprehensive test would be necessary. In addition, it is possible to reduce the number of accidents, if more stringent technical examinations are made in connection with the brakes, and we are thinking of narrowing the tolerance of wear.

Due to the growing number of cars imported from abroad, stricter import rules (creating more stringent rules for registering the vehicle, eg more comprehensive inspection of brakes and tyres) can also be a way of reducing casualties.

## ACKNOWLEDGMENTS

We thank the EFOP-3.6.1-16-2016-00017, Internationalization, Teacher, Researcher and Student Provisioning, the development of knowledge and technology transfer as tools for intelligent specialization at the Széchenyi István University project support.

## REFERENCES

- [1] UNIVERSITAS-Győr Nonprofit Ltd, Impact of the technical condition of vehicles on accidents and the consequences of accidents, study, 2017
- [2] Association of Hungarian Vehicle Importers, Press release, 2017  
<http://www.mge.hu/page.php?IID=hu&pFrom=21&pID=201&uniqueID=WCwJPnCJab&levelID=0>
- [3] DEKRA ROAD SAFETY REPORT, Passenger Transportation, Accident Prevention Strategies on Europe's Roads, DEKRA, 52-55, 2016  
[http://www.dekra.de/c/document\\_library/get\\_file?uuid=bb9ca5c9-8da9-480c-b56b-e47daa4defb8&groupId=10100](http://www.dekra.de/c/document_library/get_file?uuid=bb9ca5c9-8da9-480c-b56b-e47daa4defb8&groupId=10100)
- [4] DEKRA ROAD SAFETY REPORT, Passenger Transportation, Accident Prevention Strategies on Europe's Roads, DEKRA, 2015
- [5] DEKRA ROAD SAFETY REPORT, Passenger Transportation, Accident Prevention Strategies on Europe's Roads, DEKRA, 2014
- [6] DEKRA ROAD SAFETY REPORT, Passenger Transportation, Accident Prevention Strategies on Europe's Roads, DEKRA, 2013
- [7] Central Statistical Office, Hungarian Statistical Yearbook, 93, 2014  
[https://www.ksh.hu/docs/hun/xftp/idoszaki/evkonyv/evkonyv\\_2014.pdf](https://www.ksh.hu/docs/hun/xftp/idoszaki/evkonyv/evkonyv_2014.pdf)
- [8] Péter T., Lakatos I., Szauter F., Szabó K., Questions regarding vehicle safety and the mathematical analysis of safety in large scale networks using positive dynamic systems and probability theory methods, 13th ASME/IEEE International Conference on Mechatronic and Embedded Systems and Applications, 2017w



## DYNAMIC SIMULATION OF A SERIES WOUND DC MOTOR APPLYING THE CONTROL DESIGN AND SIMULATION MODULE OF LABVIEW

*SZIKI Gusztáv Áron PhD, SARVAJ CZ Kornél, SZÁNTÓ Attila*

*Faculty of Engineering, University of Debrecen*

*E-mail: [szikig@eng.unideb.hu](mailto:szikig@eng.unideb.hu), [sarvajcz@eng.unideb.hu](mailto:sarvajcz@eng.unideb.hu), [szanto930922@freemail.hu](mailto:szanto930922@freemail.hu)*

### **Abstract**

*In our previous publication [1] a model for serial wound DC motors was presented and a simulation program was described that is based on this model and had been developed in MATLAB environment. In the above publication the measurement process of the characteristics (electric resistances, dynamic inductances, bearing resistance torque) of the motor was also described. From the characteristics, the program simulates the operation of the motor, calculating its torque, rpm and current intensity, as a function of time. The recent publication is about the realization of the above program applying the NI LabVIEW Control Design and Simulation Module. This module enables the adjustment of input parameters (e.g. supply voltage) during the running of the program, thus the realization of real time driving simulation. In addition it can be applied with all NI hardware platforms, including data acquisition, CAN, GPIB, and field-programmable gate array (FPGA).*

**Keywords:** *series DC motor, dynamic simulation, LabVIEW, Control Design and Simulation Module*

### **1. INTRODUCTION**

At the Faculty of Engineering of the University of Debrecen we have made significant efforts regarding talent care in the last decade [2,3,4,5]. As a part of this activity student teams are regularly participants of competitions for vehicles with alternative drive (Shell Eco-marathon, Széchenyi Race, MVM Energy Race). The permanently efficient racing requires continuous development applying dynamic modelling and highly developed mathematics and computer science as in many other fields of science [6,7,8,9]. As a part of this development a simulation program was created by the authors previously in MATLAB environment, which is capable of calculating the dynamic functions (e.g. the acceleration-, velocity- and covered distance-time functions) of an electric vehicle, driven by series wound DC motor, from its technical data [10,11,12]. The above simulation program enables the calculation of optimal technical parameters at which the best dynamic characteristics (performance) can be achieved. Constructing a vehicle applying the above optimal parameters efficient racing is more possible.

A particularly important part of vehicle dynamic simulation is the modelling of the electric motor [1] and the development of a simulation program, on the basis of the model, which is capable of calculating the angular speed and torque of the motor, and also the intensity of current flowing through it, from its basic electromagnetic and dynamics characteristics as a function of time.

In the recent publication the realization of the above simulation program is presented for the series wound DC motor described in Reference [1] applying the NI LabVIEW Control Design and Simulation Module. Several input data of the electric motor – like its supply voltage (when we push or release the gas pedal of the vehicle) or the load on its shaft – are changing continuously during the race. Thus to realize a real time race simulation we had to achieve the continuous control of



these input parameters. The LabVIEW simulation environment provides an easy solution for this problem, making the values of these parameters dynamically adjustable during the simulation. In addition, LabVIEW Control Design and Simulation Module can be used with all NI hardware platforms, including data acquisition, CAN, GPIB, and field-programmable gate array (FPGA). On the other hand, LabVIEW Control Design and Simulation Module is part of the LabVIEW graphical development environment, so you can integrate other LabVIEW modules and toolkits into your applications. Along with the LabVIEW Real-Time and LabVIEW FPGA modules, you can take advantage of the LabVIEW Database Connectivity Toolset, LabVIEW DataFinder Toolkit, and more [13]. In addition, you can use other tools specific to control applications such as the LabVIEW PID and Fuzzy Logic Toolkit, the LabVIEW System Identification Toolkit, or NI VeriStand software.

## 2. SIMULATION RESULTS applying LabVIEW's Control Design and Simulation module

In this section the simulation of our previously analysed series wound DC motor [1] is presented applying the NI LabVIEW Control Design and Simulation Module. *Figure 1* shows the developed motor simulation front panel and block diagram. The input parameters can be adjusted on the front panel, and the output functions are also displayed there. The block diagram window visualizes the program code. The supply voltage of the motor ( $U_{bat}$ ), the load on its shaft ( $M_{load}$ ) and its brush voltage drop ( $U_{brush}$ ) are dynamically adjustable during the simulation. The output functions of the simulation (torque-, angular speed- and current intensity-time function) are calculated in real time mode from the actual data.

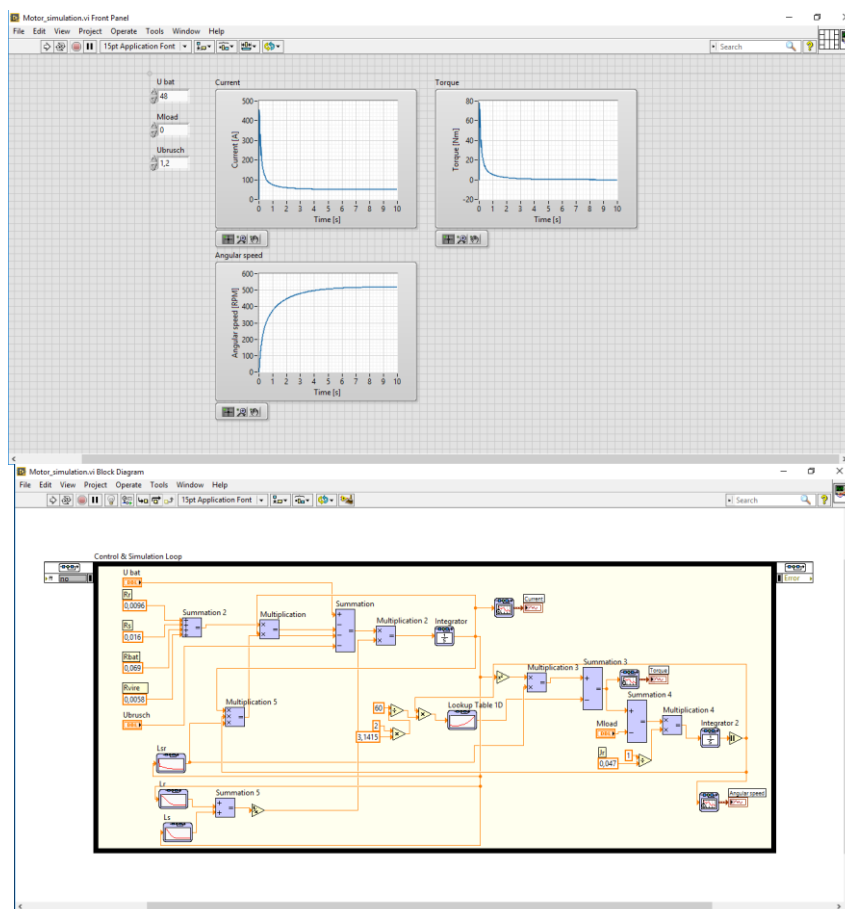


Figure 1 The front panel and block diagram of the motor simulation program in NI LabVIEW Control Design and Simulation Module



# INTERNATIONAL SCIENTIFIC CONFERENCE ON ADVANCES IN MECHANICAL ENGINEERING

12-14 October 2017, Debrecen, Hungary



The simulation results (torque-, angular speed- and current intensity-time functions) were compared with the ones that were calculated by our MATLAB-SIMULINK program [1]. The calculated functions were exactly the same applying the two different programs.

## CONCLUSIONS

The simulation of a series wound DC motor was realised applying the NI LabVIEW Control Design and Simulation Module. The simulated functions were compared with the ones obtained by the MATLAB-Simulink program previously. The calculated functions were exactly the same applying the two different programs. Nevertheless, by the application of the NI LabVIEW Control Design and Simulation Module the input parameters of the program can be adjusted even while the program is running, thus a real-time race simulation can be realised. In addition the LabVIEW Control Design and Simulation Module can be applied with all NI hardware platforms, including data acquisition, CAN, GPIB, and field-programmable gate array (FPGA).

## ACKNOWLEDGEMENT



SUPPORTED BY THE ÚNKP-17-2NEW NATIONAL EXCELLENCE PROGRAM OF THE MINISTRY OF HUMAN CAPACITIES”

## REFERENCES

- [1] Szíki, G., Sarvajcz, K., Kiss, J., Gál, T., Szántó, A., Gábora, A., Husi, G.: Experimental investigation of a series wound dc motor for modelling purpose in electric vehicles and mechatronics systems. *Measurement* 109, 111-118., 2017.
- [2] Gábora, A., Szíki, G., Szántó, A., Varga, T., Magyar, A., Balázs, D.: Prototípus elektromos tanulmányautó fejlesztése a Shell Eco-Marathon versenyre = Prototype battery electric car development for Shell Eco-Marathon competition. In: A XXII. Fialat Műszakiak Tudományos Ülésszak előadásai = Proceedings of the XXII-th International Scientific Conference of Young Engineers / szerk. Bitay Enikő, Erdélyi Múzeum Egyesület (EME), Kolozsvár, 167-170, 2017.
- [3] Juhász, G.: Szakmai versenyek az oktatás szolgálatában = Technical competitions for the education. In: Proceedings of the 1st international scientific conference on advances in mechanical engineering (ISCAME 2013) : 10-11 October 2013, Debrecen, Hungary / szerk. Mankovits Tamás, Debreceni Egyetem Műszaki Kar, Gépészmérnöki Tanszék, Debrecen, 74-78, 2013.
- [4] Nagy-Kondor, R. (2011): Technical mathematics in the University of Debrecen. *Annales Mathematicae et informaticae*, 38, 157-167.
- [5] Nagy-Kondor, R. (2005): Special characteristics of engineering students' knowledge of functions: *International Journal for Mathematics Teaching and Learning*, 10, 1-9.
- [6] Krisztián Deák, Tamás Mankovits, Imre Kocsis: Optimal Wavelet Selection for the Size Estimation of Manufacturing Defects of Tapered Roller Bearings with Vibration Measurement using Shannon Entropy Criteria, *Strojniški vestnik - Journal of Mechanical Engineering Vol 63, No 1 (2017)*, pp. 3-14.
- [7] Krisztián Deák, Imre Kocsis: Support Vector Machine with Wavelet Decomposition Method for Fault Diagnosis of Tapered Roller Bearings by Modelling Manufacturing Defects, *Periodica Polytechnica Mechanical Engineering* 61(4), pp. 276-281, 2017.



# INTERNATIONAL SCIENTIFIC CONFERENCE ON ADVANCES IN MECHANICAL ENGINEERING

12-14 October 2017, Debrecen, Hungary



- [8] Hajdu, S., Gáspár, P.: Reducing the Mast Vibration of Single-Mast Stacker Cranes by Gain-Scheduled Control. *Int. J. Appl. Math. Comp. Science* **26** (4), 791-802., 2016.
- [9] Hajdu, S., Gáspár, P.: From Modeling to Robust Control Design of Single-Mast Stacker Cranes. *Acta polytechn. Hung* **11** (10), 135-149., 2014.
- [10] Szántó Attila, Dr. Szíki Gusztáv Áron, Hajdu Sándor, Gábora András (2017): Simulation of a series wound DC motor in MATLAB environment, *Proceedings of the XXII International Conference of Young Engineers, Kolozsvár (2017)*, 367-370.
- [11] Szántó Attila, Dr. Szíki Gusztáv Áron, Hajdu Sándor (2016): Dynamic modelling of a race car driven by series wound DC motor, “Műszaki Tudomány az Észak-Kelet Magyarországi régióban (2016)” Conference Proceedings: p.587-591.
- [12] Szíki Gusztáv Áron, Hajdu Sándor, Szántó Attila (2015): Vehicle Dynamics Modelling of an Electric Driven Race Car, In: Sándor Bodzás, Tamás Mankovits (editors) *Proceedings of the 3rd International Scientific Conference on Advances in Mechanical Engineering (ISCAME 2015)*, University of Debrecen Faculty of Engineering, pp. 208-217.(ISBN:978-963-473-917-3)
- [13] <http://www.ni.com/white-paper/11281/en/>



## SOLUTION OF THERMOMECHANICAL COUPLED PROBLEM USING FEM

*SZÜLE Veronika, PERE Balázs PhD*

*Department of Applied Mechanics, University of Széchenyi István*

*E-mail: [szule.veronika@sze.hu](mailto:szule.veronika@sze.hu)*

### **Abstract**

*Vehicle components made of rubber or rubber like polymers usually exhibit large deformations. Cyclic finite deformations may induce increasing temperature in hyperelastic materials. This case where changes in deformation and in temperature occur simultaneously is called coupled thermomechanical problem. Both the mechanical and thermal processes have their own governing equations, that is why special techniques are needed for the computation. A widely used numerical method for solving such problems is the Finite Element Method (FEM). This paper summarizes the theoretical background of the solution of the coupled problem and an example will be presented of the solution of the coupled thermomechanical problem.*

**Keywords:** *hyperelastic materials, high deformations, thermodynamics, Neo-Hooke material law, coupled problem*

### **1. INTRODUCTION**

Rubber can be classified as a so-called hyperelastic polymer which has a typical geometrical and material non-linear behaviour. It means that the relationship between displacements and internal forces can be described by functions whose order is higher than linear. The geometrical nonlinearity is easy to handle mathematically, however the material nonlinearity is only described approximately [1, 2]. Furthermore, a number of material laws for rubber can be found in literature [3, 7], for example the Neo-Hooke-, the Mooney-Rivlin, the Yeoh-, and the Arruda-Boyce material models. Their applicability largely depends on the stress.

Furthermore, the task becomes more complicated because of some properties of rubber parts. The temperature of rubber increases significantly. Therefore, the temperature- and displacement fields are coupled, and it means that special solving algorithms are required [4,5]. So the equations of mechanics and thermodynamics are coupled. The mechanical properties of rubber depend on temperature and temperature changes can accelerate chemical alteration processes which lead to material deterioration by changes in the rubber network structure.

As described above, the goals of this paper are the following:

It is necessary to summarize the applied equations and the basic physical laws which are responsible for the theoretical background. Clarification of these relationships is essential because the material laws of rubber cannot violate those basic physical laws. It is necessary to extend these relationships like equilibrium of the linear and angular momentum and the first and second laws of thermodynamics to the high deformation of rubber and rubberlike polymers. For the solution of the thermomechanical exercise the Neo-Hooke material law is applied. Finally, the numerical solution and the computation of the coupled thermomechanical problem will be presented and an example will be solved.

In this paper an arrow above a letter denotes vector and double underline denotes tensor.

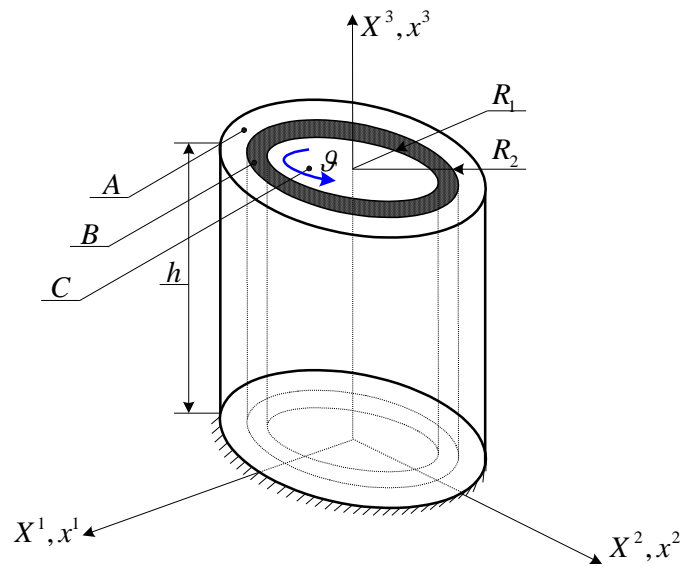


Figure 1 Mechanical model of a silent block

## 2. GOVERNING EQUATIONS

### 2.1. Equilibrium of linear momentum

The differential formulation of the equilibrium of linear momentum in the current configuration is

$$\rho \dot{\vec{v}} = \underline{\underline{\sigma}} \cdot \nabla + \vec{f} \quad (1)$$

where  $\rho$  is the mass density,  $\vec{v}$  is the velocity,  $\underline{\underline{\sigma}}$  is the Cauchy stress,  $\vec{f}$  is the volume force.

### 2.2. Equilibrium of angular momentum

The next equality shows the differential form of the balance of moments

$$\underline{\underline{\sigma}} = \underline{\underline{\sigma}}^T \quad (2)$$

### 2.3. First law of thermodynamics

When deformations repeatedly occur, significant increase in temperature can be observed. The differential form of the first law of thermodynamics is in the current configuration

$$\dot{e} \rho = [-\nabla \cdot \vec{q} + h] + \underline{\underline{\sigma}} \cdot \underline{\underline{l}} \quad (3)$$

where  $e$  is the internal energy per unit mass,  $\vec{q}$  is the heat flux,  $h$  is the heat source,  $\underline{\underline{l}}$  is the velocity gradient  $\underline{\underline{l}} = \nabla \vec{v}$ ,  $\underline{\underline{l}} = \underline{\underline{F}} \cdot \underline{\underline{F}}^{-1}$ .

### 2.4. Second law of thermodynamics

The behaviour of viscoelastic materials is described by the second law of thermodynamics. The second law of thermodynamics in the current configuration can be written as

$$\dot{\eta} T \rho \geq -\nabla \cdot \vec{q} + \frac{\vec{q} \cdot \nabla T}{T} + h \quad (4)$$

where  $\eta$  is the entropy per unit mass and  $T$  is the absolute temperature. It will be practical to



change the variable from entropy per unit mass to temperature by applying the Legendre-transformation and by using the Helmholtz-free energy

$$\psi = e - \eta T \quad (5)$$

Substituting Eqn. (5) into Eqn. (3) and subtract Eqn. (3) from Eqn. (4) the following expression is generated

$$-(\dot{\psi} + \eta \dot{T})\rho + \underline{\underline{\sigma}} \cdot \underline{\underline{l}} - \frac{\bar{q} \cdot \nabla T}{T} - D \geq 0 \quad (6)$$

which is known as Clausius-Duhem inequality [2].

### 3. CONSTITUTIVE MODEL

#### 3.1. Stress state of elastic element

The property of an elastic element is that the total mechanical energy is reversible. The free energy of the body is the function of the strain and temperature. Dissipation comes only from heat conduction.

#### 3.2. Structure of free energy function

In order to make the further calculations easier it is necessary to split Eqn. (5) to temperature-dependent and temperature-independent parts. The free energy is

$$\psi(\underline{\underline{C}}, T) = \tilde{\psi}(\underline{\underline{C}}, \tilde{T}) = \frac{T}{T_0} \psi_0(\underline{\underline{C}}) + \left(1 - \frac{T}{T_0}\right) e_0(J) + \int_{T_0}^T \hat{c}(\underline{\underline{C}}, \tilde{T}) \left(1 - \frac{T}{\tilde{T}}\right) d\tilde{T} \quad (7)$$

where  $\psi_0$  is the free energy at the reference temperature,  $e_0$  is the internal energy at the reference temperature,  $\underline{\underline{C}}$  is the right Cauchy-Green tensor and  $\hat{c}$  is the heat capacity. It is followed by an additive split of the Helmholtz free energy [3,6].

### 4. EXAMPLE

Let us consider the mechanical model of a silent block, where A, B and C are axisymmetric bodies (see *Figure 1*). The A and C bodies are rigid bodies, while B is a deformable one. The external body (A) is fixed and the internal one is imposed by a given rotation. Numerical example will demonstrate the efficiency of the algorithm, shown in *Figure 2*.

### 5. NUMERICAL SOLUTION

In order to solve the thermomechanical problem it is necessary to use the weak formulation and to do the linearization of the non-linear formulation of the mechanical problem. The position vector is determined from the weak form of the mechanical problem, the temperature field is determined from the weak form of the thermodynamical problem. The flowchart of the numerical solution is presented in *Figure 2*.

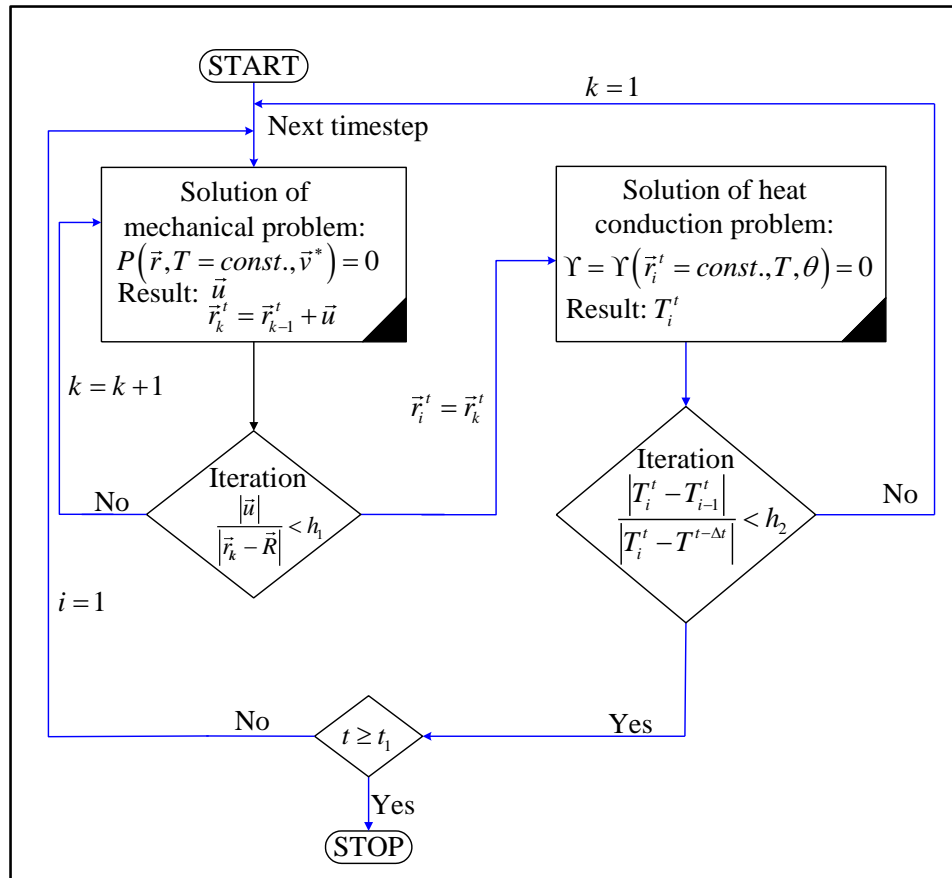


Figure 2 Flowchart of solution of the coupled thermomechanical problem

## CONCLUSIONS

The present numerical algorithm is the basis of the further fatigue and lifetime-calculations.

## REFERENCES

- [1] Bonet, J., and Wood, R. D., Nonlinear Continuum Mechanics for Finite Element Analysis, first ed., University Press, Cambridge, 1997.
- [2] Böl, M., Reese, S.: Finite element modelling of rubber-like polymers based on chain statistics, International Journal of Solids and Structures, 43, pp. 2-26, 2006.
- [3] Holzapfel, G. A., Nonlinear Solid Mechanics, A Continuum Approach for Engineering, first ed., John Wiley & Sons, Chichester 2000.
- [4] Reese S., Wriggers P.: A material model for rubber-like polymers exhibiting plastic deformation: computational aspects and a comparison with experimental results, Computer methods in applied mechanics and engineering 148, pp. 279-298, 1997.
- [5] Reese S., Wriggers P.: A material model for rubber-like polymers exhibiting plastic deformation: computational aspects and a comparison with experimental results, Computer methods in applied mechanics and engineering, Vol 148 (1997), pp. 279-298.
- [6] Böl, M., Reese, S.: Finite element modelling of rubber-like polymers based on chain statistics, International Journal of Solids and Structures, Vol 43 (2006), pp. 2-26
- [7] Pere, B.: Solution of Coupled Thermomechanical Problems Using p-FEM, 8th European Solid Mechanics Conference (ESMC2012), Graz, Austria, 9-13 July 2012 (CD-ROM, 2 pages)



## REPAIR WELDING OF LOWER RAILS OF A 30CrMoV9 STEEL TRANSPORT BEAM AND THE CONDITIONS UNDER WHICH THE WELDING PROCEDURE MUST BE CARRIED OUT

<sup>1</sup>TANASKOVIĆ *Drakče PhD*, <sup>2</sup>ĐORĐEVIĆ *Branislav*, <sup>2</sup>SEDMAK *Simon*, <sup>2</sup>VUČETIĆ *Filip*,  
<sup>1</sup>GAJIN *Marko*

<sup>1</sup>HBIS GROUP Serbia Iron & Steel d.o.o., Smederevo, 113000 Smederevo

<sup>2</sup>Innovation Center of Faculty of Mechanical Engineering, Kraljice Marije 16, 11120 Belgrade

E-mail: [brdjordjevic@mas.bg.ac.rs](mailto:brdjordjevic@mas.bg.ac.rs)

### Abstract

*Welding technology used for repairing of the lower rail of a 30CrMoV9 steel transport beam is presented in this paper. Following the previously performed repair welding, a large number of cracks were detected, located along the length of the welded joint, as well as along the transversal direction. Based on the analyses of cracks and the initial welding procedure, additional repair welding was performed, for the purpose of eliminating these cracks. Due to the base material of the rail and its characteristics (i.e. poor weldability), adequate preheating and heat treatment had to be taken into account, and particular attention needed to be devoted to the way in which the welded joint is laid. Apart from the base material quality, aforementioned parameters have considerable influence on the welded joint quality and cracks initiation.*

**Keywords:** *repair welding, 30CRMOV9 steel, crack, weldability.*

### 1. INTRODUCTION

Every welded joint contains defects, regardless of its quality. Defects in welded joints can be of metallurgical–technological nature, or due to subjective errors during the welding [1-6]. Metallurgical–technological defects occur due to insufficiently adapted metallurgical–technological metal treatment during the welding. This group of defects includes: cracks (hot, cold, lamellar and stress annealing cracks), inclusions, pores and deviations from required properties (e.g. insufficient strength or plasticity of the metal). Subjective defects include weld forming defects, such as lack of fusion, excessive overhang and edge notches. With the development of new welding technologies and materials, the amount of defects in welded joints decreases. Defects are an integral part of welded joints and it is not realistic to expect a welded joint without them.

In order to provide required levels of quality, it is necessary to perform welding in accordance with existing standards and norms. Welding procedure specifications must contain all necessary parameters (basic and auxiliary), which provide insight into the technology, and as such they can be given to the welder as independent entities [6].

This paper describes the welding technology used for repairing of the lower rails of a steel transport beam for the purpose of eliminating the existing cracks and damages caused by the previous welding process. This beam is a part of a transporter used for carrying tightly wound rolls from the coiler to the storages in the facility “Hot Rolling Mill” in HBIS Serbia Steelwork (former Steelwork Smederevo), and during exploitation, it was subjected to significant compressive load (*Figure 1*). In order to avoid the occurrence of cracks in welded joints after repair welding, all activities must be performed entirely in accordance with the prescribed technology, since the base material of the rails was 30CrMoV9 micro-alloyed high strength steel, with poor weldability.



Figure 1 a) Lower rail b) A wheel on the rail

## 2. INITIAL WELDING TECHNOLOGY USED FOR THE TRANSPORT BEAM

The original rail of the transport beam was, according to the documentation, made of 42CrMo4 steel. This rail was replaced by the one made of 30CrMoV9. It is not known which electrode was used for welding in the previous repair welding procedure. After the initially performed repair welding and weld cooling, visual control and penetrants were used to examine the weld. A significant number of large and micro-cracks were detected. One crack spread across the entire welded joint length, along the parent material with length of 5 meters. Penetrant test method also revealed a large number of smaller cracks in the longitudinal and transversal directions along the weld. Some of the crack detected by the penetrant test method can be seen in *Figure 2*.



Figure 2 Transversal cracks in the weld, detected using the penetrant test method



After analyzing the exploitation conditions to which the rail was subjected, it was determined that the cracks could not result from them, but were specifically a result of the used welding technology. Following this, additional repair welding was performed, for the purpose of eliminating the cracks. Welded joint dimensions, recommended welding procedures, selection of the additional material and all welding conditions, as well as other accompanying elements were adapted to the base material and the exploitation conditions to which the rail and the beam were subjected.

### 3. BASE MATERIALS OF BEAM AND RAIL

The base material of the transport beam was S275JR steel, with a thickness of 25 mm, whereas the base material of the rail was 30CrMoV9, with a 35 mm thickness. As mentioned in the previous text, 30CrMoV9 is an enhanced steel with poor weldability, due to its properties, mainly its chemical composition. The chemical composition of base materials of the beam and the rail is given in *Table 1*.

*Table 1* Chemical compositions of materials S275JR and 30CrMoV9 [7]

Element (%)	C	Si	Mn	P <sub>max</sub>	S <sub>max</sub>	Cr	Mo	V
30CrMoV9	0.26-0.34	0.15-0.4	0.4-0.7	0.035	0.035	2.7-3.7	0.15-0.25	0.1-0.2
S275JR	0.22	/	/	0.05	0.05	/	/	/

Mechanical properties of the base materials in their enhanced state are shown in *Table 2*.

*Table 2* Mechanical properties of materials S275JR and 30CrMoV9 [7]

Mechanical properties	Tensile strength R <sub>m</sub> (N/mm <sup>2</sup> )	Yield strength R <sub>e</sub> (N/mm <sup>2</sup> )	Elongation A (%)	Toughness (J)
30CrMoV9	800-950	520	14	41
S275JR	420-500	250	22	/

#### 3.1 Weldability of material

Weldability assessment of steels using the carbon equivalent ( $C_{ek}$ ) takes into account the influence of chemical elements on the possibility of the forming of brittle phases during the welded joint cooling. If the calculated values of  $C_{ek} < 0.3\%$ , it can be assumed that the conditions have been met for obtaining welded joints of required quality without the need for specific technological measures, i.e. the steel is of good weldability. If  $0.3\% < C_{ek} < 0.5\%$ , preheating or other measures must be applied in order to achieve the required quality, i.e. such steel is conditionally weldable. In the case that  $C_{ek} > 0.5\%$ , the possibility of obtaining a welded joint with the required level of quality still exists, however specific technological measures must be applied.

$C_{ek}$  calculated according to the Seferian method [5,8], for material 30CrMoV9 was 0.64%, which means that welded joints of required quality can be obtained with strictly controlled preheating, heat treatment and cooling.

One of the indicators of increased brittleness due to phase – structural changes, i.e. the indicator of vulnerability to cold cracks, is the hardness (HV) of the heat affected zone. It is considered that, in the case of most structural steels, the brittle phases will not form if the hardness does not exceed 350 HV. Based on the chemical composition of the structural steel and an empirical expression (1), it is possible to determine the magnitude of HV.



$$HV = 90 + 1050 \times C + 47 \times Si + 75 \times Mn + 30 \times Ni + 31 \times Cr \quad (1)$$

Calculated value of HV for steel 30CrMoV9 was 600.1, suggesting that this material is highly vulnerable to cold cracks.

For the purpose of assessing the vulnerability to hot cracks, the following empirical coefficient, HCS, is used, determined by the expression (2).

$$HCS = \frac{C \times [S + P + \frac{Si}{25} + \frac{Ni}{100}] \times 103}{3 \times Mn + Cr + Mo + V} \quad (2)$$

If  $HCS < 4$ , hot crack will most likely not form in the weld metal of steels with  $Re < 700$  MPa, whereas in the case of high strength steels, this conditions in stricter,  $HCS < 1.6$ . The calculated value of HCS for 30CrMoV9 was 2.3, and since it is a high strength steel, it is also vulnerable to hot cracks.

## 4. WELDING TECHNOLOGY

### 4.1 The selection of the welding procedure

The selection of the welding procedure was performed based on the following factors:

- Equipment potential of the contactor
- Staff potential (professional competence of the welding staff)
- Costs of welding activities
- Performance productivity
- Performance quality.

Based on the factors listed above, the manual arc welding (MAW) procedure with a coated electrode was selected for the purpose of welding. This procedure can be adjusted to all positions for all geometries and dimensions of workpiece grooves.

### 4.2 Welding equipment

During welding with a base electrode, a reverse polarity current (DC +) is used. For the selected welding procedure, devices with a steeply declining static characteristic are used, which generate DC + current as output.

### 4.3 Preparation of base material for welding

Preparation of base material of the rail for welding consists of forming the grooves for cleaning and grinding. Groove preparation is performed in several stages. First it is necessary to clean the surface by removing oil and grease, then it should be ground to metallic shine. After the visual inspection, it should be determined if there is a need to examine the surface using a magneto-flux meter in order to determine the crack length. Procedure which involves a welding machine, special electrodes and oxygen, combined with the gas procedure is be used in preparing of the groove, as it is shown in *Figure 3*.

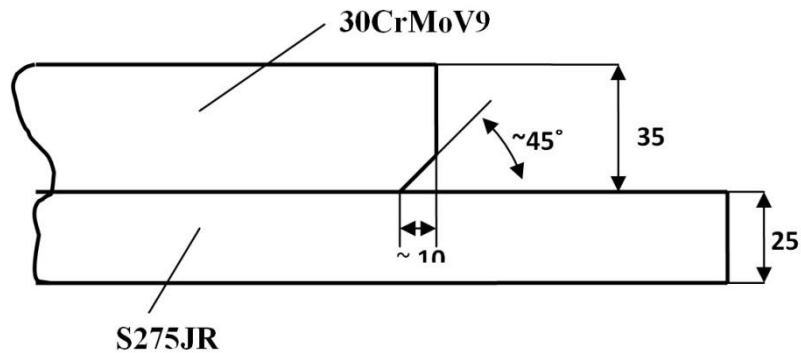


Figure 3 Groove preparation

#### 4.4 Preheating and interpass temperature

Preheating temperature for welding of 30CrMoV9 is calculated using relations (3-6). It is of great importance to comply with the preheating modes, since steel 30CrMoV9 has an increased carbon percentage (0.26-0.34%). In addition, the thickness of the piece itself causes a sudden temperature loss, thus in the case of poor compliance with the parameters (especially preheating), cracks may occur after welding.

$$HV = 360 \times [C]_h = 360 \times C + 40 \times (Mn + Cr) + 20 \times Ni + 28 \times Mo \quad (3)$$

$$[C]_d = 0.005 \times [C]_h \quad (4)$$

$$[C] = [C]_d + [C]_h \quad (5)$$

$$T_p = 350 \sqrt{[C] - 0.25} \quad (6)$$

Calculated value of preheating temperature was 200 °C, and this value was adopted as necessary during the performing of welding activities. During the preheating, regulations defined by the SRPS ISO 13916 standard [9] are applied.

Interpass temperature in the welding zone must not exceed 400 °C. The welded joint must be shielded from draft, potential rain and other external influences. After the welding has been completed, further heat treatment was not possible due to its size, but the welded layer needs to be at least wrapped in fireproof canvas, in order to ensure slow cooling. This is of great importance since this material is vulnerable to crack initiation in the case of quick cooling.

#### 4.5 Additional material

During welding of non-alloyed with low-alloyed steels, it is common practice to select an electrode which fits with the „lower value“ material, in the case of butt weld, whereas in the case of fillet welds, an electrode fitting with the „higher value“ material is selected.

The selection of additional material is made based on the quality and dimensions of the base material (30CrMoV9), the complexity of the assembly, required welded joint quality, the welding position and procedure.

Based on all of the aforementioned, the selection of the base electrode EVB 2CrMo (manufactured by Jesenice, Slovenia) was made, since this electrode fits the material of the rail. Electrode EVB 2CrMo is an alloyed base electrode used for welding of thermally stable steels Cr-Mo and CrMoV, with working temperatures up to 600 °C, corresponding steel casts and also for welding of nearly



identical alloyed steels used for enhancements (as is the case here), as well as steels used for nitriding and cementation, with strength up to 980 MPa. After welding, it is recommended tempering for 30 minutes at a temperature of 720 °C.

Chemical composition and mechanical properties of electrode EVB2 CrMo are given in *Tables 3* and *Table 4*.

*Table 3* Chemical composition of the base EVB2 EVB2 CrMo electrode [10]

Element	C	Si	Mn	Mo	Cr
%	0.08	0.45	0.7	1	2.4

*Table 4* Mechanical properties of the weld metal made of base EVB2 CrMo electrode [10]

Mechanical properties	R <sub>m</sub> (MPa)	R <sub>e</sub> (MPa)	A (%)	(KJ)
Value	620-720	470	20	95

Electrodes must be stored in a dry place and should always be dried before use in furnaces, at temperatures recommended by the manufacturer. According to the catalog, electrode EVB2 CrMo is dried at 400 °C for 1 hour. Since the electrode coating is highly hygroscopic, it is necessary to keep it in driers – quivers, at a temperature of 100 °C before welding, and particular attention should be paid to increased humidity conditions (rain). The same electrode should not be dried more than three times.

#### 4.6 Welding procedure

Welding was performed in multiple passes. For the root pass, an electrode with a diameter of 2.5 mm was used, whereas filling passes were welded using the 3.2 mm electrode. Droplets of molten material around the welded joint which may appear during welding must be removed by grinding. Each additional pass should be welded after the previous one has been cleaned. Amperage during the root pass (2.5 mm electrode) ranged from 80 to 100 A, whereas during the filling passes (3.25 mm electrode) it was between 110 and 140 A. Passes were laid in a way that resulted in the welded joint thickness of 15 mm (*Figure 4*).

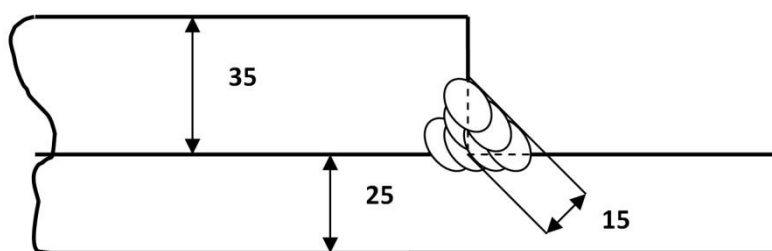


*Figure 4* Passes laying and weld thickness

In order to avoid deformation during the welding activities and heat input, welding was performed in short steps for the purpose of obtaining a continuous weld in the order shown in *Figure 5*.

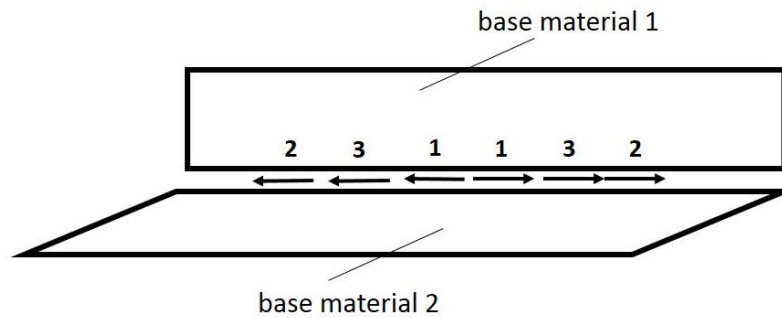


Figure 5 Order of the welding

Interpass temperature in the welded zone must not exceed 400 °C. The welded joint must be shielded from draft and potential rain. After the welding has been completed, the welded joint was wrapped in a fireproof canvas to secure slow cooling. This is of great importance since the material in question is vulnerable to crack initiation in the case of quick cooling, as previously mentioned. The appearance of the weld after welding the lower rail of the transport beam, i.e. after repairing is shown in Figure 6. As mentioned in the previous text, the joint was welded continuously by segmented joining of smaller welds.



Figure 6 Appearance of the weld after welding

## DISCUSSION AND CONCLUSIONS

Welding activities should be performed in accordance to the prescribed welding technology, and the welded should be introduced to all parts of the control process, since they are in charge of the welding activities, along with the welding coordinator. Each welder, together with the coordinator of welding procedure, should check if all of the aforementioned conditions have been met prior to welding, and if this is not the case, the welding must not be performed.

The welding procedure presented in this paper was in accordance with the prescribed welding technology for the lower rail of the transport beam. Presented technology contains the instructions for performing of welding activities. However, such instructions do not always guarantee a good result. After the initial welded joint was subjected to control, it was determined that a large number of cracks, visible even without special test methods, were present. A crack with the length of 5 m was detected along the entire length of the weld, as a consequence of inadequate cooling and the continuous weld, made by segmented joining of smaller welds. Such continuous weld was unable to absorb the deformations and bending due to cooling. In addition to this crack, a large number of small transversal cracks and longitudinal cracks were detected using the penetrant method. After this, additional repair welding, along with the defining of a new welding technology was



# INTERNATIONAL SCIENTIFIC CONFERENCE ON ADVANCES IN MECHANICAL ENGINEERING

12-14 October 2017, Debrecen, Hungary



undertaken. Hence, the continuous weld is not desirable and necessary for the purpose of connecting of the rail and the beam. Instead, it is recommended (by the original documentation as well) to perform the non-continuous welding i.e. welds with interruptions.

Weldability is considered as a range of technological properties of the base material of machine part and additional material used for welding which define its behavior under the changes that occur during welding, as well as the ability of the base and additional material to form welded joints with guaranteed safety, assuming an optimal welding technology was used [2, 5]. As shown, steel 30CrMoV9 is conditionally weldable, hence during the welding of this steel, it is necessary to, in addition to adequate preheating and additional heat treatment, take into account the way in which welding is performed and which parts are being connected. Therefore, weldability is not a fixed parameter for all materials, but depends on the welding technology details, exploitation demands, the welding process, etc.

## ACKNOWLEDGEMENT

The authors of this paper acknowledge the support from Serbian Ministry of Education, Science and Technological Development for projects TR35040 and TR35011.

## REFERENCES

- [1] Tanasković D., Tatić U., Đorđević B., Sedmak S., Sedmak A.: The effect of cracks on stress state in crane wheel hard-surface under contact loading, *Technical Gazzete*, Vol.24 No.Supplement 1, pp169-175, ISSN 1330-3651, 2017.
- [2] Katarina Gerić: *Prsline u zavarenim spojevima*, Mogorafija, FTN Izdavaštvo, ISBN 86-85211-28-X Novi Sad, 2005.
- [3] Drakče Tanasković, Branislav Đorđević, Mihajlo Arandelović, Simon Sedmak, Aleksandar Sedmak, Miloš Đukić, Uroš Tatić: Repair Welding of Crane Wheels in Steelworks Smederevo, *Advanced Materials Research (Volume 1138)*, conference: 8th International Conference on Innovative Technologies for Joining Advanced Materials (TIMA 16), pp. 180-185, ISBN 978-3-03835-768-1 (ISSN 1662-8985), Timisoara, Romania, June 02-03, 2016.
- [4] R. Jovičić, Z. Radaković, S. Petronić, E. Džindo, K. Jovičić Bubalo: Inspection, Non-Destructive Tests and Repair of Welded Pressure Equipment, *STRUCTURAL INTEGRITY AND LIFE*, Vol. 16, No 3, ISSN 1451-3749, pp. 187–192, 2016.
- [5] Zvonimir Lukačević: *Zavarivanje*, Slavonski Brod 1998.
- [6] Hal Wislon: *Welding secrets*, Second edition, Flyco Machine Company, 1990.
- [7] [www.steelnumber.com](http://www.steelnumber.com)
- [8] Tünde Kovacs, Peter Pinke: BWRA and Séférian Model for Preheating Temperature Calculation in Case of Low Alloyed and Unalloyed Steel, *Materials Science Forum*, February 2017.
- [9] SRPS EN ISO 13916:2013 - Welding - Guidance on the measurement of preheating temperature, interpass temperature and preheat maintenance temperature (ISO 13916:1996)
- [10] Elektrode Jesenice – catalogue, 2012, <http://www.elektrode.si>



## WATER LEACHING BEHAVIOUR OF CARBAMIDE SPACE HOLDER PARTICLES IN TiAl FOAMS

*THALMAIER György PhD, SECHEL Niculina, VIDA-SIMITI Ioan PhD*

*Technical University of Cluj-Napoca, 103-105 Muncii Ave., 400641 Cluj-Napoca, Romania*

*E-mail: [gyorgy.thalmaier@sim.utcluj.ro](mailto:gyorgy.thalmaier@sim.utcluj.ro), [niculina.sechel@stm.utcluj.ro](mailto:niculina.sechel@stm.utcluj.ro), [Vida.Simiti@stm.utcluj.ro](mailto:Vida.Simiti@stm.utcluj.ro)*

### **Abstract**

*In this study the characterization of the water leaching behavior of carbamide space holder particles in Ti – 48 at. % Al intermetallic foams was studied. Porous disks of Ti – 48 at. % Al intermetallic compound was manufactured by the coated space holder method by coating the spherical carbamide particles with the corresponding elemental powder mix. The powder mixture was pressed at 200 MPa and the samples were water leached. The used method is based on the ISO 2738:2001 standard. Comparing the experimental data with existing solvent debinding models could be used to elucidate the mechanisms operating during the space holder removal process through water leaching.*

**Keywords:** *Ti-Al intermetallic, porous material, coated space holder, water leaching.*

### **1. INTRODUCTION**

Metal foams are class of materials which has specific physical and mechanical. The unique properties of metallic foams make them desirable for a wide variety of applications, including filters, thermal barriers or as a core material for structural sandwich panels. Numerous studies are focus on porous light metals such as aluminium which usually prepared by different process routes (solid and liquid state) such as penetration casting, melt gas injection, powder metallurgy, and replication process [1]. Porous materials with higher melting points such as iron base alloy or intermetallic compounds are especially attractive candidates for high temperature catalyst substrates and filters due to their high strength and specific stiffness, excellent anticorrosive properties, large specific surface area and low specific weight [2, 3].

Titanium aluminide (TiAl) possesses an interesting combination of properties such as low density, high specific strength, good oxidation resistance at high temperatures and good corrosion resistance in acid and alkali mediums [4-6]. Porous TiAl-based intermetallic compounds with a mixture of metallic and covalent bonds combine advantages of ceramics and metals, exhibiting excellent performances in demanding atmospheres [6].

Porous titanium aluminides were fabricated using numerous ways, all with their ups and downs and most of the method involves space holder materials. The removal of the space holder particles is a critical step in the fabrication chain. Water is the preferred choice as a dissolving liquid with water-dissolvable space holding particles considering its abundance and price. However in depth studies of the leaching behaviour is scarce. The objective of this study was to understand the water leaching behaviour of carbamide space holding particles in the AlTi foams, since the residual carbamide can cause severe cracking in the samples during subsequent heat treatments. Leaching tests were performed using a real-time weight measurement technique developed by B. Arifvianto [7]. The results were fitted to existing solvent debinding models from powder injection moulding.



## 2. METHODS

Porous intermetallic samples were made by coating spherical carbamide particles with the corresponding elemental powder mix (52 at. % Ti and 48 at. % Al). Samples of different relative density were prepared, the ratio of the powder mixture to the carbamide being so calculated to give a porosity of 60, 70, 80, 85, and 90%. The particle size range for the carbamide particles was 2000-2500  $\mu\text{m}$  and for the metallic powders  $< 45 \mu\text{m}$ . Prior to the coating step a binder solution prepared from dissolved 2 wt % polyvinyl-alcohol in water was sprinkled onto the carbamide particles to prevent segregation.

The carbamide granules were put into a cylindrical polyethylene container, fixed in a horizontal rotating drum and the coating was carried out at 60 rpm for 10 min. The coated particles were pressed at 200 MPa in a hardened steel mold with a diameter of 15 mm. A zinc stearate powder was applied to the dies inner surface for lubrication. After pressing the samples were polished to reduce burrs that are formed during forming and then were measured and weighed.

The carbamide leaching behavior was determined using a method based on ISO 2738: 2001. The method consists in immersing each sample in 250 ml of distilled water at room temperature on an Archimedes scale to record the variation of the sample mass during the elimination of the space holder at 5 minute intervals. Dissolution of the pore former in the sample can be expressed quantitatively by its percentage removed during immersion:

$$W_d = \left( \frac{W_{0,w} - W_{t,w}}{W_{0,w} - W_{f,th}} \right) \quad (1);$$

were:  $W_{0,w}$  initial sample mass in water;  $W_{t,w}$  - sample mass at a certain time during immersion;  $W_{f,th}$  - is the final mass of the sample after removal of the pore forming agent. The final mass of the sample after the complete removal of the space holder was calculated using the following formula:

$$W_{f,th} = (1 - X) \left( \frac{\rho_m}{\rho_s} \right) W_{0,w} \quad (2);$$

Where:  $\rho_m$  - the theoretical density of the metallic powder mixture (3.88  $\text{g/cm}^3$ ),  $\rho_{sh}$  - is the space holder material's density (1.32  $\text{g/cm}^3$ ),  $X$  - the planned porosity for the sample. From these we calculated the effective diffusion coefficient using the Lin-German model from of the slope given by the equation [8].

$$\ln \frac{1}{F} = \frac{D_e t \pi^2}{(2\psi)^2} \quad (3);$$

Where  $F$  - is the residual pore forming agent fraction,  $D_e$  - the effective diffusion coefficient,  $\psi$  - is the ratio between the volume and the sample area,  $t$  - is the immersion time.

## 3. RESULTS

Figure 1 shows a continuous mass decrease of the samples. If during the measurements constant mass has not been reached, the measurement was stopped when the variation between the two consecutive measurements reached the sensitivity limit of the balance. In the first minutes of the measurement (up to 10 minutes), a rapid decrease of the mass occurs followed by a considerable slowing of the dissolution process. During these measurements no saturation phase was observed,



the last phase, saturation as described by Arifvianto in his paper [8].

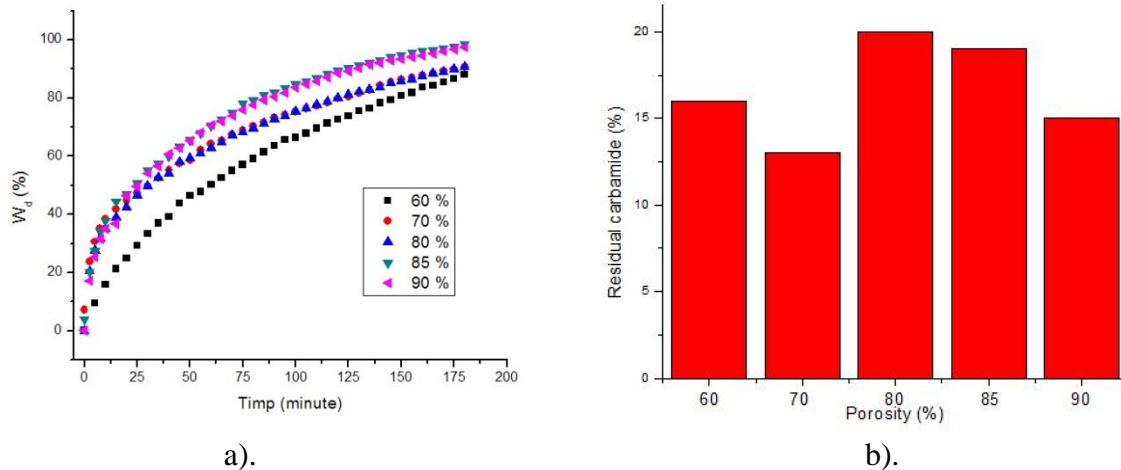


Figure 1 Dissolution of the space holder (a) and residual carbamide fraction (b)

As figure 1b suggests the residual carbamide content in the samples is less than 20% of the initial mass. These residual particles none the less can create significant problems due to the low melting temperature of the carbamide ( $\sim 133^\circ\text{C}$ ) and the low green strength of the samples. In order to further evaluate the leaching behaviors in these samples the effective diffusion coefficients were calculated from the slope of the Lin-German equation [8].

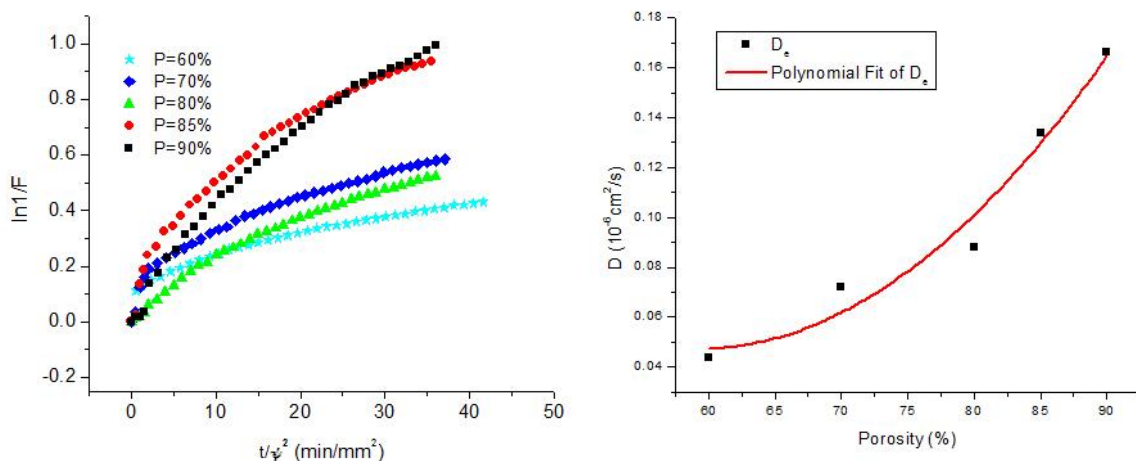


Figure 2 Application of the Lin-German model for the leaching of carbamide particles (a) and the dependence of the apparent diffusion coefficient with porosity

From the data presented in Fig. 2 the apparent diffusion coefficient was calculated in the two areas of the curve. The areas were separated at the point where the slope change was observed. In this area the pore forming agent comes in direct contact with the water and a rapid dissolution occurs. This process is specific to the removal of the pore forming agent from the first row of coated particles. The second step is a process controlled by water diffusion through the metal powder layer and the dissolution rate of the pore forming agent. It is known that carbamide has a huge solubility in water ( $>1$  kg/l at room temperature) and the permeability of a porous medium decreases linearly with its thickness, so we can conclude that the limiting factor is the water diffusion through the metal coating.



Figure 3 shows the variation of the apparent diffusion coefficient with porosity. This variation is a 2nd order polynomial type. The regression lines presented in this study appeared to be in acceptable limits since the  $R^2$  criterion is close to 1 (0.94). Experimentally it was observed on cross sections that the elimination of the pore forming agent is performed only on a depth of about 3 particles, or in the case of samples with 60% porosity, suggesting that water diffusion is conveniently achieved only in the total combined wall thickness of about 2.5 mm.

## CONCLUSIONS

In this study, space holder removal with the water leaching method was investigated using a real-time measurement technique. Fitting the data acquired into the existing solvent debinding models resulted in plots representing the three primary regimes during the leaching and space holder removal process, namely (i) rapid dissolution, (ii) dissolution and diffusion and (iii) saturation. The saturation step was not evident since the dissolution of the space holder particles from the depth of the sample is limited due to the slow water diffusion and subsequently the slow space holder removal rate. In order to have a reasonable space holder removal rate one must limit one dimension of the part, limiting it to approx. 7-8 particle deep.

## REFERENCES

- [1] M.F. Ashby, T. Evans, N.A. Fleck, L.J. Gibson, J.W. Hutchinson, H.N.G. Wadley, *Metal Foams: A Design Guide*, first ed., Butterworth-Heinemann, Woburn, 2000;
- [2] C. Park, S.R. Nutt, *Strain rate sensitivity and defects in steel foam*, *Material Science Engineering A*, 323 (2002), 358–366;
- [3] Yu.V. Milman, D.B. Miracle, S.I. Chugunova, I.V. Voskoboynik, N.P. Korzhov, T.N. Legkaya, *Mechanical behaviour of  $Al_3Ti$  intermetallic and L12 phases on its basis* *Intermetallics*, 9 (2001), 839-845;
- [4] K. Kothari, R. Radhakrishnan, N. M. Wereley, T. S. Sudarshan, *Microstructure and mechanical properties of consolidated gamma titanium aluminides*, *Powder Metallurgy*, 50 (2007), 21-27;
- [5] J. Lapin, *TiAl – based alloys: present status and future perspectives*, *Metal*, 5 (2009), 19 -21
- [6] K. Kothari, R. Radhakrishnan, M. Wereley, *Advances in gamma titanium aluminides and their manufacturing techniques*, *Progress in Aerospace Sciences*, 55 (2012), 1-16;
- [7] B. Arifvianto, M.A. Leeftang, J. Zhou, *A new technique for the characterization of the water leaching behavior of space holding particles in the preparation of biomedical titanium scaffolds*, *Materials Letters* 120 (2014) 204–207;
- [8] Shivashankar TS, German RM. *Effective length scale for predicting solvent debinding times of components produced by powder injection molding*, *J Am Ceram Soc* 1999;82:1146–52



## ELIMINATING THE POSITIONING ERROR OF GAMMA KNIFE; RECOMMENDATIONS FOR THE MECHANICAL OVERHAUL

<sup>1</sup>TIBA Zsolt PhD, <sup>2</sup>FEKETE-SZŰCS Dániel, <sup>1</sup>MENYHÁRT József

<sup>1</sup>Department of Mechanical Engineering, Faculty of Engineering, University of Debrecen  
E-mail: [tiba@eng.unideb.hu](mailto:tiba@eng.unideb.hu) [jozsef.menyhart@eng.unideb.hu](mailto:jozsef.menyhart@eng.unideb.hu)

<sup>2</sup>AFT Soft Ltd

E-mail: [fszdani@unideb.hu](mailto:fszdani@unideb.hu)

### Abstract

The gamma knife is a medical device engineered in the last third of XX century. One of these devices has been partial regenerated. The regeneration involved the change of the run-down radiation source as well as the rebuild of motors and control equipment. After the partial regeneration the device worked not properly. The failure was detected by the computer control unit. It was considered by the control unit serious problem and operation of the device was stopped. The error was provisionally ceased however during the inspection it was realized that there were significant changes in operation conditions of the machinery. In this paper we introduce the type of the error and the reason for it, the provisionally repair, as well as we give suggestion for rebuilding involving reconstruction with which the problem can be definitively eliminated. The paper does not study the device from medical point of view. The device is considered as a machinery and we introduce the operation errors and the cause of them as well as we give recommendation for the repair.

**Keywords:** Gamma knife, positioning error, cobalt-60 source, source body, collimator body

### 1. OPERATION OF THE GAMMA KNIFE

In this paper we introduce operation principle of the gamma knife in order to clear the requirements facing the machinery, however we do not deal with the medical treatment in details.

The tumour mapped by computer tomography is discredited by gamma ray concentrated in thin bundle of rays. The gamma rays are directed and focused to the tumour at different angular positions damaging the sound tissue at least.

Cobalt-60 source and loading unit

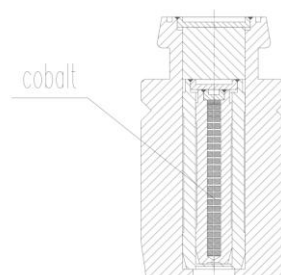
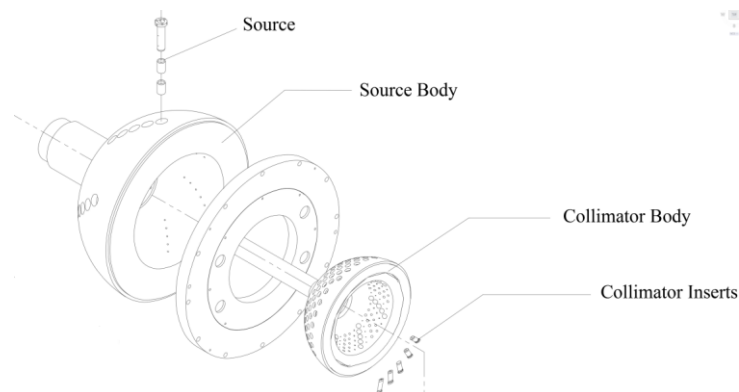


Figure 1 Enclosing the radiation source [2]



The main problem is that the gamma ray cannot be directed and focused by either optical or electromagnetic methods. The only method is the shielding [1]. The shielding is implemented by multilayer enclosing the radiation sources in case made of high mass number material. This construction provides the traveling of the bundle of rays in a small cross section, see *Figure 1* In *Figure 1* it can be seen, that the multilayer enclosing allows the gamma ray generated by the Co-60 radioactive to travel, in conformity with its actual orientation, down in a thin bundle. The second problem to be resolved is the direction of the ray bundle. It is achieved by two components which are turning adequately relative to each other, see *Figure 2* The ray sources are assembled in a hemisphere shell (source body) that can be rotated. In this hemisphere there is another hemisphere shell (collimator body) by which the sources not used in the actual therapy can be shielded.



*Figure 2* Directional-shielding hemisphere shell [2]

The operation of the mechanism:

- By turning the source body it may be achieved that one or more ray bundle get to appropriate position to be aimed at the tumour.
- By turning the collimator body it may be achieved that only the boreholes shall be coaxial with the direction of the ray sources which are at appropriate angular position to ray the tumour.
- The synchronous turning of the two hemisphere shells makes it possible that only the bundles function in terms of direction and shielding, in the therapy which are in appropriate position. Other bundles remain inactive in the therapy.

The radiotherapist can design the form of motion in time and spatial precisely with the software of control unit that enough, considering the radiation to discreate the tumour. For realizing the cause of error and the appropriate construction to eliminate it, we consider its mechanics, assembly technology and logistics.

The gamma knife device implements this procedure as follows:

- The source body is connected to a hollow shaft driven by servo-motor through a gear drive.
- The collimator body is connected to a shaft driven by another servo-motor through a gear drive. The shaft is connected to the gear drive through a coupling.
- The three-phase servo-motors are controlled by encoders.
- The power electronics of servo-motors are controlled by microcomputers.
- The motion parameters defined by the control unit (angular displacement, angular velocity, angular acceleration) are compared to the actual values.
- If the difference between the prescribed and actual values exceeds the error limit, the control computer will stop the procedure.

The spherical shells are made of high mass number material eg. lead alloy, this is why they are high-mass, loading the bearing support of the shafts very much. The effective therapy requires the



accurate direction of the bundle of rays (the tolerance is 0.1 mm order of magnitude). Concerning the accuracy let's study the following deduction:

Suppose, the distance between the tumour in the patient's skull and the radiation centre of the device is 100 mm. Let's consider the required accuracy for 0.1mm, from which the turning error of the spherical shells is:

$$\alpha = \arctg\left(\frac{0.1 \text{ mm}}{100 \text{ mm}}\right) = 0.057^\circ \quad (1.1)$$

where  $\alpha$  [°] accuracy of the positioning

The tolerance of the angular displacement determines the required technical specifications of the turning mechanism. If the bearings are seizing, the required accuracy cannot be achieved. The arising supplementary load (force of inertia) when starting and stopping the rotating parts, due to the moment of inertia of them, has to be taken into account. It follows from this, that the measure of angular velocity and angular acceleration have to be kept with high accuracy too, which supposes torque requirement. The angular positioning is provided by the servo-controller with the control software.

## 2. ERROR PHENOMENON

As it was mentioned, after the partial regeneration (change of the run-down radiation source, high power controllers, microelectronics, control software as well as the rebuild of motors) the device worked not properly. Because of it, the source body and the collimator body could not reach the angular position prescribed in the given term. The problem is represented in *Figure 3* where the actual positions of the source body, detected by the encoder of servo-motor driving the hollow shaft, is shown.

The reference parameters provided by the manufacturer are shown in *Figure 3*.

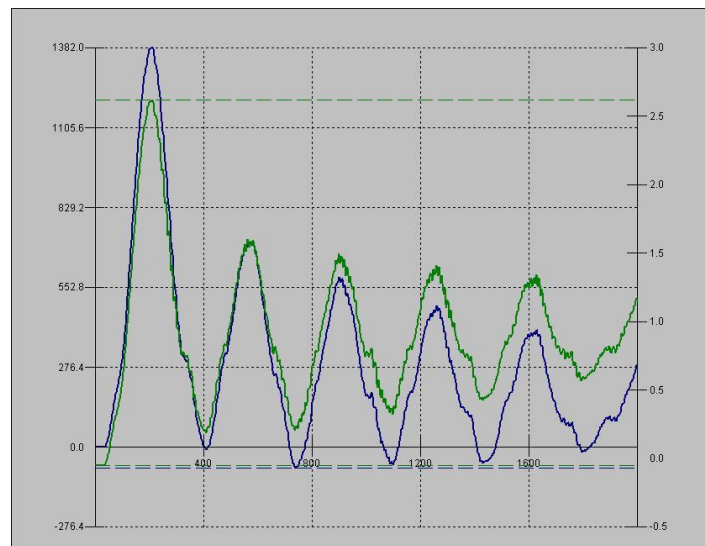


*Figure 3* Reference parameters provided by the manufacturer [3]

The interpretation of the figure:

- On the X-axis the frequency of the sampling is measured, from which the period may be concluded.
- On the Y-axis the blue curve represents the accuracy of the positioning, the green one represents the torque exerted by the servo-motor.



Measuring results after the partial regeneration shown in *Figure 4* are provided by the control computer and reference-encoders. Similarly to the previous figure, on the X-axis the frequency of the sampling (indirectly the time), on the Y-axis the positioning error (the difference of the required angular position and the actual one) are shown.

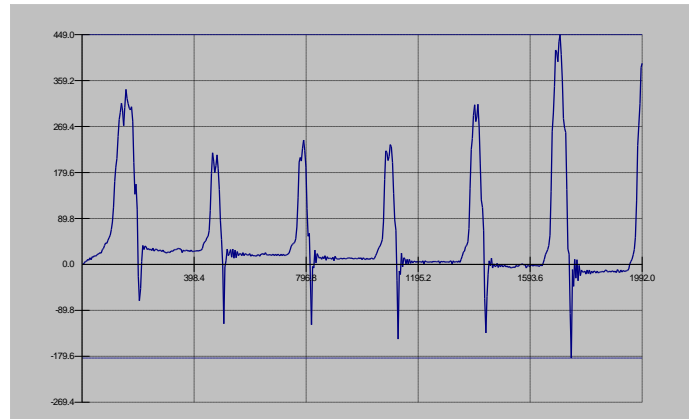


*Figure 4* Positioning error of the hollow shaft vs accuracy of the sampling [3]

It can be seen in *Figure 4* that the shaft holding the source body turns with positioning errors. The error depends on the time and recurs per 5 minutes. Later on we will refer to this measuring results and demonstrate its relation to the machinery. According to the measuring results, the measure of error exceeds about 15 times the error limit (30 encoders) defined by the manufacturer [2]. The software controlling the servo-drive, stops the movement if the positioning error exceeds the allowed one in the interest of overburden protection and effective therapy. It happened in our case as well.

### 3. PARTIAL REGENERATION OF THE GAMMA KNIFE

After detecting the error by the operating labour, the experts of Faculty of Engineering, University of Debrecen were requested for counselling. Meanwhile an external expert was contacted as well who was employed at the producer of the device. On the basis of the external expert's advice we effected a repair of the device, which was successful in terms of immediate operation. Nevertheless our persuasion is that the repair was only partial and it did not cease the causes of the malfunction. For understanding the repair work, see the *Figure 5* The measuring results of the control software showed, that the malfunction was caused by the positioning error of the source body (2) connected to the hollow shaft (4). The opinion of the external expert was (it was proved later on), that the malfunction was caused by the small clearance of the bearing (5) and it should have been increased. The prescribed working clearance is between 0.1 and 0.25 mm. Beside the bearing (5), the shaft is supported by another bearing placed behind the tooth gear, but despite the assembly drawing, it is conical roller bearing. From the shaft bearing arrangement it follows that the load of the bearing (5) exceeds far the one of another, this is why we concentrated to this. For adjusting the bearing clearance we removed the gear (6). To survey the actuation torque demand of the mechanism in the actual condition, before beginning the assembly, we measured the starting torque of the hollow shaft (4) and the source body (2) connected to it by turning the gear driving the gear (7) with a torque wrench which was 20 Nm. The starting torque of the servo motor-motor driving the hollow shaft is 11.7 Nm (catalogue data), that is obviously not sufficient. With visual inspection detected, that the lubrication of the driving gear pair was suit and there were no wear, break or any other defect on the toothed gears. Consequently the tight movement was induced not by the gearing.

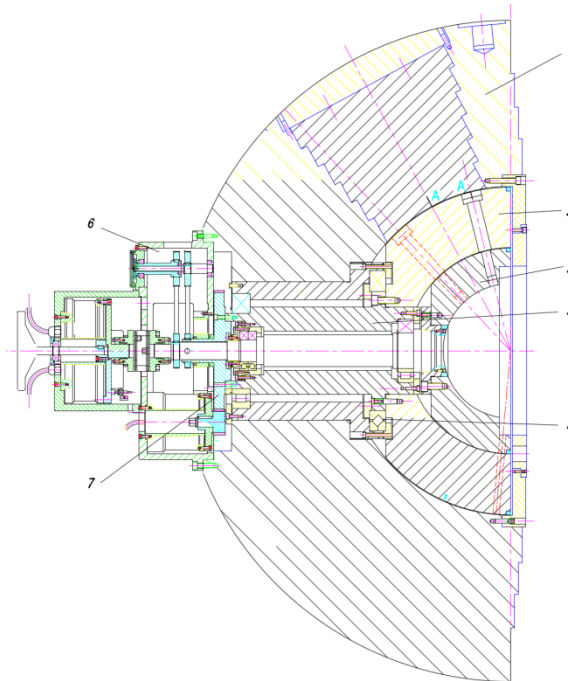


Figure 5 Sectional view of the gamma knife [based on 2]

On the basis of our experiences in the field of servo-drive we suspected that operating the servo-motor by overcurrent controlled by the power electronics would result in swinging motion. The servo-motor cannot operate smooth because of the high power demand since its overload protection decreases the current drain by this means the rpm as well. This action recurs periodically and may cause the positioning error (see Figure 4). After the torque measuring we removed the gearing and the toothed gear (7). The toothed gear is fixed to the hollow shaft with 6 pieces M8 socket head cap screws. For adjusting the bearing clearance we applied these holes. We designed and manufactured a special tool for assembling, see Figure 6.

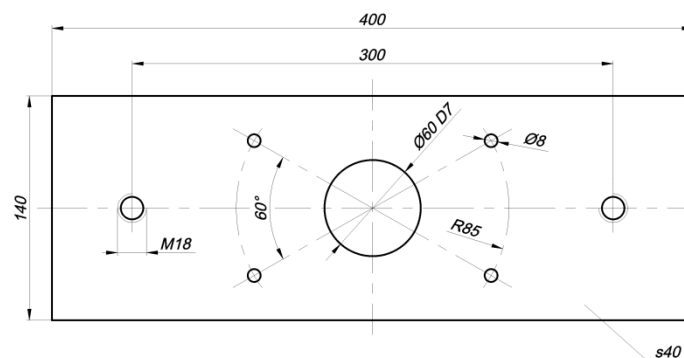


Figure 6 Bracket for adjusting the bearing clearance

We fixed the bracket shown in Figure 6 to the hollow shaft through the threaded holes with 4 pieces M8 screws. After this we supported the bracket on the vertical surface of the radioprotective shield without a gap applying the M18 threaded holes in the bracket. The displacement of the hollow shaft was measured with dial gauge. The hollow shaft was tensioned toward the gearing by synchronic turning the M18 screws against the bearing (5). Meanwhile we measured the displacement. At 0.15 mm displacement the turning of the hollow shaft became hard from which we concluded the zero clearance of the bearing supporting the source body. Despite the assembly drawing, the outer bearing's inner ring was retained by not a distance ring but a lock nut. Tensioning the hollow shaft,



this lock nut was relieved afterwards taking the pitch of the M195x2 thread into count, the nut was turned outwards. We note, that producer did not locked the nut by any method or device that raise the question of design error. After adjusting the bearing clearance to the mean value of the manufacturer specification, we disassembled the bracket. We realized that the lubrication of the outer conical roller bearing was not appropriate and corrosion could be realized on the small end face of its outer ring, to which later on we will refer. We lubricated the bearing; reset the toothed gear and the gearing. Behind the toothed gear we placed gauge sheets of 0.3 mm thickness on the fixing screws in order to ensure the adjusted bearing clearance after fixing. The bearing clearance set in after having turned the hollow shaft by 30 degree. It was proved by the position error vs time diagram evaluated by the control software (we won't detail it because of the volume limit). After the run-in the following error vs time diagram was measured:

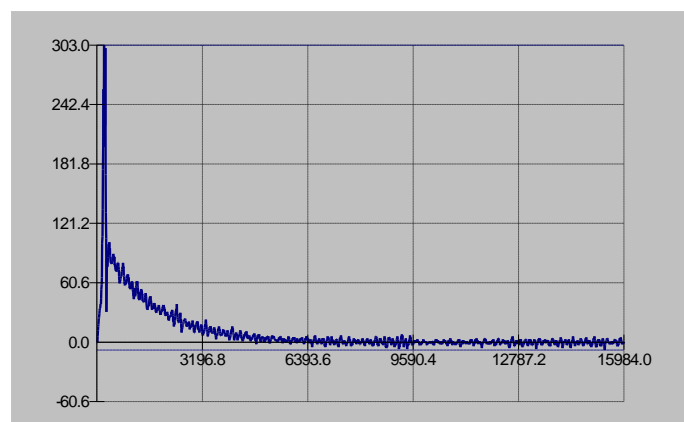


Figure 7 Positioning error vs time diagram after repairing

In the figure it may be seen, that after the transient stat the error decreased on average to the third value of the allowed limit. Accordingly we could resolve the problem – at least temporarily – the device is appropriate for the therapy.

#### 4. REVEAL OF THE CAUSE OF ERROR

Without disassembling the device, the condition of the bearing (5) cannot be assessed. This statement is very important since the disassembling is possible only after removing the radiation sources. After the partial regeneration (see chapter 3) the operating labour carried out wide-ranging tests. *Figure 8* shows one of the test result.

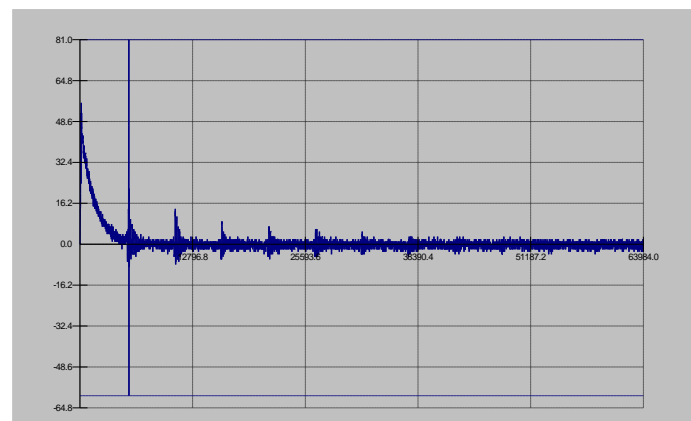


Figure 8 Positioning error after the run-in [3]



Compering the *Figure 7* and *Figure 8* it can be seen, that after adjusting the bearing clearance the error did not cease only moderated.

The explanation for the discrepancy between the two figures are the following:

- On the one hand the scaling of the *Figure 8* is much smaller than one of *Figure 7*, accordingly some discrepancies may be seen well.
  - On the other hand during the run-in the rigid body constituted by the hollow shaft and the inner ring of the bearing can move marginally in axial direction in the bearing house, consequently the axial bearing clearance can change too. The principle of aiming for the level of energy minimum gets on, thus the system aims the smallest resistance position. However it will not exclude the peak values. (The first peak may be measuring error or data communication anomaly.)
- Our opinion is that the overhaul cannot be avoidable, the operability was reinstate only temporally.

## 5. ENGINEERING ANALYSE OF THE DETERIORATION

In previous chapter 5 we gained two important experiences:

- The starting torque decreased to the quarter. The fundamental explanation for it is the bearing clearance adjustment and the subsequent lubricating of the outer bearing.
- The periodically arising positioning error has not ceased but moderated. The reason for it may be the bearing clearance adjustment as well.

The periodic time is constant. Since the hollow shaft rotates at a constant angular velocity, the cause of the fault may be found here. Furthermore we assumed that because of the radioactive radiation either a piece of the raceway scaled or a rolling element damaged. In both cases it is true, that the bearing temporarily sticks while the rolling element rolls over the damaged surface of the raceway or the rolling element contact the raceway at its damaged surface. It may explain the cause of the periodically arising positioning error.

Let's inspect at first the deterioration of the rolling element! It is well-known that during the rotation of the roller it goes around at the circuit. If one or more roller is broken or it suffered any other geometrical damage, it may be perceived by checking the rolling resistance. It is well-known as well, that in a horizontal shaft bearing, having the bearing clearance bigger than null, the load is sustained by rollers contacting the bottom part of the outer ring. From the diagram it can be seen, that measure of the positioning error is independent from the angular position of the bearing but this fact contradicts the former guesswork. If the damaged roller is in the bottom range of the bearing ring, we should detect higher resistance than in the upper one. This assumption is not proved by the measuring results, consequently the break of the rolling element or any other damage can be excluded. In the end let's assume that a piece of the raceway is broken out perhaps the outer ring is cracked or broken. In all the listed cases the bearing stays restricted operable. The deterioration must occur on the outer ring hence measure of resistance does not depends on the given angular position. The outer ring is fixed consequently it gives explanation to the problem. Unfortunately, from the available documentation the type of the bearing cannot be ascertained, therefore we have to rely on assumptions. On the basis of *Figure 9* the dimensions of the bearing may be determined. In the [4] and [5] online bearing catalogues there is no bearing having the given dimensions and construction. The bearing in question has split outer ring angular cylindrical roller type, we have not met it before. We think, it may be a special custom-built for the gamma knife device.

From our experiences gained during the partial regeneration (see chapter 5) it may be seen, that by increasing the axial bearing clearance the measure of the positioning error and the required starting torque decreased. It can be justified in terms of dynamics, the roller position is slanting relative to the axis of the bearing; in the case of positive, increasing axial bearing clearance the contact



pressure between the roller and the raceway decrease, the error moderates. Up to now the assumption is in line with our experiences.

In the following derivation we demonstrate that periodic time of the error and the contact of the roller with the damaged surface are almost same. For the deduction we used well known kinematic methods and relations.

Data:

The periodic time:  $T = 5.6$  s, on the basis of *Figure 8*.

The gear ratio according to the dimensions of *Figure 5*:

$$i = d_2 / d_1 = 300 / 60 = 5 \quad (5.1)$$

The angular velocity of the electric motor, if its signal velocity is 34000 signal/s and the number of encoder signals are 507904, thus:

$$\omega_m = \frac{2\pi}{507904} \cdot 34000 = 0.4206 \frac{1}{s} \quad (5.2)$$

The radius of the outer bearing ring raceway on the basis of *Figure 5*:  $r_k = 191$  mm,  
and the diameter of the rolling element:  $d_g = 18$  mm.

Consequently the radius of the inner bearing ring raceway:

$$r_b = r_k - d_g = 191 - 18 = 173 \text{ mm} \quad (5.3)$$

Calculation:

The angular velocity of the hollow shaft may be calculated from the angular velocity of the motor and the gear ratio:

$$\omega_t = \omega_m / i = 0.4206 / 5 = 0.08412 \frac{1}{s} \quad (5.4)$$

The inner bearing ring rotates together with the hollow shaft. The roller contacts both the inner and the outer raceways. In the case of non-slip rolling, the velocity of the contact point of the roller and the outer raceway is null, consequently it is the velocity pole of the roller. The velocity of the contact point of the roller and the inner raceway:

$$v_2 = \omega_t \cdot r_b = 0.08412 \frac{1}{s} \cdot 173 \text{ mm} = 14.55 \frac{\text{mm}}{s} \quad (5.5)$$

The angular velocity of the roller relative to its velocity pole, applying Eq. (6.3.4) and (6.3.5):

$$\omega_g = v_2 / d_g = 14.55 \frac{\text{mm}}{s} / 18 \text{ mm} = 0.8083 \frac{1}{s} \quad (5.6)$$

since the velocity of the contact point of the roller and the inner raceway are the same; and the roller turns round the velocity pole with its diameter. The velocity of the centre of the roller from the Eq. (5.6):

$$v_{gk} = \omega_g \cdot \frac{d_g}{2} = 0.8083 \frac{1}{s} \cdot \frac{18 \text{ mm}}{2} = 7.275 \frac{\text{mm}}{s} \quad (5.7)$$

The displacement of the roller's centre considering its velocity and the periodic time of the error:

$$s_{gk} = v_{gk} \cdot T = 7.275 \frac{\text{mm}}{s} \cdot 5.6 \text{ s} = 40.74 \text{ mm} \quad (5.8)$$

Analysing the Eq. (5.8) we can realize that developing the path of the roller into plane, the roller travels 40.74 mm during the periodic time derived from *Figure 4* and *Figure 8*, provided that there is a raceway fault (pitting, shelling) in the bottom part of the outer ring. On the fault of the raceway every roller roll over subjected to momentary load increase; it may be seen indirectly as an error in the diagrams. This calculation predicts that the distance between the roller centres in the bearing cage is about 40.74 mm. In the available assembly drawing, see *Figure 5*, the number of rollers cannot be ascertained, however assuming the roller diameter for 19 mm, this value seems to be



possible. This calculation proves the assumption that the raceway of the bearing is damaged. The rollers are positioned in the bearing cage equal, which is in line with the constant periodic time of the error.

## **6. REPAIRING, OVERHAUL OF THE DEVICE**

The dismantling of high-mass parts can be carried out on the basis of carefully designed material handling schedule. All the parts involved in the overhaul are inside the dome-shaped radioprotective shield. The detaching of gearing is simple; the radioprotective shield together with the inner system elements may be detached in a single unit. For this a special bucket is needed: keeping the hemisphere shell and makes it possible to turn the shield into vertical position. The assembling actions thereafter may be assisted by universal crane. The most costly part of the overhaul is removing and reset the radiation sources. The cost of the mechanical rebuild is lower. Considering this and the age of the device (30 years), it is worth applying the method from the aircraft industry namely changing all the inner elements independently from their condition. This principle does not pertain of course to the radioprotective shield and the hemisphere shell, they do not age at all. There are some special tools needed (removing the used bearing, pressing on the new one), which have to be designed and manufactured. The source body and the hollow body are fixed by screws hardly reachable; for which flexible wrench is needed. Probably it is the key issue of the assembling, and it cannot be excluded that endoscope technicians are needed to develop the special tool.

## **CONCLUSIONS**

The value of this medical device expressed in currency is very high, its role in the Hungarian public health is inestimable. This is why, it is worth dealing with extending its expected service life. The first part of the task is detailed surveying the error phenomenon and its causes. In this paper we resolved this task as the first step of the overhaul. In the next paper we will deal with the repairing in details.

## **REFERENCES**

- [1]: International Commission on Radiological Protection (1991). „1990 Recommendations of the International Commission on Radiological Protection - ICRP Publication 60”
- [2]: GammaArt6000ND Technical Documentations (American Radiosurgery Inc., 1988.)
- [3]: Yaskawa SigmaWin+ Ver. 7. (Yaskawa Inc., Galil Program WSDK, 2016.)
- [4]: On-line csapágykatalógus (SKF Inc., [www.skf.com](http://www.skf.com), 2017.)
- [5]: Medias 5.0 termékkiválasztó rendszer (Schaeffler Group, [www.fag.com](http://www.fag.com))



## LIGHTWEIGHT MANUFACTURING OF AUTOMOTIVE PARTS

*TISZA Miklós DSc*

*Institute of Materials Science and Technology, University of Miskolc*

*E-mail: [tisza.miklos@uni-miskolc.hu](mailto:tisza.miklos@uni-miskolc.hu)*

### **Abstract**

*Nowadays, developments in the automotive industry are progressing mainly in two different ways: one of the main trends is to increase the safety of cars (active and passive safety systems) while the other is to reduce the consumption and the environmental impact (engine developments, weight reduction). The demand for low consumption is endless in the automotive industry, and it is not only important due to the limited reserves of oil, but more to the increasing severity of emission rules. The European Union forced the car manufacturers to develop their cars to pass the emission rules; it is not about the competition anymore. Application of high strength steels and aluminium alloys are among the most suitable answers to meet the increased requirements in the automotive industry. In this paper, these two main trends in lightweight car manufacturing will be summarised.*

**Keywords:** *lightweight manufacturing, high strength steels and aluminium, process developments.*

### **1. RESEARCHES IN LIGHTWEIGHT MANUFACTURING AT THE UNIVERSITY OF MISKOLC**

First, we will shortly overview these researches from the point of view of applied materials. There are several ongoing research projects in these fields at the Institute of Materials Science and Technology at the University of Miskolc, as well. Application of high strength steels is the main concern in one of the big projects called AutoTech [1]. The application of lightweight materials – particularly various aluminium alloys – is the main topic in the LoCoMaTech H-2020 project [2].

### **2. APPLICATION OF HIGH STRENGTH STEELS IN CAR MANUFACTURING**

For several decades the application of conventional cold rolled steels dominated the car body manufacturing. However, in the last 20-30 years there were very intensive developments in steel making mainly initiated by the requirements to produce lightweight car body structures with lower harmful emissions, better crashworthiness and higher safety. In Figure 1. the so-called first, second and third generations of high strength steels can be seen where the total elongation ( $A_{80}$ ) is shown in the function of ultimate tensile strength ( $R_m$ ).

As it can be seen from Figure 1. increasing the strength parameters the ductility parameters – and thus the formability is significantly decreasing. Therefore, for these high strength steels the extension of formability limits is an important issue. In the AutoTech project, wide scale experimental investigations were performed to analyse the formability of different DP-steel grades (e.g. DP600, DP800 and DP1000) which are already widely used in the automotive industry. For these test results we refer to Research Reports, papers and book [1], [3] published from these investigations. Among the new, high strength materials like different grades of DP-, TRIP- and TWIN-steels, we had also an important research work on the Press Hardening Steels (PHS) and their application to produce high strength structural body elements (e.g. A and B-Pillars, etc.) applying hot forming processes.

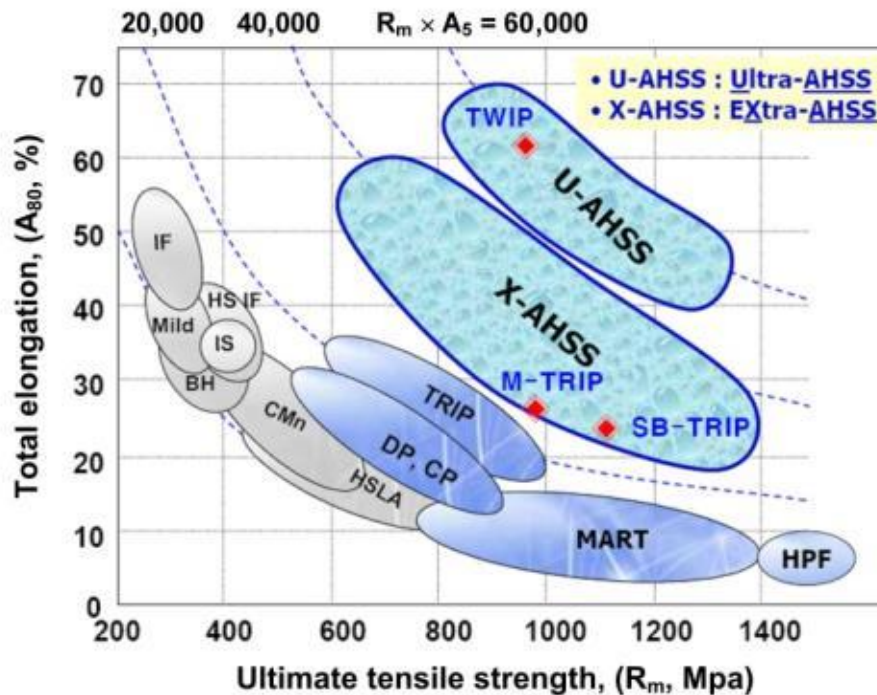


Figure 1. Total elongation vs Ultimate Tensile Strength for high strength steels

From this latter material grade – i.e. the Press Hardening Steels – different kinds of boron alloyed manganese steels should be mentioned that are widely used in car body manufacturing in hot forming conditions – particularly the 22MnB5 alloy which is regarded as the basic type of PHS steels. Since for the light metals we will focus on a new hot forming process (Hot Forming & Quenching – HFQTM) we will shortly analyse the hot forming of Press Hardening Steels for comparison with a brand new hot forming process of aluminium alloys.

Hot Press Forming (HPF) – even it is already widely used in the automotive industry – is a relatively new forming process. It was developed particularly for the application of high strength steels in car body manufacturing in the automotive industry. Nowadays, the hot stamping of high strength boron alloyed manganese steels (e.g. 22MnB5) is a well-established, industrially applied process. It is called as Hot Forming of Steels (HFS) or often termed as Press Hardening of Steels (PHS). This technology was invented in Sweden [4], then further developed in Germany [5], [6] and France [7]. Industrial plants are working all over the World [8], [9] among them in Hungary: the Kirchhoff Automotive is the main supplier for Hungarian OEM car makers with components produced by Press Hardening of Boron alloyed Manganese Steels [10].

Though, it is already an industrially well-established process, there are still many fields for further research activities, thus intensive research works are in progress on the application of various grades of high strength steels. Boron-alloyed Manganese steels are the most suitable group for hot press forming. This group includes the 22MnB5 steel as the most typical one for this application, but some other types as 8MnCrB3, 20MnB5, 27MnCrB5 and 37MnB4 can also be used in hot press forming. There are two main technological process variants applied in hot press forming of steels: one of them is called direct hot forming, the other is the indirect hot forming. In direct (or often termed as single stage) hot press forming the blank sheet is directly austenitized, then transferred to the stamping tool and cooled down rapidly with the forming tool, providing the excellent strength properties. This process cycle is shown in Figure 2. Temperature vs time for hot press forming of steels. It is absolutely essential that the forming could be finished above the  $M_s$  temperature (characteristic for the given material) to have suitable formability. After forming, the component is



cooled down together with the tool: this cooling should provide the critical cooling rate to get high strength martensitic microstructure.

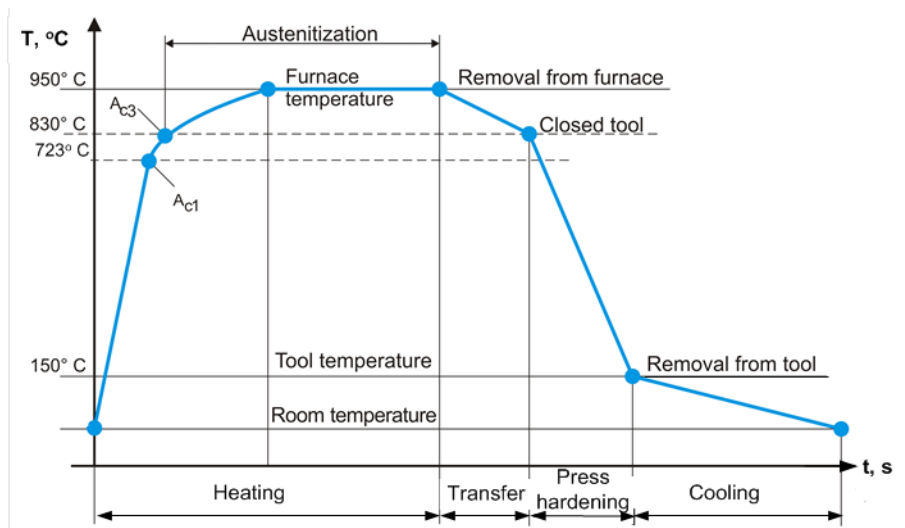
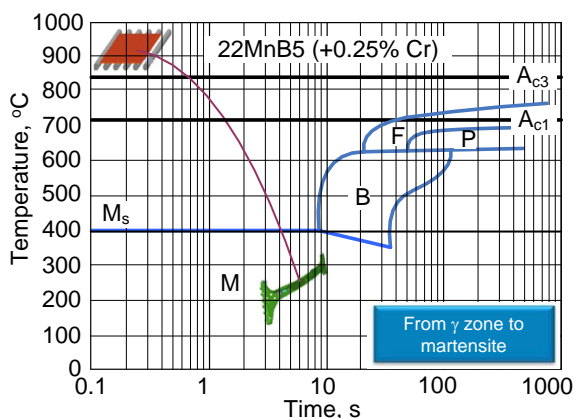
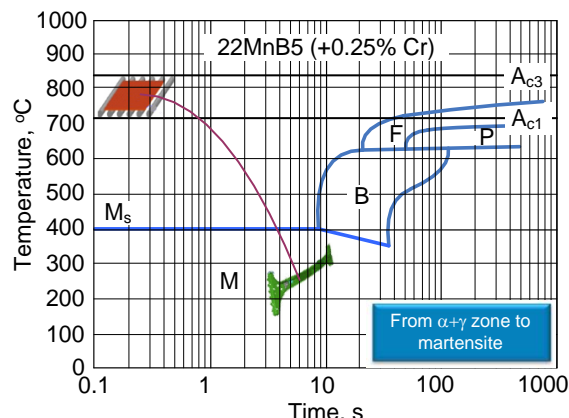


Figure 2. Temperature vs time for hot press forming of steels

Besides the two basic types of Hot Press Forming analyzed above, further process variants may be used. In these process variants, the final microstructure as well as the mechanical properties of the part can be controlled very effectively depending on the holding temperature and the controlled cooling process (Figure 3).



a) Holding temperature in the  $\gamma$ -zone



b) Holding temperature in the  $(\alpha+\gamma)$  zone

Figure 3. Process variants for Hot Forming of Steels depending on the holding temperature

In one of the most common processes, the holding temperature is selected in the homogeneous  $\gamma$ -zone above the  $A_3$  temperature of the given steel (i.e. full austenitization) and the cooling occurs over the upper critical cooling rate resulting in a fully martensite microstructure. In the second subtype, the holding temperature is in the  $(\alpha+\gamma)$  intercritical range (i.e. between the  $A_1$  and the  $A_3$  temperature). Thus the starting microstructure has ferrite and austenite. In this case, just the austenite content can be transformed into martensite and the final microstructure when the forming and cooling completed has a certain amount of ferrite, too. Though, it results in somewhat lower strength compared to the previous process variant, however it also leads to a certain amount of ductility providing better toughness properties. Also further process variants can be originated by



applying a bit lower cooling rate after the forming process. In these cases – since the cooling rate is lower than the upper critical cooling rate – the final microstructure besides martensite also contains bainite. Though, it also results in somewhat lower strength depending on the quantity of bainite, but together with an increased toughness which might be very advantageous for example increasing the crashworthiness of the structural parts due to the better energy absorption properties. These process variants are widely used in car manufacturing for producing structural elements with high load bearing capacity, like A and B pillar, sub-plate, side impact beam, etc.

### 3. ALUMINIUM ALLOYS IN AUTOMOBILES

As it was mentioned before, in lightweight manufacturing of automobiles the aluminium and its alloys play very significant role. Application of aluminium as base material for car body elements is very beneficial from the point of view of mass reduction. However, aluminium usually has lower formability than steels which leads to serious formability problems in cold forming operations. But it is also well known that the formability of aluminium is increasing significantly with the increase of the temperature. This is the main reason that significant efforts are made both in the laboratories and under industrial circumstances to apply high strength aluminium alloys in hot forming conditions. During the recent decades several new grades of high strength aluminium alloys were developed. Among them the so-called 5xxx, 6xxx and more recently the 7xxx series are mainly used in the automotive industry. Obviously with the increase of strength the formability of these alloys is reduced. It is also well known that the formability – as for most of the metals and metallic alloys – can be significantly increased at elevated temperatures. In the Imperial College of London together with some other project partners a special process was developed for the hot forming of aluminium alloys. This process is called Hot Forming and Quenching [2], [12]. This new process is patented by the Imperial College of London and the Impression Technologies UK with the name Hot Forming and Quenching (HFQ<sup>R</sup>).

The Hot Forming and Quenching of high strength aluminium alloys was developed partly utilising the principles of Press Hardening of Steels but due to the very different material science background of aluminium alloys it requires the usage of several other concepts. The basic principle behind this process is based on the unique behaviour of ageing aluminium alloys during heat treatment, which is well known from materials science [11]. This principle is shown schematically in Figure 4 with the usual Time – Temperature (T vs t) diagram.

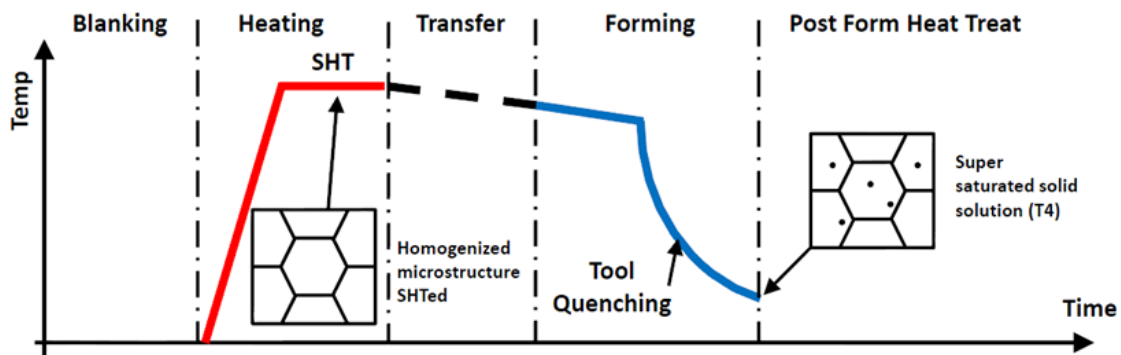


Figure 4. Basic principle of Hot Forming and Quenching<sup>TM</sup> of aluminium alloys [12]

The first part of this process is a solution heat treatment (SHT) where all the precipitations are solved above 500°C (usually between 525-580°C providing a homogenised microstructure of  $\alpha$ -solid solution. Depending on the thickness of the part it usually takes 30-60 min. However, for



aluminium alloys, the material is in a supersaturated state after the solution heat treatment and quenching in the tool having very low strength parameters and good formability; furthermore, the process requires much longer cycle time. To have sufficient high strength still we have to apply a precipitation hardening (tempering, artificial ageing) with an even much longer cycle time. Therefore, to apply this process successfully and economically in mass production in the automotive industry these cycle times should be decreased significantly. Fast heating and fast cooling methods are regarded as one of the possibilities to reduce the cycle times: these are among the most important targets in the LoCoMaTech project. Another possibility to reduce the long cycle time is the utilization of other inevitable necessary processes in the production line, i.e. using the paint baking as part of the artificial ageing process.

This basic principle is realised with the technological process solution shown in Figure 5. The 4th step is also an important part of this process since after the solution heat treatment and fast cooling aluminium alloys have low strength properties, therefore a precipitation hardening (often termed as artificial ageing) is necessary to provide the high strength properties.

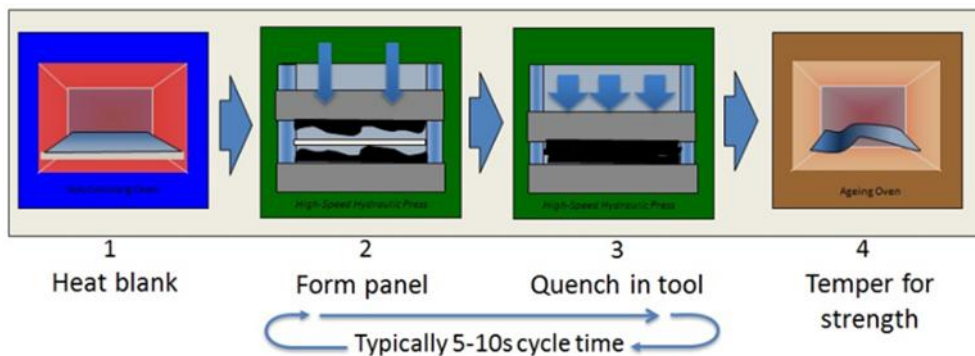


Figure 5. The technological process solution for Hot Forming and Quenching<sup>TM</sup> of aluminium alloys [12]

The process shown in Fig. 7. has some similarities with the hot forming of boron alloyed manganese steels. The substantial difference between the hot stamping of steels and the aluminium alloys mainly based on the differences of material science background and can be summarized in the followings: applying the boron alloyed manganese steels in hot forming and quenching the part is cooled in the tool with a cooling rate sufficient to provide hard martensitic microstructure having very high strength properties (usually around  $R_m = 1500-2000$  MPa) without any further heat-treatment, thus providing high strength properties within an industrially acceptable production cycle time  $t = 5$  to 10 seconds.

As it was mentioned before, this process is principally based on the hot stamping of steels, and it is also aimed in the project to develop a similar production line which already exists for the Press Hardening of Boron-alloyed Manganese steels. This is the final objective of the LoCoMaTech project [2].

## CONCLUSIONS

In this paper, some recent developments in the application of lightweight design concepts in the automotive industry were analysed from the point of view of hot forming of metallic materials. First, some basic principles of Hot Forming of Steels widely known as Press Hardening of Steels were introduced, then the Hot Forming and Quenching of aluminium alloys was analysed. Since the automotive industry requires the application of higher strength materials to overcome the reduced



# INTERNATIONAL SCIENTIFIC CONFERENCE ON ADVANCES IN MECHANICAL ENGINEERING

12-14 October 2017, Debrecen, Hungary



formability of these materials the hot forming is a promising solution. In this paper, the hot forming of steels and aluminium alloys was analysed demonstrating their similarities and differences, too.

## REFERENCES

- [1] AutoTech (2014) Formability and weldability of high strength steels applied in the automotive industry, Research Report, ID No.: TÁMOP-4.2.2.A, Jointly financed by the New Széchenyi Plan and the European Union, 2012-2014.
- [2] LoCoMaTech (2016) Low Cost Materials Processing Technologies for Mass Production of Lightweight Vehicles EU H-2020 project 2016-2019, ID No: 723517.
- [3] Tisza M (2015) Metal Forming in the automotive industry, Miskolc University Press pp. 294 ISBN 978-963-358-082-0
- [4] Lundström, E.: Method of producing a sheet steel product such as a reinforcement element in a larger structure, Patent No. 5916389, SSAB Hardtech AB, 1977.
- [5] Banik, J. et. al.: Warmumformung im der Automobilbau, Süddeutscher Verlag GmbH, Munich, 2013. pp. 1-83.
- [6] Erhardt, R., Boke, J.: Industrial application of hot forming press simulation, In: 1st International Conference on Hot Sheet Metal Forming of High-Performance, Steel, Kassel, Germany, (2008) pp. 83–88.
- [7] Chastel, Y., Dahan, Y., Massoni, E., Duroux, P., Wilsius, J., Hein, P.: Formability of quenched steels in hot stamping. In: The 9th International Conference on Technology of Plasticity, ICTP, Gyeongju, Korea, 2008. pp. 678–683.
- [8] Karbasian, H., Tekkaya A. E.: A review on hot stamping, Journal of Materials Processing Technology, vol. 210 (2010) pp. 2103-2118
- [9] Berglund, G.: The history of hardening of boron steel in northern Sweden, In: 1st International Conference on Hot Sheet Metal Forming of High-Performance Steel, Kassel, Germany, (2008) pp. 175–177
- [10] Tisza, M.: Hot forming of Boron-alloyed Manganese Steels, Materials Science Forum, 2017. Vol. 885, pp 25-30. DOI:10.4028/www.scientific.net/MSF.885.25
- [11] Tisza, M.: Physical Metallurgy for Engineers, ASM Publisher, 2001, Ohio-London, P.405.
- [12] LoCoLite (2013) An industry system enabling the use of a patented materials processing technology for Low Cost forming of Light Weight structures for transportation industries, EU FP7 NMP Project, ID No: 604240



## EXPERIMENTAL INVESTIGATION OF A FINITE LENGTH LATERAL SYSTEM IN A DIVIDING-FLOW MANIFOLD

*TOMOR András, ANTAL-JAKAB Erik, KRISTÓF Gergely PhD*

*Department of Fluid Mechanics, Faculty of Mechanical Engineering, Budapest University of Technology and Economics*

*E-mail: [tomor@ara.bme.hu](mailto:tomor@ara.bme.hu) , [ajerik93@gmail.com](mailto:ajerik93@gmail.com) , [kristof@ara.bme.hu](mailto:kristof@ara.bme.hu)*

### **Abstract**

*Flow manifolds are indispensable elements of several fluid distribution systems, e.g., in air engineering, water and wastewater treatment and polymer processing. In this study, a dividing-flow manifold of finite length laterals is investigated using Laser Doppler Velocimetry (LDV) technique in order to extend the available experimental flow field database. Volume flow rate distributions along the manifold are determined for three different Reynolds numbers. Volume flow rates of side branches are deduced from velocity data using rasters of 32 points at the outlets. The turbulent inlet velocity profile of the main conduit is also represented. The results show that the Reynolds number dependency is almost negligible in the investigated range. The presented experimental data can be further used for validation purposes.*

**Keywords:** *dividing-flow manifold, LDV measurement, volume flow rate distribution*

### **1. INTRODUCTION**

The flow manifold is a larger pipe or duct, which branches into smaller ones. When it is necessary to distribute diverse types of fluid streams into many smaller ones or to collect these minor flows, one has to use flow manifolds. There are four main types of flow manifolds: dividing, combining, U-type and Z-type. This paper focuses on dividing-flow manifolds, which can be found in several technical applications in the industry and beyond. Dividing-flow manifolds are applied in automobile industry, irrigation systems and even in musical instruments.

In order to construct effective models for flow manifold design, it is important to understand the flow mechanism in manifolds. The main design goal is usually to ensure uniform flow distribution, and an essential attribution is the pressure drop. There are four well-known approaches to investigate flow manifolds: discrete models [1, 2], analytical models [3-6], computational fluid dynamics (CFD) models [7, 8] and experimental measurements [9, 10].

Discrete models consist of systems of difference equations, which usually have to be solved iteratively by using a computer programme. In these models, knowledge of flow coefficients is indispensable.

Analytical models solve sets of differential equations, and they usually provide simple and compact solutions, which are fully explicit. However, the application of these analytical models is limited.

The newest method is the CFD, whose largest advantages are that real engineering structures can be resolved and the flow coefficients are not needed for the calculations. Nevertheless, CFD has high computational cost for optimizing complex geometries.

The high-standard experimental measurements provide the most reliable results, which can be used for the validation of other model results. The disadvantage of this method is that it is time-consuming and usually requires expensive devices. Most of the known experiments [9, 10] give old data without error bars, and the reliability of these results is questionable.

In order to provide reliable experimental data that can also be used for the validation of various



model results, Laser Doppler Velocimetry (LDV) measurements are carried out on a dividing-flow manifold. Velocity and volume flow rate distributions are determined, and the experiments are performed in the laboratory of the Department of Fluid Mechanics at the Budapest University of Technology and Economics.

## 2. EXPERIMENTAL SETUP

A dividing-flow manifold of five finite length laterals is investigated. The geometry of the manifold is shown in *Figure 1*.

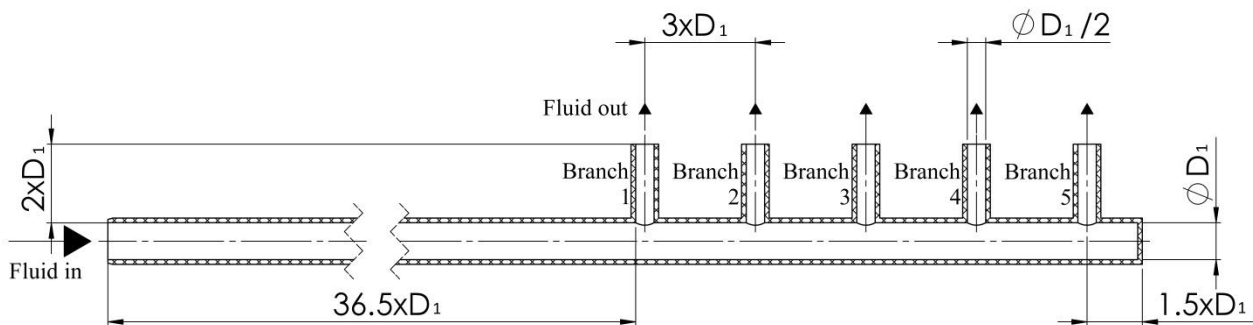


*Figure 1* Geometry of the investigated dividing-flow manifold;  $D_1 = 40$  mm

The manifold is fabricated from hydraulically smooth plexiglass pipes. The  $D_1$  diameter is chosen in such a way that the full cross-section can be accessible by the LDV optics and the manifold can be connected to standard pipes.

In the course of the experiments, the ambient pressure is 101 kPa, and the working fluid is air with a constant temperature of 30 °C. The measurement layout is shown in *Figure 2*.

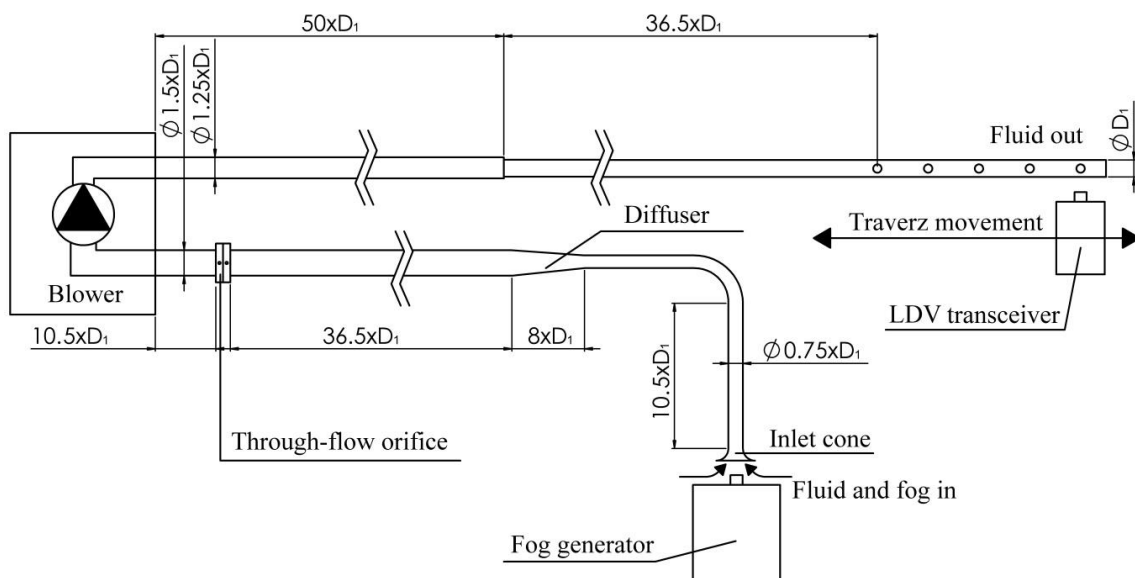


*Figure 2* Measurement layout

A blower, whose rotational speed can be regulated by a potentiometer, drives the flow. Hydraulically smooth PVC pipes are connected to the inlet and discharge side of the blower. The pipe upstream of the blower contains a standardized [11] through-flow orifice plate for measuring



the reference volume flow rate. Air is sucked in through an inlet cone, at which a fog generator produces the seeding particles. Downstream of the blower, a relatively long pipe section ensures an almost fully developed flow just upstream of the manifold. The fibre-optic LDV probe, which is attached to a three-dimensional traversing system, is located near the side branches of the manifold. The position of the probe is shown in *Figure 3*.

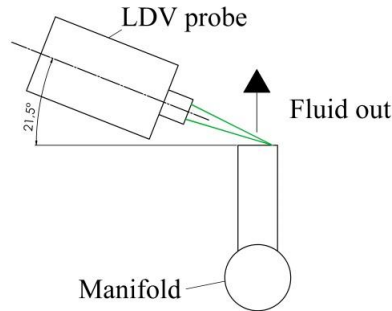


*Figure 3* Position of the fibre-optic LDV probe

A two-component LDV system is applied. However, only one component is enough for determining the volume flow rates at the side branches: only the velocity component perpendicular to the branch outlet is needed. This component is calculated from the measurement data using trigonometric functions. The system includes an air-cooled 300 mW Argon-Ion laser. The LDV transceiver has a focal length of 53 mm and a clear aperture of 7 mm. Laser light from the seeding particles that pass through the measurement volume is reflected back into the transceiver. Optical signal is digitised and analysed by an FSA3500 DSP-based signal processing unit.

Volume flow rates through side branches are deduced from velocity data. Due to the relatively short length of side branches, the flow is not fully developed at the outlets. Therefore, it is advisable to use a unique method instead of the standard measurement techniques. In this study, a raster of 32 measurement points is applied at the branch outlets. The raster is shown in *Figure 4*.

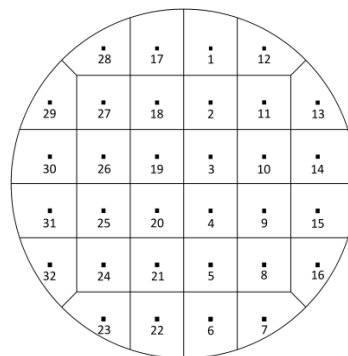


*Figure 4* Raster with 32 measurement points at the branch outlets

Volume flow rate through a side branch can be calculated as

$$q_{vi} = \sum_{j=1}^{32} A_{ij} v_{ij}, \quad (1)$$

where  $q_{vi}$  is the volume flow rate measured at the outlet of the  $i$ th side branch,  $v_{ij}$  is the velocity value measured at the  $j$ th measurement point of the  $i$ th branch outlet and  $A_{ij}$  is the area that belongs



to the  $j$ th measurement point of the  $i$ th branch. It is important to note that  $v_{ij}$  is the velocity component perpendicular to the branch outlet.

Experimental uncertainty of volume flow rates measured at the branch outlets consists of more factors. The velocity measurements using the LDV, the applied raster of 32 measurement points and the position of the probe involve uncertainties, which are estimated by auxiliary models and programs and will be reported later. The uncertainty of the reference volume flow rate measurement is estimated according to the standard [11]. Pressure drops are measured with calibrated digital manometers, whose measurement accuracy is  $\pm 2$  Pa. From this accuracy, precision error can be calculated according to the propagation of error. The total uncertainty includes also this precision error.

Measurements are carried out at three different Reynolds numbers. The three measured reference volume flow rates are  $0.0179 \pm 0.0005$  m<sup>3</sup>/s,  $0.0241 \pm 0.0006$  m<sup>3</sup>/s and  $0.0322 \pm 0.0008$  m<sup>3</sup>/s, and accordingly the Reynolds numbers at the manifold inlet ( $Re_0$ ) are  $35500 \pm 900$ ,  $48000 \pm 1200$  and  $64000 \pm 1600$ , respectively.

### 3. RESULTS AND DISCUSSION

A relatively long pipe section can be found upstream of the first branch of the manifold (*Figure 2*). However, it is often hard to ensure a fully developed turbulent pipe flow downstream of a blower even if a long pipe is connected to it. Therefore, the inlet velocity profile of the manifold is checked. The measured profile is compared to the following theoretical formula [12]:

$$v_z = v_{\max} \frac{1}{\max\left(1 - \frac{2r}{D_1}\right)^n}, \quad (2)$$

where  $v_z$  is the axial velocity component in the header,  $v_{\max}$  is the maximum velocity of the profile,  $r$  is the radial coordinate and  $n$  is a constant whose value depends on the Reynolds number. The values  $n = 6 \dots 10$  generally approximate many flows in practice [12]. At a Reynolds number of 35500,  $n$  takes the value 6.5.

The inlet profile is shown in *Figure 5*.

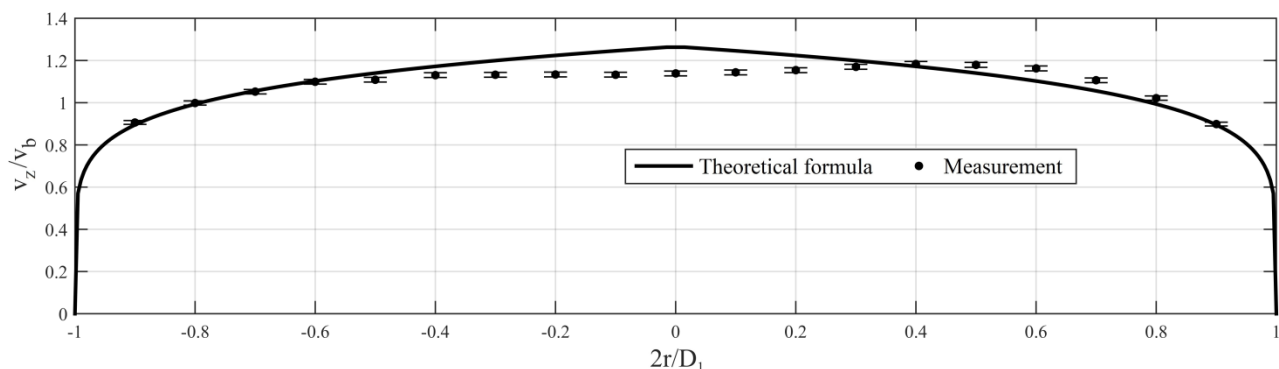


*Figure 5* Inlet velocity profile at a distance of  $2D_1$  from the first branch – comparison of measured data with a theoretical formula;  $Re_0 = 35500$  and  $v_b = 14.2$  m/s

It can be seen that there are some smaller differences between the measured inlet profile and the theoretical velocity profile of the fully developed turbulent pipe flow. However, the normalized root-mean-square error (NRMSE) is 0.0514; therefore, the inlet velocity profile is acceptable.



Volume flow rates through branches are normalized to the total volume flow rate,  $q_{vtotal}$ , which is the sum of the volume flow rates of side branches at the corresponding inlet Reynolds number. Dimensionless volume flow rate distributions along the manifold at the three different inlet Reynolds numbers are shown in *Figure 6*.

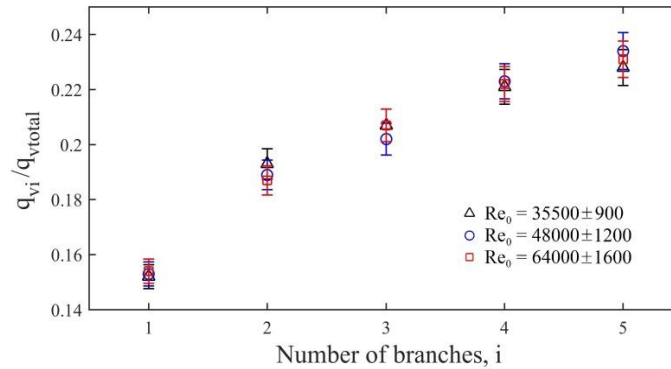


*Figure 6* Dimensionless volume flow rate distributions along the dividing-flow manifold at three different inlet Reynolds numbers

In the investigated range, the dimensionless volume flow rate distribution is almost independent of the Reynolds number at the manifold inlet. The slight differences between the results measured at different inlet Reynolds numbers are smaller than the experimental uncertainty; there is always an overlap between the corresponding error bars.

Total volume flow rates at the investigated Reynolds numbers are also determined by summing the branched off volume flow rates measured by the LDV. In order to validate the method used in this study, total volume flow rates deduced from velocity data are compared to the reference volume flow rates measured by the standardized orifice plate. The total volume flow rates are summarized in *Table 1*.

*Table 1* Total volume flow rates

$Re_0$	$q_{v0}$ (orifice) [m <sup>3</sup> /s]	$q_{vtotal}$ (LDV) [m <sup>3</sup> /s]	Relative difference [%]
35500±900	0.0179±0.0005	0.0186±0.0005	3.8
48000±1200	0.0241±0.0006	0.0251±0.0007	4.0
64000±1600	0.0322±0.0008	0.0323±0.0009	0.3

Total volume flow rates deduced from velocity data compare favourably with the reference volume flow rates.

Some characteristic velocity distributions at the branch outlets are illustrated in *Figure 7*.

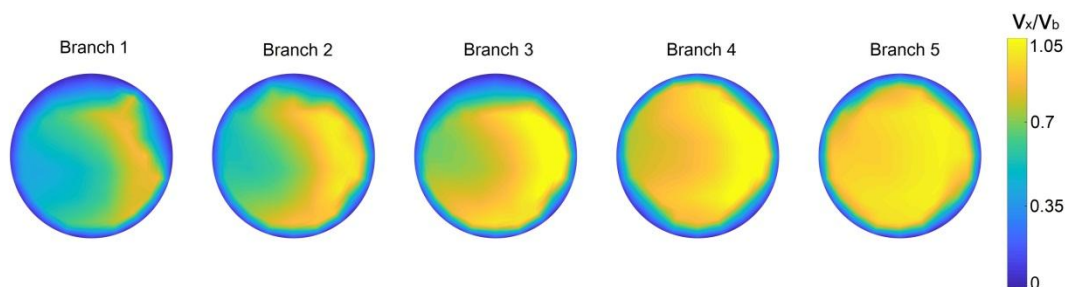


*Figure 7* Dimensionless velocity distributions at the branch outlets. Velocity component  $v_x$  is perpendicular to the branch outlets;  $Re_0 = 35500$  and  $v_b = 14.2$  m/s



## CONCLUSIONS

A dividing-flow manifold of finite length laterals was investigated using Laser Doppler Velocimetry (LDV) technique. The available experimental flow field database was extended with results of high-standard measurements. Volume flow rate distributions along the manifold were measured at three different Reynolds numbers at the manifold inlet. At the branch outlets, rasters of 32 measurement points were used for the determination of the branched off volume flow rates. As it was expected, the volume flow rate distribution depends slightly on the Reynolds number at the manifold inlet. Velocity distributions at the branch outlets were also illustrated, and the turbulent inlet velocity profile of the main conduit was also demonstrated. The presented data can be further used for the validation of other model results.

## ACKNOWLEDGMENT

This paper is supported by the ÚNKP-17-3-I New National Excellence Program of the Ministry of Human Capacities.

## REFERENCES

- [1] Datta, A.B., Majumdar, A.K.: *Flow Distribution in Parallel and Reverse Flow Manifolds*. International Journal of Heat and Fluid Flow, 2(4), 253-262., 1980.
- [2] Wang, J., Wang, H.: *Discrete Method for Design of Flow Distribution in Manifolds*. Applied Thermal Engineering, 89(1), 927-945., 2015.
- [3] Wang, J.: *Pressure Drop and Flow Distribution in Parallel-Channel Configurations of Fuel Cells: U-Type Arrangement*. International Journal of Hydrogen Energy, 33(21), 6339-6350., 2008.
- [4] Wang, J.: *Pressure Drop and Flow Distribution in Parallel-Channel Configurations of Fuel Cells: Z-Type Arrangement*. International Journal of Hydrogen Energy, 35(11), 5498-5509., 2010.
- [5] Warrick, A.W., Yitayew, M.: *An Analytical Solution for Flow in a Manifold*. Advances in Water Resources, 10(2), 58-63., 1987.
- [6] Bassiouny, M.K., Martin, H.: *Flow Distribution and Pressure Drop in Plate Heat Exchangers—I U-Type Arrangement*. Chemical Engineering Science, 39(4), 693-700., 1984.
- [7] Kulkarni, A.V., Roy, S.S., Joshi, J.B.: *Pressure and Flow Distribution in Pipe and Ring Spargers: Experimental Measurements and CFD Simulation*. Chemical Engineering Journal, 133(1-3), 173-186., 2007.
- [8] Gandhi, M.S., Ganguli, A.A., Joshi, J.B., Vijayan, P.K.: *CFD Simulation for Steam Distribution in Header and Tube Assemblies*. Chemical Engineering Research and Design, 90(4), 487-506., 2012.
- [9] Acrivos, A., Babcock, B.D., Pigford, R.L.: *Flow Distribution in Manifolds*. Chemical Engineering Science, 10(1-2), 112-124., 1958.
- [10] Kubo, T., Ueda, T.: *On the Characteristics of Divided Flow and Confluent Flow in Headers*. Bulletin of the Japan Society of Mechanical Engineers, 12(52), 802-809., 1969.
- [11] Standard ISO 5167-2:2003: *Measurement of fluid flow by means of pressure differential devices inserted in circular cross-section conduits running full – Part 2: Orifice plates*. 2003.
- [12] Munson, B.R., Young, D.F., Okiishi, T.H., Huebsch, W.W.: *Fundamentals of Fluid Mechanics*. 6th edition, John Wiley & Sons, Inc., Hoboken, New Jersey, 383-460., Chapter 8, 2009.



## CONTINUOUS PARAMETRIZATION OF HYDRAULIC LOSSES CAUSED BY DIAMETER TRANSITION IN CYLINDRICAL PIPES

*TOMOR András, MERVAY Bence, KRISTÓF Gergely PhD*

*Department of Fluid Mechanics, Faculty of Mechanical Engineering, Budapest University of Technology and Economics*

*E-mail: [tomor@ara.bme.hu](mailto:tomor@ara.bme.hu), [mervay.bence@gmail.com](mailto:mervay.bence@gmail.com), [kristof@ara.bme.hu](mailto:kristof@ara.bme.hu)*

### **Abstract**

*Connections between pipes of different diameters are frequently used in several fields of engineering. The hydraulic design of these systems is usually difficult because there are many correlations depending on the geometric parameters of the cross-section transitions as well as the flow direction. The object of this study is to find a new method for describing the loss coefficient, which, in contrast with previous correlations, is based on a continuous parametrization and independent of the flow direction. A novel reference velocity formulation is introduced to allow the use of dimensionless equations, as well as a new continuous parameter. The parameter field is thoroughly explored using computational fluid dynamics (CFD) models. The correlations obtained from the CFD calculations can be expressed by polynomial functions. This approach can significantly improve the design process of hydraulic systems.*

**Keywords:** *continuous parametrization, CFD, cross-section transition*

### **1. INTRODUCTION**

Pipe networks are crucial parts of any hydraulic systems. Pipes with different diameters have to be connected quite often, for which numerous solutions are available. The most common solution based on the flow direction is the usage of a diffuser or a confuser, but other elements can also be used, such as a sudden expansion or a sudden contraction. There are also two extreme cases, namely the flow from a pipe to a reservoir and the flow from a reservoir to a pipe. Knowing the loss coefficients of the above-mentioned elements is essential for the design of hydraulic systems [1, 2]. In the case of a single-phase flow, the loss coefficient is the function of three geometric parameters: the ratio of the diameters of the pipes, the length of the cross-section transition and the cone angle. The related literature gives different correlations based on the flow direction [3, 4]. For complex systems, the creation of hydraulic models using these correlations can be difficult. By introducing a reference velocity, a dimensionless set of equations can be obtained, that allows a continuous parametrization of hydraulic elements used for transition between different pipe diameters independently of the flow direction.

### **2. HYDRAULIC RESISTANCE MODEL**

The geometrical interpretation of a diffuser or confuser is shown in *Figure 1*. The notations can be seen in the Figure:  $v_1$ ,  $D_1$  and  $L_1$  are the velocity, diameter of the pipe and length of the inlet pipe section upstream of the cross-section transition, and  $v_2$ ,  $D_2$  and  $L_2$  are the velocity, diameter of the pipe and length of the outlet pipe section downstream of the cross-section transition, respectively.  $L_d$  is the length of the cross-section transition and  $\alpha$  is the half of the cone angle, which is positive in case of a diffuser and negative in case of a confuser. Different flow directions should be



distinguishable in the model. Sign of a velocity value is always positive when fluid enters the computational domain and flows toward the transition; consequently, signs are negative when fluid leaves the transition and computational domain.

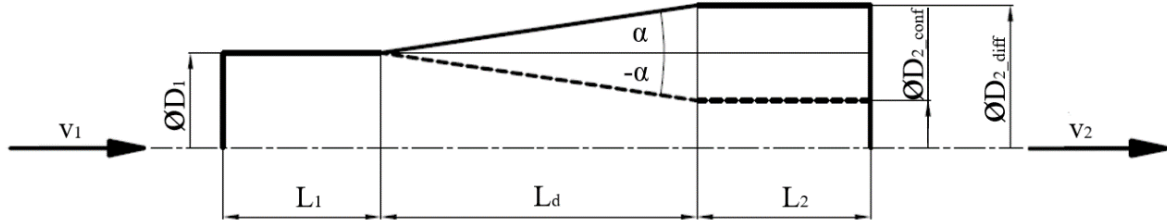


Figure 1: Geometrical interpretation. Continuous line: diffuser; dashed line: confuser

The key of the resistance model and the continuous parametrization is a novel reference velocity formulation. The reference velocity can be calculated as

$$v_{rms} = \sqrt{\frac{v_1^2 + v_2^2}{2}}. \quad (1)$$

By reordering equation (1), the equation of a circle can be obtained (2):

$$\left(\frac{v_1}{v_{rms}}\right)^2 + \left(\frac{v_2}{v_{rms}}\right)^2 = 2. \quad (2)$$

The reference velocity can also be used to obtain a dimensionless continuity equation. Equation (3) shows the rearranged, dimensionless continuity equation, where  $A_1$  and  $A_2$  are the cross-sectional areas that belong to  $v_1$  and  $v_2$ , respectively.

$$\frac{v_1}{v_{rms}} + \frac{A_2}{A_1} \cdot \frac{v_2}{v_{rms}} = 0. \quad (3)$$

It can be seen that equation (3) is the equation of a line. Let us use the substitutions given in equation (4):

$$\frac{v_1}{v_{rms}} = X; \quad \frac{v_2}{v_{rms}} = Y; \quad \frac{A_2}{A_1} = C. \quad (4)$$

Using these substitutions, the following system of equations can be written:

$$\begin{cases} X^2 + Y^2 = 2 \\ X + C \cdot Y = 0 \end{cases} \quad (5)$$

The first equation of this system is the equation of a circle of radius  $\sqrt{2}$ , whose center is at the origin. The second equation is the equation of a line passing through the origin. Therefore, the solution is always two points. The graphical representation of the system of equations is shown in Figure 2.

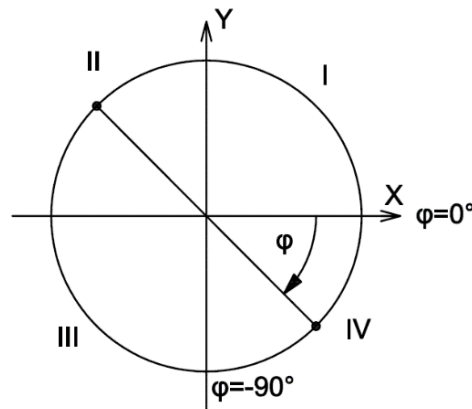


Figure 2: Graphical representation of the system of equations

Each intersection point has an  $(X, Y)$  coordinate pair; hence, each intersection point can be associated with a  $(v_1, v_2)$  velocity pair. If the slope changes, the positions of the intersection points will change; thus, the  $(v_1, v_2)$  velocity pairs associated with the points will change. It is worth mentioning that the slope of the line can only be negative, since only this type of line will give such  $(v_1, v_2)$  velocity pairs that fulfil the continuity equation because the signs of  $v_1$  and  $v_2$  have to be different. This means that only points in the second and fourth quadrant represent physically valid cases.

The position of the line can also be expressed by the variable  $\varphi$  (Figure 2). By using trigonometric formulae, a connection can be developed between the slope of the line and  $\varphi$ . This can be seen in equation (6):

$$C = \begin{cases} \frac{-1}{\tan \varphi}, & \text{if } -90^\circ < \varphi < 0^\circ \\ 0, & \text{if } \varphi = -90^\circ \\ \infty, & \text{if } \varphi = 0^\circ \end{cases} \quad (6)$$

If  $C = 1$ , the slope of the line will be  $-1$  (Figure 2). This represents a pipe without cross-section transition. There are diffusers between  $\varphi = 0^\circ$  and  $\varphi = -45^\circ$ , and there are confusers between  $\varphi = -45^\circ$  and  $\varphi = -90^\circ$ . The only difference between the second and fourth quadrant is the flow direction, but since a diffuser geometry can also be used as a confuser when the flow direction is changed, each point in the second quadrant has a counterpart in the fourth quadrant. In this paper, only the fourth quadrant is investigated.

The introduced method contains one continuous parameter ( $\varphi$ ) and is able to describe any given cross-section transition independently of the flow direction.

### 3. COMPUTATIONAL FLUID DYNAMICS MODEL

Altogether 27 different geometries are investigated. This include 10 diffusers, 10 confusers, 2 sudden expansions, 2 sudden contractions, 1 case that is a flow from a pipe to a reservoir and 1 case that is a flow from a reservoir to a pipe, and also 1 case that is a normal pipe, without cross-section transition.

The process of geometry creation is the following: first, it is decided what  $\varphi$  and  $\alpha$  values are to be investigated. Then, the inlet diameter ( $D_1 = 200$  mm), the Reynolds number ( $Re = 200,000$ ) and the reference velocity ( $v_{rms} = 1$  m/s) are chosen. Using these values, all other geometric sizes and velocities can be calculated.



Explanation of the choice of values: in case of  $\varphi$  and  $\alpha$ , the coverage of the full range of possible angles are recommended. A special attention is paid to  $\alpha=7.5^\circ$ , as the cone angle of  $15^\circ$  is commonly used in the engineering practice [5]. For  $D_1$ , 200 mm is a reasonable choice, because this diameter is common in engineering pipe systems and with a properly selected Reynolds number, (200,000 in this case), the flow will remain in the turbulent range. For  $L_1$  and  $L_2$ , see equation (7).

$$L_1 = 3 \cdot D_1; \quad L_2 = 10 \cdot D_2. \quad (7)$$

In case of the pipe to reservoir flow, ideally,  $C = \infty$ , and in case of reservoir to pipe flow,  $C = 0$ . None of these can be modelled, so in case of pipe to reservoir flow,  $C = 100$  is used, and in case of reservoir to pipe flow,  $C = 0.01$ . The investigated parameters are summarized in *Table 1*.

Table 1: Investigated parameters

$\varphi$ [°]	$\alpha$ [°]	$L_d$ [mm]	Note	$\varphi$ [°]	$\alpha$ [°]	$L_d$ [mm]	Note
0	90	0	pipe to reservoir	-60	-90	0	sudden contraction
-15	90	0	sudden expansion	-60	-60	14	confuser
-15	60	54	diffuser	-60	-45	24	confuser
-15	45	93	diffuser	-60	-30	42	confuser
-15	30	161	diffuser	-60	-15	90	confuser
-15	15	348	diffuser	-60	-7.5	182	confuser
-15	7.5	708	diffuser	-75	-90	0	sudden contraction
-30	90	0	sudden expansion	-75	-60	28	confuser
-30	60	18	diffuser	-75	-45	48	confuser
-30	45	32	diffuser	-75	-30	84	confuser
-30	30	55	diffuser	-75	-15	180	confuser
-30	15	118	diffuser	-75	-7.5	366	confuser
-30	7.5	240	diffuser	-90	-90	0	reservoir to pipe
-45	0	0	normal pipe				

Two dimensional block-structured meshes are created to reduce calculation time (*Figure 3*). The axisymmetric approach is used to model the full 3D pipes with the 2D meshes. The global mesh parameters are determined by a mesh sensitivity study. The boundary layer and the shear layer are modelled using a denser mesh, bearing in mind that the dimensionless wall distance ( $y^+$ ) in the boundary layer has to be below 1 for the appropriate near wall mesh resolution [6, 7]. The geometries and the meshes are created in ANSYS ICEM.

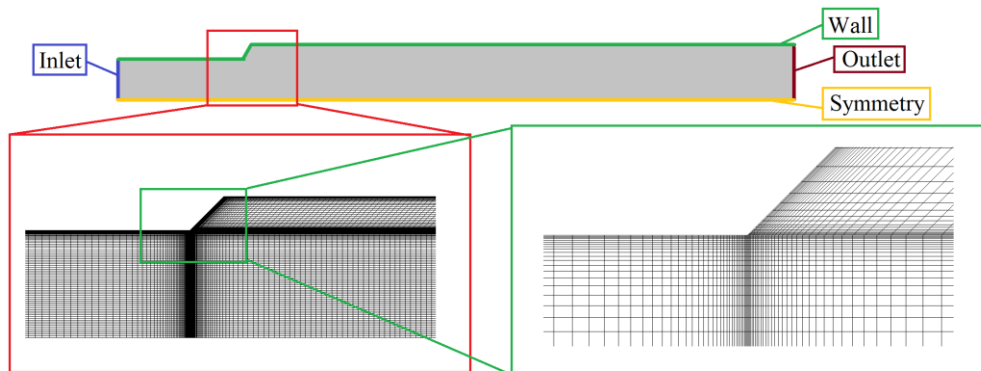


Figure 3: A typical numerical mesh and the boundary conditions; cell number: 130,000



The simulations are run in ANSYS Fluent 14.5. The calculations are steady state, the turbulence model used is k- $\omega$  SST, which is basically the combination of two turbulence models, the k- $\epsilon$  and the k- $\omega$  [8]. The fluid used is liquid water. The boundary condition at the inlet in all models is a velocity inlet. At the inlet cross-sections, velocity, turbulent kinetic energy (k) and specific turbulent dissipation rate ( $\omega$ ) quantities are prescribed using the results of auxiliary simulations. The walls are no slip walls and the outlets are pressure outlets. An axisymmetric boundary is used to model the whole 3D pipes. The Coupled scheme is used for pressure-velocity coupling and second order upwind schemes are used for the momentum, kinetic energy and dissipation calculations.

#### 4. RESULTS AND DISCUSSION

For evaluation, the loss coefficients for all geometries are calculated. The calculation of the loss coefficient ( $C_d$ ) is shown in equation (8), where  $p_{t1} - p_{t2}$  is the total pressure drop between the inlet and the outlet of the transition and  $\rho$  is the density of water:

$$C_d = \frac{p_{t1} - p_{t2}}{\frac{\rho}{2} \cdot v_{rms}^2} \quad (8)$$

The total pressure drop in the nominator is calculated as

$$p_{t1} - p_{t2} = p_{t1F} - p_{t2F} - \lambda_1 \cdot \frac{L_1}{D_1} \cdot \frac{\rho}{2} \cdot v_1^2 - \lambda_2 \cdot \frac{L_2}{D_2} \cdot \frac{\rho}{2} \cdot v_2^2 - \lambda_1 \cdot \frac{L_D}{D_1} \cdot \frac{\rho}{2} \cdot v_1^2 \quad (9)$$

In equation (9),  $p_{t1F}$  and  $p_{t2F}$  are the mass-averaged total pressure values given by ANSYS Fluent at the inlet and outlet cross-sections of the whole computational domain, respectively, and  $\lambda$  is the friction factor calculated with the well-known Blasius formula. *Figure 4* shows the loss coefficient as a function of  $\varphi$ .

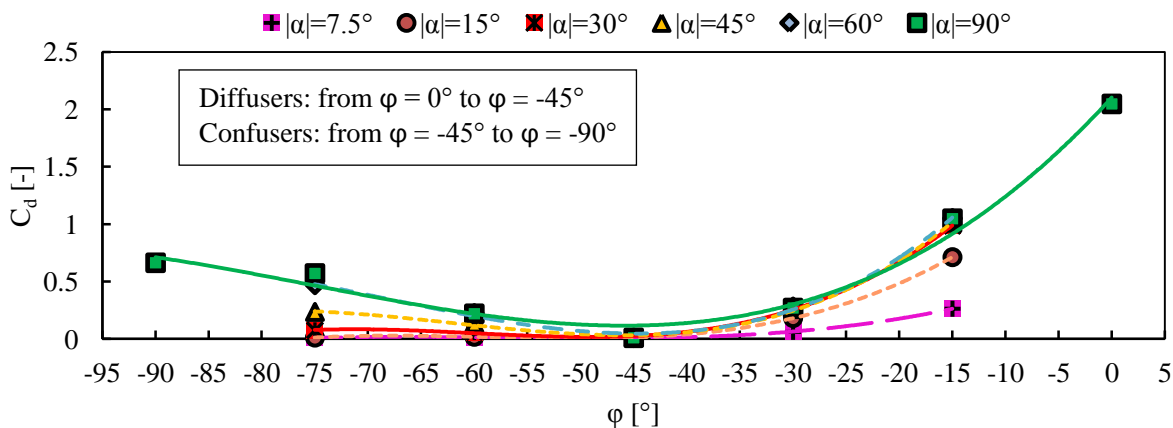


Figure 4: Loss coefficient as a function of  $\varphi$

Third degree polynomial functions are used for the fittings. It can be seen that a continuous function can be found for the whole range of  $\varphi$ . The general loss coefficient formula as a function of  $\varphi$  can be written as

$$C_d = a \cdot \varphi^3 + b \cdot \varphi^2 + c \cdot \varphi + d \quad (10)$$



Figure 5 shows the loss coefficient as a function of the half of the cone angle ( $\alpha$ ) on the whole range.

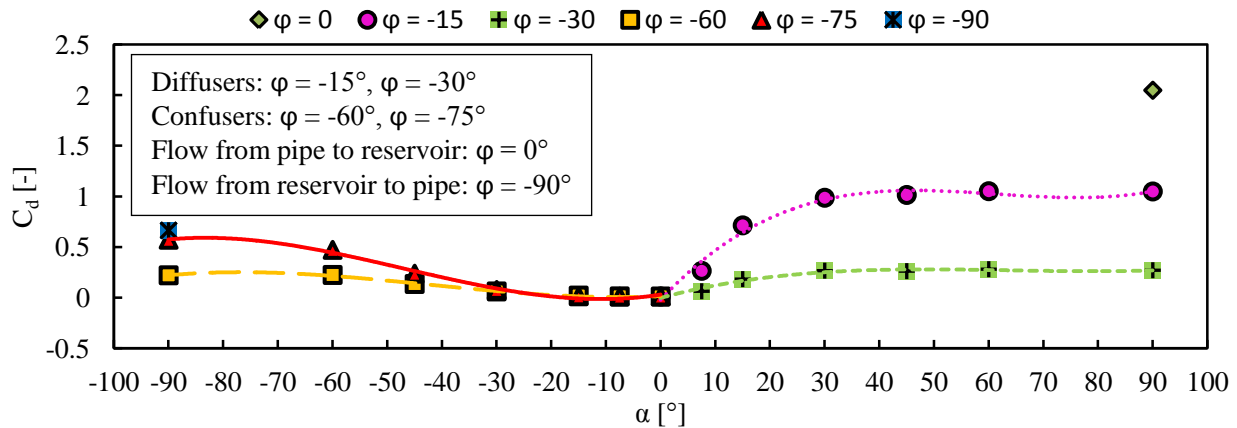


Figure 5: Loss coefficient as a function of  $\alpha$

Third degree polynomial functions can also be applied here. Therefore, the general loss coefficient formula as a function of  $\alpha$  takes the form

$$C_d = e \cdot \alpha^3 + f \cdot \alpha^2 + g \cdot \alpha + h. \quad (11)$$

The coefficients for equations (10) and (11) are summarized in Table 2 and Table 3, respectively.

Table 2: Coefficients of equation (10)

$ \alpha $ [°]	$a$	$b$	$c$	$d$
7.5	$4 \times 10^{-6}$	0.0007	0.0367	0.679
15	$9 \times 10^{-6}$	0.0016	0.0947	1.7951
30	$1 \times 10^{-5}$	0.0022	0.1298	2.4746
45	$1 \times 10^{-5}$	0.0024	0.1394	2.6099
60	$1 \times 10^{-5}$	0.0024	0.1411	2.6826
90	$7 \times 10^{-6}$	0.0016	0.1014	2.1016

Table 3: Coefficients of equation (11)

$\varphi$ [°]	$e$	$f$	$g$	$h$
-15	$5 \times 10^{-6}$	-0.001	0.0584	-0.0237
-30	$1 \times 10^{-6}$	-0.0002	0.0146	-0.0032
-60	$2 \times 10^{-6}$	0.0002	0.0028	0.0159
-90	$3 \times 10^{-6}$	0.0004	0.0086	0.0297

## CONCLUSIONS

The aim of the investigation was to calculate the loss coefficients of different cross-section transitions and different flow directions using continuous parametrization. To allow the use of dimensionless equations, a reference velocity was introduced. Different types of cross-section transitions, including diffusers, confusers, sudden expansions, sudden contractions and flow from a reservoir to pipe and pipe to reservoir were investigated using computational fluid dynamics (CFD). Relationships were described between the loss coefficient ( $C_d$ ) and the new parameter  $\varphi$ , as well as between the loss coefficient and the half of the cone angle ( $\alpha$ ). The correlations could be described with polynomial functions, allowing continuous parametrization. This parametrization can be used to make the design process of hydraulic systems more efficient.

## ACKNOWLEDGMENT

This paper is supported by the ÚNKP-17-3-I New National Excellence Program of the Ministry of Human Capacities.



# INTERNATIONAL SCIENTIFIC CONFERENCE ON ADVANCES IN MECHANICAL ENGINEERING

12-14 October 2017, Debrecen, Hungary



## REFERENCES

- [1] Rennels, D. C., and Hudson, H. M.: *Pipe Flow*, John Wiley & Sons, Inc., Hoboken, New Jersey, 101-112., Chap. 10; 113-128., Chap. 11, 2012.
- [2] Munson, B.R., Young, D.F., Okiishi, T.H., Huebsch, W.W.: *Fundamentals of Fluid Mechanics*. 6th edition, John Wiley & Sons, Inc., Hoboken, New Jersey, 383-460., Chapter 8, 2009.
- [3] Miller, D. S.: *Internal Flow Systems*, 2nd ed., BHRA (Information Services), Cranfield, Bedford MK43 0AJ, UK, 51-105., Chap. 5, 1990.
- [4] Idelchik, I. E.: *Handbook of Hydraulic Resistance*, 3rd ed., Jaico Publishing House, Mumbai, 239-330., Chap. 5, 2008.
- [5] Lajos, T.: *Az Áramlástan alapjai*, 4th ed., Mackensen Kft., Budapest, 461-504., Chap. 10, 2008.
- [6] Kiss, A., Vágó, T., Aszódi, A.: *Numerical analysis on inlet and outlet sections of a test fuel assembly for a Supercritical Water Reactor*. Nucl. Eng. Des. 295, 415–428., 2015.
- [7] Kiss, A., Aszódi, A.: *Summary for Three Different Validation Cases of Coolant Flow in Supercritical Water Test Sections with the CFD Code ANSYS CFX 11.0*. Nucl. Technol. 170, 2010.
- [8] ANSYS Inc.: *CFX Theory Guide - 2.2.2.4.3. The Shear Stress Transport (SST) Model*, 2017



## EXAMINATION OF BIOMETHANE PRODUCTION

<sup>1</sup>TÓTH Kinga, <sup>2</sup>VENCZEL Gábor, <sup>2</sup>SZAMOSI Zoltán PhD

<sup>1</sup>Department of Chemical Machinery, Faculty of Mechanical Engineering and Information Science, University of Miskolc

E-mail: [toth.kinga1029@gmail.com](mailto:toth.kinga1029@gmail.com)

<sup>2</sup>Department of Chemical Machinery, Institute of Energy Engineering and Chemical Machinery, University of Miskolc

E-mail: [venczel@uni-miskolc.hu](mailto:venczel@uni-miskolc.hu), [szamosi@uni-miskolc.hu](mailto:szamosi@uni-miskolc.hu)

### Abstract

One of the biggest environmental problem nowadays is the continuously growing organic waste production. To mitigate that, energy recovery and organic material recycling is the targeted activity. One possibility is biomethane production by biogas purification. Biogas can be used for the same purposes as natural or compressed gas as a renewable fuel. Before injection into the natural gas network or use for combustion, biogas needs to be purified. Modernization of the biogas is a multi-step gas separation process involving the removal of bulk component CO<sub>2</sub>, gas drying, removal of smaller components and compression. The product is called biomethane with a CH<sub>4</sub> content typically over 95% and a low content of pollutants. The most important part of the production is to extract as much CO<sub>2</sub> content from the biogas as possible so that the smallest part of the CH<sub>4</sub> content is wasted and reach the atmosphere with the carbon phase. Several and well established processes are commonly carried out for CO<sub>2</sub> removal: physical absorption with water or organic solvents, amine scrubbing, membrane-based processes, cryogenic processes and pressure swing adsorption.

**Keywords:** organic waste, biomethane, biogas upgrading, production technologies

### 1. INTRODUCTION

Biomethane is a pure renewable energy source. Use of bioenergy means biomass, biogas, various waste and by-products utilization for energy purposes, which is of paramount importance for the reduction of environmental load and fossil energy dependence.

In many of the world's countries, prevention and moderation of producing waste is a major political priority. Uncontrolled waste dumping is no longer acceptable today and even controlled landfill disposal and incineration of organic wastes are not considered optimal practices, as environmental standards are increasingly stricter and energy recovery and recycling of nutrients and organic matter is aimed [1].

Biogas fermentation, also called biogas technology or anaerobic digestion, is a promising waste treatment alternative because it results in the production of renewable energy sources such as methane while simultaneously removing organic pollutants [2]. Raw material of decomposition can be from a variety of things shown in *Table 1*. The raw material is filled into a sealed container where the appropriate bacteria have already been there. Then the anaerobic conditions are created (absence of oxygen) and the temperature is kept constant (usually 40 °C) [3].

Biogas is purified to biomethane to increase heating value and to minimize corrosion problems caused by acid gases. This way natural gas-like characteristics are assumed so it can be distributed to the grid. The methane content of the biogas can be used as heat and / or electricity, possibly as a



biofuel, while the end product, "bio fertilizer" may be used as an organic fertilizer, for irrigation or soil improvement.

The production and utilisation of biogas from anaerobic digestion provides environmental and socioeconomic benefits for the society as a whole as well as for the involved farmers. Utilisation of the internal value chain of biogas production enhances local economic capabilities, safeguards jobs in rural areas and increases regional purchasing power. It improves living standards and contributes to economic and social development [1].

Raw material used in anaerobic fermentation has a significant influence on the composition of the resulting biogas. Therefore, the feedstock must be carefully selected.

Table 1 The most important biogas feedstock (substrates) and their biogas yield [4]

Number	Feedstock substrate	Dry matter content (%)	Biogas yield (m <sup>3</sup> /t)	Methane (CH <sub>4</sub> ) content (%)
<i>I.</i>	Animal manures			
1.	Cow manure	25-30	40-50	60
2.	Pig manure	20-25	50-60	60
3.	chicken manure	30-35	70-90	60
4.	Cow slurry	8-11	20-30	60
5.	Pig slurry	7-8	20-35	60-70
<i>II.</i>	Crops			
1.	Corn silage	20-35	170-200	50-55
2.	Whole crops	30-35	170-220	55
3.	Beet	23-25	170-180	53-54
4.	Beet leaves	16-18	70-80	54-55
5.	Grass silage	25-50	170-200	54-55
<i>III.</i>	Food products			
1.	Molasses	80-90	290-340	70-75
2.	Grape marc	40-50	250-270	65-70
3.	Fruit residue	25-45	250-280	65-70
4.	Brewers' grains	20-25	100-130	59-60
5.	Grain stillage	6-8	30-50	58-65
<i>IV.</i>	Communal waste			
1.	Food waste	9-37	50-480	45-61
2.	Sewage sludge	5-24	35-280	60-72
3.	Green meadow	10-12	150-200	55-65

The yield of biogas varies from a given raw material to the following criteria<sup>1</sup>:

- Dry matter content,
- energy left in raw material (if it has been stored permanently, it is likely to be decomposed),
- time spent in the defrosting tank,
- raw material type and fermentation conditions,
- the purity of the raw material.

<sup>1</sup> <http://www.biogas-info.co.uk/about/feedstocks>



## 2. POSSIBILITIES OF BIOMETHANE PRODUCTION

The most important part of biomethane production is to extract as much CO<sub>2</sub> content from the biogas as possible so that the smallest possible part of the CH<sub>4</sub> content is wasted and reach the atmosphere with the carbon phase [5].

Carbon dioxide is removed by biological procedures, most commonly used in absorption such as pressurized water scrubbing, organic solvent wash, amine wash, and adsorption, such as pressure suppression adsorption and temperature fluctuations adsorption. There are some lately introduced technologies: cryogenic separation and membrane permeation.

### 2.1 Absorption

The principle of absorption is based on the different gases' different solubility in liquid. In absorption technology employing plants, raw biogas is in intense contact with some liquid within the washer which was previously filled with plastic filling. Components that are removed from biogas (mostly carbon dioxide) are typically much more soluble in the used washing liquid than methane. As a result, the remaining gas stream is saturated with methane and the contaminated water from the washer is saturated with carbon dioxide [5].

#### a) Physical Absorption: pressurized water scrubbing

The driving force of the process is the difference of solubility for CH<sub>4</sub> and CO<sub>2</sub> in water. During the process of biogas upgrading using water scrubbing column, raw biogas, pressurised (to around 9–12 bar), is introduced through the bottom of the scrubbing tower whereas water is flushed from the top of the tower. As the raw biogas moves up the column against the flow of water (counter currently) over a high surface area packing material, CO<sub>2</sub> dissolves in water and consequently CH<sub>4</sub> content increases in the gas flowing upwards in the column [6].

#### b) Organic-Physical Absorption: organic solvent wash

The process is similar to water scrubbing, but only organic solvents (e.g. polyethylene glycol) are used instead of water. Carbon dioxide (and sulphur-hydrogen) shows a higher degree of dissolution in this material than in water. As a result of improved solubility, the need for solvent and the size of the needed equipment to be used is less at the same biogas input [5].

#### c) Amine wash

The chemical absorption process for CO<sub>2</sub> removal from biogas, performed in a packed column like any other chemical scrubbing of any gas, can be optimised by selecting the best solvent, best contactor (tray or packing with respect to process conditions), best gas and liquid flow rates, and best stripping conditions [7].

### 2.2 Pressure swing adsorption

Pressure swing adsorption is one of the most known and established industrial processes for gas separation because of the compactness of the equipment, low energy requirements, low capital investment cost, and safety and simplicity of operation. Pressure swing adsorption technology uses an adsorbent material which is subjected to pressure changes to selectively adsorb and desorb the undesired gas components [8].



### 2.3 Membrane separation

Membrane-based gas permeation is one of the youngest methods for biogas upgrading but with strongly increasing importance especially during the last decade. The pre-treated biogas is provided at pressures typically between 5 and 30 bar and fed to a membrane module. Gas species with higher permeability preferentially pass the membrane to the low-pressure permeate side while species with lower permeability accumulate on the high pressure side and leave the membrane module as the retentate [9].

### 3. EXAMINATION OF THE ABSORPTION PROCESS

Among the biogas purification processes, absorption technologies, including aqueous washing, organic solvent washing, chemical washing, are the most widely used and recent studies suggest that the absorption process will remain competitive in the future. Therefore, we examined the physical absorption technologies by a modelling software which provides stable state and dynamic process simulation in an integrated environment.

In both cases, we used a raw biogas mixture of choice to compare the results. The mixture is based on the following from *Table 1*, 60% cow manure, 30% corn silage, and the remaining 10% is fruit residue. 60% of the manures, 50% of the silage corns and 70% of the fruits biogas yield is methane, which means that the whole mixture has 58% methane content. The remaining are 40% carbon dioxide and 2% other gases (ammonia, oxygen, nitrogen, H<sub>2</sub>S). First we studied what effect input data changes have to the system. The conclusion is that two factors have a significant effect on the methane content of the biomethane. These are the temperature of the inlet washing liquid and the pressure of the absorption column. The lower the temperature of the washing liquid, the higher the methane content. In contrast a linear proportionality is observed between the pressure of the column and the resulting methane content. Additionally, the methane content may be escalated to a certain extent by increasing the number of trays in the absorption column, but it is stagnant over a given tray number.

The results summarized in the following diagrams:

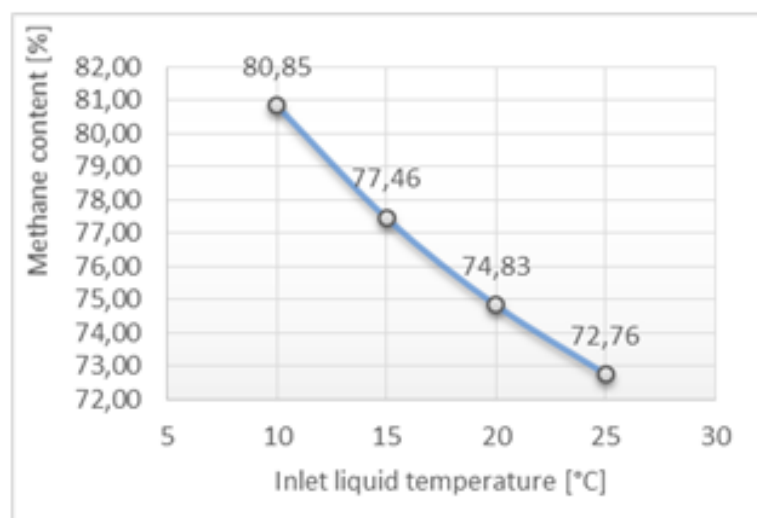


*Figure 1* Change in methane content depending on the temperature of the inlet liquid (in case of 6 trays and 8 bar pressure)

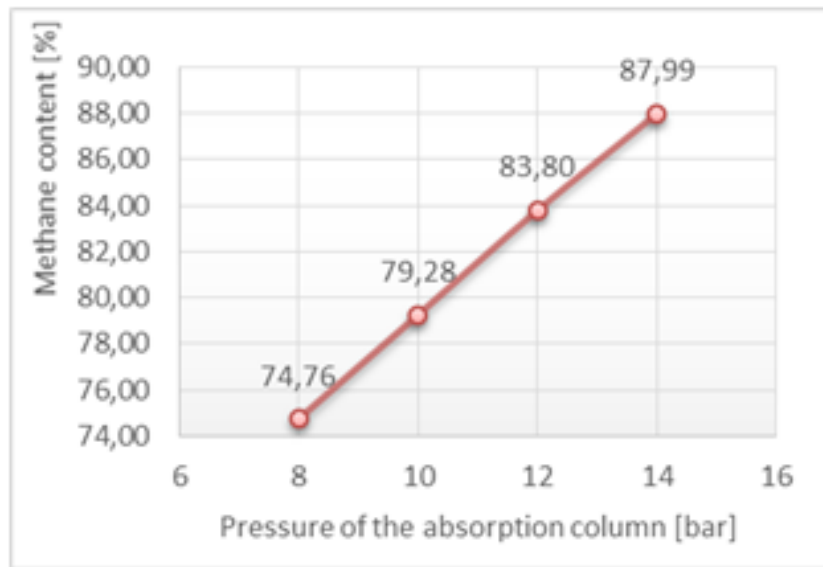


Figure 2 Change in methane content depending on the pressure of the column (in case of 20°C inlet water and 6 trays)

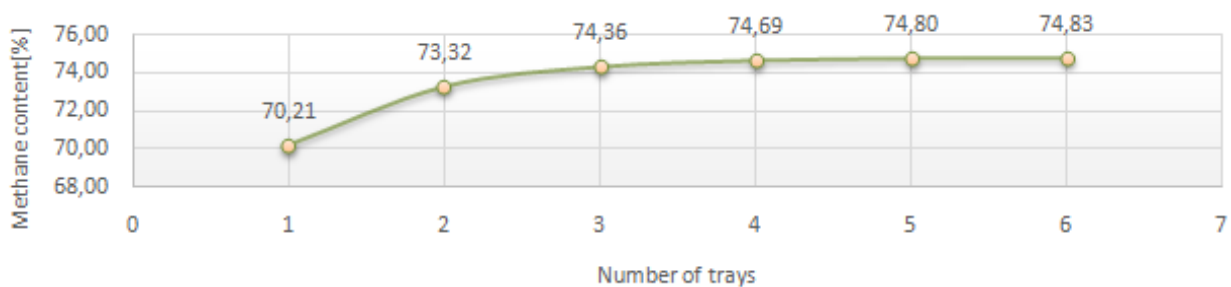


Figure 3 Change in methane content depending on the number of trays in the column (in case of 20°C inlet water and 8 bar pressure)

If you want to achieve the best results (higher methane content), the rinse liquid needs to be cooled down as much as possible before feeding and the pressure during the absorption process has to be high.

In further modelling we choose the rinse liquid to be 15 °C with 100 t/h mass flow. The raw biogas was 45°C with 1t/h mass flow. After the absorption the contaminated water should be regenerated and lead back to be recycled. Desorption is the way for this, but contrary to absorption, it needs low pressure (1 bar) and high temperature. At the top of the column leaves the ‘so called’ waste gas, at the bottom exits the clean water which needs a pressure boost and has to be cooled down before going back to the absorption process. However some water is eliminated with the waste gas at the top, so it has to be replaced. Figure 4. shows the full process.

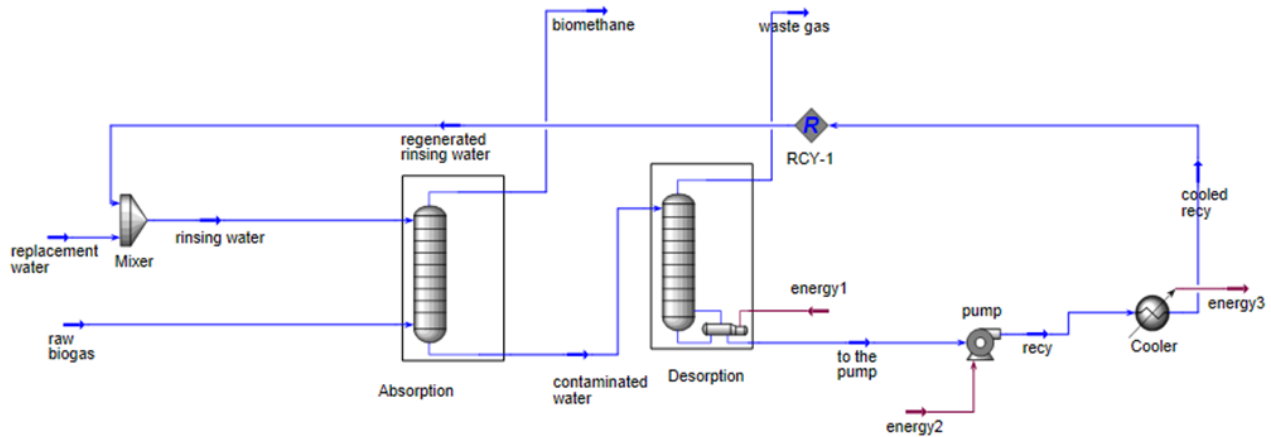


Figure 4 High pressure water scrubbing

#### 4. RESULTS

According to the model with the input data showed in table 2, the achievable biomethane contains 93,56% methane, 4,86% carbon dioxide and 1, 58% other gases.

2. Table Inlet data of the process

With 6 trays	Rinsing water	Raw biogas	Raw biogas	Biomethane
Temperature [°C]	15	45	Composition	
Pressure [bar]	14	14	Methane	93,56%
Mass flow [kg/h]	100000	1000	CO <sub>2</sub>	4,86%

#### CONCLUSIONS

It is apparent that although absorption is a simple technology, it can increase the methane content to a high level. Probably that is why it is said to be competitive in the future.

From the mixture of cow manure, corn silage and fruit residue biogas with 58% methane and 40% CO<sub>2</sub> content is formed through anaerobic digestion. We introduce this raw biogas mixture to the pressurized water scrubbing process, which resulted biomethane with 93, 56% methane and 4, 86% CO<sub>2</sub> content. Biomethane can be used in a variety of ways, and it has a lot of advantages in terms of environmental load reduction because biogas formation may occur naturally anyway and since methane is a greenhouse gas (23 times stronger than carbon dioxide), it is therefore important to reduce the volume of methane escaping to the atmosphere.

#### ACKNOWLEDGEMENT



SUPPORTED BY THE ÚNKP-17-1-I NEW NATIONAL EXCELLENCE PROGRAM OF THE MINISTRY OF HUMAN CAPACITIES

#### REFERENCES

[1] T. A. Sadi, D. Rutz, H. Prassl, M. Köttner, T. Finsterwalder, S. Volk, and R. Janssen, *Biogas*



# INTERNATIONAL SCIENTIFIC CONFERENCE ON ADVANCES IN MECHANICAL ENGINEERING

12-14 October 2017, Debrecen, Hungary



*Handbook*, no. 1. 2008.

- [2] L. Deng, Y. Liu, D. Zheng, L. Wang, X. Pu, L. Song, Z. Wang, Y. Lei, Z. Chen, and Y. Long, "Application and development of biogas technology for the treatment of waste in China," *Renew. Sustain. Energy Rev.*, vol. 70, no. August 2015, pp. 845–851, 2017.
- [3] Seai, "Upgrading Biogas to Biomethane," pp. 1–5, 2012.
- [4] D. J. Hajdú, "Biogas Plant Operation and Biogas Plant Technologies," Obekk Scientific Professional Publications, 2009, p. 15.
- [5] TUV, "Biogas To Biomethane Technology Review," *Vienna Univ. Technol.*, no. May, pp. 1–15, 2012.
- [6] R. Kapoor, P. M. V Subbarao, V. K. Vijay, G. Shah, S. Sahota, D. Singh, and M. Verma, "Factors affecting methane loss from a water scrubbing based biogas upgrading system," *Appl. Energy*, 2017.
- [7] A. L. Kohl and R. (Richard B. . Nielsen, *Gas purification*. Gulf Pub, 1997.
- [8] R. Augelletti, M. Conti, and M. C. Annesini, "Pressure swing adsorption for biogas upgrading. A new process configuration for the separation of biomethane and carbon dioxide," *J. Clean. Prod.*, vol. 140, pp. 1390–1398, 2017.
- [9] M. Miltner, A. Makaruk, and M. Harasek, "Review on available biogas upgrading technologies and innovations towards advanced solutions," *J. Clean. Prod.*, vol. 161, pp. 1329–1337, 2017.



## DESIGNING A BALANCING MACHINE FOR A PLASTIC ROTOR

UNGÁR Péter, SZABÓ Tamás PhD

Robert Bosch Department of Mechatronics, University of Miskolc

E-mail: [engarpoti@gmail.com](mailto:engarpoti@gmail.com), [szabo.tamas@uni-miskolc.hu](mailto:szabo.tamas@uni-miskolc.hu)

### Abstract

*This paper deals with the designing of a balancing machine for a specific deformable plastic rotor, which is used in a trimmer for lawn and garden purposes. In addition to the deformation of the plastic rotor caused by high rotational speed, a mechanism inside the rotor also suffers relatively high displacement. Therefore such a workpiece cannot be balanced by a traditional low rotational speed balancing machine. The construct is built with a rigid suspension. For the sake of simplicity one force gauge is used, since it meets the user requirements. The approximate balancing is performed by placing a single mass in the rotor.*

**Keywords:** *design, balancing machine, force measurement, deformable rotor.*

### 1. INTRODUCTION

A general requirement for all rotors is to reduce or eliminate its imbalance. If balancing does not address impacts caused by the imbalance of the rotor then vibrations reduce the lifetime of the equipment and it can lead to failure or, in severe cases, personal injury.

Balancing a rotor is a traditional engineering task. However, plastic rotors have a particular problem, because they suffer deformation at high speed rotation. During operation, the plastic is subjected to deformation due to the tension in it. Most balancing machines are based on low-speed vibration measurements i.e., acceleration measurements.

The basic balancing principles can be found e.g., in textbooks [1] and [2]. From the point of view of a flexible rotor, mainly the shafts of machines have been taken into account so far. Literature [3] has also done it at a low speed. Dr. Robert Ehrich, in his paper [4] balancing a turbocharger, investigated the need to perform the measurement at a high speed, because the body that is stiff enough will suffer deformation. His method is based on vibration measurement. The article outlines conditions for accurate measurements that are quite expensive and complicated to implement. The majority of balancing operators aim at examining large rotors. For example, literature [5] examines the imbalance of a turbocharger of a power plant, taking into account the flexibility of the foundation. Literature [6] also examines the imbalance by vibration measurement, thus it does not take into account the high-speed deformation.

The purpose of this article is to design a high-speed balancing machine that can be used to measure the plastic rotor under operating conditions. Determining the imbalance is based on force measurement. Since the rotor has a moving part, and under normal usage a trimmer line, approximate balancing is satisfactory. The planned machine will be regarded as a test bench.

The rest of the paper is organised as follows: balancing principles are introduced in Sec. 2. Sec. 3 deals with the construction of the balancing machine. Sensors and signal processing are detailed in Sec. 4. A measurement example is shown in Sec. 5. The last section contains the concluding remarks.



## 2. BALANCING PRINCIPLES

Two types of machines can be distinguished for the balancing of rotors: one has rigid bearings and the other flexible bearings. In the first case, the process is based on force measurement, while in the second one is based on the measured vibrations resulting from the imbalance. Thus balancing machines can be classified as rigid or soft.

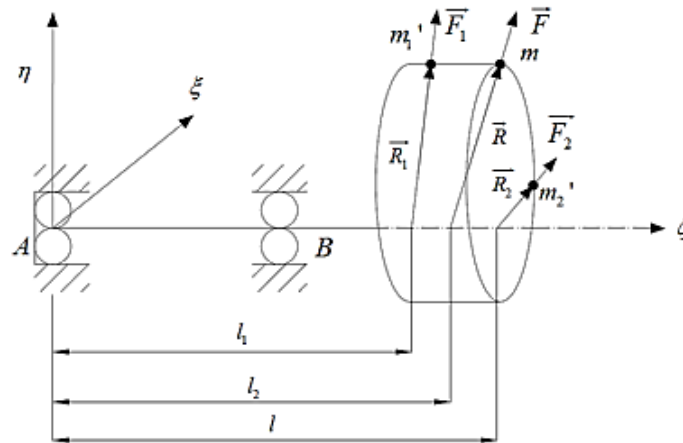


Figure 1: Balancing machine parameters

If the machine's eigen frequency is greater than the excitation frequency it is called a rigid machine. In this case the machine stand damping is large and the bearing displacement is small.

A rotor can be balanced by placing two masses in two different balancing planes. Turning it around an unbalanced body can be conceived as combinations of a perfectly balanced body, and two masses that poison it. If we can determine the position and magnitude of the two masses the rotor can be theoretically balanced. For balancing, a mass of equal weight is placed in the phase shifted by  $180^\circ$  with the two spoiling masses.

For rigid bearings, where the forces in bearings are measured, the measuring arrangement is shown in Figure 1. Based on [2], the balancing masses can be calculated as

$$m_1 = \frac{1}{R\omega^2} \frac{1}{l_2 - l_1} \sqrt{[l_2 F_A \cos\alpha + (l_2 - l_{AB}) F_B \cos\beta]^2 + [l_2 F_A \sin\alpha + (l_2 - l_{AB}) F_B \sin\beta]^2}, \quad (1)$$

$$m_2 = \frac{1}{R\omega^2} \frac{1}{l_2 - l_1} \sqrt{[l_1 F_A \cos\alpha + (l_1 - l_{AB}) F_B \cos\beta]^2 + [l_1 F_A \sin\alpha + (l_1 - l_{AB}) F_B \sin\beta]^2}. \quad (2)$$

The phases of the masses, as shown in Figure 2, are

$$\gamma = \arctg \left[ \frac{l_2 F_A \sin\alpha + (l_2 - l_{AB}) F_B \sin\beta}{l_2 F_A \cos\alpha + (l_2 - l_{AB}) F_B \cos\beta} \right], \quad (3)$$

$$\delta = \arctg \left[ \frac{l_1 F_A \sin\alpha + (l_1 - l_{AB}) F_B \sin\beta}{l_1 F_A \cos\alpha + (l_1 - l_{AB}) F_B \cos\beta} \right]. \quad (4)$$

In our approximate balancing method the masses and the phases are determined by only measuring the force in the bearing near the rotor.

This paper is proposing a possible approximate balancing using one plane only. The balancing



effect is derived from the two theoretical balancing masses. A torque equation is written by utilizing *Figure 1* for point A for the forces  $\overline{F}_1, \overline{F}_2, \overline{F}$ , where  $\overline{F}$  balances the other two ones. When the forces are written in complex vectors, the following equation is obtained

$$l_1 \overline{F}_1 + l_2 \overline{F}_2 = l \overline{F}. \quad (5)$$

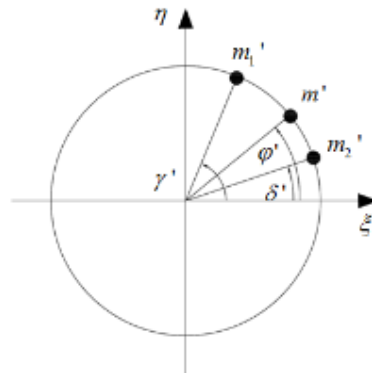


Figure 2: Phase of the masses

Using  $\overline{F} = mR\omega^2 e^{i(\omega t + \varphi)}$  for the forces, dividing both sides of (5) by  $e^{i\omega t}$ , and applying the Euler formula, we get

$$l_1 m_1 R \omega^2 (\cos \gamma' + i \sin \gamma') + l_2 m_2 R \omega^2 (\cos \delta' + i \sin \delta') = l m R \omega^2 (\cos \varphi' + i \sin \varphi'). \quad (6)$$

If the two sides are simplified, then the size of the complex members are used and arrange the equation, we obtain the balancing mass

$$m = \frac{1}{l} \sqrt{(l_1 m_1 \cos \gamma' + l_2 m_2 \cos \delta')^2 + (l_1 m_1 \sin \gamma' + l_2 m_2 \sin \delta')^2}. \quad (7)$$

The phase angle of the mass is obtained by dividing the imaginary quantities in (7) with the real values and taking the arctangent of the expression:

$$\varphi' = \text{arctg} \left[ \frac{l_1 m_1 \sin \gamma' + l_2 m_2 \sin \delta'}{l_1 m_1 \cos \gamma' + l_2 m_2 \cos \delta'} \right]. \quad (8)$$

### 3. CONSTRUCTION

A 3D rendering of the whole machine is shown in *Figure 3*. The machine is placed on a T-grooved table. The balancing is performed by using force measurement. The suspension of the machine is rigid. The aim is to measure the real imbalance, so the bearing can theoretically move freely horizontally without friction. In practice, the force measuring cell holds the bearing in place.

To achieve frictionless motion, the bearing is fixed to a car on a linear guide. This constrain allows one-directional displacement, which results in a horizontal force on the load cell.

The machine requires a drive, which is an available universal, serial engine. The motor has the following data: maximum output of 372 W, idle speed of  $26,000 \text{ min}^{-1}$  at 230V. A toroid is used to adjust the voltage of the engine, thus to change the speed.

The car can theoretically move on the linear guide. It is necessary to allow one degree of freedom of the engine relative to the mounting plate, so the shaft is not bended.

The maximum amplitude of the car is roughly  $150 \mu\text{m}$ , when it's not fixed. The force measuring



cell reduces this by at least one order of magnitude. This maximum amplitude of a few  $\mu m$  is tolerated by the gaps and joints so the shaft will not be under tension.

The shaft must be long to make the measurement, using one force measuring cell, accurate enough. By increasing the distance between the bearings, the force generated in the bearing farther from the rotor will be smaller.

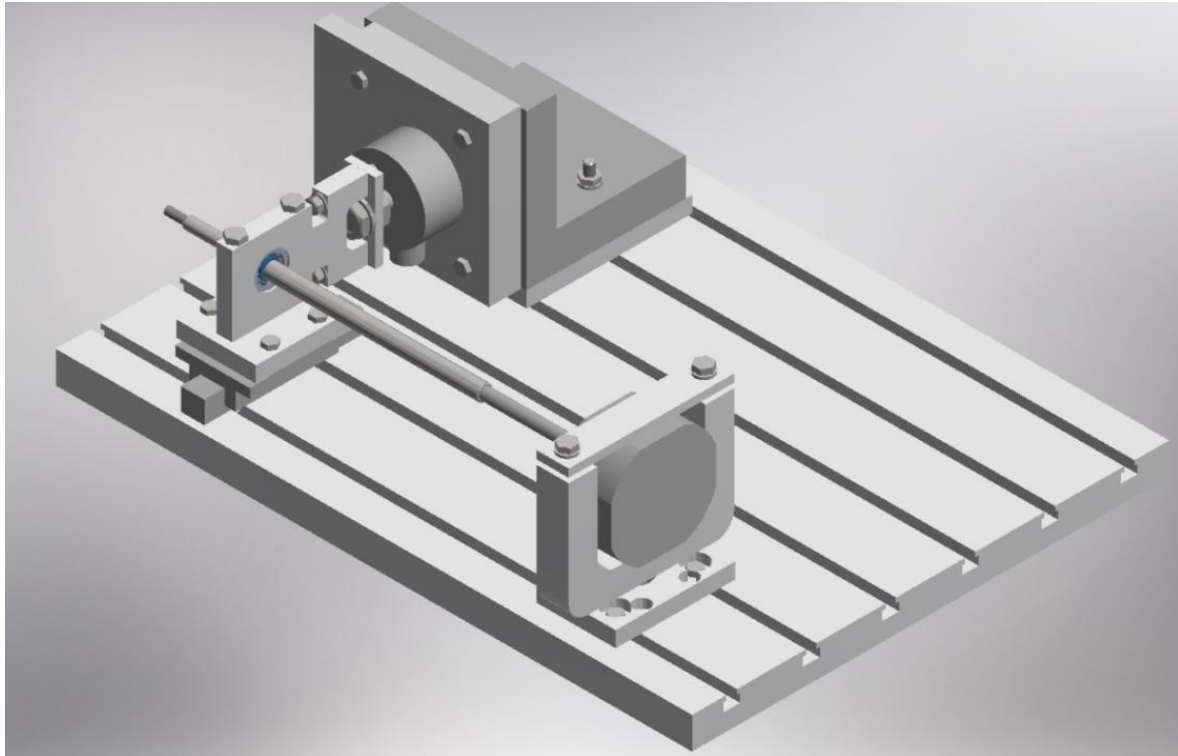


Figure 3: 3D model of the machine

Due to the lack of space technical drawings will be shown in the conference presentation.

#### 4. ELECTRONICS

The force sensor used in the machine is a Gefran TU-K1C force gauge with a 4/4 Wheatstone bridge circuit. The nominal supply voltage is 10 V, maximum 15 V. Its resolution is 2 mV/V, so the 10 V scale is divided into discrete values of 2 mVs. This allows the sensor to distinguish between 5000 different values, so it can measure in 0.2 N steps. The sensor receives excitation on a four-wired, shielded cable and outputs the measured signal levels. Two of the four wires are the positive and negative excitations, the other two are the positive, negative signals.

For measuring the phase of the rotor a two-way optical sensor is used. It detects the repetition of the outlet of the trimmer line. The sensor operates on 10-30V DC power supply.

The data acquisition hardware is a HBM Spider8 eight-channel tool. The sampling frequency is 9660 Hz/channel. Four channels are dedicated to data acquisition and measuring devices. The biggest advantage of the Spider8 is that it can directly measure two, three, four-wire, inductive, 2/4, 4/4 Wheatstone bridge connections so we do not need to design a converter. The load capacity of the channels and the maximum output is  $\pm 10V$  DC voltage. The signals are processed by a computer with the according software.



## 5. RESULTS

The measurement recorded on the test bench is shown in *Figure 4*. The red line is the force sensor's and the blue is the optical sensor's signal. The signal is basically sinusoidal. Because of the elasticity of the balancing machine, vibrations are present in the signal. They are small enough so they do not affect the approximate balancing. The negative value of the signal means that the force acting on the sensor is a pushing, the positive is a pulling force.

The phase of the imbalance is at the signal's minimum. To determine a period, the two consecutive rising edges of the optical sensor have to be taken. This will determine the  $360^\circ$  range. To determine the phase of the force, the minimum position of the signal must be searched within the range.

Based on the measurement (at  $n = 11076 \text{min}^{-1}$ ), the phase of the imbalance is  $\beta = 111^\circ$ . For a more accurate evaluation, measured forces should be averaged:

$$F_B = |F_{\max}| = \frac{64,89\text{N} + 64,54\text{N} + 63,78\text{N}}{3} = 64,4\text{N}. \quad (8)$$

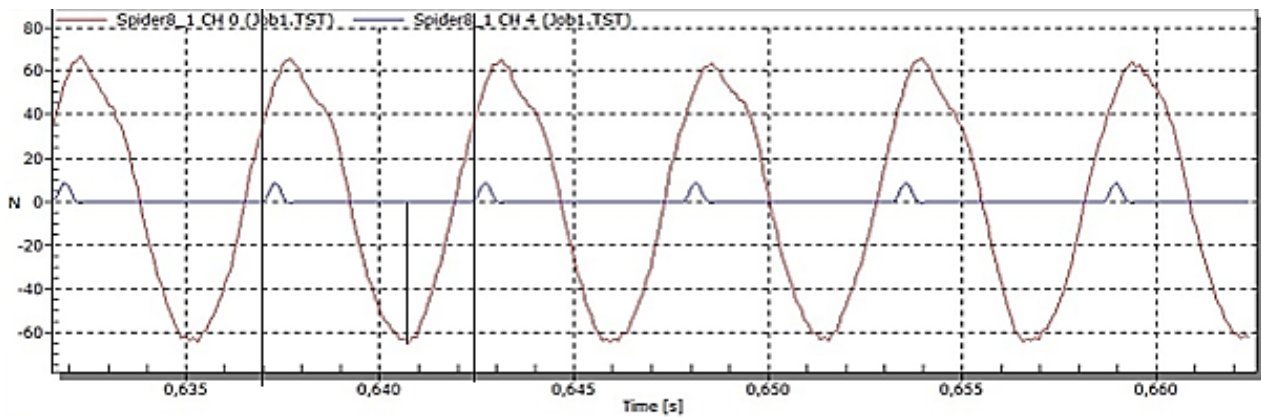


Figure 4: Measured signal

The parameters for the equations are the following:  $F_A = 0\text{N}$ ,  $R = 30\text{mm}$ ,  $\omega = 1160\text{s}^{-1}$ ,  $l_1 = 260\text{mm}$ ,  $l_2 = 305\text{mm}$ ,  $l_{AB} = 232\text{mm}$ ,  $\gamma = \delta = \beta$  in (1) and (2) the theoretical balancing masses are

$$m_1 = \frac{1}{R\omega^2} \frac{(l_2 - l_{AB})F_B}{l_2 - l_1} = \frac{(0,305\text{m} - 0,232\text{m})64,4\text{N}}{0,03\text{m} \cdot (1160\text{s}^{-1})^2 \cdot (0,305\text{m} - 0,26\text{m})} = 0,0026\text{kg}, \quad (9)$$

$$m_2 = \frac{1}{R\omega^2} \frac{(l_1 - l_{AB})F_B}{l_2 - l_1} = \frac{(0,26\text{m} - 0,232\text{m})64,4\text{N}}{0,03\text{m} \cdot (1160\text{s}^{-1})^2 \cdot (0,305\text{m} - 0,26\text{m})} = 0,001\text{kg}. \quad (10)$$

The balancing mass is calculated by using (9) and (10) in (7),

$$m = \frac{l_1 m_1 + l_2 m_2}{l} = \frac{0,26\text{m} \cdot 0,0026\text{kg} + 0,305\text{m} \cdot 0,001\text{kg}}{0,27\text{m}} = 0,0036\text{kg}. \quad (11)$$

## CONCLUSIONS

This paper dealt with the designing of a balancing machine for a specific deformable plastic rotor, which is used in a trimmer for lawn and garden purposes. A balancing machine with rigid support



was developed, which utilizes force measurement only on one bearing. The proposed balancing method was demonstrated by an example. The developed test bench device is a prototype which can be a basis for designing a balancing machine that serves practical usage.

## ACKNOWLEDGEMENT

*“The described article/presentation/study was carried out as part of the EFOP-3.6.1-16-2016-00011 “Younger and Renewing University – Innovative Knowledge City – institutional development of the University of Miskolc aiming at intelligent specialisation” project implemented in the framework of the Szechenyi 2020 program. The realization of this project is supported by the European Union, co-financed by the European Social Fund.”*

## NOMENCLATURE

- $m_1, m_2$  – theoretical balancing masses  
 $\bar{F}_1, \bar{F}_2$  – forces of the imbalances  
 $R$  – radius of the masses  
 $\omega$  – angular velocity  
 $l_1, l_2$  – distance of the balancing planes  
 $l$  – distance of the balancing mass  
 $\alpha, \beta, \gamma, \delta$  – phases of the masses  
 $F_A, F_B$  – forces in the bearings  
 $l_{AB}$  – distance of the bearings  
 $\varphi$  – phase of the balancing mass

## REFERENCES

- [1] Király Béla: *Dinamika*. Miskolci Egyetemi Kiadó, Miskolc, 2006.
- [2] Lipovszki György, Sólyomvári Károly, Varga Gábor: *Gépek rezgésvizsgálata és a karbantartás*. Műszaki Könyvkiadó, Budapest, 1981.
- [3] W. H. Miller: *Experimental Investigation Of Balancing Flexible Rotors In Large Motors And Generators*, Manager - Advanced Quality Control Engineering, Large Motor and Generator Department, General Electric Company, Schenectady, New York
- [4] Dr. Robert Ehrich: *High Speed Balance Procedure*, Manager, Development Turbo machinery, Borsig GmbH, Berlin, West Germany
- [5] Jyoti K. Sinha , M. I. Friswell , A. W. Lees and R. K. Sinha: *Robust Method for the Rotor Unbalance Estimation*, Proceedings of VETOMAC-2, 16-18 December, 2002
- [6] Tadeusz Majewski, Radoslaw Domagalski, Marco Meraz Melo: *Dynamic Compensation Of Dynamic Forces In Two Planes For The Rigid Rotor*, JOURNAL OF THEORETICAL AND APPLIED MECHANICS 45, 2, pp. 379-403, Warsaw 2007



## SELECTION OF PACKAGING SYSTEMS IN AUTOMOTIVE ENGINE SUPPLY: THE CASE OF OVERSEAS TRANSPORT

*VÖRÖSKŐI Kata*

*Department of Logistics and Forwarding, Széchenyi István University*

*E-mail: [voroskoi.kata@sze.hu](mailto:voroskoi.kata@sze.hu)*

### **Abstract**

*Packaging is a significant element in any logistics system. Disposable (one-way) packaging is also used, but returnable packaging is more common in the outbound flow of the automotive engine producer companies in the practice. Although cost is an important factor, it is not enough to only consider the costs of material and investment while choosing the right packaging system, many other aspects should be considered. That is the reason why besides the cost structure of disposable and returnable packaging further issues are examined in this paper as well. In most cases distance decides if the packaging comes back, but it also depends on the complexity of the supply chain. Transport modes can play a noticeable role (road, rail, maritime transport).*

**Keywords:** *returnable packaging, overseas transport, CKD, automotive, engines*

### **1. INTRODUCTION**

The best packaging solutions for automotive packaging are those that beside the optimal cost levels can maximize the use of packaging space so that all the products can easily be packed and stacked, at the same time reduce packaging waste [1]. Besides the support of logistics handling and containment product and environmental protection is also one of the most important functions of packaging [2].

In the automotive industry the primary function of packaging is the protection of products and parts optimised by the total costs of logistics. This way, even if shipping is performed on land or sea, by rail, trucks, vessels or multi-mode shipping, the distribution environment and logistics costs together define the possible form of packaging, and then determine the final solution from disposable to returnable packaging and systems [3]. The following packaging system are mostly used in automotive industry: one-way and returnable. Former is only suitable for one use as far as reusable containers and packaging are loaded with products and shipped to the destination, then the empty container is sent back to the supplier, refilled with products and this cycle is repeated over and over again as a closed-loop system [4]. Returnable packaging has been frequently used, for example, in the US automotive industry, in order to reduce waste, costs, transport damages and to enable JIT deliveries [5]. Standardised shipment materials are usually used as returnable packaging in the ASC, like the EUR/-EPAL pallets, racks, containers and specialty bins for certain types of parts [6].

Based on literature review and empirical study a 6 step process of automotive packaging design was created in general:

- Identification of physical characteristics of the product: dimensions and weight, surface, susceptibility to abrasion or corrosion, internal characteristics affected by vibration, fragility.



- Determination of distribution requirements: number of units, composition and attributes of the primary package, identification of the OEMs and their handling and storage requirements, the package disposal or returning criteria, total volume expected, etc.
- Choosing modes of transport and distribution channel: tradeoff analysis, knowledge of distribution environment (for example infrastructure quality, in-transit vibration and shock, humidity, extreme temperature, etc.), characteristics of the supply chain.
- Cost of packaging material and protection level of the product: comparing paper versus plastic versus metal versus, one-way or returnable packaging, standardized or special packaging, shipping unit design, cost of reuse, environmental aspects, regulations, determination of quality of protection (damage free shipment), etc.
- Redesign of the shipping unit, packaging or product if necessary.
- Development of packing methods along the whole automotive supply chain.[7]

## 2. CASE STUDY

In the case overseas CKD (completely knocked down) transport will be examined. The same returnable packaging is used for automotive engine (CKD) transport from Europe to two different destinations in India and China. The packaging comes back from China, but it will be discarded in India. In both cases it is transported by multimodal transport, namely road, rail and waterway.

The finished engines are sensitive products therefore special racks are mainly used to store and transport them. (*Figure 1*) These ensure safe and reliable transport and storage. The column is usually collapsible in order to save place while return back as empty transportation. The posts are supposed to keep the engine in place, but these can be also collapsed.



*Figure 1:* Example of returnable packaging used for overseas CKD transport

Therefore in the field of logistic packaging (industrial transportation, or even consumer packaging) the companies make decisions in order to determine the optimal packaging expenses. This decision-making situation practically means a choice between the one-way and reusable (disposable or returnable) packaging systems.[8] It is significant in the decision making process, that which costs and environmental effects disposable packaging has. The



construction of returnable packaging is more complex. Numerous factors appear and each of them should be examined separately. As returnable packaging is planned for multiple uses, packaging material should be stronger and the whole design has to handle excessive forces.

### 3. CRITERIA

In the model we suppose the following criteria/ conditions:

- 1.) The price of disposable and returnable packaging (labor cost of assembly is included) is the same:  $P_D = P_R$
- 2.) The cost of the first transport is the same (the destination is the same):  $T_{R1} = T_{D1}$
- 3.)  $W_D = U * W_R/U$  where  $W_D$  = disposal fee of disposable packaging,  $U$  = number of usage
- 4.) The complexity of the supply chain depends on the transport modes ( $\alpha$  = road,  $\beta$  = rail,  $\gamma$  = maritime) so the cost of transportation ( $T$ ) will be modified with them. Also:  $\gamma = 1 - \alpha - \beta$
- 5.)  $2 * S_D = S_R$  where  $S$  = cost of storage, because returnable packaging will be stored not only at the supplier's facility, but also at the place of destination
- 6.) Usage ratio (*Figure 2*): the more times the returnable packaging can be used, the less the unit cost will be.  $\delta$  = number of planned usage/ number of real usage

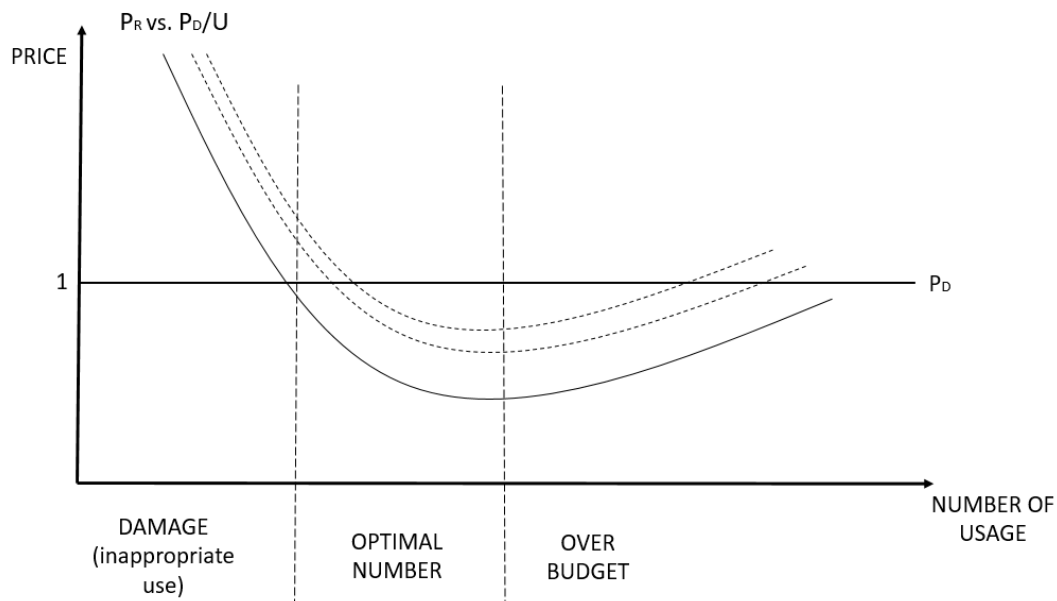


Figure 2: Usage ratio

### 4. COST STRUCTURE OF OUTBOUND PACKAGING

In this case, the engine company plays the role of system integrator, then the OEM (Original Equipment Manufacturer) complies with the vehicle-assembling factory. Returnable packaging is more common on the outbound flow of the engine companies. (*Figure 3*)

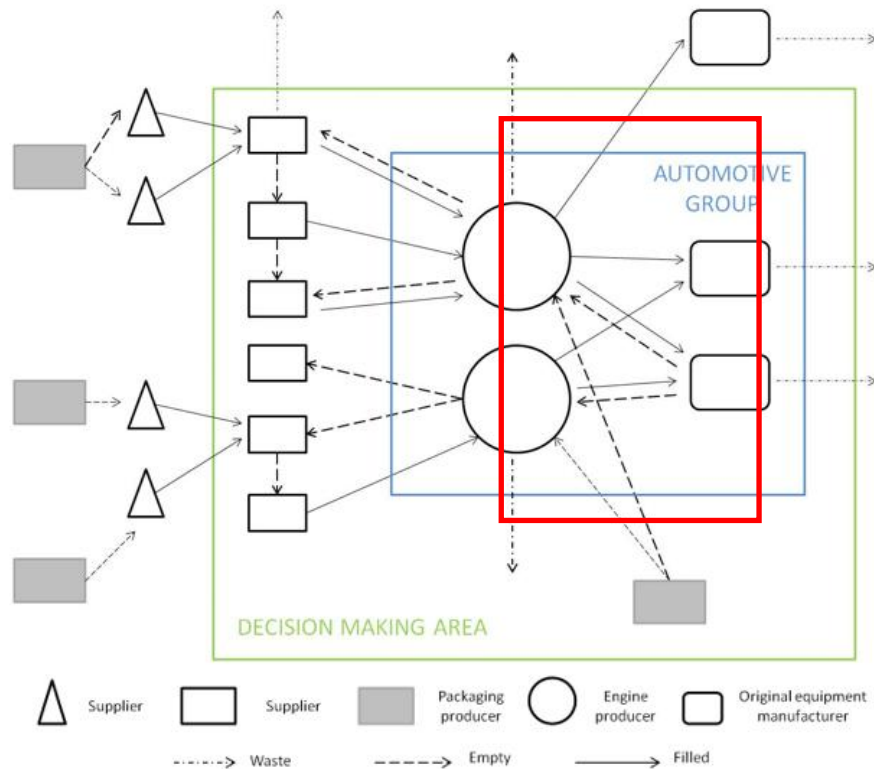


Figure 3: Packaging supply chain of an automotive engine producer

Returnable packaging has the following ingredients:

- price of returnable packaging (material cost), multiplied with the quantity (Q) and divided by the number of uses:  $(P_R * Q) / U$
- transport cost of the packaging, multiplied with the quantity and divided by the number of transports (t):  $(T_R * Q) / t$
- cost of storage (S) per unit multiplied with the quantity:  $S_R * Q$
- cost of repair (R) per unit multiplied with the quantity:  $R_R * Q$
- cost of cleaning (C) per unit multiplied with the quantity:  $C_R * Q$
- cost of administration per unit multiplied with the quantity:  $A_R * Q$
- cost of waste (W) generated divided by the number of uses:  $W_R / U$
- cost of risk of damage:  $D_R$

Based on the above mentioned total cost of returnable packaging can be described with the following equation:

$$TC_R = \sum_{i=1}^n \frac{P_R}{U} (Q_n) + \sum_{j=1}^m \frac{T_R [(Q)_j]^{\alpha+\beta+\gamma}}{T_j} + \sum_{k=1}^x S_R (Q_x) + \sum_{i=1}^n R_R (Q_n) + \sum_{i=1}^n C_R (Q_n) + \sum_{i=1}^n A_R (Q_n) + \sum_{i=1}^n \frac{W_R}{U} + D_R \quad (1)$$

where

$i = 1 \dots n$  : parts of packaging

$j = 1 \dots m$  : destinations

$k = 1 \dots x$  : destinations with storage

Disposable packaging has the following ingredients:



- purchase price of disposable packaging (material cost), multiplied with the quantity (Q): ( $P_D * Q$ ) in this case the price of disposable and returnable packaging equals
- transport cost of disposable packaging equals with the transportation cost of returnable packaging to the first destination:  $T_{R1} * Q_1 = T_D * Q_1$
- cost of storage (S) of disposable packaging equals with the half of the storage of returnable packaging on a give destination:  $\frac{1}{2} S_R * Q_X = S_D * Q_X$
- cost of repair (R) and cleaning (C):  $\emptyset$
- cost of administration of disposable packaging:  $A_D * Q$
- cost of waste (W) generated:  $W_D$

Based on the above mentioned total cost of disposable packaging can be described with the following equation:

$$TC_D = \sum_{i=1}^n P_D(Q_n) + T_D(Q_1) + \sum_{k=1}^x S_D(Q_X) + \sum_{i=1}^n A_D(Q_n) + \sum_{i=1}^n W_D \quad (2)$$

if we substitute

$$TC_D = \sum_{i=1}^n P_R(Q_n) + T_{R1}(Q_1) + \frac{1}{2} \sum_{k=1}^x S_R(Q_X) + \sum_{i=1}^n A_D(Q_n) + \sum_{i=1}^n W_D \quad (3)$$

The study has the following limitations:

- The change in global maritime fuel prices is not included in the study
- Dimensions of material flow are not considered yet. Nevertheless the world trade balance and modal shift can significantly affect transportation processes.
- $\delta$  is not included in the equation yet

## CONCLUSIONS

Automotive industry is one of the world's most significant economic sectors by its revenue. Engine transportation is carried out in different facilities all over the world. Besides waste reduction and optimal cost level the best packaging solutions for automotive packaging are those that can maximize the use of packaging space so that all the products can easily be packed and stacked. Appropriate protection of the sensitive and relatively expensive products (engines) is also crucial, especially while overseas transport where the external forces are multiplied. However managing returnable packaging systems requires more than just inverse transportation. Many other factors should be considered in the process.

## ACKNOWLEDGEMENT

The author acknowledges the financial support of this research by the Project EFOP-3.6.1-16-2016-00017. Internationalisation, initiatives to establish a new source of researchers and graduates, and development of knowledge and technological transfer as instruments of intelligent specialisations at Széchenyi István University.



# INTERNATIONAL SCIENTIFIC CONFERENCE ON ADVANCES IN MECHANICAL ENGINEERING

12-14 October 2017, Debrecen, Hungary



## REFERENCES

- [1] <http://www.mjspackaging.com/blog/what-are-the-best-packaging-solutions-for-automotive-packaging/> (access on 05. 10. 2016)
- [2] Böröcz P, Mojzes Á: *The importance of packaging in logistics*. Transpack, 8 (2), 28-32., 2008
- [3] Böröcz, P, Singh SP.: *Measurement and Analysis of Vibration Levels in Rail Transport in Central Europe*. Packaging Technology and Science, 2016
- [4] Yam K L: *The Wiley encyclopedia of packaging technology*. Wiley, USA, 2009
- [5] Witt C E: *Are reusable containers worth the cost?* Material Handling Management, 55 (7), 75., 2000
- [6] Boysen N, Emde S, Hoeck M, Kauderer M: *Part logistics in the automotive industry: Decision problems, literature review and research agenda*. European Journal of Operational Research, 242 (1), 107-120., 2015
- [7] Vöröskői K: *Packaging Perspectives In Automotive Supply Chain Management*, Euroma, Edinburgh, 2017
- [8] Vöröskői K., Böröcz P.: *Framework for the Packaging Supply Chain of an Automotive Engine Company*, Acta Technica Jaurinensis, 9 (3), 191-203., 2016



## THE INFLUENCE OF TOOL DIAMETER AND FEED SPEED ON FEED FORCE AND TORQUE MOMENT DURING STEEL S233J0 DRILLING

<sup>1</sup>ZÁKOPČAN Ján, <sup>1</sup>JAVOREK Lubomír PhD, <sup>2</sup>BACHRATÝ Michal PhD

<sup>1</sup>Faculty of Environmental and Manufacturing Technology, Technical University in Zvolen  
E-mail: [xzakopcan@is.tuzvo.sk](mailto:xzakopcan@is.tuzvo.sk), [lubomir.javorek@tuzvo.sk](mailto:lubomir.javorek@tuzvo.sk)

<sup>2</sup>Faculty of Mechanical Engineering, Slovak University of Technology in Bratislava  
E-mail: [michal.bachraty@stuba.sk](mailto:michal.bachraty@stuba.sk)

### Abstract

*In this paper, there are presented results of the thrust force and torque moment obtained during drilling of S355J0 EN10027-1 (St52-3 DIN). In the experiments, there were used drills with  $\varnothing 12\text{mm}$ ,  $\varnothing 16\text{mm}$  and  $\varnothing 20\text{mm}$  diameters and with angles of main cutting edges  $49^\circ$ ,  $54^\circ$  and  $59^\circ$ . The feed rates were  $0.10\text{mm}$ ,  $0.15\text{mm}$  and  $0.20\text{mm}$ , revolutions of drills were constantly  $350\text{ rpm}$ . Liquid Hocut 3380 was used for cooling during drilling.*

**Keywords:** *drilling; thrust force; cutting moment.*

### 1. INTRODUCTION

Drilling is probably the third most common technology of metal machining after milling and turning, especially because there is very often a requirement to make a hole so-called “already made”, which means without further processing. By drilling, the holes are prepared for thread making (by cutting or rolling) and non-compliance can cause, for example, reducing threading functionality. Tools for making holes are relatively expensive (in particular, tools made of sintered carbides or coated) and therefore, the mapping of the opening formation, such as chip formation, is essential for the tool designer when designing a drill bit that has been modeled, for example, by Kücükürk, G. (2012), who verified previously known models by his own measurements of thrust force and torque. Similar measurements were carried out by Meral, G. (2010) as part of his doctoral thesis, but in drilling alloy steels as did Tamura, S., Matsumura, T., Arrazola, P. (2012) while drilling with titanium-hardened alloy bits and modified cutting section in the edge transition with the use of internal cooling. Experiments with the drilling of materials hardened with different grids of intersecting fibers were performed by Mohan, N. (2005) and Okutan, E. et al (2013). The tracked parameters were also the thrust force and torque. There is a great deal of work in this area, and so every seemingly little piece of information can contribute to the expansion of the horizon and complete the mosaic of knowledge. The value of the thrust force must be kept within reasonable limits also in terms of the thermal load of the tool. Lowering the thrust force reduces the friction at the cutting point and hence the thermal load on the cutting edge.

By reducing the friction, we reduce the loss and therefore the energy spent on drilling. When the torque is reduced, the tool wear is reduced and, as is the case, the power required for drilling decreases. By reducing the torque, we directly reduce the power consumption that the machine takes from the network. When reducing the tool wear, we shorten the time needed to replace the tool and save money spent on buying new tools.



## 2. METHODS

### Machine

The OPTI B 50 GSM drill press stand was used for drilling. The main technical parameters are given in Table 1.

Table 1 Technical data of the machine

Height x width x length	2'454 x 610 x 1'016 mm
Spindle speeds	54 – 2'090 min <sup>-1</sup>
Autom. spindle sleeve feed	6 steps, 0.05/0.3 mm/rev
Drilling capacity in steel (S235JR)	60 mm
Number of steps	18
Total weight	820 kg
Electrical connection	400 V / 3 Ph ~50 Hz
Total connected value	3.0 / 2.4 kW
Work surface table length x width	600 x 600 mm
T-slot size	18 mm
Spindle seat	MT 4

### Tools

Drill bits with diameters 12 mm, 16 mm and 20 mm (Fig. 1) with the designation A 1141 NS HSS-E with MK2 conical shank were used for drilling. The drill bits were adjusted so that the angles of the main cutting edges were 49°, 54° and 59°.



Figure 1 Tools

### Measuring Device

A measuring device from Kistler (Fig. 2) was used to measure thrust force and cutting torque, which consisted of a dynamometer type 9272 (range -5 kN to 20 kN, torque measuring range -200 Nm to 200 Nm) multiple channel amplifier 5070A, 16-bit A / D convertor 5697A and a computer with measuring program Dyno-Ware.

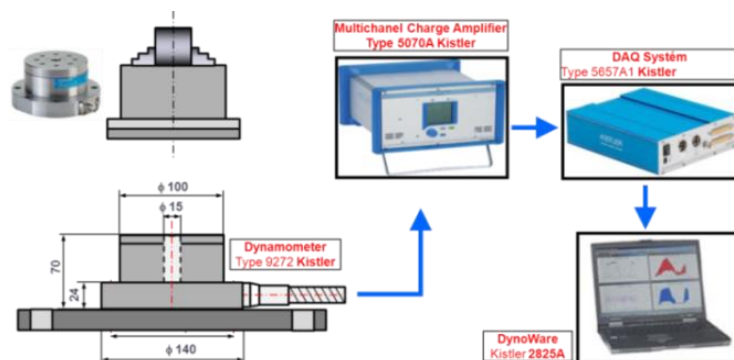


Figure 2 Measurement chain



### Materials and Conditions of the Experiment

In experiments, cube-sized samples (40mm x 40mm x 40mm), S355J0 (weldable non-alloy structural steel used for machine parts, steel structures and other comparable components according to EN 10025) were used.

The rotational speed of the tool was set at 350, 500 and 720 rpm. The feed rate per revolution was changed at three levels: 0.10, 0.15 and 0.20mm. The Hocut 3380 process fluid with 5% concentration was supplied in an amount of about 5 l/min. In this paper, the results are obtained at 350 rpm.

## 3. RESULTS

### 3.1 Influence of the feed and diameter on the thrust force

The graph (Fig. 3) shows the thrust force values at the angle of adjustment of the main cutting edges for  $2\kappa_r = 98^\circ$  of the cutting tool, the diameters of 12mm, 18mm and 20mm and the feed rates per revolution of 0.10mm, 0.15 mm and 0.20 mm. With the tool diameters of 12mm and 16mm, the feed rate does not have a significant effect on the thrust force, but with the tool diameter of 20mm, the thrust force increases almost linearly. In order to reduce the thrust force between the feeds of 0.10 mm and the 0.15 mm of the 12mm tool end, the thrust force lessens by 24 % and the decrease of the thrust force continues with feed of 0.10 mm for the 16mm and 20mm tool ends where it falls by 5 %. This measurement shows that the thrust force for  $2\kappa_r = 98^\circ$  and the feed rates of 0.15 mm and 0.20 mm increases almost linearly.

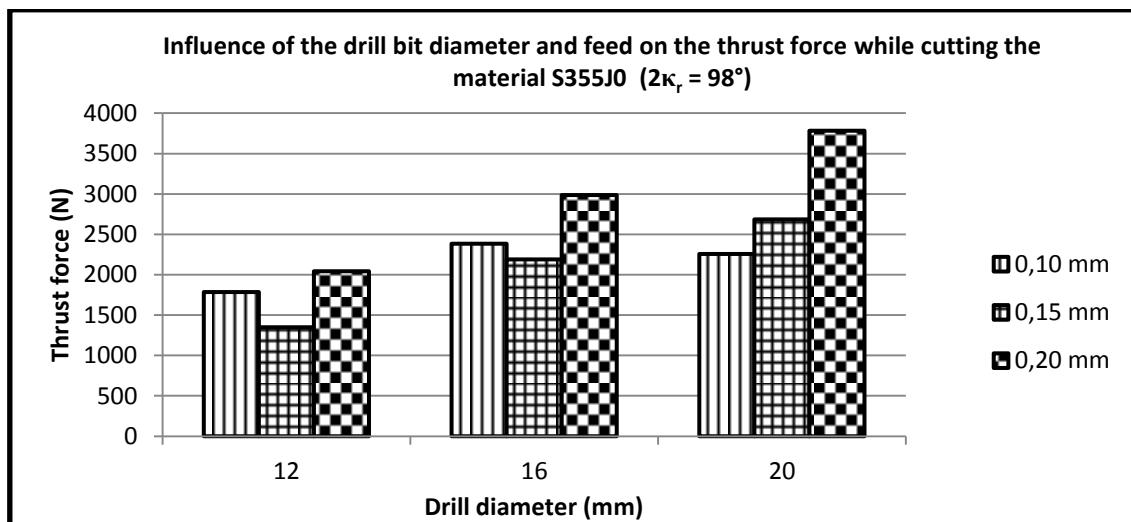


Figure 3 Influence of the drill bit diameter and feed on the thrust force ( $2\kappa_r = 98^\circ$ )

### 3.2 Influence of the feed and diameter of the tool on the torque

The graph (Fig.4) shows the torque values for  $2\kappa_r = 98^\circ$  of the cutting tool diameters of 12mm, 18mm and 20mm and feed rates per revolution of 0.10mm, 0,15mm and 0,20mm.

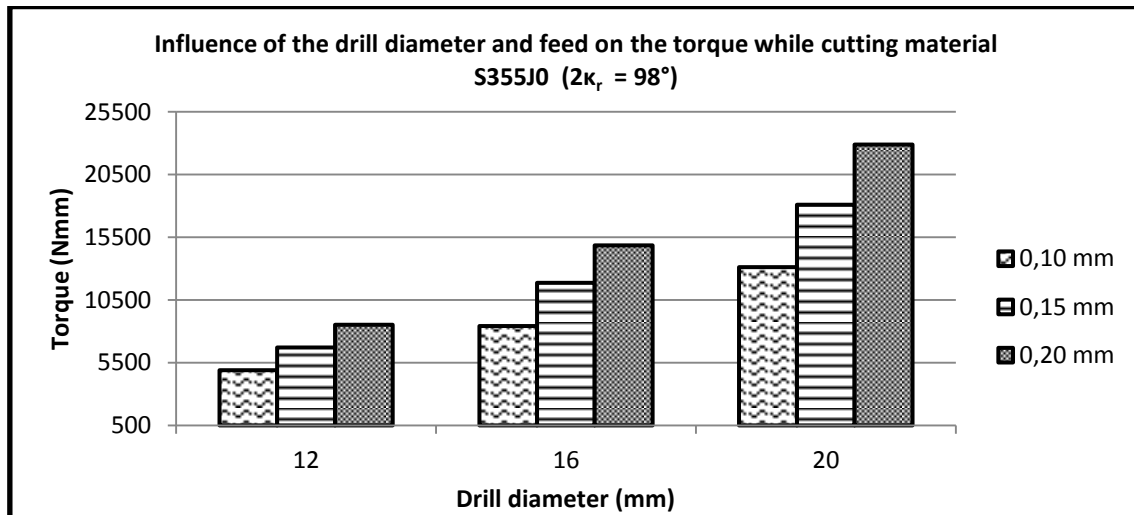


Figure 4 Influence of the drill diameter and feed on the torque ( $2\kappa_r = 98^\circ$ )

The torque for the 16mm cutting tool ends and 0.10mm feed rate increases by 72 % and for the 20mm tool end by 167 %. With 0.15mm feed rate, the torque increases by 76 % for the 16mm tool diameter and for the 20mm tool diameter by up to 169 %. With 0.20mm feed rate of the 16mm cutting tool diameter, the torque increases by 74 % and when changing the tool end to a diameter of 20mm, the torque increases by 167 %. The maximum impact on the torque for  $2\kappa_r = 98^\circ$  has a 16mm diameter tool end and the torque for feed rate of 0.20 mm is almost linear. The torque for all three feeds and cutting tool ends is almost linear.

## CONCLUSIONS

In this paper, we have verified the influence of selected technological parameters and the selected drilling diameters while drilling full holes in the material S355J0 on the value of the thrust force and torque. The tool feed rates were 0.10mm, 0.15mm and 0.20mm, the drills were 12mm, 16mm and 20mm in diameter, and a constant speed during each experiment reached 350 rpm.

The thrust force value of the tool with the diameter of 20 mm for  $2\kappa_r = 98^\circ$  increases between feed rates per revolution of 0.10mm and 0.20mm by 59%, for  $2\kappa_r = 108^\circ$  and the tool diameter of 20mm between the feed rates 0.10mm and 0.20mm increases by 69%, and for  $2\kappa_r = 118^\circ$  and the tool diameter of 20mm, the torque increases between feed rates 0.10mm and 0.20mm up to 70%, so we can state that the thrust force increases with the increasing angle of  $2\kappa_r$  and feed rate.

The torque for  $2\kappa_r = 98^\circ$  and the tool diameter of 20mm, feed rates 0.10mm and 0.20mm increases by 57%. For  $2\kappa_r = 108^\circ$  and the tool diameter of 20mm, the torque rises between the feed rates 0.10mm and 0.20mm by 58% and for  $2\kappa_r = 118^\circ$  and the tool diameter of 20mm between feed rates of 0.10mm and 0.20mm, the torque remains at 58%.

## ACKNOWLEDGMENT

The part of research work presented in this paper was solved under project KEGA 035 STU-4/2017

## REFERENCES

- [1] Javorek, L.: *Tools (Part 1)*. Publishers TU in Zvolen. 171, ISBN 97880-228-1714-1. 2012.
- [2] Kücükürk, G.: Modeling and analyzing the effects of the experimentally determined torque and thrust force on the cutting tool according to the drilling parameters. 2012.



# INTERNATIONAL SCIENTIFIC CONFERENCE ON ADVANCES IN MECHANICAL ENGINEERING

12-14 October 2017, Debrecen, Hungary



- [3] Majerik, J. et al: The verification of axial forces and torques in drilling by the noncoated cutting tools and drills with PVD TIN coatings. In Annals of DAAM. Vol. 23. No 1. 477-480. ISSN 2304-1382.
- [4] Meral, G.: An investigation of the drilling parameters' effect on cutting forces and hole quality in the drilling of AISI 1050 material. MSc Thesis, Institute of Science and Technology, Gazi University, Turkey. 2010.
- [5] Mohan, N.: Influence of process parameters on cutting force and torque during drilling of glass-fiber polyester reinforced composites. Composite Structure; 71: 407-413. 2005.
- [6] Okutani, E. et al.: A Study on the derivation of parametric cutting force equations in drilling of GFRP composites. Strojniški Vestnik-Journal of Mechanical Engineering. 59. 2. 97-105. 2002.
- [7] Tamura, S., Matsumura, T., Arrazola, P.: Cutting force prediction in drilling of Titanium Alloy. Journal of Advanced Mechanical Design, Systems and Manufacturing. Vol.6, No 6. 753-763., 2012.



## DEPENDENCE OF THE THRUST FORCE FROM THE CLEARANCE ANGLE AND FEED SPEED DURING DRILLING

<sup>1</sup>ZÁKOPČAN Ján, <sup>1</sup>JAVOREK Lubomír PhD, <sup>2</sup>BACHRATÝ Michal PhD

<sup>1</sup>Faculty of Environmental and Manufacturing Technology, Technical University in Zvolen  
E-mail: [xzakopcan@is.tuzvo.sk](mailto:xzakopcan@is.tuzvo.sk), [lubomir.javorek@tuzvo.sk](mailto:lubomir.javorek@tuzvo.sk)

<sup>2</sup>Faculty of Mechanical Engineering, Slovak University of Technology in Bratislava  
E-mail: [michal.bachraty@stuba.sk](mailto:michal.bachraty@stuba.sk)

### Abstract

The article deals with the issue of drilling holes in material C45 (steel). Specifically evaluates the thrust force with respect to change feed per revolutions (0.20mm, 0.28mm and 0.40mm) and back angle of the drills (8°, 10° and 12°). In the paper are present results for drills with ø20mm diameters and with angles of main cutting edges 59°. Revolutions of drills were constant 350 rpm. The Alfaflex process fluid with 7% concentration was supplied in an amount of about cca 5 l/min

**Keywords:** drilling, feed speed, back angle, thrust force.

### 1. INTRODUCTION

It is well known that the steel processing and metallic materials are made of over 100 years. Drilling is a widely used metal removal process in automotive, aerospace, textile machinery and other manufacturing industries for roughing and finishing cutting of holes in various components. Dynamic change in cutting force and torque moment are one of the major sources causing for example vibration or tool wearing etc. by which the machining can be monitored. Thus, accurate modelling of cutting forces is necessitated for the prediction of machining performance, for determine the mechanisms of chips removing, for option of machining parameters that affects for example the stability of machining, surface roughness, tool life ... The modelling of cutting process generally depends on real values obtained in real process. Various measuring methods of cutting force, cutting moment and other parameters were explained in literature e.g. Byrne G. (1995). Information about piezoelectric sensors that are clamped between two plates and practical experiences of users are mentioned by Elhachimi M., Torbyty S., Joyot P. (1999) or Jemelniak K., Balazinski M (2000). The thrust force and torque moment were in the focus of investigators for long time, from the beginning of metal machining, that means, that principal is the same, only properties of drilled materials and cutting materials were modified. Both parameters were analysed in Shaw M.C., Oxford Jr. C.J. (1957) or Trmal, G.J., Wyatt, J.E. (2001).

### 2. METHODS

#### Machine

Cutting process was conducted on vertical drilling machine type 2H 135 (Fig. 1) powered by a 10 kW motor with maximum spindle speed 1400 rpm. press stand was used for drilling (Fig.2). The main technical parameters are given in Table 1.



Table 1 Technical data of the machine

Parameters (L × W × H)	785 mm × 915 mm × 2350 mm
Spindle speed	(31,5 – 1400) rpm
Feed per rev.	0,1 mm – 1,6 mm
Max. diameter of drill bit	35 mm
Working table dimensions (L × W)	450 mm × 500 mm



Figure 1 Drilling machine

### Tools

Drill bits with diameters 20 mm (Fig. 2) with the designation Format HSS DIN 345N with MK2 conical shank were used for drilling. The drill bits were adjusted so that the angles of the main cutting edges was  $59^\circ$  and values of clearance angle were  $8^\circ$ ,  $10^\circ$  and  $12^\circ$ .



Figure 2 Tools

### Measuring Device

A measuring device from Kistler (Fig.3) was used to measure thrust force and cutting torque, which consisted of a Quartz 4-components dynamometer type 9272, i.e. X, Y (-5 kN to 5 kN), Z (-5 kN to 20 kN) direction, torque (cutting) moment  $M_z$  direction (range -200 Nm to 200 Nm) multiple channel amplifier 5070A, 16-bit A / D convertor 5697A. The computer software used was Kistler Dyno-Ware (type 2825D-02; version 2.5.1.2). The cutting force equipment are shown in Fig.4.

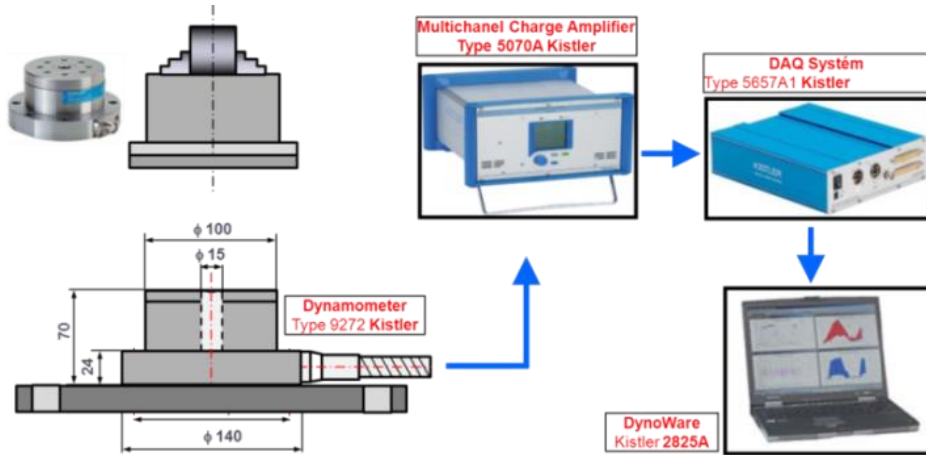


Figure 3 Measuring device

### Materials and conditions of the experiment

The experiment plan was designed based on a model of a classical experiments plan, with three independent factors. Workpiece used for machining (Fig.4) was from steel C45 ( $R_{e,min} = 430$  MPa;  $R_m = (650 - 800)$  MPa;  $HV_{10} = 179-182$ ). Depended (measured) factors were: thrust force, torque moment, surface quality of hole, tool life.



Figure 4 Workpiece after drilling

The rotational speed of the tool was set at 250, 350 and 450 rpm. The feed rate per revolution was changed at three levels: 0.20mm, 0.28mm and 0.40mm. The Alfaflex process fluid with 7% concentration was supplied in an amount of about cca 5 l/min. Depended (measured) factors were: thrust force, torque moment, surface quality of hole, tool life. The results of thrust forces and torque moment (for 250 rpm) are mentioned in this contribution.

## 3. RESULTS

### 3.1 Impact of feed rate on thrust (axial) force

On the graph (Fig. 5) is clearly visible that the change of feed rate significantly influence to the thrust force. Average value of axial force was 4378 N when the feed rate was 0.2 mm/rev. If it was changed from 0.2 mm/rev to 0.28 mm/rev the thrust force approximately increased about 25% to the average value 5442 N. When feed rate was doubled to 0.4 mm/rev average value of axial force increased on to 7431 N what is an increase about cca 75%.

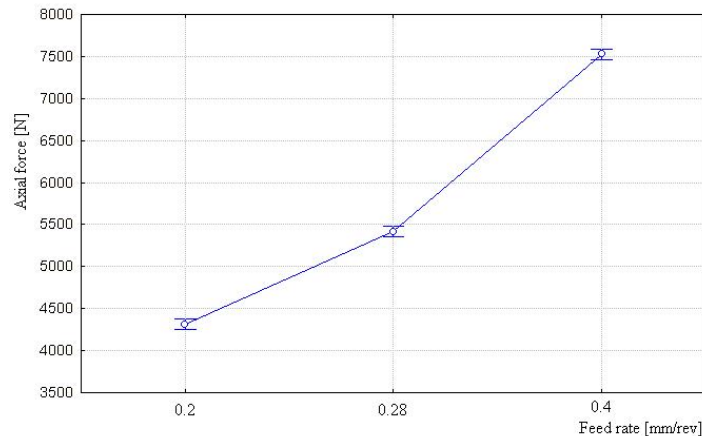


Figure 5 Axial force measured for various feed rate

### 3.2 Impact of clearance angle on axial force

With changing the clearance angle is shown, that the axial force changed. But as the graph (Fig.6) shown, the axial force in the measurement did not change linearly with the changing the clearance angle of tool. According to the measured values of clearance angle  $12^\circ$  seems to be the best because the smallest values of axial force was measured. The average value of axial force for clearance angle  $12^\circ$  and all range of feed speed was 4922 N. The angle of  $10^\circ$  during the measurement shows an increase of the average value axial force by 725 N, compared to the measuring with an angle of  $12^\circ$ . An angle of  $8^\circ$  increased average values from about 1760 N compared to values with  $12^\circ$  clearance angle. Angle of  $10^\circ$  at this measurement seems to be the worst for drilling, but its unsuitability should be verified by other experiments. When we measured with drill which clearance angle was  $10^\circ$  then occurred a destruction of cutting edge (Fig. 6)

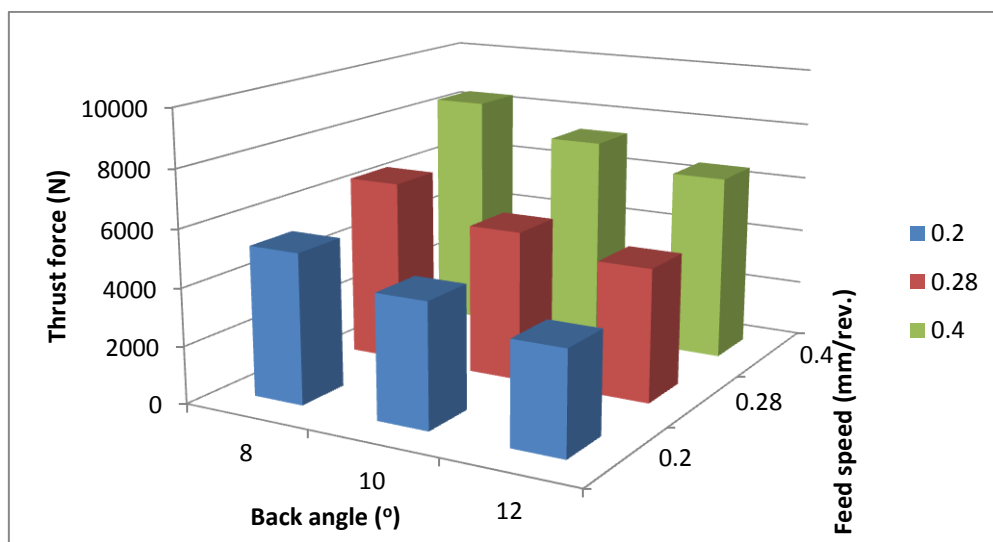


Figure 6 Influence of feed speed and back angle to thrust force

## CONCLUSIONS

This measurement showed that the thrust force during drilling steel with screw drill increased approximately linearly with increasing feed speed of tool. After doubling the feed speed increased axial force of approx. 75%. Comparing the tools in terms of impact clearance angle the experiment



# INTERNATIONAL SCIENTIFIC CONFERENCE ON ADVANCES IN MECHANICAL ENGINEERING

12-14 October 2017, Debrecen, Hungary



demonstrated the best tool with clearance angle of  $12^\circ$ . Tools with clearance angle  $8^\circ$  in this experiment shows, that the axial force increases by 2% compared to the tool with clearance angle of  $12^\circ$ . For tool with clearance angle of  $10^\circ$  the increase of thrust force was up to 11% compared to tool with clearance angle of  $12^\circ$ . To verify the measured data would be useful to repeat the measurement even using large-scale changes in the clearance angle of the tool.

## ACKNOWLEDGMENT

The part of research work presented in this paper was solved under project KEGA 035 STU-4/2017.

## REFERENCES

- [1] Byrne G. et al.: Tool Condition monitoring (TCM) – The status of research and industrial application. CIRP Annals, Vol. 44, No 2, 541-567, 1995.
- [2] Elhachimi M., Torbyty S., Joyot P.: Mechanical modelling of high speed drilling. 2: Predicted torque and experimental results. International Journal of machine tools and manufacture. Vol. 39, 569-581, 1999.
- [3] Erkki J.: A summary of methods applied to tool condition monitoring in drilling. In: International Journal of machine tools and manufacture 42, 997-1010, 2002.
- [4] Jemelniak K., Balazinski M: Laboratory versus industrial cutting force sensor in tool condition monitoring. The international Journal for manufacturing Science and production. 3, No 1, 41-47, 2000.
- [5] Rubenstein, C.: The torque and thrust force in twist drilling. I. Theory. In: International Journal of Machine Tools and Manufacture 31, No.4. 481-489, 1991.
- [6] Shaw M.C., Oxford Jr. C.J.: On the drilling of metals: 2 – the torque and thrust in drilling. Trans. Of ASME, Vol.79, 139-148, 1957.
- [7] Trmal, G.J., Wyatt, J.E.: Model for predicting the torque and thrust and its application in monitoring drilling operations. Industrial Tooling int. Conf., Southampton, 201-210, 2001.



## SUPPORTING COMPANIES

### THE ISCAME 2017 CONFERENCE AND THE 5<sup>th</sup> MECHANICAL ENGINEERING INDUSTRIAL EXHIBITION, DEBRECEN

Company name	Website	Location
Aventics Hungary Kft.	<a href="http://www.aventics.hu">www.aventics.hu</a>	Eger
CAD-CAM Solutions Kft.	<a href="http://www.cadcamsolutions.hu">www.cadcamsolutions.hu</a>	Székesfehérvár
Coloplast Hungary Kft.	<a href="http://www.coloplast.hu">www.coloplast.hu</a>	Nyírbátor
Diehl Aircabin Hungary Kft.	<a href="http://www.diehl-aerosystems.com">www.diehl-aerosystems.com</a>	Nyírbátor
eCon Engineering Kft.	<a href="http://www.econengineering.com">www.econengineering.com</a>	Budapest
Enterprise Communications Magyarország Kft.	<a href="http://www.enterprisegroup.hu">www.enterprisegroup.hu</a>	Budapest
EUROSOLID Kft.	<a href="http://www.eurosolid.hu">www.eurosolid.hu</a>	Budaörs
FAG Magyarország Ipari Kft.	<a href="http://www.schaeffler.hu">www.schaeffler.hu</a>	Debrecen
FERZOL Lemezmegmunkáló Kft.	<a href="http://www.ferzol.hu">www.ferzol.hu</a>	Tápiószőlős
Flexiforce Hungary Kft.	<a href="http://www.flexiforce.com">www.flexiforce.com</a>	Debrecen
FlexLink Systems Kft.	<a href="http://www.flexlink.com">www.flexlink.com</a>	Budapest
Haas Factory Outlet	<a href="http://www.haascnc.com">www.haascnc.com</a>	Leoben
HAJDU Autotechnika Ipari Zrt.	<a href="http://www.hajduautort.hu">www.hajduautort.hu</a>	Téglás
HAJDU Hajdúsági Ipari Zrt.	<a href="http://www.hajdurt.hu">www.hajdurt.hu</a>	Téglás
Hoya Szemüveglencse Gyártó Magyarország Zrt.	<a href="http://www.hoya.com">www.hoya.com</a>	Mátészalka
igm Robotrendszerek Kft.	<a href="http://www.igm-group.com">www.igm-group.com</a>	Győr
KE KELIT Innovative Pope Systems GmbH	<a href="http://www.kekelit.hu">www.kekelit.hu</a>	Budapest
Linamar Hungary Autóipari és Gépgyártó Zrt.	<a href="http://www.linamar.hu">www.linamar.hu</a>	Orosháza
Manz Hungary Gépgyártó Kft.	<a href="http://www.manz.com">www.manz.com</a>	Debrecen
MÁV Zrt. és MÁV-START Zrt.	<a href="http://www.mavcsoport.hu">www.mavcsoport.hu</a>	Budapest
Modine Hungária Kft.	<a href="http://www.modine.com">www.modine.com</a>	Mezőkövesd
MSK Hungary Gépgyártó Bt.	<a href="http://www.msk.hu">www.msk.hu</a>	Nyírbátor
NAGÉV RÁCS Kft.	<a href="http://www.nagev.hu">www.nagev.hu</a>	Hajdúböszörmény
Robert Bosch Automotive Steering Kft.	<a href="http://www.bosch.hu">www.bosch.hu</a>	Eger, Maklár
Rufém Kft.	<a href="http://www.rufem.hu">www.rufem.hu</a>	Bodrogolaszi
S&T Consulting Hungary Kft.	<a href="http://www.snt.hu">www.snt.hu</a>	Budaörs
SPM Instrument Budapest Kft.	<a href="http://www.spminstrument.com">www.spminstrument.com</a>	Budapest
Takata Safety Systems Hungary Kft.	<a href="http://www.takata-miskolc.hu">www.takata-miskolc.hu</a>	Miskolc
Tungaloy Hungary Kft.	<a href="http://www.tungaloytools.hu">www.tungaloytools.hu</a>	Budapest
ZF Hungária Kft.	<a href="http://www.zf.com/hu">www.zf.com/hu</a>	Eger



# INDUSTRY DAYS IN DEBRECEN

## 5<sup>TH</sup> MECHANICAL ENGINEERING INDUSTRIAL EXHIBITION

12-13 October 2017, Debrecen, Hungary



### COLOPLAST HUNGARY KFT.

Address: 4300 Nyírbátor, Coloplast u.2., 2800 Tatabánya, Búzavirág u.15.

Phone: +3642886300, +3634520500

Webpage: [www.coloplast.hu](http://www.coloplast.hu) [www.coloplast.com](http://www.coloplast.com)



#### About Coloplast

Coloplast is a Danish international company that develops products and services that make life easier for people with very personal and private medical conditions. Working closely with the people who use our products, we create solutions that are sensitive to their special needs. We call this intimate healthcare.

Our business includes ostomy care, urology and continence care, and wound and skin care. We operate globally, employing more than 10,000 people.

#### Coloplast in Hungary

Coloplast employs more than 3000 people in Hungary. There are 2 factory sites in Tatabánya and Nyírbátor and Postponement and Distribution Center in Tatabánya. We are continuously growing! Join us!

When you get a job here, you get much more than just that – you get a career! We'll push you, stretch you and reward you. Performance here goes a long way, you drive your own career development. Be ambitious and deliver results, and you'll thrive.

	Scholarship program
	Development opportunities
	Good atmosphere

 Nyírbátor:  
4300 Nyírbátor, Coloplast u.2.  
+36 42 886 300

Tatabánya:  
2800 Tatabánya, Búzavirág u.15.  
+36 34 520 500

PDC:  
2800 Tatabánya, Kerék u.3.



# INDUSTRY DAYS IN DEBRECEN

## 5<sup>TH</sup> MECHANICAL ENGINEERING INDUSTRIAL EXHIBITION

12-13 October 2017, Debrecen, Hungary



### DIEHL AIRCABIN HUNGARY Kft.

Address: 4300 Nyírbátor, Ipari park utca 9.

Phone: 06 80 200 270

Webpage: [facebook.com/diehlaircabinhungary](https://facebook.com/diehlaircabinhungary)



Diehl Aircabin Hungary Kft. is a 100% subsidiary of Diehl Aircabin GmbH., based in Laupheim Germany, and a member of the Diehl Aerosystems syndicate through the parent company.



Diehl Aircabin has established itself as a preferred partner in the international aviation industry. With its cabin modules, crew rest compartments, and air ducting, Diehl Aircabin provides an array of highly specialized aviation solutions under the general umbrella of Diehl Aerosystems.

The area of expertise of Diehl Aircabin GmbH includes product and process development, design, predevelopment, construction, and the production and qualification of cabin elements. The integration of system components such as in-flight entertainment, oxygen systems and electrical equipment also forms an important part of company's broadly based portfolio.

The story of the Hungarian company started in February 2011 when the growing pace of the German parent company made it necessary to establish a new production plant where they could move a portion of the existing Single Aisle and Long Range airplane part manufacturing. After analyzing multiple sites globally, they choose Hungary: more precisely, Nyírbátor.

In its Nyírbátor plant, Diehl Aircabin Hungary Kft. manufactures three important parts of the passenger cab for the Airbus A319/320/321, A340, A350 and A380 planes: sidewalls, door and doorframe casing and air-conditioning pipes that provide the air supply. In our plant we employ 600 employees. Currently, 75% of our employees work in two production halls. This November we opened an Engineering Centre in Debrecen and in addition create more than 150 jobs in Hungary.

For the production of these mostly handmade parts, the production of which can also be called almost "manufactorial" a highly special knowledge is knowledge required which cannot be matched completely with any current school education. Therefore, beginning with the 2016/2017 school year, our company will also join the Dual Vocational Training system which according to our plans will provide education linked to practice in professions that we specifically need. At the same time the training aims at improving the best skills and abilities of the individual. Students who graduate with good results can count on stable long term employment. For engineers and people with a higher level of education we offer more than fix and stable work: we offer a carrier opportunity.

Positions in important areas such as production preparation, process engineering, quality assurance, logistics and economy-finance are expanding in size and responsibility. When launched our comprehensive trainee program will be adjusted to our future improvements. Our headcount will nearly double after the construction of the new plant hall and the range of product will widen. As the first step of this process we would like to fill the engineering positions mentioned above. We are simultaneously hiring entrant engineers, trainees and more experienced colleagues. Moreover, we are counting on colleagues with unique qualifications such as airplane designers or engineers who have the special certification required for airplane manufacturing. We hope we have been able to increase your enthusiasm for the airplane industry.



**Fly with us to the safe future!**



# INDUSTRY DAYS IN DEBRECEN

## 5<sup>TH</sup> MECHANICAL ENGINEERING INDUSTRIAL EXHIBITION

12-13 October 2017, Debrecen, Hungary



### eCon Engineering Kft.

Address: 1116 Budapest, Kondorosi út 3. IV. emelet  
 Phone: +3612790320/101  
 Webpage: [www.econengineering.com](http://www.econengineering.com)



#### SOFTWARE SALES AND SUPPORT:

eCon Engineering Kft. was established in 2002. We emphasize our mission on the distribution of advanced engineering simulation technologies by representing such products as ANSYS, Moldex3D and Cast-Designer.

Beside the distribution of these software products we also provide solid mechanical-, fluid dynamical-, thermal- and electromagnetic analyses, injection moulding simulations, moulding optimisation and metal casting simulations during the product and design development of our customers.



The 46 years of experience and the thousands of developers worldwide are the guarantees for the market leader position of ANSYS, which was earned by its wide variety of solvers, easy operability and reliability of engineering simulations in the fields of solid mechanics, thermodynamics, fluid dynamics and electromagnetics. The ANSYS software family offers outstanding possibilities for Simulation Driven Product Development, which is indispensable in today's modern and cost-effective engineering.



The leading injection moulding simulation software provides product designers, designers/producers of moulding tools and manufacturers with the capability of predicting the outcome of their work. This way the injection moulding technology and the quality of the final product becomes much more reliable.



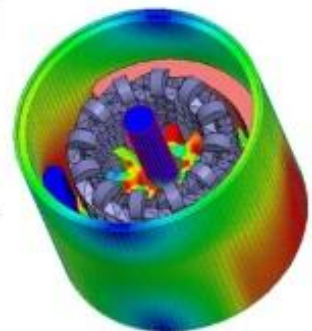
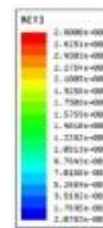
A practical cast designer and simulation software that enables the investigation of the cast parameters and eliminates the possible failures of the casting process during the design phase. It's a reliable tool for product and casting tool designers for cost- and time-effective cast design and production.

#### ANALYSIS:

Finite Element Method Analysis based development fits into the profile of eCon. With valuable experiences in the field of FEM development we offer engineering solutions for our partners.

A skilled team of 50 engineers with a wide spectrum of knowledge in the fields of mechanics, optimisation, durability and fatigue analysis, analysis of composite frames, hydrodynamics, thermodynamics, correlation analysis, dynamics, vehicle construction, medical technology and turbine physics. It's very important for us to provide our customers with a complex solution on the most professional level.

We don't only focus on just a single problem, we aim analyse the whole spectrum of possible problems and provide a comprehensive solution.



#### SINGLE-PURPOSE MACHINES:

Our company also produces special single-purpose machines, assembly lines, testers for the car and the IT industry, according to the customer's needs.

Projects include the whole production process, from the development of technology to the execution procedure, concluding with onsite installation. Guarantee servicing and full-scale project management are also included.

Our quality policy is to use our experience, developments and knowledge to fulfil and to exceed our customer expectations.





# INDUSTRY DAYS IN DEBRECEN

## 5<sup>TH</sup> MECHANICAL ENGINEERING INDUSTRIAL EXHIBITION

12-13 October 2017, Debrecen, Hungary



### ENTERPRISE COMMUNICATIONS MAGYARORSZÁG KFT.

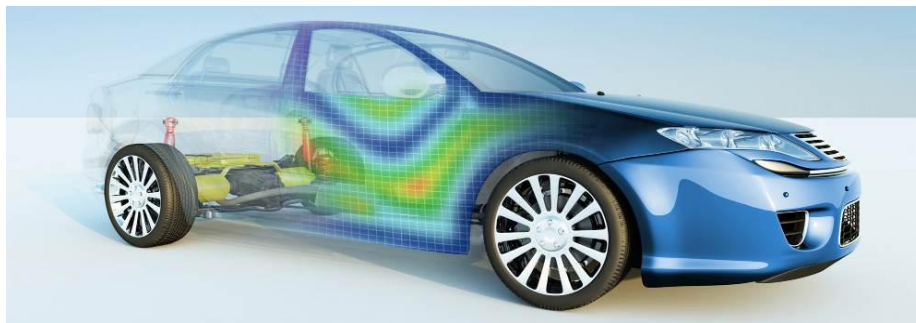
Address: H-1138 Budapest, Váci str. 117-119.

Phone: +36 (1) 471-2380 / ext. 2

Webpage: [www.enterprisegroup.hu](http://www.enterprisegroup.hu), [blog.eplm.hu](http://blog.eplm.hu), [www.digitálisipar.hu](http://www.digitálisipar.hu)



ENTERPRISE  
GROUP



### Enterprise Group PLM Business Unit – Engineering Solutions

#### CAD/CAM solutions and product lifecycle management (PLM) from design to implementation

Our PLM division provides complex engineering solutions and IT services for companies that operate in the field of industry. The market-leading solutions of Siemens PLM and Vero Software cover the entire lifecycle of products - from the original concept, through the design process, all the way to manufacturing - and support product development and recycling. Our team of experts, with decades of experience in the industry, coupled with the stable corporate background of the Enterprise Group, ensures that our clients will always receive reliable solutions that are customised to meet their own particular requirements.

PLM is a complex process which facilitates the management of a product's entire lifecycle. It includes computer-aided design (CAD) and manufacturing (CAM) solutions, but it is more complex than that, as it encompasses the full lifecycle of products. PLM offers advantages such as time-to-market acceleration, product quality improvements, prototype production cost reductions, rapid identification of potential sales opportunities and overall cost savings by recycling previously obtained data and by fully integrating engineering work processes.

Our PLM division supplies the well-known products developed by Siemens PLM Software, as well as their connected services. The division is ready to serve existing and future clients as a distributor of Solid Edge, NX, Tecnomatix Teamcenter, Femap and Preactor.

With solutions from Vero Software, the world's largest CAM-oriented CAD/CAM developer, the division is capable of comprehensively satisfying all the requirements of manufacturing companies. Among these solutions, Edgcam is recommended for production machining, Radan for sheet metal manufacturing tasks, and Alphacam for the wood and stone industries. For the Mould and Die industries, we offer Visi, as an integrated CAD/CAM solution and WorkNC, as the market leading automatic CAM software solution for 2 to 5-axis milling of complex 3D models.

Besides supplying the market's well known Siemens PLM and Vero Software products and solutions, Enterprise Group's PLM division also helps partners with the introduction of new software, as well as support and updates, training programs and constant availability. Our staff, consisting of experts with decades of experience in engineering, IT and industry related projects, can also call on the knowledge of Enterprise Group's other divisions and rely on the smooth operational background of the company when implementing their own projects.





# INDUSTRY DAYS IN DEBRECEN

## 5<sup>TH</sup> MECHANICAL ENGINEERING INDUSTRIAL EXHIBITION

12-13 October 2017, Debrecen, Hungary



### EUROSOLID Kft.

Address: Budapest, 1117 Szerémi út 7/B  
Phone: +3612168661  
Webpage: [www.eurosolid.hu](http://www.eurosolid.hu)



EuroSolid Ltd. has been dealing with the introduction and installation of CAD/CAM/PLM/MDC systems, process optimization, education and support of technical, engineering and manufacturing softwares for 20 years in Hungary. Since its foundation, our company was driven by one goal which is to help companies in product development and manufacturing fields in the most efficient way and at the highest professional standards to tackle their technical challenges.

Today EuroSolid Ltd is one of the market leaders and has more than 700 partners with references such as Michelin, Aloca, Coloplast, GE or Linamar.

Our company is the sole and exclusive distributor of SOLIDWORKS softwares in Hungary plus the only qualified education and support centre in the country. As the representative of SOLIDWORKS, our activities include professional client support, data management system installation, delivering and solving engineering tasks and performing different simulation tests with our softwares.

SOLIDWORKS is the market leading and the most integrated software system available. In the past 25 years the CAD software has grown out to become the foundation of a wide ranged product portfolio which not only includes engineering design and simulation but also electrical design, data management, quality management for inter- and post production processes, sheet-less sketch creation, rendering, technical documentation modules and so much more.

Our goal is to deliver solutions with the excellent tools, quickly-to-adapt and easy-to-learn systems of SOLIDWORKS and with the new technologies supporting design and manufacturing that ensure profitable investment and increasing productivity with optimized workflow for our clients.

## SOLIDWORKS as an Innovation Platform





# INDUSTRY DAYS IN DEBRECEN

## 5<sup>TH</sup> MECHANICAL ENGINEERING INDUSTRIAL EXHIBITION

12-13 October 2017, Debrecen, Hungary



### FAG MAGYARORSZÁG IPARI KFT.

# SCHAEFFLER

Address: 1/D Határ Road/Street, 4031 Debrecen, Hungary

Phone: 00 36-52-581-700

Webpage: <http://www.schaeffler.hu>

#### A leading global technology company

The Schaeffler Group is a global automotive and industrial supplier. Top quality, outstanding technology, and exceptionally innovative spirit form the basis for the continued success of the company. By delivering high-precision components and systems in engine, transmission, and chassis applications, as well as rolling and plain bearing solutions for a large number of industrial applications, the Schaeffler Group is already shaping “Mobility for tomorrow” to a significant degree. The technology company generated sales of approximately EUR 13.3 billion in 2016. With around 87,900 employees, Schaeffler is one of the world’s largest family companies and, with approximately 170 locations in over 50 countries, has a worldwide network of manufacturing locations, research and development facilities, and sales companies.

#### Divisions and business divisions

Schaeffler develops and manufactures precision products for approximately 60 sectors around the world. Its technologically advanced components and systems are used in applications in vehicles, machinery, plants, as well as in aerospace applications. The group distributes its products and services to numerous automotive manufacturers and industrial customers.



#### Mobility for tomorrow

Globalization, urbanization, digitalization, scarcity of resources, renewable energy, and the growing demand for affordable mobility are leading to changed, much more dynamic market requirements and business models. Based on these megatrends, the Schaeffler Group has developed its “Mobility for tomorrow” strategy concept, under which the company focuses on four areas across divisions and regions: eco-friendly drives, urban mobility, interurban mobility, and the energy chain.



Schaeffler plays an active part in shaping these focal areas through its own research and development activities and, as a leading expert in innovation and technology, offers an attractive product range to its customers and business partners.

The group’s broad portfolio of products and services ranges from components and systems for automotive drive trains to products for high-speed trains and from rolling bearings for solar power plants to innovative solutions for aerospace applications.



# INDUSTRY DAYS IN DEBRECEN

## 5<sup>TH</sup> MECHANICAL ENGINEERING INDUSTRIAL EXHIBITION

12-13 October 2017, Debrecen, Hungary



### FERZOL Kft.

Address: 2769 Tápiószőlős, Ceglédi út 15.

Phone: + 36 53 585 080

Webpage: [www.ferzol.hu](http://www.ferzol.hu)



FERZOL LTD. is present on field of metal processing and within that the sheet metal fabrication for 27 years. Our core values are unchanged since the foundation of our company: satisfying the needs of the customer – should it be a complex task or of highest quality – is our top priority. Flexibility, which is expected more and more by our customers is also of importance. This is to be met by keeping the efficiency of our production processes high and continuously improving them. To be able to perform excellently, we operate with highest level of technology and the most modern equipment.



We are proud of the unbroken progression of our company since the beginning. One of the most important conditions – besides the work of our colleagues – was the support and loyalty of our suppliers and partners. This 27 year demonstrates that the success is the result of our joint efforts. Being a 100% Hungarian owned sheet metal processing company, FERZOL LTD. commits to further growth and development which we see possible only if our customers are satisfied with our performance. Besides its traditional European markets our company supplies its products to North America and Far East as well to the following industrial segments: electronics, electrical structures, cabinets, agricultural machinery, food industry, cooling general machine and equipment manufacturing, vehicle production and car industry.

#### **We have the following key competences in sheet metal processing:**

##### **Cutting**

- 2D and 3D laser cutters
- Traditional shearing

##### **Punching**

- CNC punching machines
- Automatic sheet loading

##### **Grinding and deburring Bending**

- CNC bending machines
- Automatic panel bending machine
- Fully automatic bending cell

##### **Pressing**

- Excentric and hydraulic presses

##### **Assembly**

- Manual welding
- 3D welding robot cell
- PEM serting, toxing
- Panel gasketing

##### **Powder coating**

- Manual Iron-Phosphate technology
- Automatic Nanoceramic technology





# INDUSTRY DAYS IN DEBRECEN

## 5<sup>TH</sup> MECHANICAL ENGINEERING INDUSTRIAL EXHIBITION

12-13 October 2017, Debrecen, Hungary



### FLEXIFORCE HUNGARY Kft.

Address: 4024 Debrecen, Medvefű u. 24.

Webpage: [www.flexiforce.com](http://www.flexiforce.com)

**flexiforce**<sup>FF</sup>

### FLEXIFORCE – Everything (and more) for overhead doors



FlexiForce established in 1980 is an ambitious, multinational company with subsidiaries in the Netherlands, Hungary, Spain, Italy, Poland, China, Turkey, USA, Canada and the United Kingdom.

We are specialized in offering hardware parts, automation, panels and hardware systems for residential (garage) and industrial overhead doors. We believe in the market opportunities of our worldwide customers: independent, often local or regional, door producers.

Recently we have invested in setting up a new, state-of-art production plant of 15.000 m<sup>2</sup> in the city of Debrecen in Eastern Hungary. The facility comprises warehouse, production and offices. Winding of torsion springs, spring assembly, roll forming of angles and tracks, bending of curves and assembly of industrial and residential hardware sets are the core of the production department. Out of FlexiForce Hungary we are ready to offer supply chain service in ISC (industrial) and RSC (residential) hardware sets to OEM-customers all over Europe. The local sales team serves customers in Hungary and surrounding countries.

FlexiForce products and services support door companies in offering competitive door solutions. Our core competences lie not only in the design and quality of the products and systems, but even more in understanding the need for an efficient supply chain of products.

Meaning to have each hinge, hardware set, industrial door opener and more, available within optimal lead-time and transport distance. This is facilitated through our production and warehouse facilities in Canada, United States of America, United Kingdom, the Netherlands, Spain, Hungary, Turkey, Italy, Poland and China.

Our “close to the customer” strategy with local warehouses and local teams in place is helping our customers to successfully compete in their own market. In that way we grow our mutual business!





# INDUSTRY DAYS IN DEBRECEN

## 5<sup>TH</sup> MECHANICAL ENGINEERING INDUSTRIAL EXHIBITION

12-13 October 2017, Debrecen, Hungary



### HAJDU PUBLIC LIMITED COMPANY

Address: 4243 Téglás, külterület 135/9. hrsz.

Phone: +3652582700

Webpage: <https://www.hajdurt.hu>



Hajdu Autotechnika



Hajdu Infrastruktúra

HAJDU CÉGCSOPORT

HAJDU GROUP

#### Company History

**HAJDU Hajdúsági Ipari Zrt.**'s forerunner Hajdúsági Iparművek was founded by the Hungarian government in 1952 for the purposes of military industry. In 1957 the company started to build household appliances whose assortment as well export were constantly growing. By manufacturing its own developed as well as licensed products and setting up corresponding machinery it managed to grow into a medium-sized enterprise by the 1980s. After 1998 – with a purpose of using up its free capacities – and after 2002 (primarily due to parts produced by sheet metal forming) the company also opened up to a car industry. In 1993 it was transformed into an incorporated company and in 1994 it was privatized by Hungarian investors. The ISO 9001 quality assurance certification was introduced in 1993, whilst the ISO 14001 environmental management certification was implemented in 2001. In October 2005 HAJDU Hajdúsági Iparművek Rt. split into three separate companies. HAJDU Hajdúsági Ipari Rt. continued to produce traditional products such as hot water storage tanks, washing machines, and spin dryers.

#### The other two companies

**HAJDU Autotechnika Ipari Zrt.** deals with metalworking – it characteristically manufactures metal sheet produced automobile parts – and designing as well as manufacturing machine tools.

**HAJDU Infrastruktúra Szolgáltató Zrt.** operates an Industrial Park which also hosts both of the other HAJDU companies. It occupies quite an extensive area and offers a number of services to the enterprises that have settled there.

In 2006 HAJDU Hajdúsági Ipari Rt. was transformed into a private limited company. In 2008 new branch of business was established, focusing on developing products that use renewable energy as well as launching them onto Hungarian market. This orientation has become one of the company's main strategies. In the same year the company began realizing a two-year investment program, partly financed by European Union, which enabled a significant technological development of the production process. Between 2010 and 2015 HAJDU brand received several awards thus getting recognition for the quality of its product development and business process.

#### Our mission, philosophy, plans

HAJDU Hajdúsági Ipari Zrt. meets customer demands by providing environmentally friendly household appliances and complex systems that offer a natural helping hand to families, public institutions as well as enterprises. Our goal is to strengthen HAJDU brand's position on regional market and to meet customer demands in Europe as well as in other parts of the World. In order to achieve that we have started following ISO 9001 quality assurance standards in 1993 and ISO 14001 environmental management standards in 2001. Excellent and constant quality of our products as well as their regular development are guaranteed by systematic on-site controls performed by various accredited – both domestic and international – testing institutes (TÜV Rheiland InterCert, VDE, LCIE, etc.) Our company puts a lot of emphasis on environment protection and on minimizing negative impact on the environment. We thus strive to employ an environmentally friendly technology and use resources (materials, energy) in an economical way.





# INDUSTRY DAYS IN DEBRECEN

## 5<sup>TH</sup> MECHANICAL ENGINEERING INDUSTRIAL EXHIBITION

12-13 October 2017, Debrecen, Hungary



### HOYA LENS MANUFACTURING HUNGARY PRIVATE CO.

Address: 4700 Mátészalka, Ipari út 18.

Phone: +3644418200

Webpage: [www.hoya.com](http://www.hoya.com)



HOYA Corporation is a diversified, multinational company and leading supplier of innovative and indispensable high-tech and healthcare products. HOYA is active in two main business segments: The Life Care segment encompasses health care areas such as eyeglass lenses and the operation of contact lens retail stores, as well as medical related areas such as intraocular lenses for cataract surgery, medical endoscopes, surgical equipment and artificial bones and implants. HOYA's Information Technology segment focuses on electronics products for the semiconductor industry and LCD panels, glass disks for HDDs and optical lenses for digital cameras and smartphones. The HOYA Group comprises over 100 subsidiaries and affiliates and over 34,000 people worldwide.

#### Life Care

HOYA has diversified its business portfolio with its optical technologies providing indispensable products to people's lives. We strongly believe that by providing enduring solutions that meet needs in areas closely connected to people's lives, such as endoscopes, eyeglass lenses and intraocular lenses, it will be able to bring about changes in the quality of those lives.

#### Life Care Segment, Health Care

HOYA provides products and services to care for that most important sensory organ- the eye. HOYA started manufacturing eyeglass lenses in 1962 and contact lenses in 1972. Based on the optical and material technologies acquired since 1941, HOYA continues to contribute quality high value-added vision products to people around the world.

#### Eyeglass lenses



As a global manufacturer of eyeglass lenses, HOYA has passionately driven optical technology innovation with the aim of finding only the best vision solutions.

HOYA's unparalleled technology creates a profoundly clear vision experience for the progressive lens wearer.

Integrated Double Surface Design (iD), HOYA's patented, award-winning design technology, separates the surface geometry of progressive lenses into two components: vertical and horizontal, positioned individually on each of the two lens surfaces. Thanks to this technology, HOYA's premium progressive lenses can be individually designed; each patient's unique visual and lifestyle requirements can be integrated in the lens design to provide them with the most comfortable and accurate vision, tailored to their individual needs.

HOYA Vision Care Company is a global organization covering 52 countries with a network of over 12,000 employees and over 64,000 active accounts globally.

#### HOYA Lens Manufacturing Hungary private Co., Mátészalka

HOYA Lens Manufacturing Hungary private Co. is the largest unit of Hoya group in Europe based on the headcount and production volume as well. The past of the company and the nearness of the European market give a geopolitical advantage and stable future for the company. A Belgian investor bought 50% of Optikai Művek factory's unit in 1991. In 1994 with total ownership the enterprise with mass production has been called Buchmann Optical Művek for 8 years. Hoya has bought the Buchmann-group in 1994, so the plant in Mátészalka also became a member of the japan lens production company. By now the company do partial serving of all affiliated companies in Europe.



## **IGM ROBOTRENDSZEREK Kft.**



Address: H-9027 Győr Csörgőfa sor 1.  
Phone: +36 96 513 910, Fax: +36 96 518 600  
Webpage: [www.igm-group.com](http://www.igm-group.com)

igm was established in 1967 as a trading company for industrial devices and machine tools. In 1980, the world-wide first continuous path welding robot type was developed. As the inventor of the unique hollow shaft for welding robots, igm gained world-wide reputation for this design feature. This was the start of a successful development to one of the most important supplier of automated welding technology to the heavy machinery producers.

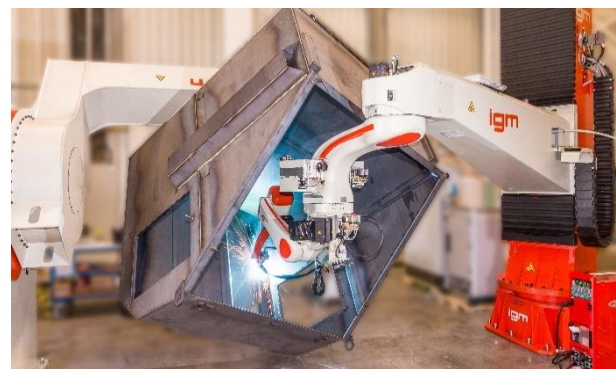
In 1990, there was the start of a joint venture in Győr regarding production of components for robot systems in Hungary. This successful cooperation led to the establishment of igm Robotrendszerek Kft. and the shift of the complete manufacturing and assembly of all robot systems to the new work shop in the industrial park of Győr in 2002. With the ongoing further expansion and modernisation of this production site igm offers a high performance and up-to-date manufacturing facility.

Today igm is Austria's most prestigious manufacturer of robots specifically developed for arc welding. Now for 50 years igm Robotersysteme AG has been a market leader in the field of arc welding automation and has developed extensive and comprehensive expertise in many diversified applications for arc welding robot systems for MIG/MAG and TIG welding process. Beside of complex, sensor guided cutting and welding robot systems, igm's portfolio comprises robot based plasma or oxy-fuel cutting and bevelling solutions. The product variety is available for individual applications in robot welding and cutting technology is unique throughout the world.

igm robotic systems are exported worldwide to manufacturer of earthmoving machinery, construction machinery, heavy road transportation vehicles and cranes, railway coaches and wagons, boilers, machine tools and shipbuilding, representing the basis of production for many internationally well-known manufacturers. With subsidiaries and sales partners in more than 20 countries, igm is today the world's only manufacturer of automated welding and cutting systems with arc, laser and electron beam technology. The current igm group sales amounts to about 140 M€ with a total of 800 employees.



Welding robot system for track roller frames



Welding robot system for waste containers



igm bevelling system



Welding robot system for fork lift masts



# INDUSTRY DAYS IN DEBRECEN

## 5<sup>TH</sup> MECHANICAL ENGINEERING INDUSTRIAL EXHIBITION

12-13 October 2017, Debrecen, Hungary



### MANZ HUNGARY GÉPGYÁRTÓ Kft.

Address: 4031 Debrecen, Határ út 1/c  
 Phone: +3652530798  
 Webpage: [www.manz.com](http://www.manz.com)



#### MANZ HUNGARY

YOUR SPECIALIST IN THE FIELD OF SMALL PARTS, LARGE WELDED SUB-CONSTRUCTIONS AND COMPLETE MOUNTED UNITS

Manz Hungary Ltd. is your partner in the field of manufacturing small and large parts, complete mounted units and welded structures.

We offer efficient and precise machining with modern tools for our customers from different industries.

#### INNOVATIVE MANUFACTURING SOLUTIONS

We support you in pilot and series production with the most efficient solutions given by our experienced specialists.

Our optimized processes and modern manufacturing solutions guarantee fast, precise and highly efficient processing.

#### YOUR BENEFIT

Our processes are adapted to the specific products and the material flow. Thanks to the cost-efficient value chain and production site in Hungary, we are able to deliver certified German quality at a fair price.

Our production site in Debrecen is advantageous with regard to manufacturing costs and location. Debrecen has its own airport and is reachable by car within two hours in Debrecen.



#### OUR EXPERTISE

CNC milling and turning machines

Large parts machining on portal milling machines

131 MIG/135 MAG and 144 TIG welding processes

Vibratory stress relief by vibratory finishing and in heat treatment furnace

Surface treatment with wet painting

Surface preparation for painting by blasting and high-pressure cleaning

Mechanical and electrical assembly of mounted units

CAD-CAM production planning (Siemens SolidEdge, EdgeCam)

#### CERTIFIED QUALITY

Manz Hungary Kft. is certified ISO 9001:2008/ISO 14001:2004



#### CONTACT

Manz Hungary Kft.  
 Határ út 1/c  
 4031 Debrecen  
 Hungary

Phone +36 52 530 798  
 Fax +36 52 530 799

[www.manz.com](http://www.manz.com)  
[oem@manz.com](mailto:oem@manz.com)  
[hungary@manz.com](mailto:hungary@manz.com)





# INDUSTRY DAYS IN DEBRECEN

## 5<sup>TH</sup> MECHANICAL ENGINEERING INDUSTRIAL EXHIBITION

12-13 October 2017, Debrecen, Hungary



### MÁV-START CO.

Address: 1087 Budapest Könyves Kálmán krt. 54-60.

Phone: +3613494949

Webpage: [www.mavcsoport.hu](http://www.mavcsoport.hu)



MÁV-START Co. is a subsidiary of MÁV Co., its primary activity is railway passenger transportation. This main activity is supported by other basic functions, like rolling stock maintenance and repair as well as traction services. Around fifteen thousand employees are working for successful operation of the Company, which is the market leader in rail passenger public transportation segment, considered as the most dominant passenger railway operator in Hungary. This operator manages to run average 3 000 trains / day, almost one million trains a year. Integrated interval Timetable is implemented almost on the whole network.

MÁV-START has a vehicle fleet stock in total of 2 700 units of passenger vehicles, from which the operationally available units are 68-71% of the total fleet. 420 vehicles are multiple units and railcars and 2 290 units are passenger couches. The average age of the fleet is around 33 years.



One of the most important objectives of MÁV-START Co. is to achieve that more individual travellers chose the opportunity of the sustainable track-based public transport and these satisfied customers become regular users of our services of increasing quality.

Using EU development resources new infrastructure is to be built at more main lines. As a result of these infrastructure developments journey time can be reduced, trains can depart more frequently, in peak hours even in 15 minutes.

In domestic traffic 42 EMUs started to operate since 2014 and another EMUs are planned to be put in operation in the next years, too. New IC+ coaches (200 km/h) designed by Hungarian experts are built in Szolnok, Hungary.



Rolling Stock Renewal Program was launched in 2013, which involved Suburb, long-distance and international coaches, bicycle transport coaches, luggage-van and restaurant cars.

Onboard free Internet access is one of the key elements of the service to be provided in Hungary. With the introduction of free WiFi the Company gets into the leading position in Central Europe.

The Company produced two demo passenger coaches positioned in intercity operation. The brand new

IC+ unit is designed as a four-axle, air conditioned, Intercity Plus coach; the 'Plus' reflects on the higher level of comfort. The maximum travelling speed is 200km/hour. This vehicle family consists of 2<sup>nd</sup> class coach, multipurpose coach and 1<sup>st</sup> class coach with buffet section.

Main features of the IC+ coaches:

- Interior: open saloon, air-conditioned, miscellaneous arrangements of seats
- Power supply for laptops, wireless internet (WLAN), video surveillance system
- Family compartments
- Disabled passengers comfort: wheelchair lift, WC, special wheelchair spaces
- Advanced design for multifunctional spaces (large luggage racks, holders for bicycles)



# INDUSTRY DAYS IN DEBRECEN

## 5<sup>TH</sup> MECHANICAL ENGINEERING INDUSTRIAL EXHIBITION

12-13 October 2017, Debrecen, Hungary



### MSK HUNGARY GÉPGYÁRTÓ Bt.

Address: 4300 Nyírbátor, MSK tér 1.

Phone: +364 511 100

Webpage: [www.msk.hu](http://www.msk.hu)



#### MSK Coverttech Group: The future is what we make of it

Innovation is built on tradition. As a family managed business, MSK Hungary Bt, with a headcount of about 350 employees, is a team member of the MSK Coverttech Group. MSK offers product-specific packaging and palletizing solutions to a number of industries.

All of our employees are respectful of our customers. We are positive that motivation and flexibility are the key components of successful participation in international competition and that is why we are one of the leading international manufacturers of heavy duty packaging machines and palletizing systems through our worldwide operations.

Value-orientation and an innovative spirit are two of the key factors that have kept the business of the Hannen family of Germany on a growth trajectory for the last 40 years. MSK offers its customers the treasure of its unique experience accumulated during the production of almost 5 000 units of packaging equipment sold. Driving innovation in our work requires us to keep expanding our current limits. MSK has experienced and creative project teams also in the field of product development who rely on their comprehensive industry competence to develop unique and outstanding packaging solutions. Owing to our state-of-the-art manufacturing methods (particularly at the central site in Nyírbátor) and continuous investments MSK stands for quality, productivity and relentless improvement.



MSK's factories count among the most modern in the industry. Accordingly, in 2010, we expanded the production area at the Nyírbátor site by approximately 5,000 m<sup>2</sup> thus reaching 21,000 m<sup>2</sup>, we installed a modern and environment-friendly powder disperser unit and we consistently renewed our CNC equipment fleet. We have recently invested approximately HUF 1 billion including the purchasing of new manufacturing equipment and the extension of our office building. Further development projects, such as the enhancement of our production capacity and the construction of a modern training center, are in the pipeline. MSK is a pioneer in a number of areas demonstrated by the high number of international patents registered by us that are exemplary for the entire industry.

#### MSK Hungary Bt. – Nyírbátor: The magic of mechanical engineering

Our relentless search for quality, innovation and reliability has made MSK one of the leading international experts of packaging and logistics systems.

MSK means the following:

- customer-specific palletizing and packaging machines
- proprietary corporate software
- complete equipment and system solutions
- development, production, servicing: all from one supplier

Information about our most recent news, development initiatives and open positions is available at:

- [www.msk.hu](http://www.msk.hu)



# INDUSTRY DAYS IN DEBRECEN

## 5<sup>TH</sup> MECHANICAL ENGINEERING INDUSTRIAL EXHIBITION

12-13 October 2017, Debrecen, Hungary



### NAGÉV RÁCS Kft.

Address: 4220 Hajdúböszörmény, Kinizsi u. 5.

Phone: +3652563113

Webpage: [www.nagev.hu](http://www.nagev.hu)



The name NAGÉV has now been well known among users of industrial walkway grating. The group, which has evolved from a 25 m<sup>2</sup> plant, is an industrial enterprise having more than thirty years of history. NAGÉV Ltd. was founded by Antal János Nagy in 1991 primarily as a private enterprise specialized in the manufacture of walkway gratings, with 100 percent sole ownership.

Since the beginning of its operation the company has been playing a significant role among domestic producers of walkway grating. The products of the company are available all around the country; many of them are installed for major investment projects. They are perfectly suitable for bridging a particular span, as well as for bearing passenger and freight traffic. The products are universal; they are linked not only to one industrial sector. The walkway gratings of NAGÉV RÁCS Ltd. are ideal for covering walking surfaces of industrial plants, power plants, public utilities, bridges, stairs, work platforms, operator's platforms and footbridges of scaffold systems, as well as for making them securely passable.

In addition to domestic customers the NAGÉV type walkway grating is well-known, recognized and demanded by foreign companies as well. In addition to industrial scale orders the manufacture of scraper grids for public use and rainwater trench drains used in front of garages represent a significant volume.

The company's activities, from its foundation to the present day, are characterized by the trinity of high quality, reasonable price and the strict compliance with the delivery dates. The products are own developments, and some of them are based on our own patent.

The NAGEV group includes Hungary's most modern and Eastern Hungary's largest hot-dip galvanizing plant. The factory in the city of Ócsa was opened in 2011, while the plant in Tiszacsege city has been operating successfully since 1998. With the completion of the high-tech facility in Ócsa an opportunity arose to galvanize industrial size steel structures in our country too.

The NAGÉV group is one of the market leaders in our country both in the walkway grating and the hot-dip galvanizing business sector.

With this brochure we would like to introduce the products of NAGÉV RÁCS Ltd. which belongs to NAGÉV Group, helping you in your design and construction work.





## **TAKATA SAFETY SYSTEMS HUNGARY KFT**

Address: 3516 Miskolc, Takata út 1.

Phone: +3646407900

Webpage: [www.takata-miskolc.hu](http://www.takata-miskolc.hu)



# TAKATA

### **Our dream**

**At Takata, we dream of a world with zero fatalities from traffic accidents. We understand the importance of every individual and hope to one day experience a global community where everyone recognizes the true value of human life.**

Takata is a leading global supplier of automotive safety systems (products include steering wheels, airbag systems, seat belts, electronics, sensors, interior trim, child restraint systems) and supplies all major automotive manufacturers in the world. Headquartered in Tokyo, Japan, Takata is currently operating 57 plants in 21 countries and employs more than 50,530 people, every one of whom is committed to turning innovative ideas into reality.

Our common goal is to reduce the number of fatalities in road traffic accidents to zero. We develop and manufacture products that help keep people safe when travelling on today's roads, aiming to provide optimum safety on the move, with a range of products for occupant and pedestrian protection. For many decades, we have been pioneering innovative technologies – producing our first seatbelts in 1952 and starting the development of airbags as early as 1969. TAKATA's mission is the development of innovative products according to high quality standards, which helps to meet the highest satisfaction of the customers.

### **„Our mission – your safety.“**

There is no end to think about safety in today's automotive society. As a company that makes seatbelts, airbags, child seats and other products that protect life, we are aware of our responsibilities to society and want to contribute to attaining the goal of creating a world that is safe. To do this, we will continue creating and further evolving safety products and systems that people can rely on. At Takata, we would be delighted developing our safety products in a world where they never had to be used, where traffic accidents do not occur anymore. That is the dream that drives us every day.

### **TAKATA at Miskolc**

The latest step toward realizing our dream has been the establishment of Takata Safety Systems Hungary Kft. in October, 2013. This new plant is our first in Hungary and the 17<sup>th</sup> in Europe and it is located in the city of Miskolc, at the Miskolc South Industrial Park. Takata Safety Systems Hungary Kft. started production of airbag technology at this new facility in October 2014. The company's investment in the new plant is € 68.3 M, with a 25 hectares big ground and up to 60.000 sqm built-in area.

**The number of the new employees at Miskolc is already 1600, who produce lifesaving automotive technology products, such as complete airbag modules, airbag components and inflators for car manufacturers across whole Europe. The new facility also features state-of-the-art systems for product development, testing, quality control and customer service.**





# INDUSTRY DAYS IN DEBRECEN 5<sup>TH</sup> MECHANICAL ENGINEERING INDUSTRIAL EXHIBITION

12-13 October 2017, Debrecen, Hungary



## TUNGALOY HUNGARY Kft.

Address: 1142 Budapest, Erzsébet Királyné útja 125.

Phone: +3617816846

Webpage: [www.tungaloytools.hu](http://www.tungaloytools.hu)



Tungaloy is one of the world's leading manufacturers of carbide cutting tools, friction materials, wear resistant items, and civil engineering products.

Headquartered in Japan, we provide our products to customers all over the world in automobile, construction, aerospace, medical, power generation, infrastructure, and heavy industries.



Continuous improvement of production technologies, combined with large investments in research and development, allows us to offer high-quality products that help manufacturing companies in a wide variety of industries increase their productivity.

**Tungaloy Hungary Ltd.** has started its operation on the hungarian market on 01.01.2012.

Tungaloy products are more than 80 years contiguous innovation's results. Thank's for that we can guarantee the profession quality worldwide. Our mission to improve the metalworking process on the hungarian market. Our central office in Budapest ensure the customers to provide hight level of support in delivery and every administrative issues day by day. The well connected logistiqué network permit the quick and troublefree delivery of the tools all over the country.

Our well qualified salesmen's target to introduce You the Tungaloy tooling solutions, and show the way how You can be more effective and economical.

Our salesman show You soon our top tree product families (**ISO turning, drilling and turning with CBN inserts**).

If You would like to know us better and inform about the best Tungaloy solutions or You have any questions about our corporation or products, please feel free to reach us on the contacts below.

**TUNGALOY HUNGARY KFT.**  
H-1142 BUDAPEST  
ERZSÉBET KIRÁLYNÉ ÚTJA 125.  
[www.tungaloytools.hu](http://www.tungaloytools.hu)  
+36 1 7816 846

Our central office in budapest also reachable in opening hours every workday between 8:00-16:00





# DEPARTMENT OF MECHANICAL ENGINEERING FACULTY OF ENGINEERING, UNIVERSITY OF DEBRECEN

2-4 Ótemető Debrecen, H-4028 Hungary



The Department of Mechanical Engineering is responsible for the mechanical engineering education on bachelor (BSc) and master (MSc) levels. The research activity of the department covers the mechanical engineering scientific area starting from the materials science to the specific fields (diagnostics, material handling, etc.). From 2015 we have introduced the dual training. At the moment we cooperate with 19 industrial partners.

## Department staff:

<b>Tamás MANKOVITS PhD</b> head of department associate professor <i>mechanics</i> <i>finite element method</i>		<b>Sándor BODZÁS PhD</b> college associate professor vice head of department <i>manufacturing,</i> <i>machine elements</i>		<b>Sándor HAJDU PhD</b> assistant professor vice head of department <i>material handling,</i> <i>mechanics</i>	
<b>Lajos FAZEKAS PhD</b> college professor  <i>logistics,</i> <i>machine repairing</i>		<b>Zsolt TIBA PhD</b> college professor  <i>machine elements</i>		<b>Ágnes BATTÁNE GINDERT-KELE PhD</b> associate professor <i>manufacturing,</i> <i>machine elements</i>	
<b>Levente CZÉGÉ PhD</b> associate professor  <i>process analysis,</i> <i>machine elements,</i>		<b>György JUHÁSZ PhD</b> associate professor  <i>machine elements,</i> <i>hydraulics and pneumatics</i>		<b>Sándor PÁLINKÁS PhD</b> assistant professor  <i>materials science,</i> <i>manufacturing</i>	
<b>Gábor BALOGH</b> assistant lecturer PhD student <i>materials science,</i> <i>manufacturing</i>		<b>Zsolt BÉKÉSI</b> assistant lecturer PhD student <i>machine elements</i>		<b>Krisztián DEÁK</b> assistant lecturer PhD student <i>diagnostics,</i> <i>mechanics</i>	
<b>József MENYHÁRT</b> assistant lecturer PhD student <i>process analysis,</i> <i>computer aided design</i>		<b>István SZÉKÁCS</b> department teacher  <i>manufacturing,</i> <i>technology</i>		<b>Márton LÉVAI</b> department teacher  <i>materials science,</i> <i>technology</i>	
<b>Péter BALSZA</b> department engineer  <i>manufacturing,</i> <i>machine elements</i>		<b>András GÁBORA</b> department engineer PhD student <i>materials science,</i> <i>technology</i>		<b>Dávid HURI</b> department engineer PhD student <i>mechanics,</i> <i>finite element method</i>	
<b>Gyula Dávid LOVADI</b> department engineer  <i>manufacturing,</i> <i>technology</i>		<b>Tamás Antal VARGA</b> department engineer  <i>mechanics,</i> <i>computer aided design</i>		<b>Zoltán Gergő GÉRESI</b> CNC technologist	
<b>Beáta KÖVÉR</b> administrative assistant		<b>Department of Mechanical Engineering Faculty of Engineering, University of Debrecen</b> 2-4 Ótemető Debrecen, H-4028 Hungary Tel.: +3652415155 E-mail: <a href="mailto:gepeszmernok@eng.unideb.hu">gepeszmernok@eng.unideb.hu</a> Website: <a href="http://old.eng.unideb.hu/gepesz">old.eng.unideb.hu/gepesz</a>			

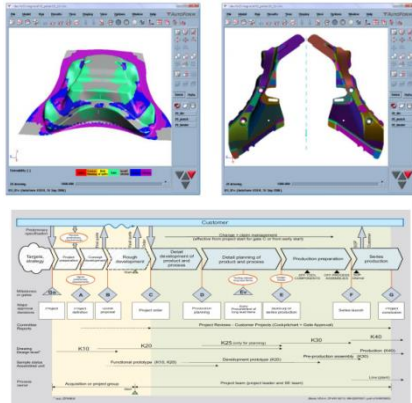


## Mechanical Engineering BSc Program Automotive Production Process Control Specialization

The aim of the teaching program includes preparing engineers to improve quality and use lean tools in the vehicle industry, enabling them to gain an understanding of the complete product development (from the supplier to the customer) and lead project teams. In cooperation with local vehicle suppliers students learn about completing cost estimation, utilizing computer software to solve manufacturing problems.



Our graduates will develop **competence or acquire knowledge** in the following areas:



- introducing and applying modern technologies, computational engineering methods and systems (manufacturing technologies, CAE)
- operating and developing mechatronical systems (electrotechnics and electronics, measuring and automatics, hydraulics and pneumatics)
- designing and redesigning plant layouts, checking KPI systems robot technology, automation, etc.
- planning material handling and manufacturing processes
- analyzing, controlling and optimizing production processes
- applying modern manufacturing management philosophies (Lean management) in the vehicle industry

The **curriculum** contains the following **subject modules**:

Basic science subjects:

48 credits

- Mathematics, Technical Mechanics, Engineering Physics, Operation and Theory of Machines, Thermodynamics and Fluid Mechanics, Technical Chemistry

Economics and humanities subjects:

20 credits

- Economics for Engineers, Microeconomics, Basics of Quality Management, Management for Engineers, State Administration and Law, Introduction to Ethics

Professional subjects:

117 credits

- Informatics, Machine Elements, CAD and CAE, 3D Computer-Aided Design, Materials Science, Technology of Structural Materials, Electrotechnics and Electronics, Thermal and Fluid Machines, Manufacturing Processes, Logistics, Industrial Safety, Computational Engineering Methods and Systems, Measuring and Automatics, Hydraulics and Pneumatics, Mechanical System Engineering, Quality Management, Safety Engineering, Material Handling and Robotics, CAM, Manufacturing Planning, Maintenance Engineering, PLC.

Optional subjects:

10 credits

Thesis:

15 credits

Duration of studies: 7 semesters, Contact hours: 2.352

ECTS credits: 210, Internship: 6 weeks

Final exam:

- Defending the thesis (oral presentation and discussion)
- Exam in two subject areas chosen by the student
  - Production Process and Control, Production Optimization, Logistics
  - Assembling Technology, CAM, Quality Management





## Mechanical Engineering BSc Program Operation and Maintenance Specialization

The aim of the teaching program is to train mechanical engineers who are able to operate and maintain machines and mechanical devices, introduce engineering technologies and apply them, organize and control work phases, mechanical developments, solve the general problems of research and planning as expected by the labor market. Those having completed the specialization have in-depth theoretical knowledge to continue their studies in the second cycle.

Our graduates will develop **competence or acquire knowledge** in the following areas:



- introducing and applying modern technologies and computational engineering methods and systems (manufacturing technologies, CAE)
- operating and developing mechatronical systems (electrotechnics and electronics, measuring and automatics, hydraulics and pneumatics)
- operating and maintaining machines and mechanical devices (mechanical system engineering, heat and fluid machines)

- organizing and controlling operational processes, mechanical developments
- planning the construction and designing of the machine parts, devices and apparatus (machine element, CAD, finite element method)
- solving the general problems of research and planning as expected by the labor market (studies of administration and law, basics of quality assurance, management for engineers, safety engineering)
- carrying out diagnostic testing, assessing the reliability of machines and devices (fracture mechanics, non-destructive testing and diagnostics)



The **curriculum** contains the following **subject modules**:

Basic science subjects:

48 credits

- Mathematics, Technical Mechanics, Engineering Physics, Operation and Theory of Machines, Thermodynamics and Fluid Mechanics, Technical Chemistry

Economics and humanities subjects:

20 credits

- Economics for Engineers, Microeconomics, Basics of Quality Management, Management for Engineers, State Administration and Law, Introduction to Ethics

Professional subjects:

117 credits

- Informatics, Descriptive Geometry, Technical Drawing, Machine Elements, CAD and CAE, 3D Computer-Aided Design, Materials Science, Technology of Structural Materials, Electrotechnics and Electronics, Measurements and Automatics, Thermal and Fluid Machines, Manufacturing Processes, Logistics, Industrial Safety, Steel Constructions, Hydraulics and Pneumatic Machines, Fracture Mechanics, Manufacturing Planning, Diagnostics, FEM, PLC, Material Handling and Robotics, Drivetrain Optimization, Machine Repairing, Maintenance Engineering.

Optional subjects:

10 credits

Thesis:

15 credits

Duration of studies: 7 semesters, Contact hours: 2.352

ECTS credits: 210, Internship: 6 weeks

Final exam:

- Defending the thesis (oral presentation and discussion)
- Exam in two subjects chosen by the student
  - Machine Repairing,
  - and one subject chosen by the student:
    - Material Handling and Robotics
    - or Maintenance Engineering

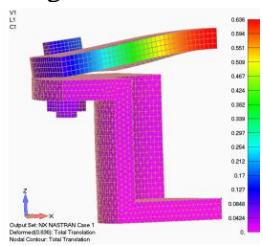




## Mechanical Engineering MSc Program Production Engineering Specialization

The aim of the teaching program is to train engineers who are able to design and elaborate production processes and the conceptions of manufacturing technologies as well as can be responsible for modelling, designing, operating, maintaining, supervising and organizing production tasks. They are capable of providing the conditions of precise and up-to-date production and its processes (optimizing and developing production processes; designing and implementing devices and systems serving the production). The specialization considers the needs of the partner industrial companies.

Our graduates will develop **competence or acquire knowledge** in the following areas:



- applying modern computational engineering methods (CAD, CAM, CAE)
- supporting, optimizing and developing production systems and processes;
- designing of manufacturing and material handling systems,
- applying management methods and systems,
- supervising and organizing in production environment,
- applying expert systems (diagnostics and condition monitoring).



The **curriculum** contains the following **subject modules**:

Basic science subjects:

22 credits

- Mathematics, Applied Statistics, Modern Physics, Dynamics of Mechanical Systems, Thermodynamics and Fluid Mechanics, Advanced Material Science

Economics and humanities subjects:

16 credits

- Basics of Management, Quality Management, Financial and Advanced Economic Knowledge, Research Methodology

Professional subjects:

46 credits

- Measurement, Signal Processing and Electronics, Design of Engineering Structures, Engineering Modelling and Simulation, Manufacturing Equipments, Design and Quality Assurance of Manufacturing Processes, Assembly Automation, Design of Material Handling Systems, Production Logistics, Maintenance and Machine Repairing Technologies, Diagnostics and Condition Monitoring, Lean Production

Optional subjects:

6 credits

Thesis:

30 credits

Duration of studies: 4 semesters, Contact hours: 1.428

ECTS credits: 120, Internship: 4 weeks

### Admission requirements for the Mechanical Engineering MSc program

Unconditional admission: Mechanical Engineering BSc:

Conditional admission by prescribing pre-master courses:

Materials Engineering BSc, Safety Engineering BSc, Energy Management BSc, Civil Engineering BSc, Industrial Design Engineering BSc, Vehicle Engineering BSc, Light Industrial Engineering BSc, Environmental Engineering BSc, Transportation Engineering BSc, Mechatronics Engineering BSc, Earth Science Engineering BSc, Technical Management BSc, Chemical Engineering BSc, Electrical Engineering BSc, Mechanical Engineering in Agriculture and Food Industry BSc

Final exam:

- Defending the thesis (oral presentation and discussion)
- Exam in two topics chosen by the student :
  - Production systems and processes (Design of Material Handling Systems, Production Logistics, Lean Production)
  - Manufacturing systems and processes (Manufacturing Equipments, Design and Quality Assurance of Manufacturing Processes)
  - Maintenance and operation (Maintenance and Machine Repairing Technologies, Diagnostics and Condition Monitoring)





Welcome in Debrecen for the

**6<sup>th</sup> International Scientific Conference on Advances in  
Mechanical Engineering (ISCAME 2018)**

and

**6<sup>th</sup> Mechanical Engineering Exhibition**

The Department of Mechanical Engineering  
Faculty of Engineering, University of Debrecen